به نام خدا

مرکز دانلود رایگان
مهندسی متالورژی و مواد

www.Iran-mavad.com

COMPREHENSIVE CORROSION

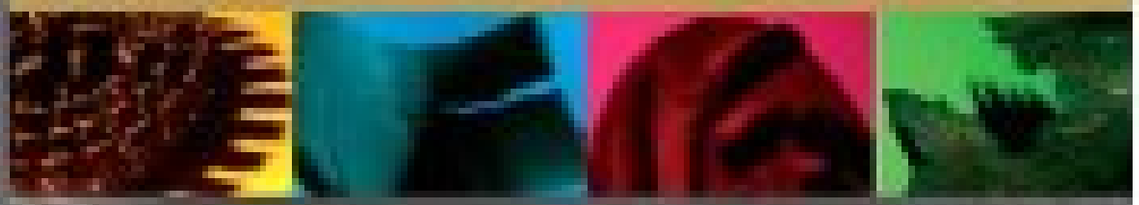

1.01 Chemical Thermodynamics

R. A. Cottis
Corrosion and Protection Centre, School of Materials, University of Manchester, P.O. Box 88, Sackville Street, Manchester, M60 1QD, UK
L. L. Shreir[†] **and G. T. Burstein**
Department of Materials Science and Metallurgy, University of Cambridge, Pembroke Street, Cambridge CB2 3QZ, UK

This article is a revision of the Third Edition article 20.2 by L. L. Shreir and G. T. Burstein, volume 2, pp 20:57–20:75,

Symbols

a Activity (strictly dimensionless – see section 1.01.2.6)
c Concentration (mol kg^{-1} or mol m^{-3} or mol dm^{-3})
***c*°** Concentration in standard state (mol kg^{-1} or mol m^{-3} or mol dm^{-3})
Cp Molar heat capacity at constant pressure (J mol^{-1} K^{-1})
E Equilibrium potential (V)
***E*°** Standard equilibrium potential (V)
F Faraday constant (96 485 C mol^{-1})
G Gibbs free energy or free enthalpy (J)
***G*°** Standard Gibbs free energy or free enthalpy (J)
H Enthalpy (J)
I Ionic strength (mol kg^{-1} or mol m^{-3} or mol dm^{-3})
K Equilibrium constant
n Number of moles
P Pressure (Pa, atm)
***p*°** Standard pressure (usually 1 atm)
Q Activity quotient
q Heat (J)
R The gas constant (8.314 J K^{-1} mol^{-1})
S Entropy (J)
T Temperature (K)
U Internal energy (J)
V Volume (m^3)
w Work (J)
z Number of electrons or equivalent positive charge
γ Activity coefficient
μ Chemical potential (J mol^{-1})
μ° Standard chemical potential (J mol^{-1})
ν Number of ions or molecules

1.01.1 Scope

Thermodynamics is concerned with the relationship between heat energy and work and is based on two general laws, the first and second laws of thermodynamics, both of which deal with the interconversion of different forms of energy. The third law states that at the absolute zero of temperature, the entropy of a perfect crystal is zero, and thus provides a method for determining absolute entropies.

[†]Deceased

The following features of the thermodynamic approach to chemical reactions should be noted:

1. It does not involve time as a variable, and does not provide information on rates.
2. It does not normally involve a knowledge of the detailed structure of the system or of the detailed mechanism of the reaction.
3. The second law is true only statistically and does not apply to individual particles or to a small number of particles, that is, thermodynamics is concerned with bulk properties of systems. Thus, thermodynamics has many limitations, but it is particularly valuable in defining the nature and structure of phases when *equilibrium* (a state that does not vary with time) has been attained; thermodynamics provides no information on the *rate* at which the reaction proceeds to equilibrium, which belongs to the realm of *chemical kinetics*.

1.01.2 Some Definitions

A *system* is any part of external reality that can be subjected to thermodynamic treatment; the material with which the system is in contact forms the *surroundings*, for example, an electrochemical cell could be the system and the external atmosphere the surroundings.

A *homogeneous* system is one in which the properties are uniform or vary uniformly throughout the system, whereas a *heterogeneous* system is one consisting of two or more homogeneous systems. Pure copper and a pure solution of $CuSO_4$ are both homogeneous systems, but copper immersed in a solution of $CuSO_4$ is a heterogeneous system characterized by an interface. The state of a system is described by its properties, which may be *intensive* or *extensive*; intensive properties are independent of quantity, for example, temperature, pressure, electrical potential, activation energy, etc., whereas extensive properties depend upon the amount of the material, for example, mass, volume, internal energy, enthalpy, entropy, free energy, chemical potential, etc.

The state of a system containing a constant amount of material depends on a few variables, for example, pressure p, volume V, and temperature T. For a given mass of pure substance, the volume can be expressed solely as a function of pressure and temperature

$$V = f(p, T) \qquad [1]$$

If pressure changes from p to $p + \mathrm{d}p$ and temperature from T to $T + \mathrm{d}T$, then the change in V is given by

$$\mathrm{d}V = \left(\frac{\partial V}{\partial p}\right)_T \mathrm{d}p + \left(\frac{\partial V}{\partial T}\right)_p \mathrm{d}T \qquad [2]$$

where $(\partial V/\partial p)_T$ is the rate of change of volume with pressure at constant temperature, and $(\partial V/\partial T)_p$ is the rate of change of volume with temperature at constant pressure. They are referred to as *partial derivatives*; the subscripts T and p denoting the variables that are maintained constant.

A *reversible* system is one that is so perfectly balanced that only infinitesimal change in an external conditions is required to reverse the direction of the process; for reversibility, the change must either be infinitesimally small or, if large, it must be carried out at an infinitely slow rate. Although these concepts are hypothetical, it is possible to approximate to reversibility by balancing the electromotive force (emf) of a reversible cell with the emf of a potentiometer circuit so that only a minute change ($<10^{-6}$ V) in the emf produced by the latter will result in a reversal of the direction of the cell reaction. An ideal reversible cell must consist of two reversible electrodes, which are so completely nonpolarizable that their potentials are unaffected by charge transfer even at high rates. This too is a hypothetical concept, but a number of electrodes will approximate to reversibility, provided the rate of charge transfer is small, and cells composed of these electrodes may be treated thermodynamically.

1.01.2.1 First Law of Thermodynamics

The first law is essentially a statement of the experimental fact that during a chemical reaction in an isolated system, *energy is conserved*, although it may be converted from one form to another.

If a system changes from state A to state B and if ΔU is the change in the internal energy of the system, then it follows from the first law that the surroundings must gain or lose an equivalent amount of energy. A convention of signs is necessary to take into account the direction of heat transfer q and work performed w: q is taken as positive if heat is transferred to the system from the surroundings and negative if the transfer is in the reverse direction; in many textbooks, w is taken as positive if work is done by the system on the surroundings and negative if it is done on the system by the surroundings, but it is preferable to allow the sign of w to develop from the

mathematics. Thus, since energy must be conserved

$$\Delta U = q - w \qquad [3]$$

where ΔU is the change in the internal energy of the system, q is the heat transferred between the system and the surroundings, and w is the work done. Equation [3] may be regarded as an algebraic expression of the conservation of energy, and it should be noted that ΔU is the difference in the internal energy of the system between its initial and final stages and that the absolute value of U is not known.

If a change from state A to state B occurs in a system at constant pressure (isobaric) so that only pV work is done, then $w = p\,\Delta V$ and

$$\Delta U = q_p - p(V_B - V_A) \qquad [4]$$

which can be written in the form

$$\begin{aligned} q_p &= U_B - U_A + p(V_B - V_A) \\ &= (U_B + pV_B) - (U_A + pV_A) \end{aligned} \qquad [5]$$

Thus, it is convenient to define another function

$$H = U + pV \qquad [6]$$

where H is the *enthalpy* or *heat content* of the system, so that

$$q_p = H_B - H_A = \Delta H \qquad [7]$$

where q_p is the heat exchanged between the system and the surroundings at constant pressure, and ΔH, like ΔU, depends only upon the initial and final states of the system.

1.01.2.2 Second Law of Thermodynamics

The first law implies that energy is interconvertible and that when one form of energy disappears another form of energy must appear in its place. However, it provides no information on (a) the transformations of energy that are possible and (b) the extent to which one form of energy can be converted into another. Some energy transformations are possible and occur spontaneously, while transformations in the reverse direction are nonspontaneous and can be made to proceed only by supplying energy from an external source. Thus, heat will flow spontaneously from a source at a higher temperature to one at a lower temperature, but it cannot pass spontaneously in the reverse direction. The heat energy flowing spontaneously can be converted by means of suitable machinery to work energy, but it is evident from the Carnot cycle (see below) that there is a theoretical limit to the extent of this interconversion.

Oxidation of hydrogen to water ($H_2 + \frac{1}{2}O_2 \rightarrow H_2O$) is thermodynamically spontaneous, and the energy released as a result of the chemical reaction appears as heat energy, but the decomposition of water into its elements is a nonspontaneous process and can be achieved only by supplying energy from an external source, for example, a source of emf that decomposes the water electrolytically. Furthermore, although the heat energy produced by the spontaneous reaction could be converted into electrical energy; the electrical energy thus obtained would not be sufficient to restore the original state of chemical energy of the system, that is, to regenerate 1 mol of H_2 and $\frac{1}{2}$ mol of O_2.

The second law, which can be stated in a number of different ways, expresses the fact that heat can only be transformed into work when it flows from a higher to a lower temperature. Clausius stated the second law as follows: "It is impossible for a self-acting machine, unaided by an external agency, to convey heat from a lower to a higher temperature."

In principle, all spontaneous processes may be harnessed and made to do work, but owing to the wastage of a proportion of the energy as heat energy there is a theoretical limit to the amount of useful work that can be obtained, and this can never be exceeded in practice. A high-efficiency power station converting chemical energy (solid or liquid fuel) into electrical energy achieves only 30–40% efficiency.

The maximum theoretical work w_{max} obtainable from a system was derived by Carnot who considered the transformation of heat energy into work when a perfect gas in a cylinder with a piston was taken through a reversible cycle (the Carnot cycle), in which the system was almost at equilibrium during each step of the cycle. It was shown that

$$w_{max} = q_2\left(\frac{T_2 - T_1}{T_2}\right) \qquad [8]$$

where q_2 is the heat absorbed from a reservoir at the higher temperature T_2 (K), and T_1 is the temperature of a second heat reservoir at a temperature lower than T_2 which receives the heat that has not been converted into work. Equation [8] is applicable to any reversible system that undergoes a cyclic process in which the original and final states of the system and the surroundings are the same. Under these circumstances, all that has changed permanently is that a quantity of heat q_2 at T_2 has been transformed into

work w_{max} together with a quantity of heat $q_1 = q_2 - w_{max}$ that is returned to the reservoir at the lower temperature T_1. It can be shown that the efficiencies of all reversible cyclic processes are the same provided T_1 and T_2 are the same, that is

$$\text{Thermodynamic efficiency} = \frac{w_{max}}{q_2} = \frac{q_2 - q_1}{q_2} = \frac{T_2 - T_1}{T_2} \quad [9]$$

It is evident from eqn [9] that (a) the efficiency increases as $(T_2 - T_1)/T_2$ increases and (b) the efficiency is zero when $T_1 = T_2$ so that no heat can be converted into work.

1.01.2.3 Entropy

The concept of entropy S is implicit in the second law, and it may be regarded as a thermodynamic property of a system that is associated with its capacity for spontaneous change. As the system undergoes spontaneous change, the entropy increases and the capacity for further spontaneous change decreases. Rearranging the q and T terms in eqn [9] and applying the convention of signs

$$\frac{q_1}{T_1} - \frac{q_2}{T_2} = 0 \quad [10]$$

and generalizing for any reversible cyclic change that proceeds isothermally at a temperature T

$$\sum \frac{q_{rev}}{T} = 0 \quad [11]$$

where Σq_{rev} is the sum of the heat absorbed or evolved reversibly. The function q_{rev}/T is a measure of the change in entropy ΔS, and this change for an isothermal process is defined as

$$\Delta S = \frac{q_{rev}}{T} \quad [12]$$

and for an infinitesimal reversible process

$$dS = \frac{\delta q}{T} \quad [13]$$

If the process is nonisothermal but finite

$$\Delta S = S_2 - S_1 = \int_{S_1}^{S_2} \frac{\delta q}{T} \quad [14]$$

It must be emphasized that the heat q_{rev}, which appears in the definition of entropy (eqn [12]), is always that which is absorbed (or evolved) when the process is conducted reversibly. If the process is conducted irreversibly and the heat absorbed is q, then q will be less than q_{rev} and q/T will be less than the entropy change ΔS eqn [12]. It follows that if an irreversible process takes place between the temperatures T_2 and T_1 and has the same heat intake q at the higher temperature T_2 as the corresponding reversible process, then the efficiency of the former must be less than that of the latter, that is

$$\left(\frac{q_1}{T_1} - \frac{q_2}{T_2}\right)_{irrev.} > \left(\frac{q_1}{T_1} - \frac{q_2}{T_2}\right)_{rev.} \quad [15]$$

Thus, from eqns. [11] and [15] it follows that for an irreversible cycle

$$\sum \frac{q}{T} > 0 \quad [15a]$$

and that more positive $\Sigma(q/T)$ is the more irreversible is the cycle. In the Carnot cycle, each stage is carried out reversibly and the entropy change is zero, and it can be shown that any complete cycle can be reduced to the sum of a large number of infinitesimal Carnot cycles so that the entropy change for any complete reversible cycle must always be zero. Thus, for any reversible process, the sum of all entropy changes for all the participating systems is given by

$$\sum dS = 0 \quad [16]$$

which provides a criterion for equilibrium.

On the other hand, in any irreversible process, although the system may gain (or lose) entropy and the surroundings lose (or gain) entropy, the system plus surrounding will always gain in entropy eqn [16]. Thus, for a real process proceeding spontaneously at a finite rate

$$\sum dS > 0 \quad [17]$$

For example, if a hot body (the system) is in contact with the surroundings at an infinitesimally lower temperature, then there will be an isothermal and reversible transfer of heat at T_2, and the loss in entropy of the hot body will be $\Delta S_b = -q_{rev}/T_2$, the gain in entropy of the surroundings will be $\Delta S_s = +q_{rev}/T_2$, and $\Delta S_b + \Delta S_s = 0$. On the other hand, if the surroundings are at a lower temperature T_1 than the body, then the transfer of heat will be irreversible and spontaneous, and the entropy changes will be $\Delta S_b = -q_{rev}/T_2$ and $\Delta S_s = +q_{rev}/T_1$. Since $T_2 > T_1$, the total change in entropy will be greater than zero, and the greater the difference between T_2 and T_1 the greater will be the gain in the total entropy of the

system as a whole, that is, the more spontaneous or irreversible is the transfer of heat.

When a substance is heated at constant pressure without change of phase through a temperature rise $\mathrm{d}T$, the heat absorbed is $C_p\,\mathrm{d}T$, where C_p is the molar heat capacity at constant pressure, and the entropy increase is

$$\int_{S_1}^{S_2} \mathrm{d}S = \int_{T_1}^{T_2} \frac{C_p}{T} = \int_{T_1}^{T_2} C_p\ \mathrm{d}\ \ln T \qquad [18]$$

Thus, the entropy increase when the substance is heated from T_1 to T_2 is

$$\Delta S = \int_{T_1}^{T_2} C_p\ \mathrm{d}\ \ln T = 2.303 \int_{T_1}^{T_2} C_p\ \mathrm{d}\ \log T \qquad [19]$$

ΔS may be evaluated by determining the heat capacity C_p at various temperatures between T_2 and T_1, and plotting the values against log T; the area enclosed by the curve multiplied by 2.303 gives the entropy increase. When there is a change of phase such as the evaporation of a liquid to saturated vapor, melting of a solid to a liquid, or transition from one crystalline form to another, the process is isothermal and reversible, and

$$\Delta S = \frac{q}{T} \qquad [20]$$

where q is the heat associated with the phase change at T.

For example, in the case of the reversible isothermal transformation of ice to water at the melting point (273 K), the heat gained by the ice will be the latent heat of fusion ($\Delta H_f = 6006\,\mathrm{J\,mol^{-1}}$) and a corresponding quantity of heat will be lost by the surrounding, and

$$\Delta S_{\text{system}} = \Delta S_{\text{ice}} + \Delta S_{\text{surr}} = \frac{6.006}{273} - \frac{6.006}{273} = 0$$

1.01.2.4 Gibbs Free Energy or Free Enthalpy

Gibbs free energy G provides a means of defining equilibrium or of the tendency of a reaction to proceed in a given direction. It is similar to the other thermodynamic functions described above in which the change in free energy ΔG is determined solely by the initial and final states of the system. The maximum work, or maximum available energy, defined in terms of the Gibbs free energy G, also called the *free enthalpy*, is

$$G = H - TS \qquad [21]$$

or, for a finite change

$$\Delta G = \Delta H - T\Delta S \qquad [22]$$

It can be shown that for a system in which the total mass, or the concentrations of the components, remains constant

$$\left(\frac{\partial G}{\partial P}\right)_{T,n_i\ldots} = V \qquad [23]$$

and

$$\left(\frac{\partial G}{\partial T}\right)_{p,n_i\ldots} = -S \qquad [24]$$

Combining eqns [21] and [24]

$$G - H = T\left(\frac{\partial G}{\partial T}\right)_{p,n_i\ldots} \qquad [25]$$

which is the important Gibbs–Helmholtz equation. Since in thermodynamics we are concerned mainly with changes in free energy and enthalpy, eqn [25] can be written as

$$\Delta G - \Delta H = T\left(\frac{\partial \Delta G}{\partial T}\right)_{p,n_i\ldots} \qquad [26]$$

Units: Free energy is an *extensive* quantity, but the *standard* free energy for 1 mol $\Delta G^{\circ}_{298\mathrm{K}}$ (in units of $\mathrm{J\,mol^{-1}}$) defined above is an *intensive* quantity.

1.01.2.5 The Chemical Potential

The energy of a system can be changed by means of thermal energy or work energy, but a further possibility is to add or subtract moles of various substances to or from the system. The free energy of a pure substance depends upon its chemical nature, its quantity (ΔG is an extensive property), its state (solid, liquid, or gas), and temperature and pressure. Gibbs called the partial molar free heat content (free energy) of the ith component of a system its *chemical potential*

$$\mu_i = \left(\frac{\partial G}{\partial n_i}\right)_{T,p,n_j} \qquad [27]$$

that is, the change in free enthalpy of the system when 1 mol of component i is added to the system, the T, p and concentration of all other substances (n_j) being maintained constant. The partial molar free energy of a pure compound is synonymous with the *standard chemical potential* μ°, which is the free enthalpy change when 1 mol of the substance is

formed from its elements under isothermal isobaric conditions. In order to evaluate the chemical potentials of compounds, and of ions in solution, it is necessary to define the following standard states:

1. The standard chemical potentials of the elements in the form that they are normally stable at the temperature and pressure under consideration are given an arbitrary value zero

$$\mu^{\circ}(\text{element}) = 0 \qquad [28]$$

2. In the case of ions in solution and of gases, the chemical potential will depend upon concentration and pressure, respectively. An arbitrary value of zero at a specified concentration is given for ions in solution, the standard chemical potential of the hydrogen ion, at the temperature and pressure under consideration

$$\mu^{\circ}_{H^+} = 0, \text{ when } a_{H^+} = 1 \qquad [29]$$

where a_{H^+} is the activity of the hydrogen ion.

1.01.2.6 Activity

The chemical potential of the hydrogen ion, or of any other ion, will vary with activity

$$\mu_i = \mu_i^{\circ} + RT \ln a_i \qquad [30]$$

where the activity a_i is a thermodynamic quantity that is related to the concentration of the ion and takes into account the fact that a solute in solution does not behave ideally at finite concentrations; only at infinite dilution, will a_i be equal to c_i numerically, where c_i is the concentration (mol kg^{-1}, mol m^{-3}, or mol dm^{-3}).

Substituting for $R = 8.314\,J\,K^{-1}\,mol^{-1}$ and $T = 298\,K$, and using the identity $\ln x = 2.303 \log x$, eqn [30] can be expressed as

$$\mu_i = \mu_i^{\circ} + 5710 \log a_i \qquad [31]$$

A similar equation is applicable to a gas, but the pressure of the gas p_g (or more strictly its fugacity) replaces the activity of the ion

$$\mu_g = \mu_g^{\circ} + 5710 \log (p_g/p^{\circ}) \qquad [32]$$

where p° refers to a standard pressure of 1 atm or $101\,325 \times 10^5$ Pa. For a nondissociating solute (e.g., urea)

$$a = \gamma c/c^{\circ} \qquad [33]$$

where γ is the activity coefficient ($\gamma \to 1$ as $c \to 0$) and c° is the concentration in the standard state.

For a 1:1 electrolyte (NaCl), a similar procedure may be adopted, but in this case not only do the constituent ions (Na^+ and Cl^-) become more ideal in behavior as the concentration decreases, but also the electrolyte becomes more completely dissociated into ions. It is not possible to determine individual ionic activity coefficient since anions and cations cannot be studied in the absence of one another. Thus, for a 1:1 electrolyte eqn [30] is written as

$$\mu = \mu^{\circ} + 2RT \ln a_{\pm} = \mu^{\circ} + 2RT \ln (\gamma_{\pm} c/c^{\circ}) \qquad [34]$$

where $a_{\pm}$ is the mean ionic activity, $\gamma_{\pm}$ is the mean activity coefficient, and $\gamma_{\pm} \to 1$ when $c \to 0$. More complex relationships are required for unsymmetrical electrolytes, such as Na_2SO_4, $La_2(SO_4)_3$, $TiCl_4$, etc.

At sufficiently low ionic strengths, the activity coefficient of each electrolyte in a mixture is given by the Debye–Hückel limiting law

$$\log \gamma_{\pm} = -\,|\,z_+ z_-\,|\,A\sqrt{I} \qquad [35]$$

where I the *ionic strength* is defined as

$$I = \frac{1}{2}\sum c_i z_i^2 \qquad [36]$$

and z_+ and z_- are the valencies of the cation and anion (NaCl is a 1:1 electrolyte, Na_2SO_4 a 2:1 electrolyte, $La_2(SO_4)_3$ a 2:3 electrolyte, etc.), and A is a constant which is $0.51\,mol^{-1/2}\,kg^{1/2}$ for water at 25 °C (c_i is in mol kg^{-1}).

Units: It should be noted that in the SI the activity of a solute is defined with reference to a standard state, that is, an ideal solution of molality 1 mol kg^{-1}. Thus, the *relative activity* of a metal ion in solution is given by

$$a_{M^{z+}} = \frac{m_{M^{z+}}}{m^{\circ}}\gamma_{M^{z+}} \qquad [37]$$

where $m^{\circ} = 1\,mol\,kg^{-1}$, $m_{M^{z+}}$ is in mol kg^{-1}, and $\gamma_{M^{z+}}$ is dimensionless. It follows that the relative activity is dimensionless, although units, such as mol kg^{-1}, g ion per litre, etc., are still being used (see below).

1.01.2.7 Gibbs–Duhem Equation

The Gibbs free energy change of a system will depend not only on temperature and pressure, but also on the chemical potentials of the species involved, and this statement may be expressed in the form of the partial differential

$$dG + \left(\frac{\partial G}{\partial T}\right)_{p,n_1,n_2\ldots} dT + \left(\frac{\partial G}{\partial p}\right)_{T,n_1,n_2\ldots} dp + \mu_1 dn_1 + \mu_2 dn_2 \qquad [38]$$

and combining with eqns [23] and [24]

$$\mathrm{d}G = -S\ \mathrm{d}T + V\ \mathrm{d}p + \sum \mu_i\ \mathrm{d}n_i \qquad [39]$$

For a process carried out under isothermal and isobaric conditions

$$(\mathrm{d}G)_{T,p} = \sum \mu_i\ \mathrm{d}n_i \qquad [40]$$

and integration of this equation for a system of given chemical composition gives

$$G_{T,p,n} = \sum n_i \mu_i \qquad [41]$$

General differentiation of this equation gives

$$\mathrm{d}G_{T,p} = \sum (n_i\ \mathrm{d}\mu_i + \mu_i\ \mathrm{d}n_i) \qquad [42]$$

Since at equilibrium $(\mathrm{d}G)_{T,p,n}$ = zero, it follows from eqn [40] that

$$\sum n_i\ \mathrm{d}\mu_i = 0 \qquad [43]$$

which is referred to as the Gibbs–Duhem equation.

For a binary solution of say A and B

$$n_\mathrm{A}\ \mathrm{d}\mu_\mathrm{A} = -n_\mathrm{B}\ \mathrm{d}\mu_\mathrm{B} \qquad [44]$$

Since

$$\mu_i = \mu_i^\circ + RT\ \ln\ a_i \qquad [45]$$

$$\mathrm{d}\mu_i = RT\mathrm{d}\ \ln\ a_i \qquad [46]$$

Hence

$$n_\mathrm{A}\mathrm{d}\ \ln\ a_\mathrm{A} = -n_\mathrm{B}\mathrm{d}\ \ln\ a_\mathrm{B} \qquad [47]$$

The Gibbs–Duhem equation is extremely important in solution chemistry, and it can be seen from eqn [47] that it provides a means of determining the activity of one component in a binary solution provided the activity of the other is known.

1.01.3 Spontaneity of a Reaction

An isothermal reaction can proceed spontaneously only if the total Gibbs free energy of the system decreases; that is, the free energy of the reactants must be greater than the free energy of the products. For a reaction

$$a\mathrm{A} + b\mathrm{B} = c\mathrm{C} + d\mathrm{D} \qquad [48]$$

$$\Delta G = \sum \mu_\mathrm{products} - \sum \mu_\mathrm{reactants} \qquad [49]$$

where ΔG is the change in free enthalpy. It follows that if $\Delta G < 0$, then the reaction will tend to proceed spontaneously in the direction shown; if $\Delta G > 0$, then the reaction will tend to proceed spontaneously in the reverse direction, and if $\Delta G = 0$, then the system will be at equilibrium and will not have any tendency to proceed in either direction.

Thus, for a spontaneous reaction

$$\Delta G = (c\mu_\mathrm{C} + d\mu_\mathrm{D}) - (a\mu_\mathrm{A} + b\mu_\mathrm{B}) < 0 \qquad [50]$$

and if all the substances are in their standard states

$$\Delta G = (c\mu_\mathrm{C}^\circ + d\mu_\mathrm{D}^\circ) - (a\mu_\mathrm{A}^\circ + b\mu_\mathrm{B}^\circ) < 0 \qquad [51]$$

1.01.3.1 Reversible Cells

By definition

$$\Delta G = -zFE \qquad [52]$$

where E (the reversible emf) is the intensity factor in the energy term and zF (the total charge per mole of ions involved in the reaction) is the capacity factor. If the activities of the reactants and products are fixed, E will be a constant, and if $a_\mathrm{A} = a_\mathrm{B} = a_\mathrm{C} = a_\mathrm{D} = 1$ is taken as the standard state, then

$$\Delta G^\circ = -zFE^\circ \qquad [53]$$

where ΔG° is the standard free enthalpy change and E° is the standard emf which is a constant for a given equilibrium at constant T.

Substituting $-zFE$ for ΔG eqn [53] in eqn [26] gives

$$\Delta H = -zFE + zFT\left(\frac{\partial E}{\partial T}\right)_p \qquad [54]$$

which provides an accurate method of evaluating ΔH and ΔS in eqn [54] from the emf of a reversible cell and the coefficient of the change of emf with temperature at constant p, since

$$-T\left(\frac{\partial(\Delta G)}{\partial T}\right)_p = zFT\left(\frac{\partial E}{\partial T}\right)_p = T\Delta S \qquad [55]$$

From eqn [49]

$$\Delta G^\circ = \sum \upsilon_i \mu_i^\circ \qquad [56]$$

where υ_i is the number of each of the ions or molecules involved in the equilibrium; combining eqns [53] and [54]

$$E^\circ = \frac{\Sigma\ \upsilon_i \mu_i^\circ}{zF} = -\frac{\Sigma\ \upsilon_i \mu_i^\circ}{96\ 500z} \qquad [57]$$

Equations [53] and [57] emphasize the essentially thermodynamic nature of the standard equilibrium emf of a cell or the standard equilibrium potential

of a half-reaction $\overset{\circ}{E}$, which may be evaluated directly from the emf measurements of a reversible cell or indirectly from $\Delta\overset{\circ}{G}$, which must in turn be evaluated from the enthalpy of the reaction and the entropies of the species involved (see eqn [22]). Thus, for the equilibrium $Cu^{2+} + 2e \rightleftharpoons Cu$ the standard electrode potential $E^{e}_{Cu^{2+}/Cu}$, and hence $\mu^{e}_{Cu^{2+}}$, can be determined by an emf method by harnessing the reaction

$$Cu^{2+} + 2Hg \rightarrow Hg_2^{2+} + Cu$$

which can be represented by a cell without a liquid junction (or liquid junction potential)

$$Hg \mid Hg_2SO_4(aq.); CuSO_4(aq.) \mid Cu$$

in which '|' represents the phase boundaries. When a cell has a liquid junction, the latter is represented by ‖ as in the cell

$$M_1 \mid M_1^{2+}(aq.) \parallel M_2^{2+}(aq.) \mid M_2$$

Although in certain cells the liquid junction can be eliminated by appropriate choice of electrolyte solution, this is not always possible. However, the liquid junction potential can be minimized by the use of a salt bridge (a saturated solution of KCl of about 4.2 M) and the liquid junction potential is then only 1–2 mV; this elimination of the liquid junction potential is indicated by ‖.

The standard electrode potential of M^{z+}/M can be evaluated accurately and conveniently provided it forms a reversible electrode and can be coupled with a reference electrode to form a reversible cell. However, a number of M^{z+}/M systems do not conform to this criterion, and calorimetric methods must be used to evaluate $\Delta\overset{\circ}{H}$ and $\Delta\overset{\circ}{S}$, and hence $\Delta\overset{\circ}{G}$ from which $\overset{\circ}{E}$ can be calculated. Thus, in the case of the $Mg^{z+}(aq)/Mg$ equilibrium, the enthalpy change during the dissolution of the metal in dilute acid at 25 °C is determined from the reaction

$$Mg(s) + 2H^+(aq) = Mg^{2+}(aq) + H_2(g);$$
$$\Delta\overset{\circ}{H} = -461\ 200\ J mol^{-1}$$

and the standard entropy change $\Delta\overset{\circ}{S}$ is evaluated from the standard partial molar entropies of the reactants and products

$$\Delta\overset{\circ}{S} = \overset{\circ}{S}(Mg^{2+}) + \overset{\circ}{S}(H_2) - \overset{\circ}{S}(Mg) + 2\overset{\circ}{S}(H^+)$$
$$= -43.3\ J\ K^{-1}\ mol^{-1}$$

Since $\Delta\overset{\circ}{G} = \Delta\overset{\circ}{H} - T\overset{\circ}{S}$

$$\Delta\overset{\circ}{G} = -461\ 200 - (298 \times 43.3)$$
$$= -448300\ J\ mol^{-1} \text{ at } 298\ K$$

$$\overset{\circ}{E}_{reaction} = \frac{-\Delta\overset{\circ}{G}}{zF} = \frac{-448\ 300}{2 \times 96\ 500} = -2.3V$$

and since $a_{H^+} = p_{H_2} = 1$, $\overset{\circ}{E}_{Mg^{2+}/Mg} = -2.3V$.

1.01.4 Chemical Potentials and Equilibrium

The relationship between the change in free energy ΔG and the equilibrium constant K is given by the van't Hoff isotherm

$$\Delta G = -RT \ln K + RT \ln Q \qquad [58]$$

and from eqn [48]

$$K = \frac{a_C^c a_D^d}{a_A^a a_B^b} \qquad [59]$$

where a denotes the equilibrium activity of the component and Q is the activity quotient. Note that the activities of the products are in the numerator and activities of reactants in the denominator.

Equation [58] shows that ΔG is dependent on K and on any arbitrary activity of reactants and products that may be introduced into the equation. When the reactants and products are in their standard states

$$a_A = a_B = a_C = a_D = 1 \text{ and } \ln Q = 0 \qquad [60]$$

Hence, from eqn [53]

$$\therefore \quad \Delta G = \Delta\overset{\circ}{G} = -RT \ln K \qquad [61]$$
$$\Delta\overset{\circ}{G} = -RT \ln K = -zF\overset{\circ}{E} \qquad [62]$$

and

$$\overset{\circ}{E} = \frac{RT}{zF} \ln K = \frac{0.0591}{z} \log K \qquad [63]$$

since at 25 °C, the term $2.303RT/F = 2.303 \times 8.314 \times 298/96\ 500 = 0.0591$ V. Combining eqns [52] and [58]

$$E = \frac{RT}{zF} \ln K - \frac{RT}{zF} \ln Q \qquad [64]$$

and from eqn [63]

$$E = \overset{\circ}{E} - \frac{0.0591}{z} \log Q$$
$$= \overset{\circ}{E} - \frac{0.0591}{z} \log \frac{a_C^c a_D^d}{a_A^a a_B^b} \qquad [65]$$

which shows how the equilibrium potential E is

dependent on the standard electrode potential $\overset{\circ}{E}$, a constant for a given equilibrium, and the activities of reactants and products. Equation [65] is termed the *Nernst* equation and is applicable only when the system is reversible. Since

$$\Delta\overset{\circ}{G} = \sum \upsilon_i \overset{\circ}{\mu_i} = -RT \ln K \qquad [66]$$

$$\log K = -\frac{\sum \upsilon_i \overset{\circ}{\mu_i}}{5710} \text{ at } 25^\circ\text{C} \qquad [67]$$

Thus, the equilibrium constant K can be evaluated from standard electrode potential $\overset{\circ}{E}$ or from the standard chemical potentials $\overset{\circ}{\mu}$.

The importance of the Gibbs free energy and the chemical potential is very great in chemical thermodynamics. Any thermodynamic discussion of chemical equilibria involves the properties of these quantities. It is therefore worthwhile considering the derivation of eqn [58] in some detail since it forms a prime link between the thermodynamics of a reaction (ΔG and $\Delta\overset{\circ}{G}$) and its chemistry.

From the defining equations of H (eqn [6]) and G (eqn [21]), differentiation gives

$$\mathrm{d}H = \mathrm{d}U + p\,\mathrm{d}V + V\mathrm{d}p \qquad [68]$$

and

$$\mathrm{d}G = \mathrm{d}H - T\,\mathrm{d}S - S\,\mathrm{d}T \qquad [69]$$

In addition, application of the first and second laws (eqns [3] and [13]) gives

$$\mathrm{d}U = T\,\mathrm{d}S - p\,\mathrm{d}V \qquad [70]$$

Combination of these gives

$$\mathrm{d}G = V\mathrm{d}p - S\,\mathrm{d}T \qquad [71]$$

This equation is particularly important because by carrying out a process isothermally ($\mathrm{d}T = 0$) the change in the value of G can be related to the volume and pressure change alone; both of these quantities are controllable and measurable. Thus, for isothermal processes

$$\mathrm{d}G = V\mathrm{d}p \qquad [72]$$

It remains only to integrate this expression. To do this, we apply initially the equation for n moles of an ideal gas

$$V = \frac{nRT}{p} \qquad [73]$$

so that

$$\mathrm{d}G = nRT\int \frac{1}{p}\mathrm{d}p \qquad [74]$$

Integration of this requires a limit to be defined. The limit is taken simply as follows. We define a standard pressure $\overset{\circ}{p}$ at which the Gibbs free energy has a standard value $\overset{\circ}{G}$. We have thereby defined a standard state for this component of the system: a standard temperature too is implicit in this since the above equations are treated for constant temperature.

Integration of eqn [74] now gives

$$G = \overset{\circ}{G} + nRT \ln \frac{p}{\overset{\circ}{p}} \qquad [75]$$

If only one mole of the gas is considered, the quantity G is called the chemical potential, μ, or the partial molar free energy. In this case, $n = 1$; and eqn [75] becomes

$$\mu = \overset{\circ}{\mu} + RT \ln \frac{p}{\overset{\circ}{p}} \qquad [76]$$

Note that the standard state has simply to be defined; there is no *a priori* reason why it should have any particular value, save for the fact that it might as well be a convenient value. A pressure of 1 atm is commonly adopted. We can thus abbreviate the equation to

$$\mu = \overset{\circ}{\mu} + RT \ln p \qquad [77]$$

provided the pressure of the gas, p, is expressed in atmospheres if the standard pressure has a numerical value of 1 atm. But note that the term inside the logarithm is actually dimensionless because of the *implicit* $\overset{\circ}{p}$.

If the gas is not ideal, so that the ideal gas equation cannot be used, we replace the pressure p in eqns [76] and [77] by the fugacity, f, such that the ideal gas equation still holds if the pressure p is replaced by the fugacity, an effective pressure, when the real pressure is p. This form is most convenient because of the numerous ways in which nonideality can be expressed and we note that the fugacity is related to, but not necessarily proportional to, the pressure. We can express the fugacity as a function of the pressure by introducing the fugacity coefficient, γ_p, as $f = \gamma_p p$, which then replaces p in eqn [77] for the nonideal case. The value of γ_p tends to unity as the gas behaves more ideally, which means that the pressure decreases.

Consider now, a simple gas phase (with ideal gases) reaction

$$\mathrm{A} + \mathrm{B} \rightarrow \mathrm{C} \qquad [78]$$

For each component, we may write eqn [77]. The free energy change, ΔG for the reaction, is then given by

$$\begin{aligned}\Delta G &= \mu_C - \mu_B - \mu_A \\ &= \mu_C^\circ - \mu_B^\circ - \mu_A^\circ + RT \ln \frac{p_C}{p_C^\circ} - RT \ln \frac{p_B}{p_B^\circ} \\ &\quad - RT \ln \frac{p_A}{p_A^\circ} \\ &= \Delta G^\circ + RT \ln \frac{(p_C/p_C^\circ)}{(p_B/p_B^\circ)(p_A/p_A^\circ)}\end{aligned} \quad [79]$$

Again, we define the standard state for a gas as 1 atm, that is, $p_A^\circ = p_B^\circ = p_C^\circ = 1$ atm so that the eqn [79] becomes

$$\Delta G = \Delta G^\circ + RT \ln \frac{p_C}{p_B p_A} \quad [80]$$

Now, since ΔG is the driving force for the reaction to proceed, equilibrium is represented by the condition that $\Delta G = 0$. Thus, the value of ΔG° is given as

$$\begin{aligned}\Delta G^\circ &= -RT \frac{(p_C^\varepsilon/p_C^\circ)}{(p_B^\varepsilon/p_B^\circ)(p_A^\varepsilon/p_A^\circ)} \\ &= -RT \ln \frac{p_C^\varepsilon}{p_B^\varepsilon p_C^\varepsilon}\end{aligned} \quad [81]$$

where the superscript ε refers to the pressure of the particular component *when the reaction is at equilibrium.* It will be recognized that the term inside the logarithm in eqn [81] is the equilibrium constant for the reaction. This relationship (together with eqn [80] is extremely important because it links the thermodynamics with the chemistry. We have derived the fact that ΔG° is simply another way of expressing the equilibrium constant for the reaction. It is important once again to bear in mind that the term inside the logarithm is actually dimensionless: each pressure is the ratio of the pressure to the standard pressure (expressed in the same units). Thus, the equilibrium constant is also strictly a dimensionless quantity. Although units are often quoted for the equilibrium constant K for the reaction (they would be atm^{-1} in the above example), units are of course inconsistent with the exponentiation of eqn [81], for which

$$K = \frac{p_C^\varepsilon}{p_B^\varepsilon p_A^\varepsilon} = \exp -\frac{\Delta G^\circ}{RT} \quad [82]$$

and the exponential term is always dimensionless. Citing of units for K (sometimes called K_p since it is a ratio of pressures as defined above) is really a method of telling one's audience what the standard states really are. Thus, we could, for example, consider 1 Pa of pressure as the standard state instead of 1 atm. It would equally be possible to use the concentration of the gas, since the ideal gas equation contains the term n/V which is the concentration (in, say, mol dm^{-3}), for which the standard state could be $1\ \text{mol dm}^{-3}$. This does not of course change the reaction, but it does change the numerical value of K and correspondingly the numerical value of ΔG°. It is not common to do this in gas phase chemistry – the usual standard state for gas is 1 atm. However, it is important to understand the principle of it, particularly in corrosion and electrochemistry, since electrochemical systems incorporate not only gases but also solids and solutions, the latter comprising solutes and a solvent. We can now express

$$\Delta G = -RT \ln K + RT \ln \frac{p_C}{p_A p_B} \quad [83]$$

Note that the term inside the second logarithm is *not* the equilibrium, unless the reaction is in equilibrium (for which $\Delta G = 0$). These pressures are the actual pressures used for the reaction, and the equation essentially describes the fact that the driving force for the reaction (as written) is represented by the excess pressure quotient of the reaction over and above the equilibrium.

All the above deal with gases and gas phase processes. We can now turn to nongaseous components of the system. There are many ways of expressing this. Probably, the simplest is to consider an ideal solution of a solute in a solvent. If the solution is ideal, the vapor pressure of the solute is proportional to its concentration, that is, $p = kc$, where c is the concentration and k is the proportionality constant. Similarly, $p^\circ = kc^\circ$ which expresses the fact that the standard pressure is related to a standard concentration. Thus, for a particular component we have from eqn [76]

$$\mu = \mu^\circ + RT \ln \frac{c}{c^\circ} \quad [84]$$

This formulation now entirely eliminates the need for a pressure and replaces it by the concentration and a standard concentration. As defined above, the standard concentration is that concentration which gives rise to the standard pressure p°. However, we have defined the original standard pressure arbitrarily as 1 atm. We can equally and validly redefine the

standard concentration of the solute as 1 mol dm^{-3} of solution (unit molar or 1 M), or 1 mol kg^{-1} of solvent (unit molal or 1 m). This, in essence, redefines the standard pressure, but that is of little consequence, since in corrosion and electrochemistry, we are usually concerned with concentrations in solution (as an electrolyte in water, for example) and with concentrations of metal in an alloy. Moreover, because the value of k may be different for different components of the system, from the point of view of the gas pressures, we may be assigning different standard states for different gases. But that does not matter either, since we are free to define the standard states in any way we choose, and we are now interested in solution components and not gases. Thus, for example, unit concentration of hydrochloric acid (say 1 m) is a far more convenient standard state than that concentration which would equilibrate with a vapor pressure of 1 atm. However, there is an added complication, already met with gases, that many solutions are not ideal. So far, the derivation has still been in terms of ideal solutions because we assumed that the pressure is proportional to the concentration; hence, the constant k is used above. Handling of this is analogous to the nonideal gas. We define a new term, the activity a, of the component which replaces the concentration in eqn [84]. Thus

$$a = \gamma \frac{c}{c^{\circ}} \qquad [85]$$

and thence for a nonideal component

$$\mu = \mu^{\circ} + RT \ln \frac{\gamma_C}{c^{\circ}} \qquad [86]$$

where c and c° are the concentration and standard concentration, respectively, expressed as molalities, and γ is the activity coefficient. We are here defining the standard concentration as 1 mole of solute per kilogram of solvent. This simply means that we are fixing the value of the chemical potential of the component as μ° when the concentration is the standard value. Note that the activity and the activity coefficient are dimensionless and a defined standard state is implied.

But that is not all. For dilute solutions, the solvent concentration is high (55 mol kg^{-1}) for pure water and does not vary significantly unless the solute is fairly concentrated. It is therefore a common practice and is fully justified to use unit mole fraction as the standard state for the solvent. The standard state of a close up pure solid in an electrochemical reaction is similarly treated as unit mole fraction (sometimes referred to as the pure component); this includes metals, solid oxides, etc.

Exactly analogous, then, to the gas phase reaction above, the value of ΔG and ΔG° can be formulated. Thus, for the following reaction, for example

$$M^{2+} + H_2O \rightarrow MO + 2H^{+} \qquad [87]$$

ΔG is given by

$$\Delta G = \Delta G^{\circ} + RT \ln \frac{(\gamma_{MO} c_{MO}/c^{\circ}_{MO})(\gamma_H c_H/c^{\circ}_H)^2}{(\gamma_M c_M/c^{\circ}_M)(\gamma_w c_w/c^{\circ}_w)} \qquad [88]$$

where the subscripts MO, H, M, and w refer to the MO, H^{+}, M^{2+}, and H_2O components, respectively. ΔG° is derived from the equilibrium activities as in eqn [81], but by using the appropriate concentration terms instead of pressure terms. Note that the equilibrium constant and the activity quotient in the above equation are again strictly dimensionless. Although dimensions are often quoted for K (sometimes called K_c) as described above (for reaction [82] this would be mol kg^{-1} or mol dm^{-3}), these are simply an expression of the standard states involved. Now, the standard state of the solid component (MO) and the solvent (H_2O) are defined by convention as the pure components (unit mole fraction). If the solution is dilute, $c_w \approx c^{\circ}_w$ and $\gamma_w = 1$. Thus the components of the equation above involving MO and H_2O are both unity. In addition, if we define the standard states of the dissolved ions as 1 M, then the relationship becomes the more familiar

$$\Delta G = \Delta G^{\circ} + RT \ln \frac{\gamma_H^2 c_H^2}{\gamma_M c_M} \qquad [89]$$

Note that if the water in the reaction is not of unit mole fraction (or nearly so), then its activity would have to be incorporated into eqn [89]. This could, for example, be as in a mixed water/methanol solution. The water concentration would then be expressed as unit mole fraction, and for accuracy, its activity coefficient relative to pure water (the standard state) would need to be known. The same is true if one of the reactants is a metal (whose standard state is the pure metal of unit mole fraction), but the reactant is in alloy form. In summary, it is common in electrochemical reactions to adopt the following standard states: for solid components and for the solvent, the standard state is unit mole fraction; for dissolved components (such as ions), the standard state is 1 mol solute per kilogram of solvent, or 1 mol solute per cubic decimeter of solution, and for gas phase components, the standard state is 1 atm pressure.

1.01.4.1 Sign Convention for Equilibrium emfs and Potentials

For ions in solution, the standard reference state is the hydrogen ion whose standard chemical potential at $a_{H^+} = 1$ is given an arbitrary value of zero. Similarly, for pure hydrogen at $p_{H2} = 1$ atm, $\mu^{\circ}_{H_2} = 0$. Thus, for the $H^+/\frac{1}{2}H_2$ equilibrium (eqn [57]),

$$E^{\circ} = -\frac{\sum \upsilon_i \mu_i}{zF} = 0.00 \text{ V} \qquad [90]$$

and the standard hydrogen electrode (SHE) is taken as the reference electrode for all other equilibria.

For a cell, the equilibrium must be written in the direction in which it proceeds spontaneously, and under these circumstances

$$\Delta G < 0 \text{ and } E > 0$$

that is, the emf of the cell will be positive. Thus, for the equilibrium between Zn and H^+, the reaction is written as

$$Zn(s) + 2H^+(aq) = Zn^{2+}(aq) + H_2(g)$$

and if $a^+_H = a^{2+}_{Zn} = a_{H_2} = 1$, $E = E^{\ominus} = +0.76\,\text{V}$. However, in the case of a half-reaction, it is quite arbitrary as to whether the equilibrium is written as a reduction (electrons on the LHS) or as an oxidation (electrons on the RHS)

$$Zn^{2+} + 2e = Zn \qquad [91a]$$

or

$$Zn = Zn^{2+} + 2e \qquad [92a]$$

since both are correct. Substituting in the Nernst equation eqn [65] for eqn [91a]

$$E = E^{\circ} - 0.030 \log \frac{1}{a_{Zn^{2+}}} = E^{\circ} + 0.030 \log a_{Zn^{2+}} \qquad [91b]$$

and for eqn [92a]

$$E = E^{\circ} - 0.030 \log a_{Zn^{2+}} \qquad [92b]$$

Thus, if the magnitudes of E are to be the same the signs of E° must be different, that is, $E^{\ominus} = -0.76\,\text{V}$ for eqn [91b] and $E^{\ominus} = +0.76$ V for eqn [92b]. If this convention is adopted, the respective electrode potentials become

$$E = -0.76 + 0.030 \log a_{Zn^{2+}} \qquad [91c]$$

$$E = +0.76 - 0.030 \log a_{Zn^{2+}} \qquad [92c]$$

and for any given activity of Zn^{2+}, the Es will be the same in magnitude but opposite in sign.

It is now internationally accepted (Stockholm Convention) that the half-reaction must be written with the electrons on the RHS:

$$Cu^{2+}(aq) + 2e = Cu \quad E^{\circ} = +0.34 \text{ V} \qquad [93]$$

$$Zn^{2+}(aq) + 2e = Zn \quad E^{\circ} = -0.76 \text{ V} \qquad [94]$$

1.02 Electrochemistry

C. Lefrou and R. P. Nogueira
Grenoble – INP – Grenoble Institute of Technology, UMR 5631 and 5266 of CNRS ''LEPMI'' and ''SIMAP'', Grenoble, France
F. Huet and H. Takenouti
Laboratoire Interfaces et Systèmes Electrochimiques, Université Pierre et Marie Curie – Paris 6, CNRS, UPR15-LISE, Paris, France

Abbreviations

CE Counter electrode
DC Direct current
IUPAC International union of pure and applied chemistry
NHE Normal hydrogen electrode
OCP Open-circuit potential

OHP Outer Helmholtz plane
OPA Operational amplifier
RE Reference electrode
SHE Standard hydrogen electrode
WE Working electrode
ZRA Zero-resistance ammeter

Symbols

a Activity of a species
$_a$ Related to the anodic reaction
$_{act}$ Related to activation control
A_1 Constant in eqn [36] (V)
b Tafel coefficient (V^{-1})
C Concentration of a species ($mol\,m^{-3}$)
$_c$ Related to the cathodic reaction
d Distance between two electrodes (m)
D Diffusion coefficient ($m^2\,s^{-1}$)
e Charge on the electron $= -1.602 \times 10^{-19}$ C
E Electrical potential (V)
E_{corr} Corrosion potential (V)
E_{eq} Equilibrium potential (V)
F Faraday constant $= 96\,486$ C mol^{-1}
g Constant in eqn [32]
G Chemical Gibbs free energy ($J\,mol^{-1}$)
$\overline{G}$ Electrochemical Gibbs free energy ($J\,mol^{-1}$)
G_I Gain of a current amplifier
G_V Gain of a voltage amplifier
$_{int}$ Related to the interface
I Current (A)
I_0 Exchange current (A)
I_{corr} Corrosion current (A)
I_{set} Set current (A)
j Current density ($A\,m^{-2}$)
j_0 Exchange current density ($A\,m^{-2}$)
j_{corr} Corrosion current density ($A\,m^{-2}$)
k Reaction rate constant ($m\,s^{-1}$)
K Constant in eqns [31] and [32] ($mol\,l^{-1}$)
$_{lim}$ Related to diffusion limitation
$_{mix}$ Related to mixed control
$_{mt}$ Related to mass transport control
M Molar mass ($kg\,mol^{-1}$)
n Number of moles (mol)
N Avogadro's number $= 6.022 \times 10^{23}$
q Electrical charge (C)
r Disk electrode radius (m)
$_{ref}$ Related to the reference electrode
R Gas constant $= 8.31$ J $mol^{-1}\,K^{-1}$
$R_{control}$ Current-control resistance (Ω)
R_{ct} Charge-transfer resistance (Ω)
R_e Electrolyte resistance (Ω)
R_m Current-measuring resistance (Ω)
R_p Polarization resistance (Ω)
S Electrode surface area (m^2)
t Time (s)
T Temperature (K)
V_{set} Set potential (V)
y Axial distance to a disk electrode (m)
z Number of electrons exchanged in a reaction
$_\infty$ Related to the bulk of the electrolyte
$[X]$ Concentration of species X ($mol\,l^{-1}$)
^{0} Related to the standard state
α Charge-transfer coefficient
β Tafel slope (V per current decade)
δ Thickness of the diffusion layer (m)
ΔX Difference in X values (X unit)
$\Delta_r \overline{G}$ $\overline{G}$ variation for reaction r ($J\,mol^{-1}$)
ε Thickness loss (m)
ϕ Flux of species ($mol\,m^{-2}\,s^{-1}$)
Φ Electrical potential (V)
γ Electrolyte conductivity ($\Omega^{-1}\,m^{-1}$)
η Overpotential (V)
ν Kinematic viscosity ($m^2\,s^{-1}$)
π Polarization (V)
θ Coverage ratio of adsorbed species
ρ Density ($kg\,m^{-3}$)
ω Electrode angular rotation rate ($rad\,s^{-1}$)

1.02.1 Introduction

The starting point of a chapter devoted to the introduction of basic aspects of electrochemistry that are absolutely vital for understanding corrosion processes can take advantage of the meaning of corrosion itself. In fact, corrosion processes encompass reactive phenomena of metal oxidation, hence yielding a progressive and more or less fast chemical deterioration of the material exposed to an aggressive environment by oxide formation or free dissolution in the form of dissolved cations. This implicates the existence of oxidation–reduction reactions, hereafter referred to as redox reactions, in which the role of the metallic surface and its interactions with the surrounding medium are particularly crucial. The basic concepts issuing from electrochemistry (roughly speaking, the branch of chemical sciences devoted to the study and investigation of reactive systems involving electrical charge transfer) are well adapted and necessary for a convenient description. These basic concepts will be helpful for the subsequent understanding of complex corrosion phenomena. The main goal of this chapter is, therefore, to provide an overview of basic electrochemical concepts, with a special focus

on electrochemical reaction near the equilibrium potential. Then, these concepts will be extended to those directly related to corrosion processes. For the sake of readability for nonexpert readers in electrochemistry, simplified representations of reactive interactions, actually much more complex, will be introduced in some cases. This is a conscious option taken by the authors to provide a self-sustained text conveying the main concepts and tools to understand the physicochemical processes associated with corrosion phenomena.

1.02.2 Current, Potential, and Interfaces

1.02.2.1 Electronic and Electrolytic Materials: The Two Sides of an Electrified Interface

Electrochemistry is a science, as well as an industrial domain, based on physicochemical phenomena taking place whenever electrical and chemical energy exchanges intervene in a reactive scheme. In this sense, most of the time electrochemistry investigates systems in which electrical currents flow, as in the case of electrochemical generators or batteries present in numerous everyday applications such as cars, mobile telephones, and so on. From this point of view, the archetypical corrosion process, that is a metallic piece freely exposed to a given aggressive environment is, to some extent, a bit marginal in the sense that the overall current flow observed from the outside of the system is zero; the system spontaneously evolves and is said to be at rest or at open-circuit. This is clearly the actual practical corrosion scenario, unless, an external source is applied as in the case of corrosion characterization or measurements and in some corrosion protection techniques such as cathodic or anodic protection. In spite of this feature, the concepts and tools involved in general electrochemistry remain valid and constitute the cornerstone of corrosion description and understanding.

It is possible to find redox reactions in a single phase, as in a bulk solution. Nevertheless, when talking about electrochemistry and more particularly corrosion, only heterogeneous systems are concerned, which means that the reactive system is composed of two or more distinct phases. As an example, let us consider a classical electrochemical system implying electrical energy exchanges such as a battery connected either to an electrical load (the battery hence discharges) or to an external electrical energy source (the battery hence charges). This is usually achieved by a multiphase 'sandwich' of at least three different materials with two different metals at the battery terminals. Since they involve electrical energy exchange, the electrochemical systems only employ conductive materials. Electrical conductivity exists as soon as the materials have mobile charges. Without going through an exhaustive survey, these key materials can be classified into three main categories according to the nature of the charge carriers: electronic conductors like metals or semiconductors, ionic conductors (or electrolytes), and finally mixed conductors (such as some conducting polymers) when the two types of electrical conduction coexist. To illustrate corrosion phenomena in the following, the text will concentrate only on metals, which are electronic conductors undergoing corrosion, and on electrolytes, which can be aqueous or organic solutions, molten salts, ionic solids, polymers, or even gases.

Besides the electrical conductivity of these materials, the specificity of the electrochemical systems comes from the way they are assembled. Regions in which the different materials (the metal and the electrolyte, for instance) are in contact and in which the electrical continuity between the electronic and ionic conductions is ensured are generally called interfaces. (The term 'interphase' would probably be more appropriate for bringing up the idea that this is not a single surface in a purely mathematical point of view, but a small physical volume usually a layer of some nanometers as roughly described hereafter in **Section 1.02.2.4.2**) The simplest electrochemical assembly is thus composed of two metals having an interface with the same electrolyte. This kind of system is referred to as a galvanic chain, where each interface is schematically represented by a vertical stroke as in the following examples:

$$\mathrm{Pt|aqueous\ solution|Au}$$

$$\mathrm{Pt|Fe^{2+},\ Fe^{3+}aqueous\ solution|Au} \qquad [1]$$

In the first example, where no corrosion process is expected at least in normal experimental conditions (concentration, temperature, etc.), both interfaces are said to be impermeable and nonreactive. In the second example, where the electrolyte is composed of an aqueous solution containing Fe^{2+} and Fe^{3+} cations, one of the most reactive couples and one often employed in analytical electrochemistry, the interfaces would still be impermeable but could then be reactive – even if corrosion of platinum and gold is considered as being negligible – since, under certain conditions, Fe^{2+} oxidation at one interface and Fe^{3+} reduction at the other should be observed. The term impermeable implies that the mobile species (the charge

carriers) at each side of the interfaces are different. Free electrons are mobile and can hence ensure the current flow across the metallic phases but are not present in the electrolyte phase, in which ions are mobile and ensure the electrical charge transport between the two metallic phases. In some more complex situations, such as certain corroding systems where a more or less ionically conductive oxide may partially or totally cover the metallic surface, hence creating an intermediate layer between the metal and the electrolyte, an interface between two ionic conductors is established and referred to as an ionic junction.

In contrast to that double interface configuration, from a macroscopic point of view, most corrosion processes take place at a single interface. This is the case, for instance, of the simplest corrosion situation: a piece of metal immersed in an electrolyte. It is obviously not possible for a net electrical current to flow in or out of this closed system. As discussed in more depth later in this chapter, this does not mean that no electrochemical reaction is taking place at the interface. It is also important to notice that this macroscopic single interface can be considered either as uniform, as for the corrosion of an almost homogeneous metallic surface (uniform or generalized corrosion) or nonuniform, as for the corrosion of a markedly heterogeneous metallic surface where inclusions or precipitates are preferentially corroded rather than the metallic matrix (an example of localized corrosion). It is then easy to understand that in the latter case two interfaces are actually concerned (metal | electrolyte | inclusion) in a microscopic approach, even if there is a single macroscopic interface.

1.02.2.2 Electrochemical Reactions

As indicated above, a common example of an electrochemical system is that of an impermeable interface between a metal and a solution containing ions where the species (charge carriers) ensuring the current flow at each side of the interface cannot traverse it. Indeed, on the one hand electrons are 'free' in the metallic lattice but trapped in the liquid phase by different cationic configurations and, on the other hand, ions can move in a liquid but are macroscopically frozen in the metallic phase by the lattice arrangement. This means that there is no straightforward continuity of the charge transport across the interface. Consequently, a steady-state current flow, for example, from the electrolyte to the metal requires the transformation at the interface of the ionic flow in the electrolyte into an electronic flow in the metal. This is done by heterogeneous chemical reactions taking place at the interface, which allow electrons to be released by mobile species in the electrolyte and incorporated into the electron 'gas' in the metallic phase (anodic reaction) or, conversely, allow electrons leaving the electronic gas at the metal side to be trapped by an electrolyte species (cathodic reaction). (Remember that one of the most important characteristics of metals is that the valence electrons are free in a state that can be likened to a gas.) These heterogeneous (since they concern both the electrolyte and metallic phases) interfacial reactions entail the loss or the gain of electrons through a charge-transfer process (either oxidation or reduction). A single oxidation or reduction reaction is known as a half-cell reaction (since another reaction of the opposite type is needed to complete the full current path and create an electrochemical cell).

Whenever the current flow is straightforwardly related to one or several heterogeneous reactions, one refers to Faradaic current or, more generally, Faradaic processes because these phenomena can be described by a quantitative law called Faraday's law. The current flow across the interface can also be related to other types of electrochemical processes, namely capacitive processes, which correspond mostly to transient phenomena and will briefly be discussed in Section 1.02.2.4.2. Of much concern in corrosion processes, Faraday's law mathematically expresses the relationship between the electrical charge transferred during a heterogeneous reaction and the amount of mass transformed at the same time. This is the Lavoisier principle of conservation of mass extended to electrons. As shown in the following example, Faraday's law is the very origin of the relationship (extremely important in corrosion engineering) between the corrosion current (experimentally measured or estimated) and the corrosion rate (in terms of mass or thickness loss), in the case of uniform corrosion. Let us consider the case of a uniformly corroding iron plate. For a divalent corrosion reaction

$$\mathrm{Fe} \rightarrow \mathrm{Fe}^{2+} + 2\mathrm{e}^{-} \qquad [2]$$

the corrosion current density (the current density is the corrosion current normalized by the geometrical surface area and is a simple and intuitive way of comparing corrosion rates independently of the size of the metallic surface considered) corresponding to the consumption of a certain quantity of Fe moles per unit time and per unit surface can be expressed by Faraday's law, as

$$\frac{1}{S}\frac{\Delta n}{\Delta t} = \frac{j}{2F} \qquad [3]$$

where $\Delta n/\Delta t$ is the number of moles of iron consumed per unit time, S is the corroding surface area, j is the corrosion current density, and F is the Faraday constant. This constant represents the electrical charge of one mole of electrons, that is, $F = -Ne$, where N is Avogadro's number and e the charge on the electron ($F = -6.022\times10^{23} \times -1.602\times10^{-19} = 96\,486\,\mathrm{C\,mol^{-1}}$). For engineering applications, the expression of the corrosion rate in terms of thickness loss per year, for instance, is more useful:

$$\frac{\Delta\varepsilon}{\Delta t} = \frac{j}{2F}\,\frac{M}{\rho} \qquad [4]$$

where M is the molar mass of the corroding compound and ρ is its density. In the case of iron corrosion ($M = 55.84\,\mathrm{g\,mol^{-1}}$ and $\rho = 7.85\,\mathrm{g\,cm^{-3}}$), a uniform corrosion current density of $5\,\mu\mathrm{A\,cm^{-2}}$, corresponds to a thickness loss of $58\,\mu\mathrm{m\,year^{-1}}$. A convenient rule of thumb is that for most metals $1\,\mathrm{A\,m^{-2}}$ corresponds to a penetration rate of approximately $1\,\mathrm{mm\,year^{-1}}$.

Let us come back to the more general description of the processes related to a current flow. One of the simplest examples in electrochemistry concerns the interface between a platinum electrode and an electrolyte containing Fe^{3+} and Fe^{2+} ions. If an external power source imposes an electron flux from the metal towards the interface, a heterogeneous chemical reaction takes place at the interface. In this example, the transformation of ferric ions into ferrous ions takes place according to the reaction:

$$Fe^{3+} + e^- \rightarrow Fe^{2+} \qquad [5]$$

This reaction indicates that a certain amount of Fe^{3+} cations, proportional to the current, is transformed into Fe^{2+} ions, capturing the electrons coming from the metal and ensuring the continuity of current flow. This interface, on which a reduction reaction occurs, is called a cathode. In the case of a current flow in the opposite direction, electrons are produced by the redox reaction. Thus, the interface is the site of an oxidation reaction and is called an anode. **Figure 1** schematically illustrates this phenomenon for reaction [5]. The arrows represent the direction in which each reacting species moves (more rigorously, they indicate the direction of the corresponding mass flow vector).

It can be seen in **Figure 1** that, even in this very simple example, the current flow entails at least three important phenomena: electron transport inside the metal, ionic transport in the electrolyte, and the heterogeneous redox reaction, that is, charge-transfer reaction.

In classical electrochemical situations, the system comprises two interfaces and the existence of a steady-state current flow implies that one of the interfaces behaves as a cathode whilst the other plays the role of an anode; that is, one of them consumes the electrons produced by the other. Two typical scenarios are depicted in **Figures 2 and 3**. They illustrate, for instance, what happens in a mobile telephone when it is being used (its battery is discharging, **Figure 2**, or being recharged, **Figure 3**).

Figure 2 presents the situation in which there is a spontaneous flow of electrons produced by an interfacial oxidation reaction at the anode. These electrons go through a resistor to be consumed at the

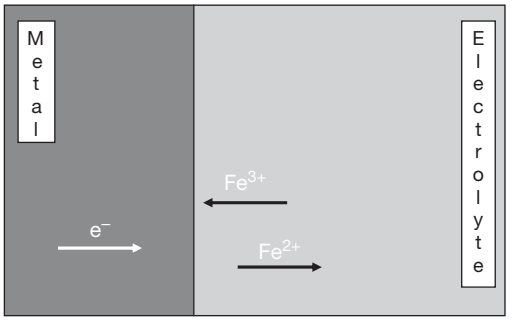

Figure 1 Schematic representation of an impermeable metal–electrolyte interface at which a reduction reaction takes place; the interface acts as a cathode.

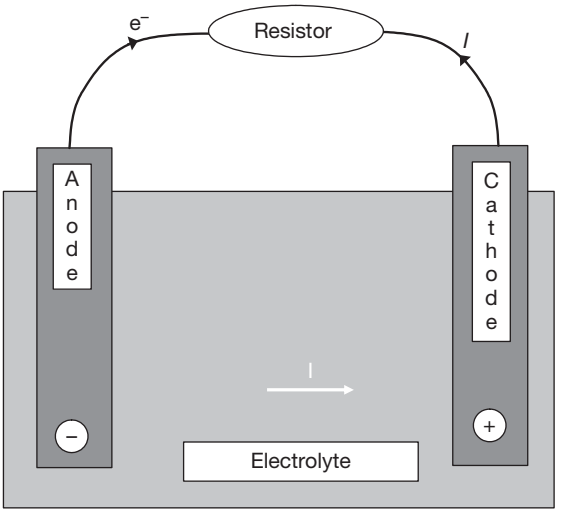

Figure 2 Electrochemical battery during discharge: electrons are delivered to the external circuit by oxidation at the anode (Red $\rightarrow$ Ox $+ ne^-$) and are consumed by reduction at the cathode (Ox $+ ne^- \rightarrow$ Red).

cathode by a reduction reaction. In that case, the chemical energy of the reactants is converted to electrical energy, which is then converted into thermal energy by the Joule effect in the resistor. For mobile telephones, the energy delivered by the electrochemical system is converted into light, sound, radio waves, etc. As soon as the discharge process leads to a chemical transformation, the recharge process requires the reverse reaction to occur. While the discharge reaction in **Figure 2** takes place spontaneously, the recharge reaction can only occur if an external power source is connected to the system, as illustrated in **Figure 3**. It is exactly like in mechanics when a ball that will spontaneously roll down a slope needs an external force to go up the slope. The electrode that was spontaneously a cathode is forced to work as an anode and the electron flow is reversed. It is worth noticing that the current and electron flows are identified by arrows in opposite directions, as illustrated in **Figures 2** and **3**, since by convention the current flow direction is given by the positive charge carriers.

In another international convention (IUPAC), largely accepted but not always respected, it is considered that the anodic and cathodic currents are positive and negative, respectively. As a consequence, when anodic and cathodic processes occur on the same electrode, as in corrosion processes, the current is then positive when it flows from the anodic areas to the electrolyte and negative when it flows from the electrolyte to the cathodic areas.

1.02.2.3 Electrochemical Reactions and Corrosion: Some Preliminary Remarks

In most corrosion processes, a single macroscopic interface is concerned. However, a system at rest, which is the most common corrosion situation, is a particular case of an electrochemical system under discharge analogous to that in **Figure 2** in the sense that the oxidation and reduction reactions are spontaneous. In contrast with **Figure 2**, no external circuit allowing the current to flow is available and the overall current flow is null since both the anodic and cathodic reactions take place at the same metallic surface. This idea can be easily handled by considering the example of galvanic coupling depicted in **Figure 4**, in which two different metals (iron and zinc) assembled together to form a single piece are exposed to an electrolyte rich in dissolved oxygen. In this situation, the zinc is an anode and hence corrodes whilst the iron tends to be protected since it plays the role of a cathode on which oxygen is reduced. It is important to notice that the fact that iron is a cathode does not mean that iron will necessarily be deposited on the metallic surface according to the reverse of reaction [2]. It means that the iron surface is the preferential site for cathodic (i.e., reduction) reactions. The exact nature of these reactions depends on the electrolyte and other important characteristics of the electrochemical systems that will be better discussed in **Section 1.02.2.4.1**. For the sake of clarity, the cathodic reaction is

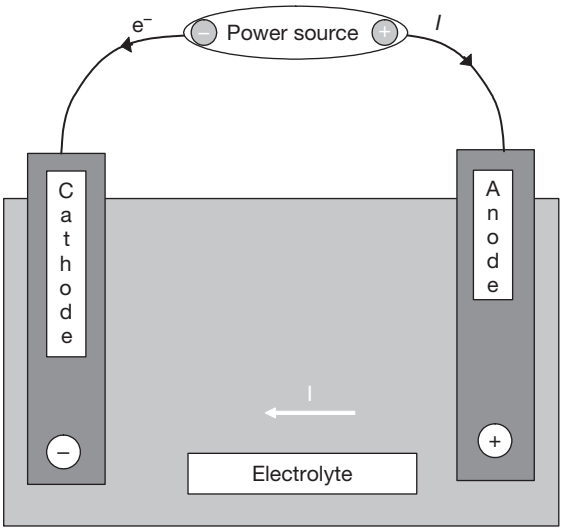

Figure 3 Electrochemical battery in charge: electrons are consumed by reduction at the cathode ($Ox + ne^- \rightarrow Red$) and produced by oxidation at the anode ($Red \rightarrow Ox + ne^-$).

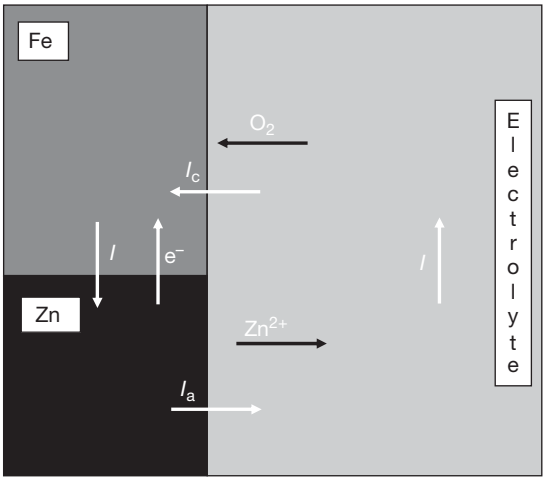

Figure 4 Null net current balance in a freely corroding system: galvanic coupling between iron and zinc in contact with an electrolyte rich in dissolved oxygen.

represented in Figure 4 by oxygen reduction, one of the most important reactions in corrosion processes.

Many similar situations with anodic and cathodic areas on the same electrode are encountered in corrosion, as when a metallic surface is not perfectly homogeneous, which is often the case. For instance, there are regions that are preferentially anodic, such as grain boundaries, intermetallic inclusions, zinc-rich phases in brasses, and so on. The existence of cathodic and anodic areas along the same surface can also be the result of inhomogeneous electrolytes, such as those in contact with partially submersed structures. Indeed, dissolved oxygen is easily available near the air–liquid interface, inducing a preferentially cathodic behavior of the metallic surface. For a completely uniform metallic surface immersed in a perfectly homogeneous electrolyte, the idea of a zero net current balance related to simultaneous anodic and cathodic reactions still holds, even if no preferential anodic or cathodic locations appear at the interface. Indeed, each surface site dynamically and randomly switch between anodic and cathodic behavior so that the overall net current is permanently zero and general corrosion occurs.

Thus, for the bimetallic surface in Figure 4 as well as for any system left at rest, the anodic, I_a, and cathodic, I_c, currents must perfectly and permanently balance out each other, so that no overall current flows to or from this closed system, so that:

$$I_{Zn} = I_a = -I_c = -I_{Fe} > 0 \qquad [6]$$

(The equality represented in eqn [6] is only true for the average behavior; short-term differences can be accommodated by charging or discharging of the double-layer capacitance, and this leads to the phenomenon of electrochemical noise.) It is important to note that in this equation, the anodic and cathodic currents are identical in absolute values. Also, this equation holds for currents, I_a and I_c, and not for current densities, j_a and j_c, defined as follows:

$$I_a = j_a S_a = -j_c S_c = -I_c \qquad [7]$$

where S_a and S_c are the surface of the anodic (zinc) and cathodic (iron) areas, respectively. Thus

$$j_a = |j_c|\frac{S_c}{S_a} \qquad [8]$$

or

$$|j_c| = j_a\frac{S_a}{S_c} \qquad [9]$$

If the surface areas of iron and zinc in Figure 4, and more generally the surfaces of preferential anodic or cathodic zones in any given electrode are different, eqn [8] clearly points out that the system may have very high partial current densities because of the surface ratio. This is extremely important in corrosion applications. As an example, let us go back to the iron–zinc example and consider the possibility of using zinc rivets to assemble large iron plates. Equation [8] immediately shows that the zinc rivets in contact with an electrolyte such as rain water corrode very rapidly because of the very high anodic (corrosion) current density related to the huge cathodic (iron)/anodic (zinc) surface ratio.

1.02.2.4 Basic Description of Metal–Electrolyte Interfaces

1.02.2.4.1 Elementary steps and intermediate interfacial species

The simplified and common aspects of electrochemical reactions taking place at metal–electrolyte interfaces considered up to now deserve a better although still simple description. The first important aspect is that the overall charge-transfer reactions involved in corrosion processes are often the consequence of complex interfacial phenomena that can be described by a more or less intricate reaction mechanism comprising several intermediate elementary steps. The reactive species implied in this mechanism are not only the ensemble of reactants and products of the overall reaction such as electrons, the metal itself, ions or dissolved gas as in the previous examples, but also other species produced as reaction intermediates.

Intermediate species can be very important in the kinetics of heterogeneous phenomena. In corrosion, these species are surface adsorbates that physicochemically adhere to the metallic surface, such as water itself, neutral species or anionic species. Let us consider two examples of complex mechanisms concerning corrosion processes. The first is the mechanism of nickel corrosion (to a first approximation, this is also the mechanism of iron dissolution) proposed in the literature[1,2]:

$$\begin{aligned} Ni + H_2O &\rightleftharpoons NiOH_{ads} + H^+ + e^- \\ NiOH_{ads} &\longrightarrow Ni^{2+} + OH^- + e^- \end{aligned} \qquad [10]$$

The simple algebraic addition of both elementary (single electron) reactions gives the global reaction [11]:

$$Ni \longrightarrow Ni^{2+} + 2e^- \qquad [11]$$

(or reaction [2] in the case of iron). This multielectronic reaction is the overall and simplified chemical representation of a more complex process. It is also

important to notice that the intermediate adsorbed species (identified by the subscript 'ads') plays an important role in the kinetics of the overall reaction. If the first ($NiOH_{ads}$ adsorption) or the second ($NiOH_{ads}$ desorption giving Ni^{2+}) elementary step is hindered, the overall Ni dissolution is slower since Ni dissolution occurs through two consecutive steps.

Adsorbates can also be produced by cathodic reactions, an important example coming from the proton reduction on metallic surfaces, roughly represented as

$$2H^+ + 2e^- \longrightarrow H_2 \qquad [12]$$

but actually composed of two (or more) intermediate elementary steps, as those of the so-called Volmer–Heyrovski route[3]:

$$H^+ + e^- \rightleftharpoons H_{ads} \qquad [13]$$
$$H_{ads} + H^+ + e^- \longrightarrow H_2 \qquad [14]$$

It is easily seen that the addition of the Volmer (reaction [13]) and Heyrovski (reaction [14]) elementary steps gives the global representation of reaction [12]. (An alternative to the Heyrovski reaction, known as the Tafel reaction, involves the direct combination of two adsorbed hydrogen atoms to form a hydrogen molecule – this dominates at low overpotentials.) Adsorbates can also play a critical role in the overall kinetics of corrosion since they constitute some of the elementary building blocks of corrosion mechanisms.[4] It is interesting to note that, under certain conditions, the adsorption site can be considered as temporarily blocked by the H_{ads} adsorbate from the point of view of corrosion,[5,6] which means that it is not able to dissolve as long as this site is occupied by H_{ads}. This is obviously not an evidence of an effective protective role of H_{ads} against corrosion, otherwise acidic solutions would not be aggressive, which is evidently far from true. It is worth recalling that the hydrogen evolution reaction in acidic media is rather fast, so that H_{ads} is transformed into H_2 at a significant rate. In addition, the active dissolution rate, for instance of iron, is also fast. Even if only 1% of the surface area is devoted to this process, the corrosion current density is far from zero. This brief discussion illustrates the complexity of corrosion kinetics. In other situations, the protective role of adsorbates as blocking agents is extremely important and is fully employed in the development of inhibitors for corrosion protection.[7,8] Very often, in the presence of organic inhibitors, the cathodic reaction rate is slowed down markedly, whereas inorganic substances, so-called anodic inhibitors, are more effective at reducing the metal dissolution rate. Since the corrosion takes place at a zero overall current, the decrease in the rates of either of these processes (anodic or cathodic) slows down the net corrosion rate.

Reactions [10]–[14] are simple mechanisms involving single-adsorbate reactions. Other important reactions, such as iron dissolution[9–14] or oxygen reduction,[15,16] can involve several adsorbates, the identification of which is often a difficult task. Besides these complex features of redox reactions with the presence or the absence of intermediate species, the current flow across the interface is also dependent on the transport of reactive species in the electrolyte. Hence, a complete or at least better description of the kinetics of the metal–electrolyte interface must encompass the behavior of these charge carriers in the interfacial region.

1.02.2.4.2 The electrical double layer

In a first approach, this description can be made simpler by considering a metal–electrolyte interface at which no redox reaction takes place so that no Faradaic current flows across it. This interface is thus impermeable and nonreactive like the first one in scheme [1] and the only observable phenomenon is the accumulation of species at both sides of the interface. When these species are electrically charged, important electrical constraints appear. Indeed, since both metallic and electrolytic phases are conductive, the attractive and repulsive electrical forces exerted on the charge carriers imposes electroneutrality (that means a net charge equal to zero) of any significant volume of metal and electrolyte. (Strictly there can be a net positive or negative charge at a point. This is described by the Poisson equation, which states that the local charge density $=-\varepsilon\varepsilon_0\, d^2\varphi/dx^2$, where φ is the local potential, ε the dielectric constant and ε_0 the permittivity of free space. However, $\varepsilon\varepsilon_0$ is so small that the net charge is negligible except in exceptional circumstances (such as at the metal–solution interface).) Significant deviations from electroneutrality can only exist at very short distances, as in a water molecule composed of two H^+ and one O^{2-}. Nevertheless, due to the intrinsic differences in the conducting mechanism in each phase (electronic conduction in the metal and ionic conduction in the electrolyte), a local deviation from electroneutrality occurs at the interface. For example, as schematically represented by a solid line in **Figure 5**, an excess of electrons at the metallic side can permanently exist provided that positive charges (for instance, an excess of cations) are in excess at the other side.

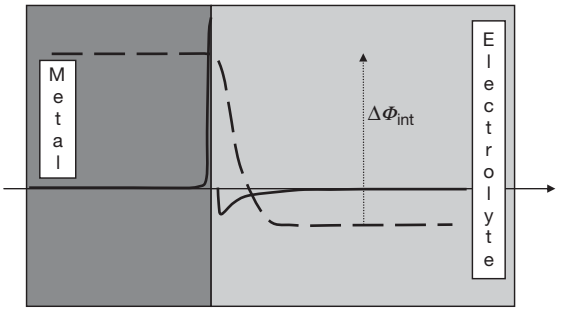

Figure 5 Schematic representation of the electrical charge density (solid line) and of the induced potential Φ (dashed line) at both sides of the interface.

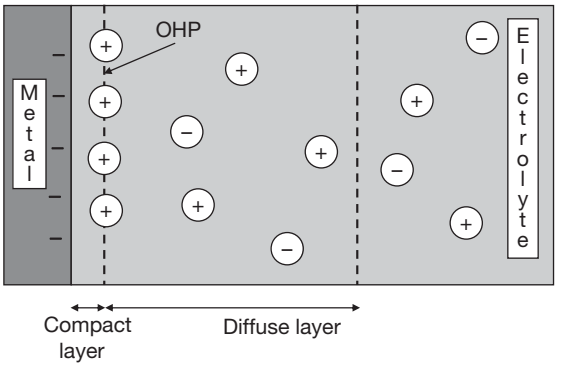

Figure 6 Simplified scheme of the electrolyte double layer: compact and diffuse layers with solvated cations and anions in the electrolyte.

Even in these conditions of local charge separation, the overall electroneutrality must be respected, which means that these face-to-face opposite charges in excess at the interface must be perfectly balanced out. These spatial and electrical configurations are essentially the same as those of an electrical capacitor composed of two parallel plates electrically charged with opposite signs. However, this electrochemical capacitor typically has a distance between the plates of only a few nanometres. The charge distribution across the interface entails a potential shift $\Delta\Phi_{int}$ across the interface, as illustrated by the dashed line in Figure 5. In steady-state conditions, the electroneutrality being respected, no current flows across the electrochemical capacitor. Nevertheless, any potential or current perturbation of the system may induce a local rearrangement of the charge distribution at each side of the interface, which leads to a transient flow of 'capacitive current.' As a consequence, the measured current in an electrochemical experiment generally includes the effects of this capacitive process, in addition to the Faradaic response.

As shown schematically in Figure 5, the distribution of the excess charge at each side of the interface is asymmetric. It is sharply confined in a virtually zero volume at the metallic side, but spread out over a nonnegligible distance at the other side. This electrolyte zone, in which the electroneutrality is not respected, is called double layer[17,18] as it is frequently divided into a first layer, close to the metallic surface, called the 'compact layer' and a second, called the 'diffuse layer,' as represented in Figure 6.[19]

In order to better understand how the double layer is configured, let us remember that ions in an electrolyte are solvated (roughly speaking, for an aqueous electrolyte, they are wrapped by water molecules). As shown in Figure 6, the distance between the closest centers of the ions and the metallic surface defines the so-called outer Helmholtz plane (OHP),[18] which is the boundary of the compact layer (thickness of about 1 nm). Under certain conditions, ions can show specific adsorption behavior at the interface (called electrosorption) so that they can penetrate into the compact layer. As a consequence, they establish a new lower minimal approach distance of the closest adsorbed ion centers that defines the inner Helmholtz plane (IHP), which logically modifies the potential profiles in this region.

Beyond the Helmholtz plane, the double layer spreads into the diffuse layer. The thickness of this layer depends on the ionic composition of the electrolyte. It is about 1 μm in pure water, whereas it may vary in an electrolytic medium from several tens to a fraction of nm depending on the salt concentration. For instance, the typical thickness of a diffuse layer varies from 6 to 20 nm when the concentration of the ionic species in the electrolyte decreases from 0.01 to 0.001 mol l^{-1}. Thus, in the presence of a supporting electrolyte (auxiliary electrolyte constituted of nonreactive ions at high concentration to increase the electrolyte conductivity) the diffuse layer becomes much thinner.

1.02.2.4.3 Current and mass transport mechanisms

As mentioned in the preceding sections, electrochemical kinetics encompasses not only interfacial reactions but also the transport of mobile species inside the conductive phases to and from the interface. Without going into mathematical details, the current in a given infinitesimal volume is the resultant of macroscopic movements of all the charged species in this

volume. A complete discussion on mass transport and its influence on electrochemical processes can be found elsewhere.[20–22] In this chapter, it is sufficient to consider that the mass transport phenomena can be macroscopically described with three types of driving force, roughly portrayed as follows:

- *Migration* is the movement of charged species under the effect of an electrical field (which is an electrical potential gradient). It may be neglected for the electroactive species in the presence of a supporting electrolyte.
- *Diffusion* is a process analogous to that of migration in which species are transported under the effect of a concentration gradient towards the regions of low concentration, which tends to homogenize the solution.
- *Convection* is the relative movement of a fluid medium, liquid or gaseous, which takes place even for macroscopically stationary electrolytes. This is the case of natural convection caused by mechanical vibrations or by density gradients, such as those induced by local differences in temperature between the wall of a reservoir and the bulk solution, by gas evolution or by the release of dense ions into solution. Convection can also be forced by mechanical stirring or, very often in electrochemistry, by using rotating disk electrodes or impinging jet cells.

In electrochemistry, under certain experimental conditions (see examples below), diffusion phenomena are negligible compared to migration and convection at a distance sufficiently far from the interface. Hence, the region in which diffusion cannot be neglected, compared to other mass transport mechanisms, is defined as the diffusion layer. This zone close to the interface plays a crucial role in the kinetics of electrochemical phenomena. It can spontaneously appear because of the interfacial depletion or abundance of reactants induced by the (electro) chemical reactions, since only the species present at the interface are able to react. Depending on the kinetics of the reactions, the interfacial concentrations can be markedly different from those in the bulk solution (the region where the concentration is homogeneous) and are a key parameter for the description of electrochemical and hence corrosion phenomena.

In the absence of convection, the current flow or simply the natural evolution of a metal–electrolyte interface at rest, as in corrosion processes, induces the formation of a diffusion layer that grows continuously with time. The changes in the electrolyte concentration generated by chemical perturbations at the interface, move progressively towards the bulk solution as the diffusion front progresses. However, convection often occurs in practice, both natural convection and especially forced convection, as in water distribution networks, pipelines, and many industrial systems. An accurate and quantitative analysis of convection phenomena is covered in another section of this book but the general result of Nernst's model illustrated in **Figure 7** can be retained. This model predicts that in spite of the presence of convection, there is a region close to the interface (called Nernst layer) in which the convective forces vanish since the electrolyte velocity at the interface is actually zero. This is the consequence of the existence of viscoelastic forces at the interface that prevent the liquid phase from sliding along the solid phase and lead to a continuous decrease of the convection effects from the bulk to the interface. The model approximates this monotonic evolution by assuming a discontinuity between the bulk and the Nernst layer. Mass transport is controlled by diffusion and migration inside this layer and the reactants exhibit concentration gradients, while outside this layer the electrolyte is stirred by convection and, therefore, the reactant concentrations are considered to be homogeneous. The thickness of the Nernst layer, also called diffusion layer, depends on the stirring conditions. Typical thicknesses are 10 and 300 µm for forced and natural convection, respectively.

1.02.2.4.4 Potential and concentration profiles across the interface

The spatial variations of the reactant concentrations and of the electrical potential in the region close to

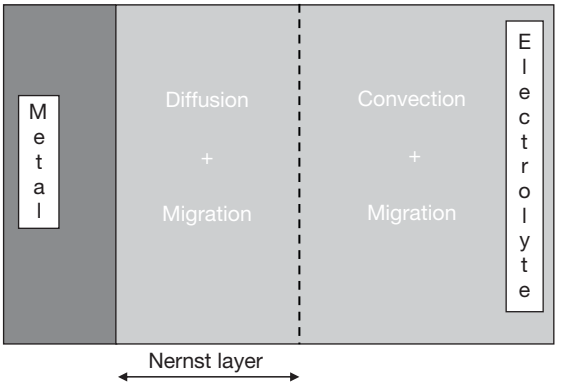

Figure 7 Simplified schematic representation of the metal–electrolyte interface for the Nernst mass-transport model.

the interface, play an important role in the accurate modeling of the kinetics of electrochemical phenomena and hence of the corrosion processes. First of all, it is important to point out the differences in the thickness of the double layer (typically a few nanometres) and that of the diffusion layer (typically a few tens of micrometres). Figure 8 presents the schematic concentration and potential profiles across the double and diffusion layers. In most cases, the diffusion layer is actually the most pertinent scale for a convenient analytical approach, so that it is sufficient to define the electrical potential and the reactant concentrations at the boundary of the double layer. Indeed, the double layer being so thin at this scale, the interfacial concentration C_{int} of a reactant, that is, the concentration at the Helmholtz plane (see the zoom in Figure 8), which is the key parameter concerning the kinetics of the mass transport and redox reactions, may be considered as constant in the double layer. In the same way, even if the potential varies strongly in the double layer, it is sufficient to consider the driving force of the redox reactions as being controlled by the interfacial potential difference $\Delta\Phi_{int}$, that is, the potential difference across the double layer. In the diffusion layer and in the electrolyte bulk, the potential will vary according to

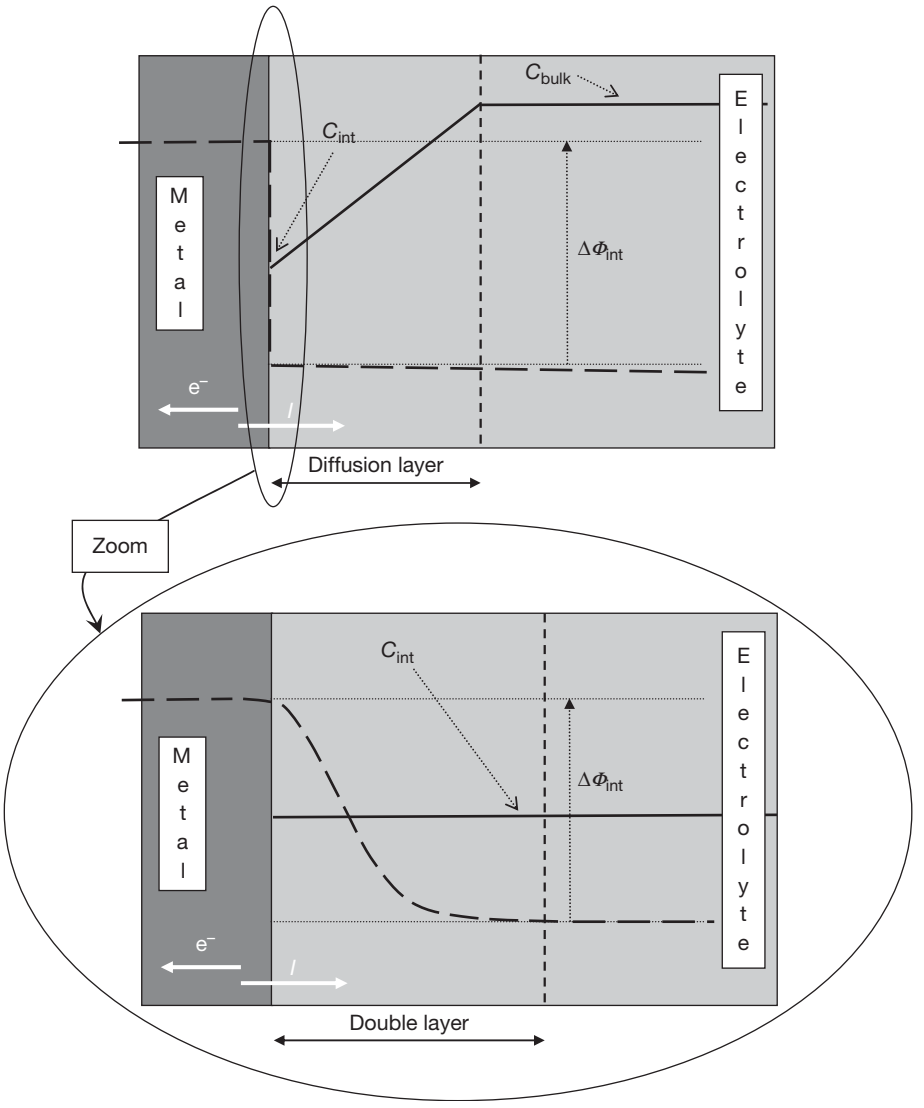

Figure 8 Schematic representation of the metal–electrolyte interface: concentration (solid line) and potential (dashed line) profiles.

the solution conductivity and current density, as in Figure 8 (ohmic drop effect, see more details in Section 1.02.6.1.2).

1.02.3 Electrochemical Equilibrium

1.02.3.1 Definition and Introductory Remarks

Electrochemical equilibrium is one of the major concepts that needs to be correctly handled to really understand corrosion processes. A proper definition should take into account the fact that the equilibrium of an electrochemical system involves the equilibrium of all materials and all interfaces. In a true equilibrium, no macroscopic gradient of any physical variable (temperature, pressure, concentration, etc.) exists in the bulk of any phase and there is no net macroscopic flux across any interface. Thus, in the framework of the present work, the electrochemical equilibrium will be frequently related to an interface state in which no overall current flows to or from the interface.

Before going further with the analysis of electrochemical equilibrium, two critical remarks must be kept in mind. Firstly, some systems can show a very slow evolution constituting a quasisteady behavior that is not a true equilibrium. As seen below, passive stainless steels can be considered as nonevolving systems under certain conditions, but they are actually far from being at thermodynamic equilibrium. The knowledge of electrochemical equilibrium characteristics is, however, still indispensable for the comprehension and the macroscopic global description of the quasisteady state of such systems and most corrosion processes. Another major point is that the equilibrium state necessarily means a net zero current, but the converse is far from being true. As already pointed out in Section 1.02.2.3, for any corroding system freely evolving in any aggressive media, the net current flowing to or from the interface is also zero, but the system will not be in a state of true equilibrium.

1.02.3.2 Electrochemical Equilibrium as a Dynamic State: the Exchange Current Density

Let us consider a static body in equilibrium. No net macroscopic movement is expected (the body does not move provided the ensemble of variables remains constant), but each constituent particle spins, vibrates, or even moves due to thermal agitation. A static object is hence an intrinsically dynamic system at the molecular level and this is not inconsistent with its macroscopic motionless state. The same holds for an electrochemical system: reaching and observing the electrochemical equilibrium absolutely does not indicate that, besides the thermal agitation, the interface is frozen without any charge transfer going on with time. For example, a copper bar immersed in a weak acid solution (no dissolved oxygen present and copper oxides are not stable) containing a certain amount of copper Cu^{2+} cations undergoes the forward–backward redox reaction at equilibrium:

$$Cu \rightleftharpoons Cu^{2+} + 2e^{-} \qquad [15]$$

In any given time interval the same number n of moles of Cu^{2+} and $2n$ of electrons is produced by metal dissolution (corresponding to an anodic current I_a) and concomitantly consumed by metal deposition on the metallic surface (corresponding to a cathodic current I_c). Dissolution and deposition are the forward and backward elementary steps of the same overall reaction [15] and take place with the same rate, thus yielding $I_a + I_c = 0$ or $|I_a| = |I_c| = I_0$, I_0 being called the exchange current. Provided that the ensemble of physicochemical parameters (temperature, pressure, etc.) is kept constant, the dynamic zero current balance between the forward and backward reactions implies that the system does not evolve with time: the Cu^{2+} concentration, as well as the mass of metallic copper, remains unchanged *ad aeternum* or, at least, as long as the equilibrium holds (as seen later, the equilibrium can be broken as a consequence of the polarization of the system under the action of a parallel reaction, such as oxygen reduction that leads to copper corrosion: the system then evolves in nonequilibrium conditions as for every corrosion process). It can then be concluded that the exchange current is an important attribute of the dynamics of the system. Indeed, the constant Cu^{2+} (or M^{z+} for a more general M^{z+}/M couple) concentration, characteristic of the electrochemical equilibrium, may result from very different interfacial behaviors. High values of I_0 (for instance, $10^{-1}\,A\,cm^{-2}$ for aqueous systems at room temperature) indicate that the system is very active with many reactive interactions per unit time in each direction (anodic and cathodic), whilst low I_0 values (typically $10^{-5}\,A\,cm^{-2}$ for aqueous systems at room temperature) indicate slow systems. This is a key concept in reaction kinetics as discussed later in this chapter.

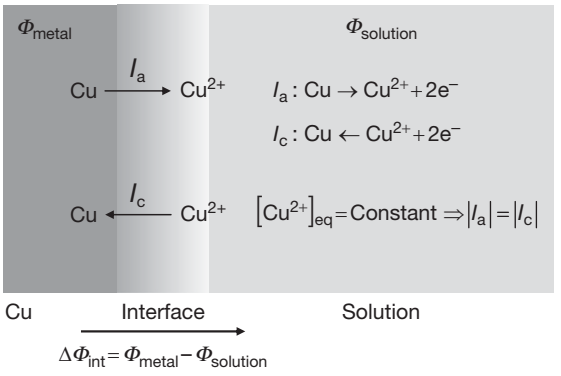

Figure 9 Schematic representation of the potential difference and current exchanges across the metal–electrolyte interface for a Cu^{2+}/Cu equilibrium.

The asymmetric distribution of electrical charges at both sides of the interface, as depicted in **Figure 9** (charged cations at one side, electrons in metallic sites at the other), entails a well-defined potential difference, $\Delta\Phi_{int} = \Phi_{metal} - \Phi_{solution}$. The $\Delta\Phi_{int}$ value thus depends on the thermodynamic characteristics of each phase – in particular their composition – and is related to the equilibrium potential, E_{eq}, as will be formalized in the next section.

1.02.3.3 Formal Expression of E_{eq}: the Nernst Law for the M^{z+}/M Couple

Classical thermochemistry deals with the transformation of a given species at constant temperature and pressure leading to the concept of Gibbs free energy. In the case of charged species intervening in electrochemistry, an electrochemical Gibbs free energy $\overline{G}$ can then be defined. As for any electrical charge q, a part of this electrochemical energy is electric and is related to the work, $q\Phi$, supplied for moving this particle inside an electrical field associated with the potential Φ. For one mole of the M^{z+} cation, the electrical contribution to the total electrochemical energy $\overline{G}$ can be written as

$$q\Phi = z|e|N\Phi = zF\Phi \qquad [16]$$

Hence, the electrochemical free energy of M^{z+} usually expressed as the addition of a chemical term, G, to the electrical term, $zF\Phi$:

$$\overline{G} = G + zF\Phi \qquad [17]$$

For any reactive system, it can be demonstrated that the thermochemical equilibrium is related to the absence of change in the reaction free energy, in this case, electrochemical, $\Delta_r\overline{G} = 0$, where the subscript r stands for any possible reaction. The electrochemical reaction free energy decomposition in chemical and electric terms as in eqn [17], entails the important conclusion that the equilibrium of a redox reaction involving z electrons sets up an interfacial potential difference $\Delta\Phi_{int}$ expressed as a function of the chemical reaction free energy. It can be demonstrated that, for reaction [18][23]:

$$M \rightleftharpoons M^{z+} + ze^- \qquad [18]$$

one has

$$\Delta_r\overline{G} = 0 \Rightarrow \Delta\Phi = \frac{\Delta_r G}{zF} \qquad [19]$$

The change in the chemical free energy can be mathematically expressed as[24,25]

$$\Delta_r G = \Delta_r G^0 + RT\ \ln\frac{a_{M^{z+}}}{a_{metal}} = \Delta_r G^0 + RT\ \ln[M^{z+}] \qquad [20]$$

where the superscript indicates that all reactants are in a standard state, and R is the gas constant ($8.31\,J\,mol^{-1}\,K^{-1}$). The symbol a denotes the species activity, which is equal to 1 in the standard state and is considered as unity in the right-hand side of eqn [20] for the metal. Besides, as an approximation that is sufficient for dilute solutions, it is assumed that the cation activity is equal to its concentration (represented by square brackets) in moles per liter.[26] According to eqn [19], the potential difference $\Delta\Phi_{int}$ associated with reaction [18] can be expressed as

$$\Delta\Phi_{int} = \Delta\Phi^0_{int} + \frac{RT}{zF}\ln[M^{z+}] \qquad [21]$$

Equation [21] is however experimentally useless, since the $\Delta\Phi_{int}$ values are not directly measurable. Indeed, even if the metallic phase can be connected to one of the terminals of a voltmeter with a conducting wire, the other terminal of the voltmeter must be connected to a probe dipped in the aqueous phase. The potential difference, $\Delta\Phi_{probe}$, between the probe (necessarily conductive to allow potential measurements) and the aqueous phase must be taken into account in addition to the potential difference, $\Delta\Phi_{M^{z+}/M}$, of the metal–solution interface in the presence of the M^{z+}/M couple under investigation. A voltage $\Delta\Phi_{M^{z+}/M} - \Delta\Phi_{probe}$ is then actually measured. To be able to give a value to the $\Delta\Phi_{M^{z+}/M}$ term, the solution is to work with a reference system to which all electrochemical potentials are referred.

The reference system chosen is the standard hydrogen electrode (SHE) related to the H^+/H_2 equilibrium, in which the reactants are in the standard state. By convention, a 0 V value is attributed to $\Delta\Phi_{probe}$ in this case at all temperatures. The SHE is difficult to realize experimentally, since it requires that the acid solution has a hydrogen ion activity of 1 (which requires a molarity greater than 1, of about 1.19 mol l^{-1} for HCl), and a hydrogen activity of 1 (which requires a partial pressure of hydrogen of 1 bar plus an allowance for the vapor pressure of the solution). A very similar electrode (with a very similar potential) is obtained by bubbling pure hydrogen gas at the surface of a Pt electrode in a normal (molar) acidic solution, which constitutes the so-called normal hydrogen electrode (NHE). **Figure 10** illustrates the experimental assembly of a NHE and the complete apparatus for the measurement of the Ag^+/Ag potential.

It is clear that the experimental set-up depicted in **Figure 10** is impractical for daily experiments. This is why several other very stable redox couples are used for reference electrodes as presented in **Section 1.02.6**. In every potential measurement, the potential determined includes both the desired metallic couple and the reference one. In such conditions, the usual notation introduces the electrode potential E as

$$E = \Delta\Phi_{M^{z+}/M} - \Delta\Phi_{ref} \qquad [22]$$

This means that the potential value read on the voltmeter in **Figure 10** is not the actual potential value of the metallic couple, it is the potential difference between two redox couples.

Finally, adding $-\Delta\Phi_{ref}$ at both sides of eqn [21] leads to the usual form of the Nernst equation applied to corrosion studies (where $[M^{z+}]$ is given in mol l^{-1}) giving the equilibrium potential, E_{eq}, of the redox reaction [18]:

$$E_{eq} = E^0 + \frac{RT}{zF}\ln\,[M^{z+}] \qquad [23]$$

or, in the more convenient decimal logarithmic scale ($RT\ln(10)/F = 0.059$ V at 25 °C):

$$E_{eq} = E^0 + \frac{0.059}{z}\,\log\,[M^{z+}] \qquad [24]$$

It is worth noting that the charge transfer process physically takes place at the metal–electrolyte interface. This means that $[M^{z+}]$ in the Nernst equation corresponds to the interfacial concentration of M^{z+}. Since there is no concentration gradient in solution at the electrochemical equilibrium, $[M^{z+}]$ is also the M^{z+} concentration in the solution bulk. However, in nonequilibrium conditions, necessarily the case when corrosion occurs, the interfacial concentration, C_{int}, is generally different from the bulk concentration, C_∞, and the electrode potential is no longer related to C_{int} or C_∞ in a simple way. Nevertheless, for some redox couples, termed Nernstian, which are almost always fast and reversible in a kinetic sense, a local near-equilibrium can be considered at the interface so that the electrode potential obeys a Nernst-like equation:

$$E(I \neq 0) = E^0 + \frac{0.059}{z}\,\log\,C_{int} \neq E_{eq} \qquad [25]$$

The Nernst equation is an extremely rich tool for a first approach of the analysis and comprehension of corrosion processes, as shown below. Let us first note that E^0, the equilibrium potential for the couple M^{z+}/M in the well-defined standard state, is a thermodynamic constant that can be easily found in tables and reference books.[27] **Table 1** gives some important examples in the context of corrosion.

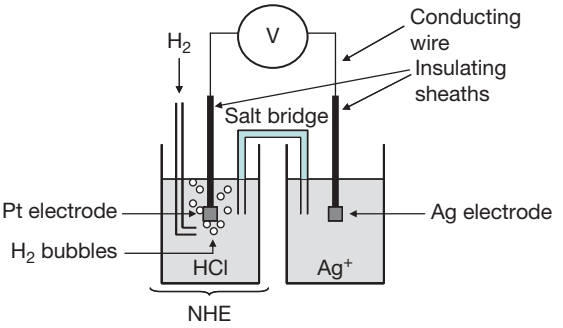

Figure 10 Experimental set-up for measuring the Ag^+/Ag potential difference, $\Delta\Phi_{Ag^+/Ag}$, versus a normal hydrogen electrode.

Table 1 Standard electrochemical equilibrium potential values of redox couples

Couple	*E^0 (V_{SHE})*
Au^{3+}/Au	1.43
Ag^+/Ag	0.79
Cu^{2+}/Cu	0.34
H^+/H_2	0
Ni^{2+}/Ni	−0.26
Fe^{2+}/Fe	−0.44
Zn^{2+}/Zn	−0.76
Al^{3+}/Al	−1.33

A first glance at Table 1 shows that noble metals such as gold and silver for which corrosion is not expected, have high positive values (hence called noble potentials), whilst those which are promptly recognized as corroding metals (Fe, Zn) have low (less noble) E^0 values. It then clearly appears that E^0 gives relevant information on the tendency of each metal to corrode. An apparent contradiction appears in the case of Al, which nonexpert common experience would describe as corrosion resistant. In reality, from a thermodynamic point of view, aluminum is actually extremely reactive and easily transformed into Al^{3+}. However, this reaction leads to the formation of a very homogeneous and corrosion-resistant film on the metallic surface, in a self-protective process called passivation, largely discussed elsewhere in this book. For the purpose of this chapter, it is important to retain this false paradox as the consequence of the fact that the Nernst equation is the result of a thermodynamic treatment concerning only the first formation of Al^{3+} and not the solid protective oxide formation, though thermodynamically predicted, as shown in the next section.

It is also easy to see from the Nernst eqn [23], that changes in cation concentration yield changes in the equilibrium potential. The equilibrium potential of any metal in contact with a solution containing the corresponding cation can be easily calculated for a given cation concentration. As an example, the equilibrium potential of Zn with $[Zn^{2+}] = 10^{-2}\,mol\,l^{-1}$ is $E_{eq} = -0.76 + 0.0295 \times (-2) = -0.82\,V_{SHE}$ according to eqn [24] and Table 1. If the potential is shifted, for instance, to $-0.7\,V_{SHE}$, the Nernst equation predicts that Zn is no longer at equilibrium with $[Zn^{2+}] = 10^{-2}\,mol\,l^{-1}$, but with $[Zn^{2+}] = 10^{2}\,mol\,l^{-1}$, that is a 10 000-fold increase in concentration. This means that Zn will corrode, liberating Zn^{2+} cations to the solution until the cation concentration predicted by the Nernst equation is reached and a new equilibrium is established. It is then clear that during a certain time needed for electrolyte homogenization at this new Zn^{2+} concentration, a positive (anodic) current appears: the system is transiently out of equilibrium. Alternatively, if the new potential value is lower than that of the initial equilibrium, it is easy to deduce that a certain amount of cations have to be reduced and deposited on the metallic Zn surface to diminish the cation concentration in solution. The value of the potential shift from the equilibrium potential

$$\eta = E - E_{eq} \qquad [26]$$

is independent of the reference employed and is called overpotential. The above discussion can be summarized as follows:

$E > E_{eq},\ \eta > 0$ possibility of metal dissolution (i.e., corrosion)

$E < E_{eq},\ \eta < 0$ possibility of electrodeposition

1.02.3.4 Some More Complex Applications of the Nernst Law

Up to now, only the archetypical corrosion redox couple M^{z+}/M has been dealt with. Nevertheless, it is important to consider the more general approach of the Nernst law used for other redox couples. Some important examples concerning acid–base properties will be treated in Section 1.02.3.5. As a first example, let us consider here a solution containing complexing ions, for instance, an aqueous electrolyte with a high concentration of chloride ions (Cl^-) in contact with an iron plate, thus undergoing corrosion. In that case, the equilibrium potential of the complex couple $FeCl^+/Fe$:

$$Fe + Cl^- \rightleftharpoons FeCl^+ + 2e^- \qquad [27]$$

can be written according to the Nernst law:

$$E_{eq} = E^0 + \frac{0.059}{2}\log\frac{[FeCl^+]}{[Cl^-]} \qquad [28]$$

Another application of the Nernst law concerns reactions with adsorbed species. As explained in the preceding sections, even if the balance of reactive phenomena could be written according to the overall M^{z+}/M redox reaction, intermediate species are frequently adsorbed on the metallic surface and play an important role in corrosion processes. Without going through the mathematical details of the exhaustive theoretical treatment of the interface, a very brief thermodynamic description of the simplest adsorption models can be presented. In the case of ideal systems, those in which no interaction between adsorbates occurs, the activity of an adsorbed species is given by its fractional covering ratio θ, defined as the ratio between the number of adsorbed species and the maximal number of adsorbed species when the surface is completely covered. In the previous example of Ni (or Fe) corrosion illustrated by reaction [10], the Nernst equation can be derived from the reaction explicitly indicating the free metallic sites available for adsorption:

$$Ni + H_2O + s \rightleftharpoons NiOH_{ads} + H^+ + e^- \qquad [29]$$

Since there is a single adsorbed species, the number of free sites is proportional to $1-\theta$ so that the Nernst law takes the following form (remember that $pH = -\log[H^+]$):

$$E_{eq} = E^0 - 0.059pH + 0.059\log\frac{\theta}{1-\theta} \quad [30]$$

Equation [30] is the mathematical representation of the so-called Langmuir isotherm, often represented as

$$\frac{\theta}{1-\theta} = \frac{K}{[H^+]} \quad [31]$$

where K is a potential-dependent thermodynamic constant.

In contrast with the assumption of the Langmuir-type isotherm, it is often necessary to take into account the possibility of interaction – attraction, repulsion – between adsorbates, mainly for high covering rates θ. This is achieved by introducing activity coefficients in the Nernst law (eqn [31]). The most usual model dealing with these nonideal electrochemical systems is the Frumkin isotherm that gathers the nonideal attributes in the form of an exponential function of the covering rate:

$$\frac{\theta}{1-\theta}\exp(g\theta) = \frac{K}{[H^+]} \quad [32]$$

where g is a constant. $g>0$ and $g<0$ correspond, respectively, to repulsive and attractive interactions between the adsorbates. With $g=0$, no interaction is expected and the Langmuir isotherm is retrieved.

1.02.3.5 Applications of the Nernst Law to Pourbaix (*E*–pH) Diagrams

An important application of the Nernst law for corrosion applications is the potential–pH diagram, also known as the Pourbaix diagram in honor of Marcel Pourbaix's exhaustive work devoted to the calculation, interpretation, and diffusion of those diagrams.[28] The importance and high usefulness of Pourbaix diagrams come from the fact that corrosion is not simply a matter of redox reactions like the basic reaction [2], but very frequently involves species with acid–base properties, such as water itself (remember that most corrosion phenomena are in fact related to aqueous corrosion). Also important for its wide applicability, is the very wide range of in-service conditions of metals that may be susceptible to corrosion. Indeed, corrosion occurs in widely differing environments in terms of both pH (from acidic environments to alkali industry, or very basic mortars and cements) and potential (highly oxidizing atmospheres, rich in oxygen or nitrates, or reducing atmospheres as in deaerated closed water circuits).

In this section, the main principles of Pourbaix diagrams and rough guidelines for their calculation are introduced. With the help of three typical and important cases (gold, iron, and aluminum), the large amount of information contained in those diagrams is shown. Their key objective is, for a given metal–electrolyte system at known constant temperature and pressure, the establishment of domains of thermodynamic stability or predominance of any potential species for the entire range of pH and electrode potential. As a result, for practical purposes, the whole inventory of service-life conditions of an interface can be represented. It then allows the global thermodynamic predictions of the behavior of a given metal–electrolyte system (corrosion, immunity, oxide formation, etc.) to be accessed readily.

While more complex diagrams, including the formation of complexes in corrosive media, can of course be established, only pure metal–water systems will be considered in this chapter. The starting point of Pourbaix diagram is based on the fact that there are three types of electrochemical equilibrium for a metal–water system, those depending only on the electrochemical potential, those depending only on the pH, and those depending on both potential and pH. The general guidelines of the diagram construction are given below for a simple example of a metal M that can dissolve into cations M^{z+} or form a solid oxide M_2O_z.

1.02.3.5.1 Purely potential-dependent equilibrium

This is the case of the simple redox reaction [18] between the pure metal and its cation for which the equilibrium is described by the Nernst equation [24], as discussed above. For a given M^{z+} concentration (different Pourbaix diagrams have to be drawn if this value is changed), E_{eq} is independent of pH and is represented in an E/pH diagram as a horizontal line, as shown in **Figure 11(a)**. Hence, regardless of the electrolyte pH, the metal M is in thermodynamic equilibrium with its cation at the given M^{z+} concentration only on this line. For $E<E_{eq}$, M^{z+} cations reduce to metal, while for $E>E_{eq}$ the metal undergoes dissolution to form cations in solution. This indicates that, for this kind of equilibrium and a given M^{z+} concentration, the thermodynamic domain of metallic stability is the whole region below the horizontal line, whilst the domain of cation predominance is the upper

region. It is important to appreciate that the position of the line is dependent on the M^{z+} concentration considered: a modification in the concentration would therefore change the stability or predominance domain of the M^{z+} species.

1.02.3.5.2 Purely pH-dependent equilibrium

When dissolved cations precipitate in the form of solid compounds in which the metal keeps the same oxidation number as the cation, for instance, for the M^{z+}/M_2O_z equilibrium, the corresponding forward and backward reactions:

$$2M^{z+} + zH_2O \rightleftharpoons M_2O_z + 2zH^+ \qquad [33]$$

convey no charge transfer. Hence, no redox reaction is present (each reactant keeps its valence on both sides of the reaction) and the equilibrium is independent of the potential, but it is a function of the pH because of the protons on the right-hand side of the equation. The corresponding line of the Pourbaix diagram can be determined with the help of the classical chemical equilibrium theory by introducing the equilibrium constant K of reaction [33][29]:

$$K = \frac{[H^+]^{2z}}{[M^{z+}]^2} \Rightarrow \log K = 2z\log[H^+] - 2\log[M^{z+}]$$

$$pK = -\log K \Rightarrow \log[M^{z+}] = \frac{pK}{2} - z\,pH \qquad [34]$$

It can be seen from reaction [33] that for low pH values (high proton concentration), the reaction equilibrium is shifted to the left side, the oxide combining with protons and producing cations. Low pH values hence entail high dissolved cation concentration. As a consequence, for a fixed M^{z+} concentration, the M^{z+}/M_2O_z equilibrium is characterized by a vertical line in the E/pH diagram (pH = constant, line 2 in **Figure 11(b)**), the left side being the predominance domain of the cations and the right side the oxide stability region. As shown in **Figure 11(b)**, lines 1 and 2 must in reality be mutually truncated at their intersection to take into account the existence of the metal oxide. One should then look for the equilibrium between M and M_2O_z, the third kind of equilibrium, which is dependent on the pH and on the potential simultaneously, to complete the Pourbaix diagram.

1.02.3.5.3 pH and potential-dependent equilibrium

As indicated above, the oxidized M species takes the form of a solid oxide M_2O_z for high pH values (M^{z+} can actually exist but its concentration is low). It is then intuitively more appropriate to consider the

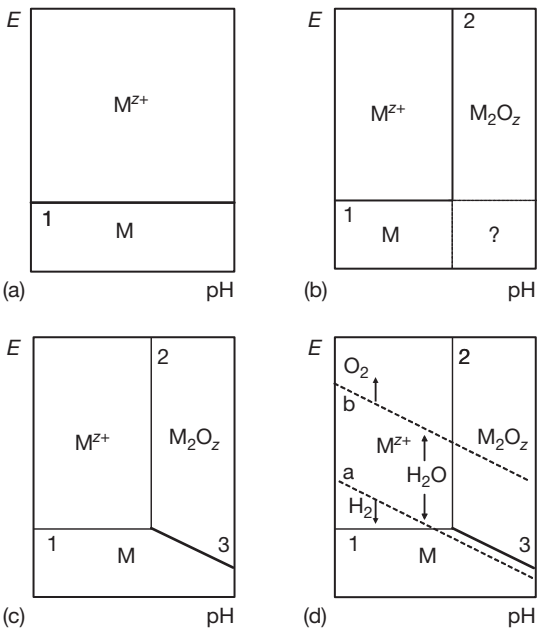

Figure 11 Building-up a generic Pourbaix diagram: (a) the metal/cation equilibrium, line 1; (b) the cation–metal oxide equilibrium, line 2; (c) the metal–metal oxide equilibrium, line 3; (d) the complete schematic Pourbaix diagram, including the water stability domain, lines a and b.

M_2O_z/M equilibrium. It is also clear that reaction requires a source of oxygen, which leads to the very important observation concerning corrosion that oxygen comes mainly from the dissociation of water molecules and not from the atmosphere, contrary to an extremely widespread idea. The overall reaction is then

$$2M + zH_2O \rightleftharpoons M_2O_z + 2zH^+ + 2ze^- \qquad [35]$$

for which the equilibrium potential can be written

$$E_{eq} = A_1 - 0.059\,pH \qquad [36]$$

where A_1 is a constant. The equilibrium, described by a linear relationship between the pH and the potential is represented by the straight line 3 of slope $-0.059\,V\ pH^{-1}$ in **Figure 11(c)**. This line, which separates M and M_2O_z, must start at the intersection of lines 1 and 2 and must be plotted towards lower potentials and more alkaline pH according to the negative slope of line 3. Indeed, in the other direction the line would be in the M^{z+} domain where neither M nor M_2O_z can exist at a steady state.

Figure 11(c) depicts the stability domains of the three species considered. Since this is a metal–water system, the diagram must also incorporate the water stability domain, according to the equilibria H_2O/H_2

and O_2/H_2O, characterized at 25 °C by the following equations:

$$E_{eq} = 0.00 - 0.059\text{pH for } H_2O/H_2$$
$$E_{eq} = 1.23 - 0.059\text{pH for } O_2/H_2O \quad [37]$$

The limits of the water stability domain are thus represented by two parallel lines, identified in **Figure 11(d)** as **a** (for the H_2O/H_2 equilibrium) and **b** (for the O_2/H_2O one), indicating that water is thermodynamically stable between these two lines: below line **a** hydrogen evolves and above line **b**, oxygen evolves, as depicted in **Figure 11(d)**, which is the final form of the schematic Pourbaix diagram for the M–H_2O system involving the three species, M, M^{z+}, and M_2O_z.

Figure 11(d) respects the usual graphic notation used for the sake of readability of the diagrams. Dashed lines indicate an equilibrium between two dissolved species (not illustrated in this simple example), such as two cations (Fe^{3+}/Fe^{2+}, for instance). Thin solid lines indicate an equilibrium between a dissolved and a solid species (lines 1 and 2), and thick solid lines indicate an equilibrium between two solid species (line 3).

Even if schematic, **Figure 11(d)** illustrates a common feature of metal–water Pourbaix diagrams, that is, metal immunity at more negative potential values, film-free metal dissolution at more positive potentials in acids and oxide formation in the neutral and alkaline pH ranges (though many metals will also corrode as oxy-anions in alkali). (The terms 'more positive' and 'more negative' are used here in place of 'higher', 'lower' and similar terms when referring to electrochemical potentials to avoid any possible confusion. Because metal potentials are often negative, there is an unfortunate tendency (particularly in the field of cathodic protection, where potentials are always negative) to say, for example, that −1.2 V is 'higher' than −1 V (and in some cases even to omit the negative sign).)

1.02.3.6 Pourbaix Diagram of Gold, Iron, and Aluminum

Let us now analyze some typical examples of Pourbaix diagrams to illustrate their usefulness. (For the sake of clarity, these are simplified diagrams that consider only some of the possible dissolved or solid species. The reader is invited to refer to the Pourbaix's Atlas of electrochemical equilibrium for more detailed pictures.[28]) **Figure 12** shows the Au–H_2O diagram at 25 °C and 1 atm. The first remarkable feature is that gold has a wide immunity domain occupying a large extent of the E/pH space. The existence

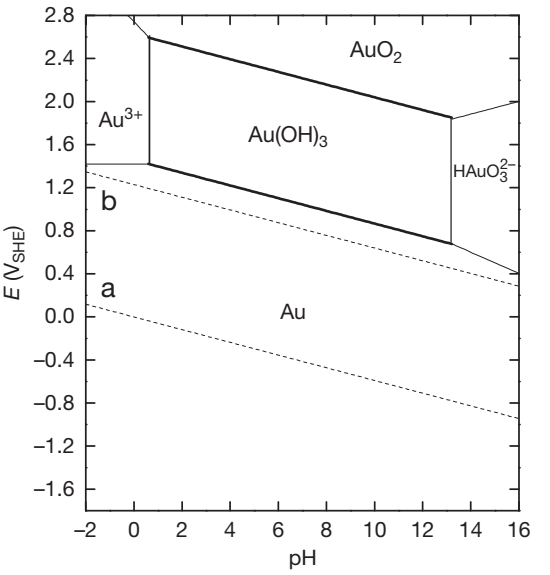

Figure 12 Simplified Pourbaix diagram for the Au–H_2O system at 25 °C. Concentration of dissolved species taken as $[X] = 10^{-6}$ mol l^{-1}.

of Au^{3+}, $Au(OH)_3$, AuO_2, and $HAuO_3^{2-}$ stability domains indicate, at first glance, that gold can undergo corrosion at very oxidizing conditions (very high potential values). A deeper look, however, shows that the gold immunity domain comprises and overhangs that of water. This means that gold is always thermodynamically stable whenever stable water is present, which obviously includes all natural environments on earth and gives a sound idea of the conditions to be achieved for gold corrosion. This is also why gold is always found in its metallic form and not in mineral compounds, unlike most of the metals.

In the case of iron, certainly the most common constructional metal, the Pourbaix diagram at 25 °C and 1 atm pressure (**Figure 13**) shows a very different behavior that explains why corrosion has always been a matter of much concern. In contrast with gold, the existence of metallic iron is thermodynamically impossible in the whole water stability domain: corrosion is hence a spontaneous process bringing iron back to its stable form in nature. Thus, iron is found in different mineral forms such as hematite (Fe_2O_3) and magnetite (Fe_3O_4) and the industrial transformation into metallic iron requires huge amounts of energy (supplied by the oxidation of carbon inside furnaces during the production of iron and steel) to break the oxygen–iron bonds. This spontaneous reverse route (iron towards oxide) is clearly demonstrated by the fact that the Pourbaix diagram in

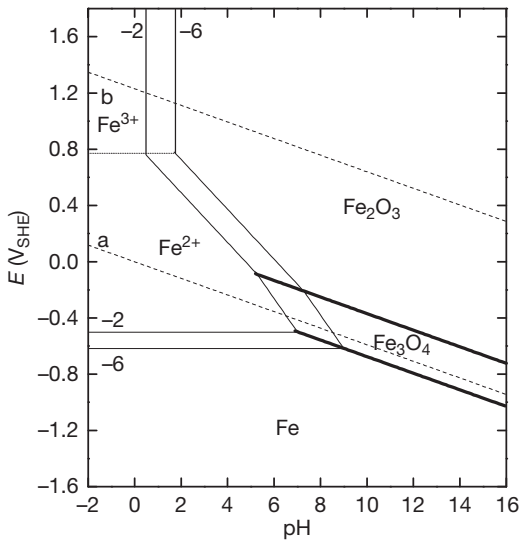

Figure 13 Simplified Pourbaix diagram for the Fe–H_2O system at 25 °C. Concentration of dissolved species taken as [X] = 10^{-2} or 10^{-6} mol l^{-1}.

Figure 13 predicts iron transformation into magnetite (less oxidized species) at more negative potentials or hematite at more positive potentials.

Figure 13 also shows a large active dissolution region (the predominance domain of the ferrous cation Fe^{2+}, followed by that of the ferric cation Fe^{3+} for potential values more positive than $E = 0.77\ V_{SHE}$), often referred to as the corrosion triangle, lying in the neutral–acid pH range, illustrating and justifying the high sensitivity of iron to corrosion in acidic environments.

As mentioned in Section 1.02.3.5.1, the stability domain of the species depends on the concentration of the dissolved species considered to be at equilibrium with the solid compounds. The concentrations used in building the diagram in Figure 13 (10^{-2} and 10^{-6} mol l^{-1}), for example, for the Fe^{2+}/Fe equilibrium, indicate the range of concentrations expected when iron corrosion is taking place. In other words, beyond these values, the stable species is no longer metallic iron, but the ferrous cation, thus leading to corrosion. The line separating the metallic iron and ferrous cation domains move up when the concentration threshold for corrosion is increased from 10^{-6} to 10^{-2} mol l^{-1}, leaving a larger iron stability domain below it.

As already discussed, overall corrosion processes at free potential are the result of coupled anodic and cathodic reactions taking place simultaneously on the metallic surface. The most common cathodic reactions occurring during iron dissolution (reaction [2]) are the hydrogen evolution (in acidic media) and the reduction of dissolved oxygen (in neutral or alkaline electrolytes in contact with air),

$$2H^+ + 2e^- \longrightarrow H_2$$
$$O_2 + 2H_2O + 4e^- \longrightarrow 4OH^- \qquad [38]$$

Note that both cathodic reactions yield an alkalinization of the interface, the first by direct consumption of H^+ and the second by production of OH^-. As a consequence, the system can locally shift from a given point inside the Fe^{2+} domain to, for instance, the hematite domain, which gives a precipitate in the form of what is generically called rust. Only ferrous species can exist at the interface, as ferric ions are stable only at much more positive potentials than normal corrosion potentials. However, in aerated solutions the ferrous ions can be oxidized in solution to ferric by dissolved oxygen, and the ferric ions can then precipitate, usually as an oxyhydroxide (α, β, γ, or δ-FeOOH) which are, roughly speaking, the different hydrated forms of hematite ($Fe_2O_3 \cdot H_2O = 2 \times FeOOH$). (The hematite is the thermodynamically stable species, the other forms are metastable but their transformation is so slow that they can be identified in corrosion products or even in minerals.) Note that the precipitation cannot occur at the metal surface because the ferric species are not stable there, so the corrosion product is necessarily porous and nonprotective.

The last illustrative example concerns aluminum, the Pourbaix diagram of which in Figure 14 shows a wide oxide domain and an extremely narrow immunity one, well below the domain of water stability. Aluminum is thus a particularly reactive metal, as already deduced from the very negative standard equilibrium potential (Table 1). It is important to note that its high corrosion resistance does not come from a marked immunity and stability, as for gold or other noble metals, but from the formation of a homogeneous and impermeable oxide layer in a very large domain of potential and pH, as shown in Figure 14. This very adherent oxide layer protects the metal from further corrosion. This process, called passivation, is also at the origin of the high corrosion resistance of several metals and alloys such as titanium and stainless steels. In the latter case, passivation of chromium, one of the main alloying elements in those steels, provides the corrosion protection.

The difference between the corrosion resistance of iron and aluminum in practical life illustrates an important aspect that must be taken into account when using Pourbaix diagrams. In fact, both diagrams

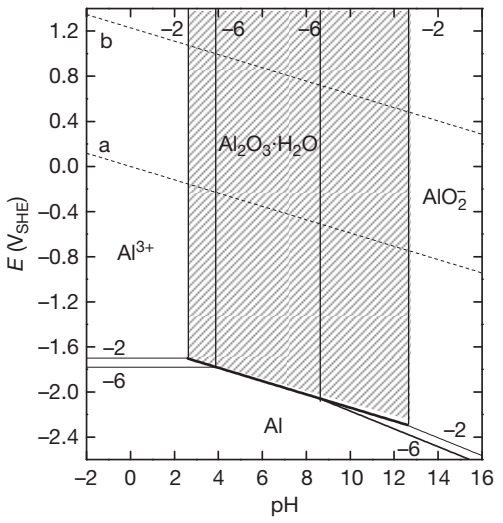

Figure 14 Simplified Pourbaix diagram for the Al–H_2O system at 25 °C. Concentration of dissolved species taken as [X] = 10^{-2} or 10^{-6} mol l^{-1}. The hatched region identifies the large passivation domain of aluminum.

predict the existence of oxide stability domains, but, in contrast with aluminum, iron is not protected by these oxides, which are usually nonadherent, friable, and easily hydrated as mentioned before. Some exceptions are nonetheless of great technological importance. In specific conditions, such as highly alkaline environments, a thin and highly protective oxide is formed on steel, which explains, for instance, the very low corrosion rate (at least initially) of reinforcing bars of low carbon steel embedded in concrete.

It is important to stress that Pourbaix diagrams are based on thermodynamic equilibria. The exchange current density is outside the scope of this approach, which gives no indication about electrode kinetics. Furthermore, corrosion is not an equilibrium process, and the anodic and cathodic reactions are completely different in nature, as explained above. In spite of these restrictions, Pourbaix diagrams constitute a very useful tool to predict if the metal is protected by immunity or passivity when the solution pH and the open-circuit potential are known.

1.02.4 Electrochemical Kinetics in the Case of a Single Forward–Backward Reaction

1.02.4.1 Qualitative Approach

Up to now in this chapter, only reactions at equilibrium, for which zero overall current characterizes the electrochemical system, have been discussed. Even when an overpotential η was imposed to the interface (see **Section 1.02.3.3** with the Zn^{2+}/Zn couple as illustration), the discussion concerned the description of the new equilibrium state with a new zero overall current towards which the system was going.

Let us now consider that a constant overpotential η is applied to the interface by means of an external device so that the system is kept out of equilibrium. This idea can be easily handled with the same example of Zn in contact with a solution of Zn^{2+} concentration $C_\infty = 10^{-2}$ mol l^{-1} ($E_{eq} = -0.82$ V_{SHE}). If this redox couple is supposed to be Nernstian (cf. **Section 1.02.3.3**), the overpotential at the interface is linked to the interfacial concentration, C_{int}, as (see eqns [24] and [25]):

$$\begin{aligned}\eta(I \neq 0) &= E(I \neq 0) - E_{eq} \\ &= E^0 + \frac{0.059}{2}\log C_{int} - \left(E^0 + \frac{0.059}{2}\log C_\infty\right) \\ &= \frac{0.059}{2}\log\frac{C_{int}}{C_\infty}\end{aligned} \quad [39]$$

When an overvoltage η of 0.12 V ($E = -0.7$ V_{SHE}), for instance, is applied to the interface, eqn [39] points out that Zn must corrode to supply Zn^{2+} cations in such amount that the interfacial concentration is 10 000 times higher than the bulk concentration. This new equilibrium will be reached after a very long time for typical volumes of electrolyte. In the transient period, a nonzero current balance ($I > 0$ corresponding to a net oxidation) is established and, since the interfacial concentration is high, the diffusion flux of the cations is directed from the metal to the electrolyte. In the other direction, $\eta < 0$ entails metallic deposition ($I < 0$ corresponding to a net reduction) so that the interfacial concentration is lower than the bulk concentration. The cation flux towards the interface can last a long time since the electrolyte reservoir is hardly changed.

In this system, the potentiostatic out-of-equilibrium conditions involve a transient behavior. In particular, the absolute value of the current decreases as a result of the thickening of the diffusion layer. Forced convection is very often used to control the interfacial concentration of the cations. As explained in **Section 1.02.2.4.3**, convection allows the thickness of the diffusion layer to be fixed and the bulk concentration to be maintained constant, provided that large volumes of electrolyte are used. In that case, the transient behavior is considerably accelerated and a steady state, different from that at equilibrium, is rapidly achieved. (In practice, a steady

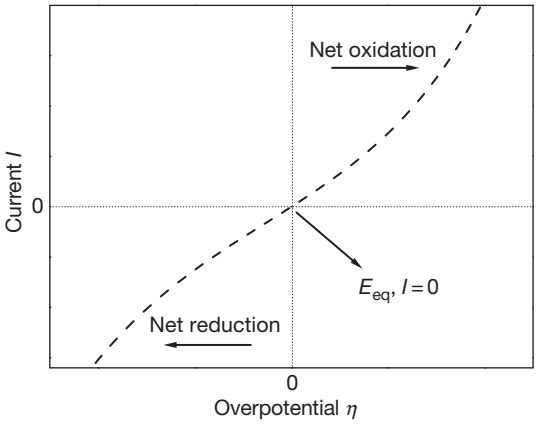

Figure 15 Schematic drawing of the current–overpotential curve involving the cathodic (net reduction) and the anodic (net oxidation) domains.

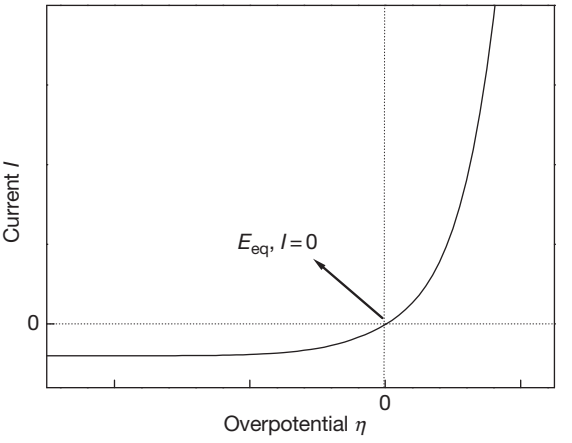

Figure 16 Schematic representation of a current–overpotential curve with a mass-transport controlled plateau in the cathodic domain.

state is impossible to obtain but the evolution of the system is so slow that it can be considered in a steady state during the experiment.) The value of the net steady-state current, at each potential or overpotential then provides important information about the kinetics of the electrochemical reaction. The ensemble of (E, I) or (η, I) couples is often plotted in the form of a current–potential or current–overpotential curve, as illustrated in Figure 15. This curve is called a polarization curve and its slope near the equilibrium depends very often on the exchange current density of the redox reaction kinetics, as shown in Section 1.02.4.2.

Since the product ηI is always positive, as illustrated in the Zn dissolution example given above, the current–potential curve increases monotonically around the equilibrium: the higher the overpotential, the higher the net current (both in absolute values). It is important to notice that nonmonotonic curves also exist, mainly in the corrosion domain, as in the case of stainless steels or passivating metals. Such a feature is, however, closely linked to systems in far-from-equilibrium conditions.

The property that the polarization curve in Figure 15 is monotonically increasing requires two conditions: first, the metal is always available at the interface so that, whatever the overpotential in the anodic part, the metal can keep supplying cations. Second, in the cathodic region, the cations must be available to ensure the increase in $|I|$ with increasing $|\eta|$. However, beyond a certain overpotential negative value, the amount of cations arriving at the interface per unit time is limited by mass transport. The consequence is that the current reaches a diffusion limiting plateau, as illustrated in Figure 16. For all electrode potentials in this region, the corresponding cation concentration at the interface is essentially zero, as discussed in the following sections.

1.02.4.2 Quantitative Approach

The qualitative description of Figure 16 shows that the actual current flow is the final result of combined kinetic phenomena, charge transfer of the redox reaction and mass transport of the cations. The following sections discuss in a more detailed and quantitative way the two limiting cases obtained when the kinetics are controlled by a single phenomenon and finally describe the general case of mixed control. Let us first restate, however, that the following development is only valid for a single forward–backward redox reaction with two reacting species present at the interface, as in the case of the elementary redox reaction:

$$\mathrm{Red} \underset{k_c}{\overset{k_a}{\rightleftharpoons}} \mathrm{Ox} + ze^- \qquad [40]$$

such as, for example, the widely employed redox couple Fe^{3+}/Fe^{2+} taking place at an inert Pt electrode. The current–potential relationships are described below for steady-state conditions and the electrolyte is assumed to be ideal: the activities of the species are equal to their corresponding concentrations, expressed in mol l^{-1}.

1.02.4.2.1 Activation-controlled systems: Butler–Volmer equation

In the activation limited case, the interfacial kinetics are the controlling factor. The influence of mass transport in the electrolyte, in particular diffusion, is negligible because it is much faster than the charge-transfer

process. Therefore, the concentrations are identical at the interface and in the electrolyte bulk:

$$[\mathrm{Ox}]_{\mathrm{int}} \approx [\mathrm{Ox}]_{\infty} \text{ and } [\mathrm{Red}]_{\mathrm{int}} \approx [\mathrm{Red}]_{\infty} \quad [41]$$

Any chemical reaction evolves according to an intrinsic speed called reaction rate. Obviously, this is also valid in the case of electrochemical reactions. As already mentioned, the zero overall current, characterizes the electrochemical equilibrium, at which the forward and backward reaction currents are equal, irrespective of the exchange current density.

The knowledge of the mechanism of the overall reaction allows the rate law of each elementary step to be derived (see **Section 1.02.2.4.1**). In the case considered here, the stoichiometry being very simple for the forward and backward heterogeneous reactions, their rate laws can be easily written in terms of the cathodic and anodic fluxes, ϕ_{cathodic} and ϕ_{anodic}, expressed in moles produced or consumed per unit time and unit surface (mol cm^{-2} s^{-1}):

$$\phi_{\mathrm{cathodic}} = k_{\mathrm{c}}[\mathrm{Ox}]_{\mathrm{int}} \approx k_{\mathrm{c}}[\mathrm{Ox}]_{\infty} \quad [42]$$

$$\phi_{\mathrm{anodic}} = k_{\mathrm{a}}[\mathrm{Red}]_{\mathrm{int}} \approx k_{\mathrm{a}}[\mathrm{Red}]_{\infty} \quad [43]$$

where both rate constants k are expressed in $\mathrm{m\,s}^{-1}$, or more usually in $\mathrm{cm\,s}^{-1}$. (From a rigorous point of view, eqn [42] should also involve the electron concentration at the interface. Nevertheless, since electrons are fully available in a metallic surface, their concentration is considered as being constant and is implicitly incorporated in the constant k_{c}.) (It should be noted that a rate constant does not necessarily have units of meters per second, in particular when the order of the reaction is not 1 or when k depends on the concentration of adsorbates in moles per square centimeters.) Each electrochemical reaction rate depends on the potential, according to the Arrhenius-type eqns [45] and [46] presented below.[4] In the standard state, which is a particular case of electrochemical equilibrium, as explained before, the fluxes of the anodic and cathodic reactions are identical with the same concentrations of the redox species so that the reaction rates are also identical and denoted k^0:

$$k_{\mathrm{c}} = k_{\mathrm{a}} = k^0 \quad [44]$$

The following expressions of electrochemical rate constants are derived:

$$k_{\mathrm{a}} = k^0 \exp\left(\frac{\alpha z F}{RT}(E - E^0)\right) \quad [45]$$

$$k_{\mathrm{c}} = k^0 \exp\left(-\frac{(1-\alpha) z F}{RT}(E - E^0)\right) \quad [46]$$

(Hereafter the usual mathematical treatment that admits global multielectron reactions ($z > 1$) is preferred. It must, however, be kept in mind that, as mentioned in **Section 1.02.2.3**, a rigorous analysis of the reaction mechanisms encompasses the existence of intermediate single electron steps with $z = 1$.) The α parameter in the exponentials, which is called charge-transfer coefficient ($0 \leq \alpha \leq 1$), indicates how the electrical energy related to a potential shift from the standard state, $zF(E - E^0)$ is shared between the anodic and cathodic reactions, as illustrated below in this section.

The overall current density related to this electrochemical reaction can be written as the algebraic sum of the anodic and cathodic currents:

$$\begin{aligned} j = j_{\mathrm{a}} + j_{\mathrm{c}} &= zF(k_{\mathrm{a}}[\mathrm{Red}]_{\infty} - k_{\mathrm{c}}[\mathrm{Ox}]_{\infty}) \\ &= zFk^0\left[[\mathrm{Red}]_{\infty} \exp\left(\frac{\alpha z F}{RT}(E - E^0)\right)\right. \\ &\quad \left. - [\mathrm{Ox}]_{\infty} \exp\left(-\frac{(1-\alpha) z F}{RT}(E - E^0)\right)\right] \end{aligned} \quad [47]$$

It must be noticed that this equation remains valid even if there is only one species in the solution. For example, if there is no Ox species introduced in the electrolyte, the cathodic terms in eqn [47] vanish and the expression of the current density is reduced to the anodic branch. As a consequence, there is no equilibrium or zero-current polarization point simply because there is no cathodic reaction counterpart: the steady-state current density tends to zero only at very high negative overpotentials. Steady-states in which only one species is present are very particular. Indeed, the development of the oxidation reaction itself produces Ox species that progressively accumulate at the interface and can in turn be reduced, hence creating a redox process.

Let us now come back to the previous example in which both Ox and Red species are initially present in the electrolyte. Instead of working with the potential difference relative to the standard state, $E - E^0$, as in eqn [47], it is more interesting to refer to the equilibrium potential and deal straightforwardly with the overpotential $\eta = E - E_{\mathrm{eq}}$ to write:

$$\begin{aligned} \frac{zF}{RT}(E - E^0) &= \frac{zF}{RT}(E - E_{\mathrm{eq}}) + \frac{zF}{RT}(E_{\mathrm{eq}} - E^0) \\ &= \frac{zF}{RT}\eta + \frac{zF}{RT}(E_{\mathrm{eq}} - E^0) \end{aligned} \quad [48]$$

According to the Nernst equation (similar to eqn [23]), E_{eq} can be written as

$$E_{eq} = E^0 + \frac{RT}{zF} \times \ln \frac{[Ox]_\infty}{[Red]_\infty} \quad [49]$$

so that

$$\frac{zF}{RT}(E - E^0) = \frac{zF}{RT}\eta + \ln \frac{[Ox]_\infty}{[Red]_\infty} \quad [50]$$

By combining eqns [48] and [50], the current density can be expressed as:

$$\begin{aligned} j &= zFk^0 \left([Red]_\infty \frac{[Ox]_\infty^\alpha}{[Red]_\infty^\alpha} \exp\left(\frac{\alpha zF}{RT}\eta\right) \right. \\ &\quad \left. - [Ox]_\infty \frac{[Ox]_\infty^{-1+\alpha}}{[Red]_\infty^{-1+\alpha}} \exp\left(-\frac{(1-\alpha)zF}{RT}\eta\right) \right) \\ &= zFk^0 [Ox]_\infty^\alpha [Red]_\infty^{1-\alpha} \left(\exp\left(\frac{\alpha zF}{RT}\eta\right) \right. \\ &\quad \left. - \exp\left(-\frac{(1-\alpha)zF}{RT}\eta\right) \right) \end{aligned} \quad [51]$$

and finally, the so-called Butler–Volmer equation is derived:

$$j = j_0 \left(\exp\left(\frac{\alpha zF}{RT}\eta\right) - \exp\left(-\frac{(1-\alpha)zF}{RT}\eta\right) \right) \quad [52]$$

where the exchange current density j_0 is

$$j_0 = zFk^0 [Ox]_\infty^\alpha [Red]_\infty^{1-\alpha} \quad [53]$$

As discussed above, at the equilibrium ($\eta = 0$), the current density is equal to 0 so that $j_a = |j_c| = j_0$. In eqn [53], the idea of exchange current density expressed as a function of two kinetic parameters, k^0 and α, of the redox system investigated is retrieved.

The two terms in the right-hand side of eqn [52] stand for the purely anodic and cathodic branches of the current–overpotential curve, respectively:

$$j_a = j_0 \exp\left(\frac{\alpha zF}{RT}\eta\right) \quad [54]$$

$$j_c = -j_0 \exp\left(-\frac{(1-\alpha)zF}{RT}\eta\right) \quad [55]$$

Figure 17 presents the anodic and cathodic branches (eqns [54] and [55]) and the sum of both currents at each potential related to the overall Butler–Volmer equation [52], which fully describes the kinetic behavior of an electrochemical interface in the case of pure activation control.

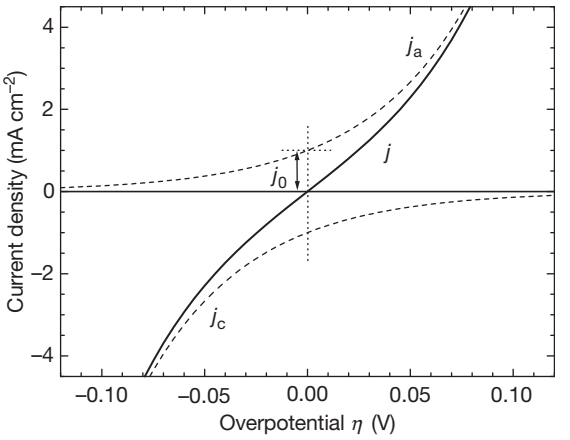

Figure 17 Current–overpotential curve of a purely charge-transfer controlled system illustrating j_a and j_c (eqns [54] and [55]) in the upper and lower halves, respectively (dashed lines) and the overall Butler–Volmer equation [52] (solid line): $\alpha = 0.5$, $z = 1$ and $j_0 = 1\ \text{mA cm}^{-2}$.

As already pointed out, the upper curve in **Figure 17** is obtained when only Red species are present in the solution (eqn [54]). In the same way, the lower curve is obtained when only Ox species are present in the solution (eqn [55]). The Butler–Volmer curve, obtained when the two species are present in the electrolyte, appears then as the addition of the two curves at each overpotential. Any current value depicted in the curve is the net result of a dynamic balance between the anodic and cathodic reactions, giving for example a zero current at equilibrium. In other words, except for very high overpotentials (see **Section 1.02.4.2.2**), the cathodic (anodic) reaction, although markedly slowed down, is still taking place on the metallic surface even at positive (negative) overpotentials, which is an important feature of corrosion processes, as seen hereafter.

The Butler–Volmer equation illustrates an important difference between purely chemical reactions and electrochemical reactions. In the first case, for given concentrations of reactants and hydrodynamic conditions, the only way of modifying the reaction rate is to change the electrolyte temperature. In the case of electrochemical reactions, however, besides the temperature (explicitly present in the argument of the exponentials but also implicitly present in the k^0 value), the electrode potential also strongly affects the reaction rate and, therefore, the resultant current. As an example, for a single electron reaction with $\alpha = 0.5$ and $T = 25\,^\circ\text{C}$ (298 K), a simple calculation from the Butler–Volmer equation indicates that an

overpotential of only 0.5 V entails a $\exp(\alpha F\eta/RT) = 17\,000$-fold increase of the anodic reaction, while the cathodic one is depressed by the same magnitude.

This example can be used to better discuss the physical meaning of the charge transfer coefficient as the kinetic parameter. This coefficient conveys information on how the electric energy supplied to the electrochemical system is shared between the anodic and cathodic reactions. The value $\alpha = 0.5$ indicates that both reactions are boosted or hindered by the same factor. The arguments of both exponentials are identical (in absolute values) for any overpotential η so that the curves are symmetric in **Figure 17**, but this is no longer the case in **Figure 18** with $\alpha = 0.8$: the anodic branch increases more steeply than the cathodic one. This slight bias relative to a symmetric behavior obtained for $\alpha = 0.5$ illustrates the fact that the response of the forward and backward reactions to a same electric energy shift ($|zF\eta|$) is different from the mutual mirrored kinetic behavior, depending on the α value.

It is also worth stressing that the final value of the current density at any overpotential is directly dependent on the exchange current density, as illustrated in **Figure 19**.

When j_0 is large, the redox couple is said to be fast and can be considered as reversible, at least for applied overpotentials not too large. High j_0 values mean that both cathodic and anodic components strongly contribute to the final net j value and small applied overpotentials are enough to produce a significant current in either direction. However, since high current values mean a high flux of reactants at the interface, the mass-transport kinetics are no longer negligible and the Butler–Volmer equation no longer valid (see **Sections 1.02.4.2.1** and **1.02.4.2.2**). On the contrary, for small j_0, that is, for slow redox couples, high overpotentials are needed to get a significant net current, as shown in **Figure 19**. The system is then said to be irreversible, not in the thermodynamic sense, but to express that it is prone to be polarized in one of the parts of the current–overpotential curve where only one of the forward and backward reactions completely governs the overall reaction. In that case, once a given species has been oxidized (reduced), the overvoltage is too large for it to be reduced (oxidized) back, so that the species has much more chances to move away from the interface than to react at the interface.

The following paragraphs deal with two approximations of the Butler–Volmer equation depending on the overpotential value. They are valid for slow redox couples and allow the kinetic parameters k^0 and/or α to be determined.

Small overpotential limit of the Butler–Volmer equation

As highlighted in **Figure 20**, in the region close to the equilibrium potential (typically $|\eta| < 10$ mV), the current–potential curve can be considered as linear. Indeed, by using the Taylor expansion at the first order (small η) of the exponentials ($\exp(x) = \sum_{k=0}^{\infty}(x^k/k!) \approx 1 + x$) in the Butler–Volmer equation, the current density is shown to be proportional to the overvoltage:

$$j = j_0 \frac{zF}{RT}\eta \qquad [56]$$

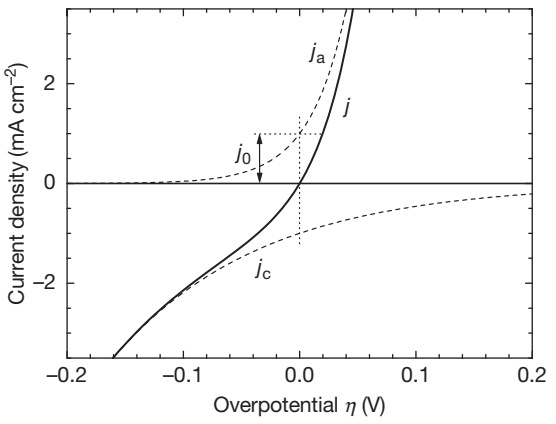

Figure 18 Current–overpotential curve as in **Figure 17** but with a biased charge-transfer coefficient $\alpha = 0.8$, $z = 1$, and $j_0 = 1$ mA cm^{-2}.

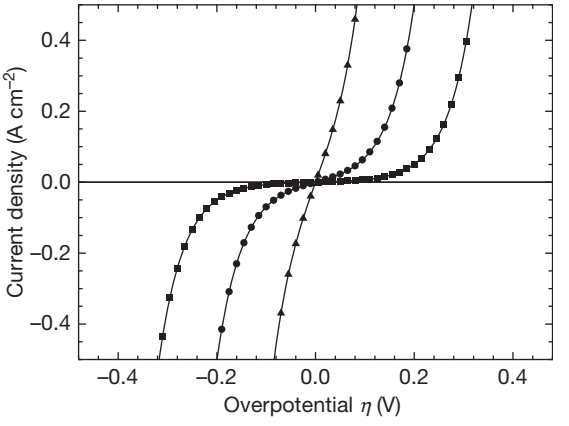

Figure 19 Effect of the exchange current density on the shape of the current–overpotential curves for $\alpha = 0.5$, $z = 1$, and $j_0 = 1$ mA cm^{-2} (■), 10 mA cm^{-2} (●), 100 mA cm^{-2} (▲).

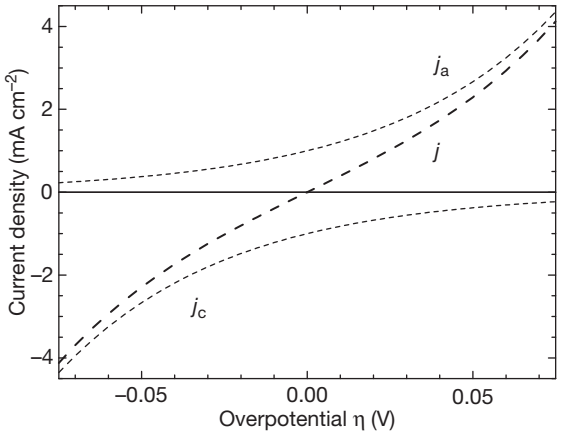

Figure 20 Small-overpotential limiting case: the linear behavior of the Butler–Volmer equation close to the equilibrium potential ($\alpha = 0.5$, $z = 1$, and $j_0 = 1\,\text{mA cm}^{-2}$).

Equation [56] does not give any information about the charge-transfer coefficient α since it depends only on the exchange current density j_0. However, the determination of j_0, through the slope of the linearized Butler–Volmer equation around the equilibrium, is an important kinetic attribute, since it is easily related to k^0 with eqn [53]. It is also important to mention that the slope of the linearized Butler–Volmer equation [56] around the equilibrium can be rewritten with the easily experimentally measurable 'polarization resistance' ($R_p = \partial\eta/\partial I$) at the equilibrium ($I = 0$), and expressed in ohms. In the particular case presented here, this resistance is equal to the charge-transfer resistance, R_{ct}, also defined as $\partial\eta/\partial I$ at $I = 0$, but under conditions where only activation polarization contributes to η (i.e., R_p includes the effects of mass transport and solution resistance, but R_{ct} does not):

$$jS = \frac{1}{R_p}\eta \Rightarrow R_p = R_{ct} = \frac{RT}{zFS}\frac{1}{j_0} \qquad [57]$$

In practice, the SR_p value in $\Omega\,\text{cm}^2$ is more commonly used (and usually also termed R_p, but with units of $\Omega\,\text{cm}^2$) because it does not depend on the surface area of the electrode.

Large overpotential limit of the Butler–Volmer equation

When a large overpotential is applied to the interface, one of the exponential terms (for instance, the cathodic one for large positive η) of the Butler–Volmer equation [52] vanishes and the corresponding reaction (cathodic in this case) can be neglected. Consequently, the following equations, similar to eqns [54] and [55], can be readily derived:

$$j \approx j_a = j_0 \exp\left(\frac{\alpha zF}{RT}\eta\right)$$

for positive large overpotential [58]

$$j \approx j_c = -j_0 \exp\left(-\frac{(1-\alpha)zF}{RT}\eta\right)$$

for negative large overpotential [59]

The system is said to be in the irreversible domain where one of the reactions is substantially hindered and can be neglected. In that case, the global current–overpotential curve tends asymptotically to the purely anodic curve or the purely cathodic curve in **Figures 17** and **18**. This happens when the ratio $|j_c/j_a| = \exp(-zF\eta/RT)$ for $\eta > 0$ or its reciprocal $|j_a/j_c| = \exp(zF\eta/RT)$ for $\eta < 0$ become small. It must be realized that these ratios are lower than 5% as soon as $|\eta|$ is greater than about $80\,\text{mV}/z$ and lower than 1% as soon as $|\eta|$ is greater than about $120\,\text{mV}/z$.

It is more convenient to express eqns [58] and [59] in a semilogarithmic scale (the $\ln 10 = 2.3$ factor stands for the conversion of the natural logarithm into the more easily handled decimal logarithm), as in the following relationships, often called Tafel laws:

$$\log j \approx \log j_a = \log j_0 + \frac{\alpha zF}{2.3RT}\eta$$

$$\text{for } \eta > \frac{0.08}{z}\,(j_a \gg |j_c|) \qquad [60]$$

$$\log(-j) \approx \log(-j_c) = \log j_0 - \frac{(1-\alpha)zF}{2.3RT}\eta$$

$$\text{for } \eta < -\frac{0.08}{z}\,(|j_c| \gg j_a) \qquad [61]$$

The terms $\alpha zF/2.3RT$ and $(1-\alpha)zF/2.3RT$ are known as the anodic and cathodic Tafel coefficients, β_a and β_c respectively.

Thus, in the irreversible domains (high η) the Butler–Volmer equation is represented by two straight lines in a semilogarithmic scale, as depicted in **Figure 21** (same data as in **Figure 18**) showing a log $|j|$ vs. η plot generally called a Tafel plot. In this case, the system is therefore said to exhibit Tafel behavior. The Tafel plot is then a powerful tool to derive kinetic parameters: the equilibrium potential and the exchange current density are obtained at the intersection of the extrapolations of the Tafel lines at $\eta = 0$, while the charge-transfer coefficient α is derived from the slope of the cathodic or anodic lines (see **Figure 21**). It is important to keep in mind that up to now the cathodic and anodic

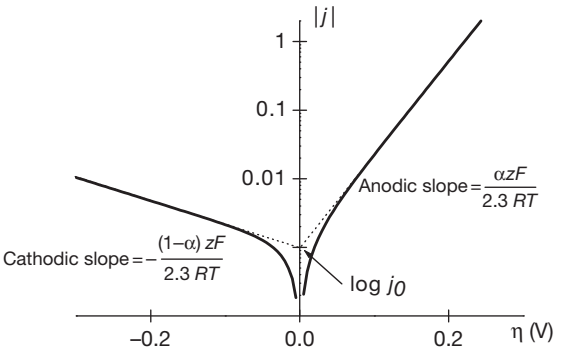

Figure 21 High-overpotential limiting case: the Tafel behavior of the Butler–Volmer equation over a wide potential domain ($z = 1$, $j_0 = 1\ \text{mA cm}^{-2}$, and $\alpha = 0.8$).

reactions are the forward and backward reactions of the same redox process and, therefore, they have the same kinetic parameters (charge-transfer coefficient α and standard rate constant k^0). The slopes of the two straight lines are then mutually linked according to

$$|(\text{Anodic slope}) - (\text{Cathodic slope})| = \frac{zF}{2.3RT} \quad [62]$$

Thus, the slope of a given branch automatically determines the slope of the other one.

In **Figure 21**, the steep increase of the anodic current for positive potentials, due to a high value $\alpha = 0.8$, is then necessarily coupled with a slower evolution of the cathodic current (in absolute value) with respect to the potential.

Another crucial aspect that deserves to be mentioned again is that Tafel behavior assumes the absence of mass transport effects (see the next section). This assumption is valid for systems requiring high overpotentials to reach significant current values, as for slow redox couples characterized by a small exchange current density. Indeed, as already discussed, mass transport has no influence on the current in that case. In contrast, for fast redox processes, that is, for redox couples with a high exchange current density, the consumption of the reacting species at the interface is faster than the supply of species by mass transport and the system no longer exhibits Tafel behavior. As a consequence, the Tafel laws (eqns [60] and [61]) cannot be experimentally observed for fast redox processes, which leads to the idea that Tafel behavior is an indication of slow kinetics. It must also be emphasized that the determination of the kinetic parameters from the linear part of the current–overpotential curves, as described in **Figure 21**, is not as simple as it may appear. Indeed, if an unambiguous linear behavior is not present, the graphic determination of j_0 and α can be seriously biased. Hence, it is widely accepted that a system can be considered as exhibiting Tafel behavior and, therefore, the kinetic parameters can be graphically estimated, only if the linear behavior extends over at least one decade of current.

1.02.4.2.2 Mass-transport limited systems: Fick's law and limiting current density

As already mentioned, mass transport plays a dominant role in the overall kinetics of the electrochemical system in some important situations. This section is then devoted to systems for which the kinetics of the redox reaction is so fast that it is completely controlled by mass transport. Only Nernstian systems, already discussed in **Section 1.02.3.3**, for which the potential and the interfacial concentrations are directly related, are now considered. This is particularly the case of fast redox systems that are reversible in a large range of overpotentials.

The qualitative description of the kinetics of the redox couple Zn^{2+}/Zn, illustrated in **Figure 16** and discussed in **Section 1.02.2.4.4**, allowed the idea of concentration profile across the interface related to a current flow to be introduced. This issue is now treated in a more quantitative way with special attention to interfaces in steady-state conditions. Let us first remember that, according to Nernst's model (see **Section 1.02.2.4.3**), convection controls the thickness, δ, of the diffusion layer at the interface, and allows the bulk concentration to be kept constant not only by electrolyte homogenization but also because the bulk is voluminous. In these conditions, the concentration profiles of the reactive species across the diffusion layer are assumed to be linear.

As an example, in the anodic branch ($\eta > 0$) of the Zn^{2+}/Zn couple, metallic Zn is transformed into Zn^{2+} cations. Therefore, the interfacial concentration of Zn^{2+}, C_{int}, is higher than that in the electrolyte bulk, C_∞, so that the concentration profile decreases, as depicted in **Figure 22**. Zn^{2+} cations in excess at the interface diffuse towards the bulk electrolyte.

Since the concentration profile is assumed to be linear inside the diffusion layer, Faraday's and Fick's laws[30,31] yield the following relationship between the current density and the concentration gradient for any M^{z+}/M couple:

$$j = -zDF\frac{C_\infty - C_{\text{int}}}{\delta} \quad [63]$$

where D is the diffusion coefficient of the cation, often

expressed in $cm^2\,s^{-1}$ (about 10^{-5} to $10^{-6}\,cm^2\,s^{-1}$ in aqueous solutions). (Fick's first law states that a diffusive flux is proportional to the diffusion coefficient D of the diffusing species in a given electrolyte and to the concentration gradient across the diffusion layer,[31] that is $j = -D(\partial C(x)/\partial x)$.)

In the cathodic branch ($\eta < 0$), the concentration increases with the distance from the electrode because of the depletion of cations at the interface, as represented in **Figure 23**. The reduction reaction that entails metallic Zn deposition on the surface, now depends on the supply of cations diffusing from the bulk towards the interface, so that eqn [63] remains valid. However, in contrast to the anodic branch where the metallic Zn can be regarded as an infinite reservoir, a limiting

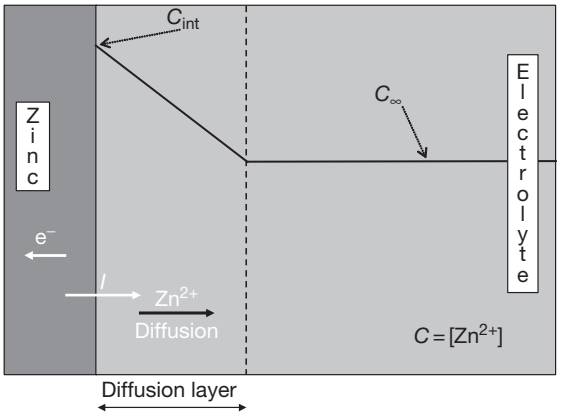

Figure 22 Zn^{2+} concentration profile across the Nernst diffusion layer for an anodic reaction according to Nernst's model.

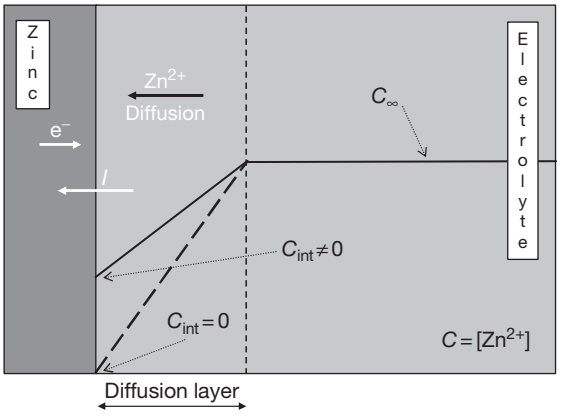

Figure 23 Zn^{2+} steady-state concentration profile across the diffusion layer for a cathodic reaction. Dashed line: limiting case with $C_{int} = 0$, corresponding to the diffusion limited current plateau in **Figure 16**.

situation is reached when the interfacial concentration becomes equal to zero. In that case, the charge-transfer activation process (redox kinetics) is so fast, relative to mass transport, that any cation reaching the interface is immediately reduced. At large negative overpotentials, this leads to the appearance of a plateau defining a limiting current in the current–potential curve, as illustrated in **Figure 16**. Introducing zero interfacial concentration in eqn [63] yields:

$$j_{lim,c} = -zDF\frac{C_\infty}{\delta} \qquad [64]$$

The effective value of the limiting current depends on the hydrodynamics (roughly speaking, the stirring conditions) of the system, which directly defines the thickness of the diffusion layer δ. Just to give an idea, for a $10^{-6}\,cm^2\,s^{-1}$ diffusion coefficient, $0.1\,mol\,l^{-1}$ concentration, 10 µm thick diffusion layer, and $z = 1$, the limiting current density is about 10 mA cm^{-2} in absolute value, according to eqn [64]. Another example concerns the rotating disk electrode, for which the Levich equation predicts the limiting current density, taking into account both the diffusion rate across the diffusion layer and the complex solution flow pattern[32]:

$$j_{lim,c} = -0.620zFD^{2/3}\omega^{1/2}\nu^{-1/6}C_\infty \qquad [65]$$

where ω is the angular rotation rate of the electrode (in $rad\,s^{-1}$) and ν is the kinematic viscosity of the solution (about $10^{-2}\,cm^2\,s^{-1}$ in common aqueous solutions). For the parameter values given above and a rotation rate of 1000 rpm ($104.7\,rad\,s^{-1}$), the current density is about $-13\,mA\,cm^{-2}$.

In addition to the quantitative expression of the limiting current given by eqn [64], the mathematical expression for the whole current–potential curve can be derived by combining eqns [39], [63], and [64]. For example, the current–potential curve of a fast redox couple M^{z+}/M, schematically represented in **Figure 16**, has the following form:

$$\eta = \frac{RT}{zF}\ln\frac{j_{lim,c} - j}{j_{lim,c}} \qquad [66]$$

1.02.4.2.3 General case: Mixed controlled systems

In the general case of an electrochemical system, interfacial charge-transfer and mass transport simultaneously intervene in the kinetics of the reactions at the interface. The mathematical expression of the current is similar to that used in the current–

potential equation [47] with interfacial concentrations instead of bulk concentrations. As an example, for the model corrosion reaction [18] in which mass transport is assumed to intervene for the cation M^{z+} only when

$$j = j_a + j_c = zF(k_a - k_c[M^{z+}]_{int}) = zFk^0\left[\exp\left(\frac{\alpha zF}{RT}(E - E^0)\right) - [M^{z+}]_{int}\exp\left(-\frac{(1-\alpha)zF}{RT}(E - E^0)\right)\right] \quad [67]$$

where k_a is now expressed in mol m^{-2} s^{-1} while k_c is still expressed in m s^{-1}. With reasoning similar to that used in eqns [48]–[51], the following relationship, similar to the usual Butler–Volmer equation, can be derived:

$$j = j_0\left[\exp\left(\frac{\alpha zF}{RT}\eta\right) - \frac{[M^{z+}]_{int}}{[M^{z+}]_\infty}\exp\left(-\frac{(1-\alpha)zF}{RT}\eta\right)\right] \quad [68]$$

where j_0 is now given by:

$$j_0 = zFk^\circ[M^{z+}]_\infty^\alpha \quad [69]$$

The interfacial concentration of M^{z+} can be evaluated with the Fick's first law (eqn [63]), which gives the following expression of the current–potential curve:

$$j = j_{act}\frac{1}{1 + j_0\dfrac{\delta}{zFD[M^{z+}]_\infty}\exp\left(-\dfrac{(1-\alpha)zF}{RT}\eta\right)} \quad [70]$$

where j_{act} stands for the 'activation current density' for which the concentration of the cations at the interface is equal to that in the solution bulk ($j_{act} = j$ in eqn [52]). Equation [70] reduces to the diffusion-limited current density in the cathodic region, already given by eqn [64] with $C_\infty = [M^{z+}]_\infty$, when η tends to $-\infty$.

Figure 24 compares the current–potential curves of a purely-activated system and a mixed controlled system with the same kinetic parameters (eqns [52] and [70]). It can be seen that at any potential the current (in absolute value) is always smaller under mixed control. Another general expression for any redox reaction may be derived from eqn [70]:

$$\frac{1}{j} = \frac{1}{j_{act}} + \frac{1}{j_{mt}} \quad [71]$$

where the mass-transport current density, j_{mt}, corresponds to the current density for a very fast redox reaction ($j_0 \to \infty$ in eqn [70]), that is, for a reaction under complete mass transport control. This simple expression highlights the cornerstone of the idea of interface control. If j_{act} is much larger than j_{mt}, eqn [71] predicts that the mixed current is very close to j_{mt}. From a physical point of view the kinetic behavior can be seen as a series connection of two steps: the slowest step determines the overall reaction rate. If the activation kinetics is fast, then the mass-transport process is the limiting step. Conversely, if the activation kinetics is slow, the diffusion process does not hinder the overall reaction rate.

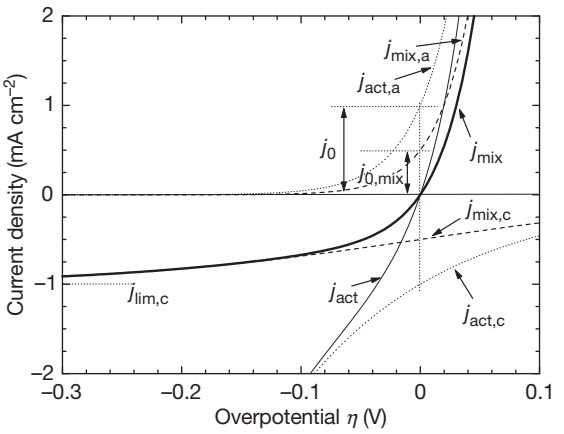

Figure 24 Comparison of the current–overpotential curves for pure activation (thin solid line and dotted lines for the anodic and cathodic currents) and mixed (activation and mass transport: thick solid line and dashed lines for the anodic and cathodic currents) kinetics with a cathodic limiting diffusion current ($z = 1$, $j_0 = 1$ mA cm^{-2}, $\alpha = 0.8$, $j_{lim,c} = -1$ mA cm^{-2}).

An important consequence of the mixed control depicted in **Figure 24** is that the exchange current density, $j_{0,mix}$, is smaller than the kinetic exchange current density j_0 derived from the k^0 and α parameters. The expression of $j_{0,mix}$ can be obtained from eqn [70] with $\eta = 0$. In the same way, the polarization resistance (reciprocal of the slope of the current–potential curve in the vicinity of E_{eq}, see eqn [57]) depends on mass transport.[33] Its expression, derived from the linear approximation of the polarization curve at small overpotentials, is:

$$R_p = \frac{1}{S}\left(\frac{\partial\eta}{\partial j}\right)_{j=0} = \frac{RT}{zFS}\left(\frac{1}{j_0} - \frac{1}{j_{lim,c}}\right) \quad [72]$$

This illustrates the fact that the overall polarization

resistance is always higher under mixed control than under activation control (for the same j_0 and α).

1.02.5 Corrosion: Far from Equilibrium Zero Net Current Systems

1.02.5.1 Qualitative Description of the Free Corrosion Scenario

Everybody knows or easily guesses the consequence of abandoning a metallic piece in an aggressive medium without specific protection, for instance, iron in seawater: the metal will be annihilated by corrosion. Regardless of the rate of the process, which depends on many factors such as the nature of the metal and of the electrolyte, temperature, pressure, and so on, this primary experimental evidence leads to an important conclusion: any corrosion process evolves under long-term out-of-equilibrium conditions. In spite of being permanently in non-equilibrium conditions, the system is, in some senses, at rest in the free corrosion scenario. In other words, no net current flux is crossing the metal–electrolyte interface.

As an obvious consequence, if the metal is being consumed by corrosion processes, oxidation reactions inevitably take place at its surface although the net current flow is zero. Therefore, at every instant the amount of current generated by these oxidation reactions (for instance, reaction [2]) must be balanced by cathodic counterparts. This implies that anodic and cathodic reactions must be occurring simultaneously. In contrast with the previous sections, this scenario cannot involve a single redox couple with a simple forward–backward reaction, otherwise the zero net current would correspond to an equilibrium condition in which the iron dissolution and deposition would perfectly balance out and no corrosion would occur. Corrosion phenomena, therefore, involve at least two different redox couples, one (or more) supplying the anodic current and the other one (or more) supplying the cathodic current and ensuring the zero current balance. This kind of self-regulated coupled system yields the two fundamental parameters of corrosion processes, the corrosion current, I_{corr}, and the corrosion potential, E_{corr}, also called rest potential or open-circuit potential (OCP). (The term coupled here refers to the fact that the anodic and cathodic reactions must deliver the same average current (in absolute value) to maintain a zero current balance, and not to coupled kinetic parameters k^0 and α as in the case of a single forward–backward reaction (with α and $1-\alpha$, respectively), as discussed before.) As described below, both E_{corr} and I_{corr} are time-evolving variables that define the intrinsic thermodynamic and kinetic characteristics of each redox couple taking part in the global reaction. This is why the corrosion potential is often referred to as a mixed potential. A simple qualitative description of a coupled system can be proposed with the example of the free corrosion of iron in acidic media: the zero net current balance is then a result of the following coupled equations:

$$\begin{aligned} &Fe \rightleftharpoons Fe^{2+} + 2e^- \\ &2H^+ + 2e^- \rightleftharpoons H_2 \end{aligned} \qquad [73]$$

The two individual equilibrium potentials, $E_{eq,Fe^{2+}/Fe}$ and $E_{eq,H^+/H_2}$, can be defined for reactions [73] if the four species are present at the metal–electrolyte interface. Their exact values depend on the experimental conditions, as described by the Nernst law (see **Section 1.02.3**). The fact that each couple behaves in a stationary way allows the steady state of the corrosion system to be defined from their individual polarization curves (see **Section 1.02.4**) and its corrosion rate to be calculated. Since iron is oxidized when corroding, its polarization point must be somewhere along the anodic branch of the Fe^{2+}/Fe η-I curve, the shape of which is a function of the thermodynamic and kinetic attributes of the couple, as illustrated in **Figure 25**. The behavior of the second couple is quite evident, since it must ensure the zero overall current by consuming the electrons supplied by the anodic reaction. H^+ is then reduced and the polarization point of the couple is located on the cathodic branch of the H^+/H_2 η-I curve. The corrosion process is then iron dissolution with hydrogen evolution according to reactions [73]. The exact situation is graphically determined by the potential for which $|I_c| = I_a$, as shown in **Figure 25**.

Since, very often corrosion processes can be considered as activation-controlled systems (at least for low current values), another useful representation for free corrosion conditions is the so-called Evans diagram, which gives the potential evolution against the logarithm of the current absolute value, as depicted in **Figure 26**, strictly Evans originally plotted E against $|I|$, i.e., using linear rather than log scales. However, the name is now widely used for diagrams plotting E against $\log |I|$.

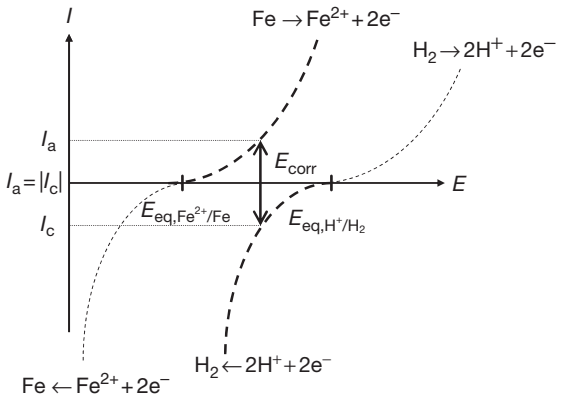

Figure 25 Schematic representation of the polarization curves of the two redox couples around their respective equilibrium potential allowing the corrosion potential E_{corr}, at which $|I_c| = I_a$, to be determined. Note that the ordinates are plotted in terms of net currents and not current densities, since the equality between the anodic and cathodic counterparts concerns the electron flux (see **Section 1.02.2.3**).

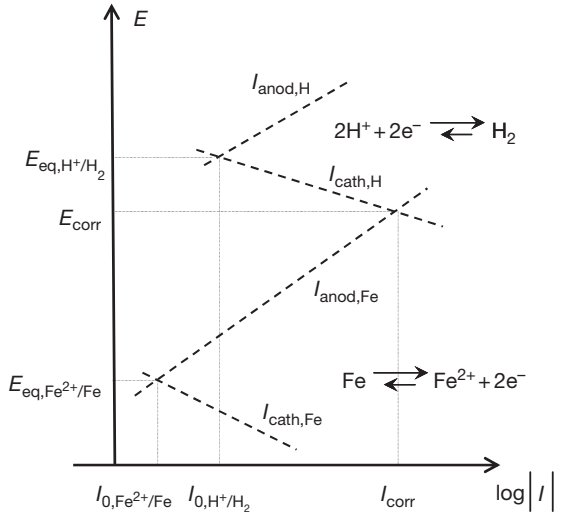

Figure 26 The Evans diagram: a simplified representation of the mixed potential and the mutually balancing cathodic and anodic electron fluxes that determine the corrosion potential and exchange current values. The figure is arbitrarily asymmetric with $E_{corr} - E_{eq,\,Fe^{2+}/Fe} > |E_{corr} - E_{eq,\,H^+/H_2}|$. The values of the exchange currents are also arbitrary.

The main advantage of the Evans diagram is to clearly illustrate the fact that when two different redox couples coexist, the electrode potential always takes a single value, the corrosion potential, which is easily determined by the intersection of two branches. The exact E_{corr} value (as well as the corrosion current value) depends on the kinetic and thermodynamic characteristics of both couples that are out of equilibrium and follow the behavior predicted by their own polarization curves, as shown in **Figure 25**. In spite of this complex behavior, E_{corr} naturally lies between the two individual equilibrium potentials. The two (or more) reactions do not usually take place with the same overpotential $\eta_{Fe^{2+}/Fe} = E_{corr} - E_{eq,\,Fe^{2+}/Fe}$ and $|\eta_{H^+/H_2}| = |E_{corr} - E_{eq,\,H^+/H_2}|$ (even if the equality $\eta_{Fe^{2+}/Fe} = |\eta_{H^+/H_2}|$ is of course not forbidden), since what they must ensure is an identical electron flux, identified to the corrosion current, I_{corr}, as depicted in **Figure 26**. Both redox couples are displaced from their respective equilibrium potential, which means that the Fe^{2+}/Fe couple shifts the proton reaction in the cathodic direction while the H^+/H_2 couple shifts the iron reaction in the anodic direction.

This idea of mixed potential is extremely important as it indicates that the reaction with the lower equilibrium potential will be anodic and that with the higher equilibrium potential will be cathodic. It then defines in principle which metal will corrode in a given situation of galvanic corrosion. (This is only necessarily true when both metals are corroding in an active state; in practical situations (which often involve one or both of the metals being passive) the standard equilibrium potentials are not reliable indicators of the behavior of galvanic couples.) Let us take the example of iron and copper in the presence of an acidic electrolyte, that is, in the presence of the H^+/H_2 couple, but in the absence of dissolved oxygen. The respective standard equilibrium potentials are -0.44, 0.34, $0\,V_{SHE}$ for iron, copper, and hydrogen, respectively. It clearly appears that iron and copper behave differently in contact with an acidic solution. The iron will corrode, driven by the proton reduction with concomitant H_2 evolution, whilst the copper will remain intact since its potential is higher than that of the H^+/H_2 couple. The importance of specifying the absence of oxygen in this example is due to the high potential of the O_2/H_2O couple ($1.23\,V_{SHE}$) that can induce the corrosion of copper as well as that of iron.

As already mentioned, it is assumed in reactions [73] that the species produced by the forward reactions are available at the interface, in particular, the Fe^{2+} cations are not all trapped in indissoluble corrosion products. Reactions [73] were intentionally represented with forward and backward arrows of different size instead of purely anodic and cathodic reactions [2] and [12]. This is of high importance because, depending on the overpotential of each reaction relative to the actual corrosion potential,

the reverse reaction (iron deposition or anodic hydrogen oxidation) can also take place on the metallic surface even though its rate will be less than the anodic and cathodic counterparts (iron dissolution and proton reduction, respectively). When the mixed potential E_{corr} entails an overpotential, high enough to bring the reaction inside the irreversible domain, the reverse reaction can be neglected, as discussed in Section 1.02.3.2. This is often the case in corrosion processes and this constitutes the basis of the simplified kinetic treatment applied to corrosion studies, which is developed in the next section.

1.02.5.2 Electrochemical Kinetics Around the Corrosion Potential

In spite of the enormous physical difference between the equilibrium and the corrosion potentials, both potentials concern systems that are released at rest and thus show a permanent zero-net current balance. In Section 1.02.4, the kinetic behavior was investigated when imposing a potential shift with respect to the equilibrium potential. It is interesting now to consider the kinetic consequences of imposing a potential shift with respect to the corrosion potential. This raises a strongly intuitive analogy between the kinetic behaviors around E_{eq} and E_{corr} that is fully verified experimentally. The first aspect in this analogy is that, as seen in Section 1.02.4.2.2, beyond a certain deviation from equilibrium, generally about a $\pm 100\,mV$ overpotential, the system can be considered to be in the irreversible Tafel domain. Considering the Pourbaix diagrams, or simply a standard equilibrium potential table, it can be seen that the differences between the equilibrium potentials of most of the typical redox couples inducing metallic corrosion are much larger than this value of $\pm 100\,mV$ (e.g., $1.23 - (-0.62) = 1.85\,V$ for Fe–O_2, and $0.62\,V$ for Fe–H^+ according to Figure 13 for $[Fe^{2+}] = 10^{-6}\,mol\,l^{-1}$ and $pH = 0$, just to mention the most common corrosion couples involving iron). This indicates that most of the common corrosion processes take place in the irreversible domain. In such conditions, and provided that the mass transport effects are negligible, the Butler–Volmer equation related to each reaction is reduced to a single anodic or cathodic branch so that the polarization curve of the overall coupled system is defined as follows:

$$j = j_{0,a}\,\exp\left(\frac{\alpha_a z_a F}{RT}\eta_a\right) - j_{0,c}\,\exp\left(-\frac{(1-\alpha_c)z_c F}{RT}\eta_c\right) \quad [74]$$

where the subscripts a and c stand for anodic and cathodic respectively and where $\eta_a = E - E_{eq,a}$ and $\eta_c = E - E_{eq,c}$. Equation [74] is implicitly derived for conditions where both processes are completely independent and in a steady state. This means, for example, that the sharing of the surface area in anodic and cathodic zones does not change with the potential, and is constant during the experiment.

Let us now define the polarization $\pi = E - E_{corr}$, analogous to the overpotential η when dealing with equilibrium systems. Assuming, as discussed above, that both couples are sufficiently far from equilibrium to be in the irreversible domain, the current–potential curve of the overall system is composed of a single anodic branch (corresponding to one of the oxidation process of the redox couples) and a single cathodic branch (corresponding to the reduction process of the other redox couple). The current−potential relationship can hence be described by the following equation, which is derived from eqn [74] and is very similar to the Butler–Volmer equation[34]:

$$j = j_{corr}\left(\exp\left(\frac{\alpha_a z_a F}{RT}\pi\right) - \exp\left(-\frac{(1-\alpha_c)z_c F}{RT}\pi\right)\right) \quad [75]$$

with

$$j_{corr} = j_{0,a}\,\exp\left(\frac{\alpha_a z_a F}{RT}\eta_{a,corr}\right) = j_{0,c}\exp\left(-\frac{(1-\alpha_c)z_c F}{RT}\eta_{c,corr}\right) \quad [76]$$

The parameters α_a and α_c are no longer mutually related as for a single transfer coefficient ($\alpha_a \neq \alpha_c$), and eqn [75] is often represented in a simpler way:

$$j = j_{corr}(\exp(b_a\pi) - \exp(b_c\pi)) \quad [77]$$

where b_a ($b_a > 0$) and b_c ($b_c < 0$) are the anodic and cathodic Tafel coefficients, respectively, expressed in V^{-1}. It is easily seen that for potentials sufficiently far from E_{corr} and in the absence of mass-transport effects, the anodic or cathodic branches yield a linear behavior in a semilogarithmic scale, as depicted in Figure 27.

The experimental Tafel slopes, β_a and β_c, expressed in volt per current decade, can be determined from Figure 27 with the following equations:

$$\beta_a = \frac{2.303}{b_a} \quad \text{and} \quad \beta_c = \frac{2.303}{b_c} \quad [78]$$

The corrosion current density can also be estimated by extrapolation of the Tafel lines at the corrosion

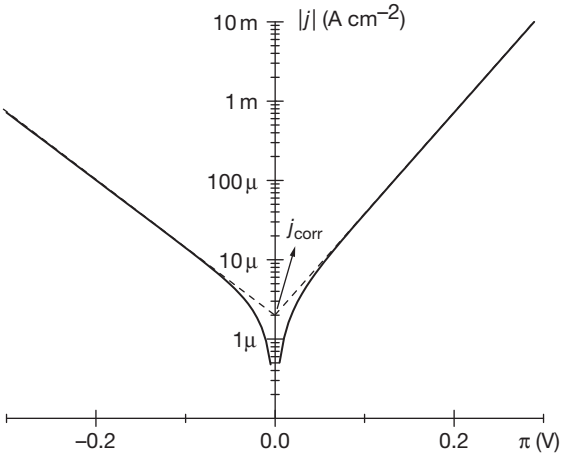

Figure 27 Kinetic behavior within a large potential domain: Tafel (linear) region and estimation of the corrosion current density. Arbitrary values of $j_{corr} = 2\ \mu A\,cm^{-2}$, $\alpha_a = 0.75$, $\alpha_c = 0.5$, $z_a = z_c = 1$.

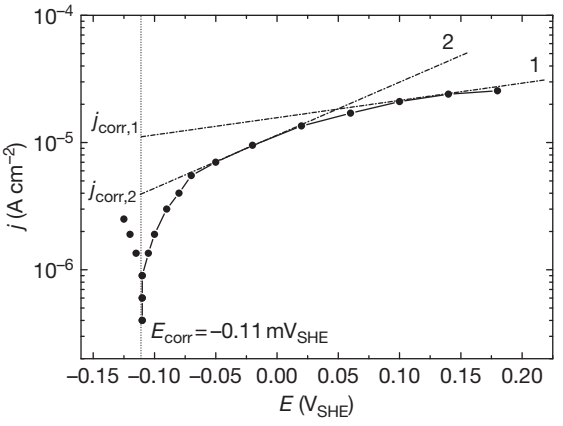

Figure 28 Anodic polarization curve of Zn in a 0.01 mol l^{-1} $NaHCO_3$ solution under O_2 bubbling at 60 °C, pH = 8.1: misestimation of the corrosion current density from a nonlinear or small-range Tafel behavior.

potential ($\pi = 0$), similar to the estimation of the exchange current density for a redox couple (**Figure 21**). It is worth emphasizing that both characteristics correspond to far-from-equilibrium conditions, each branch following its intrinsic kinetic behavior independently of the other.

From a practical point of view, the accurate determination of the corrosion current, a sort of Holy Grail for corrosion engineers, deserves two important remarks. The first, extremely relevant and often disregarded, is that the polarization curve should show a large and unambiguous region of Tafel behavior; the linear domain should encompass at least one decade of current to allow the graphical determination of the corrosion current to be carried out. Despite that, several commercial corrosion analysis programs allow manual Tafel fits from small truncated straight lines or even when there is no linear behavior at all. **Figure 28** illustrates this issue in the case of a nonlinear anodic curve measured during corrosion of Zn in a highly aerated carbonate solution at 60 °C after several hours of immersion (for illustration, the cathodic branch is ignored for the moment). The magnitude of the possible error in j_{corr} due to the arbitrary choice of two linear fits (represented by straight lines 1 and 2), corresponds to a factor of about 3 between the values of $j_{corr,1}$ and $j_{corr,2}$.

The second remark is more positive: since j_{corr} is determined at the corrosion potential, the existence of a single Tafel region (anodic or cathodic) is sufficient. This is particularly useful when the anodic branch, for example, does not present a well defined Tafel line as in **Figure 28**. If the cathodic branch exhibits a Tafel domain, which is often the case for hydrogen evolution but rare for oxygen reduction, the corrosion current can be determined by extrapolating the cathodic linear branch up to the corrosion potential. (A common error in applying Tafel extrapolation is to extrapolate the Tafel line for hydrogen evolution, even though the dominant cathodic reaction is oxygen reduction.) This is really useful, as the anodic and cathodic branches are independent without any expected symmetry or even equivalent shape. Let us come back to the previous figure but in its complete form, showing the anodic and cathodic branches (**Figure 29**). Even if the anodic reaction does not present a marked linear $\log(j_{corr}) - E$ characteristic, as seen before, the corrosion current density can be correctly estimated by means of the unambiguous and wide Tafel behavior of the cathodic branch.

In the example presented in **Figures 28** and **29**, the j_{corr} values badly estimated with the anodic branch are higher than the actual j_{corr} value. This overestimation is certainly less harmful than an underestimation, but the reverse situation cannot be simply excluded. Indeed, due to the logarithmic scale, this loose approach to the Tafel laws can yield significant errors, the impact of which in the nuclear domain, for instance, is easy to imagine and hard to mitigate.

It is worth noting, however, that it is possible to evaluate the corrosion current density with the Stern–Geary relationship in a narrow potential domain. In addition, the four unknown variables,

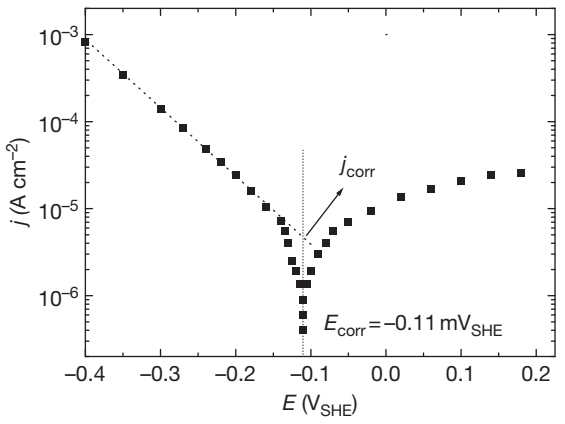

Figure 29 Complete polarization curve obtained in the same conditions as in **Figure 28**: good estimation of the corrosion current density by means of a single wide Tafel region.

j_{corr}, E_{corr}, α_a, and α_c, can be evaluated with a parameter regression calculation, provided that the potential domain is sufficiently large (about ±50 mV from E_{corr}) to give a nonlinear current–potential curve (four unknowns can then be determined instead of two for a linear curve) and, at the same time, sufficiently narrow in order that the system behavior obeys eqn [75].

One reason that the anodic branch exhibits a poorly defined Tafel domain is the dissolution mechanism itself. The metal is dissolving with multiple elementary steps, and the rate-limiting reaction step may change with the potential, as illustrated by the extensive work of Keddam *et al.* On the other hand, at the corrosion potential of iron in sulfuric acid, the coverage of the electrode surface by hydrogen atoms is close to unity,[9] and, as can be conceived readily, the surface area available for iron dissolution increases with increasing potential. This is another reason explaining the narrow linear domain of Tafel behavior of the anodic process. In contrast, the surface area at which hydrogen evolution is taking place does not change significantly so the polarization curve exhibits Tafel behavior in the cathodic domain.

It is worth mentioning that when mass-transport phenomena influence the electrochemical response, leading to a non-Tafel behavior of the two couples, the determination of the corrosion current cannot be achieved as straightforwardly as for Tafel behavior. Indeed, for a redox couple under mixed control at equilibrium (**Section 1.02.4.2.3**), it can be shown that the corrosion current is lower when mass transport is controlling the kinetics of the corrosion system. As a consequence, the polarization resistance, which is an important parameter for the assessment of corrosion current in field applications, is higher in that case.

1.02.6 The Electrochemical Cell

This section is devoted to a brief description of an electrochemical cell and of the basic instrumentation used for controlling the electrode potential (potentiostat) or the current flowing across the electrode (galvanostat). Numerous techniques, electrochemical or *in situ* spectroscopic, may be used for studying electrode reactions at equilibrium or out-of-equilibrium, such as potentiometry, amperometry, voltammetry, electrochemical impedance, electrochemical noise, scanning electrochemical microscopy, atomic force microscopy, Raman spectroscopy, etc. These techniques will not be described in this section, the reader may consult other chapters in this book, or Marcus and Mansfeld,[35] Greef *et al.*,[36] Bard and Faulkner[37] for more information.

1.02.6.1 Design of the Electrochemical Cell

Although the electrochemical phenomena occur on a single electrode in most corrosion processes, as described in **Section 1.02.2**, the understanding and quantitative analysis of these phenomena are usually performed with the help of three electrodes in contact with the same electrolyte, to measure and/or control the electrode potential and current precisely, as described briefly in the following.

Basically, the electrochemical cell comprises three electrodes immersed in an electrolyte, the working electrode (WE), which is the electrode under study, the counter-electrode (CE), the role of which is to ensure the current flow across the cell, and the reference electrode (RE) versus which the potential of the WE is measured. The electrodes may be located in single-compartment containers or in containers with two compartments separated by a membrane or a sintered glass, for example, to prevent the species produced at the counter electrode from reaching the working electrode.

Depending on the system under investigation, the reaction kinetics may be studied in stagnant solutions or in forced convection conditions. Mass-transport control in the cell may be realized by agitating the solution with gas or a stirrer, by rotating the electrode (a disk or a cylinder), or by flowing the solution in front of the WE (immersed jet cell or channel flow). Whenever feasible, controlling mass transport effectively

allows a better control and definition of the flow conditions. This helps to ensure steady state conditions, improve reproducibility, and make quantitative analysis easier with the help of the Fick and Levich equations.

1.02.6.1.1 The working electrode

The design, size, and materials of the WEs are diverse. Very often, especially in corrosion, the WE is a metallic disk or square, the lateral surface of which is embedded in an epoxy resin or covered with an electrical insulator. Care must be taken for mounting the WE since crevice effects between the sample and the insulator are possible. A thin layer of cataphoretic paint may be deposited on the lateral surface of the sample before mounting in the insulator to avoid this. The size of the WE may be very large in industrial applications but in most laboratory investigations, the surface area is of the order of $1\,cm^2$. To obtain a reproducible surface state, the WE is usually polished before the experiment with abrasive paper, alumina, or diamond paste, rinsed and placed in an ultrasonic bath to remove the polishing particles. In most cases, the WE is fully immersed in the electrolyte but in marine corrosion applications, the sample may pass through the air–electrolyte interface, which provokes water-line attack due to enhanced oxygen availability (see Section 1.02.2.3).

1.02.6.1.2 The counter-electrode

The CE is often a cylindrical grid of large surface area compared to the WE for several reasons. First, this minimizes the polarization of the CE (because of the low current density on a large electrode) and, therefore, the overall voltage required from the power source. Second, the current lines between the WE and the CE spread inside a larger electrolyte volume with a large CE, so that the electrolyte resistance is located near the WE, as shown below, which gives a lower influence of the RE position on the measured potential. When possible, the CE is positioned far from the WE so that the cylindrical shape ensures that the CE is an equipotential surface. (The ready availability of numerical modeling tools that can determine the current distribution now makes it possible to improve the design of electrochemical cells for specified situations.) Inert electrodes, metallic grids (often in platinum or titanium) or carbon sheets may be used. When a single compartment is used, the reactions taking place on the CE have to be considered with great care since they may cause changes in the concentration of the reactants in solution. In practice, the reaction occurring on the CE is that of presenting the lower CE overvoltage. In corrosion studies, they usually consist in the oxidation or reduction of a component of the electrolytic solution, such as hydrogen evolution when the WE is polarized anodically and oxygen evolution when it is polarized cathodically (or chlorine evolution in chloride solutions). Another oxidation reaction may take place when using a noninert CE, such as stainless steel (special care must be taken in that case to avoid contamination of the working electrolyte). As mentioned above, the CE must be located in a specific compartment separated with an ion-exchange membrane or a sintered glass when using a stainless steel CE or when the reaction product, such as dissolved oxygen, may alter the behavior of the WE.

1.02.6.1.3 The reference electrode

A RE is used to control and/or measure the electrode potential in almost all electrochemical investigations. However, in early work, before the common use of RE, the potential was sometimes measured with respect to a CE of large surface area. This is also the case at times for experiments performed with microelectrodes. This section is aimed at discussing the main principles of the RE and its positioning in the electrochemical cell.

The main reference electrodes

As explained in Section 1.02.3.3, the electrode potentials in the electrochemical systems are referred to a standard system called SHE, which, strictly speaking, cannot be realized, and the derived experimental RE, the NHE, is not easy to handle. A number of practical REs were, therefore, developed and are now commonly used.[18] There are two basic classes of practical RE, sometimes called secondary REs since they are calibrated against the primary reference of SHE:

- REs of the first kind consist of a metal in equilibrium with a controlled concentration of its salt. An example of this type is copper metal in a solution of copper sulfate. Then the copper ion concentration controls the potential as defined by the Nernst equation.
- REs of the second kind consist of a metal in contact with a sparingly soluble salt of the metal; this is placed in a solution with a controlled concentration of a soluble salt with the same anion. An example of this type is silver in contact with silver chloride in a solution of potassium chloride. In this case the chloride concentration in solution

controls the silver ion concentration by way of the solubility product of silver chloride, and the silver ion concentration controls the potential as defined by the Nernst equation.

Commercially-available REs include:

- $Hg|Hg_2Cl_2$ (calomel) in a saturated KCl solution, named SCE for saturated calomel electrode. This system is a very common commercial product (though tending to lose favor because of toxicity issues and a ban on the transportation of products containing mercury by air): a platinum wire is dipped into a mercury pool (**Figure 30**), which is in contact with a paste of mercury and Hg_2Cl_2, itself in contact with a saturated KCl solution ($\sim 4\,mol\,l^{-1}$ at room temperature).
- $Hg|Hg_2SO_4$ in a saturated K_2SO_4 solution. This system may be used for general purposes where the absence of chloride ions in the electrolyte is crucial.
- Hg|HgO in a KOH solution of fixed concentration, for alkaline electrolytes.
- Ag|AgCl in a KCl or NaCl solution of fixed concentration. This RE is quite easy to prepare: for instance, an Ag wire can be dipped into a concentrated KCl solution and anodically electrolyzed or it can be dipped a few minutes in a concentrated $FeCl_3$ aqueous solution in which it is spontaneously oxidized. The resulting wire is covered with an AgCl deposit and may be used in any solution of fixed chloride concentration. It is very commonly used in marine applications when the Ag|AgCl wire can be directly used in the seawater without a specific electrolyte compartment, in contrast with the above REs.
- Cu in a saturated $CuSO_4$ solution – this is the only widely used RE of the first kind. This electrode is commonly used in the field, for instance, to evaluate the efficiency of cathodic protection of buried carbon steel pipelines. It consists of a copper rod dipped in a saturated $CuSO_4$ solution, as shown in **Figure 31**.

A generic consequence of the Nernst equation for the reversible redox couple involved in these REs, is that in order to obtain a RE showing a constant potential with time, the electrolyte inside the RE must contain a salt at fixed concentration. One of the advantages of using a saturated salt solution (as in the first two examples) is that the presence of the solid salt maintains a fixed ionic concentration, given by the solubility of the salt, even if small perturbations may lead to a slight consumption of this ion. However, the saturation concentration is temperature sensitive and this kind of RE has a rather high temperature coefficient (e.g., $\sim 0.65\,mV\,°C^{-1}$ for the SCE compared to $0.06\,mV\,°C^{-1}$ for the calomel RE in $0.1\,mol\,l^{-1}$KCl).

To avoid contaminating the working solution with the salt used in the RE, a salt bridge filled with the working solution is often used, thereby increasing the distance that ions leaking out of the RE have to diffuse. Additionally, the use of the $Hg|Hg_2SO_4$ RE filled with saturated K_2SO_4 in sulfate media, or the use of the Hg|HgO RE filled with KOH in strongly alkaline media, may minimize solution contamination. Except for the Ag|AgCl RE that can be directly dipped in seawater, the use of these solid REs always introduces one or more liquid–liquid interfaces (e.g., in the porous material used to separate the RE solution from the studied solution) in the potential measurement chain. This will inevitably produce liquid junction potentials that introduce some errors in the measurement and/or control of the WE interface potential. The liquid junction potentials may reach a few tens of millivolts in specific conditions. However, when the solution in the RE is highly concentrated with a cation and an anion of similar ionic molar conductivity as, for example, in saturated KCl solution, the junction potential can be neglected.[38] In most corrosion applications, the error introduced by the junction potentials is usually of no consequence since the electrode potential does not have to be measured with an accuracy better than 1 mV.

Table 2 indicates the measured potential of the REs presented above.

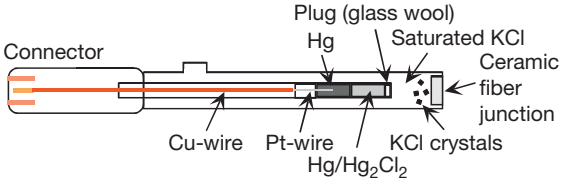

Figure 30 Scheme of the saturated calomel reference electrode.

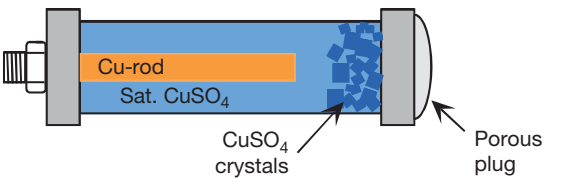

Figure 31 Scheme of the Cu|saturated $CuSO_4$ reference electrode.

Position of the reference electrode

For a simple electrochemical cell, consisting of two planar electrodes of the same size and positioned face to face, similar to a conductivity measurement cell, the potential gradient between the two electrodes is essentially uniform and the solution resistance R_e can then be calculated as follows:

$$R_e = \frac{1}{\gamma}\frac{d}{S} \qquad [79]$$

where γ, d, and S are the conductivity of the electrolyte, the distance between the two electrodes, and their surface area, respectively.

For more general cell geometries, the potential is no longer uniform in the electrolyte. Figure 32 illustrates the potential and current distributions around a disk electrode when no polarization occurs at the WE and CE and in a cell with an ideal geometry, that is, the counter electrode of hemispherical shape is located at an infinite distance, the disk electrode (radius r) is mounted in an infinite insulating plane, and the electrolyte between the disk and the CE is homogeneous.[42] In these conditions, the equipotential surfaces, which can be calculated by solving the Laplace equation in elliptic coordinates, are ellipsoids. The potential and current distribution with no polarization at the WE and CE electrodes is called primary.

Provided the diffusion layers at the WE and CE are two very thin parts of the electrolyte volume, which is often the case with forced convection, and assuming that the polarization of the electrode can be neglected (this may not be true because of the nonuniform current density), the homogeneous part of the electrolyte contributes almost the whole electrolyte resistance and the corresponding potential distribution in the electrolyte is close to that given by Figure 32. The electrolyte resistance can then be calculated from the potential distribution[42]:

$$R_e = \frac{1}{\gamma}\frac{1}{4r} \qquad [80]$$

Table 2 Potential of the main reference electrodes used in corrosion[39–41]

Electrode	*Couple*	*Potential (V_{SHE})*
NHE	Pt|H_2|1 M HCl	+0
SCE	Hg|Hg_2Cl_2|sat. KCl	+0.24
Mercurous sulfate	Hg|Hg_2SO_4|sat. K_2SO_4	+0.64
Silver chloride	Ag|AgCl|3 M NaCl	+0.21
Silver chloride	Ag|AgCl|0.1 M NaCl	+0.29
Mercuric oxide	Hg|HgO|20% KOH	+0.10
Copper sulfate	Cu|sat. $CuSO_4$	+0.32

Figure 33 shows that the normalized potential Φ^0/Φ_{int} along the disk symmetry axis decreases almost linearly with the distance y from the electrode when y is smaller than the electrode radius. This potential profile justifies the use of a Luggin–Haber probe (the tip of the RE is a capillary usually filled with the studied solution and positioned close to the WE) to reduce

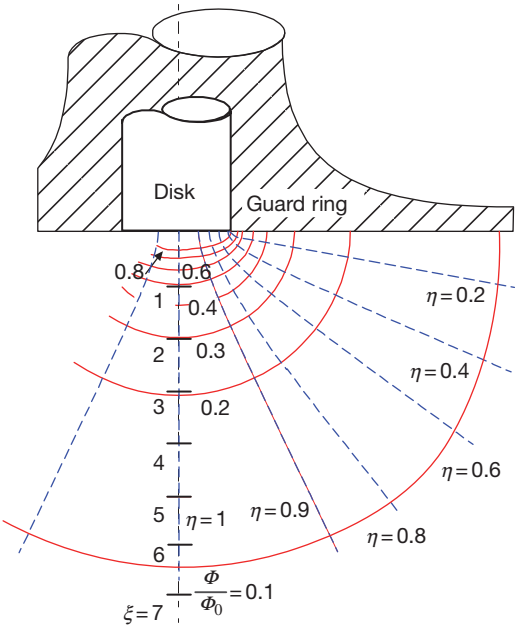

Figure 32 Primary potential (dotted lines) and current (dashed lines) distributions around a disk electrode for an ideal geometry cell. Adapted from Newman, J. *J. Electrochem. Soc.***1966**, *113*, 501–502.

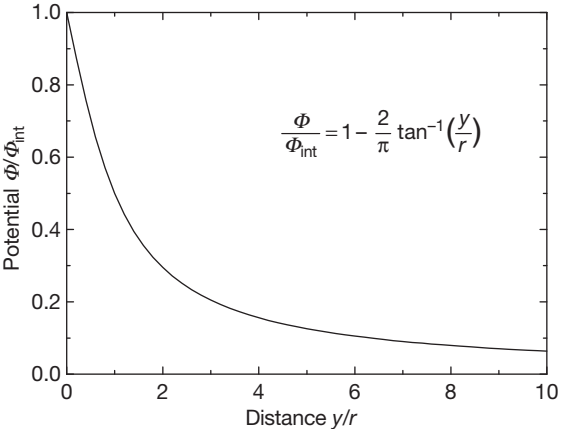

Figure 33 Potential profile along the symmetry axis of the disk electrode.

the distance between the WE and RE as much as possible and, therefore, decrease the corresponding ohmic drop, $R_e I$.[31] However, it is important to remark that the presence of the capillary close to the electrode surface induces a screening effect that may disturb the electrode potential markedly. In practice, it is then not essential to use a Luggin–Haber probe in conductive solutions since the electrolyte resistivity is low, especially in corrosion applications where the current is low as well. Because the majority of the solution resistance is concentrated close to the electrode (note in Figure 32 that 80% of the resistance occurs within $3r$ of the disc) and because the potential drop decreases as $1/r$ (the current is proportional to r^2, whereas the resistance is proportional to $1/r$), an alternative approach to the minimization of solution resistance effects is to use a very small electrode (a microelectrode), in which case the RE is situated remotely from the WE.

1.02.6.2 Potential Control and Current Control

In most recent commercial potentiostats and galvanostats, the potential or current control is performed

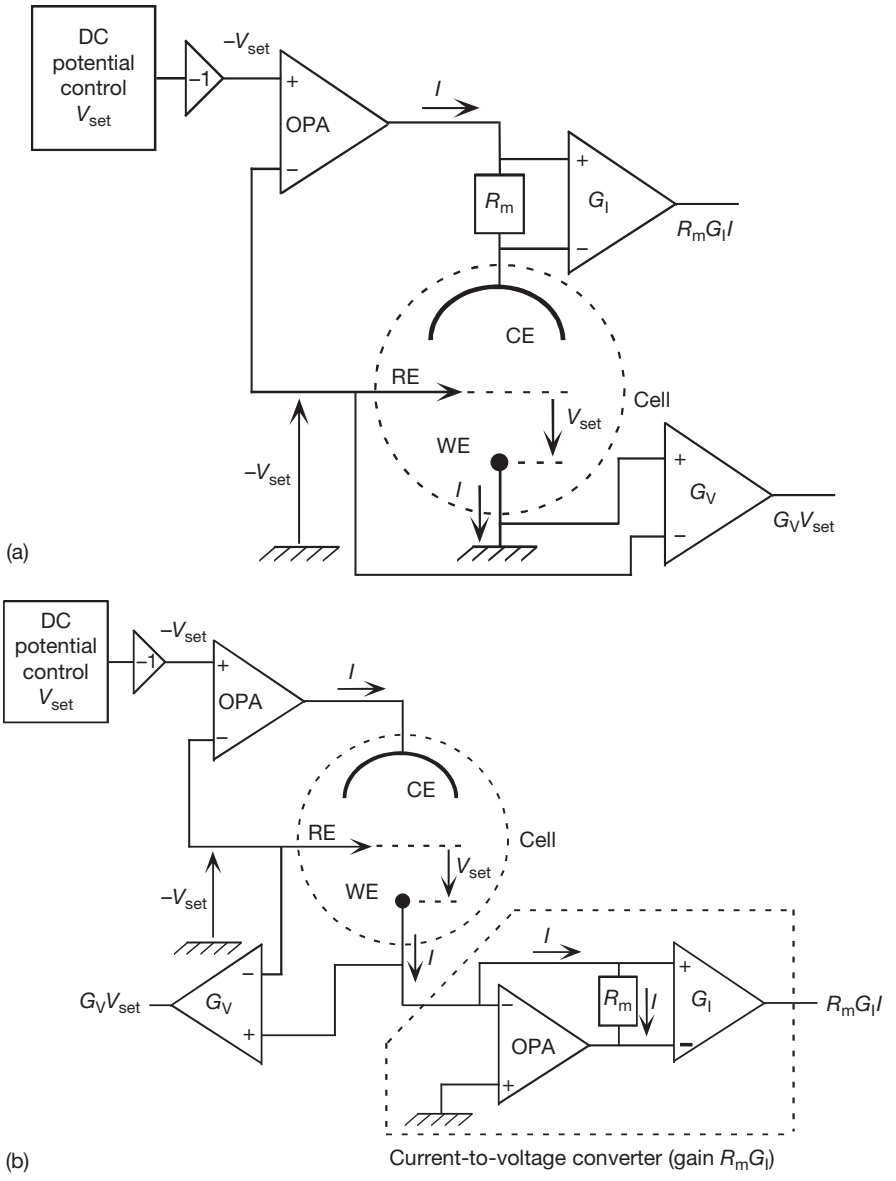

Figure 34 Schematic circuit of a potentiostat: the current is measured in the CE branch with a differential amplifier of gain G_I (a) or in the WE branch with a current-to-voltage converter of gain R_mG_I (b).

by using one or several operational amplifiers (OPA) according to the electrical schemes described below. For simplicity, only ideal OPA will be considered here, which means that no current can flow in the positive and negative inputs of the OPA and that both inputs have the same potential at any time (assuming that negative feedback is used to keep the OPA in the linear region of its behavior). Deviations from this ideal case, including nonzero input currents, limited frequency bandwidth, etc., and their consequences on the potential or current control, have been investigated thoroughly elsewhere.[43,44]

Figure 34 shows the experimental set-up used for controlling the electrochemical potential of a WE connected to the ground. Usually, this ground is floating, the chassis being connected to the earth ground for safety reasons. The voltage V_{set} (with respect to the ground) set by the user on the direct current (DC) potential control is first inverted with an amplifier of gain -1 (this is provided only in order to give the controlled potential the same sign as V_{set}, and it may be omitted in some designs). The voltage $-V_{set}$ on the positive input of the OPA is then imposed by the OPA on its negative input so that the potential difference between the RE and the WE is $-V_{set}$ as well and, therefore, the potential of the WE with respect to the RE is actually equal to V_{set}. In **Figure 34(a)**, the current I, which necessarily flows to the WE since no current can enter the negative input of the OPA through the RE, is measured from the voltage drop $R_m I$ across the resistor R_m in the CE branch. This voltage is amplified with a differential amplifier of high input impedance and gain G_I so that the gain in V/A of the current measurement is $R_m G_I$. In some equipment, the actual potential of the WE is measured with another differential amplifier of high input impedance (of gain G_V in **Figure 34**).

The current flowing to the WE can also be measured in the WE branch by using a current-to-voltage converter, also called zero-resistance ammeter (ZRA), of gain $R_m G_I$, as shown in **Figure 34(b)**. In that case, the WE is held at a virtual ground (the same potential as ground, but not connected directly to ground) via the OPA of the ZRA. This arrangement has the advantage of measuring the current actually flowing across the WE. As a consequence, in specific applications involving several WEs, it is possible to associate a ZRA with each WE to measure the current flowing into it, all WEs being at the same potential (virtual ground).

Figure 35 shows a simple way for imposing a constant current I_{set} with a potentiostat. A resistor

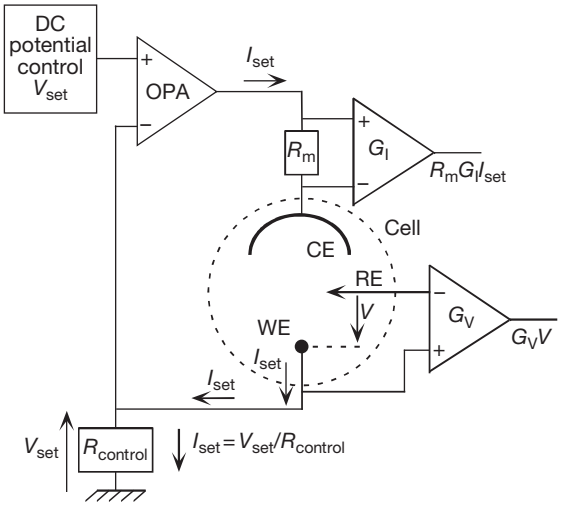

Figure 35 Schematic circuit of a simple galvanostat.

$R_{control}$ is positioned between the WE and the ground and a voltage $V_{set} = R_{control} I_{set}$ (with respect to the ground) is applied at the positive input of the OPA. In these conditions, the voltage at the negative input of the OPA is equal to V_{set} as well, so that a current $I_{set} = V_{set}/R_{control}$ crosses the resistor. Since no current can flow at the negative input of the OPA, this current I_{set} actually flows through the WE. Note that the WE is no longer grounded, which may be a drawback in some applications. To work correctly with a grounded WE, the potentiostat power supply must be isolated from ground or a galvanostat with a more complex electrical circuit must be used.

References

1. Itagaki, M.; Nakasawa, H.; Watanabe, K.; Noda, K. *Corros. Sci.* **1997**, *39*, 901–911.
2. Muñoz, A. G.; Vel, M. E.; Salvarezza, R. C. *Langmuir* **2005**, *21*, 9238–9245.
3. O'M. Bockris, J.; Khan, U. M. *Surface Electrochemistry: A Molecular Level Approach*; Plenum Press: New York, 1993; Chapter 3, pp 310–318.
4. Huet, F.; Nogueira, R. P.; Normand, B.; Takenouti, H. In *ASM Handbook Corrosion: Fundamentals, Testing and Protection* Cramer, S.D., Covino, B.S., Jr., Eds.; ASM International: Materials Park, OH, 2003; Vol. 13A, pp 52–60.
5. Plonski, I. H. *Int. J. Hydrogen Energy* **1996**, *21*, 837–851.
6. Epelboin, I.; Morel, Ph.; Takenouti, H. *J. Electrochem. Soc.* **1971**, *118*, 1282–1287.
7. Sastri, V. S. *Corrosion Inhibitors: Principles and Applications;* Wiley: West Sussex, 1998.
8. Kaesche, H. *Corrosion of Metals: Physicochemical Principles and Current Problems*; Springer: Berlin, 2003; Chapter 7, pp 144–158.

9. Keddam, M.; Mattos, O. R.; Takenouti, H. *J. Electrochem. Soc.* **1981**, *128*, 257–265, 266–274.
10. Heusler, K. E. *Z. Elektrochem.* **1958**, *62*, 582–587.
11. O'M Bockris, J.; Drazic, D.; Despic, A. R. *Electrochim. Acta* **1961**, *4*, 325–361.
12. Kelly, E. J. *J. Electrochem. Soc.* **1965**, *112*, 124–131.
13. Hilbert, F.; Miyoshi, Y.; Eichkorn, G.; Lorenz, W. J. *J. Electrochem. Soc.* **1971**, *118*, 1919–1926, 1927–1935.
14. Epelboin, I.; Keddam, M. *J. Electrochem. Soc.* **1970**, *117*, 1052–1056.
15. Greef, R.; Peat, R.; Peter, L. M.; Pletcher, D.; Robinson, J. In *Electrochemistry: Southampton Electrochemistry Group*; Ellis Horwood: West Sussex, 1985; Chapter 4, pp 139–143.
16. O'M. Bockris, J.; Khan, U. M. *Surface Electrochemistry: A molecular Level Approach*, Plenum Press: New York, 1993; Chapter 3, pp 319–348.
17. Crow, D. R. *Principles and Applications of Electrochemistry*, 4th ed.; Blackie Academic and Professional: Glasgow, 1994; Chapter 5, pp 68–71.
18. Bard, A. J.; Faulkner, L. R. *Electrochemical Methods: Fundamentals and Applications*, 2nd ed.; Wiley & Sons: Hoboken, 2001; Chapter 1, pp 12–14.
19. Stern, O. *Z. Elektrochem.* **1924**, *30*, 508–516.
20. Bagotsky, V. S. *Fundamentals of Electrochemistry*, 2nd ed.; Wiley & Sons: Hoboken, 2006; Chapter 4, pp 51–68.
21. Atkins, P. W. *Physical Chemistry*, 4th ed.; Oxford University Press: Oxford, 1990; Chapter 25, pp 763–769.
22. Fisher, A. C. *Electrode Dynamics*, 4th ed.; Oxford University Press: Oxford 1996; Chapter 2, pp 13–25.
23. Bard, A. J.; Faulkner, L. R. *Electrochemical Methods: Fundamentals and Applications*, 2nd ed.; John Wiley and Sons: Hoboken, 2001; Chapter 2, pp 60–62.
24. Oldham, K. B.; Myland, J. C. *Fundamentals of Electrochemical Science*; Academic Press: San Diego, 1994; Chapter 4, pp 117–120.
25. Bagotsky, V. S. *Fundamentals of Electrochemistry*, 2nd ed.; Wiley & Sons: Hoboken, 2006; Chapter 3, pp 39–45.
26. Compton, R. G.; Sanders, G. H. W. *Electrode Potentials*; Oxford University Press: Oxford, 1996; Chapter 1, pp 12–13.
27. *Handbook of Chemistry and Physics*, 78th ed.; Chemical Rubber Publishing Company: Boca Raton, 1997; 8-20–8-30.
28. Pourbaix, M. *Atlas of Electrochemical Equilibrium in Aqueous Solutions;* NACE: Houston, 1974.
29. Atkins, P. W. *Physical Chemistry*, 4th ed.; Oxford University Press: Oxford, 1990; Chapter 9, pp 225–237.
30. Landolt, D. In *Corrosion Mechanisms in Theory and Practice*; Marcus, P., Oudar, J., Eds.; Marcel Dekker: New York, 1995; pp 13–16.
31. Greef, R.; Peat, R.; Peter, L. M.; Pletcher, D.; Robinson, J. In *Electrochemistry: Southampton Electrochemistry Group*; Ellis Horwood: West Sussex, 1985; Chapter 1, pp 26–32.
32. Bard, A. J.; Faulkner, L. R. *Electrochemical Methods: Fundamentals and Applications*, Wiley & Sons: Hoboken, 2001; Chapter 9, p 339.
33. Scully, J. R. *Electrochemical Methods in Corrosion Science and Engineering*; Marcel Dekker: New York, 2002; Chapter 4, pp 125–150.
34. Stern, M.; Geary, A. L. *J. Electrochem. Soc.* **1957**, *104*, 56–63.
35. Marcus, P.; Mansfeld, F. *Analytical Methods in Corrosion Science and Engineering*; Taylor & Francis/CRC: Boca Raton, FL, 2006; Vol. 22: Corrosion Technology.
36. Greef, R.; Peat, R.; Peter, L. M.; Pletcher, D.; Robinson, J. In *Electrochemistry: Southampton Electrochemistry Group*; Ellis Horwood: West Sussex, 1985.
37. Bard, A. J.; Faulkner, L. R. Electrochemical Methods: Fundamentals and Applications, 2nd ed.; Wiley & Sons: Hoboken 2001.
38. Bard, A. J.; Faulkner, L. R. *Electrochemical Methods: Fundamentals and Applications*, 2nd ed.; Wiley & Sons: Hoboken, 2001; Chapter 2, pp 69–74.
39. Bard, A. J.; Faulkner, L. R. *Electrochemical Methods: Fundamentals and Applications*, 2nd ed.; Wiley & Sons: Hoboken, 2001; Appendix C, pp 808–810.
40. Bernard, M.; Busnot, F. *Usuel de chimie générale et minérale*; Dunod – Bordas: Paris, 1984; Chapter 3, p 205.
41. http://www.consultrsr.com/resources/ref/refpotls.htm.
42. Newman, J. *J. Electrochem. Soc.* **1966**, *113*, 501–502.
43. Schiller, C.-A. In *Analytical Methods in Corrosion Science and Engineering*; Marcus, P., Mansfeld, F., Eds.; Taylor & Francis/CRC Press: Boca Raton, FL, 2006; Vol. 22: Corrosion Technology, pp. 361–434.
44. Gabrielli, C. Identification of electrochemical processes by frequency response analysis Solartron, Farnborough: England, 1980; Technical Report no. 4/83; http://www.solartronanalytical.com/downloads/technotes/technote04.pdf.

1.04 Mechanical Properties and Fracture of Materials

A. H. Sherry
University of Manchester, Manchester, UK
T. J. Marrow
School of Materials, University of Manchester, Manchester, UK

Abbreviations

BS British Standard
EN Euro Norm
ASTM ASTM International
HRR Hutchinson, Rice and Rosegren
SCC Stress Corrosion Cracking
UTS Ultimate Tensile Stress (also Ultimate Tensile Strength)

Symbols

a Crack length
A Cross-sectional area
A_0 Initial cross-sectional area
B Thickness
$d\epsilon$ Increment of true strain
dL Change in gauge length under an applied load P
ds Increment of length along contour used to derive the J-integral
D Diameter
E Young's modulus
E' Young's modulus E under plane stress and $E/(1-\nu^2)$ under plane strain
F_Q Load at fracture in a fracture mechanics test
G_0–G_5 Geometry coefficients
I_n Integration parameter
J J-integral
J_c Fracture toughness under elastic–plastic conditions
K_I Mode I stress intensity factor
K_{Ic} Mode I fracture toughness under linear-elastic conditions
K_{ISCC} Threshold stress intensity factor for stress corrosion cracking
L_0 Initial gauge length
L Gauge length
n Ramberg–Osgood work hardening exponent
P Pressure
P Load
R Polar coordinate centered on the crack tip
R_i Inner radius of cylinder
R_o Outer radius of cylinder
r_p Radius of crack-tip plastic zone
T Wall thickness of cylinder
T_i Components of traction vector
U Strain energy
U_e Elastic strain energy
u_i Components of displacement vector
U_p Plastic strain energy
W Strain energy
W Width
Y Geometry parameter
Γ Anticlockwise contour around crack-tip used to calculate J-integral
α Material parameter in Ramberg–Osgood equation
ϵ True strain
ϵ_0 Reference strain in Ramberg–Osgood equation
ϵ_e Engineering strain
ϵ_{el} True elastic strain
ϵ_{pl} True plastic strain

η_p Nondimensional function of crack length
ν Poisson's ratio
θ Angular polar coordinate, centered on the crack tip
σ True stress
σ_0 Reference stress in Ramberg–Osgood equation
$\sigma_{0.2}$ Proof stress at 0.2% plastic true strain
σ_e Engineering stress
σ_{SCC} Threshold stress for stress corrosion cracking
σ_{xx} Stress in x-direction
σ_y Yield stress
σ_{yy} Stress in y-direction
σ_{zz} Stress in z-direction
$\tilde{\sigma}_{ij}(n,\theta)$ Dimensionless function of r and θ
τ_{xy} Shear stress (in the x–y plane)

1.04.1 Mechanical Properties

The mechanical properties of materials are conveniently measured and described with respect to the standard uniaxial tensile testing of round-bar or flat-plate specimens. Standard testing procedures, such as BS EN 10002–1:2001 and ASTM E8-04,[1,2] provide guidance on the measurement and interpretation of tensile load-versus-displacement (i.e., gauge length extension) data to obtain stress-versus-strain curves. Typical curves are illustrated in **Figures 1(a) and 1(b)** for a high-strength aluminum alloy and a ferritic pressure vessel steel respectively. The key regions of the stress-versus-strain curve are indicated in **Figure 2** and described in **Sections 1.04.2.1** and **1.04.2.2**. In order to interpret these, it is important to first provide a definition of stress and strain.

Consider the round tensile bar specimen illustrated in **Figure 3**, which has an initial gauge length L_0, a diameter D and is under an applied load P. The engineering stress within the specimen σ_e is defined by the applied load normalized by the *initial* cross-sectional area of the specimen, A_0, that is

$$\sigma_e = \frac{P}{A_0} \qquad [1]$$

For a round bar tensile specimen, A_0 is equal to $\pi D^2/4$, where D is the initial diameter of the bar. For a specimen of rectangular cross-section, A_0 is equal to WB, where W is the initial specimen width and B, the intial thickness. Equation [1] shows that the engineering stress is directly proportional to the load applied to the specimen. The same load applied to a specimen of smaller diameter will result in a higher applied stress.

The true stress applied to the specimen σ is defined as

$$\sigma = \frac{P}{A} \qquad [2]$$

where A is the *actual* cross-sectional area of the specimen under the load P. The true stress applied to the specimen is not directly proportional to the applied load, since the cross-sectional area of the specimen reduces progressively under an increasing tensile load. This is because the total volume of the specimen remains practically unchanged as the specimen deforms. Equation [1] therefore becomes an increasingly inaccurate measure of the true stress with increasing extension.

Engineering strain ε_e at a given applied load is defined by the increase in the gauge length of the specimen, dL, normalized by the *initial* gauge length of the specimen, L_0, that is

$$\varepsilon_e = \frac{dL}{L_0} \qquad [3]$$

Since the gauge length increases under load, the true strain ε at a given instant in the test is more accurately defined as

$$\varepsilon = \int_{L_0}^{L} \frac{dL}{L} = \ln(1+\varepsilon_e) \qquad [4]$$

where L is the *actual* gauge length of the specimen at the load of interest.

The true stress can be related to the engineering stress and strain through the following relation, which assumes constant volume[3]:

$$\sigma = \sigma_e(1+\varepsilon_e) \qquad [5]$$

1.04.1.1 Elastic Properties

The stress-versus-strain curves illustrated in **Figures 1(a) and 1(b)** exhibit a number of distinct regions. The first of these is characterized by a relationship between the applied stress and strain that is linear for most materials. Within this region, the strain accumulated under an applied tensile stress is fully recoverable upon unloading, that is, the material is 'elastic' and its shape is not permanently changed by the applied stress. The stress–strain relationship in this elastic (linear) region is defined by Hooke's law in which Young's modulus E given by

$$E = \frac{\sigma}{\varepsilon} \qquad [6]$$

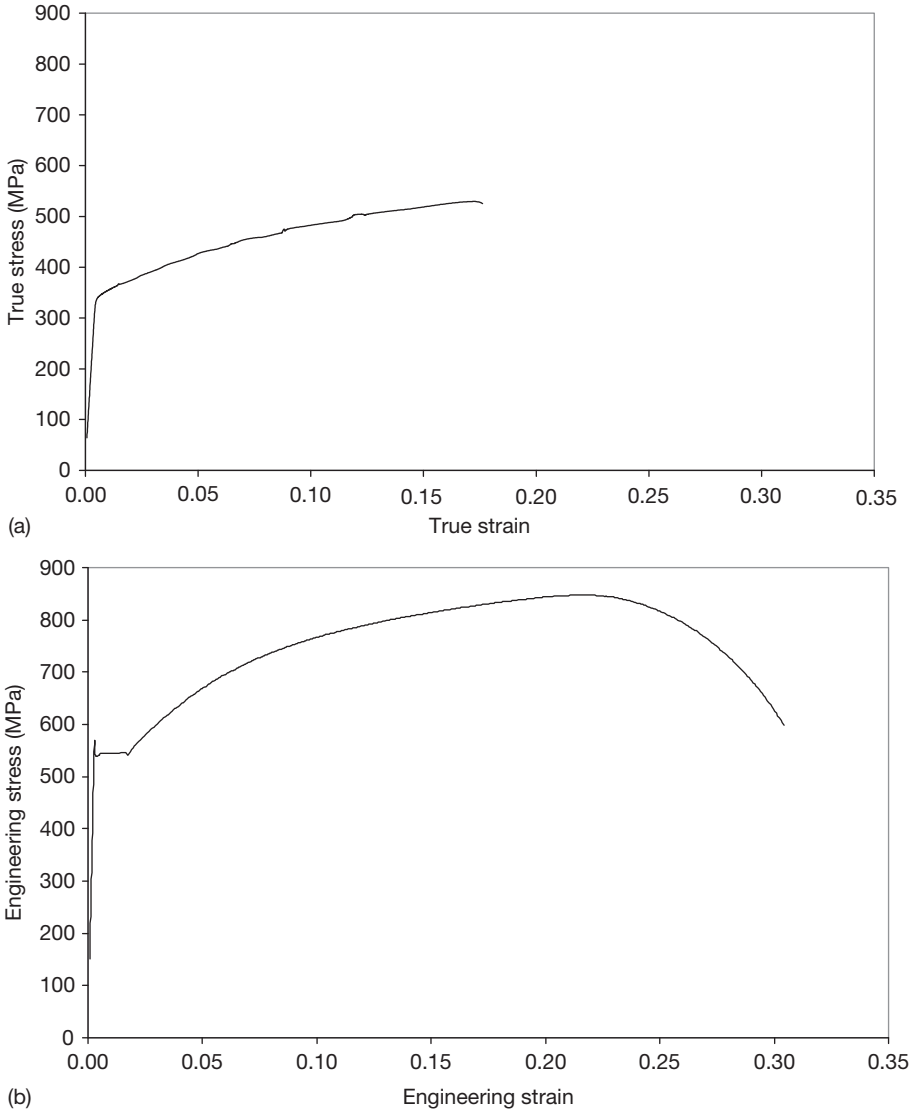

Figure 1 Typical stress–strain curves for (a) high strength aluminum alloy 2024-T351 tested at room temperature and (b) Euro-material – a quenched and tempered ferritic pressure vessel steel DIN 22Ni–MoCr37 (similar to steel type ASTM A508 Cl.3) tested at −90°C. (a) Adapted from Heerens, J.; Hellmann, D. *Eng. Fract. Mech.* **2002**, *69*, 421–449 and (b) Adapted from Bernauer, G.; Brocks, W. *Fat. Fract. Eng. Mater. Struct.* **2002**, *25*, 363–384.

Engineering stress and strain are normally sufficiently accurate to define Young's modulus for most materials with a reasonable degree of accuracy for engineering calculations. Within the linear elastic regime, eqn [6] can be used for loading in either tension or compression.

It is worth noting that the Young's modulus of many engineering materials is extremely high. For example, mild steel has a Young's modulus of ~210 GPa at room temperature. Consequently, any small inaccuracies in the measurement of displacement in this region will result in significant errors in the derived value of E. For this reason, other approaches have been developed for the accurate determination of Young's modulus. These include the measurement of the natural frequency of a vibrating loaded bar by spectroscopic techniques or derivation from the velocity of sound in the material.[3]

Although not measurable from the data shown in **Figures 1(a) and 1(b)**, Poisson's ratio ν is an important materials parameter, since it defines the ratio of the tensile strain accumulated in the loading direction to the compressive (or negative) strain accumulated in

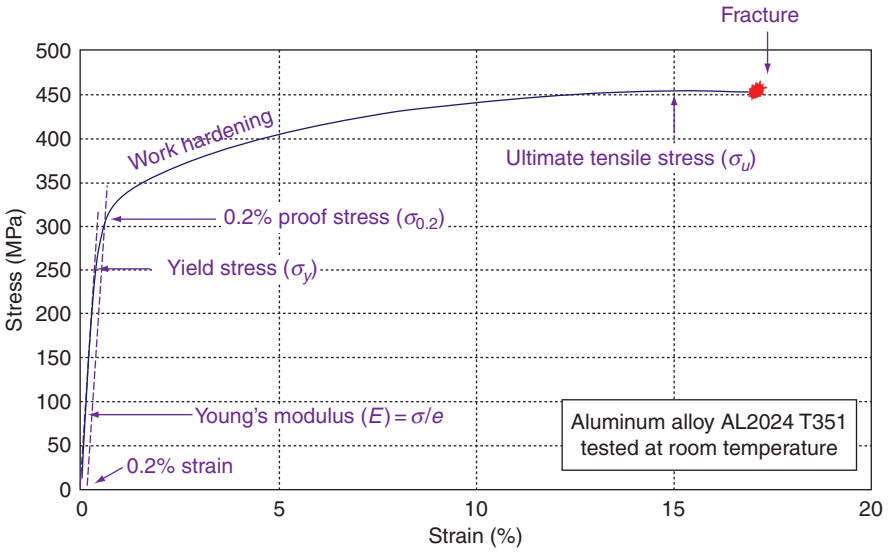

Figure 2 Key regions of a typical engineering stress–strain curve.

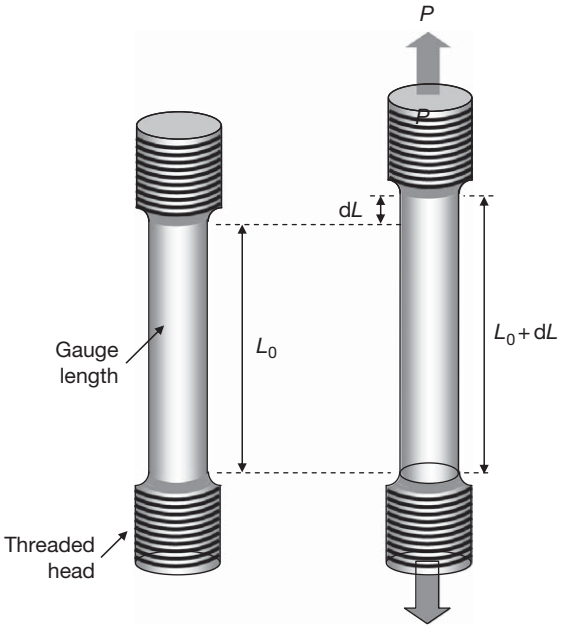

Figure 3 Schematic illustration of a round tensile specimen under an applied load *P*.

the perpendicular directions. Poisson's ratio is defined in the elastic regime and is given by

$$\nu = -\frac{\text{tensile strain}}{\text{perpendicular strain}} \qquad [7]$$

For many engineering materials, ν is close to 0.3 in the elastic regime. Poisson's ratio can be obtained by measurement of the cross-section dimensions of the specimen during testing, but accurate measurement requires other methods, similar to those used for Young's modulus.

The strain energy density or work per unit volume, U, that is expended by deforming a material is defined by the area under the true stress–true strain curve, that is,

$$U = \int_0^{\varepsilon} \sigma \, d\varepsilon \qquad [8]$$

Under linear elastic conditions, the elastic strain energy U_e is defined by

$$U_e = \frac{\sigma^2}{2E'} \qquad [9]$$

where elastic theory shows that $E' = E$ under plane stress conditions and $E/(1-\nu^2)$ under plane strain conditions. (Plane stress is defined as the condition where the out-of-plane stress is zero or negligible, i.e., in thin sheets or on the material surface. Plane strain is defined here as the condition where the out-of-plane strain is zero or negligible compared to the in-plane strains, i.e. in thick sections.)

1.04.1.2 Elastic–Plastic Properties

As the applied stress is increased in the tensile test, there comes a point where the resulting displacement can no longer be taken up by the elastic deformation of the material, and the material 'yields' plastically. Yielding, which occurs in metals by the movement of

crystallographic imperfections called 'dislocations,' is characterized by an increase in strain over and above that predicted by Young's modulus. The total strain of the specimen is thus a combination of elastic and plastic strain, that is,

$$\varepsilon = \varepsilon_{el} + \varepsilon_{pl} \quad [10]$$

where ε is the total true strain, ε_{el} is the elastic strain defined by σ/E, and ε_{pl} is the plastic strain.

The applied stress at the limit of proportionality is defined as the yield stress σ_y and is a characteristic property of the material. Loading the specimen up to a stress higher than the yield stress and subsequently unloading will result in the permanent deformation of the specimen equal to ε_{pl}. Thus, in contrast to elastic strain, plastic strain is not recovered.

The limit of proportionality is often difficult to discern accurately, and therefore, the yield stress is commonly defined by a proof stress. This is typically the 0.2% proof stress, $\sigma_{0.2}$, which is defined using a construction-line of gradient E drawn from an initial strain of 0.2%. The point at which this construction-line intersects the stress–strain curve is defined as $\sigma_{0.2}$. This is shown in **Figure 2**. This is also done in the case of materials, particularly ferritic steels that show a yield point (e.g., **Figure 1(b)**).

At applied stresses above the yield stress, the resistance to yielding increases, because the material work hardens as plastic deformation is accumulated. This is also known as cold work or strain hardening and is a consequence of an increase in the number of dislocations and their interactions with each other. The gradient of the stress–strain curve reduces in the work hardening region. This region may be characterized by a power-law relationship between stress and strain. In this way, eqn [10] may be formulated in terms of true stress and true strain to provide a full description of the stress–strain properties of materials.[4] For many materials, a suitable expression is

$$\frac{\varepsilon}{\varepsilon_0} = \left(\frac{\sigma}{\sigma_0}\right) + \alpha\left(\frac{\sigma}{\sigma_0}\right)^n \quad [11]$$

where α is a material parameter, often close to unity, σ_0 is a reference stress usually taken as the yield or 0.2% proof stress, ε_0 is the reference strain ($=\sigma_0/E$), and n is the Ramberg–Osgood work hardening exponent. This work hardening exponent is typically between 5 and 10 for ferritic steels. Equation [11] is known as the Ramberg–Osgood equation, and is illustrated in **Figure 4** with normalized stress-versus-strain curves plotted for $\alpha = 1$ and $3 \leq n \leq \infty$.

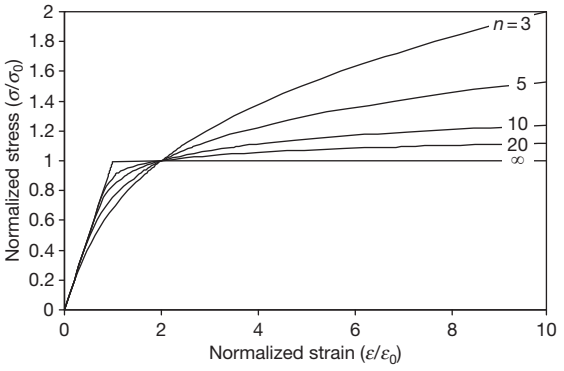

Figure 4 Normalized stress–strain curves plotted using the Ramberg–Osgood equation.

In ductile metals, at a critical strain, the tensile specimen begins to 'neck.' Up to this point, the plastic deformation occurs uniformly and stably throughout the gauge length as the rate of increase in stress due to the geometric reduction in cross-section is balanced by the rate of increase in yield stress due to work hardening. At the onset of necking, the plasticity becomes unstable and is concentrated within a localized region of the gauge length, when the geometric and work hardening factors become unbalanced. This is shown in **Figure 5(a)**. This critical strain for necking occurs at the maximum load, and thus corresponds to the maximum in the engineering stress, which is termed the ultimate tensile stress (UTS) σ_u (**Figure 2**). It can be shown by Considère's construction that, for a material following the Ramberg–Osgood equation, necking begins at a strain $\varepsilon = 1/n$.[5]

For ductile materials, fracture follows necking and normally shows a characteristic 'cup-and-cone' fracture. Ductile void growth and coalescence occurs within the neck of the specimen, and then extends by shear fracture, leading to the characteristic appearance of 'ductile dimples' from this 'microvoid coalescence' process, **Figures 5(b)** and **5(c)**.

1.04.2 Fracture Properties

1.04.2.1 The Elastic Stress Intensity Factor

The linear elastic stress intensity factor, K_I, is a parameter that quantifies the conditions of stress local to the tip of an infinitely sharp crack in an elastic material. It has the units of MPa $m^{-1/2}$. The subscript 'I' denotes that the stress intensity factor relates to Mode I loading, in which the applied loading is perpendicular to the plane of the crack, **Figure 6**. Whilst there are other modes of loading including in-plane and out-of-plane

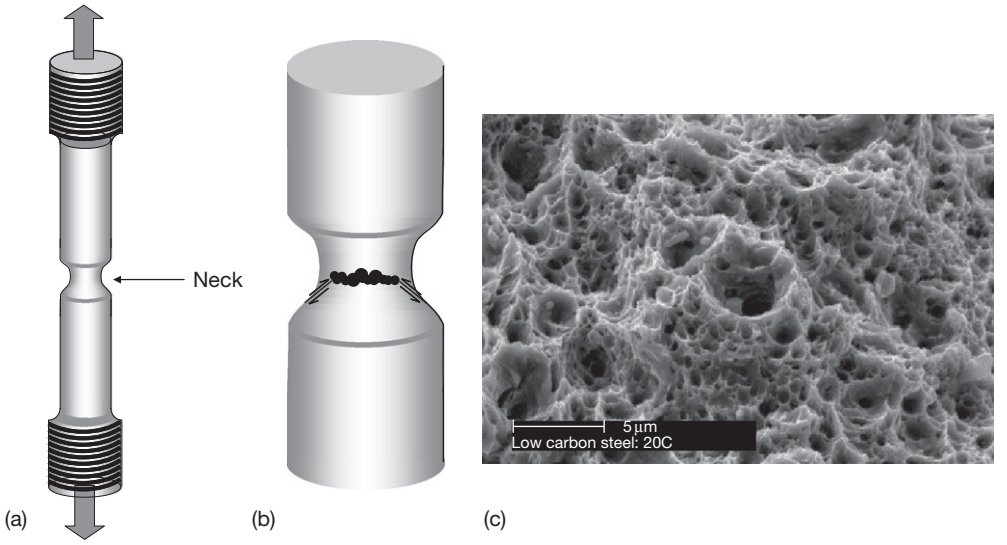

Figure 5 Schematic illustration of: (a) neck formed in tensile specimen tested beyond UTS, (b) development of cup-and-cone fracture, and (c) Scanning electron micrograph of ductile microvoid coalescence in low carbon steel.

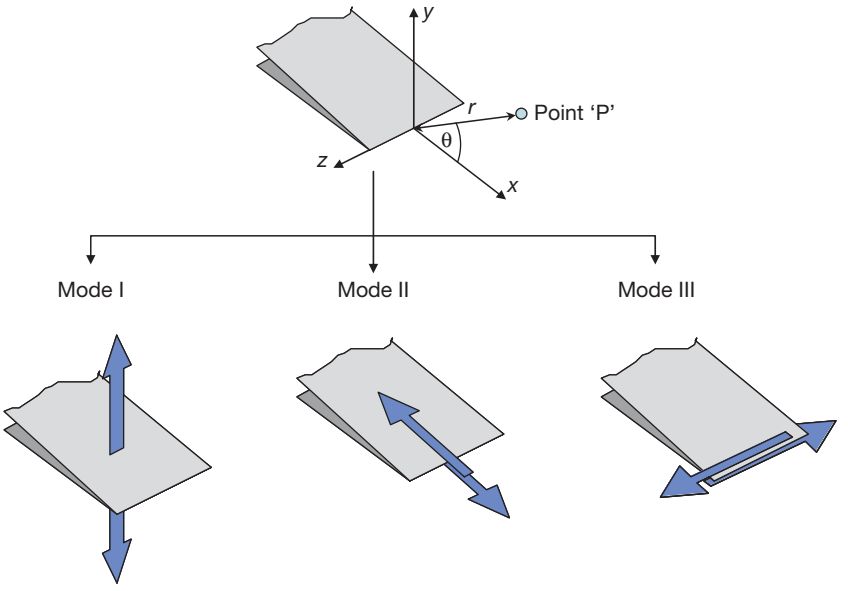

Figure 6 Definition of coordinate system and three modes of loading on a crack: Mode I opening, Mode II in-plane shear, Mode III out-of-plane shear.

shear and combinations thereof, Mode I loading is normally considered the most severe and discussion within this section is restricted to this mode.

The equations that relate K_I to the stress at a point 'P' in the vicinity of a sharp crack-tip in an elastic material (Figure 6) are given by series expressions known as the Westergaard functions. The first and dominant term in the series expansion are given below for plane strain conditions:

$$\sigma_{xx} = \frac{K_I}{(2\pi r)^{1/2}}\cos\left(\frac{\theta}{2}\right)\left[1-\sin\left(\frac{\theta}{2}\right)\sin\left(\frac{3\theta}{2}\right)\right]$$

$$\sigma_{yy} = \frac{K_I}{(2\pi r)^{1/2}}\cos\left(\frac{\theta}{2}\right)\left[1+\sin\left(\frac{\theta}{2}\right)\sin\left(\frac{3\theta}{2}\right)\right]$$

$$\sigma_{zz} = \nu\left(\sigma_{xx}-\sigma_{yy}\right)$$

$$\tau_{xy} = \frac{K_I}{(2\pi r)^{1/2}}\sin\left(\frac{\theta}{2}\right)\cos\left(\frac{\theta}{2}\right)\cos\left(\frac{3\theta}{2}\right) \qquad [12]$$

Within eqn [12], the subscripts indicate the Cartesian coordinate system that defines the plane of the crack and the loading direction, r and θ are polar coordinates of the point of interest (**Figure 6**), and v is Poisson's ratio. **Figure 7** illustrates the distribution of opening stress σ_{yy} directly ahead of a crack in an elastic material under Mode I loading, that is, increasing r with $\theta = 0°$. The stresses are proportional to K_I and hence the magnitude of the stress field within elastic material in the vicinity of a sharp crack under Mode I loading may thus be deduced from a knowledge of K_I.

A similar set of Westergaard functions relates the local strain in elastic material in the vicinity of a crack tip to K_I. Thus, as was the case for local stress, the magnitude of the strain field within elastic material in the vicinity of a sharp crack under Mode I loading may also be deduced from knowledge of K_I. The stress intensity factor is therefore a direct measure of the elastic strain energy in a stressed material that contains a crack.

Since failure by fracture is controlled by critical combinations of stress and strain in material close to the crack tip, the stress intensity factor, K_I, provides a means for quantifying the 'crack driving force' acting on a crack-like flaw in a stressed component – *albeit* strictly only within the elastic regime. The higher the value of K_I, the higher the crack driving force. In terms of thermodynamics, crack growth requires sufficient elastic strain energy to balance the energy needed to create the surfaces of the crack. This includes the work associated with the deformation and fracture mechanisms of the material. A critical stress intensity factor, which is sufficient for crack propagation, can therefore be determined.

The magnitude of K_I acting on a given crack-like flaw is dependent upon three factors: (1) the magnitude of the applied stress, (2) the size of the flaw, and (3) the geometry of the component. The general form of the equation that relates the applied stress σ and the flaw size a to K_I is as follows:

$$K_I = \sigma Y \sqrt{\pi a} \qquad [13]$$

where Y is a geometry parameter. Values for Y for common component geometries are tabulated in standards such as,[6] and are typically of the order of unity. As shown by eqn [13], the magnitude of K_I is directly proportional to the applied stress acting on the component. Thus, increasing the stress applied to a cracked component by a factor of two will double the magnitude of K_I. The stress intensity factor K_I is also dependent on the square root of the crack depth a. Y is also dependent on crack length in some geometries, but the effect is generally less strong. Consequently, under a fixed applied stress, the magnitude of K_I increases as the crack depth increases. Hence, for a crack extending gradually by a mechanism such as SCC, in which the rate of crack growth can increase with K_I, there can be an acceleration of crack growth.

An example of equations defining the stress, σ, and the geometry parameter, Y, is given in **Figure 8** for an axially cracked pipe under internal pressure, in which the crack (e.g., a stress corrosion crack) is on the inner surface[7]:

$$\sigma = \frac{pR_o^2}{\left(R_o^2 - R_i^2\right)}$$

$$Y = 2G_0 - 2G_1\left(\frac{a}{R_i}\right)_1 + 3G_2\left(\frac{a}{R_i}\right)^2 - 4G_3\left(\frac{a}{R_i}\right)^3 + 5G_5\left(\frac{a}{R_i}\right)^4 \qquad [14]$$

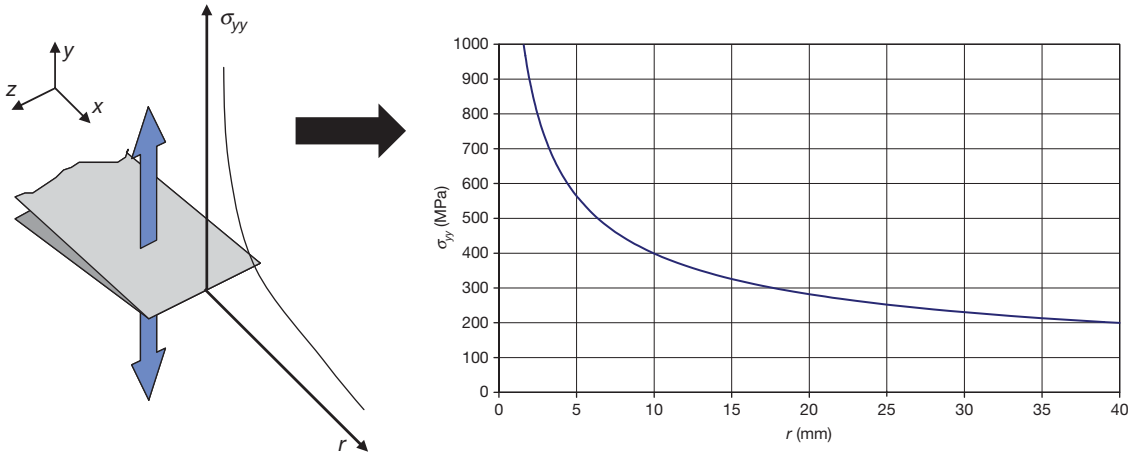

Figure 7 Elastic opening stress field ahead of a crack in an elastic material under Mode I loading with K_I = 100 MPa m$^{-1/2}$.

where σ is the circumferential stress acting on the plane of the crack due to the internal pressure, a is the crack depth, R_i is the internal radius of the cylinder, and R_o is the outside radius of the cylinder. The coefficients G_0–G_5 are tabulated in API 579.[7] Equation [14] is valid within the following geometric limits: $0 \leq a/t \leq 0.8$ and $2 \leq R_i/t \leq 1000$ where t is the wall thickness of the pipe, $t = (R_o - R_i)$.

The stress intensity factor is a valid parameter to characterize fracture properties of materials under linear-elastic conditions. However, simple inspection of eqn [12] and **Figure 7** shows that in a metal the stresses close to the crack tip will readily exceed the yield stress. Plastic deformation therefore occurs at the crack tip, in a region called the plastic zone, and the assumption of elastic conditions would strictly not be valid. However, when the plastic zone size at the tip of the crack-like flaw is small compared with the dimensions of the component, the deformation of the component may be regarded as elastic and the stress intensity factor can be valid also. Under plane strain conditions the radius of the plastic zone, r_p, may be calculated according to the following expression[8]:

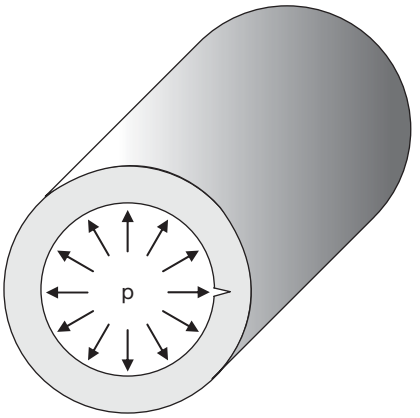

Figure 8 Schematic illustration of axially-cracked pipe.

$$r_p = \frac{1}{6\pi}\left(\frac{K_I}{\sigma_y}\right)^2 \qquad [15]$$

Fracture toughness testing standards (see **Section 1.04.3**) specify that for K_I to be a valid, the crack-tip parameter r_p must be less than ~1/50th of the characteristic dimensions of the specimen, that is

$$a, B, (W - a) \geq 2.5\left(\frac{K_I}{\sigma_y}\right)^2 \qquad [16]$$

where B is the specimen thickness, W is the specimen width, and $(W - a)$ is the uncracked ligament associated with the fracture mechanics test specimen geometry, see **Figure 9**. Where this condition is not satisfied for any of these three measures of specimen dimension, a nonlinear parameter is required to account for the plastic deformation and to thereby characterize the crack-driving force. The $\mathcal{J}$-integral provides this parameter and is briefly described in the following section.

1.04.2.2 The *J*-Integral

For a material that follows the Ramberg–Osgood stress–strain law, eqn [11], the crack-tip deformation fields may be characterized by the Hutchinson,[9] Rice, and Rosegren (HRR) fields[10] in a manner similar to that of the Westergaard functions given previously as eqn [12]. The HRR field equation for the crack-tip stress field is defined as follows:

$$\sigma_{ij} = \sigma_0\left(\frac{E\mathcal{J}}{\alpha\sigma_0^2 I_n r}\right)^{1/n+1}\tilde{\sigma}_{ij}(n,\theta) \qquad [17]$$

where I_n is an integration parameter dependent on the work hardening exponent, n, $\tilde{\sigma}_{ij}(n,\theta)$ is a dimensionless function of n and θ, and $\mathcal{J}$ is the so-called $\mathcal{J}$-integral; a contour integral following an

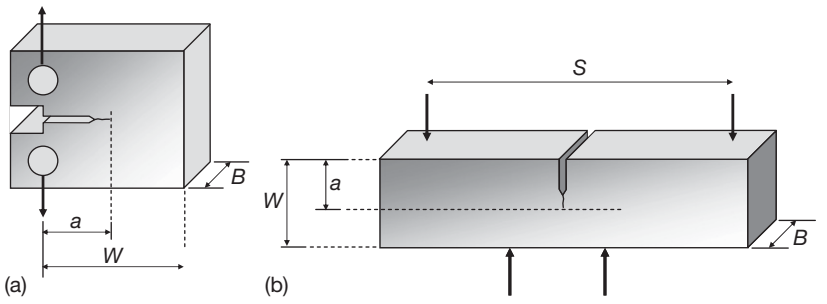

Figure 9 Schematic illustration of fracture mechanics test specimens (a) compact-tension specimen and (b) four-point bend specimen. Note arrows indicate direction of loading.

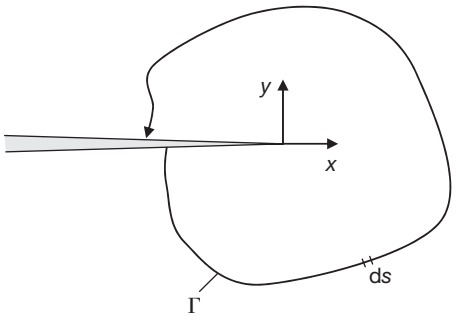

Figure 10 Anticlockwise contour around crack tip used to define the *J*-integral, eqn [18].

anticlockwise path around the tip of a crack, **Figure 10**, which defined as follows:

$$\mathcal{J} = \int_{\Gamma} \left(w \, \mathrm{d}y - T_i \frac{\partial u_i}{\partial x} \, \mathrm{d}s \right) \qquad [18]$$

where w is the strain energy density, T_i are components of the traction vector, u_i are the components of the displacement vector, and $\mathrm{d}s$ is an increment of length along the contour Γ.[8]

The $\mathcal{J}$-integral is widely used to define the crack-tip stress and strain fields for materials in the elastic-plastic regime, that is, in circumstances where eqn [16] does not hold. Under small-scale yielding conditions (i.e., in the elastic regime where the plastic zone size is small compared with the component and the assumption of elastic deformation implicit in eqn [16] is adequate), $\mathcal{J}$ is related to K_I via eqn [19][8]

$$K_I^2 = E' \mathcal{J} \qquad [19]$$

1.04.2.3 Fracture Toughness

The fracture toughness of a material is a measure of its capacity to resist failure by the onset of crack extension. It can therefore be used to determine whether a crack in a component will grow by fracture processes under certain conditions of loading. Under linear elastic conditions, the critical stress intensity factor K_I measured at the onset of fracture is used to define the fracture toughness of materials and is given the subscript 'c,' that is, K_{Ic}. The unit of K_{Ic} is MPa $m^{-1/2}$. Under conditions of more widespread plasticity, the elastic–plastic $\mathcal{J}$-integral is widely used to define the critical crack-tip conditions and hence the fracture toughness in the elastic–plastic regime, $\mathcal{J}_c$. The unit of $\mathcal{J}_c$ is kJ m^{-2}.

Fracture toughness properties of materials are conveniently measured using standard specimens containing cracks such as compact-tension (CT) specimens or Single Edge-Notched Bend (SENB) specimens, **Figure 9**. Standard sized specimens tend to be used, with B between 12.5 and 50 mm. Much larger and smaller specimens are possible, however.

Standard testing procedures provide guidance on the derivation of fracture toughness properties from tests performed on fracture mechanics specimens. These standards describe stringent test conditions to ensure that valid measurements of K_{Ic} or $\mathcal{J}_c$ are obtained. For example:

- BS7448: 'Fracture Mechanics Toughness Tests.' Part 1:1991, 'Method for determination of K_{Ic}, Critical CTOD, and Critical $\mathcal{J}$ values of metallic material.' British Standards Institute, London.
- ASTM E399-90, 'Standard Test Method for Plane Strain Fracture Toughness of Metallic Materials,' American Society for Testing and Materials, Philadelphia, 1990.

Within these procedures, the fracture toughness of the material is determined from the measured load versus displacement behavior of the specimen, tested at the temperature of interest. The displacement is measured as the crack mouth opening displacement (CMOD) along the load line, which is the line between the points of loading. Loading is generally applied in a quasi-static manner (i.e., slow displacement rates of the order of mm/min) so that dynamic loading effects do not influence the test results. Dynamic effects arise because the mechanism of yielding (i.e., movement of dislocations) is strain rate sensitive. This can cause the yield stress to rise and fracture toughness to be lowered by high strain rates, particularly in ferritic steels.

Under *linear elastic conditions*, the fracture toughness is derived from expressions that relate the applied load at fracture to the stress intensity factor. For a CT specimen, the expression is as follows[11]:

$$K_{Ic} = \frac{F_Q}{BW^{1/2}} Y \sqrt{\pi a} \qquad [20]$$

where F_Q is the load at fracture, B is the specimen thickness, W is the specimen width, and a is the crack length (**Figure 11**). The geometry term Y is a function of the crack length-to-specimen width ratio, a/W. Linear elastic conditions can be obtained in standard sized specimens in high-strength materials such as age-hardened aluminum alloys, or structural ferritic steels tested at low temperatures.

Under *elastic–plastic conditions*, the fracture toughness is derived from expressions that depend on the

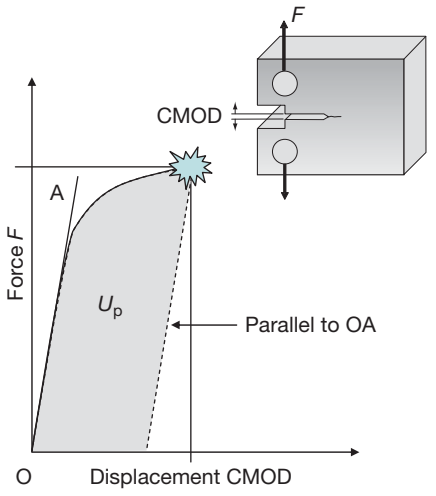

Figure 11 Schematic illustration of load F versus crack mouth opening displacement (CMOD) trace and definition of area under curve U.

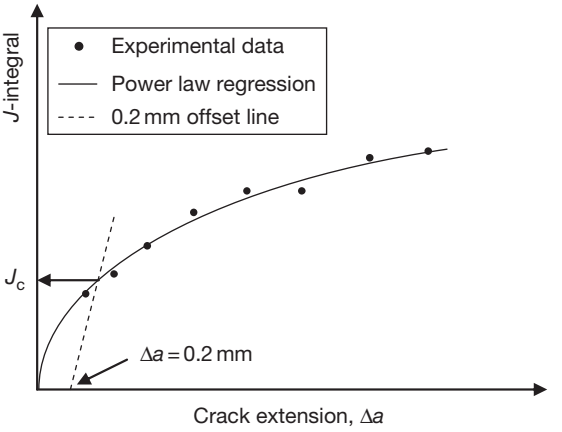

Figure 12 Schematic illustration of definition of J_c from a J R-curve.

applied load at fracture, but which also account for the additional work done by deformation in the crack tip plastic zone. For a CT specimen, the expression for $\mathcal{J}$ is as follows[11]

$$\mathcal{J} = \left[\frac{F}{BW^{1/2}}\, Y\sqrt{\pi a}\right]^2 \frac{(1-\nu)}{E} + \frac{\eta_p U_p}{B(W-a)} \qquad [21]$$

where ν is Poisson's ratio, E is Young's modulus, a is the current crack length, and U_p is the plastic strain energy. This is defined by the plastic area under the measured load-versus-displacement curve, which is the shaded region in Figure 11. The parameter η_p is a function of crack length.

The crack length, a, at which $\mathcal{J}$ is measured can be larger than the initial crack length a_0, since stable crack extension Δa can occur during test, for example, by ductile tearing. To obtain the initiation fracture toughness, $\mathcal{J}_c$, it is necessary to plot the variation of $\mathcal{J}$ as a function of Δa, either using data obtained from a number of interrupted tests, or using a single specimen tested using the unloading compliance technique.[8] A power-law curve is fitted to the valid data and the initiation toughness defined by the intersection of a 0.2 mm offset line and the $\mathcal{J}$ versus Δa power-law curve (known as the $\mathcal{J}$ R-curve) as illustrated in Figure 12.

Elastic–plastic conditions are typically obtained in standard sized specimens in tough materials, such as structural ferritic steels at ambient or elevated temperatures, or austenitic stainless steels. The measured fracture toughness, $\mathcal{J}_c$, can be used to calculate the fracture toughness, K_{1c}, using eqn [19], in order to predict the behavior of structural components that are much larger than the standard test specimen and in which linear elastic conditions would apply.

In most materials, the fracture toughness is not strongly affected by temperature. However, the fracture toughness of ferritic steels is sensitive to temperature. This is due to an effect of their body-centered cubic crystal structure on the mechanism of yielding. For example, the fracture toughness of ferritic pressure vessel steels at low temperatures can be as low as 20 MPa $m^{-1/2}$. This is the brittle fracture regime. In the ductile fracture regime, observed at higher temperatures, the fracture toughness of ferritic steel at the onset of ductile tearing is typically of the order of 200 MPa $m^{-1/2}$. The 'brittle–ductile transition temperature' describes fracture behavior between these two regimes and can be strongly sensitive to the microstructure of the steel. Neutron irradiation also affects the yield behavior and toughness of ferritic steels. The fracture toughness test is therefore a very important tool to predict the effect of temperature and other factors such as neutron irradiation, on the structural integrity of ferritic steel components containing crack-like flaws.

1.04.3 Application of Fracture Mechanics to SCC

Under a static loading condition, the growth of stress corrosion cracks is often characterized using a fracture mechanics-based approach to define the crack growth rate as a function of the stress intensity factor K_I. This approach assumes that the crack length relative to the length scale of both the material microstructure and

component is sufficient such that the crack driving force can be defined by K_I. Linear elastic conditions therefore apply, and such cracks may be described as 'long cracks.' Under such circumstances the required condition for crack growth by SCC is

$$K_I \geq K_{ISCC} \quad [22]$$

where K_{ISCC} defines the threshold stress intensity factor for sustained crack growth.

For $K_I \geq K_{ISCC}$, an initiated crack will continue to propagate, whereas for $K_I < K_{ISCC}$, an initiated crack will arrest. (Strictly, the condition for arrest is that crack propagation is not measurable. It may therefore be necessary to assume that crack growth may occur at a rate below the resolution of the measurements.) The stresses in a component can change during the lifetime, sometimes as a consequence of crack growth, and this approach can be used to determine whether a growing stress corrosion crack will arrest.

Cracks initiated at stress concentrating features (e.g., corrosion pits) can be too short to be characterized by K_I, due to either their length relative to the microstructure scale or the development of elastic-plastic deformation at the stresses needed to achieve K_I values approaching K_{ISCC}. A threshold stress σ_{SCC} may then be used to define the conditions required to propagate such cracks. Under these circumstances, the required condition for 'short crack' growth by SCC is

$$\sigma \geq \sigma_{SCC} \quad [23]$$

where σ is the applied tensile stress. For a component where $\sigma \geq \sigma_{SCC}$, an initiated short crack will continue to propagate, whereas for $\sigma < \sigma_{SCC}$, an initiated short crack will arrest. The critical stress, σ_{SCC}, is measured experimentally by observation of the behavior of cracks nucleated in statically stressed specimens.

This transition between short and long SCC cracks, and σ- or K_I-controlled crack growth may be considered using a two-parameter approach to SCC. This is illustrated schematically in **Figure 13**. The solid line defines the conditions above which SCC will be sustained (the unacceptable region). Below this line, any crack that has formed will arrest (the acceptable region). It can be seen that incorrectly applying long crack K_I-controlled behavior to short cracks can be nonconservative, that is, shallow cracks may propagate even when $K_I < K_{ISCC}$.

The prediction of component lifetime requires data for the effect of the crack-driving force on the crack growth rate. As shown by **Figure 13**, depending on the crack length, the driving force for SCC crack growth

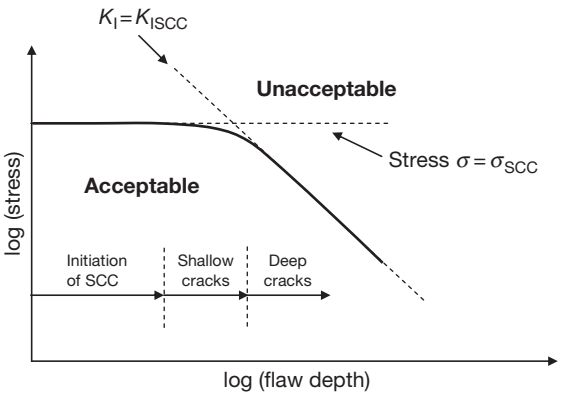

Figure 13 Schematic illustration of the two-parameter approach to stress corrosion cracking.

may either be too low and SCC does not occur (long cracks) or may be stress-controlled (short cracks). For short cracks, the crack growth rate tends to increase with stress. For long cracks, as the applied K_I increases above K_{ISCC}, the crack growth rate rises rapidly to a plateau, **Figure 14(a)**. It is important to note that the magnitude of both K_{ISCC} and the crack growth rate plateau are both material and environment dependent. For example, **Figure 14(b)**, reproduced from Reference 12, shows the influence of copper content on long SCC crack growth rates for Al–Cu–Mg alloys. Reference 13 provides guidance regarding the generation of K_{ISCC} data using precracked laboratory specimens loaded under fixed load or fixed displacement conditions.

In practice, most crack-like flaws in components in which SCC is of concern are found using NDE techniques. Cracks nucleating from weld defects are typical of this. Such cracks are often of a size that can be treated using the principles of fracture mechanics, and the K_I parameter is appropriate. However, there may be some circumstances when a stress-based approach is required – particularly when the crack initiates at a surface from pitting and significant crack growth occurs under stress-control. Under these circumstances, it is important to take full account of the stress-controlled extent of crack extension.

There are a number of further important issues that should be considered in the measurement and application of K_{ISCC} data. These include:

- K_{ISCC} will depend on the environment, material condition, and loading configuration used. For example, the loading configuration may affect the transport of chemical species to the crack tip. The conditions used to generate the data should

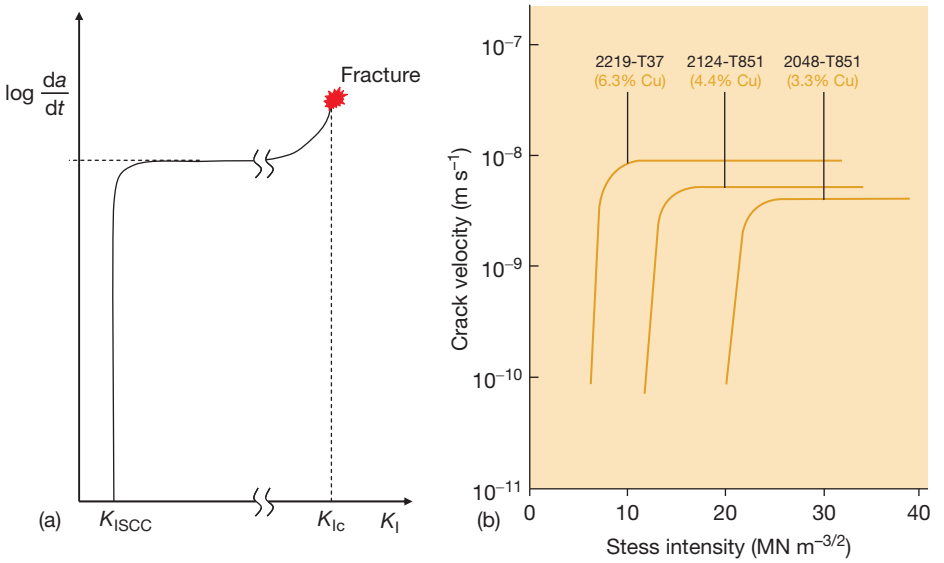

Figure 14 (a) Schematic illustration of SCC crack growth rate as a function of applied K_I, (b) SCC data for Al–Cu–Mg alloys of varying copper content. Reproduced from Cottis, R. A. Guides to good practice in corrosion control: stress corrosion cracking, NPL Report, 2000.

therefore reflect as closely as possible the service conditions of interest.

- The timescales used to generate K_{ISCC} are often shorter than typical timescales for components. For example, components in power generation may require lifetimes in excess of 40 years. As stress corrosion involves time-dependent chemical reactions, rate effects should be considered.
- While K_{ISCC} testing is conventionally carried out under static loading, service loading often includes periodic unloads and reloads (e.g., due to start-up and shutdown), in which the loading rates can be quite slow or very fast relative to the K_{ISCC} test. Under such circumstances, K_{ISCC} may be affected.

References

1. BS EN 10002-1:2001, Tensile testing of metallic materials. Method of test at ambient temperature; British Standards Institution, 2001.
2. ASTM E8-04, Standard Test Methods for Tension Testing of Metallic Materials American Society for Testing and Materials (ASTM) International, 2004.
3. Ashby, M. F.; Jones, D. R. H. *Engineering Materials: An Introduction to their Properties and Applications;* Pergamon Press: New York, 1980.
4. Patel, S. A.; Venkatraman, B.; Bentson, J. *J. Franklin Inst.* **1963**, *275*, 98–106.
5. Weil, N. A. *J. Franklin Inst.* **1958**, *265*, 97–116.
6. Murakami, Y. *Stress Intensity Factors Handbook;* Pergamon Press: New York, 1987; Vol. 1 and Vol. 2; 1992; Vol. 3.
7. API 579, Fitness for Service; American Petroleum Institute Recommended Practice, 2000.
8. Anderson, T. L. *Fracture Mechanics: Fundamentals and Applications,* 2nd ed.; CRC Press: New York, 1995.
9. Hutchinson, J. W. *J. Mech. Phys. Solids,* **1968**, pp 13–31, Vol. 16.
10. Rice, J. R.; Rosengren, G. F. *J. Mech. Phys. Solids* **1968**, *16*, 1–12.
11. BS7448, *Fracture Mechanics Toughness Tests. Part 1, Method for Determination of K_{Ic}, Critical CTOD and Critical J Values of Metallic Material;* British Standards Institute: London, 1991.
12. Cottis, R. A. Guides to good practice in corrosion control: SCC, NPL Report 2000.
13. ISO 7539-6:2003, Corrosion of metals and alloys – stress corrosion testing – part 6: preparation of pre-cracked specimens for tests under constant load or constant displacement, International Standards Organisation, 2003.

1.05 Basic Concepts of Corrosion

L. L. Shreir[†]

This article is a revision of the Third Edition article 1.1 by L. L. Shreir, volume 1, pp 1:3–1:15, © 2010 Elsevier B.V.

1.05.1 Introduction

Modern technology has at its disposal a wide range of constructional materials – metals and alloys, plastics, rubber, ceramics, composites, wood, etc., and the selection of an appropriate material for a given application is the important responsibility of the design engineer. No general rule governs the choice of a particular material for a specific purpose, and a logical decision involves a consideration of the relevant properties, ease of fabrication, availability, relative costs, etc. of a variety of materials; often, the ultimate decision is determined by economics rather than by properties, and ideally, the material selected should be the cheapest possible that has adequate properties to fulfill the specific function.

Where metals are involved, mechanical, physical, and *chemical* properties must be considered, and in this connection, it should be observed that while mechanical and physical properties can be expressed in terms of constants, the chemical properties of a given metal are dependent entirely on the precise environmental conditions prevailing during service. The relative importance of mechanical, physical, and chemical properties depends, in any given case, on the application of the metal. For example, for railway lines, elasticity, tensile strength, hardness, and abrasion resistance are of major importance, whereas electrical conductivity is of primary significance in electrical transmission. In the case of heat-exchanger tubes, good thermal conductivity is necessary, but this may be outweighed in certain environments by chemical properties in relation to the aggressiveness of the two fluids involved – thus, although the thermal conductivity of copper is superior to that of aluminum brass or the cupronickels, the alloys are preferred when high-velocity seawater is used as the coolant, as copper has very poor chemical properties under these conditions.

While a metal or alloy may be selected largely on the basis of its mechanical or physical properties, the fact remains that there are very few applications where the effect of the interaction of a metal with its environment can be completely ignored, although the importance of this interaction is of varying significance according to circumstances; for example, the slow uniform wastage of a steel structure of massive cross-section (such as railway lines or sleepers) is of far less importance than the rapid perforation of a buried steel pipe or the sudden failure of a vital stressed steel component in sodium hydroxide solution.

The effect of the metal–environment interaction on the environment itself is often more important than the actual deterioration of the metal. For instance, lead pipes cannot be used for conveying plumbo-solvent

[†]Deceased.

waters, since a lead level of >0.1 ppm is toxic; similarly, galvanized steel may not be used for certain foodstuffs owing to the toxicity of zinc salts. In many chemical processes, the selection of a particular metal may be determined by the need to avoid the contamination of the environment with traces of metallic impurities that would affect the color or taste of products or catalyze undesirable reactions; therefore, copper and copper alloys cannot be used in soap manufacture, since traces of copper ions result in the coloration and rancidification of the soap. In these circumstances, it is essential to use unreactive and relatively expensive metals, even though the environment would not result in the rapid deterioration of cheaper metals such as mild steel. A further possibility is that the contamination of the environment by metal ions due to the corrosion of one metal can result in an enhanced corrosion of another when the two are in contact with the same environment. Thus, the slow uniform corrosion of copper by a cuprosolvent domestic water may not be particularly deleterious to copper plumbing, but it can result in the rapid pitting and consequent perforation of galvanized steel and aluminum that subsequently comes into contact with the copper-containing water.

Finally, it is necessary to point out that for a number of applications, metals are selected in preference to other materials because of their visual appearance, and for this reason, it is essential that brightness and reflectivity are retained during exposure to the atmosphere; stainless steel is now widely used for architectural purposes, and for outdoor exposure, the surface must remain bright and rust-free without periodic cleaning. On the other hand, the slow-weathering steels, which react with the constituents of the atmosphere to form an adherent uniform coating of rust, are now being used for cladding buildings, in spite of the fact that a rusty surface is usually regarded as aesthetically unpleasant.

The interaction of a metal or alloy (or a nonmetallic material) with its environment is clearly of vital importance in the performance of materials of construction, and the fact that the present work is largely confined to a detailed consideration of such interactions could create the impression that this was the sole factor of importance in material selection. This, of course, is not the case, although it is probably true that this factor is most neglected by the design engineer.

1.05.2 Definitions of Corrosion

In the case of nonmetallic materials, the term *corrosion* invariably refers to their deterioration from chemical causes, but a similar concept is not necessarily applicable to metals. Many authorities[1] consider that the term *metallic corrosion* embraces all interactions of a metal or alloy (solid or liquid) with its environment irrespective of whether this is deliberate and beneficial or adventitious and deleterious. Thus, this definition of corrosion, which, for convenience, is referred to as the *transformation* definition, includes, for example, the deliberate anodic dissolution of zinc in cathodic protection and electroplating as well as the spontaneous gradual wastage of zinc roofing sheet, resulting from atmospheric exposure.

On the other hand, *corrosion* has been defined[2] as 'the undesirable deterioration' of a metal or alloy, that is, an interaction of the metal with its environment that adversely affects those properties of the metal that are to be preserved. This definition – which is referred to as the *deterioration* definition – is also applicable to nonmetallic materials such as glass, concrete, etc. and embodies the concept that corrosion is always deleterious. However, the restriction of the definition to undesirable chemical reactions of a metal results in anomalies that become apparent from a consideration of the following examples.

Steel, when exposed to an industrial atmosphere, reacts to form the reaction product rust of approximate composition $Fe_2O_3 \cdot H_2O$, which, being loosely adherent, does not form a protective barrier that isolates the metal from the environment; the reaction thus proceeds at an approximately linear rate until the metal is completely consumed. Copper, on the other hand, forms an adherent green patina corresponding approximately to bronchantite, $CuSO_4 \cdot 3Cu(OH)_2$, which is protective and isolates the metal from the atmosphere. Copper roofs installed 200 years ago are still performing satisfactorily, and it is apparent that the formation of bronchantite is not deleterious to the function of copper as a roofing material – indeed, in this particular application, it is considered to enhance the appearance of the roof, although a similar patina formed on copper water pipes would be aesthetically objectionable.

The rapid dissolution of a vessel constructed of titanium in hot 40% H_2SO_4, with the formation of Ti^{4+} aquo cations, conforms to both definitions of corrosion, but if the potential of the metal is raised (anodic protection), a thin adherent protective film of anatase, TiO_2, is formed, which isolates the metal from the acid so that the rate of corrosion is enormously decreased. The formation of this very thin oxide film on titanium, like that of the relatively thick bronchantite film on copper, clearly conforms to the *transformation* definition of corrosion, but not with the *deterioration* definition, since in these examples, the rate and extent of the reaction are not significantly

detrimental to the metal concerned. Again, magnesium, zinc, or aluminum is deliberately sacrificed when these metals are used for the cathodic protection of steel structures, but as these metals are clearly not required to be maintained as such, their consumption in this particular application cannot, according to the *deterioration*, be regarded as corrosion. Furthermore, corrosion reactions are used to advantage in technological processes such as pickling, etching, chemical, and electrochemical polishing and machining, etc.

The examples already discussed lead to the conclusion that any reaction of a metal with its environment must be regarded as a corrosion process irrespective of the extent of the reaction or of the rates of the initial and subsequent stages of the reaction. It is not illogical, therefore, to regard *passivity*, in which the reaction product forms a very thin protective film that controls rate of the reaction at an acceptable level, as a limiting case of a corrosion reaction. Thus, both the rapid dissolution of *active* titanium in 40% H_2SO_4 and the slow dissolution of *passive* titanium in that acid must be regarded as corrosion processes, even though the latter is not detrimental to the metal during the anticipated life of the vessel.

It follows that in deciding whether the corrosion reaction is detrimental to a metal in a given application, the precise form of attack on the metal (general, intergranular, etc.), the nature of the reaction products (protective or nonprotective), the velocity and extent of the reaction, and the location of the corrosion reaction must all be taken into account. In addition, due consideration must be given to the effect of the corrosion reaction on the environment itself. Thus, corrosion reactions are not always detrimental, and our ability to use highly reactive metals such as aluminum, titanium, etc. in aggressive environments is due to a limited initial corrosion reaction, which results in the formation of a rate-controlling corrosion product. Expressions such as 'preventing corrosion,' 'combating corrosion,' or even 'fighting corrosion' are misleading; with the majority of metals, corrosion cannot be avoided and 'corrosion control' rather than 'prevention' is the desired goal. The implication of 'control' in this context is that (1) neither the form nor the extent, nor the rate of the corrosion reaction must be detrimental to the metal used as a constructional material for a specific purpose and (2) for certain applications, the corrosion reaction must not result in the contamination of the environment. Corrosion control must involve a consideration of materials, availability, fabrication, protective methods, and economics in relation to the specific function of the metal and its anticipated life. At one extreme, corrosion control in certain environments may be effected by the use of thick sections of mild steel without any protective system, at the other, the environmental conditions prevailing may necessitate the use of platinum.

The scope of the term 'corrosion' is continually being extended, and Fontana and Staehle have stated[3] that '*corrosion*' includes the reaction of metals, glasses, ionic solids, polymeric solids, and composites with environments that embrace liquid metals, gases, nonaqueous electrolytes, and other nonaqueous solutions.

Vermilyea, who has defined corrosion as a process in which atoms or molecules are removed one at a time, considers that the evaporation of a metal into vacuum should come within the scope of the term, since atomically it is similar to other corrosion processes.[4]

Evans[5] considers that corrosion may be regarded as a branch of chemical thermodynamics or kinetics, as the outcome of electron affinities of metals and nonmetals, as short-circuited electrochemical cells, or as the demolition of the crystal structure of a metal.

These considerations lead to the conclusion that there is probably a need for two definitions of corrosion that depend upon the approach adopted:

1. Definition of corrosion in the context of Corrosion Science: the reaction of a solid with its environment.
2. Definition of corrosion in the context of Corrosion Engineering: the reaction of an engineering constructional metal (material) with its environment with a consequent deterioration in properties of the metal (material).

1.05.3 Methods of Approach to Corrosion Phenomena

The effective use of metals as materials of construction must be based on an understanding of their physical, mechanical, and chemical properties. The last, as pointed out earlier, cannot be divorced from the environmental conditions prevailing. Any fundamental approach to the phenomena of corrosion must therefore involve a consideration of the structural features of the metal, the nature of the environment, and the reactions that occur at the metal–environment interface. The more important factors involved may be summarized as follows:

1. *Metal* – composition, detailed atomic structure, microscopic and macroscopic heterogeneities, stress (tensile, compressive, cyclic), etc.
2. *Environment* – chemical nature, concentrations of reactive species and deleterious impurities, pressure, temperature, velocity, impingement, etc.
3. *Metal–environment interface* – kinetics of metal oxidation and dissolution, kinetics of the reduction

of species in solution, nature and location of corrosion products, film growth and film dissolution, etc.

From these considerations, it is evident that the detailed mechanism of metallic corrosion is highly complex and that an understanding of the various phenomena involves many branches of the pure and applied sciences, for example, metal physics, physical metallurgy, the various branches of chemistry, bacteriology, etc., although the emphasis may vary with the particular system under consideration. Thus, in stress-corrosion cracking, emphasis may be placed on the detailed metallurgical structure in relation to crack propagation resulting from the conjoint action of corrosion at localized areas and mechanical tearing, while in underground corrosion, the emphasis may be on the mechanism of bacterial action in relation to the kinetics of the overall corrosion reaction.

Although the mechanism of corrosion is highly complex, the actual control of the majority of corrosion reactions can be effected by the application of relatively simple concepts. Indeed, the Committee on Corrosion and Protection[6] concluded that 'better dissemination of existing knowledge' was the most important single factor that would be instrumental in decreasing the enormous cost of corrosion in the United Kingdom.

1.05.3.1 Corrosion as a Chemical Reaction at a Metal–Environment Interface

As the first approach to the principles which govern the behavior of metals in specific environments, it is preferable, for simplicity, to disregard the detailed structure of the metal and to consider corrosion as a heterogeneous chemical reaction that occurs at a metal–nonmetal interface and that involves the metal itself as one of the reactants (cf. catalysis). Corrosion can be expressed, therefore, by the simple chemical reaction:

$$aA + bB = cC + dD \qquad [1]$$

where A is the metal and B the nonmetal reactant (or reactants), and C and D, the products of the reaction. The nonmetallic reactants are often referred to as *the environment*, although it should be observed that in a complex environment, the major constituents may play a very subsidiary role in the reaction. Hence, in the 'atmospheric' corrosion of steel, although nitrogen constitutes ~75% of the atmosphere, its effect, compared with that of moisture, oxygen, sulfur dioxide, solid particles, etc., can be disregarded (in the high temperature reaction of titanium with the atmosphere, on the other hand, nitrogen is a significant factor).

One of the reaction products (say, C) will be an oxidized form of the metal, and D will be a reduced form of the nonmetal – C is usually referred to as the *corrosion product*, although the term could apply equally to D. In its simplest form, reaction [1] becomes

$$aA + bB = cC \quad \text{e.g.,}\ 4Fe + 3O_2 = 2Fe_2O_3 \qquad [2]$$

where the reaction product can be regarded either as an oxidized form of the metal or as the reduced form of the nonmetal. Reactions of this type, which do not involve water or aqueous solutions, are referred to as 'dry' corrosion reactions.

The corresponding reaction in aqueous solution is referred to as a 'wet' corrosion reaction, and the overall reaction (which actually occurs by a series of intermediate steps) can be expressed as

$$4Fe + 2H_2O + 3O_2 = 2Fe_2O_3 \cdot H_2O \qquad [3]$$

Thus, in all corrosion reactions, one (or more) of the reaction products will be an oxidized form of the metal, aquo cations (e.g., Fe^{2+} (aq.), Fe^{3+} (aq.)), aquo anions (e.g., $HFeO_2^-$ (aq.), FeO_4^{2-} (aq.)), or solid compounds (e.g., $Fe(OH)_2$, Fe_3O_4, $Fe_3O_4 \cdot H_2O$, $Fe_2O_3 \cdot H_2O$), while the other reaction product (or products) will be the reduced form of the nonmetal. Corrosion may be regarded, therefore, as a *heterogeneous redox reaction at a metal–nonmetal interface in which the metal is oxidized and the nonmetal is reduced.* In the interaction of a metal with a specific nonmetal (or nonmetals) under specific environmental conditions, the chemical nature of the nonmetal, the chemical and physical properties of the reaction products, and the environmental conditions (temperature, pressure, velocity, viscosity, etc.) are clearly important in determining the form, extent, and rate of the reaction.

1.05.3.2 Environment

Some examples of the behavior of normally reactive and nonreactive metals in simple chemical solutions are considered here to illustrate the fact that corrosion is dependent on the nature of the environment; the thermodynamics of the systems and the kinetic factors involved are considered in subsequent chapters.

Gold is stable in most strong reducing acids, whereas iron corrodes rapidly, yet finely divided gold can be quickly dissolved in oxygenated cyanide solutions that may be contained in steel tanks. A mixture of caustic soda and sodium nitrate can be fused in an iron or nickel crucible, whereas this melt would have a disastrous effect on a platinum crucible.

Copper is relatively resistant to dilute sulfuric acid, but corrodes if oxygen or oxidizing agents are present in the acid, whereas austenitic stainless steels are stable in this acid only if oxygen or other

oxidizing agents are present. Iron corrodes rapidly in oxygenated water, but extremely slowly if all oxygen is removed; if, however, oxygen is brought rapidly and simultaneously to all parts of the metal surface, the rate will become very low, owing to the formation of a protective oxide film. Lead dissolves rapidly in nitric acid, more slowly in hydrochloric acid, and very slowly in sulfuric acid. These examples show that the corrosion behavior of a metal cannot be divorced from the specific environmental conditions prevailing, which determine the rate, extent (after a given period of time), and form of the corrosion process.

1.05.3.3 Metal

Heterogeneities associated with a metal have been classified in **Table 1** as atomic (see **Figure 1**), microscopic (visible under an optical microscope), and macroscopic, and their effects are considered in various sections of the present work. It is relevant to observe, however, that the detailed mechanism of all aspects of corrosion, for example, the passage of a metallic cation from the lattice to the solution, specific effects of ions and species in solution in accelerating or inhibiting corrosion or causing stress-corrosion cracking, etc. must involve a consideration of the detailed atomic structure of the metal or alloy.

The corrosion behavior of different constituents of an alloy is well known, since the etching techniques used in metallography are essentially corrosion processes that take advantage of the different corrosion rates of phases as a means of identification, for example, the grain boundaries are usually etched more rapidly than the rest of the grain owing to the greater reactivity of the disarrayed metal.

Macroscopic heterogeneities, for example, crevices, discontinuities in surface films, bimetallic contacts, etc. have a pronounced effect on the location and the kinetics of the corrosion reaction and are considered in various sections throughout this work. Practical environments are shown schematically in **Figure 2**, which also serves to emphasize the relationship between the detailed structure of the metal, the environment, and external factors such as stress, fatigue, velocity, impingement, etc.

1.05.4 Types of Corrosion

Corrosion can affect the metal in a variety of ways, which depend on its nature and the precise environmental conditions prevailing, and a broad classification of the various forms of corrosion, in which five major types have been identified, is presented in **Table 2**. Thus, an 18Cr–8Ni stainless steel corrodes uniformly during polishing, active dissolution, or passivation, but locally during intergranular attack, crevice corrosion, or pitting; in certain circumstances, selective attack along an 'active path' in conjunction with a tensile stress may lead to a transgranular fracture. Types of corrosion are dealt with in more detail in Appendix A.

Ideally, the metal selected, or the protective system applied to the metal, should be such that no corrosion occurs at all, but this is seldom technologically or economically feasible. It is necessary, therefore, to tolerate a rate and a form of corrosion that will not be significantly detrimental to the properties of the metal during its anticipated life. Thus, provided the corrosion rate is known, the slow uniform corrosion of a metal can often be allowed for in the design of the structure; for example, in the case of a metal that shows an active–passive transition, the rate of corrosion in the passive region is usually acceptable, whereas the rate in the active region is not. It follows that certain forms of

Table 1 Heterogeneities in metal

1. *Atomic* (as classified by Ehrlich and Turnbull,[7] see **Figure 1**).
   a. Sites within a given surface layer ('normal' sites); these vary according to the particular crystal plane (**Figure 3**).
   b. Sites at edges of partially complete layers.
   c. Point defects in the surface layer: vacancies (molecules missing in surface layer), kink sites (molecules missing at edge of layer), molecules adsorbed on top of complete layer.
   d. Disordered molecules at point of emergence of dislocations (screw or edge) in metal surface.
2. *Microscopic*
   a. Grain boundaries – usually, but not invariably, more reactive than grain interior.
   b. Phases – metallic (single metals, solid solutions, intermetallic compounds), nonmetallic, metal compounds, impurities, etc. – heterogeneities due to thermal or mechanical causes.
3. *Macroscopic*
   a. Grain boundaries.
   b. Discontinuities on metal surface – cut edges, scratches, discontinuities in oxide films (or other chemical films) or in applied metallic or nonmetallic coatings.
   c. Bimetallic couples of dissimilar metals.
   d. Geometrical factors – general design, crevices, contact with nonmetallic materials, etc.

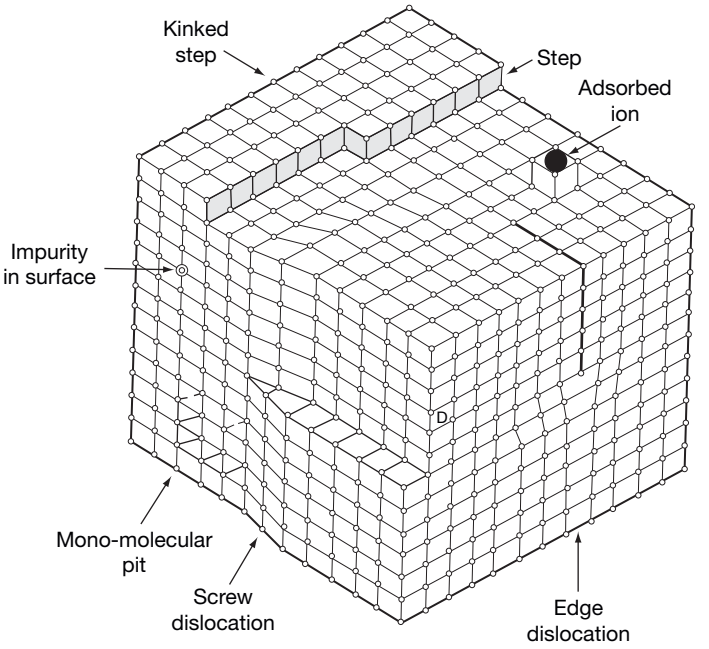

Figure 1 Surface imperfections in a crystal. Reproduced from Ehrlich, G.; Turnbull, D. *Physical Metallurgy of Stress Corrosion Fracture*; Interscience: New York and London, 1959; p 47, with permission from Interscience.

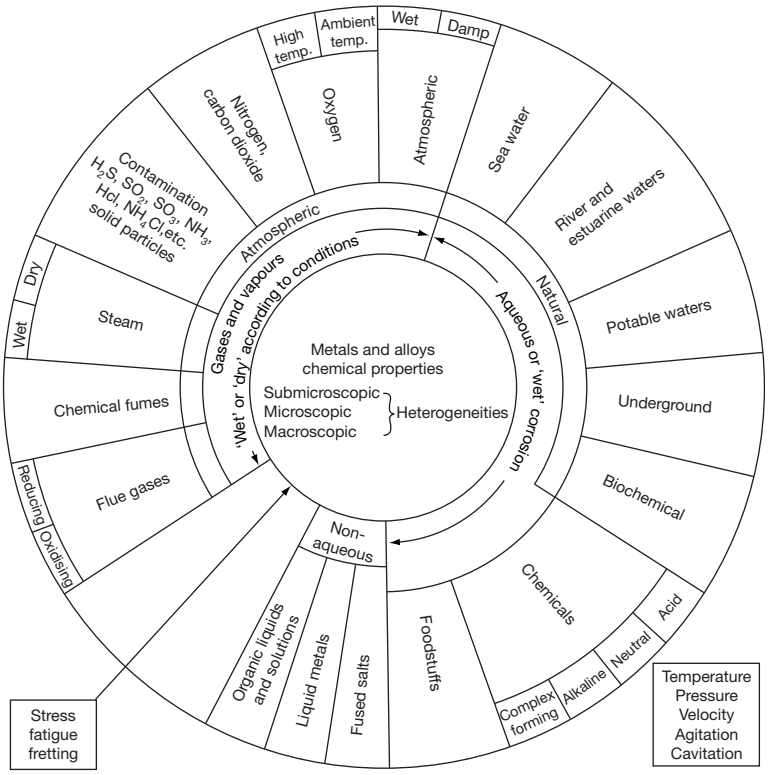

Figure 2 Environments in corrosion.

corrosion can be tolerated and that corrosion control is possible, provided that the rate and the form of the corrosion reaction are predictable and can be allowed for in the design of the structure.

Pitting is regarded as one of the most insidious forms of corrosion, since it often leads to perforation and to a consequent corrosion failure. In other cases, pitting may result in a loss of appearance, which is of major importance when the metal concerned is used for decorative architectural purposes. However, aluminum saucepans that have been in service for some time are invariably pitted, although the pits seldom penetrate the metal, that is, the saucepan remains functional and the pitted appearance is of no significance in that particular application.

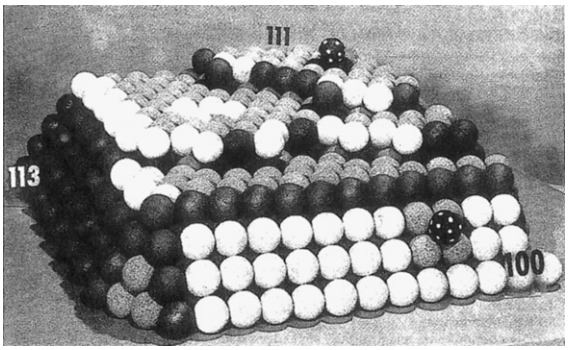

Figure 3 Hard-sphere model of face-centered cubic (fcc) lattice showing various types of sites. Numbers denote Miller indices of atom places and the different shadings correspond to differences in the number of nearest neighbors. Reproduced from Ehrlich, G.; Turnbull, D. *Physical Metallurgy of Stress Corrosion Fracture*; Interscience: New York and London, 1959; p 47, with permission from Interscience.

These considerations lead to the conclusion that the relationship between corrosion and the deterioration of properties of a metal is highly complex and involves a consideration of a variety of factors such as the rate and the form of corrosion and the specific function of the metal concerned; certain forms of corrosion such as uniform attack can be tolerated, whereas others such as pitting and stress corrosion cracking that ultimately lead to complete loss of function cannot be.

The implications of the terms *predictable* and *unpredictable* used in the context of corrosion require further consideration, since they are clearly dependent on the knowledge and expertise of the engineer, designer, or corrosion designer who takes the decision on the metal or alloy to be used, or the procedure to be adopted, to control corrosion in a specific environmental situation. On this basis, a corrosion failure (i.e., failure of the function of the metal due to corrosion within a period that is significantly less than the anticipated life of the structure) may be the result of one or more of the following possibilities:

1. *Predictable.* (1) The knowledge and technology are available, but have not been utilized by the designer; this category includes a wide variety of

Table 2 Types of corrosion

Type	*Characteristic*	*Examples*
1. Uniform (or almost uniform)	All areas of the metal corrode at the same (or similar) rate	Oxidation and tarnishing; active dissolution in acids; anodic oxidation and passivity; chemical and electrochemical polishing; atmospheric and immersed corrosion in certain cases
2. Localized	Certain areas of the metal surface corrode at higher rates than others due to 'heterogeneities' in the metal, the environment or in the geometry of the structure as a whole. Attack can range from being slightly localized to pitting	Crevice corrosion; filiform corrosion; deposit attack; bimetallic corrosion; intergranular corrosion; weld decay
3. Pitting	Highly localized attack at specific areas resulting in small pits that penetrate into the metal and may lead to perforation	Pitting of passive metals such as the stainless steels, aluminum alloys, etc., in the presence of specific ions, for example, Cl^- ions
4. Selective dissolution	One component of an alloy (usually the most active) is selectively removed from an alloy	Dezincification; dealuminification; graphitization
5. Conjoint action of corrosion and a mechanical factor	Localized attack or fracture due to the synergistic action of a mechanical factor and corrosion	Erosion – corrosion, fretting corrosion, impingement attack, cavitation damage; stress corrosion cracking, hydrogen cracking, corrosion fatigue

design features such as a wrong choice of materials, introduction of crevices and bimetallic contacts, etc., and is the most common cause of corrosion failures. (2) The knowledge and technology are available, but have not been applied for economic reasons; for example, inadequate pretreatment of steel prior to painting and the use of unprotected mild steel for silencers and exhaust systems of cars.

2. *Unpredictable.* (1) The design has been based on specific environmental conditions, which have subsequently changed during the operation of the process; in this connection, it should be noted that small changes in the chemical nature of the environment, temperature, pressure, and velocity may lead to significant changes in the corrosion rate and form: the catastrophic oxidation and the failure of steel bolts in nuclear reactors in the United Kingdom, resulting from an increase in the temperature of the carbon dioxide, is an example of an unpredictable failure due to a change in environmental conditions. (2) The knowledge of and the experience with the metal, alloy, or the environment are insufficient to predict with certainty that failure will not occur; examples could be quoted of new alloys that have been subjected to an extensive series of carefully planned corrosion tests, but have failed in service.

Professor M. Fontana[8] has made the statement that "Virtually all premature corrosion failures these days occur for reasons which were already well known and these failures can be prevented." It is apparent from this statement and from the conclusions reached by the Committee on Corrosion and Protection that category 1 is responsible for the majority of incidents of corrosion failure that could have been avoided if those responsible were better informed on the hazards of corrosion and on the methods that should have been used to control it.

1.05.5 Principles of Corrosion

It has been stated that metallic corrosion is an art rather than a science and that, at present, the available knowledge is insufficient to predict with any certainty how a particular metal or alloy will behave in a specific environment.[4] It should be appreciated that the decision to use a particular metal or alloy in preference to others in a given environment or to employ a particular protective system is based usually on previous experience and empirical testing rather than on the application of scientific knowledge – the technology of corrosion is, without doubt, in advance of corrosion science, and many of the phenomena of corrosion are not fully understood. Thus, the phenomenon of passivity, which was first observed by Faraday in 1836, is still a subject of controversy; the specific effect of certain anions in causing stress-corrosion cracking of certain alloy systems is not fully understood; and the dezincification of brasses can be prevented by additions of arsenic (or other elements such as antimony or phosphorus), but no adequate theory has been submitted to explain the action of these elements. (Editor's note: Aruguably this phenomenon is now somewhat better understand, see **Chapter 2.05, Dealloying**.)

An understanding of the basic principles of the science of metallic corrosion is clearly vital for corrosion control, and as the knowledge of the subject advances, the application of scientific principle rather than an empirical approach may be used for such purposes as the selection of corrosion inhibitors, the formulation of corrosion-resisting alloys, etc.

1.05.5.1 Terminology

The classification given in Table 2 is based on the various forms that corrosion may take, but the terminology used in describing corrosion phenomena often places emphasis on the environment or the cause of attack rather than on the form of attack. Thus, the broad classification of corrosion reactions into 'wet' or 'dry' is now generally accepted, and the nature of the process is often made more specific by the use of an adjective that indicates the type or the environment, for example, concentration-cell corrosion, crevice corrosion, bimetallic corrosion and atmospheric corrosion, high temperature corrosion, seawater corrosion, etc. Alternatively, the phenomenon is described in terms of the corrosion product itself – tarnishing, rusting, and green rot. The terminology used in corrosion is given in Table 3 and is considered in more detail in Appendix A.

Appendix A – Classification of Corrosion Processes

Existing Classifications

A logical and scientific classification of corrosion processes, although desirable, is by no means simple owing to the enormous variety of corrosive environments and the diversity of corrosion reactions, but the broad classification of corrosion reactions into 'wet' or 'dry' is now generally accepted, and the terms are in common use. The term 'wet' includes all reactions

Table 3 Terminology in corrosion

Type of attack	*Environmental*	*Cause of attack*	*Mechanical factors*	*Corrosion product*
General (uniform)	Wet[a]	Concentration cell	Stress	Rusting
Localized	Dry	Bimetallic cell	Fretting	Tarnishing
Pitting (or intense)	Atmospheric	Active–passive cell	Fatigue	Scaling
Intergranular	Immersed	Stray current (electrolysis)	Cavitation	Green rot
Transgranular	Underground	Hydrogen evolution	Erosion	Tin pest
Selective	Seawater	Oxygen absorption	Impingement	
Parting	Chemical	Impingement		
Catastrophic	Fused-salt	Hydrogen embrittlement		
Layer	Flue-gas	Caustic embrittlement		
Filiform	Biochemical			
	Bacterial			
	High temperature			
	Liquid–metal			

[a]See Appendix to this section.

in which an aqueous solution is involved in the reaction mechanism; implicit in the term 'dry' is the absence of water or an aqueous solution.

These terms are evidently ambiguous; for example, it is not always clear whether 'wet' is confined to aqueous solutions – the 'wetting' of solids by mercury indicates that liquid–metal corrosion should be classified as 'wet'. Even if the term is restricted to aqueous solutions, the difficulty arises that the mechanism of the growth of magnetite scale during the reaction of the interior of a boiler drum with dilute caustic soda at high temperatures and pressures is best interpreted in terms of a 'dry' corrosion process. Similar considerations apply to the reactions of aluminum and zirconium with high temperature water.

Considering oxidation as a typical 'dry' reaction, it follows, as shown in **Figure A1(a)**, that at the *interfaces*

$$M \rightleftharpoons (M^{z+}\bigcirc/O) + z(e\bigcirc/O) \qquad [4]$$

where $M^{z+}\bigcirc$ is an interstitial metal ion, $e\bigcirc$ an interstitial electron, and $/O$ indicates the metal–oxide interface.

If the metal dissolves to enter a vacant site, then

$$M \rightleftharpoons (M^{z+}\square/O + ze\square/O) \qquad [5]$$

where $M^{z+}\square$ represents a cation vacancy and $e\square$ a positive hole.

At the gas–oxide interface, the O_2 gas ionizes

$$\left(\frac{1}{2}O_2/\text{ads.}\right) + 2(e/X) \rightleftharpoons (O^{2-}/\text{ads.}) \qquad [6]$$

where $/X$ indicates the gas–oxide interface.

By definition, these *interfaces* can be considered as anodes and cathodes respectively.

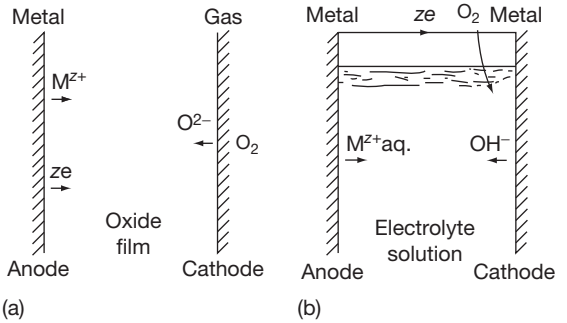

Figure A1 Anodes and cathodes in corrosion processes: (a) 'dry' corrosion and (b) 'wet' corrosion.

The corresponding 'wet' corrosion half-reactions (**Figure A1(b)**) are

$$[M^{z+} + ze]_{\text{lattice}} + H_2O \rightarrow M^{z+}\text{aq.} \qquad [7]$$

and

$$O_2 + 2H_2O + 4e = 4OH^- \qquad [8]$$

or

$$O_2 + 4H^+ + 4e = 2H_2O \qquad [9]$$

'Dry' Corrosion

These are generally metal–gas or metal–vapor reactions involving nonmetals such as oxygen, halogens, hydrogen sulfide, sulfur vapor, etc., and oxidation, scaling, and tarnishing are the more important forms. A characteristic of these reactions is that the initial oxidation of the metal, the reduction of the nonmetal, and the formation of the compound occur at one and the same place at the metal–nonmetal interface. Should the compound be volatile or

discontinuous, further interaction at the interface (or through a thin film of constant thickness) is possible, and in most cases, the reaction rate tends to remain constant with time (linear law). If the film is continuous, it will present a barrier to the reactants, and further interaction will necessitate the passage of the reactants through the film by (a) diffusion of the nonmetal or (b) diffusion and migration of ions of the reactants. The detailed mechanisms of these reactions are considered in subsequent chapters, but it is appropriate to observe that the formation of a continuous film of reactant product at a metal–nonmetal interface results in a growth rate that, when the film becomes sufficiently thick to be rate determining, decreases as the film thickens, that is, parabolic, logarithmic, asymptotic, cubic, etc.

'Wet' Corrosion

In 'wet' corrosion, the oxidation of the metal and the reduction of a species in solution (electron acceptor or oxidizing agent) occur at different areas on the metal surface with consequent electron transfer through the metal from the anode (metal oxidized) to the cathode (electron acceptor reduced); the thermodynamically stable phases formed at the metal–solution interface may be solid compounds or hydrated ions (cations or anions), which may be transported away from the interface by processes such as migration, diffusion, and convection (natural or forced). Under these circumstances, the reactants will not be separated by a barrier, and the rate law will tend to be linear. Subsequent reaction with the solution may result in the formation of a stable solid phase, but as this will form away from the interface, it will not be protective – the thermodynamically stable oxide can affect the kinetics of the reaction only if it forms a film or precipitates on the metal surface.

Further points that distinguish 'wet' from 'dry' corrosion are

1. In 'wet' corrosion, the metal ions are hydrated – the hydration energy of most metal ions is very high and thus facilitates ionization.
2. In 'wet' corrosion, the ionization of oxygen to hydroxyl must involve the hydronium ion or water.
3. In 'dry' corrosion, the direct ionization of oxygen occurs.

Corrosion in Organic Solvents

Corrosion reactions in aggressive organic solvents are becoming a more common occurrence owing to the developments in the chemical and petrochemical industries, and these reactions can lead to the deterioration of the metal and to undesirable changes in the solvent. This aspect of corrosion has recently been the subject of an extensive review by Heitz,[9] who has considered the mechanisms of the reactions, the similarities between corrosion in organic solvents and in aqueous solutions, the methods of study, and the occurrence of the phenomenon in industrial processes.

Figure A2 shows the weight loss against time curve for nickel in various solvents containing 0.05 wt% H_2SO_4 at various temperatures, and illustrates the unpredictable nature of corrosion in organic solvents. Thus, the corrosion rates in ethanol are far

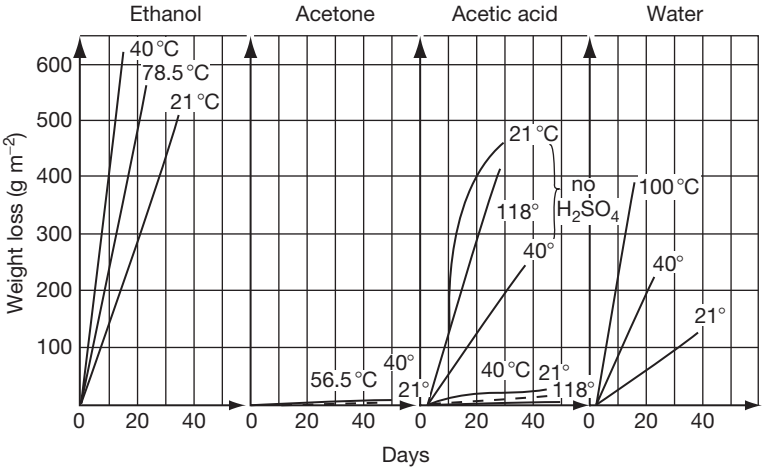

Figure A2 Corrosion of nickel in different solvents containing 0.05 wt.% H_2SO_4 at various temperatures. Reproduced from Heitz, E. In *Advances in Corrosion Science and Technology*; Fontana, M. G., Staehle, R. W., Eds.; Plenum Press, 1974; Vol. 4, p 149, with permission from Plenum Press.

greater than those in the aqueous acid, whereas in acetone, the rate is practically zero; even more surprising is the fact that in acetic acid, the addition of 0.05% H_2SO_4 actually decreases the corrosion rate.

Heitz classifies corrosion reactions in organic solvents into

1. Electrochemical reactions, which follow a similar mechanism to those in aqueous solution.
2. Chemical reactions, which involve direct charge transfer between the metal atom in the lattice of the metal and the oxidizing species.

In the case of electrochemical reactions, the partial anodic reaction results in the formation of a solvated metal cation $M^{z+}_{solv.}$, a charged or uncharged metal complex MX^-, or a solid compound MX_z, where X is a halogen ion, organic acid anion, etc.

The cathodic partial reactions are as follows:

(a) Reduction of a solvated proton to H_2 gas

$$H^+_{solv.} + e^- \rightarrow \frac{1}{2}H_2 \qquad [10]$$

(b) Reduction of acidic hydrogen of a proton donor

$$HA + e \rightarrow \frac{1}{2}H_2 + A^- \qquad [11]$$

where A^- is a carboxylic acid anion, alcoholate ion, etc.

(c) Reduction of an oxidizing gas Y

$$Y_z + zme \rightarrow zY^{m-} \qquad [12]$$

where Y can be O_2, Cl_2, F_2, Br_2, O_3, N_2O_4, etc.

(d) Reduction of oxidizing ions such as Fe^{3+}, Cu^{2+}, MnO_4^-, ClO_3^-, etc.

It is evident from these equations that in many systems, the reaction of a metal with an organic solvent follows a mechanism that is similar to the electrochemical mechanism of corrosion in aqueous solution.

Nonelectrochemical processes may be represented by the general equation

$$M + 2C_xH_yX_z \rightarrow MX_2 + C_{2x}H_{2y}X_{2x-2} \qquad [13]$$

where X is a halogen and M is a divalent metal, for example, the Grignard reaction

$$Mg + CH_3Cl \rightarrow CH_3Mg \qquad [14]$$

A further type of chemical process, which is analogous to high temperature corrosion, is the reaction of metals with organic sulfur compounds, which follow the equation

$$2M + 2RSH \rightarrow 2MS + H_2 + R_2 \qquad [15]$$

Heitz quotes a number of case studies of corrosion of metals in organic solvents and concludes that the phenomenology indicates no specific differences from that experienced in aqueous corrosion. Thus, general corrosion, pitting, crevice corrosion, intergranular corrosion, erosion–corrosion cracking, hydrogen embrittlement, etc. can all occur in organic solvents. The methods of control also follow those used for corrosion in aqueous solutions, although there are certain differences. Thus, cathodic and anodic protection are seriously limited by the resistivity of the solvent, and paint coatings deteriorate rapidly in contact with the solvent.

Suggested Classification and Nomenclature

On a basis of the preceding discussion, the classification and nomenclature outlined in **Table A1** are suggested as a possible alternative to the accepted classification of corrosion reactions into 'wet' and 'dry.'

It is considered that the main types of corrosion reactions can be classified as follows:

1. Film-free chemical interaction in which there is direct chemical reaction of a metal with its environment. The metal remains film-free, and there is no transport of charge.
2. Electrochemical reactions that involve transfer of charge across an interface. These electrochemical reactions can be further subdivided into:
   a. Inseparable anode–cathode type (insep. A/C). The anodes and cathodes cannot be distinguished by experimental methods, although their presence is postulated by theory, that is, the *uniform* dissolution of metals in acid, alkaline, or neutral aqueous solutions, in nonaqueous solution, or in fused salts. (Dr. Pryor considers that in certain cases of uniform dissolution of metals in acids (e.g., A1 in hydrochloric or sulfuric acid) or alkalis a thin film of oxide is present on the metal surface – the film is not rate-determining but its presence would indicate that reactions of this type should be classified under 2(c)).
   b. Separable anode–cathode type (sep. A/C). Certain areas of the metal can be distinguished experimentally as predominantly anodic or cathodic, although the distances of separation of these areas may be as small as fractions of a millimeter. In these reactions, there will be a macroscopic flow of charge through the metal.

Table A1 Classification of spontaneous corrosion reactions

1. *Film-free Chemical Interaction*
   (a) Metal/gas–oxide or compound volatile (e.g., reaction of molybdenum with oxygen, reaction of iron or aluminum with chlorine).
   (b) Metal/liquid
   Reactions of solid metals with liquid metals (e.g., dissolution of aluminum in mercury)
   Dissolution of metal in their fused halides (e.g., lead in lead chloride).
   Dissolution of metals in nonaqueous solutions (e.g., reaction of aluminum with carbon tetrachloride).
2. *Electrochemical*
   (a) *Inseparable anode/cathode type* (*insep. A/C*)
   Reactions with aqueous solutions. Uniform dissolution or corrosion of metals in acid, alkaline, or neutral solutions (e.g., dissolution of zinc in hydrochloric acid or in caustic soda solution; general corrosion of zinc in water or during atmospheric exposure). Reactions with nonaqueous solution (e.g., dissolution of copper in a solution of ammonium acetate and bromine in alcohol). Reactions with fused salts.
   (b) *Separable anode/cathode type* (*sep. A/C*)
   All reactions of metals in aqueous or nonaqueous solutions or in fused salts where one area of the metal surface is predominantly anodic and the other is predominantly cathodic so that the sites are physically identifiable.
   (c) *Interfacial anode/cathode type in which the metal surface is filmed*
   i. Metal/gas and metal/vapor reactions
   All reactions in which charge is transported through a film of reaction product on the metal surface – the film may or may not be rate determining (e.g., parabolic, logarithmic, asymptotic, etc., or linear growth laws, respectively).
   ii. Metal/solution reactions
   All reactions involving the uniform formation and growth of a film of reaction product (e.g., reaction of metals with high temperature water, reaction of copper with sulfur dissolved in carbon disulfide).

c. Interfacial anode–cathode type (interfacial A/C). One entire interface will be the anode and the other will be the cathode. Thus, as shown in **Figure A1(a)**, the metal–metal oxide interface might be regarded as the anode and the metal–oxygen interface as the cathode.

It is apparent that, in general, 2(a) and 2(b) include corrosion reactions that are normally classified as 'wet,' while 2(c) includes those that are normally classified as 'dry.'

The terminology suggested can be illustrated by reference to the corrosion behavior of iron:

1. Reaction of iron with oxygen at room temperature or with oxygen or water at high temperatures – interfacial A/C type.
2. Reaction of iron with oxygenated water or with reducing acids – inseparable A/C type.
3. Reaction of iron containing a discontinuous magnetite scale with oxygenated water, crevice corrosion, water-line attack, 'long-line' corrosion of buried iron pipes, etc. – separable A/C type.

Although it is realized that this classification and terminology has certain limitations, it represents a preliminary attempt to provide a more rational classification of corrosion processes than that based on 'wet' and 'dry.'

Acknowledgements

Grateful thanks are due to Dr W.B. Jepson, Dr M. Pryor, and Mr J.N. Wanklyn for the helpful discussions during the preparation of this Appendix.

References

1. Hoar, T. P. *J. Appl. Chem.* **1961**, *11*, 121; Vernon, W. H. J. *The Conservation of Natural Resources*; Institution of Civil Engineers: London, 1957; Vol. 105; Potter, E. C. *Electrochemistry*; Cleaver-Hume: London, 1956; 231.
2. Uhlig, H. H. Ed. The Corrosion Handbook; Wiley: New York/Chapman and Hall: London, 1948; Uhlig, H. H. *Corrosion and Corrosion Control*; Wiley: New York, 1971; Fontana, M. G.; Greene, N. D. *Corrosion Engineering*; McGraw-Hill, 1967.
3. Fontana, M. G.; Staehle, R. W. *Advances in Corrosion Science and Technology*; Plenum Press: New York, 1990.
4. Vermilyea, D. A. In Proceedings of the 1st International Congress on Metallic Corrosion, London, 1961; Butterworths: London, 1962; p 62.
5. Evans, U. R. *The Corrosion and Oxidation of Metals*; Arnold: London, 1960; 12.
6. Report of the Committee on Corrosion and Protection, Department of Trade and Industry, HMSO, 1971.
7. Ehrlich, G.; Turnbull, D. *Physical Metallurgy of Stress Corrosion Fracture*; Interscience: New York and London, 1959; 47.
8. Fontana, M. G. *Corrosion* **1971**, *27*, 129.
9. Heitz, E. In *Advances in Corrosion Science and Technology*; Fontana, M. G., Staehle, R. W., Eds.; Plenum Press: New York, 1974; Vol. 4, 149.

1.03 Outline of Structural Metallurgy Relevant to Corrosion

R. P. M. Procter
Corrosion and Protection Centre, School of Materials, University of Manchester, Manchester M60 1QD, UK

This article is a revision of the Third Edition article 20.4 by R. P. M. Procter, volume 2, pp 20:94–20:130, © 2010 Elsevier B.V.

Glossary

Binary A mixture of two elements (referring to phase diagrams).

Hyper-eutectic With more solute than the eutectic composition.

Hyper-eutectoid With more solute than the eutectoid composition.

Hypo-eutectic With more solute than the eutectic composition.

Hypo-eutectoid With more solute than the eutectoid composition.

Intergranular Between the grains (i.e., at the grain boundary).

Intragranular Within the grains (i.e., in the bulk of the grain).

Pro-eutectoid Formed at above the eutectoid temperature.

Quaternary A mixture of four elements (referring to phase diagrams).
Ternary A mixture of three elements (referring to phase diagrams).
Widmanstätten A lamellar microstructure first observed in iron meteorites, now used generally to describe a well defined lamellar microstructure.
α-ferrite The low temperature b.c.c. allotrope of iron.
δ-ferrite The high temperature b.c.c. allotrope of iron.

Abbreviations

b.c.c. body centered cubic
c.p.h. close packed hexagonal (sometimes also known as hexagonal close packed, h.c.p.)
f.c.c. face centered cubic

The corrosion of a metal invariably involves some kind of interaction between the metal and its environment, and in many cases, the corrosion (location, form, and rate) is significantly affected or even caused by some structural feature of the metal. It is essential, therefore, for the corrosion engineer to have some appreciation of the structure of metals; an elementary survey is provided in this chapter, which is reproduced from the 3rd edition.

The structure of pure metals is discussed in this chapter and this is followed by a description of the structure of alloys. In general, structural features are discussed in order of increasing size, that is, starting with atomic features and continuing through microscopic features to macroscopic features.

1.03.1 Structure of Pure Metals

A crystal may be defined as an orderly three-dimensional array of atoms, and all metals are aggregates of more or less imperfect crystals. In considering the structure of metals, therefore, it is convenient to start with the arrangement of atoms in a perfect metal crystal and then to proceed to the imperfections that are always present in the crystal structure.

Although there are many different crystal structures, some of which are rather complicated, most common metals fortunately have one of the three relatively simple structures: face-centered cubic (f.c.c.), close-packed hexagonal (c.p.h.), and body-centered cubic (b.c.c.). The unit cell (i.e., the smallest group of atoms possessing the symmetry of the crystal and which, when repeated in all directions, develops the crystal lattice) of each of these metallurgically common and important crystal structures is illustrated in Figure 1; the crystal structure of each of the more important metals is given in Table 1. It is clear from this table that the crystal structures of some metals change with temperature, that is, these metals are polymorphic, and this phenomenon is of very great practical significance, particularly in the case of iron, as will become apparent later.

The atoms in a metal crystal can often be satisfactorily regarded as hard spheres of about 10^{-10} m radius. A sheet of such hard balls can be most densely and closely packed together in the configuration shown in Figure 2(a); such sheets or layers of atoms are therefore known as close-packed planes. Similarly, the directions arrowed in Figure 2(a) are referred to as close-packed directions. Close-packed hexagonal and face-centered cubic crystal structures can be built up by stacking close-packed planes on top of each other in the correct sequence. Consider a sheet of eight close-packed atoms, designated by the full circles *a* in Figure 2(b); as shown, a second layer of four close-packed atoms, designated by the dotted circles *b*, may be laid on top of the first plane. Each of the *b* atoms 'sits' in one of the natural 'valleys' which occur between any three contiguous *a* atoms. There are now two such low-energy valleys in the plane of *b* atoms, one of which is immediately above an *a* atom and one of which is not (Figure 2(b)). An atom placed in the former results in an *aba* stacking of three close-packed planes, while an atom placed in the latter would result in *abc* stacking. Stacking *ababab*, etc., develops the c.p.h. crystal structure while stacking *abcabcabc*, etc., develops the f.c.c. crystal structure. The b.c.c. crystal structure cannot be built up by stacking close-packed planes on top of each other.

In the f.c.c. and c.p.h. crystal structures, each atom has 12 nearest neighbors and is therefore said to have a coordination number of 12. In the non-close-packed b.c.c. structure, on the other hand, the coordination number is only 8. In the f.c.c. structure, the four octahedral {111} planes are close packed and so are the ⟨110⟩ directions. (An account of the use of Miller indices to describe crystal planes and lattice directions is beyond the scope of this article; a very adequate treatment of this topic is, however, given in Reed-Hill)[1] In the c.p.h. structure, on the other hand, there is only one close-packed plane, the (0001) basal plane; the $\langle 11\bar{2}0 \rangle$ directions are close

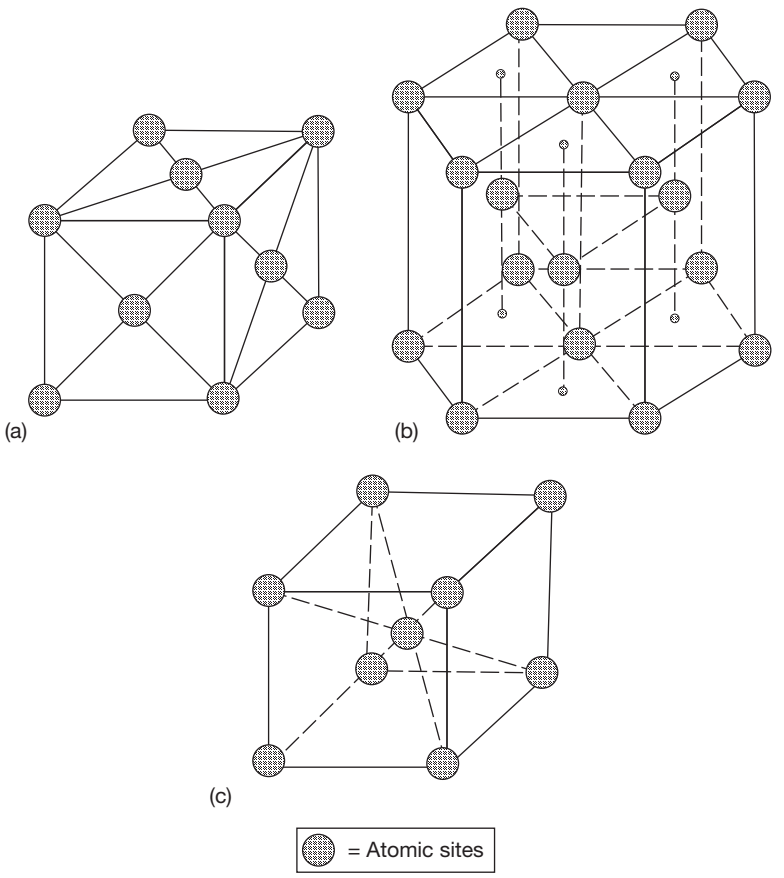

Figure 1 Unit cells of (a) the face-centered cubic (f.c.c.), (b) the close-packed hexagonal (c.p.h.), and (c) the body-centered cubic (b.c.c.) crystal structures.

packed. The different number of close-packed planes in f.c.c. and c.p.h. crystals results in the very different plastic deformation characteristics of metals with the two structures. In the b.c.c. structure, the ⟨111⟩ directions are close packed, but there are no truly close-packed planes of the type shown in Figure 2(a); the planes of closest packing, however, are {110}.

In any crystal structure, the close-packed or closest-packed planes are the lowest energy planes. On all other planes, the density of atoms is lower, and the interatomic distance and the energy of the plane are greater. Contrary to intuitive expectations, the diameter of the largest holes or interstices between atoms in the close-packed f.c.c. structure is considerably greater than the diameter of the largest interstices between atoms in the non-close-packed b.c.c. structure.

1.03.1.1 Point Defects in Crystals

The smallest imperfections in metal crystals are point defects, in particular, vacant lattice sites (vacancies) and interstitial atoms. As illustrated in Figure 3(a), a vacancy occurs where an atom is missing from the crystal structure while an interstitial occurs when an extra atom is inserted in an interstitial site (an interstice). Vacancies and interstitials are equilibrium defects because even though vacancies (and interstitials) increase the internal energy of a crystal, they also increase the entropy, and therefore, the free energy of a perfect crystal is reduced by the presence of a number of point defects. The equilibrium vacancy concentration increases exponentially with temperature and typically, in copper at room temperature, one site in 10^{14-15} may be vacant, while at 1300 K, one site in 10^{3-4} might be vacant (equivalent to 10^{17-18} vacancies per cubic millimeter). The internal energy associated with an interstitial is much greater than that associated with a vacancy; the concentration of interstitial atoms at any temperature is correspondingly very much lower than that of vacant atomic sites. Radiation damage, however, introduces many interstitials. Often, a vacancy and an interstitial are associated as a pair.

The practical importance of vacancies is that they are mobile and, at elevated temperatures, can move relatively easily through the crystal lattice.

Table 1 Crystal structure of the more important metals

Metal	*Temperature (K)*	*Crystal structure*
Alkali metals	Ambient to m.p	b.c.c.
Aluminum	Below m.p.	f.c.c.
Beryllium	Below m.p.	c.p.h.
Cadmium	Below m.p.	c.p.h.
Chromium	Below m.p.	b.c.c.
Cobalt	Below 690	c.p.h.
	690 to m.p.	f.c.c.
Copper	Below m.p.	f.c.c.
Gold	Below m.p.	f.c.c.
Iron	Below 1180	b.c.c.
	1180–1665	f.c.c.
	1665 to m.p.	b.c.c.
Lead	Below m.p.	f.c.c.
Magnesium	Below m.p.	c.p.h.
Manganese	Below m.p.	Four complex structures
Molybdenum	Below m.p.	b.c.c.
Nickel	Below m.p.	f.c.c.
Platinum	Below m.p.	f.c.c.
Silver	Below m.p.	f.c.c.
Tin	Below m.p.	Two complex structures
Titanium	Below 1155	c.p.h.
	1155 to m.p.	b.c.c.
Tungsten	Below m.p.	b.c.c.
Vanadium	Below m.p.	b.c.c.
Zinc	Below m.p.	c.p.h.
Zirconium	Below 1135	c.p.h.
	1135 to m.p.	b.c.c.

As illustrated in Figure 3(b), this is accompanied by movement of an atom in the opposite direction; indeed, the existence of vacancies was originally postulated to explain solid-state diffusion in metals. In order to 'jump' into a vacancy, an adjacent atom must overcome an energy barrier. The energy required for this is supplied by thermal vibrations. Thus, the diffusion rate in metals increases exponentially with temperature, not only because the vacancy concentration increases with temperature, but also because there is more thermal energy available to overcome the activation energy required for each 'jump' in the diffusion process.

1.03.1.2 Stacking Faults and Twins

In certain close-packed metals and alloys there are errors in the sequence of stacking of the close-packed planes. Thus, for example, the sequence of planes in a c.p.h. metal might be . . . ababa*bca*ba . . ., in which the region in italics is termed a 'stacking fault' and represents a small volume of f.c.c. material in the c.p.h. structure. Stacking faults have an energy that is higher than that of the perfect crystal structure; however, the value of the stacking-fault energy varies very widely between different metals and alloys. Stacking faults are readily visible in thin-foil transmission electron micrographs, as illustrated in Figure 4 (top).

Twins are a somewhat similar form of defect. In certain metals, adjacent areas of crystal bear a mirror-image orientation relationship to each other across the twin boundary, as illustrated schematically in Figure 5. The twin boundaries, like stacking faults,

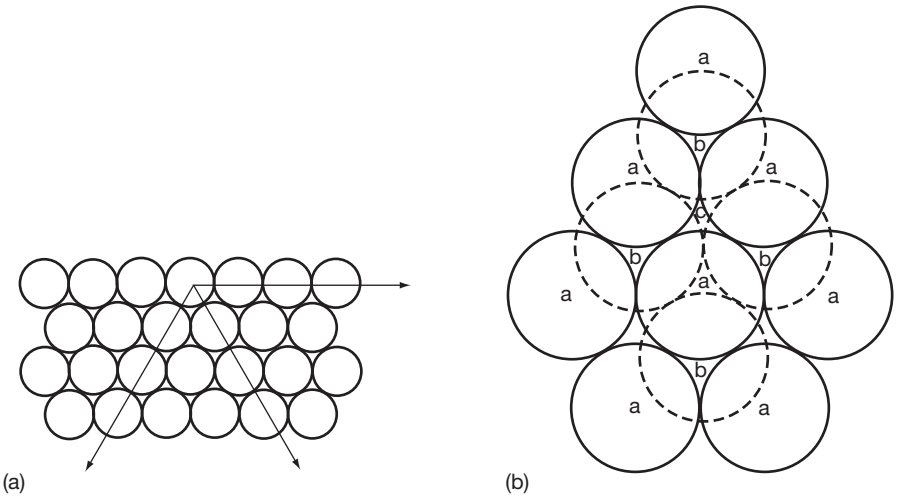

Figure 2 (a) Single close-packed sheet of atoms, with the close-packed directions arrowed and (b) stacking of three close-packed planes of atoms, showing *aba* and *abc* positions.

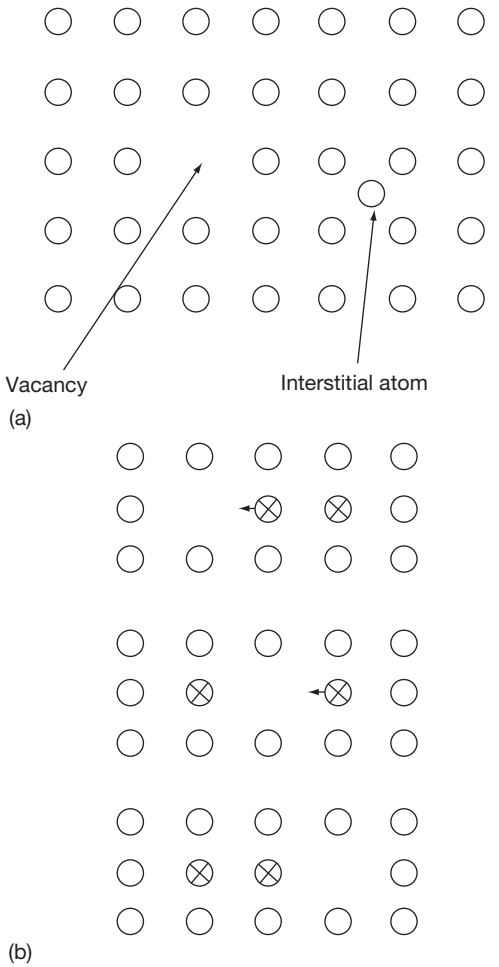

Figure 3 (a) Schematic illustration of two types of point defect and (b) three stages in diffusion by the motion of a vacancy through a crystal.

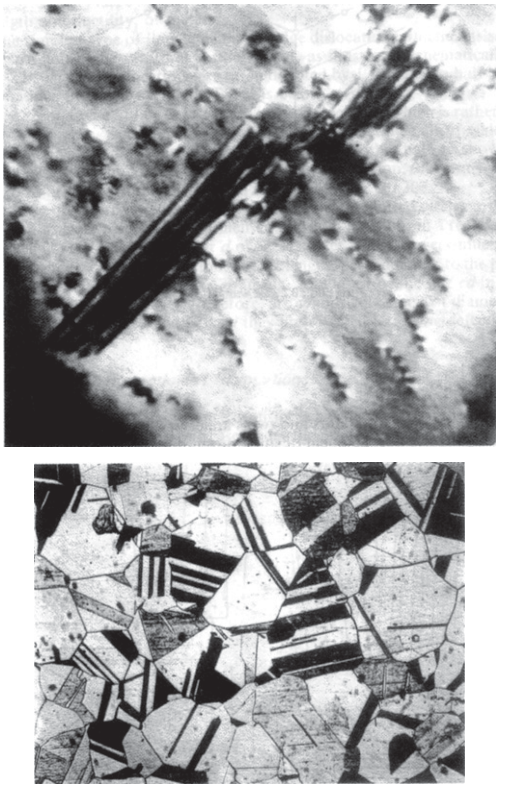

Figure 4 (top) Transmission electronmicrograph showing a stacking fault and isolation dislocations in a stainless steel (×70 000, courtesy I. Brough) and (bottom) light micrograph showing an equiaxed grain structure and twins in an annealed 70/30 brass (×200, courtesy of M. Islam).

have a somewhat higher energy than the surrounding perfect crystal structure. Twins arise during the annealing of cold-worked f.c.c. material, during the room-temperature deformation of c.p.h. materials and during the low-temperature (or shock) deformation of b.c.c. materials. Twins are often readily apparent on metallographic sections at relatively low magnifications, as shown in **Figure 4** (bottom).

1.03.1.3 Line Defects

Point defects, stacking faults, and twins are crystalline imperfections that basically involve misalignment of single atoms or of a single plane of atoms. Line defects, or dislocations, are somewhat larger-scale imperfections involving misalignment along a line of atoms.

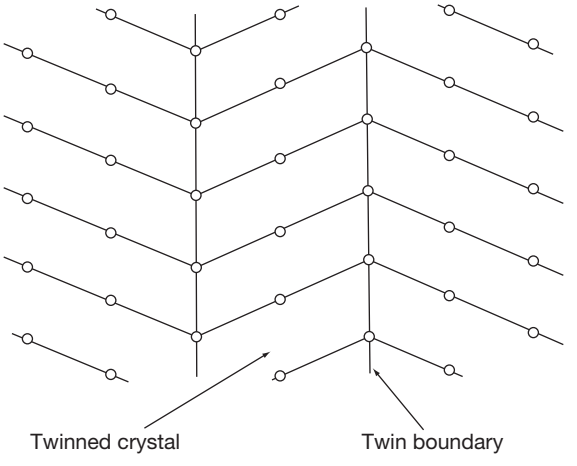

Figure 5 Twinned crystal.

Dislocations are extremely important defects, in that the dislocation density and dislocation interactions control the mechanical properties to a very large extent, in particular, the strength and ductility of metals.

The simplest type of line defect is the edge dislocation, which consists of an extra-half plane of atoms in the crystal, as illustrated schematically in Figure 6(a); edge dislocations are often denoted by $\perp$ if the extra-half plane *ab* is above the plane *sp* or by $\top$ if it is below.

The second type of line defect is the screw dislocation, which is somewhat less easy to visualize. Consider, however, a block of material, half of which is sheared one interatomic distance with respect to the other half, as shown in Figure 6(b). The line *cd* then constitutes a screw dislocation; the arrangement of atoms around a screw dislocation is shown in Figure 6(c).

To a good approximation, only atoms within the dotted circles in Figures 6(a) and 6(b) are displaced from their equilibrium position; in a real three-dimensional crystal, the diameter *d* of these circles would be very much less than the length *l* of the dislocation, that is, the length, perpendicular to the page, of the extra-half plane of atoms *ab* in Figure 6(a), or of the line *cd* in Figure 6(b). Strictly therefore, dislocations are cylindrical defects of diameter *d* and length *l*; however, since $l \gg d$, they are referred to as line defects.

1.03.1.4 Movement and Interaction of Dislocations

As with vacancies, the importance of dislocations derives from the fact that they are readily mobile, in this case under the influence of applied stresses. Figures 7(a)–7(c) illustrate the slip or glide of an edge dislocation through a crystal under the influence of a shear stress. The atom *a* in Figure 7(a) moves, under the influence of the applied stress, to position *a′* in Figure 7(b), and the extra-half plane of atoms shifts one atomic distance to the left, from plane *y* to *x*. As this process continues, the dislocation moves right through the crystal, the final result, shown in Figure 7(c), being that the crystal is sheared or slipped by one interatomic distance across the slip plane *sp*. Each step in the movement of the dislocation (i.e., from Figures 7(a) and 7(b)) clearly requires only a slight rearrangement of the atoms around the bottom of the extra-half plane, and is therefore a low-energy process; dislocations are, therefore, readily mobile under low applied stresses. However, producing the slip, shown in Figure 7(c), from a perfect dislocation-free crystal would be a very high-energy process requiring very high stresses. The difference between these two modes of slip is that in the latter, all the bonds on the slip plane are broken at the same time, while in the former, they are broken one at a time. The existence of dislocations was in fact postulated, long before they were observed, to account for the observation that the yield stress of metals is very much lower than that predicted by theoretical calculations. It is important to note that the crystal structure, after passage of a dislocation, is perfect and in no way misaligned. From Figure 8, it is clear that the dislocation line is merely

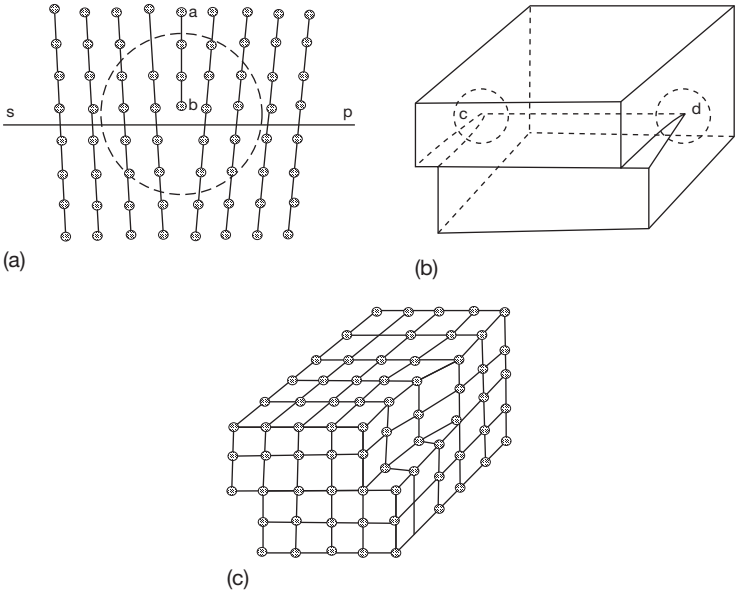

Figure 6 (a) Atomic arrangement around an edge dislocation, (b) shear required in a homogeneous solid to produce a screw dislocation, and (c) atomic arrangement around a screw dislocation.

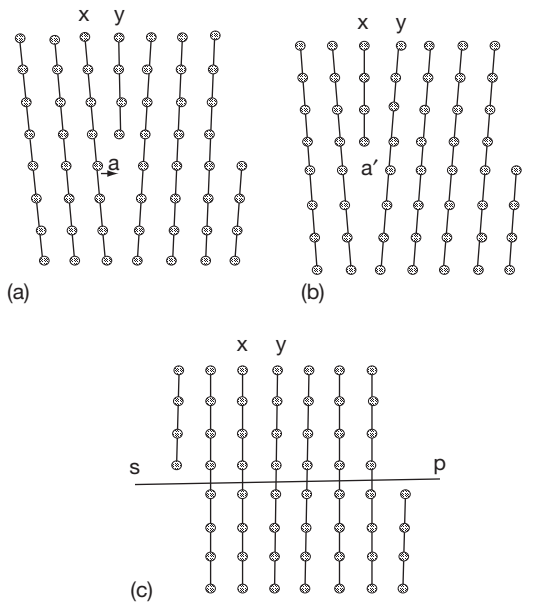

Figure 7 Three stages in plastic deformation by the motion of an edge dislocation through a crystal.

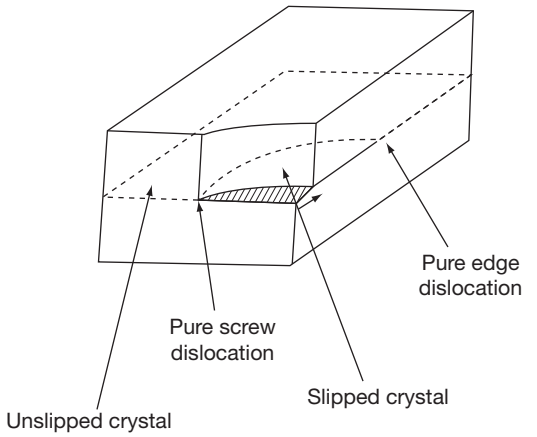

Figure 8 Schematic illustration of a mixed dislocation as the boundary between slipped and unslipped crystal. The arrow shows the Burgers vector.

the boundary between slipped and unslipped crystal. The magnitude and direction of the slip is given by what is known as the Burgers vector; in a screw dislocation, the Burgers vector is parallel to the line of the dislocation, while in an edge dislocation, it is perpendicular to it. In real crystals, dislocation lines are not straight, but are usually bowed or curved. As illustrated schematically in **Figure 8**, such dislocations are mixed, being part screw and part edge. Slip occurs on the plane containing both the Burgers vector and the line of the dislocation. In practice, it is observed that metals slip most easily on close-packed planes and in close-packed directions, that is, {111} and <110> in f.c.c. metals and usually {0001} and $<11\bar{2}0>$ in c.p.h. metals. Since f.c.c. crystals have four close-packed {111} planes, they are generally much more ductile than c.p.h. crystals, which have only one {0001} close-packed plane. In b.c.c. metals, slip occurs in <111> directions on a variety of planes. The movement of dislocations by other mechanisms, in particular by cross-slip and climb, is beyond the scope of this section.

All real metals contain dislocations; even a well-annealed metal would typically contain 10^{4-6} dislocations per square millimeter, while a heavily cold-worked metal could contain up to $10^{10}\,\mathrm{mm}^{-2}$. At first sight, this is an anomaly; dislocations were postulated to account for the low yield strength of metals, and whereas an annealed material with a low dislocation density is weak, a cold-worked metal with a high dislocation density is strong. The answer lies in the fact that when the dislocation density is low, the dislocations are generally too far apart to interact with each other very often and are more free to move under the influence of a low applied stress. On the other hand, when the dislocation density is high, the dislocations do interact, and they become tangled up with each other; dislocation motion is then difficult and the material is therefore strong. The interaction of dislocations with each other and with other structural features in metals is a very complex field; it is also, however, extremely important, as it greatly affects the strength of the metals.

The atomic bonds in a cylinder of material around dislocations are elastically stretched; dislocations, like other crystalline defects are, therefore, high-energy regions.

Dislocations are readily visible in thin-film transmission electron micrographs, as shown in **Figures 4** (top) and **9** (top). The slip step (**Figure 7(c)**) produced by the passage of a single dislocation is not readily apparent. However, for a variety of reasons, a large number of dislocations often move on the same slip plane or on bands of closely adjacent slip planes; this results in slip steps that are very easily seen in the light microscope, as shown by the slip lines in **Figure 9** (bottom).

1.03.1.5 Polycrystalline Metals: Grains and Grain Boundaries

So far, we have regarded metals as single crystals; in fact, most metals, in practice, are polycrystalline and

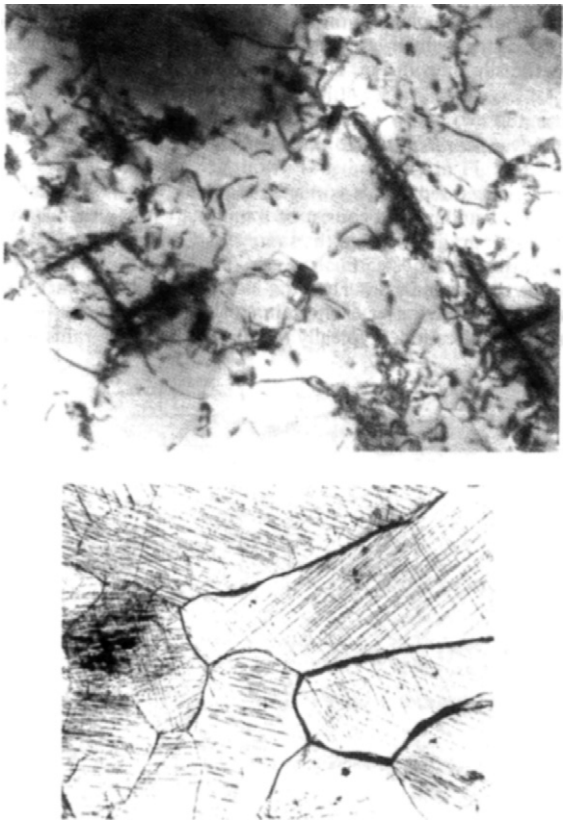

Figure 9 (top) Transmission electronmicrograph showing dislocation tangles associated with precipitates in an Al–Cu–Mg–Si alloy (×24 000, courtesy S. Blain) and (bottom) light micrograph showing slip lines in pure lead (×100).

consist of a number of crystals or grains. In a pure metal, each grain has the same crystal structure and contains vacancies, dislocations, etc., but the crystallographic orientation of each grain is different; in other words, in a polycrystalline metal, the [111] crystallographic direction of each grain points in a different spatial direction. Typically, the diameter of the grains in a coarse-grained material might be about 0.5 mm, while that in a fine-grained metal might be about 0.005 mm. However, in certain electrodeposits, the grain size is too fine to be resolved with the light microscope, while at the other extreme, jet-engine turbine blades about 150 mm long, of nickel-base superalloy, may sometimes be single crystals. The grain size of metals may be controlled by heat treatment. All the grains may be of more or less the same size and shape as in the equiaxed grain structure shown in **Figure 4** (bottom). Alternatively, if the metal has been heavily cold-worked, for example by rolling or extrusion, the grains may be

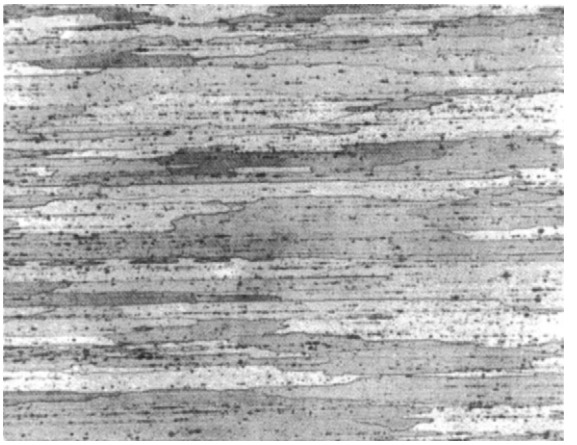

Figure 10 Light micrograph showing the highly elongated grain structure of a commercial wrought high-strength precipitation-hardening Al–Zn–Mg–Cu alloy (×40, section perpendicular to the long transverse direction).

deformed and elongated in the work direction, giving the highly directional, elongated, grain structure shown in **Figure 10**. Although the crystallographic orientation of all the grains in a polycrystalline metal is usually different and random, occasionally the orientation of most of the grains in a piece of metal is similar. Such preferred orientation can arise in a number of ways; it is important to note, however, that metals with elongated, columnar grain structures (**Figure 10**) do not necessarily have preferred orientation.

However perfect the crystal structure within a grain, there will inevitably be crystallographic mismatch and imperfection where two adjacent grains meet, that is, at grain boundaries; this region of mismatch is, however, only a few atomic diameters wide, as shown schematically in **Figure 11**, and on metallographic sections, grain boundaries only become apparent on etching. Although grain boundaries are regions of imperfection and of crystallographic mismatch, they are nevertheless quite strong, and metals do not normally fail intergranularly. Indeed, grain boundaries act as barriers to the movement of dislocations, and a fine-grained pure metal will normally be considerably stronger than a single-crystal or a coarse-grained material.

A grain boundary is a planar defect in a crystal and as such has a higher energy than the surrounding crystal. By way of comparison, the free surface energy of copper is about 1200–1800 nJ mm^{-2}, the grain boundary energy is about 300–500 nJ mm^{-2}, while the stacking-fault energy is about 80–100 nJ mm^{-2}.

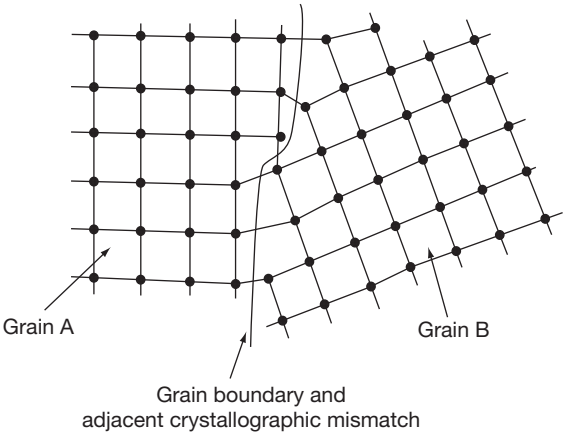

Figure 11 High-angle grain boundary.

1.03.1.6 Annealing: Recovery and Recrystallization

It must be emphasized that many of the crystalline defects already discussed are metastable and tend to be eliminated on annealing at elevated temperatures. Thus, when a cold-worked metal is heated, the energy stored in the metal during the cold-working process is released; the dislocation tangles rearrange themselves, and the internal stresses, hardness, and strength of the metal are progressively reduced. The changes occurring during this process (which is known as recovery) do not affect the optical microstructure of the metal. Recovery is followed at higher temperatures by recrystallization. New grains are nucleated throughout the metal and grow; the heavily deformed high-dislocation-density cold-worked grains are replaced by new equiaxed low-dislocation-density grains. On prolonged heating at even higher temperatures, some of these grains grow at the expense of others, and a coarse-grained material (or even a single crystal) replaces the fine-grained recrystallized structure. The changes occurring during recrystallization are readily apparent in the optical microscope and are accompanied by a drastic softening of the metal.

1.03.1.7 Macroscopic Defects in Metals

While vacancies, dislocations, etc. may be regarded as atomic defects, grains may be regarded as microscopic defects. There are also, however, what may conveniently be termed macroscopic defects in metals. Too often these are the result of poor design, poor processing or production, poor welding, careless handling or operating. Examples of these would be sharp re-entrant corners, crevices, casting defects, rolled-in mill-scale, rough-sheared edges, poorly machined surfaces, weld defects, surface scratches, etc. However, by far the most important macroscopic defect, which is inherent in the uses to which metals are put, and the ways in which they are formed, is the presence of stresses, particularly tensile stresses. These stresses may be either applied, resulting from the fact that the metal is being used in a load-bearing capacity, or residual. Residual stresses may either be microstresses arising, for example, from dislocations piled up against a grain boundary or, much more importantly, macrostresses. Residual macrostresses arise from a very wide range of effects, for example, forming, heat treating, machining, welding, and assembling operations can all give rise to high residual tensile stresses over relatively large regions.

1.03.1.8 Structure of Metal Surfaces and Surface Defects

So far the structure of pure metals has been discussed with reference to bulk characteristics and continuous crystals. However, corrosion is essentially a surface phenomenon, and it is necessary to consider how the structure and defects already described interact with free surfaces. At this stage, it is convenient to consider only a film-free metal surface, although of course, in most corrosion phenomena the presence of surface films is of the utmost importance. Furthermore, it is at free surfaces that the hard sphere model of metals first begins to become inadequate, particularly when surface films are considered, or in aqueous environments, where an electrical double layer exists.

Figure 12(a) shows schematically a smooth metal surface, although it should always be borne in mind that even a high-quality electropolished surface will not be flat but will have a roughness of about 5 nm or so high, while the roughness on a high-quality machined surface may be about 1 μm or so high. In most real materials, there will be grain boundaries meeting the surface as shown in **Figure 12(a)**. Furthermore, it is extremely unlikely that the plane of the metal surface will coincide with a low-index low-energy high-atomic-density close-packed plane, as in grain *B*. In most cases, the plane of the metal surface will be a high-index high-energy low-atomic-density plane, as in grains *A* and *C*.

On an atomic scale, metal surfaces are usually described in terms of the terrace–ledge–kink model shown in **Figure 12(b)**. Essentially, it is suggested that

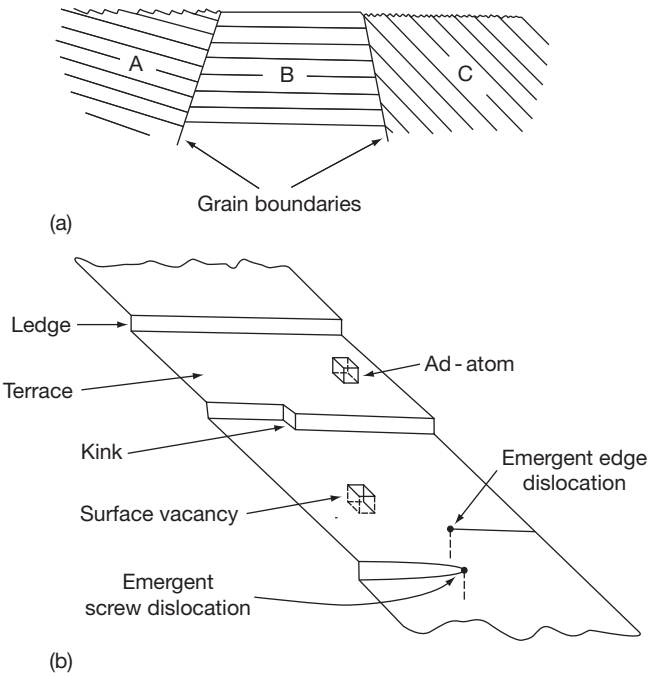

Figure 12 (a) Grains of different orientation intersecting a free surface and (b) the terrace–ledge–kink model of a free metal surface.

clean metal surfaces consist of low-energy low-index terraces separated by ledges of monatomic height, which occasionally contain monatomic kinks.

By their nature, dislocations cannot end suddenly in the interior of a crystal; a dislocation line can only end at a free surface or a grain boundary (or form a closed loop). Where a screw dislocation intersects a free surface, there is inevitably a step or ledge in the surface, one atomic layer high, as shown in **Figure 6(c)**. Furthermore, the step need not necessarily be straight and will, in fact, almost certainly contain kinks.

The coordination number of an atom lying in a (111) surface of an f.c.c. crystal is 9, compared with the bulk value of 12; an atom at a step in the surface has a co-ordination number of 7 while that of an atom at a kink in a step is only 6. The latter atom, therefore, is the most weakly bound to the metal crystal and is likely to be the first to be removed from the lattice in any active dissolution process. Clearly, however, this removal does not eliminate the kink and, in fact, it is impossible, even by repeated removal of atoms, to eliminate the step caused by a screw dislocation intersecting a free surface. There are, however, in addition to screw dislocations, many other causes of steps or ledges on metal surfaces, for example, low-index planes intersecting the surface at an acute angle (see grain *A* in **Figure 12(a)**).

As shown in **Figure 12(b)**, an edge dislocation intersecting a free surface does not cause a step. However, the atoms adjacent to the core of the dislocation, being in nonequilibrium positions, have a higher energy than other atoms in the surface. The emergent ends of both edge and screw dislocations thus represent potential sites for preferential dissolution. Finally, there may be vacancies in the surface and ad-atoms on the surface (**Figure 12(b)**).

1.03.2 Structure of Alloys

The discussion so far has been limited to the structure of pure metals and to the defects which exist in crystals composed of atoms of one element only. Of course, pure metals are comparatively rare, and all commercial materials contain impurities, including in many cases, deliberate alloying additions. In the production of commercially pure metals and alloys, impurities are inevitably introduced into the metal, for example, manganese, silicon, and phosphorus in mild steel and iron and silicon in aluminum alloys. However, most commercial materials are not even nominally pure metals but are alloys in which deliberate additions of one or more elements have been made, usually to improve some property of the metal;

examples are the addition of carbon or nickel and chromium to iron to give, respectively, carbon and stainless steels and the addition of copper to aluminum to give a high-strength age-hardenable alloy.

1.03.2.1 Components and Phases

Impure metals and alloys exhibit all the structural features and crystal defects of the pure metals already discussed. In addition, however, impure metals and alloys exhibit many structures that are not observed in pure metals and which, in many instances, have an extremely important effect on the properties, particularly the corrosion resistance. However, before dealing with the structure of impure metals and alloys, it is necessary to consider the concept of metallurgical components, phases, constituents, and equilibrium phase diagrams.

The fundamental difference between pure metals and impure metals and alloys arises from the fact that there is only one atomic species present in the former, while there are two or more present in the latter; thus, a pure metal is a single-component system, a pure binary alloy is a two-component system, while impure metals and alloys, strictly speaking, are multicomponent systems. It is, however, usually valid to neglect the impurities and, for example, to consider a commercial brass as a binary Cu–Zn alloy, that is, as a two-component system.

Gibbs' phase rule, as applied to metallurgical systems (i.e., under conditions of constant pressure) indicates that pure metals, being single-component systems, can only coexist as two phases in equilibrium at a single temperature. Thus pure copper, for example, exhibits three phases, namely solid f.c.c. copper, liquid copper, and gaseous copper. Any two of these phases, say solid and liquid copper, can coexist in equilibrium at only one temperature, that is, the melting point of copper. Pure iron exhibits four phases, namely two solid phases (f.c.c. and b.c.c. iron (see **Table 1**)) and a liquid and a gaseous phase. Alloys, on the other hand, being multicomponent systems, can exhibit two or more phases in equilibrium over a range of temperatures. The phases which are present in an alloy and their composition and distribution markedly affect many of the properties of the alloy, including its corrosion resistance.

1.03.2.2 Solid Solutions

When a pure metal *A* is alloyed with a small amount of element *B*, the result is ideally a homogeneous random mixture of the two atomic species *A* and *B*, which is known as a solid solution of *B* in *A*. The solute *B* atoms may take up either interstitial or substitutional positions with respect to the solvent atoms *A*, as illustrated in **Figures 13(a)** and **13(b)**, respectively. Interstitial solid solutions are only formed with solute atoms that are much smaller than the solvent atoms, as is obvious from **Figure 13(a)**; for the purpose of this section, only three interstitial solid solutions are of importance, that is, Fe–C, Fe–N, and Fe–H. On the other hand, the solid solutions formed between two metals, as for example in Cu–Ag and Cu–Ni alloys, are nearly always substitutional (**Figure 13(b)**). Occasionally, substitutional solid solutions are formed in which the distribution of *B* in *A* is not random (**Figure 13(c)**), and such solid solutions are said to be ordered and exhibit a superlattice. Order–disorder transitions are observed with temperature changes. Superlattices are observed in the Cu–Au, Cu–Zn, and Fe–Ni systems.

There are a number of differences between interstitial and substitutional solid solutions, one of the most important of which is the mechanism by which diffusion occurs. In substitutional solid solutions, diffusion occurs by the vacancy mechanism already discussed. Since the vacancy concentration and the frequency of vacancy jumps are very low at ambient temperatures, diffusion in substitutional solid solutions is usually negligible at room temperature and only becomes appreciable at temperatures above about $0.5T_M$, where T_M is the melting point of the solvent metal (K). In interstitial solid solutions, however, diffusion of the solute atoms occurs by jumps between adjacent interstitial positions. This is a much lower energy process that does not involve

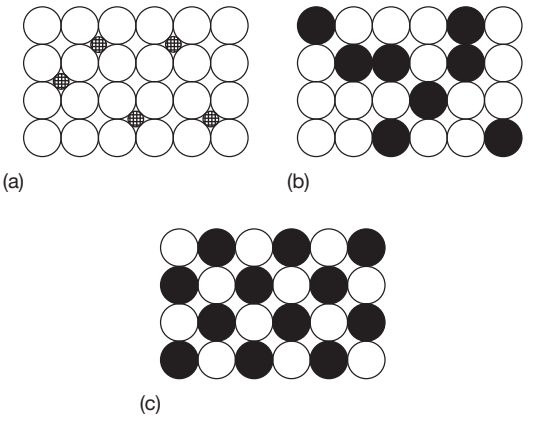

Figure 13 (a) Interstitial solid solution, (b) random substitutional solution, and (c) an ordered substitutional solid solution forming a superlattice.

vacancies, and it therefore occurs at much lower temperatures. Thus, hydrogen is mobile in steel at room temperature, while carbon diffuses quite rapidly in steel at temperatures above about 370 K.

1.03.2.3 Segregation at Dislocations and Grain Boundaries

In practice, the distribution of solute atoms in a solid solution is not ideally homogeneous. There is almost invariably a stress field around any solute atom in a solid solution, and there is therefore, a tendency for these atoms to migrate to regions of the crystal lattice that are already strained, in particular to grain boundaries and to dislocations. Thus, in impure metals and alloys, there is an inherent tendency for impurities and alloying additions to segregate at grain boundaries and around the cores of dislocations. Segregation of carbon and nitrogen to dislocations in steels has a very significant effect on their mechanical properties and is particularly responsible for their sharp yield point; similar segregation may also affect the corrosion behavior of cold-worked steels. The segregation of impurities and alloying elements to grain boundaries is clearly of relevance in any consideration of the strength and reactivity of grain boundaries and, in particular, of intergranular corrosion, temper embrittlement, etc.

In addition, it has fairly recently been recognized that impurities and alloying elements will also tend to segregate to free surfaces. The implications of this for corrosion resistance and particularly for passive-film formation have received relatively little attention.

1.03.2.4 Limited and Complete Solid Solubility

Just as the saturated solubility of sugar in water is limited, so the solid solubility of element *B* in metal *A* may also be limited, or may even be so low as to be negligible, as for example with lead in iron or carbon in aluminum. There is extensive interstitial solid solubility only when the solvent metal is a transition element and when the diameter of the solute atoms is <0.6 of the diameter of the solvent atom. The Hume-Rothery rules state that there is extensive substitutional solid solubility of *B* in *A* only if:

(a) The atomic diameters of *A* and *B* do not differ by more than 15%.
(b) The two elements have similar electronegativity. (Note: electronegativity is the power of an element to attract electrons to itself when present in a molecule or in an aggregate of unlike atoms; it is a different property from the electrode potential, which depends on the free energy difference between an element in its standard state and a compound or ion in solution.) In addition, a metal of a lower valency tends to dissolve a metal of a higher valency more readily than vice versa.

However, just as two liquids may be completely miscible and form a complete range of solutions from one pure liquid to the other, so certain metals, for example, copper and nickel, exhibit complete solid solubility over the whole range of compositions from pure copper to pure nickel. Clearly, for two metals to be soluble in each other over the whole compositional range, they must have the same crystal structure, that is, they must be isomorphous.

1.03.2.5 Intermediate Phases and Intermetallic Compounds

When metal *A* is alloyed with enough element *B* to exceed the solid solubility of *B* in *A*, a new phase is formed. This may be the other terminal solid solution of *A* in *B*. Alternatively, an intermediate solid-solution phase, with a crystal structure different from that of either of the terminal solid solutions, may be formed over a range of compositions. An example of this is the so-called β-phase in brasses, which is the stable phase at room temperature over the composition range 47–50% Zn. In some alloys, intermediate phases are formed that are best regarded as compounds. Examples are Fe_3C (cementite) in the Fe–C system and the intermetallic compounds $MgNi_2$ and Mg_2Ni formed in the Mg–Ni system. While solid solutions are stable over a range of compositions, compounds have a unique composition; cementite, for example, corresponds to Fe–25 at.%C (Fe–6.7 wt%C).

1.03.3 Equilibrium Phase Diagrams

In alloys, as in pure metals, the stable phase or phases change with changing temperature. Furthermore, in alloys, the stable phase or phases, and the composition of these phases, changes with the composition of the alloys. These changes are best represented by equilibrium phase diagrams. These define the stability and composition of the phases that can occur in an alloy system as a function of temperature and alloy composition, under conditions of constant pressure. Phase diagrams are in many ways analogous to

Pourbaix diagrams, which define the stability of phases in a metal/water system as a function of potential and pH, and like *E*–pH diagrams, phase diagrams have certain limitations. First, it must be emphasized that they are equilibrium phase diagrams and that they only predict the stability and composition of phases under equilibrium conditions. They neither give any indication of how rapidly equilibrium will be achieved in practice, nor do they give any indication of the distribution of the phases at equilibrium. Somewhat analogously, *E*–pH diagrams give no information about the rate at which a particular metal will corrode or the protectiveness of a particular passive film. Second, equilibrium phase diagrams give no information whatsoever about the existence of metastable phases, some of which are of the utmost practical significance. These limitations become particularly important under conditions of rapid temperature change. Phase diagrams, in contrast to *E*–pH diagrams, are always determined experimentally, although they can be explained, and to a certain extent, qualitatively predicted from thermodynamic data and considerations. Nevertheless, in spite of these limitations, phase diagrams are an extremely important and useful metallurgical tool.

1.03.3.1 Binary Isomorphous Phase Diagrams

Although ternary and quaternary phase diagrams are beyond the scope of this section, it is appropriate to deal with the various types of binary phase diagrams by referring to some specific alloys. The simplest phase diagram refers to an isomorphous alloy system in which there is complete solid solubility. By way of example, the Cu–Ni phase diagram is shown in **Figure 14**. This phase diagram indicates that at 1600 K, an alloy containing 70% Cu is a liquid (point *a* in **Figure 14**). On slow cooling, this alloy starts to solidify when the liquidus line is reached, that is, point *b* at about 1500 K. At this point, grains of a solid solution containing about 53% Cu are nucleated from the liquid containing 70% Cu and start to grow. As the temperature continues to fall, the composition of the liquid follows the liquidus line while that of the solid falls along the solidus line, until at 1470 K the alloy consists of a mixture of a solid solution containing 62% Cu and a liquid containing 78% Cu (**Figure 14**). Furthermore, the fraction of solid in the two-phase mixture is given by the ratio of the lengths yz/xz, while the fraction of liquid is given by xy/xz. This is known as the lever rule. On further slow cooling, the solidus line is reached, that is, point *c* at about 1430 K, when solidification of the alloy is complete; the last liquid to freeze contains about 85% Cu, while the last solid to solidify contains 70% Cu. At 1300 K, for example, and indeed at all temperatures below the solidus, an alloy containing 70% Cu is a solid (point *d* in **Figure 14**). Clearly the phase change in this transformation is liquid → solid. The microstructure of a homogeneous single-phase solid-solution alloy is

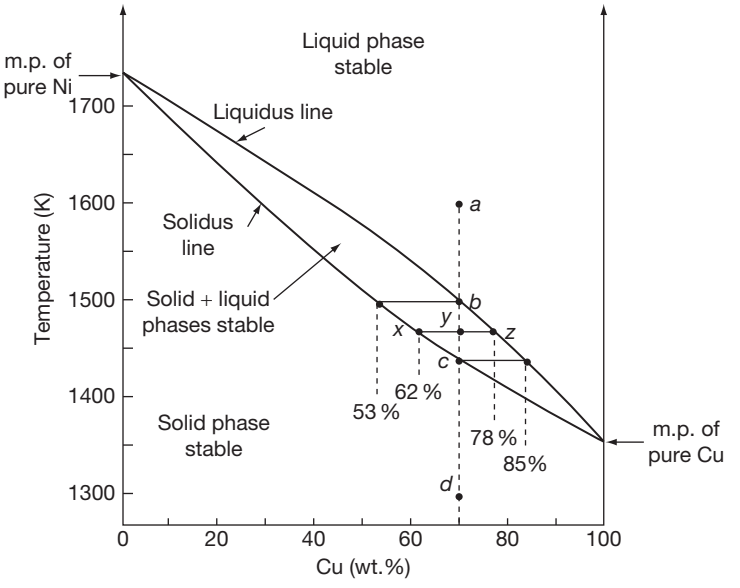

Figure 14 Nickel–copper phase diagram.

indistinguishable from that of a pure metal, as shown in Figure 4 (bottom).

1.03.3.2 Coring

If the alloy is cooled sufficiently slowly, the alloy itself and all the grains in it will be homogeneous after solidification. If, on the other hand, the alloy is cooled more rapidly, the grains will be cored, not homogeneous. During cooling, the composition changes in the solid phase involve solid-state diffusion; if the temperature falls too rapidly, therefore, there is insufficient time for diffusion. In the Cu–30Ni alloy referred to earlier, clearly the center of the grains, the first metal to have solidified, would be nickel rich (i.e., low in copper) while the grain boundary regions, the last metal to have solidified, would be copper rich. Coring is eliminated by annealing at high temperatures to permit diffusion and homogenization to take place.

1.03.3.3 Eutectic Phase Diagrams

The equilibrium phase diagram for Pb–Sb alloys represents a simple eutectic system and is shown in Figure 15. This type of phase diagram is often observed when there is negligible solid solubility of the two metals in each other, and no intermediate phases are formed. The point E is the eutectic point, T_E the eutectic temperature, and C_E the eutectic composition, in this case approximately 520 K and 13% Sb, respectively. Like a pure metal, an alloy of eutectic composition freezes at a single temperature T_E, instead of over a temperature range, as in the case of the Cu–30Ni alloy already discussed. Unlike a pure metal, however, a eutectic alloy freezes to give a mixture of two phases, in this case Pb and Sb; in general terms, therefore, a eutectic reaction involves liquid → solid α + solid β.

A hypereutectic alloy containing, say, 50% Sb starts to freeze when the temperature reaches the liquidus line (point *a* in Figure 15). At this temperature, pure proeutectic Sb nucleates; as the temperature continues to fall, more antimony is deposited from the melt, and the composition of the liquid phase moves down the liquidus line to the eutectic point. When this is reached, the remainder of the melt solidifies. The microstructure of alloys of eutectic composition varies somewhat with the alloy system, but generally consists of an aggregate of small particles, often platelets, of one of the phases comprising the eutectic in a continuous matrix of the other phase. Finally, the microstructure of the hypereutectic 50% Sb alloy already mentioned consists of primary (proeutectic) antimony surrounded by the eutectic constituent, as illustrated in Figure 16. This microstructure is clearly to be expected from the solidification sequence just described.

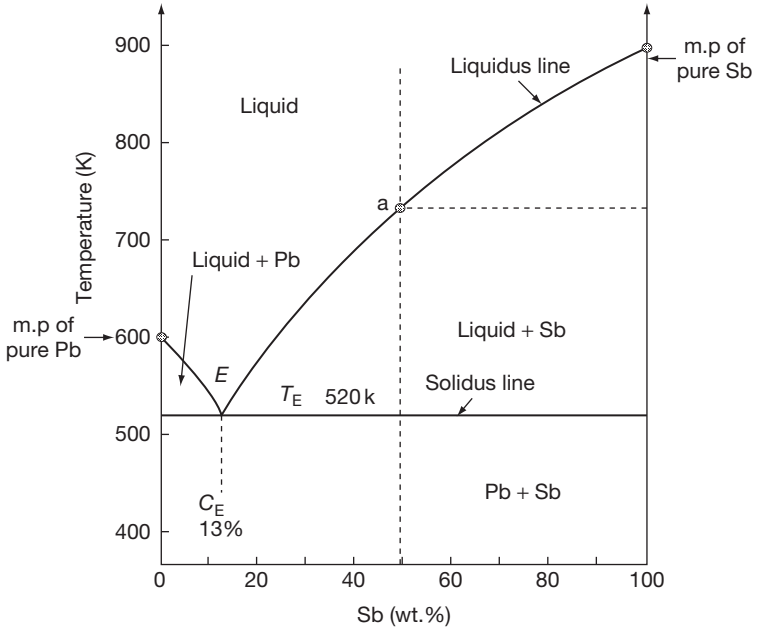

Figure 15 Lead–antimony phase diagram.

Figure 16 Light micrograph showing the microstructure of a hyper-eutectic Pb–50Sb alloy (×50).

1.03.3.4 More Complex Binary Phase Diagrams

Most phase diagrams, however, are more complex than those shown in Figures 14 and 15. Thus, in most eutectic systems, there is some appreciable solid solubility, as in the Ag–Cu phase diagram shown in Figure 17(a). At ambient temperatures, therefore, an Ag–50Cu alloy would contain two components (Ag and Cu), two phases (the α and β solid solutions), and two constituents (primary proeutectic β and the eutectic mixture of α + β). Furthermore, in many alloy systems intermediate phases and/or intermetallic compounds are formed. Figure 17(b), for example, illustrates the Mg–Sn phase diagram; this exhibits two eutectic reactions and the intermetallic compound, Mg_2Sn. Finally, a number of other reactions, in addition to the eutectic reaction, are observed; of particular importance are (on cooling in all cases):

1. The eutectoid reaction: solid α → solid β + solid γ.
2. The peritectic reaction: liquid + solid α → solid β.
3. The peritectoid reaction: solid α + solid β → solid γ.

By way of example, the Cu–Zn phase diagram shown in Figure 18 exhibits a number of different intermediate phases (β, γ, δ, etc.) and a number of peritectic reactions and a eutectoid reaction. In many instances, it is not necessary to consider a complete phase diagram. Thus Figure 19 illustrates the Al-rich end of the Al–Cu phase diagram and is used below in a discussion of precipitation hardening. Again, Figure 20 shows the Fe–Fe_3C phase diagram, the great practical importance of which is in no way reduced by the fact that one of the components in it, namely Fe_3C (cementite), is a metastable compound. The true equilibrium diagram, in which graphite appears in place of cementite, is of use only when cast irons are being considered, as opposed to steels. Other phase diagrams that are of particular significance are the iron-rich ends of the Fe–Ni and Fe–Cr systems, which are shown in Figures 21(a) and 21(b), respectively. It follows from the diagrams that Ni and C are austenite (γ-phase) stabilizers while Cr is a ferrite (α-phase) stabilizer. The fact that the interstices in an f.c.c. structure are bigger than those in a b.c.c. structure accounts for the fact that C is much more soluble in f.c.c. iron (austenite) than in b.c.c. iron (ferrite) (Figure 20).

1.03.4 The Fe–Fe_3C Phase Diagram

Because of the great practical importance of steels, it is necessary to discuss the Fe–C system in rather more detail. The Fe–Fe_3C phase diagram consists of the following three reactions

1. At 1766 K and 0.16% C the peritectic reaction: liquid Fe + δ − Fe (b.c.c.) → γ − Fe (f.c.c.).
2. At 1420 K and 4.3% C the eutectic reaction: liquid Fe → γ − Fe (f.c.c.) + Fe_3C.
3. At 996 K and 0.80% C the eutectoid reaction: γ − Fe (f.c.c.) → α − Fe_3C.

The peritectic transformation generally has little effect on the structure, properties, or corrosion resistance of steels at room temperature; an exception to this occurs in the welding of certain steels, when δ-ferrite can be retained at room temperature and can affect corrosion resistance. Furthermore, since most steels contain less than about 1.0%C (and by far the greatest tonnage contains less than about 0.3% C), the eutectic reaction is of relevance only in relation to the structure and properties of cast irons, which generally contain 2–4%C. This discussion, therefore, will be limited to the eutectoid reaction that occurs when homogeneous austenite is cooled.

1.03.4.1 Decomposition of Austenite

When austenite is cooled, the structures that result from the eutectoid reaction depend on the temperature at which the transformation takes place. In practice, of course, steels are generally continuously cooled at a rate that may vary from very rapid (quenching) to very slow (furnace cooling). However, it is useful and valid to simplify the situation by assuming that the transformation occurs isothermally. In other words, therefore, we shall consider initially,

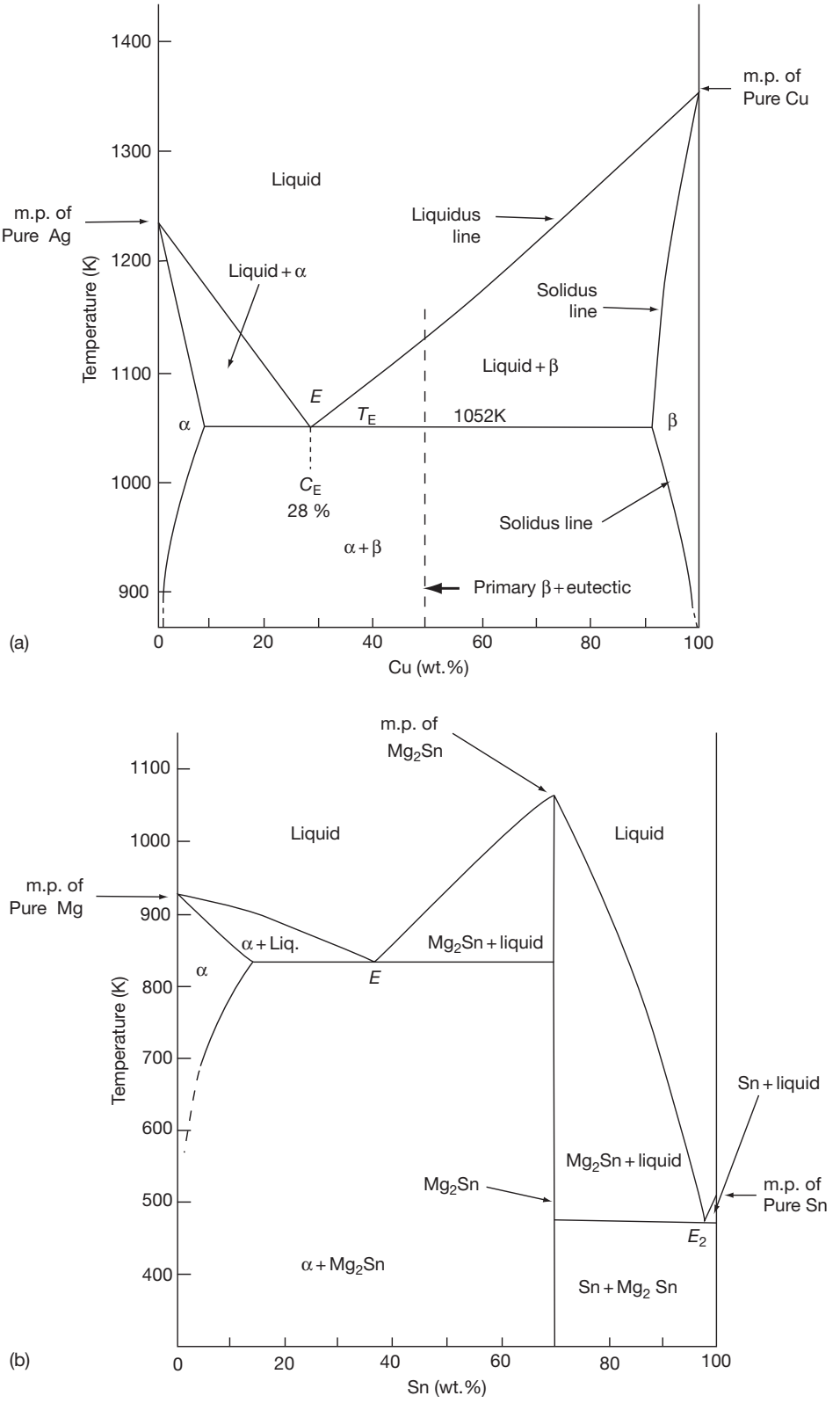

Figure 17 (a) Silver–copper phase diagram and (b) magnesium–tin phase diagram.

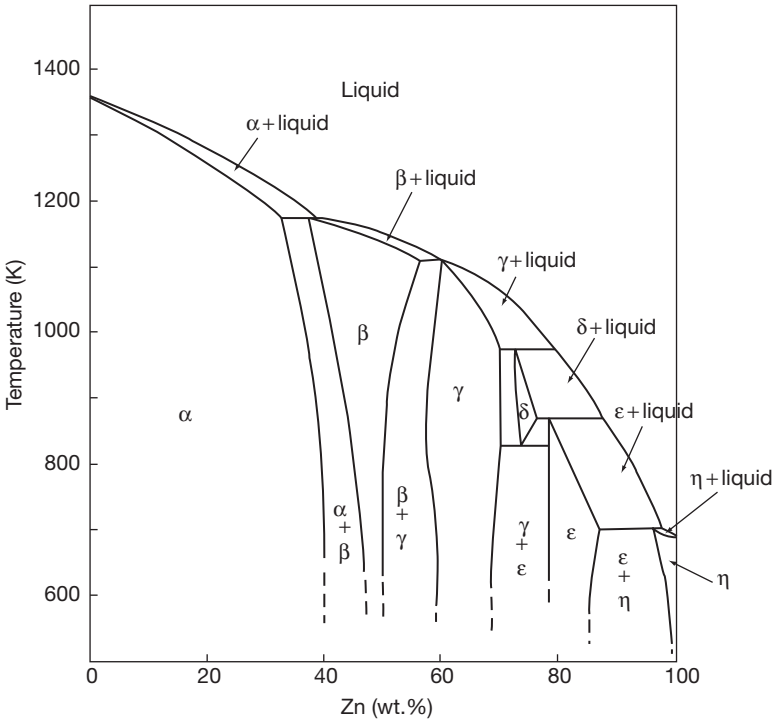

Figure 18 Copper–zinc phase diagram.

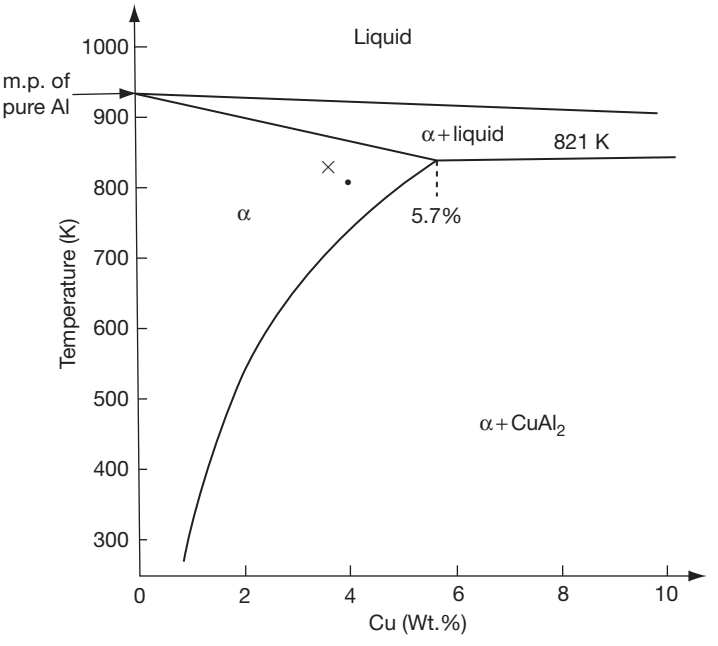

Figure 19 Aluminum-rich end of the aluminum–copper phase diagram.

the reactions that occur when a steel containing 0.8% C (i.e., of eutectoid composition) is very rapidly quenched from, say, 1400 K to some temperature $T < 996$ K, at which decomposition of the austenite takes place. In general, the structures produced on slow continuous cooling approximate to those resulting from high temperature isothermal transformation, while rapid continuous cooling results in

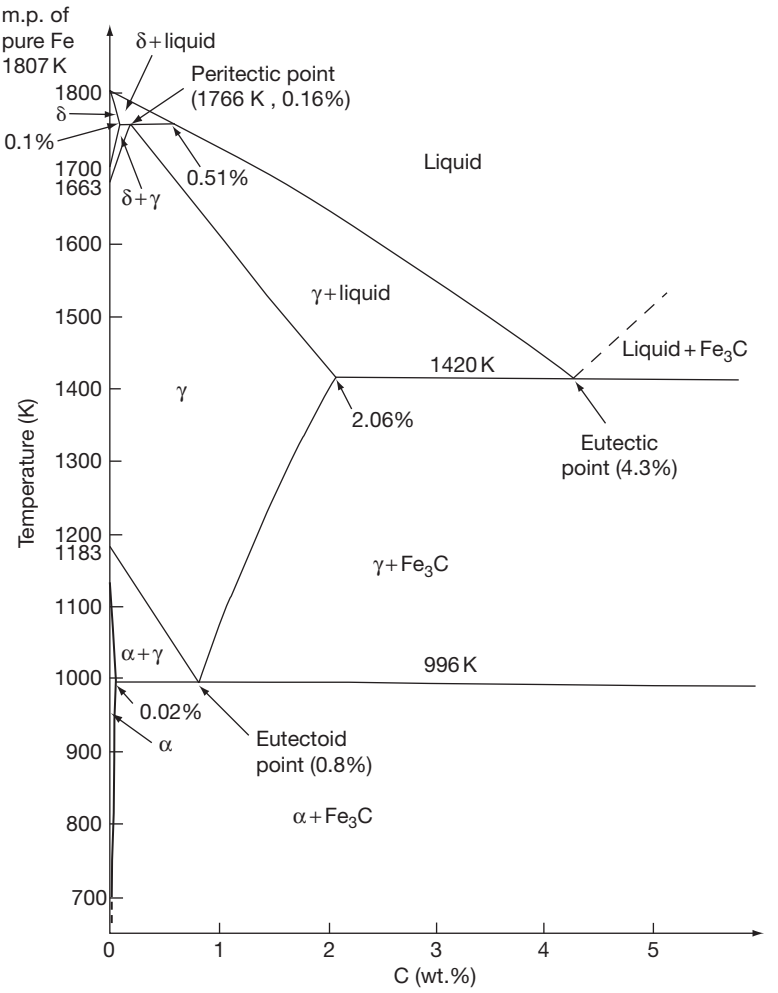

Figure 20 Iron-rich end of the metastable Fe–Fe_3C phase diagram.

structures that approximate to those obtained by intermediate-temperature isothermal transformation.

1.03.4.2 Formation of Pearlite

If austenite is allowed to transform just below 996 K, the reaction product, as predicted by the Fe–Fe_3C phase diagram, is the $\alpha - Fe + Fe_3C$ eutectoid. This eutectoid constituent is known as pearlite and consists of alternate platelets of ferrite (α-Fe) and cementite (Fe_3C), the former being the continuous phase. The decomposition of austenite to pearlite involves nucleation of pearlite, which occurs almost exclusively at austenite grain boundaries, followed by growth of pearlite; both processes involve the solid-state diffusion of carbon in iron. Immediately after quenching, therefore, the structure of the steel consists of untransformed austenite, as shown schematically in Figure 22(a). At some later time, nucleation of a number of colonies of pearlite will have occurred at the austenite grain boundaries, as shown in Figure 22(b); at this stage, about 10% of the austenite has transformed. At some still later time, growth of the pearlite will have occurred by nucleation of new α-Fe and Fe_3C platelets and by extensive edge-wise growth of existing platelets as shown in Figure 22(c); at this stage, about 90% of the austenite has transformed and eventually, transformation will be complete.

In fundamental terms, the transformation temperature affects both the driving force for the decomposition of austenite and the diffusion rate of carbon. In effect, therefore, the transformation temperature alters both the rate of nucleation and the rate of growth. This in turn manifests itself in different transformation times at different temperatures. Furthermore, the spacing of the pearlite platelets is

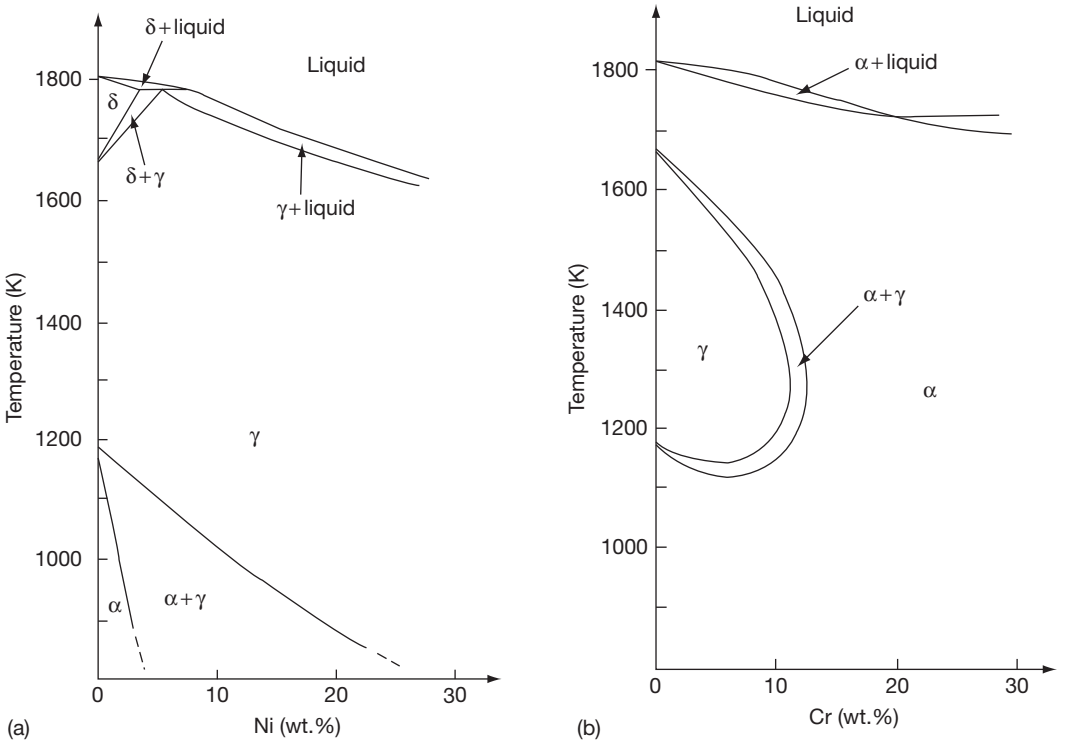

Figure 21 (a) Iron-rich end of the iron–nickel phase diagram and (b) iron-rich end of the iron–chromium phase diagram.

characteristic of the temperature at which transformation occurred; the lower the transformation temperature the finer are the platelets, and the greater the hardness and the strength of the steel. The distinction between coarse and fine pearlite structures is shown in **Figures 22(d)** and **22(e)**, respectively; in practice, the platelets in very fine pearlite may not be resolvable with a light microscope. The rate of transformation of carbon steels is also markedly affected by the presence of other alloying elements. However, a detailed consideration of the transformation and structure of low-alloy steels is beyond the scope of this section.

1.03.4.3 Formation of Bainite

At lower transformation temperatures (<770 K approximately), a second reaction, the formation of bainite, intervenes. Like pearlite, the bainite constituent in steels consists of a mixture of ferrite and an iron carbide and is formed by a time-dependent nucleation and growth process involving diffusion of carbon. Bainite, however, grows as needle-like plates, which consist of very fine particles of carbide embedded in a ferrite matrix. The carbide particles can only be resolved in an electron microscope; in the light microscope, only the acicular bainite needles are visible. The microstructure of a bainitic steel is shown schematically in **Figure 22(f)**; the appearance of bainite, however, and the structure and composition of the carbides in it, vary somewhat with transformation temperature, bainite being much harder than pearlite.

1.03.4.4 Formation of Martensite

Finally, at even lower transformation temperatures, a completely new reaction occurs. Austenite transforms to a new metastable phase called martensite, which is a supersaturated solid solution of carbon in iron and which has a body-centered tetragonal crystal structure. Furthermore, the mechanism of the transformation of austenite to martensite is fundamentally different from that of the formation of pearlite or bainite; in particular, martensitic transformations do not involve diffusion and are accordingly said to be diffusionless. Martensite is formed from austenite by the slight rearrangement of iron atoms required to transform the f.c.c. crystal structure into the body-centered tetragonal structure; the distances involved are considerably less than the interatomic distances. A further characteristic of the martensitic transformation is that it is predominantly athermal, as opposed to the isothermal transformation of austenite

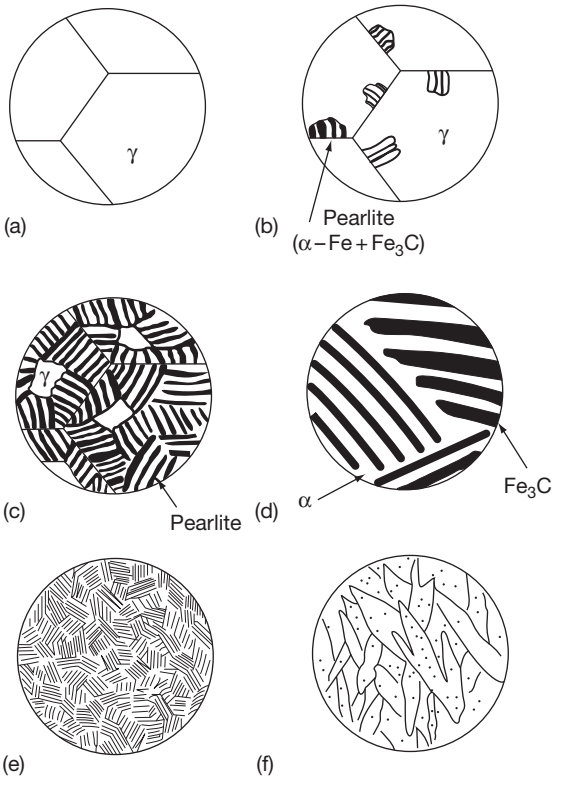

Figure 22 Some of the pearlitic and bainitic microstructures observed in eutectoid steels after various heat treatments.

to pearlite or bainite. In other words, at a temperature midway between m_s (the temperature at which martensite starts to form), and m_f (the temperature at which martensite formation is apparently complete), the steel will consist of about 50% austenite and about 50% martensite; this transformation of 50% of the austenite to martensite is effectively instantaneous, and no matter how long the steel is held at this temperature, no further transformation will occur. **Figure 23** illustrates the microstructure of a fully martensitic steel. The martensite platelets are heavily twinned, although this is only apparent in an electron microscope. In fact, in a eutectoid steel, the m_f temperature is below room temperature although in a more common hypoeutectoid steel containing about 0.2% C, $m_s \approx 720\,K$ and $m_f \approx 550\,K$. Other alloying elements also affect the temperature at which the martensite transformation takes place and usually decrease it.

1.03.4.5 Isothermal Transformation Diagrams

Time–temperature–transformation (T–T–T) diagrams are used to present the structure of steels

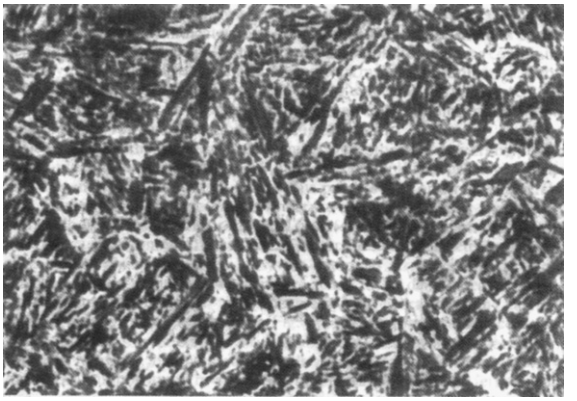

Figure 23 Light micrograph showing the microstructure of a martensitic steel (× 550).

after isothermal transformation at different temperatures for varying times. The T–T–T diagram for a commercial eutectoid steel is shown in **Figure 24(a)**. Also shown on the curves are the points at which the microstructures illustrated in **Figures 22 and 23** are observed, and the thermal treatments producing these structures. When a steel partially transformed to, say, pearlite, is quenched from point *a* in **Figure 24(a)** to below m_f, the untransformed austenite transforms to martensite.

1.03.4.6 Transformation of Hypo-Eutectoid Steels

As noted above, most steels are, in practice, hypoeutectoid. Consider, by way of example, a low-alloy steel containing 0.3%C. The Fe–C phase diagram (**Figure 20**) indicates that as a steel of this composition is cooled below about 1080 K, the equilibrium state is a two-phase structure containing primary, pro-eutectoid ferrite and austenite. On further cooling to below 996 K, the equilibrium structure consists of pro-eutectoid ferrite and pearlite. These differences are reflected in the rather more complicated T–T–T diagram used for this steel, shown in **Figure 24(b)**.

Depending on the transformation temperature, the steel may transform to ferrite plus austenite (T_1 in **Figure 24(b)**), to ferrite plus pearlite via ferrite plus austenite (T_2), directly to ferrite plus pearlite (T_3) or directly to ferrite plus bainite (T_4). The pro-eutectoid ferrite morphology, like the pearlite morphology, varies with the isothermal transformation temperature and also with the carbon content of the steel. The ferrite nucleates heterogeneously on austenite grain boundaries. Any pro-eutectoid ferrite in slightly hypoeutectoid steels (about 0.6%),

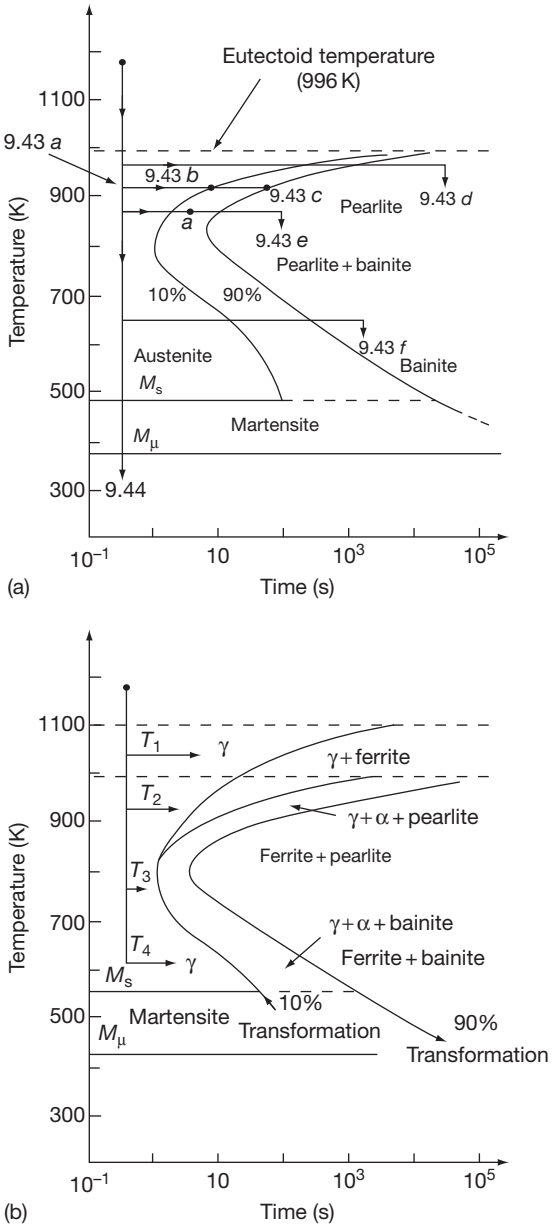

Figure 24 Isothermal time temperature transformation curves for (a) a eutectoid steel and (b) a hypo-eutectoid steel.

therefore, tends to be distributed along the austenite grain boundaries, with the grain centers transforming later to pearlite, as shown schematically in Figure 25(a). At lower carbon contents, Widmanstätten pro-eutectoid ferrite is observed, as shown schematically in Figure 25(b), while in low-carbon steels, massive ferrite is observed (Figure 25(c)). It is important to reemphasize that these pro-eutectoid ferrite structures also vary with isothermal transformation temperature and therefore, in practice, with

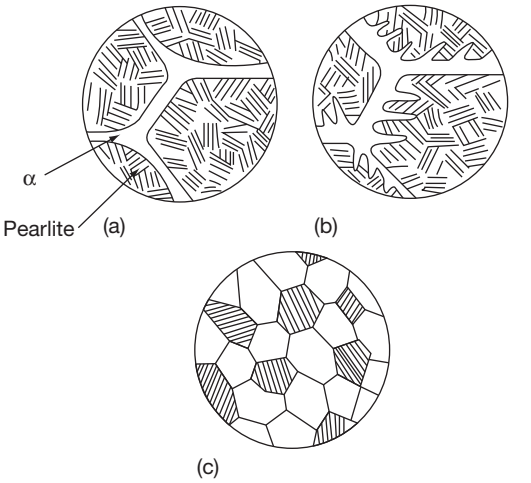

Figure 25 Schematic illustration of some of the ferritic/pearlitic microstructures observed in hypo-eutectoid steels after various heat treatments.

cooling rate; they can also be altered by subsequent heat treatment and working. Grain-boundary and Widmanstätten ferrite are generally undesirable and result in poor mechanical properties. Figure 25 illustrates some of the more important structures generally observed in two-phase alloys.

The higher the carbon content of a hypo-eutectoid steel, the more pearlite there will be in a ferritic/pearlitic structure and the greater will be the strength of the steel, other factors (grain-size, pearlite spacing, etc.) being equal.

1.03.4.7 Tempering of Martensite

As-quenched martensite is not only extremely hard, but also extremely brittle. The hardness of as-quenched martensite, which also increases with increasing carbon content, is due partly to the strain involved in retaining the carbon in solid solution in body-centered tetragonal iron, and partly, in low-carbon martensites, to their very high dislocation density. The martensite reaction in steels is not reversible and on reheating as-quenched martensite (Figure 26(a)) to various temperatures below 996 K, the carbon tends to precipitate out of the solid solution; this process is known as tempering. On tempering at about 370–520 K, the carbon precipitates out as the so-called ε-carbide, which may be written as $Fe_{2.4}C$ and has a different structure from cementite. These carbides precipitate on certain crystallographic planes and on the twin boundaries in the martensite plates, forming what is known as a Widmanstätten structure, as shown schematically in Figure 26(b).

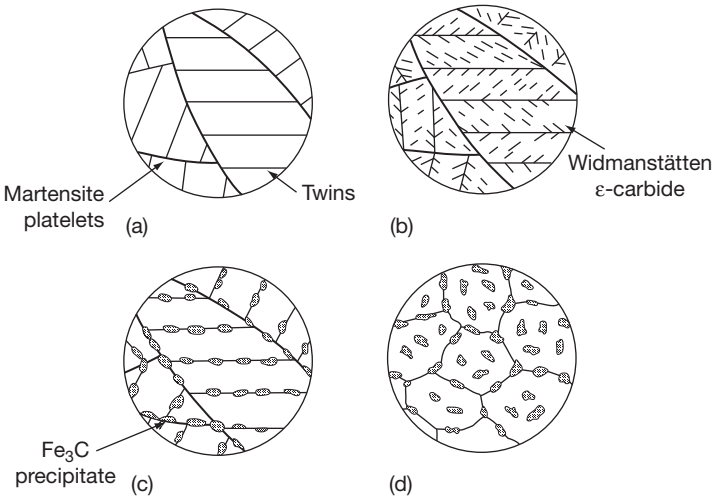

Figure 26 Some of the microstructures observed during the tempering of martensite.

On tempering at 520–770 K, cementite particles are precipitated on twin boundaries and on boundaries between martensite platelets, leaving a matrix of ferrite as shown in **Figure 26(c)**. Eventually, the cementite particles grow and become spheroidal in shape while the twinned structure breaks down and fine equiaxed ferrite grains are observed, as illustrated in **Figure 26(d)**. On tempering, as the carbon precipitates out of the solid solution, the strength and hardness of the steel falls progressively, as shown in **Figure 27**, while the toughness increases. Quenched and tempered low-alloy steels are widely used where high-strength high-toughness materials are required.

1.03.4.8 Spheroidized Structures in Steels

On tempering or annealing martensite, bainite, or even pearlite at even higher temperatures (about 970 K), a structure consisting of coarse cementite spheroids (readily visible in a light microscope) in a ferrite matrix is obtained. This is the most stable of all ferrite/cementite aggregates, and it is also one of the softest.

The structures and phase transformations observed in steels have been dealt with in some detail not only because of the great practical importance of steels, but also because reactions similar to those occurring in steels are also observed in many other alloy systems, too. In particular, diffusionless transformations (austenite → martensite), continuous precipitation (austenite → pearlite), and discontinuous precipitation (austenite → bainite and tempering of martensite) are fairly common in other alloy systems.

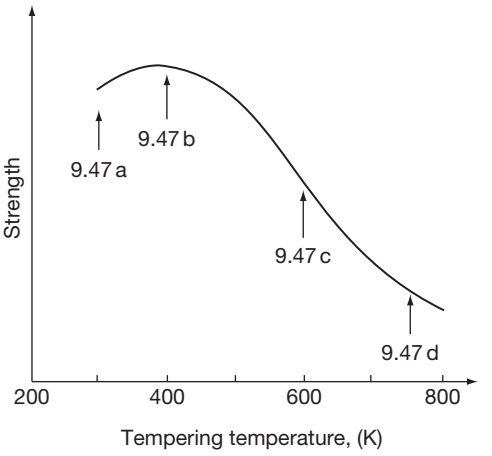

Figure 27 Effect of tempering temperature on the strength and microstructure of martensite.

1.03.5 Strengthening Mechanisms in Metals

Many of the ways of increasing the strength of metals have already been dealt with in passing. For example, cold working a metal increases its dislocation density and therefore, as already discussed, increases its strength. (The processes involved in the nucleation and multiplication of dislocations during cold working are very complex and beyond the scope of this section.) Substitutional solid solutions (e.g., austenitic stainless steels and brass) are normally stronger than the equivalent pure metals (i.e., iron and copper), as the lattice distortion involved hinders dislocation

movement. This is known as solid–solution hardening. Metals with fine grain structures, produced by grain-refining treatments, such as cold working followed by annealing to give recrystallization, are stronger than coarse-grained materials and single crystals, since grain boundaries act as barriers to dislocation movement. Steels may be quenched and tempered to produce high-strength and high-toughness materials. Clearly, all these involve altering the structure of the metal in some way. Another very important strengthening mechanism, namely precipitation hardening, also involves microstructural changes.

1.03.5.1 Precipitation Hardening

Precipitation hardening (also called age hardening and dispersion hardening) is particularly important in high-strength aluminum alloys, but it is also used to strengthen other alloys, notably certain steels and nickel-base alloys. Consider, by way of example, the Al–Cu phase diagram shown in **Figure 19**. At about 820 K, the equilibrium structure of an Al–4Cu alloy (point *X* in **Figure 19**) is the single-phase α solid solution of copper in aluminum, as shown in **Figure 28(a)**. On annealing at this temperature, that is, on solution heat treating, this equilibrium state is readily achieved. At room temperature, because the limit of solid solubility decreases with decreasing temperature, the equilibrium structure consists of the α-solid solution plus the $CuAl_2$ intermetallic compound. This equilibrium state may be achieved by very slowly cooling the alloy from 820 K to room temperature and consists of very coarse discontinuous precipitates of $CuAl_2$ in an α matrix, as shown in **Figure 28(b)**. However, on quenching the alloy to room temperature, diffusion (and therefore nucleation and growth of $CuAl_2$) is prevented, and the copper is retained in supersaturated solid solution, as shown in **Figure 28(c)**. This supersaturated solid solution is relatively soft, weak, and ductile. If this metastable supersaturated solid solution is then aged, that is, heat treated at a relatively low temperature (370–520 K), the excess copper again precipitates out of the solid solution as $CuAl_2$. In this case, however, the $CuAl_2$ particles are extremely fine, certainly submicroscopic, and under certain conditions, only just resolvable in the electron microscope. The precipitation sequence varies from alloy to alloy but is generally quite complex and involves a number of intermediate metastable precipitates. The initial precipitates or coherent zones formed during the early stages of aging (i.e., after relatively short times)

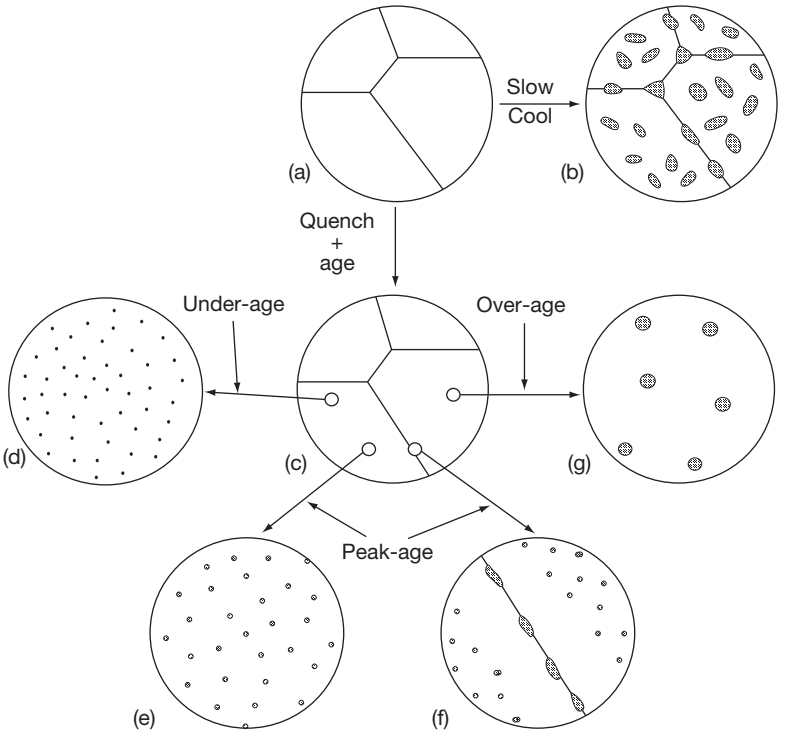

Figure 28 Some of the microstructures observed during the heat treatment of precipitation-hardening aluminum alloys.

interact with dislocations and tend to hinder their movement. This underaged condition is therefore stronger than the as-quenched condition, but since the zones are extremely fine (Figure 28(d)) and are readily sheared by moving dislocations (Figure 29(a)), it is only moderately so. On further aging, somewhat coarser, semicoherent intermediate precipitates are formed (Figure 28(e)). These interact strongly with dislocations and, being too large to be sheared, form very effective barriers to dislocation motion. Dislocations can only move through the matrix by bowing round the precipitates and leaving behind dislocation loops, as shown in Figure 29(b), and in this peak-aged condition, the alloy is strongest. If aging is continued, a relatively coarse dispersion of the equilibrium precipitate is formed. In this overaged condition (Figure 28(g)), the precipitates are too coarse and widely spaced to interact strongly with dislocation; they are relatively ineffective barriers to dislocation motion, and the alloy again has only intermediate strength. It should be emphasized, however, that even in the over-aged condition, the precipitates are still submicroscopic.

The rate at which aging occurs depends on the aging temperature. At very low aging temperatures, over-aging is not observed in a realistic timescale while at high aging temperatures, the strength falls off almost immediately. In general, the lower the aging temperature, the greater the peak hardness. These effects are illustrated schematically in Figure 30.

During aging, nucleation always occurs first at grain boundaries; the intergranular precipitates are therefore always coarser and more advanced than the intragranular precipitates. Furthermore, owing to vacancy and solute depletion, there is always a precipitate-free zone adjacent to the grain boundary. The grain-boundary structure of a peak-aged high-strength precipitation-hardening aluminum alloy is therefore as shown schematically in Figure 28(f) and in the electron micrograph in Figure 31.

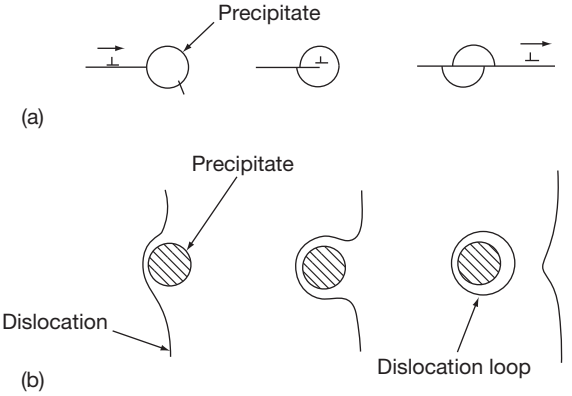

Figure 29 (a) Dislocation shearing a precipitate particle and (b) a dislocation bowing round a precipitate particle.

1.03.5.2 Complex Alloy Systems

Detailed consideration of the structure of many of the advanced and complex alloys that are of considerable technological importance (high-strength titanium alloys, nickel-base superalloys, etc.) is beyond the

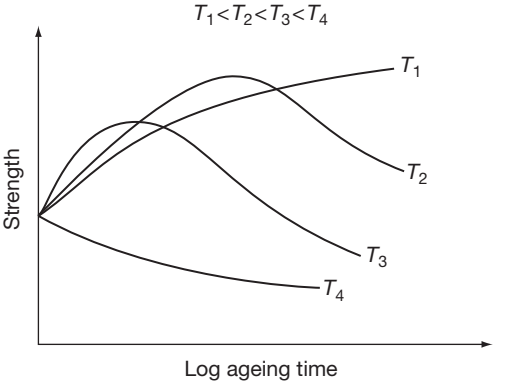

Figure 30 Curves of strength against the logarithm of the ageing time for a precipitation-hardening aluminum alloy aged at different temperatures.

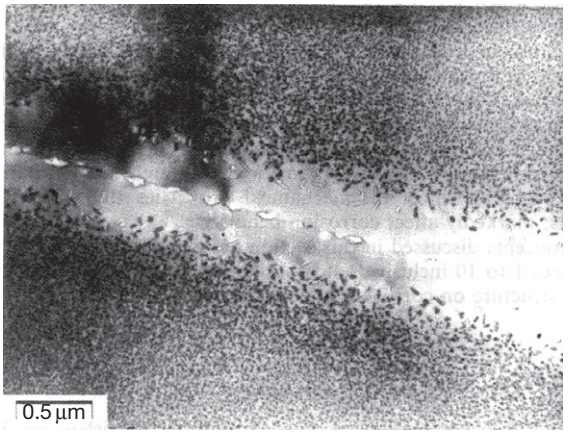

Figure 31 Transmission electronmicrograph showing intergranular and intragranular precipitation and the precipitate-free zone adjacent to the grain boundary in a high-strength precipitation-hardening Al–Zn–Mg alloy (×24 000, courtesy of G. Lorimer).

scope of this section, other than to point out that no new principles are involved. Certain titanium alloys, for example, exhibit a martensitic transformation, while many nickel-base superalloys are age hardening. Similarly, cast irons, although by no means advanced materials, are relatively complex.

1.03.5.3 Inclusions in Metals

In conclusion, it must be emphasized again that commercial materials are never pure metals or pure binary or ternary alloys. They always contain impurities that are not particularly beneficial to the properties of the material; however, so long as they are not positively detrimental (as in the case of carbon in certain austenitic stainless steels), their presence is tolerated as it would be uneconomical to remove them. Some of these impurities are in solid solution. Others, however, exist as inclusions that are quite unaffected by heat treatment, although they may be broken up by working. Examples are the Fe–Si-rich inclusions in aluminum alloys (**Figure 10**), manganese sulfide inclusions in steel, etc. However, although these impurities may have a negligible effect on mechanical properties, they can, in certain instances, markedly affect corrosion behavior.

The concepts discussed in this section are dealt with in greater depth in References Reed-Hill,[1] Rollason,[2] Bailey,[3] Smallman,[4] Cottrell,[5] Cahn,[6] Chalmers,[7] McLean,[8] Shewman,[9] and Peckner,[10] inclusive.

References

1. Reed-Hill, R. E. *Physical Metallurgy Principles*; van Nostrand Reinhold: New York, 1970.
2. Rollason, E. C. *Metallurgy for Engineers*; Edward Arnold: London, 1973.
3. Bailey, F. W. J. *Fundamentals of Engineering Metallurgy and Materials*; Cassell: London, 1972.
4. Smallman, R. E. *Modern Physical Metallurgy*; Butterworths: London, 1970.
5. Cottrell, A. H. *An Introduction to Metallurgy*; Edward Arnold: London, 1967.
6. Cahn, R. W., Ed. *Physical Metallurgy*; North-Holland: London, 1970.
7. Chalmers, B. *Physical Metallurgy*; John Wiley: New York, 1959.
8. McLean, D. *Mechanical Properties of Metals*; John Wiley: New York, 1962.
9. Shewman, P. G. *Transformations in Metal*; McGraw-Hill: New York, 1969.
10. Peckner, D., Ed. *The Strengthening of Metals*; Reinhold: New York, 1967.

1.06 Defects and Transport in Oxides and Oxide Scales

B. Pieraggi
Ecole Nationale Supérieure des Ingénieurs en Arts Chimiques et Technologique de Toulouse, Institut National Polytechnique de Toulouse, F-31077 Toulouse Cedex 04, France

Abbreviations

DIGM Diffusion-induced grain-boundary motion
PSZ Partially-stabilized zirconia
SZ Stabilized zirconia
TLK Terrace-ledge-kink

Symbols

b Burgers vector of a dislocation
n Molar fraction of free electron (mol^{-1})
p Molar fraction of positive hole (mol^{-1})
t Time (s)

x_i Mole fraction of species i (mole^{-1})
C_i Molar concentration of i (mol m^{-3})
D Diffusion coefficient (m^2 s^{-1})
J Diffusion flux (mol m^{-2} s^{-1})
K_r Equilibrium constant for the reaction r
P Pressure (bar)
Q Activation energy (J mol^{-1})
R Universal gas constant (8.314 J mol^{-1} K^{-1})
T Temperature (K)
T_m Temperature of melting (K)
$\Delta_f g$ Molar free enthalpy of formation (J mol^{-1})
$\Delta_f g_i$ Molar free enthalpy of formation of component i (defect or compound) (J mol^{-1})
ΔV_r Molar relaxation volume (m^3 mol^{-1})
δ Departure from ideal stoichiometry (mol^{-1})
ϕ Pilling–Bedworth ratio
ξ Thickness (m)
Ω Molar volume (m^3 mol^{-1})

1.06.1 Introduction

High temperature oxidation of many materials often results in the formation and growth of a continuous external oxide scale and/or in the internal oxidation of the less-noble constituents of the oxidized materials. Therefore, matter transport usually plays a very important role in scale growth and internal oxidation processes. Indeed, a growing external oxide scale separates its own substrate from the oxidizing chemical environment; thus, oxidant species and/or material constituents must be transported across the oxide scale during its growth. Similarly, internal oxidation involves the dissolution and diffusion of oxidant species within the substrate. Furthermore, heat-resisting metallic materials are protected against oxidation by the selective oxidation of their less-noble constituents, usually Cr and/or Al, leading to the growth of chromia or alumina scales that, in addition to matter transport across the scale, requires the diffusion of Al or Cr within the oxidized substrate toward the scale–substrate interface.

Therefore, processes and mechanisms of diffusion and mass transport in oxide scales and oxidized substrates are of prime importance in the understanding and modeling of the high temperature oxidation of materials. As diffusion and mass transport in solids require the presence of crystal defects, Section 1.06.2 is devoted to a general description of common crystal defects. Point defects of ionic crystal are described in Section 1.06.3. Section 1.06.4 is devoted to different aspects of diffusion and mass transport, including diffusion laws, diffusion in two-phase systems and in ternary systems, and short-circuit diffusion. Specific aspects of diffusion in oxide scales and defect structure, and diffusion in the most common oxides are reported in Section 1.06.5 before some concluding remarks (Section 1.06.6).

1.06.2 Crystal Defects

The crystal structure of any solid chemical compound defines the perfect periodical arrangement of its chemical constituents. However, many physical and chemical processes would not be possible without the existence of local discontinuities in this perfect periodic arrangement; these local discontinuities form more or less extended defective zone or crystal defects. Different kinds of crystal defects are distinguished from their geometrical dimension D: 0D for point defects, 1D for linear defects, and 2D for planar defects. These different defects are briefly described in the following subsections.

1.06.2.1 Point Defects: Thermal Defects and Constitutive Defects

Point defects are the simplest defects that can be found in any crystal phase. They are localized on single sites of the crystal structure; these sites can be regularly occupied by some chemical species or else regularly unoccupied sites of the vacant interstitial sublattice. Figure 1 defines the simplest and common point defects that can be present in pure solid chemical elements; vacancies and interstitials can also be present in disordered solid solutions. More complex defects such as divacancies or dissociated interstitials can also be formed; they are not considered here.

Interstitial sites are defined from the crystal structure. The simplest case corresponds to the close-packed stacking of hard spheres leading to the

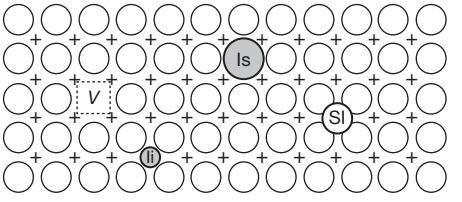

Figure 1 Schematic representation of point defects in a pure solid chemical element: v, vacancy; Is, substitutional impurity; SI, self-interstitial; Ii, interstitial impurity; the crosses mark the vacant interstitial sites.

face-centered cubic (fcc) lattice or to the hexagonal close-packed (hcp) lattice. Two kinds of interstitial site, octahedral and tetrahedral, are usually distinguished in such close-packed structure. For an fcc lattice, there is one octahedral site and two tetrahedral sites per lattice site. For fcc pure metals such as Ni or γ-Fe, small impurity atoms such as C, H, or O, for example, would occupy the octahedral sites that are the larger ones. For MO oxides of rock salt structure such as NiO and FeO and for oxides M_3O_4 (Fe_3O_4) or AB_2O_4 ($NiCr_2O_4$) of spinel structure, oxygen anions also form a close-packed fcc lattice. In rock salt structure, metal cations are only localized over octahedral sites of the fcc anionic sublattice and the tetrahedral sites always remain empty. Thus, point defects of such MO oxides would be mainly vacant octahedral sites (cation vacancies) and oxygen vacancies or self-interstitials. For spinel structure, only one-half of the octahedral sites and one-eighth of the tetrahedral sites are occupied by metal cations, which permits more complex combinations of cationic point defects as briefly described in **Section 1.06.5.4.2**.

Vacancies and self-interstitial defects are also called intrinsic defects, while substitutional or interstitial impurities are extrinsic defects. The amount of point defects in a crystal is usually defined by their concentration (defects per cubic meters), their site fraction or their molar fraction (defects per mole), which is also, the number of defects per mole of the considered crystal phase. The thermodynamic argument for the stability of defective crystals is well known and does not need to be repeated here. A detailed treatment of the thermodynamic of point defects can be found elsewhere.[1,2]

From the Gibbs phase rule, in unstressed state, pure solid chemical element, for example, pure Ni or Si, and disordered solid solutions of constant composition have no degree of freedom at constant temperature T and pressure P. The corresponding thermodynamic systems are invariant so that intrinsic point defects cannot be considered as being independent constituents of these systems; these defects are nonconservative species that need to be created/annihilated at sources or sinks.

By assuming that pressure P remains in a range such that its influence can be neglected, the mole fraction x_d of the intrinsic point defects d then only depends on temperature T:

$$x_d = \exp\left(-\frac{\Delta_f g_d}{RT}\right) \qquad [1]$$

Although point defects are a characteristic of atomic level, their usual thermodynamic quantities are commonly expressed in molar quantities ($J\,mol^{-1}$). Therefore, in eqn [1], $\Delta_f g_d$ is the molar Gibbs energy of formation of intrinsic defects d. As shown by eqn [1], the mole fraction x_d increases with T and depends only on that external independent variable, which justifies that such intrinsic defects are also called thermal defects. Vacancies are the dominant point defect in common metals and alloys; enthalpy of formation and entropy of vacancies in pure metals have been reviewed by 'Kraftmaker.'[3] Equation [1] also means that the chemical potential of vacancy is null at equilibrium. For disordered solid solution, enthalpy of formation and entropy of point defects, particularly for vacancies, would depend on solid-solution composition. However, for ideal solid solutions, there is no interaction between solution constituents and therefore no local modification of the composition in the vicinity of point defects; the chemical potential of vacancy at equilibrium is thus independent of solid-solution composition and remains null. Therefore, the equilibrium vacancy molar fraction varies monotonically as a function of composition. The situation is more complex for nonideal solid solutions where point defects would interact differently with solution constituents. For example, a constituent of larger atomic radius could trap vacancies to accommodate more easily the local volume change it introduces. Therefore, in nonideal solid solution, the dependence of defect molar fraction as a function of solution composition could be complex and the presence and rearrangement of point defects could favor localized composition change.

Under very high pressure or very large stress, the equilibrium mole fraction of intrinsic defects also depends on pressure and stress state.[4] For the simple case of a crystal submitted to a hydrostatic pressure P, the mole fraction of intrinsic defects varies as

$$x_d(P) = x_d(0)\,\exp\left(-\frac{P(\pm\Omega + \Delta v_r)}{RT}\right) \qquad [2]$$

where Ω is the crystal molar volume (the sign is '+' for vacancy formation and '–' for interstitial formation) and Δv_r is the molar relaxation volume, that is, 1 mol of the local volume variation resulting from the relaxation of the crystal lattice around a defect d. Equation [2] can be also applied to stressed crystals by replacing the pressure P by a stress tensor $\boldsymbol{\sigma}$ and the term $(\pm\Omega + \Delta v_r)$ by a formation volume tensor $\mathbf{v}_f$. Like pressure, a compressive stress has a positive sign, and hence, from eqn [2], hydrostatic pressure or compressive stress would decrease the equilibrium

molar fraction of vacancy while a tensile stress would increase it. An opposite influence would be observed with interstitial defects.

The situation is more complex for binary or multicomponent compounds. Indeed, an n-ary compound, in an unstressed state and at constant T, has $(n-1)$ degree of freedom, that is, its composition depends on $(n-1)$ composition variables that can vary independently without affecting its crystal structure. The chemical formula or ideal stoichiometric composition of such a compound is fixed by its crystallographic structure, but, as there is $(n-1)$-independent composition variables, the real chemical composition can differ from the ideal stoichiometric composition.

Several types of point defects can explain such a departure from ideal stoichiometric composition. Figure 2 defines the main types of single intrinsic point defects that can be encountered in binary compounds. The point defects of such compounds are usually described by affecting a sublattice for each independent compound constituent. But, in addition to vacancies and interstitials associated to each sublattice, antisite defects can be also present in multicomponent compounds. For a simple binary AB compound, an antisite defect corresponds to the wrong occupation of one crystal site as, for example, an atom A occupying a lattice site regularly occupied by an atom B, or inversely an atom B on a site of A. Such antisite defects are mainly observed in intermetallic and covalent compounds; they cannot be stable in ionic compounds because of the large and repulsive electrostatic interactions they would induce.

Two simple examples are provided by the crystal structure of nickel oxide NiO (rock salt structure) and the simple cubic crystal structure of nickel aluminide β-NiAl. For NiO, its departure from the ideal stoichiometry is only due to a deficit in Ni^{2+} cations, its real chemical composition can be expressed as $Ni_{1-\delta}O$ where δ is the mole fraction of cation vacancies per mole of NiO. At constant T, the departure δ varies as a function of one compositional variable that, in this case, is usually the activity (partial pressure) of oxygen. Therefore, these vacancies are not thermal defects; they are structurally linked to the crystal structure of NiO, which justifies their denomination of structural or constitutive defects. β-NiAl, contrary to NiO, is stable over a large range of chemical composition, including its stoichiometric composition. In that case, the type and concentration of structural point defects compatible with the conservation of crystal structure vary with the mole fraction of Al or Ni. For example, complex point defects such as triple defects associating one antisite Ni atom and two Ni vacancies can be found in stoichiometric β-NiAl, while Ni vacancies and antisite Ni atoms are the predominant defects in Al-rich and Ni-rich β-NiAl, respectively.

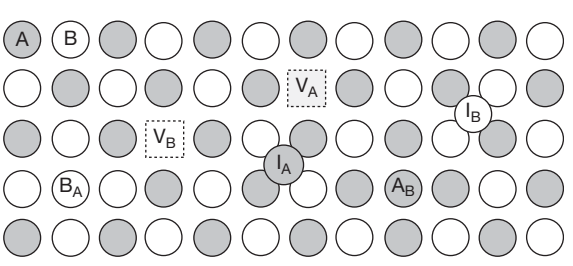

Figure 2 Intrinsic point defects in a compound AB: V_A, V_B and I_A, I_B are, respectively vacancies and interstitials of sublattices A and B. A_B and B_A correspond to antisite defects.

At constant temperature, the composition range over which a binary compound is stable, that is, the concentration limits of point defects, depends on the relative stability of this compound with respect to the closest adjacent compounds. A very stable compound, such as alumina, would have a very narrow stability range corresponding to very small departures from stoichiometry and very low defect concentrations. A less stable oxide, such as $Ni_{1-\delta}O$, would have larger stability range and thus larger defect concentration, in which case it is equal to δ/Ω.

1.06.2.2 Dislocations

Dislocations are linear defects involved in mechanical behavior, mass transport, and reactivity of materials.[5] In a crystal, a dislocation is a line that, on one slip plane, forms the boundary between a crystal region that has slipped and an adjacent unslipped region so that the glide of the dislocation line results in plastic deformation (Figure 3(a)). Such a definition has simple but important consequences. One of them is that any dislocation cannot simply end in the bulk of a crystal; a dislocation must have its extremities on a surface, an interface or a grain boundary or intersect two other dislocations to form a dislocation node or else form a dislocation loop. Dislocations are characterized by the direction of the dislocation line and the slip vector or Burgers vector **b** defining the relative displacement of slipped and unslipped crystal regions. Figures 3(b) and 3(c) illustrates schematically the two limiting types or characters of dislocations:

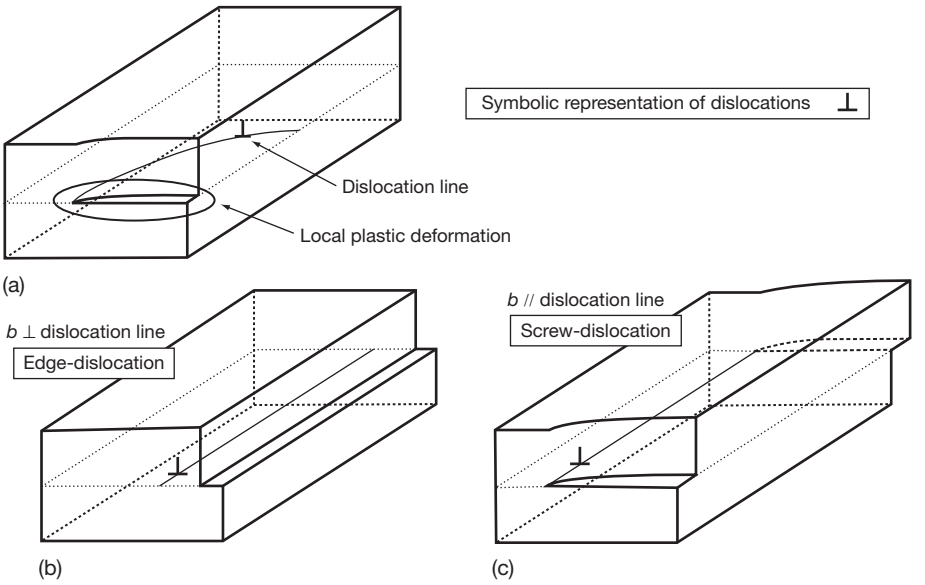

Figure 3 Schematic definition of dislocations: (a) mixed dislocation, (b) edge dislocation, and (c) screw dislocation.

1. edge dislocations for which **b** is normal to the dislocation line (**Figure 3(b)**),
2. screw dislocations for which **b** is parallel to the dislocation line (**Figure 3(c)**).

A dislocation loop has a mixed character when its Burgers vector lies in the plane of the loop, some parts are edge and some parts are screw. Such a loop may glide in its own plane. On the contrary, when the Burgers vector is normal to the loop plane, the dislocation loop, named prismatic loop, is a pure edge dislocation and cannot glide.

Dislocations induce local displacements of lattice sites from their equilibrium position. These displacements result in strain and stress fields around each dislocation. The related elastic strain energy per unit length of dislocation line is proportional to $\mathbf{b}^2$ so that the dislocation lines tend to be straight to minimize the energy added to the crystal. One other consequence is that the Burgers vector **b** of stable dislocations is the shortest translation vector of the crystal lattice, which permits to infer easily the possible Burgers vectors of dislocations for simple crystal lattices – as, for example, the fcc lattice of pure metals. These dislocations are called perfect dislocations. One perfect dislocation of Burgers vector $\mathbf{b}_1$ can dissociate into two partial dislocations of Burgers vectors $\mathbf{b}_2$ and $\mathbf{b}_3$ separated by a bidimensional defect called stacking fault. The Burgers vectors $\mathbf{b}_2$ and $\mathbf{b}_3$ of such partial dislocations are a fraction of lattice translation vectors, which justify their denomination of partial dislocations. Such a dislocation dissociation is energetically favorable, only if $\mathbf{b}_1^2 > \mathbf{b}_2^2 + \mathbf{b}_3^2$. The example of fcc metals is well known and described in many basic textbooks.[5]

The definitions of perfect edge and screw dislocations emphasize their role in plastic deformation by dislocation glide. But, dislocation motion is not restricted to gliding and dislocation lines are usually not straight. Indeed, many irregularities are commonly observed along dislocation lines resulting from dislocation intersections and also from thermal activation.[5] These irregularities can be described as more or less sharp steps distributed along a dislocation line. One step lying in the dislocation slip plane forms a kink, but such a step forms a jog when it is normal to the slip line (**Figure 4**). Kinks and jogs can move by glide, the slip plane is then stepped for jogged dislocations. On the contrary, the displacement of a jog along one dislocation moves the dislocation line in a direction normal to its slip plane; such a movement is called climb. Climb occurs at jogs by the creation/annihilation of vacancies and interstitials. Jog moving along an edge dislocation line acts as a source or sink for vacancies and interstitials, as illustrated by **Figure 5**. The interactions among the jog, dislocation climb, and intrinsic point defects play an important role in the recovery and creep as well as in point defect equilibrium – and thus on transport processes – at high temperature, that is, at $T > 0.4T_m$ for metallic materials.

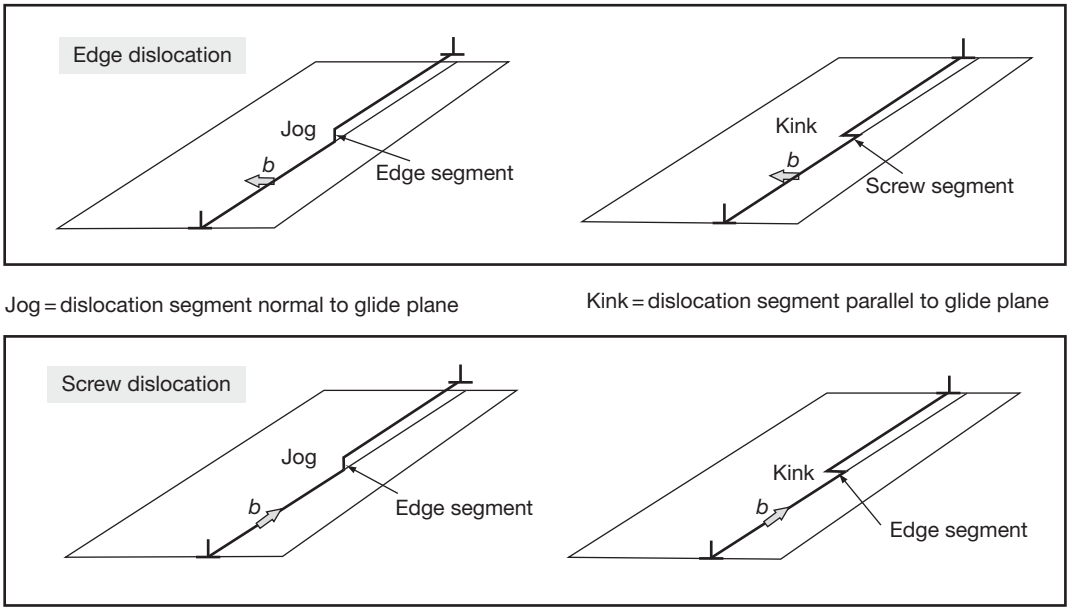

Figure 4 Kink and jog on edge and screw dislocations.

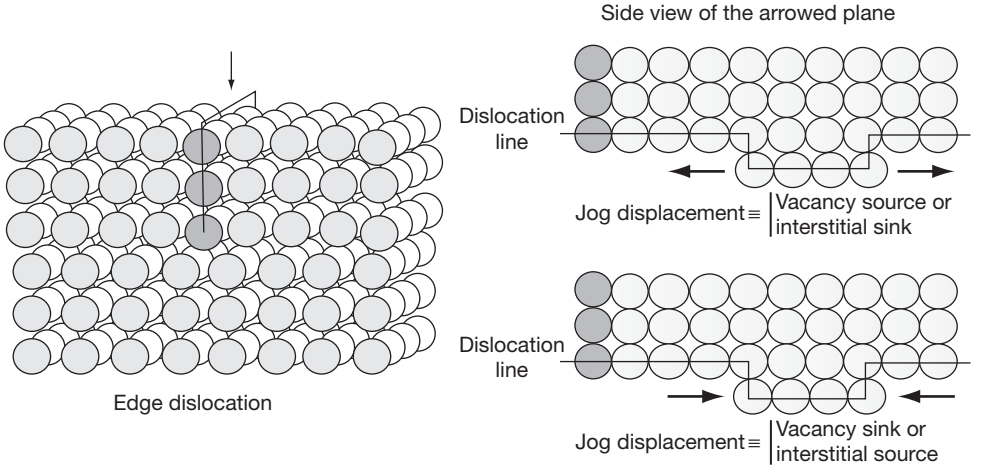

Figure 5 Schematic representation of the sink/source action of an edge dislocation from climb by jog displacement along the dislocation line.

All the above definitions are valid for disordered metallic materials. The situation is often more complex for intermetallic, covalent, and ionic compounds. The ordered structure of intermetallic compounds like β-NiAl leads to perfect superdislocations that dissociate to form antiphase boundaries bounded by dissociated dislocations. In covalent compound, most of the binding energy is localized in the nearest-neighbor bonds; the structure of glide dislocations is thus complex and involves dangling bonds so that the glide of such dislocations results in the successive breaking and reformation of chemical bonds. For ionic compounds, electrical neutrality and electrostatic interactions between ions of opposite charges results in quite complicated electrical effects for dislocations. Figure 6 shows that a dislocation in a simple 2D ionic crystal induces a local charge at the dislocation emergence. Furthermore, for the dislocation shown in Figure 6, the glide along direction x will be easier than the glide along direction z. Indeed, the glide along x maintains a separation between ions of same sign, which is not the case of glide along z

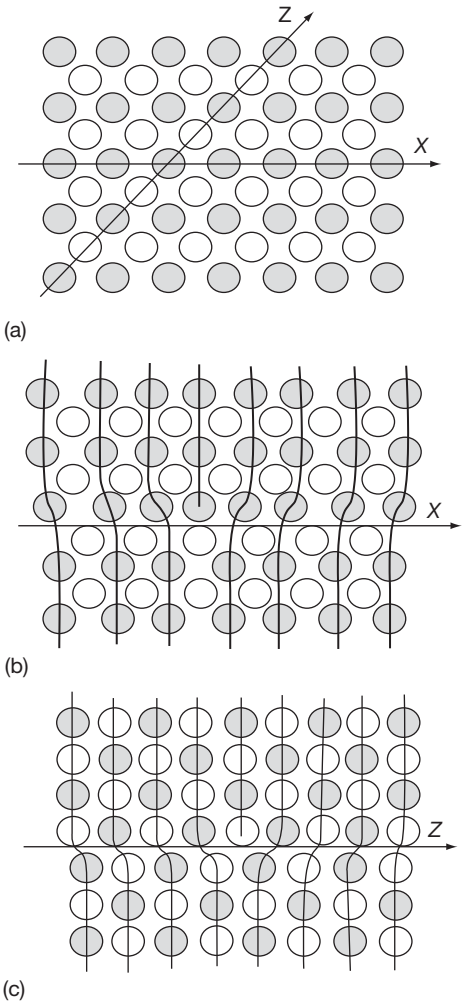

Figure 6 Dislocation glide in an ionic compound: (a) possible compact glide directions, (b) dislocation formed by glide along *z* direction, and (c) dislocation formed by glide along *x* direction.

direction. Kinks and jogs are also observed for dislocations present in ionic materials; dislocation climb by the interaction of dislocations and point defects remain the rule, which is of great importance for high temperature deformation (creep) and mass-transport processes in ionic compounds.

1.06.2.3 Surfaces

Mass and energy exchanges between a solid phase and its environment always proceed from its surface. Many processes such as, for example, adsorption and segregation, surface chemical reactions or else nucleation and crystal growth depend on the structure and properties of surfaces.[6] Atoms, molecules, or ions on a crystal surface have not the same number of nearest neighbors than in the bulk of the crystal; the surface of a solid crystal phase is thus a discontinuity, and consequently, a bidimensional crystal defect. Moreover, such a difference in surface and bulk environment is at the origin of surface energy γ, expressed in Joules per square meter, or surface tension (then expressed in the equivalent unit of $\mathrm{N\,m^{-1}}$). For a solid, surface energy depends on the surface orientation; this dependence determines the equilibrium shape of the crystal by minimizing its total surface energy.

The most common model of ideal and unrelaxed surfaces for solid crystal phases is the terrace–ledge–kink (TLK) model schematized in Figure 7. According to this model, surfaces are classified into three categories: singular, vicinal, and rough. A singular surface corresponds to a surface orientation perfectly parallel to a crystal plane of low Miller index. Such a singular surface is formed by one single terrace, that is,

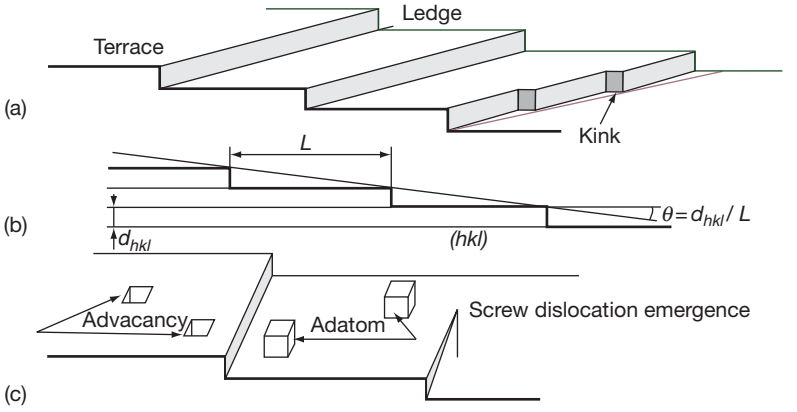

Figure 7 TKL model of crystal surface: (a) definition of terraces, ledges, and kinks, (b) relation between surface disorientation and ledge spacing, and (c) surface point defects.

a surface essentially smooth on an atomic scale. Vicinal surfaces have an orientation close to a singular surface. For disorientations along only one direction, the departure from the exact orientation is accommodated by one set of ledges, that is, steps parallel to a low-index crystal direction and delimiting successive terraces. The height of ledges is usually equal to the interplanar spacing of reticular planes parallel to the terraces; thus, the height and spacing of ledges can be easily related to the angular disorientation of the vicinal surface relatively to the singular orientation of terraces. For vicinal surfaces disoriented in two directions, the departure from the ideal orientation of terraces is accommodated by ledges and kinks forming single steps along the ledges. The spacing between successive kinks is similarly related to the surface disorientation.

Ledges and kinks have an important role in surface reactivity; as schematized in **Figure 7**, adsorption or segregation on a terrace or at a ledge or a kink are not equivalent. Similarly, ledges and kinks are important in crystal growth processes and, more generally, surface defects play an equally important role in surface reactivity. The main surface defects are also described in **Figure 7**. The formation of these defects is thermally activated; more defects are formed as temperature increases, which results in the roughening of the surface becoming disordered and more reactive.

1.06.2.4 Grain Boundaries and Interfaces

Grain boundaries and interfaces are surfaces where two single crystals of same nature and different orientation (grain boundary) or different nature and orientation (interface) join in a manner permitting some kind of matter continuity across these surfaces.[7,8] Such a surface introduces local discontinuities and thus must be considered as a bidimensional defect. By their shape, size, arrangement, and combination, grain boundaries and interfaces are important elements of the microstructure of materials and thus influence their properties. Microstructure is a nonequilibrium property of materials and as such is very sensitive to temperature, chemical composition, defect nature and concentration, mass transport processes, time, etc.

Similar to surface energy, grain-boundary energy results from the difference in local chemical environment between grain boundary and crystal, which in turn depends on the mutual orientation of the two adjacent crystals. For small disorientation, the simplest grain boundary structure is obtained by joining two similar vicinal surfaces disoriented in one direction; that is, only formed of terraces and ledges, which, as shown in **Figure 8(a)**, is similar to a symmetric tilt rotation of axis parallel to the ledge direction. The resulting grain boundary is a low-angle tilt boundary that is formed by a set of parallel and equidistant edge dislocations of Burgers vector normal to the boundary plane (**Figure 8(b)**). One other simple structure is obtained by joining two similar singular surfaces slightly disoriented in a rotation of axis normal to these surfaces, which lead to a low-angle twist boundary formed by an array of screw dislocations of Burgers vectors parallel to the boundary. From these two limiting cases, any low-angle grain boundary, also called subboundary, may be described by a more or less complex array of edge and screw dislocations. For these subboundary models, dislocation spacing is inversely proportional to disorientation angle θ so that they cannot hold when dislocation spacing is too small as that arise for $\theta > 0.10$ rad.

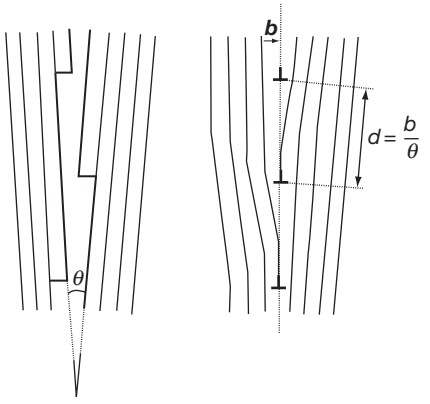

Figure 8 Formation of a parallel array of edge dislocations at low-angle tilt boundary.

However, the variation of grain-boundary energy as a function of a given disorientation angle shows minima for specific large disorientations. The simplest cases of such stable high-angle boundaries are twins similar to those usually observed for fcc or hcp metals. Several models were proposed to describe the structure of more general high-angle grain boundaries.[7,8] Dislocation models based on coincidence site lattice (CSL) are well adapted to high-angle boundaries near a twin boundary, but the description of grain boundary structure by polyhedral structural units is more realistic. The important point here is that, in addition to the orientation dependence

of grain-boundary structure and energy, there is a corresponding dependence of grain-boundary diffusivity upon disorientation.

The modeling of the structure of heterogeneous interfaces separating two different crystal phases is more complex. These interfaces are commonly classified into the three categories of coherent, semicoherent and incoherent interfaces. The coherent and semicoherent interfaces correspond to specific mutual orientations of the two adjacent crystal phases, which implies the parallelism of lattice planes and crystal directions. Independent of their structure, the mutual orientation expresses that two lattice planes and two crystal directions belonging to the specified lattice planes are both respectively parallel. For two crystals noted 1 and 2, such an orientation relationship is expressed in the following form: $(h_1k_1l_1)[u_1v_1w_1]//(h_2k_2l_2)[u_2v_2w_2]$, where the plane and direction indexes for crystal i must be such that $h_iu_i + k_iv_i + l_iw_i = 0$ $(i = 1,2)$ to express their parallelism.

Figure 9 shows that, for the simplest case of two sets of parallel lattice planes of differing spacing, the disregistry of lattice planes can be accommodated by a parallel set of interfacial edge dislocations of Burgers vector parallel to the interface plane. These interfacial dislocations are named misfit dislocations. But, as lattice plane spacings are usually incommensurable, a small elastic deformation of both lattices is often required to permit their accommodation in the region of good fit, as exaggeratedly shown in Figure 9. The resulting stress field can influence the interface behavior and properties.

A relative twist rotation of the two sets of lattice planes can be accommodated by disorientation dislocations of Burgers vectors lying in the interface plane, that is, of screw character. More generally, as schematically shown in Figure 10(a), any heterogeneous interface can be modeled by a combination of misfit and disorientation dislocations, ledges and kink, and also a specific interfacial defect named disconnection[9] and symbolized by a dissymmetric dislocation symbol. Disconnections are defects specific to heterogeneous interface (Figure 10(b)), they have partly dislocation character and partly ledge character and are formed at the junction of two half planes of the same orientation; disconnections participate in lattice misorientations.

Surfaces, grain boundaries, and interfaces can also act as sources and sinks for vacancies and interstitials.[10,11] Like for edge dislocations, the displacement of kinks along a ledge or of jog along grain boundary or interface dislocations or else the displacement of interfacial ledges and kinks would result in the creation or annihilation of vacancies or interstitials.

Remarks: The intersection of three grain boundaries, named a triple junction, is a complex line defect. The structure and properties of these line defects are neither well known nor understood and appreciated. But, these defects are more open and disordered than dislocation or grain boundaries. Therefore, their role and contribution to mass transport is likely less negligible than considered till now, particularly for fine-grained materials such as oxide scales grown at intermediate temperatures where bulk diffusion is not predominant. Similar observations apply to triple junction line defects formed at the intersection of one grain boundary and one solid–solid interface.

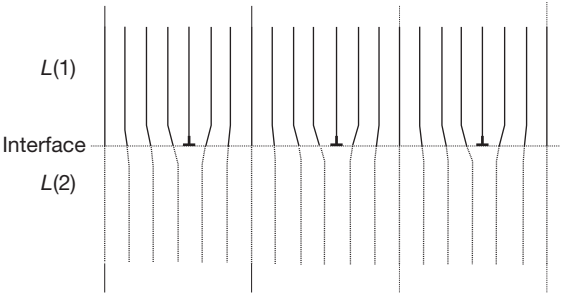

Figure 9 Misfit dislocations formed at the interface separating two parallel lattices of different interplanar spacings.

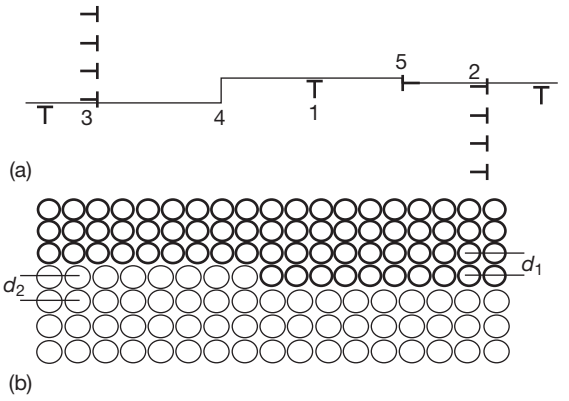

Figure 10 Interfacial defects and disconnection: (a) interfacial line defects at a semi-coherent metal–oxide interface: 1, misfit dislocation; 2, misorientation dislocation with an extra half-plane in metal lattice; 3, misorientation dislocation with an extra half-plane in oxide lattice; 4, ledge; 5, disconnection. (b) Disconnection equivalent to a misorientation dislocation of Burgers vector modulus equal to $d_2 - d_1$.

1.06.3 Point Defects in Ionic Crystals

Binary ionic compounds are formed by interpenetrating anionic and cationic sublattices that contain point defects. Several textbooks provide a detailed treatment and analysis of point defect equilibriums and defect-dependent properties of ionic compounds and metal oxides.[12–15]

Two kinds of point defect association permit to conserve the stoichiometry of a compound as illustrated in Figure 11 for an MX compound where M is a metal and X an oxidant. One association is the Frenkel defect or disorder consisting of the association of one cation vacancy and one interstitial cation. The other one is the Schottky disorder associating one cation vacancy and ν anion vacancies for an MX_ν compound. These two disorders are intrinsic defects. Indeed, an MX_ν compound maintained at its ideal stoichiometry contains only Frenkel and/or Schottky disorders, but loses one degree of freedom so that the disorder concentration or its mole fraction only depends on temperature. As for pure elements, these thermal equilibriums require operative sources or sinks of point defects. Departure of MX_ν compounds from ideal stoichiometry arises from reactions with any phase – solid, liquid, or gaseous – containing M or X in a form different to MX_ν; these reactions obviously occur at the interface between MX_ν and one of these other phases.

The thermal equilibrium of stoichiometric MX_ν compound as well as the creation/annihilation of point defects from interfacial reactions can be treated with the usual concept of chemical reactions and the associated thermodynamic tools, that is, law of mass action, chemical potentials, and activities, but such a treatment requires a specific notation for point defects. This notation must permit to express reactions balanced with respect to conservation of matter, electrical neutrality, and lattice site ratio fixed by the exact stoichiometry of the considered compound.

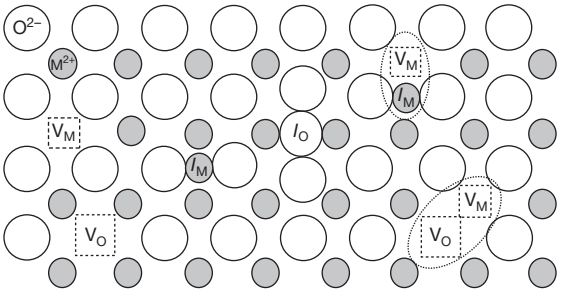

Figure 11 Intrinsic point defects of a MO oxide.

1.06.3.1 Structure and Building Elements: Kröger–Vink Notation

The commonly recommended and well-accepted notation for point defects has been suggested by Kröger and Vink and is, therefore, called Kröger–Vink notation. This notation is a symbolic representation of structure elements of defective crystals. A structure element is an atom, ion, molecule, or else vacancy or interstitial located on a specified lattice site of the perfect crystal lattice. The Kröger–Vink notation provides the following information on any kind of structure element:

1. the nature of the chemical species occupying one given lattice site in the real crystal,
2. the nature of the regular occupant of this given lattice site in the perfect crystal,
3. the effective electrical charge of the structure element.

The effective charge of a structure element is the difference between its charge in the real crystal and its charge in the neutral perfect crystal lattice. Positive effective charges are noted by dots and negative effective charges by commas or dashes; the sign '×' is used for a null effective charge. A vacancy is represented by the symbol V and an interstitial is designed by the index i affected to any species occupying an insertion site. The sites of interstitial sublattice are all noted V_i as they are always empty in the perfect crystal. All these notations are illustrated and explained in Figure 12 while the notation of all possible neutral and charged single point defects of ionic compound MX_ν is reported in Table 1. The use of Kröger–Vink notation is not restricted to ionic compounds; it can be extended to any kind of compounds; for nonionic crystal, the sign '×' for null effective charge is then usually omitted.

The reaction of formation of intrinsic defects or the interfacial reactions between an ionic crystal and its environment often result in the formation or destruction of one or more building elements of the considered compound. A building element is a combination of structure elements that can be added or removed without affecting the ideal stoichiometry or, in other words, conserves the crystal structure by keeping the ratio between the different lattice sites constant. For example, $M_M^\times + O_{O_i}^\times$ or $V_M^\times + O_O^\times$ are additive building elements of oxide MO. Building elements relative to only one sublattice can also be defined; they must keep constant the total site

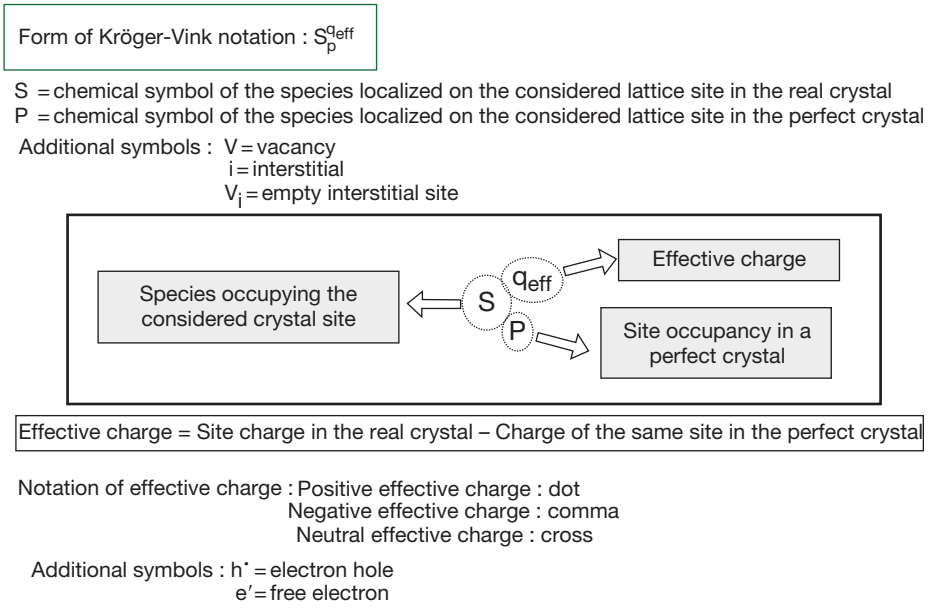

Figure 12 Kröger–Vink notation of point defects.

Table 1 Kröger–Vink notation of point defects in MO_ν oxide

Defect type	*Kröger–Vink notation*
Single point defect	
Free electron	e'
Electron hole	$h^{\cdot}$
Cationic impurity (charge $q > 2\nu$)	$I_M^{(q-2\nu)}$
Cationic impurity (charge $q < 2\nu$)	$I_M^{(2\nu-q)'}$
Neutral cation vacancy	$V_M^{\times}$
Ionized cation vacancy	$V_M^{n'}$ ($n \leq 2\nu$)
Self-interstitial cation	$M_i^{n\bullet}$
Interstitial cationic impurity	I_i^q
Anionic impurity (charge>2)	$I_O^{(q-2)'}$
Anionic impurity (charge<2)	$I_O^{(2-q)\bullet}$
Neutral anion vacancy	$V_O^{\times}$
Ionized anion vacancy	$V_O^{n\bullet}$ ($n \leq 2$)
Self-interstitial anion	$O_i^{n'}$
Interstitial anionic impurity	I_i^q
Combined defects (ν = integer number)	
Schottky	$V_M^{2\nu'} + \nu V_O^{2\bullet}$
Frenkel (or Frenkel-cation)	$M_i^{2\nu\bullet} + V_M^{2\nu'}$
Anti-Schottky	$M_i^{2\nu\bullet} + \nu O_i^{2\nu'}$
Anti-Frenkel (or Frenkel-anion)	$O_i^{2'} + V_O^{2\bullet}$

number of the considered sublattice to maintain the crystal structure and its stoichiometry; for the cation sublattice of MO, subtractive building elements such as $V_M^{\times} - M_M$ or $M_i^{\times} - V_i$ are compatible with this constraint.

1.06.3.2 Use of Kröger–Vink Notation: Formation Equilibriums of Frenkel and Schottky Disorders

The aim of this section is to illustrate the use of Kröger–Vink notation on simple examples of Frenkel and Schottky disorders formed from only neutral defects and to underline some difficulties and limits of this notation.

The formation of cationic Frenkel disorders in MX_ν only affects the cation sublattice. By using Kröger–Vink notation, the formation reaction of this disorder is

$$M_M^{\times} + V_i = M_i^{\times} + V_M^{\times} \qquad [3]$$

A similar disorder may also affect the anion sublattice (anionic Frenkel or anti-Frenkel disorder). Equation [3] fulfills the conditions of matter and lattice site balances. However, the law of mass action cannot be directly applied to eqn [3]. Indeed, like for an ionic solution for which it is not possible to vary the amount of only one ionic species while keeping all the other ones constant, it is not possible to maintain constant the number of regularly occupied cationic sites or the number of empty interstitial sites of the cation sublattice and to simultaneously create a cation vacancy or an interstitial cation. Equation [3] shows that the chemical potential, and thus the activity, of individual structure elements cannot be defined and expressed in their usual form. However, eqn [3] can be transformed to

$$0 = (M_i^{\times} - V_i) + (V_M^{\times} - M_M^{\times}) \quad [4]$$

where 0 represents the perfect lattice. The chemical potential and activity of subtractive building elements appearing in eqn [4] can then be defined and thus the law of mass action can be applied to this equation leading to

$$K_{FC} = a_{(M_i^{\times} - V_i)} a_{(V_M^{\times} - M_M^{\times})}$$

where $K_{FC} = \exp(-\Delta_f g/RT)$ is the equilibrium constant for the formation of cationic Frenkel disorder and $\Delta_f g$ the molar free energy of formation of this disorder at temperature T. The number of each subtractive building element is equal to the number of each associated point defects. Therefore, by assuming that the mole fractions of cation vacancies and interstitials are very small, an ideal behavior may be assumed and the activity of the building elements can be taken as equal to their mole fraction and therefore to the mole fraction of the associated point defects, so that

$$K_{FC} = x_{M_i^{\times}} x_{V_M^{\times}} \quad [5]$$

Although incorrect, the application of mass action law to eqn [3] leads to eqn [5] by assuming that defective and regular structure elements form a dilute ideal solid solution, the activity of regular structure elements (solvent) is then equal to 1 while the activity of defective structure elements (solutes) is equal to their mole fraction.

Both cationic and anionic sublattices are involved in the formation equilibrium of Schottky disorders. The following formation equilibrium expresses that ν independent anionic structure elements and one cationic structure element combine to form a new MX_ν unit and equivalent number of vacancies

$$M_M^{\times} + \nu X_X^{\times} = V_M^{\times} + \nu V_X^{\times} + MX_\nu \quad [6]$$

or, in the form of subtractive building elements

$$0 = (V_M^{\times} - M_M^{\times}) + \nu(V_X^{\times} - X_X^{\times}) + MX_\nu \quad [6']$$

But, eqn [6] can be simplified by considering that there is no formal difference between the MX_ν unit and the additive building element $M_M^{\times} + \nu X_X^{\times}$, which leads to the following equilibrium reaction for the formation of Schottky disorders:

$$0 = V_M^{\times} + \nu V_X^{\times} \quad [7]$$

A similar equilibrium, usually named anti-Schottky disorder, involves only interstitial defects. Under the same restrictive conditions as for Frenkel disorders, the mass action law applied to eqn [6′] or to eqn [7] leads to

$$K_{SV} = x_{V_M^{\times}} \cdot (x_{V_X^{\times}})^{\nu} \quad [8]$$

K_{SV} is the equilibrium constant for Schottky disorders involving vacancies (K_{Si} would be used for anti-Schottky disorders).

Therefore, for the sake of simplicity, but keeping in mind that such a procedure is not thermodynamically correct, the law of mass action will be applied to equilibrium reactions, written by using the Kröger–Vink notation with the restriction that the defect mole fractions remain sufficiently small to allow the assumption of ideal behavior.

1.06.3.3 Electronic Defects and Ionized Point Defects

In semiconductors and ionic compounds, the energy levels of the outer electrons form two energy bands: the valence and conduction bands separated by a forbidden band or gap. At 0 K, the valence band contains all the outer electrons while the conduction band is empty. Similar to the formation of a Frenkel defect, as the temperature increases, the energy of electrons increases up to a limit to permit the jump of electrons from the valence band to the conduction band. Such a jump creates a free or excess electron occupying a regular empty level of the conduction band and a vacant electronic level, or electron hole, in the valence band. Free electrons and electron holes are mobile electronic defects of, respectively, negative and positive effective charges. Thus, according to Kröger–Vink notation, free electrons are noted as e' and electron holes – also called positive holes – are noted as $h^{\cdot}$. The equilibrium of electronic defects is then:

$$0 = e' + h^{\cdot} \quad [9]$$

The equilibrium constant K_e is:

$$K_e = np = \exp\left(-\frac{E_g}{RT}\right)$$

where n and p are, respectively, the molar fraction of electronic defects e' and $h^{\cdot}$, and E_g the energy gap.

Point defects and electronic defects can interact to form ionized point defects. Compared with perfect crystal, point defects are in an excited state of higher energy: their outer electrons occupy energy levels localized in the forbidden bands. There are two kinds of such levels: the donor levels close to the conduction band and the acceptor ones close to the valence band; the donor levels easily release electrons to the conduction band while acceptor levels easily accept electrons from the valence band.

For example, a neutral cationic interstitial $M_i^{\times}$ induce a local excess of electrons and then acts as a donor. For a monovalent metal, the ionization equilibrium is

$$M_i^{\times} = M_i^{\bullet} + e' \qquad [10]$$

For a divalent metal, there are two ionization equilibriums, one similar to eqn [10] and the other

$$M_i^{\bullet} = M_i^{\bullet\bullet} + e' \qquad [10']$$

On the contrary, a neutral cation vacancy induces a local electron deficit and acts as an acceptor

$$V_M^{\times} = V_M^{/} + h^{\cdot} \qquad [11]$$

Similarly, a neutral anion vacancy acts as a donor and a neutral anionic interstitial as an acceptor

$$V_X^{\times} = V_X^{\bullet} + e' \qquad [12]$$
$$X_i^{\times} = X_i^{/} + h^{\cdot} \qquad [13]$$

Other ionization equilibriums are possible depending on the oxidation state of the metallic and/or oxidant constituents of MX_v. The mass action law is applicable to all these ionization equilibriums, which permits, in combination with the equilibrium of electronic defects and the condition of electrical neutrality, to determine the equilibrium molar fractions of ionized and electronic defects.

1.06.3.4 Point Defect Equilibriums in Nonstoichiometric Oxides

For any oxide MO_v, departure from ideal stoichiometry results in an O/M ratio not equal to v. This ratio is greater than v for metal deficit ($M_{1-\delta}O_v$) or oxygen excess ($MO_{v+\delta}$) and smaller than v for metal excess ($M_{1+\delta}O_v$) or oxygen deficit ($MO_{v-\delta}$). The departure from stoichiometry δ, and thus the equilibrium molar fractions of ionic point defects and electronic defects, depends on temperature and oxygen or metal activity. But, δ is usually expressed as a function of T and oxygen partial pressure P_{O_2}.

A specific type of point defect is commonly predominant in nonstoichiometric oxides such as nickel oxide $Ni_{1-\delta}O$ or zirconia $ZrO_{2-\delta}$. Equations [10]–[13] show that the ionization of point defects results in the formation of electronic defects; therefore, the predominance of one specific ionized point defect induces the predominance of one specific type of electronic defect. Thus, as the mobility of electronic defects is much higher than that of ionic defects or species, most of nonstoichiometric oxides behave like semiconductors. Nonstoichiometric oxides are p-type semiconductors if the dominant electronic defects are positive holes and inversely n-type semiconductors if free electrons are dominant.

1.06.3.4.1 p-Type oxides

Common p-type oxides present a metal deficit or an oxygen excess. Nickel oxide $Ni_{1-\delta}O$ is a typical example of a metal-deficient oxide. Over a large range of oxygen partial pressure, numerous experimental evidences have revealed that doubly charged Ni cation vacancies V''_{Ni} are the predominant point defects in nonstoichiometric $Ni_{1-\delta}O$. The formation of these vacancies can be represented by the following equilibrium:

$$\frac{1}{2}O_2(g) = O_O^{\times} + V''_{Ni} + 2h^{\cdot} \qquad [14]$$

The dependence of molar fraction, ($x_{V''_{Ni}} = \delta$), of V''_{Ni} and $h^{\cdot}$ on P_{O_2} is obtained from the mass action law applied to this formation equilibrium

$$K_{VC2} = \frac{x_{V''_{Ni}} \cdot p^2}{P_{O_2}^{1/2}} \qquad [15]$$

where K_{VC2} is the equilibrium constant. The condition of electrical neutrality implies

$$2x_{V''_{Ni}} = p$$

These two relations give

$$x_{V''_{Ni}} = \left(\frac{K_{VC2}}{2^2}\right)^{1/3} P_{O_2}^{1/6}$$

This result can be extended to cation vacancies of any charge $q \leq 2v$ that can appear in nonstoichiometric $M_{1-\delta}O_v$ oxides:

$$x_{V_M^{q/}} = \left(\frac{K_{VC_q}}{q^q}\right)^{1/(q+1)} P_{O_2}^{v/2(q+1)} \qquad [16]$$

and

$$p = q x_{V_M^{q/}}$$

The charge of predominant defects may vary with P_{O_2} depending on the free energy of formation of these defects or, which is equivalent, the equilibrium constants associated to their ionization equilibrium. For example, the cation vacancies of p-oxide $M_{1-\delta}O$ may be neutral, singly charged, or doubly charged, so that $\delta = x_{V_M^X} + x_{V'_M} + x_{V''_M}$. The molar fractions can be calculated from the three simultaneous equilibriums

$$\frac{1}{2}O_2(g) = O_O^X + V_M^{\times}$$
$$V_M^{\times} = V'_M + h^{\cdot}$$
$$V'_M = V''_M + h^{\cdot}$$

and the condition of electrical neutrality

$$p = x_{V'_M} + 2x_{V''_M}$$

This last equation determines the two domains where one charged defect dominates

$$x_{V'_M} \ll 2x_{V''_M} \Rightarrow x_{V''_M} = p/2$$
$$x_{V''_M} \ll x_{V'_M} \Rightarrow x_{V'_M} = p$$

This procedure, known as Brouwer's approximation, can be applied to any combination of ionized points defects; it simplifies greatly the calculation of defect equilibriums and their representation.

Oxides with oxygen excess caused by interstitial anions are also p-type semiconductors. However, because of the large size of oxygen anions compared to metal cations, such p-type oxides are rather uncommon in usual high temperature materials.

1.06.3.4.2 n-Type oxides

Zirconium oxide $ZrO_{2-\delta}$ and zinc oxide $Zn_{1+\delta}O$ are typical of n-type oxides. For $ZrO_{2-\delta}$, the formation of doubly charged oxygen vacancies is expressed by the equilibrium

$$O_O^{\times} = V_O^{\bullet\bullet} + 2e' + \frac{1}{2}O_2(g) \qquad [17]$$

The dependence of molar fraction of $V_O^{\bullet\bullet}$ and e' on P_{O_2} is obtained from the law of mass action

$$K_{V2a} = n x_{V_O^{\bullet\bullet}} P_{O_2}^{1/2}$$

and the condition of electrical neutrality

$$n = 2V_O^{\bullet\bullet}$$

These two relations give

$$x_{V_O^{\bullet\bullet}} = \left(\frac{K_{VA2}}{2^2}\right)^{1/3} P_{O_2}^{-1/6}$$

where K_{VA2} is the equilibrium constant.

Again, this result can be extended to oxygen vacancies of charge q $(0 \leq q \leq 2)$

$$x_{V_O^{q\bullet}} = \left(\frac{K_{VAq}}{q^q}\right)^{1/(q+1)} P_{O_2}^{-1/2(q+1)} \qquad [18]$$

Oxides like $Zn_{1+\delta}O$ with charged interstitial cations are also n-type semiconductors. The formation equilibrium of doubly charged interstitials $Zn_i^{\bullet\bullet}$ is

$$Zn_{Zn}^{\times} + O_O^{\times} + V_i = Zn_i^{\bullet\bullet} + 2e' + \frac{1}{2}O_2(g) \qquad [19]$$

where V_i is a vacant site of the interstitial cation sublattice. Comparison of eqns [17] and [19] permits to easily understand that the mole fraction of charged interstitial cations is expressed by a relation similar to eqn [18], with an equilibrium constant K_{iCn}. Equations [16] and [18] show that the mole fractions of ionic and electronic defects increase in p-type oxides and decrease in n-type oxides, at increasing P_{O_2}.

1.06.3.5 Intrinsic Defect Equilibriums Close to Stoichiometry

The nature of the dominant defect may vary depending on P_{O_2}. Some amphoteric p-type oxides can present a metal excess at low P_{O_2} and a metal deficit at higher P_{O_2}. Reverse situation may be encountered for n-type oxides with an oxygen deficit at low P_{O_2} and an oxygen excess at higher P_{O_2}.

Considering the case of an oxide MO with predominant fully ionized cationic defects, the defect equilibriums to be considered are:

- formation of doubly charged cation vacancies (equilibrium constant K_{VC2})

$$\frac{1}{2}O_2(g) = O_O^{\times} + V''_M + 2h^{\cdot}$$

- formation of doubly charged interstitial cations (equilibrium constant K_{iC2})

$$M_M^{\times} + O_O^{\times} + V_i = M_i^{\bullet\bullet} + 2e' + \frac{1}{2}O_2(g)$$

and the electronic equilibrium (eqn [9]) as both e' and $h^{\cdot}$ are involved in ionic defect equilibriums. The combination of these three equilibriums gives the equilibrium formation of a cationic Frenkel disorder (equilibrium constant K_{FC})

$$M_M^{\times} + V_i = M_i^{\bullet\bullet} + V''_M \qquad [20]$$

The condition of electrical neutrality is

$$2x_{M_i^{\bullet\bullet}} + h^{\cdot} = 2x_{V''_M + e'} \qquad [21]$$

At the stoichiometric composition, molar fractions p and n of electronic defects are equal, $p = n = K_e^{1/2}$, and similarly the molar fractions of ionic defects, $x_{M_i^{\bullet\bullet}} = x_{V''_M} = K_{FC}^{1/2}$, which from eqns [16] and [18] corresponds to $(P_{O_2})_{stoi} = K_{iC2}/K_{VC2}$. In the vicinity of their stoichiometric composition, such oxides could have different behavior and properties depending on the relative magnitude of the equilibrium constants K_e and K_{FC}. Two different situations are possible:

1. $K_e \gg K_{FC}$; in that case, $x_{M_i^{\bullet\bullet}} \ll h^{\cdot}$ and $x_{V''_M} \ll e'$ and therefore the equality $p = n = K_e^{1/2}$ hold on a more or less large range of P_{O_2} while $x_{V''_M}$ and $x_{M_i^{\bullet\bullet}}$ remain small but vary as a function of P_{O_2},

2. $K_e \ll K_{FC}$, which implies $x_{M_i}^{\bullet\bullet} \gg h^{\cdot}$ and $x_{V''_M} \gg e'$; then, the equality $x_{M_i}^{\bullet\bullet} = x_{V''_M} = K_{FC}^{1/2}$ is verified while p and n vary with P_{O_2}.

In case (1), the electronic defects predominate; such oxides are intrinsic electronic oxides; their electrical conductivity is purely electronic and independent of P_{O_2}. For the opposite case (2), the ionic defects are predominant; these oxides are intrinsic ionic oxides. Their electrical conductivity can present a significant ionic component but the electronic component is usually not negligible because of the higher mobility of electronic defects.

Out of the vicinity of stoichiometric composition, all the ionic and electronic defects coexist but their molar fraction strongly depends on P_{O_2}. From eqns [19] and [16], cation vacancies and electron holes, of molar fractions $h^{\cdot} = 2x_{V''_M}$, are predominant at P_{O_2} significantly higher than $(P_{O_2})_{stoi}$. Similarly, from eqns [20] and [18], interstitial cations and free electrons, of molar fractions $2x_{M_i}^{\bullet\bullet} = e'$, are predominant at P_{O_2} lower than $(P_{O_2})_{stoi}$.

1.06.3.6 Effect of Impurities on Defect Equilibriums

The above simplified treatment of ionic and electronic defects in oxide only considers perfectly pure oxides, which is a rather uncommon case, particularly for oxide scale grown on a metallic alloy. Indeed, the molar fractions of ionic and electronic defects are strongly affected by the presence of small amounts of impurities of different oxidation state. In some instances, the effect of impurities may be so large that it can induce an inversion of the type of predominant defects.

The influence of a trivalent impurity, like chromium, on the molar fraction of ionic defects in a nonstoichiometric p-type oxide such as nickel oxide $Ni_{1-\delta}O$ is a typical and well-known example. Chromium cations Cr^{3+} are in substitution in the cationic sublattice and constitutes a new structure element $Cr_{Ni}^{\bullet}$. The condition of electrical neutrality is then

$$x_{Cr_{Ni}^{\bullet}} + p = 2x_{V''_{Ni}} \qquad [22]$$

For $Ni_{1-\delta}O$, the departure to stoichiometry δ, and thus the mole fraction of electron holes, is lower than 10^{-3} at temperatures lower than 1300 °C. Therefore, a molar fraction of Cr higher than 10^{-2} is sufficient to induce a significant increase of vacancy and electron hole molar fractions. Indeed, for a mole fraction $x_{Cr_{Ni}^{\bullet}} \gg p$, eqns [16] and [22] leads to

$$x_{V_{Ni}^{\bullet}} = \frac{x_{Cr_{Ni}^{\bullet}}}{2} \text{ and } p = \left(\frac{2K_{VC2}}{x_{Cr_{Ni}^{\bullet}}}\right)^{1/2} P_{O_2}^{1/4}$$

Depending on $x_{Cr_{Ni}^{\bullet}}$ and P_{O_2}, the molar fraction p can reach very small values so that the intrinsic electronic equilibrium should be taken into account. Free electrons may become predominant, resulting in an inversion from p-type to n-type oxide. A similar analysis can be performed for the influence of monovalent impurities such as Li or Na. A sufficiently large amount of such impurities may induce an inversion of the type of major ionic defect from cation vacancies to interstitial cations.

This analysis can also be extended to nonstoichiometric n-type oxides. A typical example is given by zirconia $ZrO_{2-\delta}$. Its tetragonal and cubic crystal structures can be stabilized (SZ) or partially stabilized (PSZ) by the addition of CaO or Y_2O_3. A large increase in anion vacancies and an inversion from n-type to p-type are induced by these additions; ionic defects are predominant, and SZ and PSZ are extrinsic ionic oxides.

For all the possible situations, the effect of impurities can be summarized as follows:

a. For p-type oxides, the addition of cations of higher oxidation degree induces a decrease of positive holes and an increase of cation vacancies for oxides $M_{1-\delta}O_v$, or of oxygen interstitials for $MO_{v+\delta}$; cations of lower oxidation degree have the reverse effect.
b. For n-type oxides $M_{1+\delta}O$, the addition of cations of higher oxidation degree induces an increase in free electrons and a decrease in anion vacancies for $MO_{v-\delta}$ oxides or cation interstitials for $M_{1+\delta}O$ oxides, cations of lower oxidation degree has the reverse effect.

1.06.3.7 Extended Defects

At sufficiently high molar fractions, the interactions between point defects may lead to the formation of more complex defects. The most common example is wüstite, $Fe_{1-\delta}O$, where cation vacancies form ordered defect clusters. However, the formation of these defect clusters is directly linked to the large departure δ (up to 0.15) of $Fe_{1-\delta}O$ from stoichiometry. Such defect clusters are not observed in oxides, such as CoO and NiO, of smaller stoichiometry departure; for CoO, δ remains smaller than 10^{-2} up to about 1400 °C and is 10–100 smaller for NiO.

Other complex defect structures are known to be present in oxides like TiO_2 and derived suboxides

Ti_nO_{2n-1}, and also in many other oxides of transition metals. However, up to now, these complex defects and/or oxide structures have not been observed in oxide scales grown from high temperature oxidation of metallic materials.

1.06.4 Diffusion Laws and Mass Transport in Solid State

The growth of a single oxide scale or a complex corrosion scale both require the diffusion of molecular and/or ionic chemical species through the growing scale and/or the diffusion within the oxidized or corroded substrate of their chemical components toward the scale–substrate interface as usually required for the selective oxidation of the less-noble substrate component or deeper into the substrate for the more noble components. Diffusion is commonly driven by the concentration gradients of diffusing species, as expressed by diffusion laws. However, transport phenomena induced by internal or external forces can interact with concentration gradients to accelerate or slow down the motion of mobile chemical species. Useful definitions of terms specific to diffusion and matter transport in solid state are given in Kizikyalli *et al.*[16]

1.06.4.1 Diffusion Laws

Matter movement by diffusion and/or transport in a phase is quantified by the flux of moving species, that is, a number of species per time unit and per unit area normal to the movement direction. Referring this movement relatively to a defined reference frame, the total flux $\mathcal{J}_k$ of any species k along a direction x is given by

$$\mathcal{J}_k = -D_k \frac{\partial C_k}{\partial x} + \bar{v} C_k \qquad [23]$$

Fluxes and concentrations are functions of time t and abscissa x. Equation [23] is a general form of the well-known Fick's first law evidencing the two components of total flux $\mathcal{J}_k$ (in mol m^2 s^{-1}):

1. the diffusion component is expressed by the term $-D_k(\partial C_k/\partial x)$, where D_k (in $m^2\,s^{-1}$) is the diffusion coefficient of species k and C_k (in mol m^{-3}) its local concentration;
2. the transport component, induced by internal or external forces, corresponds to the term $\bar{v}C_k$ where $\bar{v}$ is the average displacement rate of all species moving relative to the reference frame.

The relative influence of these two terms is illustrated in **Figure 13** that corresponds, for example, to the broadening of a drop of colored solute in a slowly flowing fluid. The concentration profile of the colored solute at time $t_2 > t_1$ is the sum of the two contributions of eqn [23]: broadening of the concentration profile due to the diffusion under the only influence of concentration gradient and displacement x_t of this concentration profile with the fluid flow under a force such as, for example, the gravitation force.

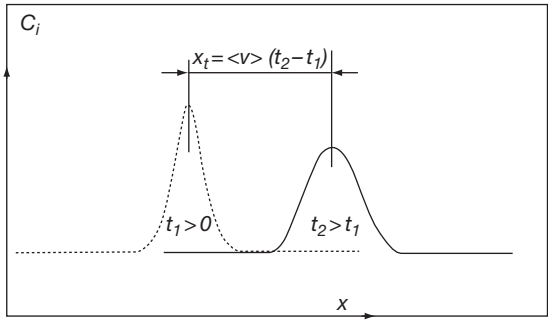

Figure 13 Diffusive and displacement components of flux relative to the fixed frame (x,C).

The displacement rate $\bar{v}$ depends on the force f acting on the moving species as expressed by the Nernst–Einstein relation

$$\bar{v} = D\frac{f}{RT} \qquad [24]$$

However, in many practical situations, there is no external or internal force acting on the moving species. Equation [23] reduces to the common form of Fick's first law

$$\mathcal{J}_k = -D_k \frac{\partial C_k}{\partial x} \qquad [25a]$$

Equations [23] and [25a] are only useful in conditions such that $\partial C_k/\partial x$ remains constant (stationary state) or can be easily assessed as in the growth of an oxide scale on a metal when both metal–scale and scale–gas interfaces are assumed to remain in equilibrium (pseudo stationary state) as the oxidation proceeds.

For all other situations, the resolution of diffusion problems required to solve the Fick's second law, the general diffusion equation expressing the conservation of matter:

$$\frac{\partial C_k}{\partial t} = -\frac{\partial \mathcal{J}_k}{\partial x} \qquad [25b]$$

For a pure diffusion process and constant diffusion coefficient D_k, this equation transforms into

$$\frac{\partial C_k}{\partial t} = D_k \frac{\partial^2 C_k}{\partial x^2} \qquad [26]$$

In eqns [23]–[26], the use of molar concentration in the expression of the local composition is essentially a practical choice. A more formal, and physically more correct, expression links the diffusion coefficient D_k to the chemical potential of species k. Indeed, Fick's laws apply only to systems assumed in local equilibrium, that is, such that the thermodynamic properties of all system constituents are determined from all the state variables required for a complete description of the system equilibrium states, independent of the local gradient of these state variables.

Equation [26] can be solved analytically. The solution depends on the initial and limit conditions; many textbooks describe the most common solutions.[17–20] For the general case of concentration-dependent diffusion coefficients, the solving of the general diffusion equation [25b] required the use of numerical methods that are now implanted in many types of mathematical software.

1.06.4.2 Lattice Diffusion and Diffusion Mechanisms

In many cases of diffusion in a crystal phase, one constituent forms an immobile sublattice that determines a fixed frame of reference where eqns [25] and [26] can be applied to diffusing species. For a given crystal phase, site-to-site jumps of diffusing species are the most common elementary steps of diffusion processes, but such jumps must preserve the major characteristics of the crystal structure of the phase. Therefore, the diffusion of atoms, molecules, or ions within a crystal phase is only possible in the presence of crystal defects. The simplest situation is the diffusion of small interstitial impurities within a fixed host lattice. Interstitial species then jump from one interstitial site to one of the closest adjacent interstitial sites. A common example of simple interstitial diffusion is the diffusion of interstitial oxygen atoms dissolved in α-Ti or α-Zr during their oxidation at high temperature. The host lattice can be also assumed immobile for the diffusion of highly diluted substitutional impurities. One impurity atom, ion, or molecule occupying a lattice site having one vacancy for nearest neighbor can jump to exchange its position with this vacancy. Such a vacancy exchange results in the motion of vacancies in a direction opposite to the diffusion of substitutional impurities. The dilute substitutional impurities can be replaced by some specific marked species of one constituent of the host lattice. For example, radioisotope ^{63}Ni can be introduced in pure nickel or nickel compounds such as NiO. These marked species can also exchange their position with adjacent vacancies of Ni lattice or cation sublattice of NiO, thus leading to random displacements and dispersion of marked species under the only influence of thermal activation. Such a diffusion process is named self-diffusion. Therefore, for a system remaining in local equilibrium, the self-diffusion coefficient D_{sd} can be expressed as the product of vacancy molar fraction x_v and vacancy diffusivity D_v

$$D_{sd} = x_v D_v \qquad [27]$$

However, vacancy diffusivity D_v is not formally equivalent to a diffusion coefficient because vacancies are nonconservative species of concentration remaining constant and equal to its equilibrium value everywhere as imposed by the assumption of local equilibrium. Equation [27] remains valid for the self-diffusion in a given sublattice as, for example, the self-diffusion of cation in the cationic sublattice of a ionic compound. However, for the diffusion of marked species or dilute impurities, the analysis is more complex than reflected by eqn [27]. Indeed, the environment of marked or impurity species changes after their jump so that all jump directions are not equivalent for such species, which leads to the introduction of a correlation factor taking into account this effect that is neglected in eqn [27].

The interstitial and vacancy exchange mechanisms are the two basic mechanisms of lattice or bulk diffusion. They are valid for many kinds of materials; however, other elementary mechanisms involving more complex defects or jump sequences may be encountered in specific situations such as, for example, diffusion in intermetallic compounds, or diffusion under high energetic fluxes as occurring in materials used in nuclear power plants. Such complex diffusion processes are out of the scope of this chapter.

Both interstitial and substitutional diffusion mechanisms involve atomic jumps requiring the overcoming of an energy barrier. Diffusion is thus a thermally activated process and the temperature dependence of diffusion coefficient is then expressed by the well-known Arrhenius relation

$$D = D_0 \exp\left(-\frac{Q_D}{RT}\right) \qquad [28]$$

where Q_D is the activation energy for the diffusion of a given species. The order of magnitude of diffusion coefficients for solids varies in the range 10^{-23} to 10^{-8} $m^2 s^{-1}$ depending on T. In metals, the diffusion of interstitial species, such as C, O, or N, is faster than

the diffusion of substitutional species. Diffusion in covalent or ionic solids is of several orders of magnitude slower than the diffusion in metallic materials.

Diffusion coefficients are important and useful properties of materials, particularly at high temperature. For self-diffusion in pure metals and some classes of materials, empirical correlations permit a rough estimate of the activation energy and the diffusion coefficient at melting point as a function of crystal structure and chemical bond.[21]

The knowledge of diffusion coefficients allows the calculation of the nominal diffusion length, $\bar{l}_D = (Dt)^{1/2}$, which provides an estimation of the size of the domain affected by the considered diffusion process. Solids or diffusion couples of size much greater than $\bar{l}_D$ along the diffusion direction are usually qualified as infinite solids for diffusion along two opposite directions, or semi-infinite solids for diffusion along only one direction.

1.06.4.3 Interdiffusion, Intrinsic Diffusion, and Kirkendall Effect in Binary Solid Solutions

In an inhomogeneous, disordered, substitutional binary solid solution, both constituents i (i = A or B) are usually able to diffuse, via the vacancy exchange mechanism, within the unique crystal lattice of such a solid solution. This diffusion process is called interdiffusion. The well-known experiments of Smigelkas and Kirkendall for the diffusion in α-brass have demonstrated that Zn and Cu diffuse simultaneously at different rates and that the faster diffusivity of Zn must be compensated by a displacement of the host lattice evidenced by the displacement of inert markers within the diffusion zone. This phenomenon, named Kirkendall effect, is schematized in **Figure 14** for two constituents A and B of constant partial molar volumes. In **Figure 14(a)**, the initial position of the contact surface is marked by fixed inert markers. As the partial molar volume of both constituents is assumed constant, the total volume of the diffusion couple remains constant; then, the fixed markers determine also the origin of the frame of reference centered on the number of moles or number-fixed frame denoted N-frame, also defined as the Matano plane M. Under this assumption of constant couple volume, this frame is immobile and its origin can also be taken at one extremity of the diffusion couple, which justify the denomination of laboratory-fixed frame of reference sometimes used for the N-frame. Moving inert markers determine the actual position

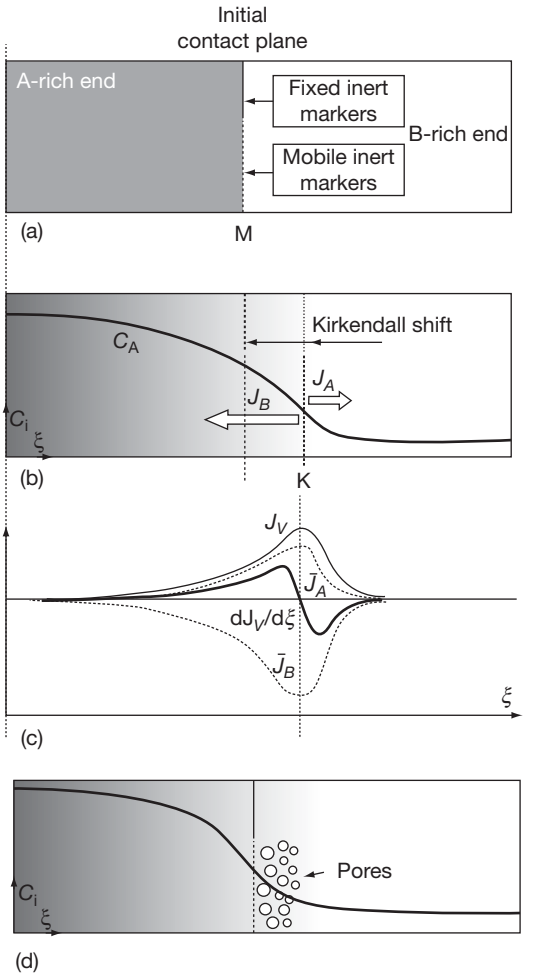

Figure 14 Kirkendall effect in a homogeneous binary A–B diffusion couple: (a) initial diffusion couple before diffusion annealing, (b) concentration profile and markers position after diffusion annealing, (c) variation of diffusion fluxes and vacancy source/sink density ($dJ_v/d\xi$), and (d) pore formation in the absence of vacancy sink.

of the initial contact surface after diffusion annealing (**Figure 14(b)**) and, therefore, visualize the drift of lattice planes within the diffusion zone; they mark the origin K, also named Kirkendall plane, of the lattice-fixed frame of reference, denoted K-frame. N- and K-frames are the more commonly considered frames of reference. The form of Fick's first law and the meaning of the corresponding diffusion coefficient depend on the chosen reference frame; a detailed analysis can be found in diffusion textbooks.[17,19]

When using N-frame, only one diffusion coefficient, denoted $\tilde{D}$ and named interdiffusion coefficient, is needed for the analysis of concentration profiles of both constituents and the calculation of interdiffusion fluxes $\tilde{J}_i$ from Fick's first law; $\tilde{D}$ is

a function of composition. Thus, the interdiffusion flux of constituents i (i = A or B), $\widetilde{\mathcal{J}}_i$ must be expressed by

$$\widetilde{\mathcal{J}}_i = \bar{\mathcal{J}}_i + v_K C_i \qquad [29]$$

- $\bar{\mathcal{J}}_i$ is the diffusion flux of i relative to the moving lattice (K-frame), it is thus named intrinsic diffusion flux; Fick's first law leads to $\bar{\mathcal{J}}_i = -\bar{D}_i(\partial C_i/\partial x)$, where $\bar{D}_i$ is the intrinsic diffusion coefficient of species i; and
- $v_K C_i$ is the transport term, v_K is the displacement rate of the moving lattice relative to the N-frame.

The conservation of matter in the N-frame implies that $\widetilde{\mathcal{J}}_A + \widetilde{\mathcal{J}}_B = 0$. This relation combined with relation [28], applied to A and B constituents, lead to the Darken equations

$$v_K = (\bar{D}_A - \bar{D}_B)\frac{\partial x_A}{\partial x} \qquad [30a]$$

$$\widetilde{D} = x_B \bar{D}_A + x_A \bar{D}_B \qquad [30b]$$

where x_A is the molar fraction of A.

The intrinsic diffusion coefficient $\bar{D}_i$ is equivalent to the self-diffusion coefficient D_i of i in the crystal lattice of the considered solid solution. The Kirkendall effect is one consequence of the difference in intrinsic diffusivities of chemical constituents of substitutional solid solutions (nonreciprocal diffusion). The relative displacement of N- and K-frames is caused by the internal chemical forces resulting from the interactions between the constituents of nonideal solid solutions, which lead to the following relation between $\bar{D}_i$ and D_i

$$\bar{D}_i = D_i\left(1 + \frac{\partial \ln \gamma_i}{\partial x_i}\right) \qquad [31]$$

where γ_i and x_i are the activity coefficient and molar fraction of constituent i. Therefore, when the two constituents form an ideal solid solution, there is no relative displacement of N- and K-frames, that is, no Kirkendall effect.

This classical treatment of Kirkendall effect in binary homogeneous systems assumes that the difference between the intrinsic diffusion fluxes of the two substitutional constituents is compensated by the action of local vacancy sinks and sources that maintain the system in local equilibrium. This local action is formally equivalent to an intrinsic vacancy flux $\bar{\mathcal{J}}_v$ permitting the conservation of lattice sites, which is expressed by the relation

$$\bar{\mathcal{J}}_A + \bar{\mathcal{J}}_B + \bar{\mathcal{J}}_v = 0$$

But local equilibrium implies that the vacancy concentration remains equal to its equilibrium value within all the diffusion couple. To achieve this requirement, the density of vacancy sources or sinks must be greater or equal to the divergence of the equivalent vacancy flux (**Figure 14(c)**). This action of vacancy sources and sinks result in the lattice drift characteristic of the Kirkendall effect in stress-free homogeneous diffusion couples. For species such as chemical elements, a Fickian diffusion flux is always the consequence of a gradient of chemical potential or concentration but such a gradient is not required for the apparent migration of vacancies that are annihilated at sinks and created elsewhere at sources and *vice versa*.

On the side of the faster diffusing species, when the density of vacancy sinks is not sufficient, the difference in the diffusion fluxes of substitutional chemical species would induce local vacancy supersaturation and associated build-up of local stress states within the diffusion zone. Return to local equilibrium in a stress-free state would be achieved by the nucleation of pores leading to the well-known Kirkendall porosity (**Figure 14(d)**). All the intermediate situations between complete or null Kirkendall shift are possible depending on local stress states and density, distribution and efficiency of vacancy sinks. Therefore, local stress states, composition-dependent volume changes, geometry, and size of the diffusion zone are among the parameters and phenomena that can interfere with nonreciprocal diffusion and must be considered in a detailed analysis and understanding of the behavior of systems when such a diffusion process occurs. Furthermore, when the partial molar volume of solution constituents are not constant and varies as a function of local composition, the total volume of the diffusion couple varies continuously as the diffusion proceeds. In addition to the increased difficulty in the analysis of diffusion profiles and fluxes, such a volume variation is also a source of local stresses that can interfere with diffusion processes and system behavior.

1.06.4.4 Diffusion in Multiphase Systems

Diffusion in multiphase systems is often only focused on the growth kinetics of intermediate phases.[22] But, the Kirkendall effect is not restricted to diffusion couples constituted of one single phase; it may also occur in diffusion couples associating several phases.

For a two-phase diffusion couple constituted of two adjacent α and β phases of an A–B binary system,

the initial contact plane can be evidenced, as for a homogenous couple, by the position of a fixed inert marker. This situation is more complex for mobile inert markers that are linked to the displacement of lattice planes. In a two-phase diffusion couple, the shift of lattice planes induced by nonreciprocal diffusion is different within the two contacting phases. Therefore, the displacement of lattice planes in both phases cannot be referred to only one frame of reference, which implies that each phase requires one specific lattice-fixed frame of reference.[23]

The difference in intrinsic diffusivity within both α and β phases requires, as for a homogeneous diffusion couple, the action of vacancy sink/source distributed within these two phases. But, the differences in the required vacancy sources and sinks in each phase implies that the same α/β interface must be able to either create or annihilate vacancies depending upon the intrinsic diffusion coefficients and the initial composition of contacting α and β phases.[23] Vacancy creation or annihilation must be considered as an inherent interfacial activity in any diffusion-driven phase transformation involving substitutional solid solutions or ordered compounds with diffusion via vacancies. Interfacial defects such as misfit and misorientation dislocations would provide the vacancy sources or sinks required by such an interface action.[10,11]

But, for a phase transformation totally or partially driven by solid-state diffusion, the role of the interface is not limited to the creation or annihilation of vacancies involved in the diffusion process, the interface has several other roles to play. For one phase growing at the expense of one other phase, the interface needs to satisfy several interrelated requirements to accommodate:

- the change in chemical composition and eventually in chemical bonding,
- the mismatch in crystal structure and molar volume, and
- the difference in phase growth or recession rate and interface displacement rate by annihilating or creating the point defects involved in the diffusion processes.

If one of these requirements is not realized, the interface and the reacting phases would not be in a state of local equilibrium. Additional constraints must then be considered and, therefore, additional state variables must be introduced to describe and quantify the properties of contacting phases and the system evolution. These constraints can be local stresses or constraints related to interface reactions, diffusion fluxes and interface movement.

1.06.4.5 Interdiffusion in Ternary Systems

Interdiffusion in ternary, and higher systems, is more complex than in binary systems. Fick's laws remain valid for the diffusion in such systems. But, for a nonideal solid solution, the flux and gradient of each component are coupled with the fluxes and gradients of all other components. Therefore, the diffusion in ternary systems cannot be treated as a simple extension of binary diffusion. The interactions between the constituents of a nonideal solid solution imply that the diffusion flux of a given constituent cannot be expressed from only one diffusion coefficient.[18,19] A (2×2) diffusion matrix must replace the single diffusion coefficient of binary systems. Furthermore, the terms of this diffusion matrix depends on the choice of one of the constituents as solvent, but the concentration profiles of each constituent are obviously independent of this choice. The interactions between the diffusing species are expressed by the off-diagonal elements of the diffusion matrix and are the cause of the complex shape of concentration profiles and diffusion paths that are commonly observed in ternary diffusion experiments.

One additional complication in ternary diffusion arises from the extra degree of freedom of ternary systems compared to binary systems. This extra degree of freedom permits the occurrence of two-phase fields in diffusion couples which also results in large variation in the morphology and microstructure of diffusion zones. Therefore, for multiphase diffusion in ternary systems, the correlation between the phase diagram, the diffusion path, the morphology and microstructure of a diffusion zone are much more complicated than for multiphase binary diffusion.[22]

Equation [28] remains valid for diffusion in a ternary, disordered, substitutional solid solution.[19] Like for binary diffusion, the difference in intrinsic diffusivities of the constituents of a ternary solid solution requires the action of vacancy sources or sinks for maintaining the systems in local equilibrium, which means that the Kirkendall effect also occurs in ternary diffusion. For diffusion in multiphase ternary systems, interfaces would have to likely act as vacancy sources or sinks, but the situation, particularly the microstructure of diffusion zone, is more complex than for binary systems and would require a specific and detailed analysis that still need to be carried out.

1.06.4.6 Short-Circuit Diffusion

For most common materials, self-diffusion and diffusion of solute elements cannot be limited to diffusion in bulk crystals for which point defects are the only defects involved in diffusion processes. Internal defects like dislocations, grain boundaries or triple junctions and interfaces are always present in common materials and are characterized by a disturbed and more open structure along which diffusion is easier. Thus, these internal defects are preferred diffusion paths leading to short-circuit diffusion. Local strains and stresses associated with these defects can be partially minimized or relaxed by the positive (attractive) or negative (repulsive) segregation of diffusing solutes. Segregation of diffusing species often interferes with diffusion processes and must not be neglected. This influence is well documented in the case of grain-boundary diffusion.[24] Diffusion along free surfaces is not considered here because surface diffusion processes and mechanisms are rather different compared to internal diffusion. The influence of short circuits on the diffusion flux of a given solute is schematized in Figure 15 for a slab of material such that the common operating short circuits, that is, dislocations, grain boundaries, and triple junctions, denoted by their respective index d, gb, and tj, are parallel to the diffusion direction. Each short circuit is then characterized by diffusion coefficients D_d, D_{gb}, and D_{tj} higher than D_b, the solute diffusion coefficient in the bulk phase.

Assuming that the boundary conditions are different but constant on each slab side and not affected by the emergence of internal defects, the total solute flux $\mathcal{J}_t$ through such a slab is the sum of the solute flux for each diffusion path

$$\mathcal{J}_t = \mathcal{J}_b + \mathcal{J}_d + \mathcal{J}_{gb} + \mathcal{J}_{tj}$$

For cross-sectional fraction areas f_b, f_d, f_{gb}, and f_{tj} of each diffusion path and constant diffusion coefficients, Fick's first law lead to the following expression of the total solute flux

$$\mathcal{J}_t = -\left(f_b D_b + f_d D_d + f_{gb} D_{gb} + f_{tj} D_{tj} \right) \frac{\Delta C}{w}$$

This relation shows that the total flux can be expressed by using an apparent diffusion coefficient D_{app} averaging the contribution of all the diffusion paths

$$D_{app} = f_b D_b + f_d D_d + f_{gb} D_{gb} + f_{tj} D_{tj} \qquad [32]$$

The dislocation density ρ_d and the average grain size d_{gb} must be known for the evaluation of fraction areas f_d, f_{gb}, and f_{tj} and of the contribution of each diffusion path. Therefore, no quantitative analysis of short-circuit diffusion can be performed without an accurate analysis of these microstructural characteristics. For the calculation of these fraction areas, a value of 0.5 nm is usually taken for the radius of dislocation cores and the thickness of grain boundaries. The relative magnitude of these diffusion coefficients is usually in the following order

$$D_b < D_d < D_{gb} < D_{tj}$$

Only bulk and grain-boundary diffusion are usually considered in the common situation encountered in oxidation of pure metals or selective oxidation of alloys.

Equation [30] is a generalization of the Hart's equation. However, for non-steady-state conditions, the use of D_{app} for the calculation of diffusion fluxes or concentration profiles from Fick's second law is only valid when the nominal diffusion length of bulk diffusion greatly exceeds the average grain size or the average dislocation spacing, which is a common situation for the diffusion in a growing oxide scale and/or its substrate. Triple junctions are very efficient short circuits but their influence is only noticeable for grain size smaller than about 100 nm[25]; therefore, one can wonder if this contribution can be neglected for fine-grained oxide scales often formed at low or intermediate temperatures.

The diffusion mechanisms along dislocations, grain boundaries, or triple junctions are neither completely known nor understood. These mechanisms are likely based on atomic jumps involving vacancies and/or interstitials although the meaning of point defects associated with dislocations, grain boundaries, or triple junctions need to be clarified. Furthermore, the

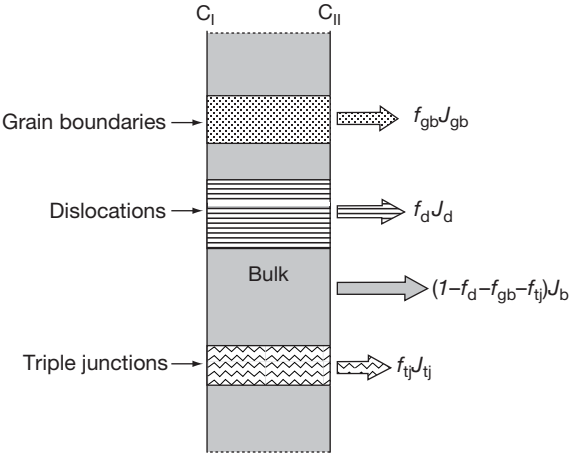

Figure 15 Schematic representation of total diffusion flux through a slab with different kinds of short circuit.

experimental determinations of solute diffusion permit only the measurement of a diffusivity parameter that includes the diffusion coefficient, the segregation factor and the thickness or cross-section area of the considered short circuit. All these factors may interfere and caution must be taken in using diffusion coefficients calculated by taking arbitrary values of segregation factors or defect width or section. The situation is even more complex for ionic compounds for which local space charges may also interfere with the diffusion processes. Experimental determinations have shown that diffusion along dislocations and grain boundaries are thermally activated and their activation energies are usually lower than that for bulk diffusion because short-circuit diffusion is easier than bulk diffusion. Therefore, as schematically illustrated in Figure 16 for grain-boundary diffusion and bulk diffusion, short-circuit diffusion is predominant at low temperatures. It is often quoted that the transition temperature for the predominance of grain-boundary diffusion is about $0.5\,T_m$ (K), where T_m is the melting temperature of bulk phase. However, it can be deduced from eqn [30] that this transition temperature would, in fact, depend on the value of fraction area f_{gb}, and thus of scale microstructure.

Finally, it must be emphasized that experimental measurements and usual treatments of dislocation and grain-boundary diffusivities are valid for stationary dislocations and grain boundaries. In many practical situations encountered in high temperature oxidation or corrosion, these defects would move and their size and density would vary, sometimes strongly, as a function of time and temperature. In that case, solute drag by moving internal defects can result in a large increase of apparent diffusion flux. In addition, the analysis can be complicated by the occurrence of specific phenomena such as diffusion-induced grain-boundary motion (DIGM) that can be observed in alloys or materials experiencing large concentration changes across moving gain boundaries.[26]

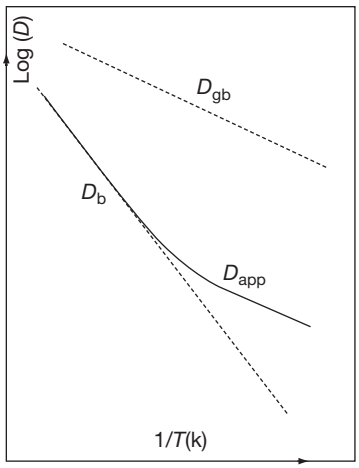

Figure 16 Arrhenius representation of bulk, grain boundary and apparent diffusion coefficients (the gb area fraction is assumed constant).

1.06.5 Diffusion and Transport in Oxides

1.06.5.1 Chemical Diffusion in Nonstoichiometric Oxides

The diffusion process induced in nonstoichiometric oxides and ionic compounds by a chemical potential gradient is named chemical diffusion. In common nonstoichiometric oxides, there is usually only one type of dominant point defect localized on one specific sublattice. Therefore, the diffusion process is restricted to the cationic sublattice for dominant defects such as cation vacancies or interstitials, and to the anionic sublattice for dominant anionic defects.

For an oxide like $M_{1-\delta}O_v$ that contains δ cation vacancy per mole of oxide, the cation concentration C_M is proportional to the departure from stoichiometry $\delta : C_M = (1-\delta)/\Omega_{MO_v}$, where Ω_{MO_v} is the molar volume of oxide MO_v. Thus, Fick's first law, applied in the laboratory frame of reference, implies that the cation flux is proportional to the δ gradient

$$\widetilde{\mathcal{J}}_M = \frac{\widetilde{D}}{\Omega_{MO_v}}\frac{\partial \delta}{\partial x} \qquad [33]$$

By taking care of the expression for cation and anion molar fractions in a nonstoichiometric oxide and neglecting the diffusion coefficient of anionic species, eqns [16], [30], and [31] lead to the following expression of $\widetilde{D}$

$$\widetilde{D} = (1+q)\frac{D_M}{\delta} \qquad [34]$$

where D_M is the self-diffusion coefficient of cation and q the absolute value of the effective charge of cation vacancies. By introducing the cation vacancy diffusivity D_{V_M} through eqn [27], the chemical diffusion coefficient is then related to the cation vacancy mobility, which does not depend on the vacancy molar fraction

$$\widetilde{D} = (1+q)D_{V_M} \qquad [35]$$

The form of this relation is general and applies to any kind of point defect by simply replacing D_{V_M} by the diffusivity D_d of the predominant defect involved in the diffusion process.

Therefore, from these relations between chemical diffusion and defect diffusivity, transport in an ionic compound can be expressed only in terms of fluxes of point defects that are the primary mobile species.

Concentration gradients and transport of charged species (ions, points and electronic defects) induce internal electric fields within ionic compounds and oxides. For an internal electric field strength E, the force f acting on transported species of charge q is $f = qE$. The flux of each species i can then be expressed from eqns [23] and [24]

$$\widetilde{\mathcal{J}}_i = -D_i \frac{\partial C_i}{\partial x} + D_i C_i \frac{q_i E_i}{RT} \qquad [36]$$

But, the condition of electrical neutrality implies that there is no net current flow within the oxide scale, which lead to the equation: $\sum q_i \widetilde{\mathcal{J}}_i = 0$. However, solving this equation by using the expression [36] for the fluxes of all charged species leads again to eqn [35].

When an external electric field is applied to an ionic compound or an oxide initially at equilibrium, the only driving force for the diffusion/transport of charged species is that induced by the electric field. The Nernst–Einstein relation [24] leads to the expression of the flux of each charged species that is related to their electrical mobility and to the expression of the contribution of the species i to the electric conductivity

$$\sigma_i = q^2 F \frac{C_i D_i}{RT} \qquad [37]$$

where F is the Faraday constant ($F = eN_A$). The total conductivity is the sum of the contribution of all the charged species. The mobility of electronic defects is largely higher than the mobility of ionic defects and thus the total conductibility is mainly electronic except in the case of some intrinsic ionic oxides. However, for nonstoichiometric oxides, the variations of electric conductivity with oxygen partial pressure P_{O_2} permit the determination of the type and charge of the predominant ionic defect as the molar fractions of electronic and ionic defects vary similarly as a function of P_{O_2} (cf. **Section 1.06.2.4**). A detailed treatment of diffusion in oxides and its relation to electric conductivity can be found in textbooks.[1,12–15]

Predominant defects are involved in mass transport. But minority point defects can be involved in other important properties of compounds. This is, for example, the case of deformation by creep at high temperature of ionic compounds that involves dislocation climb. Dislocation climb in an oxide requires the simultaneous movement of cationic and anionic species and is thus controlled by the transport rate of the slowest species, that is, the one associated to the minority defect.

1.06.5.2 Diffusion Processes in Oxide Scales

The diffusion and transport process occurring in an oxide scale can be illustrated by considering the behavior of such a scale when the chemical potential of one scale constituent differs on both its faces. This

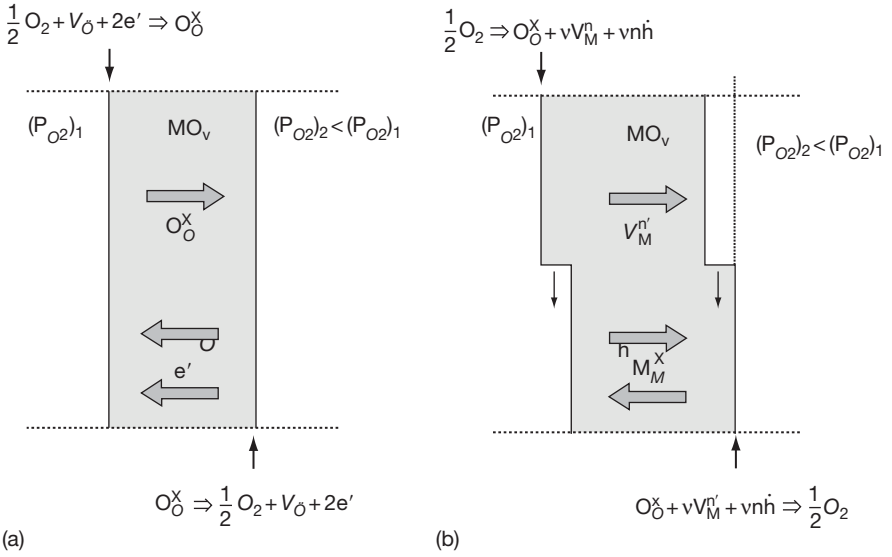

Figure 17 Diffusion fluxes and defect creation/annihilation for an MO_n oxide scale maintained in a constant oxygen gradient: (a) n-type oxide with anion vacancies and (b) p-type oxide with cation vacancies.

situation is schematized in Figure 17 for an MO_v scale separating two environments of differing oxygen partial pressure. Both sides of the oxide scale are assumed to be in equilibrium so that a gradient in the concentration of predominant defects is established within the scale. Corresponding flux of point defects can be easily calculated from eqns [33], [34], and [16] or [18] when only one type of point defect is predominant. The calculation is more complex for oxides in which anionic and cationic species are able to diffuse simultaneously.

In the case of predominant anion vacancies, as shown in Figure 15(a), the cation sublattice is not affected by the oxygen gradient so that there is no transport of cationic species and the oxide scale remains stationary. The reactions occurring on the faces of the oxide scale can be represented by the oxidation/reduction equilibrium [17] but the oxidation reaction occurs only on the high P_{O_2} and results in the annihilation of anion vacancies while the opposite reduction reaction occurs on the low P_{O_2} side and expresses the formation of anion vacancies. A constant concentration gradient of oxygen vacancies (and free electrons) is then established so that anion vacancies are continuously created at the low P_{O_2} side and annihilated at the high P_{O_2} side, which results in a constant flux of anion vacancy and a constant counter flux of oxygen anions. Therefore, in such a situation, the oxide scale acts simply as a permeable membrane that controls the oxygen flux from the high P_{O_2} compartment toward the low P_{O_2} one.

This situation is different for an oxide with predominant cation vacancies (Figure 17(b)). Indeed, the oxidation/reduction equilibrium expressed by eqn [14] involves species belonging to both anionic and cationic sublattices and results not only in the creation/annihilation of cation vacancies but also in the creation (oxidation reaction) of one new structural unit of the oxide lattice on the high P_{O_2} side and the destruction of one such unit on the low P_{O_2} side (reduction reaction). These simultaneous reactions of creation/destruction of structural unit of oxide lattice result in a net shift of the oxide scale toward the high P_{O_2} side.[1] This translation of the oxide scale can be seen as the movement of ledges operating the advance of oxide lattice planes on the oxidation side and their recession on the reduction side, as schematically shown in Figure 17(b). This steady-state shift of cationic oxide scales under a constant potential gradient of oxygen is an illustration of the Kirkendall effect in ionic compounds. Again, a constant concentration gradient of cation vacancies (and electron holes) is established through the oxide scale and cation vacancies are continuously created at the high P_{O_2} side and annihilated at the low P_{O_2} side, which result s in a constant flux of cation vacancies and an opposite constant flux of cations that causes the observed shift of the oxide scale toward the high P_{O_2} side.

This analysis can be extended to the case of two oxides, AO and BO, forming a solid solution (A,B)O where A and B cations are randomly distributed over the cationic sites of their common crystal structure; charged cation vacancies are assumed to be the predominant point defects in pure oxides and their solid solutions. In an oxygen potential gradient, the same causes producing the same effect, a shift of the crystal lattice toward the high P_{O_2} side is again observed. But, the mobility of A and B cations are usually not equal so that the faster cations, for example A cations, move faster toward the high P_{O_2} side, which results in an enrichment in A at this side, regardless of the relative thermodynamic stability of AO and BO; this process is named kinetic demixing and results in a steady-state demixing profile established through the oxide scale.[1]

1.06.5.3 Oxide Scale Microstructure and Diffusion Processes

The growth of an oxide scale on a pure metal or an alloy fits into the general category of diffusion-driven phase transformation. This general statement does not mean that diffusion is the only process governing or controlling the growth kinetics. Indeed, many other processes, linked to the role and movement of gas–oxide and/or oxide–metal interfaces, can be involved in oxide scale growth, as briefly described in Section 1.06.3.5 for a general α–β transformation.

The understanding of growth mechanisms and kinetics of an oxide scale always requires the knowledge of diffusion and transport modes within this oxide scale. Such information can be obtained by the use of inert markers and/or diffusion tracers, but the morphological and microstructural features of oxide scales can also provide quite useful information.

As for multiphase diffusion in a binary system, a Kirkendall frame of reference (K-frame) can be defined for the metal and oxide lattices. For pure metals or ideal solid solutions, the initial unoxidized surface determines the location of metal K-frame (denoted K_M) and the Matano plane (denoted M). The location of oxide K-frame (denoted K_{Ox}) depends on the growth process.

One difficulty for the oxidation of metals or alloys is linked to the large volume change usually induced

by the transformation of a metal into its oxide. This volume change is characterized by the well-known Pilling and Bedworth ratio (PBR) ϕ. For the growth of the oxide MO_v, this ratio is given by $\phi = (v_{MO_v}/\bar{v}_M)$, where v_{MO_v} is the molar volume of the growing oxide, assumed pure, and $\bar{v}_M$ the partial molar volume of metal M at the oxide–metal interface.

In many cases, this volume variation is totally accommodated or assumed to be accommodated by an elongation parallel to the growth direction. **Figure 18** schematizes, for the oxidation of a pure metal, the three different situations that can be observed in such an ideal case depending on the location of the reactions associated with the growth of the oxide lattice; M defines the position of Matano plane and K_M and K_{Ox} the position of Kirkendall planes, respectively associated to the metal and oxide lattices. The thickness of oxidized metal is equal to ξ_M and the oxide scale thickness ξ_{Ox} is then such that the ratio ξ_{Ox}/ξ_M is equal to the PBR ϕ. For the three situations of **Figure 18**, the recession of metal lattice obviously occurs at the oxide–metal interface. **Figure 18(a)** shows the relative location of M, K_M, and K_{Ox} planes for a scale of pure p-type oxide for which the oxide lattice growth occurs at the gas–oxide interface. **Figure 18(b)** defines the same location for a scale of pure n-type oxide for which the oxide lattice growth and the metal lattice recession occur simultaneously along the oxide–metal interface. The typical examples corresponding respectively to the situations depicted by **Figures 18(a)** and **18(b)** are the oxidation of pure nickel (p-type oxide) or pure zirconium (n-type oxide) in a temperature range such that the bulk diffusion of cations or anions is the only limiting growth process. In that case, the oxide scales are characterized by a homogeneous and regular microstructure consisting of columnar grains for both NiO and ZrO_2 scales but with a smaller grain size, in a section parallel to the oxide–scale interface, for ZrO_2 scales. The difference in grain size is likely due to the location of lattice growth reaction. Indeed, NiO grains grew at the oxide–gas interface where they are free to expand, which explains also their facetted morphology. On the contrary, for ZrO_2 scales, the lattice growth reaction is localized at the oxide–scale interface, the expansion of oxide grains is thus limited by the previously formed oxide; furthermore, the first formed oxide is not affected by its subsequent growth, which explains that the external morphology of such oxide scales reproduces the initial microstructure and/or morphology of its metal substrate. The smaller grain size of these scales may be also due to the continuous nucleation of new oxide grains at the scale–substrate interface and/or to local stresses and strain associated with the large value of PBR ϕ.

Figure 19 can help for a better understanding of the processes leading to the situation of **Figure 18(c)**. Indeed, **Figure 19** reveals the similar microstructures of a NiO scale (**Figure 19(a)**), grown at 800 °C,[27] and of a CoSi layer formed in a $Co_2Si/CoSi_2$ diffusion couple (**Figure 19(b)**).[28] Both NiO scale and

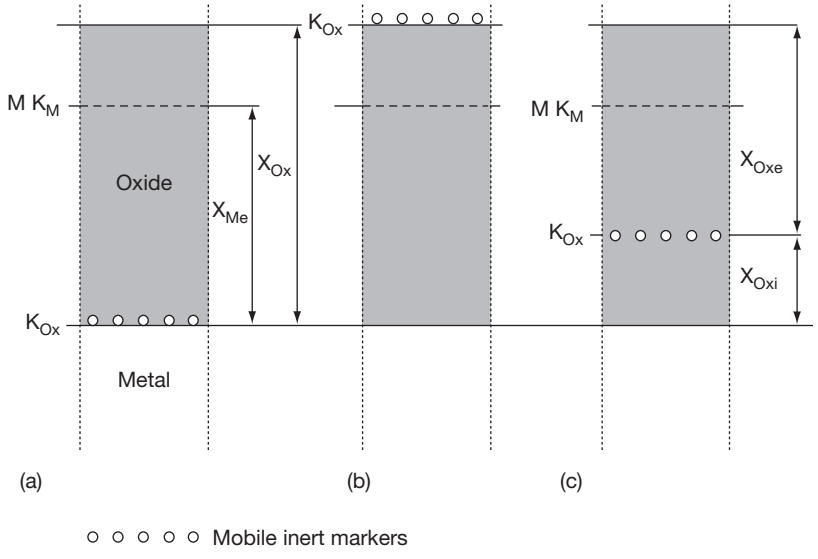

Figure 18 Relative positions of M, K_M, and K_{Ox} reference planes during the growth of an oxide scale by the oxidation of a pure metal: (a) scale growth occurring only at the external gas–oxide interface, (b) scale growth occurring only at the internal oxide–metal interface, and (c) scale growth occurring at both interfaces.

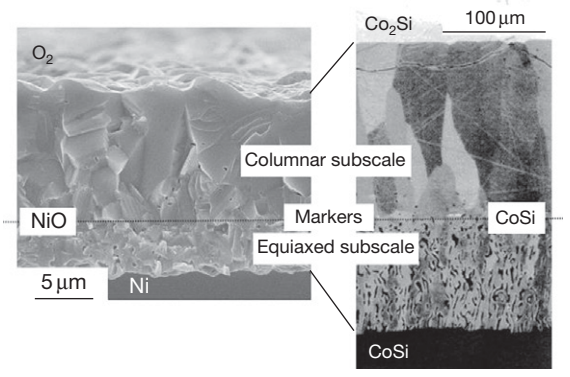

Figure 19 Similarity of the microstructure of a NiO scale grown on a high-purity nickel[27] and of a CoSi layer grown between $CoSi_2$ and Co_2Si. Reproduced from Paul, A.; van Dal, M. J. H.; Kodentsov, A. A.; van Loo, F. J. J. *Acta Mater.* **2004**, *52*, 623–630.

CoSi layer are characterized by a duplex microstructure formed by two sublayers of, respectively, equiaxed and columnar microstructure.

The growth of the columnar CoSi sublayer combines the diffusion of Si from $CoSi_2$ toward Co_2Si and its reaction at the Co_2Si/CoSi. Simultaneously, the counter diffusion of Co and its reaction at the CoSi–$CoSi_2$ interface leads to the growth of the equiaxed CoSi sublayer. Inert markers, initially located at the Co_2Si–$CoSi_2$ interface, are always located along the internal interface separating the columnar and equiaxed sublayers and they define the location of the Kirkendall plane of CoSi phase.[28]

Such a duplex microstructure is commonly observed for NiO scales grown at a temperature lower than 1000 °C.[27,29] For these duplex scales, inert marker location and ^{18}O experiments have shown that the growth of the external columnar subscale is associated to the outward diffusion of Ni cations and occurs at the scale–gas interface while the inward diffusion of oxygen is involved in the growth of the inner equiaxed subscale. Therefore, the internal interface between equiaxed and columnar sublayers marks also the initial location of the Ni surface before the formation and growth of NiO scales. These two examples clearly show that similar growth processes lead to similar microstructures. The microstructure of a growing phase directly depends on the nature of diffusing species and on the localization of growth reactions as observed in many examples of solid-state and solid–gas reactions and its microstructure differs on both sides of its Kirdendall plane.[22,28] Therefore, metallographic examinations of oxide scales provide also an easy way to determine the location of K_{Ox}. **Figure 18(c)** then corresponds to a mixed case such that oxide lattice growth occurs simultaneously at both gas–oxide and oxide–metal interfaces. The oxide scale fraction growing at the external gas–oxide interface has a thickness ξ_{oxe} and the fraction growing at the internal oxide–metal interface a thickness ξ_{oxi}. For diffusion-controlled scale growth, the relative magnitude of ξ_{oxe} and ξ_{oxi} is directly proportional to the relative magnitude of intrinsic diffusivity of species involved in the growth process, as observed in many examples of solid-state reactions.[22]

For a pure metal, the position of M and K_M planes always coincides with the position of the initially nonoxidized metallic surface. Therefore, after the growth of an oxide scale, the position of these reference planes can be accurately determined relative to a fixed reference plane such as, for example, the specimen mid-plane or any marked plane far enough from the scale–metal interface supposed to be fixed and not affected by the lattice movements induced by scale growth. These displacements can be rationalized by a factor Γ that defines the displacement ξ of any reference plane of the oxide scale as a function of the thickness of oxidized metal ξ_m: $\xi = \Gamma\xi_m$[30]; the factor Γ is defined as positive for outward displacement. For the general case of simultaneous growth at the external gas–scale interface and at the internal scale–substrate interface, the factor Γ is given by

$$\Gamma = \phi(1 - f_C) - 1 \qquad [37a]$$

The term f_C in relation [37a] is the fraction of cationic scale growth; f_C is equal to the ratio ξ_{oxe}/ξ_{ox}. Relation [37a] is easily checked from the displacement of K_{Ox} plane for pure cationic (**Figure 18(a)**) or pure anionic (**Figure 18(b)**) growth.

Figure 18 and relation [37a] remain valid for the selective oxidation of ideal disordered solid solutions; the value of ϕ is then that of the selectively oxidized constituent. Indeed, the total volume of an ideal solid solution does not depend on the spatial distribution of its constituents because the partial molar volume of each constituent is constant and equal to its own molar volume. Therefore, there is no difference between pure metal and ideal solid solution regarding the definition and location of planes M and K_M. This situation is more complex for nonideal solid solutions as the partial molar volume of each constituent varies as a function of composition. Selective oxidation of one constituent of a solid solution results in concentration gradients of all constituents in the alloy underlying the oxide scale and the resulting local variations of partial molar volumes is the

cause of local volume changes, which in turn results in local deformation and stress fields. Unfortunately, an accurate evaluation of such volume changes and related deformation field requires data that are often not available. Many oxide scales present a duplex microstructure similar to NiO scale of **Figure 19**. This is the case of α-alumina scales grown on FeCrAlY alloys oxidized at high temperature ($T >$ 1000–1100 °C); they are formed of an equiaxed outer subscale and a columnar inner subscale.[31] Like for NiO scales, this duplex microstructure is representative of the simultaneous occurrence of two growth processes, the surface separating these two subscales defines the location of K_{ox}-plane, that is, the initial location of the metal surface. But, the microstructure of alumina scales grown on high temperature alloys depends strongly on many parameters such as oxidation temperature, oxygen partial pressure or alloy composition and more particularly of the presence of reactive element such as Y, Zr, Hf, etc. Furthermore, the influence of these parameters on the nature and concentration of predominant point defects and electronic defects, diffusion mechanisms, and processes is yet neither well known nor understood. For many oxide scales, a detailed analysis and understanding of correlations between scale growth microstructure, growth mechanisms and diffusion processes is needed and is still far away to be possible. Several experimental methods now commonly used in solid-state electrochemistry can offer new insights in oxide-scale properties and scale-growth mechanism. This is notably the case of impedance spectroscopy[32] and photoelectrochemical spectroscopy.[35] Impedance spectroscopy is a powerful tool that can permit to analyze the influence of many parameters such as scale composition, scale thickness, scale microstructure, and grain size. Photoelectrochemical spectroscopy permits the determination of the local electronic properties of oxide scales, which is of particular importance for a better understanding of growth mechanisms. These techniques are particularly interesting at temperatures where bulk diffusion is not the limiting process as shown by the results obtained on the oxidation of zirconium alloys[33] or pure nickel.[34]

1.06.5.4 Point Defects and Diffusion in Common Oxides

Many works have been devoted to the study of bulk and grain-boundary self-diffusion in ionic compounds, particularly in oxides and sulfides that are commonly found in high temperature oxidation or corrosion of metallic materials.[12–14] But, only few very common oxides such as NiO monoxide, iron oxides, chromia, and alumina are briefly considered in this section. By its importance in the manufacturing of integrated circuits and its protective role in the oxidation behavior of some iron-based materials, silica is also a very common oxide. However, silica scales are amorphous and diffusion processes in amorphous solids are not considered here. Most of the studies devoted to point defects and diffusion processes in oxides are often based on measurements of electrical conductivity, scale growth kinetics or else concentration profiles of marked species. For bulk diffusion, the equations reported in **Section 1.06.5.1** permit the interpretation of experimental data regarding the diffusion mechanisms and the nature and ionization degree of defects involved in diffusion processes. But, it must be kept in mind that diffusion data obtained from oxide single crystals, very pure oxides and/or oxide samples of controlled, homogeneous and regular microstructure are not always useful for the understanding and analysis of diffusion and transport processes in oxide scales grown on complex metallic materials.

1.06.5.4.1 Nickel and cobalt monoxides

Both $Ni_{1-\delta}O$ and $Co_{1-\delta}O$ are p-type oxides of rock salt structure. Cation vacancies and positive holes are the predominant point and electronic defects; the departure from stoichiometry δ is significantly smaller for NiO. The self-diffusion coefficients of cations were determined from tracer experiments and from the analysis of scale-growth kinetics at temperatures higher than 1000 °C. The agreement between these independent determinations is excellent. The growth of NiO and CoO scales at high temperatures is one of the best examples of scale growth controlled by bulk diffusion according to the Wagner theory as demonstrated by the recent work of Mrowec and Gresik[36] on the oxidation of high-purity nickel at temperatures higher than 1100 °C. In this temperature range, NiO scales are characterized by a homogeneous microstructure consisting of large columnar grains such that the contribution of grain-boundary diffusion can be readily neglected. The following equations express the departure from stoichiometry and the variation of self-diffusion coefficient of Ni cations as a function of T and P_{O_2}

$$\delta = 0.153\left(\frac{P_{O_2}}{P^0}\right)^{1/6}\exp\left(-\frac{9620}{T}\right) \qquad [38]$$

$$D_{Ni}(cm^2s^{-1}) = 9.3 \times 10^{-3}\left(\frac{P_{O_2}}{P^0}\right)^{1/6} \times \exp\left(-\frac{27\,900}{T}\right) \quad [39]$$

Chemical diffusion coefficient $\widetilde{D}$ in NiO can be deduced from eqns [34], [38], and [39]; $\widetilde{D}$ and cation vacancy diffusivity, calculated from eqn [35], are independent of P_{O_2} and thus of the vacancy molar fraction. Diffusion data in NiO have been recently reviewed by Monceau.[37] Few measurements of self-diffusion coefficient of oxygen anions were performed at temperatures higher than 1100 °C; their values are more than five orders of magnitude smaller than self-diffusion coefficients of Ni. Other data were obtained from high temperature creep behavior of NiO, which is controlled by the diffusion of oxygen.

At temperatures lower than 1000 °C, the influence of grain-boundary diffusion cannot be neglected.[38] The grain-boundary self-diffusion of cations and anions in NiO scales has been extensively investigated and discussed.[27,29,37,38] However, the morphology and microstructure of NiO scales vary strongly as a function of time and temperature[27]; therefore, the only influence of grain-boundary diffusion is likely not sufficient for a detailed understanding of experimental scale-growth kinetics and complex evolutions of oxide-scale morphology and microstructure at $T < 1000\,°C$.

1.06.5.4.2 Iron oxides

Three oxides can be found in iron–oxygen systems: wüstite $Fe_{1-\delta}O$, magnetite Fe_3O_4, and hematite Fe_2O_3. Pure wüstite is only stable at temperatures higher than 570 °C and reduced P_{O_2}. Therefore, oxide scales grown on pure Fe above 570 °C is, from pure iron substrate up to oxygen gas phase, formed of successive three sublayers of wüstite, magnetite, and hematite. The relative thicknesses of these sublayers are almost independent of temperature and show very clearly that diffusion is largely faster in wüstite (95% of the total scale thickness) than in magnetite (4%) and hematite (1%).

Like CoO and NiO, wüstite $Fe_{1-\delta}O$ is a p-type oxide of rock salt structure but it differs by its larger departure from stoichiometry δ that can reach a value as high as about 0.15. The defects responsible for Fe self-diffusion in $Fe_{1-\delta}O$ are, like for NiO and CoO, cation vacancies but Fe self-diffusion in wüstite is about four orders of magnitude faster than Ni self-diffusion in NiO. Furthermore, contrary to NiO and CoO, Fe self-diffusion coefficients are nearly independent of δ; the formation of highly stable defect clusters combining cationic vacancies and interstitials interferes with the diffusion processes that are therefore more complex than in NiO or CoO. The main point defect of anionic sublattice are oxygen interstitials but the variation of oxygen self-diffusion as a function of temperature and P_{O_2} is complex and not yet understood. In wüstite, oxygen self-diffusion is several orders of magnitude slower than iron self-diffusion.

Magnetite Fe_3O_4 has a spinel crystal structure where the octahedral and tetrahedral sites of the fcc sublattice of oxygen anions can be occupied by Fe^{2+} and Fe^{3+} cations. The distribution of Fe^{2+} and Fe^{3+} cations over octahedral and tetrahedral sites is a function of temperature.

Magnetite is stoichiometric at room temperature and Fe^{3+} cations are equally distributed over tetrahedral and octahedral sites while Fe^{2+} cations are only in octahedral sites. This distribution of Fe^{2+} and Fe^{3+} cations corresponds to the inverse spinel structure. At temperatures higher than about 900 °C, the distribution of Fe^{2+} and Fe^{3+} cations is randomized over tetrahedral and octahedral sites and the departure from stoichiometry increases as temperature increases.

The predominant point defects are in the cationic sublattice; their nature is thus defined relatively to the normal site occupancy of one-half of octahedral sites and one-eighth of tetrahedral sites but defects localized on octahedral and tetrahedral sites are not equivalent and must be distinguished. Cation vacancies and interstitials are localized on the same sites and are formed when the proportions of occupied sites are respectively smaller (vacancy) or higher (interstitial) than 1/2 and 1/8. The majority defects are neutral cation interstitials ($Fe_{3+\delta}O_4$) at low P_{O_2} close to the wüstite–magnetite equilibrium and neutral cation vacancies ($Fe_{3-\delta}O_4$) at higher P_{O_2} close to the magnetite–hematite equilibrium. The formation equilibriums of these defects lead to defects concentration varying as $P_{O_2}^{2/3}$ for vacancies and $P_{O_2}^{-2/3}$ for interstitials.[39]

The variation of iron self-diffusion coefficient as a function of P_{O_2} is similar and expressed by the following relation[40]

$$D_{Fe}(cm^2s^{-1}) = 4 \times 10^{-11}\left(\frac{P_{O_2}}{P^0}\right)^{2/3}\exp\left(-\frac{16\,800}{T}\right) + 8 \times 10^{7}\left(\frac{P_{O_2}}{P^0}\right)^{-2/3}\exp\left(-\frac{73\,800}{T}\right)$$

The minimum of iron self-diffusion coefficients is not observed for the stoichiometric composition where the molar fraction of cation vacancies and interstitials are equal. This minimum corresponds to a P_{O_2} value such that vacancies molar fraction is higher than interstitials molar fraction, which means that interstitials are more mobile than vacancies. Oxygen self-diffusion is two orders of magnitude slower than iron self-diffusion and varies also as a function of P_{O_2} indicating that the nature of predominant anionic point defects varies also with P_{O_2}; the interpretation of the observed variations involve the formation of complex point defects at high P_{O_2}.

The crystal structure of hematite Fe_2O_3 is, like Cr_2O_3 and α-Al_2O_3 of corundum type. Corundum structure can be described as a close packing of anions, cations occupying two-thirds of the octahedral sites. Fe_2O_3 is known to be an oxygen-deficient oxide with very small departure from stoichiometry. Its defect structure is very sensitive to metallic impurities; it changes from oxygen vacancies and n-type conductivity to interstitial cations and p-type conductivity at about 800 °C. Iron and oxygen self-diffusion are apparently of the same order of magnitude but the works devoted to the influence of P_{O_2} on defect structure and self-diffusion in Fe_2O_3 cannot be interpreted on the basis of simple defect structure and lead to rather different interpretations.

1.06.5.4.3 Chromia

Heat-resisting alloys are commonly classified as chromia-forming or alumina-forming alloys according to the nature of the protective oxide scale formed upon their high temperature oxidation. However, at P_{O_2} close to atmospheric pressure, the oxidative evaporation of Cr_2O_3 in volatile CrO_3 chromic oxide limits the uses of chromia-forming alloys to about 1000 °C. Cr_2O_3, like hematite, has the corundum structure but a much more narrow range of nonstoichiometry because of its greater thermodynamic stability. Cr_2O_3 is an electronic semiconductor that can be either a p-type or an n-type semiconductor depending on T, P_{O_2}, and doping impurities. The influence of these parameters on the nature of predominant defect is complex and not yet fully understood. It is still the subject of many controversies, particularly for the role of reactive elements (RE) such as Y, Ce, etc. that modify the transport properties of Cr_2O_3, and therefore, the growth mode, the growth kinetics, and the microstructure of Cr_2O_3 scales.

The variations of electrical conductivity, chromium and oxygen self-diffusion and scale-growth kinetics as a function of P_{O_2} are complex and difficult to interpret and to compare, particularly because of their rather wide scattering. However, many data are consistent with a defect structure based on the predominance of V_{Cr}''' cation vacancies at P_{O_2} close to atmospheric pressure and on the predominance of interstitial cations $Cr_i^{3\bullet}$ at very low P_{O_2}, close to Cr_2O_3–Cr equilibrium, although anion vacancies may be important minority defects at these low P_{O_2} in agreement with experimental data showing that bulk chromium and oxygen self-diffusion coefficients are of the same order of magnitude.[41] At intermediate P_{O_2}, free electrons and electron holes are the major defects; Cr_2O_3 then behaves as an intrinsic electronic semiconductor. These differences in defect structure as a function of P_{O_2} must have a marked influence on the microstructure of Cr_2O_3 scales but there is much less work on the characterization of Cr_2O_3 scales than on NiO or α-Al_2O_3 scales.

Grain-boundary diffusion play also an important role in the growth of Cr_2O_3 scales, particularly at temperatures lower than 1000 °C. Grain-boundary diffusion of cations appears usually faster than anion diffusion. But more data on the influence of T, P_{O_2} and RE on grain-boundary self-diffusion of chromium and oxygen are needed for a better understanding of diffusion process involved in the growth of Cr_2O_3 scales.

1.06.5.4.4 α-Alumina (α-Al_2O_3)

Alumina of corundum structure, α-Al_2O_3, is the most protective and stable oxide among all the oxides commonly encountered in high temperature oxidation. Therefore, α-Al_2O_3 is also the most important oxide from the technological view point of oxidation resistance and behavior of heat-resisting alloys. Unfortunately, despite all the work conducted over its point defect structure and transport properties, there remain major problems in the understanding of α-Al_2O_3 properties and behavior that are still the subject of discussion and controversy as illustrated by a recent review.[42]

The great thermodynamic stability of α-Al_2O_3 results in a so narrow nonstoichiometry range that there is no accurate determination of its extent. As a consequence, the transport properties of α-Al_2O_3, as determined from electrical conductivity, tracer diffusion or scale-growth kinetics, are controlled by extrinsic defects associated to cationic impurities. This strong influence of impurities likely explains the wide scattering of experimental data usually observed among the numerous studies devoted to α-Al_2O_3.

One other characteristic of the transport properties of α-Al_2O_3 is the large value of the experimental activation energy reported for the bulk self-diffusion of O and Al. For oxygen diffusion, mainly studied by means of ^{18}O tracer, the reported activation energies range between 570 and 640 kJ mol^{-1}. The absence of natural Al isotope explains why there is only one study which used[26] Al markers, an artificial isotope, to measure the self-diffusion coefficient of Al.[43] The reported activation energy of Al self-diffusion is also high and found to be equal to 510 kJ mol^{-1}, a value close to the activation energy of O self-diffusion. Surprisingly, the activation energy for the diffusion of many foreign metallic cations is smaller, usually comprised between 260 and 300 kJ mol^{-1}, a value close to the mean activation energy of α-Al_2O_3 scale-growth kinetics reported by Hou[44] from a compilation of growth kinetics of numerous Ni-based and Fe-based alumina-forming alloys.

To add to the complexity of transport processes in α-Al_2O_3, the experimental activation energies of grain boundary self-diffusion of O and Al are significantly higher than the activation energies for bulk self-diffusion, a rather uncommon situation. Indeed, the reported activation energies for grain-boundary diffusion are higher than 800 kJ mol^{-1} for both O and Al. But, despite all the studies devoted to the oxidation behavior of alumina-forming alloys, there is no convincing explanation of the different activation energies for oxidation and diffusion. The complexity of α-Al_2O_3 growth is also reflected in the diversity of microstructures observed for α-Al_2O_3 scales that can be equiaxed, columnar, or duplex depending on T, P_{O_2}, and alloying elements such as RE or Pt. These different microstructures must correspond to different growth mechanisms and diffusion processes. But, a more detailed analysis of the correlation between scale microstructure, growth mechanisms and diffusion processes remains to be done.

A better understanding of defect structure and transport properties of α-Al_2O_3 could be obtained from theoretical calculations permitting the determination of the enthalpy of formation of different point defects. But, the various calculation methods and interaction potentials used in these calculations lead to somewhat differing results. The most recent calculation has shown that Schottky defects, formed by the combination $2V_{Al}^{3'} + 3V_O^{2\bullet}$, are the dominant intrinsic point defects in stoichiometric α-Al_2O_3[45] but this result is not in agreement with previous results leading to a predominance of Frenkel pairs.[46] However, because of the extrinsic behavior of α-Al_2O_3, the development of such calculations would be very useful and would lead to more consistent results and thus to a better understanding of defect structure and transport properties of α-Al_2O_3.

1.06.6 Concluding Remarks

Mass-transport processes are of fundamental importance for the understanding and modeling of high temperature oxidation and corrosion behavior of materials but, as roughly shown in **Section 1.06.5.4**, the defect structure and transport properties of most common and important oxides are far from being well known and understood. The increased capability of theoretical treatments would likely permit a more accurate modeling of chemical bonding, point defect structure and intrinsic and extrinsic behavior of common oxides in the coming years.

However, very few scale-growth kinetics can be perfectly described from the only knowledge of defect structure and bulk transport properties of the growing scale. For example, the oxidation of high-purity nickel in pure and dry oxygen is certainly the simplest situation that can be encountered in the field of high temperature oxidation of metallic materials but, at temperature lower than 1000 °C, NiO growth kinetics are several orders of magnitude faster than expected from the extrapolation of high temperature data.

Grain-boundary diffusion is currently invoked to explain faster growth kinetics at intermediate temperatures; there are indeed many experimental evidences confirming the major role of short-circuit diffusion in scale growth. But our understanding of the structure and properties of oxide grain boundaries, particularly their defect structure and the influence of intergranular segregations, needs to be considered and greatly improved without ignoring the influence of triple junctions. Furthermore, this knowledge would be useful for the analysis and modeling of the complex time-dependent evolutions of oxide-scale morphology and microstructure that interfere with short-circuit diffusion.

Surface and grain boundary are common planar defects; the interface separating two crystal phases is also a planar defect that, like surfaces and grain boundaries, can play a role in the creation or annihilation of point defects involved in scale growth or in diffusion processes within the oxidized substrate. There are many examples of solid-state reactions for which solid–solid interfaces and interfacial reactions play a major role.[47] In the field of high temperature

oxidation, one well-known example is provided by the oxidation of silicon. Indeed, molecular oxygen diffuses through the thin silica layer and reacts with the silicon substrate at the silica–silicon interface; this interfacial reaction is the controlling step for the growth of the very thin silica layers now required in the manufacturing of integrated circuits. Therefore, the roles of scale–substrate interfaces need to be more particularly analyzed in relation with some specific topics related to oxide-scale processes such as interface displacement, growth stresses and injection of point defects (vacancy or interstitial). In addition, the development of experimental techniques and methods permitting an accurate determination of the relative movement of M, K_M, and K_{Ox} planes would help in the modeling of scale-growth mechanisms. The development of such models combining diffusion processes and interface action could lead to a new approach to questions linked to the effect of impurities and of their segregation, the effect of reactive element and thus a better understanding of the dynamical behavior of scale–substrate interface during scale growth, which could open up new opportunities for the control of oxidation behavior of high temperature materials and the improvement of their oxidation resistance.

References

1. Schmalzried, H. *Chemical Kinetics of Solids*; VCH: Weinheim, 1995.
2. Hillert, M. In *Phase Equilibria, Phase Diagrams and Phase Transformations;* Cambridge University Press: Cambridge, 1998; Chapter 16. pp 427–457.
3. Kraftmaker, Y. *Phys. Rep.* **1998**, *299*, 79–188.
4. Aziz, M. *Appl. Phys. Lett.* **1997**, *70*, 2810–2812.
5. Hull, D.; Bacon, D. J. *Introduction to Dislocations*, 4th ed.; Butterworth-Heineman: Oxford, 2001.
6. Hudson, J. B. *Surface Science: An introduction*; John Wiley: New York, 1998.
7. Howe, J. M. *Interface in Materials: Atomic Structure, Thermodynamics and Kinetics of Solid–Vapor, Solid–Liquid and Solid–Solid Interfaces*; John Wiley: New York, 1997.
8. Sutton, A. P.; Balluffi, R. W. *Interfaces in Crystalline Materials*; Oxford University Press: Oxford, 2006.
9. Pond, R. C.; Hirth, J. P. *Solid State Phys.* **1997**, *47*, 287–365.
10. Hirth, J. P. *Metel Trans. A* **1991**, *22A*, 1331–1339.
11. Pieraggi, B.; Rapp, R. A.; van Loo, F. J. J.; Hirth, J. P. *Acta Metall. Mater.* **1990**, *38*, 1780–1790.
12. Kofstad, P. *Non Stoichiometry, Diffusion and Electrical Conductivity in Binary Metal Oxides*; Wiley Interscience: New York, 1972.
13. Mrowec, S. *Defects and Diffusion in Solids*; Elsevier: Amsterdam, 1980.
14. Smyth, D. M. *The Defect Chemistry of Metal Oxides*; Oxford University Press: Oxford, 2000.
15. Maier, J. *Physical Chemistry of Ionic Materials: Ions and Electrons in Solids*; John Wiley & Sons: New York, 2004.
16. Kizikyalli, N.; Corish, J.; Metselaar, R. *Pure Appl. Chem.* **1999**, *71*, 1307–1325.
17. Philibert, J. *Atom Movements, Diffusion and Mass Transport in Solids*; Les Editions de Physique/Les Ulys 1991.
18. Kirkaldy, J. S.; Young, D. J. *Diffusion in the Condensed State*; The Institute of Metals: London, 1987.
19. Glicksman, M. E. *Diffusion in Solids*; John Wiley & Sons: New York, 2000.
20. Ghez, R. *Diffusion Phenomena*; Kluwer Academic/Plenum Press: New York, 2001.
21. Brown, A. M.; Ashby, M. F. *Acta Metal* **1980**, *28*, 1085–1101.
22. van Loo, F. J. J. *Prog. Solid State Chem.* **1990**, *20*, 47–99.
23. van Loo, F. J. J.; Pieraggi, B.; Rapp, R. A. *Acta Metal Mater.* **1990**, *38*, 1769–1779.
24. Mishin, Y.; Herzig, C.; Bernardini, J.; Gust, W. *Int. Mater. Rev.* **1997**, *42*, 155–178.
25. Wang, H.; Yang, W.; Ngan, A. H. W. *Scripta Mater.* **2005**, *52*, 69–73.
26. Shewmon, P. *Diffusion in Solids*, 2nd ed.; The Minerals, Metals and Materials Society: Warrendale, 1989.
27. Peraldi, R.; Monceau, D.; Pieraggi, B. *Oxid Metel* **2002**, *58*, 249–273.
28. Paul, A.; van Dal, M. J. H.; Kodentsov, A. A.; van Loo, F. J. J. *Acta Mater.* **2004**, *52*, 623–630.
29. Haugsrud, R. *Corr. Sci.* **2003**, *45*, 211–235.
30. Manning, M. I. *Corr. Sci.* **1979**, *21*, 301–316.
31. Nychka, J. A.; Clarke, D. R. *Oxid Metel.* **2005**, *63*, 323–352.
32. Maier, J. Solid State Electrochemistry: Thermodynamics and Kinetics of Charge Carriers in Solids. In *Modern Aspects of Electrochemistry N°38*; B.E., Kluwer Academic/Plenum Publishers: New York, 2005.
33. Vermoyal, J. J.; Frichet, A.; Dessemond, L. *J. Nuclear Mat.* **2004**, *328*, 31–45.
34. Liu, H.; Mojica-Calderon, C.; Lyon, S. B.; Stack, M. M. *Solid State Ionics* **1999**, *126*, 363–372.
35. Wouters, Y.; Marchetti, L.; Galerie, A.; Bouvier, P.; Petit, J. P. Analysing Thermal Oxidation using MicroPhotoElectrochemistry (MPEC). In *Local Techniques for Corrosion Research (EFC45)*; Woodhead Publishing: Cambridge, 2007.
36. Mrowec, S.; Grzesik, Z. *J. Phys. Chem. Sol.* **2004**, *65*, 1651–1657.
37. Monceau, D.; Peraldi, R.; Pieraggi, B. *Defect Diffusion Forum* **2001**, *194–199*, 1675–1682.
38. Atkinson, A. *Rev. Modern Phys.* **1985**, *87*, 437–470.
39. Martin, M. *Solid State Phenomena* **1992**, *21–22*, 1–56.
40. Amani, B.; Addou, M.; Monty, C. *Defect Diffusion Forum* **2001**, *194–199*, 1051–1056.
41. Tsai, S. C.; Huntz, A. M.; Dolin, C. *Mater. Sci. Eng. A* **1996**, *A212*, 6–13.
42. Doremus, R. H. *J. Appl. Phys.*, **2006**, *100*, 1013011/17.
43. Le Gall, M.; Lesage, B.; Bernardini, J. *Phil. Mag. A* **1994**, *70*, 761–763.
44. Hou, P. Y. *J. Am. Ceram. Soc.* **2003**, *86*, 660–668.
45. Sun, J.; Stimer, T.; Matthews, A. *Surf. Sci. Coatings* **2006**, *201*, 4201–4204.
46. Lagerlöf, K. D. P.; Grimes, R. W. *Acta Mater.* **1998**, *46*, 5689–5700.
47. Dybkov, V. I. *Reaction-diffusion and solid-state chemical kinetics*; IPMS Publications: Kyiv, 2002.

1.07 Mechanisms and Kinetics of Oxidation

S. Chevalier
Institut Carnot de Bourgogne, UMR 5209 CNRS, University of Bourgogne, 9 Avenue Savary, BP 47870, 21078 Dijon cedex, France

Glossary

Alumina (Al_2O_3) Aluminum oxide.

Alumina (transient) Different phases of alumina (γ-Al_2O_3, δ-Al_2O_3, θ-Al_2O_3) able to transform into the stable alumina phase, α-Al_2O_3.

Alumina-forming (alloy) Alloy able to form an alumina scale.

Aluminide Intermetallic compound containing aluminum (examples FeAl, TiAl, $NbAl_3$,...).

Aluminization Surface treatment consisting of forming aluminide diffusion coating via a cementation process.

Arrhenius plot Relationship between reaction rate and temperature, $k = k_0 \exp(-E/RT)$ with E activation energy.

Cyclic oxidation Discontinuous oxidation corresponding to periods at temperature followed by rapid cooling to room temperature.

Diffusion Transport or migration of atoms, ions or molecules in a solid, liquid or gaseous media.

Diffusion (coefficients of) D_{app} is apparent diffusion coefficient, D_V is volume diffusion coefficient, D_{gb} is grain boundary diffusion coefficient.

Isothermal oxidation Continuous oxidation at a fixed temperature.

Marker (isotopic marker) Two stage oxidation experiment consisting of oxidizing a metallic substrate at high temperature in $^{16}O_2$, then in $^{18}O_2$, and locating oxygen isotopes across the thermally grown oxide scale.

Pilling–Bedworth (ratio) Oxide volume relative to native metal volume.

Residual stress Stress taking into account growth stress as well as thermal stress.

Silica (SiO_2) Silicon oxide.

Spallation Detachment of oxide scales during cooling from oxidation to room temperature.

Thermogravimetry Continuous weight change measurement as a function of oxidation time.

Wagner's theory Theory which relates kinetic parameters to diffusion of species across a growing scale.

Zirconia (ZrO_2) Zirconium oxide.

Abbreviations

AES Auger electron spectroscopy
AFM Atomic force microscopy
AISI 304 Austenitic stainless steel mainly composed of (in wt%) Fe–18Cr–10Ni
EDX Energy dispersive X-ray analysis
EPMA Electron probe micro analysis
FIB Focused ion beam
MOCVD Metal-organic chemical vapor deposition
PIPS Precision ion polishing system, ion milling using low angle Ar guns
PLS Photoluminescence spectroscopy
RE Reactive element
REE Reactive element effect
SEM Scanning electron microscopy
SIMS Secondary ion mass spectrometry
SNMS Secondary neutral mass spectrometry
TEC Thermal expansion coefficient in $^{\circ}C^{-1}$ or K^{-1}
TEM Transmission electron microscopy
XPS X-ray photoelectron spectroscopy
XRD X-ray diffraction

Symbols

$\mu_{products}$ Chemical potential of corrosion products
$\mu_{reactants}$ Chemical potential of reactants
$\Delta_r G^0$ Variation of standard free enthalpy of reaction
$\Delta_r H^0$ Variation of standard enthalpy of reaction
$\Delta m/A^0$ Weight gain per unit area
$\Delta_r S^0$ Variation of standard entropy of reaction
F17Ti Ferritic stainless steel mainly composed of (in wt%) Fe–17Cr–0.4Ti
G_r Free enthalpy of reaction
k_p Parabolic rate constant
k_l Linear rate constant
K Equilibrium constant
$Y_3Al_5O_{12}$ Garnet (called YAG for yttrium aluminum garnet)

1.07.1 Introduction

As is evident, humans need oxygen to survive. This is a paradox because this fundamental molecule can be very aggressive against most metallic materials. Even if air contains only 20% of oxygen, it is enough to provoke large-scale degradation of materials.

This degradation is directly connected to their conditions of use. The failures caused by the oxidation process can be very different depending on whether the materials are subjected to acids or salts in wet conditions, to dry conditions but at high temperature (over 500 °C) or to different aggressive atmospheres (O_2, hot corrosion, sulfur, chloride,...). Whatever the exposed conditions, the materials degrade and disintegrate more or less, following different mechanisms.[1,2]

The understanding of the mechanisms which control these different types of corrosion is fundamental to try to improve the corrosion resistance of materials and to extend their lifetime under such severe conditions. One rule is clearly established about the corrosion process; one cannot suppress corrosion. Thermodynamic data show that the formation of corrosion products is energetically favored, following the chemical reaction:

$$M \rightarrow M^{n+} + ne^{-} \quad [1]$$

Moreover, these chemical reactions are also largely dependent upon the corrosion rates. Thus, both thermodynamics and kinetics need to be considered while studying the corrosion process; they have to be carefully controlled to try to protect the base material. That is the reason why the best protection consists of decreasing the corrosion rates.

This chapter focuses on the description of fundamentals for high temperature oxidation. Specific attention will be paid to the high temperature oxidation mechanisms (from thermodynamics, kinetics, and diffusion points of view) and mainly how to relate these mechanisms to the improvement in oxidation resistance. The better the knowledge of the high temperature oxidation mechanisms is, the better is the improvement in the high temperature performance of metallic material.

High temperature oxidation performances are based on the formation of a protective oxide scale which acts as a diffusion barrier, separating the base materials from the aggressive atmospheres.[3–7] It is most of the time a huge challenge, because an effective barrier has to be dense and homogeneous, to cover the entire alloy surface, to possess mechanical properties matching those of the base materials, to consume the least possible metal,[8] to remain stable, to be able to resist complex atmospheres (presence of water vapor for example[9–11]) and above all to keep adherent to the substrate, even after thermal shocks.

Materials able to form protective chromia, Cr_2O_3, alumina, Al_2O_3, or silica, SiO_2 layers are the best candidates to be used at high temperatures in oxidizing atmospheres. These refractory oxides grown on

Fe-, Co-, or Ni-based alloys possess high melting points. Cr (12 wt%) and Al (5 wt%) are necessary to form chromia on chromia-forming alloys and to form alumina on alumina-forming alloys, respectively. The growth rate of chromia scales is much faster than that of alumina scales[12] and, at temperatures over 1000 °C, chromium oxides (especially CrO_3) start to become volatile.

As a matter of fact, chromia and alumina scales should only be employed in adequate temperature ranges, $T \leq 1000\,^{\circ}C$ for Cr_2O_3 and $T \leq 1300\,^{\circ}C$ for Al_2O_3, under isothermal exposures, that is, continuous maintenance at temperature, or under thermal cycling conditions, that is, successive exposure at oxidizing temperature followed by rapid cooling. During cycling, the oxide scales tend to spall, losing any protective effect. Thermal stresses generated during cooling and due to differences between the thermal expansion coefficient of the base metal and that of the oxide scale are mainly responsible for oxide scale spallation.[13] The thermal and/or residual stresses are known to play a huge role during the oxidation of metallic alloys.[4,14–20]

A recent study showed that the amplitude of oxide scale spallation could not be directly related to the residual stresses in the oxide layers.[21] It is also proposed that vacancy coalescence at the metal–oxide interface, as a result of the oxide scale growth, can create pores and cavities and therefore weaken scale adhesion.[22]

It appears clearly that one has to consider not only the chemical evolution of the oxide scale during its growth, but also its mechanical evolution, as well as the close relationship it establishes with the base metallic material. All these considerations are usually named 'physical-chemistry' of the oxide scales.

The proposed situation is the simplest one, as pure oxide scales grown on model materials are being considered. In fact, commercial alloys contain a lot of elements added to increase the mechanical properties, to stabilize the austenitic phase instead of the ferritic phase, to avoid or fix carbide formation (formation of σ phases for example) or to increase their corrosion resistance at ambient or high temperature. The minor element additions perturb the oxide scale formation because they may form mixed oxides, such as spinel or perovskite oxides; these oxides are known to possess poor resistance to high temperature oxidizing atmospheres compared to chromia or alumina scales. Most of the added elements segregate at the interfaces, at the oxide grain boundaries, sometimes within the oxide grains, or form mixed oxides. Some of them, called reactive elements or rare earths (RE), have considerable effects on the high temperature oxidation behavior of alloys. Their addition in small quantities is enough not only to greatly decrease the oxidation rates, but above all to drastically increase the oxide scale adherence to the base material.

The present chapter helps define adequate ways to study high temperature corrosion processes. Thermodynamics, metallurgy, kinetics and diffusion, experimental tools, and the effect of complex atmospheres will be described to answer the still open question: how to improve high temperature corrosion resistance of metals in aggressive atmospheres? Some solutions will be proposed in order to limit the degradation of metallic materials when exposed in such atmospheres at high temperature.

1.07.2 Thermodynamics

Thermodynamics can be considered the driving force for the degradation of metals and alloys in corrosive atmospheres. Effectively, pure metals or metallic elements that constitute alloys are not stable in a reactive gaseous atmosphere. Then, if one considers that the gas is oxygen, a pure metal (M) transforms to oxide (M_aO_b), following the chemical reaction:

$$\frac{2a}{b}\mathrm{M(s)} + \mathrm{O_2(g)} \leftrightarrow \frac{2}{b}\mathrm{M}_a\mathrm{O}_b\mathrm{(s)} \qquad [2]$$

In case of chromia formation for example, the chemical reaction becomes:

$$\frac{4}{3}\mathrm{Cr(s)} + \mathrm{O_2(g)} \leftrightarrow \frac{2}{3}\mathrm{Cr_2O_3(s)} \qquad [3]$$

The free enthalpy of the reaction is expressed by:

$$G_r = \sum \mu_{\text{products}} - \sum \mu_{\text{reactants}} \qquad [4]$$

where μ_{products} and $\mu_{\text{reactants}}$ are the chemical potential of the corrosion products and the reactants, respectively.

By detailing each chemical potential, this equation can be written:

$$G_r = \frac{2}{b}\mu^0_{M_aO_b} + \frac{2}{b}RT\ln\left(a_{M_aO_b}\right)^{2/b} - \frac{2a}{b}\mu^0_{M} - \frac{2a}{b}RT\ln\left(a_{M}\right)^{2a/b} - \mu^0_{O_2} - RT\ln\frac{P_{O_2}}{P^0} \qquad [5]$$

If one assumes that:

$$\Delta_r G^0 = \frac{2}{b}\mu^0_{M_aO_b} - \frac{2a}{b}\mu^0_M - \mu^0_{O_2} \quad [6]$$

$a_{M_aO_b} = 1$ (oxide is pure), $a_M = 1$ (metal is pure), and $P^0 = 1$ atm.

The classical expression of the free enthalpy of reaction is:

$$G_r = \Delta_r G^0 + RT \ln \frac{1}{P_{O_2}} = \Delta_r G^0 + RT \ln K \quad [7]$$

with K the equilibrium constant.

When the equilibrium is reached, $G_r = 0$ and then,

$$\Delta_r G^0 = -RT \ln K = RT \ln P_{O_2} \quad [8]$$

Then,

$$\ln P_{O_2} = \frac{\Delta_r G^0}{RT} \quad [9]$$

This expression means that for a partial pressure of oxygen below this critical value (value obtained when the equilibrium is reached), the metal does not oxidize. For a partial pressure of oxygen over this value, the metal can be totally oxidized.

Another possibility for expressing the variation of the reaction standard free enthalpy is:

$$\Delta_r G^0 = \Delta_r H^0 - T\Delta_r S^0 \quad [10]$$

with $\Delta_r H^0$ being the variation of the standard enthalpy of the reaction and $\Delta_r S^0$ being the variation of the standard entropy of the reaction.

These two expressions [8] and [10] allow a combination of the oxidation temperature together with the partial pressure of oxygen. Then, two diagrams will indicate the evolution of a metal or an alloy in an oxidizing atmosphere at high temperature: phase diagrams and Ellingham diagrams.[6,7,23]

Phase diagrams give the phases that can be formed depending on the temperature or the pressure. Then, if for one component (an oxide in our case), several crystallographic phases can be formed, the use of phase diagrams allows the identification of the one that is thermodynamically stable for a fixed temperature. As an example, zirconia (ZrO_2) has three allotropic structures: cubic, tetragonal, and monoclinic, which transform to each of them on decreasing the temperature, as shown in the Zr–O phase diagram.[24]

Ellingham diagrams are useful for comparing the thermodynamic stability of two oxides formed from two different metals. Their use is crucial in the case of oxidation of alloys (i.e., those which contain different minor elements), in order to know which oxides are the most thermodynamically stable.

However, this approach needs the system to be at equilibrium; most of the time, this situation is not obtained in real systems. Thermodynamics has some limits in the understanding of the corrosion behavior of metals and alloys at high temperatures. Further details on the thermodynamics of gas–metal reactions can be found in **Chapter 1.09, Thermodynamics and Theory of External and Internal Oxidation of Alloys**.

1.07.3 Kinetics

A kinetics approach is complementary to a thermodynamics approach, because it gives information about the rate of oxidation of a metal or an alloy. One can talk about heterogeneous kinetics because a metallic surface reacts with a gas, oxygen for example.[25] The mechanisms occurring during high temperature oxidation are complex. Figure 1 describes some aspects of the reaction between a metallic surface and oxygen

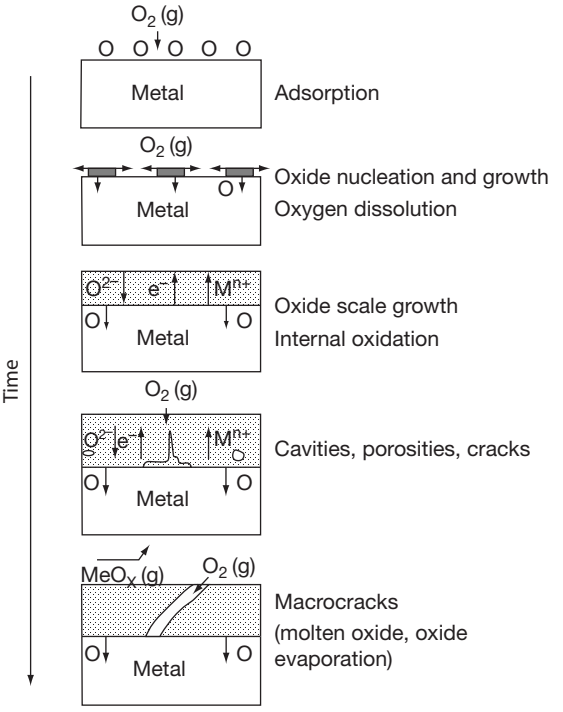

Figure 1 Schematic representation of the reaction between a metallic surface and oxygen at high temperature. Adapted from Kofstad, P. *High Temperature Corrosion*; Elsevier Applied Science, 1988; Sarrazin, P.; Galerie, A.; Fouletier, J. *Les mécanismes de la corrosion sèche. Une approche cinétique*; EDP Sciences, 2000.

at high temperature.[6,7,26] The main steps of the oxidation process can be described as follows:

- oxygen adsorption at the metal surface,
- oxide nucleation with formation of a bidimensional layer
- tridimensional growth of oxide with formation of a thin oxide layer,
- diffusion of species (from metal or from gas) across the growing scale,
- apparition of cracks or microcracks in the base metal and/or in the oxide scale,
- development of cracks at the metal–oxide interface, which can lead to scale spallation and loss of protectiveness.

Two limiting cases can be observed during the growth of an oxide layer:

- growth of a dense oxide layer, for which the transport of species takes place by solid state diffusion,
- growth of a porous oxide scale, for which the transport of species takes place by gaseous diffusion.

One can associate two kinetic regimes to these two limiting cases (**Figure 2**)[27]:

- a parabolic regime, for which in planar symmetry, diffusion of species across a growing scale is the limiting step in the oxidation process. In that case, the relationship between the weight gain per unit area ($\Delta m/A$) and the exposure time (t) is:

$$\left(\frac{\Delta m}{A}\right)^2 = k_p t \qquad [11]$$

with k_p the parabolic rate law constant ($g^2\,cm^{-4}\,s^{-1}$). The parabolic rate law constant can be also expressed in square centimeter per second, by using:

$$k_c = \left(\frac{M_{M_aO_b}}{bM_O\rho_{M_aO_b}}\right)^2 k_p \qquad [12]$$

where $M_{M_aO_b}$ and M_O are the molar mass of M_aO_b and O, respectively, and $\rho_{M_aO_b}$ is the oxide density.

The plot of $\Delta m/A = f(t^{1/2})$ or $(\Delta m/A)^2 = f(t)$ allows us to determine the domain where the parabolic rate law is verified, and also to calculate the value of k_p. The first plot is preferable because it improves the accuracy by minimizing the errors in $\Delta m/A$:

- a linear regime, for which a chemical reaction at one of the interfaces (gas-oxide and/or metal-oxide) is the limiting step in the oxidation process. In that case, the relation becomes:

$$\left(\frac{\Delta m}{A}\right) = k_l t \qquad [13]$$

with k_l the linear rate law constant ($g\,cm^{-2}$).

When a good protection against high temperature oxidation is observed, the parabolic rate law is verified. Conversely, poor oxidation resistance corresponds to a linear rate law (**Figure 2**).

Other kinetics laws can be found during the growth of oxide scales at high temperature:

- Cubic law, for which

$$\left(\frac{\Delta m}{A}\right)^3 = k_c t \qquad [14]$$

- Power law, for which

$$\left(\frac{\Delta m}{A}\right)^n = k_n t \qquad [15]$$

with $1 < n < 3$.

This last law corresponds to an intermediate case between the three previous cases. When $2 < n < 3$, the kinetic law is generally called subparabolic, which means deviation from a real parabolic law. It can be caused by the evolution of grain size during the high oxidation process, by scale cracking, oxidation of reactive element, or incorporation of metal precipitates.[28]

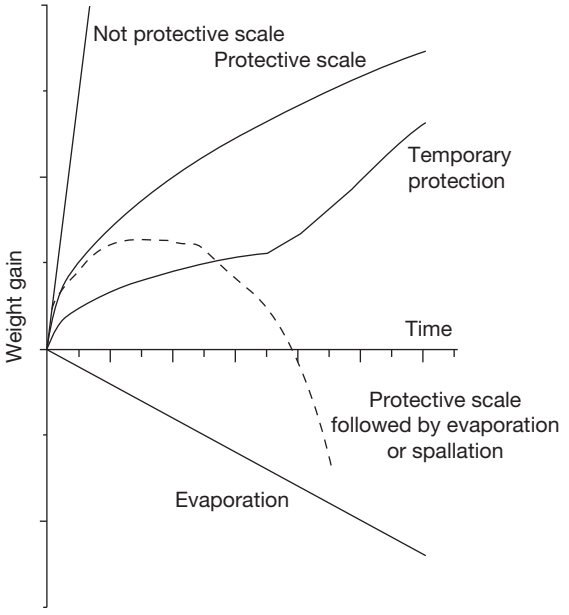

Figure 2 Schematic representation of kinetics observed during high temperature oxidation. Adapted from Antoni, L.; Galerie, A. Corrosion sèche des métaux, Techniques de l'Ingénieur, M4 228, p 9.

Other laws were identified in specific cases (thin films, beginning of the oxidation process, or low oxidation temperatures). They are:

- Logarithmic law, for which

$$\left(\frac{\Delta m}{A}\right) = A + B \ln t \qquad [16]$$

- Inverse-logarithmic law, for which

$$\left(\frac{\Delta m}{A}\right) = C - D \ln t \qquad [17]$$

Some specific cases are also obtained when mixed kinetics laws are observed, especially when chemical reaction at interface(s) takes place together with diffusion of species across the growing scale. In that case, the kinetics regime can be described by:

$$t = A + B\left(\frac{\Delta m}{A}\right) + C\left(\frac{\Delta m}{A}\right)^2 \qquad [18]$$

where A, B, and C are constants; B corresponds to $1/k_l$ and C to $1/k_p$.

A particular case corresponds to successive rate laws: parabolic then linear, which signifies a protective oxidation behavior followed by a loss of protectiveness. Both regimes are separated by a transient period. This case, illustrated in **Figure 2**, is typical of what happens during the growth of zirconia on Zr or zircaloy.[29–31]

The plot of instantaneous k_p can also give crucial information, especially on the evolution of phases in the oxide scale.[32,33] This is particularly true for alumina-forming alloys, because of the presence of several alumina phases (θ, γ, δ, α-Al_2O_3[34,35]). The plot of instantaneous k_p versus time indicates the evolution of k_p values; a constant k_p value is indicative of a stationary oxidation regime, which can be associated with the formation of a stable oxide phase, whereas an evolution of k_p with time suggests the presence of a transient phase (θ-Al_2O_3 for example). The so-plotted curves are then helpful in determining the time necessary to form a protective stable oxide phase (α-Al_2O_3 for example).

Wagner developed a theory relating the parabolic rate law constants to the diffusion coefficient of species: anions (O^{2-}, S^{2-},...) and cations (Cr^{3+}, Al^{3+},...).[36] Then, for an oxide, M_aO_b, Wagner's oxidation theory gives:

$$k_c = \frac{1}{2}\int_{p_{O_2}}^{p_{O_2}} \left[D_{anion} + \left(\frac{b}{a}\right) D_{cation}\right] d \ln P_{O_2} \qquad [19]$$

with k_c, the parabolic rate law constant ($cm^2\,s^{-1}$), $a = 2$ and $b = 3$ (for Cr_2O_3 for example), p_{O_2} is the partial pressure of oxygen for the oxide decomposition at the metal–oxide interface, and p_{O_2} is the partial pressure of oxygen at the gas–oxide interface.

This theory can be adjusted in order to fit realistic situations and to consider short-circuit diffusion paths for example. In the case of diffusion across chromia and alumina scales in the temperature range 800–1200 °C, these short-circuit paths are usually oxide grain boundaries.

1.07.4 Diffusion

The diffusion short-circuits for diffusion within oxide scales in the temperature range from 800 to 1000 °C are considered to be oxide grain boundaries. According to Harrison,[37] three diffusion regimes could be identified. The A regime is defined by $\sqrt{Dt} \gg d$, d being the oxide grain size; in that case, the volume penetration is superior to the short-circuit size, especially the grain boundaries. The C regime claims that the penetration is continuous at the grain boundaries ($\sqrt{Dt} \ll \delta$, δ being the grain boundary width). Finally, the B regime is an intermediate regime where three processes participate in diffusion: volume, grain boundary, and lateral diffusion ($\delta \ll \sqrt{Dt} \ll d/2$).

Marker experiments made during oxidation in $^{18}O_2$ lead to the determination of oxygen diffusion coefficients via oxide grain boundaries and via the oxide bulk. Taking into consideration the plots of $\ln[^{18}O] = f(x)$, the first part of the curve corresponds to the apparent diffusion of oxygen (**Figure 3**). From the three diffusion regimes, the B regime is usually chosen for the study of intergranular diffusion.[38,39] In this

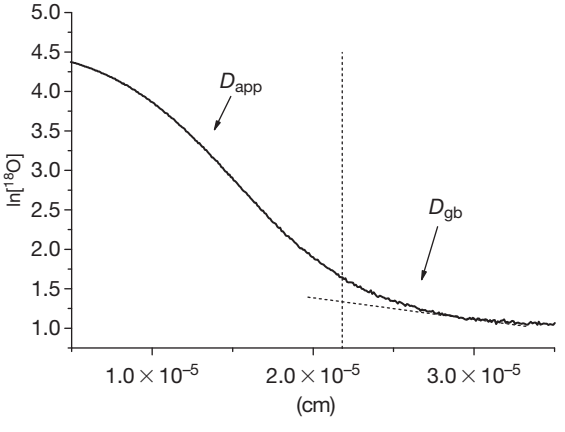

Figure 3 Plot of $\ln[^{18}O] = f(x)$ showing the zones where apparent and oxide grain boundary diffusion predominate.

regime, $\delta \ll \sqrt{Dt} \ll d/2$ with δ being the grain boundary width and d being the oxide grain size.

The apparent diffusion of oxygen corresponds to diffusion in the bulk and the oxide grain boundaries. It is expressed in the case of dislocation and bulk diffusion[40] but can be used in the case of grain boundary and bulk diffusion,[41,42] if we assume that the beginning of the oxygen distribution profile corresponds to D_{app} (A regime)[38]:

$$D_{app} = (1-f)D_b + f D_{gb} \qquad [20]$$

where f is the fraction of sites associated to the grain boundaries; f can be expressed as:

$$f = \frac{3\delta}{\phi} \qquad [21]$$

where δ is the grain boundary width (generally assumed to be 1 nm) and ϕ is the average oxide crystallite size.

D_{app} is determined from the second Fick's law solution:

$$\frac{C(x,t) - C_S}{C_0 - C_S} = \mathrm{erf}\left(\frac{x}{2\sqrt{D_{app}t}}\right) \qquad [22]$$

C_S is the oxygen 18 concentration at the oxide scale surface, C_0 is the natural concentration of oxygen 18 within the oxide layer (0.2 at.%[43]), and t is the diffusion time.

This model which associates the beginning of the distribution profile to an apparent diffusion coefficient has been recently discussed by Fielitz *et al.*[44] who proposed that the first part of the oxygen diffusion profile in polycrystalline mullite corresponded to the bulk diffusion coefficient in the B regime and not to the apparent diffusion coefficient.

The second part of the diffusion curve, $\ln[^{18}O] = f(x)$, led to determination of the oxygen grain boundary diffusion coefficient (**Figure 3**). By applying the model developed by Suzuoka[45,46] and Whipple–Le Claire[47–49] D_{gb} is expressed by:

$$D_{gb}\delta = 0.661\sqrt{\frac{4D_b}{t}}\left(-\frac{\partial \ln C}{\partial x^{6/5}}\right)^{-5/3} - D_{app} \qquad [23]$$

where $(\partial \ln C/\partial x^{6/5})$ is the slope of the curve $\ln[^{18}O] = f(x^{6/5})$.

By combining eqns [22] and [25], one obtains the following relation:

$$(1-f)D_b + \frac{0.661f}{\delta}\sqrt{\frac{4D_b}{t}}\left(-\frac{\partial \ln C}{\partial x^{6/5}}\right)^{-5/3} - D_{app} = 0 \qquad [24]$$

This relation allows the determination of the oxygen bulk diffusion coefficient, D_b. Using D_{app} and D_b, the relation [20] leads to the calculation of D_{gb}.

This calculation takes into consideration the oxide scale roughness.[50] The principle for determining the oxygen diffusion coefficients is the same, but the fraction of sites associated with grain boundaries is given by:

$$f_r = \frac{\phi/2}{\phi/2 + 2R_a} \times \frac{3\delta}{\phi} \qquad [25]$$

where R_a is the average roughness of the oxide scale.

Cation diffusion has also to be taken into account during oxide scale growth. Chromium 54 can be used as an isotopic marker in chromia (made of $^{56}Cr_2{}^{16}O_3$), and also in alumina (made of $^{27}Al_2{}^{16}O_3$). As a matter of fact and taking into account the fact that both chromium and aluminum cations diffuse in the same way, the results obtained for chromium diffusion coefficients in alumina scales are applied for aluminum cation diffusion coefficients in the same scale. Indeed, the use of a chromium isotope as a diffusive species is easier than the use of aluminum, which has no natural isotope; one can only use an artificial aluminum isotope, ^{26}Al, which is radioactive and very expensive. Very few studies have used this radioactive tracer.[51,52]

In the case of ^{54}Cr or ^{26}Al, the solution of the second Fick's law corresponding to a thin deposited layer is:

$$C(x) = C_0 \exp\left(-\frac{x^2}{4D_{app}t}\right) \qquad [26]$$

The procedure is the same as that applied for the determination of oxygen diffusion coefficients. The first part of the plot $\ln[C_{isotope}] = f(x)$ corresponds to D_{app} and the second part to D_{gb}.[53] D_{app} is calculated from the slope of $\ln[C_{isotope}] = f(x^2)$, whereas D_{gb} is determined from the Whipple–Le Claire model.

Figure 4[50,54–60] is an illustration of oxygen and chromium diffusion coefficients determined in thermally grown Cr_2O_3 scales formed on chromia-forming alloys. It appears clearly that, in thermally grown Cr_2O_3, the grain boundary diffusion coefficients (D_{gb}^{Cr} and D_{gb}^{O}) are higher than the bulk diffusion coefficients (**Figure 4**), in the considered temperature range. The large discrepancy in the diffusion coefficient values depends on the nature of the chromia-forming materials and on the presence or not of a reactive element.

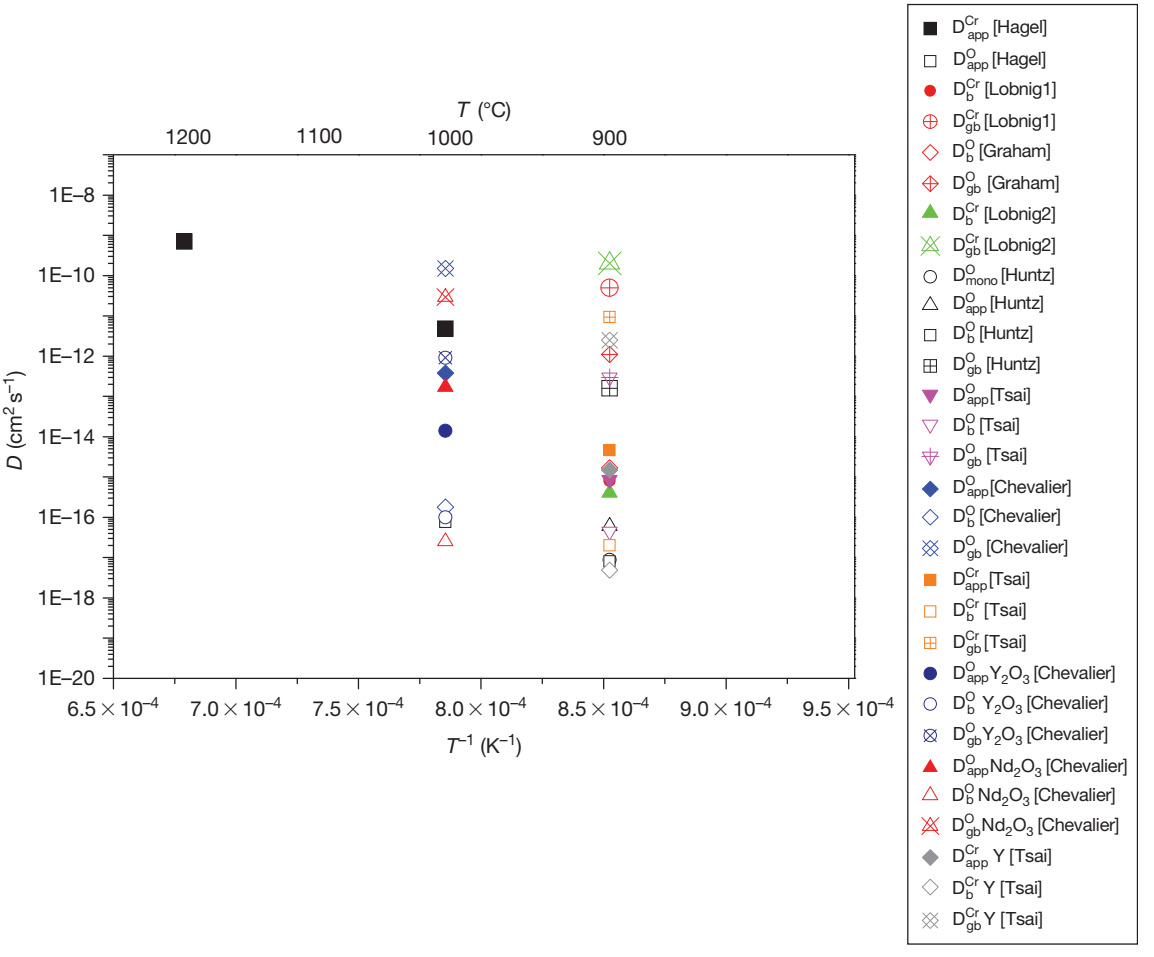

Figure 4 Comparison of oxygen or chromium diffusion coefficients in thermally grown chromia scales doped or not by RE (D^{O}_{app} is the apparent oxygen diffusion coefficient, D^{O}_{V} is the volume oxygen diffusion coefficient, D^{O}_{gb} is the grain boundary oxygen diffusion coefficient, D^{Cr}_{app} is the apparent chromium diffusion coefficient, D^{Cr}_{V} is the volume chromium diffusion coefficient, D^{Cr}_{gb} is the grain boundary chromium diffusion coefficient). The samples doped with RE are indicated by Y_2O_3, Nd_2O_3, or Y.

1.07.5 How to Investigate the High Temperature Corrosion Process

1.07.5.1 Surface Preparation

Particular attention has to be paid to the preparation of samples. Depending on the study, one has to ask if it is necessary to polish the surfaces (if the answer is positive, then one has to ask: 'up to which finishing grade? Is it necessary to achieve a mirror-like finish?') or to use sand blasting to prepare the surfaces or to degrease in ethanol or acetone (is it necessary to use an ultrasonic bath, deionized water?).

At this step in the preparation, the sample surface area has to be precisely determined, because all mass gain or loss will be divided by the sample surface area in order to make comparisons between tests.

1.07.5.2 High Temperature Corrosion Investigations

The tools used to investigate the high temperature reactivity of metallic materials are numerous: they can be basic (tubular or muffle furnaces, thermogravimetric devices,[61,62] ...) or more elaborate (corrosion under stress application,[63] oxidation with 18 oxygen,[64–68] ...).

For isothermal oxidation tests, the use of a thermobalance is of great interest, because it gives information about kinetics for more or less long exposures (see **Figure 2**). However, for most isothermal oxidation tests the duration in a thermobalance is relatively short (from 24 to 200–300 h typically) compared to real time in service conditions. Discontinuous

experiments can be used for long oxidation times; these allow the introduction of many samples (10–50 for example) all together in the same furnace (a muffle furnace is the most used) at a fixed temperature and removal of specimens after various times. By weighing each sample after such exposures, kinetic curves can be built for long periods (several thousands hours).

However, failure of oxide scales mainly occurs when the materials are subjected to thermal cycling conditions. The stresses, induced by temperature drops and rises, promote cracks and spalling, followed by drastic enhancement of the damage caused by the corrosive atmospheres.[69–74] Since thermal cycling treatments are usually more severe than isothermal oxidation, cyclic oxidation tests are widely performed in order to test the scale adherence under such severe conditions.[75–85] Cyclic oxidation experiments can be performed in a thermobalance (this means that the furnace or the sample is moved to produce cycling, but the sample is continuously weighed[86]), although, usually, net and gross weights are collected after automatic or manual cycles. The net weight gain corresponds to the specimen weight excluding any spalled scale. The gross weight gain corresponds to the specimen weight including any spalled scale collected in the crucible. The difference between the net and the gross weight gains indicates the proportion of spalled oxide scale. The results in **Figure 5** give an illustration of plots of net and gross weights for aluminide diffusion coatings on Fe–Cr alloys, which indicate cyclic behavior with and without spallation.[1]

1.07.5.3 High Temperature Corrosion Products Characterization

The complete understanding of oxide scale growth mechanisms needs a very careful analysis of the corrosion products. **Figure 6** illustrates most of the possibilities for characterizing thermally grown oxide scales.[1,87] Scanning electron microscopy (SEM) coupled with energy dispersive X-ray analyses (EDX) is probably the most useful analytical tool for observing oxide scales at the microscopic level. Coupled with XRD, it gives much necessary information about thermally grown oxide scales. However, one has also to consider optical microscopy; this gives more macroscopic information, which is often sufficient for evaluating the oxidation behavior of metals and alloys. Another convenient tool for studying oxide scales is transmission electron microscopy (TEM), which allows observations of the scale morphology at the nanometric scale, in association with local chemical analyses and microdiffraction.[88] Unfortunately, two main difficulties limit the use of this technique:

- sample preparation is very delicate and needs long and difficult manipulations,[88–90] even though the use of a focused ion beam (FIB) drastically increases the chance of success for sample preparation[91–97]),
- the correspondence between the nanometric and the macrometric scale is often difficult and needs repeated observations.

These parameters are the reasons why TEM observations are usually the last step in the characterization process, which logically evolves from macro- to nanoscale, and not the opposite!

A second very promising tool is the use of two stage oxidation experiments in $^{16}O_2/^{18}O_2$. This method consists of using an oxygen isotope, ^{18}O, as a marker in a preformed ^{16}O containing layer. The principle is to oxidize the metallic substrate first under a $^{16}O_2$ atmosphere; the reaction chamber is evacuated and $^{18}O_2$ is introduced for the second step of the test, without temperature modification. The technique has been largely used not only to study oxide scale growth mechanisms, but also to determine oxygen diffusion coefficients in many chemical systems.[44,98–102] The method can be extended to marker experiments in water vapor by making successive exposure to $H_2\,^{16}O/H_2\,^{18}O$.[103] The oxygen isotope distributions are followed using secondary ion mass spectrometry (SIMS) or secondary neutral mass spectrometry (SNMS). Very careful analyses of the oxygen isotope distribution profiles allow determination of the oxygen diffusion coefficients in growing scales. **Figure 7** shows three limiting cases corresponding to the diffusion of cations (**Figure 7(a)**), to the diffusion of anions (**Figure 7(b)**) and to mixed diffusion (**Figure 7(c)**). Bulk and grain boundary diffusion coefficients for oxygen were calculated using the models proposed by Suzuoka[45,46] and Whipple–Le Claire.[47,48]

More recently, other characterization tools have been used in the field of high temperature corrosion. These give complementary information and, together with 'more classical' analyses, they allow the determination and understanding of oxide scale growth mechanisms. Among these techniques, Raman spectroscopy,[104–108] photoluminescence spectroscopy (PLS),[35,109–114] X-ray photoelectron spectrometry (XPS),[34,35,115–117] and photoelectrochemistry[118–121] are probably the most interesting tools.

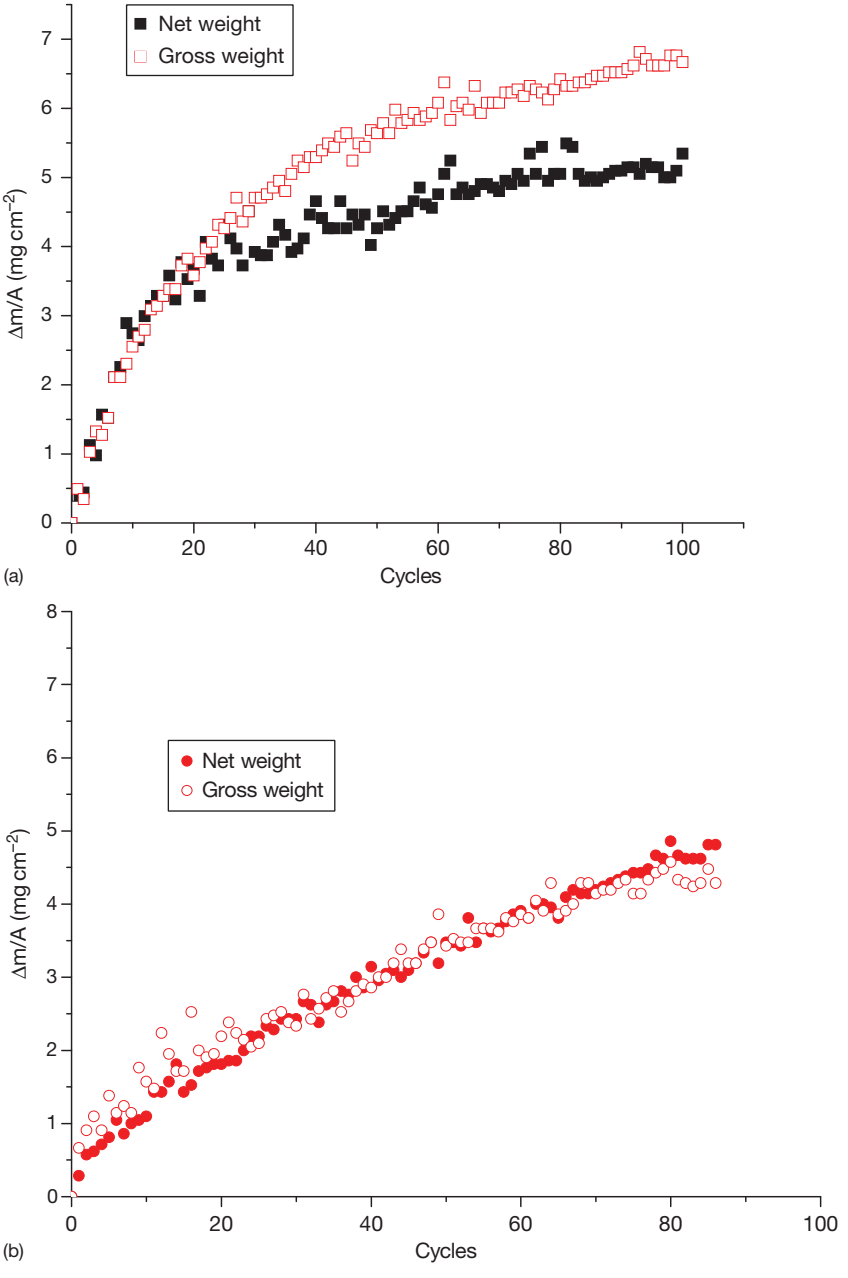

Figure 5 Cyclic oxidation kinetics (24 h cycle at 1000 °C); case of aluminized diffusion coatings: (a) the deviation between gross and net weights means oxide spallation and (b) when doped with Y_2O_3, there is no spallation. Reproduced from Chevalier, S. Traitements de surface et nouveaux matériaux: quelles solutions pour lutter contre la dégradation des matériaux à haute température?; Les Editions Universitaires de Dijon, 2007.

Generally, the study of the corrosion products is performed '*ex situ*,' which means after the specimen has cooled down to room temperature. How can one be sure that what is observed at room temperature is representative of what happened at the oxidation temperature? *In situ* analyses are able to follow the oxidation reactions at the oxidation temperature. X-ray diffraction devices equipped with high temperature furnaces were developed in order to follow the evolution of crystallographic phases during the oxidation process of metallic substrates and of the underlying substrate microstructure under oxidizing conditions.[122] The technique is also able to follow growth stress evolution during the establishment of

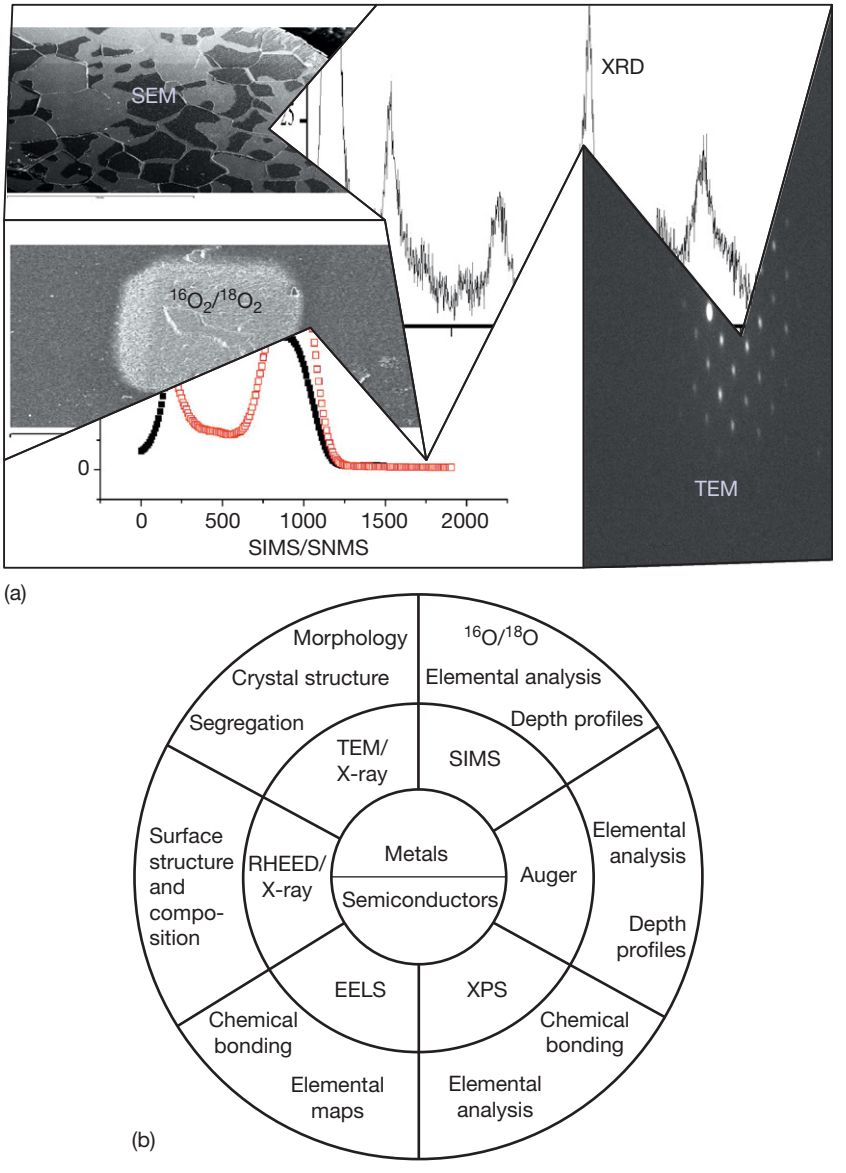

Figure 6 Illustration of characterization tools to analyze thermally grown oxide scale. Part (a) adapted from Chevalier, S. Traitements de surface et nouveaux matériaux: quelles solutions pour lutter contre la dégradation des matériaux à haute température?; Les Editions Universitaires de Dijon, 2007 and part (b) adapted from Graham, M. J. *Mater. High Temp.* **2000**, *17*, 1.

the growing scales.[123,124] More recently, texture analyses of the oxide scale as well as of the metallic substrate has been followed during the formation and growth of the corrosion products. These '*in situ*' characterizations are very useful for understanding the oxide scale growth mechanisms, for understanding the role played by minor elements on their formation and for linking the chemical properties of the scale to its mechanical properties. Figure 8 gives an illustration of the use of *in situ* XRD; it allows one to follow the phase formation and transformation during oxidation at 950 °C of a Y_2O_3 coated-Fe–30Cr alloy. It shows that the peak corresponding to the substrate (Fe–30Cr) disappears after 60 min of oxidation, which corresponds to the formation of $YCrO_3$.

1.07.5.4 Prediction and Modeling of High Temperature Oxidation

In order to prevent high temperature degradation due to oxidation, predictive modeling has been

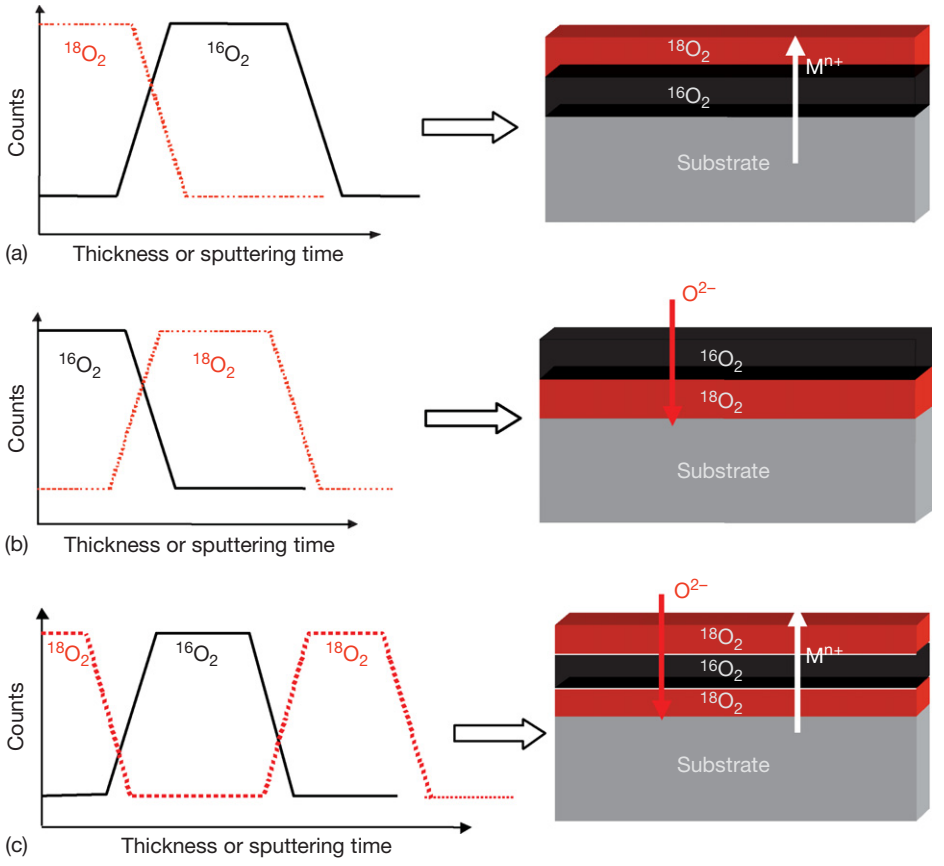

Figure 7 Three main cases encountered during two stage oxidation experiments. The location of ^{18}O compared to the ^{16}O containing scale leads to the understanding of thermally grown oxide scales, (a) diffusion of cation, (b) diffusion of anion, and (c) mixed diffusion.

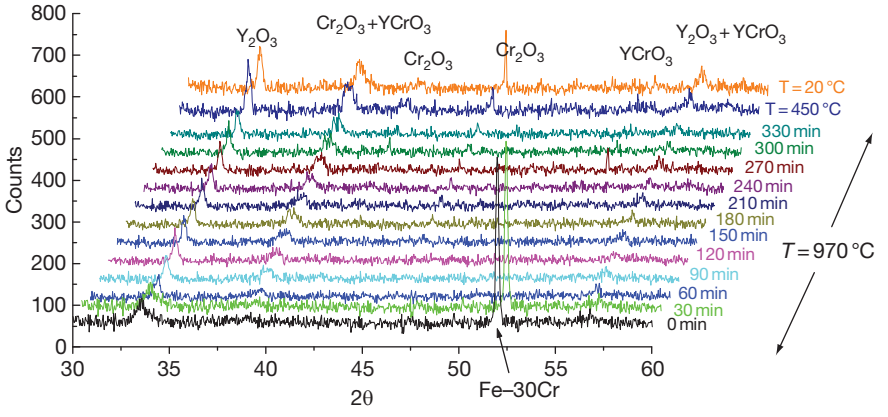

Figure 8 *In situ* XRD following phase formation and transformation during oxidation at 950 °C of a Y_2O_3 coated-Fe-30Cr alloy. Adapted from Chevalier, S. Traitements de surface et nouveaux matériaux: quelles solutions pour lutter contre la dégradation des matériaux à haute température?; Les Editions Universitaires de Dijon, 2007.

developed. This aspect is of particular interest for industrialists who need to target several thousands of hours in service condition. For alumina-forming alloys, it was shown that there was a critical Al level below which an alumina scale was no more able to grow and form a protective oxide scale. For a binary alloy, this critical value was established from Wagner's theory as:[125]

$$c_B = f\left(\sqrt{\frac{k_c}{2\tilde{D}}}\right) \text{ with } f(u) = \pi^{1/2} u(1 - \text{erf}\, u) \exp u^2 \quad [27]$$

with k_c ($cm^2\,s^{-1}$) the parabolic rate constant and $\tilde{D}$ ($cm^2\,s^{-1}$) the interdiffusion coefficient of aluminum and iron.

When the Al concentration reaches this critical value, a catastrophic oxidation phenomenon occurs, because of the formation of iron and chromium oxides, which soon leads to complete destruction of the samples. Recently, Strehl *et al.*[126] also proposed a method, based on Wagner's theory, to determine the critical Al concentration leading to catastrophic oxidation. They found that this critical value was dependent on temperature and varies from 0 wt% at 1000 °C to 3 wt% at 1300 °C. Quadakkers and Bongartz[127] established predictive diagrams for the life time of metallic materials. The proposed diagrams were obtained from kinetic considerations:

$$t_B = 4.4 \times 10^{-3}(C_0 - C_B)\rho d k^{-1/n}(\Delta m^*)^{-1/(n-1)} \quad [28]$$

where t_B corresponds to the start of catastrophic oxidation, k and n are kinetic constants and exponents established from $\Delta m^* = \Delta m/S = kt^n$, C_0 is the initial aluminum concentration, C_B is the critical Al concentration, ρ is the alloy density, d is the sample thickness, and Δm^* is the total weight gain measured during the thermal treatment. This modeling was in agreement with experimental data in order to predict the beginning of oxide scale spallation in Fe–Cr–Al foils at 1100 °C.[128]

Recent models developed by Monceau[129,130] and Smialek[131] predict the life time for alloys exposed to cyclic tests. The correlation between modeling and experimental data is clear, despite simple hypotheses.

1.07.6 High Temperature Oxidation Behavior of Metals and Alloys

1.07.6.1 Description of Chromia- and Alumina-Forming Materials

In the real world, it is rare to find pure metals; most of the time, alloys, which contain minor elements, such as Cr, Al, Si, Ti, etc., are used. Generally speaking, steels are iron-based and contain between 0.02 and 2.06 wt% carbon. Cast-irons correspond to a level of C over 2.06 wt%. Other alloys used at high temperatures are usually Ni- or Co-base.

In the field of high temperature oxidation, the classical alloys are chromia-forming (i.e., being able to form a chromia, Cr_2O_3, layer) or alumina-forming (i.e., being able to form an alumina, Al_2O_3, layer). These oxide scales, together with silica, SiO_2, layers, are the most protective scales for protection against high temperature degradation. These refractory oxides have high melting points (2330 °C for Cr_2O_3, 2054 °C for Al_2O_3 and 1713 °C for SiO_2[132,133]) and grow on Fe-, Ni-, or Co-base alloys, which contain at least 12 wt% Cr for the chromia-forming alloys,[134] associated with at least 5 wt% Al for the alumina-forming alloys.[135] One has also to distinguish ferritics (containing elements able to stabilize the α-Fe phase, such as Cr) from austenitic steels (containing elements able to stabilize the γ-Fe phase, such as Ni).[1,136] Some steels can be also martensitic or duplex in nature. The properties of the different categories of steel depend on minor element additions. As an example, **Figure 9** gives a comparison of thermal expansion coefficients, TEC, for different materials and oxides.[137] The formation of a continuous silica layer is guaranteed in the case of silicides, $MoSi_2$ or $FeSi_2$, but their physical and chemical properties are very different from those of chromia- and alumina-forming alloys. In many cases, Si is added as a minor element to the latter alloys and contributes to the formation of a discontinuous scale below the main oxide scales.[138]

As indicated previously, chromia- and alumina-forming materials usually guarantee the establishment of parabolic regimes, which are the most protective. One can note that the parabolic rate law constants for alumina-forming alloys are lower than those for chromia-forming alloys (**Figure 10**).[12] This means that the oxidation rate is lower when an alumina scale grows on an alloy surface. Growth of SiO_2 scales result in similar parabolic rate constants as those of Al_2O_3 scales.

1.07.6.2 Oxide Scale Spallation: Mechanical Properties and Stress

When they are used under appropriate conditions (maximum temperatures of 1000 and 1300 °C, for M–Cr and M–Cr–Al, respectively), Cr_2O_3 and Al_2O_3 scales possess the main protective properties needed for high temperature service conditions, at least under isothermal conditions (for a fixed temperature without thermal shocks). When exposed to thermal cycling

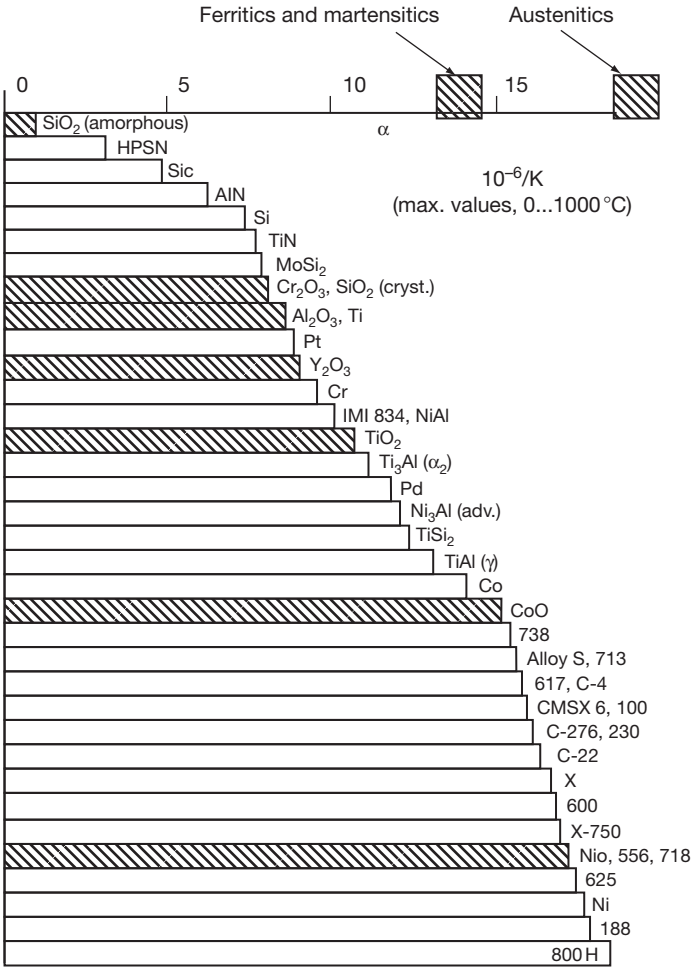

Figure 9 Comparison of thermal expansion coefficients of different materials and oxides. Reproduced from Schuetze, M. In Proceedings of the Euroconference 2000 ProEnMach, Clausthal-Zellerfeld, Germany, 20–22 Juillet 2000.

(repeated heating and cooling), the adherence of the oxide scales is often poor and limits the life time of alloys considerably.[139–142] The more the amplitude of the thermal shocks, the more is the tendency for the oxide scale to spall off or crack, making the underlying substrate free of any protection. The reasons why the oxide layers detach from the substrates are mainly due to the difference in TEC between the oxides and the substrates (**Figure 9**), which generates thermal stress. Various stresses are able to develop in the oxide scales: growth stress, thermal stress, and residual stress (as a first approximation, residual stress can be ascribed to the addition of both growing and thermal stress). They play a considerable role in the high temperature corrosion mechanisms and their determination gives fundamental information on the way to increase the corrosion resistance.[4,143–150] Another reason for stress generation in thermally grown oxide scales is associated with the volume change between the oxide and the native metal; this change is characterized by the Pilling–Bedworth ratio (PBR) and corresponds to the growth stress within the scale.[151,152] **Table 1** gives values of PBR for different oxides.[152] When PBR < 1, the volume of oxide is lower than the volume of metal and tensile stress appears in the oxide scale. When PBR > 1, the volume of oxide is higher than the volume of metal and compressive stress appears in the oxide scale. Several complementary models deal with growth stresses and attribute them to microstructural and/or diffusion considerations,[153–157] but are based on the general models established in the past.[151,158]

Geometry is also a parameter that influences the mechanical properties of the scale and has a huge

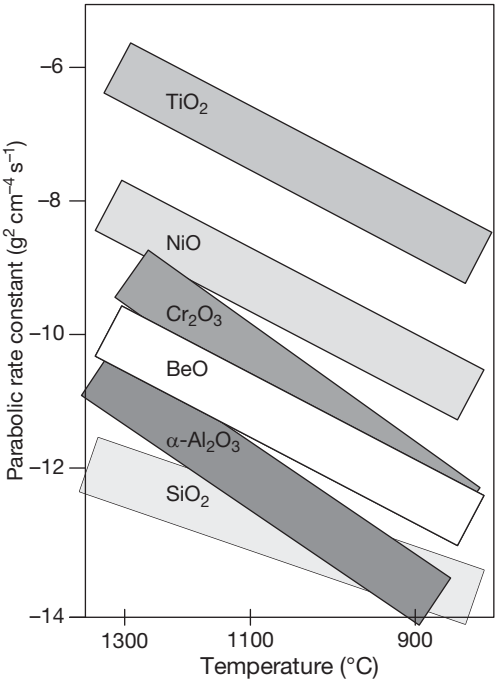

Figure 10 Parabolic rate constants in oxide scales. Adapted from Hindam, H.; Whittle, D. P. *Oxid. Met.* **1982**, *18*, 245.

Table 1 Pilling–Bedworth ratio for different oxides

Oxides	*Pilling–Bedworth ratio*
K_2O	0.45
MgO	0.81
Na_2O	0.97
Al_2O_3	1.28
ThO_2	1.3
ZrO_2	1.56
Cu_2O	1.64
NiO	1.65
TiO_2	1.76
CoO	1.86
Cr_2O_3	2.07
Ta_2O_5	2.5
Nb_2O_5	2.68
V_2O_5	3.19
WO_3	3.3

impact on the oxide scale adherence.[152] The stress generated in an oxide scale as is thermally grown on a tube is not the same as that in an oxide grown on a flat coupon.[159]

However, the amplitude of oxide spallation cannot be always ascribed to residual stress in the scale.[160] Oxide spallation is also strongly connected to the process of growth of the oxide scale. During its thermal growth, cation vacancies are generated at the metal–oxide interface; if they coalesce together, cavities are formed, weakening the interface.[161]

It appears then clearly that it is necessary to consider the chemical evolution of the oxide scale together with its mechanical evolution, as well as its relationships with the underlying substrate.

1.07.6.3 Role of Minor Elements

As indicated by their name, alloys contain minor element additions which improve their mechanical properties, their corrosion resistance, etc. As a matter of fact, thermally grown oxide scales are never pure chromia or alumina. By reacting with them, mixed oxides are formed; these include the spinel phase, $(Mn,Cr)_3O_4$,[162,163] perovskite, $MCrO_3$[164–168] or $MAlO_3$,[169] or garnet, $Y_3Al_5O_{12}$.[170–173] Nevertheless, these phases are usually less protective than chromia or alumina. Some additions have a particularly large influence on the high temperature performance of alloys; so-called reactive elements (RE), decrease the oxidation rate and strongly increase the oxide scale adherence.[1,6,174]

1.07.6.4 Reactive Element Effect (REE)

The beneficial effect of the RE on the high temperature resistance of alloys has been known for more than 50 years.[175,176] Even if the reasons why REs are so efficient are not fully understood, several hypotheses have been proposed in order to explain their beneficial effects. According to the large numbers of published papers on this problem, there is probably no single theory that is able to explain their role, irrespective of the tested materials, the native oxide scale, or the nature of the oxidizing atmosphere.[177] As an example, some RE additions give the well-known beneficial effect, whereas others can have a detrimental influence on the oxidation performance of the alloy.

A decrease in the oxidation rate and an improvement in the oxide layer adherence are usually the final result arising from RE additions.[1,178] Generally, REs favor the nucleation and the growth of scales.[179–183] They decrease the oxide grain size, and consequently change scale plasticity[184,185] and creep,[186,187] which can modify the growth and/or thermal stresses generated within the scale during its growth or on cooling to room temperature.[188–190] They prevent the detrimental sulfur effect[191–193] and suppress dislocation climb in the metal and, then, limit cation transport (poisoned interface model).[194,195] REs can also influence the

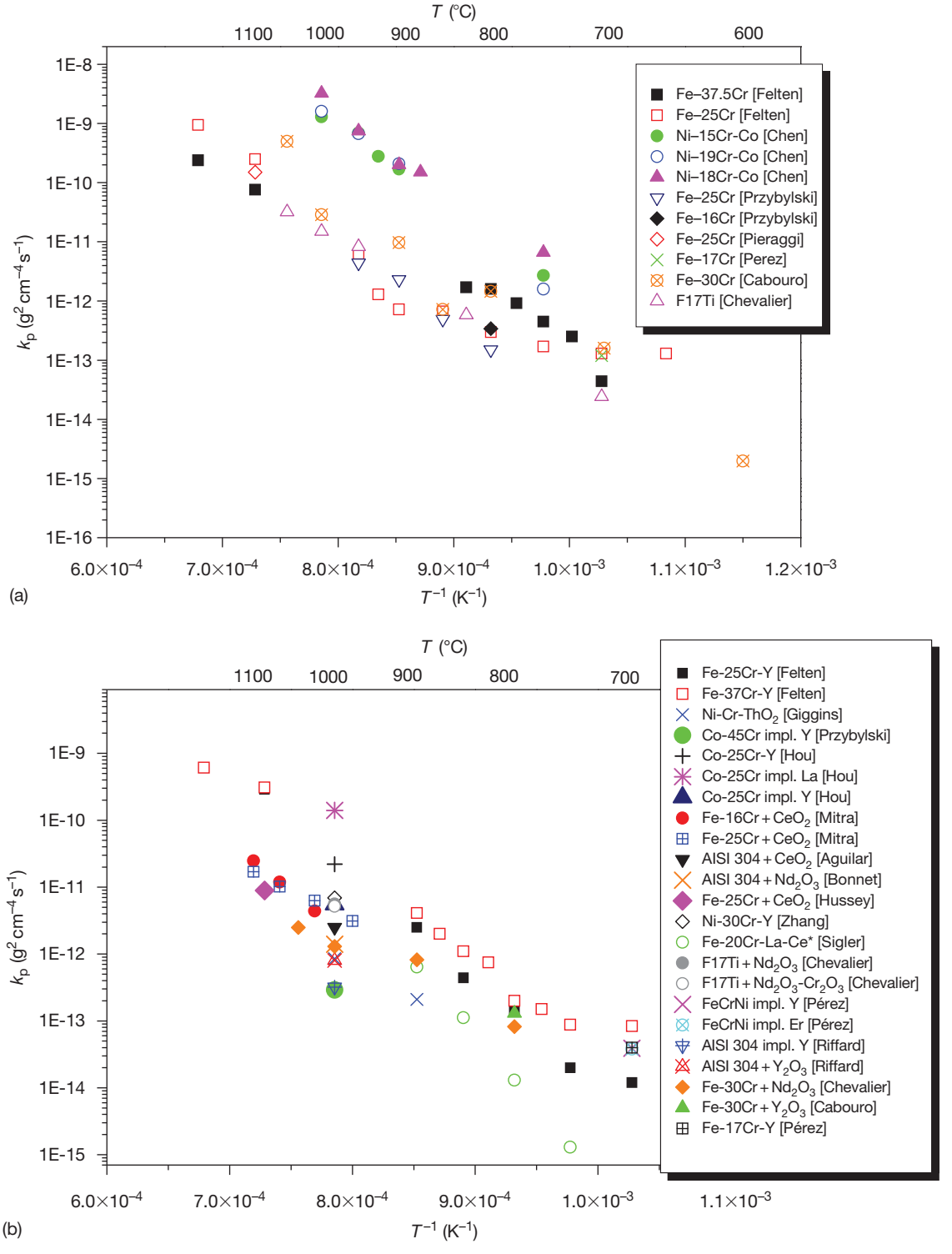

Figure 11 Parabolic rate constants established for the growth of chromia scales: (a) undoped and (b) RE doped alloys. (*Atmosphere N_2+H_2O+CO_2).

formation and/or transformation of transient phases, especially in alumina-forming alloys.[196,197]

1.07.6.4.1 Influence of RE on oxide scale growth kinetics

The RE influence on oxide scale growth rate is shown clearly on the kinetic curves for chromia-forming materials. The oxidation rate can be divided by a factor of 100 in the presence of the RE. The comparison of k_p values shown in **Figures 11(a)** and **11(b)**[198–214] illustrates this decrease. The influence of RE on alumina growth rates is much more limited.[215]

The quantity of RE introduced in the alloys plays a considerable role on the oxidation rates. When added in amounts above a critical content, the RE leads to negative effects, including a large increase in the oxidation rate.[216,217] This 'overdoping' effect is probably due to an increase in oxygen diffusion due to the presence of oxygen vacancies in the RE oxides (REO).

1.07.6.4.2 Influence of RE on oxide scale adherence

The most spectacular effect of RE introduction on oxide scale behavior is their much improved adherence to the underlying substrate.[213,218–220] Cyclic oxidation tests clearly show the resistance to spallation, since the oxide layers formed on the RE doped steels remain adherent to the alloys, even after many cycles (see example in **Figure 5**).

1.07.6.4.3 Location of RE in oxide scales

The RE is usually very difficult to detect within the oxide scale. Their presence at the surface of oxide layers as perovskite phases, $MCrO_3$[164,221–224] or $MAlO_3$,[225] garnets[217,226–228] or as not well defined phases ($CeTi_{21}O_{28}$,[229] $NdTi_{21}O_{38}$,[213] YAl_xO_y[230,231]) has been observed after long exposures in oxidizing atmospheres at high temperature.

The precise location of the RE within the oxide scale needs to be observed in TEM cross-sections.[232–247] Most of the TEM analyses have revealed the RE at the oxide grain boundaries within the thermally grown scale as well as at the metal–oxide interface. The RE solubility in Cr_2O_3 and in Al_2O_3 is very low (around 10 wt ppm for Y in Al_2O_3[248]).

Previous results have shown that the efficient dopant in thermally grown oxides (those for which the oxidation rate is decreased, the oxide scale adherence is improved and the oxide grain morphology is changed) usually segregates to the oxide grain boundaries. Nevertheless, other dopants, such as Ti, Nb, Ta, Ca, are found to segregate at the oxide grain boundaries but without giving any beneficial improvement in the oxide layer performances at high temperature.[249,250] The dopant size could play a role in its efficiency in increasing the oxidation resistance. However, the results are mainly contradictory. For example, no relationship could be found between the kinetics (k_p and mass gain) of REO coated-ferritic steels and the corresponding RE ionic radius.[1,251]

1.07.6.4.4 Influence of RE on oxide scale growth mechanism

The main consequence of the RE segregation at the oxide grain boundaries is a change in the oxide scale growth mechanism. The transport of oxygen becomes predominant in RE doped chromia layers,[252–255] as well as in alumina scales.[256–260]

Isotopic marker experiments in $^{16}O_2/^{18}O_2$ demonstrate the change in the oxide growth mechanism of RE doped oxides. The presence of the ^{18}O peak below the ^{16}O on SIMS profiles shows that oxygen transport is the main diffusion process during the scale growth.[261]

As a consequence, the morphology and the size of the oxide grains forming the scale change. Indeed, the annihilation of cation diffusion promotes the formation of equiaxed chromia grains,[262,263] instead of columnar grain for the undoped steels, and thin columnar alumina grains for alumina scales, instead of coarse oxide grains.[264,265]

The segregation of RE at oxide grain boundaries leads also to a decrease in the oxygen diffusion coefficient[1,215] even if the results appear somewhat contradictory.

The change in the oxide scale growth mechanism associated with the decrease in the oxygen diffusion are the main reasons why REs lead to improved adhesion and slower growth rates for chromia scales and improved adhesion for alumina scales.

References

1. Chevalier, S. Traitements de surface et nouveaux matériaux: quelles solutions pour lutter contre la dégradation des matériaux à haute température? Les Editions Universitaires de Dijon, 2007.
2. Huntz, A. M.; Pieraggi, B. *Oxydation des métaux et alliages*; Lavoisier: Paris, 2003.
3. Bénard, J. *L'oxydation des métaux*; Gauthier-Villars et C^ie^: Paris, 1962.
4. Béranger, G.; Colson, J. C.; Dabosi, F. *Corrosion des Matériaux à Haute Température*; Les Editions de Physique, Ecole d'Hiver du CNRS: Piau-Engaly, 1985.

5. Caillet, M.; Galerie, A.; Audisio, S.; Mazille, H. *La protection contre la corrosion*; Les Editions de Physique: Paris, 1987.
6. Kofstad, P. *High Temperature Corrosion*; Elsevier Applied Science, 1988.
7. Sarrazin, P.; Galerie, A.; Fouletier, J. *Les mécanismes de la corrosion sèche. Une approche cinétique*; EDP Sciences, 2000.
8. Green, A.; Bastow, B. In Proceedings of the 2nd International Conference on the Microscopy of Oxidation; Newcomb, S. B., Bennett, M. J., Eds.; Maney Publishing, **1993**; p 137.
9. Jianian, S.; Longjiang, Z.; Tiefan, L. *Oxid. Met.* **1997**, *48*, 347.
10. Yurek, Z. *Solid State Phenom.* **1995**, *41*, 185.
11. Henry, S. PhD Thesis, INPG, Grenoble, 2000.
12. Hindam, H.; Whittle, D. P. *Oxid. Met.* **1982**, *18*, 245.
13. Schütze, M. Proceedings of the Euroconference 2000 ProEnMach Clausthal-Zellerfeld: Germany, 20–22 Juillet, 2000.
14. Tien, J. K.; Davidson, J. M. In *Stress Effects and the Oxidation of Metals*; Cathcart, J. V., Ed.; AIME: New York, 1975; p 200.
15. Delaunay, D.; Huntz, A. M.; Lacombe, P. *Corros. Sci.* **1980**, *20*, 1109.
16. Huntz, A. M. *Mater. Sci. Technol.* **1988**, *4*, 1079.
17. Huntz, A. M.; Schuetze, M. *Mater. High Temp.* **1994**, *12*, 151.
18. Evans, H. E. *Mater. High Temp.* **1994**, *12*, 219.
19. Evans, H. E. *Int. Mater. Rev.* **1995**, *40*, 1.
20. Schuetze, M. *J. Corros. Sci. Eng.* **2003**, *6*; http://www.umist.ac.uk/corrosion/ JCSE/
21. Tolpygo, V. K.; Clarke, D. R. *Mater. Sci. Eng. A* **2000**, *278*, 142.
22. Brumm, M. W.; Grabke, H. J. *Corros. Sci.* **1993**, *34*, 547.
23. Gaboriaud, R. *Thermodynamique: Eléments fondamentaux de l'énergétique et de la cinétique chimique*; Ellipses: Paris, 1998.
24. Levin, E. M.; McMurdie, H. F. *Phase Diagrams for Ceramists*; The American Ceramic Society, 1975; p 17.
25. Barret, P. *Cinétique hétérogène*; Gauthier-Villars: Paris, 1973.
26. Soustelle, M. *Modélisation macroscopique des transformations physico-chimiques*; Masson: Paris, 1990.
27. Antoni, L.; Galerie, A. Corrosion sèche des métaux, Techniques de l'Ingénieur, 2003, M4 228, p 9.
28. Quadakkers, W. J.; Naumenko, D.; Wessel, E.; Kochubey, V.; Singheiser, L. *Oxid. Met.* **2004**, *61*, 17–37.
29. Cox, B. *J. Nucl. Mater.* **2005**, *336*, 331.
30. Pétigny, N.; Barberis, P.; Lemaignan, C.; Valot, C. H.; Lallemant, M. J. *J. Nucl. Mater.* **2000**, *280*, 318.
31. Tupin, M.; Pijolat, M.; Valdivieso, F.; Soustelle, M.; Frichet, A.; Barberis, P. *J. Nucl. Mater.* **2003**, *317*, 130.
32. Monceau, D.; Pieraggi, B. *Oxid. Met.* **1999**, *50*, 477.
33. Cadoret, Y.; Monceau, D.; Bacos, M. P.; Josso, P.; Maurice, V.; Marcus, P. *Oxid. Met.* **2005**, *64*, 185.
34. Chevalier, S.; Molins, R.; Heintz, O.; Larpin, J. P. In Proceedings of the 6th International Conference on the Microscopy of Oxidation, Birmingham, England; Tatlock, G. J., Evans, H. E., Eds.; **2005**; p 365.
35. Chevalier, S.; Galerie, A.; Heintz, O.; Chassagnon, R.; Crisci, A. *Mater. Sci. Forum* **2008**, *595–598*, 915.
36. Wagner, C. *J. Electrochem. Soc.* **1952**, *99*, 369.
37. Harrison, L. G. *Trans. Faraday Soc.* **1961**, *57*, 1191.
38. Philibert, J. *Diffusion et transport de matière dans les solides*; Les Editions de Physique, 1990; p 227.
39. Philibert, J.; Vignes, A.; Bréchet, Y.; Combrade, P. *Métallurgie: Du Minerai au Matériau*; Masson, **1998**, p 389.
40. Hart, E. W. *Acta. Metall.* **1957**, *5*, 597.
41. Smeltzer, W. W.; Haering, R. R.; Kirkaldy, J. S. *Acta Metall.* **1961**, *9*, 880.
42. Atkinson, A.; Taylor, R. I.; Hughes, A. *Philos. Mag. A* **1982**, *45*, 823.
43. Lederer, C. M.; Hollander, J. M.; Perlman, I. *Table of Isotopes*, 6th ed.; Wiley: New-York, 1967.
44. Fielitz, P.; Borchardt, G.; Schmücker, M.; Schneider, H. *Solid State Ionics* **2003**, *160*, 75.
45. Suzuoka, T. *Trans. Jpn. Inst. Met.* **1961**, *2*, 25.
46. Suzuoka, T. *J. Phys. Soc. Jpn.* **1964**, *19*, 839.
47. Whipple, R. T. P. *Philos. Mag.* **1954**, *45*, 1225.
48. Le Claire, A. D. *Philos. Mag.* **1962**, *7*, 141.
49. Nowick, A. S.; Burton, J. J. Eds. *Diffusion in Solids*; Academic Press, 1975.
50. Tsaï, S. C.; Huntz, A. M.; Dolin, C. *Oxid. Met.* **1995**, *43*, 581.
51. Le Gall, M.; Lesage, B.; Bernardini, J. *Philos. Mag. A* **1994**, *70*, 761.
52. Fielitz, P.; Borchardt, G.; Schücker, M.; Schneider, H. *Solid State Ionics* **2006**, *177*, 493.
53. Tsaï¨, S. C.; Huntz, A. M.; Dolin, C. *Mater. Sci. Eng. A* **1996**, *212*, 6.
54. Chevalier, S.; Bonnet, G.; Borchardt, G.; Colson, J. C.; Larpin, J. P. *Ceram. Polish Ceram. Bull.* **2000**, *61*, 177.
55. Hagel, W. C.; Seybolt, A. U. *J. Electrochem. Soc.* **1961**, *108*, 1146.
56. Hagel, W. C. *J. Am. Ceram. Soc.* **1965**, *48*, 70.
57. Lobnig, R. E.; Schmidt, H. P.; Hennesen, K.; Grabke, H. J. *Oxid. Met.* **1992**, *37*, 81.
58. Graham, M. J.; Eldridge, J. I.; Mitchell, D. F.; Hussey, R. J. *Mater. Sci. Forum* **1989**, *43*, 207.
59. Huntz, A. M. *J. Phys. III France* **1995**, *5*, 1729.
60. Tsaï, S. C.; Huntz, A. M.; Philibert, J. *Defects Diffusion Forum* **1997**, *143–147*, 1195.
61. Nicholls, J. R. In *Guidelines for Methods of Testing and Research in High Temperature Corrosion*; Grabke, H. J., Meadowcroft, D. B., Eds.; **1995**, p 11.
62. Grabke, H. J. In *Guidelines for Methods of Testing and Research in High Temperature Corrosion*; Grabke, H. J., Meadowcroft, D. B., Eds.; **1995**, p 52.
63. Gosmain, L. Ph.D. Thesis, Université de Bourgogne, Dijon, 2001.
64. Jedlinski, J. *Solid State Phenom.* **1992**, *21–22*, 335.
65. Göbel, M. Ph.D. Thesis. Technische Universität Clausthal, Clausthal-Zellerfeld, 1997.
66. Åkermark, T. *Oxid. Met.* **1998**, *50*, 167.
67. Berger, P.; Gaillet, L.; El Tahhann, R.; Moulin, G.; Viennot, M. *Nucl. Instr. Meth. Phys. Res. B* **2001**, *181*, 382.
68. Alibhai, A. A.; Chater, R. J.; McPhail, D. S.; Shollock, B. A. *Appl. Surf. Sci.* **2003**, *203–204*, 630.
69. Delaunay, D.; Huntz, A. M.; Lacombe, P. *Corros. Sci.* **1980**, *20*, 1109.
70. Huntz, A. M. *Mater. Sci. Technol.* **1988**, *4*, 1079.
71. Huntz, A. M.; Schütze, M. *Mater. High Temp.* **1994**, *12*, 151.
72. Evans, H. E. *Mater. High Temp.* **1994**, *12*, 219.
73. Evans, H. E. *Int. Mater. Rev.* **1995**, *40*, 1.
74. Evans, H. E. In Proceedings of the Workshop on Cyclic of High Temperature Materials; Schütze, M., Quadakkers, W. J., Eds.; IOM Communications, 1999; Vol. 27, p 3.
75. Moon, C. O.; Lee, S. B. *Oxid. Met.* **1993**, *39*, 1.
76. Smialek, J. L.; Jayne, D. T.; Schaeffe, J. C.; Murphy, W. H. *Thin Solid Films* **1994**, 253–285.
77. Jedlinski, J.; Bennett, M. J.; Evans, H. E. *Mater. High Temp.* **1994**, *12*, 169.

78. Pennefather, R. C.; Boone, D. H. *Surf. Coat. Technol.* **1995**, *76–77*, 47.
79. Chan, K. W. *Metal. Mater. Trans.* **1997**, *28A*, 411.
80. Gleeson, B.; Harper, M. A. *Oxid. Met.* **1998**, *49*, 373.
81. Strehl, G.; Al-Badairy, H.; Rodriguez, L. M.; Klöwer, J.; Borchardt, G.; Tatlock, G.; Criado, A. J. In Proceedings of the Workshop on Cyclic of High Temperature Materials; Schütze, M., Quadakkers, W. J., Eds.; IOM Communications, 1999; Vol. 27, p 82.
82. Chevalier, S.; Bonnet, G.; Valot, C.; Colson, J. C.; Larpin, J. P. In Proceedings of the Workshop on Cyclic of High Temperature Materials; Schütze, M., Quadakkers, W. J., Eds.; IOM Communications, 1999; Vol. 27, p 421.
83. Amano, T.; Watanabe, T.; Michiyama, K. *Oxid. Met.* **2000**, *53*, 451.
84. Baleix, S.; Bernhart, G.; Lours, P. *Mater. Sci. Eng.* **2002**, *A327*, 155.
85. Kulinska, A.; Choux, C.; Chevalier, S. *Intermetallics* **2008**, *16*, 1.
86. Vangeli, P. In ; Proceedings of the Workshop on Cyclic of High Temperature Materials; Schütze, M., Quadakkers, W. J., Eds.; IOM Communications, 1999; Vol. 27, p 198.
87. Graham, M. J. *Mater. High Temp.* **2000**, *17*, 1.
88. Rhüle, M.; Schumann, E. In *Guidelines for Methods of Testing and Research in High Temperature Corrosion*; Grabke, H. J., Meadowcroft, D. B., Eds.; EFC Publication 14, Maney Publishing, 1995, p 177.
89. Amelinckx, S. van Dyck, D. van Landuyt, J.; van Tendeloo, G. Eds. *Handbook of Microscopy: Applications in Materials Science, Solid-State Physics and Chemistry* Wiley-VCH, 1997, p 751.
90. Baunier, L. *Préparation des échantillons, Ecole Thématique: Microscopie des Défauts Cristallins*; St Pierre d'Oléron, 2001; p 393.
91. Langford, R. M.; Rogers, M. *Micron* **2008**, *39*, 1325.
92. Przybylski, K.; Chevalier, S.; Juzon, P.; Galerie, A.; Borchardt, G.; Heintz, O.; Larpin, J. P. *Mater. Sci. Forum* **2008**, *595–598*, 1103.
93. Tortorelli, P. F.; More, K. L.; Specht, E. D.; Pint, B. A.; Zschack, P. *Mater. High Temp.* **2003**, *20*, 57.
94. Fukuda, K.; Takao, K.; Hoshi, T.; Usui, Y.; Furukimi, O. *Mater. High Temp.* **2003**, *20*, 73.
95. Mayer, J.; Penkalla, H. J.; Dimyati, A.; Dani, M.; Untoro, P.; Naumenko, D.; Quadakkers, W. J. *Mater. High Temp.* **2003**, *20*, 167.
96. Ford, S.; Young, D. J.; McGrouther, D.; Munroe, P. R. In Proceedings of the 6th International Conference on The Microscopy of Oxidation, Birmingham, England,; Tatlock, G. J., Evans, H. E., Eds.; **2005**; p 183.
97. Svensson, H.; Stiller, K. In Proceedings. of the 6th International Conference on The Microscopy of Oxidation, Birmingham, England; Tatlock, G. J., Evans, H. E., Eds.; **2005**; p 237.
98. Kilo, M.; Borchardt, G.; Lesage, B.; Kaitasov, O.; Weber, S.; Scherrer, S. *J. Eur. Ceram. Soc.* **2000**, *20*, 2069.
99. Schmidt, H.; Borchardt, G.; Weber, S.; Scherrer, S.; Baumann, H.; Müller, A.; Bill, J. *J. Appl. Phys.* **2000**, *88*, 1827.
100. Kilo, M.; Borchardt, G.; Lesage, B.; Weber, S.; Scherrer, S.; Schroeder, M.; Schulz, O.; Martin, M. *Electrochem. Soc. Proc.* **2001**, *16*, 275.
101. Kilo, M.; Weller, M.; Borchardt, G.; Damson, B.; Weber, S.; Scherrer, S. *Defects Diffusion Forum* **2001**, *194–199*, 1039.
102. Legros, C.; Lesage, B.; Kilo, M.; Strehl, G.; Borchardt, G.; Carry, C. *Key Eng. Mater.* **2002**, *206–213*, 401.
103. Bamba, G.; Wouters, Y.; Galerie, A.; Borchardt, G.; Shimada, S.; Heintz, O.; Chevalier, S. *Scr. Mater.* **2007**, *57*, 671.
104. Mougin, J.; Le Bihan, T.; Lucazeau, G. *J. Phys. Chem. Solids* **2001**, *62*, 553.
105. Bouvier, P.; Godlewski, J.; Lucazeau, G. *J. Nucl. Mater.* **2002**, *300*, 118.
106. Kemdehoundja, M.; Dinhut, J. F.; Grosseau-Poussard, J. L.; Jeannin, M. *Mater. Sci. Eng. A* **2006**, *435–436*, 666.
107. Kadleikova, M.; Breza, J.; Vesely, M. *Microelectr. J.* **2001**, *32*, 955.
108. Krishnan, R.; Kesamoorthy, R.; Dash, S.; Tyagi, A. K.; Raj, B. *Scr. Mater.* **2003**, *48*, 1099.
109. Tolpygo, V. K.; Clarke, D. R. *Mater. High Temp.* **2000**, *17*, 59.
110. Peng, X.; Clarke, D. R.; Wang, F. *Oxid. Met.* **2003**, *60*, 225.
111. Laxman, S.; Franke, B.; Kempshall, B. W.; Sohn, Y. H.; Giannuzzi, L. A.; Murphy, K. S. *Surf. Coat. Technol.* **2004**, *177–178*, 121.
112. Murphy, K. S.; More, K. L.; Lance, M. J. *Surf. Coat. Technol.* **2001**, *146–147*, 152.
113. Sohn, Y. H.; Vaidyanathan, K.; Ronski, M.; Jordan, E. H.; Gell, M. *Surf. Coat. Technol.* **2001**, *146–147*, 102.
114. Mu, N.; Izumi, T.; Zhang, L.; Gleeson, B. *Mater. Sci. Forum* **2008**, *595–598*, 239.
115. Kuiry, S. C.; Seal, S.; Fei, W.; Quick, N. *Oxid. Met.* **2003**, *59*, 543.
116. Berthomé, G.; N'Dah, E.; Wouters, Y.; Galerie, A. *Mater. Corros.* **2005**, *56*, 389.
117. Maurice, V.; Despert, G.; Zanna, S.; Josso, P.; Bacos, M. P.; Marcus, P. *Acta Mater.* **2007**, *55*, 3315.
118. Petit, J. P.; Mermoux, M.; Wouters, Y.; Galerie, A.; Chemarin, C. *Mater. Sci. Forum* **2004**, *461–464*, 681.
119. Wouters, Y.; Bamba, G.; Galerie, A.; Mermoux, M.; Petit, J. P. *Mater. Sci. Forum* **2004**, *461–464*, 830.
120. Wouters, Y.; Marchetti, L.; Galerie, A.; Petit, J. P. *Corros. Sci.* **2008**, *50*, 1122.
121. Wouters, Y.; Galerie, A.; Petit, J. P. *Mater. Sci. Forum* **2008**, *595–598*, 1181.
122. Chevalier, S.; Strehl, G.; Borchardt, G.; Larpin, J. P.; Le Coze, J. *Matér. Technol.* **2003**, *7–8–9*, 71.
123. Bernard, F. PhD Thesis, Université de Bourgogne, Dijon, 1993.
124. Valot, C. PhD Thesis, Université de Bourgogne, Dijon, 1995.
125. Moulin, G.; Huntz, A. M.; Lacombe, P. *Acta Metall.* **1980**, *28*, 745.
126. Strehl, G.; Beaven, P.; Lesage, B.; Borchardt, G. *Mater. Corros.* **2006**, *56*, 778.
127. Quadakkers, W. J.; Bongartz, K. *Mater. Corros.* **1994**, *45*, 232.
128. Klöwer, J. *Mater. Corros.* **1998**, *49*, 758.
129. Poquillon, D.; Monceau, D. *Oxid. Met.* **2003**, *59*, 409.
130. Kartono, R.; Monceau, D.; Young, D. J. *Scr. Mater.* **2007**, *57*, 647.
131. Smialek, J. L. *Acta Mater.* **2004**, *52*, 2111.
132. www.matweb.com
133. Materials database from NIMS, www.NIMS.jp
134. Barralis, J.; Maeder, G. *Précis métallurgie: Elaboration, Structures-Propriétés, Normalisation*; Nathan: Paris, 1997.
135. Lacombe, P.; Barroux, B.; Béranger, G. *Les aciers inoxydables*; Les Editions de Physique: Paris, 1990.
136. Philibert, J.; Vignes, A.; Bréchet, Y.; Combrade, P. *Métallurgie: du minerai au matériau*; Masson: Paris, 1998.

137. Schuetze, M. In Proceedings of the Euroconference 2000 ProEnMach Clausthal-Zellerfeld: Germany, 20–22 Juillet, 2000.
138. Mikkelsen, L.; Linderoth, S.; Bilde-Sorensen, J. B. *Mater. Sci. Forum* **2004**, *461–464*, 117.
139. Schütze, M.; Quadakkers, W. J. *Cyclic Oxidation of High Temperature Materials*; IOM Communications: London, 1999.
140. Schütze, M.; Malessa, M. *Mater. Corros.* **2006**, *57*, 5.
141. Osgerby, S.; Pettersson, R. *Mater. Corros.* **2006**, *57*, 14.
142. Niewolak, L.; Malessa, M.; Coleman, S. Y.; Quadakkers, W. J.; Schütze, M. *Mater. Corros.* **2006**, *57*, 31.
143. Tien, J. K.; Davidson, J. M. In *Stress Effects and the Oxidation of Metals*; Cathart, J. V., Ed.; AIME: New York, 1975; p 200.
144. Delaunay, D.; Huntz, A. M.; Lacombe, P. *Corros. Sci.* **1980**, *20*, 1109.
145. Huntz, A. M. *Mater. Sci. Technol.* **1988**, *4*, 1079.
146. Huntz, A. M.; Schütze, M. *Mater. High Temp.* **1994**, *12*, 151.
147. Evans, H. E. *Mater. High Temp.* **1994**, *12*, 219.
148. Evans, H. E. *Int. Mater. Rev.* **1995**, *40*, 1.
149. Schütze, M. *J. Corros. Sci. Eng.*; 2003, 6 http://www.umist.ac.uk/corrosion/JCSE/.
150. Mougin, J.; Lucazeau, G.; Galerie, A.; Dupeux, M. *Mater. Sci. Eng. A* **2001**, *308*, 118.
151. Pilling, N. B.; Bedworth, R. E. *J. Inst. Met.* **1923**, *1*, 529.
152. Béranger, G.; Huntz, A. M.; Pieraggi, B. In *Corrosion des Matériaux à Haute Température*; Béranger, G., Colson, J. C., Dabosi, F., Eds.; Les Editions de Physique, Ecole d'Hiver du CNRS: Piau-Engaly, 1985; p 227.
153. Bernstein, H. L. *Metall. Trans. A* **1987**, *18*, 975.
154. Evans, H. E. *Intern. Mater. Rev.* **1995**, *40*, 1.
155. Bull, S. J. *Oxid. Met.* **1998**, *49*, 1.
156. Tolpygo, V. K.; Dryden, J. R.; Clarke, D. R. *Acta Mater.* **1998**, *46*, 927.
157. Clarke, D. R. *Acta Mater.* **2003**, *51*, 1393.
158. Rhines, F. N.; Wolf, J. S. *Metall. Trans.* **1970**, *1*, 1701.
159. Rosenband, V.; Gany, A. *Corros. Sci.* **1995**, *37*, 1991.
160. Tolpygo, V. K.; Clarke, D. R. *Mater. Sci. Eng. A* **2000**, *278*, 142.
161. Brumm, J. M. W.; Grabke, H. J. *Corros. Sci.* **1993**, *34*, 547.
162. Fergus, W. *Mater. Sci. Eng. A* **2005**, *397*, 271.
163. Quadakkers, W. J.; Greiner, H.; Hänsel, M.; Pattanaik, A.; Khanna, A. S.; Malléner, W. *Solid State Ionics* **1996**, *91*, 55.
164. Riffard, F.; Buscail, H.; Caudron, E.; Cueff, R.; Issartel, C.; Perrier, S. *Appl. Surf. Sci.* **2002**, *199*, 107.
165. Seybolt, A. U. *Corros. Sci.* **1966**, *6*, 263.
166. Downham, D. A.; Shendye, S. B. *Oxid. Met.* **1995**, *43*, 411.
167. Cristobal, M. J.; Gibson, P. N.; Stroosnijder, M. F. *Corros. Sci.* **1996**, *38*, 805.
168. Paul, A.; Odriozola, J. A. *Mater. Sci. Eng. A* **2001**, *300*, 22.
169. Tien, J. K.; Pettit, F. S. *Metall. Trans.* **1972**, *3*, 1587.
170. Cueff, R.; Buscail, H.; Caudron, E.; Riffard, F. *Mater. Sci. Forum* **2001**, *369–372*, 311.
171. Kim, K. Y.; Kim, S. H.; Kwon, K. W.; Kim, I. H. *Oxid. Met.* **1994**, *41*, 179.
172. Pint, B. A.; Hobbs, L. W. *J. Electrochem. Soc.* **1994**, *141*, 2443.
173. Pint, B. A. *Mater. Sci. Forum* **1997**, *251–254*, 397.
174. Lang, E. Ed. *The Role of Active Elements in the Oxidation Behaviour of High Temperature Metals and Alloys*; Elsevier Applied Science, 1989; p 33.
175. Pfeil, L. B. U.K. Patent 459848, 1937.
176. Pfeil, L. B. U.K. Patent 574088, 1945.
177. Quadakkers, J.; Singheiser, L. *Mater. Sci. Forum* **2001**, *369–372*, 77.
178. Lang, E. Ed. *The Role of Active Elements in the Oxidation Behaviour of High Temperature Metals and Alloys*; Elsevier Applied Science, 1989; p 111.
179. Stringer, J.; Wright, I. G. *Oxid. Met.* **1972**, *5*, 59.
180. Stringer, J.; Wilcox, B. A.; Jaffee, R. I. *Oxid. Met.* **1972**, *5*, 11.
181. Whittle, D. P.; Stringer, J. *Philos. Trans. R. Soc. Lond. A* **1980**, *295*, 309.
182. Yedong, H.; Stott, F. H. *Corros. Sci.* **1994**, *36*, 1869.
183. Ramanarayanan, T. A.; Ayer, R.; Petkovic-Luton, R.; Leta, D. P. *Oxid. Met.* **1988**, *29*, 445.
184. Zhang, Y.; Gerberich, W. W.; Shores, D. A. *J. Mater. Res.* **1997**, *12*, 697.
185. Zhu, D.; Stout, J. H.; Nelson, J. C.; Shores, D. A. *Mater. Sci. Forum* **1997**, *251–254*, 437.
186. Tolpygo, V. K.; Dryden, J. R.; Clarke, D. R. *Acta Mater.* **1998**, *46*, 927.
187. Tolpygo, V. K.; Clarke, D. R. *Oxid. Met.* **1998**, *49*, 187.
188. Huntz, A. M. *Mater. Sci. Eng. A* **1987**, *87*, 251.
189. Forest, C.; Davidson, J. H. *Oxid. Met.* **1995**, *43*, 479.
190. Sarioglu, C.; Stiger, M. J.; Blachere, J. R.; Janakiraman, R.; Schumann, E.; Ashary, A.; Pettit, F. S.; Meier, G. H. *Mater. Corros.* **2000**, *51*, 358.
191. Funkenbusch, A. W.; Smeggil, J. G.; Bornstein, N. S. *Metal. Trans. A* **1985**, *16*, 1164.
192. Lees, D. G. *Oxid. Met.* **1987**, *27*, 75.
193. Smialek, J. L. In Proceedings of the International Conference on the Microscopy of Oxidation; Bennett, M. J., Lorimer, G. W., Eds.; **1990**; p 258.
194. Pieraggi, B.; Rapp, R. A. *J. Electrochem. Soc.* **1993**, *140*, 2844.
195. Pieraggi, B.; Rapp, R. A.; Hirth, J. P. *Oxid. Met.* **1995**, *44*, 63.
196. Rommerskirchen, I.; Kolarik, V. *Mater. Corros.* **1996**, *47*, 625.
197. Montealegre, M. A.; Gonzalez-Carrasco, J. L. *Intermetallics* **2003**, *11*, 169.
198. Chen, J. H.; Rogers, P. M.; Little, J. A. *Oxid. Met.* **1997**, *47*, 381.
199. Felten, A. J. *J. Electrochem. Soc.* **1961**, *108*, 490.
200. Pérez, J.; Cristobal, M. J.; Hierro, M. P.; Arnau, G.; Botella, J. *Oxid. Met.* **2000**, *54*, 87.
201. Brylewski, T.; Prazuch, J.; Przybylski, K. *Ceram. Polish Ceram. Bull.* **2000**, *61*, 221.
202. Brylewski, T.; Nanko, M.; Maruyama, T.; Przybylski, K. *Solid State Ionics* **2001**, *143*, 131.
203. Pieraggi, B.; Rapp, R. A. *J. Phys. IV* **1993**, *3*, 275.
204. Cabouro, G.; Caboche, G.; Chevalier, S.; Piccardo, P. *J. Power Sources* **2006**, *156*, 39.
205. Giggins, C. S.; Pettit, F. S. *Metall. Trans.* **1971**, *2*, 1071.
206. Przybylski, K.; Garratt-Reed, A. J.; Yurek, G. J. *J. Electrochem. Soc.* **1988**, *135*, 509.
207. Hou, P. Y.; Stringer, J. *Oxid. Met.* **1988**, *29*, 45.
208. Mitra, S. K.; Roy, S. K.; Bose, S. K. *Oxid. Met.* **1990**, *34*, 101.
209. Bonnet, G.; Larpin, J. P.; Colson, J. C. *Solid State Ionics* **1992**, *51*, 11.
210. Hussey, R. J.; Papaiacovou, P.; Mitchell, D. F.; Graham, M. J. *Mater. Sci. Eng. A* **1989**, *120*, 147.
211. Zhang, Y.; Zhu, D.; Shores, D. A. *Acta Metall. Mater.* **1995**, *43*, 4015.
212. Sigler, D. R. *Oxid. Met.* **1996**, *46*, 335.
213. Chevalier, S.; Bonnet, G.; Larpin, J. P.; Colson, J. C. *Oxid. Met.* **1997**, *47*, 53.

214. Riffard, F.; Buscail, H.; Caudron, E.; Cueff, R.; Issartel, C.; Perrier, S. *Appl. Surf. Sci.* **2002**, *199*, 107.
215. Chevalier, S. In *Developments in High-Temperature Corrosion and Protection of Materials*; Gao, W., Li, Z., Eds.; Woodhead Publishing: Cambridge, England, 2008; Chapter 10.
216. Klöwer, J.; Li, J. G. *Mater. Corros.* **1996**, *47*, 545.
217. Klöwer, J. *Mater. Corros.* **2000**, *51*, 373.
218. Chevalier, S.; Bonnet, G.; Larpin, J. P.; Colson, J. C. *Corros. Sci.* **2003**, *45*, 1661.
219. Chevalier, S.; Larpin, J. P. *Mater. Sci. Eng. A* **2003**, *363*, 116.
220. Chevalier, S.; Dawah Tankeu, A. P.; Buscail, H.; Issartel, C.; Borchardt, G.; Larpin, J. P. *Mater. Corros.* **2004**, *55*, 610.
221. Seybolt, A. U. *Corros. Sci.* **1966**, *6*, 263.
222. Downham, D. A.; Shendye, S. B. *Oxid. Met.* **1995**, *43*, 411.
223. Cristobal, M. J.; Gibson, P. N.; Stroosnijder, M. F. *Corros. Sci.* **1996**, *38*, 805.
224. Paul, A.; Odriozola, J. A. *Mater. Sci. Eng. A* **2001**, *300*, 22.
225. Tien, J. K.; Pettit, F. S. *Metall. Trans.* **1972**, *3*, 1587.
226. Kim, K. Y.; Kim, S. H.; Kwon, K. W.; Kim, I. H. *Oxid. Met.* **1994**, *41*, 179.
227. Pint, B. A.; Hobbs, L. W. *J. Electrochem. Soc.* **1994**, *141*, 2443.
228. Pint, B. A. *Mater. Sci. Forum* **1997**, *251–254*, 397.
229. Aguilard, G. Ph.D. Thesis Université de Bourgogne, Dijon, 1992.
230. Pint, B. A.; Garratt-Reed, A. J.; Hobbs, L. W. *J. Am. Ceram. Soc.* **1998**, *81*, 305.
231. Wu, Y.; Hagihara, K.; Umakoshi, Y. *Intermetallics* **2004**, *12*, 519.
232. Yurek, G. J.; Przybylski, K.; Garratt-Reed, A. J. *J. Electrochem. Soc.* **1987**, *134*, 2643.
233. Przybylski, K. *Mater. Sci. Eng. A* **1989**, *121*, 509.
234. Przybylski, K.; Yurek, G. J. *Mater. Sci. Forum* **1989**, *43*, 1.
235. Chevalier, S.; Bonnet, G.; Przybylski, K.; Colson, J. C.; Larpin, J. P. *Oxid. Met.* **2000**, *54*, 527.
236. Ul-Hamid, A. *Oxid. Met.* **2002**, *58*, 23.
237. Przybylski, K.; Garratt-Reed, A. J.; Pint, B. A.; Katz, E. P.; Yurek, G. J. *J. Electrochem. Soc.* **1987**, *134*, 3207.
238. Pint, B. A.; Garratt-Reed, A. J.; Hobbs, L. W. In Proceedings of the 2nd International Conference on the Microscopy of Oxidation; Newcomb, S. B., Bennett, M. J., Eds.; **1993**; p 463.
239. Schumann, E.; Yang, J. C.; Graham, M. J.; Rhüle, M. *Mater. Corros.* **1995**, *46*, 218.
240. Schumann, E.; Yang, J. C.; Graham, M. J.; Rühle, M. *Mater. Corros.* **1996**, *47*, 631.
241. Pint, B. A.; Garratt-Ree, A. J.; Hobbs, L. W. *J. Phys. IV* **1993**, *3*, 247.
242. Pint, B. A.; Alexander, K. B. In Proceedings of the 3rd International Conference on the Microscopy of Oxidation; Newcomb, S. B., Little, J. A., Eds.; **1996**; p 153.
243. Pint, B. A.; Alexander, K. B. *J. Electrochem. Soc.* **1998**, *145*, 1819.
244. Mennicke, C.; Schumann, E.; Le Coze, J.; Smialek, J. L.; Meier, G. H.; Rhüle, M. In Proceedings of the 3rd International Conference on the Microscopy of Oxidation; Newcomb, S. B., Little, J. A., Eds.; **1996**; p 95.
245. Newcomb, S. B.; Dunin-Borkowski, R. E.; Boothroyd, C. B.; Czyrska-Filemonowicz, A.; Clemens, D.; Quadakkers, W. J. In ; Proceedings of the 3rd International Conference on the Microscopy of Oxidation; Newcomb, S. B., Little, J. A., Eds.; **1996**; p 166.
246. Kohno, M.; Ishikawa, S.; Ishi, K.; Satoh, I. In Proceedings of the 3rd International Conference on the Microscopy of Oxidation; Newcomb, S. B., Little, J. A., Eds.; **1996**; p 55.
247. Molins, R.; Germidis, A.; Andrieu, E. In Proceedings of the 3rd International Conference on the Microscopy of Oxidation; Newcomb, S. B., Little, J. A., Eds.; **1996**; p 3.
248. Sato, E.; Carry, C. *J. Am. Ceram. Soc.* **1996**, *79*, 2156.
249. Pint, B. A.; Alexander, K. B. In Proceedings of the 3rd International Conference on the Microscopy of Oxidation; Newcomb, S. B., Little, J. A., Eds.; **1996**; p 153.
250. Pint, B. A.; Alexander, K. B. *J. Electrochem. Soc.* **1998**, *145*, 1819.
251. Chevalier, S.; Larpin, J. P. *Acta Mater.* **2002**, *50*, 3105–3114.
252. Quadakkers, W. J.; Speier, W.; Holzbrecher, H.; Nickel, H. In Proceedings of the International Conference on the Microscopy of Oxidation; Bennet, M. J., Lorimer, G. W., Eds.; **1990**; p 149.
253. Papaiacovou, P.; Hussey, R. J.; Mitchell, D. F.; Graham, M. J. *Corros. Sci.* **1990**, *30*, 451.
254. Hussey, R. J.; Sproule, G. I.; Graham, M. J. *J. Phys. IV* **1993**, *3*, 241.
255. Quadakkers, W. J.; Norton, J. F.; Penkalla, J.; Breuer, U.; Gil, A.; Rieck, T.; Hänsel, M. In Proceedings of the 3rd International Conference on the Microscopy of Oxidation; Newcomb, S. B., Little, J. A., Eds.; **1996**; p 221.
256. Quadakkers, W. J.; Speier, W.; Holzbrecher, H.; Nickel, H. In Proceedings of the International Conference on the Microscopy of Oxidation; Bennet, M. J., Lorimer, G. W., Eds.; **1990**; p 149.
257. Jedlinski, J.; Borchardt, G. *Oxid. Met.* **1991**, *36*, 317.
258. Czyrska-Filemonowicz, A.; Szot, K.; Wasilkowska, A.; Ennis, P. J.; Breuer, U.; Gil, A.; Quadakkers, W. J. In Proceedings of the 3rd International Conference on the Microscopy of Oxidation; Newcomb, S. B., Little, J. A., Eds.; **1996**; p 185.
259. Quadakkers, W. J.; Clemens, D.; Bennett, M. J. In Proceedings of the 3rd International Conference on the Microscopy of Oxidation; Newcomb, S. B., Little, J. A., Eds.; **1996**; p 195.
260. Chevalier, S.; Przybylski, K.; Borchardt, G.; Larpin, J. P. *Mater. Sci. Forum* **2004**, *461–464*, 53.
261. Chevalier, S.; Bonnet, G.; Borchardt, G.; Colson, J. C.; Larpin, J. P. *Mater. Sci. Forum* **2001**, *369–372*, 327.
262. Pint, B. A.; Garratt-Reed, A. J.; Hobbs, L. W. *Mater. High Temp.* **1995**, *13*, 3.
263. Turker, M.; Hugues, T. A. *Oxid. Met.* **1995**, *44*, 505.
264. Turker, M.; Hugues, T. A. *Oxid. Met.* **1995**, *44*, 505.
265. Chevalier, S.; Przybylski, K. Unpublished results.

1.09 Thermodynamics and Theory of External and Internal Oxidation of Alloys

B. Gleeson
Department of Mechanical Engineering and Materials Science, The University of Pittsburgh, 647 Benedum Hall, Pittsburgh, PA 15261, USA

Symbols

a_i Chemical activity of phase or component i
D_i Diffusion coefficient of component i ($m^2\ s^{-1}$)
K Equilibrium constant for a given reaction
k_l Linear rate constant ($m\ s^{-1}$) or ($kg\ m^{-2}\ s^{-1}$)
k_p Parabolic rate constant ($m^2\ s^{-1}$) or ($kg^2\ m^{-4}\ s^{-1}$)
N_i Mole fraction of component i
P_i Partial pressure of gaseous species i
R Universal gas constant (8.314 $J\ mol^{-1}\ K^{-1}$)
T Temperature (K)
t Time (s)
V_m Molar volume of metal or alloy ($m^3\ mol^{-1}$)
X Thickness of metal consumed due to scaling (m)
x Scale thickness (m)
ΔG° Gibbs free enthalpy in the standard state ($J\ mol^{-1}$)
ΔW Weight change ($kg\ m^{-2}$)
γ_i Chemical activity coefficient of solute i
ν Stoichiometric factor for the oxide BO_ν

1.09.1 Introduction

High temperature corrosion plays an important role in the selection of materials in modern industry. Numerous commercial processes such as electric power generating plants, aerospace, gas turbines, heat-treating, and mineral and metallurgical processing operate at temperatures exceeding ~500°C.[1] Oxidation is often the most important high temperature corrosion reaction in these commercial processes. Indeed, most high temperature alloys are designed to react with the oxidizing environment in such a way that a protective oxide scale forms.[2] The degradation resistance of a high temperature alloy depends on sustaining the formation of this protective scale.

The properties of the scale determine the extent to which protection can be provided. Ideally, the scale should exhibit a slow growth rate, good adherence to the alloy substrate, a high stability, and be continuous and free of defects such as microcracks or large

voids. In general, a chromia, alumina, or silica scale can meet these requirements for high temperature oxidation resistance, with chromia-forming alloys being the most extensively used in high temperature industrial applications.

Almost all theoretical treatments of high temperature corrosion assume local equilibrium. In the majority of cases, this proves to be a reasonable assumption, although it is usually insufficient for predicting the nature and phase constitution of the reaction product. This is because reaction kinetics dictate the pathway for scale development. The following discusses key fundamental aspects associated with the thermodynamics and kinetics of high temperature corrosion. From a thermodynamic standpoint, it will be shown that relative partial pressures of the gaseous components in the reacting atmosphere are important for predicting the composition of the product scale. From a kinetic standpoint, it will be shown that limiting equations can be established for predicting both scaling kinetics and critical concentrations in the alloy for transitioning to and sustaining protective scaling behavior.

1.09.2 Pure Metal Reactions

In the context of this discussion, the metal and gas react to form a solid surface scale. The prototypical gas will be oxygen; however, it should be realized that the fundamental treatments equally apply to other gases, such as sulfur and nitrogen. Moreover, the oxidant may be simple, like O_2, S_2, and N_2, or it may be more complex, like H_2O, H_2S, and NH_4. For the sake of clarity, the following discussion will consider oxide-scale formation. An oxide scale may be a single layer or it may be comprised of two or more layers of varying compositions that depend on the temperature and oxidizing conditions. There are two important factors in discussing the oxidation of metals: thermodynamics and kinetics. Metallic elements react with oxygen to form oxides if it is energetically feasible. Thermodynamics show whether or not a reaction can take place. When the oxidation reaction is possible, kinetics shows how fast the reaction will be. In practical applications, kinetics is of more importance because it determines the extent of metal consumption and the overall reaction pathway (i.e., assemblage and structure of the reaction product). Oxidation theory of pure metals provides the foundation for understanding the more complicated processes associated with alloy oxidation.

1.09.2.1 Thermodynamics of a Single-Oxidant Reaction

Consider the high temperature reaction of a metal, M, with an oxidant gas, in this case oxygen. The metal initially absorbs oxygen and then chemical reaction ensues to form an oxide. For the metals of relevance to this review, the resulting oxide is solid. Thus, the oxide first nucleates and then grows to form a scale on the metal surface. Depending on its growth kinetics, the scale may or may not protect the underlying metal.

The formation of an oxide may be generally described by the reaction

$$\frac{2x}{y}\mathrm{M} + \mathrm{O}_2 = \frac{2}{y}\mathrm{M}_x\mathrm{O}_y \qquad [1]$$

Presented in this manner, the high temperature oxidation of metals may seem to be among the simplest of reactions; however, the reaction path and behavior often involve a number of phenomena and processes that depend on a variety of factors.[3,4] In fact, at the same temperature for a given gas–metal reaction, one can observe drastically different rates of reaction (linear, parabolic, or any other rate) when the gaseous composition of the atmosphere is altered and the relative partial pressures of the gaseous components are different.[5]

Under equilibrium conditions, the law of mass action for reaction [1] gives[6]

$$K_1 = \frac{a_{\mathrm{M}_x\mathrm{O}_y}^{2/y}}{a_{\mathrm{M}}^{2x/y}\, a_{\mathrm{O}_2}} \qquad [2]$$

where K_1 is the temperature-dependent equilibrium constant and a_i is the chemical activity of species i. In most cases, the solids (metal and oxide) are assumed to be in their pure standard state, so that their activities are defined as unity. At relatively high temperatures and moderate pressures, the oxidant gas can be treated as being ideal; that is, the activity of oxygen can be approximated by its partial pressure in atmospheres. Thus, eqn [2] simplifies to

$$K_1 = 1/P_{\mathrm{O}_2} \qquad [3]$$

where P_{O_2} is the oxygen partial pressure.

Thermodynamically, reaction [1] for any metal can take place spontaneously from left to right when its overall Gibbs free energy change, ΔG, is negative. For reaction [1], the Gibbs free energy change under isobaric conditions is given as:

$$\Delta G = \Delta G^\circ + RT\ \ln K_1 \qquad [4]$$

where ΔG° is the standard Gibbs free energy of formation of the oxide at absolute temperature

T and R is the gas constant. If $\Delta G = 0$, the system is at equilibrium, and if $\Delta G > 0$, the reaction is thermodynamically unfavorable. At equilibrium ($\Delta G = 0$),

$$\Delta G^\circ = -RT \ln K_1 = RT \ln P_{O_2} \quad [5]$$

Thus, knowing that at equilibrium both the forward and reverse reaction rates are equal, the dissociation pressure of the oxide can be defined from [5] as:

$$P_{O_2}^{diss} = \exp\left(\frac{\Delta G^\circ}{RT}\right) \quad [6]$$

The metal M can only be oxidized to the oxide M_xO_y at the temperature T if the ambient partial pressure of oxygen is larger than the dissociation pressure defined by eqn [6].

For the usual conditions of constant temperature and pressure, the auxiliary function ΔG° is usually described by the simple relation

$$\Delta G^\circ = \Delta H^\circ - T\Delta S^\circ \quad [7]$$

where ΔH° is the enthalpy of reaction and ΔS° is the entropy change under standard-state conditions. Tabulated values of ΔH° and ΔS° for the determination of ΔG° at any given temperature are readily available.[7–9] A small selection of useful values is given in **Table 1**.

Equation [7] shows that a plot of ΔG° versus T gives a straight line. This line would change in slope when a new phase forms (i.e., at melting or boiling temperature). A Gibbs energy–temperature diagram, usually called an Ellingham diagram,[6] summarizes the temperature dependence of ΔG° for various common oxidation reactions at a standard state ($p_{O_2} = 1$ atm). Such a diagram is shown in **Figure 1** for oxides.

Table 1 Standard energies of reaction[7,8] for pure solid metal (except liquid Al) and various common gasses

Reaction	$\Delta G^\circ = \Delta H^\circ - T\Delta S^\circ$ ($J\,mol^{-1}$)	
	ΔH° ($J\,mol^{-1}$)	$-\Delta S^\circ$ ($J\,mol^{-1}\,K$)
$\frac{2}{3}Al(l) + \frac{1}{2}O_2 = \frac{1}{3}Al_2O_2$	−565 900	128
$Co + \frac{1}{2}O_2 = CoO$	−233 886	70.7
$3CoO + \frac{1}{2}O_2 = Co_2O_4$	−183 260	148.1
$\frac{2}{3}Cr + \frac{1}{2}O_2 = \frac{1}{3}Cr_2O_2$	−373 420	86
$Fe + \frac{1}{2}O_2 = FeO$	−264 890	65.4
$3FeO + \frac{1}{2}O_2 = Fe_2O_4$	−312 210	125.1
$2Fe_2O_4 + \frac{1}{2}O_2 = 3Fe_2O_2$	−249 450	140.7
$Mn + \frac{1}{2}O_2 = MnO$	−412 304	72.8
$Ni + \frac{1}{2}O_2 = NiO$	−234 345	84.3
$\frac{1}{2}Si + \frac{1}{2}O_2 = \frac{1}{2}SiO_2$	−451 040	86.8
$H_2 + \frac{1}{2}O_2 = H_2O$	−246 440	54.8
$CO + \frac{1}{2}O_2 = CO_2$	−282 420	86.8
$O_2 + \frac{1}{2}S_2 = SO_2$	−362 420	72.4
$NiO + Cr_2O_2 = NiCr_2O_4$	−1 376 880	332
$NiO + Al_2O_2 = NiAl_2O_4$	−1 933 667	408

The calculated ΔG° value would be for the mole numbers shown in the particular reaction considered.

Figure 1 shows the relative thermodynamic stability of the indicated oxides. The lower the line on the diagram, the more negative the standard free energy of formation and, hence, the more stable the oxide. For example, the lines for Al_2O_3, SiO_2, and Cr_2O_3 are lower than those for FeO, NiO, and CoO in the Ellingham diagram, so the former oxides are more stable and therefore meet an important criterion for being protective scales. It is further seen in Figure 1 that the ΔG° versus T lines for most of the oxides are parallel and positively sloped. This is a consequence of the fact that the entropy of a gas is much larger than that of a solid. Thus, for the metal oxidation reactions represented by eqn [1],

$$\Delta S^\circ = \frac{2}{y} S^\circ_{M_xO_y} - \frac{2x}{y} S^\circ_M - S^\circ_{O_2} \approx -S^\circ_{O_2}. \quad [8]$$

It follows from eqn [7] that $\partial\Delta G^\circ/\partial T = -\Delta S^\circ \approx S^\circ_{O_2}$, which is greater than zero.

The P_{O_2} can be read directly from Figure 1 by using the P_{O_2} scale along the bottom and the right side of the diagram. A straight line drawn from the index point labeled 'O' (at $\Delta G^\circ = 0$, $T = 0$ K) at the upper left of the diagram, through a specific temperature point on an oxide line, intersects the P_{O_2} scale at the dissociation oxygen partial pressure ($P_{O_2}^{diss}$) for that oxide at that particular temperature. Accordingly, the oxides lower on the diagram are more stable and consequently have lower $P_{O_2}^{diss}$ values. For instance, from Figure 1, it is found that the dissociation pressure for NiO is $\sim 10^{-10}$ atm at 1000°C, while that for Cr_2O_3 is $\sim 10^{-22}$ atm, and for SiO_2 and Al_2O_3, it is 10^{-26} and 10^{-34} atm, respectively. The significance of this is that it is difficult thermodynamically to preclude the oxidation of Cr, Si, and Al.

Similar free-energy diagrams, which can be interpreted in exactly the same way, have been constructed for sulfides, carbides, and nitrides.[5] Moreover, Lou *et al.*[10] presented an excellent review on the use of Ellingham diagrams for treating gas–solid reactions.

Low oxygen partial pressures are in practice achieved using oxygen-bearing gas mixtures. The most common gas mixtures are H_2O/H_2 and CO_2/CO. The partial pressures of oxygen are then established from the equilibria:

$$H_2O = H_2 + \frac{1}{2}O_2;\ K_9 = \frac{P_{H_2} P_{O_2}^{1/2}}{P_{H_2O}} \quad [9]$$

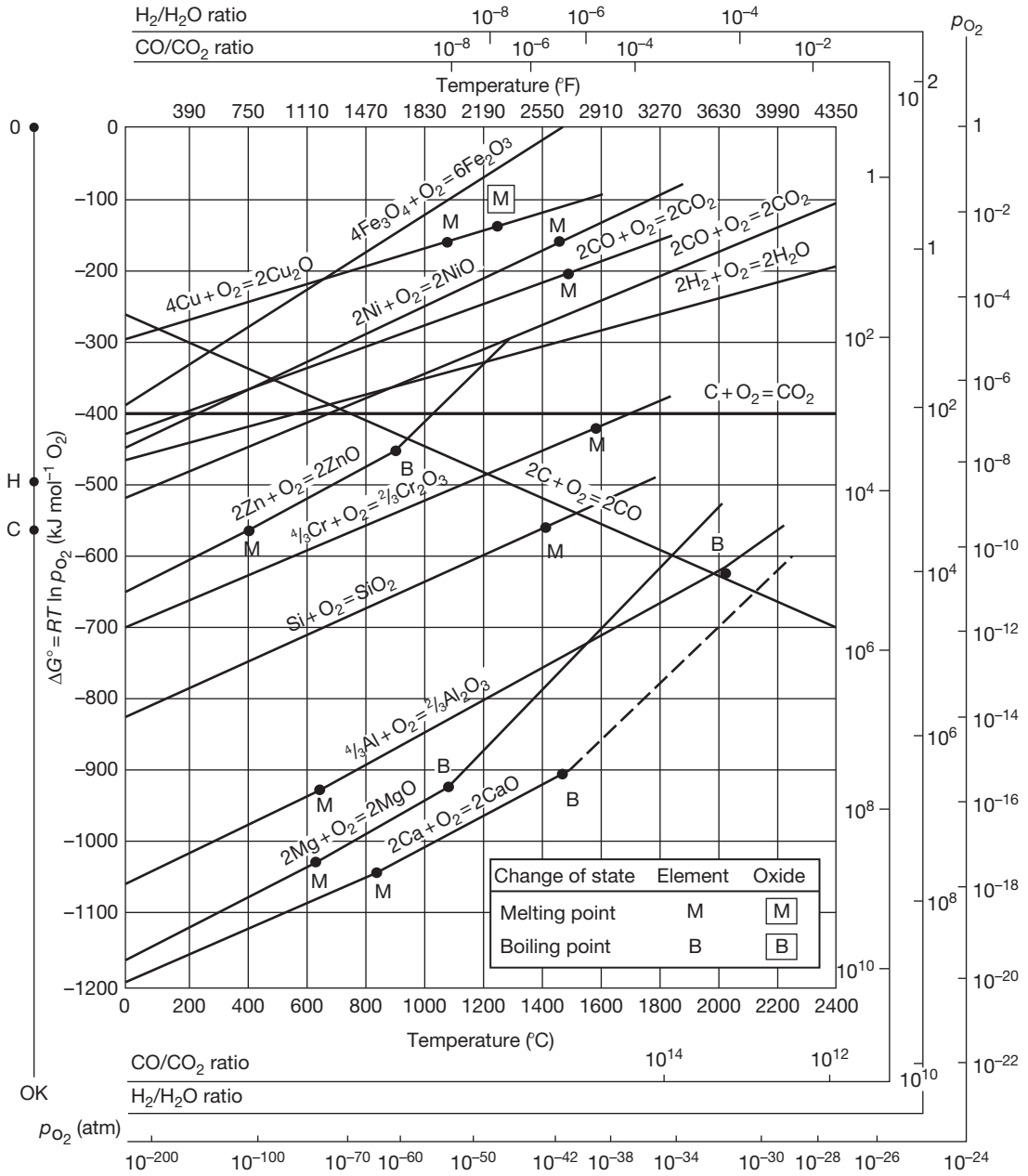

Figure 1 Ellingham diagram showing the standard Gibbs energies of formation of selected oxides as a function of temperature. Reproduced from Gaskall, D. R. *Introduction to the Thermodynamics of Materials*, 5th ed.; Taylor & Francis: New York, 2008.

and

$$CO_2 = CO + \frac{1}{2}O_2; K_{10} = \frac{P_{CO}P_{O_2}^{1/2}}{P_{CO_2}} \qquad [10]$$

where K_9 and K_{10} are the temperature-dependent equilibrium constants for reactions [9] and [10], respectively. Thus, the P_{O_2} may be determined from these equilibrium constants if the equilibrium P_{CO}/P_{CO_2} or P_{H_2}/P_{H_2O} ratios are known. In oxygen-lean gases containing both H_2O and CO_2, the P_{O_2} is usually determined by the H_2–H_2O reaction [9] since steam is more reactive than CO_2. Moreover, for a controlled laboratory experiment, it is preferred practice to facilitate the equilibrium by using a

platinum-containing catalyst in the reaction zone of the furnace.

In addition to the direct oxidation with oxygen, the overall metal oxidation reactions in these gas mixtures are:

$$xM + yH_2O = M_xO_y + yH_2 \qquad [11a]$$

and

$$xM + yCO_2 = M_xO_y + yCO \qquad [11b]$$

From **Figure 1**, the H_2/H_2O and CO/CO_2 ratios can be obtained by using the same method as for determining $P_{O_2}^{diss}$, using the index points labeled 'H' and 'C' at the left of the diagram instead of point 'O.'

The growth of a scale is usually sufficiently slow for local equilibrium to be closely approached. In fact, it is found that the Gibbs phase rule[6] can be applied to rationalizing the phase assemblage of a growing scale. Specifically, the Gibbs phase rule under isothermal and isobaric conditions is given as

$$P + F = C \qquad [12]$$

where P is the number of phases at a given location in the scale, F represents the degrees of freedom, and C number of components in the system. For the oxidation of a pure metal, $C = 2$ (i.e., metal and oxygen), and for diffusion to occur there must be a gradient in the chemical activity across the scale, so that $F = 1$. Thus, $P = 1$, meaning that only one phase can exist at a given plane (parallel to the metal/scale interface) within the scale. In practical terms, this means that a metal capable of forming multiple oxides must form those oxides as distinct scale layers. For example, at 1 atm O_2 and temperatures above 560 °C, pure iron oxidizes to form a triple-layered scale in the sequence $Fe|FeO|\ Fe_3O_4\ |Fe_2O_3\ |O_2$, with the oxide position being dictated by the necessity for the oxygen content to progressively increase when traversing from the iron to the oxygen at the scale surface. A similar line of reasoning can be used to show that a pure metal oxidized isothermally will not form internal oxide precipitates, but instead must form an external product.

1.09.2.2 Thermodynamics of Dual Oxidant Reactions

The thermodynamic aspects of multioxidant corrosion have been discussed by Giggins and Pettit.[11] Often, however, the complexity of a given process environment precludes an accurate determination of which type of corrosion should predominate. In such cases, it may be necessary to conduct field-exposure tests to properly evaluate the corrosion behavior of the candidate alloys. Even so, the assumption of thermodynamic equilibrium provides a reasonable starting point for assessment.

Quite often, two-dimensional phase stability diagrams are used to assess the high temperature corrosion of a metal M exposed to a dual-oxidant atmosphere. To illustrate this, the possible reactions of M exposed to oxidizing–sulfidizing atmosphere are determined by considering the following:

$$M + \frac{1}{2}O_2 \leftrightarrow MO \qquad [13]$$

$$M + \frac{1}{2}S_2 \leftrightarrow MS \qquad [14]$$

$$MO + \frac{1}{2}S_2 \leftrightarrow MS + \frac{1}{2}O_2 \qquad [15]$$

The equilibrium from reactions [13] and [14] defines the critical $P^*_{O_2}$ and $P^*_{S_2}$ values (i.e., dissociation pressures) for M/MO and M/MS equilibrium, respectively, while reaction [15] defines critical P_{S_2}/P_{O_2} ratios for MS/MO equilibria. With regard to the latter, it can be easily shown for reaction [15] that $\log(P_{S_2}) = \log(P_{O_2}) - 2\log K_{15}$, where K_{15} is the equilibrium constant for this reaction. Thus, a plot of $\log(P_{S_2})$ versus $\log(P_{O_2})$ should have a line of slope equal to the unity that separates MS stability from MO stability. **Figure 2** shows the general construction of an M–S–O phase-stability diagram. It is noted that a more complete diagram may include higher-order oxides and sulfides, as well as sulfates (MSO_4).[11] Only the simpler diagram is discussed here since the main important points can still be made.

The diagram in **Figure 1** shows the stability range of a metal and its oxide and sulfide products as a function of the two principal reactants: oxygen and

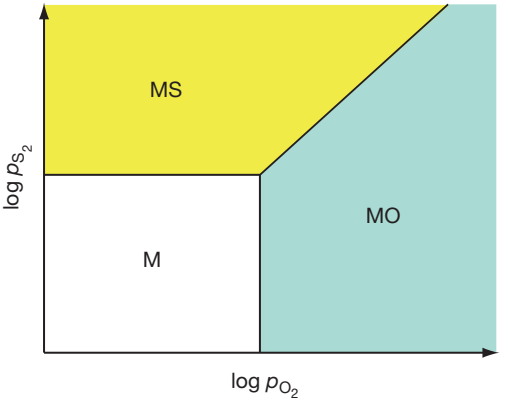

Figure 2 Schematic representation of a simple phase-stability diagram for a metal and its oxide and sulfide.

sulfur. A given atmosphere is defined by either equilibrium or nonequilibrium P_{O_2} and P_{S_2} values and would therefore be represented by a point in the stability diagram. The location of that point identifies the phase that is in stable equilibrium with that particular atmosphere. However, as shown in **Figure 3**, other phases can form even if only oxide stability is predicted. This depends on the reacting gas, the P_{O_2}–P_{S_2} combination, and whether the scale develops open pathways for gaseous penetration (e.g., microcracks). Internal sulfidation is particularly apt to occur in SO_2-containing atmospheres due to the local equilibrium dictated by the reaction $O_2 + \frac{1}{2} S_2 \rightarrow SO_2$, which has an equilibrium constant denoted as K_3. As indicated in **Figure 3**, the formation of an internal sulfide beneath an external oxide scale can only be completely avoided if

$$P_{SO_2} < K_3 P^*_{O_2} \sqrt{P^*_{S_2}} \qquad [16]$$

Although phase-stability diagrams are very useful for interpreting reaction products and gaining insights into reaction pathways, they do not have any predictive capabilities from a practical standpoint.

On the basis of equilibrium thermodynamics of reaction [15], the transition from sulfidation to oxidation of metal M should occur when

$$\left(\frac{P_{O_2}}{P_{S_2}}\right)^{1/2} > K_{15} \qquad [17]$$

The thermodynamic boundary separating sulfide and oxide stability in a phase stability diagram is determined by replacing '>' with '=' in eqn [17]. **Figure 4** shows the phase-stability diagram for the Type 310 stainless steel at 875 °C.[12] Superimposed on this diagram are experimental data indicating the type of scale formed on 310 under different P_{O_2}–P_{S_2} combinations. It is seen that sulfide-to-oxide transition at a given P_{S_2} actually occurs at a higher P_{O_2} than that predicted from equilibrium calculations. The experimentally-determined boundary is dictated by kinetic factors and, accordingly, is referred to as the kinetic boundary. For the case of the 310 stainless steel shown in **Figure 4**, the actual P_{O_2} values for the transition from chromium–sulfide to chromium–oxide formation are about three orders of magnitude higher than the equilibrium values. The kinetic factors which influence the location of the kinetic boundary include composition and surface finish of the alloy, and gas composition. Although theoretical prediction of the location of a kinetic boundary is not possible, LaBranche and Yurek[13] showed that for H_2–H_2O–H_2S gas mixtures there is a critical H_2O/H_2S ratio associated with the kinetic boundary. The value of this ratio is dictated by the competitive formation of the oxide and the faster-growing sulfide. It was found by LaBranche and Yurek that oxide formation on pure chromium at 900°C could only occur when the area fraction of Cr_2O_3 was greater than ~0.9 in the early stages of exposure, which corresponds to $H_2O/H_2S > 10$.

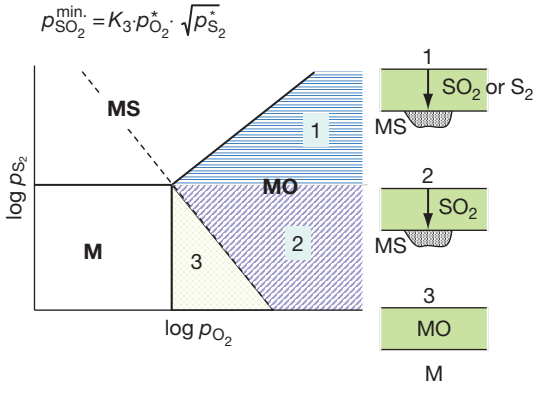

Figure 3 Application of the phase-stability diagram in identifying possible modes of attack.

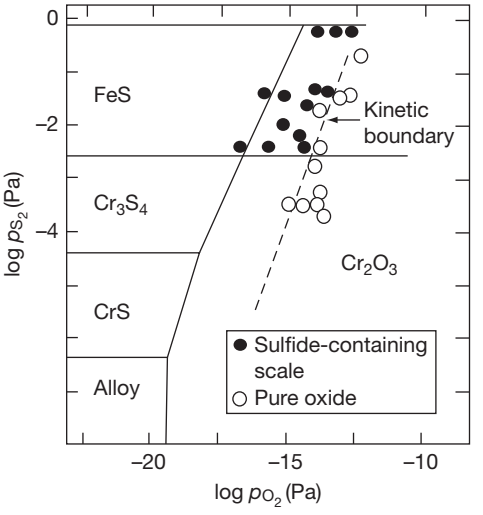

Figure 4 Thermodynamic phase-stability diagram for type 310 stainless steel at 875°C, showing the experimentally-determined kinetic boundary. Reproduced from Stroosnijder, M. F.; Quadakkers, W. J. *High Temp. Technol.* **1986**, *4*, 141.

1.09.2.3 Kinetics of Scale Formation

The reaction of a metal with an oxidant to form a product scale is concomitant with a weight gain due to pick-up of the oxidant (e.g., grams of oxygen gained). Accordingly, the scaling rate may be quantified by the change in the scale thickness, x (cm), or by weight gain, ΔW (mg cm^{-2}). In the case of oxidation, these two parameters are directly related by

$$x = \frac{V_{ox}}{yM_O}\Delta W \qquad [18]$$

where V_{ox} is the molar volume of oxide in cm^3 mol^{-1}, y is the stoichiometric amount of oxygen in oxide M_xO_y, and M_o is the atomic weight of oxygen.

The formation of oxide scale is also related to the consumption of metal, and the relationship between ΔW and the thickness of the metal consumed (X) is given by

$$X = \frac{V_m}{\gamma M_O}\Delta W \qquad [19]$$

where V_m is the molar volume of metal in cm^3 mol^{-1} and γ is the stoichiometric factor for the oxide scale product (i.e., $\gamma = y/x$ for M_xO_y). For most metals, the oxidation rates follow one or more of the three possible kinetic laws: linear, logarithmic, and parabolic. These kinetic laws are discussed in the following.

Formation of an oxide scale will separate the two reactants, metal and gaseous oxygen. In order for the reaction to proceed further, at least one of the reactants must progress through the scale to form more oxide at the oxide/gas, oxide/metal, or both interfaces. The mechanisms by which the reactants progress through the scale can therefore be an important part of the overall mechanism and kinetics by which high temperature oxidation reaction proceeds. Another aspect of the oxidation process, which can sometimes be rate controlling, is the kinetics of the interfacial reaction steps.

1.09.2.3.1 Parabolic rate law

At high temperature, initial scale growth is usually very rapid; however, the reaction rate will eventually decrease when scale thickness reaches ~0.5 μm and the transport of reacting species through the scale becomes rate controlling. When the rate-controlling step in the oxidation process is the diffusion of reactant(s) through the oxide layer and with the boundary conditions for diffusion being time independent, the scaling kinetics will follow the parabolic rate law. Parabolic kinetics results from the fact that the scale thickness, x, increases with time, t, and, since this corresponds to the increasing diffusion distance, the oxidation rate decreases. Thus, the instantaneous oxidation rate is quite simply inversely proportional to the oxide thickness, that is,

$$\frac{dx}{dt} = \frac{k_p'}{x} \qquad [20]$$

where k_p' is a proportionality constant. Integration of eqn [20] gives

$$x^2 = k_p t + C \qquad [21]$$

where k_p is taken to be the parabolic rate constant ($k_p = 2\,k_p'$) with typical units of cm^2 s^{-1}. Another form of the parabolic rate equation is given by the weight gain (g cm^{-2}):

$$\Delta W^2 = k_p t + C \qquad [22]$$

where the units of k_p in this case are g^2 cm^{-4} s.

The parabolic rate law is the standard for analysis of high temperature oxidation kinetics, in which diffusion through the relatively thick scale controls reaction rates. The diffusion-controlled scale-thickening process is thermally activated, meaning that the rate increases exponentially with temperature, as given by the Arrhenius equation:

$$k_p = k_o \exp\left(\frac{-Q}{RT}\right) \qquad [23]$$

Here, k_o is a constant that is a function of the oxide composition and the gas pressure, and Q is the activation energy for oxide-scale growth. Figure 5[1] shows the temperature dependence of the k_p values for the oxides of Fe, Co, Ni, Cr, Al, and Si. The figure shows a range of k_p values for Al_2O_3 and Cr_2O_3 growth because these oxides do not show intrinsic behavior and are instead very sensitive to impurities (i.e., doping).

Deviations from parabolic kinetics are generally analyzed in terms of chemical and metallurgical effects on the rates of the relevant diffusing process(es). The parabolic rate law will not hold in the very early stages of oxidation, before the scale has developed sufficient continuity and thickness. In the case of hafnium and zirconium, the time exponent in eqn [21] is found to be ~3 (cubic kinetics) rather than 2 (parabolic kinetics) at high temperatures. This has been attributed to the simultaneous dissolution of oxygen into the substrate metal during oxidation.[14] It has also been shown for NiO-[15] and Al_2O_3-scale[16] growth that subparabolic kinetics can occur if both short-circuit diffusion through the scale predominates and the average grain size of the scale increases with oxidation time.

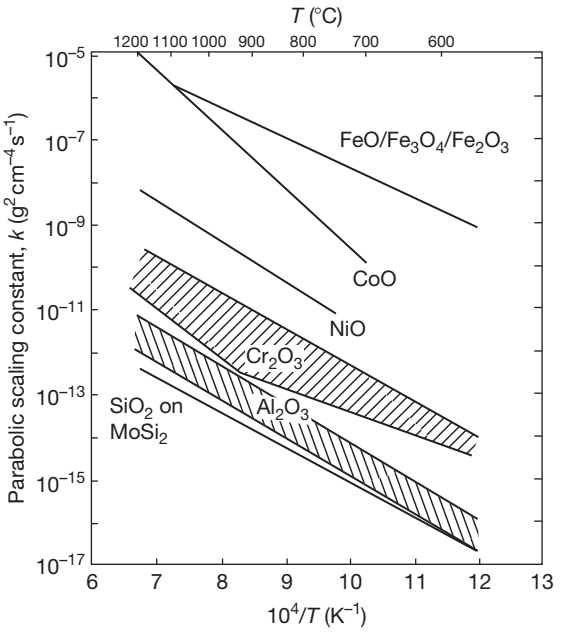

Figure 5 Parabolic oxidation rate constant for various oxide scales as a function of temperature. Reproduced from Gleeson, B. In *Corrosion and Environmental Degradation*, *Vol. II*: Volume 19 of the Materials Science and Technology Series; Schütze, M., Ed.; Wiley-VCH: Weinheim, Germany, 2000.

1.09.2.3.2 Linear rate law

Under certain conditions, the oxidation of a metal proceeds at a constant rate according to a linear rate law, that is,

$$x = k_l t \qquad [24]$$

where x is the scale thickness and k_l is the linear rate constant. A linear rate law may result when a phase-boundary reaction controls the kinetics rather than a transport process. An example is CO_2 dissociation at the scale surface controlling the oxidation kinetics of steel in a CO_2-rich atmosphere.[17]

Linear kinetics is also possible if the oxide is volatile or molten, if the scale spalls or cracks, or if a porous, nonprotective oxide forms on the metal.[4] Since the rate of oxidation never slows down, consumption of the metal occurs in a relatively short time in comparison to a metal scaling according to parabolic kinetics. Examples of metals that scale in a nonprotective, linear manner due to continual scale cracking are Nb and Ta.[18]

In the early stages of a metal oxidation process, the scale may be sufficiently thin that linear oxidation kinetics prevails. As the scale thickens, a transition to parabolic kinetics will usually ensue.[19] Conversely, microcracking and porosity may develop as the scale thickens, reducing the protectiveness of the oxide. The parabolic rate law may then fail, and the kinetics approaches linearity at some time after the start of reaction and scale growth. That is, a constant oxidation rate can develop after a period of parabolic behavior. In this special case of parabolic scaling superimposed on a relatively constant rate of scale cracking and healing, the overall kinetics is said to be 'paralinear.'[20]

1.09.2.3.3 Logarithmic rate law

At low temperatures (e.g., $T < 300$–$400\,^{\circ}C$), oxidation rates are often inversely proportional to time, that is,

$$\frac{dx}{dt} = \frac{k}{t} \qquad [25]$$

where k is a constant. Integration of [25] leads to the logarithmic rate law

$$x = k_a \log(k_b t + 1) \qquad [26]$$

where k_a and k_b are constants. Logarithmic oxidation is usually obeyed for relatively thin scales at low temperatures.

1.09.2.4 Transport Properties of Metal Oxides

Metallic oxides are seldom stoichiometric, meaning that the metal-to-oxygen atom ratio is not exactly that given by the stoichiometric chemical formula, even though the compound is electrically neutral. The same can be stated for sulfides and nitrides, but the focus here will be on oxides as the prototypical systems. The ionic charge imbalance in a nonstoichiometric oxide is compensated by electronic charges, that is, electron and electron holes. As a consequence, nonstoichiometric oxides exhibit both electronic and ionic conductivities. These conductivities are temperature dependent, which, from the electronic standpoint, classifies the nonstoichiometric oxides as semiconductors.

Electronic semiconductors are categorized as n-type (excess of electrons) or p-type (excess of electron holes). The n-type oxides may have either an excess of cation interstitials or an excess of oxygen vacancies (i.e., a deficiency in filled sites on the oxygen sublattice, MO_{1-x}) as the principal ionic defects. Some examples of n-type oxides are TiO_2, Fe_2O_3, $NiFe_2O_4$, ZnO, Al_2O_3, and SiO_2.[18] For n-type oxides, the principal ionic defect concentration, C, is found to be proportional to the negative power of the oxygen partial pressure[21]:

$$C \propto P_{O_2}^{-1/n} \quad [27]$$

where n is a positive integer which depends upon the charge of the ionic defect in the oxide and the oxide's stoichiometry.

The p-type oxides may have either an excess of cation vacancies (i.e., a deficiency in filled sites on the metal sublattice, $M_{1-x}O$) or an excess of oxygen interstitials. Some common p-type oxides include NiO, CoO, FeO, $FeCr_2O_4$, $CoCr_2O_4$, and $NiAl_2O_4$. For p-type oxides, the principal ionic defect concentration is related to the oxygen partial pressure by[21]:

$$C \propto P_{O_2}^{1/n} \quad [28]$$

During the oxidation process, ions transport by two ways: the cation migrates outward to scale/gas interface and the anion migrates inward to metal/scale interface (**Figure 6**). Thus, two reactions could potentially happen at the two interfaces to result in scale growth, although it is typically found that one reaction predominates. In other words, either metal or oxygen diffusion predominates in the thickening of a given oxide scale.

For the defective structures treated so far, it has been assumed that the oxides are pure; however, it is thermodynamically impossible to produce perfectly pure compounds or materials. It is therefore necessary to consider the effects of impurities on the defective structure of oxides. It is noted, however, that the presence of impurities can sometimes be neglected if the intrinsic defect concentration in the host oxide is relatively large. As an example of the so-called 'doping effect,'[21] the following is found for a p-type, metal-deficient oxide $M_{1-x}O$:

- The addition of substitutionally dissolved foreign cations of lower valence increases the concentration of electron holes and decreases the concentration of cation vacancies.
- The addition of substitutionally dissolved foreign cations of higher valence decreases the concentration of electron holes and increases the concentration of cation vacancies.

Thus, for the p-type, metal-deficient NiO, doping with Cr^{3+}, will cause an increase in the nickel vacancy concentration, which in turn will cause an increase in the effective diffusivity of nickel in the NiO. This increase in diffusivity is manifested as an increase in the k_p for NiO-scale growth. Indeed, it is found experimentally that NiO grows faster on dilute Ni–Cr alloys than on pure Ni.[22]

1.09.2.5 Wagner's Theory of Metal Oxidation

Carl Wagner's theory of metal oxidation[23,24] provides a fundamental understanding of the essential features of the high temperature growth of a continuous scale. The model ideally assumes that the scale is dense, single-phase, continuous, and adheres to the metal over the entire metal surface. The basic assumption of the theory is that lattice diffusion of the reacting atoms or ions through the dense scale is rate controlling (i.e., the microstructure of the oxide scale was not considered). **Figure 7** gives a set-up of the model.[14]

As indicated in **Figure 7**, the scale growth involves fluxes of both ionic and electronic charged species. The driving forces for these fluxes are related to the chemical potential gradient and electrostatic field that develop in the growing scale. The relative

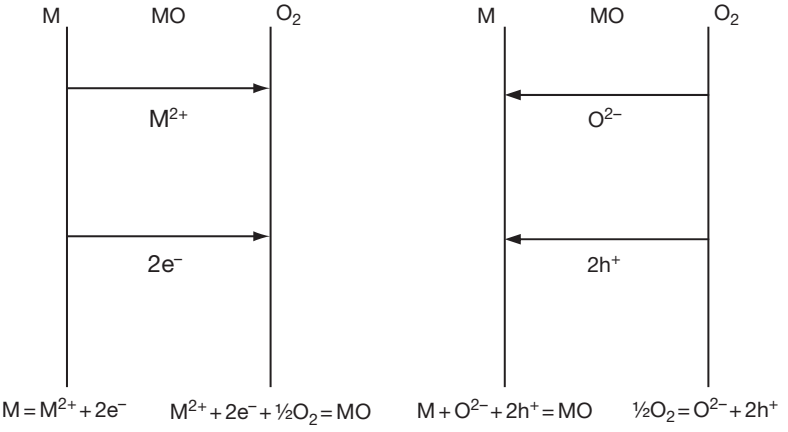

Figure 6 Ionic and electronic transport processes and interfacial reactions in the growth of a nonstoichiometric oxide scale MO.

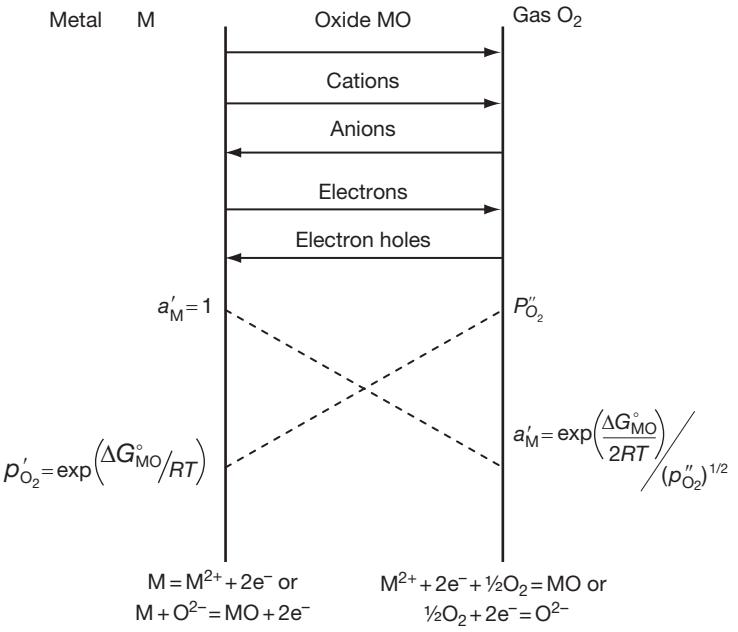

Figure 7 Transport processes according to Wagner's theory. Adopted from Birks, N.; Meier, G. H. *Introduction to High Temperature Oxidation of Metals*; Edward Arnold: London, 1983.

migration rates of cations, anions, electrons, and electron holes must also be balanced such that no net charge build up occurs within the scale.

Wagner derived an expression for the parabolic rate constant in terms of the electronic and ionic conductivities of the oxide or, alternatively, in terms of the self-diffusion coefficients of the reacting ions in which parameters can be measured relatively easily. Limiting cases of Wagner's derivation are as follows[14]:

$$k' = \frac{1}{RT}\int_{\mu''_M}^{\mu'_M} D_M \, d\mu_M \qquad [29]$$

and

$$k' = \frac{1}{RT}\int_{\mu''_X}^{\mu'_X} D_X \, d\mu_X \qquad [30]$$

where k' is the parabolic rate constant with units of cm^2s^{-1}, D_M and D_X are the self-diffusion coefficients for metal, M, and nonmetal, X, through the scale, respectively, and μ_M and μ_X are the chemical potentials for the metal and nonmetal. Equation [29] is valid when cation diffusion predominates and eqn [30] is valid when anion diffusion predominates. The good agreement between parabolic rate constants calculated from diffusivities and the oxidation rate constants measured experimentally have provided validation for Wagner's theory.[25,26]

Because the diffusion flux within the oxide is proportional to the defect concentration, eqn [28] can be used for a p-type oxide to arrive at the following relation for the oxidation rate:

$$k' \propto [(P^o_{O_2})^{1/n} - (P^i_{O_2})^{1/n}] \qquad [31a]$$

where $P^o_{O_2}$ and $P^i_{O_2}$ are the oxygen pressures at the scale/gas interface and metal/scale interface respectively, and n is an integer related to the cation vacancy or oxygen interstitial charge. For an n-type oxide, use of eqn [27] gives:

$$k' \propto [(P^i_{O_2})^{-1/n} - (P^o_{O_2})^{-1/n}] \qquad [32a]$$

where in this case n is related to the oxygen vacancy or cation interstitial charge. In most cases, the ambient oxygen pressure $P^o_{O_2}$ is much greater than $P^i_{O_2}$, which is the dissociation pressure ($P^{diss}_{O_2}$). Thus, eqns [31a] and [32a] can be approximated to give

$$k' \propto (P^o_{O_2})^{1/n} \text{ for a p-type scale} \qquad [31b]$$

and

$$k' \propto (P^i_{O_2})^{-1/n} \text{ for a n-type scale} \qquad [32b]$$

These equations show that the growth rate of a p-type oxide is directly dependent on the oxygen partial pressure in the atmosphere. By contrast, the

growth rate of an n-type oxide is independent of the external oxygen partial pressure.

Oxides formed in practice are usually more complex than what was assumed by Wagner. First, a multilayer scale can form on a number of metals, such as Fe, Cu, and Co. For instance, and as discussed earlier, a three-layered $FeO/Fe_3O_4/Fe_2O_3$ scale forms on iron above ~570 °C at atmospheric pressure. Treatments of the growth kinetics of multilayered scales have been presented by a number of authors.[27–30] In general, these treatments relate overall oxidation scaling kinetics to the intrinsic growth rates of the individual layers in the scale. Second, scales forming on metal surfaces are usually polycrystalline in structure, and in many cases, these structures are fine-grained. The activation energy for grain-boundary diffusion is lower than that for lattice diffusion by up to a factor of three. As a consequence, grain-boundary diffusion will tend to predominate at lower temperatures and can cause the scaling kinetics to be orders of magnitude higher than what would be predicted based on lattice diffusion.[26]

As indicated above, Wagner's theory considered the ideal case of scale formation in which the scale is assumed to be a compact and perfectly adherent barrier, that is, free of voids, pores, and fissures. The assumptions made by Wagner were indeed appropriate; however, deviations from Wagner's theory have been shown.[31] Many studies have shown that pores form and develop preferentially along grain boundaries in the scale.[32,33] The presence of voids in scales clearly represents a deviation from ideal scale growth. In some extreme cases, it may be necessary to take into account the void volume fraction in Wagner's model; but often the void formation may be considered to be a secondary process that does not significantly affect the overall scaling kinetics.

As the scale grows, stresses develop due to differences in the molar volume of metal and oxide(s). The resulting growth stresses are typically compressive.[34,35] More significant stresses can develop under thermal cycling conditions due to a mismatch in the coefficient of thermal expansion (CTE) between oxide scale and metal. Increasing stresses may eventually result in crack formation and even scale detachment.[35] Cracking of a protective oxide scale can result in the parabolic oxidation kinetics being interrupted by a sudden increase in rate when the gas can react directly with the metal surface. As oxide begins to cover the metal surface again, parabolic oxidation is resumed. The overall oxidation of the metal becomes approximately a paralinear process of periodic cracking and healing of a protective oxide.

1.09.3 Alloy Reactions

The fundamentals of pure-metal oxidation provide a basic understanding of alloy oxidation, but the latter is generally much more complex as a result of some, or all, of the following[14]:

(a) The various metal components in an alloy will have different affinities for oxygen, as indicated in the Ellingham diagram in **Figure 1**.
(b) More oxides may be formed, including ternary and higher oxides.
(c) A degree of solid solubility may exist between the oxides.
(d) The various metal ions will have different mobilities in the oxide phases.
(e) The various metals will have different diffusivities in the alloy.
(f) The extra degree of thermodynamic freedom provided by an additional metal component in the alloy may result in subsurface oxide precipitation (i.e., internal oxidation).

When it is considered that scales can crack, contain voids, spall, and even form multiple layers of irregular thickness, the situation becomes even more complex. The following provides a brief overview of the fundamental aspects of alloy oxidation.

1.09.3.1 Thermodynamics of Alloy Oxidation

As in the case of a pure metal, alloy oxidation is driven by an overall decrease in free energy. However, the alloy components are not in their pure state, which corresponds thermodynamically to their chemical activities being less than unity. For dilute solution of metallic component B in A, the average solvent A atom exists essentially in the same chemical surrounding environment as in its pure state, with only a small number of neighboring solute B atoms. Thus, in the limit of a very dilute solution, the A atoms follow Raoult's law,[6] such that:

$$\lim_{N_A \to 1} a_A = N_A \qquad [33]$$

where a_A and N_A are the chemical activity and mole fraction of solvent A, respectively. Also, according to Henry's law, the chemical activity of solute B is given as:

$$\lim_{N_B \to 0} a_B = \gamma_B N_B \qquad [34]$$

where γ_B is the activity coefficient of solute B for the A–B system. It can be easily shown that the dissociation P_{O_2} for an AO scale in contact with an A–B alloy is

greater than what would be calculated for AO in contact with pure A. Specifically,

$$\frac{P_{O_2}}{P^*_{O_2}} = \left(\frac{1}{a_A}\right)^2 \quad [35]$$

where a_A is the activity of A in the A–B alloy, and P_{O_2} and $P^*_{O_2}$ are the dissociation pressures for the A–B alloy and pure A, respectively.

It is typically the activity of the solute that is most important when assessing the thermodynamics of alloy oxidation; although, the results are often of limited utility. This can be shown as follows. Consider the oxidation of an A–B alloy in which the solute B forms a more stable and protective oxide. Assuming that the only stable oxides are AO and BO and that these oxides are insoluble in one another, the important reaction to consider is

$$AO + \underline{B} \rightarrow BO + \underline{A} \quad [36]$$

where $\underline{B}$ and $\underline{A}$ correspond to B and A in the alloy solution. The law of mass action for this reaction gives

$$K_{36} = \frac{a_A}{a_B} \approx \frac{N_A}{\gamma_B N_B} \quad [37]$$

Thus, reaction [36] will only proceed to the right if $\frac{a_A}{a_B} < K_{36}$, which means that there is a critical a_B, or conversely N_B, for this to occur. In most practical cases of interest, the solute–metal oxide BO is significantly more stable than the base-metal oxide AO, causing K_{36} to be much larger than unity. This, in turn, results in a very small minimum N_B value for BO to be thermodynamically stable in contact with the A–B alloy. In the case of an Ni–Cr alloy, N_{Cr} must be greater than $\sim 10^{-9}$ at 1000 °C for the displacement reaction $3NiO + 2\underline{Cr} \rightarrow Cr_2O_3 + 3\underline{Ni}$ to be thermodynamically stable.[36] Such a low Cr content is orders of magnitude below what is necessary kinetically to sustain Ni–Cr/Cr_2O_3 stability, let alone to kinetically establish a continuous Cr_2O_3 scale. For the latter, the critical Cr mole fraction, N^{crit}_{Cr}, in Ni–Cr alloy exposed to air at 1000 °C is experimentally found to be ~0.2.[37]

1.09.3.2 Criterion for the Sustained Exclusive Growth of a Protective Scale

If a continuous BO_υ scale on an A–B alloy is established under a particular set of conditions, it may be necessary to determine if its growth can be sustained under a different set of conditions. (The stoichiometric factor υ for the oxide BO_υ will be used for the remainder of this chapter in order to provide more general kinetic-based expressions.) An example of this could be the preoxidation of an alloy at a low P_{O_2} followed by in-service exposure to a higher P_{O_2} and/or different temperature. The sustained growth of a continuous BO_υ scale requires a sufficient supply of B from within the alloy to the alloy/scale interface. The resulting subsurface concentration gradient of solute B is represented schematically in **Figure 8**, in which N^i_B is the mole fraction of B in the alloy at the alloy/scale interface. The maximum possible rate of B supply in the alloy can be imposed by setting N^i_B equal to zero, thereby producing the steepest possible diffusion gradient of B. Under steady-state conditions, this maximum rate of B supply would have to equal the rate of B consumption due to BO_υ scale growth. Determination of the minimum B content in the alloy, $N^o_{B(min)}$, necessary for the sustained exclusive growth of a BO_υ scale on an A–B alloy was originally considered by Wagner,[38] who further assumed that: (1) the diffusion coefficient of B in the alloy, D_B, is independent of concentration; (2) the BO_υ scale obeys parabolic thickening kinetics with a rate constant k_p; (3) solvent metal A is insoluble in BO_υ; and (4) the recession of the alloy/scale interface may be neglected. Wagner derived the criterion

$$N^o_{B(min)} > \frac{V_m}{\upsilon M_O}\left(\frac{\pi k_p}{2D_B}\right)^{\frac{1}{2}} \quad [38]$$

where V_m is the equivalent molar volume of the alloy and M_O is the atomic weight of the oxidant, which is oxygen in this discussion ($M = 16\,g\,mol^{-1}$). Many researchers have used the criterion in eqn [38] to predict the minimum content of B necessary for a bare alloy to form an exclusive BO_υ scale layer. However, this is not a correct use of the criterion, since its derivation was based on supply rather than establishment. The

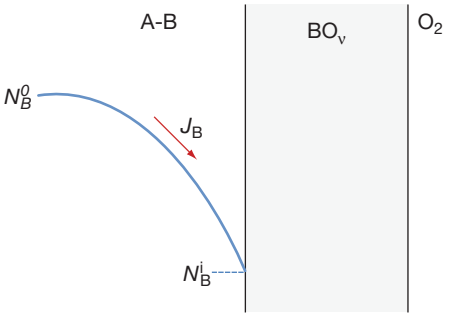

Figure 8 Schematic representation of the concentration profile of *B* in a binary alloy *A–B* which is forming an exclusive scale layer of BO_υ.

criterion given in [38] gives only the minimum possible B content in the alloy necessary to supply B at a sufficient rate to the alloy/scale interface for the sustained growth of an established BO_υ scale layer. The actual B content necessary for both the establishment and sustained growth of a BO_υ scale will very likely be higher than $N^o_{B(min)}$ owing to transient and kinetic effects.

1.09.3.3 Internal Oxidation

Internal oxidation is used here in a generic sense to represent a process in which a diffusing oxidant from the surface reacts with a less-noble solute component in the alloy to form discrete particles.[39] Internal oxidation is not desired because it changes the optimized mechanical properties of an alloy and may result in internal stress and weakening of the grain boundary.

For a dilute binary alloy A–B, the dissolved oxygen atoms can react with less-noble B atoms in the alloy in the manner,

$$\underline{B}+\upsilon\underline{O} \rightarrow BO_\upsilon \qquad [39]$$

The necessary condition for BO_υ formation in the alloy may be formulated in terms of the equilibrium solubility product K_{sp}, such that:

$$[a_B][a_O]^\upsilon > K_{sp} \qquad [40]$$

The degree to which the solubility product must be exceeded (i.e., the degree of supersaturation) before precipitation occurs depends on a number of factors, such as the stability, composition, and crystal structure of the precipitating BO_υ phase. For instance, if the crystal structure and lattice dimensions of BO_υ are such that it can form a coherent interface with the alloy matrix, then only a small degree of supersaturation is likely to be necessary for BO_υ precipitation. In general, the greater the stability of BO_υ, the lower will be its K_{sp} value. It is for this reason that the internal precipitates commonly observed in oxidized high temperature alloys are of the stable oxides Al_2O_3, SiO_2, TiO_2, and Cr_2O_3.[40,41] Multiple internal oxidation zones can also develop if more than one reaction product is stable.[42,43] The sequence of the thermodynamically possible phases progresses from metal-rich in the innermost zone of the alloy to oxidant-rich at the surface.

The internal oxidation zone extends to the depth at which the activity of dissolved oxygen becomes too small for the formation of the oxide BO_υ. The kinetics of internal oxidation are generally found to be diffusion-controlled and the depth of the internal oxidation zone, ξ, in an alloy undergoing no external scale formation can be described by the following kinetic expression, assuming no enrichment of B in the internal oxidation zone[44,45]:

$$\xi = \left(\frac{2N^s_O D_O t}{\upsilon N^o_B}\right)^{1/2} \qquad [41]$$

where N^s_O is the solubility of the oxidant in the alloy, D_O is the diffusivity of the oxidant in the alloy, N^o_B is the initial solute concentration in the A–B alloy, and t is the time. The product $N^s_O D_O$ is the oxygen permeability in alloy. The solubility of oxygen in the alloy depends upon the oxygen partial pressure at the alloy surface in accordance with Sievert's law,[6] that is,

$$N^s_O \propto P^{1/2}_{O_2} \qquad [42]$$

Thus, the depth of internal oxidation would be expected to decrease with decreasing P_{O_2} in the manner $\xi \propto P^{1/4}_{O_2}$.

The above discussion considers only internal precipitation in the absence of external scale formation. In the case of AO_υ scale formation, the value of N^s_O is no longer fixed by the environment but is instead fixed by the equilibrium between at the alloy/scale interface (assuming no through-scale access by the oxidant) according to the reaction,

$$\underline{A} + \frac{\upsilon}{2}O_2 = AO_\upsilon \qquad [43]$$

The effective thickness of the internal precipitation zone in the situation of concurrent AO_υ-scale formation decreases in a most pronounced manner from that predicted in the absence of an external scale at large k_p and N^o_B values.[46] A large k_p value for AO_υ-scale growth corresponds to a large amount of metal recession, which means the total attack is still high, even though the internal precipitation zone is relatively low.

The preceding theoretical considerations are based on models assuming predominant lattice diffusion of both oxygen and the alloying element. As such, the theoretical treatments are only expected to apply to relatively high temperatures or to very large-grained materials, with the extreme being single crystals. As the temperature is reduced, grain-boundary effects will become increasingly important. This is due to relatively rapid diffusion along grain boundaries, enhanced concentration or segregation of the oxidant and the alloying element at grain boundaries, and a preferred tendency for nucleation at grain boundaries.[4]

1.09.3.4 Transition from Internal Oxidation to External Scale Formation

The transition from internal to external oxide formation typically occurs with a relatively small increase in the alloy content of the less-noble component B in the A–B alloy, at which oxidation leads to the formation of a surface scale of BO_υ, and the alloy no longer undergoes internal oxidation. Considering again the alloy system A–B, there are two limiting possible situations: one is when only one of the components can oxidize and the other is when both of the components can oxidize. For the first case, if the oxygen partial pressure is low (i.e., below the stability of AO_υ formation), the component B in the alloy surface nucleates as BO_υ in an A-rich matrix. If B can diffuse fast enough to reach the surface and maintain a sufficient supply for BO_υ formation, a complete surface layer of BO_υ will be established. However, if this condition is not met, then BO_υ will precipitate as internal particles within the alloy. So, the internal or external formation of BO_υ depends on the balance between the outward flux of B and the inward flux of atomic oxygen into the alloy.

Wagner[47] proposed that the condition for the transition from internal to external BO_υ formation occurs when a critical volume fraction of BO_υ, f^*, is attained. Under this condition, the influx of oxygen is so restricted that sideways growth of the internal BO_υ precipitates is kinetically favored to the extent that BO_υ eventually forms as a continuous layer on the alloy surface. Under conditions of no or a negligibly small rate of metal recession, the following criterion for the transition from internal to external BO_υ formation was obtained:

$$N_{B^*}^{o} \geq \left[f^* \left(\frac{V_m}{V_{ox}} \right) \pi \frac{N_O^S D_O}{2 \upsilon D_B} \right]^{1/2} \qquad [44]$$

where $N_{B^*}^{o}$ is the critical mole fraction of B in the alloy, V_m is molar volume of the alloy, V_{ox} is molar volume of the oxide, and D_B is the diffusion coefficient of solute B in the alloy. Rapp[44] reported excellent agreement between experimental and reasonably predicted values of $N_{In^*}^{o}$ as a function of oxygen partial pressure in Ag–In alloys oxidized at 550°C. The value of f^* is usually taken to be 0.3 in accordance with the results from this study by Rapp.

From the criterion given by eqn [44], it is seen that $N_{B^*}^{o}$ can be decreased by decreasing the product of N_O^s and D_O (i.e., decreasing the permeability of oxygen) and/or increasing D_B. Indeed, the direct and indirect control of these variables in numerous experimental studies conducted over the past 40 years have validated this criterion.[1]

1.09.4 Epilogue

Advances in the high temperature stability of materials are critically needed to realize the full performance and potential of many current and future commercial systems. These advances must lead to significantly enhanced capabilities that will allow high temperature components to operate robustly for prolonged periods in harsh environments, such as those involving aggressive gases, deposits, photon or radiation fluxes, stresses, high or low pressures, or some combination of these conditions. For example, coal gasification, biomass conversion, and gas-cooled nuclear reactor systems typically produce complex, multioxidant gaseous environments that can be highly aggressive from the standpoint of surface degrading structural components. The resulting multioxidant process environments are often non-equilibrium and can involve both gaseous and deposit-induced attack. Fundamentally, the high temperature stability of a material in an aggressive environment relates to reactions and transport at and across its external surfaces. Similar to what was discussed in this chapter, these reactions are defined in terms of some combination of chemical potential, temperature and pressure and can be highly complex. Different processes, many of them coupled, are involved from the onset of reaction, that is, the absorption and dissociation of gaseous molecules at the surface, to the steady-state growth of a protective surface scale that develops. Indeed, the ability to control the growth and stability of this scale and to predict its behavior under different types of extreme chemical environments for extended periods of time will require a much greater basic understanding of the underlying reactions and transport processes involved. The basic starting points have been presented in this chapter, but still much more research and development are needed to improve the reliability and durability of materials exposed to aggressive conditions.

References

1. Gleeson, B. In *Corrosion and Environmental Degradation, Vol. II:* Volume 19 of the Materials Science and Technology Series; Schütze, M., Ed.; Wiley-VCH: Weinheim, Germany, 2000.

2. Lai, G. Y. *High-Temperature Corrosion of Engineering Alloys;* ASM International: Materials Park, OH, 1990.
3. Kofstad, P. *High Temperature Oxidation of Metals*; John Wiley and Sons: New York, 1966.
4. Young, D. *High Temperature Oxidation and Corrosion of Metals*; Elsevier: Amsterdam, 2008.
5. Alcock, J. C. B.; Easterbrook, E. Thermodynamics and Kinetics of Gas-Metal Systems. In *Corrosion, Volume 1: Metal/Environment Reactions*, 3rd ed.; Shreir, L. L., Jarman, R. A., Burstein, G. T., Eds.; Butterworth-Heinemann: London, 1994.
6. Gaskall, D. R. *Introduction to the Thermodynamics of Materials*, 4th ed.; Taylor & Francis: New York, 2008.
7. Kubaschewski, O.; Alcock, C. B. *Metallurgucal Thermochemistry*, 5th ed.; Pergamon Press: Oxford, 1979.
8. Barin, I.; Platzki, G. *Thermochemical Data of Pure Substances*; VCH: Weinheim, 1995.
9. JANAF Thermochemical Data, Army-Navy-Air Force Thermochemical Panel, Dow Chemical Company, Midland, MI, 1962–1963.
10. Lou, V. L. K.; Mitchell, T. E.; Heuer, A. H. *J. Am. Ceram. Soc.* **1984**, *68*, 49.
11. Giggins, C. S.; Pettit, F. S. *Oxid. Met.* **1980**, *14*, 363.
12. Stroosnijder, M. F.; Quadakkers, W. J. *High Temp. Technol.* **1986**, *4*, 141.
13. LaBranche, M. H.; Yurek, G. J. *Oxid. Met.* **1987**, *28*, 73.
14. Birks, N.; Meier, G. H. *Introduction to High Temperature Oxidation of Metals*; Edward Arnold: London, 1983.
15. Peraldi, R.; Monceau, D.; Pieraggi, B. *Oxid. Met.* **2002**, *58*, 275.
16. Naumenko, D.; Gleeson, B.; Wessel, E.; Singheiser, L.; Quadakkers, W. J. *Metall. Mater. Trans. A* **2007**, *38A*, 2974.
17. Lee, V. H. J.; Gleeson, B.; Young, D. J. *Oxid. Met.* **2005**, *63*, 15.
18. Bradford, S. A. Fundamentals of Corrosion in Gases. In *Metals Handbook*, 9th ed.; *Corrosion;* ASM International: Metals Park, OH, 1987; Vol. 13.
19. Pettit, F. S.; Wagner, J. B. *Acta Met.* **1964**, *12*, 35.
20. Sheasby, J. S.; Smeltzer, W. W. *Oxid. Met.* **1981**, *15*, 215.
21. Kofstad, P. *Nonstoichiometry, Diffusion and Electrical Conductivity in Binary Metal Oxides*; Wiley-Interscience: New York, 1972.
22. Giggins, C. S.; Pettit, F. S. *Trans. AIME* **1969**, *245*, 2495.
23. Wagner, C. *Z. Phys. Chem.* **1933**, *21*, 25.
24. Wagner, C. *Atom Movements*; ASM: Cleveland, 1951; p 153.
25. Raynaud, G. M.; Clark, W. A. T.; Rapp, R. A. *Metall. Trans. A* **1984**, *15A*, 573.
26. Atkinson, A. *Rev. Mod. Phys.* **1985**, *57*, 437.
27. Garnaud, G.; Rapp, R. A. *Oxid. Met.* **1977**, *11*, 193.
28. Hsu, H. S. *Oxid. Met.* **1986**, *26*, 315.
29. Gesmundo, F.; Viani, F. *Corros. Sci.* **1978**, *18*, 217.
30. Wang, G.; Gleeson, B.; Douglass, D. L. *Oxid. Met.* **1989**, *31*, 415.
31. Yurek, G. J. *Corrosion Mechanisms*; Marcel Dekker Inc.: New York, 1987; p 397.
32. Dravinieks, A.; McDonald, H. *J. Electrochem. Soc.* **1948**, *94*, 139.
33. Mrowec, S. In *Proceedings of JIM International Symposium on High Temperature Corrosion of Metals and Alloys;* Mt Fuji, Japan, 17–20 November 1982; p 115.
34. Stringer, J. *Corros. Sci.* **1970**, *10*, 1970, 513.
35. Schütze, M. *Protective Oxide Scales and Their Breakdown*; Institute of Corrosion and Wiley Series on Corrosion and Protection; John Wiley & Sons Ltd: England, 1991.
36. Birks, N.; Rickert, H. *J. Inst. Met.* **1963**, *91*, 1963, 308.
37. Wood, G. C.; Wright, I. G.; Hodgkiess, T.; Whittle, D. P. *Werkst. Korros.* **1970**, *20*, 900.
38. Wagner, C. *J. Electrochem. Soc.* **1952**, *99*, 369.
39. Douglass, D. L. *Oxid. Met.* **1995**, *44*, 81.
40. Gleeson, B.; Harper, M. A. *Oxid. Met.* **1998**, *49*, 373.
41. Wei, F. I.; Stott, F. H. *High Temp. Technol.* **1989**, *7*, 59.
42. Schnaas, A.; Grabke, H. J. *Oxid. Met.* **1978**, *12*, 387.
43. Kane, R. H. *Corrosion* **1981**, *37*, 187.
44. Rapp, R. A. *Corrosion* **1965**, *21*, 382.
45. Wagner, C. *Z. Elektrochem.* **1959**, *63*, 772.
46. Gesmundo, F.; Viani, F. *Oxid. Met.* **1986**, *25*, 269.
47. Wagner, C. *Z. Elektrochem.* **1959**, *63*, 772.

1.08 Stress Effects in High Temperature Oxidation

M. Schütze
Karl Winnacker Institut der DECHEMA e.V., Theodor-Heuss-Allee 25, D-60486 Frankfurt am Main, Germany

Glossary

Acoustic emission Acoustic signals ('noise') arising from the generation of transient elastic waves produced by sudden redistribution of stress in a material (e.g., cracking, micro-cracking, and dislocation movement).

Buckling Failure by elastic instability under the effect of compressive stresses where the structural member (e.g., scale) bends sidewards in the center of an unattached area.

Coefficient of thermal expansion (CTE) Degree of expansion/contraction divided by the change in temperature.

Creep Time-dependent plastic deformation at high temperatures ('flow').

Depletion Drop in element concentration in an alloy during high temperature exposure. For example, by the consumption of this element for surface oxide formation.

Elastic modulus/Young's modulus (1) Slope of the stress–strain curve in elastic deformation, (2) resistance of a material against elastic deformation.

Healing Closure of cracks or other defective sites in a layer or oxide scale by diffusion or scale growth processes.

Microcracking Formation of cracks or crack networks where the single cracks are in the range of microns, or less.

Growth stresses Mechanical stresses originating from scale or layer growth directly due to volume changes.

Protrusions Local extension of the surface scale into the metal substrate.

Poisson ratio Ratio of transverse strain (contraction strain) divided by the extension strain (axial strain).

Physical defect Defects in a physical structure (material), for example, pores, voids, crevices, cracks, etc.

Residual stress Stresses remaining in a structure even after removing external load.

Subsurface zone Area in a material directly underneath the surface.

Thermogravimetry Test procedure in which the mass change of a specimen due to high temperature corrosion is recorded by a balance.
Thermocycling Test procedure in which a specimen is subjected to regularly repeated temperature cycles.

Abbreviations

COSIM Computer code for predicting oxide spallation
CTE Coefficient of thermal expansion
DTMO Differential test in monofacial oxidation
NASA National Aeronautics and Space Administration
ODIN Computer code for predicting alloy depletion
PBR Pilling-Bedworth-ratio
RT Room temperature (ambient temperature)
XRD X-ray diffraction

Symbols

c Physical defect size
d_{met} Thickness of the metal substrate
d_{ox} Oxide scale thickness
r Interfacial amplitude
t Time
t_B Time to the beginning of breakaway oxidation
A_o Length of a defect free interface
A_{sep} Separated length of an interface
C_c Minimum alloy concentration to form a protective oxide scale (critical concentration limit)
D (inter-)Diffusion coefficient
E^* Effective elastic (Young's) modulus
E_{met} Elastic (Young's) modulus of the metal
E_{ox} Elastic (Young's) modulus of the oxide
G_c Critical surface energy
K Stress intensity factor
K_c Fracture toughness
k_i Oxidation rate constant for the recession of the oxide/metal interface
K_{Ic} Fracture toughness under mode I load
$N_{A,b}$ Atom fraction of element B in an alloy
PBR Value of the Pilling-Bedworth-Ratio
R Radius of a scale delamination
T Temperature
ν_{met} Poisson ratio of the metal
ν_{ox} Poisson ratio of the oxide
α_m Mean coefficient of thermal expansion (CTE) of a multi-scale system
α_{met} Coefficient of thermal expansion (CTE) of the metal
α_{ox} Coefficient of thermal expansion (CTE) of the oxide
ε_c Critical strain to failure
δ_{el} Elastic strain
ε_{ext} External strains resulting from component operation
ε_{geo} Geometrically induced oxide growth strains
ε_{int} Intrinsic oxide growth strains
ε_{ox} Strain in the oxide
ε_{pl} Plastic strain
ε_{therm} Thermally induced oxide strains from temperature changes
$\dot{\varepsilon}$ Strain rate
$\dot{\varepsilon}_c$ Critical strain rate for scale crack healing
λ 'Wave length' of an interface
σ Elastic stress
σ_c Critical stress for failure
σ_{ext} External stresses resulting from component operation
σ_{geo} Geometrically induced oxide growth stresses
σ_{int} Intrinsic oxide growth stresses
σ_{ox} Stress in the oxide
σ_{therm} Thermally induced oxide stresses from temperature changes
ω Stress relaxation factor
ΔT Temperature change
γ_i Intrinsic surface energy
γ_o Fracture surface energy

1.08.1 Introduction

The role of stresses in oxidation is of significance because these stresses can determine the lifetime of a high temperature component from a corrosion point of view.[1] High temperature corrosion resistance is based on the protective effect of dense, slowly growing, and adherent oxide scales, that is, if any chemical or mechanical damage occurs to these scales, the corrosion resistance of the materials will be endangered. This chapter deals with the key aspects describing scale integrity under the effect of stresses, also taking into account the role of the superimposed oxidation processes. The latter is important as, at elevated temperature, stresses and oxidation should not be looked at separately as they are active simultaneously and interact with each other.

Therefore, not only the topics of mechanical scale failure (cracking, spalling, delamination, etc.), but also the mechanisms of scale damage healing and metal subsurface zone depletion are addressed.

An example where the whole complexity of this interaction becomes evident is the so-called 'breakaway mechanism' by which the protective period in oxidation ends and the nonprotective period starts.[2] From a technical point of view this is the end of the lifetime of a component, at least under the aspect of high temperature corrosion. Although the breakaway effect can also be described solely based on chemical mechanisms (loss of chemical stability of the protective oxide),[3] under industrial conditions mechanical stresses are always present and the breakaway effect is considerably determined from a joint interaction of chemical and mechanical mechanisms.[3,4] In the simplest case the latter may be initiated from (intermediate) cooling, but also at constant operation temperature oxide growth stresses can reach critical limits where the integrity of the scales is endangered.[5]

Generally, the following stresses in oxidation can be distinguished[1]:

1. Intrinsic growth stresses σ_{int} resulting from the chemical nature of the oxidation process. These can arise when new oxide is formed inside the existing oxide, for example, by counter diffusion of oxide forming species. Other sources of such stresses can be epitaxial relationships between metal surface and oxide in particular at the beginning of oxidation or phase transformations in the oxide scale, the metal, or coating subsurface zone.
2. Geometrically induced growth stresses σ_{geo} resulting from particular narrow surface curvatures where effects of the differences in volume of oxide formed and metal consumed come into play.
3. Thermally induced stresses σ_{therm} resulting from temperature changes and the different values of the coefficients of thermal expansion (CTE) for metal/alloys and oxides.
4. External stresses σ_{ext} resulting from operation, for example, centrifugal stresses, gravity, constraints in structures, etc.

All these stresses have to be accommodated by elastic or plastic/creep deformation in the oxide/metal system. Otherwise, if critical stress values are exceeded, mechanical failure of the scale results as a stress relief mechanism. In this case, however, the protective effect of the scale may be lost unless it can be restored by scale healing mechanisms.

Equation [1] summarizes this situation in terms of the strain values resulting from the different types of stresses:

$$\varepsilon_{int} + \varepsilon_{geo} + \varepsilon_{therm} + \varepsilon_{ext} = \varepsilon_{el} + \varepsilon_{pl} \quad [1]$$

Failure occurs when the elastically stored energy in the form of ('elastic') stress σ reaches or exceeds a critical value σ_c:

$$\sigma = E_{ox}\varepsilon_{el} \geq \sigma_c \quad [2]$$

where E_{ox} is the elastic modulus of the oxide scale.

Failure occurs in terms of strains when

$$\varepsilon_{int} + \varepsilon_{geo} + \varepsilon_{therm} + \varepsilon_{ext} = \varepsilon_{el} + \varepsilon_{pl} = \varepsilon_c \quad [3]$$

where ε_c is the critical strain for the different failure mechanisms (see **Section 1.08.4**). As will be shown later, oxide scales usually behave in a brittle manner, even at service temperatures of high temperature components, so that at mechanical scale failure $\varepsilon_{pl} \ll \varepsilon_{el}$ or $\varepsilon_c \approx \varepsilon_{el}$.

In addition to the failure mechanism, ε_c is also a function of the oxide/metal system and the oxidation parameters. High values of ε_c automatically mean high tolerance of the system against failure by mechanical stresses.

The following sections deal in some detail with the key issues of the role of stresses in oxidation. For an even more detailed description of this topic, the reader is referred to a textbook which is devoted solely to this field.[1]

1.08.2 Scale Stresses Arising from Oxide Growth

1.08.2.1 Intrinsic Growth Stresses in Oxide Scales

1.08.2.1.1 Experimental observations

Most standard investigations of the oxidation behavior of materials do not take into account that the formation of growth stresses in the scales may take place during the oxidation process.[6] The existence of such stresses has, however, already become evident in an optical observation of the oxide scale surfaces as shown as an example in **Figure 1**.[7] In this example the scale shows a perpendicular arrangement of waves that have partially detached from the substrate. The formation of such waves is an indication that additional volume had been created in the existing oxide which had to be accommodated by a stress relaxation mechanism like detachment. This situation has been observed by a number of authors.[8–15]

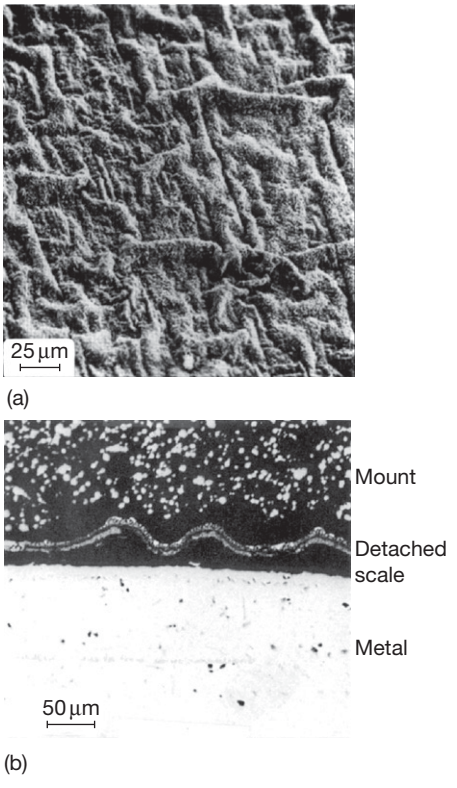

Figure 1 'Wave' formation in the oxide scale due to lateral growth stresses on a heat resistant 18 Cr steel after 100 h oxidation at 1000 °C in air.[7] (a) SEM image of the surface and (b) optical micrograph of a cross-section.

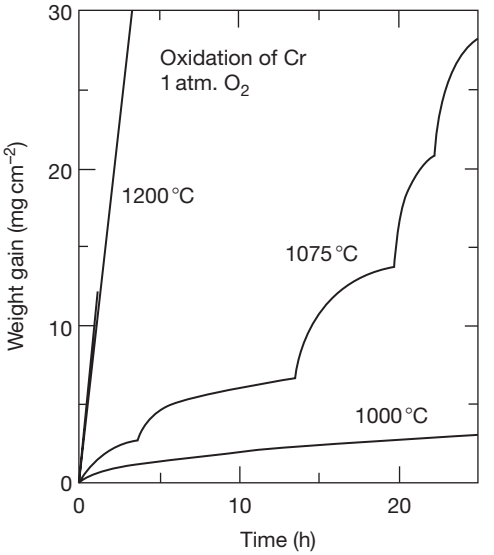

Figure 2 Repeated cracking of scales leading to a sequence of 'parabolic' stages in the overall oxidation of pure Cr at 1000–1200 °C in O_2.[8,9]

As the example in Figure 1 shows, the formation of waves was possible without damage to the existing oxide so that its protective effect remained.

Thermogravimetric investigations of the oxidation of pure chromium revealed that such (isothermal) growth stresses could even be sufficiently high to crack the existing oxide and initiate the formation of new oxide on the fresh metal surface exposed underneath the waves.[8,9] This becomes evident in the mass change versus time curve shown in Figure 2. After each cracking process, the start of a new parabolic partial curve is observed and in the extreme case of very high growth stresses at the highest test temperature, in these investigations the cracking frequency has become so high that a quasilinear mass change curve is found.

Besides the phenomenological observations, a number of measurements have been performed in order to quantify the level of these growth stresses. The measurement techniques reported in the literature are the following:

1. Measurement of the bending of a thin metal strip which is protected on one side and oxidized on the other side.[16–22] This test is sometimes called differential test in monofacial oxidation (DTMO).[21,22]
2. Measurement of the bulging of a thin metal plate protected on one side and oxidized on the other side.[23]
3. Measurement of the change in diameter of a helix or a spiral made of a thin metal strip oxidized either on one side[24,25] or on both sides.[26] On the spiral, the length change can also be measured.
4. Measurement of the increase in length of thin metal strips or tubes resulting from creep and elastic deformation of the substrate due to the stresses from the oxide growth.[27–30]
5. Measurement of the curvature or a radius change of a U-shaped thin foil specimen.[31] A somewhat similar method is the catenary method which makes use of a wire sample suspended as a catenary between two supports and where a change in the shape of the catenary curve is recorded during oxidation.[32]
6. Measurement of the bending of an oxidized strip as one of the sides is polished away stepwise and the thickness is progressively reduced.[33]
7. Measurement of the frequency shift due to scale stresses in Raman spectroscopy/photo luminescence.[34–39]

8. Using changes in the photocurrent due to stresses by applying a microphotoelectrochemistry technique.[39]
9. Measurement of the distortion of the oxide lattice using X-rays.[40–45]
10. Measurement by using synchrotron radiation instead of standard X-ray sources which allows one to study thinner oxides and with greater time resolution.[45,46]

In particular, the foil bending measurements can be combined with acoustic emission recording, which allows the detection of any cracking or delamination processes resulting from the build-up of scale stresses.[5,21,22] All these measurements have been described in great detail in the respective publications where the drawbacks and the advantages of the different methods are also discussed. In the following section, only the results from measurements are addressed.

One of the systems that has been investigated in some detail is NiO on nickel or Ni–Cr.[20,21,47–49] The reason for this is that a single phase oxide of significant thickness is formed, which allows nickel oxide scales to be looked at as a model system. A typical example of the course of the stress curves as a function of oxidation time is given in **Figure 3(a)**. In many cases, such curves start with a very short tensile period before they change into a steeply increasing compressive slope, which reaches a maximum and then falls off slightly. Often after longer times, the level of stress starts to oscillate around a certain value as is also indicated in this example for the two polycrystalline nickel versions. Interestingly the oxide formed on the nickel single crystal shows a further increase of the growth stresses which falls together with the effect that no acoustic emission occurs for the single crystal specimen while on the two polycrystalline specimens significant acoustic emission takes place, starting after ~10 h of exposure, **Figure 3(b)**. Acoustic emission is an indication that, evidently, micro cracking and oxide delamination has taken place because of the formation of growth stresses allowing direct access of oxygen through the scale to the oxide/metal interface and the formation of new fine-grained oxide at these positions. As a consequence, the typical two layered structure on nickel is formed as an oxide scale while on the single crystal nickel only a single oxide layer appears. In Przybilla and Schütze,[21] this could be explained in a model by the presence of impurities in the polycrystalline nickel materials which facilitates interfacial delamination while the nickel single crystal was ultra pure and the oxide scale was adherent. This effect was later also confirmed by Huntz *et al.*[48] The maximum growth stress values which were observed in these tests were around −550 MPa at 900 °C.

Much higher stresses are reported, for example, for chromia layers growing at 750 °C in pure oxygen.[38] In this case, values of up to −2.4 GPa were reached as measured by Raman spectroscopy. Similar values were measured under the same conditions for steels of the composition Fe–18Cr and Fe–18Cr–TiNb. For the oxide scales on pure iron or mild steel, respectively, different values were observed for magnetite and hematite in the same oxide scale.[45] In magnetite, these stresses reached values of tensile nature up to 135 MPa at 400 °C while those in the same scale for hematite were compressive and went up to −270 MPa. Interestingly when oxidizing gray cast iron the stresses in both partial layers were of compressive nature at 400 °C. For magnetite, they reached −60 MPa, while for hematite the maximum was around −570 MPa. In all cases, there was first an increase up to a maximum in the value of the stresses while during further oxidation, a decrease or an oscillation around a certain level occurred. This was similar to the observations described for NiO on polycrystalline Ni in **Figure 3**.

The largest number of investigations on oxide growth stresses focused on the behavior of alumina scales on iron or nickel based substrates. In most cases, surprisingly high compressive stress values were found, which make it hard to believe that the oxide scale could survive such stresses without any mechanical damage. As an example, a tensile stress value of 600 MPa on β-NiAl alloys that had been oxidized at 1100 °C can be quoted.[46] It should, however, be mentioned that large contradictions also occur between the measured values of different investigations. As an example, the measurements by Hou *et al.*[50] can be quoted with much lower values, which were explained by stress relaxation processes. Hou *et al.*[50] also reveals that in the early stages the growth stress in θ-Al_2O_3 is compressive and is converted into tensile stresses when the formation of α-Al_2O_3 begins. Only when a complete α-Al_2O_3 layer had formed at the metal/oxide interface did the stresses in α-Al_2O_3 become compressive, reaching a steady state level around −75 MPa at 1100 °C. Other sources report growth stresses on NiAl oxidized at 1100 °C in the range of around zero.[44]

For FeCrAl(Y) alloys and iron-based aluminides extremely high stresses had been found, for example, up to −1.6 GPa.[51] Surprisingly there is, however, a big

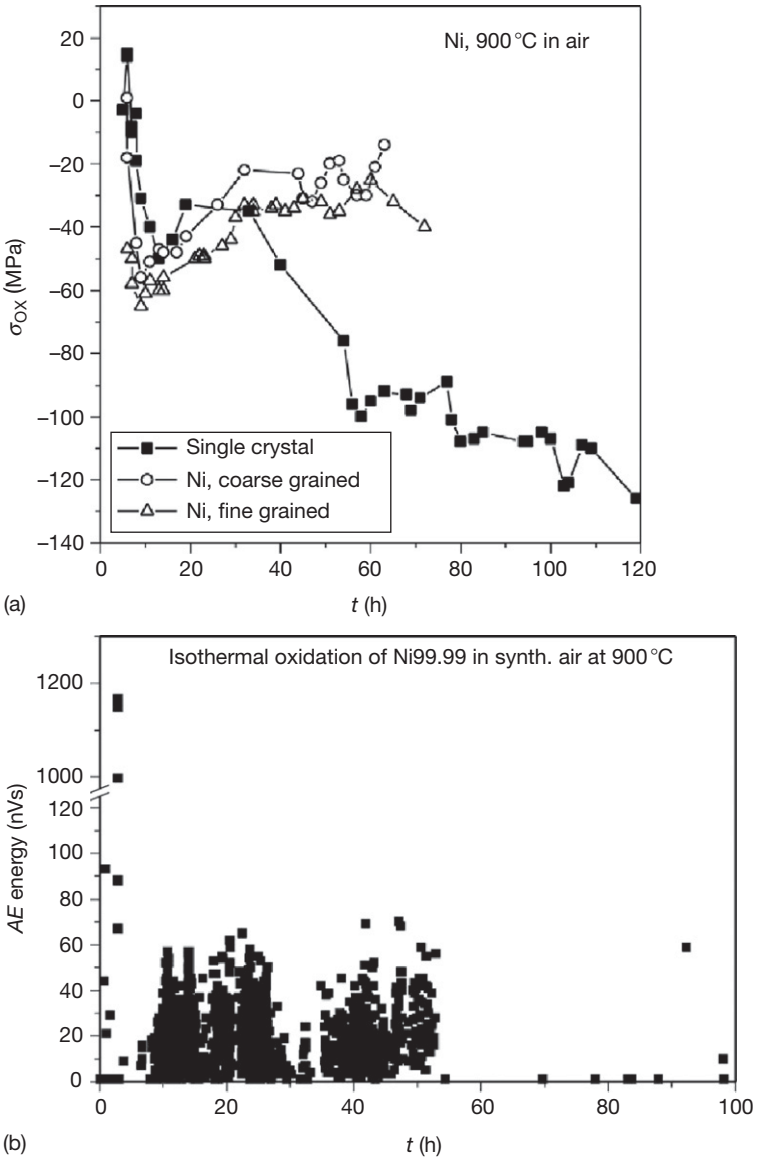

Figure 3 (a) Growth stress in NiO scales on nickel as a function of oxidation time at 900 °C in air as determined by XRD measurements[21,49] (single crystal = 99.9999% Ni, Ni coarse or fine grained = 99.99% Ni). (b) Acoustic emission activity in a plain oxidation test with Ni99.99 at 900 °C in air. Reproduced from Przybilla, W.; Schütze, M. *Oxid. Met.* **2002**, *58*, 103–145.

scatter between very high compressive and very high tensile stresses, depending also on the measurement technique. While in high temperature X-ray measurements compressive values as high as −1.7 GPa were observed,[44] similar investigations at the same temperature by synchrotron X-ray radiation led to tensile stresses of the same order of magnitude.[46] Tensile growth stresses of ∼1 GPa were also observed by Mennicke *et al.*[52] which addresses, however, also the point that significant stress relaxation may take place during isothermal, and in particular, thermocycling oxidation of the materials. Interestingly Mennicke *et al.*[52] also detected that there is no significant difference in the growth stresses as well as in the residual stresses after cooling or with regard to stress relaxation during thermocycling, between oxides formed on Y-doped and undoped FeCrAl materials. Evidently, the presence of a reactive element in this case did not lead to a change of the oxidation mechanism in a way that influences the intrinsic growth stress situation.

Limited information is available on TiO_2 as well as TiO_2/Al_2O_3 mixtures on titanium and titanium aluminides, respectively. While for titania the values are compressive and exceed −1000 MPa,[39] those of the mixed oxide scale on the titanium aluminides can be compressive as well as tensile, both in the range of ∼100 MPa.[22]

In Table 1 a rather incomplete summary of the existing information in the literature on the level of intrinsic growth stresses in oxides is attempted, which indicates that there is still a significant scatter between the data and definitely more work is needed to get a clearer view of the role and the level of intrinsic growth stresses in oxide scales.

Finally an interesting aspect, which was observed for ferritic steels forming Cr-rich oxide scales, is addressed. Here it turned out that water vapor-containing environments lead to higher compressive

Table 1 Results from growth stress measurements of oxide scales

Oxide	*Substrate*	*Temperature (°C)*	*Max. abs. value[a] (MPa)*	*Technique*	*Ref.*
NiO	Ni	627	−90		53
	Ni	1027	+12/+110		53
	Ni	940	+1365		53
	Ni Grade A	900	+20		54
	Ni SX 99.999	900	−130/+15	X-ray	49
	Ni 99.99	900	−55/+15	X-ray	49
	Ni 99.0	900	−65/+15	X-ray	49
	Ni 99.99	900	−550/+250	DTMO	21
	Ni 99.0	900	−400/+300	DTMO	21
	Ni 99.99	800	−1500/+700	DTMO	21
Fe_2O_3	Mild Steel	400	−270	X-ray	45
	Grey Cast Iron	400	−5770	X-ray	45
Fe_3O_4	Mild Steel	400	+135	X-ray	45
	Grey Cast Iron	400	−60	X-ray	45
Cr_2O_3	Cr 99.7	750	−2400	Raman	38
	Fe–18Cr	750	−2800	Raman	55
	Fe–18Cr–TiNb	750	−2200	Raman	55
	Cr	875	+200		19
	Cr	940	−350		1
θ-Al_2O_3	β-NiAl	1000/1100	−480	Synchrotron	50
α-Al_2O_3	β-NiAl	1000/1100	−75/+500	Synchrotron	50
Al_2O_3	NiAl	1100	0	X-ray	44
	FeCrAlY	1100	−1300/−200	X-ray	44
	FeCrAl	1100	−400	X-ray	44
	FeCrAlY	1000	−1700/−500	X-ray	44
	FeCrAl	1000	−1000	X-ray	44
	FeCrAlY	1100	+1100/+500	Synchrotron	46
	FeCrAlY	1000	+500	Synchrotron	46
	FeCrAlY	1200	+800/+100	Synchrotron	46
	Kanthal	1000	+260	Synchrotron	46
	Kanthal	1200	−150	Synchrotron	46
	NiAl	1100	+600/−300	Synchrotron	46
	NiAl + Hf	1100	+500		46
	FeNiCrAl	1000	−400	DTMO	18
	FeNiCrAlY	1000	−80	DTMO	18
	FeCrAl	1300	−340	DTMO	56
TiO_2	Ti99.6		−1000	Raman	39
TiO_2/Al_2O_3	TiAl2Cr	800	+100/−100	DTMO	22
	TiAl	900	−130	DTMO	22
Cr-(Fe)-oxide	P91 steel	650/dry air	−200	DTMO	5
	P91 steel	650/10% H_2O	−1200	DTMO	5
	Nf 616	650/dry air	−120	DTMO	5
	Nf 616	650/10% H_2O	−900	DTMO	5

[a]Max. abs. value means that this was the highest value measured independent of the stress direction. The latter is indicated by the (+) or (−) sign: (+), tensile; (−), compressive.

stresses than dry air.[5] While the stresses in dry air oscillate around a constant value over oxidation time, there is a significant stress relaxation in the humid environment, which leads after a while to a drop of the growth stresses to values close to those in dry air.

1.08.2.1.2 Modeling

The earliest attempt to model the formation of growth stresses in oxide scales during the oxidation process, dates back to 1923 and was performed by Pilling and Bedworth.[57] In their model, they described the volume change that is involved in the transition from the metal lattice to the cation lattice of the oxide when only the oxygen anions are diffusing during the oxide growth process. The ratio of the volume of the oxide formed by the oxidation process to the metal consumed in this reaction is termed the Pilling–Bedworth ratio (PBR). Values of the PBR are given in **Table 2** for several oxides and metal substrates. The key assumption in this model is that the oxide scales grow inwardly and they would be compressed if the PBR were greater than one. Tensile stresses would develop in the oxide if the PBR were less than one. Consequently, if oxide scales grow outward by the diffusion of metal cations, the oxide scale must remain free of growth stresses as the new oxide grows freely on the scale surface. Assuming inward scale growth will occur, the resulting strain in the oxide can be calculated according to the following equation[60]:

$$\varepsilon_{ox} = \omega[(\mathrm{PBR})^{1/3} - 1] \qquad [4]$$

where the factor ω is introduced to take account of possible stress-reducing processes. Assuming elastic behavior, the corresponding growth stress in the oxide would be:

$$\sigma_{ox} = \frac{-E_{ox}}{1 - \nu_{ox}}\varepsilon_{ox} \qquad [5]$$

where E_{ox} is the elastic modulus of the oxide, and ν_{ox} is the Poisson ratio.

The PBR values have been used for many years, and are sometimes still used, to explain the formation of growth stresses in oxide scales. Nowadays, however, it is generally agreed that this model is too simplistic an explanation, especially because it does not take into account the outward growth of oxides by metal cation transport, which is a dominant mechanism for many technical alloys. In the meantime a number of more sophisticated models have been developed[61] describing, for example, the formation of growth stresses based on the formation of new oxide in the existing oxide scale, as shown in **Figure 4**.[2] The first model of this type was developed by Rhines and Wolf, based on the assumption that counter diffusion takes place in the oxide scale with the inward movement of oxygen along grain boundaries and the outward movement of metal cations within the oxide grains.[142] The reactions of the two species at the oxide grain boundaries would lead to the formation of new oxide at these positions with a volume increase that also generates strains in a lateral direction. As counter diffusion of the oxide-forming species during scale growth has also been shown in several

Table 2 PBR values for some technically important oxides and metal substrates[2,17,57–59]

System	*PBR*
α-Al_2O_3/Al	1.28
CoO/Co	1.86
Cr_2O_3/Cr	2.07
Cr_2O_3/Fe–25Cr–20Ni	2.1
CuO/Cu	1.70
$FeCr_2O_4$/Fe–18Cr–8Ni	2.1
Fe(FeCr)$_2O_4$spinel/Fe–Cr	2.1
FeO/α-Fe	1.68
Fe_2O_3/α-Fe	2.14
Fe_2O_3/Fe_3O_4	1.02
Fe_3O_4/α-Fe	2.1
Fe_3O_4/FeO	1.2
MgO/Mg	0.84
MnO/Mn	1.77
MoO_3/Mo	3.27
NiO/Ni	1.65
SiO_2/Si	2.15
TiO_2/Ti	1.73
ZrO_2/Zr	1.57

Reproduced from Kofstad, P. *High Temperature Corrosion*; Elsevier Applied Science: London, 1988.

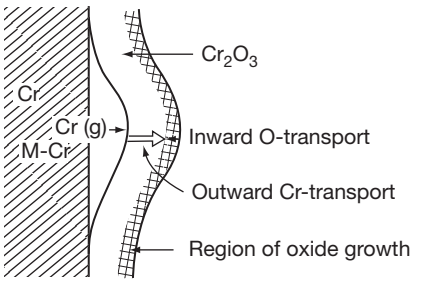

Figure 4 Schematic representation of the growth of chromia scales by counter transport of oxygen and chromium in the scale. Reproduced from Kofstad, P. *High Temperature Corrosion*; Elsevier Applied Science: London, 1988.

investigations by isotope and SIMS measurements,[62] this approach has also become the basis for many of the more advanced and more recent models in the literature.[63–65] Clarke was able to express the growth strain rate in terms of a number of parameters including the parabolic rate constant, the scale thickness, and the oxide grain size.[63] This lateral growth strain rate increases with the parabolic rate constant and decreases with increasing oxide grain size and scale thickness. While these models in several cases can predict the measured order of magnitude of scale stresses correctly, they still have the problem that any stress relaxation process, which will inevitably take place under practical conditions, is not reflected. Nevertheless, all these models can help a better understanding of the complex situation in the oxidation of particular technical alloys, which is in most cases away from the simple parabolic growth mechanism usually described in textbooks.

1.08.2.2 Geometrically Induced Growth Stresses

On curved substrate surfaces, the growth of oxide scales can lead to growth stresses originating from the surface geometry. The reason is that metal is consumed by the oxidation process so that the original metal surface recedes and at the same time there is a difference between the original metal volume consumed by the oxidation process and the volume of the resulting oxide, see PBR. Figure 5 illustrates the potential situations that can exist, based on the extreme cases of scale growth by cation diffusion alone and by anion diffusion alone for PBR > 1.[66]

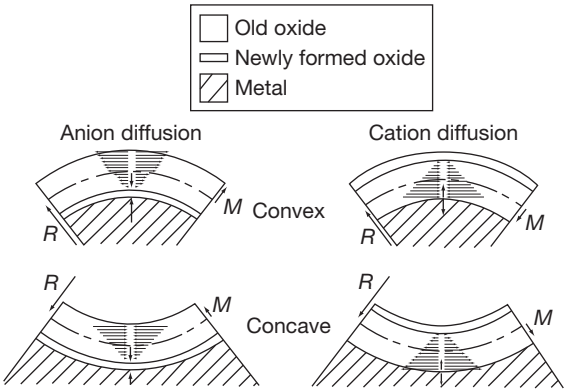

Figure 5 Growth stresses in the oxidation of curved surfaces. Reproduced from Christl, W.; Rahmel, A.; Schütze, M. *Oxid. Met.* **1989**, *31*, 1.

In the case of anion diffusion, the new oxide is formed at the interface between oxide scale and metal. As most of the technical oxides have a PBR > 1, it means that additional volume is created at the interface, which shifts the existing oxide scale outward. As a consequence, tensile stresses will arise in circumferential direction on convex surfaces, while compressive stresses will be present perpendicular to the interface between oxide and metal. The circumferential stresses are the highest in the 'oldest' part of the oxide, which is the one on the scale surface. The part that was formed last is almost stress-free with regard to the circumferential direction. On concave surfaces the same situation leads to compressive circumferential and perpendicular stresses, as shown in the lower left part of Figure 5. For cation diffusion, new oxide is formed on top of the existing oxide and is, thus, the stress-free part of the system. The oldest part is at the oxide/metal interface and, thus, shows the highest circumferential stresses. These are compressive for convex surfaces and tensile for concave surfaces. The stresses perpendicular to the oxide/metal interface are tensile in both cases.

As described by Schütze,[1] these scale stresses can be calculated quantitatively, based on the oxidation rate data and the surface curvature. The general tendency is that the higher the oxide growth rate and the smaller the surface curvature radius, the more marked will be the oxide scale stresses resulting from the geometrical situation. As a result, fast-growing oxide scales, especially at sharp edges, are greatly endangered from high geometrical growth stresses. As will be shown later, tensile stresses especially can lead to delamination of the scale or scale cracking, so that low curvature radii such as edges can always be sites of preferred attack by high temperature corrosion as the protective oxide scale may suffer damage at these spots first.

1.08.2.3 Other Types of Growth Stresses

Among the stresses arising from oxide growth, there are many other sources of stress that can be considered intrinsic growth stresses, but are of significance only in very specific cases. In the literature, the role of epitaxial stresses has been discussed often, where stresses develop as a consequence of the difference in lattice parameters of the oxide and the substrate. Such stresses should be maximum at the oxide/metal phase boundary and will fall off toward the oxide surface.[67] It can be expected that with the increasing thickness of the oxide scale, such epitaxial

stresses will have less significance, which means that they play a role only in extremely thin films and at low temperatures.[58]

Another cause for growth stresses in oxide scales can be changes in the oxide composition.[68] For example, it has been observed that for various Fe–Cr alloys, the transition from initially formed $(Cr, Fe)_2O_3$ to a scale with increasing Cr and decreasing Fe content, leads to the formation of tensile stresses in course of time.[69] The explanation for this effect was a decrease in atomic volume associated with this transition. Another example is the change from the transient alumina scales consisting of θ-Al_2O_3, at the beginning of oxidation to the later α-Al_2O_3, which, due to the different crystal structures, also induces stresses in the oxide, which usually lower the compressive stress level in the scale.[50] Further effects can be present in the case of phase changes in the metal subsurface zone where for example, the consumption of aluminum by oxidation and, thus, a phase change from β-NiAl to γ-NiAl leads to a volume change.[70] The situation of stresses induced by selective internal oxidation is discussed by Hänse *et al.*[71] also. Although such stresses are present in the metal subsurface zone they will have an effect on the oxide scale itself. Such internal oxides or oxide protrusions of the scale/metal interface can introduce stresses not only by the growth of the oxide under isothermal conditions but also during cooling, leading to detrimental local stress concentrations.[72] Another source of local differences in (growth) stress levels can be multiphase substrates on which different types of surface oxides are formed, with locally different oxide growth rates.[72]

Finally, it should be mentioned that the involvement of volatile species in the oxidation process can also have a dramatic effect on the stress situation in the oxide scale. This is particularly known as the so-called active oxidation, which takes place in oxidizing halogen-containing environments.[73–75] In this case, volatile metal halides, which are formed at the oxide/metal interface by the reaction of halogen from the gas phase with the metal migrate in an outward direction through the oxide scale and, with increasing oxygen partial pressure, are deposited as solid oxides within the scale. As a result, additional volume is created within the existing oxide scale, leading to high compressive stresses followed by the cracking and opening up of the oxide scale for further ingress of halogens to the metal. These very high growth stresses are the reason why a protective effect of the oxide scale cannot be maintained under halogenizing conditions.

Dissolution and precipitation processes in the oxide have also been speculated to create growth stresses that can lead to cracking and by this to a change in the oxidation kinetics. An example for this is the mixed TiO_2/Al_2O_3-oxide scale on intermetallic titanium aluminides, where the initially formed Al_2O_3 barrier in the scale becomes dissolved after a while and reprecipitated as discrete Al_2O_3 particles in a TiO_2 matrix. This process seems to lead to precipitation stresses and microcracking in the scale after an incubation period, and initiates the so-called breakaway effect, where the oxidation rates increase significantly compared to the former protective period.[76]

1.08.3 Thermally Induced Scale Stresses Resulting from Temperature Changes

1.08.3.1 Experimental Observations

The CTE of substrate material and oxide scale are usually different from each other and during temperature changes these differences can lead to significant stresses in the oxide/metal system. **Table 3** shows a compilation of measured and theoretically calculated CTE data. This compilation should serve as orientation as the CTEs are a function of temperature with, in most cases, a more or less linear dependency where the higher CTE values are at the higher temperature. **Table 3** reports the maximum values found in the literature. For a more exact quantitative consideration of the stress situation in oxide/metal systems during temperature changes, it is recommended that the reader either refers to the original literature or measures the CTE data in laboratory tests. As high temperature components have to be cooled down from their operation temperature during inspection intervals or if they are subjected to thermocyclic operation, it is necessary to regard the role of temperature induced stresses in the oxide/metal system in some depth. As general experience shows, these stresses are the most critical for the protective effect of the oxide scales and can reach values as high as 3 GPa and even more.[78]

For thermally grown oxide scales, the temperature-induced stress cannot be measured directly, as discussed in **Section 1.08.1**. After a temperature change new stresses develop in the scale; however, these new thermal stresses are added on top of the preexisting intrinsic growth stresses, geometrically induced growth stresses, and external stresses (see eqns [1]–[3]). Moreover, stress relaxation phenomena

Table 3 Orientational ('maximum') values of the coefficients of thermal expansion (CTE) for several technically relevant substrates, coatings, and oxide phases

	CTE α (10^{-6} K)		CTE α (10^{-6} K)
SiO_2 (amorphous)	0.9	Incoloy 956	15.0
HPSN	3.0	738	15.3
Si	4.6	Alloy S, 713	15.4
SiC	4.9	NiPt39Al	15.6
AlN	6.2	617, Hast C-4	15.6
TiN	7.8	CMSX 6, IN 100	15.8
$MoSi_2$	7.9	Hast C-276, 230	15.9
Cr_2O_3, SiO_2 (cryst.)	8.1	Hast C-22	16.1
Al_2O_3	8.4	NiCrAlY	16.4
Ti	8.6	Hast X	16.5
Pt	8.8	600	16.6
Y_2O_3	8.9	X-750	16.7
Cr	9.5	NiO, 556, 718	17.1
IMI 834, NiAl	9.9	625	17.2
TiO_2	10.5	Ni	17.5
Ti_3Al (α2)	10.9	188	17.8
RuAl	11.0	Austenitic steels	17.0–19.0
Pd	11.6	800H	18.3
Ni_3Al	11.9		
NiCo17Cr14AlY	18.5		
$TiSi_2$	12.1	Fe_3Al	19.5
TiAl	12.9	$FeAl_2$	19.5
Ferritic steels	12.0–14.0	FeAl	21.8
Co	13.9	Fe–28Al–2Cr	22.5
CoAl	14.0	Al	23.8
FeCrAlY	14.5	Fe–28Al–5Cr–0.1Zr	24.0
CoO	14.9	Fe_2Al_5	24.2

Reproduced from Schütze, M.; Malessa, M.; Rohr, V.; Weber, T. *Surf. Coat. Technol.* **2006**, *201*, 3872–3879.

such as scale microcracking, detachment, and plastic deformation of the substrate also change the scale stress state. The superposition of all these stress generators and relaxors are sometimes called the 'residual' scale stress, which is often measured at room temperature (RT) after high temperature exposure by Raman spectroscopy, optical fluorescence spectroscopy, and X-ray diffraction (XRD).[79–86] The measured RT residual stresses, even though they are not a direct measure of temperature-induced stress, provide insight into the scale stress situation, which has been demonstrated for the reactive element effect [79–81] and some sample geometry effects.[82–84]

An example for the case of the reactive element effect is given in **Figure 6** where the Raman technique

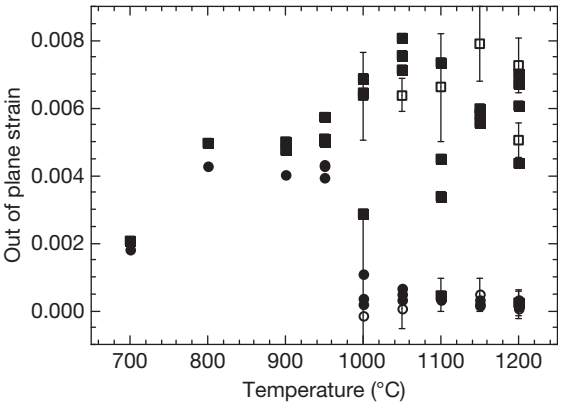

Figure 6 A comparison of out-of-plane Al_2O_3 residual scale strains after cooling as a function of oxidation temperature, as determined by XRD (open circles and open squares) and Raman spectroscopy (full circles and full squares). The materials investigated were FeCrAl (circles) and FeCrAl + 0.1Zr (squares).

was also verified by XRD measurements. At exposure temperatures above ~1000 °C the alloy without the reactive element Zr spalls, after cooling to RT, and the measured strains go to zero. The alloy with Zr does not spall after cooling and the scale strain remains high. At temperatures below 1000 °C there is no significant difference in the strain levels between the two alloys. This aspect of the reactive element effect has been experimentally confirmed for the reactive elements Zr, Y, and Hf in a variety of FeCrAl, NiCrAl, NiCoCrAl, and NiAl alloys.[79–81] The transition temperature (1000 °C in **Figure 6**) above which the reactive element effect is observed can differ from alloy to alloy, for example on NiCoCrAl and even some FeCrAl. The reactive element effect is observed at temperatures above 1100 °C.[79–81] This is caused by the variation in thermal strain due to the different CTEs of the respective alloys as shown in **Table 3**. Generally speaking, the higher the alloy CTE the lower the exposure temperature required to produce an influence of the reactive element effect.

The Raman technique has also been used to investigate the role that sample geometry plays in residual stresses.[82–84] These investigations show that the higher compressive residual stresses are found in the sample center and decrease as the sample edge or corner is approached.[82] The stress analysis performed by finite element modeling shows that the stress component perpendicular to the sample surface is near zero at the sample center and becomes increasingly more tensile as the sample edge or

corner is approached. This tensile stress, if large enough, is expected to cause scale spallation at the edges and corners of samples.

1.08.3.2 Modeling

A quantitative assessment of the level of stresses induced by temperature changes can be performed using the following equation[87]:

$$\sigma_{ox} = \frac{-E_{ox}\Delta T(\alpha_{met} - \alpha_{ox})}{(E_{ox}/E_{met})(d_{ox}/d_{met})(1-\nu_{met}) + (1-\nu_{ox})} \quad [6]$$

where E_{met}, E_{ox} are the elastic moduli of the metal and the oxide, respectively, ν_{met}, ν_{ox} are the Poisson ratios of the metal and oxide, respectively, d_{met}, d_{ox} are the thickness of the metal substrate and the oxide scale, respectively, and α_{met}, α_{ox} are the thermal expansion coefficients of metal and oxide. The elastic moduli and, as already mentioned, in most cases also the CTE, are not independent of temperature, so eqn [6] is accurately applicable only for limited temperature intervals. For larger temperature changes σ_{ox} has to be calculated by making a summation of the incremental values over small temperature intervals. Equation [6] can be simplified if thin oxide scales on thick substrates are considered:

$$\sigma_{ox} = \frac{-E_{ox}\Delta T(\alpha_{met} - \alpha_{ox})}{1-\nu_{ox}} \quad [7]$$

In the case of multilayer oxide scales, where the different layers have different CTE, the stress σ_i of each individual layer i of n layers can be calculated by[88]

$$\sigma_i = \frac{E_i}{1-\nu_i}\Delta T\frac{\alpha_m - \alpha_i}{1-\alpha_i\Delta T} \quad [8]$$

where α_m is the mean thermal expansion coefficient of the combined scale:

$$\alpha_m = \frac{\sum_i^n d_i E_i \alpha_i/[(1-\nu_i)(1-\alpha_i\Delta T)]}{\sum_i^n d_i E_i/[(1-\nu_i)(1-\alpha_i\Delta T)]} \quad [9]$$

Also for thermally induced stresses, the surface curvature may play a role for the sign and the level of the thermally induced stresses (Figure 7). In most cases, the CTE of the oxide scale will be lower than that of the metal substrate (left part of Figure 7) so that on convex surfaces compressive stresses will be found in the circumferential direction and tensile stresses perpendicular to the oxide/metal interface. On concave surfaces, the circumferential stresses are compressive and those at the oxide/metal interface in the perpendicular direction also become compressive. The case where the CTE of the oxide is higher than that of the metal is shown in the right part of Figure 7.

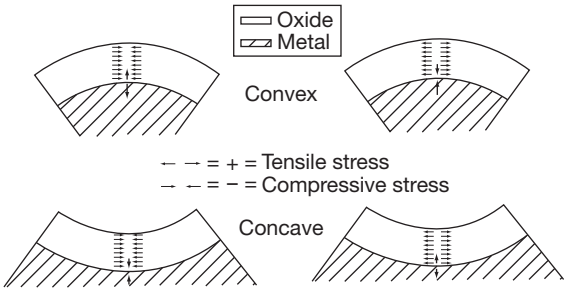

Figure 7 Direction of the cooling stresses on curved surfaces.[1] Left part: $\alpha_{met} > \alpha_{ox}$. Right part: $\alpha_{met} < \alpha_{ox}$.

The situation where the CTE of the oxide is higher than that of the substrate metal occurs only in some specific situations. One of these situations can be found in the unalloyed or low alloy steels where, due to the change from the normal to the inverse spinel structure in magnetite or chromium–iron spinels, a large variation of the value of the CTE takes place (see Figure 8). Such cases require a more sophisticated quantitative treatment, which is described elsewhere.[1,66] As a result, a rather complex stress distribution in the multilayer oxide scale can be observed, leading to a locally different sensitivity to cracking or spalling of the oxide layer system.[1]

1.08.4 The Effect of Stresses on the Integrity of the Oxide Scale

1.08.4.1 Measured Critical Strain Values to Scale Failure

Since the protective effect of a dense surface oxide scale guarantees the corrosion resistance of the technical high temperature materials under service conditions, one of the key issues is to maintain the integrity of the scales or at least to know the mechanical limits before failure of the scales occurs. This failure can consist of various forms of damage depending on the prevailing stress situation in the scale/metal composite system, the mechanical properties and structure of the scale, and the temperature and deformation rates:

1. fracture of a scale or a component of the scale perpendicular to the direction of tensile stress,
2. fracture of the scale or a component of the scale by the action of shear or buckling stresses in the scale,

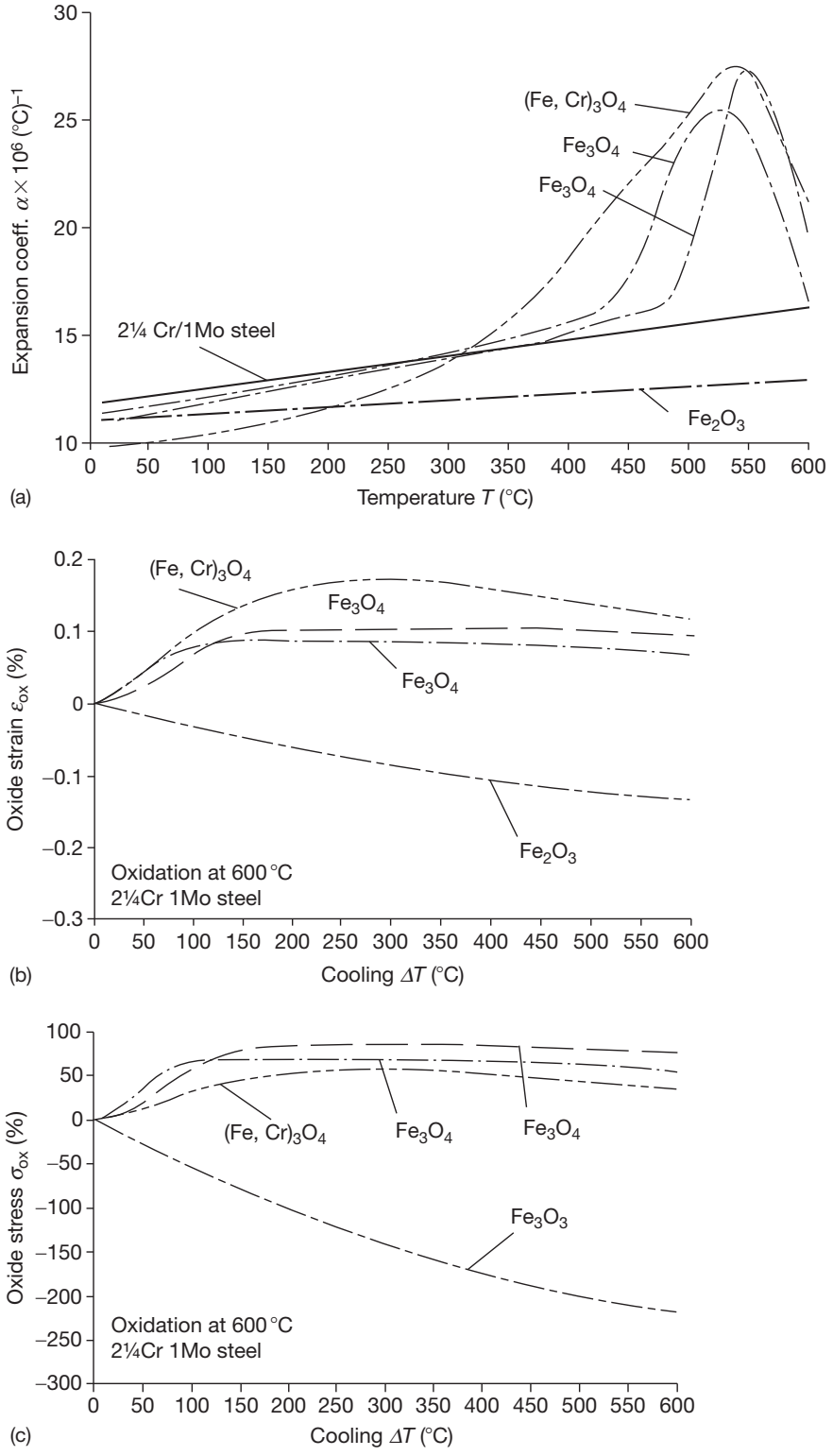

Figure 8 Role of differences in CTE values for the example of the oxide scale formed on a 2.25 Cr1Mo steel at 600 °C in air.[1,66] (a) Variation with temperature of CTE,[89,90] (b) strains in the oxide on cooling from 600 °C, and (c) stresses in the oxide on cooling from 600 °C.

3. formation of microcracks in the scale,
4. disbonding of the scale from the metal or separation along the interfaces between the components of the scale,
5. spalling of parts of the scale under compressive stresses.

Before these failure situations are addressed by model considerations in Section 1.08.4.2, it will be helpful to look at experimental data on the strains to scale failure.

The measurement of critical strains to scale failure requires some experimental effort. The most critical part in these measurements is to record the moment of scale failure either by optical or acoustic means. The most elegant technique has been proved to be the acoustic emission analysis, which has been applied to the measurement of scale failure in a number of investigations.[1] The simplest way would be to attach an acoustic waveguide to the specimen by clamping or spot welding in order to lead the signals from the hot zone of the test environment to the colder part outside the test rig and a piezoelectric transducer. In equipment that is more sophisticated, large size specimens that reach out into the colder part where the piezoelectric transducer can be attached directly.[66] If the respective parameters are known, especially the CTE, even the cooling step after oxidation can be used to assess critical strains for scale failure together with temperature and acoustic signal recording.[1] More accurate methods, however, are based on tensile or compressive testing machines in which simple uniaxial tension and compression or more sophisticated four point bending tests can be performed. Both types of tests have been used successfully and are described in detail in the literature.[1,91–93] An example of the test arrangement for a tensile test is shown in Figure 9.[7]

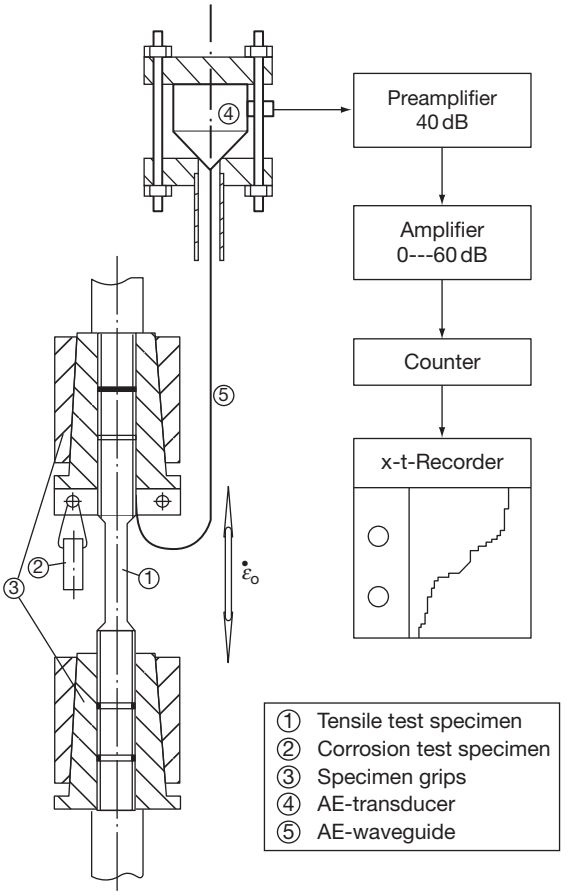

Figure 9 Schematic of a test arrangement for measuring critical strains to oxide scale failure at oxidation temperature in a furnace using a tensile test machine equipped with an acoustic emission measurement device and a waveguide. Reproduced from Schütze, M. *Oxid. Met.* **1985**, *24*, 199–232.

The critical strain values to scale failure existing in the literature from such measurements have been summarized elsewhere[92] and are shown in Table 4. It turns out that, with the exception of nickel oxide on nickel, under compressive strains where a specific stress relief mechanism of simultaneous microcracking and crack healing in the scale ('pseudoplasticity') comes into play,[93] almost all other values lie in the range between 0 and ~1%. This confirms the brittleness of the protective oxide scales indicating that oxides, even if they are grown as metal oxide scales on metallic substrates, show ceramic nature. Also, the fracture toughness values which can be derived from these critical strain values (see Section 1.08.4.2) as shown in Table 5[92] confirm the brittleness of oxide scales. These values can be used for model-based assessments of critical failure strains (see Section 1.08.4.2).

Besides the standard tensile or compression test, or the rather universal four point bending test, a number of special tests for scale adhesion measurements have been developed. These have been described elsewhere.[1,106,107] Most of these techniques are only applicable at RT since they rely on the strength of an organic glue. Recently a new type of test has been developed, which is called the 'inverted blister test'.[107] In this case, the energy that is necessary to enlarge an area of detached scale by increasing the hydrostatic pressure in a complex arrangement through a central hole so that the substrate metal (which is a thin foil)

Table 4 Experimental data on scale failure strains given in the literature

Oxide	*Substrate*	*Temperature (°C)*	ε_c *(%)*	*Mode*	*Ref.*
Al_2O_3	18CrAl steel	800	0.08–0.16	Tensile	7
Al_2O_3	FeCrAlY	RT	0.4–1.3	Tensile	94
Al_2O_3	FeCr alloy	RT	0.05	Tensile	95
Al_2O_3	MA 956	600	0.5–0.6	Tensile	96
Al_2O_3	FeCr alloy	RT	−1.4	Compressive	95
Cr_2O_3	AISI 310	RT	0.78–0.95	Tensile	97
Cr_2O_3	Alloy 800	800	0.09–0.50	Tensile	7
Cr_2O_3	Nimonic 75	700	0.002–0.005	Tensile	98
Cr_2O_3	Nimonic 75	800	0.005–0.008	Tensile	98
Cr_2O_3	Nimonic 75	1000	0.013–0.018	Tensile	98
Cr_2O_3	AISI 310	RT	−(0.29–0.79)	Compressive	97
Cr_2O_3	Alloy 800	RT	−(0.6–0.8)	Compressive	1, 97
NiO	Pure Ni	800	0.2–0.7	Tensile	1
NiO	Pure Ni	800	0.13–0.48	Tensile	7
NiO	Pure Ni	900	0.04–0.11	Tensile	99
NiO	Pure Ni	RT	−(0.9–2.2)	Compressive	1
NiO	Pure Ni	RT	−(0.8–2.7)	Compressive	93
NiO	Pure Ni	400	−(0.8–2.0)	Compressive	93
NiO	Pure Ni	600	−(0.7–4.0)	Compressive	93
NiO	Pure Ni	800	−(1.2–3.2)	Compressive	93
FeO	Low alloy steel	600–900	0.01–0.02	Tensile	89
Fe_3O_4	Mild steel	RT	0.05–0.08	Tensile	89
Fe_3O_4	Pure iron	RT	0.1–0.33	Tensile	89
Fe_3O_4	Pure iron	RT	0.1–0.13	Tensile	89
Fe_3O_4	Pure iron	300	0.05–0.08	Tensile	89
Fe_3O_4	AISI 316	RT	0.11–0.20	Tensile	89
Fe_3O_4	AISI 316	800	0.17–0.31	Tensile	89
Fe_3O_4/Fe_2O_3	Mild steel	RT	0.15–0.45	Tensile	100
Fe_3O_4/Fe_2O_3	Mild steel	550	0.05–0.42	Tensile	100
Fe_3O_4/Fe_2O_3	2.25Cr1Mo steel	600	0.1	Tensile	89
Fe_3O_4/Fe_2O_3	AISI 316	RT	0.13–0.22	Tensile	89
Fe_3O_4/Fe_2O_3	AISI 316	600	0.27–0.35	Tensile	89
Fe_3O_4/Fe_2O_3	Mild steel	500	0.01–0.02	Tensile	98
$FeO/Fe_3O_4/Fe_2O_3$	Mild steel	600	0.01–0.02	Tensile	98
$FeO/Fe_3O_4/Fe_2O_3$	Mild steel	700	0.02–0.03	Tensile	98
$FeO/Fe_3O_4/Fe_2O_3$	Mild steel	800	0.03–0.06	Tensile	98
Fe_3O_4/Fe_2O_3	Mild steel	RT	−(0.18–0.55)	Compressive	101
Fe_2O_3	2.25Cr1Mo steel	600–300	−0.6	Compressive	66
TiO_2/Al_2O_3	Ti50Al	900	0.15–0.50	Tensile	102
TiO_2/Al_2O_3	Ti50Al2Nb	900	0.15–1.30	Tensile	102
TiO_2/Al_2O_3	Ti47Al1Cr Si	900	0.6–1.7	Tensile	99

Reproduced from Schütze, M.; Ito, S.; Przybilla, W.; Echsler, H.; Bruns, C. *Mater. High Temp.* **2001**, *18*, 39–50.

deforms plastically (forming a growing blister at the detached area) and separates from the oxide, is measured. Although this test looks intriguing, it is not easy to use.

Hou *et al.*[108] contains a number of adhesion energy data with a scatter even within one metal/oxide system of up to three orders of magnitude. This shows the difficulties of such types of measurements. Much of the scatter will certainly also arise from the presence and the level of impurities at the oxide/metal interface. Sulfur especially is known to play a detrimental role on scale adhesion as it weakens the interface and enhances interfacial pore formation.[109–111] For example, in NiAl, increasing the interface sulfur content from zero to ~2.5% reduced the interfacial strength by a factor of ~10.

1.08.4.2 Model Considerations

Because oxide scales are brittle phases even at high temperatures, as is obvious from the experimental data, a model description of scale failure is possible,

Table 5 Oxide fracture toughness data calculated from critical strain and defect data given in the literature

Oxide	*Substrate*	*Temperature (°C)*	*K_{Ic} (MPa $m^{1/2}$)*	*Mode*	*Ref.*
Al_2O_3	Bulk	RT	3.0–6.0	Bending test	99
Al_2O_3	Bulk	RT	2.5	Calculated from γ_0	103, 104
Al_2O_3	FeCrAl	RT	0.4	Through scale	95
Al_2O_3	Kanthal APM	700	1.0	Through scale	105
Al_2O_3	18CrAl steel	800	0.3–1.0	Through scale	104
Al_2O_3	MA 956	1100	0.4–1.7	Through scale, initiation at macro pores	105
Al_2O_3	MA 956	1100	0.6–2.1	Through scale, initiation at macro pores	105
Cr_2O_3	Bulk	RT	1.8	Calculated from γ_0	103, 104
Cr_2O_3	Nimonic 75	700	1.8–2.5	Through scale	98
Cr_2O_3	Nimonic 75	800	2.0–3.2	Through scale	98
Cr_2O_3	Nimonic 75	900	4.0–5.5	Through scale	98
Cr_2O_3	Alloy 800	800	1.2	Through scale	104
NiO	Bulk	RT	1.2	Calculated from γ_0	103, 104
NiO	Nickel	RT	0.5	Through scale	98
NiO	Nickel	RT	0.3–0.4	Through scale, initiation at pores	99
NiO	Nickel	RT	0.75–1.3	Through scale, initiation at microcracks	99
NiO	Nickel	RT	3.6	Scale detachment, parallel to interface	99
NiO	Nickel	800	2.6–6.0	Through scale	104
NiO	Nickel	900	1.2	Through scale	98
FeO	Bulk	RT	0.9	Calculated from γ_0	103, 104
Fe_3O_4	Bulk	RT	1.4	Calculated from γ_0	103, 104
Fe_3O_4	2.25Cr1Mo steel	600	0.2	Through scale	104
Fe_3O_4	Bulk	RT	1.6	Calculated from γ_0	103, 104
FeO/Fe_3O_4	Pure iron	570	2.0	Through scale	98
FeO/Fe_3O_4	Pure iron	670	2.2–4.0	Through scale	98
FeO/Fe_3O_4	Pure iron	740	2.3–5.3	Through scale	98
FeO/Fe_3O_4	Pure iron	800	5.8–9.3	Through scale	98
$FeCr_2O_4$	Bulk	RT	1.5	Calculated from γ_0	103, 104
Fe_2MnO_4	Bulk	RT	0.8	Calculated from γ_0	103, 104
TiO_2	Titanium	RT	1.3	Through scale	103, 104
TiO_2/Al_2O_3	Ti47Al1CrSi	RT	0.2	Scale detachment, parallel to interface	99
TiO_2/Al_2O_3	Ti47Al1CrSi	700	1.2	Scale detachment, parallel to interface	99
TiO_2/Al_2O_3	Ti50Al	900	1.5–3.0	Through scale	102
TiO_2/Al_2O_3	Ti50Al2Nb	900	1.0–3.3	Through scale	102
TiO_2/Al_2O_3	Ti47Al1CrSi	900	2.7–7.0	Through scale	99
TiO_2/Al_2O_3	Ti47Al1CrSi	900	1.4–4.0	Scale detachment, parallel to interface	99
SiO_2	Bulk	RT	0.9	Calculated from γ_0	103, 104
MnO	Bulk	RT	0.9	Calculated from γ_0	103, 104
CoO	Bulk	RT	1.0	Calculated from γ_0	103, 104

Reproduced from Schütze, M.; Ito, S.; Przybilla, W.; Echsler, H.; Bruns, C. *Mater. High Temp.* **2001**, *18*, 39–50.

based on fracture mechanics approaches. Such approaches always assume that so-called physical defects (pores, voids, micro cracks, etc.) are present in a structure and are responsible for its failure. From this assumption, a critical stress σ_c can be calculated from the critical surface energy G_c which is released by the growth of the existing physical defect, E^* which is the effective Young's modulus (calculated from the values of different phases if the crack passes along the phases[112,113]) and c, which characterizes the size of the physical defect:

$$\sigma_c = \left(\frac{E^* G_c}{\pi c}\right)^{1/2} \quad [10]$$

Assuming linear elastic behavior, the numerator in eqn [10] can be replaced by the fracture toughness K_c.

$$K_c = \left(E^*_{ox} G_c\right)^{1/2} \quad [11]$$

which is valid for the plain stress situation that usually predominates in thin scales. In the case of plain strain, the right hand side of eqn [11] must be multiplied by the factor $1/\sqrt{(1-\nu^2)}$. The fracture toughness K_c or K_{Ic} is a material property characterizing the resistance of the oxide to crack growth. Crack growth starts to occur once the stress intensity factor K at the tip of the defect in the scale reaches or exceeds the value of this fracture toughness. Values of the fracture toughness are given in **Table 5**. If the fracture toughness and the size of the physical defects in the oxide scale or the scale/metal system are known, critical strain values can be assessed by model equations at which damage to the scale occurs. The respective equations for the different damage situations are summarized here and represented schematically in **Figure 10**.

1. Through scale cracking (tensile):

$$\varepsilon_c^t = \frac{K_{Ic}}{f E_{ox}\sqrt{\pi c}} \quad [12]$$

2. Beginning of interfacial crack growth/delamination (compressive)[115]

$$-\varepsilon_c^i = \frac{K_{Ic}}{f\sqrt{\pi c}} \frac{\left(1+\frac{r}{d}\right)(1+\nu_{ox})}{2E_{ox}} \quad [13]$$

3. Buckling (compressive)[116]

$$-\varepsilon_c^b = \frac{1.22}{1-\nu_{ox}^2}\left(\frac{d}{R}\right)^2 \quad [14]$$

4. Crack deflection at scale buckles toward surface (compressive)[10]

$$-\varepsilon_c^{bf} = 3.6\left(\frac{d}{R}\right)^2 \quad [15]$$

5. Spalling (compressive)[116]

$$-\varepsilon_c^s = \sqrt{\frac{2\gamma_o}{dE_{ox}(1-\nu)}} \quad [16]$$

ε_c is the critical strain in the oxide (i.e., the strain parallel to the oxide/metal interface) at which the respective type of failure occurs. K_{Ic} is the mode I (i.e., plain tensile straining) fracture toughness of the plane in which failure starts, E_{ox} is the Young's

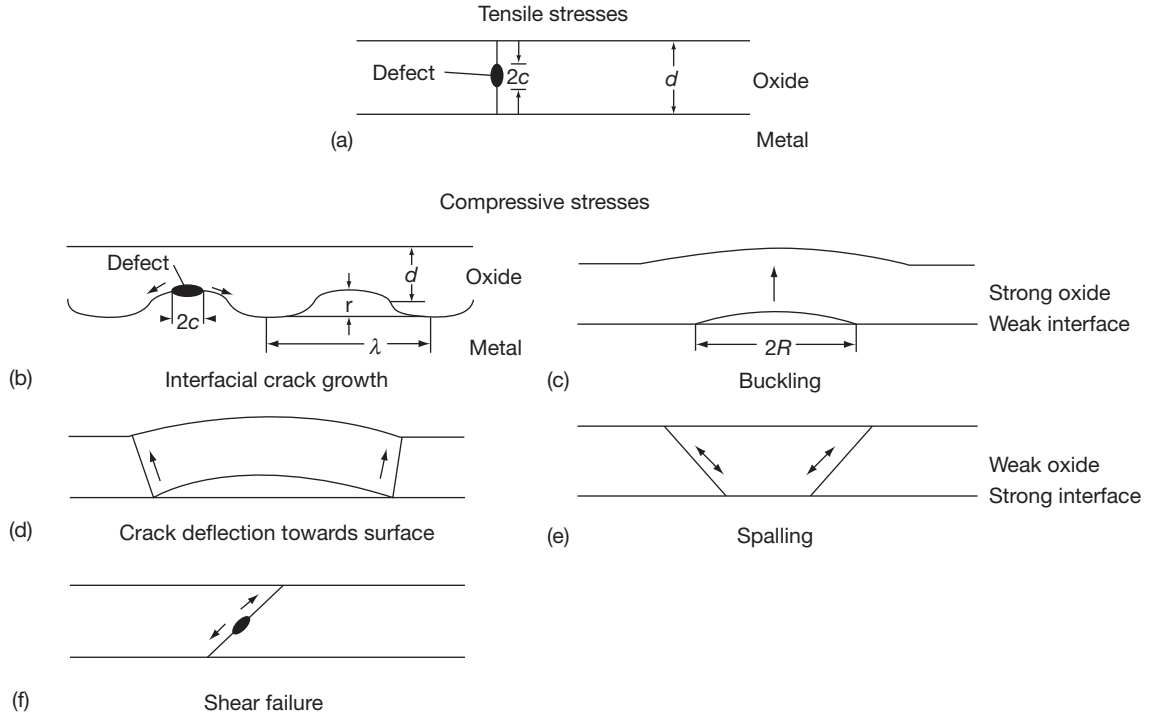

Figure 10 Schematic of the different potential modes of scale failure. Reproduced from Schütze, M. In *High Temperature Corrosion of Advanced Materials and Protective Coatings*; Saito, Y., *et al*. Ed.; North Holland: Amsterdam, 1992; 29.

modulus of the oxide, and $2c$ is the size of an embedded physical defect (pore, void, microcrack, etc.) which is responsible for failure. The size of a surface defect would be c. f is a geometrical factor (for embedded defects $f = 1$) and d is the scale thickness. The remaining parameters are the interfacial roughness (amplitude r), the Poisson ratio ν_{ox}, and the radius of an already existing delamination R. Finally, γ_0 is the surface energy needed for the creation of two new surfaces by cracking or detachment. This energy is an effective energy, which is influenced by the geometrical parameters of the failure plane in the following way[103,117]:

$$\gamma_0 = \gamma_i \left(1 + \frac{0.1 E_{ox}}{2\gamma_i} \frac{r}{\lambda}\right) \left(\frac{A_0 - A_{sep}}{A_0}\right) \qquad [17]$$

where the additional parameter λ represents the 'wavelength' of a rough interface, A_0 the surface without separations and A_{sep} that part of the surface where delaminations/separations already exist (i.e., A_{sep} is an equivalent to c). γ_i is the intrinsic surface energy, which is a material's parameter and, thus, similar to K_{Ic} independent of the microgeometry:

$$K_{Ic} = \sqrt{2\gamma_i E_{ox}} = \sqrt{G_c E^*_{ox}} \qquad [18]$$

Equation [16] actually corresponds to the original equation of U.R. Evans.[118] However, as shown by eqns [17] and [18] this rather simple equation should be extended by micromechanics parameters.

It should be mentioned here that for the size of physical defects also, especially where size depends on the oxidation process, some kinetic data exist in the literature, at least to a small extent.[21,99,102] Furthermore, these values can also be determined from metallographic examinations of oxidized specimens. The same is valid for the other geometrical parameters such as scale thickness and waviness of the oxide/metal interface.

Sometimes there is a criticism that the physical defect sizes needed for scale failure, particularly for the buckling situation, are much larger than is commonly observed on scales in metallographic investigations, that is, the scales fail before the appearance of critical physical defect sizes. As the literature shows, critical buckling constellations can grow from many small cavities to the necessary size.[119] Furthermore, small defects can interact with each other in a mechanical sense if they are lying close enough to each other so that a much larger 'effective' defect size determines the failure behavior of the scale.[1] Rules on how to calculate the effective physical defect size are given elsewhere.[1,120]

A number of Young's moduli and Poisson ratios are given in **Tables 6 and 7**. Further values of the elastic constants, especially for elevated temperatures, can be found elsewhere.[1]

Figures 11 and 12 show how the model equations can be used to calculate the dependency of the critical strain to failure on the respective scale parameters. Assuming a physical defect size of ~1 μm or less, this results in critical strain values of a few tenths of a percent under tensile strain for Al_2O_3, Cr_2O_3, and Fe_3O_4 (see **Figure 11**). A comparison with actually measured critical strain values in **Table 4** shows that this is very much in the same order of magnitude and confirms that the model approaches are suitable for a first assessment of the sensitivity to mechanical failure of such oxide scales.

Table 6 Surface fracture energies, elastic moduli, and fracture toughness values at room temperature (RT) (calculated from atomistic data)

Oxide	*γ_i (J m^{-2})*	*E_{ox} (MPa)*	*K_{Ic} (MPa m$^{1/2}$)*
FeO	3.0	130 000	0.9
CoO	3.0	156 000	1.0
NiO	3.6	191 000	1.2
MnO	2.7	148 000	0.9
Fe_3O_4	4.5	208 000	1.4
$FeCr_2O_4$	5.0	233 000	1.5
Fe_2MnO_4	3.0	108 000	0.8
Al_2O_3	7.7	419 000	2.5
Cr_2O_3	5.8	283 000	1.8
Fe_2O_3	6.0	219 000	1.6
Y_2O_3	4.8	123 000	1.1
SiO_2	4.4	85 600	0.9

Reproduced from Robertson, J.; Manning, M. I. *Mater. Sci. Technol.* **1990**, *6*, 81–91.

Table 7 Values of Poisson ratios ν_{ox} at RT

Oxide	*v*
Al_2O_3	0.24
Cr_2O_3	0.29
FeO	0.36
Fe_2O_3	0.19
Fe_3O_4	0.29
NiO	0.32
SiO_2	0.07
TiO_2	0.28
CoO	0.36
MnO	0.34
$FeCr_2O_4$	0.31
$MnFe_2O_4$	0.39
Y_2O_3	0.38

Reproduced from Robertson, J.; Manning, M. I. *Mater. Sci. Technol.* **1990**, *6*, 81–91.

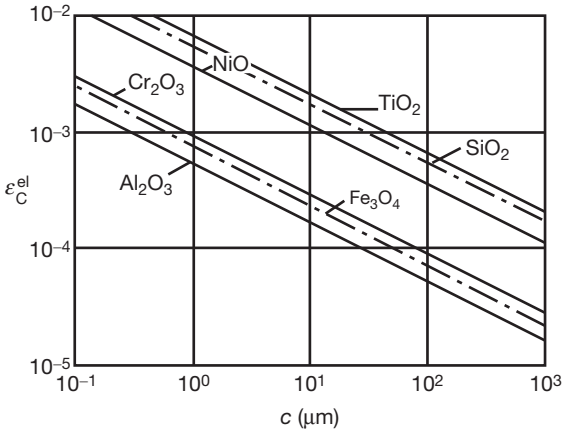

Figure 11 Strain values to scale cracking ε_c under tensile stress for different oxides as a function of the physical defect size c calculated using eqn [12]. Reproduced from Schütze, M. *Oxid. Met.* **1995**, *44*, 29–61.

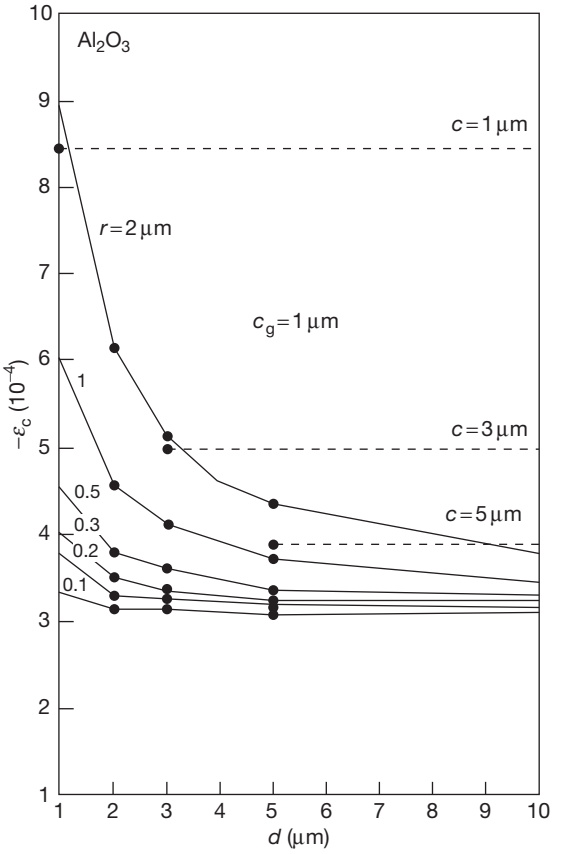

Figure 12 Strain values to the beginning of scale delamination ε_c under compressive stress for Al_2O_3 and a physical defect size $c_g = 1$ μm at the scale/metal interface calculated using eqn [13]. r denotes the 'interfacial amplitude' (see **Figure 10(b)**). Reproduced from Schütze, M.; Ito, S.; Przybilla, W.; Echsler, H.; Bruns, C. *Mater. High Temp.* **2001**, *18*, 39–50.

Similar values are observed for the beginning of crack growth (scale detachment) along the metal/scale interface, as represented in **Figure 12**. These values are slightly lower than those observed in experimental investigations for global scale failure under compression, which is, however, sensible, as the beginning of crack growth or delamination along the scale/metal interface is not yet the complete failure by spalling or detachment of large parts of the scale. Therefore, the situation in **Figure 12** represents rather a conservative approach to scale failure under compressive stresses. See Schütze[1,104] for an in-depth discussion of the models available for the theoritical description of scale failure occurs. Schütze[1] also contains a discussion of the influence of oxide creep, if existing, on the critical strains to failure. It can, however, be stated here that this influence is limited and only becomes evident at very low defect or grain sizes of the oxide. For most technical situations, the oxide scale will behave in a brittle manner as described by the model equations shown, even at the operation temperature of a high temperature component.

1.08.5 Maintaining the Protective Effect of Oxide Scales Even After Mechanical Failure under Stresses

1.08.5.1 Healing of Cracks or other types of Damage in the Protective Oxide Scale

As the discussion on the cracking behavior of oxide scales shows that brittle failure is to be expected, it is even more important to discuss the mechanism of oxide damage healing. It can be stated that all current technical metallic alloys would not survive for a long time in operation, from a high temperature corrosion point of view, if healing of oxide scale damage did not take place. The reason is that in almost all cases of high temperature, service strains or stresses of the types described so far (be it external or internal stresses of the system) will arise and endanger the integrity of the brittle oxide scale. What distinguishes a growing 'ceramic' oxide scale from a 'dead' artificially applied ceramic layer is that, during high temperature exposure, the oxidation process and, thus, the growth of the oxide scale, continues. At the same time, this growth process represents the healing potential of the oxide/metal system, which allows it

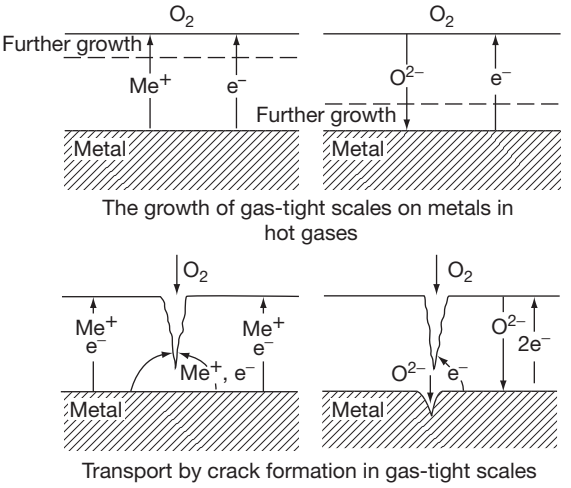

Figure 13 The two extreme cases of material transport through oxide scales (inward growth and outward growth) and their effect on scale crack healing. Reproduced from Bruch, U.; Döhle, K.; Pütz, J.; Rahmel, A.; Schütze, M.; Schuhmacher, K. D. *Proceedings of the International Congress on Metallic Corrosion*; NRC, Ottawa, 1984; Vol. 3, 325–329.

to protect itself even after intermediate mechanical damage.

The principles of the crack healing process are illustrated schematically in **Figure 13**. As the diffusion length at a crack is shorter than in the undamaged part of the oxide scale, this means that the local oxide growth rates will also be higher than in the rest of the scale. With increasing time and continuously increased thickening at these damaged spots, the overall scale becomes smooth again so that with time the crack is closed. **Figure 14** shows that this is not a theoretical consideration alone but that cracks can be closed almost completely by this healing process, leaving only scars in the oxide surface, which are hard to detect by optical means, (**Figure 14(c)**). As observed in experiments, healing of oxide cracks requires that a certain critical deformation rate of the substrate is not exceeded.[122] Otherwise the crack faces of the oxide scale would move apart at a higher rate than can be accommodated by the oxidation process from the faces of the scale crack. **Figure 15**

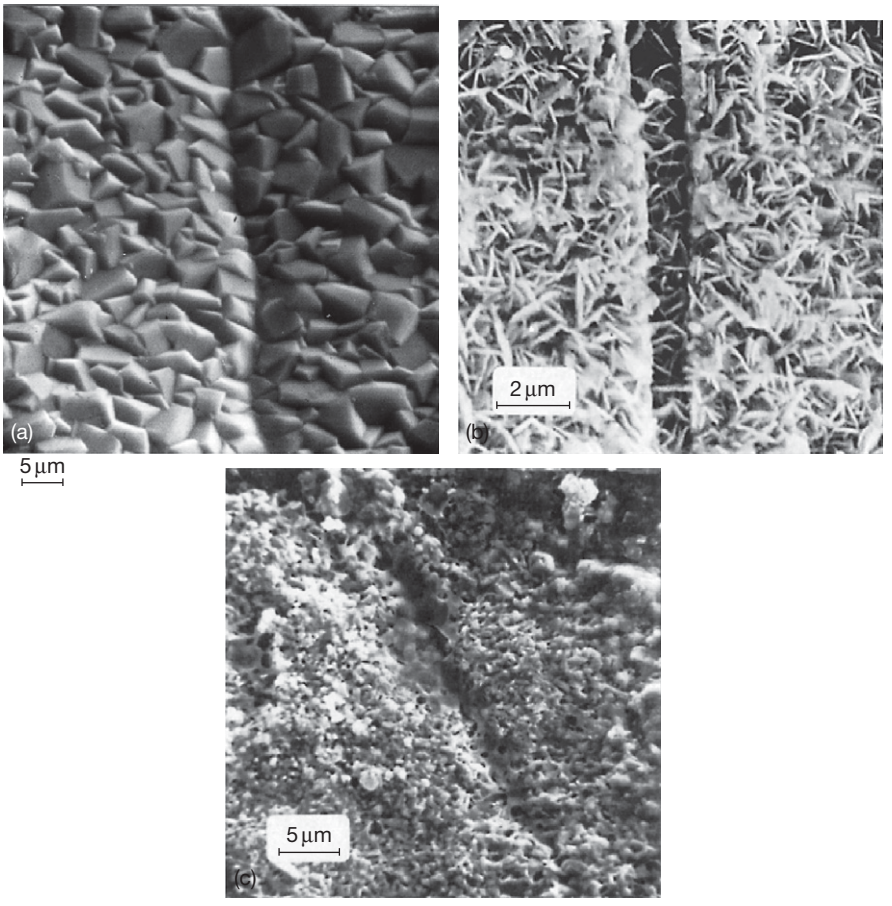

Figure 14 Examples of healed scale cracks in SEM surface investigations. (a) NiO scale on Ni99.2 after oxidation and straining at 800 °C, (b) oxide scale on Alloy 800H after oxidation and straining at 800 °C, and (c) same scale as (b) but later stage in the healing process.

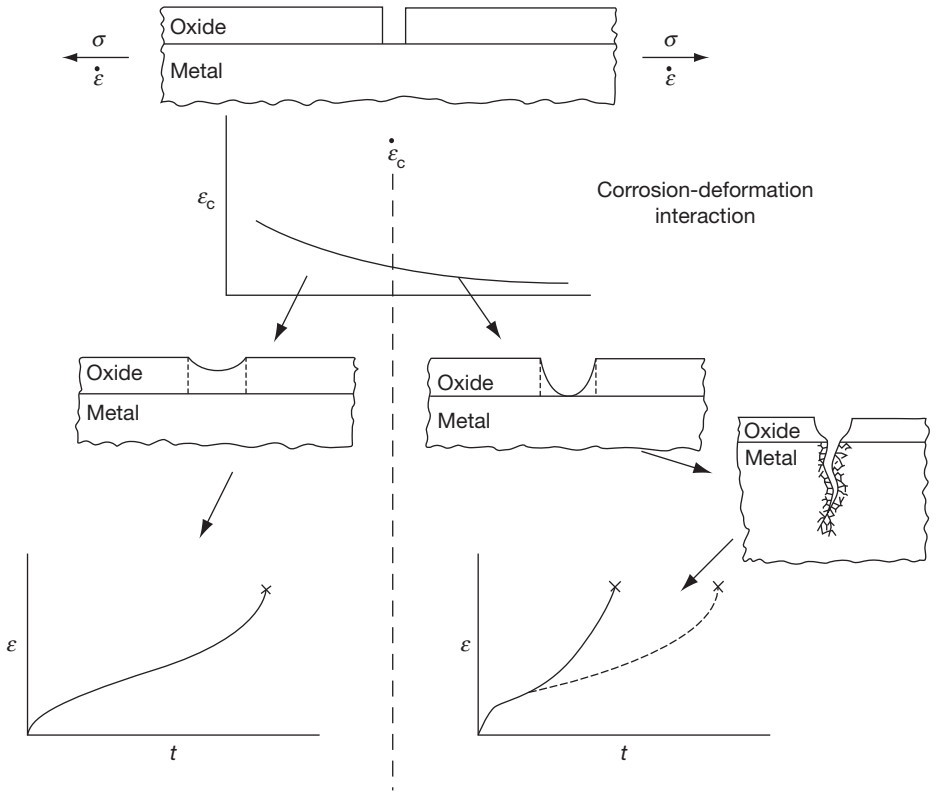

Figure 15 Schematic illustration of the role of a critical deformation rate $\dot{\varepsilon}_c$ of the substrate for scale crack healing. Left: below $\dot{\varepsilon}_c$ instant healing of the scale crack is possible and in the creep curve ε–t no acceleration of creep due to corrosion damage occurs. Right: above ε_c healing is impeded and internal corrosive attack at the unprotected site reduces the load bearing metal cross-section ending up in accelerated creep.

illustrates this schematically, indicating that above this critical strain rate, crack healing would be impeded and internal corrosion in particular along grain boundaries could facilitate crack formation in the metal subsurface zone as observed by Wagner.[123] At lower strain rates, the healing process would be able to close the cracks again, restoring the protective effect of the scale. This situation has been modeled by superimposing the oxidation process on the movement of crack phases by continued deformation and the details of this model development as described by Barbehön *et al.*[124] The model calculations provided quantitative values of the critical strain rates, which were in the range of 10^{-6} to 10^{-8} s^{-1} and in good agreement with the experimentally determined values.[1,102]

1.08.5.2 The Influence of Subsurface Zone Depletion on Maintaining the Protective Effect of Oxide Scales Under Stresses

Contrary to what is required by the theoretical models of oxidation[125] it is usual that significant depletion of the protective scale-forming alloy takes place in the metal subsurface zone directly underneath the oxide scale. Evidently, in most technical cases, an equilibrium situation is not achieved and the oxidation process requires a faster supply of scale forming species from the substrate than can be achieved by the alloy. As shown in **Figure 16** this is at least true for many of the technical alloys in their normal operating temperature range (further examples are given elsewhere[1,4]). This may be different at very high temperatures and for materials with high self-diffusion coefficients of the scale forming elements, where the level of this element is equal over the whole material thickness (i.e., no gradient), for example, FeCrAl alloys at 1200 °C.[127]

The drop in the alloy concentration directly underneath the oxide scale means that it is no longer the original alloy that was in contact with the oxide scale or the environment, if the oxide scale fails. In order to make this aspect clearer one should take a look at **Figure 17**, which shows the parabolic rate constant as a function of the chromium content in iron chromium steels at 1000 °C.[128] From this figure

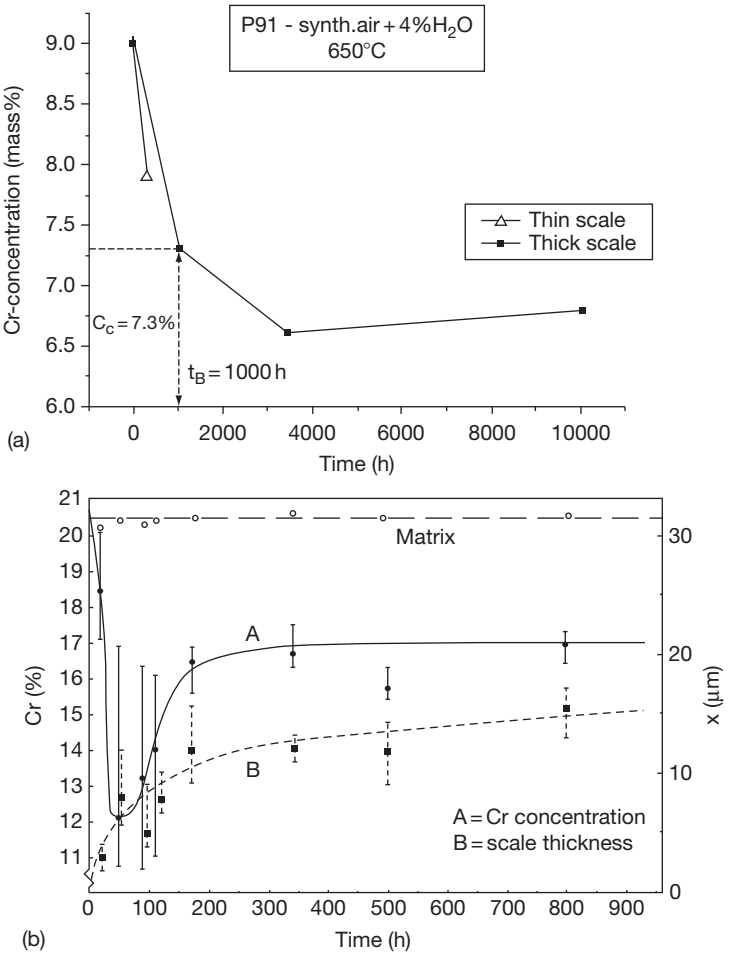

Figure 16 Cr depletion during oxidation as a function of oxidation time measured by EPMA directly underneath the oxide scale in the metal subsurface zone. (a) P91 in air with 4% water vapor at 650 °C,[4] (b) alloy 800 in laboratory air at 800 °C,[126] A = Cr concentration, B = oxide scale thickness.

it becomes clear that steel, containing originally 20% of chromium which forms a more or less pure chromia scale, would behave much worse after significant depletion of chromium in the metal subsurface zone if the scale should crack or spall. At these spots, a material with significantly lower chromium concentration would be exposed to the oxidizing environment and, consequently, fast-growing iron-rich oxides would grow at these spots strongly deteriorating the protective effect of the scale. For this, it is not necessary that the scale is cracked by external stresses; even intrinsic growth stresses or geometrically induced growth stresses can lead to scale damage as shown in **Figure 18**, where nodule formation of fast-growing iron-rich oxides has taken place at machining marks on an undeformed specimen of 9% chromium steel, which protruded through the thin chromium-rich oxide scale on the original surface.[129] As can be seen from **Figure 16** and also Schütze[4] for this kind of material a steep drop in the chromium content takes place during oxidation.

Generally, four different cases can be distinguished with regard to the influence of depletion in the metal subsurface zone on the healing capability of damaged oxide scales. This is summarized schematically in **Figure 19** for the example of chromia formers. In case (a) subsurface zone depletion takes place at a measurable rate but the values do not fall below the critical Cr-limit, which is necessary to form the protective scale. This situation guarantees the long-term healing capability of the oxide/metal system under operation. In case (b) there is a steep drop in the concentration of the protective scale forming the alloy at the beginning of oxidation but

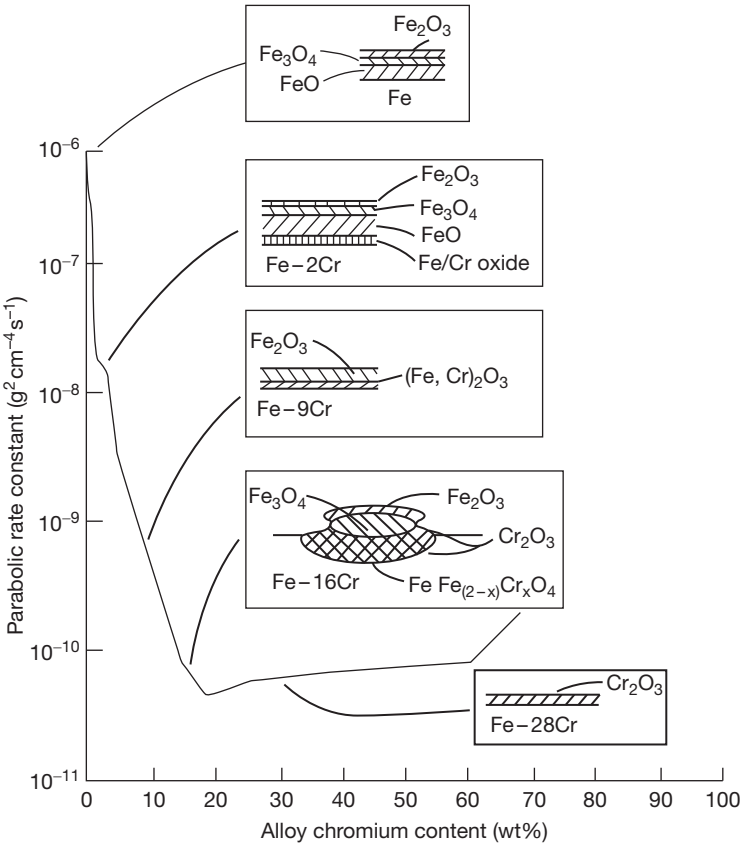

Figure 17 Schematic showing the effect of Cr in Fe–Cr alloys on oxidation rate and oxide scale structure at 1000 °C in oxygen. Reproduced from Whittle, D. P.; Wood, G. C.; Evans, D. J.; Scully, D. B. *Acta Metall.* **1967**, *15*, 1747.

rediffusion of this element from the metal interior fills the reservoir directly underneath the oxide scale again so that the critical limit is undercut only temporarily. If oxide scale cracking can be avoided in this first period of exposure time, then the healing capability would be restored and would last for the rest of the lifetime of the component. Case (c) represents the situation where rediffusion from the metal interior is not able to fill the alloying reservoir in the metal subsurface zone to the extent which allows protective healing of the oxide scale, and case (d) shows the even worse situation where the composition of the subsurface zone falls below the thermodynamic stability limit of the oxide scale in contact with the metal substrate. In the latter case, therefore, even without any mechanical damage to the oxide scale, the scale would no longer be stable from a chemical point of view and would be converted into a nonprotective type of oxide.

The situation of subsurface zone depletion and rediffusion from the metal interior has been modeled by a number of authors and for different material systems.[130–138] Two of these models have been converted into an open source code software tool. The first is called COSIM and is available from NASA.[139] The second is called ODIN[140] and allows the treatment of the situation of two-dimensional structures, which is of importance at edges and corners. As discussed in **Section 1.08.2**, these sites are most endangered from the viewpoint of the stress situation in the oxide scale. A pragmatic diagram has been developed by Whittle using Wagner's considerations on the formation of a continuous protective oxide scale,[141] (**Figure 20**).[142] Further details are given elsewhere.[1] The diagram in **Figure 20** marks four regions with increased healing potential. In region (1), the chromium content is not sufficient to establish a protective chromia scale. In region (2), a protective scale can be established but after the first cracking or spalling the amount of chromium would not be sufficient for protective healing. This region would correspond to cases (c) and (d) in **Figure 19**.

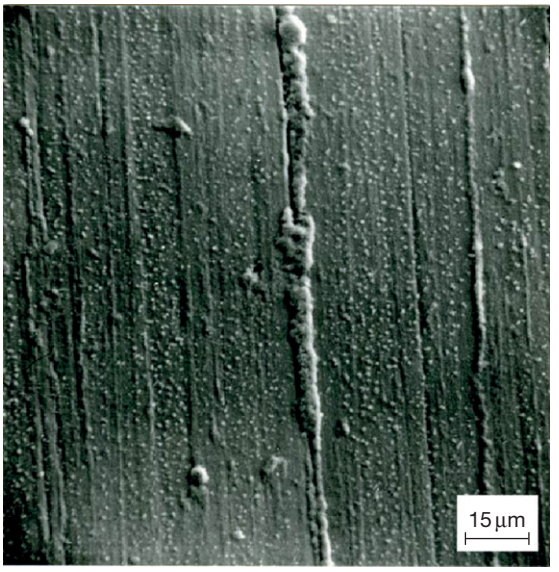

Figure 18 Oxide nodule formation by faster growing Fe-rich Cr-(Fe)-oxide at machining marks on an undeformed specimen of a 9% Cr steel after 850 h in isothermal oxidation at 650 °C in air. Reproduced from Wulf, G. L.; McGirr, M. B.; Wallwork, G. R. *Corros. Sci.* **1969**, *9*, 739.

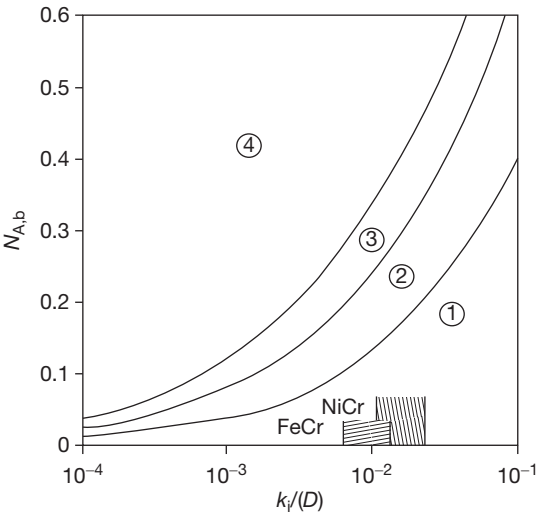

Figure 20 Critical values for the atom fraction $N_{A,b}$ of the protective scale-forming element A as a function of the k_i/D.[142] This figure is an example for chromia formers. k_i = oxidation rate constant for the recession of the oxide/metal interface, D = interdiffusion coefficient of A in the alloy, also shown are the bandwidths of the k_i/D ratio for Fe–Cr and Ni–Cr alloys (see text for explanation).

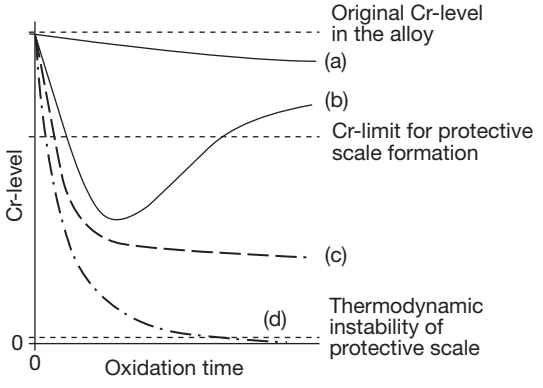

Figure 19 Schematic of the four cases of subsurface zone depletion of the protective scale forming element (in this example Cr for chromia formers): (a) Drop of the alloy concentration at a slow rate. The concentration does not fall below the Cr-limit for protective scale formation. (b) Temporary drop below the protective limit but rediffusion from the alloy interior = temporary jeopardizing of the protective effect. (c) Final drop below the protective limit but not below the thermodynamic stability limit of the oxide on the alloy; in case of scale damage the protective effect would be finally lost. (d) Same situation as (c) but drop below the thermodynamic stability limit = 'chemical destruction' of the protective scale without the need of superimposed stresses.

Region (3) shows the area in which healing can take place at least once after cracking or spalling and only region (4) guarantees repeated protective healing for longer operation times. The latter region would be equivalent to case (a) in **Figure 19**. Similar diagrams can of course be established also for alumina formers and help in the assessment of the choice of the right material for long-term operation. All these models can be used for a first theoretical assessment of the healing potential of materials. In most cases, very reasonable results can be expected. There is still, however, a need for a broader experimental basis to verify these models.

1.08.6 Concluding Remarks

It is the aim of this chapter to illustrate the important role of the mechanical aspects of oxidation behavior, particularly oxidation resistance of metallic materials at high temperatures. In a number of cases where the observed oxidation behavior could not be explained by the classical models of oxidation theory, the presence of stresses in the oxide/metal system was the reason for the discrepancies. As shown in the

relatively concise treatment of this topic in this chapter, a number of well-elaborated models describing the role of stresses, and also the healing of scale damage and subsurface zone depletion for the protective effect of the oxide scales, exist. Furthermore, a limited number of experimental data are available to characterize at least the more common situations, but at this point more work is needed. The model basis is now sufficiently broad to develop comprehensive computer codes regarding the complex synergistic interplay of the different chemical and mechanical mechanisms. This has indeed been started[141] and may in the near future allow a better quantification of the role of stress effects in oxidation, especially under industrial conditions. At the same time, the basis of experimentally determined data that can be fed into computer calculations has to be broadened. This chapter provides a general understanding of this rather complex situation in which stresses and oxidation interact with each other, leading sometimes to unexpected oxidation behavior. For a more detailed treatment of the topic the reader is referred to the textbook literature.[1]

References

1. Schütze, M. *Protective Oxide Scales and Their Breakdown*; John Wiley: Chichester, 1997.
2. Kofstad, P. *High Temperature Corrosion*; Elsevier Applied Science: London, 1988.
3. Evans, H. E.; Donaldson, A. T.; Gilmour, T. C. *Oxid. Met.* **1999**, *52*, 379–402.
4. Schütze, M.; Renusch, D.; Schorr, M. *Mater. High Temp.* **2005**, *22*, 113–120.
5. Donchev, A.; Fietzek, H.; Kolarik, V.; Renusch, D.; Schütze, M. *Mater. High Temp.* **2005**, *22*, 139–146.
6. Isecke, B.; Schütze, M.; Strehblow, H. H. In *Springer Handbook of Materials Measurement Methods*; Czichos, H., Saito, T., Smith, L., Eds.; Springer Verlag: Berlin, 2006: Chapter 12: Corrosion.
7. Schütze, M. *Oxid. Met.* **1985**, *24*, 199–232.
8. Kofstad, P.; Lillerud, K. P. *J. Electrochem. Soc.* **1980**, *127*, 240.
9. Lillerud, K. P.; Kofstad, P. *J. Electrochem. Soc.* **1980**, *127*, 2397.
10. Evans, A. G.; Crumley, G. B.; Demaray, R. E. *Oxid. Met.* **1983**, *20*, 193.
11. Caplan, D.; Sproule, G. I. *Oxid. Met.* **1975**, *9*, 459.
12. Ecer, G. M.; Meier, G. H. *Oxid. Met.* **1979**, *13*, 119.
13. Golightly, F. A.; Stott, F. H.; Wood, G. C. *Oxid. Met.* **1976**, *10*, 163.
14. Golightly, F. A.; Wood, G. C.; Stott, F. H. *Oxid. Met.* **1978**, *14*, 217.
15. Miner, R. G.; Nagarajan, V. *Oxid. Met.* **1981**, *16*, 313.
16. Pawel, R. E.; Cathcart, J. V.; Campbell, J. J. *J. Electrochem. Soc.* **1963**, *110*, 551.
17. Stringer, J. *Corros. Sci.* **1970**, *10*, 513.
18. Delaunay, D.; Huntz, A. M.; Lacombe, P. *Corros. Sci.* **1980**, *20*, 1109.
19. Zhao, J. G.; Huntz, A. M. *J. Mater. Sci.* **1984**, *19*, 3166.
20. Huntz, A. M.; Calvarin Amiri, G.; Evans, H. E.; Cailletaud, G. *Oxid. Met.* **2002**, *57*, 499.
21. Przybilla, W.; Schütze, M. *Oxid. Met.* **2002**, *58*, 103–145.
22. Przybilla, W.; Schütze, M. *Oxid. Met.* **2002**, *58*, 337–359.
23. Tylecote, R. F. *Mem. Sci. Rev. Metall.* **1965**, *62*, 241.
24. Jaenicke, W.; Leistikow, S. *Z. Phys. Chem.* **1958**, *15*, 175.
25. Jaenicke, W.; Leistikow, S.; Städler, A. *J. Electrochem. Soc.* **1964**, *111*, 1031.
26. Engell, H.; Wever, F. *Acta Metall.* **1957**, *5*, 695.
27. Buresch, F. E.; Bollenrath, F. *J. Nucl. Mater.* **1967**, *24*, 270.
28. Cathcart, J. V.; Liu, C. T. *Oxid. Met.* **1973**, *6*, 123.
29. Roy, C.; Burgess, B. *Oxid. Met.* **1970**, *2*, 235.
30. Donaldson, A. T.; Evans, H. E. *J. Nucl. Mater.* **1981**, *99*, 38.
31. Kang, K. J.; Hutchinson, J. W.; Evans, A. G. *Acta Mater.* **2003**, *51*, 1283–1291.
32. Zhao, J. G.; Zhang, Y. T. *Mater. Sci. Eng. A* **1989**, *120*, 245.
33. Huntz, A. M.; Zhao, J. G.; Boumaza, A.; Moulin, G. *Mater. Sci. Technol.* **1988**, *4*, 470.
34. Vosberg, V. R.; Fischer, W.; Berger, M. G.; Clemens, D.; Quadakkers, W. J.; Nickel, H. *Fresenius J. Anal. Chem.* **1996**, *355*, 745–747.
35. Zouboulis, E.; Renusch, D.; Grimsditch, M. *Appl. Phys. Lett.* **1998**, *72*, 1.
36. Birnie, J.; Graggs, C.; Gardiner, D. J.; Graves, P. R. *Corros. Sci.* **1992**, *33*, 1.
37. Tolpygo, V. K.; Clarke, D. R. *Mater. High Temp.* **2000**, *17*, 59–70.
38. Mougin, J.; Rosman, N.; Lucazeau, G.; Galerie, A. *J. Raman Spectrosc.* **2001**, *32*, 739–744.
39. Wouters, Y.; Galerie, A.; Bouvier, P.; Mermoux, M.; Petit, J. P. *Microscopy of Oxidation*; Science Reviews: Strixton, UK, 2005; Vol. 6, pp 145.
40. Lawless, K. R.; Gwathmey, A. T. *Acta Metall.* **1956**, *4*, 153.
41. Pyun, Y. J.; Homma, T.; Takakuwa, K. *J. Jpn. Int. Metall.* **1983**, *47*, 663.
42. Liu, C.; Lebrun, J. L.; Huntz, A. M.; Sibieude, F. *Z. Metallk.* **1993**, *84*, 140.
43. Goedjen, J. G.; Stout, J. H.; Guo, Q.; Shores, D. A. *Mater. Sci. Eng. A* **1994**, *177*, 115.
44. Sarioglu, C.; Schumann, E.; Blachere, J. R.; Pettit, F. S.; Meier, G. H. *Mater. High Temp.* **2000**, *17*, 109–115.
45. Corkovic, S.; Pyzalla, A. R. *Mater. Corr.* **2004**, *55*, 341.
46. Tortorelli, P. F.; More, K. L.; Specht, E. D.; Pint, B. A.; Zschack, P. *Mater. High Temp.* **2003**, *20*, 303–309.
47. Calvarin-Amiri, G.; Huntz, A. M. *R. Molins Mater. High Temp.* **2001**, *18*, 91–99.
48. Huntz, A. M.; Lefeuvre, A.; Andrieux, M.; Severac, C.; Moulin, G.; Molins, R.; Jomard, F. *Microscopy of Oxidation*; Science Reviews: Strixton, UK, 2003; Vol. 5, pp 393.
49. Gnäupel-Herold, T.; Reimers, W. In *Proceedings of the International Conference on Residual Stresses*; Frisson, T., Odin, M., Anderson, A., Eds.; Linköping University: Linköping, Sweden, 1997.
50. Hou, P. Y.; Paulikas, A. P.; Veal, B. W. *Microscopy of Oxidation*; Science Reviews: Strixton, UK, 2005; Vol. 6, pp 373.
51. Echsler, H.; Alija Martinez, E.; Singheiser, L.; Quadakkers, W. J. *Mater. Sci. Eng. A* **2004**, *384*, 1–11.
52. Mennicke, C.; Clarke, D. R.; Rühle, M. *Oxid. Met.* **2001**, *55*, 551–569.
53. Homma, T.; Pyun, P. J. *High Temperature Corrosion*; Jap. Int. Metals: Tokyo, 1983; 161.

54. Liu, C.; Huntz, A. M.; Lebrun, J. *Mater. Sci. Eng. A* **1993**, *160*, 113.
55. Galerie, A.; Toscan, F.; Dupeux, M.; Mougin, J.; Lucazeau, G.; Valot, C.; Huntz, A. M.; Antoni, L. *Mater. Res.* **2004**, *7*, 83–88.
56. Dionnet, B. PhD Thesis, University of Limoges, 1993.
57. Pilling, N. B.; Bedworth, R. E. *J. Inst. Metals* **1923**, *29*, 529.
58. Hancock, P.; Hurst, R. C. *Adv. Corros. Sci. Technol.* **1974**, *4*, 1.
59. Weast, R. C. *Physical Constants of Inorganic Compounds Handbook of Chemistry and Physics*, 6th ed.; CRC, 1984; B68, B161.
60. Bernstein, H. L. *Metall. Trans.* **1987**, *A18*, 975.
61. Stott, F. H.; Atkinson, A. *Mater. High Temp.* **1994**, *12*, 195–207.
62. Chevalier, S.; Strehl, G.; Favergeon, J.; Desserrey, F.; Weber, S.; Heintz, O.; Borchardt, G.; Larpin, J. P. *Mater. High Temp.* **2003**, *20*, 253–259.
63. Clarke, D. R. *Acta Mater.* **2003**, *51*, 1393–1407.
64. Krishnamurthy, R.; Srolovitz, D. J. *Acta Mater.* **2003**, *51*, 2171–2190.
65. Limarga, A.; Wilkinson, D. S.; Weatherly, G. L. *Scripta Mater.* **2004**, *50*, 1475–1479.
66. Christl, W.; Rahmel, A.; Schütze, M. *Oxid. Met.* **1989**, *31*, 1.
67. Taniguchi, S. *Trans IDIJ* **1985**, *25*, 3.
68. Appleby, W. K.; Tylecote, R. F. *Corros. Sci.* **1970**, *10*, 325.
69. Howes, V. R.; Richardson, C. N. *Corros. Sci.* **1969**, *9*, 385.
70. Singheiser, L. Forschungszentrum Jülich, Private communication.
71. Hänsel, M.; Boddington, C. A.; Young, D. J. *Corros. Sci.* **2003**, *45*, 967–981.
72. Quadakkers, W. J.; Tyagi, A. K.; Clemens, D.; Anton, R.; Singheiser, L. In *Elevated Temperature Coatings: Science and Technology III*; Hampikian, J. M., Dahotre, N. B., Eds.; The Minerals, Metals and Materials Society: Warrendale, 1999; pp 119–138.
73. Lee, Y. Y.; McNallan, M. J. *Metall. Trans.* **1987**, *18A*, 1099.
74. Bramhoff, D.; Grabke, H. J.; Schmidt, H. P. *Werkst. Korr.* **1989**, *40*, 642.
75. Schwalm, C.; Schütze, M. *Mater. Corros.* **2000**, *51*, 34, 73, 161.
76. Schmitz-Niederau, M.; Schütze, M. *Oxid. Met.* **1999**, *52*, 225–240.
77. Schütze, M.; Malessa, M.; Rohr, V.; Weber, T. *Surf. Coat. Technol.* **2006**, *201*, 3872–3879.
78. Huntz, A. M.; Schütze, M. *Mater. High Temp.* **1994**, *12*, 151–161.
79. Renusch, D.; Grimsditch, M.; Koshelev, I.; Veal, B. W. *Oxid. Met.* **1997**, *48*, 471.
80. Uran, S.; Grimsditch, M.; Veal, B.; Paulikas, P. *Oxid. Met.* **2001**, *56*, 551–569.
81. Koshelev, I. K.; Paulikas, A. P.; Uran, S.; Beno, M. B.; Jennings, G.; Linton, J.; Veal, B. W. *Oxid. Met.* **2003**, *59*, 469–481.
82. Renusch, D.; Muralidharan, G.; Uran, S.; Grimsditch, M.; Veal, B. W.; Wright, J. K.; Williamson, R. L. *Oxid. Met.* **2000**, *53*, 171.
83. Uran, S.; Veal, B. W.; Grismditch, M.; Pearson, J.; Berger, A. *Oxid. Met.* **2000**, *54*, 73–85.
84. Wright, J. K.; Williamson, R. L.; Renusch, D.; Grimsditch, M.; Veal, B. W.; Hou, P. Y.; Cannon, R. M. *Mater. Sci. Eng. A* **1999**, *262*, 246.
85. Lipkin, D. M.; Clarke, D. R.; Hollatz, M.; Bobeth, M.; Pompe, W. *Corros. Sci.* **1997**, *39*, 231.
86. Tolpygo, V. K.; Dryden, J. R.; Clarke, D. R. *Acta Mater.* **1998**, *46*, 927.
87. Tien, J. K.; Davidson, J. M. In *Stress Effects and the Oxidation of Metals Proceedings*; Cathcart, J. V., Ed.; TMS-AIME: New York, 1975; p 200.
88. Metcalfe, E.; Manning, M. I. The spalling of steam grown oxide from austenitic and ferritic alloys. Report RD/L/R/1966 Central Electricity Generating Board, CERL, Leatherhead, 1977.
89. Armitt, J.; Holmes, D. R.; Manning, M. I.; Meadowcroft, D. B.; Metcalfe, E. The spalling of steam grown oxide from superheater and reheater tube steels. Report FP686 EPRI, Palo Alto, 1978.
90. Manning, M. I.; Metcalfe, E. Steamside spalling from Type 316 superheater and reheater tubes. Report RD/L/N15/75 Central Electricity Generating Board, CERL, Leatherhead, 1975.
91. Saunders, S. R. J.; Nagl, M. M.; Schütze, M. *Mater. High Temp.* **1994**, *12*, 103–109.
92. Schütze, M.; Ito, S.; Przybilla, W.; Echsler, H.; Bruns, C. *Mater. High Temp.* **2001**, *18*, 39–50.
93. Küppenbender, I.; Schütze, M. *Oxid. Met.* **1994**, *42*, 109–144.
94. Golightly, F. A.; Stott, F. H.; Wood, G. C. *Werkstoffe Korr.* **1979**, *30*, 487–491.
95. Banks, J. P.; Gohil, D. D.; Evans, H. E.; Hall, D. J.; Saunders, S. R. J. In *Materials for Advanced Power Engineering*; Contsouradis, D., *et al.* Ed.; Kluwer Academic: Dordrecht, 1994; pp 1543–1552.
96. Guttmann, V.; Mediavilla, A.; Ruano, O. *Mater. High Temp.* **1993**, *11*, 42–50.
97. Nagl, M. M.; Saunders, S. R. J.; Guttmann, V. *Mater. High Temp.* **1994**, *12*, 163–168.
98. Hancock, P.; Nicholls, J. R. *Mater. High Temp.* **1994**, *12*, 209–218.
99. Bruns, C.; Schütze, M. *Oxid. Met.* **2001**, *55*, 35–68.
100. Nagl, M. M.; Evans, W. T.; Hall, D. J.; Saunders, S. R. J. *J. Phys. III* **1993**, *3*, 933–941.
101. Nagl, M. M.; Evans, W. T.; Saunders, S. R. J.; Hall, D. J. *Mater. Sci. Technol.* **1992**, *8*, 1043–1049.
102. Schmitz-Niederau, M.; Schütze, M. *Oxid. Met.* **1999**, *52*, 241–276.
103. Robertson, J.; Manning, M. I. *Mater. Sci. Technol.* **1990**, *6*, 81–91.
104. Schütze, M. *Oxid. Met.* **1995**, *44*, 29–61.
105. Hukelmann, F. Doctoral Thesis, Technical University of Clausthal, 2000.
106. Hou, P. Y.; Atkinson, A. *Mater. High Temp.* **1994**, *12*, 119–125.
107. Mougin, J.; Dupeux, M.; Galerie, A.; Antoni, L. *Mater. Sci. Technol.* **2002**, *18*, 1217–1220.
108. Hou, P. Y.; Saunders, S. R. J. *Mater. High Temp.* **2005**, *22*, 121–129.
109. Hou, P. Y.; Priimak, K. *Oxid. Met.* **2005**, *63*, 113–129.
110. Funkenbusch, A. W.; Smeggil, J. G.; Bornstein, N. S. *Metall. Trans.* **1985**, *16A*, 1164.
111. Smialek, J. L. *Metall. Trans.* **1991**, *22A*, 739.
112. Suga, T. *Doctoral Thesis University of Stuttgart* **1983**.
113. Suga, T.; Kvernes, I.; Elssner, G. *Z. Werkstofftechn.* **1984**, *15*, 371.
114. Schütze, M. In *High Temperature Corrosion of Advanced Materials and Protective Coatings*; Saito, Y., *et al.* Ed.; North Holland: Amsterdam, 1992; 29.
115. Evans, H. E.; Mitchell, G. P.; Lobb, R. C.; Owen, D. R. J. *Proc. R. Soc. London A.* **1993**, *440*, 1.
116. Evans, A. G.; Hutchinson, J. W. *Acta Metall.* **1989**, *37*, 909.
117. Evans, U. R. *An Introduction to Metallic Corrosion*; Arnold Publishers: London, 1948.
118. Zimmermann, D.; Tolpygo, V. K.; Rühle, M.; Clarke, D. R. *Z. Metallk.* **2003**, *94*, 157–162.

119. Hancock, P.; Nicholls, J. R. *Mater. Sci. Technol.* **1988**, *4*, 398.
120. Schütze, M. *Oxid. Met.* **1986**, *25*, 409.
121. Bruch, U.; Döhle, K.; Pütz, J.; Rahmel, A.; Schütze, M.; Schuhmacher, K. D. *Proceedings of the International Congress on Metallic Corrosion*; NRC, Ottawa, 1984; Vol. 3, 325–329.
122. Schütze, M. *Werkstoffe Korr.* **1987**, *38*, 597.
123. Wagner, C. *Z. Elektrochemie* **1959**, *63*, 772.
124. Barbehön, J.; Rahmel, A.; Schütze, M. In *High Temperature Alloys for Gas Turbines and Other Applications*; Betz, W., *et al.* Ed.; D. Reidel Publishers: Dordrecht, 1986; 1267.
125. Quadakkers, W. J.; Bongartz, K. *Mater. Corr.* **1994**, *45*, 232–241.
126. Wright, I. G. In *Metals Handbook* 9th ed., ASM International: Metals Park, 1987; Vol. 13, Corrosion, 97.
127. Barbehön, J.; Rahmel, A.; Schütze, M. *Oxid. Met.* **1988**, *30*, 85.
128. Whittle, D. P.; Wood, G. C.; Evans, D. J.; Scully, D. B. *Acta Metall.* **1967**, *15*, 1747.
129. Wulf, G. L.; McGirr, M. B.; Wallwork, G. R. *Corros. Sci.* **1969**, *9*, 739.
130. Evans, H. E.; Lobb, R. C. *Corros. Sci.* **1984**, *24*, 223.
131. Nicholls, J. R., *et al.* In *Lifetime Modelling of High Temperature Corrosion Processes*; Schütze, M., Quadakkers, W. J., Nicholls, J. R., Eds.; EFC-Publication No. 34: Maney, Leeds, 2001.
132. Wright, I. G.; Pint, B. A.; Hall, L. M.; Tortorelli, P. F. In *Lifetime Modelling of High Temperature Corrosion Processes*; Schütze, M., Quadakkers, W. J., Nicholls, J. R., Eds.; EFC-Publication No. 34: Maney, Leeds, 2001; p 339–358.
133. Nesbitt, J. A. In *Lifetime Modelling of High Temperature Corrosion Processes*; Schütze, M., Quadakkers, W. J., Nicholls, J. R., Eds.; EFC-Publication No. 34: Maney, Leeds, 2001; pp 359–378.
134. Evans, H. E.; Taylor, M. E. *Oxid. Met.* **2001**, *55*, 17–34.
135. Pragnell, W. M.; Evans, H. E. *Oxid. Met.* **2006**, *66*, 209–230.
136. Renusch, D.; Echsler, H.; Schütze, M. *Mater. Sci. Forum* **2004**, *461–464*, 729–736.
137. COSIM – A finite difference computer model to predict tenary concentration profiles associated with oxidation and interdiffusion of overlay coated substrates. Funding No. WU-714-04-20-00. Contact: J.A. Nesbitt, NASA John Glenn Research Centre, Cleveland.
138. Pragnell, W. M. PhD thesis, University of Birmingham, 2005.
139. Wagner, C. *J. Electrochem. Soc.* **1952**, *99*, 369.
140. Whittle, D. P. *Oxid. Met.* **1972**, *4*, 171.
141. Schütze, M.; Malessa, M.; Renusch, D.; Tortorelli, P. F.; Wright, I. G.; Dooley, R. B. *Mater. Sci. Forum* **2006**, *522–523*, 393–400.
142. Rhines, F. N.; Wolf, J. S. . *Metall. Trans.* **1970**, *1*, 1701.

1.10 Oxidation of Metals and Alloys

P. Y. Hou
Lawrence Berkeley National Laboratory, Materials Sciences Division, 1 Cyclotron Rd., Berkeley, CA 94720, USA

Abbreviations

AE Acoustic emission
AES Auger electron spectrometry
EDS Energy dispersive spectroscopy
EELS Electron energy loss spectroscopy
ppm Parts per million
RE Reactive element
SEM Secondary electron microscopy
SIMS Secondary ion mass spectrometry
SNMS Secondary neutral mass spectrometry
STEM Scanning transmission electron microscopy
TEM Transmission electron microscopy

UHV Ultra high vacuum
YAG Yttrium aluminum garnet

Symbols

b Oxide grain size
D Diffusivity
Δ*G* Gibb's free energy
k_p Parabolic rate constant
pO_2 Partial pressure of oxygen
R Gas constant
T Temperature
δ Grain boundary width

1.10.1 Introduction

This chapter provides an overview of the corrosion behavior of different metals and alloys where oxygen is the only oxidant. Isothermal oxidation studies conducted in air and oxygen are considered, but any effects due to the presence of nitrogen in air, or humidity in the atmosphere are not included; these topics are covered in **Chapter 1.13, Nitridation of Alloys** and **Chapter 1.17, Oxidation in Steam and Steam/Hydrogen Environments**. Only pure metals and model alloys are discussed to illustrate the oxidation process; the behavior of more complicated commercial alloys is addressed in **Chapter 1.23, High Temperature Corrosion of Chromia-forming Iron, Nickel and Cobalt-base Alloys** and **Chapter 1.24, High Temperature Corrosion of Alumina-forming Iron, Nickel and Cobalt-base Alloys**. The principles that govern many aspects of high temperature oxidation that are considered in this chapter, such as oxidation kinetics, transport mechanisms through oxides, defect formation, stress generation and relaxation, microstructural evolution, and scale failure mechanisms, are thoroughly covered elsewhere in this volume. In this chapter, only experimental results on these phenomena will be summarized, without details of mechanistic discussions. The purpose here is to provide a short view of the current understanding of the oxidation behavior of a range of metals and alloys. More extensive discussions can also be found in textbooks on the oxidation of metals and alloys.[1–3]

The chapter is divided into sections on similar types of oxides that are formed on metals and alloys. The oxidation of Ni, Co, and Fe is first summarized, followed by that of refractory metals (Nb, Mo, Ta, W) and their alloys, and then by SiO_2-, Cr_2O_3-, and Al_2O_3-forming alloys. In each section, results on the nucleation, growth and protectiveness of the oxide formed are presented with the following topics covered whenever data are available: initial stage scale development, oxidation rates, transport mechanisms and dominating diffusion paths, development of oxide phases including oxide phase transformation, and evolution of scale microstructure and its relationship to the growth mechanism and scaling rate. A section (**Section 1.10.7.2**) on impurity segregation (mainly S, but also C) at different oxide–alloy interfaces, and its effect on oxide scale adhesion is included. The data cover a range of Al_2O_3-forming alloys, with or without Pt or reactive elements (REs), and some Cr_2O_3-forming alloys. In **Section 1.10.7.1**, the RE effect on Cr_2O_3- and Al_2O_3-forming alloys, and some work with NiO on Ni, is presented. Mechanisms that have been proposed for the RE effects on oxide nucleation, growth and adhesion are briefly reviewed.

Figure 1 compares the range of oxidation rates at different temperatures for the major oxides discussed in this chapter. Above 1100 °C, the oxide on Si has the slowest growth rate, but the establishment of a protective surface SiO_2 layer is difficult; more details are presented in **Section 1.10.4**. The kinetics for

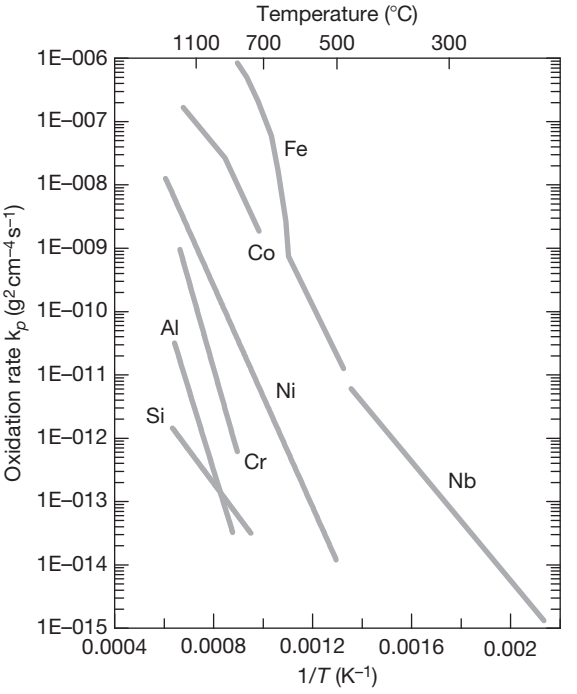

Figure 1 Summary of parabolic oxidation rate constants for some of the metals discussed in this chapter.

refractory metals, such as Nb, are only parabolic at low temperatures. Linear kinetics and oxide volatilization are often observed at higher temperatures (Section 1.10.3). The rate for Co oxidation shows two activation energies that are associated with the formation of Co_3O_4 above a growing CoO layer at lower temperatures; more details are discussed in Section 1.10.2.2. For iron, the lower temperature rate is dominated by the growth of magnetite (Fe_3O_4), while, at high temperatures, above ~570 °C, the rate is mainly dominated by the growth of the very nonstoichiometric wustite (FeO); since deviation from stoichiometry decreases with increasing temperature, the activation energy is seen to diminish with temperature. Details of iron oxidation are presented in Section 1.10.2.3.

1.10.2 Oxidation of Nickel, Cobalt, and Iron

The high temperature oxidation behaviors of Fe, Ni, and Co are similar in that the oxide growth is mainly controlled by the outward diffusion of cations because they form oxides that are metal-deficient at high temperatures and over a wide range of oxygen partial pressures.[4] From studies of nonstoichiometry, electrical conductivity, and self-diffusion coefficients, the predominant point defects in the major oxides formed on these metals are determined to be metal vacancies. Among these metals, iron oxidizes the fastest, as iron oxide and, hence, has the highest concentration of defects and the highest diffusion rate. The next lowest rate is for Co and then Ni (see Figure 1).

As Ni forms only one oxide, NiO, over a wide range of temperatures and oxygen potentials,[5] it is relatively the simplest system. Consequently, it has often been chosen as a model to study the fundamentals of high temperature metal oxidation, where oxide growth is controlled by cation diffusion. In this section, Ni oxidation is discussed first and in detail, because many concepts applicable to Ni are also relevant to the other metals, for example, initial stage of oxidation, metal and oxygen transports, the importance of oxide grain boundaries as transport paths, the generation of oxidation stresses and the development of duplex structures. Specific characteristics for Co and Fe oxidation follow.

1.10.2.1 Nickel

Nickel forms only one oxide, NiO, over a wide range of temperatures and oxygen potentials,[5] and much is known of its oxidation mechanism and the scale microstructure that develops.[6–12]

1.10.2.1.1 Transient stage oxidation

According to the surface studies of Mitchell *et al.*,[13,14] the initial stage oxidation of Ni proceeds in three stages. The first is the chemisorption of oxygen and the formation of a two-dimensional oxygen surface structure, which is different for different Ni orientations. The second involves nucleation and lateral growth of NiO. Nucleation occurs on sites that are present at the onset of oxidation, but such sites were not identified; lateral growth takes place at the periphery of nuclei by direct capture of oxygen from the gas phase. Stage 3, which starts before the completion of stage 2, involves logarithmic thickening of the oxide nuclei (up to their tested temperature of 300 °C). The nucleation and growth kinetics depend on temperature and the partial pressure of oxygen, but not significantly on metal orientation. At higher oxidation temperatures, however, the shape, size, and density of NiO nuclei have been found to depend strongly on Ni orientation,[15] in agreement with later results[16,17] showing that substrate orientation can strongly affect oxide grain size and oxide-scale thickness within a wide range of oxidation temperatures, from 450 to 1200 °C.

1.10.2.1.2 Oxide structures

The structure of NiO can be either simplex (single layer), which consists of a layer of columnar grains, or duplex (double layer), which has a columnar outer layer similar to that on the simplex scale, and an equiaxed, fine-grained, porous inner layer; examples of these are shown in Figure 2. In both structures, the columnar grains are textured,[18,19] where the degree of texture becomes more apparent for thicker scales. There have been experimental indications that the type of texture varies with Ni orientation,[20,21] and these differences may create different NiO grain boundary characters, thus affecting the oxidation rate.[20] However, the mechanism by which a different texture develops and exactly how it affects transport through the oxide is not yet clear. Even with an apparently single layer of columnar NiO, TEM studies[22] have found that a layer of fine-grained oxide with differently orientated grains can exist at the oxide–metal interface, where the oxide grains are only submicron in size. The reason for their formation is not clear; it is also not known if such a layer exists under all oxidation conditions. The

consequence of having this layer of fine-grained oxide at the interface may be to relax the growth and even the thermal stresses, since these fine grains may exhibit superplasticity.

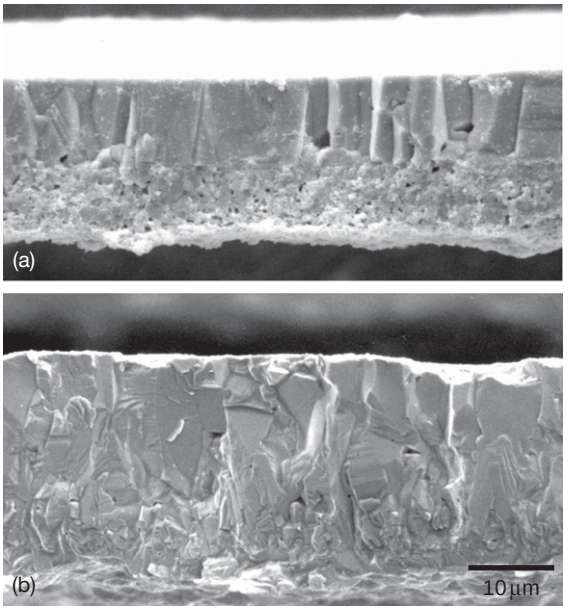

Figure 2 Typical NiO microstructure (a) duplex, columnar outer and fine grained, porous inner layers formed on normal purity Ni, 99.6–99.7%. (b) Single columnar layer formed on high-purity Ni, >99.95%. Reproduced from Hou P. Y.; Cannon, R. M. *Mater. Sci. Forum* **1997**, *251–254*, 325–332.

It is not known if the fine-grained oxide layer at the oxide–metal interface is the prelude to the thicker inner scale that is observed in a duplex structure. The thickness ratio of the inner and outer layers has been noted to depend on the oxidation temperature, the surface preparation[23] and, most importantly, the metal purity. For a given oxidation condition, less pure Ni is more prone to develop duplex scales than high purity Ni[24, 25]; furthermore, the duplex structure is always found on dilute Ni-based alloys.[10,26] Smoother surfaces and higher temperatures tend to decrease the duplex layer formation. **Figure 3** illustrates the range of temperatures and times at which different microstructures of NiO develop on high purity Ni.[17] At 900 °C or above (up to 1200 °C), the scale is one single compact layer, but, at temperatures below ~850 °C, it can be duplex or a porous single layer, depending on the oxidation time. In both cases, the first formed scale is a single layer, but less dense oxide forms at higher temperatures; with time, the scale can become duplex, where an inner, more fine-grained layer develops. Greater amounts of porosity are often found in the inner layer of the duplex structure. The mechanisms by which they develop are not clear, although several have been proposed; a review of these proposals can be found in the article by Kyung and Kim.[27] Some of these mechanisms attribute oxide growth stress as the cause for the onset of a porous, and eventually duplex, scale

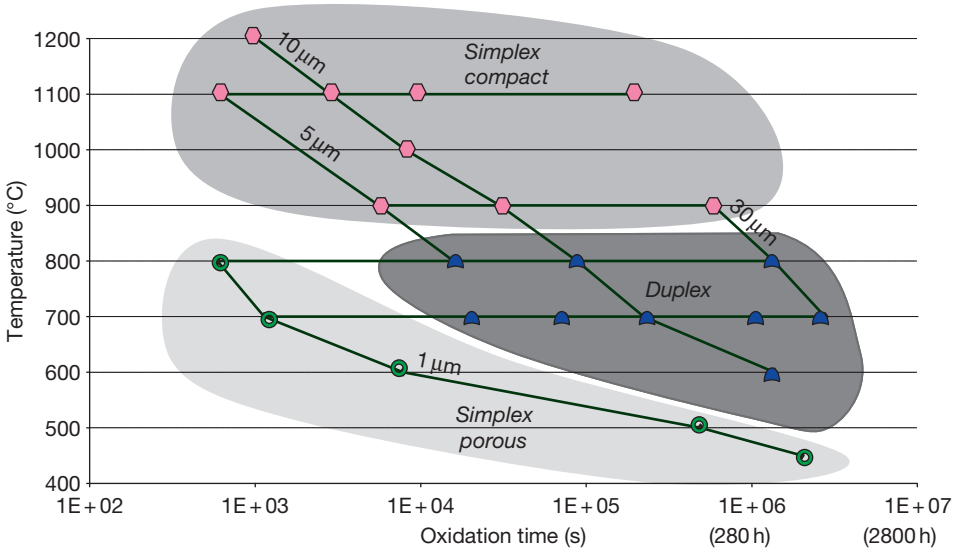

Figure 3 Formation of different NiO microstructures in relation to oxidation temperature, time, and oxide scale thickness. Oxidation was carried out on high purity Ni (>99.999%) in oxygen, after polishing to a 0.25 µm diamond surface finish and annealing at 1350 °C in Ar–5% H_2. Reproduced from Peraldi, R.; Monceau, D.; Pieraggi, B. *Oxid. Met.* **2002**, *58*, 249–273.

formation[28–30]; others point to the importance of the inward transport of oxygen through the initially formed single layer.[31,32] For whatever reason porosities are present in the oxide, a quasiequilibrium model of gaseous transport through these pores was developed to explain the formation of the inner layer.[33,34] In the case of Ni oxidation, it was suggested by Caplan *et al.*[35] that the duplex structure was also related to carbon impurity in the Ni. It was found that carbon, segregated at Ni grain boundaries, could induce grain boundary cavitation as a result of metal creep under the oxide growth stress. These cavities were then incorporated into the oxide as the oxidation front progressed inward. In nondecarburized Ni, cavities that formed inside the oxide contained C-containing gases, so $CO–CO_2$ was suggested to act as a carrier gas for the inward transfer of oxygen across these cavities.

1.10.2.1.3 Growth rate and transport processes through NiO

The growth of NiO at 700–1300 °C generally follows parabolic kinetics, although, usually, these are only exactly parabolic at temperatures above ~1000 °C. Reported parabolic rate constants have recently been complied by Peraldi *et al.*[36] over a wide range of temperatures, with data from different surface preparations, metal purities and orientations and partial pressures of oxygen. There has not been enough work done in the low-temperature range (<500 °C), and existing data show too much discrepancy to warrant a clear understanding of the behavior in this temperature regime. Oxidation rate values at very high temperatures (>1000 °C) have much less scatter than at intermediate temperatures (from 500 to 1000 °C). Furthermore, the activation energy for all the high temperature data are similar, ranging between 180 and 240 kJ mol^{-1}, which is similar to the activation energy for Ni lattice diffusion, at 154–254 kJ mol^{-1}. Tracer studies by Atkinson *et al.*[37] have also shown that NiO growth above 1000 °C is controlled by Ni lattice diffusion, but the growth is dominated by Ni grain boundary diffusion below this temperature.[38] In the intermediate temperature range, a decrease in the rate constant is often observed with oxidation time,[38–40] which can be attributed to a decreased grain boundary area due to grain growth,[41] attesting to the tracer studies[38] that oxide growth is dominated by grain boundary, rather than lattice, diffusion. Results from different works in this regime displayed greater scatter; some data showed apparently slower oxidation rates and lower activation energies than those at the high temperatures. These differences may be due to differences in sample purity, orientation and surface treatment, all of which have been reported to affect NiO growth rates. Impurities from the Ni, or minor alloying elements incorporated into the NiO, can change its defect concentration and, hence, affect the Ni cation transport rates.[42,43] Experimental measurements,[44] however, indicate that impurities often decrease the grain boundary diffusion rate of Ni. Thus, it would appear that the effects of impurities in increasing the oxidation rate of Ni most probably result from an altered oxide microstructure. Indeed, the most significant way the oxidation rate can be affected seems to be a change in the microstructure of the NiO scale, from simplex to duplex,[12] where the inner layer of the duplex scale is often fine-grained and porous.

Although the overall growth of the NiO scale is largely controlled by the outward diffusion of Ni through lattice or grain boundary diffusion *via* nickel vacancies,[2] a noticeable degree of oxygen diffusion through the scale is often observed. As seen from the oxygen isotope studies conducted by Atkinson *et al.*[7] (**Figure 4**), the thicker the inner layer, the more inward penetration of oxygen, and the inner layer thickness is directly related to Ni purity. Gaseous transport of oxygen is believed to occur through a porous oxide, whether in a porous simplex scale or in a porous inner layer in a duplex scale and, hence, contributes to, and increases, the oxidation rate. The oxygen tracer studies show that most of the inner layer growth takes place at or near the scale–metal interface via oxygen inward transport through the scale.[37] The path for oxygen transport, particularly through the outer layer, has been suggested, by Atkinson *et al.*,[37] to be microcracks or fissures, in the scale caused by growth stresses. The conclusion was made simply because the rate of oxygen transport is too fast to be accounted for by solid state diffusion.

The topic of stresses in thermally grown NiO can be dated back to 1947 when Evans[45] reported the observations of buckling and curling of NiO scale after its removal from the underlying Ni substrate. This indicated the presence of a compressive residual stress in the NiO film, and a possible stress gradient through it, with higher compression at the scale–metal interface.[46] Later studies[47] further demonstrated the existence of a compressive growth stress by measuring the degree of Ni elongation during oxidation. Others[48] have come to the same conclusion by

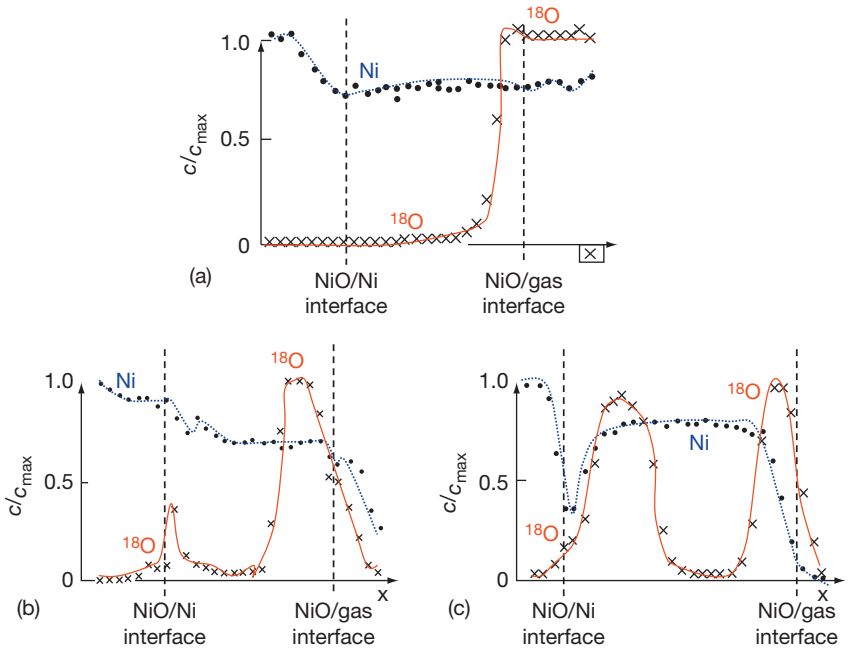

Figure 4 Ni and ^{18}O traces through NiO scales formed at 1000 °C on (a) {100} Ni crystal, (b) 99.998% high-purity polycrystalline Ni, and (c) 99% low-purity polycrystalline Ni. Each specimen was first oxidized in $^{18}O_2$ then in equal amount of time in $^{18}O_2$, under 50 torr of total oxygen pressure. (After Atkinson, Taylor and Goode[7]).

studying the flexure of thin strips of Ni samples as a result of oxide growth. More recent studies using *in situ* X-ray diffraction techniques, however, have found the growth stress to be slightly tensile[49–51] at 900 °C, but compressive at lower temperatures, that is, 800 °C[52] and 600 °C.[51]

An implication consistent with the stress studies seems to be that the first formed simplex scale is under compression, but the growth stress in duplex NiO scales is mildly tensile near the outer surface and strongly compressive near the scale–metal interface, with the total net stress still being compressive.[25] The tensile stress in the outer duplex layer may assist microcrack formation, although direct observations of these gaseous transport paths have not been made. Acoustic emission studies conducted at 800 and 900 °C[53] have shown some activities during Ni oxidation, indicating possible cracking of the oxide. However, the experiment was done on a thin film of Ni that was allowed to bend during oxidation, in order to determine the level of growth stress. It is unclear how the bending of the sample under the oxide growing condition affected the AE signals. Since oxidation is a dynamic process, where cracks can form and heal at any time within the scale, it may be impossible to identify these fast gaseous transport paths, if they do exist, unless microstructures can be studied *in situ* at the oxidation temperatures.

1.10.2.2 Cobalt

Three cobalt oxides exist, namely Co_3O_4, Co_2O_3, and CoO, and have respectively the spinel, hexagonal, and cubic structures. Co_2O_3 is unstable above 300 °C, so is not found in oxidation products of Co, where tests are usually conducted between 400 and 1400 °C.[5] From the results reported in the review by Wood *et al.*,[5] average activation energies are calculated to be $107 \pm 26\,kJ\,mol^{-1}$ between 500 and 800 °C, and $213 \pm 47\,kJ\,mol^{-1}$ between 800 and 1400 °C. Clearly, there is a sharp, but unexplained, increase in oxidation rate with temperature above 600–700 °C. Kofstad[2] has compiled some of these oxidation rates, between 800 and 1150 °C, and noted yet another change in activation energy at about 950 °C, which is associated with the formation of Co_3O_4. The activation energy for self-diffusion of Co in CoO in the range 800–1300 °C is 144 or $160\,kJ\,mol^{-1}$,[4,54] which lies in the range of oxidation activation energies. These results suggest that CoO growth is controlled by cation movement via vacant lattice sites.

Above ~900–950 °C, only CoO is formed, but below this temperature, Co_3O_4 can exist as a thin layer at the scale–gas interface above the CoO. The proportion of Co_3O_4 in the scale seems to increase with decreasing temperature, from 800 to 600 °C.[55] The relative thickness of the two layers is a function not only of temperature, but also of the partial pressure of oxygen. These dependencies, from 500 to 900 °C, have been summarized by Hsu and Yurek.[56] Both layers grow by cation outward diffusion, with probably lattice and grain boundary diffusion dominating in the CoO and Co_3O_4 layers respectively, due to the difference in grain size between the two layers. The growth rate of CoO at 600 °C has been found to be about five times greater than that of Co_3O_4,[57] so the overall oxidation rate is usually considered to be controlled by the growth of the CoO layer. It should also be noted that, once a complete Co_3O_4 layer exits at the surface, the overall oxidation rate becomes independent of the ambient oxygen pressure, as the partial pressure of oxygen at the CoO/Co_3O_4 interface is given by the decomposition pressure of Co_3O_4 in equilibrium with CoO.

Like NiO, the CoO layer can be single- or double-layered.[55] It also appears that a double-layered structure is favored with alloying addition in dilute Co alloys,[58] while pure Co tends to form a single layer.[59] Pt markers placed on the sample surface prior to oxidation reside at the inner–outer oxide layer interface,[55,60,61] suggesting that, analogous to NiO, the outer layer grows by the outward movement of cobalt ions and the inner one by the inward diffusion of oxygen gas or anions. More recent work using the ^{18}O isotope[62] has confirmed these earlier studies; between 1000 and 1300 °C. The CoO formed on dilute Co–Cr alloys develop duplex structures, where the inner layer thickness increased with increasing Cr content. Growth of the scale is dominated by cation outward transport, but oxygen inward diffusion becomes more apparent with a thicker inner layer.

1.10.2.3 Iron

The rate of iron oxidation is governed by the stabilities of its various oxide phases, FeO, Fe_3O_4, and Fe_2O_3, which are in turn a function of the oxidation temperature and the ambient partial pressure of oxygen. The temperature and pO_2 ranges at which each of these oxides are stable is shown in **Figure 5** so, at 900 °C and 10^{-18} atm, for example, iron will not be oxidized, because none of its oxides is thermodynamically stable under such a condition. In air or oxygen

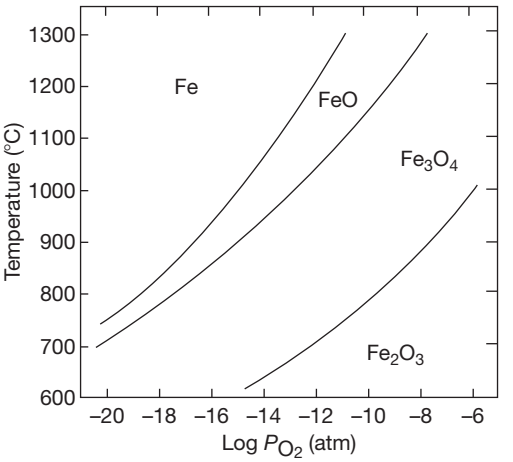

Figure 5 Regions of stability for different iron oxides as a function of oxygen partial pressure and temperature. Reproduced from Kofstad, P. *High Temperature Corrosion*; Elsevier Applied Science: London, UK, 1988.

and above 570 °C, the oxide scale is multilayered, consisting of hematite (Fe_2O_3) at the scale–gas interface, magnetite (Fe_3O_4) in between and wustite (FeO) at the scale–metal interface. Below 570 °C, wustite is unstable, so the scale only consists of Fe_2O_3 and Fe_3O_4. While these observations are true for bulk scales, FeO has been found to be stable in very thin films at temperatures down to 400 °C[63] and within narrow cracks at 500 °C.[64] A cross-section of a scale formed at 525 °C is given in **Figure 6**, where the scale consists only of Fe_3O_4 and Fe_2O_3, and the Fe_3O_4 layer is seen to consist of two different layers.[65] Similar to NiO and CoO, duplex Fe_3O_4 or FeO layers are often observed, and the amount of porosity in them increases with oxide thickness.

Wustite is metal deficient, $Fe_{1-y}O$. The nonstoichiometry, y, is a function of the partial pressure of oxygen and temperature. Between 800 and 1250 °C, it varies from 0.05 at the iron–wustite phase boundary to about 0.1–0.15 (higher at higher pO_2) at the wustite–magnetite boundary.[66–70] Unlike CoO and NiO, the deviation from stoichiometry decreases with increasing temperature at a constant partial pressure of oxygen, which means that the enthalpy of defect formation is negative. Magnetite has the spinel structure. At pO_2 values above the stoichiometric composition, the oxide is metal deficient ($Fe_{3-y}O_4$), where y increases with increasing pO_2 and decreases with increasing temperature, as occurs for wustite. At lower pO_2 values, the oxide has a cation excess, with the dominant defect being iron ions on interstitial sites.[71] Because of these properties, Fe

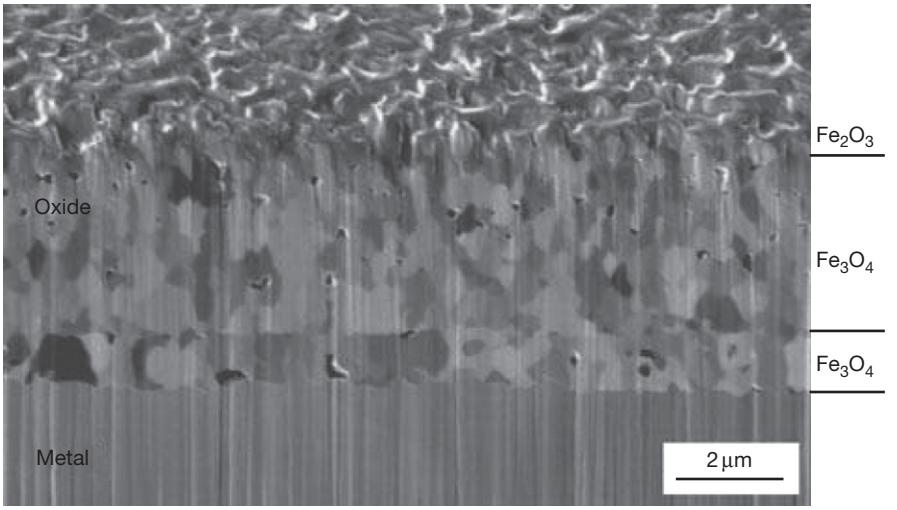

Figure 6 Focus ion beam image of ion milled cross-section of oxide formed on iron after 1 hr oxidation in oxygen at 525 °C. The oxide is seen to consists of three layers, with the top being hematite and the bottom two magnetite. Reproduced from Jonsson, T.; Jardnas, A.; Svensson, J. -E.; Johansson, L. -G.; Halvarsson, M. *Oxid Met.* **2007**, 67, 193–214.

diffusion in magnetite as a function of pO_2 shows a minimum near its stoichiometric composition for each temperature.[72] Among the three iron oxides, Fe_2O_3 has the smallest degree of nonstoichiometry.

Both FeO and Fe_3O_4 grow predominantly by cation transport of Fe^{2+} in FeO and Fe^{2+} and Fe^{3+} in Fe_2O_3. The dominant transport path in FeO seems to be Fe lattice diffusion,[73] but oxide grain boundaries have been shown to be more important for Fe_3O_4 below 600 °C, and at all temperatures for Fe_2O_3.[74–76] The measured activation energy for Fe_2O_3 growth is about 169–222 kJ mol^{-1},[77] which is much lower than that expected from measurements of tracer diffusivities of iron or oxygen.[78] Oxygen tracer diffusion studies on the growth of Fe_2O_3 during the oxidation of iron at 550 °C have shown that, while the primary diffusion species through the oxide is Fe ions, fast, inward oxygen diffusion occurs down cracks in the scale.[79] A simplified schematic diagram for the diffusion-controlled growth of multilayered scales on iron above 570 °C is illustrated in **Figure 7**, and the reactions that occur at each interface are noted. The range of oxidation rates, in an Arrhenius plot, can be found in **Figure 1**. Above 570 °C, a distinct break associated with the formation of FeO in the scale occurs. The activation energy above this temperature is not constant, because of the large change in stoichiometry of FeO with temperature.

A strong orientation relationship exists between the iron surface and the composition and thickness of the initial oxide that forms. The first-formed oxide layer, at around 200 °C, consists of Fe_2O_3 and

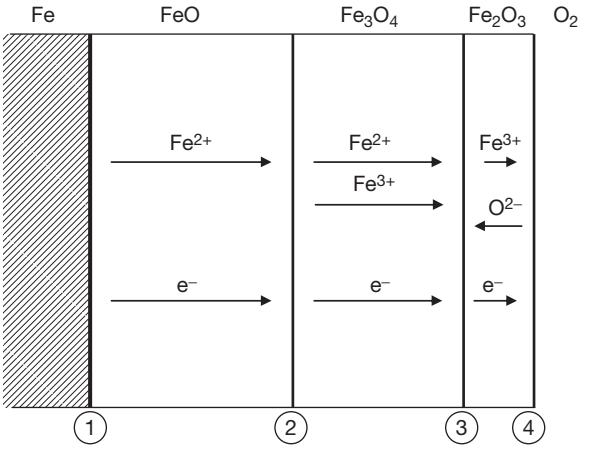

1. $Fe = Fe^{2+} + 2e^-$
2. $4FeO = Fe^{2+} + 2e^- + Fe_3O_4$
3. $3Fe_3O_4 = Fe^{n+} + ne^- + 4Fe_2O_3$
4. $Fe_2O_3 = 2Fe^{3+} + 6e^- + 3/2O_2$
   $1/2O_2 + 2^{e-} = O^{2-}$

Figure 7 Schematic illustration of the oxide layers formed upon iron oxidation above 570 °C, the dominant diffusing species through each layer and the reactions that take place at each interface are indicated.

Fe_3O_4,[80] where a higher proportion of Fe_3O_4 exists on the lower index planes close to (100), (110), and (111), than on the higher index planes. The initial oxide composition and thickness are also found to depend on surface preparation and the presence of impurities[81]; for example, on cold-worked surfaces, the scale tends to contain less Fe_3O_4.[82] Between 350

and 500 °C, Fe_3O_4 nucleates first, and then grows laterally over the entire surface.[83] Subsequent growth of the Fe_3O_4 layer follows parabolic kinetics, where the rate is dominated by the diffusional transport of Fe^{2+} and Fe^{3+} ions through oxide grain boundaries. With time, and if the pO_2 is sufficiently high, Fe_2O_3 nucleates in the Fe_3O_4 surface.[84] When the Fe_2O_3 overgrows to form a continuous layer, the overall oxidation rate is substantially decreased, because the growth rate of Fe_2O_3 is slower than that of Fe_3O_4, and growth of the Fe_3O_4 layer is decreased due to the lower effective pO_2 at the Fe_3O_4/Fe_2O_3 interface. Therefore, the oxidation of iron often shows an unusual dependence on oxygen pressure, with a higher overall oxidation rate at lower pO_2 values, due to a slower rate of Fe_2O_3 nucleation, so a complete surface layer of Fe_2O_3 is achieved less easily to help impede the faster growth of Fe_3O_4.

It is well known that most technical steels oxidize faster in the presence of water vapor than in dry air. The reasons are currently under intense investigation. For unalloyed iron, a strong water vapor effect is not always observed. The difference in behavior between dry and moist environments seems to be affected by the oxidation temperature,[85,86] as well as the experimental procedure and the purity of the samples.[87] When a water vapor effect was observed, it appears that the oxide scale is more plastic when it was formed in the presence of moisture.[85,87]

1.10.3 Oxidation of Refractory Metals and Their Alloys

Refractory metals are by definition metals with high melting points. If this were the only criterion, that is, melting point greater than 1925 °C,[88–90] eleven metals would fall into this category. Other definitions are more restrictive and include the requirements that the metal has a body-centered-cubic (bcc) crystal structure and forms oxides whose melting points are lower than that of the metal.[89] These are niobium (Nb), tantalum (Ta), molybdenum (Mo), tungsten (W), and rhenium (Re), in increasing melting points that range from 2468 to 3180 °C. Although the high melting points make these metals attractive candidates for high temperature applications, their usage has been limited due to several problems, such as insufficient yield strength at high temperatures, difficulties in fabrication and poor oxidation resistance. Even at 300 °C, oxidation can be significant (Figure 1); above 1100 °C, the rates are simply too high to completely preclude their use. Alloying has improved the high temperature strengths, as well as the oxidation resistances, allowing refractory alloys to be used in a number of high temperature structural applications, principally in areas of propulsion and energy conversion, such as rockets and reentry systems.[91] Among the five metals listed above, Nb, Ta, Mo, and W have received greater attention in research and have wider industrial applications; therefore, these will be the ones discussed here.

1.10.3.1 Oxidation of Ta, Nb, Mo, and W Metals

Although these are simple metals, their oxidation behaviors are very different and more complicated than those of Fe, Ni, and Co described in the previous section. This is because in addition to the usual complications associated with oxidation, such as oxide nucleation, growth and diffusion processes in the oxide and the metal, these metals can have relatively high oxygen solubility, and large numbers of oxides that can form under different temperatures and oxygen pressures and, in some cases, are volatile, especially oxides of Mo and W. The equilibrium vapor pressures of some refractory metal oxides at $pO_2 = 1$ atm are summarized[92] in Figure 8. Most studies on the oxidation of refractory metals, including reaction mechanisms, metal recession rates and their pO_2 dependence, were performed prior to 1970, and a thorough description can be found in Ref. 2. This section only briefly summarizes the unique oxidation behavior of these metals and discusses their alloys and coatings or surface treatments that have been attempted to improve oxidation resistance.

1.10.3.1.1 Tantalum and niobium

Tantalum forms only one thermodynamically stable solid oxide, Ta_2O_5. However, nucleation of this oxide appears to be difficult, especially at lower temperatures and oxygen pressures. As a result, oxidation of Ta during the initial stage involves extensive dissolution of oxygen in the metal and the formation of different metastable TaO_x type oxides at different temperatures. Between 300 and 500 °C, the oxides grow in the form of platelets on the metal surface and extend into the metal along preferred crystallographic orientations.[93,94] As temperature increases, Ta_2O_5 begins to nucleate on the surface platelets but, below 800 °C, it is not able to develop into a dense surface layer; reaction is believed to be controlled by oxygen-chemisorption equilibrium and the nucleation and growth of Ta_2O_5, leading to a porous surface film

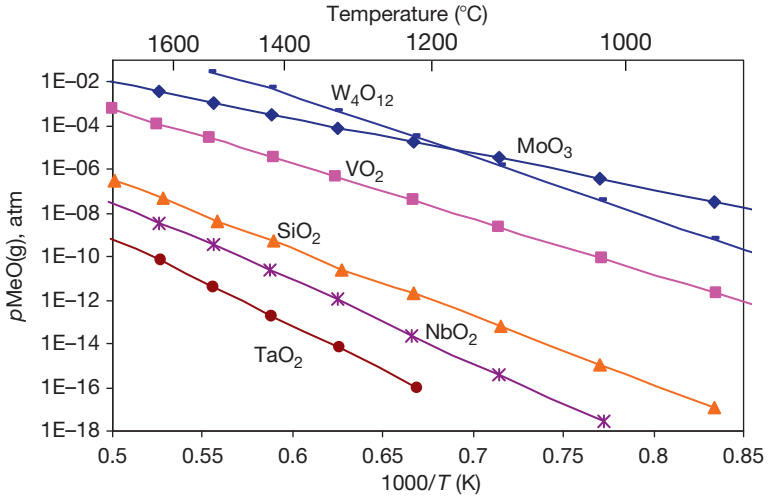

Figure 8 Equilibrium vapor pressure of some refractory metal oxides and silicon dioxide at pO_2 = 1 atm. Reproduced from Ramberg, C. E.; Beatrice, P.; Kurokawa, K.; Worrell, W. L. In *High Temperature Silicides and Refractory Alloys*; Proceedings of the Matererial Research Society Symposium, Boston, MA, Nov.–2 Dec. 1993; Briant, C.L., Petrovic, J. J., Bewlay, B. P., Vasudevan, A. K., Lipsitt, H. A., Eds.; Material Research Society: Pittsburgh, PA, 1994; pp 243–253.

and a linear oxidation rate.[94] A consequence of oxygen dissolution into the metal is metal embrittlement, which can be significant and should not be ignored.[95]

Above 800 °C, between 1 atm to 0.01 torr O_2, a complete Ta_2O_5 layer can develop after an initial incubation time that is associated with the nucleation and growth of Ta_2O_5 in similar ways as at lower temperatures.[96] Growth of the first formed Ta_2O_5 layer exhibits parabolic kinetics, which should be dominated by oxygen inward transport through the scale. This conclusion, although made only from the morphology of the scale, is consistent with the oxidation pressure dependence of the rate constants.[96] Since conductivity experiments show that Ta_2O_5 exhibits p-type conductivity at pressures close to 1 atm O_2 and n-type conductivity at lower oxygen pressures,[97] it was concluded that transport through the compact Ta_2O_5 predominantly occurs *via* oxygen vacancies at lower pO_2 and by interstitials at higher pO_2. After the short parabolic period, the oxidation rate becomes linear.[96] This behavior was interpreted to involve a repetitive, continuous, and probably statistically distributed cracking of the scale down to the metal, whereby exposing the metal–oxide interface beneath the cracks to oxygen. Oxygen then chemisorbs on the freshly exposed metal surface and reaction rates again become dominated by the nucleation and regrowth of Ta_2O_5. Indeed, substantial amounts of compressive growth stresses have been found during oxidation up to 550 °C by deflection of Ta, as well as Nb.[98] The sources of the stresses are oxygen dissolution during the initial stage and oxide film formation afterwards. The stress distribution across the scale to the metal region affected by oxygen dissolution cannot be determined from the bending test, but tensile stress can develop in the oxide film at some stage if there is compression in the substrate near the oxide–metal interface, and this tensile stress can easily induce scale fracture. Under compression, oxides are less easy to crack, but scale failure, especially by buckling of the surface film, is common under biaxial compression. The fact that blisters were found on the oxides formed on Ta and Nb[99] suggests this kind of failure.

Above 1050 °C, the post-parabolic oxidation rate is no longer linear, but decreases with time,[100] probably due to increased sintering of the oxide grains that densify the film, and enhanced plasticity to relieve some of the growth stresses that cause cracking. At temperatures greater than 1200 °C, however, reaction rates at 1 atm oxygen can be so fast that severe sample heating or even ignition can occur. Above ~1500 °C, evaporation of TaO and TaO_2 becomes important.

The oxidation behavior of niobium is in many ways analogous to that of tantalum, but the behavior is even more complex due to the fact that Nb forms several stable oxides: NbO, NbO_2, which has the rutile structure, and several polymorphs of Nb_2O_5. During the initial stage, oxidation proceeds principally by dissolution of oxygen in the metal, and this is subsequently followed by the formation of NbO, NbO_2 or a mixture of both. At higher temperatures, ~450–500 °C, a

surface layer of NbO_2 forms at low pO_2 ($\sim 10^{-4}$ to 10^{-5} torr)[101,102] and Nb_2O_5 develops near atmospheric pressures.[103,104] Both types of oxides can be protective for a period of time, showing parabolic growth rate controlled by the inward diffusion of oxygen, but the surface layer eventually breaks down, giving rise to linear kinetics, where the rate is controlled by oxygen adsorption and the nucleation and growth of Nb oxide at the oxide–metal interface. Usually, oxidation kinetics are parabolic to paralinear over the temperature range 400–600 °C, but linear from 700 to 900 °C.[105] Like Ta, oxidation can only be studied in low pO_2 environments above 1200 °C, because the rate is too rapid near atmospheric pressure.[102] At and above 1500 °C, oxidation is affected by the presence of liquid Nb_2O_5, which melts at 1490 °C; at even higher temperatures, evaporation of Nb_2O_5 becomes increasingly important.

1.10.3.1.2 Tungsten and molybdenum

When W is heated in the temperature range ~200–700 °C in oxygen, it grows a multilayered oxide film that desorbs above ~900 °C into predominantly volatile WO_2, with very small amounts of WO and WO_3.[106] WO_{3-x} forms in the temperature range 568–908 °C, and its growth rate has been expressed as: $D = 6.83 \times 10^{-2} \exp(-29\,890/RT)$, with the activation energy given in calories per mole.[107] Growth of the WO_{3-x} film was determined to be dominated by oxygen diffusion via oxygen vacancies. At higher temperatures (~1100–2900 °C),[108] the oxidation rate is dominated by the formation of a variety of volatile products, namely WO_2, W_2O_6, WO_3, and W_3O_9, where the polymeric oxides, $(WO_2)_2$ and $(WO_3)_2$, are believed to form through the interaction between WO_2 molecules. Due to the extensive volatilization, the oxidation of tungsten is dominated by the adsorption and dissociation of oxygen, the surface interaction of oxygen atoms with the metal and the subsequent desorption of tungsten oxide.[109] The reaction rates are a strong function of not only temperature, but also oxygen pressure, as illustrated in **Figure 9**, where the experimental data are those from Bartlett.[110]

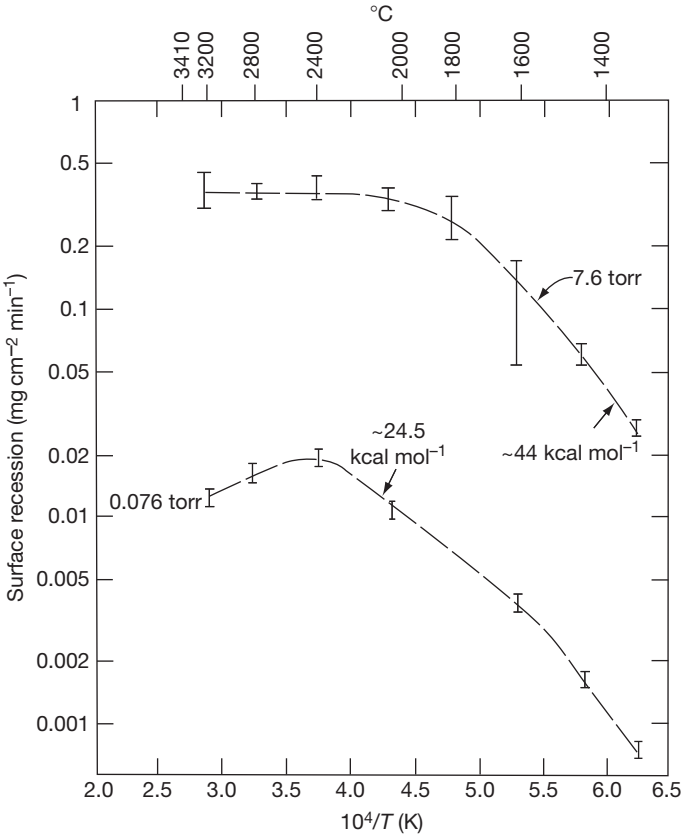

Figure 9 Tungsten surface recession rate as a function of temperature under high and low oxygen partial pressures. Reproduced from Kofstad, P. *High Temperature Corrosion*; Elsevier Applied Science: London, UK, 1988.

Under low oxygen pressures, generally below $\sim 10^{-4}$ atm,[111] the oxidation rate is governed by surface processes or reactions; above ~1300 °C, the oxide evaporates as soon as it is formed, and the metal remains free of surface oxide during oxidation.[112] The metal recession rate is slower at higher pressures, because a surface boundary layer exists, which limits the rate of oxygen arrival at the metal surface. Furthermore, the surrounding gas acts as a blanket that reflects escaping molecules back to the surface; the fraction of this back-reflection process is a function of the total gas pressure of the system. Consequently, metal recession rates are slower than expected from surface reactions alone. Furthermore, the high pressure regime is affected by the gas flow rate, because the thickness and effect of the boundary layer are decreased with higher flows.

The oxidation of Mo is similar to that of W. At 190 °C in air, molybdenum is coated with an oxide film, which hinders further oxidation up to 350 °C. Over 350 °C, oxidation recommences. At 500 °C, the rate increases quickly as MoO_3 sublimates intensively, exposing the metal. When oxidized in air, molybdenum oxides show valencies of 4 and 6.[113] Oxidation behaviors at higher temperatures are dictated again, as with W, by volatilization of oxides. The principal products are the gaseous dioxide and trioxide, MoO_2 and MoO_3, respectively. Between ~1200 and 2300 °C,[114] the trioxide was found to be the more important species at lower temperatures, and the dioxide was the dominant product at higher temperatures. At the lowest temperatures and highest oxygen pressures, small amounts of polymeric oxides, $(MoO_2)_2$ and $(MoO_3)_2$ were also detected.

1.10.3.2 Oxidation of Refractory Alloys

The focus of this section is not to review the effect of alloying additions on the oxidation of refractory metals, but to discuss advances made that can improve the oxidation behavior and, hence, the usefulness of this class of material.

Some of the investigators, who studied the oxidation behavior of refractory metals prior to 1970, also examined the oxidation mechanism of some refractory alloys. For example, W addition to Ta has been studied to evaluate its effect on Ta oxidation; the amount of W added varied from 10 wt%[115–117] to 50 wt%.[118] In most cases, no significant beneficial effects were found, except at 1200 °C, where 50 wt% W was reported to decrease the Ta oxidation rate by nearly a factor of 10, but the effect quickly diminished at higher temperatures.[117] Dilute Nb–Hf and Nb–Zr alloys, often considered for applications where strength and resistance to alkali metals are required, have also been studied.[119,120] Although the oxidation rate in air can be decreased with the addition of Hf or Zr, the benefit is not significant. Furthermore, internal oxide precipitates of Hf and Zr develop, and they may further embrittle the alloy. Careful heat treatments can control the size, morphology, and distribution of the internal particles, allowing them to produce a strengthening effect in the alloy,[119] but this type of controlled morphology is difficult to maintain in long-term applications. Also, protective surface oxides do not form on alloys such as Ta–8W–1Re–0.7Hf–0.25C and Mo–36Re (all in wt%); with the Mo–Re alloy, weight gains associated with the formation of MoO_2 were found at temperatures above 400 °C for $P_{O2} < 10^{-3}$ Pa (10^{-5} torr) in vacuum, but weight losses took place with evaporation of MoO_3 at 10^{-2} Pa.[121] Oxygen dissolution and internal oxidation were also reported to affect the mechanical property of these alloys.[122] The oxidation rate of Nb in air from 800 °C to above 1000 °C can be decreased by alloying with Hf, Zr, W, Mo, Ti, or Ta.[123] However, the preferred fabricable alloys still require further protection by coating.

The development of oxidation resistant Nb alloys that can be used for aerospace applications had received considerable interest,[124] since Nb is less dense but stronger than Ni-based superalloys at high temperatures. Attempts have been made by alloying to promote the formation of an Al_2O_3 scale as a protective layer. Svedberg[125] conducted an extensive investigation of the oxidation resistance of Nb-alloys in air at 1200 °C and found the slowest rate for $NbAl_3$, which developed an alumina inner layer adjacent to the metal–oxide interface and an $NbAlO_4$ outer layer at the oxide–gas interface. The oxidation rate was approximately parabolic, but the rate constant was still 2 orders of magnitude higher than that of NiA1, which forms a protective alumina scale in O_2 at 1200 °C. Perkins and Meier[126] have also studied factors affecting the selective oxidation of Al and the formation of protective alumina scales on Nb–Al alloys. It was shown that protective alumina scales are not formed on $NbAl_3$ in air at 1350 °C due to the formation of an Al-depleted Nb_2Al layer at the scale–alloy interface. Protective alumina scales can be formed on Nb–Al alloys with 37.5–50 at.% Al in air at 1400–1600 °C by adding Ti to increase the solubility and diffusivity of Al and adding Cr and/or V to decrease the solubility–diffusivity product of O in the alloy. An alloy with 25.4Nb–29.1Ti–2.8Cr–3.5V–39.2Al

(wt%) was developed and was able to form a protective alumina scale in air at temperatures above 1000 °C that was even stable up to 1400 °C. Furthermore, this alloy oxidized with kinetics comparable to those of NiAl.[127] However, the melting point of the alloy was relatively low, about 1600 °C, which resulted in poor mechanical strengths at high temperatures. Attempts to raise the melting point were made by replacing Nb (melting point ~2500 °C) with Ta (m.p. ~3000 °C), and led to an increase in the alloy melting point by ~300 °C. However, the microstructures of the Ta–Al–Ti–V–Cr alloys are thermally unstable. Technical efforts have also been made to improve the strength and oxidation resistance of the Nb–Al–Ti–V–Cr alloys by adding dispersion particles.[128] It was found that Al_2O_3 and Y_2O_3 were thermally and chemically stable with respect to Nb alloys, but SiC, Nb_5Si_3 and AlN reacted extensively with the alloys at high temperatures.

Some efforts have also been carried out through alloying of Cr to produce a refractory metal based alloy that is a good Cr_2O_3 former,[129] but the results have not been successful, mainly due to the difficulties in controlling the alloy microstructure and also from the formation of volatile oxides, especially those of W and Mo.

In general, despite quite a bit of effort and some limited successes, successful development of high temperature refractory-based alloys with the ability to form a protective oxide scale over an extended period has not been achieved. Even though some of these alloys have potentially useful properties, the alloying elements usually lead to detrimental effects in at least one crucial alloy property.[130] These drawbacks have severely limited the applicability of refractory alloys. One approach to improve the oxidation resistance has been to use coatings, and these will be briefly discussed in the next section.

1.10.3.3 Coatings on Refractory Metals and Alloys for Oxidation Protection

Coatings, whether applied as an external layer, or produced in the alloy surface region, have been used to improve the oxidation resistance of refractory alloys. In some cases, they are very effective.[131] These include $MoSi_2$,[132,133] niobium silicide, both in its pure form and alloyed with Fe and Cr,[130] $(Mo,W)(Si,Ge)_2$,[134] and aluminides.[127] The oxidation behavior of some of the silicides is described in **Section 1.10.4.2**. Although these coatings can, for the most part, provide adequate oxidation protection, they tend to be very brittle. Even a small mismatch in the thermal expansion coefficients between the base metal and the coating can lead to cracks, especially when the coating is under residual tension. The cracks can heal under some conditions, but often they allow oxygen penetration into the base metal, which then oxidizes rapidly. Consequently, the use of coatings to protect these metals is not always an adequate solution to the oxidation problem.

Other types of coatings have continually been evaluated, but have showed little success. On tungsten, amorphous W–N–Ni coatings with different N and Ni contents have been demonstrated to improve the oxidation resistance up to 800 °C,[135] by forming two nickel-rich, external oxide layers of NiO and $NiWO_4$. The oxidation rate was controlled by the outward diffusion of either Ni^{2+} or W^{6+} ions through the oxide layers. However, for the coating to remain effective, it has to stay amorphous. Crystallization induced a dimensional stress capable of destroying the protective oxide layers. FeCrAl-, SiCrFe-, and $MoSi_2$-based coatings have been deposited onto molybdenum with various techniques (plasma spraying, slurry deposition and physical vapor deposition) to different thicknesses with a range of varying thermal post-treatments.[136] The best coating lifetime, however, was only a few thousand hours at 1200 °C and a few hundred hours at 1450 °C under isothermal oxidation tests in air. Although a noticeable improvement from uncoated metal, durability has not been proved for these coated systems for them to be used reliably in engineering applications.

Surface treatments have included laser alloying, ion implantation and aluminizing, all of which aim at modifying the surface composition of an alloy so that it can develop a protective oxide scale, while not changing the alloy bulk properties. Ion implantation of different species can have a beneficial influence on the thermal oxidation kinetics of niobium in pure oxygen at temperatures below 500 °C.[137] Si and Al were most beneficial. However, the treatment only delayed the appearance of the linear catastrophic kinetics, but showed no long-term effects. When Al or Si powders were deposited onto niobium by laser melting, forming aluminized or siliconized surface coatings, the effect was longer lasting, but the coatings still failed with time.[138] Likewise, coatings produced by pack cementation with Cr and Al also failed under longer times and at higher temperatures; one of the reasons for the failure was interdiffusion, where the scale forming element is lost from the coating by diffusing into the alloy, while alloying elements diffuse into the coating and change its oxidation

properties. Diffusion barriers have been tested to show some success. When a Re–Ni film that contained more than 70 at% Re was applied onto a Nb–5Mo–15W (wt%) alloy via electroplating, followed by pack cementation with Cr and Al, the alloy was able to develop a protective Al_2O_3 scale, with a Re–Cr rich σ-phase layer in the inner layer of the coating, which decreased the mutual diffusion between the outer Al reservoir layer and the alloy substrate.[139] However, the most severe condition tested so far was isothermal oxidation at 1100 °C for 100 h in air. No cyclic oxidation tests have been performed to evaluate the durability of the coating.

1.10.4 Oxidation of Silica-Forming Alloys

Pure silica (SiO_2) is one of the most impermeable oxides at high temperatures. The low activation energy for the diffusion of oxygen in SiO_2 makes it a more protective oxide scale than Al_2O_3 at temperatures above ~1080 °C (see **Figure 1**). However, this rate can increase by a factor of 2–8 in the presence of water vapor or certain impurities such as Na or Al.[140,141] More than 15 different crystalline forms of SiO_2 have been reported.[142] Silica also exists in amorphous form (quartz glass). In both crystalline and vitreous (fused) quartz, tracer studies have shown that the diffusivity of oxygen is much faster than that of silicon.[143] The diffusion rate of oxygen in fused quartz, is around 10^{-13} cm^2 s^{-1} at 1200 °C, and about 1.5 orders of magnitude lower at 1000 °C.[144,145] Formation of volatile SiO, however, should limit the application of SiO_2-forming alloys in environments of low oxygen activity.[146]

1.10.4.1 Si-Containing Alloys

Silicon additions to Fe, Co, and Ni-based alloys have strong adverse effects on their mechanical properties; therefore, like Al, only small amounts can be added. Similar to aluminum, the presence of a third element in the alloy, such as Cr, can greatly enhance SiO_2 formation, where a SiO_2 healing layer is often found beneath either a Cr_2O_3 healing layer or an external Cr_2O_3 scale. (An example of a partial SiO_2 healing layer beneath an external Cr_2O_3 can be seen in **Figure 10**.) According to Stott *et al.*,[147] healing layers of SiO_2 are harder to establish than Al_2O_3 because the Gibbs free energy of formation (ΔG) for SiO_2 and Cr_2O_3 are closer than that between Al_2O_3 and Cr_2O_3 (−125, −162, and −202 kcal mol^{-1} O_2 at 1000 °C, respectively, for SiO_2, Cr_2O_3, and Al_2O_3). The smaller differences in ΔG_{SiO_2} and $\Delta G_{Cr_2O_3}$ give rise to a lower driving force for SiO_2 nucleation at, or near, the scale–alloy interface, resulting in a lower density of internal oxide precipitates, hence making the formation of a healing layer more difficult.

Experimentally, it has been suggested that SiO_2 forms as a complete layer beneath a Cr_2O_3 scale when a 20Cr–25Ni–Nb stainless steel containing 0.45–0.75 wt% Si was oxidized at 750–900 °C.[148] However, there was no strong evidence indicating that this layer was not partial, but complete at the interface. Later work on the same 20Cr–25Ni–Nb alloy oxidized at 825 °C in CO_2, has shown by TEM that the silica layer at the interface was amorphous.[149] The addition of various amounts of Si to a similar steel, 20Cr–25Ni–TiN, oxidized at 850 °C in CO_2-based gas containing 2% CO showed a minimum parabolic rate at ~0.9 wt% Si, and X-ray mapping of polished scale cross-sections showed the presence of a silica interlayer between the external Cr_2O_3 and the alloy.[150] However,

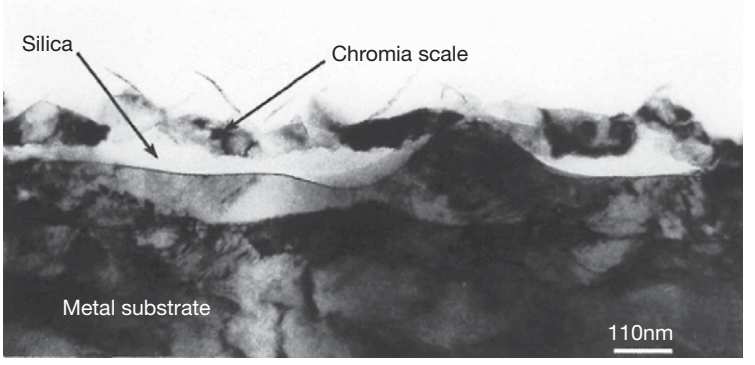

Figure 10 Cross-sectional transmission electron micrograph showing SiO_2 healing layer beneath an external Cr_2O_3 scale formed on commercial Ni–20 wt% Cr alloy containing 1.3 wt% Si, oxidized in air for 2 min at 950 °C. Reproduced from Ahmad, B.; Fox, P. *Oxid. Met.* **1999**, *52*, 113.

the decrease in alloy oxidation rate was no more than 2.5 times, and this rate was considered to be controlled by Cr diffusion through the SiO_2 layer. For example, Cr_2O_3 internal oxides were often found beneath the silica interlayer, suggesting that the layer did not form continuously over the entire alloy surface. Similar base metal cation transport through SiO_2 layers was also proposed for Fe–14 and –20 wt% Si alloys,[151] where Fe seemed to diffuse through an apparently complete SiO_2 layer to form Fe_2O_3, resulting in a linear oxidation rate.

Whether the SiO_2 layer, formed at the oxide–alloy interface, is continuous or intermittent is often considered to depend on the Si concentration in the alloy, as well as the oxidation time and temperature. For example, Douglass and Armijo[152] reported that an almost continuous SiO_2 layer formed after oxidizing Ni–20Cr–1Si (wt%) at 1200 °C for 2 weeks, while Saito and Maruyama[153] observed a continuous SiO_2 layer on a similar Ni–20Cr–1Si alloy oxidized for 50 h at 1250 °C. However, the method of detection can affect these results. While most works rely on microprobe or EDS/SEM analyses, where relatively thick (close to a micron) layers are observed, much thinner films can be detected by STEM. An amorphous silica healing layer, a few nanometers thick, has been found on a Ni–20Cr–1Si (wt%) alloy after only 5 min oxidation at 950 °C in air.[154] Upon oxidation, the initial scale consisted almost exclusively of Cr_2O_3. Thin, partial layers of silica were detected at the metal–oxide interface (**Figure 10**) after 2 min at 950 °C, and they thickened locally with oxidation times. After >25 min, these regions spread along the metal–oxide interface until an almost continuous silica layer had formed.

Healing layers of silica have also been reported in Ni–Si alloys.[155] The addition of 1 wt% Si had little effect on the oxidation rate of nickel at 1000 °C, but was sufficient to establish a partial-healing layer of amorphous SiO_2. The layer was incorporated into the inner part of the duplex NiO scale but did not react with the oxide. Increasing the silicon concentration to 4 or 7% facilitated the development of apparently continuous amorphous SiO_2 layers at the base of the scale, resulting in decreased rates of oxidation. However, these layers were unable to prevent the continued transport of Ni^{2+} ions into the NiO scale and oxygen into the alloy. Furthermore, the SiO_2 layers provided planes of weakness that resulted in considerable damage under thermal stresses during cooling, causing severe scale spalling, where failure occurred within the SiO_2 layer.

The structure of the SiO_2 that formed during high temperature oxidation seemed to be amorphous at or below 1000 °C,[149,154] but a crystalline form of either cristobalite or tridimite developed at ~1100 °C, depending on alloy composition and oxidation time.[156] In general, the amorphous phase is favored at low temperatures and is the first formed phase, while crystalline forms are favored at high temperatures or after longer time periods. Transformation from amorphous to the cristobalite phase involves a substantial volume change, which generates higher stresses within the silica layer that may contribute to the often observed preferential spalling.[157]

In summary, even though SiO_2 can provide effective protection against high temperature oxidation, Si added to Fe-, Co-, or Ni-based alloys is not able to develop into protective SiO_2 scales in the same way that Cr and Al can in forming Cr_2O_3 and Al_2O_3. In most cases, the SiO_2 may not be a complete layer that acts as a diffusion barrier. Even if it were, base metal cations and oxygen seem to diffuse rather rapidly through it, which may involve transport through short-circuit paths, such as cracks and pores.[158] Furthermore, the presence of a SiO_2 layer, whether partial or complete, often has a detrimental effect on oxide scale adhesion, where preferential cracking and spalling take place within this layer.

1.10.4.2 Silicides

Because of their high melting points and low densities, silicides have long been considered for high temperature applications, but their poor ductility is a major drawback, which has hampered their development as high temperature structural components.[159,160] When a protective SiO_2 scale can form, the silicides should also possess adequate oxidation resistance. From thermodynamic considerations, most Si-rich M_xSi_y silicides, where M = Ti, V, Nb, Ta, Cr, Mo, W, Mn, Tc, Re, Fe, Ru, Os, Co, Rh, Ir, Ni, Pd, or Pt, are predicted to be capable of forming protective SiO_2 layers at temperatures greater than 900 °C.[161] However, like the Si-containing alloy discussed above, kinetic considerations ultimately determine whether or not a protective SiO_2 scale will develop. Higher temperatures and longer oxidation times usually favor the formation of a complete surface SiO_2 layer; for example, SiO_2 was found to cover the entire $MoSi_2$ surface at temperatures greater than 1000 °C, but at lower temperatures, portions of the surface were covered by MoO_3.[162]

The high temperature oxidation and corrosion of some silicides, namely $MoSi_2$, Mo_5Si_3, $TiSi_2$, Ti_5Si_3, V_5Si_3, Cr_3Si, and Fe and Ni silicides have recently

been summarized by Brady *et al.*[163]; emphasis was placed on Mo and Ti silicides, because their oxidation behaviors have been most extensively studied. Readers interested in the details of silicide oxidation should refer to this publication. Only brief summaries are given here.

During the initial stages of silicide oxidation, oxides of the metal and silica usually form simultaneously. For example, $TaSi_2$ or $NbSi_2$, upon oxidation, form mixed oxides of both silica and Ta_2O_5 or Nb_2O_5.[164,165] Diffusion across the surface scale at this point is therefore not dictated by the transport through SiO_2, but through the mixed MeO_x–SiO_2 layer. Although the Nb and Ta silicides could eventually be protected by a thick mixed-oxide layer, spallation problems due to growth stresses become critical as scale thickness increases, and the oxide scales on $TaSi_2$ and $NbSi_2$ can crack extensively.[164,165] In some systems, the mixed oxide layer can be rather protective. Several studies[166,167] have suggested that the oxidation kinetics of $TiSi_2$ are parabolic, due to the formation of a protective scale that consists of a silica layer near the silicide–scale interface and islands of TiO_2 at the scale–gas interface. Ti, which is soluble in SiO_2 up to ~10 at.%,[168] apparently diffuses to the outer surface, forming islands of TiO_2 and leaving a protective silica–titania glass on the inside. In other systems, the metal oxide that coexists and continues to grow with the SiO_2 may eventually disrupt the protectiveness of the silica.[169–171]

Many of the metal oxides can be volatile under some oxidation conditions, which complicates the scale development process. Equilibrium vapor pressures of some refractory metal oxides, together with SiO_2, are presented in **Figure 8**. Mo and W oxides, for example, are highly volatile. As these oxides, initially formed with silica on $MoSi_2$ or WSi_2, volatilize, the scale layer becomes more silica-rich and oxygen transport to the silicide–scale interface decreases. This decrease in oxygen transport and the associated decrease in the oxygen activity at the silicide–scale interface continue as the metal oxides continue to volatilize. Eventually, the oxygen activity at the interface decreases to a value where the base metal oxide is unstable, then the Mo or W silicide is protected by a relatively pure SiO_2 layer.[172, 173] This process is favored as the oxidation temperature is raised. At temperatures >1200 °C, volatilization is rapid, and the silica layer can be purified within the first hour of oxidation.[174]

Pesting is often a problem with molybdenum silicides, where extensive oxidation disintegrates the silicide to powder or fragments. For $MoSi_2$, this occurs in the temperature range ~300–550 °C.[163] The rapid disintegration is usually preceded by an incubation period,[175] the duration of which is affected by microstructure, applied stress, temperature, and oxygen partial pressure. The susceptibility to pesting seems to depend on the material microstructure and stoichiometry. When the $MoSi_2$ is dense with small amounts of connected porosity, and is free of cracks, pesting does not occur.[176–179] An example of the pesting behavior and its sensitivity to specimen porosity is seen in **Figure 11**, from Kurokawa *et al.*,[179] where noticeable pesting of the porous sample took place shortly after 56 h at 500 °C, leading to total disintegration of the sample after 100 h, but weight gain of the dense sample was less than $2 \times 10^{-3}\,g\,cm^{-2}$ up to the end of the test, at ~111 h. The oxides that formed in various stages of disintegrated $MoSi_2$ are MoO_3 and amorphous SiO_2.[177,180,181] Pest disintegration appears to be caused by the formation of voluminous Mo oxides in extended defects. This introduces stresses that provide the driving force for fast crack propagation and fragmentation of the relatively brittle solid. It appears that susceptibility to pesting increases with Mo concentration for Mo:Si ratios >0.5 and decreases when $MoSi_2$ is Si-rich (68–70 at.%).[181]

Mo–Si–B alloys, with melting points above 2000 °C, are being considered for high temperature applications, such as turbine blade materials.[182]

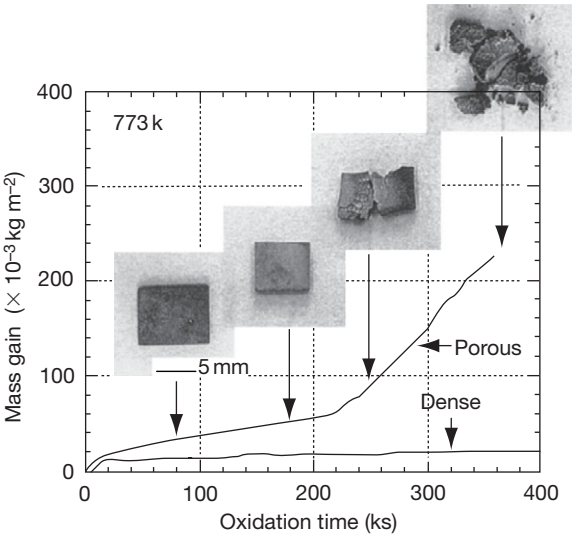

Figure 11 Oxidation kinetics of dense and porous $MoSi_2$ at 500 °C in air, and the appearance of the porous sample at four different times. Reproduced from Kurokawa, K.; Houzumi, H.; Saeki, I.; Takahashi, H. *Mater. Sci. Eng. A* **1999**, *261*, 292–299.

Several compositions of this alloy are able to develop a protective surface borosilicate glass that offers good oxidation resistance at high temperatures. The development of this glass layer is similar in principle to the oxidation of $MoSi_2$. Above 800 °C, the first formed oxides are rich in MoO_3, which volatilizes, while the silicon and boron oxides slowly form a complete layer of borosilicate. Once this silicate layer is established, the rate of alloy recession is decreased. However, development of the protective silicate layer is very sensitive to the oxidation temperature, alloy composition, particularly the B to Si ratio, and other factors.[183] Increasing the B/Si ratio decreases the viscosity of the glass and allows it to cover the surface of the sample faster, but this also increases the oxygen diffusivity through the glass and lowers the high temperature oxidation performance. Furthermore, at low temperatures, ~650–750 °C, the formation of a protective borosilicate layer is slow compared to the loss of Mo by the formation and volatilization of MoO_3, and this leads to pesting of the material.[184,185] Current efforts in improving the oxidation resistance of these alloys involve the development of coatings.[186]

1.10.5 Oxidation of Chromia-Forming Alloys

Chromium oxidizes at high temperatures to form one oxide, the corundum Cr_2O_3, which consists of hexagonally close-packed oxygen ions with Cr cations occupying two-thirds of the octahedral sites. The structure is the same as α-Al_2O_3 and α-Fe_2O_3. Cr_2O_3 reacts with oxygen to form volatile CrO_3 according to the equation $0.5Cr_2O_3 + 0.75O_2 = CrO_3$, at temperatures above 850–900 °C; the reaction rate increases with increasing partial pressure of oxygen in the atmosphere and with increasing gas flow rates[187]; it becomes rather pronounced at temperatures above 1000 °C,[188] thus limiting the use of Cr_2O_3 forming alloys to temperatures less than 900 °C. In the presence of moisture, Cr_2O_3 reacts with water vapor to form a number of volatile chromium hydroxides.[189] The reaction rates depend on temperature, total pressure, partial pressure of water and the reaction gas flow rate. These volatilization reactions have been shown to cause severe problems in solid oxide fuel cell environments, where Cr_2O_3 forming alloys are being considered as a low-cost interconnect material.[190–193] The most common and extensively used Cr_2O_3-forming alloys are stainless steels. Ferritic steels have the base composition of Fe–Cr with 13–18 wt% Cr to ensure the formation of a slow growing scale of Cr_2O_3, or mixed Fe–Cr spinel and Cr_2O_3, for corrosion protection. Common austenitic steels contain higher concentrations of Cr (18–30 wt%) and an austenite stabilizer, such as Ni or Mn. The present chapter describes the development, growth and adhesion of Cr_2O_3 scales observed for Cr and model Cr_2O_3-forming alloys.

1.10.5.1 Transport Properties and Oxidation Rates

Cr_2O_3 is an electronic semiconductor.[4] It changes from a p-type to an n-type semiconductor from near-atmospheric oxygen pressures to oxygen activities close to the Cr/Cr_2O_3 interface. There are evidences[4] showing that Cr self-diffusion (mainly lattice diffusion) depends on oxygen activity, and it can vary by 3–4 orders of magnitude under a given temperature. The dominant defect structures may be Cr vacancies or interstitials respectively, at high and low oxygen activities.[194] Earlier diffusion studies by Hagel and Seybolt[195] on sintered polycrystalline Cr_2O_3 showed a three orders of magnitude higher Cr diffusivity over that of oxygen. Compared with Cr diffusion rates found in single crystal Cr_2O_3,[196] which is nearly five orders of magnitude lower than the rates reported by Hagel and Seybolt, the earlier rates should be dominated by short circuit diffusion, mainly via oxide grain boundaries.[74] Consequently, growth of Cr_2O_3 scales has often been considered to be dominated by cation outward transport, mainly through Cr_2O_3 grain boundaries.[197] Location of inert markers subsequent to oxidation of essentially Cr_2O_3-forming alloys seems to support this conclusion,[198] where markers that had been deposited on specimen surfaces prior to oxidation resulted near the scale–metal interface after oxidation, suggesting an outward growth mechanism.

More recent diffusion studies,[199] utilizing oxygen and chromium isotopes, ^{18}O and ^{54}Cr respectively, showed that the rates of O and Cr bulk diffusion are similar, but Cr grain boundary diffusion is greater than that of oxygen. The parabolic oxidation rate constants calculated from these diffusion data agreed with experimentally determined values, but suggested that Cr_2O_3 scale growth is in fact controlled by counter diffusions of oxygen and chromium along oxide grain boundaries. Moreover, SIMS studies[200] on different areas of Cr_2O_3 showed different transport properties on the same sample of Cr after it was

oxidized in natural oxygen (^{16}O) and then, without cooling to room temperature, in oxygen enriched in ^{18}O. Results showed that, in some places, the oxide grew primarily by chromium transport while, in others, it grew primarily by oxygen transport and, in still others, it grew by a mixture of both. It was postulated that these apparent different transport processes were related to different degrees of high *versus* low angle oxide grain boundaries, presuming that the two have different transport properties, whether intrinsic or due to different degrees of impurity segregation.

Above 700 °C in air or atmospheric oxygen, the kinetics of Cr_2O_3 growth are generally interpreted as parabolic, although periodic increases in the reaction rates have been observed in some cases[201]; these will be treated later under breakaway oxidation. The parabolic oxidation rates on Cr metal prior to 1980 had been compiled by Hindam and Whittle,[202] with data scattered between the two solid lines in **Figure 12**; all of the experiments included here were conducted in oxygen. Reported rates from more recent studies also fall within this wide band of scattered data. It is rather astonishing that such a large range of rates, over three orders of magnitude, can exist for a simple metal. The most likely explanation for these differences may be the relative adhesion of the Cr_2O_3 scale, resulting in different degrees of scale buckling and convolution during oxidation, or even local breakaway resulting in small nodule formation (see **Figure 13** for typical microstructures). Buckling, driven by the compressive growth stress in the oxide film,[203] often occurs; an example is given in **Figure 14**. These buckles increase the amount of oxide per unit area of metal, hence giving rise to an apparent increase in oxidation rate. Continued scale growth beneath a buckle is achieved by Cr vapor transport,[204] which can be faster than solid state diffusion through the scale. Several other factors may also contribute to the scatter. Formation of volatile oxide species, especially at higher temperatures, can be a problem. Although most studies corrected for the sample weight loss due to CrO_3 formation, the possible effect of water vapor and the formation of other volatile species were not considered. Metal purity can also be a contributor to rate variations. Dissolution of metallic impurities in Cr_2O_3 can exert a doping effect, that is, changing its defect concentration and, hence, its oxidation kinetics. Nonmetallic impurities, such as S and C, have also been suggested to affect the transport rate through Cr_2O_3.[205,206] However, it is also possible that these impurities caused a decrease in scale adhesion, consequently, leading to increases in the rate by forming more convoluted or buckled oxides. Different surface treatments, such as electropolishing, etching or mechanical abrasion, have also been shown to have profound effects on subsequent oxidation rates,[207] mainly due to the development of very different oxide grain sizes on these surfaces.[208] Likewise, sample pretreatment, such as annealing, cold working, rolling, etc., or the rate at which specimens are heated to the oxidation temperature can all have an effect, since they can influence the development and

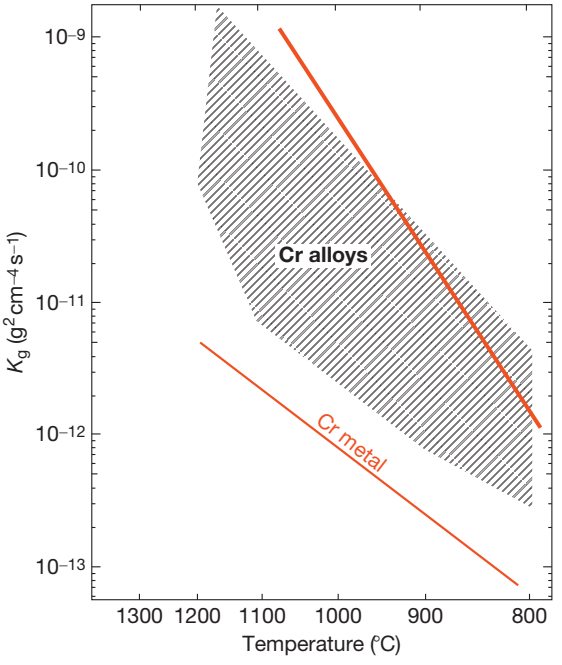

Figure 12 Range of parabolic rate constants from the oxidation of pure Cr (bonded between the solid lines) and binary Co, Ni and Fe–Cr alloys (the shaded area), complied by Hindam and Whittle.[202]

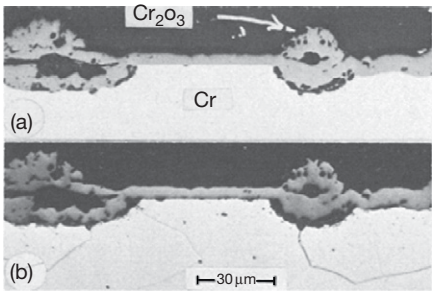

Figure 13 Optical micrograph of polished cross-section of etched Cr oxidized for 42 h at 1200 °C, giving examples of localized oxide nodule, or ridge, formation on pure Cr. Reproduced from Caplan, D.; Sproule, G. I. *Oxid. Met.* **1975**, *9*, 459–472.

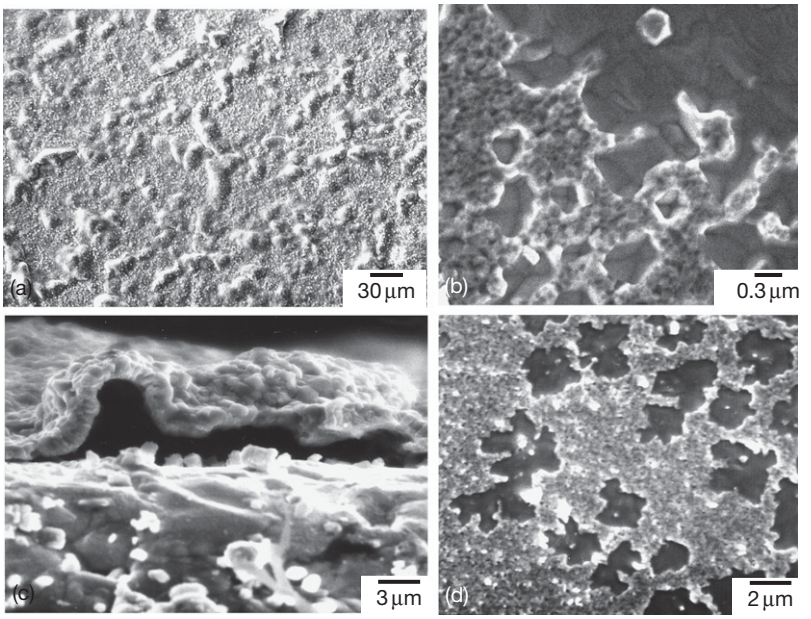

Figure 14 Examples of buckled Cr_2O_3 scale formed on commercial grade 99.8% Cr at 1000 °C. (a) Scale surface and (c) cross-section after oxidation for 30 min. (b) and (d) are metal surfaces after scale removal and oxidation for 5 and 10 min, respectively.

grain size of the first formed Cr_2O_3. Although it appears that the grain size and microstructure of the Cr_2O_3 scale dictates its growth rates, no clear correlations can be identified between the rate and the various factors mentioned above.

The oxidation rates of Cr_2O_3 forming alloys of Ni, Co, or Fe–Cr have also been complied by Hindam and Whittle,[202] and those data are also plotted, as a shaded band, in **Figure 12**. It is seen that, even with different base metals, less scattering occurs during alloy oxidation. This is probably related to better Cr_2O_3 adhesion on alloys than on Cr. It is also possible that base metals incorporated into these Cr_2O_3 scales dominate other impurities that might influence the oxidation rate. Both Ni and Co have small, but significant solubility in Cr_2O_3, while Fe_2O_3 and Cr_2O_3 are completely isomorphous.

1.10.5.2 Cr_2O_3 Layer Development on Alloys

When a Cr-containing alloy is oxidized, its oxidation rate usually changes with its Cr concentration, as illustrated in **Figure 15** for binary Co–Cr alloys.[209] The rate increases with the first few percent of Cr addition, due to duplex scale formation and the increased oxidation rate from oxygen inward transport, as described for Ni and Co alloys in **Section 1.10.2**. Afterwards, the rate constant is rather unaffected by additional Cr until a critical Cr concentration is reached. This is the concentration necessary to form a complete Cr_2O_3 layer, whether as an external surface layer or a healing layer beneath some base metal oxides. Once the Cr_2O_3 layer is formed, the oxidation rate

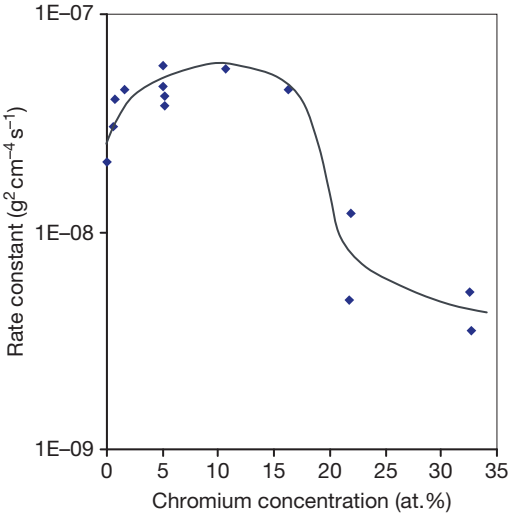

Figure 15 The change of oxidation rate, at 1000 °C 760 torr oxygen, of Co–Cr as a function of alloy Cr concentration. Data from Wright and Wood[209] include parabolic rate constants from initial and steady states.

becomes dominated by its subsequent growth. Ni–Cr and Fe–Cr alloys behave similarly.[210]

The minimum Cr concentration necessary for the establishment of a continuous Cr_2O_3 layer is usually around 13–25 wt% in oxygen at atmospheric pressure. However, this selective oxidation process depends heavily not only on partial pressures of oxygen, but also on oxidation temperature; sample surface treatments and substrate grain size are also influencing factors. Consequently, alloys with compositions around the narrow transition range can develop nonprotective or protective scales with minor changes in operating conditions. For example, a Ni–14.6 wt% Cr[211] can either form a protective Cr_2O_3 scale or a Ni-rich oxide, depending on how it was heated to the oxidation temperature. The former protective scale developed when heating was done in vacuum ($\sim 10^{-5}$ torr), but the latter behavior was found when the sample was heated in air, attesting to the pO_2 dependence of the selective oxidation process. Fine-grained[212] or cold-worked alloys[213] can also assist the establishment and maintenance of the Cr_2O_3 layer, often at Cr concentrations lower than otherwise predicted. This is because alloy grain boundaries are faster diffusion paths, so the healing Cr_2O_3 layer is preferentially established at the intersections of these grain boundaries with the surface. The effect has been clearly demonstrated on a Ni–Cr alloy.[214] For Fe–Cr alloys with comparable compositions to Ni–Cr, Cr_2O_3 is more readily established initially because of the greater alloy interdiffusion coefficient in the bcc Fe–Cr structure compared with that in the fcc Ni–Cr structure, and the lower oxygen solubility and diffusivity in Fe–Cr. Consequently, less Fe than Ni oxides are present above the Cr_2O_3 layer formed on Fe–Cr and Ni–Cr respectively. Detailed discussions of the selective oxidation process and factors affecting it can be found elsewhere in this volume.

1.10.5.3 Scale Morphology and Breakaway Oxidation

The first-formed, thin Cr_2O_3 scales are uniform and adherent. However, under these apparently adherent scales are often debonded areas or facetted interfacial voids (**Figure 14(b)**), which can be seen after the scale has been spalled away from the force of a scratch. The debonded areas had a smooth, often thermally etched appearance, where the scale and substrate were not in intimate contact at the reaction temperature, and their fraction increased with oxidation time (**Figure 14(d)**). Elsewhere, the metal surface exhibits oxide grain 'imprints,' where the scale had maintained contact with the alloy. It is evident that the fraction of these debonded areas can be significant, and the extent of scale detachment is found to be strongly related to alloy purity.[215]

With longer oxidation times, Cr_2O_3 scales formed on Cr can be heavily buckled (or convoluted) or show localized nodule formation (**Figures 13, 14(a), and 14(c)**). Development of the nodules seen in **Figure 13** has been shown to be related to oxide grain size. When the Cr surface was etched prior to oxidation, large grained Cr_2O_3 developed on some metal orientations, while finer grained oxide formed on other orientations and on alloy grain boundaries.[208] The fine grained oxide grew considerably faster, and apparently inward and outward from the original alloy surface, and is most likely due to faster transport rates via oxide grain boundaries. Both kinds of oxide, thin film or nodule, remained in good contact with the metal. However, such good contacts are not often observed. Typically, scale buckling occurs, as seen in **Figure 14** in plan view and in cross-section. The buckles appeared to have formed preferentially along alloy grain boundaries, similar to those observed by Howes,[216] who in a later paper[217] investigated buckling above alloy grain boundaries under a scanning electron microscope. It was suggested that the preferential separation was due to faster Cr boundary diffusion from the alloy, hence higher cation vacancy flux, but not all grain boundaries developed buckles, so the exact reason why scales are buckled on some locations but not on others is not clear. Depending on the sample surface treatment, oxidation conditions and probably other factors, such as metal purity, the extent of buckling can be rather severe, resulting in very convoluted oxides. Cracking of these extremely convoluted, or buckled oxides can occur at the oxidation temperature and allow oxygen access to the bare metal surface underneath; repeated cracking and healing at temperature eventually leads to the formation of a multilayered oxide, as shown in **Figure 16**. In the case of chromium-containing alloys, this process is unlikely, except for high Cr contents,[218,219] because selective oxidation of Cr to form Cr_2O_3 leads to an appreciable Cr depletion in the alloy beneath the scale–alloy interface. When the protective Cr_2O_3 is damaged, base metal oxides may develop, resulting in the formation of large nodules that are usually double layered, with an outer layer of almost purely base metal oxide, and an inner layer of mixed base metal and Cr oxides. Depending on the growth rate of the base

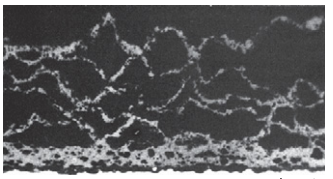

Figure 16 Optical micrograph showing layers of Cr_2O_3 scales formed on Cr metal after oxidation at 1090 °C for 21 h. Reproduced from Caplan, D.; Sproule, G. I. *Oxid. Met.* **1975**, *9*, 459–472.

metal oxide and the diffusion rate of Cr in the alloy, a healing layer of Cr_2O_3 may again form at the base of the nodule and thus stop its growth. Otherwise, the fast growing nodule continues to grow vertically and laterally, and eventually destroys the protective Cr_2O_3 scale.

Associated with the failure of the protective Cr_2O_3 layer to allow fast base metal oxide growth are accelerated oxidation kinetics that can be observed as a fast increase in specimen weight gain, and called 'breakaway oxidation.' When the Cr_2O_3 forms again as a healing layer, the oxidation rate can revert to that dominated by Cr_2O_3 scale growth. In cases where breakaway and healing happen continuously at different locations, the weight gain may still show an apparent parabolic behavior, but with a much faster rate than that found for Cr_2O_3 only. Breakaway oxidation usually occurs more easily on Fe–Cr than Ni–Cr or Co–Cr alloys,[220] due to a poorer scale adhesion on Fe–Cr alloys, for reasons that are not clear. When breakaway does happen for Ni–Cr alloys,[211] the situation is worse, because chromium depletion at the alloy–oxide interface is greater and longer lasting than for Fe–Cr alloys.

The driving force for buckling has to be the compressive stress that develops in the Cr_2O_3 film.[203] Although earlier works have concluded that oxidation stresses are negligible compared with thermal stresses,[221,222] direct measurements of stresses in Cr_2O_3 at oxidation temperatures have been achieved more recently. Using *in situ* Raman spectroscopy, Kitamura *et al.*[223] determined that the growth stress in Cr_2O_3 formed at 900 °C in air is highly compressive, with a maximum level of 700 ± 100 MPa. Although still a fraction of the thermal stress, measured to be about 3500 MPa, the magnitude is higher than that observed on any Al_2O_3 forming alloys, recently performed with *in situ* synchrotron X-ray techniques.[224,225] A study by Zhu *et al.*[226] using hot stage X-ray diffraction, also reported compressive stresses in Cr_2O_3, although the level was not as high as that found by Kitamura *et al.*[223] Counter diffusion of oxygen and chromium and internal oxide growth resulting from these fluxes has been suggested[47] to be the cause of such stresses.

More severe Cr_2O_3 buckling and convolution have been observed on Cr oxidized at low pO_2 values.[194] The scales were heavily wrinkled or even totally detached from the metal except at specimen corners. It was suggested that the difference in behavior in lower pO_2 is due to a higher oxide plasticity at low oxygen pressures. The greater plasticity would indeed allow the scale to deform without cracking, but there still appears to exist a higher driving force that causes the greater deformation. It is possible that higher growth stresses were generated at lower pO_2. If the stress generation mechanism was that of internal growth, as proposed by Rhines and Wolf,[47] it is possible that the relative diffusion rates of Cr and O may differ under different pO_2 values.

1.10.6 Oxidation of Alumina-Forming Alloys

At temperatures above 900 °C, alloys or coatings that develop Al_2O_3 scales are most commonly employed for practical applications, due to the relative ease with which alumina can develop into a complete layer and the slow growth rate and long-term chemical stability of Al_2O_3. There are mainly two types of commercial Al_2O_3-forming alloys: the aluminides, such as FeAl and NiAl, and the MCrAl type alloy that is often the base of superalloys, where 'M' represents the base metal and can be a mixture of Fe, Ni, and Co. For the aluminides, at least ~19 at.% Al is needed to achieve the selective oxidation of Al to develop a protective Al_2O_3 scale and suppress the oxidation and growth of iron oxides[227,228]; ~22 at.% Al is needed for Ni–Al, where a thin layer of Ni-containing oxide, NiO and/or $NiAl_2O_4$, is present at the scale outer surface and the Al_2O_3 forms at the scale–alloy interface as a healing layer. In accordance with the theory on selective oxidation, these critical Al compositions can vary depending on oxidation temperature and environment, and also on alloying additions. The addition of about 18–20 at.% Cr in MCrAl type alloys decreases the amount of Al necessary to establish the protective Al_2O_3 layer to no more than 10 at.%. Iron aluminides have limited industrial usage, due to their low high temperature strengths.[163] Platinum is often added to nickel

aluminides[229] to enhance the oxidation resistance, mainly by increasing the Al_2O_3 scale adhesion. Small amounts of Ti, Zr, Hf, Y, or a combination of these are added to MCrAl type alloys also to enhance Al_2O_3 adhesion; these are the so-called 'REs,' which have higher oxygen affinities than Al, and their effects on the oxidation behavior of Al_2O_3-forming alloys will be presented in **Section 1.10.7.1**.

1.10.6.1 Scale Development

Only Al_2O_3 is formed on β-NiAl[230–232] and β-FeAl[233] at elevated temperatures (>800 °C). On γ′-Ni_3Al, an external layer of Ni-rich oxide, either NiO and/or $NiAl_2O_4$, is always present, beneath which is the Al_2O_3 layer.[234–236] Unlike Ni_3Al, Fe_3Al alloys do not seem to develop a noticeable Fe-rich surface layer.[237,238] When such alloys are heated slowly to 1100 °C in air,[239] the first detected oxide, using Raman spectroscopy, was Fe_2O_3, whose intensity increased from 500 to 700 °C, then dropped to zero with continued oxidation at higher temperatures. Above 900 °C, the scale consisted of only Al_2O_3 and Fe_2O_3 was no longer detected. This difference between the Fe-based and the Ni-based alloys is believed to be associated with faster diffusion rates of Al relative to Fe in Fe_3Al than of Al compared to Ni in Ni_3Al.[238]

On MCrAl type alloys, the addition of Cr promotes Al_2O_3 formation, by the well-known third element effect,[240] where the alloy is suggested to initially develop Cr_2O_3, causing a decrease in the partial pressure of oxygen at the scale–alloy interface to facilitate the Al_2O_3 formation. Therefore, steady-state scales that form on these alloys are always almost pure Al_2O_3. However, the initial scale still has appreciable amounts of the base metals, because all metals and alloys exposed in the ambient atmosphere contain a thin layer of native oxide that is a few nanometers thick. An example is given in **Figure 17(a)** for FeCrAl where the surface oxide consists of an outer layer rich in Fe and an inner layer slightly enriched with Cr. When the alloy is heated to elevated temperatures in air or oxygen, this native oxide quickly thickens and aluminum starts to enrich at the scale–alloy interface (**Figure 17(b)**). Further oxidation results in a fully established aluminum oxide layer at the scale–alloy interface (**Figure 17(c)**). Subsequent scale growth only involves thickening of this alumina layer, where all the initially formed Fe and Cr oxides become incorporated into the Al_2O_3 layer. Integrating the depth profile curves in **Figure 17** over distance shows that the initial stage oxide clearly contains high levels of base metals, in this case Fe and Cr, whose concentrations decrease as the scale develops into a complete layer of the thermodynamically most stable oxide, in this case Al_2O_3.[241] This process of initial stage base metal oxidation and the subsequent incorporation of their oxides into the final scale are expected for all alloys.[242] The amount that is incorporated depends

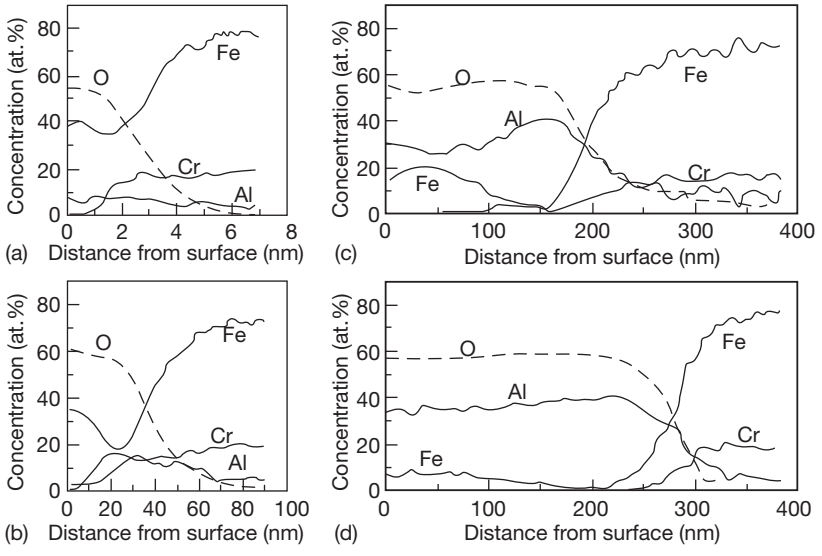

Figure 17 Auger depth profiles through the surface oxide on a FeCrAl alloy (a) the native oxide prior to oxidation, (b)–(d) oxides formed after the alloy was introduced into a 1000 °C furnace and oxidized in air for 1, 3, and 11 min, respectively. Reproduced from Hou, P. Y. *J. Am. Ceram. Soc.* **2003**, *86*, 660–668.

strongly on the alloy composition, the oxidation temperature and the partial pressure of oxygen in the environment, or sometimes even on the alloy surface finish.[243] The behavior of FeCrAl similar to that reported here has been shown using other surface techniques[244,245]; NiCrAl[246] also forms transient Ni and Cr oxides. The effect of these base metals in Al_2O_3 on its transport, and hence growth properties, are addressed later in this section.

When Al_2O_3 is first developed, regardless of the alloy system, it is never the thermodynamically most stable α form, especially upon heating, but consists of alumina that have often been identified as the cubic θ[230,231] or γ[232,235,247–250] phase, or a mixture of the two.[230,252] The more stable hexagonal α-Al_2O_3 phase later nucleates at the transition alumina–alloy interface,[249–251] while the initially formed transition alumina transforms to the α form with time. The development of α-Al_2O_3 is faster at higher temperatures[252] and with the presence of Cr[253] and/or Fe[238,239] in the alloy, but seems slower with higher concentrations of Al or the presence of a RE, such as Hf, Y or Zr.[254]

The first-formed alumina are often referred to as 'transition' or 'metastable' alumina. At present, there are no clear indications as to why a certain form of transition alumina is formed; either θ or γ has been found without any systematic differences in alloy type, oxidation temperature, detection methods or oxidation environment, for example, the presence of moisture. Even the δ[230] and κ phases have been reported in some cases. Since there are many polymorphs of alumina, and many routes by which one phase can transform to the other,[255] it is possible that many different types of alumina can be present during the initial stage of oxidation.[256] TEM studies[230,232,235,236] often showed that the transition alumina formed epitaxially, having a cube-on-cube orientation relationship with the alloy, while the degree of preferred orientation decreased with oxidation time. Limited high-resolution TEM studies[257] indicated that the interface between the transition alumina and the alloy, in this case a single crystal NiAl, was coherent, but became incoherent once α-Al_2O_3 nucleated. The morphology of the transition aluminas is often described as platelet or needle-like. TEM analyses[258,259] have identified the plane of the platelets to be (110), whether they are θ or γ-Al_2O_3; and the platelets are often heavily twinned along the [111] direction.[259] This structure is probably related to the high compressive growth stresses present in the initially formed transition alumina layer,[260] whereas twinning and needle-like growth are means to relieve the growth stress. Surface smoothing of the platelets occurs with time as a spheroidization phenomenon driven by a decrease in surface energy.[258]

When α-Al_2O_3 is nucleated at the transition alumina–alloy interface, its orientation is random, and it forms an incoherent interface with the alloy.[232] On FeCrAl type alloys, these nuclei are finer grained[250,261] than those on NiAl[260,262] or NiPtAl,[263] where they tend to form large circular plates that extend faster laterally than vertically[260,262,264]; an example of these circular plates found on Ni–55 at.% Al is shown in **Figure 18(a)**. The number density of these circular plates depends on the alloy grain orientation[260] and increases on rougher surfaces.[263] The first formed α-Al_2O_3 is always under tension,[224,225,260] which can be as high as 400–600 MPa. Since there is ~5% volume shrinkage associated with the θ-to-α transformation, this result indicates that most of this alpha phase is developed by oxide phase transformation, rather than from oxidation, that is, growth of a new oxide grain at the interface. The high tensile stress, which exceeds the

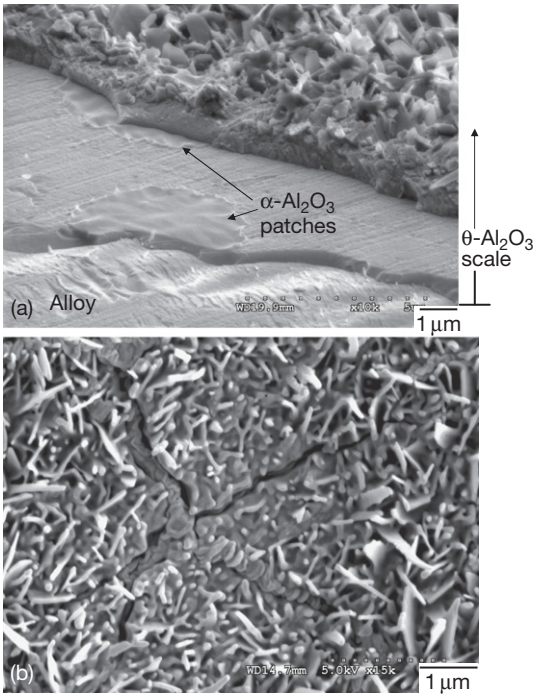

Figure 18 Examples of alumina scale morphology resulting from the transformation of θ to α alumina during oxidation with SEM micrographs showing (a) cross-section of scale formed on Ni–55 at.% Al, 1100 °C, 40 min. (b) Surface of oxide on the same alloy after 11 h at 1100 °C. Reproduced from Hou, P. Y.; Paulikas, A. P.; Veal, B. W. *Mater. High Temp.* **2006**, *22*, 373–381.

toughness limit of α-Al_2O_3,[265] often causes cracking of the first-formed α-Al_2O_3 grains. Ridges of oxides, which are associated with α-Al_2O_3 grain boundaries, develop and fill the cracks after the transformation is completed (**Figure 18(b)**). The alpha nuclei eventually impinge and develop into a complete α-Al_2O_3 layer above the alloy, and subsequent scale growth becomes dominated by the transport of O and Al through this alpha layer, while the initially formed transition alumina transform to the α-Al_2O_3 phase with time.

When Cr and/or Fe are present in the alloy, the transformation to α-Al_2O_3 is accelerated. Since Cr_2O_3 and Fe_2O_3 have the same corundum structure as α-Al_2O_3, they have been suggested to serve as templates that facilitate the nucleation and growth of the α phase at a temperature below which this transition happens in the bulk at 1000 °C.[239,253] TEM studies have found small particles of α-Al_2O_3 present in the first-formed transition alumina layer on FeCrAl[250] and Fe_3Al[238] alloys. Although it is not clear how their formation is related to the Cr_2O_3 and/or Fe_2O_3 that were present on the alloy surface at the onset of oxidation, their presence in the initial Al_2O_3 layer must also help to facilitate the alumina transformation and the development of a complete α-Al_2O_3 layer.

1.10.6.2 Oxidation Rates

Oxidation of alumina scales usually follows parabolic kinetics, indicating diffusion-controlled growth. The growth rate of the transition alumina is about 1 order of magnitude faster than that of the α-Al_2O_3.[248] Due to the phase transformation and the different growth rates of the different aluminas, oxidation kinetics usually show two parabolic stages separated by a gradual transition.

The parabolic rate constants of many binary and ternary Al_2O_3-forming alloys, known prior to 1982, have been compiled by Hindam and Whittle.[202] Their summary included alloys that contained a RE, such as Y, Ce, or Th, and contributions from transitional alumina phases were not always eliminated. It was also noted that, in some cases, strict parabolic behavior was not observed, so the rate constants were only determined from the weight change near maximum exposure times. Despite these reservations, all the data fell in a scatter band of about 16, with scale thickness for a given time varying by a factor of 4. The scatter is much smaller than that observed for Cr_2O_3 scales (**Figure 12**), probably because transport through Al_2O_3 scales is less sensitive to impurities.

As common base metals such as Fe, Ni, Co, and Cr can be incorporated into the Al_2O_3 scale during initial stage oxidation, and some of these elements have been shown to have a profound effect on the high temperature creep properties of Al_2O_3,[266–271] hence affecting O and/or Al transport; it is worthwhile to examine whether these incorporated base metals affect oxidation rates. Before that, one needs to realize how much of these base metals are present in a growing α-Al_2O_3 scale and whether they segregate at the grain boundaries. TEM studies have found a decrease from 4 to 0.3 at.% Fe and Cr in the scale as it increases from 0.4 to 5 μm for Al_2O_3 scales grown on FeCrAl alloy at 1000–1200 °C,[272] indicating that the scale becomes purer as it thickens with oxidation time. In other words, all these impurities were incorporated during the initial stage, attesting to the protectiveness of the Al_2O_3 scale. The Fe and Cr concentrations in the Al_2O_3 appeared uniform when relatively large areas, that is, 14 μm^2, were examined, but they varied greatly from point to point under a 17 nm beam size. This kind of distribution was also found for Ni and Cr in Al_2O_3 formed on NiCrAl.[293] These local high concentrations probably resulted from small grains of base metal oxides or spinels left from the initial stage of oxidation. The lattice parameter of α-Al_2O_3 grains within the scale was enlarged with higher concentrations of Fe, Ni, and Cr,[272] suggesting that at least some of these elements are dissolved in the Al_2O_3. Point analyses made at many grain boundaries and within the grains adjacent to the boundary found 38% of the boundaries with higher concentrations of Fe, but none had higher concentrations of Cr. Since Cr_2O_3 forms a complete solid solution with Al_2O_3,[273] Cr is expected to dissolve in Al_2O_3 and not segregate on grain boundaries. Fe may have segregated, but its segregation may be charge related, hence pO_2 dependent. Recent work by Harmer *et al.*[274] using EELS shows that Fe^{2+} segregates at Fe-doped Al_2O_3 grain boundaries, but not Fe^{3+}. The behavior is consistent with the fact that Fe^{3+} has an appreciable solubility in Al_2O_3, about 3–5 at.%,[275] but the solubility is only a few parts per million for Fe^{2+}.[276]

In order to better correlate alloy composition to oxidation rates, data cited in the Hindam and Whittle paper[202] are reevaluated, and those representing steady-state growth rates from Ni-, Fe-, or Pt-based alloys that are undoped with REs are compared with more recently published results.[277–302] These rates

are plotted in Figure 19 as a function of the inverse of the oxidation temperature. All the studies included here are from laboratory tests performed on high purity binary M–Al or ternary M–Cr–Al type alloys, so M (Fe, Ni, or Pt) and Cr should be the most abundant impurities incorporated in the Al_2O_3 scale. Most tests were carried out at one atmosphere oxygen, but some in air. Different symbols in Figure 19 distinguish different types of alloys. The data showed much scatter from study to study even for alloys with the same composition. Some general trends, however, seem apparent. PtAl alloys, on average, tend to have the slowest oxidation rates, but this conclusion is not supported by all the PtAl data. The presence of Cr does not seem to make any difference to oxidation rates. The Fe-based alloys seem to oxidize with the highest rates, which would agree with the higher creep rates observed for Fe-doped Al_2O_3.[266] However, the higher oxidation rates may also be related to increases in surface area that resulted from wrinkling of the scale and the underlying alloy.[303,304] FeCrAl and Fe_3Al type alloys are especially prone to wrinkling. Such increase in surface area can be as high as 10%,[304] but none of the oxidation rates cited here had been corrected for it.

In summary, the growth rates of α-Al_2O_3 scales from 1000 to 1300 or 1400 °C on Fe-, Ni-, Co-, and Pt-based binary or ternary alloys without any RE addition can vary over two orders of magnitude, with an average activation energy of about 240 kJ mol^{-1}. Although base metal components are incorporated in the growing alumina during the initial stage of oxidation, and depending on their size and solubility in Al_2O_3, may segregate to oxide grain boundaries, their effect on oxidation rates seems small. In a way, this is surprising, because Al_2O_3 is a very stoichiometic oxide, whose transport property is dictated by impurity contents.[305] No explanations are apparent for the large variation in reported oxidation rates. Perhaps part of this scatter is indeed due to the presence of different types and/or amounts of impurities under different test conditions. To date, there is no good understanding of which impurities these may be. Tolpygo *et al.*,[306] for example, have shown that grit blasted coating surfaces develop much thicker Al_2O_3 scales (by a factor of ~3) than other surfaces, due to the incorporation of impurities, such as Li, Na, K, Ca, Mg, and/or Si, in the surface

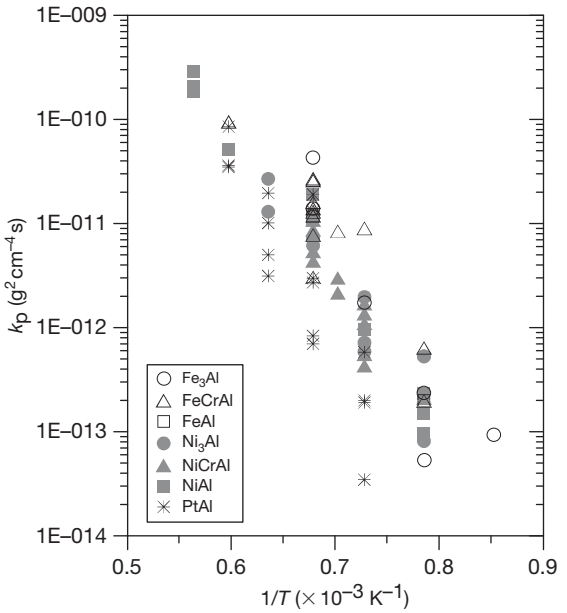

Figure 19 Parabolic rate constants showing the Al_2O_3 scale growth rate on different Fe, Ni, and Pt-based alloys. Reproduced from Hou, P. Y. *J. Am. Ceram. Soc.* **2003**, *86*, 660–668.

1.10.6.3 Oxide Growth Mechanism

The transition alumina has been shown to grow predominantly by aluminum outward transport.[231,307] From several earlier inert Pt marker studies,[301,308] α-Al_2O_3 was believed to grow predominantly by O inward diffusion, since markers that were placed on the alloy surface prior to oxidation remained on the scale surface afterwards, indicating inward growth of the scale. The minor amount of aluminum outward transport is believed to contribute to lateral growth of the scale, causing extensive scale convolution, or wrinkling[298]; an example is given in Figure 20. Based on the degree of such a convolution, whether the scale is detached from the substrate or wrinkled with it, the extent of lateral growth on polycrystalline FeCrAl alloy, for example, can be as high as 20–50%.[303,304] This shows that the amount of Al outward transport is not trivial. More recent two-stage oxidation studies using $^{18}O/^{16}O$[309–315] indicated clearly that a considerable amount of Al outward transport indeed occurs during scale growth. In this type of study, the oxidation at each stage is done in an atmosphere enriched with one of the oxygen isotopes. The isotope distribution throughout the scale is subsequently determined using spectroscopic methods. Secondary ion mass spectroscopy (SIMS) is the most commonly employed technique.[311,313–315] Secondary neutral mass spectroscopy[312] (SNMS) and other techniques[309,310] have also been used.

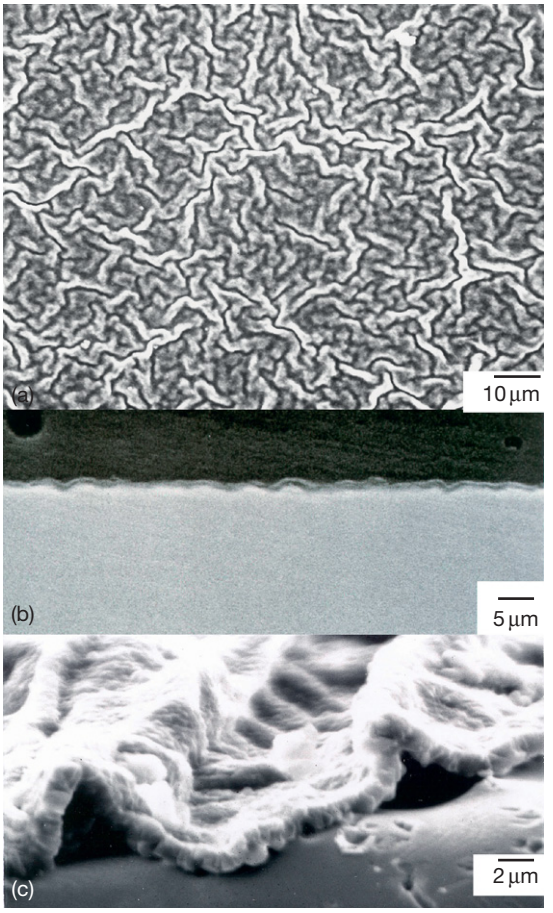

Figure 20 Wrinkling of alumina scale formed on FeCrAl at 1000 °C in oxygen: (a) oxide surface and (b) polished cross-section after 3 h, (c) fractured cross-section after 120 h.

From the location and the distribution profiles of the second stage isotope, the dominant transport species and its path can be determined.[37,310,316] A typical profile from the results of Quakakkers *et al.*[312] is presented in **Figure 21** as an illustration. The alumina scale was formed at 1000 °C on a FeCrAl alloy after oxidation first in $^{16}O_2$ for 2.5 h to ensure a completely transformed and stable α-Al_2O_3 layer, then without cooling, the specimen was continually oxidized in $^{18}O_2$ for 5 h to allow new oxides to grow so its location could be determined later. A large peak of the second isotope, in this case ^{18}O, is present at the scale–gas interface. Portions of it come from oxygen isotope exchange but, due to the slow rate of this process,[37] its contribution should be small. The majority of ^{18}O found at the outer surface is therefore due to new oxide formation from Al that diffused through the scale and reacted with oxygen from the atmosphere. A significant amount of ^{18}O also exists within the first

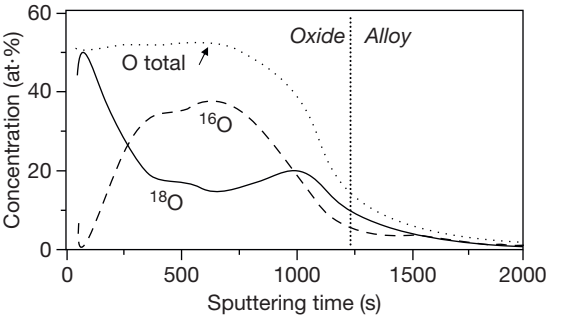

Figure 21 An example of oxygen isotope profiles from Quadakkers *et al.*[312] after two-stage oxidation of an FeCrAl alloy oxidized at 1000 °C first in $^{16}O_2$ for 2.5 h, then in $^{18}O_2$ for 5 h.

formed oxide and at the scale–alloy interface. This is the result of oxygen diffusion through the Al_2O_3 scale forming new oxides at the scale–alloy interface. If the outer and inner portions are integrated and their areas compared, one obtains an outward to inward growth ratio of 0.45. This method is of course not quantitatively precise, but can be used to compare the effect of dopants on the transport properties through alumina scales.

Although the isotope studies clearly show that α-Al_2O_3 grows mainly by oxygen inward transport, but with an appreciable amount of Al outward transport, the transport path, that is, lattice, grain boundary or other short circuit diffusion paths, cannot be revealed. The grain size of transition alumina that grows initially on alloy surfaces upon oxidation is extremely fine, in the range of a few nanometers.[238,246] Even with more mature scales, that is, α-Al_2O_3, that have grown to several microns thick, the oxide grain size is still no more than 1 or 2 μm.[281,282] Owing to these small grain sizes, and the slow oxygen lattice diffusivity found by tracer studies,[317] grain boundaries have always been considered the dominant transport paths through alumina scales. More recently, microstructural evidence has also shown the importance of grain boundary transport through α-Al_2O_3 scales.[263] While some oxide ridges, such as those shown in **Figure 18**, develop during the initial stage from alumina transformation, continued ridge growth can still occur through an adherent α-Al_2O_3 layer. Furthermore, polished cross-sections, as seen in **Figure 22**, often show thicker scales above and below an Al_2O_3 grain boundary,[263] giving clear indications that this is the preferred transport path through the scale, and growth of the oxide took place at the scale–alloy interface and on the oxide surface, as suggested by oxygen tracer studies.

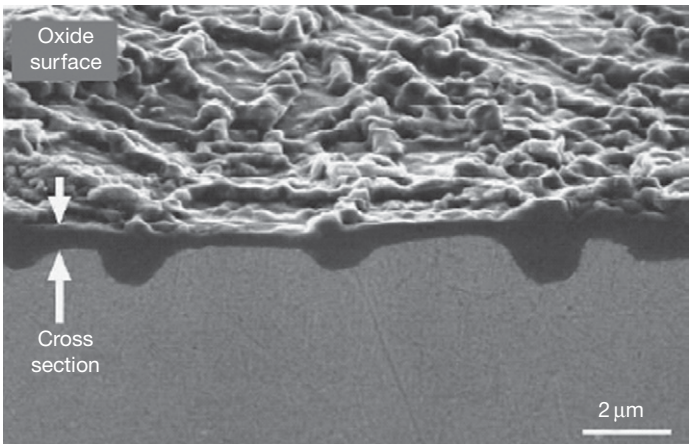

Figure 22 SEM image of polished cross-section of alumina formed on NiPtAl, showing oxide ridges above and below the alumina grain boundary. Oxidation was carried out at 1200 °C for 50 h in air. Reproduced from Tolpygo, V. K.; Clarke, D. R. *Mater. High Temp.* **2000**, **17**, 59–70.

The growth of an Al_2O_3 oxide scale that follows parabolic kinetics is controlled by the diffusion of O and Al through the scale layer according to the following equation

$$k_p = \int_{P_{O_2}} \left[1.5\left(D_L^{Al} + \frac{\delta D_b^{Al}}{d} \right) + \left(D_L^{O} + \frac{\delta D_b^{O}}{d} \right) \right] d \ln P_{O_2} \quad [1]$$

where k_p is the parabolic rate constant, d is the oxide grain size and Ds are the respective diffusivities. Assuming the Ds are not functions of P_{O_2} and that the contribution from lattice diffusion is insignificant, an effective diffusivity, D_{eff}, which is a combination of the boundary diffusivities of Al and O, can be obtained as

$$D_{eff} = k_p d / \ln P_{O_2} \quad [2]$$

The P_{O_2} is the oxygen potential difference across the alumina scale. The parabolic rate constant, k_p, in its usual units of $g^2\,cm^{-4}\,s^{-1}$, can be converted to the units of Ds in $cm^2\,s^{-1}$ using the density of alumina. Assuming thermodynamic equilibrium at the Al_2O_3–alloy interface, the P_{O_2} there would be that of the dissociation pressure of Al_2O_3 at the oxidation temperature. From most reported microstructure of oxide scales, the average oxide grain size can be taken as roughly 0.5, 1, 1.5, and 2 µm respectively for oxidation at 1000, 1100, 1200, and 1300 °C. The range of D_{eff} thus calculated using eqn [2] from the range of k_ps shown in **Figure 19** is presented as a shaded area in **Figure 23**. On this figure are also plotted different cation and anion diffusivities experimentally determined in bulk alumina. A grain boundary width, δ, of 10 nm is chosen to convert grain boundary diffusivity, usually presented as δD with units of $cm^3\,s^{-1}$.

Oxygen diffusion from tracer studies in single crystals undertaken by several investigators[317–321] all agree within an order of magnitude and with similar activation energies. Good agreement was also found with D_L^O obtained from dislocation loop annealing studies by Lagerloff *et al.*[322] The apparent oxygen diffusivity determined on polycrystalline Al_2O_3 by Oishi and Kingery[317] showed enhanced rates by 1–2 orders of magnitude; the lower temperature branch may be related to impurities, but the exact reason is unknown. To deduce a boundary diffusivity from these data is not straightforward, as the study only measured the total uptake of ^{18}O. The boundary diffusion of oxygen obtained by Prot and Monty[323] has a drastically different activation energy from that of Oishi and Kingery.[317] Tracer studies of Al diffusion have been limited due to the low activity of ^{26}Al. The only data are from Paladino and Kingery[324] and a more recent work by Le Gall *et al.*[325] Although Palodino and Kingery[324] used polycrystalline Al_2O_3, the grain size was 130–200 µm and the behavior was believed to be of bulk diffusion. In that case, this result should be comparable to those from Le Gall *et al.*,[325] whose study was performed on single crystal Al_2O_3, but was slightly contaminated with Si.[320] Yet the two sets of data differ by nearly four orders of magnitude. The discrepancy between these two tracer studies may lie in the difference in the Si content of their samples, or simply due to experimental difficulties using the ^{26}Al tracer. These results show that diffusion data on Al_2O_3 are

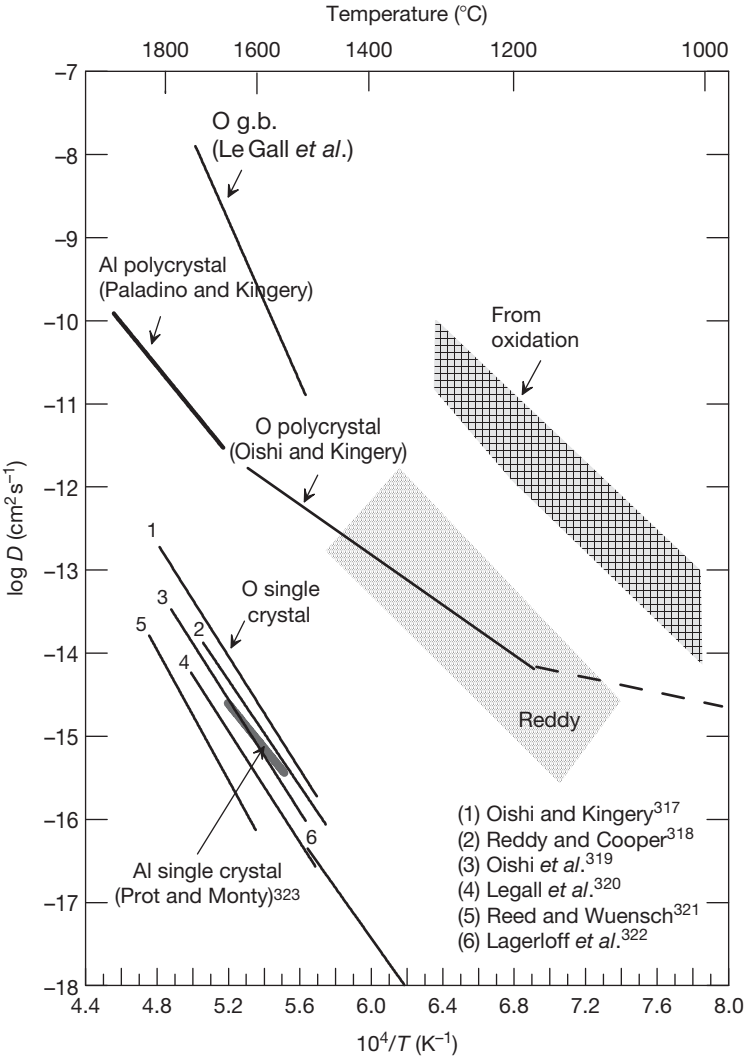

Figure 23 Comparison of diffusion rates calculated from oxidation kinetics with published tracer diffusivity data.

rather scattered. One can only conclude that D_{gb}^{O} (oxygen boundary diffusion) is much faster than that of D_{L}^{O}, and the same may be true for Al. A conclusion on the relative magnitude of the Al and O boundary diffusivity is more difficult. They may be more comparable than the difference between Al and O lattice diffusions. These general conclusions agree qualitatively with the current view on O and Al transports through Al_2O_3 scales, and also with diffusion rates compiled from creep and sintering studies.[326] However, qualitatively, diffusivities from creep tend to be at least an order of magnitude higher than the rates determined from tracer studies. This could be either due to contributions from other deformation mechanisms, such as basal slip and cavitation, or from trivial amounts of grain boundary migration that perturb the tracer profiles, giving rise to a higher D_L, thereby causing deconvolution to yield ratios of D_b/D_L that are too low by a few orders of magnitude.[327]

Oxidation studies are usually performed at much lower temperatures than creep, sintering or tracer diffusion studies, making direct comparisons less straight forward, where diffusivities are extrapolated assuming activation energies to be constant over a wide range of temperatures. The effective diffusivity determined from the range of k_ps from α-Al_2O_3 scale growth (shaded band in **Figure 23**) is seen to lie slightly above the available δD_b^{Al} values from tracer studies. Compared to δD_b^{O}, it is more than two orders of magnitude higher than most of the tracer data, except the calculated lower temperature branch of Oishi and Kingery.[317] These comparisons suggest that

Al boundary transport in Al_2O_3 scale growth is not trivial, which agrees with the results of two-stage oxidation studies using $^{18}O_2/^{16}O_2$[310] and with the conclusion obtained from oxide wrinkling analysis[328] and oxide microstructures.[263]

1.10.6.4 Scale Adhesion

Although Al_2O_3 grows slowly to offer good oxidation protection, it spalls extensively during cooling on alloys that do not contain any RE. Part of the reason is the high thermal stress, as high as several gigaPascals,[329] that exists between Al_2O_3 and these Al_2O_3-forming alloys, and partly due to a weak Al_2O_3–alloy interface. Unlike Cr_2O_3, Al_2O_3 almost always fails adhesively, where the oxide delaminates along the interface, exposing bare alloy surfaces after scale spallation. Interfacial pores are often present after oxidation, acting as interfacial defects, which can further deteriorate scale adhesion. Sulfur impurity is known to weaken the interface and REs to strengthen it. These effects are discussed in detail in the next section. Discussion of Al_2O_3 adhesion here only involves alloys without any RE addition.

Intermetallic alumina formers, such as NiAl and FeAl, are particularly susceptible to forming large cavities at the scale–alloy interface. Several experimental studies on NiAl[232,235,330–332] and FeAl[333–335] have investigated the pore formation behavior in these systems. On NiAl,[331] more voids were observed on the Ni-rich alloys, where diffusion of Ni in the alloy is much faster than that of Al. The authors attributed the pore formation mechanism to the Kirkendall effect, where the different Ni and Al diffusion rates can cause a net flux of vacancy to the scale–alloy interface, which condenses out into voids. Indeed, the mechanism of pore formation has often been attributed to vacancy condensation. These can be vacancies that arrive at the scale–alloy interface from the growing scale as a result of cation outward transport,[336,337] or from any unequal diffusion of the alloying elements in the substrate,[338] such as that from the Kirkendall effect. It has been suggested[339,340] that vacancies can be injected into the metal to be annihilated or to form voids there. However, if the oxide–metal interface acts as a perfect vacancy sink, such rejection should not take place; instead, vacancies will be annihilated at the scale–metal interface.[341,342] Harris,[343] on the other hand, disputed the vacancy condensation model entirely and suggested that tensile stress induced in the alloy by the compressive growth stress in the oxide caused voiding. Similar views are shared by others,[344] suggesting that interfacial pore formation is a result of uneven stress distribution at the scale–alloy interface.

Although the exact mechanism of void formation is still not established, it is clear that on Ni or Fe aluminides, voids almost 10 times larger than the oxide grain size and as deep as the scale thickness can exist from the very beginning of oxidation,[335] even during the heating stage; an example is shown in **Figure 24**. On FeAl, it has been shown that most voids nucleated during the initial stage of oxidation, where the first-formed transition alumina grew predominantly by cation outward transport. Moreover, the density of these voids increased dramatically with the presence of surface impurities, such as C, Cl, P, S, or a combination of these.[345] Impurities, whether present at the alloy surface prior to oxidation or inside the alloy that diffuses to the surface during oxidation, have been suggested to enhance pore formation by lowering the metal surface energy.[346]

Other than the often large pores found at oxide–metal interfaces, various types of porosity have also been reported within the Al_2O_3 scale. One particularly common appearance is a row of fine pores at the boundary between the first-formed outer transition

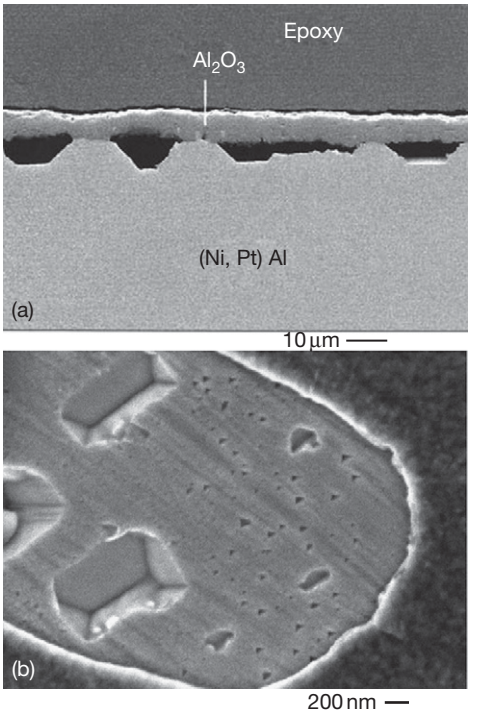

Figure 24 Examples of voids formed at the alumina–aluminide interfaces: (a) on a Ni–44Al–6Pt–3.5Co–1.5Cr (at.%) alloy after 300 h at 1150 °C,[385] and (b) on Fe–40Al after 3 min at 1000 °C.[335]

alumina layer and the subsequently developed α-Al_2O_3 inner layer. These pores most likely resulted from the alumina transformation that is associated with a volume reduction. Other types of small pores, some at Al_2O_3 grain boundaries, especially at triple point junctions, and some even at oxide grain centers, are commonly observed. A few explanations have been given for their occurrence,[246,328,332] but there has not been much discussion on this topic. As most of these pores are small, about a fraction of the alumina grain size, and randomly distributed inside the scale, they usually do not contribute to scale failure.

Buckling of Al_2O_3 scales at the growth temperature, as often found with Cr_2O_3 scales, is rarely observed, except after extensive scale convolution,[347] sometimes referred to as rumpling[348] or wrinkling.[349] In the beginning of the convolution, the oxide remains attached to the alloy at all locations, and the alloy and scale wrinkle together. An example of such morphology is seen in **Figure 20(b)**. The compressive growth stress in the oxide is believed to be the driving force[266,350,351] that causes an initially planar oxide–alloy interface to convolute as a stress relaxation mechanism. With further oxidation, the rumpling amplitude increases and its wavelength decreases. This phenomenon seems to occur only for Fe-based Al_2O_3 formers without a RE addition, such as FeAl and FeCrAl[352]; some believe the process is related to the alloy's mechanical properties, but others have suggested that it may be related to the rates of interface diffusion.[351,352] It is important to note that this type of wrinkling happens at the oxidation temperature, with only a small contribution during the first few hundred degrees of cooling.[353] The phenomenon is very different from that observed on coatings during thermal cycling oxidation.[354,355] A consequence of the wrinkling morphology is the establishment of very uneven stress distribution along the oxide–metal interface.[353] High tensile stress thus present at the peaks can cause scale separation from the alloy, and after prolonged oxidation, this indeed occurs. Therefore, even though a convoluted, rough interface like the ones discussed here can impede crack propagation,[356] the outcome is that it provides a tensile stress component at the interface that can act as a crack initiator.

1.10.7 Effect of Minor Alloying Elements and Impurities

The most beneficial minor alloying additions in combating high temperature oxidation are the so-called 'REs,'[357] such as Y, Ce, Hf, and Zr. They are often added in the alloy and found in the protective oxide scales. Studies have shown that they segregate strongly at alumina and chromia grain boundaries and alter the scale growth process.[358,359] The first part of this section describes the RE effects and discusses some of the mechanisms that have been proposed to explain these effects.

Impurities that are incorporated into the growing scale can come from many different sources. An apparent one is the common surface contaminants that are present before oxidation, such as Na and K,[360] but their concentrations are usually low and can vary significantly from test to test. The most abundant impurity sources are base metal components (discussed in the previous section), such as Fe, Ni, or Co, which are incorporated as oxides during the initial stage of oxidation.[241,361] Nonmetallic impurities that are present in almost all commercial grade alloys may segregate to the scale–alloy interface during oxidation. In particular, the segregation of sulfur is believed to greatly deteriorate scale adherence.[362,363] This phenomenon is also addressed in this section, after the discussion on RE effects.

1.10.7.1 Reactive Elements

The addition of oxygen active elements, such as Y, Hf, Ce, or Zr, is known to have profound beneficial effects on the oxidation behavior of Cr_2O_3- and Al_2O_3-forming alloys. This so-called 'RE effect' was discovered 70 years ago[364] and was first termed the rare earth effect, because rare earth metals added as melt deoxidants to Nichrome (Ni–20 wt% Cr) heating elements were found to increase cyclic lifetimes substantially by increasing the adhesion of Cr_2O_3 scale to the alloy. The amounts of the rare earth additions were 0.01–0.5 wt%. In a later patent,[365] it was found that elements from groups IIA, IIIA, IVA, and VA of the periodic table could produce similar beneficial effects. Indeed, subsequent work carried out by various other investigators confirmed that a wide range of additions affect Cr_2O_3- and Al_2O_3-forming alloys similarly, as long as the additions form a more stable oxide than Cr_2O_3 or Al_2O_3.

Early results have been extensively reviewed by Whittle and Stringer,[357] where they concluded that the effects on Cr_2O_3-forming alloys are fourfold; they (1) enhance the selective oxidation of chromium, (2) decrease the oxide growth rate, (3) change the oxide growth mechanism from predominantly cation outward to oxygen inward transport and (4) improve the oxide scale adhesion. For Al_2O_3-forming alloys,

however, the effect was only to improve the scale adhesion. This last conclusion arises because the ratio of cation to anion transport is much lower in Al_2O_3 than Cr_2O_3; also, Al_2O_3 growth rate is significantly lower than that of Cr_2O_3, so any effect on cation transport and oxidation rate would be small and, therefore, difficult to measure. Furthermore, most Al_2O_3-forming alloys studied prior to that time were MCrAl type alloys, where M was Fe, Ni or Co. These alloys already have Cr as an added third element to help promote Al_2O_3 formation; hence, any effect of RE, on the selective oxidation of Al, could not be observed. Advances with improved analytical techniques and studies of NiAl and FeAl alloys have since shown that actually effects (1) and (2) also apply to Al_2O_3 formers.[366] Each of these effects is described and discussed separately later in this section. Other than these, RE additions also alter the oxide grain structure from equiaxed to columnar[367] (an example can be seen on **Figure 25**), and the average oxide

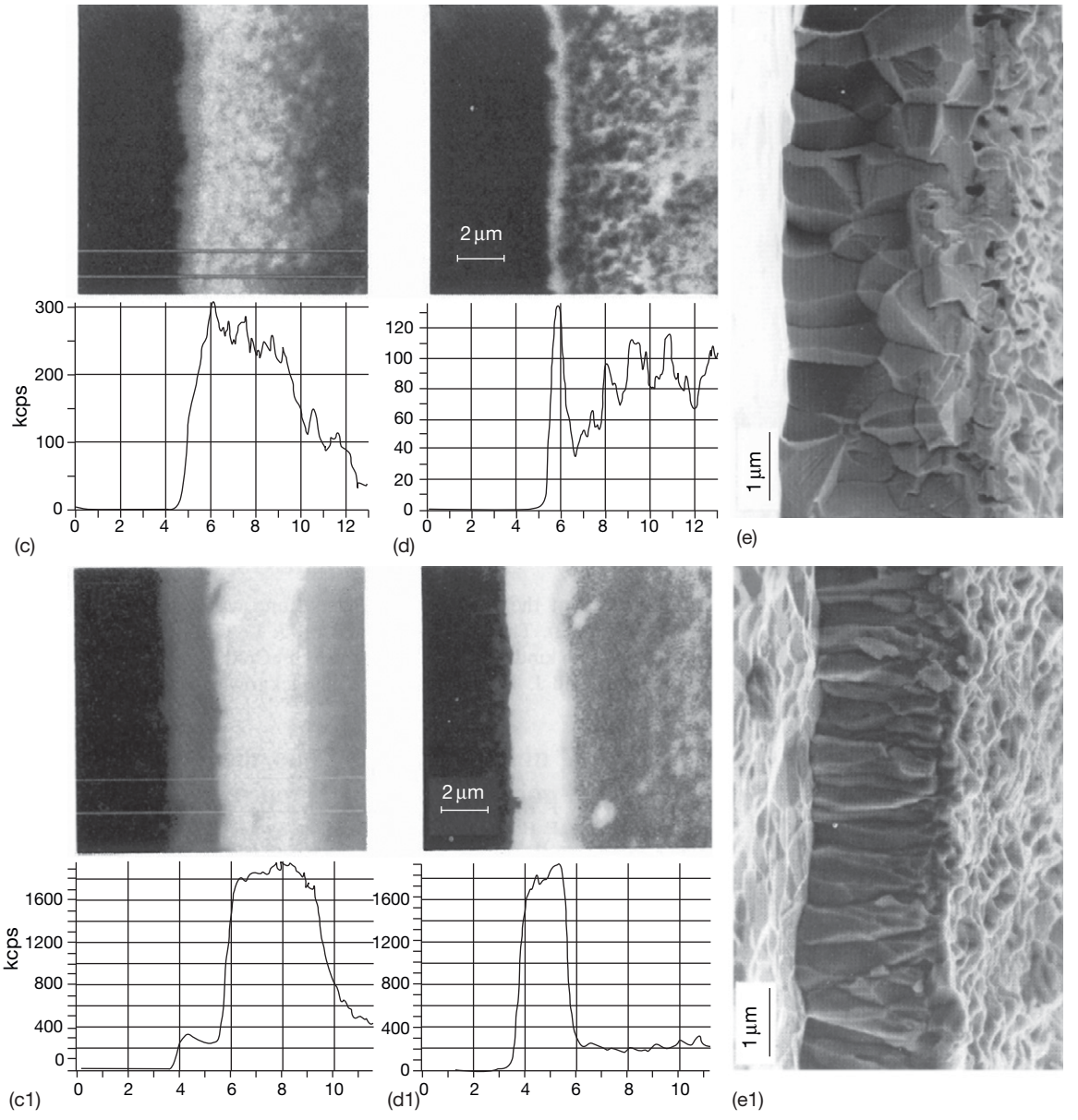

Figure 25 Effect of Y addition (bottom set of figures) in FeCrAl on oxygen transport and oxide microstructure.[315] (a) and (c) are map and line traces of ^{16}O; (b) and (d) are those for ^{18}O. The specimens were oxidized at 1200 °C first for 1.5 h in $^{16}O_2$, then 3.5 h in $^{18}O_2$.

grain size is decreased by about a factor of 1.5–2. The RE effects are most pronounced between 1000 and 1200 °C. At 900 °C or below, they become marginal; above 1300 °C (tested for Al_2O_3 formers), the effects break down.

Other than alloying additions of REs, a fine dispersion of a few volume percent of RE oxide particles, usually incorporated by mechanical alloying, are just as effective. Furthermore, superficially applied RE or RE oxide,[368] via ion-implantation or a thin coating of RE oxides or nitrates that convert to the oxides, seems equally effective. However, these surface applications, although sometimes useful for mechanistic studies,[369,370] are not effective for long-term applications that are often required for industrial usage, due to insufficient supply of the RE. The distribution[368] and concentration[278] of RE in alloys are extremely critical for their effectiveness on oxidation. While earlier studies usually use a few tenths of a weight percent, more recent works suggest that a more favorable concentration may be only a few hundred parts per million.[371] Whether this range of concentration is 'optimal' for all applications and systems is, however, questionable. The most favorable concentration may depend on the type of RE, the alloy system, the oxidation conditions or a combination of them. Overdoping of RE can produce detrimental rather than beneficial effects. Excess RE in the alloy can form a second phase, such as Y garnet, which oxidizes to YAG that promotes internal oxidation and acts as a crack initiator, hence decreases scale adhesion. An uneven distribution of RE oxide dispersions is also undesirable, for it causes nonuniform oxidation, where areas without any RE oxides can exhibit fast and nonprotective oxidation behavior.

The relative effectiveness of the different REs is unknown, although there do appear to be differences. It is also not yet clear whether one type of RE is more effective in a certain type of alloy system, although the same RE incorporated in different types of alloys can show different effects.[372] Hafnium, for example, has been shown to be exceptionally effective in NiAl alloys, decreasing the oxidation rate by almost a factor of 10.[372] The early patent[365] also noted that the effectiveness of RE decreased on passing from group II to group V, but increased with increasing atomic weight within a particular group, which is similar to recent suggestions made by Pint and Alexander,[283] pointing out that the relative effectiveness may be related to the atomic size of these elements. In summary, the relative effectiveness of REs and their optimal concentrations in a given alloy system and for a given application is still an open question and is currently under investigation. Another question worth pursuing is the benefits of codoping,[373] that is, adding more than one type of RE in an alloy. This may be the future area for optimization of the RE effect for commercial applications.

1.10.7.1.1 Promoted selective oxidation

The beneficial effect of REs on selective oxidation is to decrease the amount of Cr or Al in the alloy necessary to develop the protective Cr_2O_3 or Al_2O_3 scales. For alloys that already have sufficient amounts of Cr or Al, the effect is to decrease the time required for these scales to be established, hence decreasing the amount of base metal oxide formation. RE oxide dispersions seem to be more effective than RE additions in this respect, while surface applied RE or RE oxides do not show the same effectiveness.[374]

It has been suggested that RE or its oxides in the alloy increase Cr diffusion,[375] or acts as preferential nucleation sites,[376] to promote the establishment of the Cr_2O_3 layer. However, diffusion studies[377] on Y_2O_3- and ThO_2-containing Ni–Cr and Co–Cr alloys have shown that the presence of RE dispersions alone does not enhance the diffusivity of chromium in the alloy; rather, Cr diffusion increases with a decrease in alloy grain size. Indeed, both RE and their oxide dispersions tend to stabilize a fine alloy grain size; this has been shown for Cr_2O_3-[378] and Al_2O_3-forming alloys.[379] Furthermore, subgrain structures created by the oxide dispersions can also enhance diffusion.[377,380] It is known that a Cr_2O_3 layer develops on Ni–Cr alloys more readily over alloy grain boundaries than over the bulk of the grains, and on cold-worked surfaces than on polished ones.[381] Therefore, it appears that the major effect of RE or RE oxides is to decrease the alloy grain size, thus allowing faster diffusion of the scale-forming element from the bulk to promote an earlier development of a protective scale.

1.10.7.1.2 Decreased growth rate and changed growth direction

Above 900 °C, RE additions can decrease the growth rate of Cr_2O_3 scales by nearly an order of magnitude.[357] While the oxidation rates of undoped alloys are approximately parabolic, those doped with RE are often described as asymptotic or cubic. Similar decreases can be achieved by surface-applied RE or RE oxides, or even with RE implanted into an

existing thin oxide film,[370,382] suggesting that RE incorporation into the oxide is essential in decreasing the scale growth rate. Below 900 °C, the effect is minimal, with an approximately twofold decrease in rates.[383]

When rates on RE-doped and undoped Al_2O_3-forming alloys are compared and plotted over a wide temperature range, the data are scattered over about two orders of magnitude and show no apparent effect of RE on scale growth rate.[202,241,357] Therefore, earlier reviews[202,357] have concluded that RE has no effect on Al_2O_3 scale growth rate. However, the scatter may be related to differences in the process of adding RE to the alloys, and the different experimental conditions and procedures. If data with or without RE additions obtained from the same research group on the same type of alloy are compared,[241] the results show a consistent decrease in oxidation rate with the addition of RE (**Table 1**). In this summary, no distinction was made on the different types of RE, even though some RE may be more effective than others in some cases. Some of the rates were averaged from several tests of an undoped alloy, or from alloys doped with different REs, giving rise to the relatively large error bars. Still, a clear trend can be seen from these results showing that all RE additions in Ni- and Fe-based alloys decrease the oxidation rate by about a factor of two. On the PtAl alloy, the addition of Zr decreased the rate by a factor of four, but only one set of data exist for this alloy, so it would be premature to conclude that the RE effect on scale growth rate is greater on Pt-based than on Ni- or Fe-based alloys.

Other than the decrease in rate, RE additions also affect the relative transport rates of oxygen and Cr or Al through the scale. The effect was more prominent for Cr_2O_3-forming alloys, so it was often realized with earlier Pt marker studies.[384] Not until oxygen isotopes were used, was the effect also verified for Al_2O_3-forming alloys, where a noticeable amount of Al outward transport is decreased with the addition of REs; an example can be seen in **Figure 25**. An estimate from the relative percentage of the two oxygen isotope distributions, averaged over seven data sets over the temperature range of 900–1100 °C,[241] showed that the outward transport of Al is decreased by about a factor of four. These oxygen tracer studies, performed on different types of alloys with different REs, showed similar results. However, microstructural observations on the extent of grain boundary ridge development on Al_2O_3 surfaces showed obvious differences between the type of alloy and RE.[385,386] These studies were made during a second stage oxidation after polishing the top layer of the first-formed oxide. In the first study, it was found that different REs behaved similarly on FeCrAl-based alloys, but 0.05 at.% addition of Zr in Ni–50Al was more effective in decreasing Al outward transport than the same amount of Y addition. In a second, more quantitative study, Y was found to be more effective on FeCrAl-based alloys than Zr. It was concluded that the ratio of inward diffusion of oxygen to outward diffusion of aluminum depends not only on the oxidation temperature, but also on the RE dopant, as well as its form in the alloy. There are apparent discrepancies between the two reports, but the results are interesting in that they point to possible different degrees of the RE effect in different systems.

Utilizing analytical TEM, Yurek and coworkers investigated oxide scales in cross-sectional samples and first demonstrated that RE segregates to Cr_2O_3[359] and Al_2O_3[358] grain boundaries. A similar segregation has since been observed for many RE-containing alloys, where different REs, such as Y, Zr, Hf, La, and Ti, added in different forms (metallic, oxide dispersion, ion-implantation, or surface coating) and in different types of alloys, have been found to segregate at Al_2O_3 grain boundaries.[237,281–283,358,387–392] The amount that is segregated has been quantified to

Table 1 Effect of RE addition on oxidation rates

Alloy system	*Oxidation condition*	*Rate w/o RE*	*RE type*	*Rate with RE*	*Refs*
NiAl	1200 °C	$(1.4 \pm 0.4) \times 10^{-11}$	Ti, La, Zr, Hf, Y	$(8.0 \pm 4.1) \times 10^{-12}$	277, 279, 280, 283, 387
Ni_3Al		7.1×10^{-12}	Y	$(4.3 \pm 3.1) \times 10^{-12}$	
Fe_3Al		$(1.3 \pm 0.2) \times 10^{-11}$	Hf, Zr, Y	$(4.9 \pm 2.4) \times 10^{-12}$	
FeCrAl		$(1.8 \pm 0.6) \times 10^{-11}$	Nb, Ti, Sc, Hf, Gd, Ba, Nd, La, Zr, Y	$(7.1 \pm 2.8) \times 10^{-12}$	
PtAl		$(1.6 \pm 0.4) \times 10^{-11}$	Zr	4.1×10^{-12}	
FeCrAl		7.8×10^{-12}	Y	4.1×10^{-12}	287
FeCrAl	1150 °C	8.5×10^{-12}	Ti	2×10^{-13}	290
NiCrAl	1100 °C	1.1×10^{-12}	Y, Hf	$(4.5 \pm 2.1) \times 10^{-13}$	

be about 0.2 monolayer.[392] When the segregation was followed as a function of oxidation temperature and time,[393] it was determined that the RE not only segregates at Al_2O_3 grain boundaries, but also diffuses through it to the scale surface, where it can precipitate out as fine oxide particles.

Based on the segregation result, and the change in the oxygen isotope distribution, Yurek and coworkers[358] proposed that the presence of RE at the oxide interface decreases cation grain boundary diffusion, but probably does not affect oxygen diffusion; consequently, scale growth becomes dominated by oxygen inward transport. This proposal has been explained in detail by Pint,[393] stating that the oxygen potential across the scale drives the RE to diffuse from the alloy, through the scale to the outer surface, where the diffusion path is the oxide grain boundaries, and this is where RE segregates. Although there are ample evidences of RE segregation to growing Cr_2O_3 and Al_2O_3 oxide grain boundaries, creep studies have also indicated that RE additions to sintered Al_2O_3 significantly decreased the creep rate,[270,271] implying a decrease in Al grain boundary diffusivity, the exact mechanism by which RE at oxide grain boundaries affects cation, but not anion, diffusion is not known. Analysis of the effect of impurities on grain boundary structure[394,395] may shed some light on the boundary diffusional processes. Another question worth considering, which may be closely related to the transport mechanism of cations and anions in oxide grain boundaries, is why Al and O do not react at the boundary, as both diffuse through it. Such a reaction should result in internal plating of oxide at the grain boundary, or lateral growth,[47] which would generate in-plane compressive stress. It is possible that once such stress is generated, it prevents further reaction, until the stress is relieved. Clarke,[396] using a dislocation climb model, has determined for Al_2O_3 scale that only 10^7 molecules per micron length of grain boundary can generate ~0.5 GPa of growth stress.

1.10.7.1.3 Improved scale adhesion

The most industrially relevant beneficial effect of the RE additions is the improved scale adhesion, especially for Al_2O_3-forming alloys and coatings. It has been demonstrated repeatedly that additions of RE or RE oxides in the alloy greatly increase the spallation resistance of Al_2O_3 and Cr_2O_3 scales during cooling, thereby significantly increasing the lifetime of an alloy or coating under cyclic oxidation conditions. Associated with the greater spallation resistance are noticeable microstructural changes, particularly at the scale–alloy interface. Chromia scales without any RE tend to detach from the alloy at the oxidation temperature, leading to widespread buckling, and, hence, cracking and spalling during cooling. Alumina scales, on the other hand, often develop many discrete interfacial voids, which act as defects to assist in scale failure, or become wrinkled, as often seen in Fe-based alloys, which give rise to tensile stresses at some locations at the interface that lead to scale delamination. Apart from these microstructure changes, there are also significant chemical changes at the scale–alloy interface, which can significantly affect the strength of the interface. This effect will be discussed in more detail later in this section under the 'sulfur effect.' Surface additions of REs or RE oxides have been shown to exert a similar beneficial effect on Cr_2O_3 scale adhesion,[397] but do not seem to do so on Al_2O_3-forming alloys.[398]

Many earlier explanations of the possible role of REs in improving scale adhesion have been summarized and described.[357,366,399–401] A few of them are no longer being considered, except for special cases. For example, in the case of fine-grained scales that develop on nanocoatings,[402,403] that is, alloy coatings consisting of columnar grains with grain widths in the tens of nanometer range, the small grains are envisaged to be highly plastic and, hence, are able to relieve much of the growth stress and decrease the driving force for spallation. However, recent *in situ* stress measurements using synchrotron radiation have shown that the magnitude of the growth stress is far less important than the interface chemistry or microstructure in dictating scale failure.[404] Oxide pegging, where fine stringers of Al_2O_3 oxide grow internally from the external scale into the substrate, have been suggested to impede crack propagation due to the large interfacial contact areas associated with the peg microstructure, and to relieve stresses by the two-phase peg-containing region.[405] Morphology of the pegs is critical to their effectiveness,[406] where a fine and more uniform distribution of small pegs is much more efficient in combating scale spallation than large ones, which are even capable of initiating scale failure. Although pegging may be important, there are several alloy systems, including Cr_2O_3-forming alloys, which do not form any pegs, but still remain adherent under severe cyclic oxidation conditions.

To date, the most accepted mechanism by which RE affects scale adhesion is related to the chemical change that occurs at the scale–alloy interface when RE is present. This can be a decrease in interface

S concentration and/or the presence of RE at the interface. The proposed mechanism related to sulfur segregation[362,407,408] is usually known as the 'sulfur effect.' The hypothesis is that the oxide–metal interfaces are intrinsically strong, but the indigenous sulfur that is present in metals and alloys, possibly as low as around 5–30 ppm, segregates to the interface during oxidation, thus weakening the bonding and rendering the scale nonadherent. The role of the REs, as a result of their strong sulfide-forming ability, is to react and tie up the sulfur, thereby preventing it from segregating to the interface.

There has been some debate on whether it is possible for a large and negatively charged sulfur ion to segregate to an intact oxide–metal interface.[346] Indeed, if the interface were always coherent, it might not have enough space to accommodate a large segregand, especially one that is negatively charged as are the oxygen ions in the oxide. However, oxide–metal interfaces are not always coherent; coherency is often lost after prolonged oxidation.[409] At such interfaces, as with high angle grain boundaries,[410,411] segregation may be easier. When pO_2 and interfacial strains are taken into consideration, first principle calculations show that S segregation to Al_2O_3/Ni(Al) interfaces is in fact thermodynamically favored.[412] Ample evidences also exist from Auger analysis studies, showing that sulfur can indeed segregate to growing oxide–metal interfaces,[413,414] not only on interfacial void surfaces, but also on intact interfaces. The latter location was further vindicated when sulfur was detected by analytical transmission electron microscopy (TEM) on cross-sectional specimens of Cr_2O_3[415] and Al_2O_3[416–419] scales, indicating that true interfacial segregation of S to an oxide–metal interface is possible, even though such detection is often difficult, due to beam-induced desorption.[417]

The effect of S segregation on interfacial strength has been demonstrated experimentally on Al_2O_3 grown on NiAl[420] and on diffusion bonded Al_2O_3 on Ni,[421] showing greatly decreased interfacial strength with submonolayer of S coverage. Furthermore, first principle calculations also demonstrated a large bond-weakening effect of S at oxide–metal interfaces.[412] When an alloy is desulfurized, for example by a high temperature H_2-annealing process, its ability to retain the scale under severe thermal cycling conditions is also greatly improved. This conclusion has been repeatedly demonstrated for Al_2O_3-forming alloys,[363] and also for Cr_2O_3-forming alloys.[422] These results further attest to the detrimental effect of S on scale adhesion.

Although it is clear that S can segregate at oxide–metal interfaces and weaken the interfacial strength, the role of the RE is still uncertain. The presence of RE in the alloy can indeed prevent S segregation to the interface,[423] but by what mechanism? It is conceivable that RE can getter sulfur by forming a sulfide, but RE oxide dispersions are equally effective in improving scale adhesion. The RE oxides are more stable than their sulfides, so the gettering mechanism does not seem to apply. Since REs are known to segregate to oxide–alloy interfaces,[237,392] as they do to oxide grain boundaries, it has been suggested[393,424] that RE at the interface prevents S from segregating there, by blocking available sites for S segregation, similar to surface site competition or poisoning. Pieraggi *et al.*[424,425] further suggested that the segregated large RE ions can pin interfacial dislocations, which are necessary in annihilating interfacial point defects generated by the scale growth process. Blocking these interfacial reaction steps can then retard the scaling kinetics and even alter the scaling mode, for example, from predominantly cation transport to that of anion transport. This 'poisoned interface' model attempts to explain the RE effects on scale growth kinetics, transport process and adhesion. However, there has not been convincing experimental evidence to support it.

The presence of RE at the interface may exert a bond strengthening effect. This has been demonstrated experimentally[423] on Fe_3Al-based alloys that were undoped, doped with Zr and desulfurized. When interfacial composition and strength were compared, it was found that, although eliminating the sulfur in the alloy greatly improved scale adhesion, the presence of RE at the interface further strengthened the scale–alloy interface. The bond strengthening effect of RE at Al_2O_3–metal interfaces has also been established by earlier theoretical analyses,[426] and, recently, by more rigorous first principle calculations.[427]

All the above discussions on the RE effect have been based mainly on Al_2O_3- and some on Cr_2O_3-forming alloys. A few studies have also been done on the oxidation of nickel and other pure metals.[428] For the work on nickel, surface application techniques were often used, such as sol–gel coatings of RE oxides[429] or ion-implantation of REs.[430] The observed effects are not as strong as those reported for Al_2O_3- and Cr_2O_3-forming alloys. Oxidation rates are usually decreased by 2–3 times and the oxide grain sizes are also decreased, by a factor of ~2. Since the adhesion of NiO on Ni is usually good, it is not clear if these surface-applied REs affect NiO adhesion.

1.10.7.2 Nonmetallic Impurities

1.10.7.2.1 Sulfur

The segregation of indigenous sulfur impurity from an alloy to the scale–alloy interface during high temperature oxidation is often considered the major cause that weakens the interface, a conclusion drawn mainly from works performed on Al_2O_3-forming alloys.[362,363,408,431] The originally proposed hypothesis[362,408,431] states that the oxide–metal interface is intrinsically strong, but is weakened by the segregation of indigenous sulfur, which is often present in the alloy in parts per million levels, hence making the scale nonadherent. Evidence of the detrimental effect of sulfur on scale adhesion has been provided by the performance of many different desulfurized or low S alloys.[292,432,433] When the sulfur content in the alloy is decreased to less than 3 ppm or so, often by a high temperature H_2-annealing process, scale spallation under thermal cycling can be significantly decreased.[433]

The proposed 'sulfur effect' shows how interface chemistry may affect scale adhesion. Sulfur is well known to segregate to alloy grain boundaries and weaken them,[434] and theoretical studies have shown bond weakening effects of S on Al_2O_3–metal interfaces.[412,426] Limited mechanical testing on the strength of diffusion-bonded Al_2O_3–metal interfaces in the presence of a foreign element has also demonstrated strong effects of interface chemistry.[435,436] However, most of these studies did not characterize the effect that these segregands had on interface microstructure, particularly on the defect type, size, and distribution. This is especially important, as more debonded areas seem to exist when impurities are present at these interfaces.[412,435] As all commercial metals and alloys contain parts per million levels of nonmetallic impurities that readily segregate to surfaces when the alloy is heated; it is often assumed that the same kind of segregation takes place at oxide–metal interfaces. Whether this is always the case is not obviously clear. Some researchers have questioned whether it is energetically favorable for a large and electronically negative sulfur to segregate to an oxide–metal interface.[346,437]

Studies of the chemical changes at Al_2O_3–alloy interfaces as a function of oxidation time have in recent years been carried out for MCrAl type of alloys, where M is Fe[414,438] or Ni,[413] iron aluminides,[439–441] nickel aluminides,[420,442] or NiPtAl[443,444]; a few studies have also been conducted on Cr_2O_3/NiCr[445] and Cr_2O_3/Cr.[446] In most cases, the interfacial chemistry was evaluated using conventional Auger electron microscopy (AES) with a typical probe size of about 1 μm, after spalling the oxide scale in ultrahigh vacuum (UHV) by scratching an oxidized specimen surface,[420, 438,443,445,446] or bending a thin strip of oxidized sample.[414] The chemical composition of the alloy surface was then examined. With the scratch technique, the underside of the oxide, or the oxide side of the interface, could also be examined, and that location was always found to be free from segregands. Any impurity, if present at the interface, resided on the alloy side after scale spallation. One of these studies also utilized a field emission AES,[439] of probe size ~30 nm, and verified that sulfur was indeed present at the interface, rather than at small interfacial void surfaces. Furthermore, the amount of interface sulfur was found to be significantly higher than that calculated from interface sweeping, that is, accumulation of impurity atoms in the alloy onto the moving oxide–metal interface when it advances into the alloy as a result of an inwardly grown scale. Occasionally, sulfur could also be detected by using scanning electron transmission microscopy (STEM) on thin cross-sectional samples,[415–419] but such detection is usually difficult, partly due to the small amount of S segregated at the interface, and partly to S desorption under the electron beam.[417] However, results from these few TEM investigations have further demonstrated that sulfur can segregate to intact oxide–alloy interfaces that are pore-free.

AES studies of the build-up of sulfur as a function of oxidation time on several Al_2O_3–alloy interfaces are summarized in **Figure 26**, where each datum point was obtained from a different specimen oxidized for a given time. Although sulfur was found to be the major segregand at these scale–alloy interfaces, the segregation behavior, in terms of rate and amount, varied significantly for different alloys and differed from surface segregation. A few general conclusions can be made from these interfacial segregation results: (i) On MCrAl type alloys, the amount of interfacial sulfur is high due to strong co-segregation of S with Cr[413,438]; cosegregation of C also occurs on FeCrAl during cooling, but not on NiCrAl, due to the faster C diffusion rate in the bcc FeCrAl than in the fcc NiCrAl. (ii) On Fe or Ni aluminides, S is only present at the Al_2O_3–alloy interface when a complete layer of α-Al_2O_3 is developed.[413,420] On FeAl, the amount saturated at the Al_2O_3–alloy interface is about 0.5 monolayer, while much higher concentrations are found on surfaces of interfacial voids due to

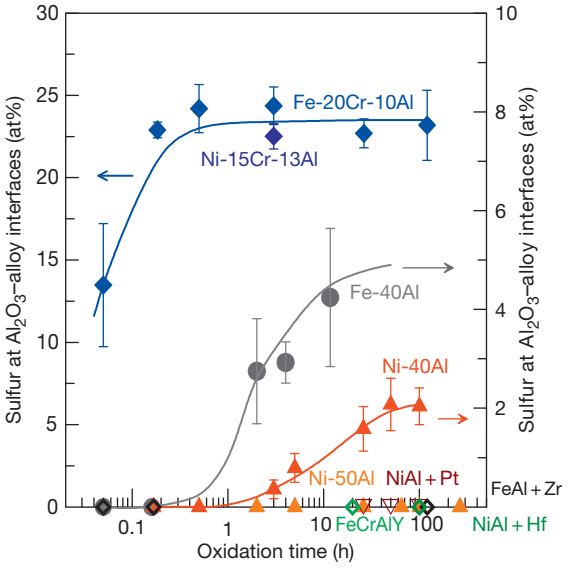

Figure 26 Summary of the amount of sulfur detected at different alumina–alloy interfaces as a function of oxidation time.

cosegregation of Al and S.[439] On NiAl, the saturation level is lower, only about 0.2 monolayer, which may be related to the lower level of sulfur impurity in nickel aluminides compared with that in iron aluminides (a few parts per million *vs.* tens of parts per million). (iii) Segregation on NiAl depends on alloy stoichiometry, in that no S segregates at α-Al_2O_3/Ni–50Al interfaces, but small amounts are present at α-Al_2O_3/Ni–40Al.[420] Finally, Pt[443] and REs (Hf, Zr, and Y)[423] prevent S segregation to the interface. Mechanical testing on some of these alloy systems directly related the amount of S at the interface to interfacial strengths,[420,423] and found that the strength decreases most sharply with the first few submonolayers of sulfur. Another related detrimental effect of sulfur on scale adhesion is its ability to enhance interfacial void formation, probably by decreasing the energy of void nucleation by decreasing the metal surface energy when S is segregated to a void embryo.[332,345] In fact, different types of common surface impurities, such as C, P, Cl, and Na, have also been shown to greatly increase the interfacial pore density on FeAl.[345,447]

Although it is now clear that sulfur, as an impurity in the alloy, can segregate to the growing oxide–metal interface to enhance interfacial void formation and decrease the interfacial bond strength, a few studies have shown a surprising beneficial effect of sulfur. For example, under steam oxidation environments, Cr cosegregated with S to the alloy surface, a high Cr ferritic steel, and promoted the formation of a protective Cr_2O_3 layer.[448] In FeCrAl, samples containing greater than 100 ppm sulfur seemed to develop Al_2O_3 scales that were more adherent than those with 3 or 30 ppm S.[449] It is not clear if this 'improved adhesion' is related to the formation of a thin layer of sulfide at the Al_2O_3–alloy interface; the mechanism is rather unclear and the method of determining scale adhesion not quantitative.

Sulfur has also been suggested to affect the growth mechanism of Al_2O_3 or Cr_2O_3 scales. Some studies have reported that the effect of excess sulfur, in the alloy or from the oxidizing atmosphere, is to produce a less protective surface oxide film, as seen from the outgrowth of Cr_2O_3 nodules on a layer of Al_2O_3 on a NiCrAl alloy,[450] or an Al_2O_3 layer that was more easily cracked at the oxidation temperature.[432] These results can be explained by the less adherent scales that usually form in the presence of sulfur. However, in other cases where scale damage or breakaway was not apparent or not studied, excess sulfur seemed to affect transport rates through the oxide, giving rise to thicker scales with higher S concentrations in the alloy.[417] Consequently, sulfur in the oxide scale, particularly at grain boundaries, was suggested to enhance cation outward transport,[415,417,451] where S acts as an electron donor and increases the number of Al vacancies.[451] However, the exact effect of S on oxide growth rates is not fully substantiated, for there are cases where sulfur was detected everywhere within the oxide layer, but it did not show any effect on scale growth rate.[418]

1.10.7.2.2 Other impurities

For all of the metals discussed in this chapter under most conditions, oxidation rates are controlled by diffusional transport across the oxide scale. Therefore, impurities that are incorporated into the growing oxide must have an effect on the rates of cation and/or anion diffusion, on oxide creep and perhaps also on the oxide microstructure. These impurities can be segregated at oxide grain boundaries, as in the case of REs (**Section 1.10.7.1**), or dissolve in the oxide, to affect grain boundary transport, diffusional creep, and/or change the oxide defect concentration, thereby affecting the rates of cation or anion transport through the oxide film. For NiO, it is clear that impurities enhance duplex scale formation[452] (see **Section 1.10.2.1**), in ways that are still not clearly understood.

Although the type and concentration of impurities must be important in high temperature oxidation,

evaluations of their effects have not been made systematically. Ample examples on the effect of impurities, whether on sample surfaces from the environment[306,345] or from within the alloy,[453,454] serve to underline their importance, as well as the complexity of the oxidation process.

1.10.8 Concluding Remarks

Oxidation is considered by some as a perfect topic for teaching material science, because it covers all aspects of the field, from basic thermodynamics to gas–solid interaction, defect chemistry, similar and dissimilar interfaces, bulk and short circuit diffusions, phase transformation, deformation, fracture mechanics and more. Indeed, the oxidation of even pure metals and simple binary alloys involves extremely complicated processes, many of which are interrelated. The summary given here and the many references sited are intended to provide future researchers with a foundation of the extensive works that have been done, so that the same conclusions need not be repeated. In every section of this chapter, many questions obviously remain for future scientists to unravel. It is important to bear in mind that quantitative analysis is extremely important. Although some aspects of the oxidation processes are difficult to quantify, one should strive to do it as much as possible, even if semiquantitatively. It is also important to always consider the *dynamic* nature of the oxidation process and take notice of the knowledge gained from other disciplines, as oxidation covers a wide range of scientific principles.

What is most lacking in past research, in my view, is the understanding of the coupling of different phenomena and the identification of the generality of certain phenomenon, that is, how and/or whether an experimentally observed trend for one system applies to others. An example of this is the sulfur effect, which has been extensively studied and substantiated for Al_2O_3 formers, but it is not certain if the same applies for Cr_2O_3, NiO, Fe_2O_3, or other systems. Related to this question is the nature of the oxide–metal interface on different types of alloys. There seems to be a myth that interfaces formed on alloys whose scales grow mainly by anion transport are stronger than those that grow by cation transport. Quantitative experimental work has to be conducted to provide answers. First principle calculations may also be employed to help elucidate many questions related to metal–oxide interfaces and how structure and chemistry affect their strength. The above example is only one of many that can be raised. While engineering investigations are often system specific, scientific research should provide knowledge that has broad relevance. Coupling of phenomena is an area that has received little attention. For example, it has been proposed[328] that the magnitude of the oxidation stress should be related to the oxide microstructure and *vice versa*. How structure and chemistry affect stress generation and how the stress in turn affects structure due to relaxation are questions that remain unclear. Many such *couplings* can be identified. Studying them undoubtedly raises the level of experimental difficulty, but with increasingly advanced instrumentation and theoretical tools, new results and insights should be attainable.

References

1. Kubaschewski, O.; Hopkins, B. E. *Oxidation of Metals and Alloys*, 2nd ed.; Academic Press: New York, 1962.
2. Kofstad, P. *High Temperature Corrosion*; Elsevier Applied Science: London, UK, 1988.
3. Birks, N.; Meier, G. H.; Pettit, F. S. *Introduction to the High-Temperature Oxidation of Metals*, 2nd ed.; Cambridge University Press: Cambridge, UK, 2006.
4. Kofstad, P. *Nonstoichiometry, Diffusion, and Electrical Conductivity in Binary Metal Oxides*; Wiley-Interscience: London, 1972; Chapter 11, pp 221–257.
5. Wood, G. C.; Wright, I. G.; Ferguson, J. M. *Corros. Sci.* **1965**, *5*, 645–661.
6. Vasyutinskiy, B. M.; Kartmazov, G. N. *Fiz. Metal Metalloved* **1963**, *15*, 132.
7. Atkinson, A.; Taylor, R. I.; Goode, P. D. *Oxid. Met.* **1979**, *13*, 519–537.
8. Harris, A. W.; Atkinson, A. *Oxid. Met.* **1990**, *34*, 229–258.
9. Sawhill, H. T.; Hobbs, L. W.; Tinker, M. T. *Adv. Ceram.* **1983**, *6*, 128–138.
10. Moon, D. P. *Oxid. Met.* **1989**, *31*, 71–89.
11. Kim, C. K.; Fan, S. K.; Hobbs, L. W. In *Microscopy of Oxidation*; Bennett, M. J., Lorimer, G. W., Eds.; Institute of Metals: London, UK, 1991; pp 374–380.
12. Peraldi, R.; Monceau, D.; Pieraggi, B. *Mater. Sci. Forum* **2001**, *369–372*, 189–196.
13. Mitchell, D. F.; Sewell, P. B.; Cohen, M. *Surf. Sci.* **1976**, *61*, 355.
14. Mitchell, D. F.; Graham, M. J. *Surf. Sci.* **1982**, *114*, 546–562.
15. Martius, U. M. *Can. J. Physics* **1956**, *33*, 466–472.
16. Balmain, J.; Savall, C.; Molins, R.; Severac, C.; Haut, C.; Huntz, A. M. *Mater. Sci. Forum* **2001**, *369–372*, 125–132.
17. Peraldi, R.; Monceau, D.; Pieraggi, B. *Oxid. Met.* **2002**, *58*, 249–273.
18. Ueno, T. *Trans. Jpn. Inst. Met.* **1973**, *14*, 267.
19. Lebrun, J. L.; Huntz, A. M.; Beranger, G.; Aubry, A.; Zhao, J. G. In *Residual Stresses in Science and Technology*; Ceck, G., Denis, D., Simon, A., Eds.; Elsevier Science: London, UK, 1988; p 135.
20. Czerwinski, F.; Zhilyaev, A.; Szpunar, J. A. *Corr. Sci.* **1999**, *41*, 1703–1713.
21. Desserrey, F.; Valot, C.; Montesin, T.; Larpin, J. P. *Mater. Sci. Forum* **2002**, *408–412*, 1007–1012.

22. Hobbs, L. W.; Sawhill, H. T.; Tinker, M. T. *Rad. Effects* **1983**, *74*, 291–297.
23. Homma, H.; Khoi, N. N.; Smeltzer, W. W.; Embury, J. D. *Oxid. Met.* **1971**, *3*, 463–473.
24. Kim, C. K.; Fan, S. K.; Hobbs, L. W. In *Microscopy of Oxidation*; Bennett, M. J., Lorimer, G. W., Eds.; Institute of Metals: London, UK, 1991; pp 374–380.
25. Hou, P. Y.; Cannon, R. M. *Mater. Sci. Forum* **1997**, *251–254*, 325–332.
26. Stawbridge, A.; Stott, F. H.; Wood, G. C. *Corros. Sci.* **1993**, *35*, 855–862.
27. Kyung, H.; Kim, C. K. *Mater. Sci. Eng.* **2000**, *B76*, 173–183.
28. Mrowec, S. *Corros. Sci.* **1967**, *7*, 563.
29. Evans, A. G.; Rajdev, D.; Douglass, D. L. *Oxid. Met.* **1972**, *4*, 151.
30. Kofstad, P. *Oxid. Met.* **1985**, *24*, 265.
31. Atkinson, A.; Smart, D. W. *J. Electrochem. Soc.* **1988**, *135*, 2886.
32. Robertson, J.; Manning, M. I. *Mater. Sci. Technol.* **1988**, *4*, 1064.
33. Gibbs, G. B.; Hales, R. *Corros. Sci.* **1977**, *17*, 487.
34. Yurek, G. J.; Schmalzried, H. *Ber. Bunsenges. Phys. Chem.* **1975**, *79*, 255.
35. Caplan, D.; Hussey, R. J.; Sproule, G. I.; Graham, M. J. *Oxid. Met.* **1980**, *14*, 279–299.
36. Peraldi, R.; Monceau, D.; Pieraggi, B. *Oxid. Met.* **2002**, *58*, 275–295.
37. Atkinson, A.; Taylor, R. I.; Goode, P. D. *Oxid. Met.* **1979**, *13*, 519–543.
38. Atkinson, A.; Taylor, R. I.; Hughes, A. E. *Philos. Mag. A* **1982**, *45*, 823–833.
39. Gulbransen, E. A.; Andrew, K. F. *J. Electrochem. Soc.* **1954**, *101*, 128.
40. Herchl, R.; Khoi, N. N.; Homma, T.; Smeltzer, W. W. *Oxid. Met.* **1972**, *4*, 35.
41. Rhines, F. N.; Connell, R. G., Jr. *J. Electrochem. Soc.* **1977**, *124*, 1122.
42. Horn, I. Z. *Z. Metalkunde* **1949**, *40*, 73.
43. Wood, G. C.; Stott, F. H.; Forrest, J. E. *Werk. Korr.* **1977**, *28*, 395–404.
44. Atkinson, A.; Taylor, R. I. *J. Phys. Chem. Solids* **1986**, *47*, 315.
45. Evans, U. R. *Symposium on Internal Stresses in Metals and Alloys,* London, 1947, pp 291–310.
46. Ueno, T. *Trans. Jpn. Inst. Met.* **1974**, *15*, 167–172.
47. Rhines, F. N.; Wolf, J. S. *Metall. Trans.* **1970**, *1*, 1701–1710.
48. Ueno, T. *Jpn. J. Appl. Phys.* **1975**, *14*, 2081–2082.
49. Liu, C.; Huntz, A. M.; Lebrun, J. L. *Mater. Sci. Eng. A* **1993**, *160*, 113–126.
50. Goedjen, J. G.; Stout, J. H.; Guo, Q.; Shores, D. A. *Mater. Sci. Eng. A* **1994**, *177*, 115–124.
51. Homma, T.; Pyun, Y. J. In *Proceedings of JIMIS-3: High Temperature Corrosion Trans. Jpn. Inst. Met., Suppl.* **1983**, 161–166.
52. Wolf, J. S.; Cavin, B. In *Advances in X-ray Analysis*; Golfrich, J. V., *et al.* Ed.; Plenum, 1994; p 449.
53. Przybilla, W.; Schutze, M. *Oxid. Met.* **2002**, *58*, 103–145.
54. Carter, R. E.; Richardson, F. D. *J. Met* **1954**, *6*, 1244.
55. Phalnikar, C. A.; Evans, E. B.; Baldwin, W. M. *J. Electrochem. Soc.* **1956**, *103*, 367–429.
56. Hsu, H. S.; Yurek, G. J. *Oxid. Met.* **1982**, *17*, 55–76.
57. Martin, M.; Hilbrandt, N.; Koops, U. In *Proceedings of the Symposium on High Temperature Corrosion and Materials Chemistry*; Electrochemical Society: Pennington, NJ, 1998; pp 106–117.
58. Kofstad, P. K.; Hed, A. Z. *J. Electrochem. Soc.* **1969**, *116*, 224–229.
59. Pettit, F. S.; Wagner, J. B. *Acta Metall.* **1964**, *12*, 41.
60. Wagner, C.; Koch, E. *Z. Phys. Chem.* **1936**, *1332*, 439.
61. Mrowec, S.; Werber, T. *Roczniki Chem.* **1962**, *36*, 159.
62. Przybylski, K.; Szwagierczak, D. *Oxid. Met.* **1982**, *17*, 267–295.
63. Gulbransen, E. A.; Ruka, R. *Trans. AIME* **1950**, *188*, 1500.
64. Pinder, L. W. C.E.G.B. Report, MID/SSD/80/0050/R, August 1980.
65. Jonsson, T.; Jardnas, A.; Svensson, J. -E.; Johansson, L. -G.; Halvarsson, M. *Oxid. Met.* **2007**, *67*, 193–214.
66. Vallet, P.; Raccah, P. *Mem. Sci. Rev. Metall.* **1965**, *67*, 1.
67. Swarooop, B.; Wagner, J. B., Jr. *Trans. AIME* **1967**, *239*, 215.
68. Bransky, I.; Hed, A. Z. *J. Am. Ceram. Soc.* **1968**, *57*, 231.
69. Fender, B. E.; Riley, F. D. *J. Phys. Chem. Solids* **1969**, *30*, 793.
70. Giddings, R. A.; Gordon, R. S. *J. Am. Ceram. Soc.* **1973**, *56*, 111.
71. Dieckmann, R. In *High Temperature Corrosion*; Rapp, R. A., Ed.; NACE: Houston, TX, 1983; p 70.
72. Dieckmann, R. In *Oxidation of Metals and Associated Mass Transport*; Dayananda, M. A., Rothman, S. J., King, W. E., Eds.; Metallurgical Society: Warrendale, PA, 1986; p 7.
73. Garnaud, G.; Rapp, R. A. *Oxid. Met.* **1977**, *11*, 193.
74. Atkinson, A. *Rev. Mod. Phys.* **1985**, *57*, 437–470.
75. Atkinson, A.; Taylor, R. I. *High Temperature – High Pressure* **1985**, *14*, 469.
76. Atkinson, A.; Taylor, R. I. *J. Phys. Chem. Solids* **1985**, *46*, 469.
77. Channing, D. A.; Graham, M. J. *Corros. Sci.* **1972**, *12*, 271.
78. Channing, D. A.; Dickerson, S. M.; Graham, M. J. *Corros. Sci.* **1973**, *13*, 933.
79. Francis, R.; Lees, D. G. *Corros. Sci.* **1976**, *16*, 847.
80. Sewell, P. B.; Cohen, M. *J. Electrochem. Soc.* **1964**, *111*, 501–508.
81. Caplan, D.; Graham, M. J.; Cohen, M. *Corros. Sci.* **1970**, *10*, 1.
82. Svedung, I.; Hammar, B.; Vannerberg, N. G. *Oxid. Met.* **1973**, *6*, 21.
83. Howe, C. I.; McEnany, B.; Scott, V. D. *Corros. Sci.* **1985**, *25*, 195.
84. Boggs, W. E.; Kachik, R. H.; Pellisier, G. E. *J. Electrochem. Soc.* **1965**, *112*, 539.
85. Rahmel, A.; Robolski, J. *Corros Sci.* **1965**, *5*, 333.
86. Fukumoto, M.; Hayashi, S.; Maeda, S.; Narita, T. *J. Inst. Met.* **2001**, *65*, 115.
87. Tuck, C. W.; Odgers, M.; Sachs, K. *Corros. Sci.* **1969**, *9*, 271.
88. Wittnauer, J. *J. Met* **1900**, *42*, 7.
89. Buckman, R. W., Jr. In *Alloying*; Walter, J. L., Jackson, M. R., Sims, C. T., Eds.; ASM International: Metals Park, 1988; p 419.
90. Pugh, J. *J. Met.* **1958**, *212*, 335.
91. Nieh, T. G.; Wadsworth, J. In *High Temperature Silicides and Refractory Alloys*; Proceedings of the Matererial Research Society Symposium; Briant, C. L., Petrovic, J. J., Bewlay, B. P., Vasudevan, A. K., Lipsitt, H. A., Eds.; Mater. Res. Soc.: Pittsburgh, PA, 1994; Vol. 322, p 315.
92. Ramberg, C. E.; Beatrice, P.; Kurokawa, K.; Worrell, W. L. In *High Temperature Silicides and Refractory Alloys*; Proceedings of the Matererial Research Society Symposium, Boston, MA, Nov.–2 Dec. 1993; Briant, C. L., Petrovic, J. J., Bewlay, B. P., Vasudevan, A. K., Lipsitt, H. A., Eds.; Material Research Society: Pittsburgh, PA, 1994; pp 243–253.
93. Kofstad, P. *J. Inst. Met.* **1962**, *90*, 253–264.

94. Pawel, R. E.; Cathcart, J. V.; Campbell, J. J. *Acta Metall.* **1962**, *10*, 149.
95. Pint, B. A.; DiStefano, J. R. *Oxid. Met.* **2005**, *63*, 33–55.
96. Kofstad, P. *J. Electrochem. Soc.* **1963**, *110*, 491.
97. Kofstad, P. *J. Electrochem Soc.* **1962**, *109*, 776.
98. Pawel, R. E.; Campbell, J. J. *Acta Metall.* **1966**, *14*, 1827.
99. Cathcart, J. V.; Campbell, J. J.; Smith, G. P. *J. Electrochem. Soc.* **1958**, *105*, 442.
100. Kofstand, P. *J. Less Common Met.* **1963**, *5*, 158.
101. Inouye, H. In *Cohimbium Metallurgy*; AIME Metallurgical Society Conferences, 10; Douglass, D. L., Kunz, F. W., Eds.; Interscience Publishers: New York, 1961.
102. Kofstad, P.; Espevik, S. *J. Electrochem. Soc.* **1965**, *112*, 153.
103. Earl, A.; Gulbransen, A.; Andrew, K. F. *J. Electrochem. Soc.* **1958**, *105*, 4–9.
104. Sheasby, J. S.; Wallwork, G. R.; Smeltzer, W. W. *J. Electrochem. Soc.* **1966**, *113*, 1255.
105. Strafford, K. N. *Corros. Sci.* **1979**, *19*, 49–62.
106. King, D. A.; Madey, T. E.; Yates, J. T., Jr. *J. Chem. Phys.* **1971**, *55*, 3247–3253.
107. Sikka, V. K.; Rosa, C. J. *Corros. Sci.* **1980**, *20*, 1201–1219.
108. Schissel, P. O.; Trulson, O. C. *J. Chem. Phys.* **1965**, *43*, 737–743.
109. Walsh, P. N.; Quets, J. M.; Graff, R. A. *J. Chem. Phys.* **1967**, *46*, 1144–1153.
110. Bartlett, R. W. *Trans. Metal Soc., AIME* **1964**, *230*, 1097.
111. Bartlett, R. W. *Trans. Metall. Soc. AIME* **1964**, *230*, 1097.
112. Perkins, R. A.; Crooks, D. D. *J. Met.* **1961**, *13*, 490.
113. Zhetbaev, A. K.; Ibragimov, S. H. S. H.; Shokanov, A. K. *J. Phys.* **1980**, *41*, 387–388.
114. Berkowitz-Mattuck, J. B.; Cuchler, A.; Engelke, J. L.; Goldstein, N. *J. Chem. Phys.* **1963**, *39*, 2722–2730.
115. Voitovich, R. F. *Fiz. Metal. Metalloved* **1961**, *12*, 376.
116. Kofstad, P. *J. Inst. Met.* **1962–63**, *91*, 411.
117. Dooley, R. B.; Stringer, J. *J. Less Common Met.* **1971**, *25*, 15–26.
118. Klopp, W. D.; Maykutii, D. J.; Jaffeet, R. I. *Trans. Am. Soc. Met.* **1961**, *53*, 637.
119. Corn, D. L.; Douglass, D. L.; Smith, C. A. *Oxid. Met.* **1991**, *35*(1–2), 139–173.
120. DiStefano, J. R.; Chitwood, L. D. *J. Nucl. Mater.* **2001**, *295*, 42–48.
121. DiStefano, J. R.; Chitwood, L. D. AIP. AIP Conference Proceedings, no. 552, 2001; pp 1076–1081. [Conference Paper; Journal Paper].
122. DiStefano, J. R.; Pint, B. A.; DeVan, J. H. *Int. J. Refract. Met. Hard Mater.* **2000**, *18*(4–5), 237–243.
123. Babitzke, H. R.; Siemens, R. E.; Asai, G.; Kato, H. Bureau of Mines Report of Investigations 6558, US Department of the Interior, 1964.
124. Nieh, T. G.; Wadsworth, J. In *High Temperature Silicides and Refractory Alloys*; MRS Proceedings; Briant, C. L., Petrovic, J. J., Bewlay, B. P., Vasudevan, A. K., Lipsitt, H. A., Eds.; **1993**; Vol. 322, p 315.
125. Svedberg, R. C.; Foroulis, Z. A.; Pettit, F. S. *J. Electrochem. Soc.* **1976**, 331.
126. Perkins, R. A.; Meier, G. H. *J. Met.* **1990**, *42*, 17–21.
127. Perkins, R. A.; Chiang, K. T.; Meier, G. H. *Scripta Metall.* **1988**, *22*, 419–424.
128. Lee, J. S.; Stephens, J. J.; Nieh, T. G. In *High Temperature Niobium Alloys*; Stephens, J. J., Ahmad, I., Eds.; TMS: Warrendale, PA, 1991; p 143.
129. Diliberto, S.; Rapin, C.; Steinmetz, P.; Vilasi, M.; Berthod, P. *J. Mater. Sci.* **2003**, *38*, 2063–2072.
130. Perkins, R. A.; Meier, G. H. *J. Met.* **1990**, *42*, 17.
131. Wittenauer, J. *J. Met.* **1990**, *42*, 7.
132. Wadsworth, J.; Nieh, T. G.; Stephens, J. J. *Int. Met. Rev.* **1988**, *33*, 131.
133. Ux, M.; Wittenauer, J. P. *J. Met.* **1992**, *44*, 25.
134. Mueller, A.; Ge, W.; Rapp, R. A.; Courtright, E. L. *J. Electrochem. Soc.* **1992**, *139*, 1266–1275.
135. Louro, C.; Cavaleiro, A. *J. Mater. Proc. Tech.* **1999**, *92–93*, 162–168.
136. Martinz, H. -P.; Rieger, M. *Mater. Sci. Forum* **1997**, *251–254*, 761–768.
137. Pons, M.; Caillet, M.; Galerie, A. *Mater. Chem. Phys.* **1986**, *15*, 45–60.
138. Pons, M.; Caillet, M.; Galerie, A. *Mater. Chem. Phys.* **1987**, *16*, 423–432.
139. Fukumoto, M.; Matsumura, Y.; Hayashi, S.; Sakamoto, K.; Kasama, A.; Tanaka, R.; Narita, T. *Oxid. Met.* **2003**, *60*, 355.
140. Deal, B. E.; Grove, A. S. *J. Appl. Phys.* **1965**, *36*, 3770.
141. Opila, E. J. *J. Am. Ceram. Soc.* **1994**, *77*, 730.
142. Duquesnoy, A.; Marion, F. *C.R. Hebd. Seances Acad. Sci.* **1963**, *256*, 2862.
143. Kroger, F. A. In *High Temperature Corrosion*; Rapp, R. A., Ed.; NACE: Houston, 1983; p 89.
144. Sucov, E. W. *J. Am. Ceram. Soc.* **1965**, *46*, 190.
145. Haul, R.; Dumbgen, *Z. Elektrockem* **1962**, *66*, 636.
146. Robinson, R. C.; Smialek, J. L. *J. Am. Ceram. Soc.* **1999**, *82*, 1817–1825.
147. Stott, F. H.; Wood, G. C.; Stringer, J. *Oxid. Met.* **1995**, *44*, 113–145.
148. Evans, H. E.; Hilton, D. A.; Holm, R. A.; Webster, S. J. *Oxid. Met.* **1980**, *14*, 235.
149. Bennett, M. J.; Desport, J. A.; Labun, P. A. *Math. Phy. Sci.* **1987**, *412*, 223–230.
150. Evans, H. E.; Hilton, D. A.; Holm, R. A.; Webster, S. J. *Oxid. Met.* **1983**, *19*, 1.
151. Adachi, T.; Meier, G. H. *Oxid. Met.* **1987**, *27*, 347.
152. Douglass, D. L.; Armijo, J. S. *Oxid. Met.* **1970**, *2*, 207.
153. Saito, Y.; Maruyama, T. *Mater. Sci. Eng.* **1987**, *87*, 275.
154. Ahmad, B.; Fox, P. *Oxid. Met.* **1999**, *52*, 113.
155. Stott, F. H.; Gabriel, G. J.; Wood, G. C. *Oxid. Met.* **1987**, *28*, 329–345.
156. Adachi, T.; Meier, G. H. *Oxid. Met.* **1987**, *27*, 347.
157. Saito, Y.; Maruyama, T.; Amano, T. *Mater. Sci. Eng.* **1987**, *87*, 275–280.
158. Meier, G. *Mater. Sci. Eng.* **1989**, *120*, 1.
159. Sauthoff, G. *Intermetallics*; VCH: New York, 1995; pp 99–117.
160. Willaims, J. C. In *Structural Intermetallics*; Nathal, M. V., Darolia, R., Liu, C. T., Martin, P. E., Miracle, D. B., Wagner, W., Yamaguchi, M., Eds.; TMS: Warrendale, PA, 1997; pp 3–8.
161. Jiang, H.; Petersson, C. S.; Nicolet, M. A. *Thin Solid Films* **1986**, *140*, 115.
162. Meier, G. H. *Mater. Corros.* **1996**, *47*, 595.
163. Brady, M. P.; Pint, B. A.; Tortorelli, P. F.; Wright, I. G.; Hanrahan, R. J., Jr. In *Corrosion and Environmental Degradation; Materials Science and Technology*; *Vol II*, Schutze, M., Ed.; Wiley-VCH: Germany, 2000, pp 296–308.
164. Lublin, P.; Sama, L. *Am. Ceram. Soc.* **1967**, *46*, 1083.
165. Lavendel, H. W.; Elliot, A. G. *Trans AIME* **1967**, *239*, 143.
166. Schwettmann, F. N.; Graff, R. A.; Kolodney, M. *J. Electrochem. Soc.* **1971**, *118*, 1973–1977.
167. Abba, A.; Galerie, A.; Cailet, M. *Oxid. Met.* **1982**, *17*, 43–54.
168. Evans, D. L. *J. Am. Ceram. Soc.* **1970**, *53*, 418.
169. Meschter, P. J. *Metall. Trans. A.* **1992**, *23A*, 1763.
170. Glushko, P. I.; Postogvard, G. I.; Pugachev, N. S.; Dudnik, S. F.; Podtykan, V. P. *Prot. Met.* **1977**, *13*, 187.
171. Melsheimer, S.; Fietzek, M.; Kolarik, V.; Rahmel, A.; Schutze, M. *Oxid. Met.* **1997**, *47*, 139.

172. Berkowitz-Mattuck, J.; Dils, R. R. *J. Electrochem. Soc.* **1965**, *112*, 583.
173. Mochizuki, T.; Kashiwagi, M. *J. Electrochem. Soc.* **1980**, *127*, 1128.
174. Ramberg, C. E.; Worrell, W. L. *J. Am. Ceram. Soc.* **2001**, *84*, 2607–2616.
175. Aitken, E. A. In *Intermetallic Compounds*; Westrook, J. H., Ed.; Wiley: New York, 1967; p 491.
176. Berkowitz-Mattuck, J. B.; Blackburn, P. E.; Felten, E. J. *Trans. AIME* **1965**, *233*, 1093.
177. Berztiss, D. A.; Cerchiara, R. R.; Gulbransen, E. A.; Pettit, F. S.; Meier, G. H. *Mater. Sci. Eng. A* **1992**, *155*, 165.
178. Yanagihara, K.; Przybylski, K.; Maruyama, T. *Oxid. Met.* **1997**, *47*, 277.
179. Kurokawa, K.; Houzumi, H.; Saeki, I.; Takahashi, H. *Mater. Sci. Eng. A* **1999**, *261*, 292–299.
180. Bartlett, R. W.; McCamont, I. W.; Gage, P. R. *J. Am. Ceram. Soc.* **1965**, *48*, 551.
181. McKamey, C. G.; Tortorelli, P. F.; DeVan, J. H.; Carmichael, C. A. *J. Mater. Res.* **1992**, *7*, 2747.
182. Dimiduk, D. M.; Perepezko, J. H. *MRS Bull* **2003**, *28*, 639.
183. Thom, A. J.; Summers, E.; Akinc, M. *Intermetallics* **2002**, *10*, 555.
184. Supatarawanich, V.; Johnson, D. R.; Liu, C. T. *Intermetallics* **2004**, *12*, 721.
185. Parthasarathy, T. A.; Mendiratta, M. G.; Dimiduk, D. M. *Acta Metall.* **2002**, *50*, 1857.
186. Sakidja, R.; Rioult, F.; Werner, J.; Perepezko, J. H. *Scripta Mater.* **2006**, *55*, 903.
187. Young, C. T.; Tenney, D. R.; Herring, H. W. *Metall. Trans.* **1975**, *6A*, 2253.
188. Caplan, D.; Cohen, M. *J. Electrochem. Soc.* **1961**, *108*, 438.
189. Opila, E. J.; Jacobson, N. S. In *Fundamental Aspects of High Temperature Corrosion*; Shores, D. A., Rapp, R. A., Hou, P. Y., Eds.; The Electrochemical Society: Pennington, NJ, 1997; Vol. 96-26, pp 269–280.
190. Kofstad, P.; Bredesen, R. *Solid State Ionics* **1992**, *52*, 69.
191. Huang, K.; Hou, P. Y.; Goodenough, J. B. *Solid State Ionics* **2000**, *129*, 237.
192. Brylewski, T.; Nanko, M.; Maruyama, T.; Przybylski, K. *Solid State Ionics* **2001**, *143*, 131.
193. Quadakkers, W. J.; Piron-Abellan, J.; Shemet, V.; Singheiser, L. *Mater. High Temp.* **2003**, *20*, 115–127.
194. Kofstad, P.; Lillerud, K. P. *J. Electrochem. Soc.* **1980**, *127*, 2410–2419.
195. Hagel, W. C.; Seybolt, A. U. *J. Electrochem. Soc.* **1961**, *108*, 1146.
196. Atkinson, A.; Taylor, R. I. In Proceedings of the 3rd International Conference on Nonstoichiometric Compounds, State College: PA, 1984.
197. Hughes, A. E.; Atkinson, A.; Chadwick, A. T. In *Defect Properties and Processing of High-Technology Nonmetallic Materials*; North-Holland: New York, NY, 1984; pp 27–37.
198. Giggins, C. S.; Pettit, F. S. *Metall. Trans.* **1971**, *2*, 1071.
199. Tsai, S. C.; Huntz, A. M.; Dolin, C. *Mater. Sci. Eng. A.* **1996**, *212*, 6–13.
200. Dong, W.; Bishop, H. E.; Johnson, D.; Lees, D. G.; Lorimer, G. W. *Oxid. Met.* **2000**, *54*, 509.
201. Lillerud, K. P.; Kofstad, P. *J. Electrochem. Soc.* **1980**, *127*, 2397–2410.
202. Hindam, H.; Whittle, D. P. *Oxid. Met.* **1982**, *18*, 245–262.
203. Evans, A. G.; Cannon, R. M. *Mater. Sci. Forum* **1989**, *43*, 243–268.
204. Kofstad, P.; Lillerud, K. P. *Oxid. Met.* **1982**, *17*, 177.
205. Ben Abderrazik, G.; Moulin, G.; Huntz, A. M. *Oxid. Met.* **1990**, *33*, 191–235.
206. Fox, P.; Lees, D. G.; Lorimer, G. W. *Oxid. Met.* **1991**, *36*, 491.
207. Caplan, D.; Harvey, A.; Cohen, M. *Corros. Sci.* **1963**, *3*, 161.
208. Caplan, D.; Sproule, G. I. *Oxid. Met.* **1975**, *9*, 459–472.
209. Wright, I. G.; Wood, G. C. *Oxid. Met.* **1977**, *11*, 163.
210. Wood, G. C.; Hodgkiess, T.; Whittle, D. P. *Corros. Sci.* **1966**, *6*, 129–147.
211. Wood, G. C.; Hodgkiess, T. *J. Electrochem. Soc.* **1966**, *113*, 319.
212. Moulin, P.; Armanet, F.; Beranger, G.; Lacombe, P. *Mere. Sci. Rev. Metall.* **1977**, *74*, 143.
213. Warzee, M.; Maurice, M.; Sonnen, C.; Waty, J.; Berge, P. H. *Rev. Met.* **1964**, *61*, 593.
214. Stott, F. H.; Bartlett, P. K. N.; Wood, G. C. *Mater. Sci. Eng.* **1987**, *8*, 163.
215. Hou, P. Y. unpublished results.
216. Howes, V. R. *Corros. Sci.* **1968**, *8*, 221.
217. Howes, V. R. *Corros. Sci.* **1968**, *8*, 729.
218. Mortimer, D.; Post, M. L. *Corros. Sci.* **1968**, *8*, 499.
219. Wood, G. C.; Whittle, D. P. *J. Electrochem. Soc.* **1968**, *115*(126), 133.
220. Wood, G. C. *Oxid. Met.* **1970**, *2*, 11–57.
221. Daghigh, S.; Lebrun, J. L.; Huntz, A. M. *Mater. Sci. Forum* **1997**, *251*, 381–388.
222. Hou, P. Y.; Stringer, J. *Act. Metall.* **1991**, *39*, 841–849.
223. Kitamura, K.; Nishiyama, Y.; Otsuka, N.; Kudo, T. *Mater. Sci. Forum* **2006**, *522–523*, 489–495.
224. Tortorelli, P. F.; More, K. L.; Specht, E. D.; Pint, B. A.; Zschack, P. *Mater. High Temp.* **2003**, *20*, 303–310.
225. Hou, P. Y.; Paulikas, A. P.; Veal, B. W. *Mater. Sci. Forum* **2004**, *461–464*, 671–680.
226. Zhu, D.; Stout, J. H.; Nelson, J. C.; Shores, D. A. *Trans. Tech. Pub.* **1997**, *251–254*, 437–444.
227. Tortorelli, P. F.; Natesan, K. *Mater. Sci. Eng.* **1998**, *A258*, 115.
228. DeVan, J. H.; Tortorelli, P. F. *Corros. Sci.* **1993**, *35*, 1065.
229. Pint, B. A.; Wright, I. G.; Lee, W. Y.; Zhang, Y.; Pruessner, K.; Alexander, K. B. *Mater. Sci. Eng. A* **1998**, *245*, 201.
230. Doychak, J.; Smialek, J. L.; Mitchell, T. E. *Metall. Trans. A* **1989**, *20*, 499.
231. Rybicki, G. C.; Smialek, J. L. *Oxid. Met.* **1989**, *31*, 275.
232. Yang, J. C.; Nadarzinski, K.; Schumann, E.; Rühle, M. *Scripta Metall.* **1995**, *33*, 1043.
233. Smialek, J. L.; Doychak, J.; Gaydosh, D. J. *Oxid. Met.* **1990**, *34*, 259.
234. Kuenzly, J. D.; Douglass, D. L. *Oxid. Met.* **1974**, *8*, 139.
235. Doychak, J.; Rühle, M. *Oxid. Met.* **1989**, *31*, 431.
236. Schumann, E.; Rühle, M. *Acta Metall. Mater.* **1994**, *42*, 1481.
237. Alexander, K. B.; Prussner, K.; Hou, P. Y.; Tortorelli, P. F. In *Microscopy of Oxidation*; Newcomb, S. B., Little, J. A., Eds.; The Institute of Metals, 1997; Vol. 3, pp 246–264.
238. Zhang, X. F.; Thaidigsmann, K.; Ager, J.; Hou, P. Y. *J. Mater. Res.* **2006**, *21*, 1409–1419.
239. Renusch, D.; Grimsditch, M.; Koshelev, I.; Veal, B. W.; Hou, P. Y. *Oxid. Met.* **1997**, *48*, 471.
240. Wagner, C. *Corros. Sci.* **1965**, *5*, 751.
241. Hou, P. Y. *J. Am. Ceram. Soc.* **2003**, *86*, 660–668.
242. Wood, G. C.; Hodgkiess, T. *Nature* **1966**, *211*, 1358–1361.
243. Sauer, J. P.; Rapp, R. A.; Hirth, J. P. *Oxid. Met.* **1982**, *18*, 285–294.
244. Jedlinski, J.; Borchardt, G.; Bernaski, A.; Scherrer, S.; Ambos, R.; Rajchel, B. In *Microscopy of Oxidation*; Newcomb, S. B., Bennett, M. J., Eds.; The Institute of Metals, 1993; Vol. 2, pp 445–454.
245. Quaddakkers, W. J.; Elschner, A.; Speier, W.; Nickel, H. *Appl. Surf. Sci.* **1991**, *52*, 271–287.

246. Smialek, J. L.; Gibala, R. *Metall. Trans. A* **1983**, *14A*, 2143–2161.
247. Pint, B. A. In *Fundamental Aspects of High Temperature Corrosion*; Shores, D. A., Rapp, R. A., Hou, P. Y., Eds.; Electrochemical Society, 1996; pp 74–85.
248. Brumm, M. W.; Grabke, H. J. *Corros. Sci.* **1992**, *33*, 1677–1690.
249. Yang, J. C.; Schumann, E.; Levin, I.; Ruhle, M. *Acta Mater.* **1998**, *46*, 2195–2201.
250. Andoh, A.; Taniguchi, S.; Shibata, T. *Mater. Sci. Forum* **2001**, *369–372*, 303–310.
251. Yang, J. C.; Nadarzinski, K.; Schumann, E.; Rühle, M. *Scripta Metall.* **1995**, *33*, 1043–1048.
252. Sigler, D. R. *Oxid. Met.* **1991**, *36*, 57–80.
253. Hagel, W. C. *Corrosion* **1965**, *21*, 316.
254. Jedlinski, J. *Oxid. Met.* **1993**, *39*, 55–60.
255. Frémy, N.; Maurice, V.; Marcus, P. *Surf. Interf. Anal.* **2002**, *34*, 519–523.
256. Doychak, J.; Ruhle, M. *Oxid. Met.* **1989**, *31*, 431–452.
257. Yang, J. C.; Schumann, E.; Müllejans, H.; Rühle, M. *J. Phys. D: Appl. Phys.* **1996**, *29*, 1716–1724.
258. Doychak, J. K. Doctoral thesis, Case Western Reserve University: Cleveland, OH, 1986.
259. Yang, J. C.; Schumann, E.; Levin, I.; Rühle, M. *Acta Metall.* **1998**, *46*, 2195–2201.
260. Hou, P. Y.; Paulikas, A. P.; Veal, B. W. *Mater. High Temp.* **2006**, *22*, 373–381.
261. El Kadiri, H.; Molins, R.; Bienvenu, Y.; Horstemeyer, M. F. *Oxid. Met.* **2005**, *64*, 63–97.
262. Lipkin, D. M.; Schaffer, H.; Adar, F.; Clarke, D. R. *Appl. Phys. Lett.* **1997**, *70*, 2550–2552.
263. Tolpygo, V. K.; Clarke, D. R. *Mater. High Temp.* **2000**, *17*, 59–70.
264. Steiner, C. J. -P.; Hasselman, D. P. H.; Spriggs, R. M. *J. Am. Ceram. Soc.* **1971**, *54*, 412–413.
265. Schutze, M. In *Proceedings of the Workshop on High Temperature Corrosion of Advanced Materials and Protective Coatings*; Saito, Y., Onay, B., Maruyama, T., Eds.; Elsevier Science, 1992; pp 39–49.
266. Lessing, P. A.; Gordon, R. S. *J. Mater. Sci.* **1977**, *12*, 2291–2302.
267. Ikuma, Y.; Gordon, R. S. *J. Am. Ceram. Soc.* **1983**, *66*, 139–147.
268. Hollenberg, G. W.; Gordon, R. S. *J. Am. Ceram. Soc.* **1973**, *56*, 140–147.
269. Sugita, T.; Pask, J. A. *J. Am. Ceram. Soc.* **1970**, *53*, 609–613.
270. Cho, J.; Harmer, M. P.; Chan, H. M.; Richman, J. M.; Thompson, A. M. *J. Am. Ceram. Soc.* **1997**, *80*, 1013–1017.
271. Wang, C. M.; Cho, J.; Chan, H. M.; Harmer, P.; Richman, J. M. *J. Am. Ceram. Soc.* **2001**, *84*, 1010–1016.
272. Hou, P. Y.; Zhang, X. F.; Cannon, R. M. *Scripta Metall.* **2004**, *51*, 45–49.
273. Levin, E. M. Robbins, C. R.; McMurdie, H. F. Eds. *Phase Diagram for Ceramists*; The American Ceramic Society, 1964; p 309.
274. Drahus, M. D.; Chan, H. M.; Rickman, J. M.; Harmer, M. P. *J. Am. Ceram. Soc.* **2005**, *88*, 3369–3373.
275. Muan, A. *Am. J. Sci.* **1958**, *256*, 413–422.
276. Novokhatskii, I. A.; Velov, B. F.; Gorokh, A. V.; Savinskaya, A. A. *Russ. J. Phys. Chem.* **1965**, *39*, 1498–1499.
277. Wright, I. G.; Pint, B. A.; Tortorelli, P. F. *Oxid. Met.* **2001**, *55*, 333–337.
278. Pint, B. A.; More, K. L.; Tortorelli, P. F.; Porter, W. D.; Wright, I. G. *Mat. Sci. Forum* **2001**, *369–372*, 411–418.
279. Pint, B. A.; Garratt-Reed, A. J.; Hobbs, L. W. In *Microscopy of Oxidation*; Newcomb, S. B., Bennett, M. J., Eds.; The Institute of Materials, 1993; Vol. II, pp 463–475.
280. Pint, B. A.; Hobbs, L. W. *Proc. Electrochem. Soc.* **1992**, 92–100.
281. Pint, B. A.; Hobbs, L. W. *Oxid. Met.* **1994**, *41*, 203–233.
282. Pint, B. A.; Garratt-Reed, A. J.; Hobbs, L. W. *J. Phys IV.* **1993**, *C9-3*, 247–256.
283. Pint, B. A.; Alexander, K. B. *J. Electrochem. Soc.* **1998**, *145*, 1819–1829.
284. Sheasby, J. S.; Jory, D. B. *Oxid. Met.* **1978**, *12*, 527–539.
285. Felten, E. J.; Pettit, F. S. *Oxid. Met.* **1976**, *10*, 189–223.
286. Giggins, C. S.; Pettit, F. S. *J. Electrochem. Soc.* **1971**, *118*, 1782–1790.
287. Tien, J. K.; Pettit, F. S. *Metall. Trans.* **1972**, *3*, 1587–1599.
288. Pettit, F. S. *AIME Met. Soc. Trans.* **1967**, *239*, 1296–1305.
289. Stasik, M. S.; Pettit, F. S.; Meier, G. H.; Ashary, A.; Smialek, J. L. *Scripta Metall. Mater.* **1994**, *31*, 1645–1650.
290. Sarioglu, C.; Stiger, M. J.; Blachere, J. R.; Janakiraman, R.; Schumann, E.; Ashary, A.; Pettit, F. S.; Meier, G. H. *Mater. Corros.* **2000**, *51*, 358–372.
291. Hindam, H. M.; Smeltzer, W. W. *J. Electrochem. Soc.* **1980**, *127*, 1622–1630.
292. Smialek, J. L. *Metall. Trans. A* **1978**, *9A*, 309–320.
293. Smialek, J. L.; Gibala, R. In *High Temperature Corrosion*; Rapp, R. A., Ed.; NACE: Houston, TX, 1981; pp 274–283.
294. Nanko, M.; Ozawa, M.; Maruyama, T. *J. Electrochem. Soc.* **2000**, *147*, 283–288.
295. Xu, C. H.; Gao, W.; Gong, H. *Intermetallics* **2000**, *8*, 769–779.
296. Kuenzly, J. D.; Douglass, D. L. *Oxid. Met.* **1974**, *6*, l39–l78.
297. Kumar, A.; Nasrallah, M.; Douglass, D. L. *Oxid. Met.* **1974**, *8*, 227–263.
298. Golightly, F. A.; Stott, F. H.; Wood, G. C. *J. Electrochem. Soc.* **1979**, *126*, 1035–1042.
299. Kahn, A. S.; Lowell, C. E.; Barrett, C. A. *J. Electrochem Soc.* **1980**, *127*, 670–679.
300. Nicolas-Chaubet, D.; Haut, C.; Picard, C.; Millot, F.; Huntz, A. M. *Mater. Sci. Eng. A.* **1989**, *120–121*, 83–89.
301. Amano, T.; Yajima, S.; Saito, Y. *Trans. Jpn. Inst. Met.* **1979**, *20*, 431–441.
302. Amano, T.; Yajima, S.; Saito, Y. *Trans. Jpn. Inst. Met.* **1985**, *26*, 433–443.
303. Hou, P. Y.; Cannon, R. M.; Zhang, H.; Williamson, R. L. In *Fundamental Aspects of High Temperature Corrosion*; ECS Fall Meeting, San Antonio, TX, 6–11 October 1996; Shores, D. A., Rapp, R. A., Hou, P. Y., Eds.; Electrochemical Society: Pennington, PA, 1997; ECS Proceedings, Vol. 96-26, pp 28–40.
304. Tolpygo, V. K.; Clarke, D. R. *Acta Metall.* **1998**, *46*, 5135–5166.
305. Kroger, F. A. *Ann. Rev. Mater. Sci.* **1977**, *7*, 449–475.
306. Tolpygo, V. K.; Clarke, D. R.; Murphy, K. S. *Metall. Trans. A* **2001**, *32*, 1467–1478.
307. Jedlinski, J.; Borchardt, G.; Mrowec, S. *Solid State Ionics* **1992**, *50*, 67–74.
308. Hindam, H. M.; Smeltzer, W. W. *Oxid. Met.* **1980**, *14*, 337–349.
309. Young, E. W. A.; De Wit, J. H. W. *Solid State Ionics* **1985**, *16*, 39–46.
310. Reddy, K. P. R.; Smialek, J. L.; Cooper, A. R. *Oxid. Met.* **1982**, *17*, 429–449.
311. Jedlinski, J.; Borchardt, G. *Oxid. Met.* **1991**, *36*, 317–337.
312. Quadakkers, W. J.; Elschner, A.; Speier, W.; Nickel, H. *Appl. Surf. Sci.* **1991**, *52*, 271–287.
313. Prescott, R.; Mitchell, D. F.; Sproule, G. I.; Graham, M. J. *Solid State Ionics* **1992**, *53–56*, 229–237.
314. Pint, B. A.; Martin, J. R.; Hobbs, L. W. *Oxid. Met.* **1993**, *39*, 167–195.

315. Mennicke, C.; Schumann, E.; Ruhle, M.; Hussey, R. J.; Sproule, G. I.; Graham, M. J. *Oxid. Met.* **1998**, *49*, 455–466.
316. Basu, S. N.; Halloran, J. W. *Oxid. Met.* **1987**, *27*, 143–155.
317. Oishi, Y.; Kingery, W. D. *J. Chem. Phys.* **1960**, *33*, 480–486.
318. Reddy, K. P. R.; Cooper, A. R. *J. Am. Ceram. Soc.* **1982**, *65*, 634–638.
319. Oishi, Y.; Ando, V.; Suga, N.; Kingery, W. D. *J. Am. Ceram. Soc.* **1983**, *66*, C130–C131.
320. Le Gall, M.; Huntz, A. M.; Lesage, B.; Monty, C.; Bernardini, J. *J. Mater. Sci.* **1995**, *30*, 201.
321. Reed, D. J.; Wuensch, B. J. *J. Am. Ceram. Soc.* **1980**, *63*, 88–92.
322. Lagerlof, K. P. D.; Peltka, B. J.; Mitchell, T. E.; Heuer, A. H. *Rad. Effects* **1983**, *74*, 87–107.
323. Prot, D.; Monty, C. *Philos. Mag.* **1996**, *73*, 899–917.
324. Paladino, A. E.; Kingery, W. D. *J. Chem. Phys.* **1962**, *37*, 957–962.
325. Le Gall, M.; Lesage, B.; Bernardini, J. *Philos. Mag.* **1994**, *70*, 761–773.
326. Cannon, R. M.; Rhodes, W. H.; Heuer, A. H. *J. Am. Ceram. Soc.* **1980**, *63*, 46–53.
327. Glaeser, A. M.; Evans, J. W. *Acta Metall.* **1986**, *34*, 1545.
328. Cannon, R. M.; Hou, P. Y. In *High Temperature Corrosion and Materials Chemistry*; Hou, P. Y., McNallan, M. J., Oltra, R., Opila, E. J., Shores, D. A., Eds.; The Electrochemical Society, 1998; pp 594–607.
329. Lipkin, D. M.; Clarke, D. R. *Oxid. Met.* **1996**, *45*, 267–280.
330. Hutchings, R.; Loretto, M. H.; Smallman, R. E. *Met. Sci.* **1981**, *15*, 7.
331. Brumm, M. W.; Grabke, H. J. *Corros. Sci.* **1993**, *34*, 547.
332. Pint, B. *Oxid. Met.* **1997**, *48*, 303.
333. Rommerskirchen, I.; Eltester, B.; Grabke, H. J. *Mater. Corros.* **1996**, *47*, 646.
334. Xu, C. H.; Gao, W.; Gong, H. *High Temp. Mater. Proc.* **2000**, *19*, 371.
335. Hou, P. Y.; Niu, Y.; Van Lienden, C. *Oxid. Met.* **2003**, *59* (1/2), 41–61.
336. Dravnieks, A.; McDonald, H. J. *J. Electrochem. Soc.* **1948**, *94*, 139.
337. Dobson, P. S.; Smallman, R. E. *Proc. R. Soc. Lond. A* **1966**, *293*, 423.
338. Kumar, A.; Nasrallah, M.; Douglass, D. L. *Oxid. Met.* **1974**, *8*, 227.
339. Hales, R.; Smallman, R. E.; Dobson, P. S. *Proc. R. Soc. Lond. A* **1968**, *307*, 71.
340. Douglass, D. L. *Mater. Sci. Eng.* **1969**, *3*, 255.
341. Evans, H. E. *Mater. Sci. Technol.* **1988**, *4*, 1089.
342. Pieraggi, B.; Rapp, R. A.; Hirth, J. P. *Oxid. Met.* **1995**, *44*, 63.
343. Harris, J. *Acta Metall.* **1978**, *26*, 1033.
344. Zimmermann, D.; Bobeth, M.; Ruhle, M.; Clarke, D. R. *Zeit. Metall.* **2004**, *95*, 84–90.
345. Hou, P. Y.; Van Lienden, C. *Mater. High Temp.* **2003**, *20*, 357.
346. Grabke, H. J.; Wiemer, D.; Viefhaus, H. *Appl. Surf. Sci.* **1991**, *47*, 243.
347. Hou, P. Y.; Stringer, J. *J. Phys* **1993**, *4*(C9), 231–240.
348. Golightly, F. A.; Stott, F. H.; Wood, G. C. *Oxid. Met.* **1976**, *10*, 163.
349. Tolpygo, V. K.; Clarke, D. R. *Acta Mater.* **1998**, *46*, 5153.
350. Wood, G. C.; Stott, F. H. *Mater. Sci. Technol.* **1987**, *3*(7), 519.
351. Suo, Z. *J. Mech. Phys. Solids* **1995**, *43*, 829.
352. Yang, Z. G.; Hou, P. Y. *Mater. Sci. Eng. A* **2005**, *391*(1/2), 1–9.
353. Wright, J. K.; Williamson, R. L.; Renusch, D.; Veal, B.; Grimsditch, M.; Hou, P. Y.; Cannon, R. M. *Mater. Sci. Eng. A* **1999**, *262*, 246.
354. Balint, D. S.; Xu, T.; Hutchinson, J. W.; Evans, A. G. *Acta Metall.* **2006**, *54*, 1815–1820.
355. Davis, A. W.; Evans, A. G. *Metall. Trans.* **2006**, *A37A*, 2085–2095.
356. Schutze, M.; Saito, Y.; Onay, B.; Maruyama, T. Proceedings of the Workshop on High Temperature Corrosion of Advanced Materials and Protective Coatings; Saito, Y., Onay, B., Maruyama, T., Eds.; Elsevier Science, 1992; pp 39–49.
357. Whittle, D. P.; Stringer, J. *Philos. Trans. R. Soc. London A* **1980**, *295*, 309.
358. Przybylski, K.; Garrett-Reed, A. J.; Pint, B. A.; Katz, E. P.; Yurek, G. J. *J. Electrochem. Soc.* **1987**, *134*, 3207.
359. Cotell, C. M.; Yurek, G. J.; Hussey, R. J.; Mitchell, D. F.; Graham, M. J. *Oxid. Met.* **1990**, *34*, 173–200.
360. Tolpygo, V. K.; Grabke, H. J. *Scripta Metall.* **1998**, *38*, 123–129.
361. Delaunay, D.; Huntz, A. M.; Lacombe, P. *Corros. Sci.* **1984**, *24*, 13–25.
362. Funkenbusch, A. W.; Smeggil, J. G.; Bornstein, N. S. *Metall. Trans.* **1985**, *16A*, 1164–1166.
363. Smialek, J. L. *Metall. Trans.* **1991**, *22A*, 739–752.
364. Pfeil, L. B. U.K. Patent No. 459848, 1937.
365. Pfeil, L. B. U. K. Patent No. 574088, 1945.
366. Pint, B. A. In *Proceedings of John Stringer Symposium on High Temperature Corrosion*; ASM Materials Solution Conference, Indianapolis, IN, 5–8 November 2001; Tortorelli, P., Wright, I. W., Hou, P. Y., Eds.; ASM International: OH, 2003; pp 52–62.
367. Pint, B. A. In *Fundamental Aspects of High Temperature Corrosion*; Shores, D. A., Rapp, R. A., Hou, P. Y., Eds.; Electrochemical Society, 1997; Vol. 96-26, pp 74–85.
368. Stringer, J.; Hou, P. Y. In *Proceedings of the Symposium on Corrosion and Particle Erosions at High Temperatures*; TMS Annual Meeting, Las Vegas, NV, 27 February–3 March; Srinivasan, V., Vedula, K., Eds.; 1989; pp 383–401.
369. Jedlinski, J.; Godlewski, K.; Mrowec, S. *Mater. Sci. Eng. A* **1989**, *120–121*, 539–543.
370. Hou, P. Y.; Brown, I.; Stringer, J. *Nucl. Inst. Meth. B* **1991**, *59/60*, 1345–1349.
371. Pint, B. A. *J. Am. Ceram. Soc.* **2003**, *86*, 686–695.
372. Pint, B. A. *Oxid. Met.* **1998**, *49*, 531–559.
373. Pint, B. A.; More, K. L.; Wright, I. G. *Mater. High Temp.* **2003**, *20*, 375–386.
374. Hou, P. Y.; Stringer, J. *Oxid. Met.* **1988**, *29*, 45–73.
375. Davis, H. H.; Graham, H. C.; Kvernes, I. A. *Oxid. Met.* **1971**, *3*, 431.
376. Stringer, J.; Wilcox, B. A.; Jaffee, R. L. *Oxid. Met.* **1972**, *5*, 11.
377. Seltzer, M. S.; Wilcox, B. A.; Stringer, J. *Met. Trans.* **1972**, *3*, 2391; Seltzer, V. *J. Metal Trans*. **1972**, *3*, 2357.
378. Nanni, P.; Stoddart, C. T. H.; Hondros, E. D. *Mater. Chem.* **1976**, *1*, 297.
379. Pint, B. A.; Leibowitz, J.; DeVan, J. H. *Oxid. Met.* **1999**, *51*, 183–199.
380. Pint, B. A.; Garratt-Reed, A. J.; Hobbs, L. W. *Mater. High Temp.* **1995**, *13*, 3–16.
381. Giggins, C. S.; Pettit, F. S. *Trans. TMS–TIME* **1969**, *245*, 2509.
382. Li, M. S.; Qian, Y. H.; Zhou, Y. C. *Oxid. Met.* **2004**, *61*, 529.
383. Huang, K.; Hou, P. Y.; Goodenough, J. B. *Mater. Res. Bull.* **2001**, *36*, 81–95.
384. Giggins, C. S.; Pettit, F. S. *Met. Trans.* **1971**, *2*, 1071.
385. Tolpygo, V. K.; Clarke, D. R. *Mater. High Temp.* **2003**, *20*, 261–271.

386. Nychka, J. A.; Clarke, D. R. *Oxid. Met.* **2005**, *63*, 325–352.
387. Dickey, E. C.; Pint, B. A.; Alexander, K. B.; Wright, I. G. *J. Mater. Res.* **1999**, *14*, 4531–4540.
388. Ishii, K.; Kohno, M.; Ishikawa, S.; Satoh, S. *Mater. Trans., JIM (Japan)* **1997**, *38*, 787–792.
389. Mennicke, C.; Schumann, E.; Le Coze, J.; Smialek, J. L.; Meier, G. H.; Ruhle, M. In *Microscopy of Oxidation*; Newcomb, S. B., Little, J. A., Eds.; Institute of Materials: UK, 1997; Vol. 3, pp 95–104.
390. Ramanarayanan, T. A.; Raghavan, M.; Petkovic-Luton, R. *Oxid. Met.* **1984**, *22*, 83–100.
391. Versaci, R. A.; Clemens, D.; Quadakkers, W. J.; Hussey, R. *Solid State Ionics* **1993**, *59*, 235–242.
392. Schumann, E.; Yang, J. C.; Ruhle, M.; Graham, M. J. *Oxid. Met.* **1996**, *46*, 37–49.
393. Pint, B. A. *Oxid. Met.* **1996**, *45*, 1–37.
394. Duffy, D. M.; Tasker, P. W. *Philos. Mag. A* **1984**, *50*, 155–169.
395. Lartigue-Korinek, S.; Dupau, F. *Acta Metall. Mater.* **1994**, *42*, 293–302.
396. Clarke, D. R. *Acta Metall.* **2003**, *51*, 1393–1407.
397. Hou, P. Y.; Stringer, J. *J. Electrochem. Soc.* **1987**, *134*, 1836–1849.
398. Hou, P. Y.; Shui, Z. R.; Chuang, G. Y.; Stringer, J. *J. Electrochem. Soc.* **1992**, *139*, 1119–1126.
399. Wood, G. C.; Stott, F. H. In *High Temperature Corrosion*; Rapp, R. A., Ed.; NACE, 1981; p 227.
400. Prescott, R.; Graham, M. J. *Oxid. Met.* **1992**, *38*(3/4), 233–254.
401. Strawbridge, A.; Hou, P. Y. *Mater. High Temp.* **1994**, *12*, 177–182.
402. Yang, S. L.; Wang, F. H.; Niu, Y.; Wu, W. T. *Mater. Sci. Forum* **2001**, *369–372*, 361–368.
403. Wu, Y. N.; Qin, M.; Feng, Z. C.; Liang, Y.; Sun, C.; Wang, F. H. *Mater. Lett.* **2003**, *57*(16–17), 2404–2408.
404. Hou, P. Y.; Paulikas, A. P.; Veal, B. W. *Mater. Sci. Forum* **2006**, *522–523*, 433–440.
405. Hindam, H.; Whittle, D. P. *Trans. Jpn. Inst. Met. Suppl.* **1983**, 261.
406. Allam, I. A.; Whittle, D. P.; Stringer, J. *Oxid. Met.* **1978**, *12*, 35; **1979**, *13*, 381.
407. Ideda, Y.; Nii, K.; Yoshihara, K. *Trans. Jpn. Inst. Met. Suppl.* **1983**, *24*, 207.
408. Lees, D. G. *Oxid. Met.* **1987**, *27*, 75.
409. Hou, P. Y.; Bennett, M. J.; Ruhle, M. In International Workshop on High Temperature Oxidation; Gorisch, Germany, 15–19 August 1994, Douglass, D. L., Kofstad, P., Rahmel, A., Wood, G. C., Eds.; *Oxid. Met.* **1996**; 45, pp 529–620.
410. Balluffi, W. In *Interfacial Segregation*; Johnson, W. C., Blakely, J. M., Eds.; ASM: Metals Park, OH, 1997; pp 193–237.
411. Seah, P.; Hondros, E. D. *Proc. R. Soc. Lond. A.* **1973**, *335*, 191–212.
412. Zhang, W.; Smith, J. R.; Wang, X. G.; Evans, A. G. *Phys. Rev. B.* **2003**, *67*, 245414.
413. Hou, P. Y. *J. Corr. Sci. Eng.* 2003, 6, Paper 75.
414. Al-Badary, H.; Tatlock, G.; Le Coze, J. In *Microscopy of Oxidation*; Newcomb, J. B., Little, J. A., Eds.; The Institute of Metals, 1997; Vol. 3, pp 105–114.
415. Fox, P.; Lees, D. G.; Lorimer, G. W. *Oxid. Met.* **1991**, *36*, 491–503.
416. Hou, P. Y.; Prüßner, K.; Fairbrother, D. H.; Roberts, J. G.; Alexander, V. *Scripta Metall.* **1999**, *40*, 241–247.
417. Prussner, K.; Schumann, E.; Ruhle, M. In *Proceedings of the Symposium Fundamental Aspects of High Temperature Corrosion*; Shores, D. A., Rapp, R. A., Hou, P. Y., Eds.; Electrochemical Society: Pennington, NJ, 1997; pp 344–351.
418. Molins, R.; Rouzou, I.; Hou, P. Y. *Mater. Sci. Eng. A* **2007**, *454–455*, 80–88.
419. Prüßner, K.; Schumann, E.; Rühle, M. In *Fundamental Aspects of High Temperature Corrosion*; Shores, D. A., Rapp, R. A., Hou, P. Y., Eds.; The Electrochemical Society, 1996; p 344.
420. Hou, P. Y.; Priimak, K. *Oxid. Met.* **2005**, *63*, 113–130.
421. Kiely, J. D.; Yeh, T.; Bonnell, D. A. *Surf. Sci.* **1997**, *393*, L126.
422. Hou, P. Y.; Smialek, J. L. *Scripta Metall.* **1995**, *33*, 1409–1416.
423. Hou, P. Y. *Oxid. Met.* **1999**, *52*, 337–351.
424. Pieraggi, B.; Rapp, R. A. *Mater. High Temp.* **1994**, *12*, 229–235.
425. Pieraggi, B.; Rapp, R. A.; Hirth, J. P. *Oxid. Met.* **1995**, *44*(1–2), 63–79.
426. Hong, Y.; Anderson, A. B.; Smialek, J. L. *Surf. Sci.* **1990**, *230*, 175–183.
427. Yong, J.; Smith, J. R.; Evans, A. G. γ-Ni/Al_2O_3 Adhesion: Aluminum Activity and Impurity Effects, Presented at the Workshop on Science and Technology of Thermal Barrier Systems, University of California, Santa Barbara, CA, 9–11 January 2007.
428. Strawbridge, A.; Rapp, R. A. *J. Electrochem. Soc.* **1994**, *141*, 1905–1915.
429. Czerwinski, F.; Szpunar, J. A.; Smeltzer, W. W. *J. Electrochem. Soc.* **1996**, *143*, 3000–3007.
430. George, P. J.; Bennett, M. J.; Bishop, H. E.; Cotell, C. M.; Garratt-Reed, A. J. *Surf. Coat. Technol.* **1992**, *51*(1–3), 45–51.
431. Ikeda, Y.; Nii, K.; Yoshihara, K. *Trans. Jpn. Inst. Met. Suppl.* **1983**, *24*, 207.
432. Smeggil, J. G. *Mater. Sci. Eng.* **1987**, *87*, 261–265.
433. Smialek, J. L.; Jayne, D. T.; Schaeffer, J. C.; Murphy, W. H. *Thin Solid Films* **1994**, *235*, 285–292.
434. Seah, P.; Hondros, E. D. *Proc. R. Soc. Lond. A* **1973**, *335*, 191–212.
435. Lipkin, D. M.; Clarke, D. R.; Evans, A. G. *Acta Met.* **1998**, *46*, 4835–4850.
436. Bonnell, D. A.; Kiely, J. *Phys. Stat. Sol.* **1998**, *166*, 7–17.
437. Grabke, H. J.; Wagemann, B. *Oxid. Met.* **1995**, *43*, 97–114.
438. Hou, P. Y. *Mater. Corros.* **2000**, *51*, 329.
439. Hou, P. Y.; Moskito, J. *Oxid. Met.* **2003**, *59*(5/6), 559–574.
440. Hou, P. Y. *J. Mater. Sci. Lett.* **2000**, *19*, 577–578.
441. Hou, P. Y. *Mater. Sci. Forum* **2001**, *369–372*, 23.
442. Rivoaland, L.; Maurice, V.; Josso, P.; Bacos, M. -P.; Marcus, P. *Oxid. Met.* **2003**, *60*, 137–157.
443. Hou, P. Y.; McCarty, K. F. *Scripta Metall.* **2006**, *54*, 937–941.
444. Cadoret, Y.; Bacos, M. -P.; Josso, P.; Maurice, V.; Marcus, P.; Zanna, S. *Mater. Sci. Forum* **2004**, *461–464*, 274.
445. Hou, P. Y.; Stringer, J. *Oxid. Met.* **1992**, *38*, 323–345.
446. Hou, P. Y. In *High Temperature Corrosion and Materials Chemistry*; Hou, P. Y., McNallan, M. J., Oltra, R., Opila, E. J., Shores, D. A., Eds.; The Electrochemical Society, 1998; pp 198–210.
447. Hou, P. Y. In *Proceedings of the John Stringer Symposium on High Temperature Corrosion*; ASM Materials Solution Conference, Indianapolis, IN, Nov. 5–8, 2001; Tortorelli, P., Wright, I. W., Hou, P. Y., Eds.; ASM International: OH, 2003; pp 164–173.
448. Murata, Y.; Nakai, M.; Nagai, K.; Morinaga, M.; Sasaki, Y.; Hashizume, R. *Mater. Sci. Forum* **2006**, *522–523*, 147–154.

449. Amano, T.; Watanabe, T.; Michiyama, K. *J. Jpn. Inst. Met.* **1997**, *61*, 1077–1085.
450. Quadakkers, W. J.; Wasserfuhr, C.; Khanna, A. S.; Nickel, H. *Mater. Sci. Technol.* **1988**, *4*(12), 1119–1125.
451. Huang, T. T.; Richter, R.; Chang, Y. L.; Pfender, E. *Metall. Trans. A* **1985**, *16A*, 2051–2059.
452. Molins, R.; Andrieux, M.; Huntz, A. M. *Mater. High Temp.* **2005**, *22*, 335–342.
453. Ben Abderrazik, G.; Moulin, G.; Huntz, A. M. *Oxid. Met.* **1990**, *33*, 191–235.
454. Mayer, J.; Penkalla, H. J.; Dimyati, A.; Dani, M.; Untoro, P.; Naumenko, D.; Quadakkers, W. J. *Mater. High Temp.* **2003**, *20*, 413–419.

1.11 Sulfidation and Mixed Gas Corrosion of Alloys

R. John
Shell Global Solutions (US) Inc., Westhollow Technology Center, P.O. Box 4327, Houston, TX 77210, USA

1.11.1 Sulfidation

1.11.1.1 Types of Equipment and Processes

Corrosion of metals and alloys used in equipment processing high temperature, corrosive, gases containing sulfur, H_2S, and COS is a concern in processes used in gas processing, combustion gas process heaters, petroleum refineries (hydrocracking, coking, vacuum flashing, hydrotreating, and catalytic reforming) coal/coke/oil gasification, petrochemical production, gasification of black liquor in pulp/paper production, and fossil fuel-fired power generation. Corrosion is often the phenomenon, which defines the maximum allowable temperature or maximum allowable gas species concentrations for metals and alloys in equipment.

1.11.1.2 Corrosion Mechanism

The key variables, which influence the kinetics are exposure time, partial pressures P_{H_2} and P_{H_2S} (for H_2 and H_2S gases) or P_{CO} and P_{COS} (for CO and COS gases), alloy composition and temperature. Sulfidation corrosion forms sulfide corrosion products, damages the metal and alloy by losses in wall thickness (penetration), and occurs upon exposure of metals to gases containing sulfur, COS, or H_2S. Sulfidation by H_2S is predominately discussed in this chapter. Sulfidation reduces the useful thickness of the metal by the formation of surface sulfide scale and internal sulfide phases. The sum of these two thicknesses is defined as the total metal penetration. The first step in determining the potential for equipment to sulfide is to assume that sulfidation is the dominant corrosion mechanism. The key indicator of sulfidation is that most of the corrosion products are sulfides. Sulfides will be found on the exposed surface and within the alloy microstructure near to the surface, depending upon the alloy and exposure conditions. X-ray analyses by diffraction and fluorescence of a surface scale sample are common methods to determine the presences of sulfides. An alternate

method is to evaluate the thermochemical interactions between the alloy and gas, and the compounds formed. Surface metal loss (scaling) by sulfidation can be detected by methods, which measure the metal thickness, such as ultrasonic and mechanical methods. Sound metal loss by internal sulfidation can only be detected by metallography, as shown schematically in Figure 1.

The time dependence of sulfidation has been controversial[1–5] with reports of a parabolic time dependence (metal loss proportional to time$^{0.5}$), linear time dependence (metal loss proportional to time), power law dependence (metal loss proportional to time^{x}), and various combinations of these dependencies. If the corrosion product sulfide scale remains undisturbed on the alloy surface and sufficient time has passed (in excess of 1000 h), currently available information suggests that the time dependence is parabolic. Removal or cracking of the surface sulfide scale tends to increase the rate of sulfidation, because the presence of the scale is a partial barrier, which tends to slow the sulfidation rate as time passes. The idealized time parabolic dependence of sulfidation of G10200 carbon steel at 350 °C in 0.05 atm H_2S in H_2 after several thousand hours is shown in Figure 2. Some studies suggest an initial linear time dependence for several thousand hours. Sulfidation data measured after several hundred hours (as is often the case for available data) are unlikely to be useful in estimating sulfidation corrosion rates for long-term service. Sulfidation data are properly used when the time dependence is considered.

Increasing the concentration of H_2S tends to increase the sulfidation rate of alloys. Figure 3 shows the effect of several alloys widely used in process equipment. Dashed lines represent extrapolations of the available data, while solid lines represent interpolations of the available data. The line for carbon steel stops for low concentrations of H_2S because FeS is not stable at low concentrations of H_2S (as shown in Figure 4), and the carbon steel cannot corrode at combinations of sufficiently high temperature and sufficiently low partial pressure of H_2S. It is incorrect to indicate that steels with significant concentrations of Cr cannot corrode at conditions representing low H_2S concentrations and high temperatures indicated by this line. This is because alloys with Cr form CrS at lower H_2S concentrations and higher temperatures

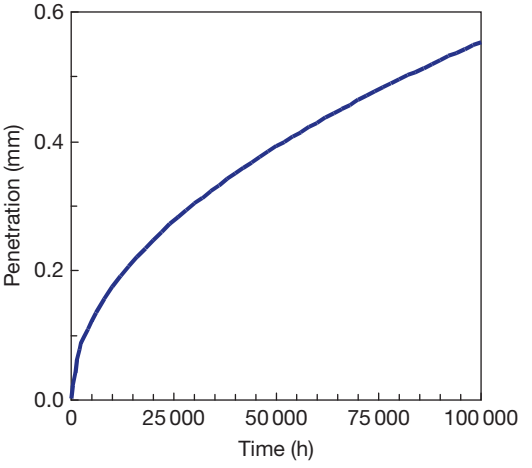

Figure 2 Effect of time upon the sulfidation corrosion of carbon steel (G10200) after 1 year in 0.05 atm H_2S and H_2 at 623 K.

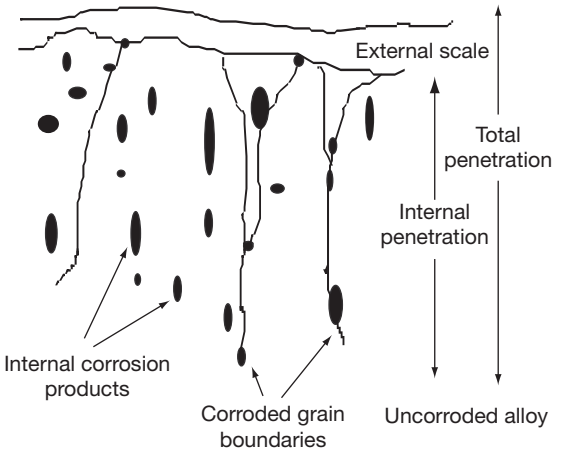

Figure 1 Schematic view of total penetration measurement for a typical corrosion product morphology.

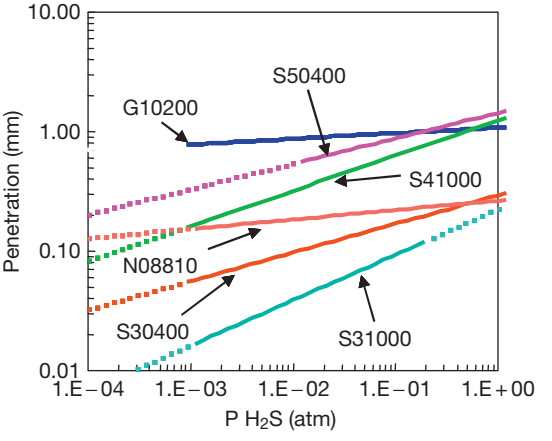

Figure 3 Effect of H_2S partial pressure upon the sulfidation corrosion after 1 year in H_2–H_2S gases at a total pressure of 1 atm at 723 K.

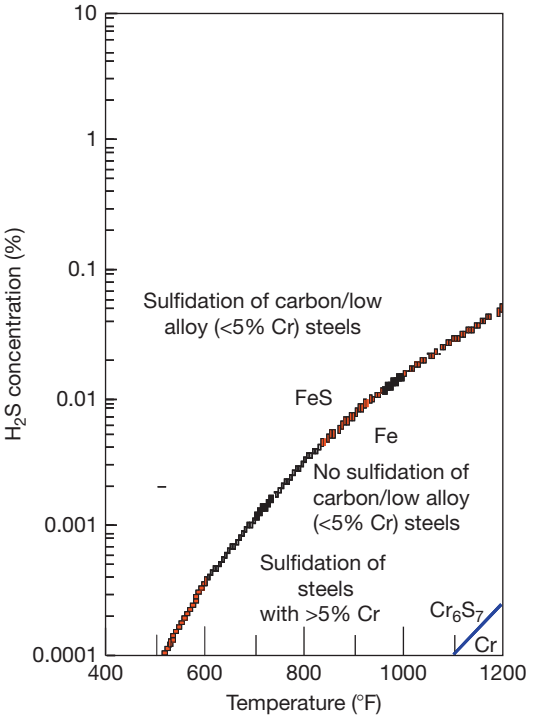

Figure 4 Conditions for possible sulfidation, based upon H_2S concentrations in H_2–H_2S gases and temperatures above the FeS/Fe line for carbon/low alloy (<5% Cr) steels and above the Cr_6S_7/Cr line for alloys with >5% Cr, 400–1200 °F (204–648 °C, 473–921 K).

than that needed to form FeS on steels. Figure 4 shows the limits of H_2S concentration and temperature corresponding to sulfide corrosion products of Fe and Cr, as shown beneath the lines. Alloys with greater than 5% Cr can corrode in conditions where low alloy steels cannot corrode. The corrosion rates may be low (such as 0.025–0.25 mm $year^{-1}$) but still significant for conditions where steels are traditionally thought to be immune to sulfidation. The ranges of H_2S concentration represented in Figures 3 and 4 span the low H_2S range of catalytic reformers to the high H_2S concentrations expected in modern hydrotreaters in crude oil distillation equipment in petroleum refineries. These curves are in good agreement with the traditional data.[1–5]

Sulfidation caused by sulfur-containing compounds in liquid hydrocarbons in the absence of a gas phase (such as that found in petroleum distilling units) is not discussed in this chapter. The sulfur concentrations in liquid hydrocarbons and the sulfur evolvable as gaseous H_2S have not yet been clearly related. However, the effective H_2 and H_2S concentrations are likely dominant variables in the liquid hydrocarbons. If the effective gas concentration of H_2S could be estimated, the approach discussed should be suitable for estimating the metal losses, as related to the maximum allowable temperatures/H_2S concentrations and appropriate materials of construction.

High-Ni alloys used either as base metals or as welding filler metals are a special concern in sulfidation conditions. Sulfidation of high-Ni alloys can be especially rapid and yield corrosion rates greater than 2.5 mm $year^{-1}$ if the temperature exceeds 530 °C, which is the melting point of a potential corrosion product which forms as a mixture of Ni and nickel sulfide. A reasonable approach for high-Ni alloys is that they should not be used in sulfidation conditions when metal temperatures will exceed 530 °C. High-Ni alloys with high-Cr levels (such as N06625 or N08825) can be very suitable, with low corrosion rates at lower temperatures.[6–8] The phase behaviors of FeS and NiS are described in Figures 5–8.

The first step in assessing the rate of sulfidation is to evaluate the potential for the formation of sulfide corrosion products. Confirmation of formation of sulfides on existing equipment or a thermochemical evaluation of the corrosive gas to produce sulfides may be done by the analyses of corrosion products, use of well-known compilations,[7–13] or ASSET program.[10] Once sulfidation is expected, one can predict sulfidation rates by using either the traditional sulfidation curves for corrosion in H_2S–H_2 gases or the curves of the type shown in previous work,[7–13] including the effects of temperature, gas composition, and alloy composition.

Most corrosion data for alloys exposed to high temperature gases have been reported in terms of weight change/area for relatively short exposures and inadequately defined exposure conditions. The weight change/area information is not directly relatable to the thickness of corroded metal (penetration), which is often needed to assess the strength of the equipment components. Corrosion is best reported in penetration units, which indicate the sound metal loss, as discussed earlier.[12,13] Corrosion in high temperature gases is affected by key parameters of the corrosive environments such as temperature, alloy composition, time, and gas composition. Summaries of metal penetrations are used in this chapter, which goes beyond the traditional corrosion weight change data by reporting total metal penetration for an extensive number of alloys over a wide range of conditions. Compositions of some alloys discussed in this chapter are shown in Table 1.

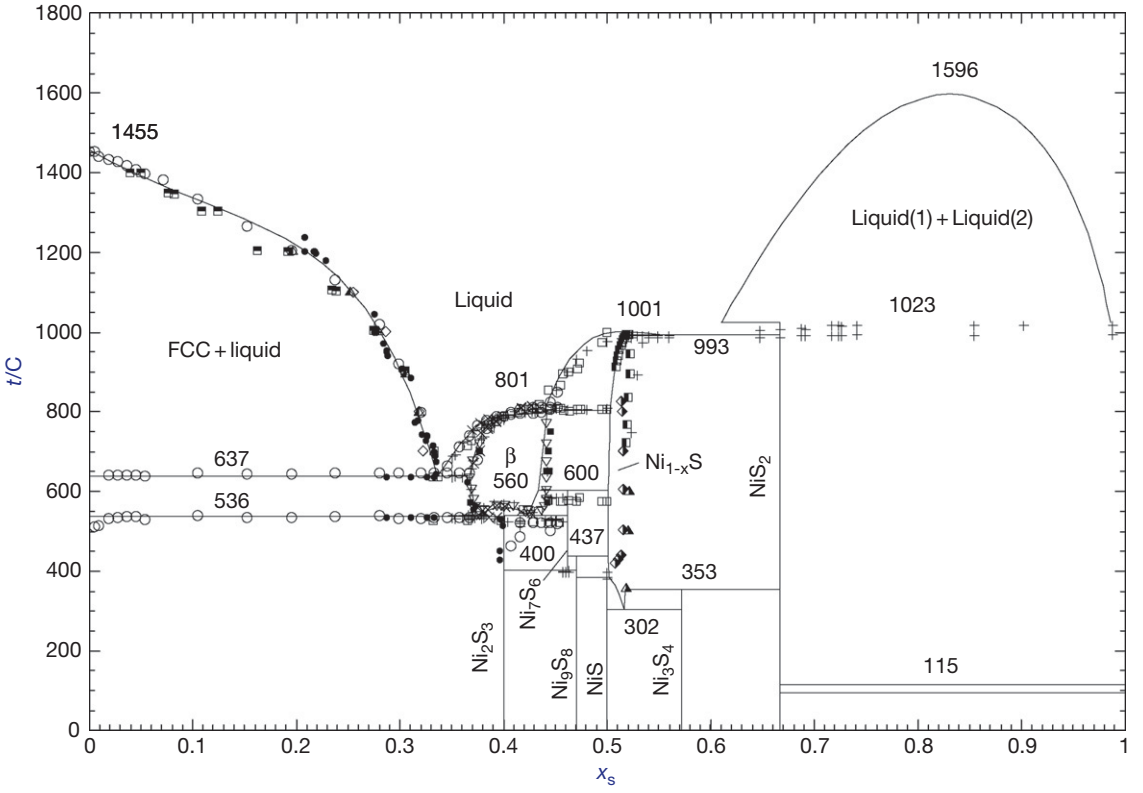

Figure 5 Calculated condensed phase diagram with experimental data for Ni–S system.

1.11.1.3 Compilations of Sulfidation Corrosion Rate Predictions

Sulfidation rate data for some commercial alloys are summarized in **Figures 9–12**. **Figure 9** shows sulfidation predictions of several simple metals (copper, carbon steel, and nickel). **Figure 10** shows sulfidation predications of a range of alloys often used in these types of conditions. **Figure 11** shows sulfidation predictions of some of the most resistant alloys available. **Figure 12** shows sulfidation predictions of several alloys similar to the 18% Cr–8% Ni steels. These steels experience different sulfidation rates, even though the Cr and Ni concentrations are similar. The different concentrations of Mo, Ti, and Nb among these alloys do significantly influence the sulfidation kinetics which is not well known; it is widely assumed that these steels corrode with kinetics similar to the common 18% Cr–8% Ni steel UNS S30400.

The effects of temperature and H_2S concentration upon sulfidation of steels often used in oil refining services are shown in **Figures 3** and **9–12**, which represent metal losses expected after 1 year of exposure. Increasing the temperature and H_2S concentration increase the sulfidation rate. Temperature increases of 50 °C will typically double the sulfidation rate, while increasing the H_2S concentration by a factor of 10 may be needed to double the sulfidation rate. Therefore, likely changes of H_2S concentrations in processes are generally less significant, in terms of influencing corrosion, than the likely temperature variations. Increasing the Cr content of the alloy greatly slows the sulfidation, as seen in progression from 9% Cr (S50400), 12% Cr (S41000), 18% Cr (S30400), 20% Cr (N08810), and 25% Cr (N08825 and N06625). The ranges of H_2S concentration represented in these figures span the low H_2S range of catalytic reformers to the high H_2S concentrations expected in modern hydrotreaters. These curves are in good agreement with the traditional data.[8–13]

1.11.1.4 Time Dependence to Predict Sulfidation

A large compilation of test data was evaluated with respect to the time dependence of the corrosion. The following rate equation can be used to calculate corrosion by sulfidation.[8] The equation incorporates the

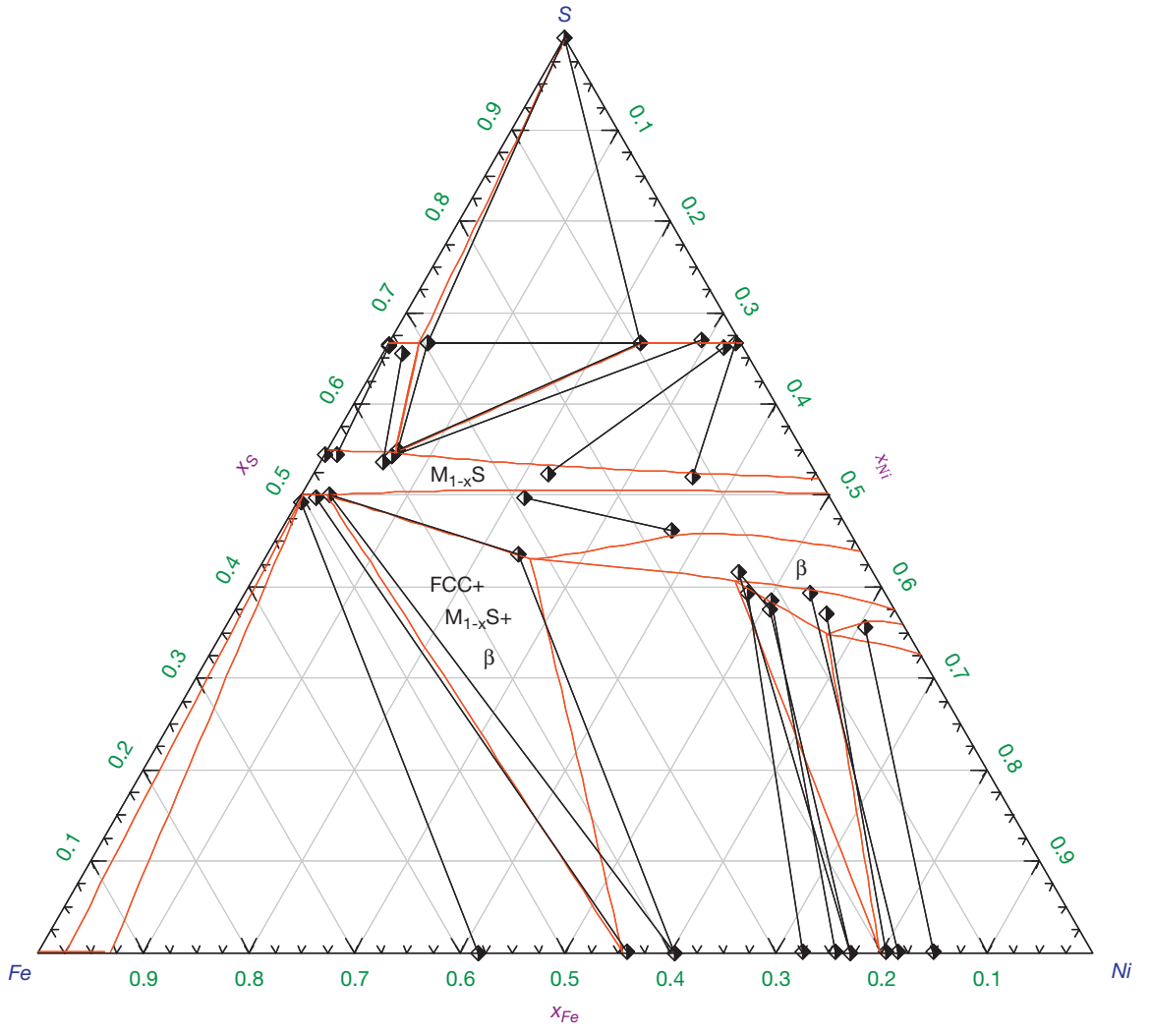

Figure 6 Calculated isotherm of the Fe–Ni–S system at 998 K.

well-known time parabolic and linear behaviors, which have been observed. Parabolic behavior occurs initially and then tends towards linear time dependence as the surface scales crack or partially spall as they thicken and become less adherent. The transition towards linear dependence often results from development of an effective steady-state thickness of surface corrosion product, as caused by cracking, spalling, or other failure mechanisms.

$$\log((\text{Penetration}/\text{Hours}^{0.5}) + (M \times \text{Hours})) = A + B \times \log(P_{H_2S}) + C \times \log(P_{H_2}) + D/T \quad [1]$$

In this equation, penetration represents sound metal loss by corrosion, T is the absolute temperature, and P_{H_2S} and P_{H_2} represent the partial pressures of the respective species. A, B, C, D, and M are constants that are calculated separately for each alloy. The form of the equation includes both linear and parabolic time dependencies. The M factor empirically describes how much time passes before the time dependence becomes linear and varies for each alloy.

Graphical illustrations of correlations for a couple of example alloys (S30400 and N08810) are shown in **Figure 13**. These alloys are fairly typical and in that Fe–Ni–Cr alloys are widely used in many different types of process equipment, and they are also well correlated with the methodology described in this article. In fact, the data are well correlated over about three orders of magnitude of variation in the measured corrosion for wide ranges in the important environmental variables of temperature, partial pressure of H_2, and partial pressure of H_2S.

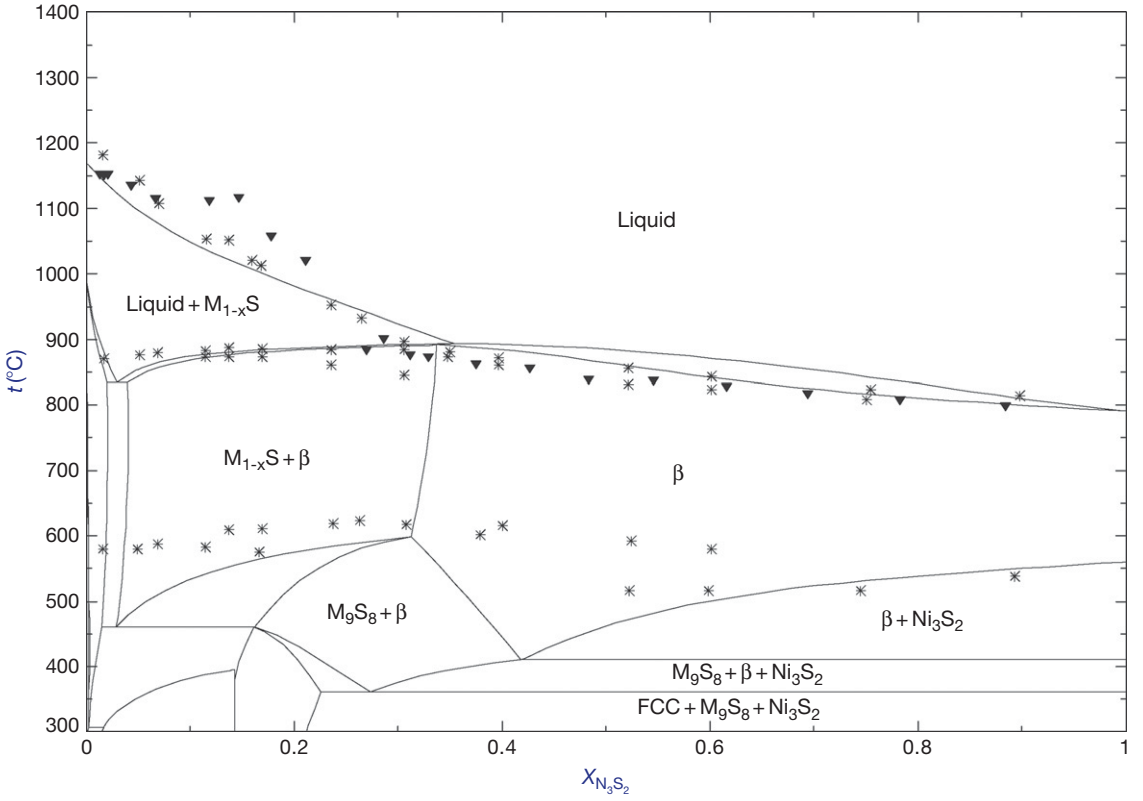

Figure 7 Calculated section of the FeS–Ni_3S_2 with experimental data.

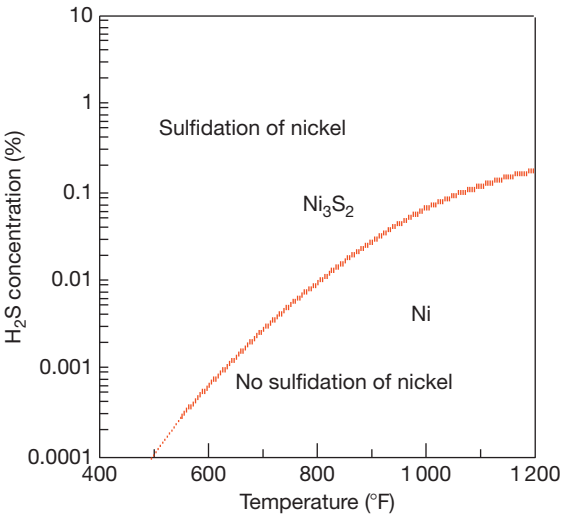

Figure 8 Conditions for possible sulfidation of nickel based upon combinations of H_2S concentrations in H_2–H_2S gases and temperatures above the Ni/Ni_3S_2 line for Ni-base alloys. 400–1200 °F (204–628 °C).

1.11.1.5 Laboratory Simulation

Laboratory simulation of sulfidation corrosion is generally carried out with flowing H_2–H_2S gases or CO–COS gases at constant temperature, starting with a polished metal surface. The combination of gas flow rate and H_2S (or COS) concentration must be high enough to prevent significant consumption of H_2S during the test exposures. Post-exposure examination is carried out with weight change and microscopic methods to assess the amount of metal consumed by scale formation and also the amount of the metal containing internal corrosion products.

1.11.2 Corrosion by Mixed Gases

The corrosion mechanism names for mixed gas corrosion indicate the stable alloy corrosion products formed and result from a competition between the different possibilities and are named after the corrosion

Table 1 Compositions of alloys discussed

UNS	Fe	Cr	Ni	Co	Mo	Al	Si	Ti	W	Mn	Cu	RE	Nb
S30415	69.66	18.30	9.50	0.00	0.42	0.00	1.23	0.00	0.00	0.56	0.23	0.05	0.00
S30815	65.60	20.90	11.00	0.00	0.00	0.00	1.77	0.00	0.00	0.64	0.00	0.00	0.00
N06025	9.45	25.35	62.63	0.00	0.00	2.09	0.06	0.14	0.00	0.09	0.01	0.00	0.00
S41000	86.50	12.30	0.50	0.00	0.10	0.00	0.60	0.00	0.00	0.00	0.00	0.00	0.00
G10200	99.42	0.00	0.00	0.00	0.00	0.00	0.04		0.00	0.38	0.00	0.00	0.00
S30400	71.07	18.28	8.13	0.14	0.17	0.00	0.49	0.00	0.00	1.48	0.19	0.00	0.00
S31000	52.41	24.87	19.72	0.05	0.16	0.00	0.68	0.00	0.00	1.94	0.11	0.00	0.00
S31600	68.75	17.00	12.00	0.00	2.25	0.00	0.00	0.00	0.00	0.00	0.00	0.00	0.00
S34700	68.14	17.75	10.75	0.00	0.00	0.00	0.55	0.00	0.00	1.80	0.00	0.00	0.96
S44600	74.12	24.36	0.36	0.02	0.20	0.00	0.33	0.00	0.00	0.45	0.10	0.00	0.00
R30188	1.32	21.98	22.82	38.00	0.00	0.00	0.37	0.00	14.55	0.82	0.00	0.04	0.00
N07214	2.49	16.04	76.09	0.14	0.10	4.71	0.10	0.00	0.10	0.20	0.00	0.00	0.00
N06230	1.30	21.90	59.70	0.28	1.20	0.38	0.42	0.02	14.20	0.49	0.01	0.00	0.00
R30556	32.50	21.27	21.31	18.09	2.88	0.17	0.33	0.00	2.38	0.96	0.00	0.00	0.00
N06600	7.66	15.40	75.81	0.00	0.00	0.32	0.16	0.00	0.00	0.29	0.32	0.00	0.00
N06601	13.53	23.48	60.00	0.06	0.16	1.26	0.50	0.27	0.00	0.31	0.38	0.00	0.00
N06617	0.76	22.63	53.20	12.33	9.38	1.15	0.15	0.27	0.00	0.02	0.05	0.00	0.00
N06625	2.66	21.74	62.79	0.00	8.46	0.10	0.41	0.19	0.00	0.10	0.00	0.00	3.52
N08810	44.22	21.22	31.71	0.00	0.00	0.33	0.60	0.41	0.00	0.92	0.51	0.00	0.00
C11000	0.00	0.00	0.00	0.00	0.00	0.00	0.00		0.00	0.00	100.00	0.00	0.00
N08120	34.53	25.12	37.44	0.11	0.37	0.11	0.57	0.02	0.10	0.73	0.18	0.00	0.66
N12160	8.00	28.00	34.30	27.00	0.00	0.00	2.70	0.00	0.00	0.00	0.00	0.00	0.00
S67956	75.22	19.40	0.28	0.05	0.00	4.50	0.11	0.33	0.00	0.09	0.00	0.00	0.00
N02270	0.00	0.00	99.99	0.00	0.00	0.00	0.00	0.00	0.00	0.00	0.00	0.00	0.00

RE means rare earth elements.

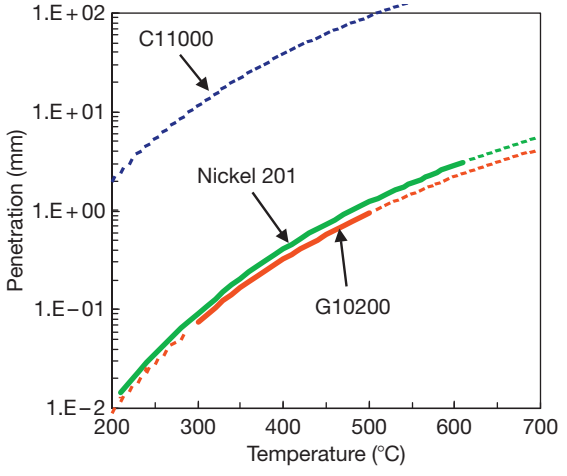

Figure 9 Effect of temperature upon sulfidation of some simple metals after 1 year in 0.5 atm H_2 and 0.05 atm H_2S.

products, which dominate. Examples are: sulfidation/oxidation means that sulfides and oxides form, oxidation/carburization means that carbides and oxides form, oxidation/nitridation means that nitrides and oxides form, and so on. Corrosion leads to the formation of corrosion products, which leads to metal loss (penetration), and occurs upon exposure of metals to gases, which contain the reactive species needed to form the corrosion products. An X-ray analysis by diffraction of a surface scale sample is a common method to determine the identity of corrosion products. An alternate method is to evaluate the gas composition. Surface metal loss (scaling) can be detected by methods, which measure the metal thickness, such as ultrasonic and mechanical methods. Sound metal loss by internal corrosion can only be detected by metallography, as schematically shown in Figure 1.

The time dependence of high temperature corrosion is controversial[3–5] and depends on the combination of alloy, temperature, time, and corrosion mechanism. Reported time dependencies include: parabolic (metal loss proportional to time$^{0.5}$), linear (metal loss proportional to time), power law (metal loss proportional to time^{x}), and various combinations of these dependencies. If the corrosion product scale remains undisturbed on the alloy surface and sufficient time has passed (in excess of 1000 h), a reasonable approximation is that the time dependence is parabolic. Removal or cracking

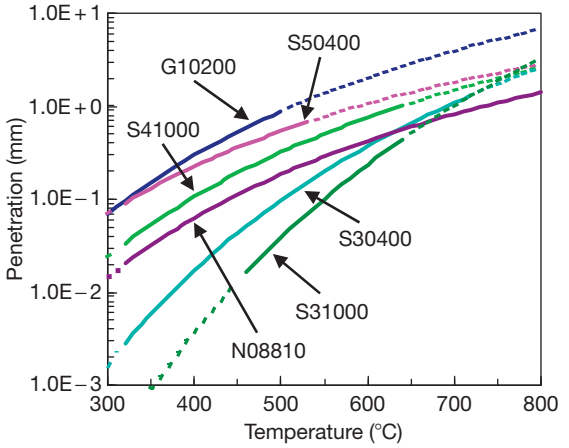

Figure 10 Effect of temperature upon sulfidation corrosion of some alloys commonly used in sulfidizing conditions after 1 year at 0.5 atm H_2 and 0.05 atm H_2S.

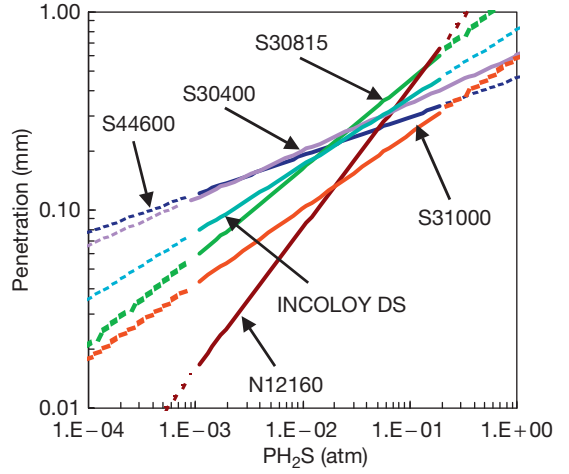

Figure 11 Effect of H_2S partial pressure upon sulfidation corrosion of some very resistant alloys at 550 °C after 1 year.

of the surface scale will tend to increase the rate of corrosion, because the presence of the scale is a partial barrier, which tends to slow corrosion as time passes, but corrosion still continues. Some studies suggest initial linear time dependence for several thousand hours. Corrosion data measured after hundreds of hours (as is often the case for available data) are unlikely to be useful in estimating sulfidation corrosion rates for long-term service. Corrosion data are properly used when the time dependence is considered. The corrosion mechanisms considered and some of the important variables are listed below:

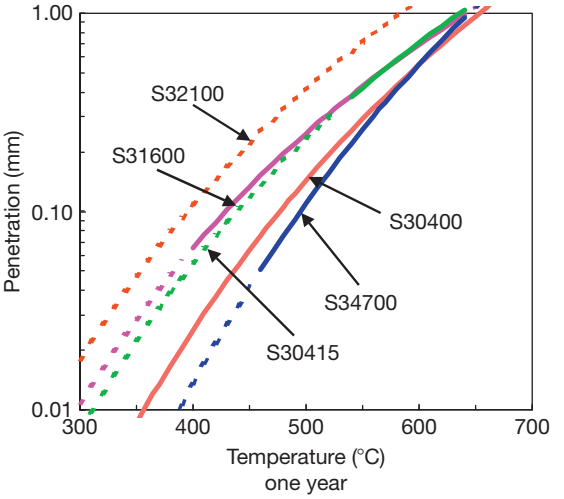

Figure 12 Effect of temperature upon sulfidation corrosion of '18-8' steels exposed to 0.5 atm H_2 and 0.05 atm H_2S after 1 year.

- Sulfidation/oxidation by CO–CO_2–COS and H_2–H_2O–H_2S gases – key variables, which influence the kinetics, are exposure time, P_{O_2}, P_{S_2}, alloy composition, and temperature;
- Oxidation/nitridation by O_2–N_2 gases – key variables, which influence the kinetics, are exposure time, partial pressures of O_2 and N_2, alloy composition, and temperature;
- Oxidation/carburization by CH_4–H_2O gases – key variables, which influence the kinetics, are exposure time, P_{O_2}, activity of carbon (a_C), alloy composition, and temperature.

1.11.2.1 Thermochemical Calculations to Predict Oxide–Sulfide–Carbide–Nitrides on Alloys

Since many alloys may be used in a wide range of gases, which can induce corrosion producing mixtures of corrosion products, it is wise to examine the types and combinations of potential corrosion products. One approach is to use thermochemical calculations to predict the stable corrosion products defined by equilibrium reactions between the alloy, gas, and alloy temperature. The surface of equipment exposed to large amounts of flowing gas can be approximated by a small amount of alloy exposed to a large amount of gas. For example, a ratio of 1 mol alloy to 1000 mol of gas will not deplete the gas of important corrosives in the calculation. This

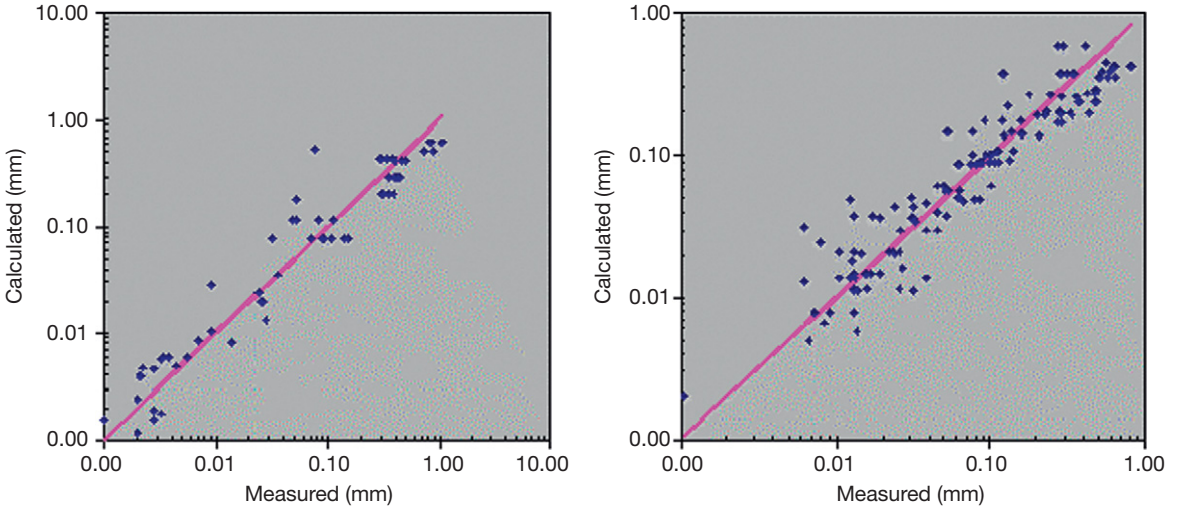

Figure 13 Example of correlations of sulfidation data for S30400 (left) and N08810 (right) using the formalism described in this chapter. Corrosion by mixed gases.

approach ignores differing reaction and diffusion rates of the species in the alloys and corrosion products. The calculation also assumes that the major elements in the alloys will determine the type of dominant corrosion products, which is typically true and will ignore any subtleties of corrosion product morphologies and kinetics.

To this end, a capability to perform thermochemical models for complex corrosion product phases was developed to enable the required calculations. The elements considered in the thermochemical calculations are:

W–La–Mo–Nb–Cu–Ni–Co–Fe–Mn–Cr–Ti–Ar–Cl–S–Si–Al–F–O–N–C–H

With all of the known corrosion product phases having been analyzed in terms of the thermochemical solution behaviors of the known species in each phase, the assumption of pure and single component condensed phases, which is a common assumption, is no longer required. In order to structure the calculations, the thermochemical literature was extensively reviewed. Thermochemical data such as free energies of formation, heat capacities, heats of mixing, heats of fusion, heats of evaporation, and second-order phase transition were also considered and compiled. Models were then constructed to describe the solution thermodynamics of the complex sulfide, alloys, carbides, oxides, and intermetallic phases, as described.[22–24] The elements considered to occur in the solution phases, are:

- Al–Co–Cr–Fe–Mn–Ni–Si–Ti in oxides,
- Fe–Ni–Co–Cr in sulfides,
- W–Mo–Nb–Cu–Ni–Co–Fe–Mn–Cr–Ti–Si–Al in carbides and nitrides,
- W–La–Mo–Nb–Cu–Ni–Co–Fe–Mn–Cr–Ti–Si–Al–N–C in the alloy liquid and solid-solution phases.

The effort included development of mathematical models, based on the known solutions and described the thermodynamic properties as functions of temperature and composition. The models were optimized using all the available thermodynamic and phase diagram data from the literature in order to obtain a set of model parameters for the two-component, three-component, and higher-order subsystems. The resulting models were then used to estimate the thermodynamic properties of the *N*-component solutions from the database of parameters for lower-order subsystems. Examples of the species groupings are listed below:

- Spinel – (Fe^{2+}, Fe^{3+}, Co^{2+}, Co^{3+}, Cr^{2+}, Cr^{3+}, Ni^{2+}, Mg, Al) [Fe^{2+}, Fe^{3+}, Co^{2+}, Co^{3+}, Cr^{3+}, Ni^{2+}, Mg, Al]$_2O_4$;
- Corundum – Fe_2O_3–Cr_2O_3–Al_2O_3;
- Monoxide – FeO–CoO–NiO–CaO–MgO–ZnO–CuO.

For oxide phases in the Fe–Co–Ni–Cr–O system, thermodynamic data are available mainly for the following subsystems:

- Fe–O, Co–O, Ni–O, Cr–O
- Fe–Cr–O, Fe–Ni–O, Fe–Co–O

The models were evaluated by comparison to the available thermodynamic and phase equilibrium data. Comparison between the model results and known phase diagrams indicated that the model predictions could reproduce the measured data within the experimental error limits from 25 °C to above the liquidus temperatures at all compositions and oxygen partial pressures from metal saturation to equilibrium with oxygen. Examples of the high-quality fits of the thermochemical models to the measured data are shown in **Figures 5–7**. The model for the sulfide liquid phase contains Fe–Ni–Co–Cr–S and uses the quasichemical model pair approximation[22–24] to take into account strong short-range ordering. For solid nonstoichiometric sulfide solutions in the Fe–Ni–Co–Cr–S system, appropriate thermodynamic models were developed. Parameters of these models were optimized to reproduce all solid–solid and solid–liquid phase equilibria.

The main data that were considered in the models were:

- Solid sulfide/liquid sulfide equilibrium, partial pressure data of S in the liquid sulfide over the whole composition range from pure metals to sulfur-rich liquid
- Sulfur activity over the liquid sulfide and over solid (Fe, Ni)S solutions
- Sulfide/metal/oxide/gas equilibria
- Heats of mixing, heat content, heat capacities, etc.
- Metal activity data
- Metal–liquid sulfide equilibrium data
- Liquid–oxide equilibrium data.

This technology is embodied in the ASSET (Alloy Selection System for Elevated Temperatures) technology and is widely available.[10,25,32,33]

1.11.2.2 Sulfidation/Oxidation by CO–CO_2–COS and H_2–H_2O–H_2S Gases

Sulfidation corrosion in the presence of oxidizing gases is called sulfidation/oxidation, which occurs when both sulfide and oxide corrosion products form. The key variables, which influence the kinetics, are exposure time, partial pressures of O_2 and S_2, in gases like CO–CO_2–COS or H_2–H_2O–H_2S or CO–CO_2–COS–H_2–H_2O–H_2S, alloy composition, and temperature. The corrosion leads to metal losses by both surface scaling and internal corrosion product formation (penetration).

Significant research has been carried out over the last 20 years by investigators such as Perkins,[14,15] Natesan,[16–18] Bakker,[19] and John[20,21] to define how the gas composition influences the kinetics of alloy corrosion in sulfidizing/oxidizing conditions. It is well accepted that the thermochemical interactions of the alloys and the exposure conditions influence the stabilities (and formation) of the corrosion products and the rates of corrosion. The referenced studies and others show that the corrosion products, which form may not necessarily be those expected, are based upon simplified thermochemical expectations using Fe–S–O, Cr–S–O, and Ni–S–O systems for the computations and assuming pure component corrosion products. In fact, gas mixtures corroding real alloys expected to form pure Cr_2O_3-type corrosion products actually require gas P_{O_2} values of 2 or 3 orders of magnitude greater than the calculated value thought to form Cr_2O_3. This has been interpreted to be a 'kinetic boundary,' meaning that an excess P_{O_2} value is needed to precipitate and grow the Cr_2O_3. This is different in concept from a thermochemical criterion for the relative stabilities of corrosion products, as defined by combinations of P_{O_2} and P_{S_2}, at a given temperature. It was suggested that the high growth rates of sulfides cause high P_{O_2}s required to form the Cr_2O_3-rich corrosion products. However, thermochemical calculations possible with the models now available can calculate the real corrosion product compositions. These thermochemical solution calculations now suggest that the 'kinetic boundaries' are really equilibrium phase boundaries, when the real phase compositions and thermochemistry are considered.

On the basis of the logic presented above, the strategy adopted by John[20,21] has been used to correlate sulfidation/oxidation corrosion with the relative stabilities of the Cr_2O_3 and CrS phases as expressed in terms of P_{O_2} and P_{S_2}, as shown below:

$$2CrS + 3/2O_2 = Cr_2O_3 + S_2 \quad [2]$$

$$\frac{P_{O_2}^{3/2} K_2}{P_{S_2}} = \frac{A_{Cr_2O_3}}{A_{CrS^2}} \quad [3]$$

where K_2 is the equilibrium constant for reaction [2]. A measure of the relative stability of Cr_2O_3 and CrS (or the activity factor AF), is defined below:

$$AF = \log(A_{CrS^2}/A_{Cr_2O_3}) \quad [4]$$

where A indicates the activity of the subscripted species. High AF values correspond to high activities of CrS (A_{CrS}) values and rapid corrosion, while low AF values reflect low A_{CrS} values and slow corrosion.

It has been experimentally well demonstrated that sulfidation/oxidation kinetics correlate with AF and that sulfidation/oxidation kinetics are parabolic with time, a parabolic rate constant is written in terms of the gas composition, as related by eqns [3] and [4] and then used to correlate corrosion by sulfidation/oxidation with exposure conditions:

$$\log(K_p) = A + B(\log(P_{S_2}) - 1.5\log(P_{O_2})) + C/T \quad [5]$$

where K_p is a parabolic rate constant for the reactions leading to total penetration, A, B, and C are experimentally determined constants, and T is temperature. This relationship has been demonstrated to correlate alloy corrosion by sulfidation/oxidation for many different alloys over wide ranges of temperatures and gas compositions.[8–10,20,21] An example of this type of correlation between measured corrosion and exposure conditions is shown in Figure 14 for a common heat-resistant alloy N06600. Once these types of correlations for an alloy are established, alloy corrosion in sulfidation/oxidation conditions can be made for many alloy/condition combinations. The utility of these correlations is obvious. Accurate predictions of sulfidation/oxidation for wide ranges of conditions in terms of gas composition, temperature, and time can be made and expressed in very practical engineering units related to change in wall thickness.

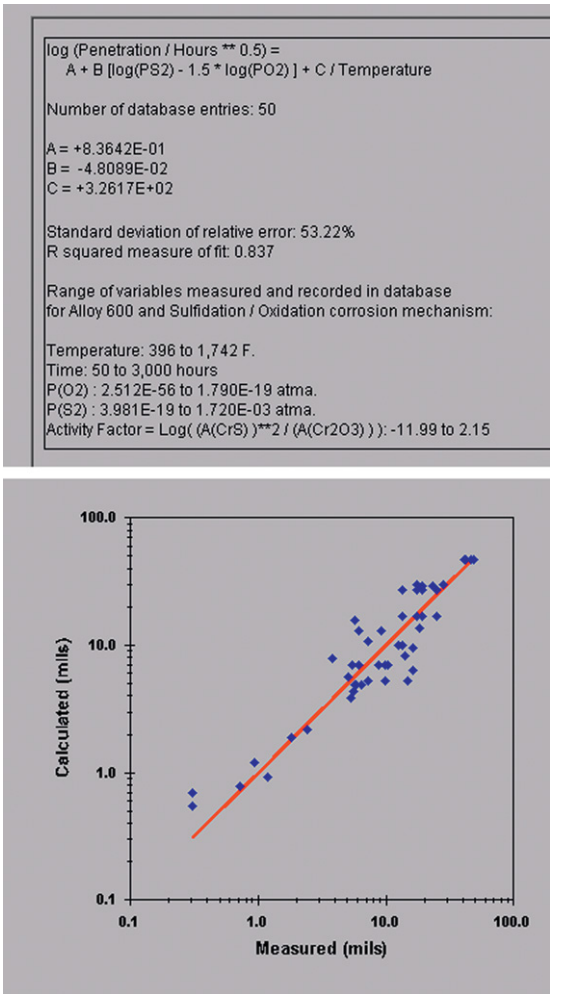

Figure 14 Illustration of sulfidation/oxidation correlation for alloy N06600 in various combination of exposure conditions, in terms of temperature, time, P_{O_2} and P_{S_2}.

1.11.2.3 Thermochemistry and Corrosion Mechanism

The utility to predict the formation of alloy corrosion products is illustrated in Figures 15–17. The results compare very well with practical experience and summarize the stable corrosion products for ranges of gas compositions and temperatures. Nickel-base alloys like N06600 and N06625 form liquid sulfide at temperatures slightly above 1100 °F (866 K), while an Fe–Cr–Ni stainless steel like S30400 and a heat-resistant Ni–Cr–Co alloy like N12160 form liquid sulfide corrosion products only at much higher temperatures. Nickel-base alloys form liquid nickel sulfide corrosion products, if any portion of the corrosion product layer is in conditions, which stabilize the liquid. Through the thickness of the corrosion product, one might think of a gradient of H_2S, as the corroding alloy at the alloy/corrosion product interface consumes sulfur species. Increasing the amount of Cr will increase the amount of oxide in the corrosion product for a nickel-base alloy (as found in N06025) but will not prevent the formation of the liquid sulfide. An iron-based stainless steel, like S30400, does not form liquid sulfide, but does form large amounts of solid sulfides. A Ni–Cr–Co alloy like N12160 with high concentrations of Cr, Si, and Co shows large concentrations of oxides and no liquid sulfide formation, until higher H_2S concentrations are present, which should be excellent for resistance to corrosion in these conditions, as is the case for the Ni–Cr–Co alloy.

1.11.2.4 Laboratory Simulation

It is important to remember that the usual goal of laboratory corrosion tests is to produce information, which will help decisions related to industrial equipment. Industrial equipment often requires lifetimes of years at high pressures, high temperatures

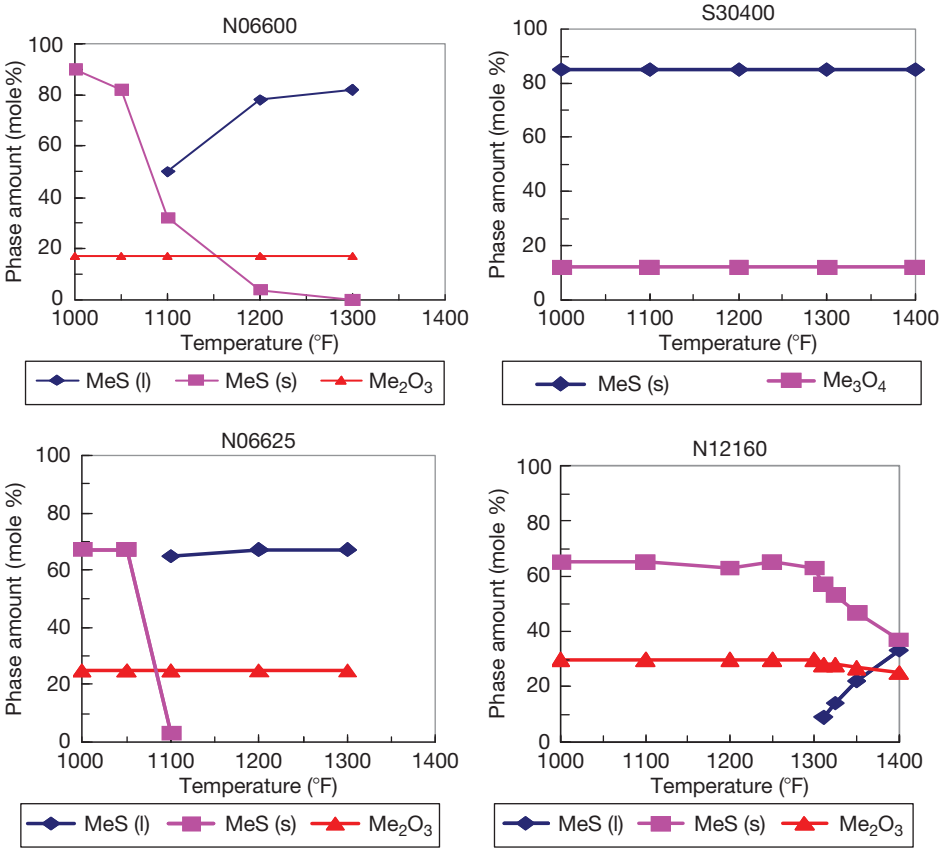

Figure 15 Calculated corrosion products for a small amount of alloy exposed to a large amount of 5% H_2–65% H_2–30% H_2O at 1 atm, 1000–1400 °F (811–1033 K).

and requires considerable expense and time to fabricate. Laboratory tests aim to quickly and cheaply define the likely corrosion phenomena and kinetics prior to building the industrial equipment. For the case of sulfidizing/oxidizing conditions, some important issues will now be discussed, including the effects of temperature, exposure time, and gas composition.

Laboratory corrosion tests often intend to accelerate corrosion relative to exposures in industrial equipment and to speed assessment of many alloys and their corrosion with coupons. This is cheaper, faster, and more reliable than gathering corrosion data by inspecting full-scale equipment in operating processes. Examples of process equipment where sulfidation/oxidation may occur are processes in petroleum refining such as hydrocrackers, hydrotreaters, coal/coke/oil gasifiers, crude-oil distilling columns, vacuum flashers, sulfur-removal plants, coking units, and flexicokers. Corrosion will be discussed in terms of the total metal penetration, which is defined as the sum of the metal lost by surface scale formation plus the thickness of the subsurface metal layer that is affected by the corrosion exposure. Such a subsurface layer may have internal precipitates of corrosion products, pores, voids, or cracks, which have been produced by reaction with the corrosive environment. This is illustrated in the schematic view of a cross section of a corroded alloy shown previously in **Figure 1**. Some of the alloys studied are shown in **Table 1**.

Many process gases contain H_2–H_2O–H_2S gas mixtures, which will determine the partial pressures of O_2 and S_2 (P_{O_2} and P_{S_2}) and which are in turn well known to determine the sulfidation/oxidation corrosion behaviors for Cr-containing alloys. As the following reactions show, chemical thermodynamics can be used to calculate the P_{O_2} and P_{S_2} values for C-based gases (CO–CO_2–COS):

$$CO + 1/2O_2 = CO_2 \quad [6]$$

$$K_{eqn[6]} = \frac{P_{CO_2}}{P_{O_2}^{1/2} P_{CO}} \quad [7]$$

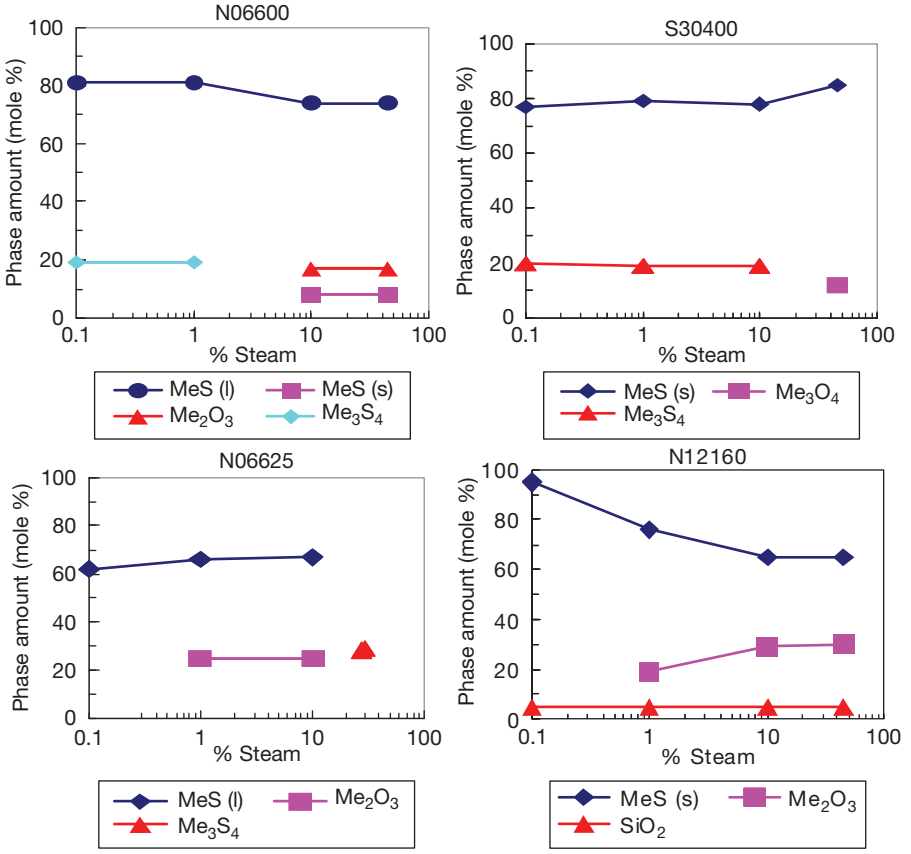

Figure 16 Calculated corrosion products for a small amount of alloy exposed to a large amount of gas of 5% H_2S, 50% H_2, and *X*% H_2O at 1 atm at 921 K.

$$P_{O_2} = \frac{P^2_{CO_2}}{K^2_{eqn[6]} P^2_{CO}} \quad [8]$$

$$CO + 1/2S_2 = COS \quad [9]$$

$$K_{eqn[9]} = \frac{P_{COS}}{P^{1/2}_{S_2} P_{CO}} \quad [10]$$

$$P_{S_2} = \frac{P^2_{COS}}{K^2_{eqn[9]} P^2_{CO}} \quad [11]$$

While the P_{O_2} and P_{S_2} values can be calculated for H-based gases (H_2–H_2O–H_2S):

$$H_2 + 1/2S_2 = H_2S \quad [12]$$

$$K_{eqn[12]} = \frac{P_{H_2S}}{P^{1/2}_{S_2} P_{H_2}} \quad [13]$$

$$P_{S_2} = \frac{P^2_{H_2S}}{K^2_{eqn[13]} P^2_{H_2}} \quad [14]$$

$$H_2 + 1/2O_2 = H_2O \quad [15]$$

$$K_{eqn[15]} = \frac{P_{H_2O}}{P^{1/2}_{O_2} P_{H_2}} \quad [16]$$

$$P_{O_2} = \frac{P^2_{H_2O}}{K^2_{eqn[15]} P^2_{H_2}} \quad [17]$$

where K_{eqn} values are the equilibrium constants for the reaction number indicated.

The H-based gases are found in many industrial processes. However, use of these gases as test gases in small-scale laboratory testing involves some practical difficulties, including producing, handling, and controlling small amounts of H_2O vapor (steam). Using H_2O in the test gases requires attention to several concerns: continuous production of small quantities of steam and heat tracing of the test apparatus to prevent steam condensation during the tests. Condensation of the steam would change the gas composition and the corrosion conditions in the tests. H_2–H_2O–H_2S gases are widely used in corrosion testing. However, there is an alternative.

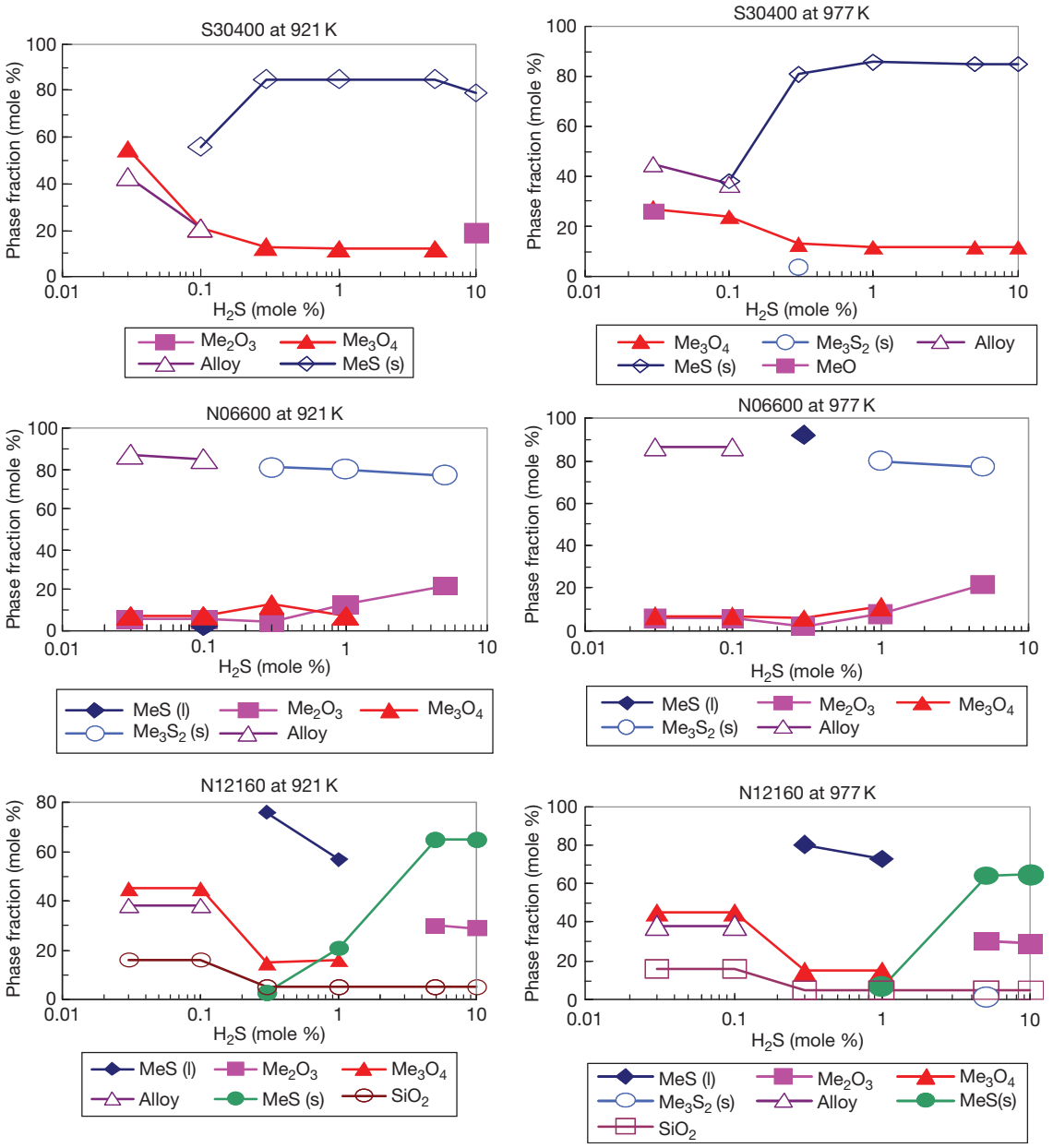

Figure 17 Effect of H_2S concentrations upon formation of liquid corrosion products for several alloys exposed to *X*% H_2S, 60% H_2, 30% H_2O, and balance Ar at 1 atm.

We can also use CO–CO_2–COS gases to simulate the P_{O_2} and P_{S_2} values of the H_2–H_2O–H_2S gases. Use of CO–CO_2–COS gases, rather than H_2–H_2O–H_2S gases avoids the difficulties of managing steam in small amounts and losses due to condensation. The ambition is to make laboratory tests easier and more reliable, particularly during long-term corrosion tests.

C-based gases can simulate the P_{O_2} and P_{S_2} values and corrosion behaviors of H-based gases. An example of a comparison of some values of P_{O_2} and P_{S_2} for a C-based gas of 32% CO–1% COS–balance CO_2 at 1 atm, which was chosen to simulate the H-based gas of 10% H_2–10% H_2S–25% H_2O–balance Ar at 1 atm is shown in Table 2. The P_{O_2} and P_{S_2} values closely match

between the C- and the H-based gases. Figure 18 illustrates the excellent agreement for P_{O_2} and P_{S_2} values between these C- and H-based gases over the temperatures of 1200–1800 °F (648–982 °C) for the example compositions shown. C-based and H-based gases can interchangeably simulate equivalent thermochemistries of the corrosive conditions, as defined in terms of P_{O_2} and P_{S_2}. Figure 19 shows that the AF values for C-based and H-based gases can also be closely matched. It is not important that the values of AF, P_{O_2}, and P_{S_2} in the laboratory test conditions exactly match the conditions of industrial interest, because correlations between these variables can be defined and used to interpolate/extrapolate/predict corrosion for ranges of conditions of interest, once a correlation is established.

1.11.2.5 Kinetics

It is not sufficient to only confirm that AF, P_{O_2}, and P_{S_2} thermochemical values of gases can be correlated between H-based and C-based gases in order to assure that corrosion is adequately related between the gas

Table 2 Summary of calculations comparing P_{S_2}, P_{O_2}, and AF values in C-based and H-based gases, where AF(activity factor) = $\log((a_{CrS})^2)/(a_{Cr_2O_3})$, corrosion correlates with, $\log(\text{Penetration}/\text{Hours}^{0.5}) = A + B[\log(P_{S_2}) - 1.5\log(P_{O_2})] + C/\text{absolute temperature}$

		Temperature (°F)			
		1200	1400	1600	1800
H_2–H_2S–H_2O gases	P_{S_2} atm	8.3 E−06	1.0 E−04	7.5 E−04	3.3 E−03
	P_{O_2}, atm	3.0 E−22	3.2 E−19	8.5 E−17	7.8 E−15
	AF	−7.54	−6.51	−5.69	−5.04
	MeS	79	79	79	79
	Me_2O_3	18	18	18	18
CO–COS–CO_2 gases	P_{S_2} atm	9.7 E−05	9.7 E−05	5.9 E−04	1.7 E−03
	P_{O_2}, atm	4.9 E−23	1.4 E−19	8.0 E−17	1.5 E−14
	AF	−6.37	−5.99	−5.76	−5.76
	MeS	79	79	79	85
	Me_2O_3	18	18	18	0
	Me_3O_4	0	0	0	11

The table is calculated for 10% H_2–10% H_2S–25% H_2O–balance Ar and 32% CO–1% COS–balance CO_2 at 1 atm and corrosion product quantities are calculated for UNS S34700.

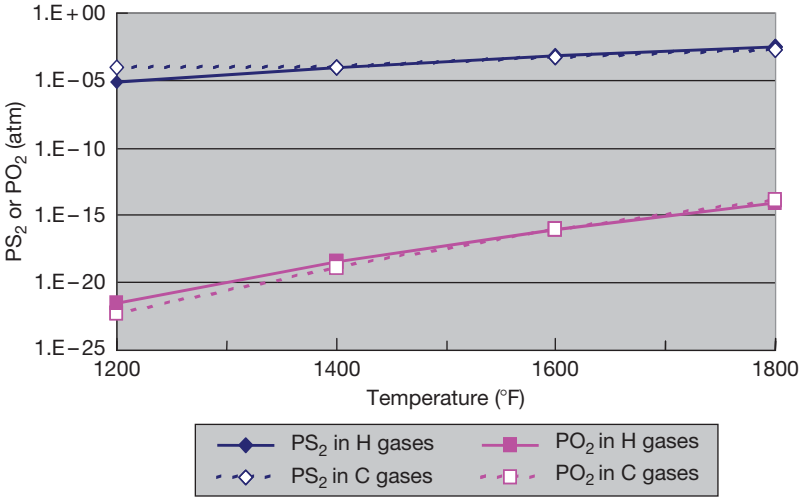

Figure 18 Summary of calculations comparing P_{S_2} and P_{O_2} values in C- and H-based gases where C-based gas means CO–CO_2–COS and H-based gas means H_2–H_2O–H_2S.

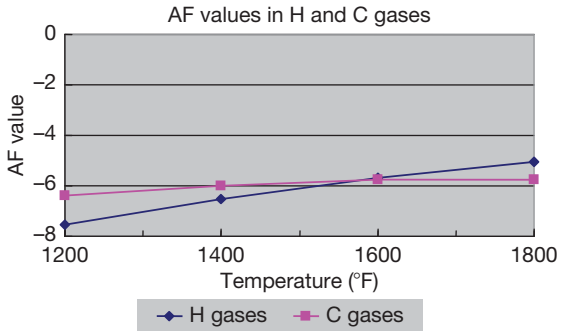

Figure 19 Summary of calculations comparing AF in C- and H-based gases where C-based gas means $CO–CO_2–COS$ and H-based gas means $H_2–H_2O–H_2S$.

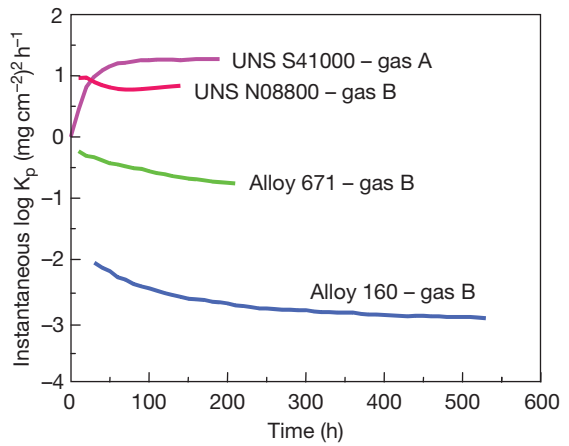

Figure 20 Effect of time upon the instantaneous parabolic rate constants for sulfidation/oxidation of several alloys at 600 °C. Gas A is 2% CO–2% COS–balance CO_2 and Gas B is 48% CO–48% CO_2 and 4% COS.

types. The relation between measured corrosion kinetics for the gas types and their compositions must also be examined. Many studies either suggest or assume that the time dependence of the extent of hot gas corrosion is parabolic. Figure 20 shows that the measured values of the instantaneous parabolic rate constants for a number of alloys exposed to sulfidizing/oxidizing conditions can vary greatly from the initial exposure time. It may take up to 500 h before the parabolic rate constant becomes constant (meaning it is independent of time). Exposure times greater than 500 h may be needed to measure real parabolic rate constants useful to predict very long-time corrosion behavior. Indeed, after the initial time of changing kinetics, the long-term corrosion behavior can be

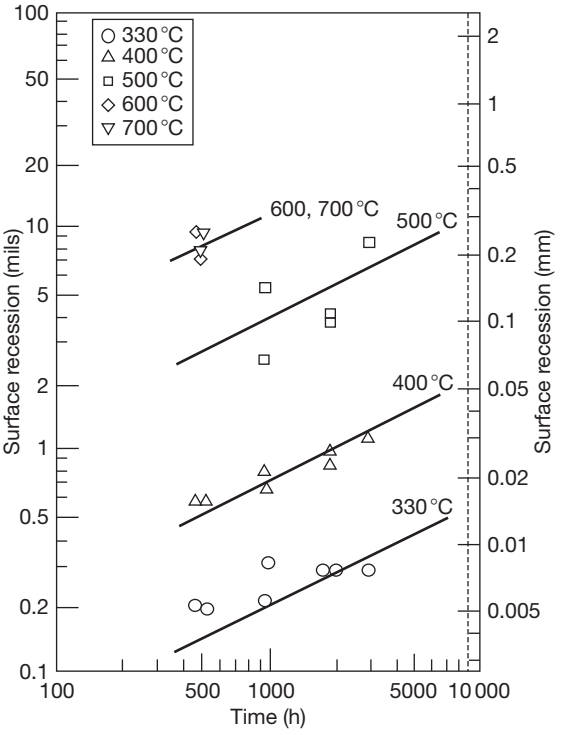

Figure 21 Sulfidation/oxidation corrosion of alloy UNS N06625 in a gas of initial composition of 0.1% H_2S–79.1% H_2–20.8% CO at 1 atm.

shown to be parabolic for many thousands of hours for many Fe–Ni–Cr heat resistance alloys, with an example shown in Figure 21.

Once the time dependence is understood, the next question becomes whether real corrosion behavior in equilibrium and nonequilibrium H-based and C-based gases can be correlated in the same way. This question arises because many industrial processes handle gases, which are not equilibrated and alloy corrosion occurs by contact with nonequilibrium gases. Nonequilibrium gases occur when the combinations of gas flow rates, temperatures, and gas phase reaction rates do not allow sufficient time to equilibrate the gases.

Corrosion in equilibrated and nonequilibrated gas compositions has been compared. Previous corrosion tests[25,26] showed that if the P_{O_2} and the P_{S_2} values are matched between $CO–CO_2–COS$ gases and $H_2–H_2O–H_2S$ gases, then the corrosion behaviors of Fe–Ni–Cr alloys are equivalent in terms of the corrosion products formed, corrosion product morphologies, and the measured corrosion kinetics. This is illustrated in Figure 22, where the gas compositions of various C-based and H-based gases at equilibrium and not at equilibrium were used to

expose N08800. All the different types of gases induce similar corrosion behavior, once the AF (or P_{O_2} and P_{S_2} values) are considered. These gases cover variations of about 10 orders of magnitude in both P_{O_2} and P_{S_2}. The open symbols are C-based gases, while the closed symbols are H-based gases. The solid points are equilibrium gases and open points are nonequilibrium gases. **Figure 22** shows that there is no distinction between the C-based and H-based gases, in terms of correlating P_{O_2} and the P_{S_2} with corrosion behavior for alloy UNS N08800. This is true for a variation of nearly six orders of magnitude change in the gravimetric parabolic rate constants for alloy N08800, showing that C-based and H-based gases can be used interchangeably to simulate corrosion conditions, as long as the P_{O_2} and P_{S_2} values are assessed. This approach has been used for a large number of heat-resistant alloys based on various combinations of Fe–Ni–Cr–Co–Al.

After demonstrating that AF (or P_{O_2} and P_{S_2} values) can define the corrosion condition for the alloy; an alternative approach is to prepare the phase stability diagram shown in **Figure 23**. The diagram includes iso-AF lines, which suggest lines of equal corrosion kinetics, as defined by AF (or P_{O_2} and P_{S_2}) values. The next step is to then add isocorrosion contours, which

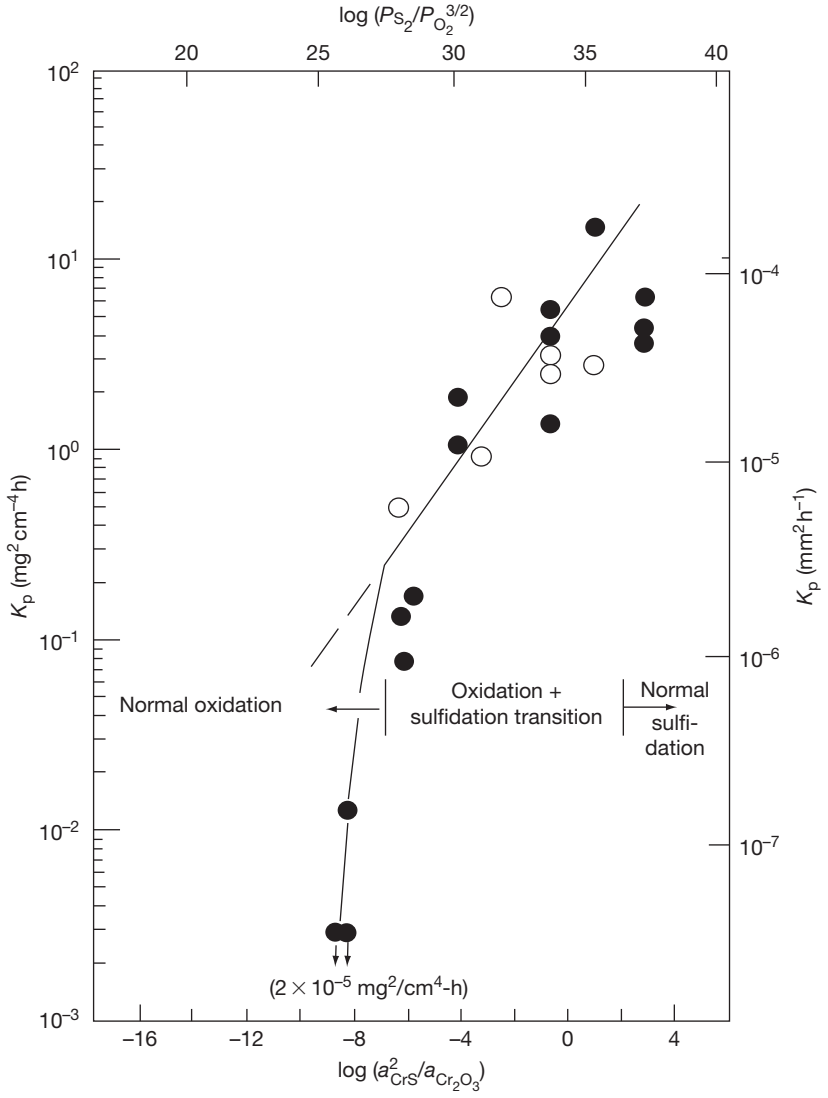

Figure 22 Effect of gas composition expressed in terms of AF (comparing C-based and H-based gases) upon the instantaneous parabolic rate constant (K_p) for UNS N08800 exposed to sulfidizing/oxidizing conditions at 600 °C.

are parallel to the phase boundary between the CrS and Cr_2O_3 phase fields for the diagram for Cr–S–O–C at 600 °C, as shown in **Figure 24**. This accomplishment is quite remarkable in using thermochemical information on corrosion product stability diagrams to compile and correlate corrosion kinetics of real engineering alloys in complex gases. Indeed, a collection of these types of diagrams could be constructed for numerous combinations of alloys and exposure conditions of gas compositions and temperatures. However, the utility represented in ASSET,[10,25,32,33,52,53] avoids the cumbersome preparation of many diagrams and allows accurate predictions as needed.

One concern with CO–CO_2–COS gases in laboratory tests is that compositions and temperatures must be maintained to keep carbon activities (a_Cs) < 1, in order to avoid carbon deposition, which could present practical problems in terms of unexpected changes in the gas composition and potential plugging of gas flow lines. A potential reaction between CO and CO_2, which can lead to carbon deposition, is shown below.

$$CO_2 + C = 2CO \qquad [18]$$

$$a_C = \frac{P_{CO}^2}{K_{eqn[18]} P_{CO_2}} \qquad [19]$$

where a_C is the activity of solid C described in reaction [18] and calculated in eqn [19]. In order for the CO–CO_2–COS gases to adequately simulate the corrosivity of the H_2–H_2O–H_2S gases, conditions must also not allow solid carbon to form. This can be confirmed experimentally by analyses of the corrosion products and can also be assessed by calculating the stabilities of the potential phases, while considering oxides, carbides, sulfides, and alloy phases. Formation of carbides in conditions which induce sulfidation/oxidation is rare, since oxides and sulfides are usually much more stable than carbides. Safety and toxicity concerns with COS are similar to those with H_2S, and the methods to remove COS and H_2S from exiting test gases by passage through aqueous NaOH solutions before exhausting them into the atmosphere. Performing these types of corrosion tests requires careful control of the test atmosphere. For example, the air must be adequately removed from the test chamber before the high temperature test gas contacts the alloy coupons. The test chamber must be purged with gases

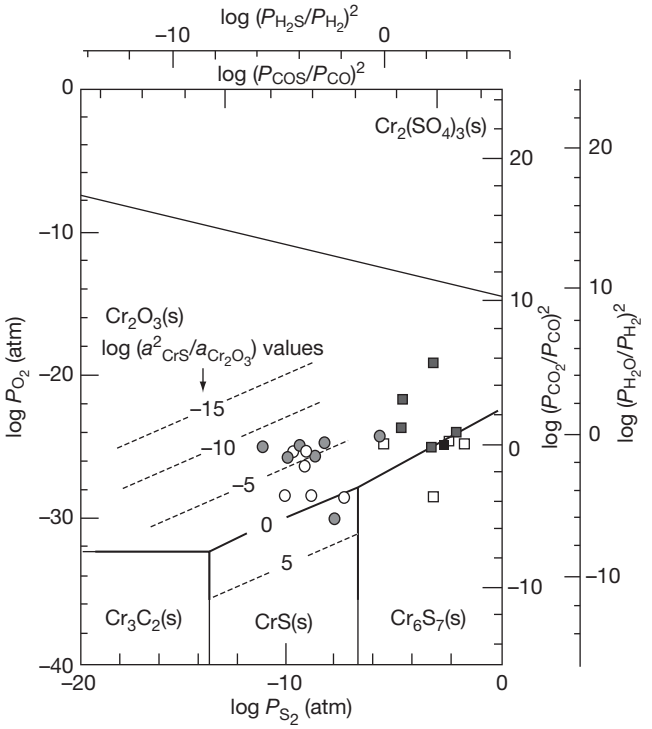

Figure 23 Calculated thermochemical phase stability diagram for C–S–O system at 600 °C. Round points represent H-based gases and square points represent C-based gases. Solid points represent equilibrium gases and open points are nonequilibrium gases.

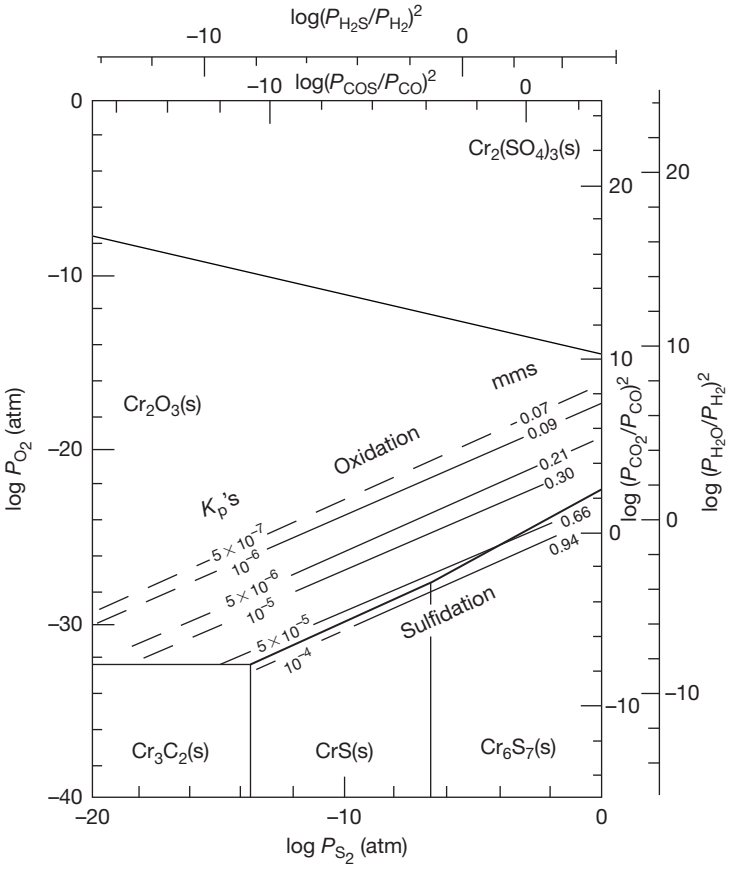

Figure 24 Isocorrosion contours for alloy N08800 on the calculated Cr–S–O thermochemical phase stability diagram at 600 °C. Values for K_p's in square millimeter per hour and metal loss (in mm) after 1 year of exposure are shown.

like N_2 or inert gases until the O_2 decreases to values below 0.001 atm. Then, H_2 can be introduced to the test chamber at temperatures above 1000 °F to scavenge the remaining low levels of O_2 by reaction to form H_2O before the corrosion test exposure starts.

Another concern that might be raised is whether C-based gases can adequately simulate H-based gases in terms of any potential effects of water vapor upon the corrosion behavior. The reported observations to date suggest that the effects of water vapor upon oxidation are associated with oxidizing conditions where volatile, oxidized, hydrated species form. The conditions that produce sulfidation/oxidation have P_{O_2} values of perhaps 10^{-25} to 10^{-10} atm, and the majority of corrosion products are sulfides. The P_{O_2} values are well below those associated with conditions showing oxidation to be affected by water vapor.

Let us examine the utility of these concepts. The presence of oxidizing gases such as H_2O or CO_2 slows the sulfidation rate because they increase the stability of slow-growing oxide corrosion products. The corrosion can be much slower than expected if only H_2S–H_2 were present. This can be important because gases, sometimes thought to contain only H_2S–H_2, also contain some H_2O vapor, because of exposure of the gas to liquid water. A gas exposed to water at room temperature (from processes such as a water wash) may contain up to 2–3% water in the gas, if saturated with water at room temperature. Sulfidation rates predicted using only the H_2S–H_2 concentrations would overestimate the corrosion, if H_2O were really present. This slower corrosion rate by sulfidation/oxidation can be predicted using the approaches described in this article. This is illustrated in **Figures 25** and **26** for several alloys at 600 °C in sulfidizing/oxidizing gases. The extent of corrosion occurring at the right-hand P_{O_2} in **Figure 26** and the low AF values in **Figure 26** corresponds to simple oxidation, while progression to the left-hand side of the axis corresponds to lower P_{O_2}s and the high values of AFs are expected in O_2-depleted conditions. When the P_{O_2} becomes low enough and oxides are no longer stable, sulfidation

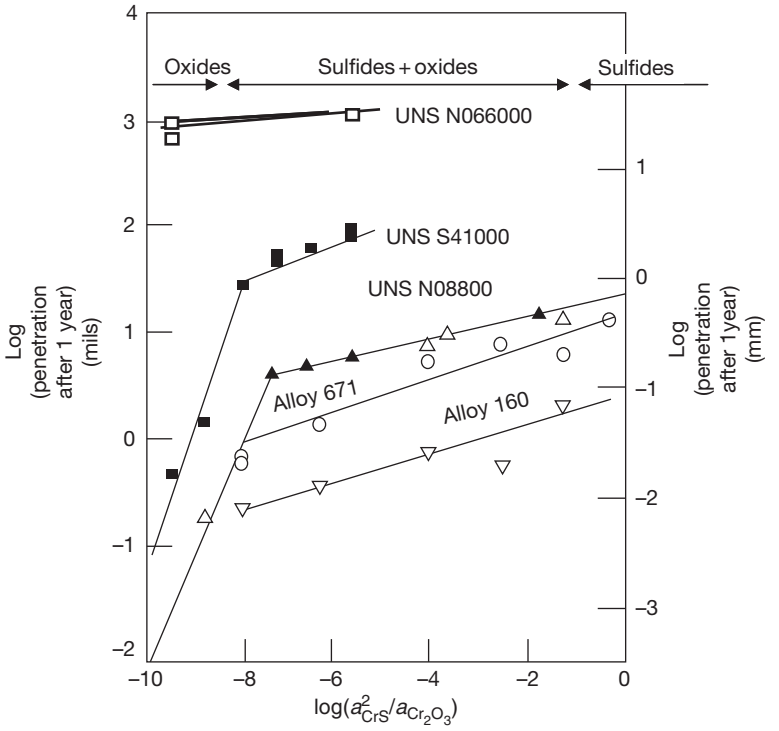

Figure 25 Influence of gas composition measured in terms of AF upon corrosion of high-chromium alloys corroding by sulfidation/oxidation.

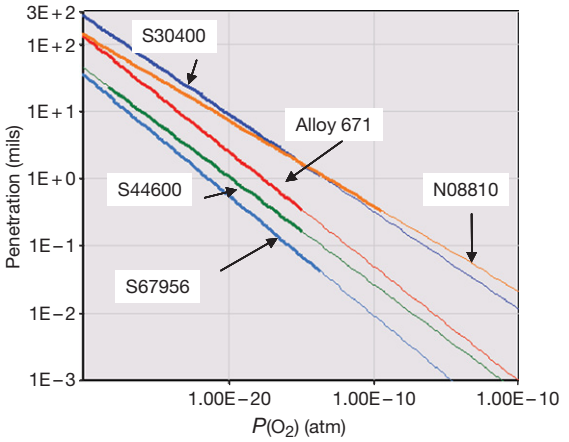

Figure 26 Effect of O_2 partial pressure upon sulfidation/oxidation of alloys after 1 year of time and exposure to S_2 partial pressure of 10^{-7} atm at 700 °C.

becomes the dominant corrosion mechanism. The minimum corrosion in this scenario is oxidation in O_2-containing gases and the maximum corrosion is sulfidation in H_2S–H_2 gases. Several alloys are shown in Figure 26, with both thick and thin portions of the lines. The thick portions represent predictions based upon interpolations for conditions for which there are compiled corrosion data for that alloy. The thin portions of the lines represent corrosion predictions based upon extrapolations for conditions outside the data represented by the data compilation. Figures 25 and 26 clearly show that data compilations for a number of commercially important alloys can represent many orders of magnitude of variation in the exposure conditions, as summarized in terms of the P_{O_2}, P_{S_2}, temperature and exposure time. Figure 27 shows how variations in steam concentrations can affect the sulfidation/oxidation of S030400, which is typical for many alloys. Figure 28 shows an example of a correlation for sulfidation/oxidation for alloys S30400.

1.11.2.6 Corrosion Influenced by Gas History

Another way to examine the approach to equilibrium for an alloy corroding by sulfidation/oxidation is to examine how promptly changes in gas composition influence subsequent alloy corrosion behavior, since the gas thermochemistry should determine the alloy corrosion behavior. Data reported some time ago[21] for sulfidation/oxidation of UNS N08800 exposed to gases, which induced sulfidation/oxidation, showed

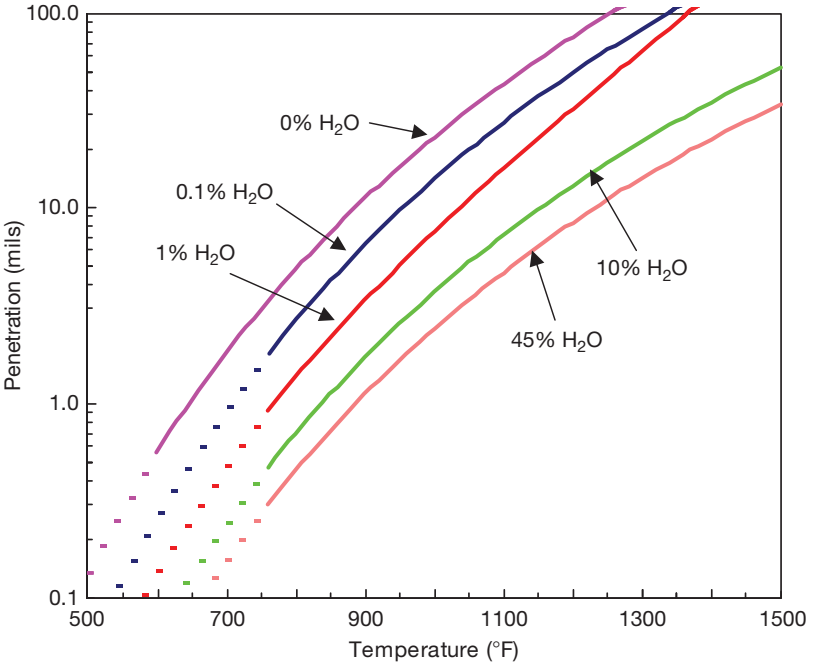

Figure 27 Effect of temperature and steam concentration upon metal penetration by sulfidation/oxidation of S30400 after 1 year in 5% H_2S, 50% H_2O, *X*% H_2O and balance Ar.

that corrosion kinetics changed promptly as the gas composition and temperature were changed to correspond to that measured when the alloy had always been exposed to that environment. The previous exposure history of the corroding alloy had no effect upon the corrosion behavior after a few hundred hours. This was demonstrated by comparing the parabolic rate constants for the time periods corresponding to the same gaseous exposure, independently of the prior exposure. The alloy corrosion kinetics change within only a hundred hours to match those expected for the new gaseous exposure. There have been several examples of summing the expected amounts of corrosion expected because of different portions of complex exposure as if they were produced by individual exposures.

1.11.3 Oxidation/Nitridation by N_2–O_2 Gases

1.11.3.1 Types of Equipment and Processes Where Nitridation Occurs

Stainless steels and other heat-resistant alloys are used because of their excellent corrosion resistances and mechanical properties in different kinds of service, such as vessels and pipelines in oil and gas equipment and other components. Their high temperature corrosion behaviors depend upon the composition of the gases and temperatures. Surface scales and internal (subsurface) oxidation are both possible and seen in many different applications. Corrosion by both nitridation and oxidation are possible when alloys are exposed to atmospheres rich in nitrogen at temperatures higher than 1000 °F (537 °C), nitrides such as CrN and Fe_4N may form and affect the alloy mechanical properties. Nitridation is similar to carburization in that both are high temperature corrosion mechanisms for metals and alloys which do not produce surface scales and do not cause losses in wall thickness, as experienced by other high temperature corrosion mechanisms, such as oxidation and sulfidation. The main consequence of nitridation (like carburization) is embrittlement of the alloys making them vulnerable to fracture. There is also a slight increase in volume (decrease in density) as the nitrogen dissolves into the alloy (or carbon in the case of carburization). The interstitial solution of the nitrogen into the austenite phase distorts the lattice.[41–44]

The high temperature oxidation of UNS 30400 steel and other stainless steels in the presence of 60% H_2–40% N_2, NH_3–H_2O mixtures, and other H_2–N_2 mixture, has already been studied by several authors from the phase transformation point of view.[45–47] It is also well known that nitrogen and carbon dissolving into alloys increase hardness yield strength, tensile strength, and wear resistance[48] and

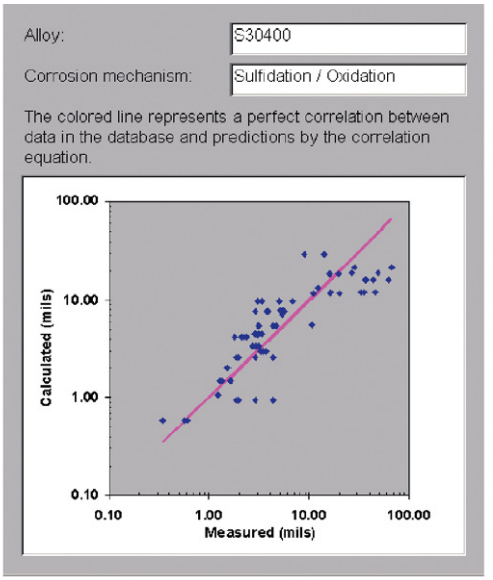

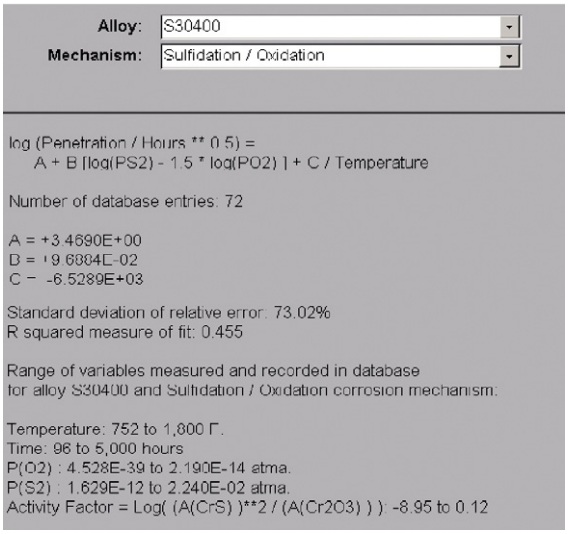

Figure 28 Example of the analysis of the sulfidation/oxidation corrosion database for S30400 and the quality of the corrosion correlation.

lower toughness. Nevertheless, there is almost no previous work dealing with the conditions, which define the competition between nitridation and oxidation at high temperatures for these materials. Nitridation primarily forms internal nitride corrosion products and can be described in terms of sound metal loss (penetration) by measuring the depth of the formation of the internal nitrides. The process occurs upon exposure of metals in gases containing pure N_2, $N_2 + H_2$, NH_3, air, and mixtures of O_2-depleted air and other gases at temperatures above 300–430 °C (600–800 °F). This corrosion depends upon the gas composition, alloy composition, time, and temperature.[42,44]

A recent corrosion evaluation study was performed on stainless steel tubes used in as a component part in a reactor.[41] The material was UNS S30400 and was exposed to a nitriding, carburizing, and oxidizing environment, containing mainly NH_3 and CO_2, at temperatures between 390 and 450 °C. The atmosphere had a high nitridation potential. Alloy nitrides were stable and formed. The authors explained that the corrosion process includes ingress (solution) of nitrogen into the steel and then formation of a nitrided layer, once the solubility products of the nitrides are exceeded. This formation of CrN particles at temperatures above 425 °C in the near-surface layer causes a volume expansion of about 11% and a corresponding increase in compressive stresses in the surface that can lead to crack formation. Temperatures lower than 425 °C lower the Cr mobility, even if the N_2 concentration in the atmosphere is high.

Issartel *et al.*[45,46] analyzed this occurrence of nitridation and the effect of the temperature upon spalling in terms of the corrosion products formed in UNS S30400 stainless steel in air at 800 and 900 °C (1122 and 1652 °F) by using X-ray diffraction and SEM. Their results support the presence of austenite at lower than expected temperatures in a nontreated sample because the nitridation treatment on the steel surface produced a solid solution of N in the austenite. In this case, no nitrides form in the alloy surface. Riffard *et al.*[47] used *in situ* X-ray diffraction to follow the formation of nitrides at the testing temperature. At the beginning of the oxidation test, CrN formed together with Fe_2O_3. Cr_2O_3 quickly appears and leads to a protective oxide scale formation growing according to a parabolic rate law. During oxidation, *in situ* X-ray diffraction also shows that Fe_2O_3 transforms to $FeCr_2O_4$. These results confirm that nitridation enhances internal oxidation at high temperature.

Internal nitridation is also observed on numerous commercial high temperature alloys.[49–51] In the case of nickel-base alloys, which are often used for high temperature applications, internal nitridation is aided by repeated spalling and cracking of the protective oxide made of either Al_2O_3 or Cr_2O_3. Nitrogen penetrates into the near-surface area of the alloy and forms stable nitrides, such as, TiN and AlN.[51] These surface precipitates embrittle the high temperature and low-temperature mechanical properties of the material. Additionally, dissolution of the high-volume fraction of the initial small precipitates of the cubic γ'-phase

occurs [Ni_3(Al, Ti)], which provides the excellent creep resistance of Ni-base superalloys at high temperature. Formation of nitrides can reduce creep and stress rupture properties of Ni-base superalloys at high temperatures, lowering the maximum allowable stress and/or temperature for a particular application.

The transition from oxidation to nitridation in O_2–N_2 gases of varying composition for several different types of alloys (Fe–Cr alloy UNS 410000, Fe–Ni–Cr alloy UNS 30400 and Ni–Cr–Al alloy UNS N07214) is a function of temperature, O_2 partial pressure, and alloy composition in O_2–N_2 gases at 1600 °F. The stable alloy phases and corrosion products were calculated by ASSET[52–54] by thermochemical equilibrium calculations for varying gas compositions. The predictions of the phase behavior were compared to and agreed with experimental observations made with carefully exposed coupons of the alloys.[53,54]

1.11.3.2 Thermochemistry and Corrosion Mechanism

Oxidation/nitridation by O_2–N_2 gases occurs in various industrial equipment involved in fossil fuel combustion, fertilizer manufacturing, or ammonia production. The key variables influencing the kinetics are exposure time, partial pressures of O_2 and N_2, alloy composition, and temperature. The effects of variation from a high P_{O_2} to low P_{O_2} can induce changes in the corrosion products and rates of corrosion. The oxidation behavior can vary from predominantly surface oxidation (scaling) to oxidation by internal oxidation as the P_{O_2} decreases depending upon alloy composition. Progression to lower levels of P_{O_2}, will induce nitridation to dominate over oxidation. These observations impact how laboratory tests can best simulate corrosion behavior by oxidation or nitridation and also in terms of applications where low levels of P_{O_2} may be different from the expected in O_2–N_2 gases.

1.11.3.3 Predicting Corrosion Product and Alloy Phase Formation in Nitriding/Oxidizing Conditions

Three different alloys were investigated: two iron-base stainless steels, under the specification AISI 304 (UNS S30400) and 410 (UNS S41000), and a nickel-base alloy named 214 (UNS N07214). The nominal chemical compositions of these alloys are reported in Table 1. The stable corrosion products for conditions of interest were predicted using ASSET and are the likely surface corrosion products for the alloys exposed to the O_2–N_2 gases. Corrosion data reported in the literature have been compared to these predictions, in terms of corrosion product formation and the metal losses observed.

Figures 29 and 30 show the calculated phases for UNS S30400 and UNS S41000 stainless steels, as functions of the O_2 partial pressure (in O_2–N_2 gases) at 1 atm and 1600 °F (871 °C). The results show that both alloys form the M_2O_3 phase at O_2 partial pressures higher than 0.001 atm. The corrosion products are about 75% Fe_2O_3 and 25% Cr_2O_3. Alloy UNS S30400 has around 8 wt% Ni and differs from UNS S41000 in that a significant fraction of the spinel phase $(Fe/Ni)_3O_4$ forms over a broad range of O_2 partial pressures, as shown in Figure 29. The 0.5 wt% Ni composition in the alloy UNS S41000 is insufficient to contribute to the significant formation of the spinel phase ($FeNi_2O_4$), which occurs for only a very narrow range of O_2 partial pressure.

In the case of stainless steel UNS S30400 shown in Figure 29, levels of O_2 between 0.04 and 0.0634 atm induce formation of an MeO phase (where Me is mostly Fe with small amounts of Cr and Ni). Lower levels of O_2 tend to produce some M_2O_3 phase (where M is mostly Cr) with a maximum content of 15%; then, this phase decreases slowly. For this alloy, very low levels of O_2, tend to form nitrides. Chromium nitrides formation (CrN and Cr_2N) starts at 0.0125 atm of O_2 and continue to increase in concentration at lower P_{O_2}s until the Cr reacts to make nitride.

For the UNS S41000 stainless steel shown in Figure 30, a comparable result was observed. There is more MeO phase (FeO) – maximum 85% at an O_2 partial pressure of 64×10^{-5} atm – and the presence of this phase increases at 0.075–0.0275 atm O_2. At O_2 partial pressures below 3×10^{-5} to 15×10^{-5} atm O_2, the formation of iron ferrite forms with the reduction of austenite. This steel has 12.3 wt% of Cr. At very low levels of O_2, the formation of nitrides starts. As seen from Figure 30, the UNS S41000 stainless steel forms Cr nitrides (CrN and Cr_2N) but less than the values found in UNS S30400. The lower Cr content (12.0 wt %) of UNS S41000 naturally forms less nitride phase than UNS S30400 which has a higher Cr content (18.4 wt%). At even lower partial pressures of O_2 (5×10^{-6} atm), the amount of Cr_2N decreases to 3–4%.

Increasing the amount of Ni, as found in the alloy UNS N07214 increases the amount of oxides, which depend upon the presence of nickel, such as MeO oxides, where Me can be Fe or Ni. Figure 31 illustrates

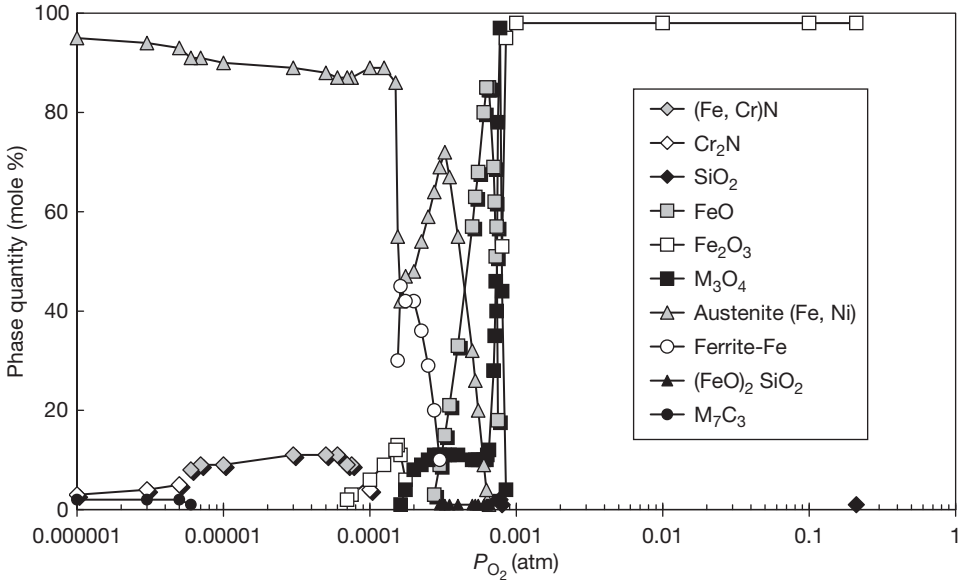

Figure 29 Effect of O_2 partial pressure upon the stable phases for UNS S30400 stainless steel exposed to O_2–N_2 gases at 1 atm and 871 °C (1600 °F).

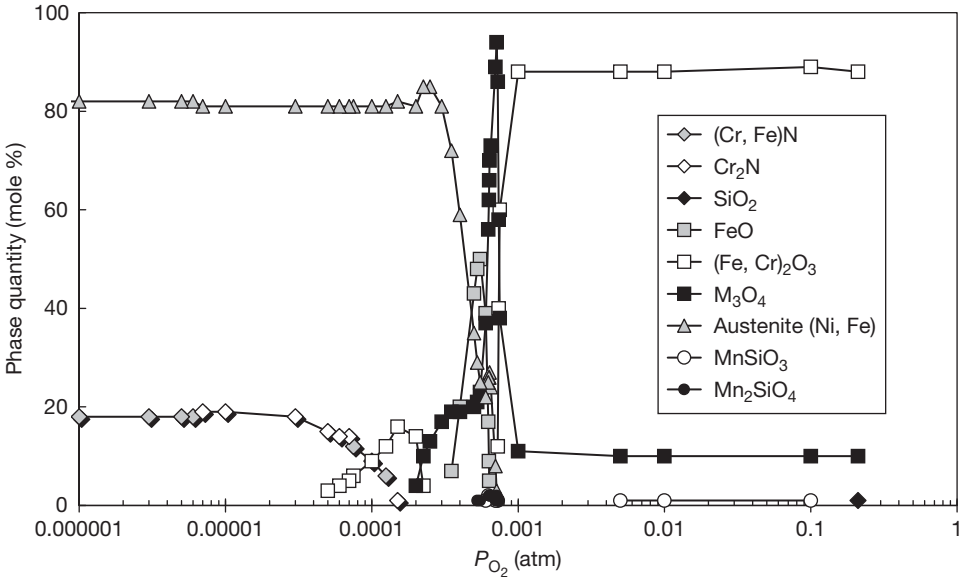

Figure 30 Effect of O_2 partial pressure upon the stable phases for UNS S41000 stainless steel exposed to O_2–N_2 gases at 1 atm and 871 °C (1600 °F).

this by showing stable NiO at O_2 partial pressures above 6×10^{-3} atm and spinel phases consisting of $NiCr_2O_4$ and $NiO{\cdot}Al_2O_3$ at O_2 partial pressures between 3×10^{-3} and 6×10^{-3} atm, as shown in **Figure 31**.

Because alloy 214 (nickel-base UNS N07214) has a high Ni content (76 wt%) and low Fe content (2.5 wt%), the results are very different. **Figure 31** shows the effect of the O_2 partial pressure at 1 atm and 1600 °F (871 °C). At O_2 partial pressures above 0.006 atm of O_2, NiO is the dominant phase (80 wt%), but this phase decreases dramatically at lower O_2 partial pressures and disappears at 0.003 atm of O_2. The reduction in the amount of NiO occurs simultaneously with an increase in the amount of the Ni-rich austenite phase. It is well known that the oxidation rates of nickel alloys such as UNS N07214

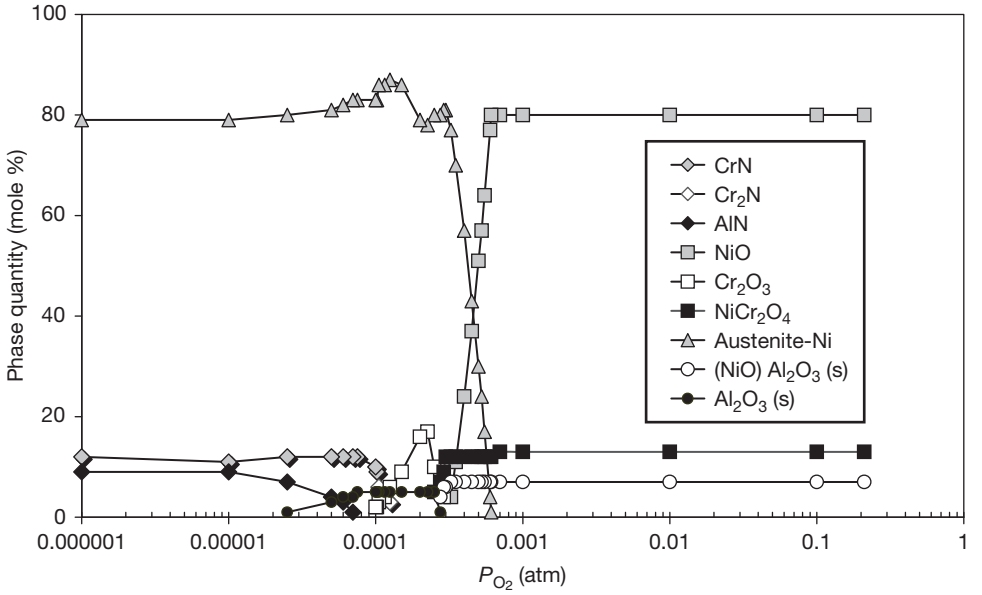

Figure 31 Effect of O_2 partial pressure upon the stable phases for nickel-base alloy UNS N07214 exposed to O_2–N_2 gases at 1 atm and 871 °C (1600 °F).

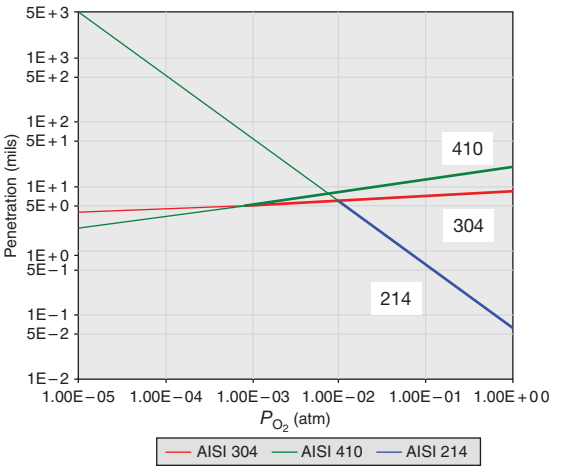

Figure 32 Predicted effect of P_{O_2} upon oxidation corrosion of UNS S30400, UNS S41000, and UNS N07214 at 871 °C (1600 °F) after 1 year of exposure time (obtained by using ASSET predictions). The thickened portion of each line correspond to interpolations of actual data (corrosion rates) obtained in the range of pressure from 1 to 0.001 atm for 304 and 410; and from 1 to 0.01 atm for 214.

depend strongly upon the O_2 partial pressure in the gas. Low O_2 partial pressures (about 0.01 atm, and less) favor subsurface oxidation and rapid total penetration. At 25×10^{-3} atm and above of O_2, the formation of Cr_2O_3 and Al_2O_3 occurs while $NiCr_2O_4$ and the $NiO{\cdot}Al_2O_3$ (spinel structure) cannot form. At 10^{-3} atm of O_2 and less, nitrides became stable.

Low levels of O_2 and high levels of N_2, such as found in 3×10^{-3} atm O_2 and 0.997 atm N_2 increase the stability of the austenite phase (FCC), since nitrogen is well known as an austenite stabilizer. This behavior was observed in the stainless steels considered in this study at 1600 °F (871 °C). The N_2 partial pressure of about 1 atm in the gas phase when O_2 partial pressures are sufficiently low (10^{-4} to 3×10^{-3} atm), allows formation of nitrides – mostly in the form of CrN and Cr_2N with limited solubility for Fe into the nitride phases. These compounds can be detected by bulk analysis of the corrosion product scale with X-ray diffraction.

Figure 32 shows the predicted effect of O_2 (in O_2–N_2 gases) at 871 °C (1600 °F) after 1 year of exposure time obtained by using ASSET for UNS S30400, UNS S41000, and UNS N07214. Stainless steels UNS S30400 and UNS S41000 have comparable penetrations under different O_2 partial pressures. Penetration of UNS S30400 is almost independent of O_2 while penetration of UNS S41000 slightly decreases when O_2 concentration decreases. In the case of nickel-base alloy UNS N07214, the penetration decreases with increasing O_2 concentration and internal oxidation is the dominant oxidation mechanism. These predicted rates are based on the correlations of measured oxidation data. The corrosion rates were predicted for 1.0 to 0.001 atm, as indicated in the bold lines in Figure 32.

As shown in Figure 33, the influence of O_2 concentration upon oxidation is complex over the

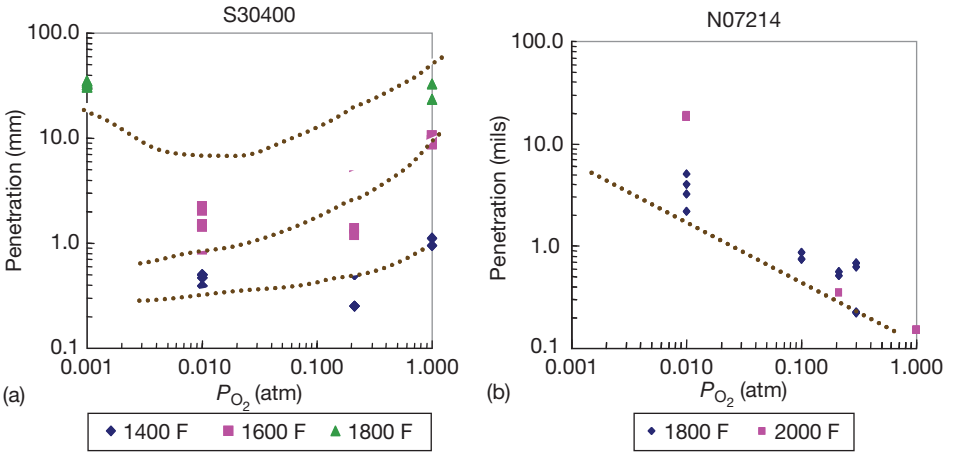

Figure 33 Effect of O_2 partial pressure upon metal penetration of (a) UNS S30400 and (b) UNS N07214 exposed to different temperatures for 1000 h.

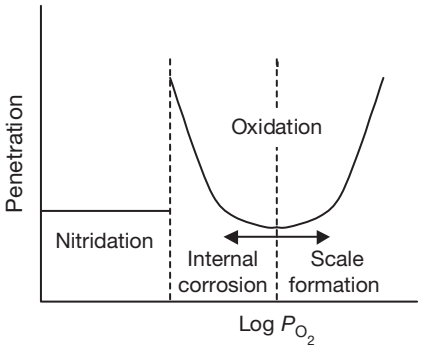

Figure 34 Schematic representation of the transition from oxidation to nitridation, for a fixed temperature, exposure time, and alloy.

temperature range of 871–1177 °C (1400–2000 °F) for alloys exposed to different O_2 concentrations at a constant exposure time of 1000 h. Alloys S30400 and S41000 show higher penetrations at higher P_{O_2}s and lower P_{O_2}s, with a minimum at some intermediate P_{O_2}. Microstructures show that penetration for these alloys is mostly scale formation at high P_{O_2}s, while internal oxidation dominates at low P_{O_2}s. The minimum penetration at some intermediate P_{O_2} is caused by the transition between dominance by scale formation and internal oxidation.

Al_2O_3-forming alloys such as N07214 exhibit slower oxidation as the O_2 concentration increased the amount of oxide present as Al_2O_3–Cr_2O_3–Fe_2O_3. Figure 34 illustrates the different types of corrosion expected over a range of N_2–O_2 gas composition. Internal oxidation competes with scaling as defined by the P_{O_2}. At low O_2 pressures, such as 10^{-4} atm of O_2, nitrides form and grow within the metal matrix.

1.11.4 Oxidation/Carburization by CH_4–H_2O Gases

1.11.4.1 Types of Equipment and Processes Where Carburization Occurs

Corrosion of metals and alloys used in equipment processing high temperature, corrosive, gases containing carbon, hydrocarbons and gases like CO or CO_2 have the potential to induce carburization. Examples of some processes might be gas processing, combustion gas process heaters, petroleum refineries (hydrocracking, coking, vacuum flashing, hydrotreating, and catalytic reforming) coal/coke/oil gasifying, petrochemical production, gasification of black liquor in pulp/paper production, and fossil fuel-fired power generation. Carburization may limit the maximum allowable temperature or maximum allowable gas species concentrations for metals and alloys in equipment.

1.11.4.2 Thermochemistry and Corrosion Mechanism

Oxidation/carburization by CH_4–H_2O, CO, or CO_2 gases is possible. The key variables influencing the kinetics are exposure time, P_{O_2}, activity of carbon (a_C), partial pressure of H_2S, alloy composition, and temperature. Alloys exposed to mixtures of C–CH_4–H_2O can experience corrosion by oxidation and carburization. The transition between carburization and

oxidation behaviors of commercial alloys will be discussed.

In carburizing atmospheres, carbon is transferred from the environment into metal components. This process is carburization, which is a high temperature corrosion phenomenon.[57–66] This can change mechanical properties of metals and alloys mostly at temperature >800 °C when carbon diffuses into alloys and react with metals to form internal carbide precipitates.

A result of carburization is an increase in hardness of the carburized materials. Low alloy steels are often exposed to carbonaceous environments to produce hard surfaces to increase wear resistance, corrosion resistance, and abrasion resistance. So, with the proper heat treatment in a gas atmosphere, the consequence of carburization is beneficial.

Carburization is also a corrosion process that affects high temperature alloys, especially in petrochemical industry processes. It is a common contribution to failure of ethylene pyrolysis tubes and can degrade the corrosion resistance and mechanical properties of metals and alloys. In some cases, coke deposition occurs at the inner walls of tubes during hydrocarbon cracking. The decoking process is used to remove coke deposits. Steam or steam–air mixtures are often used to remove coke. The removal processes oxidize the coke to CO and CO_2 and by thermal shocking/spalling of the deposits. The decoking process also introduces oxidation as a corrosion concern.

Carburization occurs when carbon enters the surface layer of a metal or alloy. The dissolved carbon remains in solution or reacts with the metal to form carbides. Both mechanisms strengthen or harden the surface of the metal. In most cases, carburization leads to precipitation of carbides like $M_{23}C_6$ and M_7C_3 inside the alloy surface. The internal carbide formation causes a volume increase of the carburized zone and potential cracking which leads to deterioration of mechanical properties of metals. The increased carbon levels also lead to loss of ductility, which can lead to various forms of fracture.

The carburization rate of an alloy is affected by alloy composition, exposure gas composition, temperature, and time. This chapter discusses carburization in terms of the total sound metal loss (penetration), which is the sum of surface metal loss by scaling plus internal carburization.

1.11.4.3 Corrosion Products Prediction

ASSET was used to calculate stable corrosion products and alloy phases of several alloys exposed to CH_4–H_2O gas mixtures at 1800 °F (982 °C). Three alloys are summarized: UNS S34700, UNS S44600, and UNS N06025. UNS S34700 is an Fe–Cr–Ni stainless steel stabilized with small additions of niobium and tantalum. The alloy exhibits an excellent resistance to intergranular corrosion and can be used for prolonged service from 800 to 1500 °F (427–816 °C). UNS S44600 is an Fe–Cr ferritic heat-resisting alloy with excellent resistance to oxidation and to various forms of hot corrosion. The alloy is most commonly used for service between 1500 and 2200 °F (815 and 1200 °C). UNS N06025 is a high carbon Ni–Cr–Fe alloy with additions of Al, Ti, Y, and Zr. The alloy exhibits exceptional resistance to oxidation at high temperatures and possesses very good high temperature carburization resistance. This alloy can be used for pressure vessels with service temperatures up to 1150 °C.

Corrosion products and alloy phases were calculated at 1800 °F (982 °C) under various CH_4–H_2O gas mixtures by assuming that equilibrium conditions are satisfied, as shown in **Figure 35** for alloy UNS S34700, **Figure 36** for alloy UNS S44600, and **Figures 37 and 38** for alloy UNS N06025. Each figure shows the stable corrosion products such as oxides and carbides, the alloy phases and their relative phase amounts.

The effect of gas composition on Me_3O_4 (spinel) composition was investigated. The concentration of metals (Fe, Cr, and Ni) in spinel were calculated, as shown in **Figure 35** for UNS S34700, **Figure 36** for UNS S44600, and **Figure 37** for UNS N06025. For these three alloys, the amount of spinel increases with increasing H_2O in gas mixture. The major metals in the spinel are Fe and Cr. For UNS S34700 and UNS S44600, the concentration of Fe in spinel increases with increasing H_2O and the concentration of Cr in spinel (Me_3O_4) decreases with increasing H_2O. For UNS S44600, which is a nickel-based alloy, the concentration of Ni in spinel (Me_3O_4) increases with increasing H_2O.

Carburization tests were performed on several alloys at 1800 °F (982 °C) for 720 h under different gas atmospheres. One group of samples was under flowing pure CH_4 gas, which decomposed to produce massive amounts of solid carbon. The other group was under H_2–1.2% CH_4, which yields a carbon activity of one at the test temperature of 1800 °F (982 °C).

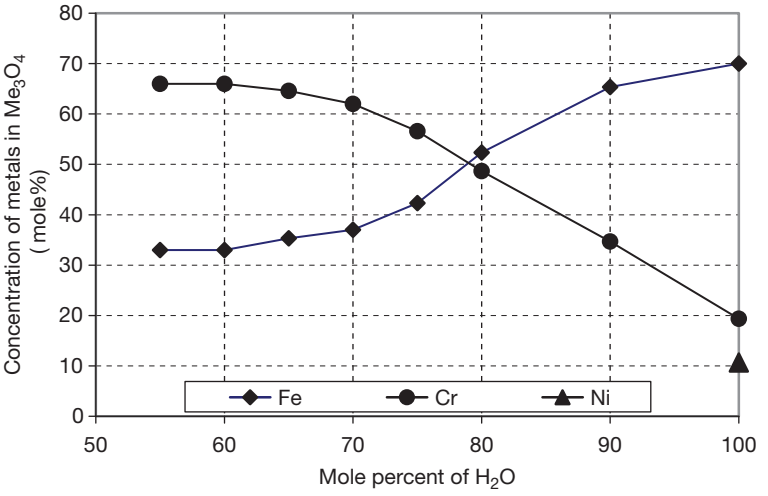

Figure 35 Effect of gas composition upon Me_3O_4 composition in alloy UNS S34700 at 1800 °F (982 °C).

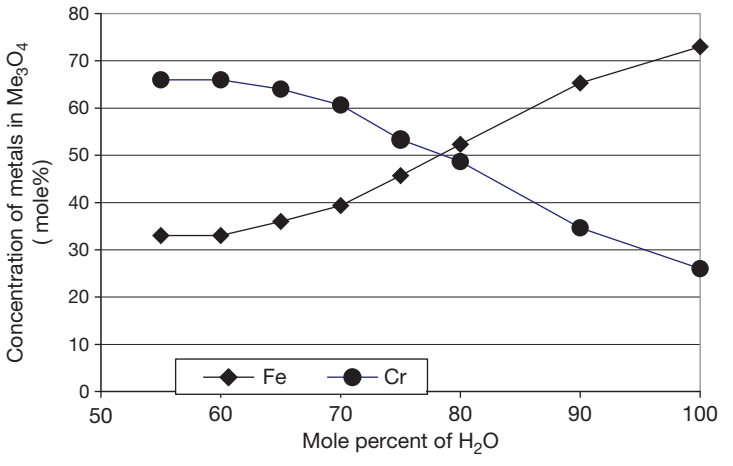

Figure 36 Effect of gas composition upon Me_3O_4 composition in alloy UNS S44600 at 1800 °F (982 °C).

The carburization corrosion rates were measured and shown in **Figure 39** for samples under H_2–1.2% CH_4 gas mixtures and **Figure 40** for samples under pure CH_4. Also carburization rates for 1 year were calculated based on the measured corrosion rates for 720 h and assuming parabolic kinetics for 1 year, as shown in **Figures 39 and 40**. The carburization results show that UNS S34700 has better carburization resistance than UNS S44600 and UNS N06025 in both testing gas environments.

The carburization corrosion rates for alloys in pure CH_4 are much higher than those in H_2–1.2% CH_4. Under pure CH_4 gas atmosphere at 1800 °F (982 °C), tested alloys were heavily coated with solid carbon on the surface and their carburization rates are much higher than the same samples in the H_2–1.2% CH_4 gas mixture. Carbon activity would have been one if the gas mixture had been at equilibrium. Since available data for well-known alloys like UNS N08810, HP, and HK show increasing carburization at higher carbon activities, the carbon activity must have been larger than one in the pure CH_4 gas atmosphere and the gas must not have been at equilibrium at 1800 °F (982 °C).

1.11.5 Summary

The various corrosion mechanisms are named for the corrosion products that form in high temperature gas phase corrosion of metals and alloys, which occur in a variety of industrial processes. The thermochemistry

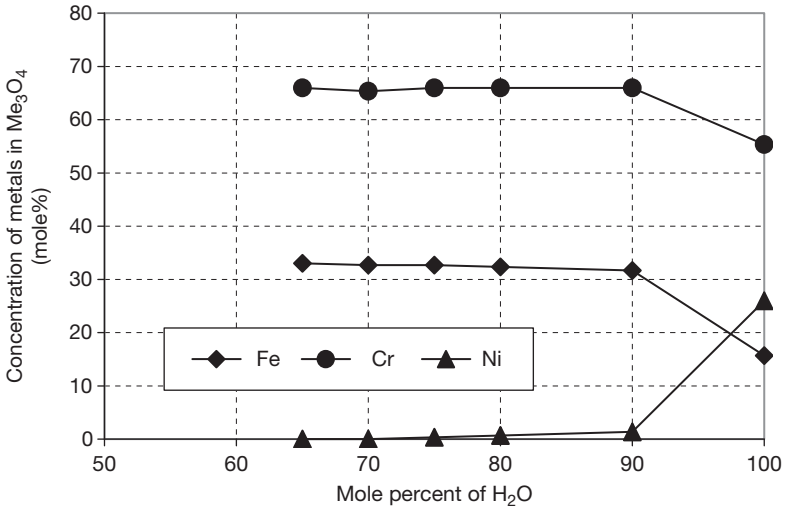

Figure 37 Effect of gas composition upon Me_3O_4 composition in alloy UNS N06025 at 1800 °F (982 °C).

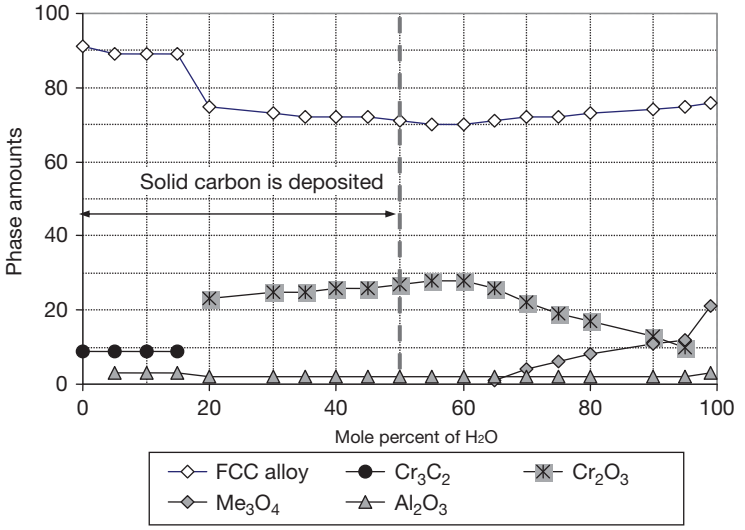

Figure 38 Equilibrium corrosion products of UNS N06025 under CH_4–H_2O gas mixture atmospheres at 1800 °F (982 °C).

of the interactions between the alloying elements and the species in the gas phase determines which corrosion products form. In most instances, increasing the temperature increases the rate of corrosion. However, the effect of changes in the gas species concentrations upon the rate of corrosion may have nonobvious effects upon the rate of corrosion, particularly when corrosion is producing a mixture of corrosion products. Much of the effects of mixed gas corrosion can be thought of in terms of a competition between the different corrosion products, which likely impact corrosion behaviors in various ways. Effects of changing gas species concentrations upon corrosion for mixed gas corrosion have been discussed for several classes of corrosion mechanisms. Any changes in gas composition, which induce greater stability of slower growing corrosion products, will tend to slow the rate of corrosion in mixed gases. For example, increasing the P_{O_2} in a gas, which is causing sulfidation/oxidation, will tend to favor slower oxide growth at the expense of growth of faster growing sulfides, thereby, slowing the rate of corrosion. This chapter has reviewed the current knowledge of how thermochemistry in terms of the P_{O_2} and P_{S_2} values of gases can describe corrosion behaviors for sulfidation/oxidation conditions and can even be used to select a test

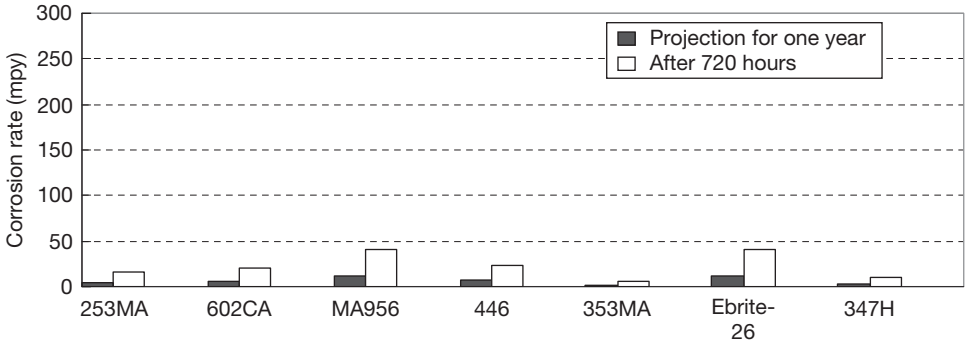

Figure 39 Carburization rates for alloys in H_2–1.2% CH_4 at 1800 °F (982 °C).

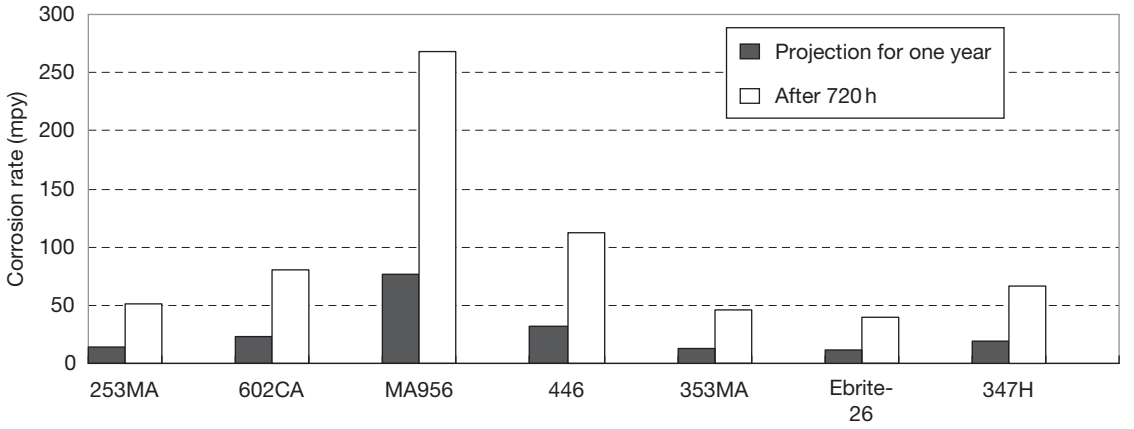

Figure 40 Carburization rates for alloys in CH_4 at 1800 °F (982 °C).

gas which is very different from the industrial gas in question. Industrial corrosion in H_2–H_2O–H_2S gases can be simulated in laboratory tests using CO–CO_2–COS, which are suggested because they are experimentally more convenient. Test exposure times must be long enough to achieve long-term corrosion behavior, as measured by the time needed for the parabolic rate constant to become independent of time, which is at least 500 h at 600 °C for a number of alloys discussed. Once long-time (time independent) parabolic time dependence is achieved, then the extent of corrosion over thousands of hours can be well correlated with a parabolic time dependence. Once the effects of gas composition, exposure time, and temperature are well understood for a given alloy and corrosion mechanism, it is also possible to predict alloy corrosion for many hot-gas corrosion mechanisms for wide ranges of conditions using correlations, even considering changing gaseous and temperature exposures, by summing the corrosion expected in the various sets of exposure conditions.

Corrosion can be well discussed and used in terms of total metal penetration, which is the sum of metal thickness lost by scale formation plus the metal thickness affected by internal corrosion product formation. Alloys vary widely in their relative amounts of total metal penetration for various corrosion mechanisms and exposure conditions, which is due to either internal penetration or scale formation.

The corrosion behaviors of alloys vary from surface to internal corrosion and were studied by assessing the stable corrosion products and alloy phases as functions of the ambient gas composition. There are transitions in corrosion behavior as the gas exposure changes, causing changes in the stable corrosion products. The metal loss information for alloys in several corrosive environments was reviewed and advice given on how to predict the probable corrosion

mechanism and amount of metal penetration as functions of the important variables. A new capability was developed and reviewed with the ability to predict formation of the basic types of corrosion products and thickness losses by corrosion for wide ranges of conditions of gas composition, temperatures, and times for many alloys.

Acknowledgments

Support by the following organizations are recognized and appreciated: US Department of Energy – Office of Industrial Technologies via cooperative agreement DE-FC02-00CH11020, Shell Global Solutions (US) Inc.; Shell International E&P Inc, Arthur L. Young of Humberside Solutions Ltd., Arthur D. Pelton of Centre for Research in Computational Thermochemistry in Université de Montréal, William T. Thompson of the Royal Military College of Canada, Oak Ridge National Laboratory, Foster Wheeler Development Corporation, KEMA, Caterpillar, Special Metals Corporation, Texaco, Haynes International, Usinor Industeel, Kvaerner Pulping Oy, Materials Technology Institute of the Chemicals Process Industries (MTI), Dupont, Exxon/Mobil, Rolled Alloys, VDM Fluor Daniel and Air Products. The experimental testing effort owes its deepest gratitude to Owen Kriegel and Paul F. Schmidt of Shell Global Solutions (US) Inc and research staff at ORNL. Data contributions from Haynes International, VDM and Special Metals Corporation are acknowledged. Ian G. Wright of Oak Ridge National Laboratory is thanked for his many contributuions. Technical contributions from Yali Li and Juan Gonzalez are acknowledged.

References

1. Haycock, E. W. In *High Temperature Metallic Corrosion of Sulphur and Its Compounds*; Foroulis, Z. A., Ed.; Electrochemical Society: Princeton, NJ, 1970; p 110.
2. Haycock, E. W.; Sharp, W. H. Corrosion of ferrous alloys by H_2S at high temperatures, Session from the 24th Meeting of the American Petroleum Institute, New York 1959.
3. Guzeit, J. In *Process Industries Corrosion – The Theory and Practice*; National Association of Corrosion Engineers: Houston, TX, 1986.
4. Backensto, E. B.; Drew, R. E.; Stapleford, C. C. In Corrosion; NACE, 1956; Vol. 12, p 22.
5. Sorell, G.; Hoyt, W. B. In Corrosion; NACE, 1956; Vol. 12, p 213t.
6. Lai, G. Y. *High-Temperature Corrosion of Engineering Alloys*; ASM International: Materials Park, OH, 1990; Literature from Haynes International Marketing, ''Technical Information, Oxidation Resistance of Haynes High Temperature Alloys''.
7. Stoklosa, A.; Stringer, J. *Oxid. Met.* **1977**, *11*, 263.
8. John, R. C.; Pelton, A. D.; Young, A. L.; Thompson, W. T.; Wright, I. G.; Besmann, T. M. Assessing corrosion in oil refining and petrochemical processing, Presented at Symposium on High Temperature Corrosion in Energy Related Systems, Angra dos Reis, Rio de Janeiro, 1–4 September 2002.
9. John, R. C.; Fort, W. C., III; Tait, R. A. *Mater. High Temp.* **1993**, *11*, 124.
10. John, R. C.; Young, A. L.; Thompson, W. T. *Corrosion/97*; National Association of Corrosion Engineers: Houston, TX, 1997; Paper 142.
11. Lai, G. Y. In Corrosion/84; National Association of Corrosion Engineers: Houston, TX, 1984; Paper 73. Data from brochures Haynes 188 and Pocket Guide to Haynes Alloys from Cabot Corp, 1986.
12. John, R. C. Second International Conference on Heat Resistant Materials, Gatlinburg, TN, 11–14 September 1995.
13. John, R. C. In Corrosion/96; National Association of Corrosion Engineers: Houston, TX, 1996; Paper 171.
14. Perkins, R. A. In *High Temperature Corrosion*; Rapp, R. A., Ed.; National Association of Corrosion Engineers: Houston, TX, 1981; pp 345–353.
15. Perkins, R. A. Proceedings of the Third Annual Conference on Materials for Coal Conversion and Utilization. U. S. Department of Energy, CONF-781018, October, 1978.
16. Natesan, K.; Chopra, O. K. In Proceedings of the Conference on Properties of High-Temperature Alloys; Foroulis, Z. A., Pettit, F. S., Eds.; The Electrochemical Society: New Jersey, 1976; pp 493–510.
17. Natesan, K. In *High Temperature Corrosion*; Rapp, R. A., Ed.; National Association of Corrosion Engineers: Houston, TX, 1981; pp 336–344.
18. Baxter, D. J.; Natesan, K. In *High Temperature Corrosion in Energy Systems*; Rothman, M. F., Ed.; TMS-AIME/MSD-ASM: Detroit, 1985, pp 237–252.
19. Bakker, W. T. Mixed oxidant corrosion in nonequilibrium syngas at 540 °C; Electric Power Research Institute: Palo Alto, CA, 1995.
20. John, R. C. In *High Temperature Corrosion in Energy Systems*; Rothman, M. F., Ed.; TMS-AIME/MSD-ASM: Detroit, 1985, pp 501–514.
21. John, R. C. In *High Temperature Materials/Corrosion – Fundamental Aspects of High Temperature Corrosion II*, Shores, D. A., Yurek, G. J., Eds.; Electrochemical Society, 1987, pp 86–99.
22. Waldner, P.; Pelton, A. D. *J. Phase Equilib. Diff.* **2005**, *26*, 23–28.
23. Waldner, P.; Pelton, A. D. Thermodynamic modeling of the Ni–S system, in press.
24. Waldner, P.; Pelton, A. D.; Thermodynamic modeling of the Fe–Ni–S system, in press.
25. John, R. C. In *Life Prediction of Corrodible Structures*; NACE, ISBN 1-877914-60-6 1994; Vol. 1.
26. John, R. C. Meeting of Electrochemical Society, 4–9 May 1986; paper no. 358.
27. John, R. C. *Fundamental Aspects of High Temperature Corrosion – II, Simultaneous Sulphidation and Oxidation of Alloy 800 in Mixed Gases*; Electrochemical Society, 1987; p 86.
28. Natesan, K. In *High Temperature Corrosion*; Rapp, R. A., Ed.; NACE: Houston, TX, 1983; p 336.
29. Baxter, D. J.; Natesan, K. *Oxid. Met.* **1989**, *31*, 305.
30. Rhamel, A.; Schorr, M.; Valesco-Tellez, A.; Pelton, A. *Oxid. Met.* **1987**, *27*, 199.

31. Perkins, R. A.; Morse, G.; Coons, W. C. Materials for syngas coolers, Report AP-2518, EPRI Research Report 1654-5, Palo Alto, CA, August 1982.
32. John, R. C.; Thompson, W. T.; Karakaya, I. In Corrosion/88 1988; Paper 136.
33. John, R. C.; Pelton, A. D.; Young, A. L.; Thompson, W. T.; Wright, I. G. MS&T Conference, Cincinnati, OH, 15–19 October 2006.
34. Kofstad, P. *High temperature Corrosion*; Elsevier Applied Science, 1988.
35. *Process Industries Corrosion*; National Association of Corrosion Engineers, 1975.
36. Norton, J. F.; Bakker, W. T. Eds. *Materials for Coal Gasification Power Plant*; Butterworth-Heinemann, 1993.
37. Bakker, W. T. Dapkunas, S.; Hill, V. Eds. *Materials for Coal Gasification*; ASM International, 1988.
38. Embury, J. D. Ed. *High Temperature Oxidation and Sulphidation Processes*; Pergamon Press, 1990.
39. Rapp, R. A. Ed. *High Temperature Corrosion*; National Association of Corrosion Engineers, 1983.
40. Streiff, R. Stringer, J. Krutenat, R. C.; Caillet, M. Eds. *High Temperature Corrosion – Advanced Materials and Coatings*; Elsevier Science, 1989.
41. Grabke, H. J. *Mater. Corros.* **2005**, *56*(6), 384–388.
42. Grabke, H. J.; Strauss, S.; Vogel, D. *Mater. Corros.* **2003**, *54*(11), 865–901.
43. Kothari, D. C.; *et al. Mater. Sci. Eng. A* **1989**, *116*, 89–95.
44. Agudo, L.; Sanchez, C.; Nachez, L.; Feugeas, J. N.; Staia, M. H. *Revista de la Facultad de Ingenieria, Universidad Central de Venezuela* **2005**, *20*(1), 71–76.
45. Issartel, C.; *et al. Corros. Sci.* **2004**, *46*(9), 2191–2201.
46. Issartel, C.; Buscail, H.; , Caudron, E.; *et al. Appl. Surf. Sci.* **2004**, *225*, 14–20.
47. Riffard, F.; Buscail, H.; Caudron, E.; Cueff, R.; Issartel, C.; Perrier, S. *J. Phys. IV* **2004**, *118*, 369–375.
48. Rawers, J. C. *Proc. Inst. Mech. Eng. L J. Mater. Des. Applic.* **2004**, *218*(L3), 239–246.
49. Han, S.; Young, D. J. *Oxid. Met.* **2001**, *55*(3–4), 223–242.
50. Krupp, U.; Christ, H.-J. *Oxid. Met.* **1999**, *52*(3–4), 277–298.
51. John, R. C. In Proceedings of the 4th International Symposium on High Temperature Corrosion and Protection of Materials, Les Embiez, France, 20–24 May 2000.
52. John, R. C.; Pelton, A. D.; Young, A. L.; Thompson, W. T.; Wright, I. G. Predicting equipment lifetimes with high temperature corrosion data, Presented at the 6th International Symposium on High Temperature Corrosion and Protection of Materials, Les Embiez, France, 16–21 May 2004; Proceedings of the Material Science Forum, 2004; Vols. 461–464, 599–610.
53. Thompson, W. T.; Bale, C. W.; Pelton, A. D. Facility for the analysis of chemical thermodynamics (FACT), Ecole Polytechnique, Royal Military College of Canada in Kingston, McGill University Montreal, Montreal, 1985.
54. Christ, H. J.; Berchtold, L.; Sockel, H. G. *Oxid. Met.* **1986**, *26*(1–2), 45–76.
55. Pedraza, F.; Grosseau-Poussard, J. L.; Abrasonis, G.; Riviére, J. P.; Dinhut, J. F. *J. Appl. Phys.* **2003**, *94*(12), 7509–7519.
56. Udyavar, M.; Young, D. J. *Corros. Sci.* **2000**, 42, 961–883.
57. Grabke, H. J. *Carburization: A High Temperature Corrosion Phenomenon*; MTI, 1998.
58. Kofstad, P. *High Temperature Corrosion*; Elsevier Applied Science, 1988.
59. Grabke, H. J.; Muller, E. M.; Speck, H. V.; Konczos, G. *Steel Res.* **1985**, *56*(5), 275–282.
60. Grabke, H. J.; Müller-Lorenz, E. M.; Schender, A. *ISIJ Int.* **2001**, *41*, S1–S8.
61. John, R. C.; Pelton, A. D.; Young, A. L.; Spencer, P., Thompson, W. T. Alloy Carburization at Temperatures of 1200–2100°F (650–1150°C); NACE – Corrosion, 2003, Paper 03474.
62. Nava Paz, J. C.; Grabke, H. J. *Oxid. Met.* **1993**, *39*(5/6), 437–456.
63. Ben-Haroe, I.; Rosen, A.; Hall, I. W. *Mater. Sci. Technol.* **1993**, *9*, 620–626.
64. Bullock, E.; Frampton, P. D.; Norton, J. F. *Microstruct. Sci.* **1981**, *9*, 215–224.
65. Klöwer, J. *Mater. Corros.* **1996**, *47*, 685–694.
66. Driver, D.; Barrand, P. *J. Iron Steel Inst.* **1964**, *202*, 614–615.

1.12 Carburization and Metal Dusting

D. J. Young
School of Materials Science and Engineering, University of New South Wales, UNSW Sydney, NSW 2033, Australia

Abbreviations

EDS Energy dispersive spectrometry (of X-rays)
FIB Focused ion beam
ppm Parts per million (concentration)
SAD Selected area diffraction
TEM Transmission electron microscopy

Symbols

α Ferrite; solubility
γ Austenite
γ_i Activity coefficient of species *i*
ε Tortuosity factor, reflecting diffusional blocking by precipitate
ν Stoichiometric coefficient
a_i Activity of species *i*
erf Error function
erfc Complementary error function
g Critical volume fraction necessary to form external scale (of oxide or carbide)
k_d Metal disintegration (dusting) rate constant
$k_p^{(i)}$ Parabolic rate constant for internal carburisation
r_n Rate constant for reaction *n*

t Time
w/o Weight percent
x Position co-ordinate
A Surface area
B_i Mobility of species i
D_i Diffusion coefficient of species i
E_A Activation energy for kinetic process
ΔG_f^o standard Gibbs free energy of formation
$\Delta \bar{H}_C$ Partial molar enthalpy of carbon dissolution
K_n Equilibrium constant for reaction n
K_{sp} Solubility product
N_i Mol fraction of species i
$N_i^{(o)}$ Original mol fraction of species i in solid prior to diffusion
$N_i^{(s)}$ Mol fraction of species i at surface of alloy
Q Activation energy for diffusion
R General gas constant
$\Delta \bar{S}_C^{XS}$ Partial molar excess entropy of carbon dissolution
T Temperature
V_i Molar volume of species i
W Weight
X Scale thickness
X_i Width of internal precipitation zone

1.12.1 Introduction

Carbonaceous gases are generated by the combustion of fossil fuels: coal, oil, and natural gas. The reactions

$$C + \frac{1}{2}O_2 = CO \quad [1]$$

$$CO + \frac{1}{2}O_2 = CO_2 \quad [2]$$

$$CH_4 + 2O_2 = CO_2 + 2H_2O \quad [3]$$

are often carried out using excess air, so that the exhaust gases contain free molecular oxygen plus CO_2 and H_2O. Despite the use of excess air or oxygen, locally reducing conditions can form and persist in large-scale combustion units. Such conditions can lead to carbon attack, as will be discussed in the following sections.

A number of other high temperature processes are conducted under reducing conditions so as to produce hydrogen or CO, rather than their oxidation products. Steam reforming of natural gas

$$CH_4 + H_2O = CO + 3H_2 \quad [4]$$

at temperatures around 800–900 °C is widely used to produce hydrogen. This process is carried out by passing the gases through catalyst beds in externally heated alloy tubes. Somewhat similar tubular reactors are used in the pyrolysis or 'steam cracking' process for making ethylene or propylene; for example,

$$(H_2O) + C_2H_6 = C_2H_4 + H_2 + (H_2O) \quad [5]$$

In this case, the steam is added as a diluent in order to reduce the amount of solid carbon produced by gas-phase pyrolysis.

Feedstock materials, hydrocarbons, have been rising in price, and the need for improved process efficiencies has led to higher operating temperatures. Simultaneously, tube wall thicknesses have been reduced to improve heat transfer. Thus, process engineering changes have led to higher tube metal temperatures and reduced load-bearing sections. These increased demands on material properties have been met by a series of advances in alloy design. The tubes are centrifugally cast, austenitic chromia formers. Their compositions have evolved from the old HK 40 grade (Fe–25Cr–20Ni), through the HP grades (Fe–25Cr–35Ni) to high-nickel alloys containing 45% or even 60% Ni. The increased alloy levels have provided significant improvements in creep properties, but the materials are still subject to corrosion by carbon.

The process of coal gasification is of potential importance in achieving high-efficiency electric power generation. Steam is contacted with coal at high temperature, producing synthesis gas

$$C + H_2O = CO + H_2 \quad [6]$$

Although coal gasification has been employed for a long time, its use on the scale and at the intensity required to support gas turbine-driven power generation is relatively new. However, the carbon corrosion mechanisms can be expected to be related to those observed in steam reforming and steam cracking plants.

Under combustion conditions, the oxygen potential is usually high enough to guarantee oxide scale formation. The questions of interest then concern interaction of CO_2 with the oxide. In contrast, synthesis gas and other carbonaceous gases handled in the chemical and petrochemical industries are characterized by high a_C values and low oxygen potentials. Typically, these gases are oxidizing to chromium and aluminum, but not to iron or nickel. The questions of interest, therefore, concern the ability of Cr_2O_3 and Al_2O_3 scales to exclude carbon from the alloy, and the consequences of oxide scale failure when carbonaceous gas species contact the metal surface.

We consider first the simple case where the oxygen potential is so low that no oxide forms, and corrosion by carbon alone results. If the carbon activity, a_C, is less than 1, but large enough to stabilize a metal carbide, the reaction is described as carburization. Such reactions are rapid and destructive. However, if the gas is supersaturated with respect to carbon ($a_C > 1$), an even greater threat emerges. Catalysis of carbon deposition by the metal can lead to its disruption and fragmentation in an extremely rapid corrosion process known as metal dusting. Dusting mechanisms are different for ferritic and austenitic alloys, and they are discussed separately. Alloy design strategies for slowing carburization and metal dusting are shown to be of limited value. However, alloying to achieve protective oxide formation can delay carbon access to the metal. This approach is discussed together with other surface treatments in the final section of this chapter.

1.12.2 Gaseous Carbon Activities

The common gas-phase processes producing carbon are the synthesis gas reaction

$$CO + H_2 = H_2O + C \quad [7]$$

the Boudouard reaction

$$2CO = CO_2 + C \quad [8]$$

and hydrocarbon cracking, for example,

$$CH_4 = 2H_2 + C \quad [9]$$

The standard free energies of these reactions are listed in Table 1. It is necessary to recognize that all three reactions are very slow as homogenous gas-phase processes. They will not reach equilibrium in a typical laboratory reactor, unless catalyzed. Although many materials of practical interest – iron, nickel, cobalt, and their alloys – are catalytically active to these reactions, their oxide scales are inert.

Table 1 Gas phase equilibria relevant to carburizing

Reaction	$\Delta G_f^\circ = A + BT(J)$	
	A	*B*
$CO + H_2 = H_2O + C$	−134 515	142.37
$2CO = CO_2 + C$	−170 700	174.5
$CH_4 = 2H_2 + C$	+87 399	−108.74

As seen in Figure 1, temperature effects are very different for these carbon-producing reactions. Thus, methane, and hydrocarbons in general, can produce significant carbon activities only at high temperatures. On the other hand, the synthesis gas and Boudouard reactions produce increasing carbon activities as the temperature is lowered.

It is because these gases are difficult to equilibrate that they can become supersaturated with respect to carbon; that is, $a_C > 1$. An example is synthesis gas produced in a steam reforming unit, which will normally have $a_C < 0.5$. As the gas is cooled from reaction temperature, however, the rate of reaction [7] is so slow that the gas fails to adjust its composition by depositing carbon. The gas-phase carbon activity calculated from

$$a_C[7] = \frac{K_7 p_{H_2} p_{CO}}{p_{H_2O}} \quad [10]$$

can then be much greater than 1. It is recognized that the same gas also produces carbon via reaction [8], and one can calculate

$$a_C[8] = \frac{K_8 p_{CO}^2}{p_{CO_2}} \quad [11]$$

In general, $a_C[7] \neq a_C[8]$, because the gas is not at equilibrium. In this situation, it is appropriate to consider reactions [7]–[9] as separate, independent processes, as will be demonstrated in Sections 1.12.6 and 1.12.7. Nonetheless, because reaction [7] is usually faster than [8], it is common to calculate a_C from eqn. [1].

Carburization experiments require $a_C \leq 1$. The use of CH_4/H_2 gas mixtures to control carbon activity is inadvisable at temperatures below ~1000 °C, because of the slow rate of reaction [9] and the usually brief residence time of a laboratory reactor. It is preferable to use mixtures of H_2 and C_3H_6, as the latter pyrolyzes readily.

1.12.3 Carburization

Carbides are much less stable than oxides, as seen from the examples in Table 2. Thermodynamic data for other carbides can be found in a review by Shatynski.[1] Of the common alloy base metals, nickel and cobalt do not form carbides under the conditions of interest. Iron forms cementite, Fe_3C, at temperatures below 763 °C only if $a_C > 1$. Exposure of these metals to reducing carbonaceous gases leads to dissolution of carbon at the metal surface and its

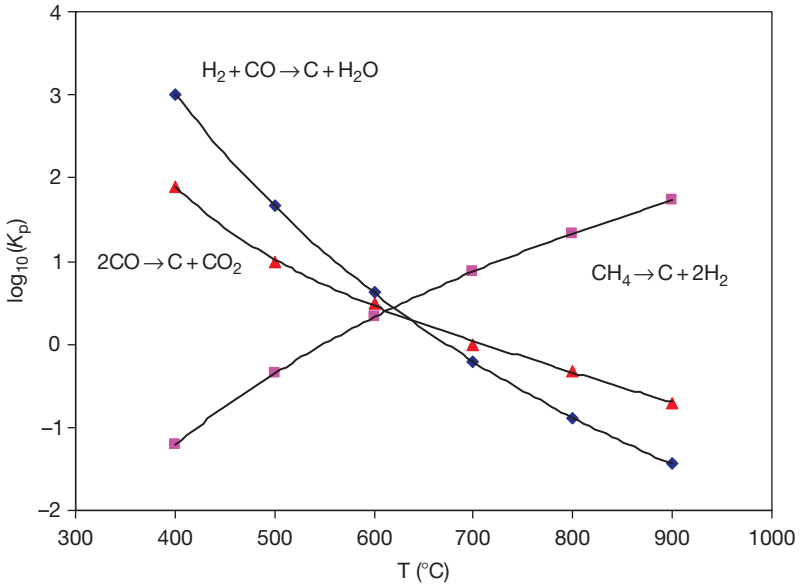

Figure 1 Equilibrium constants for gas-phase carbon producing reactions.

Table 2 Properties of metal carbides

Carbide	$\Delta G_f^\circ = A + BT(J)$		V_{MC_y}* *(cm³)*	*MP (°C)*
	A	*B*		
$Cr_{23}C_6$	−411 200	−38.7	7.91	1580
Cr_7C_3	−174 509	−25.5	8.26	1665
Cr_3C_2	−84 353	−11.53	8.98	1895
NbC	−130 122	+1.67	13.47	3480
SiC	−113 386	+75.7	13.70	2700
Al_4C_3	−266 520	+96.2	15.24	~1400
Fe_3C	29 037	−28.0	8.31	1650

*Volume per mole of metal

diffusion inwards, but no carbide phase is formed if $a_C < 1$. If the metal surface is at equilibrium with the gas phase, the surface concentration of dissolved carbon $N_C^{(s)}$ (mole fraction), can be found from the relationship

$$N_C^{(s)} = Ka_C \qquad [12]$$

Data for carbon dissolution in iron and nickel is summarized in Table 3, where the carbon solubility in nickel is seen to be much lower than in γ-Fe. If inward carbon diffusion causes no phase change in the solvent metal, and if furthermore D_C is independent of composition, then the resulting carbon concentration profile is found by solving Fick's second law to obtain

Table 3 Partial molar enthalpy and entropy for carbon dissolution in metal

Metal	$\Delta\bar{G}_C$ *(kJ mol⁻¹)*	ΔS_c^{xs} *(J mol⁻¹ K⁻¹)*	*Ref*
Ni	54	5	2
γ-Fe	44.04	17.62	3

$$\frac{N_C - N_C^{(o)}}{N_C^{(s)} - N_C^{(o)}} = \text{erfc}\left(\frac{x}{2\sqrt{D_C t}}\right) \qquad [13]$$

Here, $N_C^{(o)}$ represents the original carbon level in the metal prior to carburization. The rate at which the carburization zone widens is given approximately by

$$X_i^2 = 4D_C t \qquad [14]$$

As D_C values in austenite are high, the process is fast. Using data for D_C,[4, 5] it is found that carbon penetrates about 3 mm into each of γ-Fe and Ni in 24 h at 1000 °C.

The heat-resisting alloys used in contact with carbon-rich gases are usually chromia formers. As seen in Table 2, chromium also forms reasonably stable carbides. It is commonly observed[6–8] that exposure of these alloys to gas compositions such that no chromia scale can form leads to internal chromium carbide precipitation, rather than external scale formation. The conditions under which this

reaction morphology develops are now examined using model Fe–Cr, Ni–Cr, and Fe–Ni–Cr alloys, for which the necessary data is available.

1.12.4 Internal Carburization of Model Alloys

1.12.4.1 Reaction Morphologies and Thermodynamics

Chromium carbides are the expected reaction products and their formation within the alloy is the outcome of competition between rival processes. Scale formation is favored by rapid diffusion of chromium from the alloy to its surface, whereas internal precipitation is favored by rapid carbon ingress. Wagner's analysis[9] of this situation allows calculation of the minimum value of $N_{Cr}^{(o)}$ at which scaling is favored over internal precipitation

$$N_{Cr}^{(o)} = \left(g_{CrC_v} \frac{\pi}{2v} \frac{V_A}{V_{CrC_v}} \frac{N_C^{(s)} D_C}{D_{Cr}} \right)^{1/2} \quad [15]$$

where g is the critical volume fraction necessary to form a continuous carbide layer, V_A and V_{CrC_v} are the molar volumes of alloy and carbide, D_C and D_{Cr} are the diffusion coefficients in the alloy of the indicated solutes, and v is the stoichiometric constant for the carbide CrC_v. Choosing Nimonic 75 (approximately Ni–20Cr) as a basis for calculation, we can specify $V_A = 6.58\ cm^3\ mol^{-1}$. Values for carbon permeability $(N_C^{(s)} D_C)$ and D_{Cr} listed in **Table 4**, together with V_{CrC_v} from **Table 2** and the supposition $g = 0.3$, lead to estimates of $N_{Cr}^{(o)} = 15$, 20, and 37 required to form scales of Cr_3C_2, Cr_7C_3, and $Cr_{23}C_6$, respectively, at 1000 °C. Of course, values of $N > 1$ lack physical significance and result from inaccuracies in the data. The conclusion is simply that Ni–Cr alloys are unlikely to form carbide scales exclusively, because the inward carbon flux is so high and the molar volume of chromium carbide is small.

The conditions necessary for carbide precipitation are now examined more closely. In the case of $Cr_{23}C_6$, we can write

$$(M) + 23\underline{Cr} + 6\underline{C} = Cr_{23}C_6(+M), \Delta G_P \quad [16]$$

the free energy change for which can be calculated from data for carbide formation

$$23Cr + 6C = Cr_{23}C_6, \Delta G_f^\circ \quad [17]$$

and alloy component dissolution

$$Cr = \underline{Cr}, \Delta \bar{G}_{Cr} \quad [18]$$

$$C = \underline{C}, \Delta \bar{G}_C \quad [19]$$

in the solvent metal, M. Thus,

$$\Delta G_P = \Delta G_f^\circ - 23\Delta \bar{G}_{Cr} - 6\Delta \bar{G}_C \quad [20]$$

and we evaluate the carbide solubility product

$$N_{Cr}^{23} N_C^6 = K_{sp} = \exp[(\Delta G_f^\circ - 23\Delta \bar{H}_{Cr} - 6\Delta \bar{H}_C)/RT] \quad [21]$$

with $\bar{H}_i$ being the partial molar heat of dissolution. A similar treatment for Cr_7C_3 leads to the result

$$N_{Cr}^{7} N_C^3 = K_{sp} = \exp[(\Delta G_f^\circ - 7\Delta \bar{H}_{Cr} - 6\Delta \bar{H}_{Cr})/RT] \quad [22]$$

Standard values (**Table 2**) for ΔG_f°, carbon solubility data for γ-Fe and Ni (**Table 3**), and activity coefficient data for Fe–Cr[10] and Ni–Cr[11] allow calculation of carbide solubility product values shown in **Tables 5** and **6**.

Carbon solute levels in γ-Fe and Ni in equilibrium with $a_C = 1$ are also shown in the tables, along with the corresponding minimum chromium concentrations necessary to stabilize each carbide. Iron base alloys are predicted on this basis to be more susceptible to internal carbide precipitation. This prediction is tested by comparing the calculated minimum N_{Cr} values required for carbide precipitation with the

Table 4 Permeability data for carburization

Alloy	*T (°C)*	$N_C^{(s)} D_C$	D_{Cr}
γ-Fe	900	4.3×10^{-9}	4.4×10^{-13}
	1000	1.4×10^{-8}	3.7×10^{-12}
	1100	5.5×10^{-8}	2.3×10^{-11}
Ni	900	7.9×10^{-10}	8.0×10^{-13}
	1000	3.6×10^{-9}	7.2×10^{-12}
	1100	1.4×10^{-8}	4.7×10^{-11}

Table 5 Chromium carbide precipitation in Fe–Cr alloys

Alloy	*900 °C*	*1000 °C*	*1100 °C*
$N_C^{(s)}$ (γ-Fe)	0.057	0.066	0.098
$K_{sp}(Cr_{23}C_6)$	1×10^{-29}	3.6×10^{-27}	2.6×10^{-24}
N_{Cr}(min)	0.12	0.14	0.17
$K_{sp}(Cr_7C_3)$	3×10^{-16}	3.8×10^{-15}	3.4×10^{-14}
N_{Cr}(min)	0.02	0.03	0.03

Table 6 Chromium carbide precipitation in Ni–Cr alloys

Alloy	*900 °C*	*1000 °C*	*1100 °C*
$N_C^{(s)}$	0.007	0.011	0.016
$K_{sp}(Cr_{23}C_6)$	9.9×10^{-26}	8.4×10^{-24}	3.7×10^{-22}
N_{Cr}(min)	0.29	0.32	0.34
$K_{sp}(Cr_7C_3)$	9.8×10^{-14}	9.4×10^{-13}	6.5×10^{-12}
N_{Cr}(min)	0.10	0.13	0.17

Table 7 Internal carbides found in Ni–Cr and Fe–Cr at 1000 °C at ambient $a_C = 1$

Alloy	$N_{Cr}^{(o)}$	*Surface carbides*	*Internal carbides*	*Ref.*
Ni–Cr	0.11	None	None	12
	0.22	Cr_3C_2	Cr_7C_3	12
	0.33		Cr_7C_3	13
Fe–Cr	0.05	M_3C	M_7C_3[a]	14
	0.08	M_3C	M_7C_3	14
	0.11	M_3C	M_7C_3	14
	0.18	M_7C_3	$M_7C_3 + M_{23}C_6$	14
	0.26	M_7C_3	$M_7C_3 + M_{23}C_6$	14

[a]M: chromium-rich (Cr + Fe).

experimental results for 1000 °C summarized in Table 7. The appearance of the carbide precipitation zones in Fe–Cr alloys is illustrated in Figure 2. As predicted, Fe–Cr alloys of high chromium content formed both carbides, whereas Ni–Cr formed only Cr_7C_3. Furthermore, the prediction that no carbide should form in Ni–Cr with $N_{Cr}^{(o)} < 0.13$ is borne out.

The success of this simple thermodynamic treatment indicates that local equilibrium is attained, and a steady-state diffusion description should be applicable. However, whilst the assumption that the chromium carbides are pure phases – the basis for eqns. [21] and [22] – is reasonable for the Ni–Cr–C system, it is a poor approximation for Fe–Cr–C. As seen in the phase diagram of Figure 3, iron solubilities in the carbides are high, and cannot be neglected. It is possible to calculate K_{sp} values for the mixed carbides $(Cr,Fe)_{23}C_6$ and $(Cr,Fe)_7C_3$, but a simpler approach is to construct diffusion paths representing the locus of phase constitutions along lines through the reaction zone. As $D_C \gg D_{Cr}$, these paths are constructed on the basis that only carbon diffuses and hence the N_{Cr}/N_{Fe} ratio remains unchanged within the reaction zone.

The diffusion path in Figure 3 for $N_{Cr}^{(o)} = 0.08$ is seen to cross the $\gamma + M_7C_3$ two-phase region, corresponding to internal precipitation of this carbide, before entering the single-phase M_3C zone, in agreement with experimental observation (Table 7). An alloy with $N_{Cr}^{(o)} = 0.18$ is seen to develop a carbon diffusion path which crosses successive two-phase regions $\gamma + M_{23}C_6$ and $\gamma + M_7C_3$ before entering the single-phase M_7C_3 field. Again, this corresponds with the experimental observation (Table 7) of two internal precipitation zones, with $M_{23}C_6$ forming in the inner (lower a_C) zone.

As iron solubility in the carbides increases with a_C, the Fe/Cr ratio in the precipitates is predicted to decrease with increasing depth within the precipitation zone. Microanalysis in a transmission electron microscope of carbides precipitated within an Fe–Ni–Cr alloy[16] revealed the partitioning of chromium between precipitate and matrix in the carburized alloy. As seen in Figure 4, the results are in reasonable agreement with measured equilibrium values, and again it is concluded that local equilibrium is achieved throughout the precipitation zone. Two more important inferences can be drawn from the phase diagram of Figure 3. Carburization is predicted to transform the alloy matrix of a high-chromium Fe–Cr alloy from ferrite to austenite as a result of chromium depletion and carbon saturation. As shown in Figure 2, this transformation is observed at the precipitation front. Secondly, if $N_{Cr}^{(o)}$ is less than ~0.4, then $(Fe,Cr)_3C$ is predicted to form at or near the alloy surface if the gas phase a_C value is high enough. This is important in metal dusting reactions (Section 1.12.6), but can be ignored when studying carburization reactions at $a_C \leq 1$. Furthermore, in austenitic alloys the nickel content destabilizes Fe_3C, and the phase is not observed.

1.12.4.2 Carburization Kinetics

Internal carburization is a particular form of internal oxidation, and its kinetics can therefore[6–8,12] be described using Wagner's theory.[9] Because $N_C^{(s)} D_C \gg N_{Cr}^{(o)} D_{Cr}$, the rate at which the carbide precipitation zone deepens is given by

$$X_i^2 = 2k_p^{(i)} t \qquad [23]$$

$$k_p^{(i)} = \frac{\epsilon N_C^{(s)} D_C}{v N_M^{(o)}} \qquad [24]$$

where $N_M^{(o)}$ is the original alloy concentration of metal M which forms carbide MC_v. Thus, carburization rates are predicted to vary inversely with concentration of reactive solute metal. Data for a series of Fe–Cr

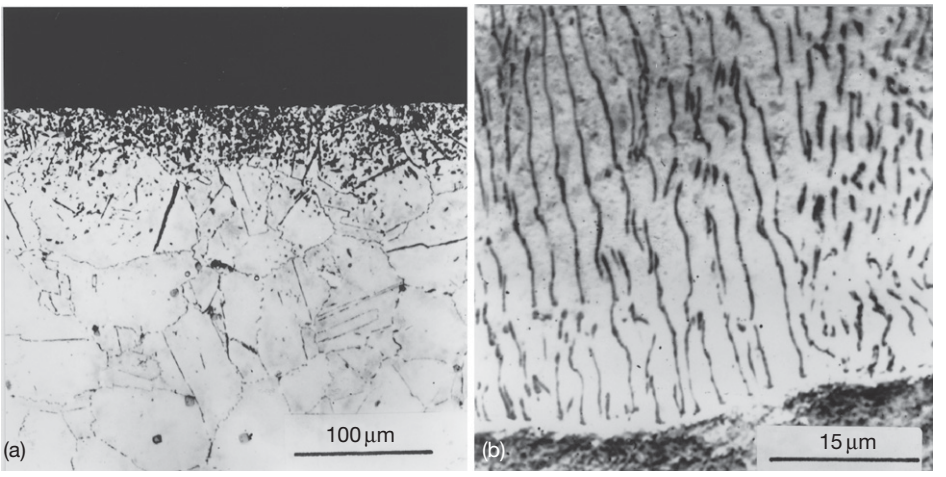

Figure 2 Internal carburization of Fe–Cr at 1000 °C (a) Fe–7.5Cr forms M_7C_3 precipitates and (b) Fe–17Cr forms innermost zone of $M_{23}C_6$ precipitates.[14]

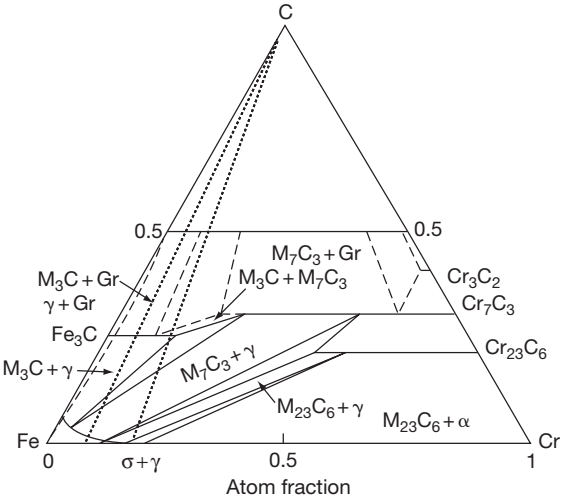

Figure 3 Isothermal section at 1000 °C of the Fe–Cr–C phase diagram.[15] Dotted lines show carburization diffusion paths for $D_C \gg D_{Cr}$.

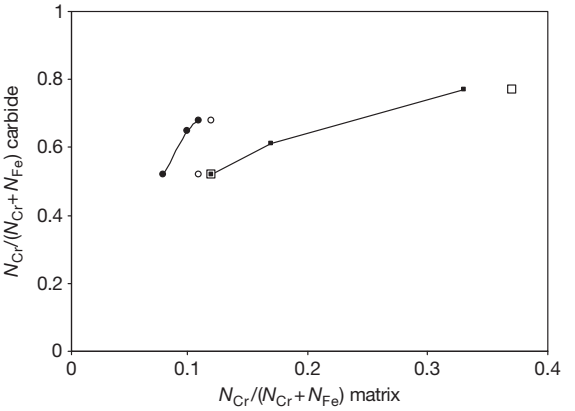

Figure 4 Partitioning of Cr between precipitates and matrix in carburized alloy[16] (filled symbols) and in equilibrium studies[15] (open symbols). Circles for M_7C_3 and squares for $M_{23}C_6$.

alloys[14,17] is shown in Figure 5. The kinetics are seen to be parabolic, and plots of $k_p^{(i)}$ against $1/N_{Cr}^{(o)}$ are linear except at high $N_{Cr}^{(o)}$ values. The slopes of these lines were used together with $v = 0.71$ (for $(Cr_{0.6}Fe_{0.4})_7C_3$ formed by low-chromium alloys) and the assumption $\epsilon = 1$ to calculate carbon permeabilities. Comparison in Table 8 with values found from $N_C^{(s)}$[3] and D_C[4] measurements shows good agreement, demonstrating the utility of eqn. [24] in describing carburization rates. This is at first sight surprising, as eqn. [24] is based on the assumption that $K_{sp} \ll 1$, and the concentration of chromium in the matrix being close to zero. However, as will be seen in Section 1.12.4.3, the effect on carburization rates is small.

A further prediction of eqn. [24] is that carburization rates are determined by the permeability of the metal matrix, regardless of the identity of the precipitating carbide, providing that changes in the stoichiometric coefficient v are taken into account. Permeability values calculated for nickel by Allen and Douglass[12] from their carburization measurements of Ni–V, Ni–Cr, and Ni–Nb alloys are seen in Table 9 to be in approximate agreement with each other and with values found from independently

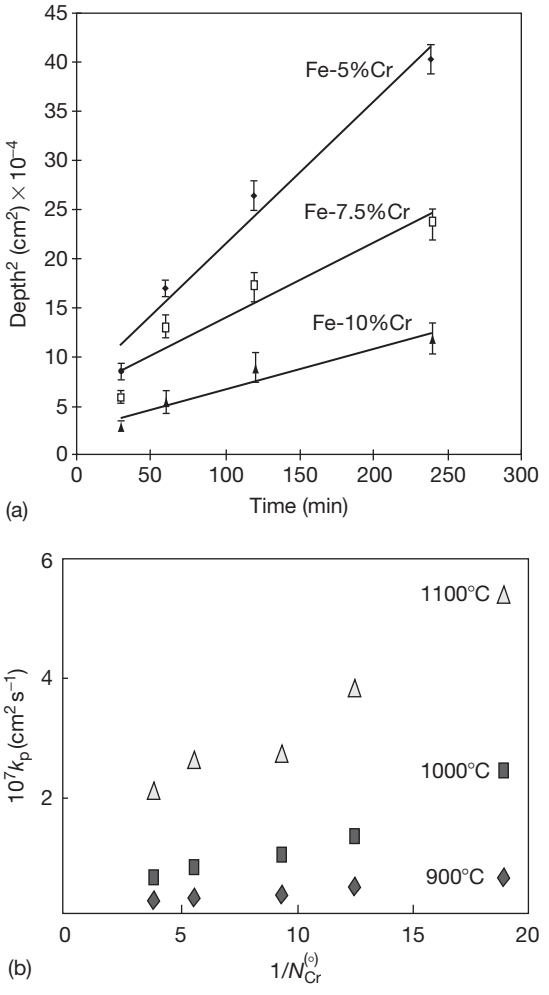

Figure 5 Carburization of Fe–Cr alloys (a) representative kinetics at 1000 °C and (b) effect of alloy chromium content on carburization rate.[14,17]

measured values of $N_C^{(s)}$[2] and D_C.[5] It is concluded that internal carburization of both Fe and Ni base alloys is controlled by interstitial diffusion of carbon through the depleted metal matrix lattice. The temperature effect on the rate is described by the empirical equation:

$$k_p^{(i)} = k_o^{(i)} \exp(-E_A/RT) \qquad [25]$$

Logarithmic differentiation of eqn. [24] yields

$$E_A = \Delta\bar{H}_C + Q \qquad [26]$$

where Q is the activation energy of diffusion. In the case of Fe–Cr alloys, the extent of iron dissolution in the carbides varies with temperature as does the

Table 8 Carbon permeabilities $N_C^{(s)}D_C$ ($cm^2\,s^{-1}$) in Fe–Cr

	900 °C	*1000 °C*	*1100 °C*
Carburization kinetics	6.6×10^{-9}	2.5×10^{-8}	6.2×10^{-8}
From $N_C^{(s)}$ and D_C	4.3×10^{-9}	1.4×10^{-8}	5.5×10^{-8}

Table 9 Carbon permeabilities ($N_C^{(s)}D_C$) ($10^{10}\,cm^2\,s^{-1}$) deduced from carburization kinetics of Ni–base alloys[12]

Alloy	*T (°C)*			
	700	*800*	*900*	*1000*
Ni–12V	0.40	2.2	11	44
Ni–20Cr	0.21	0.8	8	55
Ni–3Nb	0.30		6	14
From $N_C^{(s)}$ and D_C	0.19	1.6	7	36

stability of the carbides, and the simple description of eqn. [26] cannot be expected to apply. In the case of Ni–Cr alloys, however, nickel dissolves to only a small extent in the carbides, and Cr_7C_3 is the only stable internal carbide over a wide range of temperature for $N_{Cr}^{(0)} \approx 0.2$. The value of $E_A = 190\,kJ\,mol^{-1}$ measured by Allen and Douglass[12] for Ni–20Cr agrees with the prediction of eqn. [26] based on $\Delta\bar{H}_C = 54\,kJ\,mol^{-1}$ [2] and $Q = 138\,kJ\,mol^{-1}$ [5].

Chromia-forming alloys are usually based on Fe–Ni, and the applicability of eqn. [24] to Fe–Ni–Cr model alloys is now tested. Carburization of 25Cr alloys at 1000 °C and $a_C = 1$ produces two reaction zones. Diffraction studies identified the near-surface zone precipitates as M_7C_3, and those in the inner zone as $M_{23}C_6$. Carburization kinetics of a series of Fe–Ni–Cr alloys have been found[18] to be parabolic at 1000 °C, and the rate constants are seen in **Figure 6** to vary considerably with alloy nickel content. If nearly all the chromium is precipitated as carbide, then the reaction is sustained by carbon dissolution in and diffusion through the remaining Fe–Ni matrix. Ignoring the dissolution of some of the iron into carbide, we approximate the matrix as having the same N_{Ni}/N_{Fe} ratio as the parent alloy. On this basis, one can use values of $N_C^{(s)}$ measured by Wada *et al.*[2] for Fe–Ni alloys and for D_C measured by Bose and Grabke[19] to predict carburization rates from eqn. [24]. Measured and predicted rates were found[18] to agree very well. It is therefore concluded that the Wagner theory provides a satisfactory basis for describing the carburization of alloy compositions close to those of

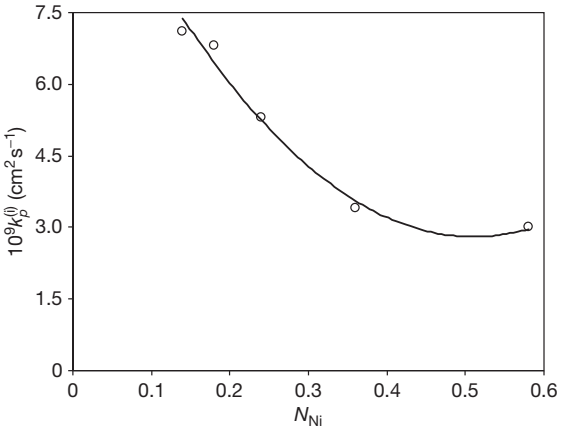

Figure 6 Variation of carburization rate at 1000 °C with Ni content of Fe–Ni–25Cr alloys.[18]

commercial heat-resisting alloys. Before going on to consider practical alloys, it is worth considering the microstructures and distributions of carbide precipitates.

1.12.4.3 Carbide Microstructures and Distributions

Particles of M_7C_3 precipitated in austenite are globular, and develop no rational orientation relationship with the matrix. In contrast, $M_{23}C_6$ possesses a cubic structure and develops a strong cube-in-cube orientation relationship with the fcc γ-matrix[20]

$$[001]_\gamma[001]_{M_{23}C_6} : (100)_\gamma(100)_{M_{23}C_6} \qquad [27]$$

Usually, the $M_{23}C_6$ precipitates are small, cuboidal, or needle-shaped particles (e.g., **Figure 7**). The small precipitate size reflects the fact that they grew for only a short time: a result of the continued nucleation of new particles as the reaction front advanced into the alloys. This in turn was due to rapid carbon diffusion, which quickly produced sufficient supersaturation to favor homogeneously distributed nucleation. In other circumstances, the same carbide can form elongated lamellar or lath shaped precipitates oriented parallel to the reaction direction (**Figure 7**). As the value of $k_p^{(i)}$ is 30–50% higher when the aligned microstructure is adopted, the reasons for its development are of interest.

Lamellar or cellular $M_{23}C_6$ microstructures have been reported to develop in ferritic alloys,[14,16,21,22] in high-nickel austenitics,[18] and in a variety of heat-resisting alloys carburized at low temperatures.[23,24] It is also observed in previously nitrided Fe–Ni–Cr

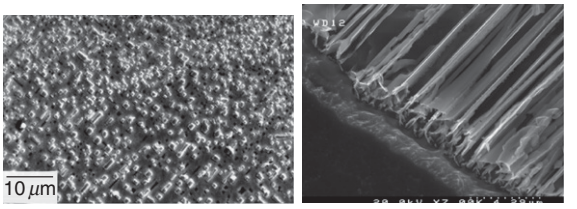

Figure 7 Cuboidal and lath-shaped $M_{23}C_6$ precipitates at the reaction front in Fe–20Ni–25Cr carburized at 1000 °C.

alloys.[18,20] A distinctive common feature in these cases is the formation of a grain boundary at the carbide precipitation front. In the case of ferritic alloys (**Figure 2(b)**), the boundary corresponds to the phase transformation

$$\alpha\text{-}(Fe,Cr) + x\underline{C} \rightarrow \gamma\text{-}(Fe,C) + Cr_{23}C_6 \qquad [28]$$

In high-nickel alloys, lamellar carbides develop in colonies in the alloy interior. It seems likely that they nucleated at alloy grain boundaries and then grew into the adjacent grain in a discontinuous precipitation process which is now described.

A clear view of the boundary at the carbide precipitation front is shown in **Figure 8** for an Fe–20Ni–25Cr alloy first subjected to a brief period of internal nitridation to form a boundary just beneath the surface. Subsequent carburization led to the pictured microstructure: the dark grain on the right is unreacted austenite, the light grain on the left is chromium-depleted matrix, and the precipitates are $M_{23}C_6$. The selected area diffraction pattern shows the same cube-in-cube orientation relationship [27] between precipitate and matrix. The crystallographically oriented sides of the precipitates were always the close-packed (111) planes. No rational orientation relationships were found between unreacted austenite and either reacted austenite or carbide. Microanalysis results in **Figure 8** show a step function change in N_{Cr} at the austenite/depleted austenite grain boundary, but no sign of lateral diffusion within the matrix. The mechanism is that of discontinuous precipitation[20,25]

$$\gamma + \underline{C} = \gamma^D + Cr_{23}C_6 \qquad [29]$$

where γ^D denotes depleted austenite. The change in crystallographic orientation from parent γ to product γ^D is obvious in **Figure 8**. This reorientation resulted from the free energy reduction achieved when the austenite formed coherent interfaces with the precipitates which grew approximately unidirectionally, parallel to the carbon diffusion direction.

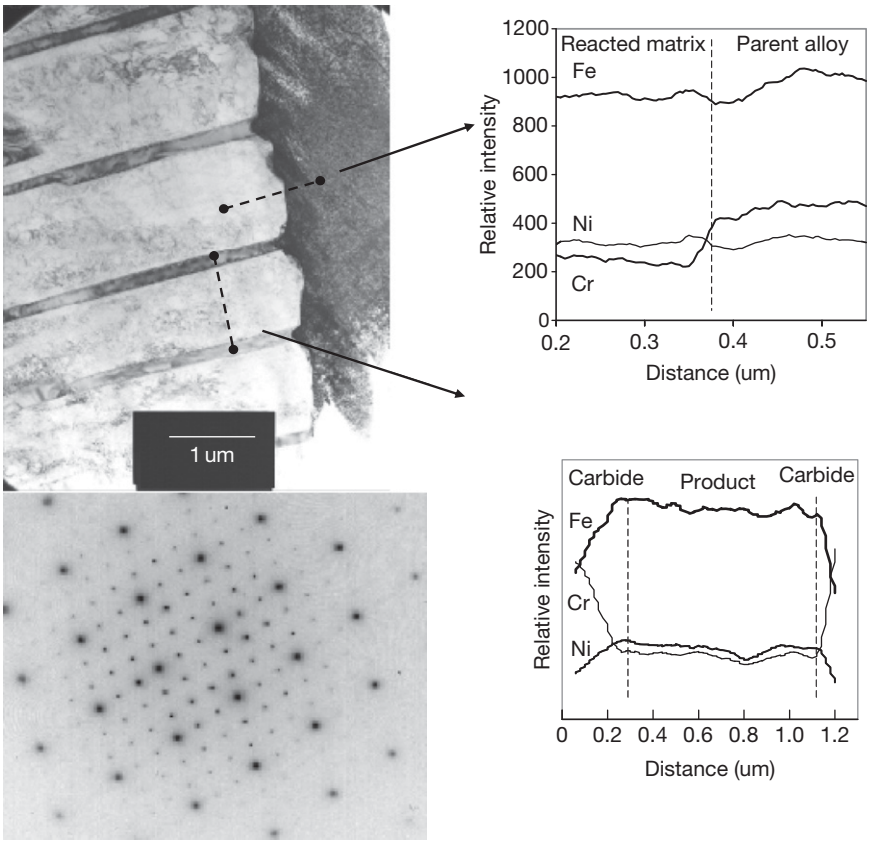

Figure 8 $M_{23}C_6$ precipitation front in Fe–20Ni–25Cr after brief prenitridation and subsequent carburization at 1000 °C, $a_C = 1$.[20,25]

The incoherency of the γ/γ^D interface is evident in its curvature, and this provided rapid chromium diffusion towards the advancing carbide precipitate tips, sustaining their growth and producing the discontinuous change in N_{Cr} seen at the interface.

It is concluded that lamellar carbide precipitates develop when a grain boundary is present. The boundary provides more rapid chromium diffusion to the precipitates, favoring their continued growth rather than nucleation of new ones. As seen in **Figure 5(b)**, carburization rates for Fe–Cr alloys with high N_{Cr} values are higher than predicted by eqn. [24]. These are the alloys which form lamellar precipitates, and the acceleration is attributed to boundary diffusion of carbon along the multiple carbide–austenite interfaces. As $N_C^{(s)} D_C$ in austenite is in any case large, the increase in rate is relatively small: 30% faster in Fe–Cr and 30–50% faster in Fe–Ni–Cr alloys at 1000 °C.

Carbide precipitate distributions are nonuniform, because K_{sp} is not small. Thus, as depth within the precipitation zone increases, a_C and N_C decrease causing N_{Cr} to increase according to the solubility product equilibria [21] and [22]. As a result, the amount of chromium precipitated is less. The qualitative effect on carburization rate can be seen from eqn. [24]: because the effective value of $N_{Cr}^{(o)}$ is lowered, the penetration rate is faster. This effect has been analyzed[26,27] for the general case of low-stability precipitates. Deviation from the Wagner assumption of vanishingly small K_{sp} values is expressed via a solubility parameter

$$\alpha = 1 - N_{Cr}^{(s)}/N_{Cr}^{(o)} \qquad [30]$$

where $N_{Cr}^{(s)}$ is the matrix equilibrium chromium concentration at the surface of the reacted alloy. If $\alpha = 1$, $K_{sp} = 0$ and the Wagner model applies; if $\alpha = 0$, no precipitation occurs and an error function solution describes the carbon profile. Considering Fe–Cr alloys, we find from eqn. [22] and the data of **Table 5** that $N_{Cr}^{(s)} = 0.028$. Taking a representative value of

$N_{Cr}^{(o)} = 0.25$, then a value of $\alpha = 0.9$ is arrived at. For this value, Ohriner and Morall[26] calculate that $k_p^{(i)}$ is increased by a factor of 2 above that predicted from eqn. [24]; that is, the penetration depth is increased by ~40%. However, uncertainties in measured values of D_C, $N_C^{(s)}$, and $k_p^{(i)}$ total at least this amount. A similar conclusion is reached for $Cr_{23}C_6$ precipitation. It is, therefore, concluded that despite the approximate nature of its assumptions, the simple result eqn. [24] provides good order of magnitude prediction for model alloy carburization. A more precise prediction can be made using the numerical treatment of the Ohriner–Morall theory developed by Christ.[28]

1.12.5 Internal Carburization of Heat-Resisting Alloys

Many laboratory studies of the carburization of heat-resisting alloys have been reported.[6–8,28–45] These are in general agreement with the findings from industrial exposures[46] that carburization rates vary with Fe/Ni ratio and decrease with increased levels of Cr, Nb, Si, and sometimes W and Ti.

The usual appearance of a cast heat-resistant alloy after carburization is shown in **Figure 9**. Murakami's etch reveals finely precipitated, cuboidal $M_{23}C_6$ particles in the inner zone and coarser, spherical M_7C_3 particles near the surface. The original cast alloy structure is seen to the right: austenite dendrites with primary interdendritic $M_{23}C_6$. Near the carburization front, preferential precipitation is seen along dendrite boundaries. Some fragmentary external carbide scale is also seen. This is usually Cr_3C_2 on high-nickel alloys and M_7C_3 on low-nickel materials. The difference arises from the changed Fe/Cr ratios.[35] Thus, reaction morphologies are consistent with local equilibrium. Moreover, as the internal carburization kinetics are parabolic, it is clear that the process is diffusion controlled.

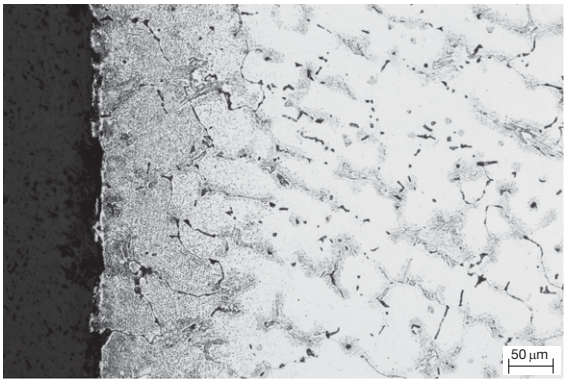

Figure 9 Cast alloy Fe–45Ni–19Cr after carburization for 24 h at 900 °C.

Despite the complexity of these alloys, their relative performance under nonoxidizing conditions can be understood in terms of Wagner's equation [24]. The procedure is to model the heat-resisting alloys as Fe–Ni–Cr ternaries, and approximate the carburization zones as chromium carbide precipitates in an Fe–Ni matrix. Carburization rates are then predicted from eqn. [24] to change with carbon permeability, $N_C^{(s)} D_C$. This permeability shows a minimum at Ni/Fe ≈ 4 : 1,[2,10] which was shown by Rahmel *et al.*[47] to be reflected in relative penetration depths of a range of alloys. Clearly, the Fe/Ni ratio has a significant effect on carburization rate. However, this approach neglects the effect of N_M, and a more detailed calculation is required.

The quantity N_M represents mainly chromium. In calculating its value, the alloy chromium content must, therefore, be corrected for the amount already removed from the matrix into interdendritic carbide during casting. This is done on the assumption that all of the alloy carbon was precipitated as pure $Cr_{23}C_6$. Added contributions to N_M are calculated on the basis of NbC and other MC carbide formation, as well as the molybdenum carbides $(Mo_2Fe)C$ and (CrMoFe)C. As seen earlier, the application of eqn. [24] is nonetheless an approximation because M_7C_3 and $M_{23}C_6$ carbides contain substantial levels of iron.[15] Consequently, the value of N_M calculated as described above is an underestimate. On the other hand, however, an overestimate of N_M results from the error in the mass balance underlying eqn. [24]. This latter error arises because the solubility products of Cr_7C_3 and $Cr_{23}C_6$ are large, and significant levels of chromium remain unreacted in the depleted matrix.

Carburization leads to approximately equimolar amounts of M_7C_3 and $M_{23}C_6$; hence, a value of $v = 0.345$ is used in eqn. [24]. No value for ε is available. Predicted k_p values based on $\epsilon = 1$ are compared in **Table 10** with measured[40] quantities for a selection of alloys. It is seen that close order of magnitude agreement is achieved for the 30, 35, and 45 Ni grades, but not for the 60Ni grades. The latter contain aluminum, and will be discussed below. We consider first the effects of other alloy components.

Table 10 Carburization rate constants (k_p) ($10^7\,cm^2\,s^{-1}$) for heat-resisting alloys

Cast Alloy	*1100 °C*		*1000 °C*		*900 °C*	
	Measured	*Calc*	*Measured*	*Calc*	*Measured*	*Calc*
Fe–30Cr–30Ni (Nb, Ti, Zr)	1.45	2.05	0.13	0.33	0.10	0.11
Fe–25Cr–35Ni (Nb)	0.64	2.15	0.28	0.37	0.18	0.10
Fe–26Cr–36Ni (Nb, low C)	0.44	1.32	0.17	0.24	0.06	0.06
Fe–35Cr–45Ni	0.44	0.50	0.10	0.08	0.04	0.03
Fe–19Cr–45Ni (Mo,Hf)	0.41–0.43	0.99	0.13–0.22	0.18	0.05–0.08	0.03
Fe–30Cr–45Ni (Hf)	0.63	0.62	0.10–0.15	0.15	0.04–0.05	0.02
Fe–25Cr–60Ni–2.4Al	0.14	0.87	0.04	0.17	0.03	0.03
Fe–25Cr–60Ni–3.6Al	0.01	0.95	0.01	0.19	0.02	0.03
Fe–25Cr–60Ni–4.8Al	0.02	0.90	ND	0.18	ND	0.03
602CA (2.3 Al, wrought)	0.14	0.82	0.04	0.17	0.03	0.03

ND, not determined.

1.12.5.1 Effect of Carbon

Cast alloys usually contain high levels of carbon, which segregates as $M_{23}C_6$ during alloy solidification, thereby affecting N_M as described above. The success of this description is tested by comparing carburization rates for the alloy Fe–25Cr–35Ni–Nb with high and low carbon. At 1000 °C, the ratio $k_p(\text{High C})/k_p(\text{Low C})$ predicted from eqn. [24] to be 1.5 compares well with the measured value of 1.7. Agreement at the other temperatures is also good. It is concluded that the method used to calculate the effect of original alloy carbon is successful. On this basis, it would follow that cast alloys have lower carburization resistance than their wrought (low carbon) equivalents. In fact, the opposite effect is found,[8,38] as a result of rapid grain boundary diffusion of carbon in wrought alloys.

1.12.5.2 Effect of Molybdenum

Molybdenum can be added for solution strengthening of an alloy, and is also a carbide former. Two alloys containing 24Cr, 32Ni, 0.8Nb, and 0.44C, with and without the addition of 3 w/o Mo were found[38] to carburize at $a_C = 1$ at significantly different rates. The carbides Mo_3C and Cr_7C_3 are of comparable stability, and can therefore co-exist if the metals are at similar activity levels. In fact, the carbides $(Mo_2Fe)C$, (CrFeMo)C, and Cr_7C_3 were all identified by X-ray diffraction analysis of the carburized alloy C. Equation [24] is now used to test the possibility that precipitation of molybdenum carbides slows the rate.

A level of 3 w/o molybdenum, forming a carbide of stoichiometry $Mo_{1.5}C$ (an average of the two observed carbides), is equivalent in its consumption of carbon to a level of 2.5 w/o chromium, forming Cr_7C_3. The value of N_M in the molybdenum-bearing alloy is on this basis calculated to be 13.6% higher than for the comparison alloy. Taking into account the effects of alloy compositional changes in D_C, N_C, and N_M gives predicted relative reductions in the k_p values when Mo is added of 40% at 900 °C, 23% at 1050 °C, and 10% at 1150 °C. The measured reductions were 44% at 900 °C, 24% at 1050 °C, and 16% at 1150 °C. This suggests that eqn. [24] enables the effect of molybdenum to be modeled, subject to the reliability of the N_C and D_C data. Furthermore, it also predicts correctly the effect of temperature on the efficacy of this element in reducing carburization.

1.12.5.3 Effect of Silicon

It has long been known[29] that silicon slows carburization, even under gas conditions where no silicon-rich oxide can form. The stability of SiC is a great deal less than that of $Cr_{23}C_6$ and Cr_7C_3 and no SiC will form in these chromium-rich alloys. Increasing the alloy silicon content therefore has no effect on N_M. Under the reducing conditions of these experiments no SiO_2 is formed, and the beneficial effects to be expected of silicon on carburization rates under reducing conditions, therefore, result from modification of the carbon solubility and/or diffusivity. These modifications are due to thermodynamic interaction between the dissolved silicon and carbon.

Silicon is known to reduce both $N_C^{(s)}$ and D_C. Roy *et al.*[48] have examined the effect of silicon on carbon diffusion in Fe–Si–C. A comparison of carburization rates of two cast heat-resisting steels which differed only in their silicon levels showed[38] that increasing the silicon level decreased the rate by more than

would be predicted from Roy's diffusion data. The other major contributory factor is the depression of carbon solubility by silicon. The effect has been measured in liquid iron alloys, where the resulting change in carbon solubility is significant, but no data directly applicable to heat-resisting alloys is available.

1.12.5.4 Effect of Niobium and Reactive Elements

Niobium is often added to cast heat resistant alloys for strengthening purposes. It is also found in some wrought alloys, where it improves weldability. Reactive elements such as Ce and Hf are added to modify carbide shapes and to improve oxide scale spallation resistance. All are strong carbide formers and have strong effects on carburization resistance. The benefits of niobium have been reported several times.[8,45,49] The variation of $k_p^{(i)}$ with niobium concentrations is shown in **Figure 10** for several heat-resisting alloys. The effect of niobium can be distinguished from variations in $N_C^{(s)} D_C/D_M$ also plotted in this figure. Even if all the alloy niobium was available in solution to precipitate NbC, the effect of adding 1–2 w/o Nb on N_M is very small, much less than the substantial reductions in $k_p^{(i)}$ seen at higher niobium levels.

Similar effects have been noted for additions of Ce[39] and Hf.[40] These elements are present at low concentrations, typically around 0.1–1.0 w/o, and their effect on the value of N_M is negligible. Nonetheless, their addition is found to reduce carburization rates substantially. It is possible that carbides of Nb, Ce, and Hf precipitate preferentially at sites where interference with carbon diffusion is maximal. As carbon penetration is more rapid at primary carbide/dendrite boundaries (**Figure 9**), reactive metal carbide precipitation at these interfaces could exercise a disproportionate effect on the overall rate.

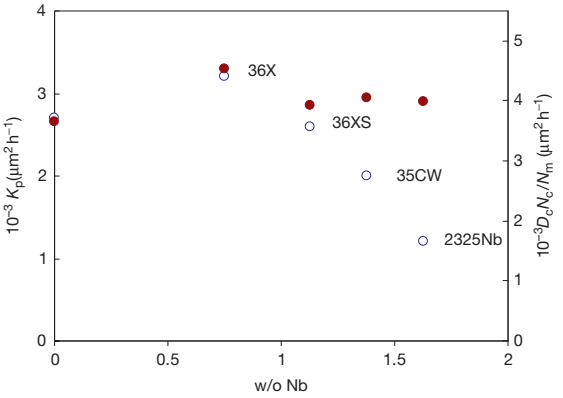

Figure 10 Carburization rate constants for commercial 25Cr–35Ni alloys at 1000 °C as a function of niobium content (○) compared with $N_C^{(s)} D_C/N_M$ (●). Data from Ref. 8.

1.12.5.5 Effect of Aluminum

The 60Ni alloys in **Table 10** were predicted from eqn. [24] to carburize at rates similar to the 45Ni alloys. At 900 °C, the wrought alloy 602 CA and two cast versions reacted at close to the predicted rates. At higher temperatures, the rates were much slower than predicted. The explanation is clear from the micrographs of **Figure 11**, where a protective, external scale is seen to form on high-N_{Al} alloys. The scale was α-Al_2O_3, which is thermodynamically stable at the water vapor impurity levels which are unavoidable in reaction gases. However, external scale formation is possible only when a sufficient flux of alloy solute aluminum is available, and internal oxidation can be avoided (see eqn. [15]). This flux increases with both alloy N_{Al} and temperature, through its effect on D_{Al}, qualitatively accounting for the observed pattern of behavior. When this scale formed, it functioned as a barrier limiting carbon access to the underlying metal. Thus, at 900 °C, no alumina formed and the 60Ni alloys all carburized at the expected rates. At 1000 and 1100 °C, alumina scales grew on all alloys, and carburization was slowed. The scale was discontinuous on the low-aluminum alloys, and carburization was not completely suppressed. A minimum aluminum content of ~4 w/o was required to achieve complete protection.

1.12.5.6 Alloying for Carburization Protection

The kinetics of alloy carburization are very well described by diffusion theory, and a rational approach to alloy design is therefore available. Unfortunately, however, most methods of suppressing internal attack on chromia-forming alloys are either impractical or only modestly successful. It is not possible to adjust chromium levels to achieve exclusive external carbide growth. Modifications of alloy carbon permeability through adjusting the Fe/Ni ratio or alloying with other metals yield only small improvements in carburization rates. Silicon decreases carbon solubility and diffusivity quite strongly, but metallurgical limits on alloy silicon concentrations mean that only modest improvements in carburization resistance can be obtained. The only really successful alloy additive

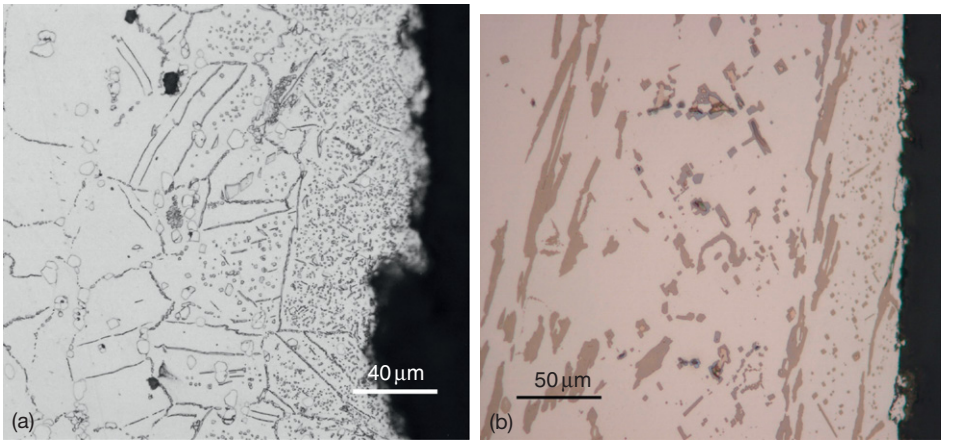

Figure 11 Effect of Al_2O_3 formation on carburization of 60Ni alloys (a) low-Al at 900 °C and (b) high Al at 1100 °C.

is aluminum, and it functions by forming an oxide scale. The general question of protection against carburization by oxide scale formation is considered in Section 1.12.8.

1.12.6 Metal Dusting of Iron and Ferritic Alloys

Metal dusting is a catastrophic form of corrosion in which metals exposed to carbon-supersaturated gas disintegrate, forming metal-rich particles (the 'dust') dispersed in a voluminous carbon deposit. Early reports of industrial failures[50–53] were followed by the laboratory research of Hochman[54–56] concerning the dusting of iron, nickel, cobalt, and chromia-forming ferritic and austenitic alloys. Subsequently, work by Grabke[57–61] quantified and extended Hochman's observations. The description of the process, as provided by Hochman and Grabke, for pure iron is shown schematically in Figure 12.

1.12.6.1 Metal Dusting of Iron

When iron is exposed to carbon-rich gas at oxygen potentials too low to form iron oxide, the metal catalyzes reactions such as [7]–[9], but the resulting carbon is dissolved in the metal. Hochman and Grabke suggested that this leads to carbon supersaturation of the iron, and the subsequent precipitation of metastable Fe_3C phase which they observed. The appearance of the cementite is shown in Figure 13. According to the proposed mechanism, once the iron surface is covered with cementite, carbon deposits on the carbide. The carbon activity at the cementite surface is then supposed to be unity (rather than the supersaturated value of the gas phase); the cementite becomes unstable and decomposes via the reaction

$$Fe_3C = 3Fe + C \qquad [31]$$

producing finely divided iron and carbon. The iron particles produced in this way are catalytically active, and lead to accelerated carbon deposition. The kinetics of carbon deposition were observed[61] in the short term to follow the quadratic rate law

$$\Delta W_C/A = k_C t^2 \qquad [32]$$

where $\Delta W_C/A$ is the carbon weight per unit area, before becoming approximately linear. The form of eqn. [32] was explained by Grabke *et al.*[61] as being due to the generation of catalytically active particles by metal consumption in the dusting process:

$$\Delta W_M/A = k_d t \qquad [33]$$

where $\Delta W_M/A$ is the metal wastage expressed as a mass loss per unit area. If the catalytic particles are of uniform surface area and activity, then the rate of carbon deposition is proportional to the mass of metal consumed

$$\frac{d(\Delta W_C/A)}{dt} = k \times k_d t \qquad [34]$$

Integration of this expression yields eqn. [32]. In the long term, individual particles are encapsulated by carbon and deactivated as catalysts. The rate at which this happens approximately balances the rate of new particle generation, as coking rates become approximately constant.

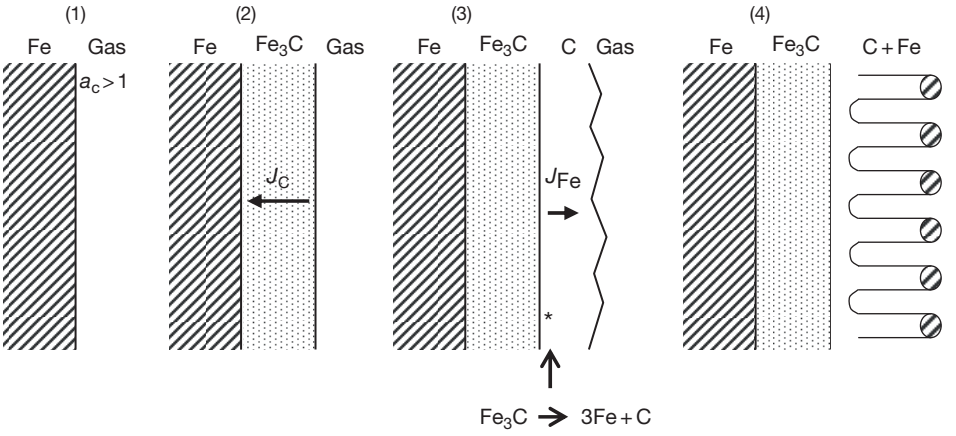

Figure 12 Hochman–Grabke model for dusting of pure iron.

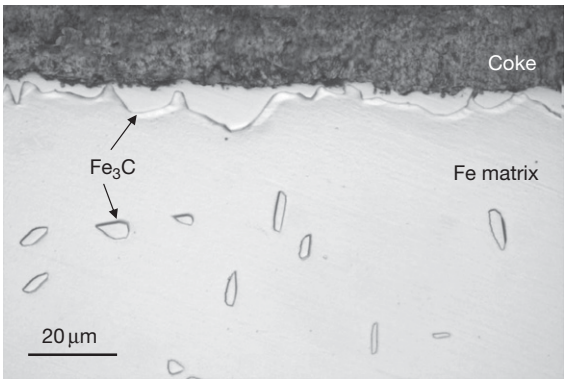

Figure 13 Cementite produced by reaction of pure iron with $CO/H_2/H_2O$ ($a_C = 2.9$, $p_{O_2} = 2 \times 10^{-23}$ atm).[62]

Transmission electron microscopy (TEM)[63–66] has revealed that the carbon at the cementite surface is mainly graphite at temperatures above ~500 °C. It was suggested that the iron resulting from cementite decomposition dissolved in the graphite, diffused outwards and precipitated as metal particles which catalyzed further carbon deposition. The evidence for this was the measurement by EDS of a small concentration of iron in the graphite. However, it is difficult to understand the driving force which would cause iron to diffuse from a low-activity source, the cementite, towards a high activity destination, metallic iron particles.

Further examination of the particles by both X-ray and electron diffraction[23,67–70] has established that they are Fe_3C. As seen in **Figure 14**, much of the coke deposit is filamentary. These filaments usually carry faceted Fe_3C particles at their tips. The particles are oriented with their [001] direction parallel to the carbon tube axis.[71] This allows Fe_3C planes in the {010} and {100} families to be parallel to the tube axis. The *d*-spacing of the (020) plane in 0.337 nm and that of the (300) plane is 0.169 nm. These correspond closely to the (0002) and (0004) *d*-spacings of graphite (0.337 and 0.168 nm, respectively). Accordingly, it is suggested that alignment of these planes with the graphite basal planes, which form the multiple walls of the nanotube, leads to formation of low-energy graphite–carbide interfaces and a preferred growth orientation for the carbon tubes.

A mass transport model for filamentary coke deposit is shown in **Figure 14(c)**. The exposed Fe_3C facets are in contact with the gas, and catalyze carbon production. This carbon diffuses through the particle to the Fe_3C-graphite interface where growth of the carbon tube continues. The model is analogous to that originally proposed by Baker *et al.*[72] for catalysis of carbon filaments grown by metallic particles. There remains, however, the question of how the Fe_3C particles are formed.

If iron does, in fact, dissolve in graphite, it could diffuse outward if a carbon activity gradient was in effect, as illustrated in **Figure 15(a)**. The iron flux is given by

$$\mathcal{J}_{Fe} = B_{Fe} N_{Fe} \frac{\partial \mu_C}{\partial x} \qquad [35]$$

and results from the thermodynamic Fe–C interaction. Here, B_{Fe} is the mobility of iron in graphite. When the solute iron reaches a position at which a_C is high enough to stabilize cementite, that phase precipitates. To test this model, one needs values for iron solubility and its diffusion coefficient in graphite, and these are lacking. It is clear that an extremely high value for D_{Fe} would be required to explain why the decomposition

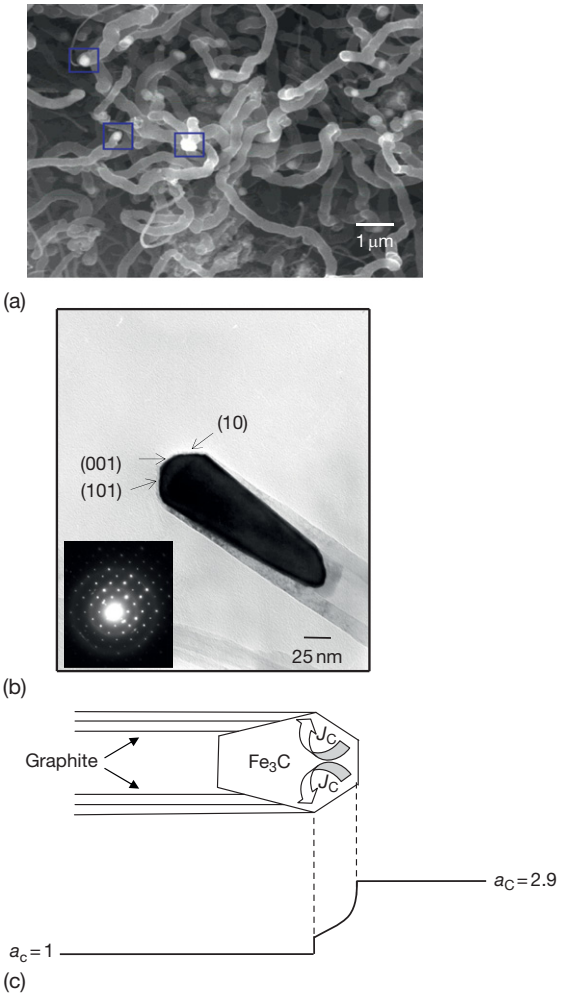

Figure 14 Coke filaments with Fe_3C particles at their tips (a) SEM view, (b) TEM image, and (c) mass transfer model.

reaction [31] leads to 75 at % iron, but produces none of that phase at the decomposition site.

Studies of cementite decomposition in CH_4–H_2 gas mixtures[73] have shown that the reaction products are iron and graphite. In that case, the reaction is controlled by the diffusion of carbon through the product ferrite, driven by the carbon activity gradient between the high value at the Fe_3C/Fe phase boundary and its value of unity at the Fe/C(gr) boundary:

$$\text{Rate} = D_C\left(C^{Fe_3C/Fe} - C^{C/Fe}\right) \qquad [36]$$

where $C^{Fe_3C/C}$ and $C^{C/Fe}$ are carbon concentrations at the ferrite–cementite and ferrite–graphite interfaces, D_C is the carbon diffusion coefficient in ferrite, and the variation in the diffusion path length is ignored. The concentration of carbon is related to

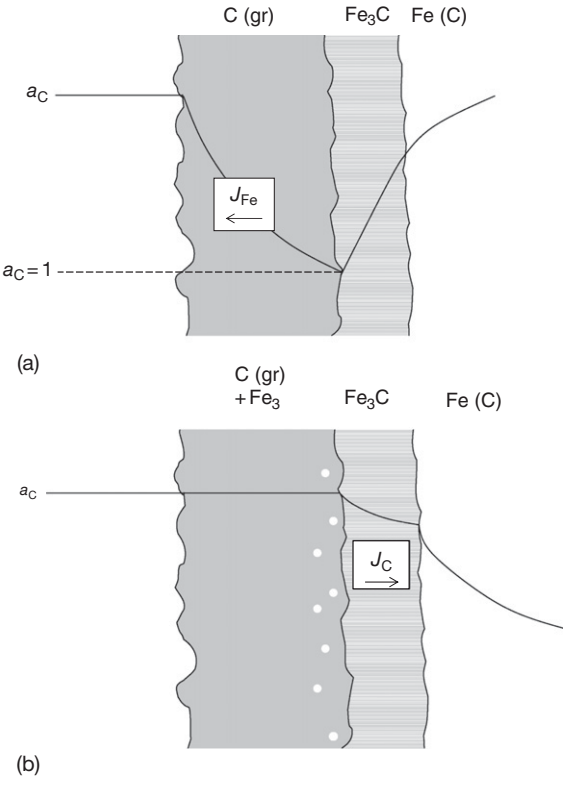

Figure 15 Mass transport models for metal dusting when cementite is formed: (a) cementite decomposition and iron diffusion through graphite and (b) cementite disintegration coupled with inward graphite growth.

its activity by a coefficient γ_C, with $a_C = \gamma_C C$. Approximating γ_C as a constant and setting $a_C = 1$ at the iron–graphite interface, we obtain

$$\text{Rate} = D_C\left(a_C^{Fe_3C/Fe} - 1\right)/\gamma_C \qquad [37]$$

Using standard data for D_C[74] and $a_C^{Fe_3C/Fe}$,[75] it is found that the temperature dependence of cementite decomposition predicted by eqn. [37] is in very good agreement with experimental observation (**Figure 16**). Cementite decomposition by that mechanism is clearly not occurring in the iron dusting reaction depicted in **Figures 13** and **14**.

The alternative mechanism of Fe_3C particle production is mechanical disintegration resulting from volume expansion.[67,76] Because Fe_3C is a carbon diffuser,[77,78] the cementite layer grows inward and is consequently under compressive stress. Precipitation of graphite could occur at internal defects in a nucleation and growth process.[67] Such a process would be similar to the way carbon forms and grows at the rear

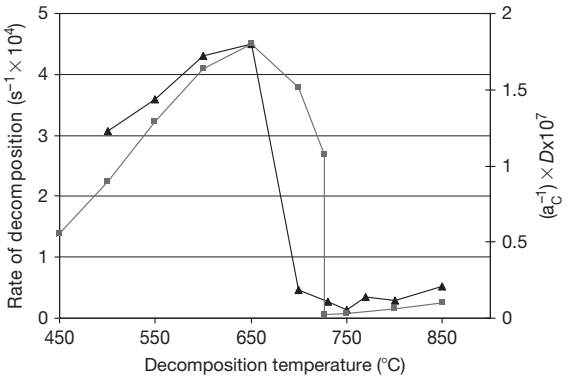

Figure 16 Rate of Fe_3C decomposition measured (▲) in H_2/CH_4 and calculated (▪) from D_C and a_C in ferrite.[73]

of Fe_3C particles (Figure 14). Growth of these precipitates could then disrupt the cementite surface. Examination of the C(gr)/Fe_3C interface in Figure 17 shows that graphite is growing into the cementite layer, and that nanoparticles of Fe_3C are detached from the bulk carbide. For these to exist, a_C must be high enough to stabilize the phase. It is therefore concluded that the graphite layer does not function as an effective barrier to the gas, and that a_C at the coke–cementite interface is probably close to the value in the ambient gas.

This conclusion is supported by the observation[79] that the surface cementite layer continues to thicken, and that the carbon content of the iron specimen increases as dusting proceeds. It is clear that carbon is diffusing through the cementite scale and into the iron, and that the description of Figure 15(b) applies. However, these experiments were of limited duration (up to ~40 h) and at a single temperature. Once the iron sample reaches a steady state of carbon supersaturation, the mechanism may well change[80] when an inward flux of carbon is no longer possible. Moreover, it is likely that the mechanism changes with gas composition and temperature. Zhang *et al.*[81] have reported that at $T = 700°C$, and low p_{CO} values, the surface Fe_3C scale decomposes to form a surface layer of ferrite. At still higher temperatures, no cementite layer is seen, and graphite deposits directly into the metal.

1.12.6.2 Iron Dusting in the Absence of Cementite

Given the important role played by cementite in the dusting of iron, it is reasonable to enquire whether dusting might be prevented if Fe_3C formation was suppressed. Cementite can be destabilized with respect to graphite by alloying with silicon to raise the solute carbon activity. Unfortunately, silicon also oxidizes in the gases under discussion, as will be discussed in the following sections. Germanium, on the other hand, forms a much less stable oxide, and by virtue of its chemical similarity to silicon, might be expected to suppress Fe_3C formation. This is indeed the case, as shown in Figure 18, where graphite is seen to be growing directly into a ferritic Fe–Ge alloy, in the absence of any cementite. The nanoparticulate material near the disintegrating interface is also α-Fe (Ge), as are the particles found on coke filaments.

Alloying with germanium suppressed Fe_3C formation, but did not prevent metal dusting. Instead, dusting occurred more rapidly by the growth of graphite directly into the alloy. Metal particles were formed by disintegration of the bulk metal, as the graphite grew inwards. Again it is suggested that this was a consequence of the volume expansion accompanying nucleation and growth of graphite within the metal. This process was more rapid than the corresponding one involving Fe_3C. It is noteworthy that the Fe–Ge/graphite interface morphology is similar to that developed between nickel and graphite (where no carbide forms) during dusting (see Section 1.12.7). However, the dusting rate was much faster for the ferritic material. It is concluded that suppression of Fe_3C formation does not prevent dusting when this alternative mechanism is available.

1.12.6.3 Effects of Temperature and Gas Composition on Iron Dusting

As noted by Grabke,[82] iron dusting and coking kinetics are very complex, and more detailed studies are needed to arrive at a comprehensive, self-consistent picture. As seen in Figure 19, somewhat different temperature dependencies have been reported under different gas conditions. Grabke *et al.*[61] considered the temperature dependence at $T < 540\,°C$ to reflect rate control by cementite decomposition, which is independent of gas composition. Ramarayanan *et al.*[65,84] identified two temperature regimes: $T < 450\,°C$ where the coke was amorphous and the rate was controlled by physical disintegration of Fe_3C, and $450 < T < 570\,°C$ where the chemical decomposition of Fe_3C was thought to become important. Its rate increased as the graphitization of coke increased with temperature, which was thought to provide a diffusion pathway for dissolved iron. The decline in dusting rates reported by Ramarayanan *et al.* at $T > 570°C$ was attributed by them to a

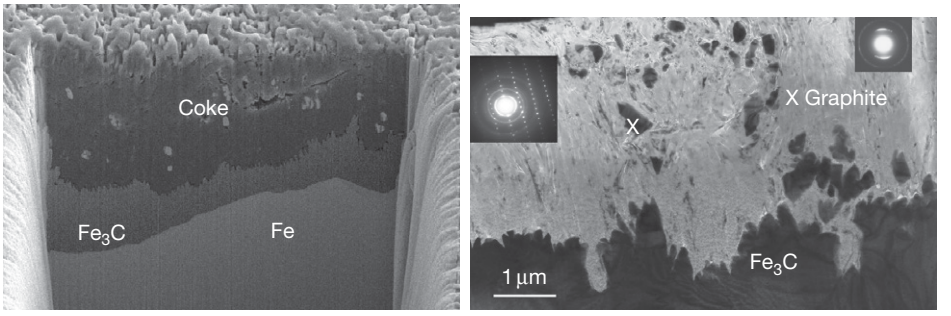

Figure 17 Graphite–cementite interface developed during dusting of iron at 680 °C: (a) FIB milled section and (b) TEM bright field with SAD identifying nanoparticles as Fe_3C.[62]

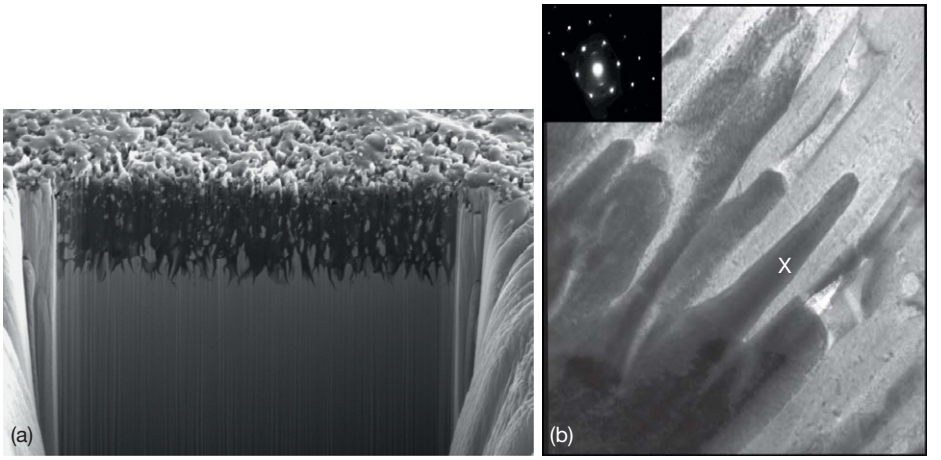

Figure 18 Fe–10Ge alloy after 10 h reaction in $H_2/H_2O/CO$ ($a_C = 2.9$, $p_{O_2} = 2 \times 10^{-23}$ atm): (a) FIB cross-section and (b) TEM cross-section with SAD identifying α-Fe.[62]

decrease in a_C with increasing temperature. Muller-Lorenz and Grabke[83] observed an increased dusting rate in the range 540–620 °C, reporting it to vary with the product $p_{CO}p_{H_2}$, and concluded that carbon transfer was rate-controlling.

Part of the reason for this confusion is the way in which a_C varies with temperature (**Figure 1**) and gas composition (eqns. [10] and [11]) in $CO/H_2/H_2O$ gas mixtures. Thus, the driving force for carbon precipitation ($a_C - 1$) is related to gas composition variables which themselves appear in kinetic expressions. Distinguishing the two effects can be difficult, and is impossible if the gas compositions are not carefully controlled. Thus, the use of CO/H_2 gases without H_2O to buffer the composition means that a_C is uncontrolled, and will vary with the extent of carbon deposition. As carbon deposition rates are rapid around 550 °C, both a_C and p_{CO} can vary considerably in a nominal $CO–H_2$ gas mixture.

The dependence of both coking and dusting rates on the composition of $CO/H_2/H_2O$ gases determined by Muller-Lorenz and Grabke[83] is shown in **Figure 20**. Similar results were found for iron dusting at 550 °C by Chun *et al.*[65] In both cases it was concluded that the rate-determining step in the dusting process was reaction [7] leading to

$$\text{Rate} = r_7 p_{CO} p_{H_2} \qquad [38]$$

However, this analysis neglects the effect of a_C. Experiments[85] in which a_C was constant revealed that keeping the product $p_{CO}p_{H2}$ constant, but varying the individual partial pressures changed both coking and dusting rates. Obviously, the simple description of eqn. [38] fails.

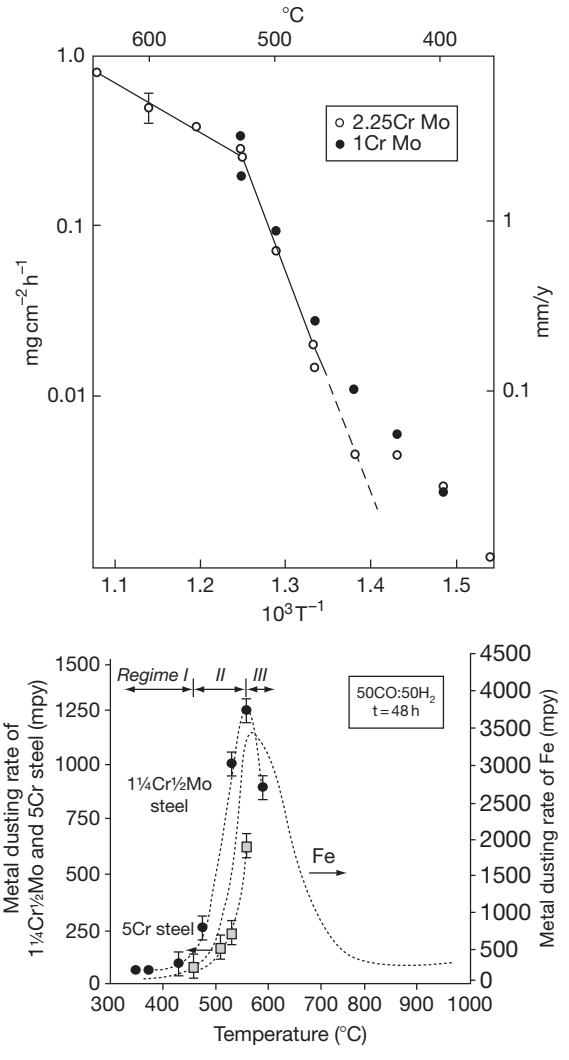

Figure 19 Temperature effects on metal dusting for iron and low-alloy steels: LHS in $CO/H_2/H_2O$[83]; RHS in $CO–H_2$.[84]

Considering the coking process first, it is seen that the Boudouard reaction [8] is likely to be important at high p_{CO} values. Furthermore, when p_{H_2} is high, it is likely that methanation (the reverse process in [9]) will occur under catalyzed conditions. Ignoring the reverse reactions in [7] and [8] along with the forward process [9], we can write

$$\frac{d(\Delta W_C/A)}{dt} = r_7 p_{CO} p_{H_2} + r_8 p_{CO}^2 - r_{-9} p_{H_2}^2 \qquad [39]$$

where r_i are the rate constants. As seen in **Figure 21**, this expression is successful in describing coking rates with $r_7 = 35.5, r_8 = 4.5$, and $r_{-9} = 5.6$ mg cm^{-2} atm^{-2} h^{-1}. It is concluded that coke deposition can be described in terms of gas–solid kinetics.

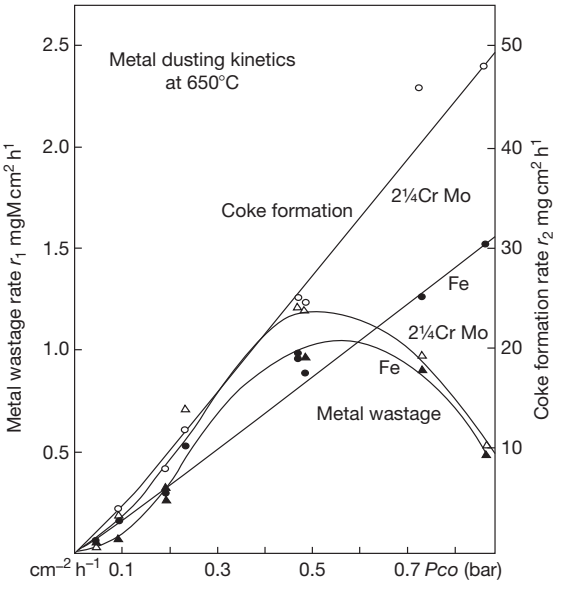

Figure 20 Dependence of coking and dusting rates on p_{CO} in $H_2/CO/H_2O$ mixtures.[83]

More information is required on the variation of dusting kinetics with gas composition. Available data for dusting in $CO/H_2/H_2O$ mixtures at 500°C[86] indicates the rate increases with a_C. Data at 550 °C[84] for metal consumption rates of iron exposed to CO/H_2 mixtures reveal a maximum at $p_{CO} = 0.5$ atm $= p_{H_2}$. If the unavoidable water vapor impurity level was the same in all gases used, then $a_C = K_7 p_{CO} p_{H_2}/p_{H_2O}$ also had its maximum at this composition.

1.12.6.4 Dusting of Low-Alloy Steels

Dusting of $2\frac{1}{4}$Cr–1Mo and 1Cr–$\frac{1}{2}$Mo steels is seen in **Figures 19** and **20** to be similar to pure iron in rate and dependence on temperature and gas composition. Reaction morphologies are also similar,[82] and it may be concluded that mechanisms are the same. The reasons for the slightly faster dusting rates observed on $2\frac{1}{4}$Cr–1Mo steel have not been established. However, it is to be noted that in $CO/H_2/H_2O$ gases, the p_{O_2} values are high enough to oxidize the chromium. Although no Cr_2O_3 scales can form on such a dilute alloy, conversion of the steel surface to Fe_3C may lead to encapsulation of chromium-rich oxide particles. These might act as nuclei for graphite precipitates, thereby accelerating the cementite disintegration.

Addition of silicon to iron has two effects: a partial destabilization of Fe_3C with respect to C(gr) and the promotion of SiO_2 formation at the oxygen potentials

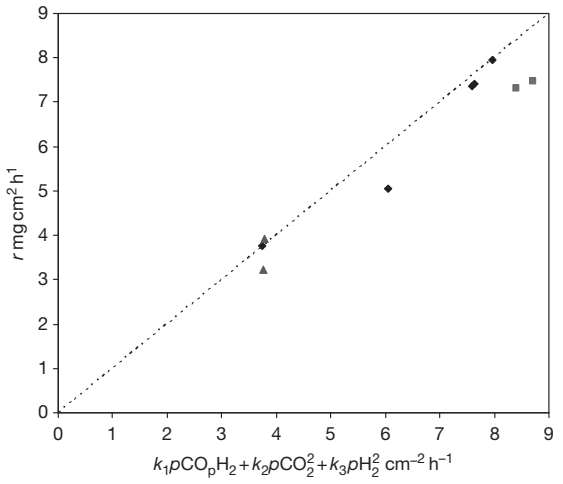

Figure 21 Variation of coking rates on iron according to eqn. [38].[85]

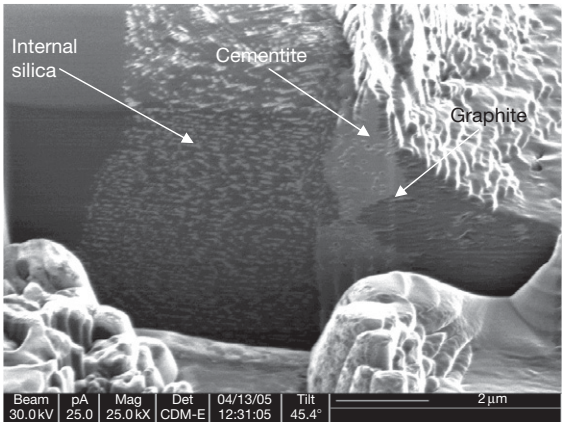

Figure 22 FIB image of Fe–*x*Si after dusting in $CO/H_2/H_2O$ ($a_C = 2.9$, $p_{O_2} = 10^{-23}$ atm) at 680 °C.[87]

of $CO/H_2/H_2O$ gases. At low-silicon alloy levels, the SiO_2 forms as a dendritic internal precipitate rather than an external scale (**Figure 22**). Thus, the SiO_2 provides little or no protection against carbon access to the metal. The Fe_3C layer formed by Fe–Si alloys is thinner than on iron, coking is faster, and metal wastage is also more rapid.[87] The internal SiO_2 precipitates are incorporated into the Fe_3C scale as it grows into the alloy. These might act as graphite nucleation sites, thereby accelerating cementite disintegration and dusting.

1.12.6.5 Dusting of Ferritic Chromium Steels

The behavior of these alloys when exposed to $CO/H_2/H_2O$ gas mixtures depends on whether a chromia scale is formed and retained. If the alloy chromium level is too low to form a Cr_2O_3 scale, the steel will dust at essentially the same rate as a $2\frac{1}{4}$Cr–1Mo steel.[88] If the steel forms a continuous, adherent chromia scale, resistance to dusting under isothermal conditions is very good, because the scale prevents carbon entry. The factors determining the success or otherwise of a steel in resisting dusting are those governing its ability to quickly form a continuous Cr_2O_3 scale by diffusing chromium to the surface.

The effect of temperature on D_{Cr} is clear from the studies of Grabke *et al.*[60] Steels containing 17 and 26 Cr showed complete resistance to dusting at 650 and 600 °C, but underwent a slight extent of attack at 550 °C. Thus, the susceptibility to dusting increased as the temperature and D_{Cr} decreased. The effective value of D_{Cr} can be increased at the low temperatures involved here by creating a deformed and fine-grained alloy surface. This is done by surface grinding, shot peening, etc., and has been shown[88] to lead to better dusting resistance. In the absence of such treatment (or after its effects have been annealed out), the ferritic nature of the alloy is itself important, because of the higher D_{Cr} value compared to austenitic materials. A comparison of the dusting performance of model ferritic and austenitic 25Cr alloys in **Figure 23** illustrates this point. These alloys had been electropolished to remove any cold-worked surface material, so that alloy chromium transport was via lattice diffusion.

Alloys which successfully develop continuous, protective chromia scales are nonetheless subject to long-term dusting attack. Under isothermal exposure conditions, growth stress accumulation in the scale leads ultimately to mechanical failure. A series of such events can exhaust the capacity of an alloy to regrow its protective scale, and metal dusting ensues.[88,89] Discontinuous exposures combine the effects of accumulated growth stress and occasional thermal shock. These have also been shown to produce alloy depletion and eventual dusting.[60,82,88,90] Short-term thermal cycling experiments induce the same failure mode, and are useful as accelerated corrosion tests.[91] In all cases, the chromia scale breaks down locally, allowing carbon to enter the chromium-depleted metal. Rapid inward diffusion of carbon leads to internal precipitation of chromium carbides, thereby preventing any subsequent rehealing of the scale. The depleted iron matrix forms a surface cementite layer[23,92] which disintegrates producing numerous cementite particles which catalyze further coke deposition.[23] This localized attack produces a

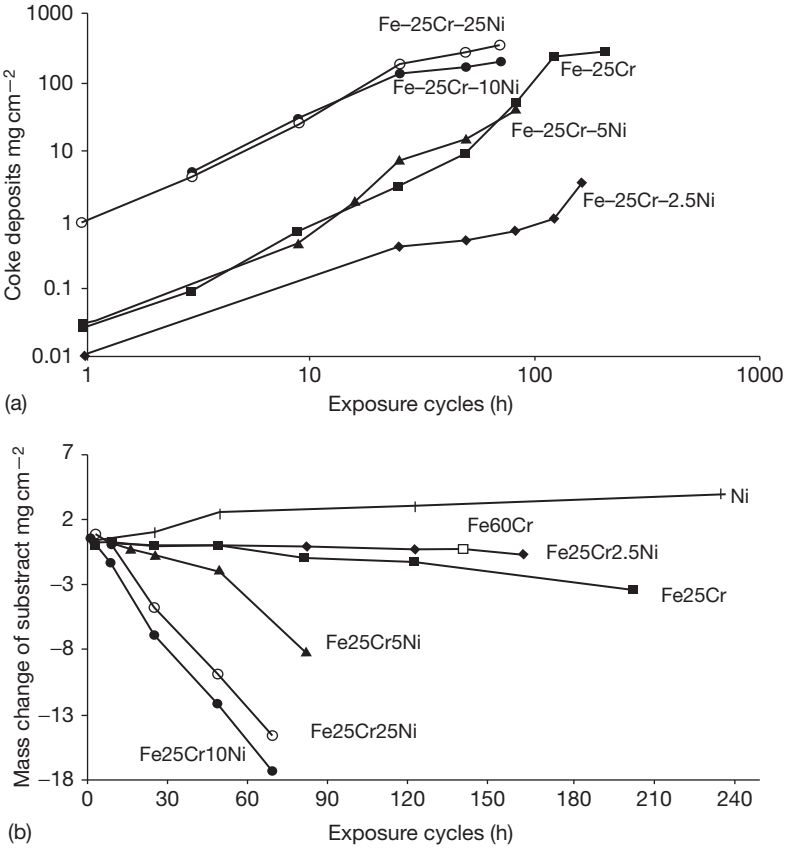

Figure 23 Coke deposition and metal wastage kinetics for electropolished 25Cr alloys at 680 °C in CO/H_2/H_2O (a_C = 2.9, $p_{O_2} = 10^{-23}$ atm).[23]

pitted surface (**Figure 24**). As the reaction proceeds, more pits form and they widen and coalesce until the attack becomes general.

If the alloy chromium level is high enough, dusting of ferritics can be prevented. An Fe–60Cr alloy survived one thousand 1-h cycles at 680 °C, forming only Cr_2O_3,[23] which was impermeable to carbon. Furthermore, the chromia was catalytically inactive, and no coke deposited.

1.12.6.6 Dusting of FeAl and FeCrAl Alloys

Iron aluminides and FeCrAl alloys are able to develop alumina scales, and their ability to resist dusting is, therefore, of interest. The high-diffusion coefficients characteristic of the ferritic FeCrAl materials (typically Fe–20Cr–5Al) means that they are able to reheal scales quickly, thereby preserving the surface barriers to carbon entry.

Dusting of the intermetallic Fe_3Al at 650 °C in CO–H_2–H_2O was investigated by Strauss *et al.*,[93] who reported extensive attack at localized pits. After addition of 2.2% Cr to the alloy, dusting was confined to the unpolished specimen edges. With 4.8% Cr and 0.15% Zr, pitting was completely suppressed, and only a thin coke layer formed. Dusting was associated with formation of a surface layer of Fe_3C. Further work on Fe–15Al and Fe–26Al by Schneider and Zhang[94,95] showed that dusting was also associated with internal precipitation of the κ-carbide, Fe_3AlC_x. Attack on Fe–15Al was general, but was reduced to localized pitting by alloying with 2.9% of Nb or Ta, and almost stopped by adding 2% of either V or Ti. Increases in temperature or alloy aluminum content led to reduced dusting rates. As pointed out by the authors, the observations are consistent with protection against dusting due to Al_2O_3 scale formation. However, at the relatively low temperature of 650 °C, the binary intermetallic does not reliably form a continuous scale. Alloy additions of Cr, Nb, Ta, V, and Ti all improve alumina scale formation. Nonetheless, once the scale is

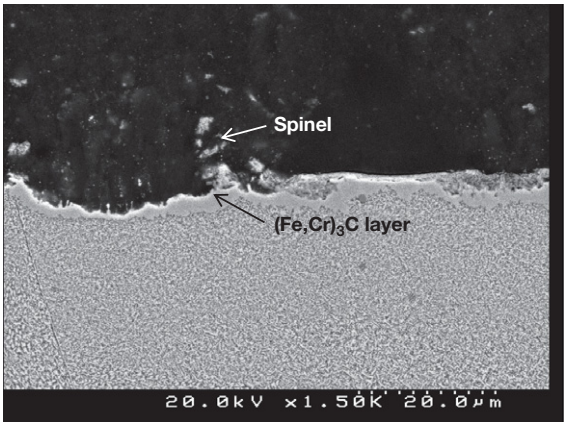

Figure 24 Onset of dusting for Fe–25Cr reacted at 680 °C in $CO/H_2/H_2O$ (a_C = 2.9, p_{O_2} = 10^{-23} atm) showing local internal carburization, surface cementite layer and its disintegration.

damaged, rapid carbon entry leads to internal carburization of the alloy and prevents subsequent alumina rehealing. The mechanism is, thus, very similar to that of attack on ferritic Fe–Cr alloys.

The FeCrAl materials provide much better dusting resistance. Baker and Smith[90] reported that an oxide dispersion-strengthened alloy, MA956, demonstrated very good dusting resistance at 621 °C up to 9000 h in a $CO–H_2–H_2O$ gas which was oxidizing to aluminum. Good performance has also been reported[80,91] for FeCrAl materials at 650 °C in similar atmospheres. Internal precipitation of the κ-carbide was observed after several thousand hours,[80] and filamentary coke growth was catalyzed by Fe_3C particles[91] when the scale was damaged by repeated thermal shocks.

1.12.7 Dusting of Nickel and Austenitic Alloys

Metal dusting of nickel and austenitic alloys differs from the reaction of ferritic materials in that cementite is not formed and the corresponding nickel carbide is unstable. An examination of the dusting behavior of pure nickel provides a good basis for understanding the reaction of austenitic, heat-resisting alloys.

1.12.7.1 Metal Dusting of Nickel

Exposure of nickel to carbon-rich gases at oxygen potentials where the metal does not oxidize leads to catalysis of reactions [7]–[9] producing carbon. Hochman[56] and Schneider *et al.*[95] reported the rate of carbon uptake to be much slower than the corresponding process on iron. The kinetics are approximately linear[94,95] after an induction period of length varying with temperature and gas composition. Metal consumption kinetics have not been measured directly. It is usually assumed that the carbon deposit contains an approximately constant nickel concentration (1–2 w/o), and on this basis linear dusting kinetics would be deduced. Chun *et al.*[96] measured metal surface recession after 7 h reaction in unbuffered CO/H_2 gas mixture of proportions 25:1, and found average rates to be of order 1 mm $year^{-1}$ at temperatures above 600 °C.

Reaction morphologies vary with ambient conditions, and the available information is incomplete. The 25:1 CO/H_2 gas produced external attack, whereas at a CO to H_2 ratio of 1:1, extensive internal graphitization also resulted. The appearance of coarse-grained nickel after exposure to a $CO/H_2/H_2O$ gas is shown in **Figure 25**. Cold working the metal surface prior to reaction induced recrystallization of the near-surface region, and graphite formation at the multiple grain and sub-grain boundaries. It is clear that carbon dissolves in the nickel and diffuses inwards, supersaturating the metal until graphite precipitates nucleate and grow at favorable sites. Nava Paz and Grabke[58] reported earlier that $CO/H_2/H_2O$ mixtures with low p_{CO} led to internal graphitization, whereas high p_{CO} mixtures induced surface deposition.

Coke accumulated on the external nickel surface in three forms: a more-or-less uniform layer on to the surface, clusters of approximately spherical particles, and filaments.[97] The spheres contain nickel particles and the filaments carry particles at their tips. The presumed correlation between coke mass and metal consumption is seen to be reasonable. Nickel is catalytically active to all of reactions [7]–[9], and it was proposed long ago[72] that reactions such as

$$CO + H_2 = H_2O + \underline{C} \qquad [40]$$

where $\underline{C}$ represents dissolved carbon, occur on the bare facets of the nickel particles. The carbon then diffuses rapidly through the particle and precipitates at the rear faces, causing elongation of the carbon filament. If the exposed nickel faces cannot dissolve carbon quickly enough, the particle is encapsulated with graphite, forming a roughly spherical particle. The accumulation of the outer, loose-coke deposit is thereby explained. Of more interest, however, is the

Figure 25 Graphitization of nickel exposed to $CO/H_2/H_2O$ (a_C = 19) for 100 h at 650 °C.

development of coke at the metal surface, and the way in which parent metal is 'dusted' to form the catalytic nanoparticles.

Zeng and Natesan[98] used Raman spectroscopy, which is sensitive to the degree of carbon crystallinity, to show that the surface carbon layer was more graphitic than the outer coke. Grabke *et al.*,[99,100] Pippel *et al.*,[64] and Chun *et al.*[96] all used TEM to examine the nickel–carbon interface. These authors agreed that the carbon was graphite, that the graphite basal planes were oriented approximately normal to the nickel surface when dusting occurred, and that nickel was dissolved (1–2 w/o) in the graphite. The mechanism deduced from these observations was one of outward diffusion of solute nickel through the graphite, followed by precipitation of nickel particles in the outer regions of the graphite layer. The fundamental difficulty with this mechanism is essentially the same as was identified earlier in the iron dusting case. No driving force is apparent for mass transfer from bulk nickel to particulate metal, which would presumably be at a higher energy level as a result of its surface area.

A TEM image of the graphite layer and nickel concentrations analyzed within it using EDS[101] are shown in **Figure 26(b)**. Very little concentration gradient is apparent, suggesting either that no diffusion occurs or that D_{Ni} in graphite is extremely high. Examination of the microstructure in **Figure 26** shows that in fact nickel nanoparticles are distributed throughout the graphite layers. Thus, the surface layer is a two-phase, two-component material in which isothermal diffusion could not occur if local equilibrium was in effect. It is nonetheless possible that a single-phase graphite–nickel solution might form under other reaction conditions and the nickel diffusion model could apply. In the example of **Figure 26**, it appears that mechanical disintegration of the metal is a consequence of the inward growth of graphite and the accompanying volume expansion. Such a process was in fact deduced from the original electron microscopy studies,[64,96,99,100] and the proposed diffusion of nickel through graphite is of secondary importance.

The mechanism of graphite nucleation and growth is of fundamental importance to the dusting process. It is proposed[96,99,102] that the free edges of graphite basal planes act as attachment sites for carbon atoms, permitting their extension into the metal (**Figure 27**, left). The supply of carbon necessary for this process can only be maintained if direct gas access to the metal continues throughout the reaction. Even when the surface is covered with graphite and coke, no effective barrier to the gas is formed. Most of the coke is obviously porous, and even the more dense graphite layer is extensively fissured.

The factors controlling graphite formation on nickel have been investigated intensively because carbon fouling (coking) of industrial nickel catalysts is an important practical problem. Direct surface observation[103] using low energy election diffraction showed that a preferred epitaxial relationship developed between the graphite basal plane (0001) and Ni(111) faces. A computer simulation of this arrangement is shown in **Figure 27** (right). Electron diffraction[104] confirmed that (111), (113), and (220) nickel faces were found at filament–metal interfaces. The same preferred epitaxies are observed in metal dusting.

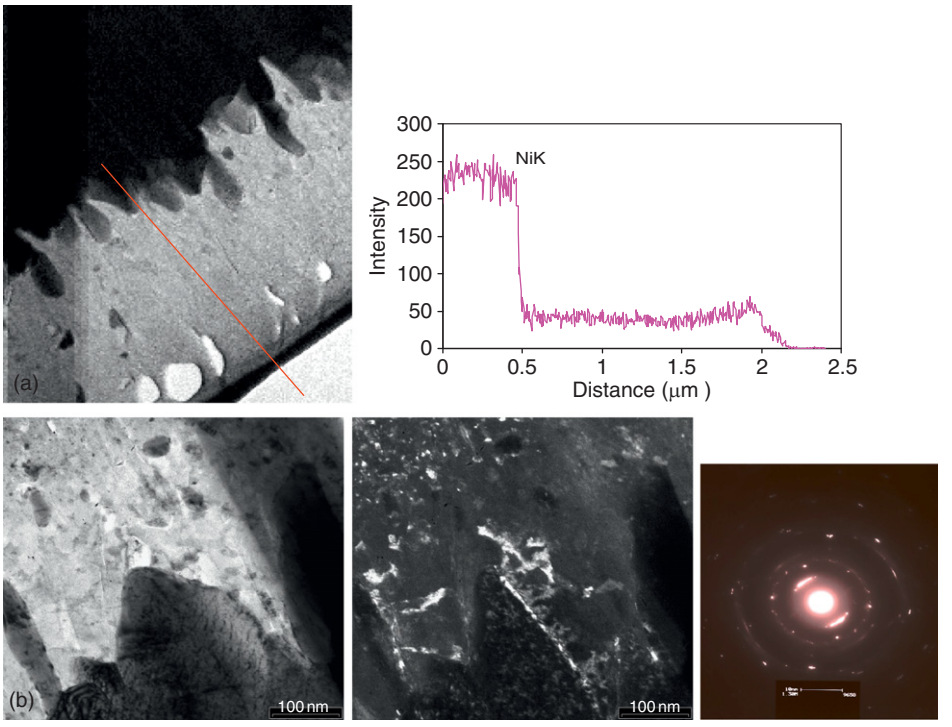

Figure 26 (a) TEM bright field view and EDS line scan through uniform graphite layer on nickel and (b) bright and dark field images using (111) nickel reflection reveal particulate metal in graphite ($CO/H_2/H_2O$, $a_C = 19$, $T = 680\,^{\circ}C$).[101]

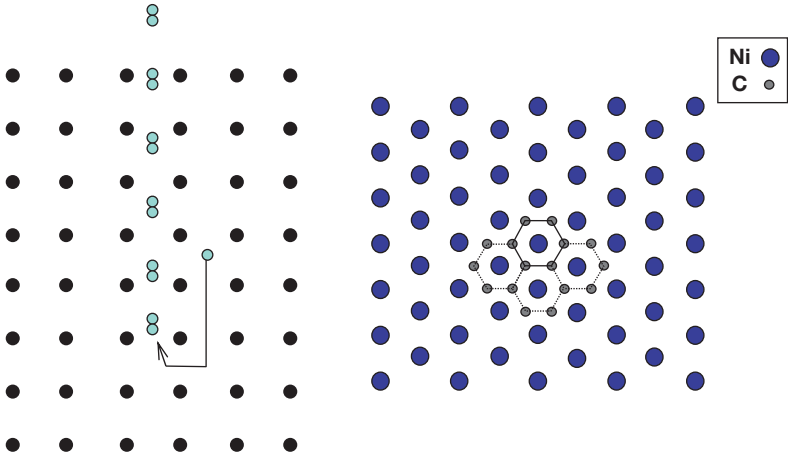

Figure 27 Left: Schematic view of graphite growth into nickel. Right: Computer simulation of the epitaxial relationship between the graphite basal plane and a Ni(111) surface.

Examination by TEM of reacted nickel single crystal and polycrystalline surfaces[64,96,100] revealed that graphite basal planes developed parallel to nickel (111) and (110) surfaces, but at right angles to a (100) surface. In the short term, no dusting occurred at the (111) or (110) surfaces, but on the (100) surface graphite grew into the nickel, causing its disintegration. This pattern of behavior is clearly consistent with the reaction model of **Figure 27**, which requires the graphite basal planes to be oriented at an angle to the surface. Of course, the model is somewhat over simplified. Consider, for example,

a (111) surface which is in fact intersected by planes such as $(11\bar{1})$, providing favorable inward growth directions for graphite. These will be accessible at surface jogs, kinks, etc., and dusting does, in fact, ultimately commence on these surfaces.[64,96,100]

Figure 28 shows graphite growing into the metal, along nickel (111) and (113) planes. Penetration of graphite basal planes between adjacent planes of the nickel lattice destroys its structure. It has been suggested[98,101] that the graphite nucleates within the metal interior. This is self evidently the case for internal graphitization (Figure 25). Such a process is analogous to the dissolution–precipitation mechanism producing carbon filaments from nickel nanoparticles. Some insight into the process can be gained from a consideration of alloying effects.

1.12.7.2 Dusting of Nickel Alloys in the Absence of Oxide Scales

The dusting of austenitic Ni–Fe alloys at 650 °C in $CO/H_2/H_2O$ gases such that no oxidation occurred was studied by Grabke *et al.*,[105] who found that both coking and metal wastage rates increased monotonically with iron concentration. The changes in coking rate reflected a combination of changing catalytic activity and dust particle size. Regardless of alloy iron content within the range 0–70%, the reaction morphologies were the same as for pure nickel. The dependence of dusting rate on alloy composition can be understood in part from carbon permeability data. The higher permeability of iron-rich alloys would provide a greater flux to the graphite nucleation and growth sites, supporting more rapid graphitization and metal dusting. On this basis, however, pure nickel would be predicted to dust more rapidly than alloys with ~80% Ni, which have the lowest $N_C^{(s)} D_C$ values. In fact, the metal dusted more slowly than the alloy. More information is required for high Ni/Fe ratios, which are typical of Inconel alloys.

Alloying copper with nickel has been found[106,107] to decrease coking and dusting rates sharply (Figure 29). The coke deposit on alloys containing at least 10 w/o copper consisted solely of filaments. Thus, metal wastage via the process leading to graphite particle clusters was suppressed. Copper is known to be immune to dusting attack, but its effect on nickel alloy dusting was much greater than one of simple dilution. Similar results have been reported[108–110] for the effect of copper on catalytic coking by nickel. This can be understood[108,110,111] if the catalytically active sites consist of y near-neighbor atoms. Then the carbon deposition rate on an alloy, r, is described by

$$r = r_{Ni}(1 - N_{Cu})^y \qquad [41]$$

where r_{Ni} is the rate on pure nickel. The effect of copper can be described by this equation with $y = 18$, as shown by the calculated lines in Figure 29.

A catalytic site of 18 near-neighbor atoms is physically unrealistic if surface reactions of simple molecules (e.g., eqn. [40]) are involved. However, if graphite nucleation is the process being catalyzed, then a stable

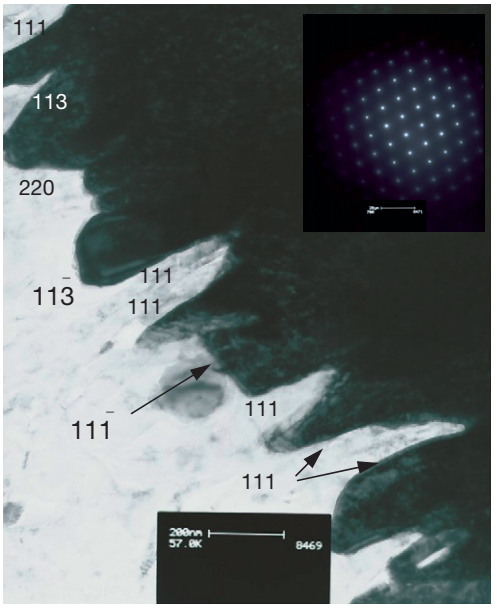

Figure 28 Nickel facets at graphite–metal reaction front determined by SAD.[101]

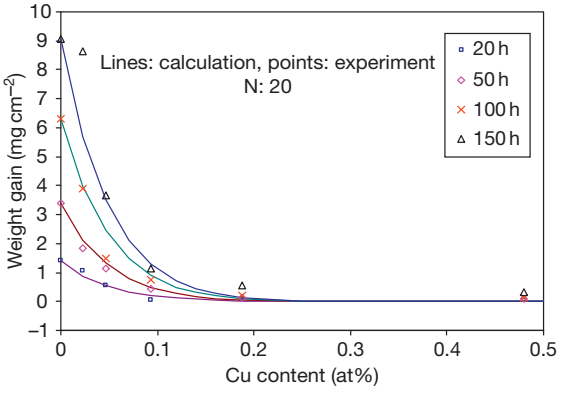

Figure 29 Carbon uptake on Ni–Cu alloys at 680 °C in $CO/H_2/H_2O$ (a_C = 19). Continuous lines calculated from eqn. [41].[106]

nucleus presumably requires at least one hexagonal carbon ring. As seen in **Figure 27** (right), it would require 7 near-neighbor nickel atoms on a free surface or 14 atoms on adjacent (111) planes for internal nucleation. It is therefore concluded that the copper effect is consistent with internal graphite nucleation.

Copper alloying also affects carbon solubility in the metal. The solubility is reported[112] to be reduced from a maximum of 0.18% in nickel to ~0.01% in Ni–90Cu. However, Mclellan and Chrashka[113] showed that carbon solubility was unaffected by the presence of up to 40% copper. More information is required for carbon permeability, but on the basis of existing data, graphite nucleation appears to be more strongly affected.

1.12.7.3 Effects of Temperature and Gas Composition on Nickel Dusting

Average metal recession rates in a 50–50 mixture of CO–H_2 were found[96] to increase with temperature to a maximum at about 800 °C, and to remain constant at higher temperatures. The carbon activity in those experiments was uncontrolled, and interpretation of the high temperature results is therefore difficult. The low-temperature results were correlated with an observed increase in carbon graphitization with increasing temperature. Chun *et al.*[96] suggested that dusting was controlled by outward diffusion of nickel dissolved in graphite, and therefore accelerated with increased graphitization of the coke. However, it could also be argued that only graphite, and not amorphous carbon, was capable of growing into the metal, because graphite can develop a crystallographic orientation relationship with the metal. Increasing graphitization would, therefore, increase the extent of nickel disintegration. Carbon uptake rates in a gas mixture of H_2–24CO–2H_2O were found by Schneider *et al.*[99] to have a maximum at about 625 °C, and decreased sharply at higher temperatures, reflecting the lower carbon activities reached at higher temperatures in a gas of fixed composition.

Direct measurements of the dependence of metal consumption (i.e., dusting) rates on gas composition are lacking, but data is available for coking rates. At a fixed temperature of 650 °C, carbon uptake rates vary with gas composition in a complex way. Experiments in which p_{CO} and a_C (as calculated from eqn. [10]) were varied independently[97] showed that carbon uptake rates were not directly related to a_C. Using instead an elementary kinetic description for reactions [7]–[9], one arrives at eqn. [39]. **Figure 30** demonstrates the success of this description with $r_7 = 0.73$, $r_8 = 0.06$, and $r_{-9} = 0.27\ \mathrm{mg\,cm^{-2}\,atm^{-2}\,h^{-1}}$. This indicates that coke formation is controlled by the CO + H_2 reaction [7] at moderate p_{CO} levels and by the Boudouard reaction [8] at high p_{CO} levels. The methanation process is important when p_{H_2} is significant. It needs to be recognized that different dependencies are likely at different temperatures, and that the relationship between coking and dusting rates is likely also to be temperature dependent. More work is required to obtain a full understanding of the effects of environmental variables on nickel dusting.

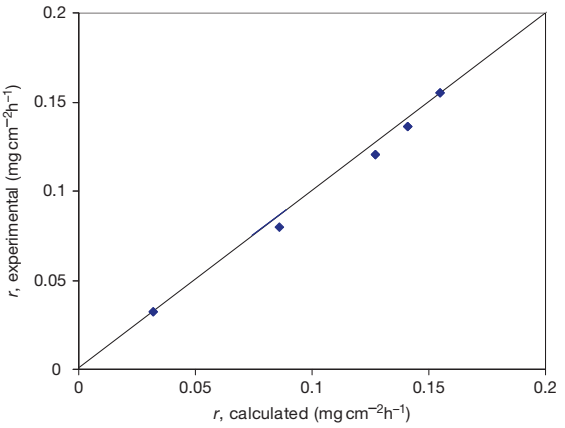

Figure 30 Carbon uptake kinetics on nickel according to eqn. [39].[97]

1.12.7.4 Dusting of Austenitic Alloys

Grabke *et al.*[102,105] found that the dusting of binary Fe–Ni alloys varied in reaction morphology and rate with nickel content. Essentially, low-nickel content alloys behaved like pure iron, forming a surface layer of cementite, whereas high-nickel alloys graphitized directly without forming carbide. The nickel level necessary to suppress cementite formation at 650 °C was reported as 30%[105] and also as 5–10%.[102]

The dusting of austenitic chromia-forming alloys is prevented for so long as the oxide scale acts as a barrier to carbon ingress.[56] The onset of dusting has been characterized by Grabke *et al.*[58,60,105] and the general features of the process are now clear. Selective oxidation of chromium produces a chromium-depleted subsurface alloy region. Local scale damage allows gas access to the metal. If sufficient chromium remains, the Cr_2O_3 scale reheals; if not, other reactions follow. If p_{O_2} is too low for nickel or iron oxides to form, carbon enters the alloy, precipitating chromium carbides.

At these low-temperatures, D_{Cr} is small, and the carbides are very fine. Removal of chromium from the matrix renders future oxide healing of the surface impossible, and gas access to the chromium-depleted surface continues. The metal is essentially an Fe–Ni alloy, and at high-nickel levels it undergoes graphitization and disintegration in the same way as pure nickel.

Thermal cycling dusting studies[23] on model Fe–*x*Ni–25Cr alloys revealed considerable variation in metal wastage rate with nickel content (**Figure 23**). A 2.5Ni alloy was ferritic, and formed a surface layer of M_3C, which disintegrated into cementite dust. Alloys with 5 and 10Ni had duplex $\alpha+\gamma$ microstructures, in which the austenite was clearly carburized more rapidly than the ferrite. Dusting produced nanoparticles of M_3C from the 5Ni alloys and both M_3C and austenite from the 10Ni alloy. A 25Ni alloy was fully austenitic, and disintegrated to yield austenite dust. This shift from carbide to austenite particles with increasing nickel levels is the same as that of binary Fe–Ni alloys,[102,105] and reflects the mechanism of attack on chromium depleted surfaces.

The variation of dusting rate with Fe/Ni ratio shown in **Figure 23** reflects mainly the difference in D_{Cr} accompanying the change from ferritic to austenitic structures. Because the alloy surfaces were electropolished and any cold-worked surface regions removed, chromium was available to the surface only via lattice diffusion. Thus, rehealing was more effective, and frequency of dusting initiation less, in the alloy sequence $\alpha > (\alpha+\gamma) > \gamma$. At still higher nickel levels, improved performance resulted from the lowering of alloy carbon permeability.

A growing body of results on the dusting resistance of austenitic alloys is becoming available. It is generally agreed[60,90,105,114] that higher nickel levels are beneficial and that a minimum chromium level of about 25% is required.[114,115] At these levels, scale breakdown allows formation of two internal carbide zones, usually spheroidal M_7C_3 near the surface and lamellar or Widmanstatten $M_{23}C_6$ at greater depths.[23,116] Alloy additions of silicon and aluminum improve the ability of the scale system to exclude carbon by forming oxide subscales.[59,90,117–119] Additions of carbide forming metals (Mo, W, Nb) form stable carbides. Their ability to getter carbon allows unreacted chromium to reheal the surface scale, delaying the onset of dusting.[119] However, subsequent oxidation of these refractory metal carbides leads to volume expansion, and disruption of the protective scale.[120] It has been shown[121] that additions of copper improve the dusting resistance of 310 stainless steel and alloy 800, just as copper decreases the dusting of nickel itself. This effect is limited by the alloy solubility for copper, which increases with nickel concentration.

Szakalos *et al.*[24,80,122] have pointed out that the fine internal carbides formed after scale failure can be oxidized *in situ*, leading to disruption of the metal and contributing to the dusting process. This is, in fact, the 'green rot' corrosion process,[123] in which the large volume expansion accompanying carbide oxidation fractures the metal. Under dusting conditions, this could occur simultaneously with graphitization of the chromium-depleted surface metal. The two possible reactions for internal carbides near the surface are the oxidation process and simple dissolution, providing a chromium flux toward the surface. The competition between the two processes will depend on oxygen and carbon permeabilities, and D_{Cr} within the subsurface alloy region. Rates of carbon and oxygen dissolution into the region are also likely to depend on gas compositions.

1.12.8 Protection by Oxide Scaling

As noted earlier, industrial gas streams which cause carburization are almost always oxidizing to chromium, and therefore also to silicon and aluminum. Heat-resisting alloys used at temperatures up to about 1000 °C are usually chromia formers, and the protective nature of their scales is what preserves the alloys from carburization. Using radioactive ^{14}C, Wolf and Grabke[124] showed that the solubility of carbon in Cr_2O_3 and Al_2O_3 at 1000 °C is below the detectability limit of 0.01 ppm. Nonetheless, chromia scales grown on alloy surfaces can be permeable to carbon, presumably by transport through defects or along internal surfaces. Grabke *et al.*[125] showed that radiotracer carbon in a $CO/CO_2/H_2/H_2O$ gas mixture slowly permeated scales on preoxidized Fe–Cr alloys. Simultaneous internal carburization and external Cr_2O_3 growth has been observed[126] on Fe–28Cr exposed to CO/CO_2 at 900 °C. However, a Ni–28Cr alloy reacted in the same way formed no internal carbides, indicating a more gas-tight scale.

Cast heat-resisting steels form scales consisting of mixed carbides and oxides, the proportion of oxide increasing with ambient p_{O_2}. At high-oxygen activities, the scale is mainly Cr_2O_3 with an outermost layer of manganese-rich spinel and, depending on alloy silicon levels, a more or less continuous SiO_2 layer at the alloy–scale interface. For as long as they maintain their mechanical integrity, these scales completely block carbon access to the underlying

alloys. The appearance of scales grown at 1000 °C, low p_{O_2} values and $a_C = 1$ and the corresponding diffusion paths mapped on the thermochemical diagram are shown in **Figure 31**. The scale grown at $p_{O_2} = 10^{-22}$ atm is a mixture of oxide (dark) and carbide (light) with a sublayer of SiO_2 (black). The protectiveness of these scales depends on alloy silicon content, as shown in **Figure 32**, where a level of about 1.8 w/o is seen to reduce the carburization rate dramatically at 1050 °C. Kane[29] reported a value of 2 w/o at 1093 °C. At $p_{O_2} = 10^{-24}$ atm, Cr_2O_3 is unstable, but SiO_2 still forms (**Figure 31**). Exposure to these conditions[127] led to a scale of carbide over a thin silica layer at the alloy surface. This scale was not protective, and alloys carburized rapidly, even at silicon levels up to 2.4 w/o. It is concluded that conditions producing both SiO_2 and Cr_2O_3 are necessary to provide a carbon-resistant scale.

The location of the stability boundary between chromium carbide and oxide shown in **Figure 31** is temperature dependent:

$$3Cr_2O_3 + 4C = 2Cr_3C_2 + \frac{9}{2}O_2 \qquad [42]$$

$$\Delta G^\circ = 3192100 - 797.3T \qquad [43]$$

In the presence of a coke deposit, $a_C = 1$, and the value of p_{O_2} corresponding to the equilibrium [42] is calculated to be as shown in **Figure 33**. In a steam cracking reactor, the H_2/H_2O ratio is approximately 1. The equilibrium p_{O_2} values calculated for

$$H_2 + \frac{1}{2}O_2 = H_2O$$

are seen to be much higher than the Cr_3C_2/Cr_2O_3 values, and the oxide is stable. However, as pointed out by Grabke *et al.*,[6] the oxygen activity beneath a carbon deposit can be a great deal less. If the carbon deposit is gas tight, then the gas species will be CO and CO_2, with the ratio p_{CO}^2/p_{CO_2} set through the Boudouard equilibrium [42] with unit carbon activity. If the total pressure $p_{CO} + p_{CO_2} = 1$ atm, the corresponding p_{O_2} is found from the thermodynamics

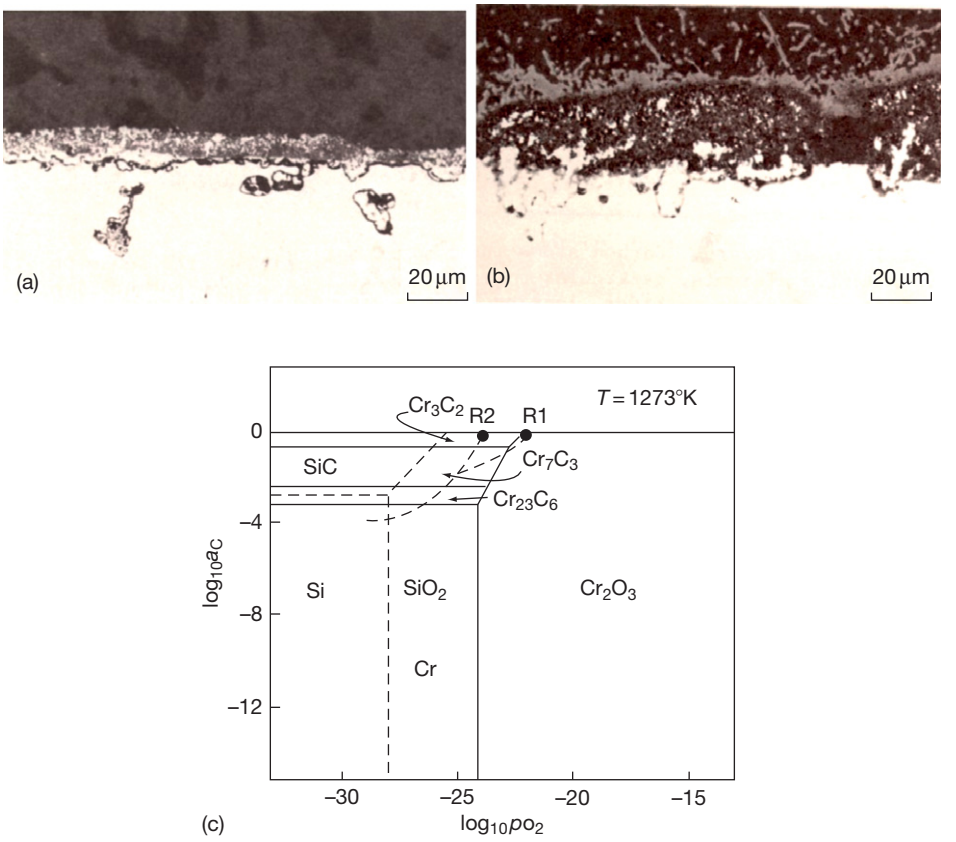

Figure 31 Scales grown on 25Cr–35Ni heat-resisting steels at 1000 °C and $a_C = 1$, (a), $p_{O_2} = 10^{-22}$ atm, (b) $p_{O_2} = 10^{-24}$ atm[127] and (c) diffusion paths.

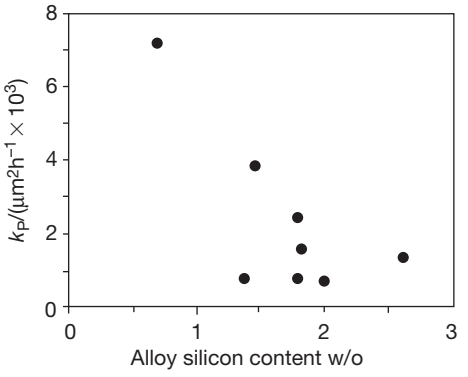

Figure 32 Dependence of carburization rate on alloy silicon content at 1050 °C, $a_C = 1$, $p_{O_2} = 3 \times 10^{-20}$ atm.[128]

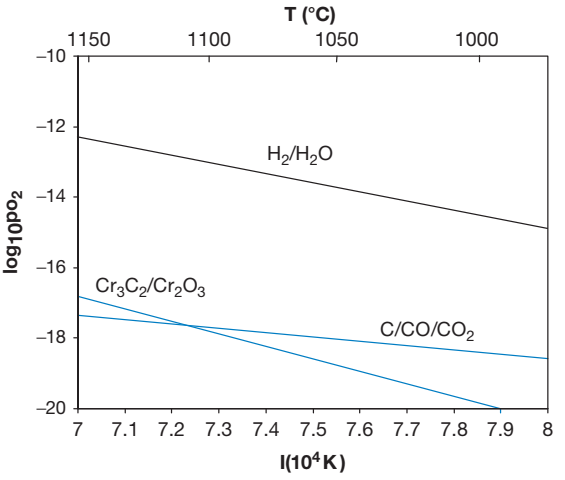

Figure 33 Thermodynamics of oxide to carbide conversion compared with CO/CO_2 mixture at $p_T = 1$ atm in equilibrium with graphite, and with oxygen potential controlled by H_2/H_2O equilibrium in steam cracking furnaces.

of [2] to be low at high temperatures (Figure 33). If $T \geq 1100°C$, carbon will reduce the oxide and degrade the protective nature of the scale.

Both Cr_2O_3 and Al_2O_3 scales provide effective barriers to carbon entry and metal dusting, but will eventually fail by cracking or spallation. If sufficient chromium or aluminum remains at the alloy surface, then scale rehealing occurs. If not, carbon dissolves in the depleted alloy and diffuses inward, to precipitate carbides.[129] At high carbon activities, metal dusting follows. The competition between outward metal diffusion to form a scale and inward carbon diffusion should in principle be described by an equation such as eqn. [15]. Unfortunately, no rigorous test of this description is available. Qualitative support is provided by the finding[91,130] that several heat-resisting alloys can be ranked in metal dusting resistance during temperature cycling according to their $N_{Cr}^{(o)} D_{Cr} / N_C^{(s)} D_C$ values.

A practical problem arises in the use of oxide scales for protection against carbon. Preoxidation procedures used to develop a chromia scale prior to service can also develop an outer scale layer of spinel, MCr_2O_4. If subsequent service conditions provide an oxygen potential below the spinel stability level, it is reduced leaving particles of metal,

$$MCr_2O_4 = Cr_2O_3 + M + \frac{1}{2}O_2 \qquad [44]$$

These particles act as catalytic sites, accelerating the onset of coking. This in turn can lead to scale disintegration and the commencement of dusting. Exposing austenitic chromia formers to oxidizing and carburizing conditions has been shown[131] to lead to rapid scale failure, accelerated carburization, and in some cases the commencement of dusting. In order to avoid this effect it is necessary to adjust the preoxidation conditions so that the oxides formed at that stage are stable during subsequent service.

1.12.8.1 Protection by Adsorbed Sulfur

The introduction of gaseous sulfur species such as H_2S to industrial process steams is widely practiced in order to minimize carburization and metal dusting. Sulfur adsorbs on the metal surface, impeding carbon access.[34,132,133] Under these conditions, rehealing of damaged oxide scales is favored over carbon penetration. The effect increases with p_{S_2}, but the sulfur pressure must be kept below the value at which CrS can form.

Adsorbed sulfur also provides protection against metal dusting, delaying the onset of the process and allowing more time for oxide rehealing. Data assembled by Schneider *et al.*[134] for the effect on iron is shown in Figure 34. The H_2S/H_2 ratios required to yield protection increase with temperature because sulfur adsorption is strongly exothermic. In the case of iron, sulfur adsorbs on cementite and prevents the nucleation of graphite.

1.12.8.2 Protection by Coatings

As is clear, long-term protection against metal dusting and carburization can only be achieved by forming a stable oxide scale which is capable of rapid rehealing. Coatings with high concentrations of scale forming elements can be used to provide this

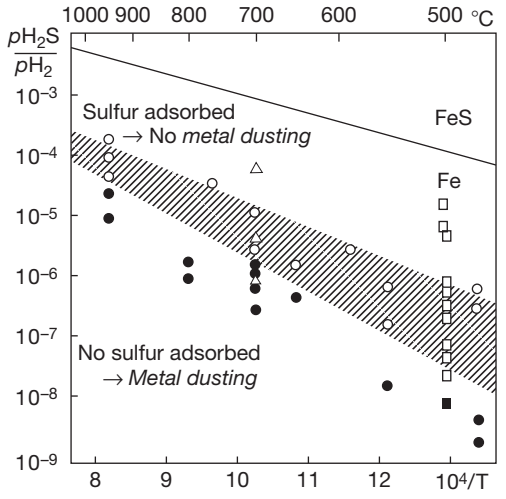

Figure 34 Effect of sulfur on metal dusting. The hatched region represents the transition to an iron surface saturated with sulfur.[134]

protection. Chemical vapor deposition[135–140] and flame spraying[141] have been used to produce carburization resistant coatings, and their utility under metal dusting conditions has also been tested.[142] Aluminum diffusion coatings were found to be protective for a series of ferritic steels (2.25–28Cr) and the austenitic alloy 800. However, long-term exposure led to pore development under the scale and cracking. Silicon diffusion coatings did not develop protective scales. A flame sprayed γ-TiAl coating was successful on a ferritic material, but failed on alloy 800 as a result of thermal mismatch. This work showed that alumina scales provided better protection against carbon than did chromia.

1.12.9 Conclusions

Carburization reactions at $a_C \leq 1$ are described by the classical theory of internal oxidation. Local equilibrium is achieved within the reacting alloy, solid-state diffusion of dissolved carbon controls the rate, and parabolic kinetics result. Wagner's diffusion theory provides good quantitative predictive capability, despite the approximate nature of some of its assumptions.

Metal dusting reactions at $a_C > 1$ proceed according to complex mechanisms which are still not fully defined. Local equilibrium is not achieved within the gas or at the gas–solid interface. It is, therefore, necessary to consider both the thermodynamic state of the gas and the kinetics of the several parallel gas–solid reactions possible. This requires specification of the complete gas composition, including minority species, as well as temperature. Considerably more work is needed to define temperature and gas composition effects on dusting rates.

Ferritic materials at moderate temperatures form Fe_3C. This phase is either disintegrated by precipitation within it of graphite or, in other gases, decomposed to yield metallic iron. Unfortunately, the boundaries between the two regimes are still not defined. Austenitic materials form no iron carbide, and are disintegrated by precipitation and growth of graphite within the metal. A similar mechanism operates for ferritic materials when cementite formation is prevented by high temperatures or alloying.

Protection against carburization and dusting requires the provision of a surface barrier between metal and gas, either an adsorbed sulfur layer or an oxide scale. When attack by carbon does occur, it is catastrophically rapid. For this reason, protective measures must be employed, and their continued effectiveness monitored.

References

1. Shatynski, S. R. *Oxid. Met.* **1978**, *13*, 105.
2. Wada, T.; Wada, H.; Elliott, J. F.; Chipman, J. *Met. Trans.* **1971**, *2A*, 2199.
3. Wada, T.; Wada, H.; Elliott, J. F.; Chipman, J. *Met. Trans.* **1972**, *3*, 2865.
4. Smith, R. P. *Acta Met.* **1953**, *1*, 578.
5. Grabke, H. J.; Peterson, E. M. *Scripta Met.* **1978**, *12*, 1111.
6. Grabke, H. J.; Gravenhorst, U.; Steinkusch, W. *Werkst. u. Korros.* **1976**, *27*, 291.
7. Schnaas, A.; Grabke, H. J. *Oxid. Met.* **1978**, *12*, 387.
8. Smith, G. M.; Young, D. J.; Trimm, D. L. *Oxid. Met.* **1982**, *18*, 229.
9. Wagner, C. *Z. Elektrochem.* **1959**, *63*, 772.
10. Kubaschewski, O.; Alcock, C. B. *Metallurgical Thermochemistry*, 5th ed.; Pergamon: Oxford, 1983.
11. Mazandarany, F. N.; Pehlke, R. D. *Met. Trans.* **1973**, *4A*, 2070.
12. Allen, A. T.; Douglass, D. L. *Oxid. Met.* **1999**, *51*, 199.
13. Ramanarayanan, T. A.; Slolovitz, D. J. *J. Electrochem. Soc.* **1985**, *132*, 2268.
14. Ahmed, O.; Young, D. J. In *High Temperature Corrosion and Materials Chemistry*; McNallan, M. J., Opila, E. J., Maruyama, T., Narita, T., Eds.; The Electrochemical Society, Inc.: Pennington, NJ, 2000; Vol. II; p 77.
15. Benz, R.; Elliott, J. F.; Chipman, J. *Met. Trans.* **1974**, *5*, 2235.
16. Ford, S. Ph.D. Thesis, University of New South Wales, 2005.
17. Young, D. J.; Ahmed, O. *Mater. Sci. Forum* **2001**, *369–372*, 93.
18. Udyavar, M.; Young, D. J. *Corros. Sci.* **2000**, *42*, 861.
19. Bose, S. K.; Grabke, H. J. *Z. Metallk.* **1978**, *69*, 8.
20. Ford, S.; Young, D. J.; McGrouther, D.; Munroe, P. R. *Mater. High Temp.* **2005**, *22*, 351.
21. Bunin, K. P. *Izv. Chern. Metall.* **1973**, *2*, 123.
22. Mozchan, V. I. *Izv. Chern. Metall.* **1979**, *8*, 92.

23. Toh, C. H.; Munroe, P. R.; Young, D. J. *Oxid. Met.* **2002**, *58*, 1.
24. Szakalos, P.; Lundberg, M.; Petterson, R. *Corros. Sci.* **2006**, *48*, 1679.
25. Ford, S.; Munroe, P. R.; Young, D. J. In *John Stringer Symposium*; Tortorelli, P. F., Wright, I. G., Hou, P. Y., Eds.; ASM International: Materials Park OH, 2003; p 77.
26. Ohriner, E. K.; Morall, J. E. *Scripta Met.* **1979**, *13*, 7.
27. Kirkaldy, J. S. *Canad. Met. Q.* **1969**, *8*, 35.
28. Christ, H. J. *Mater. Corros.* **1998**, *49*, 258.
29. Kane, R. H. *Corrosion* **1981**, *37*, 187.
30. Chu, W. F.; Rahmel, A. *Oxid. Met.* **1981**, *15*, 331.
31. Roach, D. B.; Wright, I. G. *The Study of the Carburisation Resistance of Heat Resistant Casting Alloys*; 1st Interim Report on Project No 60, Batelle, Columbus Labs, OH, 1974.
32. Ledgeff, K.; Rahmel, A.; Schorr, H. *Werkt. Korros.* **1980**, *31*, 121.
33. Ramanarayanan, T. A.; Petkovic-Luton, R. *Corrosion* **1981**, *37*, 712.
34. Barnes, J.; Corish, J.; Norton, J. F. *Oxid. Met.* **1986**, *26*, 333.
35. Kinniard, S. P.; Young, D. J.; L Trimm, D. *Oxid. Met.* **1986**, *26*, 417.
36. Mitchell, D. R. G.; Young, D. J. *Foundry Trade J.* **1992**, *166*, 253.
37. Mitchell, D. R. G.; Young, D. J. *J. Mat. Sci. Lett.* **1993**, *12*, 1076.
38. Mitchell, D. R. G.; Young, D. J.; Kleeman, W. *Mater. Corros.* **1998**, *49*, 231.
39. Becker, P.; Ouamara, F.; Young, D. J. In *High Temperature Corrosion Materials Chemistry IV*; Opila, E., Hou, P., Moruyama, T., Pieraggi, B., Schifler, D., Wachina, E., Eds.; The Electrochemical Society, Inc.: Pennington, NJ, 2003; p 178.
40. Becker, P.; Young, D. J. *Oxid. Met.* **2007**, *67*, 267.
41. Klower, J.; Heubner, U. *Mater. Corros.* **1998**, *49*, 237.
42. Young, D. J. *Mater. Corros.* **1999**, *50*, 675.
43. Forseth, S.; Kofstad, P. *Mater. Corros.* **1998**, *49*, 266.
44. Grabke, H. J. *Carburisation – A High Temperature Corrosion Phenomenon*; MTI Publication No. 52, Materials Technology Institute of the Chemical Processing Industries: St. Louis, MI, 1997.
45. Grabke, H. J.; Wolf, I. *Mater. Sci. Eng.* **1987**, *87*, 23.
46. Lewis, H. *B. Corros. J.* **1968**, *3*, 166.
47. Rahmel, A.; Grabke, H. J.; Steinkusch, W. *Mater. Corros.* **1998**, *49*, 221.
48. Roy, S. K.; Grabke, H. J.; Wepner, W. *Arch. Eisenhuttenwes.* **1980**, *51*, 91.
49. Hemptenmacher, J.; Grabke, H. J. *Werkst. Korros.* **1983**, *34*, 333.
50. Camp, E.; Phillips, C.; Cross, L. *Corrosion* **1954**, *10*, 149.
51. Hubbell, W. G. *The Iron Age* **1946**, *157*, 56.
52. Burns, L. *Corrosion* **1950**, *6*, 169.
53. Lefrancois, P. A.; Hoyt, W. B. *Corrosion* **1963**, *19*, 360t.
54. Hochman, R. F. *Proc. 3rd Int. Cong. Met. Corrosion,* University of Moscow Press, 1969.
55. Hochman, R. F.; Klett, M. G. *Proc. 5th Int. Cong. Met. Corrosion,* NACE: Houston, TX, 1974.
56. Hochman, R. F. In *Proc. Symp. Properties of High Temperature Alloys with Emphasis on Environmental Effects*; Foroulis, Z. A., Pettit, F. S., Eds.; Electrochemical Society: Pennington, NJ, 1977; p 571.
57. Grabke, H. J.; Hemptenmacher, J.; Munker, A. *Werkst. Korros.* **1984**, *35*, 543.
58. Nava Paz, J. C.; Grabke, H. J. *Oxid. Met.* **1993**, *39*, 437.
59. Grabke, H. J.; Krajak, R.; Nava Paz, J. C. *Corros. Sci.* **1993**, *35*, 1141.
60. Grabke, H. J.; Krajak, R.; Muller-Lorenz, E. M. *Werkst. Korros.* **1993**, *44*, 89.
61. Grabke, H. J.; Bracho-Troconis, C. B.; Muller-Lorenz, E. M. *Werkst. Korros.* **1994**, *45*, 215.
62. Motin, M. A. A.; Munroe, P. R.; Brady, M. P.; Young, D. J. *Scripta Mater.* **2007**, *56*, 281.
63. Pippel, E.; Woltersdorf, J.; Grabke, H. J.; Strauss, S. *Steel Research* **1995**, *66*, 217.
64. Pippel, E.; Woltersdorf, J.; Schneider, R. *Mater. Corros.* **1998**, *49*, 309.
65. Chun, C. M.; Mumford, J. D.; Ramanarayanan, T. A. *J. Electrochem. Soc* **2002**, *149*, B348.
66. Schmid, B.; Walmsley, J. C.; Grong, O.; Odegard, R. *Met. Mat. Trans. A.* **2003**, *34*, 345.
67. Zeng, Z.; Natesan, K.; Maroni, V. A. *Oxid. Met.* **2002**, *58*, 147.
68. Zhang, J.; Schneider, A.; Inden, G. *Corros. Sci.* **2003**, *45*, 1329.
69. Zhang, J.; Schneider, A.; Inden, G. *Corros. Sci.* **2003**, *45*, 281.
70. Zhang, J.; Schneider, A.; Inden, G. *Mater. Corros.* **2003**, *54*, 770.
71. Toh, C. H.; Munroe, P. R.; Young, D. J. *Mater. High Temp.* **2003**, *20*, 527.
72. Baker, R. T. K.; Barber, M. A.; Harris, P. S.; Yeates, F. S.; Waite, R. J. *J. Catal.* **1972**, *26*, 51.
73. Longbottom, R.J.; Ostrovski, O.; Zhang, J.; Young, D.J. *Met. Mat. Trans. B*. **2007**, *38*, 175.
74. Smith, R. P. *Transactions, AIME* **1962**, *224*, 105.
75. Turkdogan, E. T. *Physical Chemistry of High Temperature Technology*; Academic Press: New York, 1980.
76. Koszman In *Proc. Symp. on High Temp. Gas-Metal Reactions in Mixed Environments*; Jannson, S. A., Foroulis, Z. A., Eds.; Met. Soc. AIME: New York, 1973; p 155.
77. Ozturk, B.; Fearing, V. L.; Ruth, J. A.; Simkovich, G. *Met. Trans. A.* **1982**, *13*, 1871.
78. Schneider, A.; Inden, G. *Calphad* **2007**, *31*, 141.
79. Young, D. J.; Motin, M. A. A.; Zhang, J. Defects and Diffusion, accepted for publication.
80. Szakalos, P. *Mater. Corros.* **2003**, *54*, 752.
81. Zhang, J.; Schneider, A.; Inden, G. *Mater. Corros.* **2003**, *54*, 763.
82. Grabke, H. J. *Mater. Corros.* **2003**, *54*, 736.
83. Muller-Lorenz, E. M.; Grabke, H. J. *Mater. Corros.* **1999**, *50*, 614.
84. Chun, C. M.; Ramanarayanan, T. A. *Oxid. Met.* **2004**, *62*, 71.
85. Yin, H. ME Thesis, University of New South Wales 2006.
86. Schneider; Vielhaus, H.; Inden, G.; Grabke, H. J.; Muller-Lorenz, E. M. *Mater. Corros.* **1998**, *49*, 336.
87. Motin, M. A. A. PhD Thesis, University of New Southwales 2009.
88. Grabke, H. J.; Muller-Lorenz, E. M.; Eltester, B.; Lucas, M.; Monceau, D. *Steel Research* **1997**, *68*, 179.
89. Frabiezewski, A. S.; Watkins, W. R.; Hoffman, J. J.; Dean, S. W. *Corrosion 2000*; NACE: Houston, TX, 2000; paper no. 532.
90. Baker, B. A.; Smith, G. D. *Corrosion 2000*; NACE: Houston, TX, 2000; paper no. 257.
91. Toh, C. H.; Munroe, P. R.; Young, D. J.; Foger, K. *Mater. High Temp.* **2003**, *20*, 129.
92. Grabke, H. J. *Mater. Corros.* **1998**, *49*, 303.
93. Strauss, S.; Krajak, R.; Palm, M.; Grabke, H. J. *Mater. Corros.* **1996**, *47*, 701.
94. Schneider; Zhang, J. *Mater. Corros.* **2003**, *54*, 778.
95. Schneider; Zhang, J. *J. Corros. Sci. Eng.* **2003**, *6*, paper H043.

96. Chun, C. M.; Mumford, J. D.; Ramanarayanan, T. A. *J. Electrochem Soc.* **2000**, *147*, 3680.
97. Zhang, J.; Young, D. J. *Corros. Sci.* **2007**, *49*, 1496.
98. Zeng, Z.; Natesan, K. *Chem. Mater.* **2003**, *15*, 872.
99. Schneider, R.; Pippel, E.; Woltersdorf, J.; Strauss, S.; Grabke, H. J. *Steel Research* **1997**, *68*, 326.
100. Wei, Q.; Pippel, E.; Woltersdorf, J.; Strauss, S.; Grabke, H. J. *Mater. Corros.* **2000**, *51*, 652.
101. Zhang, J.; Munroe, P. R.; Young, D. J. *Acta Mater*. **2008**, *56*, 68.
102. Pippel, E.; Woltersdorf, J.; Grabke, H. J. *Mater. Corros.* **2003**, *54*, 747.
103. Shelton, J. C.; Patil, H. R.; Blakely, J. M. *Surf. Sci.* **1974**, *43*, 493.
104. Yang, R. T.; Chen, J. P. *J. Catal.* **1972**, *26*, 51.
105. Grabke, H. J.; Krajak, R.; Muller-Lorenz, E. M.; Strauss, S. *Mater. Corros.* **1996**, *47*, 495.
106. Zhang, J.; Cole, D. M. I.; Young, D. J. *Mater. Corros.* **2005**, *56*, 756.
107. Nishiyama, Y.; Otsuka, N. *Mater. Sci. Forum* **2006**, *522–523*, 581.
108. Bernardo, C. A.; Alstrup, I.; Rostrup-Nielsen, J. R. *J. Catal.* **1985**, *96*, 517.
109. Alstrup; Tavares, M. T.; Bernardo, C. A.; Sorensen, O.; Rostrup-Nielsen, J. R. *Mater. Corros.* **1998**, *49*, 367.
110. Tavares, M. T.; Alstrup, I.; Bernardo, C. A. *Mater. Corros.* **1999**, *50*, 681.
111. Dalmon, J. A.; Martin, G. A. *J. Catal.* **1998**, *49*, 367.
112. DKI German Copper Institute Booklet: *Copper nickel alloys: Properties, Processing, Application*. http://www.copper.org/applications/cuni/txt_DKI.html.
113. Mclellan, R. B.; Chraska, P. *Mater. Sci. Eng.* **1970**, *6*, 176.
114. Grabke, H. J.; Muller-Lorenz, E. M.; Klower, J.; Agarwal, D. C. *Mater. Performance* **1998**, *37*, 58.
115. Maier, M.; Norton, J. F.; Puschek, P. *Mater. High Temp.* **2000**, *17*, 347.
116. Perkins, R. A.; Coons, W. C.; Radd, F. J. In *Properties of High Temperature Alloys*; Foroulis, Z. A., Pettit, F. S., Eds.; Electrochemical Society, Inc.: Princeton, NJ, 1976; p 733.
117. Maier, M.; Norton, J. F. *Corrosion 99*; NACE: Houston, TX, 1999; paper 75.
118. Zeng, Z.; Natesan, K.; Grimoditch, M. *Corrosion* **2004**, *60*, 632.
119. Strauss, S.; Grabke, H. J. *Mater. Corros.* **1998**, *49*, 321.
120. Litz, J.; Rahmel, A.; Schorr, M. *Oxid. Met.* **1988**, *29*, 95.
121. Zhang, J.; Young, D. J. *Corros. Sci.* **2007**, *49*, 1450.
122. Szakalos, P.; Pettersson, R.; Hertzman, S. *Corros. Sci.* **2002**, *44*, 2253.
123. Betteridge, W. *The Nimonic Alloys*; E. Arnold: London, 1959.
124. Wolf; Grabke, H. J. *Solid State Commun.* **1985**, *54*, 5.
125. Grabke, H. J.; Ohla, K.; Peters, J.; Wolf, I. *Werkst. Korros.* **1983**, *34*, 495.
126. Zheng, X. G.; Young, D. J. *Oxid. Met.* **1994**, *42*, 163.
127. Tomas, P.; Young, D. J.; L Trimm, D. In *Proc. Int. Congress Met. Corros.* National Research Council of Canada: Ottawa, 1984; Vol. 1; p 58.
128. Mitchell, D. R. G.; Young, D. J.; Kleeman, W. *Corrosion 92*; NACE: Houston, TX, 1992; paper 302.
129. Dillinger, L.; Buchheit, R. D.; Van Echo, J. A.; Roach, D. B.; Hall, A. M. *Microstructures of Heat-Resistant-Alloys*; Steel Founders' Society of America: Rocky River, OH, 1970.
130. Young, D. J. *Mater. Sci. Forum* **2006**, *522–523*, 15.
131. Harper, M. A.; Ducasse, M.; Young, D. J. *Corrosion* **1995**, *51*, 191.
132. Grabke, H. J.; Peterson, E. M.; Srinivasan, S. R. *Surface Sci.* **1977**, *67*, 501.
133. Grabke, H. J.; Moller, R.; Schnaas, A. *Werkst. Korros.* **1979**, *30*, 794.
134. Schneider; Viefhaus, H.; Inden, G.; Grabke, H. J.; Muller-Lorenz, E. M. *Mater. Corros.* **1998**, *49*, 336.
135. Southwell, G.; MacAlpine, S.; Young, D. J. *J. Mater. Sci. Eng.* **1987**, *88*, 81.
136. Ganser, B.; Wynns, K. A.; Kurlekar, A. *Mater. Corros.* **1999**, *50*, 700.
137. Rapp, R. A. *Corrosion 89*; NACE: Houston, TX, 1989; paper 532.
138. Streiff, R. In *Elevated Temperature Coatings: Science and Technology II*; Dahotre, N. B., Hampikian, J. M., Eds.; TMS, 1996; p 407.
139. Wachtell, R. L. In *Science and Technology of Surface Coating*; Chapman, B. N., Anderson, J. C., Eds.; Academic Press: London, 1974; p 105.
140. Kung, S. C.; Rapp, R. A. *Oxid. Met.* **1989**, *32*, 89.
141. Schutze, M. German Patent: DE 197 43 421.5 (1998).
142. Rozado, C.; Schutze, M. *Mater. Corros.* **2003**, *54*, 831.

1.13 Nitridation of Alloys

U. Krupp
Faculty of Engineering and Computer Sciences, University of Applied Sciences Osnabrück, Albrechtstraße 30, 49076 Osnabrück, Germany

Abbreviations

CALPHAD Calculation of phase diagrams
CSL Coincident site lattice

Symbols

c_i Concentration of a species i
c_B^{ξ} Concentration of the nitride-forming alloying element B at the reaction front ξ
c_B^0 Initial concentration of the nitride-forming alloying element B in the alloy
c_N^0 Nitrogen concentration at the surface (can be set equal to the max. nitrogen solubility in the alloy)
c_N^{ξ} Nitrogen concentration at the reaction front ξ
D_i Diffusivity of a species i ($m^2\ s^{-1}$)
g^* Critical volume fraction for the transition from internal to external oxidation/nitridation
j_{bulk} Diffusive flux through the bulk ($m^{-2}\ s^{-1}$)
j_{if} Diffusive flux along interfaces (precipitates, grain or phase boundaries) ($m^{-2}\ s^{-1}$)
j_{prec} Diffusive flux through the precipitates ($m^{-2}\ s^{-1}$)
K Equilibrium constant
L_{SP} Solubility product
P Permeability ($m^2\ s^{-1}$)
$p(H_2)$ Hydrogen partial pressure (Pa)
$p(NH_3)$ Ammonia partial pressure (Pa)
$p(N_2)$ Nitrogen partial pressure (Pa)
$p(O_2)$ Oxygen partial pressure (Pa)
R Universal gas constant ($J\ mol^{-1}\ K^{-1}$)
t Exposure time (s)
T Temperature (K, °C)
x, y Coordinates (m)
V_i Molar volume of a species i ($m^3\ mol^{-1}$)
ΔG_0 Standard free energy of formation ($J\ mol^{-1}$)
ε Labyrinth factor
γ Parameter
ν Stoichiometric coefficient
ξ Depth of the internal reaction front (precipitation depth) (m)

1.13.1 Introduction

Nitridation of alloys refers mostly to a kind of surface-modification process applied to high-strength steels, to improve wear and fatigue resistance (case hardening).[1] Here, the nitridation process is carried out in an ammonia-containing atmosphere, exhibiting high nitrogen activity, leading to the formation of Fe nitrides, as well as V, Cr, and Al nitrides, in the case of alloy steels. However, nitrogen-based gas atmospheres are often considered inert and used for welding and heat-treatment purposes. Nitridation as a kind of high temperature corrosion becomes relevant for technical components operating at temperatures well above 800°C, for example, gas-turbine blades or tubes

in power generation and chemical industry. At these temperatures, dissociation of N_2 into atomic nitrogen at metal surfaces is sufficient, so that alloying elements with a high affinity to nitrogen, such as Ti, Al, and Cr, can form nitrides. Provided that diffusive penetration of nitrogen is fast, the nitrides form internally; it is a form of corrosive attack that is very similar to internal oxidation and has been termed internal nitridation.[2] Figure 1 shows an example of internal nitridation leading to failure of a natural-gas-fired burner tube made of the Ni-base alloy 601.

In most technical cases, internal nitridation has been observed in heat-resistant alloys together with superficial oxide-scale formation and internal oxidation. Hence, quantitative prediction of the degree of nitridation attack requires a thorough analysis of the relevant diffusive transport mechanisms and the thermodynamic stabilities of the species participating in the high temperature corrosion processes. The relationship between the gas atmosphere and the formation of metal nitrides is discussed in Section 1.13.2, while Section 1.13.3 focuses on some implications during internal corrosion reactions occurring during the operation of components made of technical heat-resisting alloys. Section 1.13.4 provides an insight into applying computer modeling to complex internal-corrosion processes.

1.13.2 Thermodynamics and Kinetics of Nitridation Processes

1.13.2.1 Nitrogen-Containing Gas Atmospheres

The risk of nitridation of alloys is prevalent in atmospheres with high nitrogen activities a_N, that is, nitrogen-based atmospheres (N_2) or, in particular, ammonia-bearing atmospheres (NH_3) with nitrogen activities up to the range of $a_N = 10^{10}$. The resulting atomic-nitrogen concentration at the metal surface can be calculated using the following equations[2]:

$$\frac{1}{2}N_2 \Leftrightarrow N_{dissolved},\ c(N_{dissolved}) = K\sqrt{p(N_2)} \quad [1]$$

$$NH_3 \Leftrightarrow \frac{3}{2}H_2 + N_{dissolved},$$

$$c(N_{dissolved}) = K\frac{p(NH_3)}{p(H_2)^{3/2}} \quad [2]$$

It should be mentioned that at moderate and low temperatures atomic nitrogen (eqn [2]) recombines to form molecular N_2. Hence, nitridation requires either a high flux of nitriding gas or high temperatures.

The relevant nitride-forming alloying elements Ti, Al, and Cr are at the same time prone to oxidation. The formation of the respective nitrides or oxides depends on the standard free energy of formation (cf. Section 1.13.2.3) and the relationship between the nitrogen and oxygen partial pressures. With the help of thermodynamic data for the stability of the different oxide and nitride compounds, this relationship can be represented by means of stability diagrams.

The competitive situation between oxidation and nitridation is prevalent during high temperature exposure to gases containing both oxygen and nitrogen. This is the case for air and for nearly all combustion atmospheres. In the case of cracks in thermally-grown oxide (TGO) scale and/or metal substrate, the nitrogen activity can reach much higher values than the oxygen activity, which is reduced due to oxidation. This can lead to situations where locally the $p(N_2)/p(O_2)$ ratio reaches values at which Al, Ti, and Cr form nitrides instead of oxides.[3,4] An example of such a situation is shown in Figure 2.

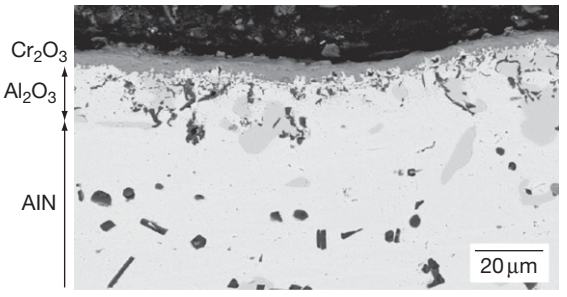

Figure 1 Internal-oxidation and -nitridation attack of a failed natural-gas burner tube of alloy 601 operated at $T = 1100°C$.

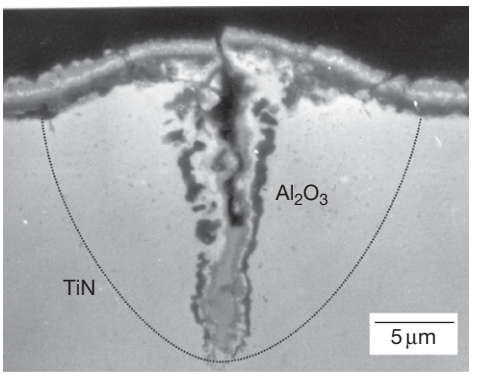

Figure 2 Crack in the superalloy CMSX-6 caused by fatigue at 950 °C showing internal oxidation and nitridation.

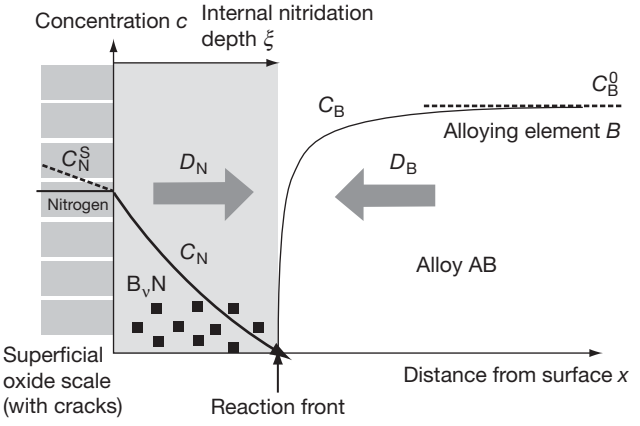

Figure 3 Concentration profiles during internal precipitation of B_vN according to Wagner's classical theory of internal oxidation.

1.13.2.2 Diffusion-Controlled Internal Nitridation

Provided that the degree of N_2 dissociation at the metal surface is fast enough, that is, $p(N_2)$ can be assumed to be equal to the nitrogen concentration in the gas phase, the nitridation process is determined by inward diffusion of nitrogen into the alloy and outward diffusion of the nitride-forming alloying element, cf. Figure 3. Under these conditions, the nitrogen concentration at the surface is constant ($c_N(x=0) = c_N^s$), while the concentration of the nitride-forming alloying element far away from the internal-nitridation zone is always equal to the nominal bulk concentration ($c_B(x > \xi) = c_B^0$). In the most simple case of just one nitride compound precipitating in a specimen or component where two- or three-dimensional geometrical features are negligible, the nitridation process can be described by Fick's second law of diffusion with c_N, c_B, D_N, D_B being the concentrations and diffusivities of nitrogen N in the alloy and the nitride-forming alloying element B, respectively:

$$\frac{\partial c_{N/B}}{\partial t} = D_{N/B}\frac{\partial^2 c_{N/B}}{\partial x^2} \qquad [3]$$

In general, internal nitridation can be treated in an analogous way to internal oxidation, where the classical theory of Carl Wagner[5] can be applied. Assuming parabolic progress of the internal-nitridation depth ξ, that is,

$$\xi(t) = 2\gamma\sqrt{D_N t} \qquad [4]$$

the diffusion equation [3] can be coupled with the concentrations c_N^ξ and c_B^ξ at the reaction front ξ based on the solubility product $L_{SP} = c_B c_N$ of the respective nitride compound B_vN (cf. Figure 3 and Section 1.13.2.3)

$$c_N(x,t) = c_N^s - \frac{c_N^s - c_N^\xi}{\operatorname{erf}\gamma}\operatorname{erf}\left(x/2\sqrt{D_N t}\right) \qquad [5]$$

$$c_B(x,t) = c_B^0 - \frac{c_B^0 - c_B^\xi}{\operatorname{erfc}\left(\gamma\sqrt{\frac{D_N}{D_B}}\right)}\operatorname{erfc}\left(x/2\sqrt{D_B t}\right) \qquad [6]$$

and taking into account that the diffusive flux of nitrogen and the nitride-forming alloying element at the reaction front must be equivalent (according to the stoichiometry B_vN).

$$\lim_{\varepsilon\to 0}\left[-D_O\left(\frac{\partial c_N}{\partial x}\right)_{x=\xi-\varepsilon} = vD_B\left(\frac{\partial c_B}{\partial x}\right)_{x=\xi+\varepsilon}\right] \qquad [7]$$

For nitride compounds of high stability, like the common ones TiN and AlN, the concentrations c_N^ξ and c_B^ξ can be neglected, that is, $L_{SP} = 0$ (type I behavior). Furthermore, interstitial nitrogen diffusion (cf. Table 1) should be by orders of magnitude faster than substitutional diffusion of the metallic alloying elements, that is, $D_B/D_N \ll c_N^s/c_B^0 \ll 1$. According to Wagner's theory of internal oxidation, the internal-nitridation depth can be calculated as

$$\xi^2(t) = \underbrace{2\frac{c_N^s D_N}{v c_B^0}}_{k_N} t \qquad [8]$$

with k_N being the nitridation constant. Even though eqn [8] provides a good estimate for many internal carburization, oxidation, and nitridation phenomena, technical corrosion processes involve mostly simultaneous formation of various compounds of different

thermodynamic stability,[6,7] for example, in NiCrAlTi alloys, the progress of the internal TiN precipitation front is governed by the consumption of nitrogen due to CrN/Cr_2N and AlN formation and the surface nitrogen concentration c_N^s, which might be decreasing because of the possible growth of an outer Al_2O_3 and/or Cr_2O_3 scale. This is schematically represented in **Figure 4**.

The problem becomes more complex when nitrides of moderate or low thermodynamic stability like CrN, Cr_2N, or Fe nitrides have to be accounted for. For such situations, where the solubility product L_{SP} is considerably high (eqn [9]), the theory of Laflamme and Morral[8] (type II behavior) or numerical approaches[9,10] (**Section 1.13.4**) should be considered.

$$0 < L_{SP}/c_N^s c_B^0 < 1 \qquad [9]$$

In most studies, nitrogen diffusion coefficients were not determined directly, but by evaluating nitridation kinetics,[11] for example, experimental determination of the permeability $P = c_N D_N$ by measuring the precipitation depth ξ[12] (cf. eqn [8]). Diffusion data for nitrogen in Ni and γ-Fe alloys are given in **Table 1**.

Table 1 Diffusion coefficients ($m^2\ s^{-1}$) for nitrogen in Ni alloys and Fe–20Ni

	N in Ni alloys	*N in Fe–20Ni*
700 °C	9.5×10^{-13} to 2.3×10^{-12}	1.2×10^{-12}
800 °C	3.2×10^{-12} to 8.5×10^{-12}	3.9×10^{-12}
900 °C	1.4×10^{-11} to 4.0×10^{-11}	1.5×10^{-11}
1000 °C	2.2×10^{-11} (24)	–

Source: Douglass, D. L. *J. Met.* **1991**, *11*, 74–79.

The assumption that internal nitridation is governed by bulk diffusion of nitrogen according to Fick's second law is an oversimplification. As demonstrated by Stott and Wood,[13] for internal oxidation, the diffusive flux j of nitrogen through the precipitation zone should be threefold (cf. **Figure 4**): bulk diffusion through the solvent j_{bulk}, diffusion through the precipitates j_{prec} (should be negligible), and diffusion along the precipitate/bulk interfaces or grain boundaries j_{if}. Since the flux contributions have to be multiplied by the respective diffusion area, the blocking effect of the precipitates ($j_{prec} \cong 0$) plays an important role for the transition from internal nitridation to external nitride-scale formation (cf. **Section 1.13.2.4**). A phenomenological approach to account for the flux-blocking effect of the internal precipitates was suggested by Schnaas and Grabke[14] using a labyrinth factor ε in eqn [8]:

$$\xi^2(t) = 2\frac{\varepsilon c_N^s D_N}{\nu c_B^0} t \qquad [10]$$

Douglass[11] reports diffusion coefficients for nitrogen in nickel being two orders of magnitude higher than for oxygen and attributes this observation to trapping effects, where a higher binding energy between oxygen atoms and the traps could exist.

It has been observed in several studies[15,16] that internal nitridation (similar to internal oxidation[17–19]) does not only imply diffusion of the reacting species, but also mechanical stresses arising from the higher specific volumes of the nitride compounds as compared to the substrate. This leads to a flux of the nonreacting alloying elements towards the surface,

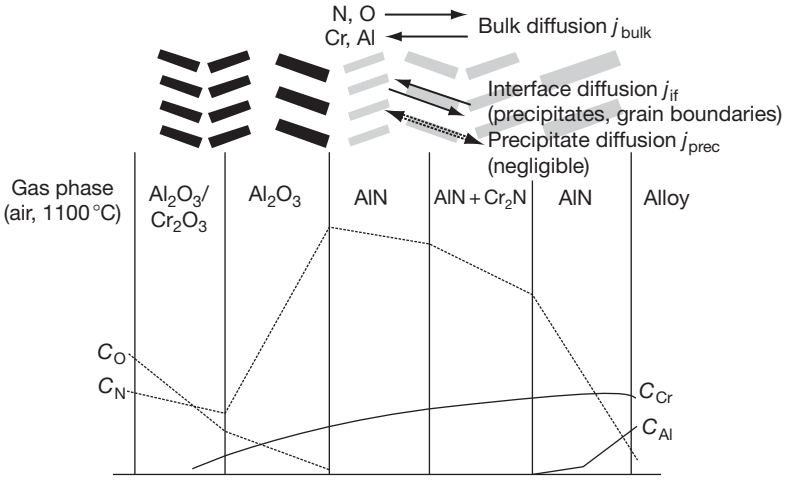

Figure 4 Schematic representation of the concentration profiles during oxidation and nitridation of Ni–Cr–Al alloys[6] and relevant diffusion fluxes.[13]

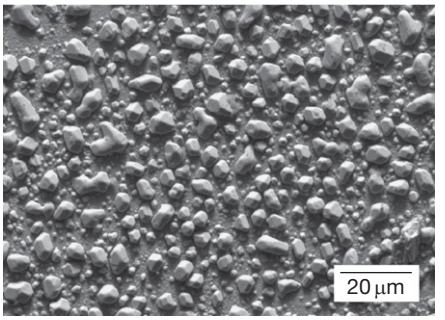

Figure 5 Formation of solvent surface protrusions after internal nitridation of Ni–10Cr–2Ti for 150 h at 1100 °C in low-oxygen N_2–45% He–5% H_2 atmosphere.

where they form protrusions (Figure 5). Hence, internal nitridation kinetics must be influenced by additional factors like Nabarro–Herring creep,[18] dislocation pipe diffusion,[18] and/or grain-boundary sliding.[19]

1.13.2.3 Influence of the Chemical Composition – Thermodynamics of Internal Nitridation

Although diffusive fluxes are relevant for the lateral progress of the reaction front, the kind of nitride that is formed depends on thermodynamic-stability conditions: local thermodynamic equilibrium can be assumed in cases of sufficiently high reaction rates. Figure 6(a)[20] represents the condition for thermodynamic equilibrium in terms of the standard free energy of formation ΔG_0, which is correlated with the equilibrium nitrogen partial pressure $p(N_2)$:

$$\ln p(N_2)_{equ} = \frac{-\Delta G_0}{RT} \qquad [11]$$

In addition to the technically most relevant nitrides Fe_4N, ε-$Fe_{2-3}N$, TiN, AlN, CrN, and Cr_2N, in Ni-based alloys with high Cr contents, the ternary π phase can also occur.[21–23] The π phase of a stoichiometry of $Cr_{10}Ni_7N_3$ is formed by a peritectic reaction of Cr_2N with Ni.[22] An estimation of the nitrides/oxides being formed for given nitrogen and oxygen partial pressures $p(O_2)$ and $p(N_2)$, respectively, is possible with the help of thermodynamic stability diagrams. An example for the system Ni–Cr–Al–Ti–N–O is shown in Figure 6(b). To account for complex higher-order interaction terms determining the internal-corrosion behavior of complex technical alloys, the CALPHAD method, implemented,

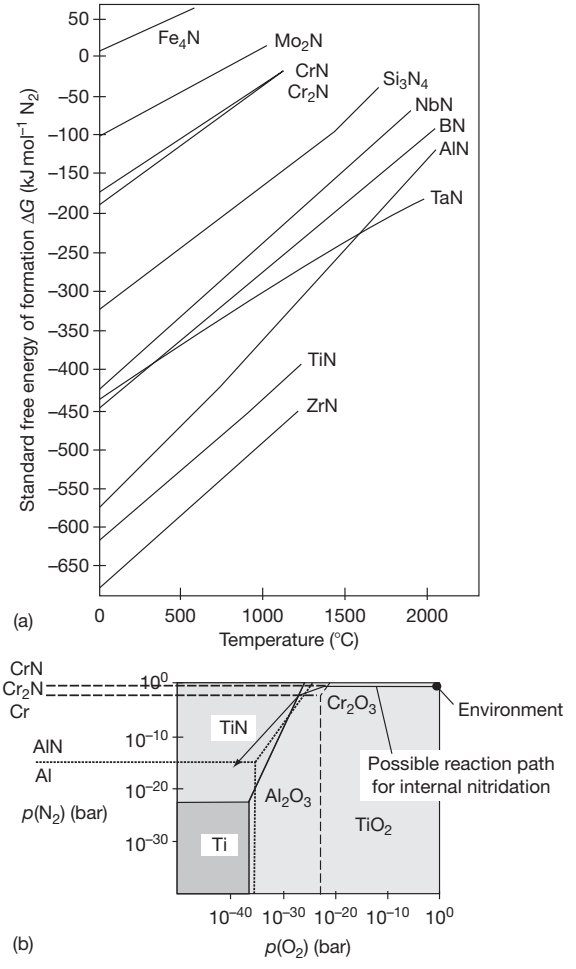

Figure 6 (a) Standard free energy diagram of selected nitridation reactions and (b) stability diagram for nitridation and oxidation in N_2/O_2 gas mixtures (1000 °C).

for example, in the software packages FactSage™, ChemApp™, and ThermoCalc™, is applied.

In general, from the thermodynamic point of view, the susceptibility to nitridation depends on (i) the concentration of the nitride-forming elements, and, in particular, on (ii) the nitrogen concentration being dissolved in the alloy. Although the nitrogen solubility in steels at elevated temperatures is rather high (in the order of 10^{-1} at.%), it drops substantially when increasing the Ni or Co content in the alloys. This was shown by Barnes and Lai[2] experimentally and by Krupp *et al.*[12,24] by means of CALPHAD calculations, using the thermodynamic software ChemApp™. It should be mentioned that the solubility data reported for nitrogen in Ni alloys show large scatter, ranging from 0.0015 at.% (Wriedt and Gonzalez[25] for

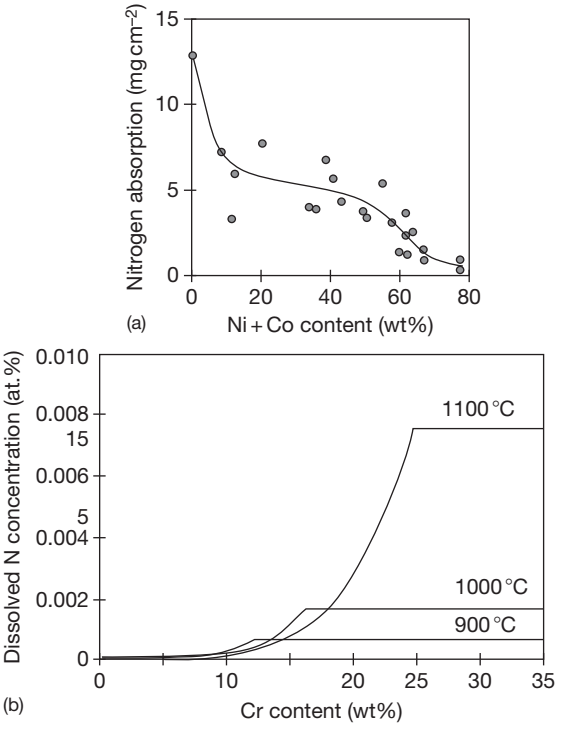

Figure 7 Effect of the chemical composition of (a) the nitridation resistance of Ni-, Fe-, and Co-base alloys[2] and (b) the nitrogen solubility in Ni–*x*Cr alloys (ChemApp™ calculation according to Gorr *et al.*[24]).

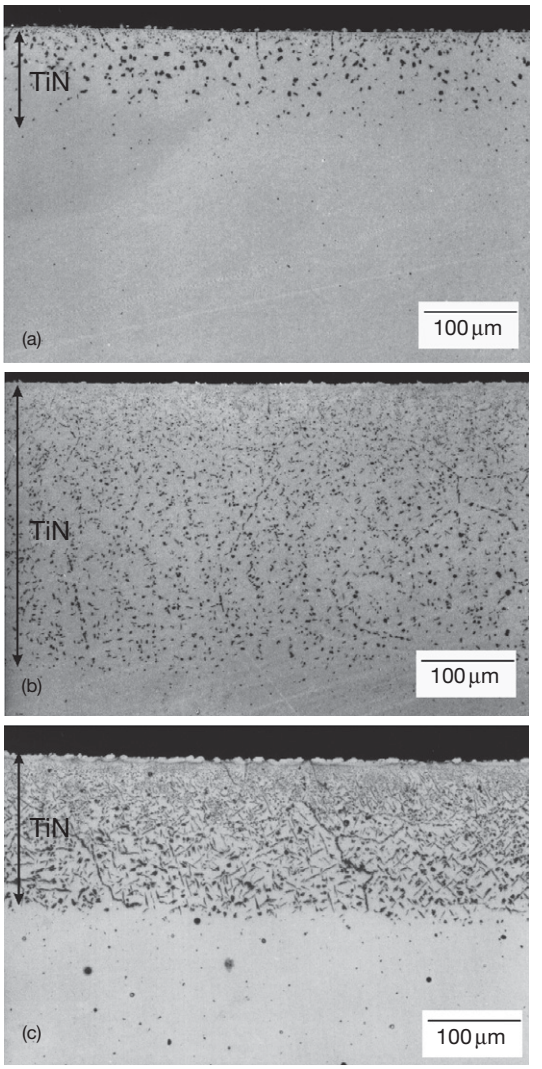

Figure 8 Internal-nitridation attack (TiN) of Ni–*x*Cr–*y*Ti model alloys after 100 h exposure at 1100 °C to low-oxygen N_2–45%He–5%H_2 atmosphere: (a) 5 wt% Cr–2 wt% Ti, (b) 20 wt% Cr–2 wt% Ti, (c) 20 wt% Cr–6 wt% Ti.[12]

pure Ni) and 0.004 at.% (Chang[26] derived from measurements (LECO nitrogen analyzer) for Ni–10%Cr) to 0.16 at.% (Allen and Douglass for Ni–V[27] alloys). Figure 7 shows data for the nitrogen concentration absorbed or dissolved in Ni-containing alloys.

The low nitrogen solubility in Ni-based alloys, which can be assumed to be equal to the maximum N concentration in the alloy surface layer (c_N^s), is directly related to the susceptibility to internal nitridation, where, according to eqn [8], the precipitation depth depends on the permeability $c_N^s D_N$, the exposure time t, and the concentration of the nitride-forming alloying element c_B^0. These relationships are represented by results obtained for the nitridation of various Ni–*x*Cr–*y*Ti model alloys,[12] as shown in Figure 8.

1.13.2.4 The Transition from Internal to External Nitridation

Assuming eqn [8] to be valid, the mole fraction of nitrides B_vN in the internal-nitridation zone is approximately equal to the original mole fraction c_B^0 of the nitride-forming alloying element B. However, if the diffusivity of B is not negligible as compared to the nitrogen diffusivity, that is, $D_N c_N^s \leq D_B c_B^0$, then the mole fraction of nitrides B_vN in the internal-nitridation zone becomes substantially higher than c_B^0. According to Wagner,[5] coalescence of the nitride precipitates into a compact nitride scale can be expected once a critical volume fraction g^* of the nitrides (typical values: $g^* = 0.2, \ldots, 0.3$) is exceeded, corresponding to a solute concentration

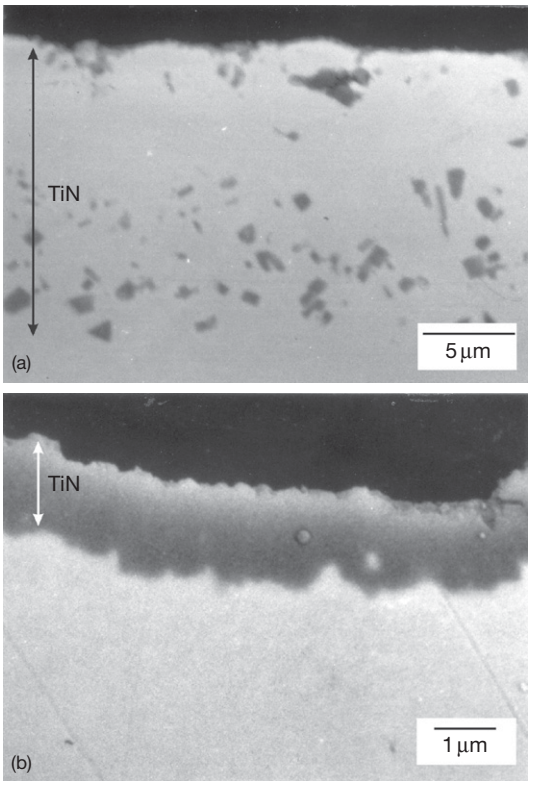

Figure 9 Internal-nitridation attack (TiN) of Ni–*y*Ti model alloys after 800 h exposure at 900 °C to low-oxygen N_2–45% He–5% H_2 atmosphere: (a) 2 wt% Ti and (b) 6 wt% Ti.

$$c_B^0 < \frac{\pi g^* D_N V}{2\nu D_B V_{B_\nu N}} c_N^s \qquad [12]$$

for which internal nitridation instead of superficial nitride-scale formation occurs, with V and $V_{B_\nu N}$ being the molar volumes of the alloy and the nitride compound, respectively. Hence, the critical solute concentration c_B^0 increases with (i) increasing nitrogen solubility c_N^s, (ii) increasing nitrogen diffusivity D_N, and (iii) decreasing solute diffusivity D_B. This is the reason why for Ni–6Ti with very low N solubility, superficial TiN-scale formation was observed (**Figure 9**, Ni–2Ti shows little internal-nitridation attack under the same conditions), while Ni–20Cr–6Ti shows deep internal-nitridation attack (cf. **Figure 8**).

Equation [12] has to be considered when designing alloys to form superficial nitride scales for improved wear resistance at elevated temperatures. However, in such cases, the high specific volume of the nitrides compared with that of the substrate alloy, needs to be taken into account (cf. **Section 1.13.3.1**).

1.13.3 Internal Nitridation of Heat-Resistant Alloys

1.13.3.1 Internal Nitridation of Fe- and Ni-Based Superalloys

Because of the very low nitrogen solubility in Ni compared to Fe, Ni-based alloys, for example, alloy 600 and 601,[2,28] exhibit a substantially higher resistance to internal nitridation than Fe-based alloys, such as alloy 800/800H or AISI 314.[2,29] In the case of NH_3-containing atmospheres, the high temperature corrosion behavior of both, Ni- and Fe-based alloys can be catastrophic, generally leading to external and/or internal nitridation attack.[30] Very high nitrogen activities in combination with some amount of oxygen lead to the formation of nonprotective porous oxide–nitride scales. According to Strauß *et al.*,[31] in low- and high-alloy Cr steels, sponge-like scales of Fe_3O_4 or $FeCr_2O_4$ are formed in 70% NH_3–30% H_2O atmosphere being obviously permeable for NH_3 with the consequence of strong internal nitridation in the form of needle-like Cr nitrides. Because of the high specific volume of the Cr nitrides, compressive stresses are induced in the internal-nitridation zone, leading to intercrystalline cracks and a disintegration of the polycrystalline microstructure. Ni alloys may form very instable Ni_3N that releases gaseous nitrogen when decomposing, leading to pore formation. In the case of Cr-containing Ni-based alloys, the combination of pores and internal Cr nitrides causes fast surface-layer degradation in ammonia atmosphere.[31]

Since Cr nitrides are of only moderate thermodynamic stability, their formation is limited to atmospheres with very high nitrogen activities or alloys containing Cr concentrations above ~20 wt%, hence exposure of most technical NiCr alloys to air does not cause any nitridation. However, alumina-forming superalloys, often alloyed with Ti for γ' strengthening, often show massive internal nitridation under service conditions, for example, gas-turbine blades operating in air or combustion atmosphere.[32] Below a superficial Cr_2O_3 scale, the oxygen partial pressure drops to a value sufficient only for the formation of Al_2O_3 and TiO_2. On the other hand, Cr_2O_3 is observed to be permeable to atomic nitrogen;[33] hence the ratio $p(N_2)/p(O_2)$ increases below the chromia scale. For conditions where no dense Al_2O_3 subscale can be formed because of overall or local depletion of the Al concentration below a critical value, a situation that is often promoted by service under thermal-cycling conditions, further penetration of nitrogen is possible, allowing stable AlN and TiN

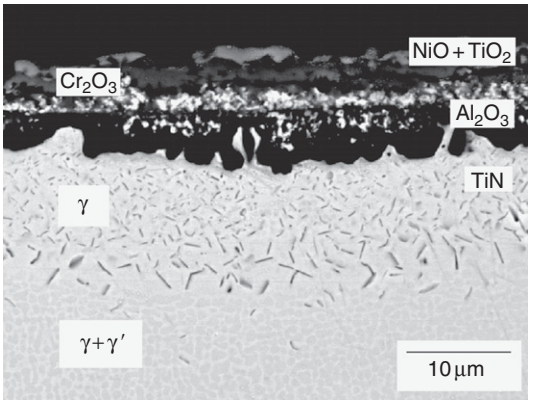

Figure 10 Internal nitridation in the single-crystalline Ni-base superalloy SRR99 after 100 h exposure at 1000 °C to air.

precipitates to be formed according to the local combination of $p(N_2)$ and $p(O_2)$ (cf., thermodynamic stability diagrams, **Figure 6(b)**). The process of internal nitridation of alumina-forming Ni- or Fe-based superalloys is shown for the single-crystalline superalloy SRR99, as an example, in **Figure 10**.

For superalloys with Cr concentrations not above 20 wt% and nitrogen activities below $a_N = 1$, occurrence of only the most stable nitride TiN, the somewhat less stable nitride AlN, and, depending on the gas and alloy composition, NbN and VN,[27] is possible.

In cast Ni-based superalloys, for example, the single-crystalline alloys used for the first stages gas-turbine blades, the susceptibility to internal nitridation varies locally due to dendritic segregations. The high nitrogen diffusivity (cf. **Section 1.13.2.2**) leads to a fast progress of the internal-precipitation front, which is accompanied by a dissolution of the strengthening γ' phase ($Ni_3(AL,Ti)$) due to the nitridation (and oxidation-) caused consumption of the γ'-forming alloying elements Al and Ti (see **Figure 10**). A particular deep dissolution can be observed in alloys where the γ' phase is stabilized by a high Ti content ($c_{Ti} > 2$ wt%).

Even though it can be assumed that internal nitridation of superalloys is controlled by nitrogen diffusion, the parabolic rate law was shown in an explicit way only for model systems or in pure nitriding gas atmospheres.[6,12] It can be assumed that the morphology of the internal reaction products itself is of significance for the precipitation kinetics. The AlN precipitates are by orders of magnitude larger than the TiN precipitates (see **Figures 10** and **14**). Hence, the formation of AlN nuclei requires much higher supersaturation and particle growth must be partly controlled by Al diffusion in a much more pronounced way than is the case for TiN precipitates.

Ni-based alloys with Cr concentrations above ~20 wt% are prone to the formation of a third group of nitrides: Cr_2N and the ternary π phase ($Cr_{10}Ni_7N_3$, cf. **Section 1.13.2.3**). The π-phase nitrides reported by several authors[21–23] are of coarse morphology and were discussed as a possible strengthening phase in the bulk[34] or as surface layer of heat-resistant alloys.

1.13.3.2 Mechanical Effects on Internal Nitridation Kinetics

Generally, the mechanisms governing internal-corrosion cannot be analyzed without taking mechanical stresses into account. In particular, large, needle-like precipitates act as crack initiation sites and cause an embrittlement of the internally-corroded surface layer. According to a study by Klöwer *et al.*,[29] the small submicrometer TiN precipitates are much less harmful than the blocky AlN precipitates. However, in cases where the initial Ti concentration is rather high ($c_{Ti} \geq 2$ wt%), the alloy grain boundaries can be completely covered by TiN, leading to intercrystalline cracking as shown for a nitrided model alloy in **Figure 11(a)**. Hence, nitridation leads to a dangerous decrease in the ductility of technical high temperature alloys.

As a second effect, the nitridation reaction is accompanied by a strong increase in the specific volume v of the nitrides, for example, $v_{CrN} = 0.17\ cm^3\ g^{-1}$, $v_{AlN} = 0.19\ cm^3\ g^{-1}$, $v_{TiN} = 0.31\ cm^3\ g^{-1}$, as compared to the specific volume of Ni-base superalloys, $v_{Ni\text{-}base} \cong 0.13\ cm^3\ g^{-1}$. This volume increase has been shown by various authors to cause damage in the form of cracks or grain disintegration[14,31] and/or to drive outward solvent diffusion leading to substrate–metal protrusions.[15–19] **Figure 11(b)** shows the tip of a wedge-shaped specimen of the Ni-based superalloy CMSX-4 after thermal cycling at 1100 °C (1 h dwell times interrupted by 15 min cooling periods).[35] The combination of geometry-induced growth stresses and differences in the coefficient of thermal expansion ($CTE_{oxide} \ll CTE_{alloy}$) led to repeated spalling of the alumina scale, near-surface depletion of the Al reservoir, and, eventually, strong internal-oxidation and nitridation attacks in combination with cracks and fast oxidation of the solvent ('breakaway' oxidation).

As mentioned earlier, stress-driven and stress-enhanced diffusion contributes vitally to the kinetics

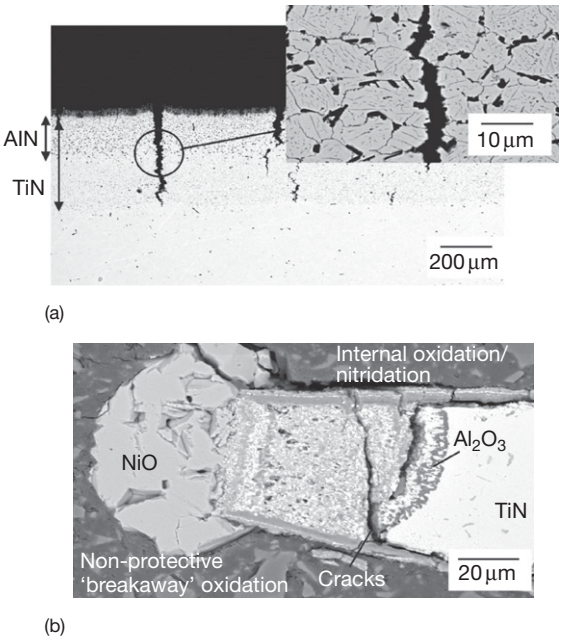

Figure 11 Cracks in an internally nitrided surface layer in alloy 80A (100 h, 1000 °C, low-oxygen N_2–45% He–5% H_2 atmosphere) due to tensile testing and (b) 'breakaway oxidation' and internal oxidation/nitridation of a wedge-shaped specimen of the single-crystalline Ni-base superalloy CMSX-4 after thermal cycling exposure at 1100 °C – 1 h dwell times in air.

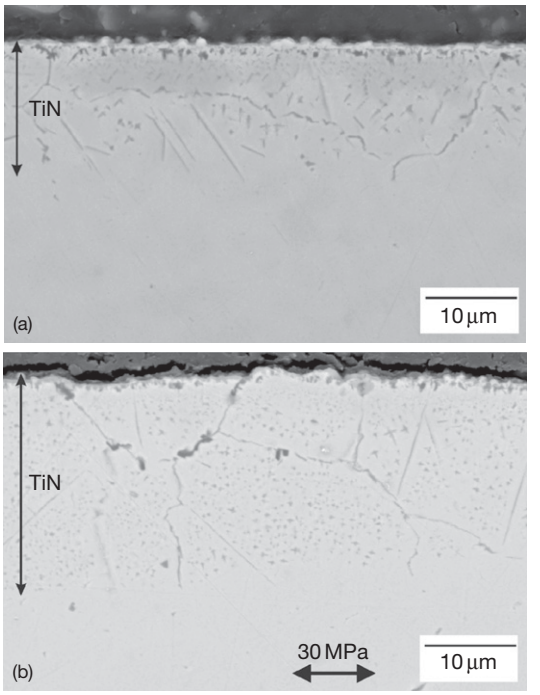

Figure 12 Internal nitridation within (a) a mechanically unloaded specimen and (b) a creep-loaded specimen ($\sigma = 30$ MPa) of the Ni-base superalloy alloy 80A exposed at $T = 900$ °C for $t = 48$ h to low-oxygen N_2–45% He–5% H_2 atmosphere.

of internal nitridation. Figure 5 shows NiCr protrusions on top of an internally nitrided Ni–10Cr–2Ti alloy. Chang *et al.*[15] could prove the direct relationship between the depth of internal TiN precipitation and the degree of coverage by surface protrusions. The most probable mechanism for the respective outward transport of solvent has been assumed to be dislocation-pipe diffusion[15,18] rather than Nabarro–Herring creep or grain-boundary sliding. Furthermore, it was shown by Krupp *et al.*[36] and Dong *et al.*[37] that the internal-nitridation rate was substantially increased when superimposing a mechanical creep load (Figure 12); again, this can be attributed to dislocation-pipe diffusion, contributing to internal precipitation when the dislocation density is increasing due to dislocation creep.

1.13.3.3 Protection Against Internal Nitridation Attack

In the literature on high temperature corrosion of technical superalloys, there is agreement that a dense and adherent Al_2O_3 scale provides the most effective protection against internal nitridation. Nitrogen permeation is obviously very slow. However, it should be mentioned that in a nitrogen-based atmosphere with very low oxygen partial pressures in the range of $p(O_2) < 10^{-23}$ bar, a very thin alumina scale of submicrometer thickness is formed, which is not able to block nitrogen permeation.[4] Even though preoxidation of an alumina-forming alloy or any other alloy that has been aluminized could prevent internal oxidation, there is still the risk of local spalling and/or cracking of the scale. If under service conditions no healing layer can be formed, such a situation would cause a transition to internal oxidation and nitridation.

As a second possibility to protect a material against internal nitridation, nitride-forming alloying elements, such as Ti and Al, should be avoided. However, this is difficult because of the high significance of Al for alumina-scale formation and γ' stabilization. The latter effect, γ' destabilization because of Al and Ti reduction, can be partly accommodated by adding Ta and Nb, though the latter also is a nitride former.[27] Similar to many alloying elements in high-alloyed Ni-based superalloys, the risk of brittle-phase formation, for example, by high Nb concentrations, needs to be taken into account when considering new alloy compositions. Attempts to replace Al as the most

effective TGO former at very high temperatures, for example, by Si, has never been successful; hence, even for coated alloys, a minimum Al concentration for healing-layer formation must be maintained.

In the case of polycrystalline alloys, the susceptibility to internal-oxidation and internal-nitridation attack might be reduced by grain-boundary-engineering-type processing. It was shown for oxidation of alloy 718 in air that by increasing the fraction of low-energy CSL boundaries (coincident site lattice) the oxidation rate was reduced.[38] There is a chance that a combination of near-surface grain refinement and high temperature exposure could (i) reduce the ratio between the inward oxygen flux and the outward aluminum flux, that is, promoting superficial Al_2O_3 formation even at low initial Al concentrations, and (ii) reduce the inward nitrogen flux by an increasing number of CSL boundaries exhibiting low grain-boundary diffusivity.

1.13.4 Modelling and Computer Simulation of Internal Nitridation

According to the preceding sections, internal nitridation is governed by solid-state diffusion of the reacting metallic and nonmetallic species (i) through a superficial oxide scale, (ii) through an internal-precipitation zone, and (iii) through the substrate alloy. In general, this problem can be treated by the diffusion differential equation for all the species participating in the nitridation process, using either the gradients in the chemical potential or, in a simplified way, the concentration gradients.[9,10,39] In the latter case, the equations need to be coupled with a mass balance and a Gibbs-energy criterion, accounting for the local solubility product, that is, the concentrations of the diffusing species in thermodynamic equilibrium.

Possible ways to solve the diffusion equation

$$\frac{\partial c}{\partial t} = \nabla(D\nabla c) \qquad [13]$$

numerically are provided by the finite-difference and the finite-element method. Although the latter one is of a large flexibility with respect to diffusion in complex geometries, the finite-difference approach is easier to handle and to link with computational thermodynamics. Here, the derivatives in eqn [13] (simplified for two-dimensional diffusion problems) are replaced by difference quotients using time steps of a length Δt and location steps of flexible widths Δx and Δy, respectively,

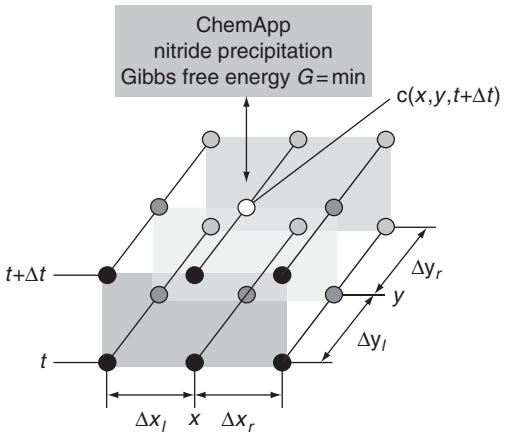

Figure 13 Schematic representation of the two-dimensional finite-difference mesh (Crank–Nicolson scheme) for simulation of internal-corrosion processes in combination with ChemApp™.

according to the Crank–Nicolson scheme (Figure 13, l = left-hand side, r = right-hand side)[40].

$$\frac{c(x,y,t+\Delta t)-c(x,y,t)}{\Delta t} = \frac{D_x(x,y)}{2}\left(\frac{c(x-\Delta x,y,t)-2c(x,y,t)+c(x+\Delta x,y,t)}{\Delta x_l(x,y)\cdot\Delta x_r(x,y)} + \frac{c(x-\Delta x,y,t+\Delta t)-2c(x,y,t+\Delta t)+c(x+\Delta x,y,t+\Delta t)}{\Delta x_l(x,y)\cdot\Delta x_r(x,y)}\right) + \frac{D_y(x,y)}{2}\left(\frac{c(x,y-\Delta y,t)-2c(x,y,t)+c(x,y+\Delta y,t)}{\Delta y_l(x,y)\cdot\Delta y_r(x,y)} + \frac{c(x,y-\Delta y,t+\Delta t)-2c(x,y,t+\Delta t)+c(x,y+\Delta y,t+\Delta t)}{\Delta y_l(x,y)\cdot\Delta y_r(x,y)}\right) \qquad [14]$$

Equation [14] applied simultaneously to all the species involved in the internal-nitridation process allows the stepwise solution of two-dimensional diffusion problems in a two-dimensional area with location-dependent diffusion coefficients accounting for the different diffusion paths, that is, bulk diffusion, grain-boundary-diffusion, etc. Coupling of the equations can be established by the integrable thermodynamics interface ChemApp™, which represents the thermodynamic software FactSage™. The interface recalculates the set of concentrations at a certain time step according to thermodynamic equilibrium until the diffusion calculation continues.

The numerical approach can be applied to solve complex internal-nitridation phenomena, which cannot be treated by Wagner's classical theory of internal oxidation, for example, (i) internal precipitation of compounds of moderate thermodynamic stability such as Cr nitrides (cf. Figure 14(a)), (ii) simultaneous internal

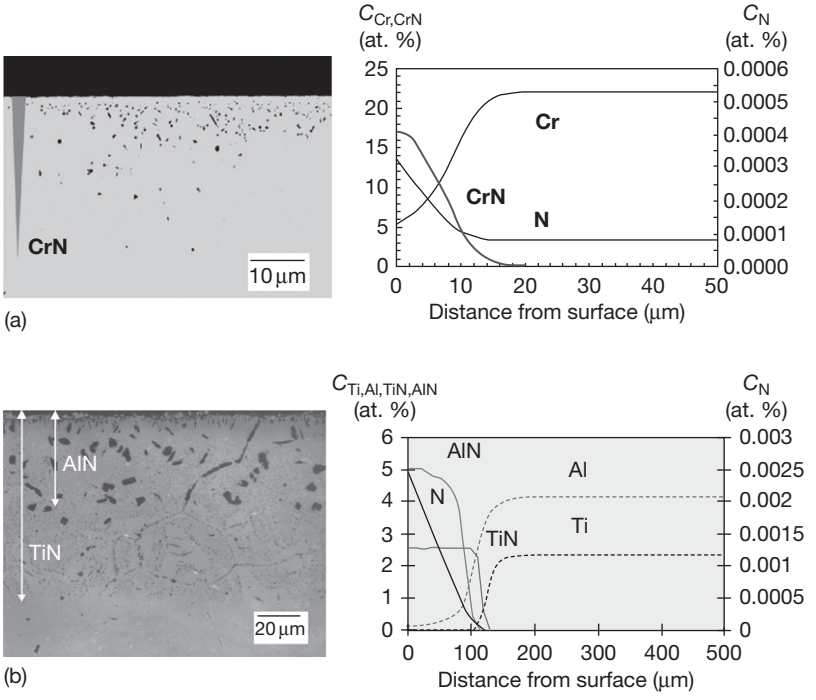

Figure 14 Cross-sectional view and simulated concentration profiles of (a) internal precipitation of CrN in Ni–20Cr (800 °C, 200 h) and (b) simultaneous internal precipitation of TiN and AlN in Ni–20Cr–2Al–2Ti (1100 °C, 150 h) in both cases exposure to low-oxygen N_2–45% He–5% H_2 atmosphere.

and/or intergranular precipitation of more than one nitride and/or oxide compound (cf. **Figure 14(b)**), or (iii) internal corrosion as a consequence of local damage of a superficial oxide scale by cracking or spalling.

1.13.5 Concluding Remarks

Although for many technical applications nitridation treatments are used to produce wear-resistant surface layers on steels, in high temperature corrosion, the term nitridation refers to a deep embrittlement attack caused by nitride compounds. Nitridation occurs not only in ammonia atmospheres with a high nitrogen activity but also in pure nitrogen or even in air or combustion atmospheres at temperatures above 800 °C, where N_2 dissociation is fast enough to allow atomic nitrogen to penetrate into the metal surface by solid-state diffusion. The nitridation rate depends mainly on the diffusivity of nitrogen in the alloy and the thermodynamic stability of the nitrides being formed internally; the precipitation depth as a function of exposure time follows in many cases a parabolic rate law as was proposed by Wagner[5] for internal oxidation. Most technical applications of heat-resistant alloys with alloying elements of high nitrogen affinity, such as Al, Ti, Cr, Nb, and V, imply superimposition of oxidizing and nitriding environments. Hence, whether a superficial oxide scale can protect the substrate against internal corrosion attack depends strongly on the mechanical integrity of the scale and the ability to form a healing layer by means of sufficient supply of the oxide-forming alloying element to the metal surface. Here, the critical factors are (i) the local ratio between the oxygen and the nitrogen activity, and (ii) the solute concentration being required for transition from internal oxidation to external scale formation. These factors may change when mechanical stresses are superimposed, which arise due to thermal cycling or due to volume changes caused by internal precipitation. The mutual interactions between the diffusivity of the reacting species through a superficial oxide scale and the metallic bulk, the thermodynamics and nucleation kinetics of nitrides, and the parameters caused by the service conditions, that is, temperature changes, composition of the gas phase, etc., are complex and only touched upon in this chapter. A thorough analysis is not possible by means of an analytical approach; it requires a numerical treatment taking the various aspects of solid-state reactions into account.

Acknowledgments

The author acknowledges the experimental and theoretical work of Dr. S.Y. Chang, Dr. R. Orosz, Dr. V. Braz da Trindade Filho, and Dr. U. Buschmann, as well as the strong support by Prof. Dr. H.-J. Christ, head of Institut für Werkstofftechnik of the University of Siegen, Germany, where a great part of the research work discussed in this chapter was carried out. The research was financially supported by Deutsche Forschungsgemeinschaft and the European Commission, which is gratefully acknowledged.

References

1. Gupton, P. S. *The Heat Treatment Source Book*; ASTM: Metals Park, 2001.
2. Lai, G. L. *High-Temperature Corrosion of Engineering Alloys*; ASM International, Materials Park, 1990.
3. Bennett, M. J.; Nichols, J. R.; Borchardt, G.; Strehl, G. *Mater. High. Temp.* **2002**, *19*, 117–125.
4. Krupp, U.; Christ, H.-J. *Met. Mat. Trans.* **2000**, *31*, 47–56.
5. Wagner, C. *Z. Elektrochem.* **1959**, *63*, 772–782.
6. Han, S.; Young, D. J. *Oxidat. Met.* **2001**, *55*, 223–242.
7. Young, D.J. In Proceedings Corrosion Science in the 21st Century, 7–11 July 2003, Manchester, UK; J. Corros. Sci. Eng [online].
8. Laflamme, G. R.; Morral, J. E. *Acta Met.* **1978**, *26*, 1791.
9. Nesbitt, J. *Oxidat. Met.* **1995**, *44*, 309–338.
10. Engström, A.; Höglund, L.; Ågren, J. *Met. Mat. Trans.* **1994**, *25*, 1127–1134.
11. Douglass, D. L. *J. Met.* **1991**, *11*, 74–79.
12. Krupp, U.; Christ, H.-J. *Oxidat. Met.* **1999**, *52*, 277–298.
13. Stott, F. H.; Wood, G. C. *Mater. Sci. Technol.* **1988**, *4*, 1072–1078.
14. Schnaas, A.; Grabke, H. J. *Werkst. Korrosion* **1978**, *29*, 635–644.
15. Chang, S. Y.; Krupp, U.; Christ, H.-J. *Mater. Sci. Eng.* **2001**, *301*, 196–206.
16. Kodenstov, A. A.; van Dal, M. J. H.; Cserhati, C.; Daróczi, L.; van Loo, F. J. J. *Acta Mater.* **1999**, *11*, 3169.
17. Douglass, D. L. *Oxidat. Met* **1995**, *44*, 81–111.
18. Yi, C.; Guan, S. W.; Smeltzer, W. W.; Petric, A. *Acta Met. Mater.* **1994**, *42*, 981–990.
19. Stott, F. H.; Shida, Y.; Whittle, D. B.; Wood, G. C.; Bastow, B. D. *Oxidat. Met.* **1982**, *18*, 127.
20. Bürgel, R. *Handbuch Hochtemperatur-Werkstofftechnik*; Vieweg: Braunschweig Wiesbaden, 1998.
21. Krupp, U.; Chang, S. Y.; Christ, H.-J. *Z. Metallkunde*, **2000**, *12*, 2006–2012.
22. Kodentsov, A. A.; Van Dal, M. J. H.; Cserhati, C.; Daroczi, L. *Acta Mater.* **1999**, *47*, 3169–3180.
23. Ono, N.; Kajihara, M.; Kikuchi, M. *Met. Trans. A* **1992**, *23*, 1389–1393.
24. Gorr, S.; Chang, S.Y.; Krupp, U.; Christ, H.-J. Unpublished data.
25. Wriedt, H. A.; Gonzalez, O. D. *Trans. AIME* **1961**, *221*, 532.
26. Chang, S. Y., PhD thesis, University of Siegen, 2001.
27. Allen, A. T.; Douglass, D. L. *Oxidat. Met.* **1999**, *52*, 505–536.
28. Tjokro, K.; Young, D. J. *Oxidat. Met.* **1995**, *44*, 453–474.
29. Klöwer, J.; Brill, U.; Rockel, M. *Mater. Corros.* **1997**, *48*, 511–517.
30. Rubly, R. P.; Douglass, D. L. *Oxidat. Met.* **1991**, *35*, 259–278.
31. Strauß, S.; Grabke, H. J.; Vogel, D. *Mater. Corros.* **2003**, *54*, 895–902.
32. Barnes, J.; Lai, G. Y. In *Proceedings Corrosion and Particle Erosion at High Temperatures*; Srinivasan, V., Vedula, K., Eds.; TMS: Warrendale, 1989; 617.
33. Krupp, U.; Chang, S.-Y.; Christ, H.-J. In *Proceedings EFC-Workshop Life Time Modelling of High-Temperature Corrosion Processes*; Schütze, M., Quadakkers, W. J., Nichols, J. R., Eds.; EFC Publications No. 34, 2001; pp 148–164.
34. Brill, U. Habilitation thesis, RWTH Aachen Technical University Aachen, Germany, 1997.
35. Orosz, R.; Krupp, U.; Christ, H.-J. *Mater. Corros.* **2006**, *57*, 154–158.
36. Krupp, U.; Orosz, R.; Christ, H.-J.; Buschmann, U.; Wiechert, W. *Mater. Sci. Forum* **2004**, *461–464*, 37–44.
37. Dong, J. X.; Sawada, K.; Yokokawa, K.; Abe, F. *Scripta Mater.* **2001**, *44*, 2641–2646.
38. Krupp, U.; Wagenhuber, Ph. E. G.; Kane, W. M.; McMahon, C. J., Jr. *Mater. Sci. Technol.* **2005**, *21*, 1247–1254.
39. Krupp, U.; Christ, H. J. *Oxidat. Met.* **1999**, *52*, 299–319.
40. Krupp, U.; Trindade, V. B.; Christ, H.-J.; Buschmann, U.; Wiechert, W. *Mater. Corros.* **2006**, *57*, 263–268.

1.14 Corrosion in Molten Salts

M. Spiegel
Salzgitter-Mannesmann-Forschung GmbH, Ehinger Strasse 200, 47259 Duisburg, Germany

Abbreviations

CE Counter electrode
RE Reference electrode
WE Working electrode

Symbols

a_i Activity of species *i*
E Voltage (V, mV)
I Current (A cm^{-2})
K Equilibrium constant
M^{n+} Cation of charge *n*+
n Charge
p_i Partial pressure of species *i*
Z Complex resistivity (Ω)

1.14.1 Introduction

Molten salts are present in many technical processes. As sulfate- and chloride-containing deposits on boiler tubes from conventionally-fired plants such as waste-, biomass-, and coal-fired boilers, they are responsible for severe corrosion-induced failures. For many years, salt deposits on gas turbines (especially Na_2SO_4) were identified as the major corrosive species that limit the lifetime of the turbine blades. Molten salts are also present as electrolytes, for example, $((Li,K)_2CO_3)$ in molten carbonate fuel cells. As the economic impact of corrosion due to molten salts (i.e., hot corrosion) is significant, great research efforts have been conducted on the mechanisms and prevention of molten salt-induced corrosion.

High temperature corrosion processes beneath molten salts are generally complicated as many different steps are involved. The metal is separated from the gas phase by the melt and transport of oxidizing species from the gas phase to the metal–melt interface that occurs. Hence, the solubility of gases in the salt is an important factor in hot corrosion. Subsequent to diffusional transport of the dissolved gas species through the molten salt, interfacial reactions take place at the metal–melt interface and corrosion products are formed, partially soluble in the salt, and transported towards lower concentrations by diffusion in the salt film.

The nature of the molten salts is generally ionic and the corrosion process involves electrochemical reactions, that is, oxidation of the metal and reduction

of melt components and dissolved gases. This requires investigation by electrochemical techniques. The complexity of the corrosion mechanism and the interdependence of many physical and chemical steps require a systematic description of the processes involved. Due to the different chemical and electrochemical properties of a particular melt, it is impossible to give a general approach, as this is the case for oxidation processes.

As a consequence, the following chapters look much more deeply into corrosion mechanisms in sulfate and carbonate melts, as examples of very different mechanisms involved.

1.14.2 Principles and Mechanisms of Corrosion in Sulfate Melts

1.14.2.1 Thermodynamic Considerations

Sulfate melts contain SO_4^{2-} oxyanions. According to the models of Flux[1] and Flood and Forland and Motzfeld,[2] the SO_4^{2-} anion dissociates, giving SO_3 and O^{2-} ions, eqn [1]:

$$SO_4^{2-} = SO_3 + O^{2-} \quad [1]$$

As cations (e.g., Na^+) are also present in the melt, equilibrium [1] can be written as eqn [2]:

$$Na_2SO_4 = Na_2O + SO_3 \quad [2]$$

The *basicity* of the melt is defined by the $p(O^{2-})$ value, eqn [3]:

$$pO^{2-} = -\log a_{O^{2-}} \quad [3]$$

According to eqn [3], a small pO_2 value is given by a high O^{2-} activity and the melt is defined to be basic. Correspondingly, a high pO_2 value is given by a small O^{2-}activity and the melt is defined to be acidic.

The overall basicity of the melt can be changed by the gas phase composition. From eqn [2], it becomes clear that:

$$a(O^{2-}) = Kp(SO_3)^{-1} \quad [4]$$

Hence, by variation of $p(SO_3)$ in the gas phase, the value of $a(O^{2-})$ is increased.

1.14.2.2 Solubility of Gases in Sulfate Melts

From eqn [4], it becomes immediately clear that the melt chemistry is influenced by variations in the gas phase in the atmosphere, especially by variations in $p(O_2)$ and $p(SO_3)$ values. In order to reach chemical equilibrium through the whole melt film, the gases under consideration need to be soluble in the molten salt, where they can act as oxidizing agents for the metal and, therefore, detrimentally influence the corrosive nature of the salt.

Experimental investigations of the solubility of O_2 and SO_2 in molten Na_2SO_4 were carried out by Andresen *et al.*[3] For O_2 and SO_2, a low solubility was observed, following Henry's law. Flood and Forland[2] published some work on the solubility of SO_3 in the melt. At low concentration of SO_3, the solubility follows Henry's law but, at higher concentrations, deviation from Henry's law was observed according to a reactive solubility of SO_3 with the sulfate ion, eqn [5]:

$$SO_4^{2-} + SO_3 = S_2O_7^{2-} \quad [5]$$

In summary, the solubility of O_2 and SO_2 in Na_2SO_4 is negligibly low, whereas the solubility of SO_3 is significantly high.

1.14.2.3 Oxidizing and Reducing Reactions of Sulfate Melt Species

From an electrochemical point of view, the corrosion process is only possible if the anodic oxidation of the metal as it occurs in corrosion is forced by a complementary cathodic reduction of either the melt components or the dissolved gases. In order to study the electrochemical behavior of a sulfate melt, polarization experiments in a pure Na_2SO_4 melt have been performed with noble metal electrodes when the following anodic and cathodic reactions were identified, eqns [6]–[11]:

Reduction (cathodic) reactions (increasing overpotential):

$$SO_4^{2-} + 2e^- = SO_3^{2-} + O^{2-} \quad [6]$$

$$SO_4^{2-} + 6e^- = S + 4O^{2-} \quad [7]$$

$$SO_4^{2-} + 8e^- = S^{2-} + 4O^{2-} \quad [8]$$

Oxidation (anodic) reactions:

$$SO_4^{2-} = SO_3 + \frac{1}{2}O_2 + 2e^- \quad [9]$$

Reduction of SO_3 and O_2, produced by equilibrium eqn [1], is also possible:

$$SO_3 + 2e^- = SO_2 + O^{2-} \quad [10]$$

$$\frac{1}{2}O_2 + 2e^- = O^{2-} \quad [11]$$

The decomposition of the sulfate as described previously only occurs in highly basic melts under

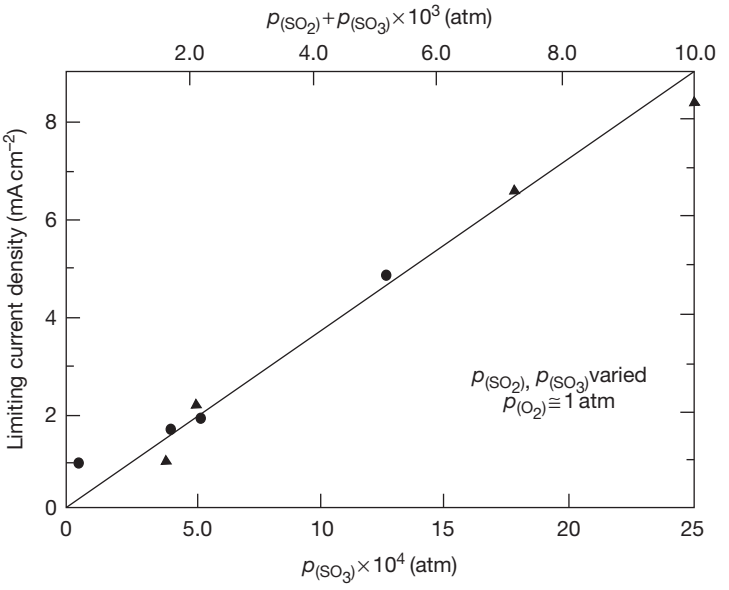

Figure 1 Limiting diffusion current at Pt electrodes beneath a thin Na_2SO_4 melt as a function of $p(SO_2,SO_3)$ at constant $p(O_2)$ at 896 °C.

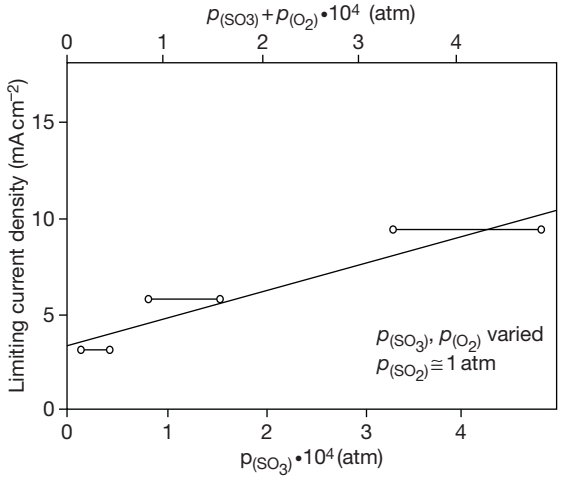

Figure 2 Limiting diffusion current at Pt electrodes beneath a thin Na_2SO_4 melt as a function of $p(SO_3)$ at constant $p(SO_2, O_2)$ at 896 °C.

reducing conditions or at high cathodic or anodic overpotentials. In principle, this is possible in deep melts or if the melt is trapped in pores within the oxide scale.

The situation is completely different if gas species are dissolved in the melt. This has been shown by measurements of the limited diffusion current in a thin Na_2SO_4 film at 896 °C.[4] The experiments were carried out in an $O_2 - (SO_3 + SO_2)$ gas mixture, showing that the limiting diffusion current increases with increasing $p(SO_3, SO_2)$ values at constant $p(O_2)$ (**Figure 1**) and also increases with increasing $p(SO_3)$ values at constant $p(O_2, SO_2)$ (**Figure 2**).

As SO_3 is dissolved as $S_2O_7^{2-}$ in the melt, the major oxidizing species in a thin Na_2SO_4 melt film in the presence of SO_3 is $S_2O_7^{2-}$ ions. The reduction reactions were investigated by chronopotentiometric measurements in a Na_2SO_4 melt at 900 °C in an $O_2 + 1\%$ $(SO_2 + SO_3)$ atmosphere[5] and the results show two transition times (**Figure 3**), attributed to the following reduction steps, eqns [12] and [13]:

$$S_2O_7^{2-} + e^- = SO_4^{2-} + SO_3^- \qquad [12]$$

$$SO_3^- + e^- = SO_3^{2-} = SO_2 + O^{2-} \qquad [13]$$

The reduction of O_2 is also possible in an O_2^- and SO_3^- containing atmosphere, but to a much smaller extent, due to the low solubility of O_2 in the sulfate melt.

For very basic melts without SO_2/SO_3 being present in the gas atmosphere, the reduction of oxygen ions occurs, as shown by chronopotentiometric measurements in a Na_2SO_4 melt, with the addition of 5 mol% Na_2O_2 in air at 900 °C. Two major reactions were identified, eqns [14] and [15]:

$$O_2^- + 3e^- = 2O^{2-} \qquad [14]$$

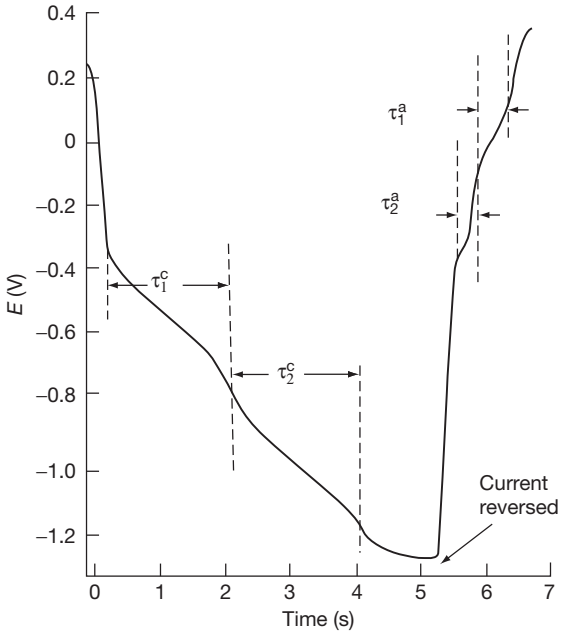

Figure 3 Chronopotentiometric curve for Na_2SO_4 in O_2 + 1% (SO_2 + SO_3) at 900 °C.

$$2O_2^- + 4e^- = 2O^{2-} + O_2^{2-} \qquad [15]$$

In general, corrosion mechanisms in sulfate melts mainly involve gaseous species dissolved in the molten salt. The same is true for molten carbonates, which is considered in the next section.

1.14.3 Principles and Mechanisms of Corrosion in Carbonate Melts

Molten carbonates are also oxyanion melts, containing O^{2-} ions, stemming from the dissociation of the carbonate ions, eqn [16]:

$$CO_3^{2-} = CO_2 + O^{2-} \qquad [16]$$

In accordance with the definition of the acid/base characteristic of sulfate melts, the basicity of carbonate melts is defined by eqn [17]:

$$pO^{2-} = -\log a_{O^{2-}} \qquad [17]$$

1.14.3.1 Solubility of Gases

The dissolution of oxygen in carbonate melts takes place by a chemical reaction between the O_2 molecules and the basic component of the melt (i.e., Na_2O); hence, it does not obey Henry's Law. Based on impedance measurements in a $(Li,K)_2CO_3$ melt at 615–800 °C, the following reduction steps for oxygen species take place by dissolution in the carbonate melt,[6] eqns [18] and [19]:

1. Peroxide mechanism:

$$2CO_3^{2-} + O_2 = 2CO_2 + 2O_2^{2-} \qquad [18]$$

Peroxide ions are mainly present in K-rich melts.

2. Superoxide mechanism:

$$2CO_3^{2-} + 3O_2 = 2CO_2 + 4O_2^- \qquad [19]$$

The superoxide mechanism does not take place in pure Li_2CO_3 melts, that is, superoxide-ions are not present in predominately Li-rich melts.

According to experiments by Cleas *et al.*[7] in a molten Na_2CO_3–K_2CO_3 melt at 800 °C, the solubility of CO_2 in carbonate melts is rather high. The results of cyclovoltametric experiments indicate a very weak anodic reduction peak for CO_2 to CO, but a significant solubility of CO_2 in the carbonate melt by chemical reaction of CO_2 with the carbonate ion, according to eqn [20]:

$$CO_2 + CO_3^{2-} = C_2O_5^{2-} \qquad [20]$$

1.14.3.2 Oxidizing and Reducing Reactions of Carbonate Melt Species

Anodic polarization of a carbonate melt with inert Au-electrodes is limited by the oxidation of the carbonate ion according to the reaction given in eqn [16]. The cathodic process is generally the deposition of alkali-metal according to:

$$M^{n+} + ne^- = M \qquad [21]$$

There is also evidence that, when in contact with O_2- and CO_2-containing gases, some contributions to the cathodic current are due to the following reduction reactions, eqns [22]–[24]:

$$CO_2 + \frac{1}{2}O_2 + 2e^- = CO_3^{2-} \qquad [22]$$

$$\frac{1}{2}O_2 + 2e^- = O^{2-} \qquad [23]$$

$$CO_2 + 2e^- = CO + O^{2-} \qquad [24]$$

Special interest has to be paid to the electrochemical behavior of oxygen species, stemming from the reactive dissolution of oxygen in the carbonate.[8]

The following reduction steps take place after reactive dissolution by the peroxide and superoxide mechanisms in a $(Li,K)_2CO_3$ melt at 615–800 °C for oxygen species, eqns [25]–[30]:

1. Peroxide mechanism:

$$2CO_3^{2-} + O_2 = 2CO_2 + 2O_2^{2-} \quad [25]$$

peroxide reduction steps:

$$O_2^{2-} + 2e^- = 2O^{2-} \quad [26]$$

$$O^{2-} + CO_2 = CO_3^{2-} \quad [27]$$

2. Superoxide mechanism:

$$2CO_3^{2-} + 3O_2 = 2CO_2 + 4O_2^- \quad [28]$$

superoxide reduction steps:

$$O_2^- + e^- = O_2^{2-} \quad [29]$$

$$O_2^{2-} + 2e^- = 2O^{2-} \quad [30]$$

Hence, in corrosion studies in oxygen-containing environments, the reduction of oxygen species is the relevant reduction reaction.

1.14.4 Solubility of Oxides in Sulfate and Carbonate Melts

Metal surfaces are protected by a dense and adherent oxide layer, formed upon high temperature oxidation. Corrosive attack of metals and alloys in molten salts is due to the solubility of oxide scales by basic and acidic dissolution whereas the solubility of oxides is a function of melt basicity and depends on the chemical composition of the passive layer.

By a combination of thermodynamic stability diagrams of the salt phase to be investigated and the oxide phase under consideration, phase stability diagrams can be constructed to predict the behavior of any oxide in any molten salt. Figure 4 shows the Na–Fe–S–O phase diagram for prediction of corrosion of iron in a Na_2SO_4 melt at 1200 K. This diagram was constructed from superposition of the Na–S–O- and Fe–S–O-stability plots. The diagram shows clearly the basic corrosion products: $NaFeO_2$ at high $a(Na_2O)$ and the acidic corrosion products $FeSO_4$ and $Fe_2(SO_4)_3$ at low $a(Na_2O)$.

In order to investigate the solubilities of oxides in molten salts as a function of melt basicity, experiments were carried out by Rapp *et al.*[8] in molten Na_2SO_4 at 1200 K. The melt basicity was fixed by a variation in the gas atmosphere, that is, $p(SO_2)$ and $p(O_2)$, and by the addition of Na_2O_2 to the molten salt. Figure 5 shows solubility plots for various oxides in molten Na_2SO_4 at 1200 K as a function of melt basicity, that is, $-\log a(Na_2O)$. The characteristic shape of the plots represents the amphoteric dissolution behavior of oxides in molten sulfates. Basic solubility occurs at high $a(Na_2O)$ (left hand side of each curve), acidic solubility occurs at low $a(Na_2O)$ (right hand side of each curve). A characteristic minimum is

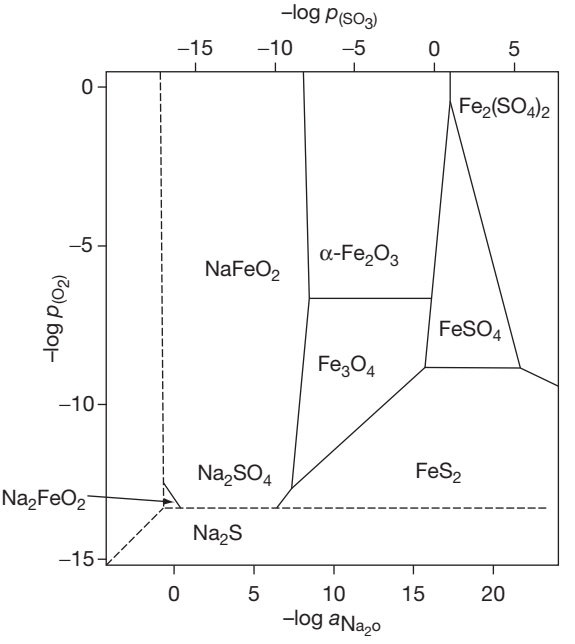

Figure 4 Na–Fe–S–O phase diagram for prediction of corrosion of iron in a Na_2SO_4 melt at 1200 K.

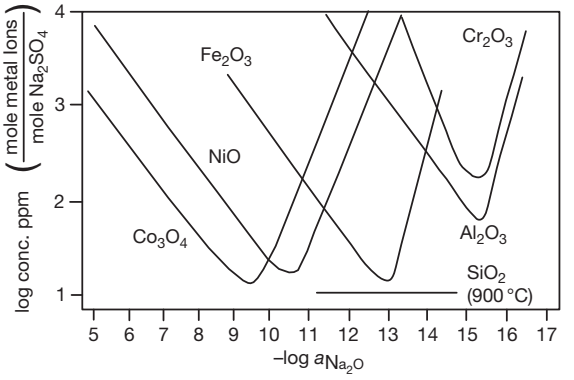

Figure 5 Solubility plots of various oxides in molten Na_2SO_4 at 1200 K as a function of melt basicity, for example, $a(Na_2O)$.

reached, where the dissolution mechanism changes from basic to acidic.

Basic dissolution of oxide scales occurs when oxide ions are present in the molten salt from the dissociation of the sulfate ion according to the reaction given in eqn [31]:

$$SO_4^{2-} = SO_2 + \frac{1}{2}O_2 + O^{2-} \quad [31]$$

During oxidation of the bare metal surface by SO_4^{2-} in a basic melt, metal oxide and additional oxide ions are formed according to eqn [32]:

$$M + SO_4^{2-} = MO + O^{2-} + SO_2 \quad [32]$$

Hence, the O^{2-} ion concentration on top of the metal oxide is higher than in the entire melt and dissolution of oxide takes place according to eqn [33]:

$$MO + O^{2-} = MO_2^{2-} \quad [33]$$

In the case of basic dissolution, the metal oxide is dissolved as a complex oxide ion.

Such dissolution reactions were investigated by Rapp and coworkers[12] for several oxides, such as Al_2O_3,[9] Fe_2O_3,[10] Cr_2O_3,[11] NiO, and Co_3O_4, in a Na_2SO_4 melt at 1200 K.

Acidic dissolution occurs by SO_3, which is dissolved in the molten sulfate as $S_2O_7^{2-}$ ions. In principle, the following reaction takes place, eqn [34]:

$$MO + SO_3 = M^{2+} + SO_4^{2-} \quad [34]$$

The oxides are dissolved as metal ions in the sulfate melt and metal sulfates are formed.

Hwang and Rapp[13] have shown that the solubility of different oxides is not independent and a synergistic effect is observed, showing accelerated dissolution of both oxides with respect to the single oxide phase. At 1200 K, Fe_2O_3 and Cr_2O_3 powder were dissolved in a Na_2SO_4 melt with a certain basicity, given by an atmosphere of oxygen containing 1 vol.% SO_2. In **Figure 5**, this condition is placed between the solubility minima of Cr_2O_3 and Fe_2O_3 in the melt.

Hence, Cr_2O_3 is dissolved by basic fluxing, eqn [35]:

$$Cr_2O_3 + \frac{3}{2}O_2 + 4Na_2SO_4 = 2Na_2CrO_4 + 2Na_2S_2O_7 \quad [35]$$

The presence of $Na_2S_2O_7$ leads to acidic fluxing of the Fe_2O_3, according to eqn [36]:

$$Fe_2O_3 + 3Na_2S_2O_7 = Fe_2(SO_4)_3 + 3Na_2SO_4 \quad [36]$$

The accelerated dissolution is due to the short diffusion distance for SO_3 in the melt.

As in the case of sulfates, the solubility of oxides in carbonate melts also depends on the partial pressure of CO_2 in the gas phase, that is, on the basicity of the melt. As NiO is the cathode material in molten carbonate fuel cells, its solubility is of major interest and has been investigated in detail. **Figure 6** shows the solubility plot for NiO in a $(Li_{0.62}K_{0.38})_2CO_3$ mixture as a function of $p(CO_2)$ in the gas phase at temperatures of 923–1023 K.[14]

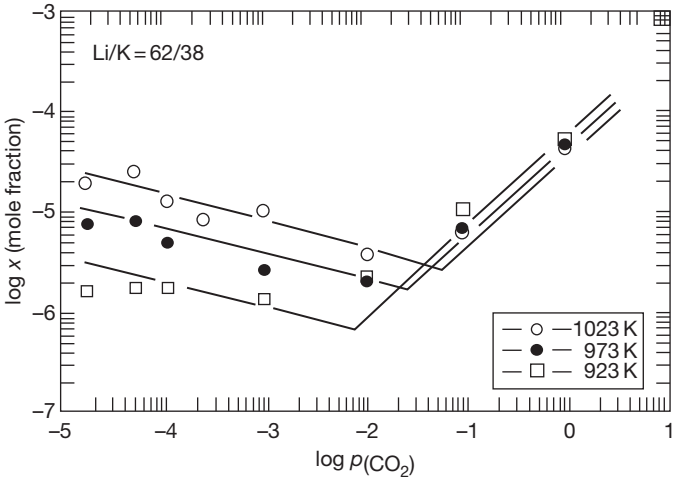

Figure 6 Solubility plot of NiO in a $(Li_{0.62}K_{0.38})_2CO_3$ mixture as a function of $p(CO_2)$ in the gas phase at temperatures of 923–1023 K.

Two different solubility regimes are observed, showing a negative slope (low $p(CO_2)$) and a positive slope (high $p(CO_2)$). These two regimes correspond to the basic (low $p(CO_2)$) dissolution and acidic dissolution (high $p(CO_2)$) of NiO in the carbonate melt, according to eqns [37] and [38]:

basic dissolution:

$$NiO + CO_3^{2-} + NiO_2^{2-} + CO_2 \qquad [37]$$

acidic dissolution:

$$NiO + CO_2 = Ni^{2+} + CO_3^{2-} \qquad [38]$$

Further investigations of the basic dissolution of NiO in other carbonates have shown that the solubility also depends on the nature of the carbonate. The solubility of NiO at 910 °C in a CO_2–O_2–Ar atmosphere is highest for Rb_2CO_3 and lowest for Na_2CO_3, especially in the acidic regime.[15]

Evidence is also given to the fact that the basic solubility of NiO in K_2CO_3 melts at constant $p(CO_2)$ depends slightly on the $p(O_2)$ value in the gas phase. This dependence is due to the following basic dissolution reaction:

$$K_2O + 2NiO + \frac{1}{2}O_2 = 2KNiO_2 \qquad [39]$$

1.14.5 Corrosion Mechanisms in Sulfate Melts: The Rapp and Goto model

As discussed earlier, the oxidation of the metal beneath a highly basic molten sulfate film generates O^{2-}-ions at the oxide–melt interface by the reduction of O_2 or by the reduction of the sulfate-ion, eqns [40]–[42].

$$M = M^{2+} + 2e^- \qquad [40]$$

$$O_2 + 2e^- = O^{2-} \qquad [41]$$

and:

$$M + SO_4^{2-} = MO + O^{2-} + SO_2 \qquad [42]$$

Accordingly, the region close to the oxide surface is much more basic than the entire salt film and basic dissolution of the oxide occurs. In the ideal case, the dissolved species form a separate layer, comparable to a Nernst concentration interface. From this interface, transport of the dissolved oxide species and also oxidant gas occur within their concentration gradients in the melt film towards the melt/gas or the gas/oxide interface. In addition to the concentration gradient in the melt film, a basicity gradient also exists, from regions of high $p(O^{2-})$ at the melt/oxide interface to low $p(O^{2-})$ at the melt/gas interface. By reaching regions of low $p(O^{2-})$, the solute is no longer stable and precipitation of solid oxide occurs by the reverse of the dissolution reactions, eqn [43]:

$$MO_2^{2-} = MO + O^{2-} \qquad [43]$$

This precipitation creates a permanent sink for the solute, promoting the continuous flux of the dissolved oxide in the melt film. On the other hand, the consumption of oxidant gas O_2 by the formation of O^{2-} ions and subsequent dissolution reaction at the melt–oxide interface creates the gradient for oxidant diffusion. **Figure 7** shows a schematic plot of the gradients and transport processes within the melt film.

Rapp and Goto[16] analyzed the basic fluxing conditions and developed a criterion for the continuous fluxing of oxide scales, eqn [44]:

$$\left(\frac{d_{(sol.)}}{dx}\right)_{x=0} \prec 0 \qquad [44]$$

As long as the negative solubility gradient (Rapp–Goto criterion) is valid, basic fluxing proceeds and the rate of the corrosion process is enhanced.

An important proof of the Rapp–Goto criterion was given later by Otsuka and Rapp,[17] who performed an electrochemical experiment (potentiometric measurements) on preoxidized nickel at 1173 K in an O_2–0.1% SO_2 gas atmosphere and covered by a thin film of Na_2SO_4. The authors continuously recorded the basicity and oxygen activity of the melt as a function of time. **Figure 8** shows the results, plotted on the Ni–Na–S–O phase diagram. At the beginning of the corrosion reaction, the melt was found to be basic.

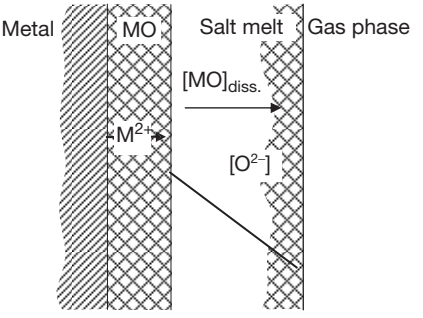

Figure 7 Schematic plot of the solubility gradient and transport processes within the melt film. The oxide precipitates at the melt–gas interphase.

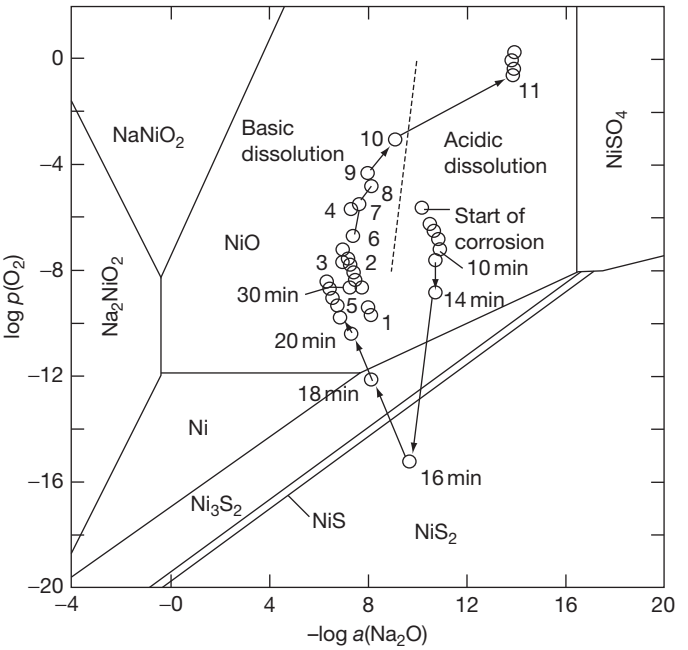

Figure 8 Basicity and oxygen activity measurements during corrosion of preoxidized Ni beneath a Na_2SO_4 film at 1173 K in O_2–SO_2, plotted in the Ni–Na–S–O phase diagram.

During the corrosion reactions, the basicity of the melt increases and Ni-sulfide becomes stable. As the composition of the gas atmosphere was not changed, the results show quite clearly that the local chemistry of the melt is influenced by the local corrosion reactions.

Acidic fluxing requires a higher $p(SO_3)$ value in the gas phase and/or some alloying elements such as Co or Ni, from which molten eutectic mixtures are able to form with the sulfate deposit (alloy-induced acidic fluxing). The main feature of acidic fluxing is the solubility of certain metal sulfates, formed by reaction of the alloying elements and SO_3 from the gas phase, within the salt deposit. Generally, no sulfide formation occurs by acidic fluxing.

1.14.6 Methods of Investigation of Corrosion in Molten Salts

1.14.6.1 Electrochemical Techniques

Being electrochemical in nature, fundamental studies of hot corrosion mechanisms require electrochemical techniques. The simplest electrochemical measurement is polarization of the sample and the measurement of the induced current. As in aqueous corrosion, polarization studies provide information mainly about the potential dependent behavior of a piece of metal in the melt, that is, active dissolution, the passive range and breakthrough potentials. For such studies, the melt is placed in an alumina crucible, situated in a vertical, closed-end furnace, as shown in Figure 9.

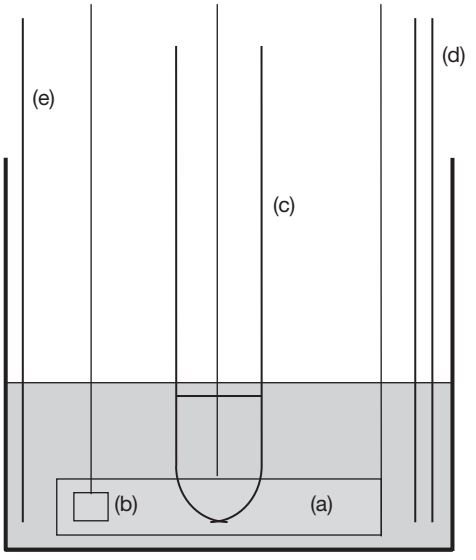

Figure 9 Typical set-up of the inner crucible of a high temperature electrochemical cell with counter-electrode (a), the working-electrode (b), the reference electrode (c), the gas inlet tube (d), and the thermocouple (e).

In order to avoid electronic distortions from the furnace heating wires, a cylindrical vessel made of stainless steel is usually placed between the alumina

crucible and the furnace. The vessel is electrically connected to the furnace in order to avoid electrical charges on the surface. The alumina crucible is closed by a heat-resistant pyrex-glass flange with spaces for the electrodes, the thermocouple and the gas-inlet tube. The electrode wires and the thermocouple are shielded by small-diameter alumina tubes. These *alumina tubes* are fixed with cayon fittings in the glass flange.

For the polarization studies, a three electrode set-up is necessary, consisting of a working electrode (WE), a counter electrode (CE), and a reference electrode (RE). The WE is usually the metal to be investigated or, for studies of the polarization behavior of the melt itself, Au or Pt are appropriate; the latter are also suitable for the counter electrode.

The main difference in aqueous corrosion studies is the design of the reference electrodes. The most useful types are closed-end tubes of either internally-platinized Y_2O_3-stabilized ZrO_2, mullite or glass membranes, depending on the composition of the melt and the temperature. Glass membranes, especially Pyrex®, Supremax® and Duran 50®, are Na^+ and K^+ ion-conducting membranes and are also useful for studies in molten salts, especially at temperatures up to 700 °C. Similar to the mullite reference electrode, a silver wire is dipped into the molten chloride or sulfate to be investigated; usually this melt additionally contains $AgCl_2$ or Ag_2SO_4 in concentrations of 1–10 mol%.[18]

For example, **Figure 10** shows a polarization curve for a 2.25Cr–1Mo–steel in a eutectic (Ca–K–Na) sulfate mixture at 850 °C in an N_2–5 vol.% O_2 gas mixture, using a mullite–Ag/$AgSO_4$ reference electrode. After an active region, the material behaves in a passive manner in the potential range of approximately −0.25 to 0.25 V; this is followed by an increasing current. Investigation of the sample within the passive region shows the formation of a porous Fe_2O_3 scale on the metal surface.[19]

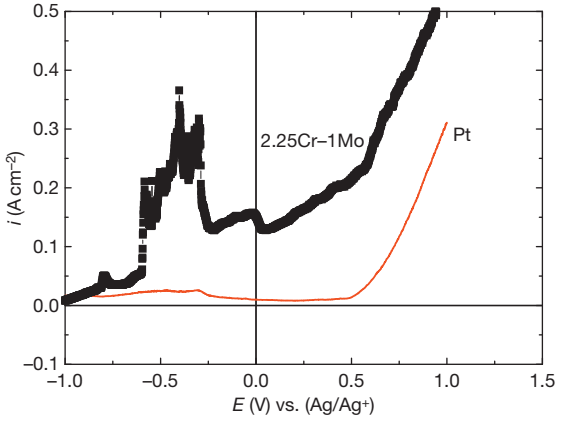

Figure 10 Polarization curve of a 2.25Cr–1Mo–steel in a eutectic (Ca–K–Na)–sulfate mixture at 850 °C in an N_2–5 vol% O_2 gas mixture; the curve for Pt is shown for comparison.

Extended investigations are possible by using cyclic voltammetry. **Figure 11** shows a cyclic voltammogram of pure iron in a eutectic 62 wt% Li_2CO_3–38 wt% K_2CO_3 melt at 650 °C in synthetic air, containing 25 vol.% CO_2. The details regarding reference electrode and set-up are described elsewhere.[20] Upon anodic polarization, the voltammogram shows three different anodic peaks (A, B, C) and two cathodic peaks (D, E).

According to detailed investigation by SEM and XRD on samples, held at different anodic potentials, the following reactions were identified:

$$\text{A: } Fe + CO_3^{2-} = FeO + CO_2 + 2e^- \quad [45]$$

$$\text{B: } Fe + 4FeO + 4CO_3^{2-} + 5Li^+ = Li_5Fe_5O_8 + 4CO_2 + 3e^- \quad [46]$$

$$\text{C: } Li_5Fe_5O_8 + 2CO_3^{2-} = LiFe_5O_8 + 2Li_2CO_3 + 4e^- \quad [47]$$

Impedance spectroscopic measurements are occasionally used in molten-salt corrosion studies. In general, most of the impedance spectra emphasize diffusion-controlled kinetics for the active corrosion of metals in molten salts. This behavior is expected as the activation energy for charge-transfer reactions is easily reached at higher temperatures.

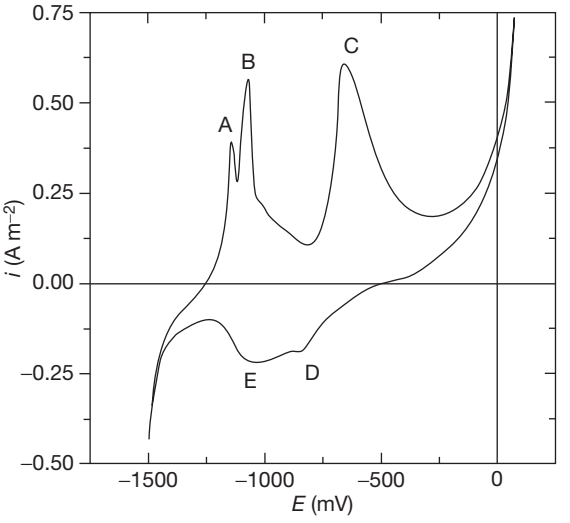

Figure 11 Cyclic voltammogram of pure iron in a eutectic 62 wt% Li_2CO_3–38 wt% K_2CO_3 melt at 650 °C in synthetic air, containing 25 vol% CO_2.

The paper by Zheng *et al.*[21] gives some theoretical impedance models for hot corrosion of metals in molten salts. In general, the authors propose large semicircles in the Nyquist plot for nonactive metals, resulting from a rate-limiting charge-transfer reaction. For active metals, the total impedance may result from the scaling of the metals when the Nyquist plot should show two capacitance loops, *and* with the rate-limiting step being the charge-transfer reaction. For porous scales on the surface, a line should be shown in the low frequency range; this is related to a diffusion-controlled process.

One example is the hot corrosion of a preoxidized nickel specimen under a thin Na_2SO_4 melt film in a 0.1 wt% SO_2–O_2 gas mixture at 1200 K.[22] By variations in the oxide scale thickness and the purity of the material, different regimes of corrosion were investigated, that is, the passive state, the pseudopassive state and the active state. The passive state for 99.9975% *of* pure nickel, preoxidized in pure O_2 for 2 h at 1200 K, is controlled by diffusion of $S_2O_7^{2-}$ ions in the salt melt. The corresponding Nyquist plots of impedance data show linear behavior in the low frequency range with a slope of 45°, as shown in **Figure 12**.

1.14.6.2 Other Methods

Multisample exposure tests are the most useful tests for estimating long-term corrosion data behavior of a certain material by fitting the corrosion data to general kinetic laws. The furnace set-up, used for the tests, is connected to a gas-flow device. In addition, salt needs to be deposited on the sample surface. This can be done by different techniques:

- evaporation of the salt with subsequent condensation on the cooler sample surface (Dean test)
- full salt immersion (crucible test, thick salt film)
- surface coverage of the sample (thin salt film)
- slurry or from an aqueous solution (thin salt film)

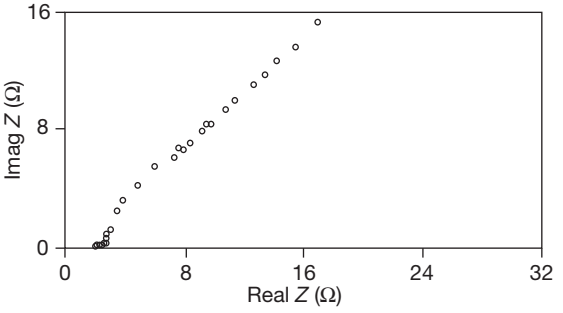

Figure 12 Nyquist plot of impedance data of the passive state of 99.9975% pure nickel in a Na_2SO_4 melt in an 0.1 wt% SO_2–O_2 gas mixture at 1200 K, showing linear behavior in the low frequency range, with a slope of 45°.

Determination of the extent of corrosion can be obtained by measurements of the scale thickness or of the remaining metal thickness or by the determination of the total weight loss after removal of the corrosion products. The last method is particularly favored if a high amount of oxide is dispersed in the solidified salt.

According to the standard guidelines for exposures of samples coated with thin salt films, as developed in the TESTCORR project,[23] the extent of corrosion should be determined on a logarithmic time scale, that is, after 1, 3, 10, 30, 100, 300, and 1000 h of exposure and redeposition of salt should be made *after* every 20 h.

In order to study short-term kinetics, thermogravimetric experiments are useful; these allow the identification of possible incubation times or the influence of gas phase composition. However, it has to be shown that the overall mass change is not influenced by reactions of the salt itself, for example, significant evaporation or reaction of the salt with the gas phase.

1.14.7 Examples of Hot-Salt Corrosion in Industrial Practice

1.14.7.1 Gas Turbines: Corrosion Beneath Na_2SO_4 Deposits

The need for the early work on hot corrosion beneath Na_2SO_4 melts was based on gas-turbine blade failures as a consequence of Na_2SO_4 deposition. It has been established that deposition of Na_2SO_4, formed by salt from the air and sulfur from the fuel, is responsible for these kinds of attack. Especially the work by Goebel and Pettit[24] as well as by Bornstein and DeCrescente[25,26] recognized that the formation of sulfides on the metallic engine parts results from the presence of a thin salt film on the metal surface. As a consequence, extensive research was conducted on alloys coated with Na_2SO_4 and how they reacted in different environments. In the following discussion, some general principles on the reaction mechanisms will be discussed. The corrosion kinetics of metals are significantly enhanced by several orders of magnitude compared to the oxidation without any salt, as shown in **Figure 13** for nickel reaction beneath a Na_2SO_4 deposit at 900 °C in an O_2–SO_2 containing atmosphere.[27]

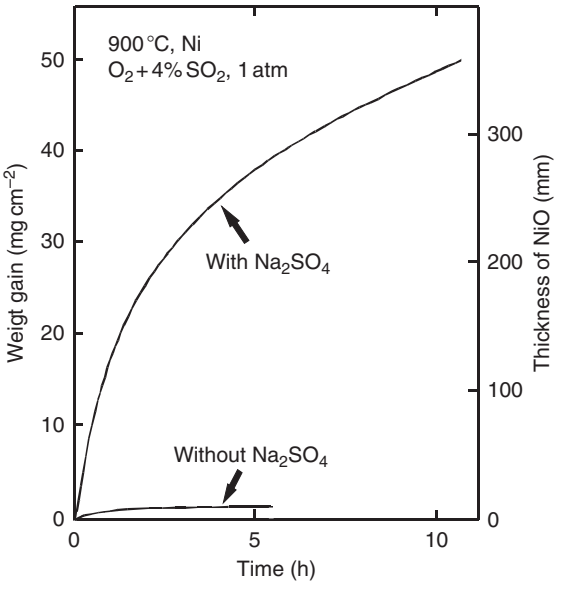

Figure 13 Comparison of the reaction kinetics of pure nickel with and without deposit of Na_2SO_4 in 1 atm O_2–4% SO_2 at 900 °C. Reproduced from Edeleanu, C.; Littlewood, R. *Electrochim. Acta* **1960**, *3*, 195.

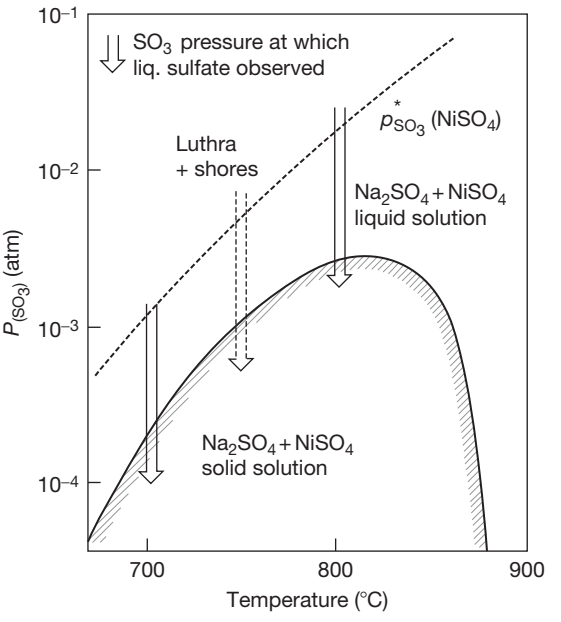

Figure 14 Comparison of the theoretical values of the critical SO_3 pressure needed to form a $Na_2SO_4 + NiSO_4$ melt with the lowest pressures occurring where a molten sulfate was observed and 'hot corrosion' was initiated.[28,29,34,35]

Two main corrosion mechanisms have been identified: Type I and Type II hot corrosion. Type I usually occurs at temperatures above the melting point of Na_2SO_4 ($T > 884\,°C$); here, the und die oxide scale is dissolved in the salt melt due to basic fluxing (see **Section 1.14.4**). Type II hot corrosion occurs at temperatures below the melting point of Na_2SO_4. One example for this is the corrosion of nickel beneath a solid Na_2SO_4 salt deposit in SO_3-containing gas. In the early stages of corrosion, a Na_2SO_4–$NiSO_4$ solid solution is formed:

$$NiO + SO_3 + Na_2SO_4 = Na_2SO_4 - NiSO_4(ss) \quad [48]$$

In the preceding reaction, the amount of $NiSO_4$ increases, the Na_2SO_4–$NiSO_4$ mixture starts to melt and accelerated corrosion is observed. The melting point of the mixture strongly depends on the $p(SO_3)$ value in the gas phase, that is, it decreases with the increasing value of $p(SO_3)$ and the melting point of the Na_2SO_4–$NiSO_4$ mixture decreases,[28,29] **Figure 14**.

In aircraft engines, *mostly* Type II hot corrosion is mainly observed in nickel- and cobalt-based materials. Extensive studies were preformed on Co–Cr, Co–Al, Ni–Cr, Ni–Cr–Al, and Co–Cr–Al–Y alloys.[35,36] A detailed corrosion mechanism for Co-based alloys in O_2^- and SO_3^- containing gases was presented by Luthra.[30] In this model, the SO_3 is dissolved in the melt and transported via SO_4^{2-} ions from the melt–gas to the melt–oxide interface at which $CoSO_4$ is formed. In only O_2-containing gases, Co^{2+} ions are dissolved from the oxide and transported to the melt–gas interface at which they are oxidized by O_2 to Co^{3+} ions and Co_3O_4 is formed. Some Co^{3+} ions also diffuse back to the melt–oxide interface where they are reduced to Co^{2+} ions again. Alloying elements Mo, W, and, also, V (present as a fuel impurity) form the acidic oxides: MoO_3, WO_3, and V_2O_5. The effect of $NaVO_3$ on the acidic fluxing of CeO_2, HfO_2, and Y_2O_3 was studied in detail by Zhang and Rapp.[31] The authors show that fluxing was accelerated by the presence of acidic solutes in the melt. This behavior was shown to result from complexing reactions between the solute VO^{3-} ions and oxide ions, provided by the acidic dissolution of *ceria in* the respective oxide.

1.14.7.2 Waste Incineration: Corrosion in Chloride Melts

In waste-fired boilers, solid and molten salts are formed by condensation of aerosols within the flue gas on cooled material surfaces that function as heat-exchanger tubes. The presence of salts accelerates the corrosion process, especially if they are associated with the formation of molten phases on the material surface or in the oxide scales.

Figure 15 shows a characteristic failure situation, in which the salt-covered part of the tube is significantly damaged.

The molten phases are mainly chlorides, such as KCl, NaCl, $ZnCl_2$, and $PbCl_2$.[32] Due to the significant amount of heavy metals, these salt mixtures form molten eutectics at temperatures as low as 250 °C, as shown in Table 1.

A typical salt melt-induced attack of a superheater tube ($T \approx 550$ °C) from a waste-fired boiler is shown in Figure 16. The morphology of the scale is typical for molten salt attack, that is, a thick and dense chromium-rich oxide scale in contact with the metal and iron-oxide and nickel-oxide precipitates in the former molten salt.[33]

The behavior of metals and their oxides in molten chlorides has not been studied as extensively as in sulfate systems. Chloride melts are mostly simple ions and initially free of oxygen, which is different from sulfates. In some cases, molecular species exist, for example $AlCl_3$ or $HgCl_2$.

Theoretical thermodynamic considerations by Edeleanu and Littlewood[34] have shown that the corrosion tendency of a metal in chloride melts depends on the stability of the specific metal chloride. Furthermore, the solubility of the metal chloride or metal oxide depends on the total pressure and, more importantly, on contaminants in the molten salt, especially oxygen. In pure chloride melts, a passivation of the metal is impossible, because most of the metal chlorides are soluble. Electrochemical experiments on iron and nickel in a KCl–NaCl melt at 700 °C in argon showed a very negative corrosion potential with respect to platinum and no passivation of the metal was observed. As corrosion products, Fe_3O_4, Fe_2O_3, and NiO were observed on top of the melt at the melt–gas interface.[36] Obviously, oxidation of the soluble metal chlorides occurs in contact with the oxygen-containing gas.

The cathodic reaction during metal oxidation is the reduction of contaminants in the melt, especially dissolved oxygen. Ishitsuka und Nose[35] studied the solubility of some metal oxides in pure NaCl–KCl melts at 727 °C and in NaCl–KCl–Na_2SO_4–K_2SO_4 melts at 550 °C. The basicity of the melt was set at $-\log a_{O}^{2-} = -2$ for basic, $-\log a_{O}^{2-} = -7$ for intermediate and $-\log a_{O}^{2-} \geq 17$ for acidic conditions. The results show a typical amphoteric solubility, as already known from sulfate melts. For some oxides, no solubility minima were observed, that is, for example, NiO/Cr_2O_3 is thought to be dissolved as chromate, corresponding to a basic solubility.

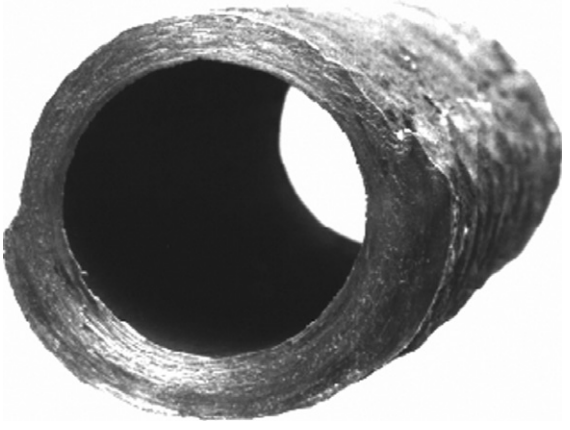

Figure 15 Characteristic failure situation of a superheater tube from a waste-fired boiler. The ash-covered part of the tube is significantly damaged.

Table 1 Eutectic mixtures and melting points of salts found in deposits from waste fired plants

Composition (wt%)	*Melting point (°C)*
48$ZnCl_2$–52KCl	250
82$ZnCl_2$–18KCl	262
84$ZnCl_2$–16KCl	262
73$ZnCl_2$–27$PbCl_2$	300
31NaCl–69$PbCl_2$	410
21KCl–79$PbCl_2$	411
17NaCl–83$PbCl_2$	415
39$ZnCl_2$–50KCl–11$PbCl_2$	275
35$ZnCl_2$–48NaCl–17$PbCl_2$	350
16NaCl–40KCl–44$PbCl_2$	400
K_2SO_4–Na_2SO_4–$ZnSO_4$	384
KCl–$ZnCl_2$–K_2SO_4–$ZnSO_4$	292

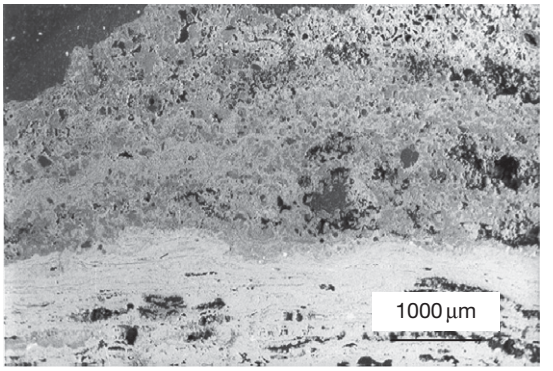

Figure 16 Typical melt-induced attack of a superheater tube ($T \approx 550$ °C) from a waste-fired boiler. The morphology of the scale is typical for molten salt attack that is, a thick and dense chromium-rich oxide scale in contact with the metal and iron-oxide and nickel-oxide precipitates in the molten salt.

In summary, it seems to be evident that corrosion in chloride melts is based on the solubility of metals and oxides as metal chlorides in the molten salt.

In deposits from waste incineration, mainly KCl–$ZnCl_2$ mixtures are present in the ashes and fast corrosion occurs at relatively low temperatures. The main corrosion mechanism is dissolution of metal in the molten salt as soluble metal chlorides. **Figure 17** shows a schematic plot of the mechanisms involved, as described by Ruh.[36]

At the metal–salt interface, the metal is dissolved as metal chloride by forming a ternary eutectic with the salt deposit. The concentration of dissolved metal chloride is high at the inner interface and low at the salt–gas interface. As a consequence, the metal chloride diffuses outward towards the oxygen-containing gas and is oxidized to oxide again.

It has been found that iron-based low alloyed steels show much more corrosion than nickel-based materials. The proposed model is supported by thermodynamic calculations of the solubility of iron, chromium, and nickel beneath a $ZnCl_2$–KCl melt. **Figures 18–20** show ternary phase diagrams for the $FeCl_2$–$ZnCl_2$–KCl, $CrCl_2$–$ZnCl_2$–KCl, and $NiCl_2$–$ZnCl_2$–KCl systems at 320 °C.

The solubility of $FeCl_2$ is quite high whereas the solubility of $CrCl_2$ is low and almost no solubility occurs for $NiCl_2$. This reflects the stability of the different alloys based on the corrosion mechanism as described above.

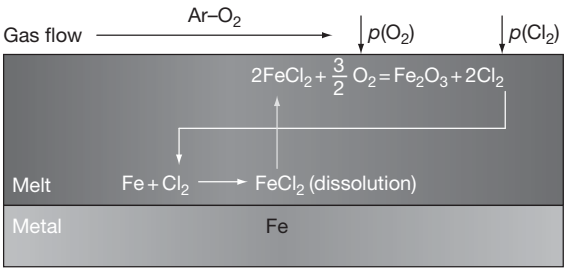

Figure 17 Reaction scheme for the mechanisms involved in chloride-induced corrosion beneath a molten $ZnCl_2$–KCl eutectic from deposits in waste-incineration plants.

1.14.7.3 Corrosion in Molten Carbonate Fuel Cells

Molten carbonate fuel cells are high temperature fuel cells, working at 650 °C with a molten 62 wt% Li_2CO_3–38 wt% K_2CO_3 eutectic mixture as the electrolyte, CO_2 and O_2 as oxidant gases and H_2 as the fuel. The relevant reactions are:

Cathode:

$$CO_2 + \frac{1}{2}O_2 + 2e^- = CO_3^{2-} \qquad [49]$$

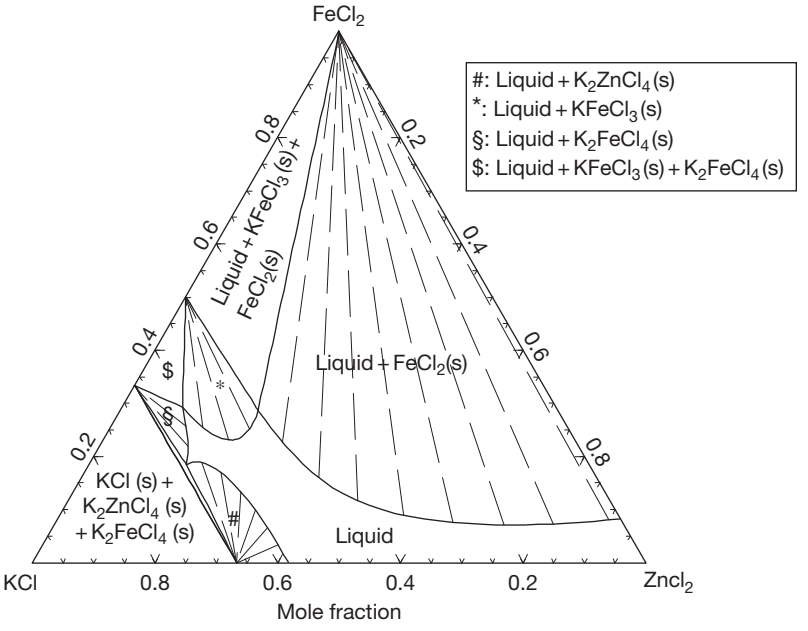

Figure 18 Solubility of $FeCl_2$ in a $ZnCl_2$–KCl eutectic mixture at 320 °C.

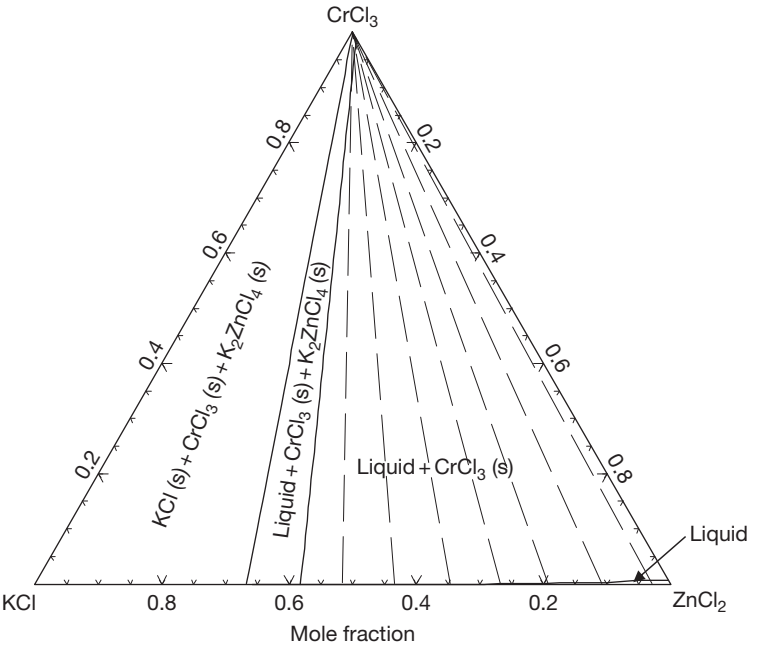

Figure 19 Solubility of $CrCl_2$ in a $ZnCl_2$–KCl eutectic mixture at 320 °C.

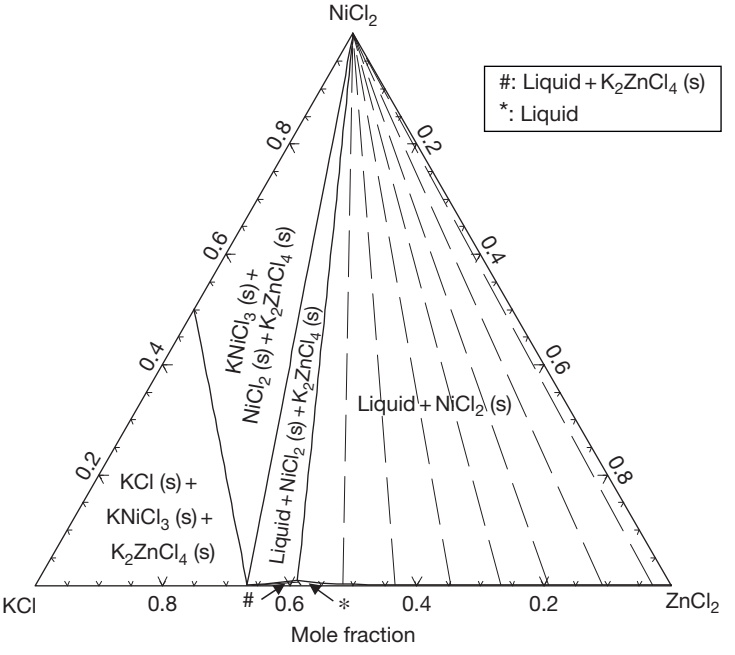

Figure 20 Solubility of $NiCl_2$ in a $ZnCl_2$–KCl eutectic mixture at 320 °C.

Anode:

$$H_2 + CO_3^{2-} = H_2O + CO + 2e^- \qquad [50]$$

In practice, the stack technology is applied, by stapling some of the modules to a bigger device. The main corrosion problems occur at the cathodic side, where NiO is used as the cathode material and stainless steel as the current collector. Both parts are in contact with the gas phase (O_2, CO_2) and the molten carbonate, leading to hot corrosion

attack. NiO forms as the cathode materials starts to dissolve in the melt and reprecipitates in the electrolyte, leading to a short circuit and breakdown of the cell voltage. Furthermore, corrosion of the cathodic-current collector by the molten carbonate occurs and the cell voltage decreases due to the growth of poorly-conducting oxide phase*s*, that is, $LiCrO_2$. Laboratory research is still going on in order to find metallic materials with good corrosion resistance, that form corrosion products with reasonable electric conductivity, such as spinels, doped with Co and/or Mn.

References

1. Lux, H. Z. *Elektrochem. Angew. Phys. Chem.* **1939**, *45*, 303.
2. Flood, H.; Forland, T.; Motzfeld, K. *Acta Chem. Scand.* **1952**, *6*, 257.
3. Andresen, R. E. *J. Electrochem. Soc.* **1979**, *126*, 328.
4. Shores, D. A.; Fang, W. C. *J. Electrochem. Soc.* **1981**, *128*, 346.
5. Fang, W. C.; Rapp, R. A. *J. Electrochem. Soc.* **1983**, *130*, 2335.
6. Nishina, T.; Uchida, I.; Selman, J. R. *J. Electrochem. Soc.* **1994**, *141*, 1191.
7. Claes, P.; Thirjon, B.; Glibert, *J. Electrochim. Acta* **1996**, *41*, 141.
8. Rapp, R. A. *Corrosion* **1986**, *42*, 568.
9. Jose, P. D.; Gupta, D. K.; Rapp, R. A. *J. Electrochem. Soc.* **1985**, *132*, 735.
10. Zhang, Y. S.; Rapp, R. A. *J. Electrochem. Soc.* **1985**, *132*, 734.
11. Zhang, Y. S. *J. Electrochem. Soc.* **1986**, *133*, 655.
12. Gupta, D. K.; Rapp, R. A. *J. Electrochem. Soc.* **1980**, *127*, 2194.
13. Hwang, Y.-S.; Rapp, R. A. *J. Electrochem. Soc.* **1990**, *137*, 1276.
14. Ota, K.; Mitsushima, S.; Kato, K.; Kamiya, N. In *Proceedings of the second Symposium in MCFC-Technology*; Electrochemical Society, 1990; Vol. 90–16, 318.
15. Orfield, M. L.; Shores, D. A. *J. Electrochem. Soc.* **1988**, *135*, 1662.
16. Rapp, R. A.; Goto, K. In *Proceedings of the Fused Salt Symposium*; Braunstein, J., Ed.; The Electrochemical Society: Princeton, NJ, 1979; Vol. 2.
17. Otsuka, N.; Rapp, R. A. *J. Electrochem. Soc.* **1990**, *137*, 46.
18. Lee, K. N.; Shores, D. A. *J. Electrochem. Soc.* **1990**, *137*, 859.
19. Spiegel, M. Proceedings EUROCORR'00, London, 2000.
20. Biedenkopf, P.; Spiegel, M.; Grabke, H. J. *Mater. Corros.* **1997**, *48*, 731.
21. Zheng, C. L.; Eang, W.; Wu, W. T. *Corros. Sci.* **2001**, *43*, 787.
22. Wu, Y. M.; Rapp, R. A. *J. Electrochem. Soc.* **1991**, *138*, 2683.
23. Tomkings, A. B., *et al.* TESTCORR, Code of Practice, ERA Report 2000-0546, 2001, Unpublished data.
24. Goebel, J. A.; Pettit, F. S. *Metall. Trans.* **1970**, *4*, 1943.
25. Bornstein, N. S.; DeCrescente, M. A. *Trans. Met. Soc. AIME* **1969**, *24*, 1947.
26. Bornstein, N. S.; DeCrescente, M. A. *Metall. Trans.* **1971**, *2*, 2875.
27. Lillerud, K. P.; Kofstad, P. *Oxid. Met.* **1984**, *21*, 233.
28. Luthra, K. L.; Shores, D. A. *J. Electrochem. Soc.* **1980**, *127*, 2202.
29. Luthra, K. L. *Metall. Trans. A* **1982**, *13*, 1647, 1843, 1853.
30. Luthra, K. L. *J. Electrochem. Soc.* **1985**, *132*, 1293.
31. Zhang, Y. S.; Rapp, R. A. *Corrosion* **1987**, *43*, 384.
32. Spiegel, M. *Mater. Corros.* **1999**, *50*, 373.
33. Spiegel, M. *Mater. Corros.* **2000**, *51*, 303.
34. Edeleanu, C.; Littlewood, R. *Electrochim. Acta* **1960**, *3*, 195.
35. Ishitsuka, T.; Nose, K. *Mater. Corros.* **2000**, *51*, 177.
36. Ruh, A.; Spiegel, M. *Corros. Sci.* **2006**, *48*, 679.

1.16 Types of Environments

B. A. Baker
Special Metals Corporation, 3200 Riverside Drive, Huntington, WV 25705, USA

Abbreviations
AHF Anhydrous hydrofluoric acid
LME Liquid metal embrittlement
MSW Municipal solid waste

1.16.1 Introduction

High temperature corrosion in gaseous environments is commonly interpreted as that taking place above the temperature at which corrosive liquids may condense, causing dew point corrosion. While most high temperature corrosion processes typically take place at quite high temperatures, above about 450 °C, such phenomena can take place at even lower temperatures. For example, formation of pyrosulfates of potassium and sodium can contribute significantly to corrosion rate in coal-fired boiler furnace walls within the temperature range of ~250–350 °C.[1]

While interaction with gaseous environments comprises much of the breadth of knowledge of high temperature corrosion, interdiffusion can occur between high temperature materials and other solids, for example, between a silicon carbide furnace hearth and a furnace belt carrying product through the furnace, or between a graphite sample holder and metallic furnace components. Contact with molten materials may occur, such as interaction between alkali salts of sulfur or halides and metal alloys, which can result in the formation of lower-melting eutectics. Processes governing corrosion resulting from contact with molten salts are analogous to aqueous corrosion processes in that an electrolyte is present; galvanic effects may thus be operable. Lower-melting metals and alloys are another source of possible corrosion.

Laboratory studies have contributed significantly over the years to deepen the knowledge base of high temperature corrosion processes. Prediction of corrosion rates for many high temperature corrosion phenomena may be performed based upon the modeling of the kinetics of governing reactions; predictive software tools have been developed which provide this function for a wide range of high temperature alloys.[2]

Extraneous factors, which may be difficult to simulate in the laboratory, often account for the difficulty in mimicking commercial processes. Such factors include, but are not limited to, pressure, gas velocity, impurities, and mechanical and thermal stress.

Pressure: The effect of pressure upon the mobility of reacting ions through a surface layer such as an oxide is not pronounced. However, if the dissociation pressure of a corrosion product is within the given range of conditions, then pressure may exert a profound effect. The effect of temperature is far more prominent, typically.

Gas velocity: Very high velocity gas streams may promote erosion; this, in conjunction with corrosive species which may be present, can result in accelerated wastage rates via an erosion–corrosion mechanism. Conversely, exposure of materials high in molybdenum or vanadium to stagnant high temperature oxidizing atmospheres can lead to what is termed 'catastrophic oxidation' – molybdenum trioxide, MoO_3, melts

at 795 °C and vanadium pentoxide, V_2O_5, melts at 690 °C. If adequate gas flow is not provided, these oxides do not volatilize and serve to promote additional oxidation.[3,4]

Impurities: Simulation of industrial corrosion environments is frequently very difficult because of the improbability of pinpointing the concentration of various low-level impurities. This often stems from a lack of knowledge about the specific nature of the industrial environment.

Stress: Stress-accelerated grain boundary oxidation has been found to contribute to cracking phenomena in high temperature materials. For example, Soontrapa[5] documented a case occurring in an age-hardenable Fe–Ni material. Interaction between this mechanism and stress-corrosion cracking in simulated primary water at 360 °C, mimicking conditions found in a pressurized water reactor, has been reported by Panter[6]; cracking in austenitic stainless steels at 610 °C has also been attributed to this mechanism.[7]

Thermal cycling can produce stresses sufficient to cause cracking and buckling of corrosion layers, possibly leading to eventual spalling of the corrosion layer completely from the surface. The tendency for this to occur can depend upon the differential expansion coefficients between the oxide and substrate as well as the strength of the oxide itself versus that of the substrate. Subsurface oxides can serve to provide mechanical stability during thermal cycling as well.

1.16.2 Oxidizing Environments

Oxidation is certainly the most important mode of high temperature corrosion. While certain processes do involve simple oxidation by air, such as the external surfaces of electrically heated components, it is more common that oxidizing species are accompanied by other reacting components from the atmosphere. The combustion of natural gas is one very common example, where typically a percentage of excess air is employed, producing a gas which contains primarily O_2, N_2, H_2O, CO_2, and CO. While the majority of the oxidizing potential is provided by O_2 in such an atmosphere, other species may have very meaningful effects upon observed oxidation behavior. For example, water vapor is known to have a significant effect upon ferritic and austenitic stainless steel oxidation behavior, in the formation and volatilization of $CrO_2(OH)_2$.[8–11] In cases where combustion is carried out with a substoichiometric air-to-fuel ratio, the oxygen pressure becomes a function of the pCO/pCO_2 and pH_2/pH_2O ratios. In such 'reducing' combustion atmospheres, oxidation, while occurring concurrently, may not often be the predominant mode of corrosion. For example, if the sulfur level in the combusted fuel is sufficiently high, sulfidation could become the principal mode of corrosion.

Oxidation in pure steam is a significant consideration in the specification of materials for steam superheater tubes and steam header pipes in power generating plants. Recent advances in power plant design have targeted very high steam temperatures up to 760 °C and increased pressure levels in boosting the efficiency of future plants. Oxidation rates of austenitic stainless steels and even nickel-based alloys are concerns under these conditions.[12,13]

Some industrial processes utilize pure oxygen at elevated temperatures; for example, conversion of titanium tetrachloride to titanium oxide. Pure oxygen rather than air can be utilized for combustion of coal and other fuels (oxy-fuel combustion) in the interest of reducing NO_x levels in emissions, and producing a purified CO_2 stream for enhanced utilization or disposal.[14] Reforming processes, which involve combining a hydrocarbon feedstock (typically methane) with steam to produce syngas and ultimately hydrogen, can also utilize oxygen in place of a fraction of supplied steam.

1.16.3 Nitridation

Nitridation can give concurrent results with oxidation in air, or in combustion environments employing air as the oxidizing gas. This is predominant in materials having additional elements such as aluminum, titanium, and niobium – nitrides formed are typically internal – for which nitride formation is particularly thermodynamically favorable. Such nitridation can occur under static conditions, but is more prevalent upon exposure to dynamic loading conditions. Internal nitrides are often found to be associated with the tips of creep cracks formed in air or combustion environments.[15] In nickel-based alloys, the diffusivity of nitrogen is determined to be nearly two orders of magnitude greater than that of oxygen.[16] This explains the observation of internal nitrides extending to greater depths than internal oxides after exposure to such environments.

Nitrogen or cracked ammonia is often used as a protective atmosphere during the heat treatment of stainless steels. Sintering of powder metal components is performed in a nitrogen-based atmosphere.

Purposeful nitridation of the surface of metallic components is frequently carried out to impart strength and wear resistance. Furnace components exposed repeatedly to the same nitriding atmosphere must possess good resistance. Typically, in nitrogen and ammonia-based environments, alloys high in nickel content (having low nitrogen solubility and diffusivity) and low in elements which are strong nitride formers (aluminum, titanium, niobium, chromium) are favored for sustained service. Uncracked ammonia is a particularly harsh nitriding environment. Interaction of the uncracked ammonia with the metal surface results in direct diffusion of nascent nitrogen. Ammonia, which has been dissociated into H_2 and N_2, possesses less nitriding potential compared to pure nitrogen.

A mixture of nitrogen and water vapor is utilized in processes employing the Kalina Cycle. Corrosion effects in such atmospheres have been studied by Grabke.[17] Interestingly, the performance of austenitic stainless steels was found to supersede the performance of nickel-based materials in this specific environment.

1.16.4 Environments Promoting Carbon Ingress

Carburization, a high temperature form of corrosion promoted by carbon ingress and subsequent internal carbide precipitation, may proceed via one of the following reactions resulting in carbon formation:

$$2CO = CO_2 + C \quad [1]$$
$$CO + H_2 = H_2O + C \quad [2]$$
$$CH_4 = 2H_2 + C \quad [3]$$

High temperature carburization in hydrocarbon-based environments is encountered commonly in heat treatment processes. Here again, materials having high nickel content (low carbon solubility and diffusivity) and low levels of strong carbide formers (chromium, titanium, niobium, tungsten, molybdenum) are commonly favored. High levels of aluminum or silicon can enhance the performance in such environments as well, where even very low levels of oxygen may allow the formation of a protective scale.

Environments that are concurrently oxidizing and carburizing allow for a wider range of material usage, if the oxygen pressure is high enough to promote the formation of chromium oxide. For example, Fe–Ni–Cr materials, often having chromium levels at or above 25% and silicon additions, are commonly used as radiant tubes in ethylene-cracking furnaces. Under normal operating conditions, chromium oxide protects the tubes against rapid carburization in the carburizing–oxidizing environment at the ID of the tubes. At very high temperatures, at and above ~1100 °C where chromium oxide is not stable, silicon oxide can afford protection, as shown by Nishiyama.[18] Coke formation also occurs in the ethylene cracking environment. Laboratory testing to truly simulate such an environment would thus need to incorporate an atmosphere for which the carbon activity exceeds unity. Production of carbon fiber products also typically involves exposure to solid carbon deposits at elevated temperatures.

Steam reformers, converting natural gas or other hydrocarbon feed stocks to a gas rich in hydrogen and carbon monoxide, can promote carburization if temperatures exceed the normal 700–850 °C, or if carbon activity becomes excessive in the normally oxidizing gas atmosphere.[19]

Gas carburizing of steels takes place in an endothermic combustion environment with added hydrocarbons. Such atmospheres typically have a carbon activity below unity. Carburization of furnace components such as supporting grates, fans, and radiant furnace tubes is often observed; heat treatment baskets and belts are also affected.

Another form of carburization, termed 'green rot' involves alternating exposure of a nickel-based material having an intermediate chromium level (first encountered with 80% Ni–20% Cr heating element materials) to a nonoxidizing (reducing) carburizing atmosphere followed by an environment containing sufficient oxygen to oxidize chromium. Internal carbides formed during the reducing cycle are subsequently preferentially oxidized upon exposure to the oxidizing environment. This phenomenon has been combated by the use of nickel-based materials having higher Cr levels, or niobium addition.

Carbon dioxide cooled nuclear reactors, which operate at temperatures lower than the helium-cooled variant, can experience carburization of components, despite the fact that the CO_2 environment is oxidizing and has low carbon activity. This occurs at the oxide scale–metal interface if CO_2 penetrates the scale.[19] Numerous reactors employing CO_2 cooling are in operation in the United Kingdom.

Carburization can occur in coal combustion and coal gasification processes, despite the fact that the prevailing form of attack is typically sulfidation, often via contact with incompletely combusted carbonaceous material at elevated temperatures.

Metal dusting is a form of carburization which occurs when carbon activity exceeds unity at intermediate temperatures, ~400–800 °C. The most frequently encountered occurrence of this phenomenon is seen in processes which form syngas via the combination of steam and hydrocarbon feedstock (reforming) at high temperature (750–850 °C). The resulting syngas mixture contains H_2, CO, CO_2, and H_2O as well as residual CH_4 and other hydrocarbons. Industrial processes involving syngas production include production of hydrogen, fertilizers, and synthetic fuels as well as gasification of various feedstocks including coal and biomass. Typically, higher ratios of pCO/pCO_2 and pH_2/pH_2O produce higher calculated carbon activity and consequently higher propensity for metal dusting. Carbon activity, by virtue of reactions [1] and [2], rises as temperature is lowered; at some point as temperature drops, sluggish kinetics result in decreased metal dusting activity. Nickel-based alloys having high levels of oxide scale forming elements, chromium and aluminum, and low iron content tend to exhibit the most favorable performance in these environments. Environments with very high CO levels encountered in iron ore reduction promote metal dusting as well. Metal dusting corrosion is also encountered occasionally in the heat treating industry. Petroleum refineries experience metal dusting in hydrodealkylation processes and catalyst regeneration systems. Nuclear plants employing CO_2 for cooling can experience metal dusting as well. Metal dusting can occur in molten carbonate and solid oxide fuel cells. Exposure in hydrocarbon-based environments can also result in metal dusting attack.[20]

Incorporation of even ppm levels of H_2S into environments, known to promote metal dusting, has been found to suppress the phenomenon.[20,21]

1.16.5 Environments Containing Halides

Chlorine and hydrogen chloride are found in numerous industrial processes. Concentrations, which may have an impact upon high temperature corrosion behavior, range from ppm levels to pure gas streams. Other gaseous components can have an effect on material performance; environments which contain oxygen and/or water vapor can accelerate corrosion behavior for some materials.

Municipal solid waste (MSW) combusted to produce electrical power typically contains sufficient chloride-containing plastic materials (primarily PVC) to promote a severe form of corrosion on the fireside wall of waterwall and superheater tubing. Metal temperatures range typically from 400 to 650 °C. Deposition of alkali chlorides (often containing heavy metals such as lead and zinc), which may be molten or partially molten, onto metal surfaces results in the formation of metal chlorides. In addition, the flue gas contains HCl vapor. The HCl vapor can react with oxygen in the oxidizing combustion environment to form chlorine gas, according to the following equation:

$$2HCl + \frac{1}{2}O_2 = Cl_2 + H_2O \qquad [4]$$

Volatilized metal chlorides, formed via interaction with the generated chlorine, may react with oxygen in the flue gas to form additional chlorine, creating a self-sustaining mechanism:

$$FeCl_2 + 2\ CrCl_2 + 2O_2 = FeCr_2O_4 + 3Cl_2 \qquad [5]$$

Vapor pressures for various metal chlorides as a function of temperature are shown in **Figure 1**.[22]

Typical MSW combustion gas also contains SO_2; residual levels of HCl in the gas commonly range from 400 to 600 ppm, whereas SO_2 levels are typically in the range of 100–200 ppm. It is generally agreed that the mechanism of corrosion in MSW boilers is related primarily to the presence of chlorine-containing species. To combat this form of corrosion, metallic coatings are typically applied via weld overlay or thermal spray onto the fireside tube surface. These materials are typically Ni–Cr–Mo alloy systems. At temperatures above 800 °C in oxidizing–chloridizing atmospheres, the high vapor pressure of molybdenum oxychlorides makes molybdenum-containing materials a less desirable choice.[23] At such high temperatures, Ni–Cr–Al materials typically exhibit better performance.

Combustion of biomass in boilers can have a mechanism of corrosion in waterwalls and superheaters similar to that seen in MSW boilers. Wood and straw products, for example, contain significant levels of potassium and chlorine, producing KCl in the gas phase. Condensation on cooler metal surfaces from the gas phase in turn can create more complex alkali salts with alloying elements from the metal substrate. As in MSW boilers, metallic coatings are typically applied by weld overlay, thermal spray, etc. Materials utilized to combat the intermediate-temperature form of chloride salt attack are also typically Ni–Cr–Mo alloy systems.

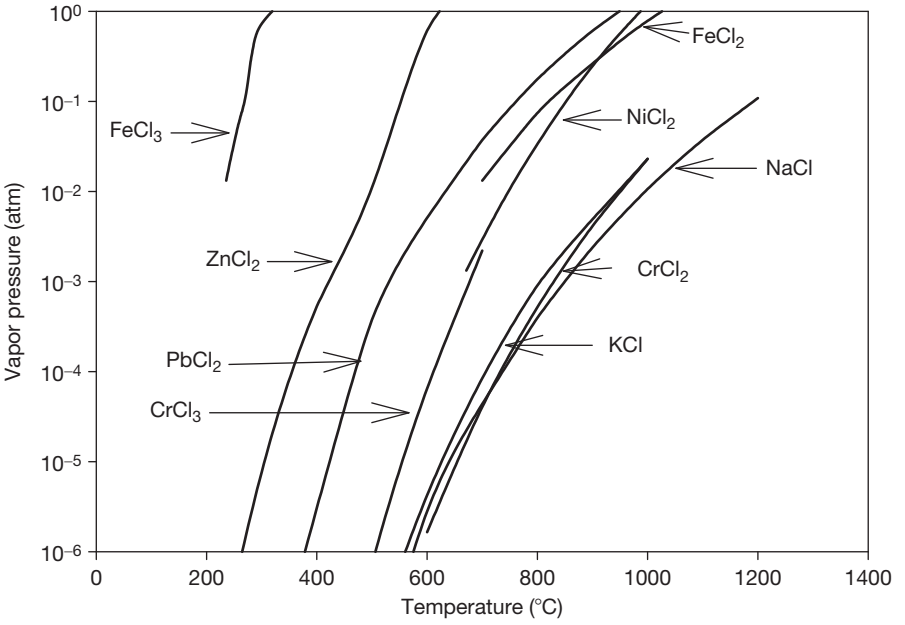

Figure 1 Vapor pressure versus temperature for metal chlorides.

Production of ethylene dichloride, an intermediate of vinyl chloride monomer, involves creation of chlorine-bearing high temperature environments.

Production of titanium and silicon dioxides involves oxidation of a chloride precursor at high temperature.

Formation of metal chlorides from ores is a common step in metals production, capitalizing upon the very high vapor pressure of many metal chlorides.

Chemical vapor deposition processes may incorporate the utilization of high temperature HCl vapor.

Certain coals can contain low levels of chlorine, which can exacerbate coal ash corrosion effects in boiler tubing and superheater tubing.[24] Chloride layers have been discovered at the scale-to-metal interface in exposed tubes. Even a very modest quantity of chlorine at high temperatures can evoke severe corrosion effects because of the previously described self-perpetuating mechanism.

Fluorine can promote very severe forms of corrosion as well. Anhydrous hydrofluoric acid (AHF) is used in the alkylation catalysis for gasoline manufacture and for the manufacture of chlorofluorocarbon refrigerants and propellants. Uranium oxide is fluorinated at high temperatures with hydrofluoric acid to produce HF_6. Centrifuging then typically follows for the separation of HF_6 containing U235 from that incorporating U238. Production of modern refrigerants involves elevated-temperature exposure to chlorine- and fluorine-containing environments.

Bromine and iodine have similar effects, though less severe than those of chlorine or fluorine.

1.16.6 Sulfur-Containing Environments

Sulfidation occurs in a variety of forms and environments, and can result from a number of different sulfur-containing species. Exposure to H_2–H_2S gas mixtures in refining environments is a classical form of sulfidation. Exposure of nickel-containing materials in such an environment above the Ni–NiS eutectic melting temperature (~645 °C) can have catastrophic results. However, at lower temperatures, nickel-based materials can provide very good performance. Attack rate is dependent simply on the partial pressure of sulfur, determined by the pH_2/pH_2S ratio. These conditions are encountered in petroleum refining in hydrotreating, hydrocracking, and hydrodesulfurising processes.

Environments containing significant partial pressures of both sulfur and oxygen are termed sulfidizing-oxidizing; this is typical of most sulfur-containing environments. Corrosion behavior is dictated by both the oxygen and sulfur partial pressures. Again, in general, high nickel alloys are not desired for such environments; however, with sufficient levels of scale-forming elements such as chromium or aluminum, protection can be afforded. An example of such an environment

would be that produced by the combustion of natural gas containing significant levels of H_2S. Commercial food preparation operations involving meat products can produce sulfidation–oxidation in oven components by virtue of the sulfur present in the disulfide bonds of proteins. Oil-fired boilers commonly burn low-grade fuel containing significant sulfur levels.

1.16.6.1 Coal-Fired Boiler Corrosion

The sulfur content of coal used for energy generation can be as high as 5% or more, producing combustion gases containing H_2S, SO_2, and SO_3 and resulting in the deposition of flue ash containing alkali sulfate salts onto metal surfaces cooler than the gas (furnace walls, superheaters and reheaters). These salts may react with SO_2 or SO_3 to form pyrosulfates or more complex alkali–iron trisulfates. Low-melting combinations of the various species may be formed. For example, potassium sulfate (K_2SO_4) and potassium pyrosulfate ($K_2S_2O_7$) form a molten salt mixture at 407 °C when the SO_3 concentration is 150 ppm. The mode of sulfidation promoted by deposits containing such salt mixtures is commonly termed 'coal-ash corrosion.'

While the sulfidizing–oxidizing environments noted so far are typically strongly oxidizing in nature, certain environments exhibit a higher ratio of sulfur pressure to oxygen pressure. These types of environments are generated by combustion under significantly substoichiometric conditions. Typically, oxides afford protection to the point where breakaway corrosion initiates, followed by significant sulfidation attack. Coal gasification processes typify this type of environment. Low-NO_x burners in coal combustion operate under conditions which produce a reducing environment in the vicinity of the burners, with metal temperatures possibly as high as 600 °C. This can result in the presence of H_2S rather than SO_2 in the combustion gas. High wastage rates of waterwall tubes in such boilers can result. Weld overlays are applied to combat corrosion; Ni–Cr–Mo welding products are commonly utilized. Thermal spray coatings and chromium/chromium–silicon coatings are also often utilized.

Blowing deposits from superheaters and reheaters using steam soot blowers is commonly employed, which promotes a form of erosion–corrosion. Water lances or water canons may be used to remove slag deposits from waterwalls via thermal shock. This can contribute to circumferential cracking by a mechanism involving corrosion-assisted thermal fatigue.

Steam superheaters and reheaters in coal-fired boilers are subject to severe coal-ash corrosion problems as well, because of deposition of combustion ash containing sulfate salts. Temperatures are significantly higher than that at the waterwall surface. Such conditions often necessitate not only high-strength austenitic materials for tubing, but also consideration of protective claddings. Nickel–chromium materials have been found to perform well; tubes clad with a 50Ni–50Cr material are often utilized.

Recent interest in developing the technology required for the construction and operation of coal-fired plants having steam temperatures of up to 760 °C has necessitated consideration of a different class of materials. Elevating the operating temperature of the waterwall and superheaters will have an effect upon coal-ash corrosion dynamics. One recent study by McDonald involved insertion of a test loop into the low-NO_x boiler burning Ohio coal containing 3% sulfur, in the interest of simulating conditions in a superheater operating at temperatures higher than conventional; at 1050–1210 °F.[25] Results indicated that the conditions were harsh for many materials and that, tubes weld-overlaid or clad with Ni–Cr materials having very high Cr levels exhibited the most favorable performance.

1.16.6.2 Oil-Fired Boiler Corrosion

Fuel oils consisting of residuals from petroleum refining cause oil-ash corrosion in boilers. Compounds formed from residual vanadium, sulfur, and sodium account for this mode of corrosion. Vanadium forms V_2O_5; similarly, sodium forms sodium oxide (Na_2O) or sodium sulfate (Na_2SO_4). These compounds can combine to form fused salts that can have very low melting temperatures.[26] The resulting molten vanadate compounds cause fluxing of otherwise protective oxide scales, promoting very aggressive corrosion attack and metal wastage. The concentration of SO_3 in the flue gas exerts significant influence upon the stability of the fused vanadate salts, as discussed by Seiersten and Kofstad.[27] As in coal-fired boilers, Ni–Cr overlay coatings are commonly applied over the ferritic or austenitic steels used in steam superheaters and reheaters in the interest of optimizing corrosion resistance.

The mode of corrosion resulting from exposure to deposited sulfate is termed 'Type I' hot corrosion in gas turbines, whereby sulfur-containing salts become molten, resulting in dissolution of protective oxides, and resultant ingress of sulfur and formation of internal sulfides. Type I hot corrosion occurs typically in the temperature range of 850–950 °C, and primarily

in aerospace applications. Coatings are normally used for protection of metallic components against this mode of corrosion; for example nickel- and cobalt-based MCrAlY systems have been used with success. Cobalt-based coatings offer particularly good resistance to Type I hot corrosion. Type II hot corrosion, also resulting from sulfate salt deposition, typically occurs at temperatures below 800 °C. This form of hot corrosion results from localized formation of low-melting eutectics, resulting in localized pitting with the absence of gross sulfide formation, and is more commonly encountered in land-based and marine gas turbine applications. Typically, cobalt-based coatings are not as resistant to Type II hot corrosion as nickel-based coatings.

1.16.7 Molten Metals

Liquid metals are often considered for use as heat transfer media, because of their attractive physical properties – high thermal conductivity and heat capacity. Also, their operating pressures are very low compared to water. Lead, lead–bismuth, and sodium have all been considered as coolants for nuclear reactors. Sodium metal is used to fill hollow high-performance engine valve stems, in the interest of transmitting heat along the valve stem and to the cooling jacket. The properties of molten potassium make it suitable as the working fluid for a two-phase Rankine cycle, enabling operation at temperatures higher than that for typical steam-based systems.[28]

Solar Stirling engines have employed the use of sodium as the working fluid as well. The range of heat capacities and boiling points for the various metals used for heat transfer applications serve to dictate the range for the use. For example, lead is useful up to 500 °C, sodium 700 °C, and lithium 1300 °C.[29]

Molten aluminum is an extremely harsh environment for all types of metals and alloys.

Molten zinc is commonly used in the hot-dip galvanizing process for coating steel for corrosion resistance enhancement. Galvanizing tanks and handling accessories require resistance.

When under stress, metals may become susceptible to liquid metal embrittlement (LME). Instances of LME are often associated with welding, brazing, or soldering.

1.16.8 Molten Salts

Molten-salt technology is critical for several industries.[30] As with molten metals, molten salts are utilized in nuclear and solar energy systems as a medium for heat transfer and storage because of high thermal conductivity and heat capacity. A mixture of sodium and potassium nitrates has been used for energy storage in solar collectors.

Extraction of aluminum is performed by dissolving alumina in cryolite. Extraction of various reactive metals, such as titanium, magnesium, sodium and others is accomplished using molten salts, often chlorides.

Molten salt batteries use molten salts as an electrolyte. They are used in services where very high power density is required. These characteristics make such batteries a promising technology for powering electric vehicles. Operating temperatures as high as 700 °C, however, pose significant challenges.

Molten carbonate fuel cells are currently being developed for natural gas and coal-based power plant applications, as well as other industrial and military applications. These fuel cells do not require an external reformer to produce hydrogen. Instead, fuels are converted to hydrogen within the fuel cell itself.

Molten salts are used frequently in the heat treating industry for case hardening, annealing and stress relieving, quenching and tempering, as well as cleaning. As corrosion rate in molten salts is typically a form of oxidation, attack is commonly exacerbated at the salt-to-air interface.

In the chemical industry, molten salts are used for cracking and catalysis, curing and vulcanizing plastics, synthesis of organics and gases, and in pyrolysis of scrap and hazardous materials.

References

1. Reid, W. T. *External Corrosion and Deposits*; American Elsevier: New York, 1971.
2. John, R. C., *et al. Mater. Sci. Forum* **2004**, *461–464*, 599–610.
3. Meijering, J. K.; Rathenau, G. W. *Nature* **1950**, *165*, 240.
4. Brennor, S. S. *J. Electrochem. Soc.* **1955**, *102*(1), 16.
5. Soontrapa, C. Master's Thesis, Massachusetts Institute of Technology, 2005.
6. Panter, J.; Viguer, B.; Cloué, J. M.; Foucault, M.; Combrade, P.; Andrieu, E. *J. Nucl. Mater.* **2006**, *348*(1–2), 213–221.
7. Le Calvar, M.; Scott, P. M.; Magnin, T.; Rieux, P. *Corrosion* **1998**, *54*(2), 101–105.
8. Asteman, H.; Svensson, J. E.; Johansson, L. G.; Norell, M. *Oxid. Met.* **2000**, *54*(1–2), 11–26.
9. Young, D.; Pint, B. *Oxid. Met.* **2006**, *66*(3–4), 137–153.
10. Peraldi, R.; Pint, B. A. *Oxid. Met.* **2004**, *61*(5–6), 463–483.
11. Rakowski, J. M. *J. Eng. Gas Turbines Power* **2004**, *126*(4), 768–873.

12. Program on Technology Innovation. Oxide Growth and Exfoliation on Alloys Exposed to Steam EPRI, Palo Alto, CA, 2007; 1013666.
13. Holcomb, G. R. *Oxid. Met.* **2008**, *69*(3–4), 163–180.
14. Natesan, K.; Rink, D. L. In Proceedings of the 21st Annual Conference on Fossil Energy Materials, Oak Ridge National Laboratory/U.S. Department of Energy, April 30 to May 2, 2007.
15. Welker, M.; Rahmel, A.; Schütze, M. *Metall. Trans. A* **1989**, *20A*, 1541–1551.
16. Douglass, D. L. *JOM*; **1991**, *74.*
17. Grabke, H. J.; Strauss, S.; Vogel, D. *Mater. Corros.* **2003**, *54*(11), 895.
18. Nishiyama, Y.; Otsuka, N.; Nishizawa, T. *Corrosion* **2003**, *59*(8), 689–700.
19. Grabke, H. J. *Carburisation – A High Temperature Corrosion Phenomenon*; Materials Technology Institute of the Chemical Process Industries: St. Louis, MO, 1998.
20. Grabke, H. J. In *European Corrosion Congress, Eurocorr'99*; Aachen, September 1999.
21. Grabke, H. J.; Müller-Lorenz, A.; Schneider, A. *ISIJ Int.* **2001**, *41*(Supplement), S1–S8.
22. Brandes, E. A.; Brook, G. B. Eds. *Smithells Metals Reference Book*; Butterworth-Heinemann: Oxford, 1992.
23. Oh, J. M.; McNallan, M. J.; Lai, G. Y. *Metall. Trans. A* **1986**, *17A*, 1087–1094.
24. Effect of Coal Chlorine on Waterwall Wastage in Coal-Fired Boilers with Staged Low NOx Combustion Systems, EPRI, Palo Alto, CA; American Corporation, St. Louis, MO; Dairyland Power Cooperative, La Crosse, WI, 2002, 1004082.
25. McDonald, D. K. Coal Ash Corrosion Resistant Materials Testing Program Evaluation of the First Section Removed in November 2001, The Babcock and Wilcox Company, submitted to DOE (DE-FC26-99FT40525) and OCDO (CDO/D-98-2).
26. Reid, W. T. *External Corrosion Deposits in Boilers and Gas Turbines*; Elsevier: Amsterdam, 1971.
27. Siersten, M., Kofstad, P. *High Temp. Technol.* **1987**, *5*(3), 115.
28. Radovanovic, M. *Fluidized Bed Combustion;* Taylor & Francis: London, 1986; 267.
29. Baboian, R. *Corrosion Tests and Standards: Application and Interpretation*, 2nd ed.; ASTM International: West Conshohocken, PA, 2005.
30. Lovering, D. G. Ed. *Molten Salt Technology*; Plenum Press: New York, 1982; 1.

1.18 Fireside Corrosion

N. Otsuka
Corporate R&D Laboratories, Sumitomo Metal Industries, Ltd., 1-8 Fusocho, Amagasaki, Japan

Glossary

Acidic dissolution (of metal oxides) A dissolution reaction to form acidic solutes such as $Fe_2(SO_4)_3$, $NiSO_4$, $Cr_2(SO_4)_3$. See basic dissolution.

Basic dissolution (of metal oxides) A dissolution reaction to form basic solutes such as $NaFeO_2$, $NaNiO_2$, Na_2CrO_4. See acidic dissolution.

Basicity (of fused sodium sulfate) Defined as $-\log a_{Na_2O}$. The basicity of sodium sulfate is affected by the SO_3 concentration of the ambient gas atmosphere.

Biomass Plant matter grown for use as a biofuel. Biomass is grown from several plants, including swichgrass, hemp, corn, willow, and sugarcane. Chips of wood are also included.

Bitumen A mixture of organic liquids that are highly viscous, black, sticky, entirely soluble in carbon disulfide, and composed primarily of highly condensed polycyclic aromatic hydrocarbons.

Bituminous coal A relatively hard coal containing a tar-like substance called bitumen. It is of higher quality than lignite coal but of poorer quality than anthracite coal.

Black liquor A solvent of the cooking process for Kraft pulping. Black liquor is rich in sodium and organic portions such as lignin and hemicelluloses. It is fired in boilers to obtain heat and to recover sodium as sodium sulfide and sulfates from it.

Borio index An index obtainable from coal chemistry. This index is used to estimate the relative severity of high-S coal regarding the fireside corrosion of metal components.

Catastrophic oxidation See hot corrosion.

Fireside corrosion A type of corrosion encountered for high temperature metal components exposed to hot combustion gases.

Fluxing of oxide scale A reaction that takes place when protective oxide scales form on high temperature steels and alloys come in contact with molten salts. Protective metal oxides dissolve in molten salts and lose their protection against corrosive environments.

High temperature hot corrosion (HTHC) See Type I hot corrosion.

Hot corrosion An accelerated (or catastrophic) oxidation of metals and alloys whose surface is coated with fused salt and/or corrosive slag films in high temperature gaseous environments.

Kinetic boundary (of Cr_2O_3 protection) A boundary shown in the P_{O_2}–P_{S_2} phase stability diagram of chromium which

separates the regime of the uniform formation of protective Cr_2O_3 scale from that of the formation of fast-growing Cr/Fe sulfide scale on high temperature stainless steels and alloys.

Lignite coal Often referred to as brown coal, which is the lowest rank of coal and used almost exclusively as fuel for steam-electric power generation. It is brownish-black and has a high inherent moisture content, sometimes as high as 66%, and very high ash content compared to bituminous coal. It is also a heterogeneous mixture of compounds for which no single structural formula will suffice.

Low-temperature hot corrosion (LTHC) See Type II hot corrosion.

Naphtha A group of various liquid hydrocarbon intermediate-oil-refining products used primarily as feedstock for producing a high-octane gasoline component via the catalytic reforming process. Naphtha is also used in the petrochemical industry for producing olefins in steam crackers and in the chemical industry for solvent applications.

Oil ash corrosion See vanadium attack.

Orimulsion A new type of fossil fuel coming from vast reserves of bitumen in the Orinoco Belt in Venezuela. This fuel is dispersed by water in a condition of emulsion.

Oxidizing gas A gas atmosphere containing oxidizing gas species such as O_2, CO_2, SO_x, and H_2O. Generally, oxidation of steels and alloys takes place upon exposure to this environment.

Reheater A heat exchanger made of steel tubes which are used in steam generating boilers to reheat steam coming from a steam turbine in order to be used again in a steam turbine. Their metal temperature is among the highest in boiler tubes, and they are prone to fireside corrosion.

Reducing gas A gas atmosphere containing reducing gas species such as H_2, CO, and hydrocarbon (CH_4, etc). For some combustion gases where sulfur-bearing gas species such as H_2S are included, sulfidation (see sulfidation below) may take place for steels and alloys upon exposure to this gas atmosphere.

Salt-fluxing model A corrosion mechanism based on the destructive dissolution of originally protective metal oxide scale into thin fused salt film, followed by reprecipitation of these metal oxides as thick, porous, nonprotective reaction products.

Sulfidation A type of corrosion caused by reaction of metal and alloys with sulfur-bearing species such as gaseous hydrogen sulfide or liquid alkali sulfates. The major reaction products are metal sulfides.

Superheater A heat exchanger made of steel tubes which are used in steam generating boilers in order to raise the temperature and pressure of steam (to superheat) to be used in steam turbines. Their metal temperature is among the highest in boiler tubes, and they are prone to fireside corrosion.

Syngas (or synthetic gas) A gas mixture containing CO and H_2. Syngas is used as a fuel gas for combustion or as a raw material to obtain ammonia, methanol, and hydrogen.

Type I (or high temperature) hot corrosion Occurs at a relatively high temperature (900–1000 °C) at which pure Na_2SO_4 (melting point 884 °C) is liquid.

Type II (or low-temperature) hot corrosion Occurs at 600–750 °C, well below the melting point of pure sodium sulfate (884 °C). This corrosion results from the reaction of protective oxide scale with liquid phase of sodium and potassium complex metal sulfates.

Vanadium attack A type of corrosion caused by the reaction of molten vanadate compounds with protective metal oxide scales. The major degradation reaction is the dissolution of the protective metal oxide scales into molten oxides, and fast transport of the dissolved oxygen in molten oxide layer from flue gas to metal surface supports the corrosion reaction.

Abbreviations

BLRB Black liquor recovery boiler
HTHC High temperature hot corrosion
LTHC Low temperature hot corrosion
MSW Municipal solid waste
ppm parts per million
PVC Polyvinyl chloride plastic

Symbols

k_p Parabolic rate constant ($cm^2\ s^{-1}$)
$-\log a_{Na_2O}$ Basicity of melt
P_{O_2} Oxygen partial pressure (atm)
P_{S_2} Sulfur partial pressure (atm)

1.18.1 Introduction

Fireside corrosion is often encountered in metal components of energy-converting systems which are aimed at generating steam and electricity upon combusting fossil fuel such as coal and oil, biomass, municipal and industrial solid waste. Turbine blades and vanes, boiler tubes and plate-fin type heat-exchangers, hangers and tube supports, etc., which are exposed to hot combustion gases, are the major concerns. Corrosion is normally influenced by the type of fuel, combustion conditions, and design factors of respective system. In this chapter, fireside corrosion is explained from the point of fuel chemistry, and the effect of combustion conditions and design factors on corrosion is emphasized. Corrosion resistance of steels and alloys is introduced as well.

1.18.1.1 Fuel Chemistry

Examples of elemental analyses of major fuels used for generating electricity are shown in Table 1. Fuels consist of combustible elements such as carbon and hydrogen, with slight addition of impurities such as nitrogen, sulfur, and chlorine. In this table, municipal solid waste (MSW) burnt in waste incinerators and black liquor fired in Kraft pulping mill are shown for comparison. From the point of fireside corrosion, vanadium, sulfur, and chlorine in fuel are the important impurity elements.[1] Alkali metals

Table 1 Elemental analyses of major fuel (wt.%, example)

Element	*Heavy oil*	*Coal*	*Natural gas*[a]	*Municipal solid waste*[b]	*Black liquor*[c]
Ultimate					
C	85	76.2	76.5	22	28.4
H	12	5.13	23.5	8.7	5.2
O	0.35	6.15	–	60.4	44.3
N	0.2	1.63	–	0.3	–
S	2.4	1.73	–	0.02	2.7
Cl	–	0.275	–	0.4	3.0
Ash	0.05	8.89	–	8.18	–
Metals					
Fe	–	1.1	–	0.2	–
V	0.01	–	–	–	–
Ca	–	0.1	–	0.9	–
Mg	–	0.04	–	0.1	–
Na	50 ppm	0.03	–	0.06	13.0
K	50 ppm	0.03	–	0.04	3.4
Zn	–	–	–	70 ppm	–
Pb	–	–	–	10 ppm	–
Heat value[d]	10 400	7509	10 800	2440	3700

[a]Liquified natural gas (LNG): CH_4–6% C_2H_6–4% C_3H_8–2% C_4H_{10}.
[b]51 wt.% water involved.
[c]For closed cycle, $S/Na_2 = 0.3$, 20% water involved.
[d]$kcal\ kg^{-1}$, high-heat value.
Source
Heavy oil: Thermal and Nuclear Power Engineering Society, *The Thermal and Nuclear Power*, **1988**, *39*, 1453–1485.
Coal: Blough, J. L.; Stanko, G. J. In *Fireside Corrosion testing of Candidate Superheater Tube Alloys, Coatings, and Claddings-Phase II*, Corrosion/97, NACE International: Houston, TX, 1997; Paper no. 140.
MSW: Otsuka, N. In *Thermodynamic Equilibrium Calculations of Deposits on Superheater Tubes in Waste Incinerators*, Corrosion/2000; NACE International: Houston, TX, 2000; Paper 00229.
Black Liquor: Pejryd, L.; Hupa, M. In *Bed and Furnace Gas Composition in Recovery Boilers-Advanced Equilibrium Calculations*, Proceedings of TAPPI Pulping Conference, 1984; pp 579–590.
Reproduced from Otsuka, N. *Corr. Sci.* **2002**, *44*, 265–283.

sodium and potassium, along with alkali earth metals calcium and magnesium, relate to corrosion as well. In the case of oils used in utility and industrial boilers, various types of oils such as crude oil, heavy oil, light oil, and naphtha, or mixtures of these are combusted. Similarly, with respect to coals, lignite , bituminous , anthracite coals, etc. with varying sulfur and chlorine contents, are fired. Therefore, a large variety does exist in the fuel chemistry. For most of the oils fired in boilers, vanadium is included typically from 0 to as high as 300 ppm[1] (parts per million by weight). Sulfur content ranges from 0.1 to 3.2 wt%[2], and sodium and potassium, from 0 to 100 ppm.[1] Sulfur concentration generally correlates with vanadium content; high-sulfur oil contains high concentration of vanadium.[2] Chlorine content of oil is in most cases low, up to 100 ppm.[3] For fuel coal, sulfur and chlorine are the significant impurities relevant to corrosion. Similar to oil, their composition varies depending on their origin and how they are blended. Sulfur is generally present from less than 0.5% to 3% (in extreme cases up to 7%),[1] while chlorine, from less than 0.01% to as much as 0.8%.[1] Fuel coal contains sodium from 0 to 700 ppm while potassium from 0 to 2500 ppm.[4] Vanadium content of coal is generally negligible. In contrast, natural gas does not virtually contain impure elements of vanadium, sulfur, and chlorine. This is considered one major reason why fireside corrosion in gas-fired boilers and turbines is slight. For municipal solid waste (MSW), almost half of their weight is water, and they contain chlorine in the order of 1000 ppm. The sources of chlorine are inorganic, primarily as NaCl and organic such as polyvinyl chloride plastic (PVC). Note that sulfur concentration of waste is minor. Heavy metals such as lead and zinc in waste are noticed as well. Black liquor is a solvent of cooking process for Kraft pulping and is rich in sodium with organic portion such as lignin and hemicelluloses. This fuel, burnt in boilers to recover sodium and heat, contains large amounts of sulfur and chlorine. Ranges of chlorine and sulfur contents of various fuels are illustrated in **Figure 1**. From the point of chlorine and sulfur concentrations, coal and black liquor are categorized as high-chlorine high-sulfur fuel, oil as high-sulfur low-chlorine fuel, municipal solid waste as high-chlorine low-sulfur fuel, and natural gas as low-chlorine low-sulfur fuel. According to the literature,[5] biomass fuel can be categorized as low-sulfur medium-chlorine fuel, since their sulfur content ranges from 0.02% to 0.1%, whereas chlorine, from 0.01% to just below 1%.

1.18.1.2 Flue Gas Composition

Examples of flue gas composition in boilers firing various types of fuels are presented in **Table 2**. These values may vary depending on the location of boilers, combustion conditions such as air–fuel ratio as described in the following section, and the degree of combustion reactions proceeding toward the final thermodynamic equilibrium conditions. Note that the flue gas of heavy oil contains SO_2 of the order of 0.1%; that of coal has similar SO_2 concentration with slight HCl; those of natural gas and black liquor are virtually free of SO_2 and HCl; and that of municipal solid waste contains HCl of the order of 0.1% with traces of SO_2.

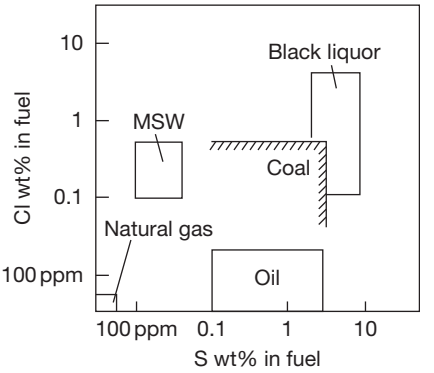

Figure 1 Chlorine and sulfur contents of major fuels.

Table 2 Flue gas composition for complete combustion (vol.%, example)

	Heavy oil	*Coal*	*Natural gas*	*Municipal solid waste*	*Black liquor*
O_2	3	4.2	3.3	9.0	1.2
CO_2	14.5	13.6	9.1	10.9	14.2
H_2O	10.5	5.5	16.7	19.5	16.8
SO_2	0.1	0.12	–	19 ppm	–
HCl	–	0.02	–	0.11	4 ppm

Data taken from
Heavy Oil: Thermal and Nuclear Power Engineering Society, *Therm. Nucl. Power* **1988**, *39*, 1453–1485.
Coal: Calculated for the coal in **Table 1** for air–fuel ratio of 13 in weight at 1300 °C.
Natural gas: Calculated for the natural gas in **Table 1** for air–fuel ratio of 20 in weight.
MSW: Kawahara, Y.; Hagiwara, H.; Nakamura, M.; Shibuya, E; Yukawa, K. In *An Evaluation of Corrosion Resistant Alloys by Field Corrosion Test in Japanese Refuse Incineration Plants*, CORROSION/95; NACE International: Houston, TX, 1995; Paper no. 564.
Black Liquor: Calculated for the black liquor in **Table 1** for air–fuel ratio of 3.77 in weight at 1000 °C.

1.18.1.3 Combustion Conditions

Flue gas composition is significantly affected by the combustion conditions. Concentration of gaseous species upon firing 1.7% S coal (chemical composition is given in Table 1) was calculated at 1300 °C, assuming thermal equilibrium, and presented in Figure 2 as a function of air–fuel ratio. In this chapter, air–fuel ratio is defined by the ratio of their weights; air–fuel ratio of 10 represents combustion of 100 g fuel with 1000 g air. Where combustion takes place in complete or in air-excess conditions such as for the air–fuel ratio of more than 10, oxidizing gas species such as O_2, SO_2, and NO prevail. Complete combustion is termed here when carbon and hydrogen in fuel is totally oxidized to carbon dioxide and water vapor, and no additional oxygen is present in the flue gases. This corresponds to air–fuel ratio of 10 in Figure 2. In contrast, when combustion reactions proceed in air-deficient conditions where air–fuel ratio is less than 10, reducing gas species such as CO, H_2, and H_2S replace the oxidizing gas species of O_2, SO_2, and NO. This is termed the partial combustion. Concentration of CO_2 and H_2O is not significantly affected by the air–fuel ratio. Carbon dioxide and water vapor can coexist with oxidizing gas species of O_2 and SO_2 and reducing gas species of CO and H_2. Normally, from the point of combustion efficiency, fuel is fired in slightly air-excess conditions. Therefore, except at locations where equilibrium is not established, flue gas generally oxidizes the metal components. Partial combustion is encountered for gasification process of coal and residual oil. For these cases, flue gas, called synthetic gas (syngas) in some cases, is generally reducing, and contains gaseous H_2S, resulting from sulfur in fuel. For some industrial boilers, slightly air-deficient combustion is favored at their furnaces, in order to minimize formation of gaseous nitrogen oxides. Gaseous H_2S exists in the flue gases locally. Oxygen and sulfur partial pressures of these combustion gases are calculated as a function of air–fuel ratio at 1300 °C and presented in Table 3. As expected, low P_{O_2}-high P_{S_2} gas atmospheres are indicated upon combustion at low air–fuel ratio, whereas high P_{O_2}–low P_{S_2} gas atmospheres are characterized for combustion at high air–fuel ratio. Therefore, from the equilibrium point of view, corrosion environments for air-excess combustion are categorized as 'oxidizing,' while that for partial combustion as 'sulfidizing' when fuel contains considerable amounts of sulfur. The effect of temperature on flue gas composition upon combusting 1.7% S coal is basically minor for conditions of air-excess combustion (Table 4 for air–fuel ratio of 12), but slight changes are noticed for conditions of partial combustion (Table 5 for air–fuel ratio of 6).

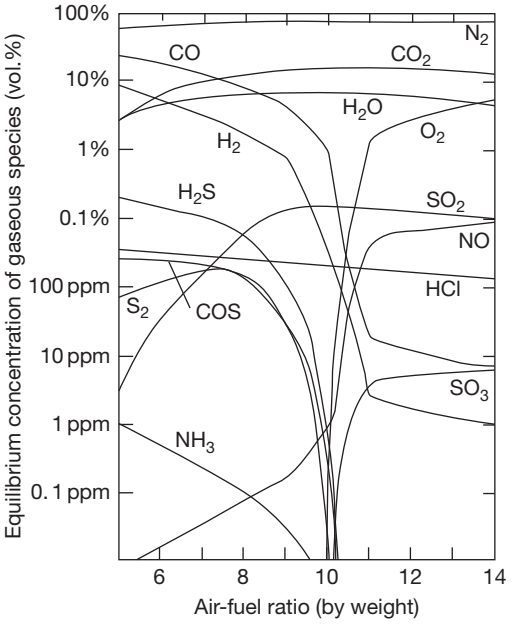

Figure 2 Equilibrium concentration of gaseous species in flue gas upon combustion of 1.7% S coal at 1300 °C. Calculated based on the coal chemistry presented in Table 1. Air–fuel ratio is given by weight; for example, air–fuel ratio of 10 represents combustion of 100 g coal with 1000 g air.

1.18.1.4 Deposit Chemistry

Fireside corrosion of metal components is significantly affected, in many cases, by the chemical and physical properties of deposits piled up on metal surface from flue gas. Usually, chemical and physical properties of these deposits vary drastically,

Table 3 Equilibrium oxygen partial pressure P_{O_2} and sulfur partial pressure P_{S_2} of flue gases upon combustion of 1.7% S coal as a function of air–fuel ratio at 1300 °C (calculated)

Air–fuel ratio	P_{O_2}	P_{S_2}
5	3×10^{-12}	8×10^{-5}
6	2×10^{-11}	1×10^{-4}
7	8×10^{-11}	2×10^{-4}
8	3×10^{-10}	2×10^{-4}
9	2×10^{-9}	3×10^{-5}
10	5×10^{-8}	4×10^{-8}
11	0.01	4×10^{-19}
12	0.03	8×10^{-20}
13	0.04	3×10^{-20}

Coal composition is taken from Table 1. Air-fuel ratio is defined by weight; for example, air-fuel ratio of 10 represents combustion of 100 g coal with 1000 g air.

Table 4 Equilibrium flue gas composition upon combusting 1.7% S coal in an air-excess condition (vol.%, air–fuel ratio of 12, calculated)

Temperature (°C)	N_2	O_2	CO_2	H_2O	SO_3 (ppm)	SO_2	NO (ppm)	OH (ppm)	CO (ppm)	H_2 (ppm)	P_{S_2}[a]
200	76.4	2.8	14.7	5.9	1252	–	–	–	–	–	3×10^{-86}
400	76.4	2.8	14.7	5.9	1239	0.001	–	–	–	–	6×10^{-56}
600	76.4	2.8	14.7	5.9	787	0.04	3	–	–	–	6×10^{-40}
800	76.4	2.8	14.7	5.9	152	0.11	27	–	–	–	4×10^{-31}
1000	76.3	2.9	14.7	5.9	31	0.12	134	4	–	–	2×10^{-25}
1200	76.3	2.9	14.7	5.9	9	0.12	425	30	3	–	2×10^{-21}
1400	76.3	2.9	14.7	5.9	4	0.12	1022	144	43	5	2×10^{-18}

[a]Partial pressure. Coal composition is taken from **Table 1**. Air-fuel ratio is defined by weight; for example, air-fuel ratio of 12 represents combustion of 100 g coal with 1200 g air.

depending on the type of fuel and location of the component in the system. A layered structure is usually observed for these deposits,[6,7] with different chemistry and porosity in each position. Deposit chemistry of the innermost layer, which contacts directly the metal to its oxide scale, is considered important to examine the corrosion. Examples of the deposit chemistry obtained for superheater tubes of boilers firing various fuels are presented in **Table 6**. Tube deposit of heavy oil is rich in vanadium and sulfur, and the major constituents are Na_2SO_4 and V_2O_5 (explained later). Tube deposit of coal comprises ash constituents of silicon and aluminum oxides, and sulfur compounds such as $(Na,K)_2SO_4$[7] are also indicated. For those firing municipal solid waste, chlorides of sodium and potassium with slight inclusion of lead and zinc salts are characterized. Deposit of black liquor consists of mixtures of sodium and potassium sulfates, carbonates, and chlorides. Corrosive compounds in these deposits can be predicted to a certain extent, from the fuel chemistry, assuming that the corrosive compounds are vanadium oxides, sodium and potassium salts such as sulfates, chlorides, and carbonates, and compounds of heavy metals such as lead and zinc.[8] This is schematically illustrated in **Figure 3**. This sketch is constructed with the assumption that combustion terminates at thermodynamic equilibrium, and deposition of corrosive salts such as sulfates and chlorides takes place by vapor condensation from flue gas on metal surface. For example, in the case of high-Cl high-S coal, sodium and potassium in the fuel do not react with chlorine, but they preferentially react with sulfur to generate sulfate salts.[8] Chlorine in coal reacts to form gaseous HCl. Therefore, sodium/potassium chlorides are normally not found in their tube deposits. Similarly, for municipal solid waste, sodium, potassium, lead, and zinc react primarily with sulfur to form their sulfates, and the remaining react with chlorine to generate their chlorides. Hence, upon firing municipal solid waste, SO_x concentration in flue gas is generally very low, since sulfur in waste is totally captured upon reaction to form sulfate salts. The important point is that the chemical affinity of sulfur to react with sodium and potassium is much greater than that of chlorine; for fuel abundant in sulfur, there is no chance for chlorine to react with sodium/potassium to form their chlorides, and for this fuel chloride salts are generally not incorporated in the deposits. For black liquor, abundant sodium enables reaction with sulfur and chlorine in the fuel to form its sulfide and chloride. In this case, sulfur and chlorine in the fuel are completely consumed, and the remaining sodium can react with carbon to form its carbonate. Therefore, in tube deposits of black liquor recovery boilers sulfates, chlorides, and carbonates are present. In this way, one may predict the deposit chemistry, to the first-order approximation, upon knowing the fuel chemistry of the respective system. Critical temperature at which the corrosive salts in the deposits start to melt varies with the salt systems. For V_2O_5–Na_2SO_4 salt mixtures relating to oil deposits, this is reported to be 600 °C[9]; for Na_2SO_4–K_2SO_4–Fe_2O_3 salt mixtures representing coal deposits, it is recognized as 552 °C[10]; for $(Na,K)_2SO_4$–(Na,K)Cl (–$(Na,K)_2CO_3$) salt mixtures relevant to black liquor deposits, it is estimated to be around 500 °C[11]; for sulfates and chlorides of sodium, potassium, and heavy metals such as lead and zinc representing municipal solid waste deposits, it can be as low as 300 °C.[12] Involvement of chloride salts of sodium and potassium in the deposits generally lowers their melting points, and its effect on temperature is drastic for sulfates and chlorides of heavy metals such as lead and zinc.

Table 5 Equilibrium flue gas composition upon combusting 1.7% S coal in a partial combustion condition (vol.%, air-fuel ratio of 6, calculated)

Temperature (°C)	N_2	CO_2	CO	CH_4	H_2O	H_2	H_2S	SO_2	COS	NH_3	P_{O_2}[a]	P_{S_2}[a]
200	73.7	15.3	5 ppm	0.46	10.2	0.08	0.24	–	2 ppm	11 ppm	4×10^{-45}	3×10^{-14}
400	72.9	16.1	0.35	0.68	7.7	2	0.24	–	26 ppm	34 ppm	3×10^{-32}	2×10^{-11}
600	67.5	12	10.2	0.23	3	6.8	0.21	–	0.02	23 ppm	3×10^{-25}	2×10^{-9}
800	64.9	7.9	17	12 ppm	3	6.9	0.19	–	0.02	6 ppm	8×10^{-20}	2×10^{-7}
1000	64.9	7	18	–	3.9	6	0.19	–	0.02	2 ppm	1×10^{-15}	5×10^{-6}
1200	64.9	6.4	18.6	–	4.6	5.4	0.17	9 ppm	0.03	–	1×10^{-12}	6×10^{-5}
1400	64.9	5.9	19.1	–	5	4.9	0.13	0.01	0.02	–	2×10^{-10}	2×10^{-4}

[a]Partial pressure. Coal composition was taken from Table 1. Air–fuel ratio is defined by weight; for example, air–fuel ratio of 6 represents combustion of 100 g coal with 600 g air.

Table 6 Composition of Superheater Deposits (wt%, example)

	Heavy oil	*Coal*			*Municipal solid waste*	*Black liquor*
		Outer layer	*Intermediate layer*	*Inner layer*		
Si as SiO_2	–	23.5	23.3	7.6	15.3	–
Al as Al_2O_3	–	14	11.5	1.7	9.5	–
Fe as Fe_2O_3	11.2	36	11	70.5	1.8	–
Ti as TiO_2	–	0.9	< 0.1	< 0.1	1.4	–
Ca as CaO	1.17	1.3	< 0.1	< 0.1	17.4	–
Mg as MgO	0.88	1.3	1.1	< 0.1	2.9	–
Na as Na_2O	17.8	0.3	1.7	0.15	8.4	44.3
K as K_2O	–	2.9	13.5	1.3	12.3	5.2
V as V_2O_5	49.7	–	–	–	–	–
Ni as NiO	2.24	< 0.1	< 0.1	0.3	–	–
Cr as Cr_2O_3	–	< 0.1	< 0.1	7.0	1.2	–
Pb as PbO	–	–	–	–	0.1	–
Zn as ZnO	–	–	–	–	1.0	–
C as CO_2	1.6	–	–	–	0.4	14.3
S as SO_3	21.6	7.3	27.5	10.0	15	34.6
Cl	–	0.02	< 0.01	< 0.01	9.2	1.5
pH	3.8	3	2.2	4.3	8.2	–
Water soluble %	–	9	45.4	9.0	–	–

Data taken from
Heavy oil: superheater deposit for 1.6–1.8%S, 130–150 ppm V_2O_5, from Fukahori, K.; Uera, H.; Harada, Y. *The Thermal and Nuclear Power*, **1977**, *28*, 639–649, Coal: Blazewicz, A.J.; Gold, M. ASME publication, 79-WA/Fu-6, 1980, Municipal solid waste: Otsuka, N. CORROSION/97, paper no.157, NACE: Houston Texas, 1997, Black liquor: Backman, R.; Skrifvars, B.-J.; Hupa, M.; Siiskonen, P.; Mäntyniemi, J. *J.Pulp and Paper Sci.*, **1996**, *22*, J119–J126.

1.18.2 Gas-Phase Corrosion

In this section, fireside corrosion caused not by slag deposits but by gaseous species in flue gas is explained. Gas-phase corrosion can be separated into two categories, that is, high temperature oxidation in oxidizing gas atmospheres and sulfidation in reducing gas atmospheres.

1.18.2.1 Oxidizing Conditions

In most energy-converting systems, combustion is conducted under slightly excess-air conditions and their flue gases normally contain oxidizing gas species such as O_2, CO_2, H_2O, and SO_x. From engineering point of view, scaling of metal components exposed to these oxidizing gas atmospheres can generally be predicted from the available data reported in air, since the effects of CO_2 and SO_x on scaling is in most cases minor.[13] Approximate temperature limits of steels and alloys considered to be applicable for these oxidizing gas conditions are summarized and shown in Table 7. For carbon steel and low-alloyed steels of up to 5% Cr, exposing these steels to flue gases of higher temperature results in heavy scaling, and metal loss due to scaling increases exponentially upon raising the oxidation temperature. This behavior is shown in Figure 4. For steels of more than 9%Cr, stainless steels, and nickel-base alloys, uniform formation of Cr_2O_3 scale is established at lower temperatures, and their weight gains are slight. Above a critical temperature, which depends on respective alloy system, breakaway oxidation results for these steels and alloys and Cr_2O_3 scale loses its protection to high temperature oxidizing gases.[14] Temperature limits shown in Table 7 for stainless steels and nickel-base alloys are determined from the onset of breakaway oxidation. Parabolic rate constants of major metal oxide scales are summarized in Figure 5. Among the metal oxide scales which can uniformly form on metal surfaces, the growth rates of Cr_2O_3, Al_2O_3, and SiO_2 are relatively low, compared to those of Fe_3O_4, CoO, and NiO. Therefore, these metal oxide scales can be used as 'protective' oxide scales for steels and alloys as far as breakaway oxidation does not take place. The effect of water vapor on oxidation of engineering steels and alloys forming Cr_2O_3 scale must be pointed out. As shown in Figure 6, water vapor in flue gas atmosphere can significantly enhance the breakaway oxidation, especially of stainless steels.[14] For some stainless steels, oxidation experiments conducted in laboratory air during hot, wet season (e.g., P_{H_2O} of 0.1 atm at 40 °C with 100% humidity) can be different from those performed in cold, dry air

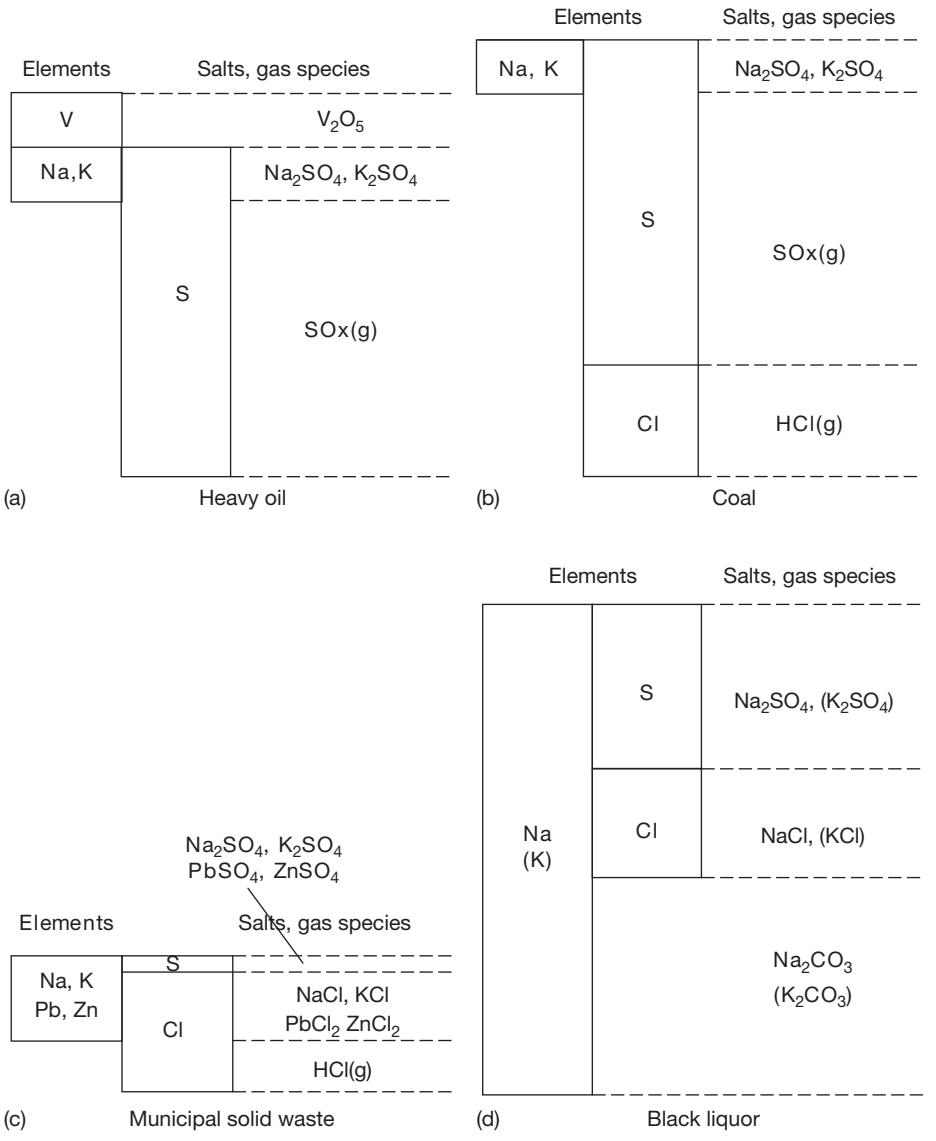

Figure 3 A simplified relationship between the elements in fuel and corrosive salts in tube deposits.

(e.g., P_{H_2O} of 0.006 atm at 0 °C with 100% humidity). Partial pressure of water vapor as a function of dew point of flue gas can be found in the literature.[15] Since flue gases resulting from combustion of natural gas contain greater amount of water vapor, its effect on oxidation of steels and alloys should be examined carefully. Oxidation rates of boiler tube materials exposed to 100% steam, often used to estimate the metal temperatures for ferritic steels, are summarized in the literature.[16]

1.18.2.2 Reducing Conditions

For gasifiers of coal, residual-oil, etc., combustion is regulated under air-deficient conditions. In these cases, reducing gas species of H_2 and CO coexist with CO_2 and H_2O, in flue gases and H_2S is incorporated when fuel contains sulfur.[17] For high temperature components exposed to these gas mixtures, sulfidation of steels and alloys occurs. For reducing conditions, gas atmospheres are normally high in P_{S_2} and low in P_{O_2}, and simultaneous formation of metal sulfides and oxides takes place. Since the driving force for the formation of metal oxide scale is small, uniform formation of protective metal oxide scales is relatively difficult to be established. In these cases, formation of metal sulfides overwhelms that of metal oxides, since the growth rate of metal sulfide scales is generally much higher than those of metal oxide scales.[18,19] Corrosion rates are

Table 7 Approximate temperature limits (°C) in air

Steel	*Composition (wt%)*	*Fontana & Green*	*Morris*		*Kane*
			Intermittent service	*Continuous service*	
Plain carbon	0.1C	480	–		510
T12	1Cr–0.5Mo	–	–		565
T22	2.25Cr–1Mo	–	–		580
T5	5Cr–0.5Mo	620	–		620
T9	9Cr–1Mo	670	–		650
AISI type 410	11Cr	760	815	705	700
AISI type 430	17Cr	840	870	815	840
AISI type 442	21Cr	950	1035	980	–
AISI type 446	25Cr	1030	1175	1095	–
AISI type 304, 321, 347	18Cr–8Ni–(Ti,Nb)	900	870	925	900
AISI type 316	18Cr–10Ni–2Mo	900	870	925	–
AISI type 309	23Cr–12Ni	1090	980	1095	1040
AISI type 310	25Cr–20Ni	1150	1035	1150	1090
Hastelloy X	Ni-base superalloy	1200	–		–
Hastelloy C	Ni-base superalloy	1150	–		–
Cr		900	–		–
Ni		780	–		–
Cu		450	–		–
Brass	70Cu–30Zn	700	–		–

Temperature below which oxidation rate in negligible. Negligible is defined as less than about 0.31 mg cm^{-2} h^{-1} (for weight gain, Fontana & Greene). For Morris and Kane, criteria is not presented.
Source: Fontana, M. G.; Greene, N. D. *Corrosion Engineering*; McGraw-Hill, 1967; p 369.
Morris, L. A. *Met. Eng. Q. Am. Soc. Met.* **1968**, *8*, 30–47.
Kane, R. H. In *Process Industries Corrosion*; Moniz, B. J., Pollock, W. I., Eds.; NACE: Houston, TX, 1986; pp 45–65.

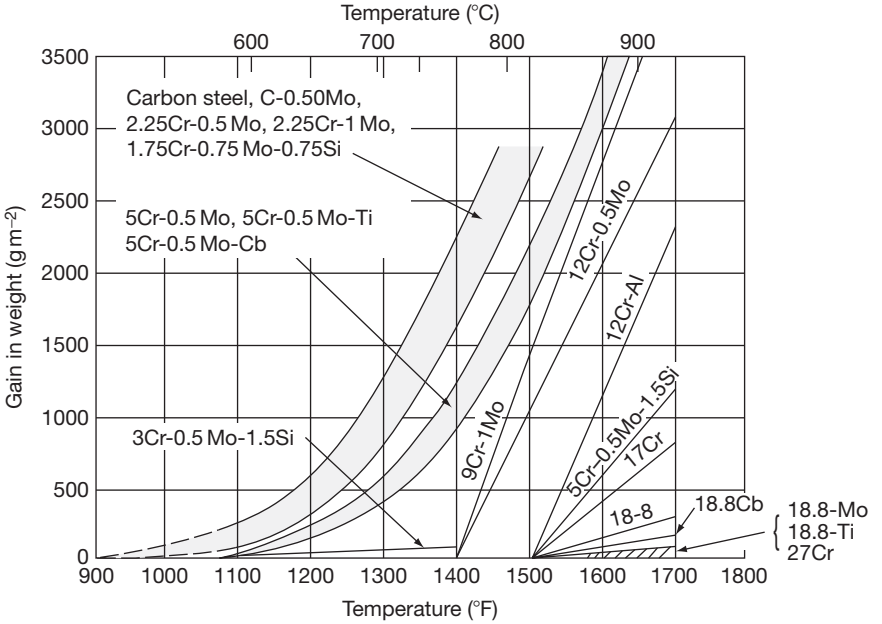

Figure 4 Oxidation behavior of engineering steels and alloys exposed to air for 1000 h. Reproduced from Kane, R. H. In *Process Industries Corrosion – The Theory and Practice*, Moniz, B. J., Pollock, W. I., Eds.; NACE: Houston, TX, 1986; pp 45–65.

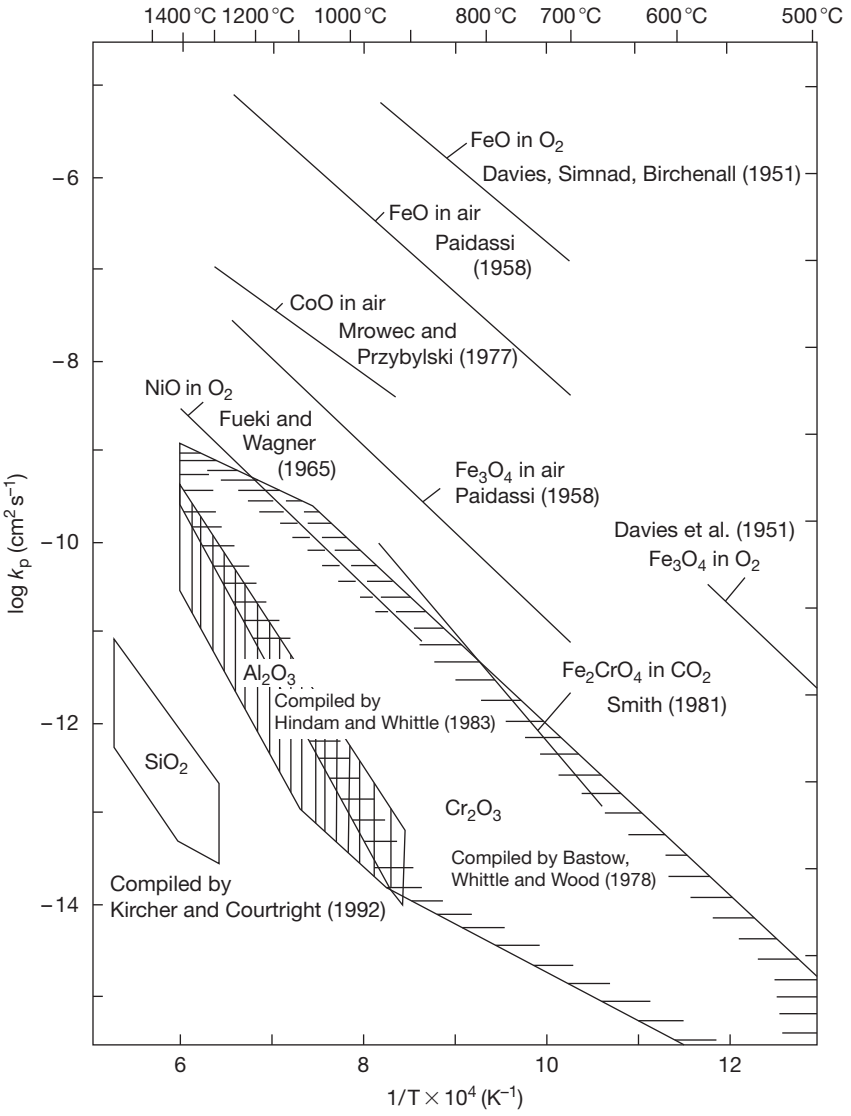

Figure 5 Parabolic rate constants (in scale thickness) of major oxide scales. Data were taken from Davies, M. H.; Simnad, M. T.; Birchenall, C. E. *J. Met.* **1951**, 889–896; Paidaiis, J. *Revu Metall.* **1957**, *LIV*, 569–585; Mrowec, S.; Przybylski, K. *Oxid. Met.* **1977**, *11*, 365–381; Fueki, K.; Wagner, J. B. *J. Electrochem. Soc*. **1965**, *112*, 384–388; Smith, A. F. *Werkst. Korros*. **1979**, *30*, 100–104; Hindam, H.; Whittle, D. P. *Oxid. Met.* **1982**, *18*, 245–284; Bastow, B. D.; Whittle, D. P.; Wood, G. C. *Oxid. Met.* **1978**, *12*, 413–438; Kircher, T. A.; Courtright, E. L. *Mater. Sci. Eng. A* **1992**, *155*, 67–74.

influenced not by slow-growing metal oxide scales but by fast-growing metal sulfide scales. Therefore, sulfidation can cause serious corrosion damage for metal components. In order to estimate the sulfidation rates of industrial steels and alloys, data taken from simple binary H_2S/H_2 gas mixtures are often referred,[20] since these data are considered to indicate the maximum corrosion rates of steels and alloys in respective P_{S_2} gas atmospheres. Iso-corrosion rate curves of engineering steels are presented in **Figure 7** as a function of temperature and H_2S concentration in H_2S–H_2 gas mixture of naphtha desulfurizers. These data represent exclusive formation and growth of sulfide scales where formation of protective oxide scales is minimized. For certain flue gas system containing not only H_2S and H_2 but also some oxidizing gas species of CO_2 and H_2O, formation of the protective Cr_2O_3 scale may result for stainless steels and nickel-base alloys, if thermodynamic condition favors. Once formation of uniform Cr_2O_3 scale is achieved, sulfidation by H_2S is hindered, and steels and alloys are protected by the uniform Cr_2O_3 scale. In coal

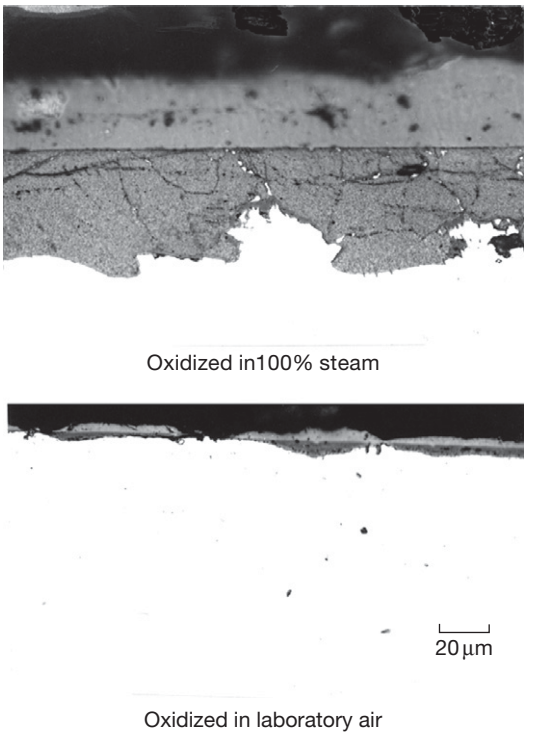

Figure 6 Cross section of TP321H steel (18% Cr–8% Ni–0.4% Ti) reacted with 100% steam (top) and laboratory air (bottom) at 650 °C for 1000 h under atmospheric condition.

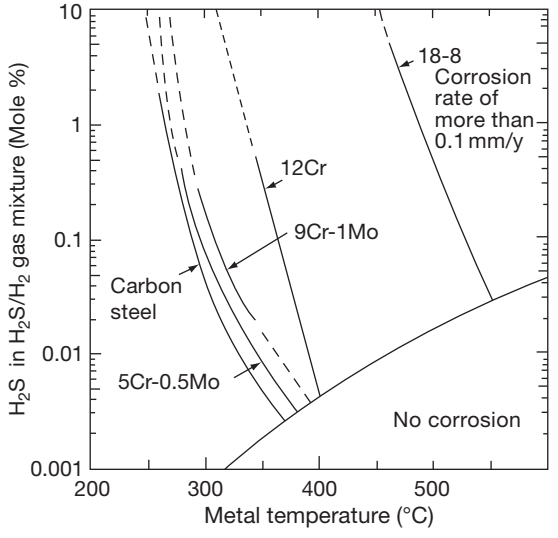

Figure 7 Isocorrosion rate curves of engineering steels for high temperature H_2S/H_2 corrosion in naptha desulfurizers. Corrosion rate of 0.1 mm year^{-1}. Adapted from Gutzeit, J. In *Process Industries Corrosion – The Theory and Practice*; Moniz, B. J., Pollock, W. I., Eds.; NACE: Houston TX, 1986; pp 367–372.

gasifiers, P_{S_2}–P_{O_2} boundary of uniform formation of Cr_2O_3 scale on steels and alloys deviates from that predicted from the thermodynamics. This boundary is referred as the kinetic boundary of Cr_2O_3 scale, shown in Figure 8 for example. Higher oxygen potential (or lower sulfur potential) is needed to secure the uniform formation of Cr_2O_3 scale, since greater driving force is needed for the growth of Cr_2O_3 to compete with that of the fast-growing metal sulfides.

1.18.3 Molten Salt Corrosion in Power Generating Systems

In this section, fireside corrosion caused predominantly by molten salts is outlined. High temperature metal components subject to fireside corrosion in energy-converting systems are exposed to hot combustion gases, and their metal temperatures are normally lower than the ambient flue gases, especially for heat exchanger materials placed in hot combustion gases to obtain heat from them. Depending on fuel chemistry, sodium/potassium sulfates and their chlorides, vanadium oxides, and chlorides and sulfates of heavy metals such as lead and zinc, which are present as vapor phases in flue gases, are considered as corrosive salts. They tend to vapor-condense on 'cold' metal surface from surrounding hot gas atmospheres. These vapor-condensed salts concentrate at the innermost metal-side of the deposit layer, since these sites are the coldest location in the deposits and hence the driving force for vapor-condensation of these salts is considered the greatest. For conditions where these salts become molten, reaction of these salts with protective metal oxide scales may initiate and fluxing reaction would take place, resulting in degradation of these protective metal oxide scales.[6,21] Metal oxide scales, initially formed as protective oxide layer on metal surfaces by gas-phase reaction, react with fused salts and dissolve into the salts. These dissolved metal ions precipitate out as oxide particles at the gas-side of the salt layer. Hence, once fluxing of metal oxide scale initiates, protective metal oxide scale is converted into porous, nonprotective oxide particles. At the reaction front, oxidation of metal constituents takes place in much higher rates than the case where the formation of protective oxide scales is established. At these sites, sulfidation as well as chlorination may simultaneously occur depending on the chemistry of molten salts. Since the final product of this corrosion is generally metal oxides, the overall reaction of molten salt corrosion can be interpreted as 'oxidation' of metals. This is

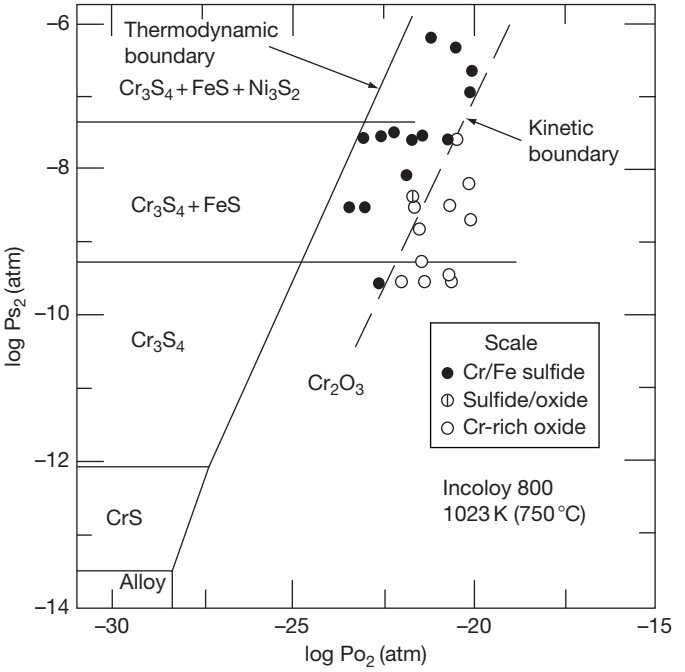

Figure 8 Kinetic boundary of Cr_2O_3 protection found for Alloy 800 as a function of oxygen and sulfur partial pressures in sulfidizing gas atmospheres at 750 °C. Reproduced from Natesan, K. In High Temperature Corrosion, 2–6 March 1981, San Diego, CA; Rapp, R. A., Ed.; NACE: Houston, TX, 1981; pp 336–344.

one reason why the molten salt corrosion is termed as 'accelerated oxidation' or 'catastrophic oxidation.'[6] In molten salt corrosion, severe corrosion does not take place when the surrounding gas atmosphere does not contain any oxygen, even though sufficient amounts of molten salts are present on metal surfaces. Generally, oxygen is the predominant oxidant for fireside corrosion, while carbon dioxide and water vapor are not that influencing. The role of molten salts is interpreted to enable fluxing of metal oxide scales,[21] and the ability to facilitate fast transportation of oxygen in molten salt layer to reaction sites is another important property of molten salts to maintain the high reaction rates of this corrosion.[9] A schematic behavior of molten salt corrosion is presented in **Figure 9**. Frequently, incubation time is experienced at the beginning of the corrosion,[6] where the corrosion rates remain relatively low. In this period, formation of protective oxide scales and condensation of corrosive salts are considered to take place. For conditions where salts become fused, that is, metal temperatures exceed that of the melting points of the salt mixture, accelerated oxidation takes place, and fireside corrosion initiates. When the metal temperatures remain lower than the melting point of the salt mixture, accelerated oxidation do not take place, and corrosion remains slight. Therefore, it is of

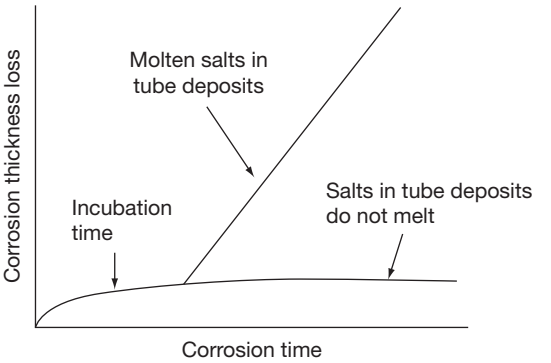

Figure 9 Schematic corrosion behavior caused by fused salts.

great importance to know the melting point of the deposits and to compare it with the metal temperature of the component. Finally, the importance of flue gas temperature on corrosion should be pointed out. It is generally accepted that the corrosion rate of this type depends not only on metal temperature, but also on flue gas temperature to which the metal components are exposed. Exposing metal components to flue gas of higher temperature generally result in higher corrosion rates.[22,23] This is interpreted from greater concentration of corrosive salts in the deposits, since the

flue gas of higher temperature normally contains higher concentration of vapor species of corrosive salts, and the driving force for vapor-condensation of these salts onto metal surface is apparently greater than those exposed to flue gas of low temperatures, which is attributed to the temperature difference between the flue gas and the base metal.[8]

1.18.3.1 Vanadium Attack

Vanadium attack, referred as oil ash corrosion as well, has been recognized as severe fireside corrosion for boiler tubes, turbine components, furnace tubes, and reformer tubes in boilers, combustors, and reformers which fire oil containing vanadium.[3,9] Oil, rich in vanadium and sodium of approximately more than 1–10 ppm, is recognized to have potential corrosivity to metals.[24] Vanadium reacts with oxygen in combustion air to form V_2O_3, V_2O_4, and finally volatile V_2O_5 in flue gases.[2] Gaseous V_2O_5 vapor condenses on metal surface as ash deposits. Depending on the deposition rates of V_2O_5 and of other vapor-condensed species such as Na_2SO_4, etc., the deposit chemistry varies, but vanadium (as oxide) can constitute up to 80% of the deposits although vanadium concentration in fuel is typically less than 300 ppm.[3] In many cases, vanadium oxides react with other constituents such as sodium to form low melting point compounds. This is shown in **Figure 10**. Note that for Na_2O–V_2O_5 system, melting points can be as low as 530–540 °C, which corresponds to the metal temperature of superheater and reheater tubes in practical boilers.[3] In addition to vanadium pentoxide, sodium vanadates of Na_2O–V_2O_4–$5V_2O_5$, $4Na_2O$–V_2O_4–$11V_2O_5$, Na_2O–V_2O_5, and $3Na_2O$–V_2O_5 can be involved in superheater and reheater deposits. Melting points of superheater and reheater deposits taken from 350–500 MW boilers firing oil of 30–40 ppm V, 8–15 ppm Na, and 1–1.5% S are plotted as a function of (Na + S)/V atomic ratio of their deposits and shown in **Figure 11**.[25] Clearly, vanadium-rich deposits start to melt at 480–500 °C, whereas those lean in vanadium remain solid until heated to above 800 °C. Sulfate-rich deposits have normally high melting points.

Vanadium attack is interpreted to result from fluxing of protective metal oxide scales and fast transfer of dissolved oxygen in molten oxide layer.[9] A laboratory corrosion test revealed that accelerated corrosion of TP304 stainless steel occurred when reacted with pure molten V_2O_5, but the corrosion rate even increased when sodium sulfate was added to vanadium pentoxide; maximum corrosion resulted

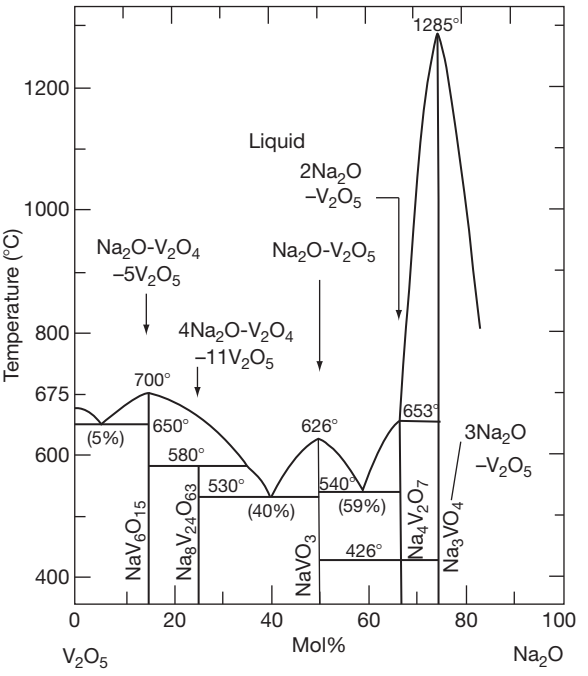

Figure 10 Melting point of Na_2O–V_2O_5 system. Reproduced from Roth, R. S.; Dennis, J. R.; McMurdie, H. F. *Phase Diagrams for Ceramists*; The American Ceramic Society, 1987; Vol. VI, p 98.

for V_2O_5–20 mol% Na_2SO_4 salt mixture.[9] This was explained from the ability for vanadium pentoxide–alkali salt mixtures to absorb oxygen. Indeed, vanadium pentoxide–alkali salt mixtures absorb oxygen upon heating from solid to liquid phase through the reversible change from vanadylvanadate to alkali acid vanadates, according to the following equation[9]

$$m\mathrm{Na_2O}\cdot(n-p)\mathrm{V_2O_5}\cdot p\mathrm{V_2O_4}+1/2p\mathrm{O_2}=m\mathrm{Na_2O}\cdot n\mathrm{V_2O_5}$$

Capability to accommodate great amount of oxygen in the melt and ability for fast diffusion of oxygen through its layer to metal surface seem to be the characteristics of this liquid phase.

The effect of metal temperature on corrosion is significant. In order to minimize the corrosion, limiting metal temperature to below the critical temperature, which relates to the melting points of the ash deposits, is considered an effective measure to alleviate the corrosion.[3] The effect of flue gas temperature on corrosion is reported to be important as well. When placing heat-exchanger tubes and plates to flue gases of higher temperature, vapor-deposition of corrosive vanadium and sodium compounds enhances, and concentration of these compounds on metal surface

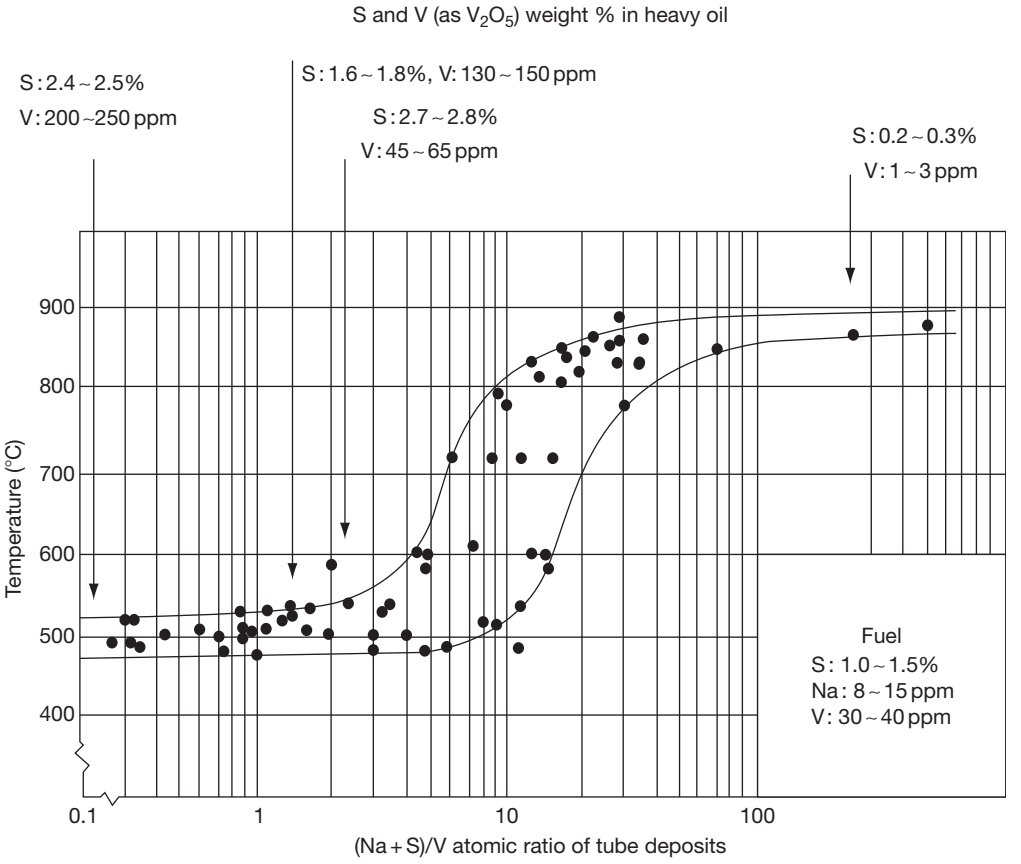

Figure 11 Melting point of tube deposits taken from superheater and reheater tubes of 350–500 MW boilers firing heavy oil. Steam temperatures were 540–571 °C. Reproduced from Harada, Y.; Nakamori, S. *Boushoku Gijutsu* **1980**, *29*, 615–621.

increases. This facilitates formation of molten salts at these sites, and the corrosion aggravates accordingly. For boiler tubes, regions of gas and metal temperatures where corrosion may occur are empirically recognized in practice. This is presented in Figure 12. This criterion depends on several factors such as fuel chemistry, boiler design, and combustion conditions, but in order to increase metal temperature, the lowering of the flue gas temperature is generally needed. Lowering excess air used for combustion of oil should have a certain effect to reduce the corrosion rate, since removing 'free' oxygen in the flue gas obviously would help in minimizing supply of major oxidizing gas species of the corrosion reaction. However, using low excess combustion air is reported not always successful when applied to practical power plants, because of the complexity of combustion and flue gas mixing in real boilers.[3] The effect of inhibitors and fuel additives on corrosion has been widely recognized, and addition of inhibitors to fuel oil is successfully applied to some boilers in practice.[25]

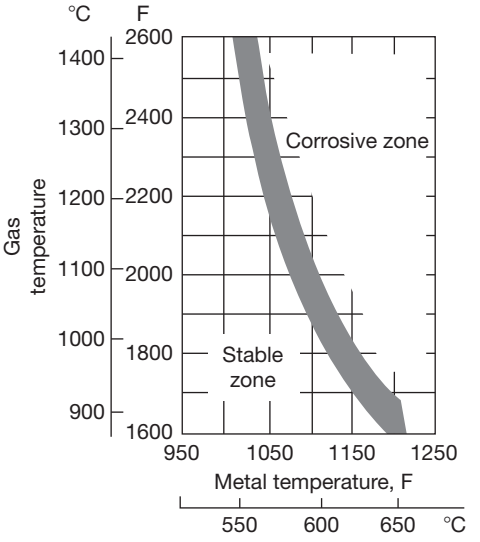

Figure 12 Regions where boiler tubes are subject to fireside corrosion as a function of tube metal temperature and flue gas temperature. Reproduced from Hansen, W. H.; Kessler, G. W. *Trans. ASME* **1965**, 210–214.

These inhibitors are designed to react with vanadium to form compounds of high melting points. Out of a number of inhibitors, MgO and its derivatives are used in practice because of its effectiveness and relatively low cost.[3,25] For example, addition of water-soluble $Mg(OH)_2$ to fuel oil, at an atomic Mg/V ratio of 2, is reported to have been successful in reducing the corrosion rate of TP321H (18% Cr–10% Ni–0.4% Ti) superheater tubes in a practical boiler to about one-third, the steam temperature of which was 571 °C.[25]

According to **Figure 13**, high-chromium steels and alloys seem to have better resistance to vanadium attack. Nickel-based alloys have generally higher corrosion rates than the iron-based alloys, suggesting that nickel is detrimental compared to iron. For boiler tube application, high-Cr ferritic steels of 9% Cr and 12% Cr are reported to have better resistance than the austenitic 18-8 stainless steels.[26,27] This is interpreted to be attributed, again, to nickel in 18-8 steels, since nickel is a harmful alloying element to combat the corrosion, the reason for which still seems to remain unclear.

Recently, a new type of fossil fuel coming from vast reserves of bitumen existing in the Orinoco Belt in Venezuela has become recognized as an useful fuel to generate electricity.[28] This fuel, arising from the technology for dispersing natural bitumen in water, is called orimulsion. Orimulsion contains water of around 30 wt%. An example of the elemental analysis is 60.1% carbon, 10.1% hydrogen, 26.4% oxygen, 0.35% nitrogen, 2.85% sulfur, and 0.2% ash (by weight).[28] It should be noted that this fuel contains vanadium of 310 ppm and sodium of 30 ppm. Vanadium attack on metal components is predicted. Field tests were conducted in real boilers firing orimulsion, and fireside corrosion of boiler materials turned out to be not that severe. This was attributed to high concentration of magnesium in the fuel, that is, 370 ppm, which acted as inhibitor to raise the melting points of the ash deposits, and hence alleviating corrosion for metal components. Information on the concentration not only of corrosive impurities but also of other impurities such as alkali earth elements is needed to evaluate the corrosivity of fuel.

1.18.3.2 Sulfate-Induced Corrosion

Fireside corrosion has often been encountered in blades and vanes of land-based and aircraft gas

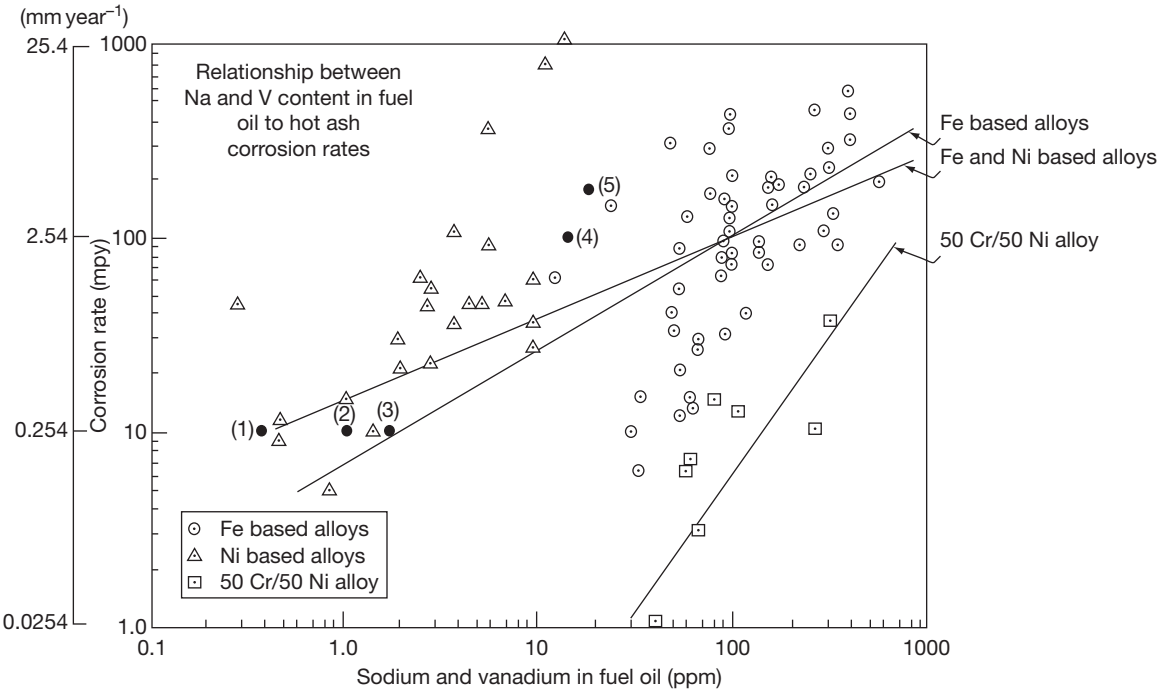

Figure 13 Relationship between Na + V content in fuel oil to corrosion rates. Reproduced from Demo, J. J. *Mater. Perform.* **1980**, 9–15. Data of iron-based alloys are from boiler and furnace/reformer tubes, those of nickel-base alloys predominantly from turbine blades, and those of 50Cr–50Ni alloy from tube supports and hangers. Solid marks with numbers represent industrial and semiworks experience points of iron-based reformer alloys.

turbines because of thin film of pure liquid sodium sulfate, which is vapor-condensed from flue gas onto metal surface.[6,21] The source of sodium comes from either the fuel or the air intake. Sodium, commonly present in sea salt as sodium chloride, reacts with sulfur in fuel to form sodium sulfate, according to the well-known reaction[6]:

$$2NaCl + SO_3 + 1/2O_2 = Na_2SO_4 + Cl_2$$

At turbine conditions, sodium chloride is considered thermodynamically unstable. Metal temperatures of the components are generally above the melting point of sodium sulfate, that is, 884 °C. This is often termed as Type I hot corrosion or high temperature hot corrosion (HTHC).[21] For utility boilers firing high-sulfur coal, fireside corrosion of superheater and reheater tubes can take place. This is categorized as Type II hot corrosion, or low-temperature hot corrosion (LTHC), since this corrosion occurs in the temperature range of 600–750 °C, well below the melting point of pure sodium sulfate.[21,29] In this section, fireside corrosion of Type II hot corrosion is introduced firstly.

It is well recognized that for boilers firing pulverized coal of high sulfur concentration, external corrosion of superheater and reheater tubes takes place.[7,10,29,30,31] The corrosion rate of boiler tubes starts to significantly increase at around 565 °C (1050 °F) when the metal temperature exceeds the melting point of their tube deposits, exhibits a maximum at around 650–700 °C, and decreases drastically upon further increase in the metal temperature.[7,10] The drastic decrease in the corrosion rate at above 700 °C is interpreted to be from the solidification of liquid phases, the temperature of which depends upon the partial pressure of SO_3 in flue gas and the chemistry of the complex sulfates.[32] Hence, the corrosion behavior is characterized as 'bell-shaped' form.[7,10] Corrosion rate of tube steels is influenced not only by the metal temperature, but also by the flue gas temperature, suggesting a great effect of vapor-condensation of corrosive salts from flue gas on metal surface.[23] This is shown in **Figure 14**. Tube deposits contain corrosive salts of sodium and potassium sulfates and iron oxide (hematite, Fe_2O_3), in addition to ash constituents such as complex oxides of aluminum, silicon, etc. Sodium and potassium sulfates can form complex sulfates of low melting-points upon reaction with hematite, that is, sodium and potassium iron trisulfates of $(Na,K)_3Fe(SO_4)_3$. Under a simulated flue gas atmosphere of 0.25% SO_2–3.6% O_2–15.0% CO_2–balanceN_2, sodium iron

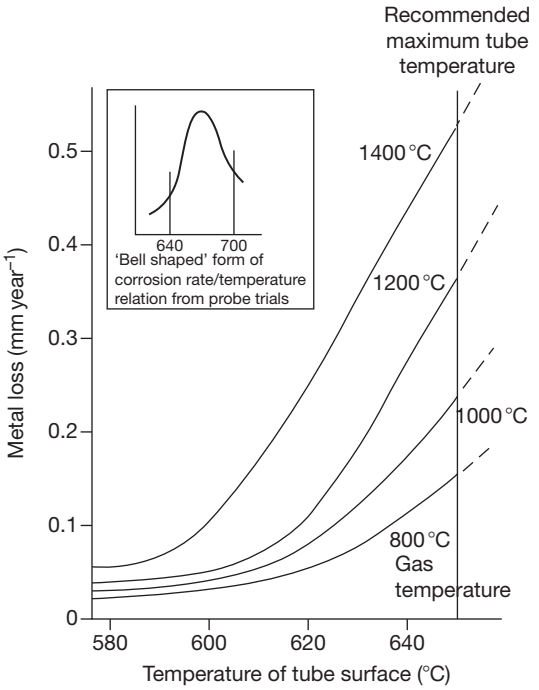

Figure 14 An example of the corrosion rates of superheaters and reheaters as a function of tube surface temperature and flue gas temperature. The inset shows the 'bell-shaped' corrosion behavior of this type of corrosion. Reproduced from Cutler, A. J. B.; Flatley, T.; Hay, K. A. *Metallurgist and Materials Technologist*, **1981**, February, 69–81.

trisulfate, $Na_3Fe(SO_4)_3$ becomes fused at 624 °C, whereas potassium iron trisulfate, $K_3Fe(SO_4)_3$, at 618 °C.[10] The melting point of these complex sulfates is affected by the sodium–potassium ratio, and the lowest melting-point 552 °C is obtained for compounds between 1:1and 2:1 molar mixture of potassium to sodium iron trisulfates.[10] Hence, for most laboratory tests simulating fireside corrosion of Type II attack, synthetic ash of $Na_{1.5}K_{1.5}Fe(SO_4)_3$ (1.5 mol Na_2SO_4–1.5 mol K_2SO_4–1 mol Fe_2O_3 mixture) is used as predominant corrosives to simulate this environment.[33] It should be noted that these sodium and potassium complex iron trisulfates are stable only in gas atmospheres containing SO_2. Temperature range for the liquid-phase stability of these complex sulfates seems to be affected by SO_2 (and therefore SO_3) concentration in the flue gases. For example, temperature regime where severe corrosion occurs for TP321H steel (18% Cr–10% Ni–0.4% Ti) becomes broader when exposed to gas atmospheres of higher SO_2 concentration. This is shown in **Figure 15**.[33] For flue gas of low SO_2 concentration,

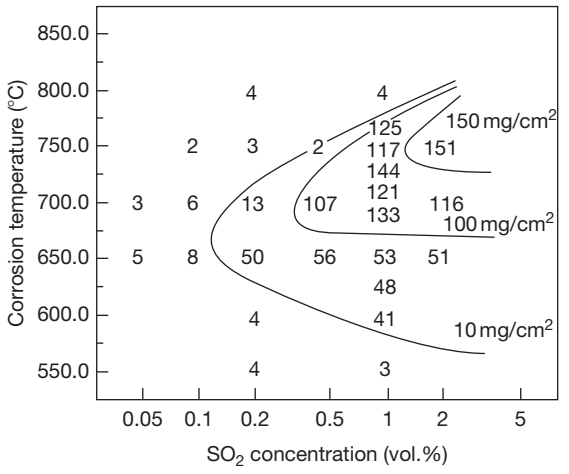

Figure 15 The effect of SO_2 vol.% in gas atmosphere on high temperature corrosion of TP321H steel specimen reacted with 1.5 mol Na_2SO_4–1.5 mol K_2SO_4–1 mol Fe_2O_3 in *x*% SO_2–5% O_2–15% CO_2–N_2. Numbers in the figure designate corrosion weight loss. Reproduced from Fukuda, S. T.; Hamada, H.; Sakaguchi, Y. In Proceedings of the 32th Meeting of the Japanese Society of Corrosion Engineering, 1985, August, Sapporo, B-302, pp 239–246.

sulfates of potassium and sodium do not seem to react with iron oxides to form stable complex sodium and potassium iron trisulfates, and these ash deposits remain solid at tube metal temperatures. This result clearly demonstrates the importance of SO_2 (and therefore SO_3) concentration in flue gases, since one can predict the occurrence/absence of fireside corrosion of superheater and reheater tubes of coal-fired boilers, when the SO_2 concentration of flue gas is specified. Therefore, for firing low-S coal where the SO_2 concentration of flue gas is less than 0.1%, sulfate-induced corrosion is expected to be slight.

There is an index representing the corrosivity of high-S coal of 1.4–8.2% S (proximate, by weight) from the coal chemistry. This index is often referred to as the Borio index, determined from the concentration of acid-soluble alkali and alkali earth elements (in ppm), and Fe_2O_3 (in wt%) of coal.[4] Procedure to obtain this index is shown in **Figure 16**. In order to obtain acid-soluble sodium and potassium concentrations in coal, precise measurement seems to be necessary. Test procedure for this is described in the literature as follows,[4] 'set 2 g portion of coal sample (~70% through 200 mesh) to a 250-m L Erlenmeyer flask and add 40 m L of 5% HCl solution. Fix air condenser and digest the sample for 16 h at a gentle boil. After digestion, filter through #40 Whatman filter paper of 15 cm into 100-ml volumetric flask. Wash filter and contents at least four times with small amounts of water, and make it up to 100 ml volume. This solution should be carefully measured.'[4] As expected, corrosivity of high-S coal is related to the concentration of acid-soluble sodium and potassium compounds, hematite content, and calcium and magnesium contents. To combat the corrosion, high-Cr steels and alloys perform well, which will be explained later in detail.

The mechanism of Type II hot corrosion seems to resemble that of Type I hot corrosion. Therefore, corrosion reaction offered for Type I hot corrosion is explained. For Type I hot corrosion observed at turbine blades and vanes, corrosion products consist generally of relatively thin outer oxide layer, a thick mixed oxide/metal layer, and a thin metal zone containing sulfides below the mixed oxide/metal layer.[6] Sulfides are generally rich in chromium, but in some cases nickel-rich or cobalt-rich sulfides are found for materials which experienced rapid degradation, presumably, due to liquid formation of Ni–Ni_3S_2 or Co–Co_4S_3 eutectics.[6] The eutectic temperatures are 645 and 877 °C, for Ni–Ni_3S_2 and Co–Co_4S_3 eutectics respectively.[34] Early interpretation of this corrosion was derived to explain the formation of sulfides in the base metal and called the sulfidation model.[34] According to this model, corrosion can be divided into two stages. At a triggering stage, which is 'sporadic and unpredictable,' reduction of sodium sulfate by an unspecified reducing agent generates elemental sulfur, which reacts with base metal components to form their sulfides. Hence, for this model, oxidizing agent is considered sodium sulfate. These metal sulfides react with base metal elements to form low melting point eutectics such as Ni–Ni_3S_2. At an enhanced oxidation stage, metal is penetrated by the metal–metal sulfide liquid eutectics, and oxidation of these liquid eutectics by oxygen was proposed to proceed more rapidly than the sulfur-free alloy. Formation and enhanced oxidation of metal–metal sulfide eutectics was the early mechanism. Since chromium sulfides are normally present in the corrosion products of the degraded turbine blades and vanes, and metal–metal sulfide eutectics such as Ni–Ni_3S_2, etc. are not always indicated,[6] more generalized interpretation seems to be necessary. Chromium does not form any metal–metal sulfide eutectic. Recent understanding of this type of corrosion is based on destructive dissolution of originally protective metal oxide scale into thin fused salt film, followed by reprecipitation of these metal oxides as thick, porous, nonprotective reaction products.[21] This is called the salt-fluxing model. The overall reaction is again accelerated/catastrophic

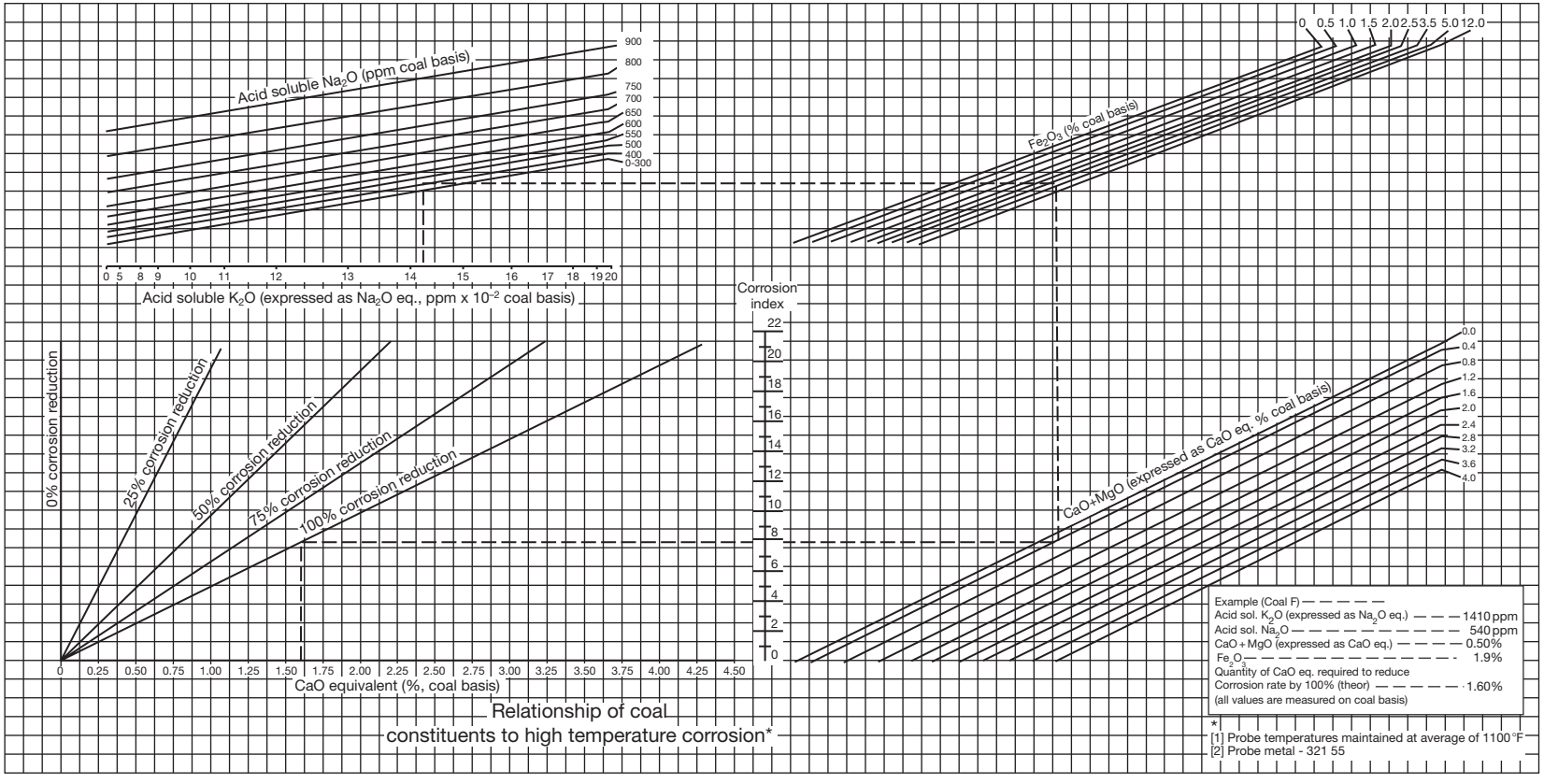

Figure VII-13. Relationship of cool constituents to high temperature corrosion VII-29

(a) (b) (c)

Figure 16 Relation of coal constituents to high temperature corrosion of boiler tubes. Reproduced from Borio, R. W.; Wilson, E. B. The control of high temperature fire-side corrosion in utility coal-fired boilers, OCR R6D Report No. 41, April 1969, Office of Coal Research, Department of the Interior, Washington, DC.

oxidation of metals, and deterioration of protective metal oxide scale through dissolution/fluxing reactions is an important step for initiating and maintaining the corrosion. Oxygen in flue gas is necessary to maintain the corrosion; without oxygen, reaction cannot proceed even when abundant fused salts are present on metal surfaces. The fluxing reactions of metal oxide scales are significantly affected by the 'basicity' of fused salts, which is defined as $-\log a_{Na_2O}$ for pure sodium sulfate.[21] Basicity of sulfate melts is affected by the activity of SO_3 in flue gas, according to the following reaction:

$$Na_2SO_4 = Na_2O \text{ (in the melt)} + SO_3(g)$$

This is similar to the thermal stability of the complex sodium/potassium iron trisulfates where the stability of its liquid phase is influenced by SO_3 concentration.[33] It should be pointed out that basicity of fused sulfate salts is influenced by the partial pressure not of SO_2, but of SO_3. Generally, SO_3 concentration of flue gas is approximately two orders of magnitude less than SO_2 (see **Table 4**, for example).

Solubility of major metal oxides in fused sodium sulfate at 927 °C is presented in **Figure 17**.[21] Clearly, solubility of metal oxides depends on the basicity of sulfate melt, and two types of dissolution reactions are noticed, except for SiO_2. The one is categorized as the acidic dissolution, which takes place in an acidic melt lean in O^{2-} ion.[21] For NiO, for example, the reaction is written as $NiO = Ni^{2+} + O^{2-}$. The other one is termed as the basic dissolution, which occurs in a basic melt rich in O^{2-} ion. The reaction is designated as $2NiO + O^{2-} + 1/2O_2 = 2NiO_2^-$.

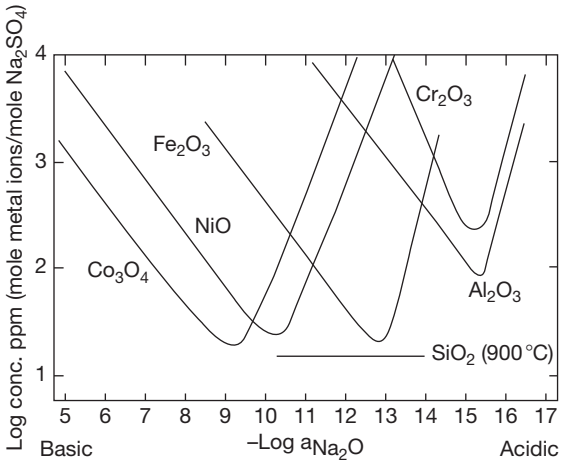

Figure 17 Oxide solubility of major oxides in fused Na_2SO_4 at 927 °C and 1 atm O_2. Reproduced from Rapp, R. A. *Corrosion* **1986**, *42*, 568–577.

In order to establish self-sustaining hot corrosion of steels and alloys, it seems necessary for fused sodium sulfate to locate its melt chemistry at a specific condition where simultaneous dissolution and reprecipitation of metal oxide scales are sustained. The basicity at which self-sustaining hot corrosion can occur may depend upon the alloy system; for pure nickel, this corresponds to the basicity at which basic dissolution of NiO is secured.[35] One explanation for it may be provided by the solubility gradient model, which can be found in the literature.[36] For fused salt film of sodium sulfate, maintaining its melt basicity in basic conditions is considered rather difficult since the melt chemistry enabling NiO basic dissolution is quite far from the melt conditions equilibrated with acidic flue gas atmosphere containing SO_3. In acidic melts, pure nickel, if protected by dense metal oxide scales, did not produce any rapid attack.[35] Current understanding for this is to incorporate the effect of sulfidation reaction of the base metal by fused sodium sulfate, which generates O^{2-} ion and shifts its basicity to more basic conditions.[21] For pure nickel, the sulfidation reaction is given by the following equation:

$$SO_4^{2-} + 4Ni = 3NiO + NiS + O^{2-}$$

Direct contact of fused salts with the base metal, presumably at cracks, flaws, and grain boundaries of its protective oxide scale results in altering the basicity to more basic, where self-sustaining corrosion is facilitated. Since formation of protective oxide scales is considered to precede vapor-condensation of molten salts, 'incubation time' is usually required for fused salts to permeate the protective oxide scale[37] and to arrive at the point where direct contact of fused salt and base metal becomes possible. For acidic melts, oxide solubility is the lowest for Cr_2O_3 and Al_2O_3, as shown in **Figure 17**. Therefore, these metal oxide scales, along with SiO_2, is expected to function as protective oxide scales in acidic melts. This may be one reason why the steels and alloys forming uniform Cr_2O_3, Al_2O_3, and SiO_2 scales have good resistance to hot corrosion. On the contrary, molybdenum, tungsten, and vanadium, commonly added to strengthen their alloys, are regarded as harmful alloying elements for hot corrosion.[38] Oxides of these alloying elements can be categorized as 'acidic' oxides, which are thermodynamically stable in acidic melts. Thermodynamic stability of major metal oxides relevant to alloy constituents of high temperature materials is calculated at 927 °C, P_{O_2} of 1 atm and shown in **Figure 18**. In this figure, unit activities of condensed phases in mutual equilibrium are assumed. Oxides of

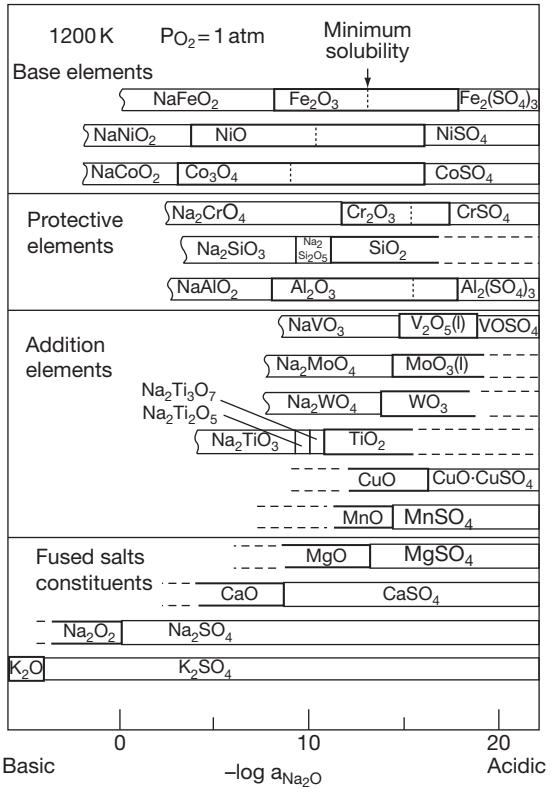

Figure 18 Basicity of major oxides at 1200 K, $P_{O_2} = 1$ atm relevant to high temperature corrosion.

molybdenum, tungsten, and vanadium are stable in acidic melts, while oxides of sodium and potassium are stable in basic melts. In 'neutral' melts, basic dissolution may take place for acidic oxides; described for molybdenum oxide as follows:

$$MoO_3(s) + O^{2-} = MoO_4^{2-}$$

This reaction shifts the basicity of molten salts to more acidic. At the reaction front of metal/salt interface of nickel-base alloys containing molybdenum and the like, oxidation and subsequent dissolution of these alloying elements may take place simultaneously and a very acidic condition can be established locally, which forces acidic fluxing of otherwise protective Cr_2O_3 and Al_2O_3 scales. This may be one explanation for the detrimental effect of molybdenum and tungsten on corrosion.

For Type II hot corrosion, the beneficial effect of chromium on corrosion is prominent as well, as shown in Figure 19 for example. High-Cr alloys such as alloy 671 are used to combat fireside corrosion in these environments. It should be pointed out that for 18-8 stainless steel family additional elements of molybdenum and titanium to steels degrade their

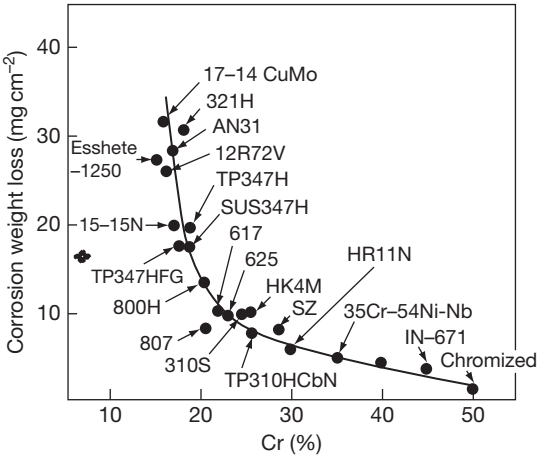

Figure 19 Laboratory corrosion test results of high temperature steels and alloys. The test was conducted at 650 °C for 5 h in 1% SO_2–5% O_2–15% CO_2–N_2 Test specimens were reacted with 1.5 mol Na_2SO_4–1.5 mol K_2SO_4–1 mol Fe_2O_3 salt mixture by salt-coating method.

corrosion resistance, whereas with niobium the opposite occurs. The beneficial effect of niobium on corrosion seems to remain unclarified, although recent modern 18-8 stainless steel tubes contain small amount of niobium.

This explanation is valid for fireside corrosion encountered in components exposed to environments firing fossil fuel containing sulfur. In general cases, SO_2 concentration in these flue gases lies in the range of less than several thousand parts per million, and SO_3 concentration in the range of less than 100 ppm. However, for extreme cases such as boilers firing solid sulfur, SO_3 concentration of flue gas may surpass hundreds of parts per million, and fused-salt corrosion attributed to liquid sodium/potassium pyrosulfates of $Na_2S_2O_7$ and $K_2S_2O_7$ can take place.[39] Since the melting point of Na_2SO_4–$Na_2S_2O_7$ and K_2SO_4–$K_2S_2O_7$ systems is reported to be low, down to around 400 °C (Figure 20), fireside corrosion resulting from the formation of liquid phase of sodium and potassium pyrosulfates can occur for boiler tubes. Again, it must be pointed out that these liquid phases are only stable for conditions where SO_3 (not SO_2) concentration in flue gas exceeds 200 ppm for potassium pyrosulfate and 2000 ppm for sodium pyrosulfate, which is very rare for boilers firing conventional fuel.

1.18.3.3 Fireside Corrosion Induced by Chlorine in Fuel

Fireside corrosion relating to chlorine in fuel is encountered for boiler components in waste incinerators and

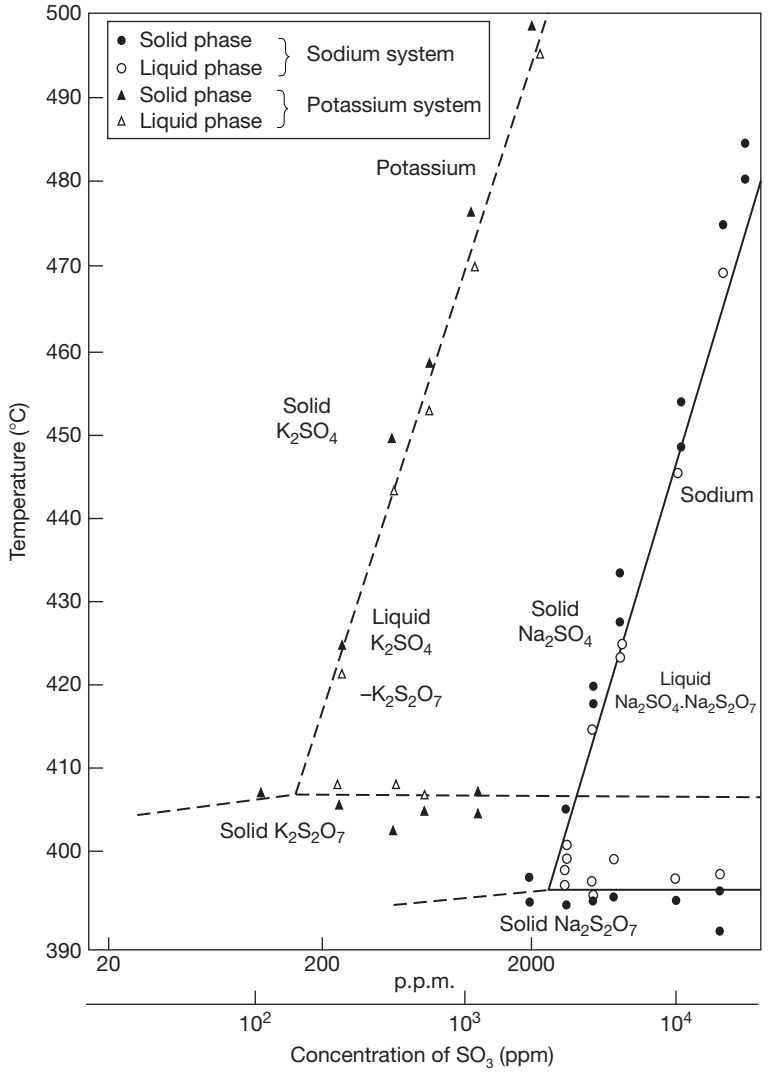

Figure 20 Temperature range of liquid $K_2S_2O_7$–K_2SO_4 and $Na_2S_2O_7$–Na_2SO_4 in the presence of various partial pressures of SO_3. Reproduced from Coats, A. W.; Dear, D. J.; Penfold, D. *J. Inst. Fuel* **1968**, 129–132.

in black liquor recovery boilers (BLRB). It is generally accepted that chloride salts, deposited on metal surface via vapor-condensation, play an important role in corrosion.[40] In order to deposit chloride salts from flue gas on metal surface, chloride vapor species must be present in flue gas atmospheres.

Fireside corrosion of waste incinerators has been intensively studied for steel tubes of their heat recovery boilers.[40–42] Except for aqueous corrosion experienced at below the dew-point temperatures, corrosion can start at above 320 °C, which is indeed surprisingly low compared to other types of fireside corrosion encountered in real systems. A schematic temperature dependence of boiler tubes on corrosion in waste incinerators is presented in **Figure 21**.[41] Since hydrogen chloride is always present in flue gases in the order of hundreds and thousands of parts per million, the early interpretation of corrosion was the gas-phase attack of metals by hydrogen chloride.[42] Since one of the reaction products can be highly volatile iron trichloride (Fe_2Cl_6, boiling point 315 °C, see **Figure 22**), corrosion products are expected not to function as corrosion barrier for boiler tubes, and high corrosion rates can be expected even at low temperatures. However, laboratory tests examining gas-phase corrosion of tube steels by hydrogen chloride turned out that its corrosion rate is significantly low at 400 °C, which cannot explain

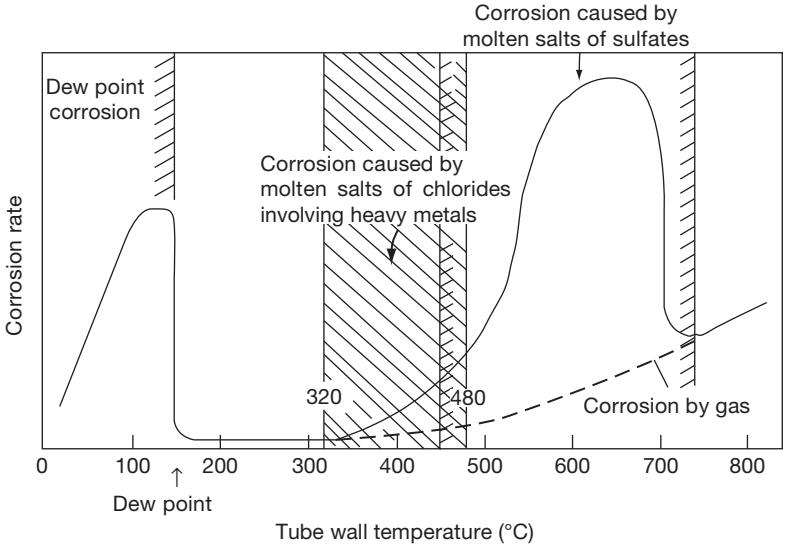

Figure 21 Corrosion behavior of carbon steel boiler tube in waste incinerator as a function of tube wall temperature (schematic). Adapted from Von Fa¨ßler, K.; Leib, H.; Spa¨hn, H. *Mitteilungen der VGB* **1968**, *48*, 126–139.

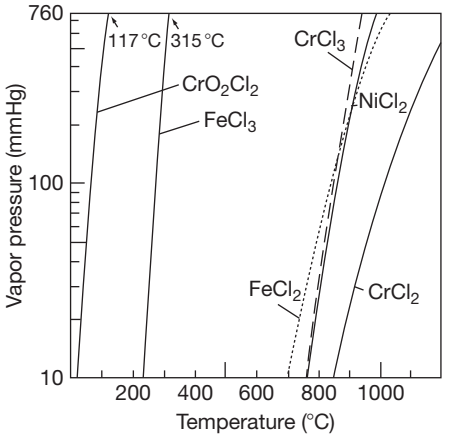

Figure 22 Vapor pressure of Fe, Cr, and Ni chlorides. Data taken from Kubaschewski, O.; Alcock, C.B. *Metallurgial Thermochemistry*, 5th ed.; Pergamon Press, 1979.

the corrosion occurring in real boilers.[43] Therefore, gas-phase corrosion by chlorine was proposed instead as the root cause for the corrosion since the corrosion rate of tube steel by chlorine gas is appreciably higher than hydrogen chloride.[41] Gaseous chlorine is never found in furnace flue gases. Therefore, local formation of chlorine gas in tube deposits through the following Deacon reaction:

$$4HCl + O_2 = 2Cl_2 + 2H_2O$$

was suggested.[41] Tube deposits were explained to function as catalyst of the Deacon reaction. Sulfur may corrode steels through the formation of sodium and potassium pyrosulfates ($(Na,K)_2S_2O_7$) of low melting points, which react with tube steels (and their protective oxide scales) to form liquid alkali iron trisulfates ($(Na,K)_3Fe(SO_4)_3$) at below 500 °C.[41] Gas-phase corrosion by chlorine, and corrosion by liquid phases are the early mechanisms.[40,41] According to this mechanism, corrosion of carbon steel boiler tubes by chlorine and sulfur occurs simultaneously. Corrosion products of these reactions are the corresponding iron chlorides ($FeCl_2$, Fe_2Cl_6), iron oxides (Fe_3O_4, Fe_2O_3), and iron sulfide (FeS) for steel boiler tubes.[40]

According to the Deacon reaction, increasing corrosion temperature should result in lowering the partial pressure of Cl_2, and hence would lead to a decrease in the corrosion rate of tube materials. However, in real furnaces, severe fireside corrosion of boiler tubes normally occurs when metal temperature of tube steels exceeds certain critical temperature, which depends on several factors such as tube location, operational conditions, boiler design, waste chemistry, etc.[44] This is apparently inconsistent with the model based on the Deacon reaction. In addition, in order to stabilize molten phases of pyrosulfate salts, high concentration of gaseous SO_3 (of more than several hundreds parts per million) is needed in the ambient flue gases (see **Figure 20**), which is apparently not the case in real waste incinerators. The concentration of SO_3 in flue gas of waste incinerators is normally below ppm level. Extensive field

tests conducted in the late 1990s revealed that fireside corrosion of boiler tubes becomes significant for the area where their metal temperatures exceed the melting point of tube deposits.[12,46] Most slag deposits contain not only sodium and potassium chlorides, but also chlorides and sulfates of heavy metals such as lead, zinc, tin, which can lower the melting point of tube deposits, down to below 300 °C.[12] Therefore, the corrosion can be interpreted as molten salt corrosion as well. In many cases, molten phase is indicated in tube deposits where fireside corrosion is prominent. Similar to fused sodium sulfate, acid–base equilibrium for chloride melts with hydrogen chloride and water vapor in flue gas is proposed,[46] and solubility measurements of major metal oxides in eutectic NaCl–KCl and NaCl–KCl–Na_2SO_4–K_2SO_4 melts as a function of the melt 'basicity' were performed experimentally.[47] Since tube deposits in waste incinerators generally contain considerable amounts of solid ash constituents such as $CaSO_4$, Al_2O_3, and SiO_2, which do not melt at tube metal temperatures, tube deposits are expected to be in partial fusion when corrosion reaction takes place. Laboratory test revealed that the corrosion rate of tube materials drastically increases when the tube deposits start to melt, and the enhanced corrosion rate is influenced by the volume faction of fused salts in tube deposits.[48] For more molten phases in the deposit, higher corrosion rate is expected. This is schematically illustrated in Figure 23. Therefore, enrichment of heavy metals such as lead and zinc in tube deposits will not only lower the melting points of the deposits, but may also augment the volume fraction of molten phases at a certain temperature, resulting in an increased corrosion rate for boiler tubes.

Generally, among iron, chromium, and nickel, iron and chromium have poor resistant to high temperature chlorine environments. This is interpreted from the ability to form highly volatile chlorides at low temperatures, for example, iron trichloride for iron and chromium oxychloride for chromium. This is shown in Figure 22. Corrosion resistance of steels and alloys in waste incinerators seems to follow this trend, and high-Ni alloys have normally good resistance to the environment. However, according to the field tests, chromium seems to be effective as well, which is different from the argument of chloride volatility. Nickel-base alloys with high chromium seem to perform well. It is interesting to note that the effect of molybdenum on corrosion is beneficial, which is opposite to those experienced for sulfate-induced corrosion. Corrosion resistance of steels and alloys seems to increase with increasing their Cr + Mo + Ni concentration, shown in Figure 24 for example. High-Cr, high-Ni, high-Mo alloys such as alloy 625 (22% Cr–61% Ni–9% Mo) are recognized to be resistant in this environment.

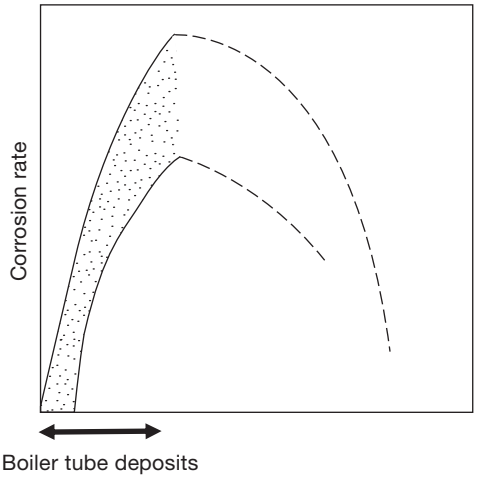

Figure 23 A schematic illustration explaining the effect of volume fraction of fused salts on corrosion.

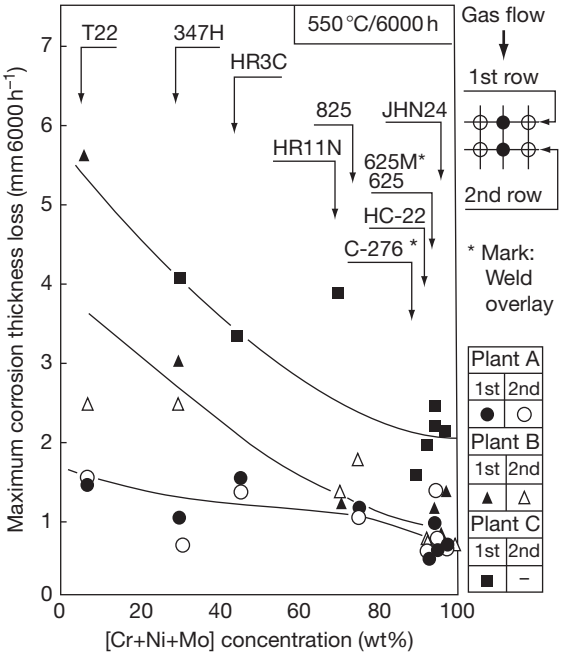

Figure 24 Tube wall thickness loss of corrosion probes as a function of alloy Cr + Mo + Ni concentration after exposure at 550 °C for 6000 h in waste incinerators. Reproduced from Kawahara, Y.; Orita, N.; Nakamura, M.; Ayukawa, S.; Hosoda, In Corrosion 97; NACE: Houston, TX, 1999; paper no. 91.

For black liquor recovery boilers, chloride salts are incorporated in superheater and reheater tube deposits, similar to those in waste incinerators.[49] However, their melting points are generally above 500 °C, considerably higher than the waste incinerators. This is attributed to the absence of heavy metals such as zinc and lead in the fuel. For black recovery boilers, stress corrosion cracking of their floor tubes seems to be the major concern.[50]

References

1. Stringer, J. *Mater. Perform.* **1993**, 53–59.
2. Fukahori, K.; Uera, H.; Harada, Y. *Therm. Nucl. Power* **1977**, *28*, 33–43.
3. Paul, L. D.; Seeley, R. R. In *Corrosion/90*; NACE: Houston, TX, 1990; Paper no. 267.
4. Borio, R. W.; Wilson, E. B. The control of high-temperature fire-side corrosion in utility coal-fired boilers, OCR R6D Report No.41, April 1969, Office of Coal Research, Department of the Interior: Washington, DC.
5. Simms, N. J.; Kilgallon, P. J.; Oakey, J. E. In Materials for Advanced Power Engineering 2006, Proceedings of the 8th Liège Conference Part III, Forschungszentrum Jülich GmbH Zentralbibliothek, Verlag, 2006; pp 1503–1512.
6. Stringer, J. *Ann. Rev. Mater. Sci.* **1977**, *7*, 477–509.
7. Nelson, W.; Cain, C., Jr. *Trans. ASME, Series A* **1960**, *82*, 194–204.
8. Otsuka, N. *Corros. Sci.* **2002**, *44*, 265–283.
9. Cunningham, G. W.; Brasunas, A. *Corrosion* **1956**, *12*, 389t–405t.
10. Cain, C.; Nelson, W. *Trans. ASME, Series A* **1961**, *83*, 468–474.
11. Levin, E. M.; Robbins, C. R.; McMurdie, H. F. *Phase Diagrams for Ceramists;* The American Ceramic Society, 1964; Vol. I, p 495.
12. Daniel, P. L.; Paul, L. D.; Barna, J. In Corrosion/1987; NACE: Houston, TX, 1987; Paper no. 400.
13. Edström, J. O. *JISI* **1957**, *185*, 450–466.
14. Kofstad, P. *High Temperature Corrosion;* Elsevier Applied Science, 1988.
15. Weast, R. C.; Astle, M. J.; Beyer, W. H. *CRC Handbook of Chemistry and Physics*, 68th ed., CRC Press: Boca Raton, FL, 1987; pp D189–D190.
16. Armitt, J.; Holmes, R.; Manning, M. I.; Meadowcroft, D. B.; Metcalfe, E. The spalling of steam-grown oxide from superheater and reheater tube steels, EPRI FP-686, TPS 76-655, Final Report, February 1978.
17. Bakker, W. T. Mixed oxidant corrosion in nonequilibrium syngas at 540 °C EPRI TR-104228, March 1995.
18. Mrowec, S.; Werber, T. In *Corrosion of Metals*; Department of Commerce, National Technical Information Service, 1978; Chapter 13, pp 444–474.
19. Young, D. J. *Rev. High-Temp. Mater.* **1980**, *4*(4), 299–346.
20. Gutzeit, J. In *Process Industries Corrosion – The Theory and Practice*; Moniz, B. J., Pollock, W. I., Eds.; NACE: Houston, TX, 1986; pp 367–372.
21. Rapp, R. A. *Corrosion* **1986**, *42*, 568–577.
22. Hansen, W. A.; Kessler, G. W. *Trans. ASME* **1965**, *87*, 210–214.
23. Cutler, A. J. B.; Flatley, T.; Hay, K. A. *Metallurgist and Materials Technologist*, 1981, February, pp 69–81.
24. Demo, J. J. *Mater. Perform.* **1980**, *19*, 9–15.
25. Harada, Y.; Nakamori, M. *Boushoku Gijutsu* **1980**, *29*, 615–621.
26. Alexander, P. A.; Marsden, R. A.; Nelson-Allen, J. M.; Stewart, W. A. *J. Inst. Fuel* **1964**, *37*, 59–69.
27. Holland, N. H. *J. Inst. Fuel* **1970**, *43*, 97–103.
28. Marruffo, F.; Chirinos, M. L.; Sarmiento, W.; Hernandez-Carstents, E. In *17th Congress of the World Energy Council, Division II,* 13–18 September; World Energy Council: Houston, TX, 1988; Vol. 73, pp 73–87.
29. Plumley, A. L.; Jonakin, J.; Vuia, R. E. A review study of fire-side corrosion in utility and industrial boilers, Presented at Corrosion Seminar at MacMaster University and Engineering Institute of Canada, Hamilton, Ontario, 19–20 May 1966.
30. Blazewicz, A. J.; Gold, M. *An ASME Publication 79-WA/Fu-6,* The American Society of Mechanical Engineers, 1979.
31. Blough, J. L.; Stanko, G. J.; Bakker, W. T. In *Ultra-Supercritical Power Plants,* CORROSION/2000, NACE: Houston, TX, 2000, Paper no. 250.
32. Luthra, K. L.; Shores, D. A. *J. Electrochem. Soc.* **1980**, *127*(10), 2202–2210.
33. Fukuda, Y.; Sato, T.; Hamada, H.; Sakaguchi, Y. In *Proceedings of the 32th Meeting of the Japanese Society of Corrosion Engineering,* August 1985, Sapporo, B-302, pp 239–246.
34. Simons, E. L.; Browning, G. Y.; Liebhafsky, H. A. *Corrosion* **1955**, *11*, 505t–514t.
35. Otsuka, N.; Rapp, R. A. *J. Electrochem. Soc.* **1990**, *137*, 46–52.
36. Rapp, R. A.; Goto, K. S. In *Proceedings of the 2nd International Symposium on Molten Salts;* Braunstein, J., Ed.; The Electrochemical Society: Pennington, NJ, 1979; pp 159–177.
37. Pettit, F. S.; Meier, G. H. In *Oxidation and Corrosion of Superalloys*; Superalloys 85, The Metallurgical Society of AIME: Warrendale, PA, 1985; pp 651–687.
38. Goebel, J. A.; Pettit, F. S.; Goward, G. W. *Met. Trans.* **1973**, *4*, 261–278.
39. Coats, A. W.; Dear, D. J. A.; Penfold, D. *J. Instit. Fuel* **1968**, *41*, 129–132.
40. Krause, H. H. *J. Mater. Energy Syst.* **1986**, *7*(4), 322–332.
41. Von Fäßler, K.; Leib, H.; Spähn, H. *Mitteilungen der VGB* **1968**, *48*(2), 126–139.
42. Von Huch, R. *Bresnnst.-Wärme-Kraft* **1966**, *18*, 76–79.
43. Brown, M. H.; DeLong, W. B.; Auld, J. R. *Ind. Eng. Chem.* **1947**, *39*, 839–844.
44. Wright, I. G.; Krause, H. H.; Dooley, R. B. In *Corrosion/95*; NACE: Houston, TX, 1995; Paper no. 562.
45. Krause, H. H.; Wright, I. G. In *Corrosion/95*; NACE: Houston, TX, 1995; Paper no. 561.
46. Otsuka, N.; Kudo, T. In *High Temperature Corrosion of Advanced Materials and Protective Coatings*; Saito, Y., Önay, B., Maruyama, T., Eds.; North-Holland: Tokyo, Japan, 1992; pp 205–211.
47. Ishitsuka, T.; Nose, K. *Mater. Corros.* **2000**, *51*, 177–181.
48. Otsuka, N.; Tsukaue, Y.; Nakagawa, K.; Kawahara, Y.; Yukawa, K. In *Corrosion/97*; NACE: Houston, TX, 1997; paper no.157.
49. Tran, H. N.; Barham, D.; Hupa, M. *Mater. Perform.* **1988**, *27*(7), 40–45.
50. Barna, J. L.; Mattie, R. J.; Rogan, J. B.; Allison, S. F. *Pulp Paper* **1989**, *63*(6), 90–98.

1.15 High Temperature Tribocorrosion

I. A. Inman, P. S. Datta, and H. L. Du
Ellison Building, Northumbria University, Newcastle upon Tyne, NE1 8ST, UK
C. Kübel
Group Leader Electron Microscopy, Forschungszentrum Karlsruhe, Institute for Nanotechnology, Postfach 3640, 76021 Karlsruhe, Germany
P. D. Wood
Ricardo Plc, Shoreham Technical Centre, Shoreham-by-Sea, West Sussex, BN43 5FG, UK

Glossary

Abrasion The removal of material from a solid surface by the mechanical action of another solid. The second solid may be in the form of a second body (the opposing sliding surface) or third body (wear debris).

Abrasive wear The removal of surface material from an object by the action of another agent or medium. This may be the surface of another object or by hard particles trapped between the two interacting surfaces – referred to as 'two body' and 'three body' abrasion respectively. The hard particles or surface must be 1.3 times harder than the soft material from which material is removed.

Adhesion/cohesion The action of intermolecular forces at surfaces or interfaces in close contact, holding those surfaces together. Such forces may include chemical bonding (chemical adhesion), intersolubility (diffusive adhesion), Van der Waals forces (dispersive adhesion) and electrostatic forces (electrostatic adhesion). Surface interlocking may also occur (mechanical adhesion) via material filling surface voids or pores. Adhesion is of greater influence during contact of clean metallic surfaces (and thus during severe wear), as there are no contaminants to prevent this contact. Adhesion is also more effective in a vacuum, where there is no surrounding atmosphere to affect it. Adhesion is normally used to describe attraction between dissimilar molecules and cohesion between like molecules.

Asperity A protruding, raised area of (sliding) surface.

Block-on-cylinder A test configuration used to study unidirectional sliding wear, with the 'block' (either stationary or in reciprocating motion) as the sample material and the 'cylinder' (normally rotating) as the counterface.

Coefficient of friction Dimensionless value describing the resistance experienced by two surfaces in movement against each other. The higher the value, the greater the ability to resist movement. The 'frictional force' is that which needs to be applied to overcome this resistance to movement.

Compacted oxide layer Often wear-protective layers of oxide are formed as a 'tribocorrosion' product, when two metals (or a metal and ceramic) are slid against each other at high temperature in an oxygen-containing atmosphere.

Compacted particles Debris forming a compacted oxide layer.

Counterface (countersurface) The material or surface sliding against the sample.

Critical oxide thickness (ξ) According to Quinn's oxidational wear model,[1] this is the maximum thickness of compacted oxide layer or 'glaze' that can develop and remain mechanically stable. Beyond this, the oxide becomes unstable, generating a wear particle.

Critical transition temperature The minimum temperature according to Jiang[2] at which sintering can occur within a compacted oxide layer, allowing a solid wear-protective layer (or 'glaze') to form on top of it before it is broken down.

Cross-slip Transfer of (screw) dislocation glide from one slip plane to another during deformation.

Cutting The physical deformation due to a harder asperity or third body being pushed through a softer material where adhesion is high. The movement of the harder material over the softer material results in the creation of a deeper groove upon the sample surface than seen with 'wedge-forming' or ploughing, with long strips of debris forming at the point of contact.

Dissimilar interface system A configuration where the sample and counterface are of different materials.

Ejection The removal of wear debris from the sliding wear interfaces such that it can no long play an 'active' part in the wear process.

Fretting Damage due to repeated relative motion of sliding surfaces against each other, for example, due to vibration or oscillation.

Glaze Compacted oxide layer, usually referring to a more wear protective, sintered form generated (normally) at elevated temperatures.

High angle annular dark field in STEM Images formed by gathering scattered electrons with an annular dark field detector. An 'annular dark field' (ADF) image generated only by very high angle, incoherently scattered electrons, is highly sensitive to variations in atomic number of the elements in the sample (Z-contrast images) and is hence known as 'high angle annular dark field' or HAADF.

HIPped (hot isostatically pressed) A method of alloy or material production by powder metallurgy methods, using a combination of temperature and (isostatic) pressure to produce the final item.

Intermetallic Materials composed of defined proportions of two or more metallic elements and possibly one or more nonmetallic elements. Such materials typically have a highly ordered crystal lattice structure composed of the constituent parts, but not necessarily the same as any of the constituent parts.

Ion-implantation The implantation of ions of one material into the crystal lattice of another solid, thereby bringing about a desired change in the physical properties of that solid (i.e., doping).

Material transfer Transfer of material at the wear interface from one wear surface to the other.

Mechanical alloying The mixing of two or more solid phase materials to produce material of different composition and possibly phase to either of the original materials. During sliding wear (i.e., severe wear), this may happen where the two parent sliding surfaces are of different composition, due to material transfer between and mixing at the sliding interface. This mechanically alloyed material may then potentially readhere to either parent sliding surface.

Mild wear Wear in which direct contact between the sliding surfaces are separated by corrosion debris (generally oxide), often less than 1 μm diameter. This debris may take the form of compacted oxide or 'glaze' layers. Where the two sliding surfaces are metallic, the debris being generally nonmetallic prevents adhesion and (metallic) transfer. Coefficient of friction values are thus usually much lower. Wear values are generally, but not always, lower than severe wear, however, such debris can act abrasively and instead enhance wear.

'Orowan' stress The stress required to bow a dislocation between particles or impurities, acting as obstacles within a crystal lattice.

Oxide dispersion strengthened (ODS) alloy An alloy in which a fine dispersion of oxides have been introduced, to strengthen the material

by interfering with the operation of slip systems during material deformation.

Phase transition Thermally or mechanically induced change in crystallographic structure, for example, from 'face-centered cubic' to 'body-centered cubic' in iron or mild steel, or 'face-centered cubic' to 'hexagonal close-packed' in cobalt-rich alloys

Pin-on-disk A test configuration used to study sliding wear, with the 'pin' (or in some cases 'button' or 'coupon') as the sample material and the 'disk' as the counterface. The 'pin' may be held stationary against a rotating 'disk' to study unidirectional sliding wear, or moved backwards and forward against a stationary 'disk' to study reciprocating or fretting wear.

Ploughing A general term, covering the three related terms of 'ploughing,' 'wedge-forming' and 'cutting,' being defined as the physical deformation due to a harder material ploughing through a softer material or rather the work required to carry this out. Ploughing is also referred to more specifically as the physical deformation due to a harder material being pushed through a softer material where adhesion forces are weak. The grooves created are shallower than with 'cutting' or 'wedge-forming,' with lower penetration of the harder asperity or third body into the softer material. Formation of wear debris particles cannot be clearly seen at the point of contact.

Positron annihilation (PA) A major technique in Materials Science, originally applied in condensed-matter physics, now widely used in metals and alloys to provide information on defect structures.

Retention The continued residency of wear debris at the wear interface, such that it may continue to play an active part in the wear process.

'Run-in' wear A normally brief period of severe wear due to initial metal-to-metal contact almost always observed before mild wear is established.

Sample The material or surface undergoing wear testing.

Scanning electron microscopy (SEM) A type of microscope in which the surface of a sample is scanned with a high energy beam of electrons. An image of the sample surface is created from secondary electrons that are ejected from it.

Scanning transmission electron microscopy (STEM) A variation of TEM in which the electrons pass through the specimen and the electron optics focus the beam into a narrow spot over the sample in a raster. The rastering of the beam across the sample is used to perform various analyses such as annular dark field (ADF) imaging, energy dispersive X-ray (EDX) analysis and electron loss spectroscopy (EELS) simultaneously, allowing direct correlation of image and quantitative data.

Scanning tunneling microscopy (STM) An imaging technique based on the concept of quantum tunneling. In STM a conducting surface is brought very near to the surface (metallic/semiconductor) when a bias between the two allows electrons to tunnel through the vacuum between them. At low voltage the tunneling current is a function of local density of states (LODS) at the Fermi level of the sample. The changes in current accompanying the tip movement over the surface are translated into an image.

Scanning tunneling spectroscopy (STS) A technique employed within an STM, to probe the local density of electronic states, and band gap of surfaces and materials on surfaces at the atomic scale. The technique allows observation of changes in constant current topographies with tip-sample bias, local measurements of *IV* curves and tunneling conductance d*I*/d*V*. This allows investigations of small areas (5 Å diameter, the area in which the tunneling current flows).

Scuffing Roughening of surfaces by plastic flow, whether or not there is material loss or transfer.

Selected area diffraction pattern (SAD) This technique is generally performed inside a TEM, in which electrons pass through a thinned sample (see 'TEM'). As the wave length (a fraction of a nanometer) and the spacing between atoms are comparable, the atoms act as diffraction gratings to the electrons. Some of the electrons are scattered to particular angles determined by the material crystal structures (allowing

identification and analysis) and form a spot pattern image on the TEM screen.

Severe wear The wear encountered typically where two metallic surfaces are in direct sliding contact, without an intervening compacted oxide or 'glaze' layer, or other protective coating. Such wear is characterized by high coefficient of friction values, high levels adhesion, plastic deformation and to varying degrees (mainly metallic), material transfer between the surfaces. Also typical of severe wear is the generation of large, flat, angular, generally metallic wear debris with sizes of up to 0.1 mm (or greater) due to 'delamination.'

Slip direction The direction on the slip plane with the highest linear density.

Slip plane The crystallographic close packed plane in which dislocation movement can occur.

Slip system A combination of slip planes and directions defined by crystallographic arrangement (i.e., body-centered cubic, face-centered cubic, hexagonal close-packed).

'Third body'/'three body' wear The interaction of two wear surfaces during sliding, in combination with a third agent (i.e., debris). This third agent may be termed 'active' (it is retained between the wear surfaces and modifies the wear process) or 'passive' (it is ejected and has no effect).

Torque transducer A device for measuring torque in a rotating system. In tribology, changes in torque due to sliding surface contact can be used to determine the coefficient of friction.

Transmission electron microscopy (TEM) A widely used technique in Materials Science where an electron beam is transmitted through a thinned sample placed in vacuum with a typical energy of 100–400 keV. The electron beam is then focused by a series of magnetic field lenses into a typical spot of diameter 1–10 nm. A TEM image is created from those electrons that pass through the sample.

Tribocorrosion, tribo-oxidation The enhanced generation of corrosion product (normally oxide) during sliding wear. The conjoint action of tribology and corrosion/oxidation.

Tribology The study of the science and technology of interacting surfaces in relative motion, and including the related subjects of lubrication, friction and wear. Derived from the Greek verb τριβο ('tribo'), meaning 'to rub.'

'Two body' wear The interaction of two wear surfaces during sliding, in the absence of a third agent (i.e., wear debris) between the wear surfaces.

Unidirectional sliding Where the sample and counterface move in only one direction relative to each other.

Van der Waals' forces Attractive forces between unbonded atoms and molecules (significant for very small particles of less than 5 μm in diameter).

Vickers hardness number (VHN) A parameter defining the hardness of an engineering material. The Vickers hardness number is that obtained by application of a predefined load through a diamond pyramidal (or Vickers) indenter. The size of the indent created is used to obtain a measure of materials' hardness.

Wear behavior, wear regime, wear mechanism The type of wear observed (i.e., mild or severe wear).

Wear debris The material removed from sliding surfaces during wear. This may be metallic (dominant during severe wear) or oxide (dominant during mild wear).

Wear map, wear mechanism map A plot that shows the effect on wear mechanism of two or more sliding variables (i.e., load, temperature, sliding speed), allowing prediction of wear mechanism where the values of these variables are known.

Wear rate The rate of material removal during sliding.

Wear volume The volume of material removed during sliding.

Wedge-forming The physical deformation due to a harder asperity or third body being pushed through a softer material where adhesion is moderate. Material is pushed up ahead of asperities on the counterface, resulting in a grooved wear scar with transverse cracks. The depth of groove created is lower than for the 'cutting' model, but higher than for 'ploughing.'

Symbols

d Distance for which sliding contact is maintained
f Mass fraction of oxide
p Mean pressure (load/area)
r Distance affecting mutual action of Van der Waals' forces
t i) Time of sliding
ii) Time required to grow oxide layer of critical thickness
v Speed
A i) True area of contact
ii) Hamaker constant
A_p Arrhenius constant
D Depth of wear
E Activation energy for bonding
F i) Force of attraction
ii) Contact frequency
H i) Material indentation hardness
ii) Indentation hardness
K_a Probability of a wear particle being generated
K_p Oxidation rate (parabolic rate constant)
K_1 '*K* factor' ($K_1=K_a/H$)
K_{1c} Fracture toughness
L Sliding distance
P Applied load
Q_p Activation energy for oxidation
R i) Radius of particle of sphere
ii) Gas constant
T, T_o Temperature in Kelvin (absolute temperature)
V Sliding speed
W Work volume
γ Surface energy
γ_o Surface energy at standard temperature and pressure
ρ Oxide average density
τ Length of time of each encounter (contact between surfaces)
ξ Critical oxide layer thickness
Δm Growth of oxide per unit area
$1/K_a$ Number of encounters (contacts between surfaces) required to generate an oxide layer of critical thickness

1.15.1 Introduction

High temperature wear is a serious problem in many situations, including power generation, transport, materials processing, and turbine engines.[3–7] Such wear is accentuated by faster surface oxidation kinetics, loss of mechanical hardness and strength of materials forming the contacting surfaces, and changes in adhesion between these surfaces caused by the joint action of temperature and tribological parameters. Efforts to prevent wear have included the use of oxidation resistant and thermally stable materials, coatings, and materials with preoxidized surfaces.[3–10] However, the choices of coatings and materials are severely restricted by high temperature environmental conditions.[3–5]

An alternative method of generating wear-resistant surfaces on coated and uncoated materials is to take advantage of certain events that accompany the high temperature wear process, such as oxidation, debris generation, and elemental transfer between contacting surfaces.[3–5,11] These events under certain conditions of temperature, pressure, and speed can lead to 'glaze' formation on contacting surfaces, enhancing resistance to further wear.[2–5,11–30] Although 'glaze' formation and the general issues relating to wear at elevated temperatures have been extensively studied,[2–5,11–30] it is still difficult to predict the precise conditions that promote 'glazed' surface formation. Many aspects of high temperature wear, including debris generation, debris oxidation, material transfer between surfaces, and enhanced elemental diffusion, still need clarification. At present, there is incomplete understanding of the formation, nature, microstructure, and defect structure of high temperature wear-resistant surface 'glaze.'

This chapter is not intended to catalogue all previous work. Instead, the objective is to concentrate on generic principles, modeling, and scientific theories, which where possible will facilitate understanding of the high temperature wear process. There is a heavy reliance on the information generated in the authors' own laboratory, where extensive use has been made of current microscopical techniques.

The chapter is structured as follows: Section 1.15.2 deals with some general principles of wear, Sections 1.15.3 and 1.15.4 consider published research while Section 1.15.5 discusses some results of nanoscale investigations of 'glaze' formation; Section 1.15.6 concludes with some final remarks.

1.15.2 Wear Theory

1.15.2.1 Early Wear Theory

1.15.2.1.1 Archard and Hirst – Distinction between mild and severe wear

In 1956, Archard and Hirst[31,32] categorized wear into two groups: mild wear and severe wear.

'Mild wear' occurs when the debris produced (generally oxide) prevents direct metal-to-metal contact. Although Quinn[33] does not specifically mention

the oxidation reaction in his review of oxidational wear when discussing the definition of mild wear, the majority of studies into sliding wear have concentrated on the oxidation reaction. Debris produced is of very small size (<1 μm) and complete coverage is not necessarily achieved, with oxide in many cases only forming on load-bearing areas such as asperities. Electrical contact resistance is high because of the presence of the oxide on the wear surfaces.

The absence of such oxides allows contact between the metallic interfaces, with adhesion, plastic deformation, and, to varying degrees, material transfer between the surfaces. This is typical of the 'severe wear' situation, examples of which have already been observed in the lower temperature sliding wear of Incoloy MA956 against Incoloy 800HT, in the work of Wood[3] and Rose[4] (these authors refer to these alloys as MA956 and Incoloy 800); the 270 °C case shown in **Figure 1** is one such example. Debris particles tend to be large, flat and angular, up to 0.1 mm or greater. Contact resistance on surfaces that have undergone severe wear tends to be very low, due to the exposure of the metallic surface.

Temperature affects the nature of wear as it influences the kinetics of oxidation. Other factors such as relative humidity[34] and partial pressure of oxygen also affect the nature of wear as explained by Lancaster[26] and Stott *et al.*[14,35] **Figure 2** shows a smaller range of severe wear in an oxygen atmosphere at 300 °C, compared to that in air.

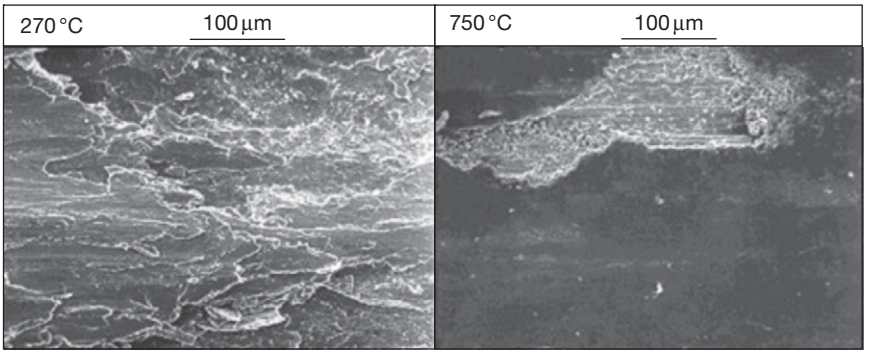

Figure 1 Wear surfaces produced during the sliding of Incoloy MA956 against Incoloy 800HT at 270 and 750 °C[4] (load = 7 N, sliding speed = 0.654 m s^{-1}, sliding distance = 9418 m). At 270 °C, a highly worn, heavily deformed surface is produced. There is direct metal-to-metal contact, allowing high levels of adhesion accompanied by plastic deformation, material transfer and the production of large flat angular debris. At 750 °C, a compacted oxide layer has been created from the debris, giving physical protection via enhanced hardness and also separating the metallic surfaces, preventing contact and adhesion.

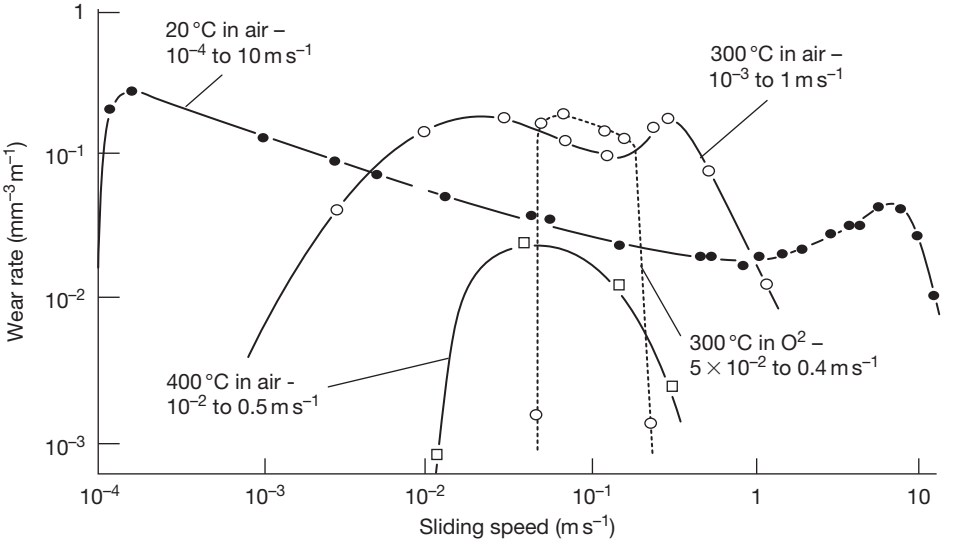

Figure 2 Variation in wear rate with sliding speed at 20, 300, and 400 °C in air and also 300 °C in pure oxygen for α/β brass sliding against steel[26] (approximate sliding speed ranges for severe wear at each temperature given in italics).

The model that Archard and Hirst[31] proposed assumes a true area of contact, occurring between a small number of asperities on the contacting surfaces. The true area of contact can be calculated by eqn [3]:

$$A = P/H \quad [1]$$

where P is the applied load and H is the indentation hardness of the material. If W is the worn volume and L is the sliding distance producing the wear, then W/L is dependent on, and is therefore proportional to, the area of the friction junctions or true area of contact.

$$W/L \propto A \quad \text{or} \quad W/L = K_a L \quad [2]$$

This gives:

$$W/L = K_a P/H \text{ or } W = K_a PL/H \quad [3]$$

the dimensionless parameter K_a being the constant of proportionality and also the probability of a wear particle being generated. It is also referred to as the 'wear coefficient.' An alternative form ($K_1 = K_a/H$) is:

$$W = K_1 PL \quad [4]$$

K_1 being referred to as the 'K factor.'[31] Taking eqn [3] and rearranging allows K_a to be expressed in terms of wear depth, sliding velocity, and pressure.

Dividing by the apparent area of contact gives:

$$d/L = p(K_a/H) \quad [5]$$

where d is the depth of wear (volume divided by area) and p is the mean pressure (load over area). If v is sliding speed and t is the time of sliding, $L = vt$, then

$$d/vt = p(K_a/H) \text{ or } t = dH/K_a pv \quad [6]$$

$$K_a = dH/pvt \quad [7]$$

The above implies that the level of wear is proportional to the sliding distance and applied load; Archard and Hirst showed this to be true over a limited range[31] (**Figure 3**).

The Archard model[31] is effective assuming that there are no changes in the wear surface as a result of the sliding process. However, changes do occur in many cases, leading to changes in wear rate resulting from little or no variation in experimental or operational parameters,[27,28,36,37] and thus, changes in K_a value may be observed. Previous experimental work[3–5] has demonstrated that such changes can occur, with changes in friction being coincident with a switch from early severe wear to mild oxidational wear, without any alteration of experimental parameters. This was usually denoted by decreases in the mean coefficient of friction and also in the variability of the coefficient of friction versus time trace. For example, during early severe wear at 750 °C, mean values typically between 0.7 and 1 could be obtained for Nimonic 80A versus Incoloy 800HT. On reaching the mild wear stage, values of between 0.4 and 0.5 were typically obtained.

A direct link between hardness and wear rate is not always observed. Archard and Hirst proposed the theory of mild and severe wear discussed in this section, to resolve these difficulties.[31]

1.15.2.1.2 Classification by mechanism

Many approaches to classifying wear have been attempted; Quinn's 1983 review[33] lists a number of these and tries to classify them under Archard and Hirst's mild and severe wear[31] headings (**Table 1**). For example, Burwell and Strang[38] propose seven different classifications of mild and severe wear, which Quinn argues are actually special cases of Archard and Hirst's mild and severe wear (with many of their classifications, including elements of both).[31] Ludema[39] talks in terms of 'scuffing' ('roughening of surfaces by plastic flow, whether or not there is material loss or transfer') and 'run-in,' Quinn seeing 'scuffing' as a form of adhesive wear and 'run-in' as corrosive or mild wear (due to the generation of oxides on the wear surface). Finally, Tabor[40] does not distinguish between adhesive and corrosive wear, preferring to classify both as adhesive wear, with Burwell and Strang's remaining mechanisms being referred to as 'nonadhesive wear' (surface fatigue, abrasion, and fretting) or a mixture of both (cavitation and erosion).

The classification of wear mechanisms clearly remains a matter of debate, although Quinn[33] proposes that each of the forms of wear described should be considered in terms of either mild or severe wear in any given situation. However, it is the view of the current authors that it is not possible to talk simply in terms of mild and severe wear. For example, when material is lost by abrasion, the loss of material by the ploughing action of asperities on a wear surface does not necessarily require adhesion or corrosion to remove material. Also, loss of material by delamination wear is a fatigue-related process, caused by repeated loading and unloading of surface layers as asperities of the opposite surface pass over it, assisting the propagation of subsurface cracks, eventually leading to material loss. Although adhesion or reaction with a corrosive environment may accelerate the process, again neither is necessary for fatigue and crack propagation to occur.

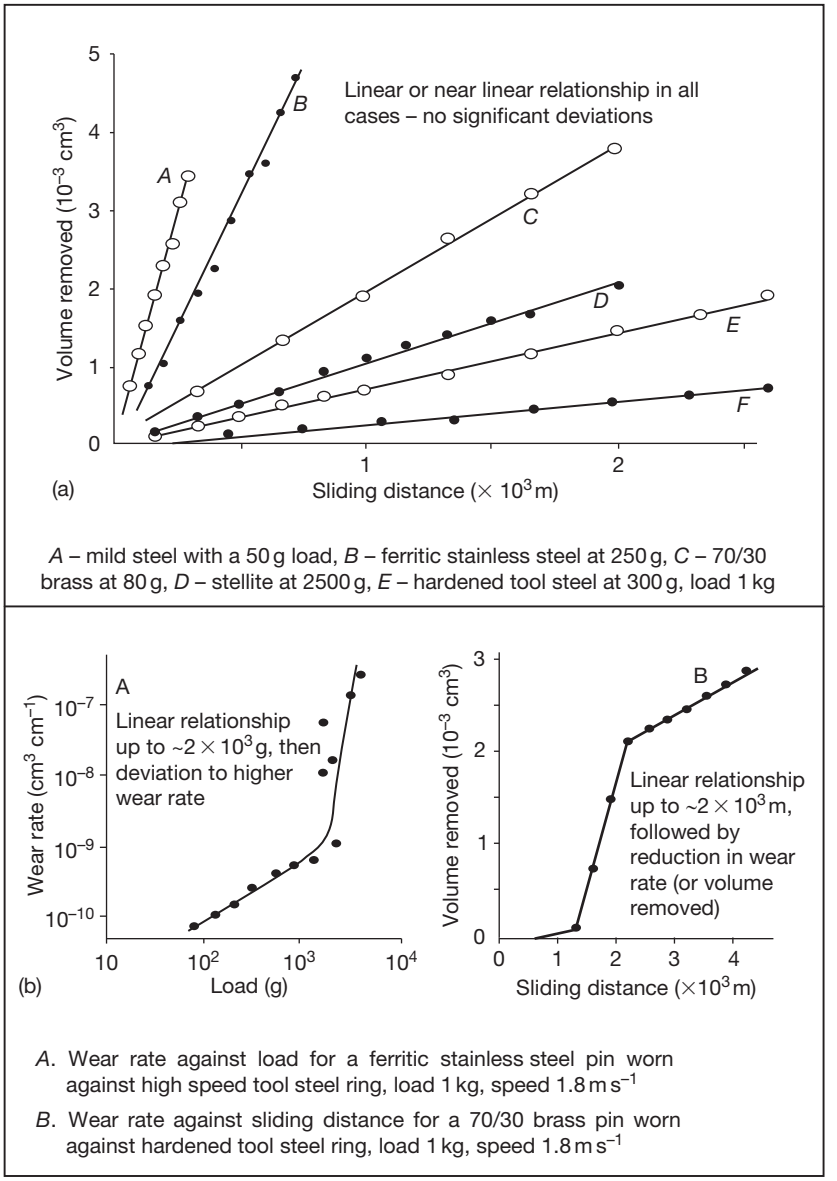

Figure 3 Experimental data from Archard and Hirst's Work on like-on-like sliding at 1.8 m s^{-1}. Reproduced from Archard, J. F.; Hirst, W. *Proc. Royal Soc. London A* **1956**, *236*, 397–410.

Table 1 Quinn's comparison of the various classifications of wear

Burwell and Strang [25]	*Tabor*	*Ludema*	*Quinn [16]*
Adhesive wear Corrosive wear	Adhesive wear	Scuffing ''Run-in''	Severe wear Mild wear
Surface fatigue (pitting) Abrasion Fretting	Nonadhesive wear	Mechanisms of scuffing and ''run-in''	Mechanisms of mild and severe wear
Cavitation Erosion	Mixtures of adhesive and non-adhesive wear	Not covered in Ludema's review	

Source: Reproduced from Quinn, T. F. J. *Tribol. Int.* **1983**, *16*, 257–270.

The different behaviors of oxide debris are not accounted for either. Inman *et al.*[5,21–24] observed that during sliding wear, an oxide could either be protective or abrasive or even in limited quantities affect the severe wear process. It was thus suggested that mild and severe wear could be subcategorized into 'standard severe wear' (no oxide present, adhesion and delamination dominating), 'abrasion-assisted severe wear' (oxide abrasively assists the adhesion/delamination dominated wear process), 'protective mild wear' (oxide prevents metallic contact and forms a protective layer as loose debris or 'glaze'), and 'abrasive mild wear' (oxide debris prevents metallic contact, but remains loose and promotes wear by abrasion).[24] Another suggested classification system is that of Rabinowicz,[41] who identifies abrasive and fatigue wear, as well as adhesive and corrosive wear, as distinct categories of wear in their own right. Each of these four categories of wear is now discussed.

1.15.2.2 'Two and Three Body' Wear

1.15.2.2.1 Overview

Much of the discussion so far has been concerned with what happens when two surfaces move relative to one another, generating wear debris. The consideration of wear without the interaction of debris is referred to as 'two body' wear. However, the generation of debris particles introduces a 'third body' into the sliding process, which can then go on to have a significant effect on the wear process.

This debris may be retained within the interface area, where it may become an 'active' participant[42] in the wear process or may be ejected immediately after its formation, in which case, it is referred to as 'passive' debris. Active debris tends to be fine and may be a mixture of metallic and oxide particles. On the other hand, 'passive' debris particles are in general much larger and, because of their immediate removal from the wear interface on formation, may retain much of their original form and structure. In metallic wear, 'passive debris' is more likely to be metallic.

The work of Rose[4] and Inman *et al.*[5,21–23] clearly illustrates this difference. For sliding of Nimonic 80A and Incoloy MA956 versus Stellite 6, at lower temperatures (390 °C and lower at 0.654 m s^{-1}, 270 °C and lower at 0.905 m s^{-1}), debris particles tended to be of a fine nature; these were largely retained at the interface, commuted, and converted to a layer of loose, discrete (usually) oxide particles. The retention of this debris as a 'third body' then acted to keep the interfaces separated and wear values low. This is an example of 'active' debris.

At intermediate temperatures up to 630 °C for Nimonic 80A versus Stellite 6 and 510 °C for Incoloy MA956 versus Stellite 6, debris was ejected as larger metallic particles that did not remain at the wear interface and thus did not separate the two wear surfaces. This is an example of 'passive' debris.

At higher temperatures, larger amounts of fine oxide debris were generated; in the case of Incoloy MA956 versus Stellite 6, this again separated the interfaces and also formed protective compacted oxide or 'glaze' layers. Nimonic 80A slid against Stellite 6 also formed protective layers at 0.314 m s^{-1}; however, at 0.654 and 0.905 m s^{-1}, wear levels increased because of oxide debris acting abrasively against the Nimonic 80A surface. These latter observations are once again examples of 'active' debris.

In addition to promoting mild wear, the negative effect of abrasion has also been noted; as with hard and soft surfaces in the two body wear models already discussed, for a third body to have an abrasive effect at the wear interface possibly leading to increased wear, it is normally expected that the hardness of the third body will be at least 1.3 times greater than that of either of the contacting materials.[33]

Active participation of third bodies has been noted by other researchers, notably Iwabuchi *et al.*,[43–45] who studied the effects of the introduction of iron oxide (Fe_2O_3) particles to the wear interface, noting that, where the particles were supplied under fretting test conditions, the severe running-in wear volume for a standard carbon steel (S45C) was decreased 10-fold.[45] Increased surface roughness also proved to be a positive factor in that the particles were more effectively retained. Introduction of a large enough quantity of Fe_2O_3 particles eliminated the severe wear running in stage.

Iwabuchi also studied the effects of particle size[43] and found that with a surface roughness of maximum asperity height 20 μm, a particle size of 0.3 μm (the smallest studied) was found to give the lowest wear rate during mild wear. However, particle sizes of 1 μm were observed to decrease the wear rate in the severe wear stage the most. Ideally, the same size particle would result in both; for practical use to be made of such observations, a compromise needs to be made. It is also to be noted that Iwabuchi expressed uncertainty as to whether the 0.3 μm particle size is the most effective only for the 20 μm maximum asperity height or for other asperity heights as well.

The current authors suggest that the optimum size will vary and also change as the wear test proceeds, for the simple reason that, as the larger asperities are

removed, until such time as an oxide layer forms, the particle size that can be contained in the recesses will also decrease. Conversely, during severe wear, roughening of the wear surface may allow for a larger particle size to be retained. A limiting factor is that there will probably be an upper limit of particle size, partially due to comminutation and ejection of larger debris and also a limit to the size of particle that can convert from metal to oxide.

Iwabuchi also points out that the tendency to form a protective compacted layer of oxide is affected by other parameters; varying test parameters such as load and sliding speed showed that, for certain conditions, the oxide particles acted as an abrasive and increased the wear rate. **Figure 4** is a wear map of load versus amplitude, where different combinations of load and amplitude produce different outcomes as regards the influence of the introduced oxide particles.[42] For very low loads and amplitudes, the introduction of the oxide particles has a positive effect, lowering the level of wear. For medium loads and amplitudes, the oxides have a negative effect and wear levels are higher because of the abrasive action of the oxides. Moreover, increasing load for moderate amplitude or amplitude for moderately high load again results in a positive influence and wear levels are low.

Leheup and Pendlebury[46] took a different approach, by the use of an interfacial air flow in a like-on-like 'cup-on-flat surface' sliding test at various temperatures for Fe–18% Cr–9% Ni stainless steel. The effect of temperature was quite marked, with removal of the debris at room temperature leading to increased wear. At temperatures of 400 and 500 °C, formation of compacted oxide layers did still occur; this was considered to be due to the ready sintering and adherence of the loose oxide particles at these temperatures. The attractive effects of Van der Waals' forces (acting to retain smaller particles between the wear surfaces) were also considered, as detailed in **Sections 1.15.2.2.3** and **1.15.2.2.4**. Colombie *et al.*[47] obtained similar results with increased wear on blowing nitrogen through the wear interface at frequent intervals; the more frequent the intervals, the greater the observed wear. Magnetic fields can also have an effect with ferromagnetic materials; Hiratsukam *et al.*[48] showed that the field direction could influence whether debris was retained (thus decreasing wear) or ejected (thus increasing wear).

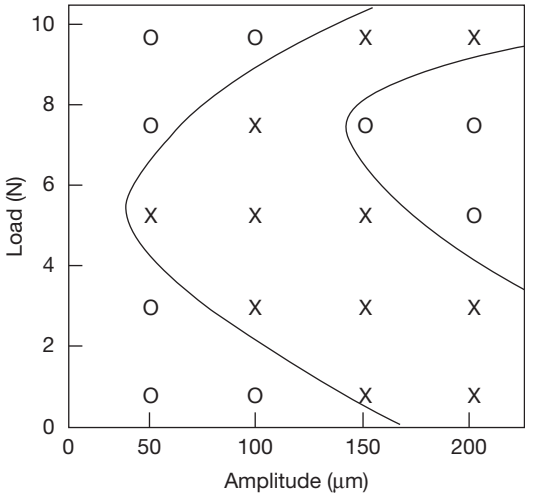

Figure 4 Effectiveness of wear reduction on S45C plain carbon steel due to the introduction of Fe_2O_3 particles.[42] (○) Positive effect, oxide separates wear surfaces and wear is low, (×) negative effect, oxide acts as an abrasive and increases wear.

Rigney[49] also questioned the validity of the traditional models of wear if they do not take into account third bodies resulting from transfer and mixing; in addition to separating or screening 'first bodies' (sample and counterface), third bodies can have other effects as they are able to flow and transmit load, accommodate velocity gradients, and are also created, destroyed, and regenerated during sliding. Resulting behavior can depend on dimensions, compositions (may be the same as either of the 'first body' materials or a mixture of both), properties (the materials may undergo stresses close to their mechanical limits), and hardness. Chemical composition is a key to the observed properties of the third body.

Despite the evidence, it is still the case that many models of wear do not take into account the action of the third body, with debris assumed to be ejected on formation. Much work has been done using experimental rigs in which debris is retained at the wear interface, including fretting wear and much of the pin-on-disk work.[1,2,6,10,14,17–19,33,35,43,46,50–71] Even in situations where ejection is favored, such as the block-on-cylinder approach,[3,4] debris has remained at the interface and has played a significant part in the promotion of mild wear.

1.15.2.2.2 Surface films and preoxidation – Third body or not?

Also absent from the traditional models, is consideration of the effect of any surface films, adsorbed gases or other volatile species that may be present in most situations. Clearly, the wear process will be affected by the nature of the surfaces.[72,73]

This is also true for preoxidized films,[3,48,49,52] where early metal-to-metal contact has been decreased or eliminated to varying degrees, followed by earlier formation of compacted oxides in a number of cases. Although not a 'third body' in their own right (they are directly attached to one or both 'first body' surfaces at the beginning of sliding), the sliding action will create extra loose material from the surface oxide layer, which will proceed to act as a third body where retention is preferred over ejection.

1.15.2.2.3 Behavior of particles at the interface

The behavior of third body material at the wear interface goes beyond just acting as an agent for separation of the sliding surfaces or removing material from them. Rigney's observations[49] on load transmission, velocity gradients and debris particle creation, destruction, and regeneration are one example of this.

In addition, the particles may undergo varying degrees of motion at the interface because of the movement of the sliding surfaces. Halliday and Hirst[53] noted accumulation and 'rolling' of debris particles during fretting corrosion tests on mild steel specimens, which they commented as being responsible for the decrease in friction during testing. They also noted that some sliding debris must be present, as the observed coefficient of friction would have been in the region of 0.002 for rolling alone, rather than the values near or below 0.05 observed after the run-in phase was completed. Halliday and Hirst also established that the presence of the oxide particles prevented wear due to welding (adhesion) of the surfaces together.

Conversely, Suh and Sin[74] noted an increase in friction and wear by ploughing due to the presence of debris particles; this was confirmed by the removal of the debris, after which the coefficient of friction fell from a high 'steady-state' value and gradually rose again as further debris was generated. It is to be commented here, that Suh and Sin used a unidirectional crossed rotating-cylinder-on-stationary-cylinder configuration, while Halliday and Hirst conducted tests with an 'oscillatory-cylinder-on-two-block-fretting-wear' configuration. Thus, it would have been likely that debris retention in Halliday and Hirst's work would have been much greater, allowing for the observed generation of Fe_2O_3 oxide particles.

Also, Suh and Sin's work[74] largely describes a metal–metal interaction, with most testing being carried out in a purified argon atmosphere. Even where an inert atmosphere is not used (as with AISI 1020 steel), there was nothing to suggest the generation of oxide debris and thus all interactions can be assumed to be metal–metal in their case. Hence, a direct comparison between their work and that of Halliday and Hirst may not be wholly appropriate. However, Rose[4] and Inman *et al.*[5,21,22,24] report high levels of wear for Nimonic 80A versus Stellite 6 at elevated temperature, where only oxide debris was generated during all but the earliest part of the sliding process. Here, it is the oxide debris that acts as a third body and aids material removal.[5,21,22,24]

Rice *et al.*[75] showed that the effects of debris parameters on coefficient of friction are more important than asperity parameters. On modeling and comparing the influence of variations in density and size of particles at the interface with that of asperities on coefficient of friction, the sensitivity of coefficient of friction to changes in particle density and size was much the greater.

When particle parameters alone were considered, it was observed that increases in density lead to a much faster increase in the coefficient of friction to a high steady state value. Increased particle sizes also lead to increases in the coefficient of friction values, or conversely, smaller particle sizes are preferred for a lower friction regime. Of most interest in the work of Rice *et al.*,[75] was the observation that, if particle density was increased while particle size was decreased (which could be regarded as analogous to particle break-down early in the wear process), then there was a sharp increase in friction, followed by a steady decrease with time.

It is to be noted that Suh and Sin,[74] Rice *et al.*[75] did not consider the movement of debris, as the debris was 'entrapped.' However, their approach[75] does allow for estimation of friction where particle size means that movement is not a primary consideration; Hesmat[76] proposes a lower size limit of 20 μm for debris to be a contributor to abrasive wear. At higher values, the results of Suh and Sin[74] and Rice *et al.*[75] are, therefore, more applicable.

Debris movement for smaller particles is clearly a key consideration, as the fall in friction due to, for instance, rolling invalidates any models that fail to consider it. Jiang *et al.*[19] proposed the following series of mechanisms for wear debris movement under sliding conditions, each mechanism accounting for a different mode of perceived particle movement (**Figure 5**).

1. *Rotating:* A particle is entrapped in front of another fixed or immovable particle or object. It cannot move from its current position when impacted by

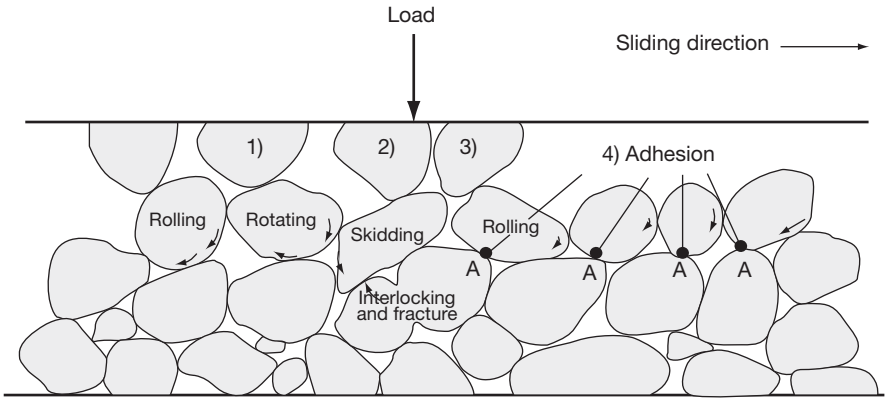

Figure 5 Mechanisms of possible movement of particles during sliding of particulate materials.[19] 1 – Rotating, 2 – relative skidding, 3 – rolling, 4 – adhesion or sintering affected rolling mechanism.

an asperity from the opposite surface and is only able to rotate around its own center.

2. *Relative skidding:* A fixed or locked grain in one half of the sliding pair slides or 'skids' against a fixed grain attached to the opposite surface.
3. *Rolling:* The particles are able to freely move or roll along with the opposite sliding surface (and are not entrapped by it as with the 'rotation' mechanism).
4. *Adhesion or sintering affected rolling mechanism:* Adhesion developing between adjacent particles hinders the rolling of particles, affecting (increasing) friction compared with the 'free' rolling mechanism.

The mechanisms of movement can change and any particle may be subject to a different mechanism at different time points. It is also possible that a particle will become 'interlocked' or 'entrapped'[54] and be unable to move, and thus be liable to fracture, due to a build-up of stress upon it. Further appraisal of these mechanisms[54] does not specifically mention the fourth mechanism, adhesion and sintering general factors affecting the resulting particle layer as a whole.

It is also possible that for a given range of particle sizes, powder 'flow' may occur. Hesmat[76] observes that particles of an intermediate size, between 5 and 20 μm, may undergo 'quasihydrodynamic flow' under sliding conditions. Larger particles will behave as *in situ* elastic bodies and contribute to abrasive wear, while smaller particles will compact and behave as a nearly solid body, moving along with the 'first body' interface and protecting it. At these smaller sizes, Van der Waals' forces and other attractive forces will become important factors and inhibit the flow process.

However, it is to be pointed out that the debris particles produced using the block-on-cylinder configuration,[3,4] in the 5–20 μm size range specified by Hesmat for flow, were noted to be highly irregular in shape, being 'flat and angular' as a result of delamination wear. Also, they were metallic, meaning that adhesion between metallic surfaces would also be a major influence; Hesmat's work was with oxide particles. The combination of these influences would thus inhibit any flow process and eliminate the quasihydrodynamic flow region; high levels of metallic wear were observed[3,4] during the 'severe wear' stages, with associated high levels of adhesion due to transfer and back-transfer of material between metallic interfaces. Where oxidational wear did occur, particles were 5 μm in size or less, when, as Hesmat points out, Van der Waals' and other attractive forces and compaction come into play. This means that quasihydrodynamic flow cannot play a significant part in the sliding wear process as observed between the selected test alloys in the current configuration, favoring ejection of material from the wear interface. Hesmat's lower limit of 20 μm for abrasive wear could, therefore, be revised downward to the 5 μm upper limit for forces of attraction and compaction.

1.15.2.2.4 The effect of forces of attraction between third bodies

As already noted,[76] attractive forces such as Van der Waals' forces become a factor when considering very small particles (for oxides, 5 μm or less). Electrostatic forces between particles, and between particles and tribosurfaces, also exist, but these are only about 1% of Van der Waals' forces for nonconductive solids.[77]

If F is the force of attraction and assuming the particle is spherical, this can be directly related to particle size by:

$$F = \frac{AR}{6r^2} \quad [8]$$

where A is the Hamaker constant; R, the radius of the particle or sphere; r is the equilibrium separation.

The Hamaker constant[50] is dependent on the surface energy of the sphere:

$$A = 9\pi r^2 \gamma \quad [9]$$

where r is the distance affecting mutual action of Van der Waals' forces (which can be estimated at 0.3–0.5 μm), and γ is the surface energy.

Van der Waals' forces are extremely short ranged in nature, produced by dipole induction between neighboring bodies. This accounts for the attraction observed between the smaller wear particles (<5 μm)[76] and the wear surfaces.[78]

Surface energy is temperature-dependent, thus making the Hamaker 'constant' and the force of attachment F temperature-dependent. An Arrhenius relationship exists between surface energy and temperature:

$$\gamma = \gamma_0 \exp\left(-\frac{E}{RT}\right) \quad [10]$$

where R is the gas constant; E, the activation energy for 'bonding'; and T is the absolute temperature.

The amount of work done in relation to wear is fairly minimal, compared with the formation of compacted oxides and 'glazes,' as discussed in **Section 1.15.2.3**, with the work of Hesmat[76] being one of the more comprehensive studies of the potential behavior of debris and particles at the wear interface in relation to their size. It is suggested, here, that the role of Van der Waals' forces in the accumulation and grouping together of particles is perhaps more important, especially at more elevated temperatures. For sintering and fusion of finer oxide particles to form glazes, an attractive force must be present to hold the particles in position long enough to allow significant sintering reactions to occur.

The importance of sintering in the formation of debris layers in itself cannot be ignored. Zhou *et al.*[79] showed that for iron, nickel, and iron–25% nickel powders, significant sintering can occur on raising the temperature above room temperature (denoted by the significant shrinkage of specially prepared compacts), where the particle size is defined as 'ultrafine,' in this case, 30–40 nm. In comparison, more traditional fine particles of around 5 μm did not show a significant response (in terms of shrinkage) until above 500 °C. This does not mean that sintering did not occur with the larger particles; it is more that a greater response was obtained for the smaller particles because of their greater relative surface area, and hence, the contact area. With particles of 300–400 nm, a ready sintering response may be detectable in a wear situation.

The effect of shrinkage of the compacts, as occurs in all powder compacts on sintering, is worth noting. As sintering and thus shrinkage undoubtedly occur in accumulations of wear debris at not-necessarily-greatly-elevated temperatures, this will no doubt have an influence on the formation of compacted oxide layers during the wear process. To date, no attempt has been made to address this issue or its importance on the sliding wear process.

1.15.2.3 Mild Wear and Mechanisms of Compact Oxide Formation

1.15.2.3.1 Introduction to compacted oxides or 'glazes'

As stated in **Section 1.15.2.1**, Archard and Hirst[31,32] defined mild wear as that occurring where the surface is extremely smooth and consisting partially or wholly of the product of reaction between the material under sliding and the surrounding atmosphere or fluid. An oxidation reaction is required for the creation of the corrosion product, although, as already stated, the corrosion product itself need not necessarily be an oxide.

The term 'glaze' is misleading, as it implies a glassy amorphous material, which was thought to be the case until Lin *et al.*[6] proved it to be crystalline by means of electron diffraction; the term 'compacted oxide layer' is a more accurate description. 'Glaze' and 'compacted oxide' tend to be used fairly interchangeably throughout literature, and despite the crystalline nature of these surfaces, the term 'glaze' has remained in common use. More recently, Datta *et al.*[15,80] have demonstrated that the compacted oxide layers formed in some systems and under certain conditions have a nanocrystalline structure and are highly disordered as discussed further in **Section 1.15.4.3**.

Compacted oxide layers tend to form under conditions of moderately high temperature, low loading, and usually low sliding speed. For a compacted oxide layer to form and a resultant decrease in wear to occur, many researchers specify that a minimum temperature that is dependent on conditions and

alloy composition must be exceeded. With increasing temperature, the formation of these compacted oxides becomes more rapid, with a consequent decrease in the 'severe wear' running in period, the debris from which can be a major source of material needed for the formation of the compacted oxide layers. Compacted oxide formation is not restricted to low sliding speed, as the effect of frictional heating due to high sliding speed can raise the temperature above the critical temperature required for the formation of the compacted oxide layers.

Many researchers have extensively studied the decrease in wear by the formation of compacted oxides at high temperatures. In addition to Archard and Hirst,[31,32] others such as Lancaster,[26] Bhansali,[81] Razavizadeh and Eyre,[82] Stott *et al.*,[2,6,10,14,17–19,35,50,55–61] Quinn[1,33,62–64] and Garcia,[83] have contributed to the knowledge of compacted oxide formation. Recent work[3–5,20–25] has additionally concentrated on the sliding of dissimilar interfaces and their effects on the mode of wear. The key issues on oxide formation are discussed as follows.

Wear that is dependent on the tendency to oxidation is highly dependent on temperature. The tendency to oxidation with respect to temperature can be described by the following Arrhenius type equation:

$$K_p = A_p \exp\left(\frac{Q_p}{RT_0}\right) \quad [11]$$

where K_p is the oxidation rate, A_p is the Arrhenius constant, Q_p is the activation energy (for oxidation), R is the gas constant, and T_0 is the absolute temperature in Kelvin.

Stott in conjunction with Lin and Wood,[6,55–59] and later Glascott and Wood[10,50,54,60,61] proposed various modes and mechanisms of 'glaze' formation based on the generation and behavior of oxide debris at the sliding interface. Jiang *et al.* building on studies of third body interactions[19] (later revised by Stott[54]) and adhesive processes between particles,[17] proposed a descriptive model for debris behavior at the sliding interface,[2] based on their generation, commutation, sintering to form 'glaze' layers (above a critical temperature), layer break-up, and debris removal. These mechanisms and modes of formation are discussed in more detail in **Section 1.15.4**.

1.15.2.3.2 Quinn's oxidational wear model

Quinn's model of wear[62] assumes a dependence upon the wear rate of oxide film formation on the wear interface. At a critical thickness ξ, the oxide layers are no longer able to withstand the forces acting tangentially on them, and suffer failure and break away. Combining Quinn's and Archard's models[31] allows the critical thickness to be used to relate wear rate to material oxidation rate, showing an increase in wear rate with temperature.

From Archard's wear equation [5], the wear volume W is related to the applied load P and the total sliding distance L, giving

$$W = \frac{K_a PL}{H} \text{ or } W = K_a AL\left(A = \frac{P}{H}\right)$$

K_a can be regarded as the probability of a wear particle being generated in any given encounter (assuming unit sliding distance in the following derivation, making W the wear rate). Thus, $1/K_a$ is the number of encounters required to produce a wear particle.

In oxidational wear, a wear particle cannot be produced until the critical thickness for mechanical stability ξ is reached; thus $1/K_a$ is the number of encounters required to generate an oxide layer of this thickness. If t is the time required to grow the layer and τ is the length of time of each encounter, then

$$t = \frac{\tau}{K_a} \quad [12]$$

If V is the sliding speed and d is the distance along which the sliding contact is maintained, then

$$t = \frac{\tau}{V} \quad [13]$$

and eqn [14] can be modified to

$$t = \frac{\tau}{VK_a} \quad [14]$$

In a given time period t, the growth of oxide per unit area will be Δm. Assuming parabolic oxidation

$$\Delta m^2 = K_p t \quad [15]$$

where K_p is the parabolic rate constant. If f is the mass fraction of oxide, that is, oxygen, and ρ is the oxide average density, then

$$\Delta m = f\xi\rho \quad [16]$$

and

$$f^2\xi^2\rho^2 = K_p t \quad [17]$$

Substituting eqn [2] into eqn [16] gives

$$K_a = \frac{dK_p}{Vf^2\xi^2\rho^2} \quad [18]$$

The rate constant can normally be calculated using an Arrhenius relationship, as described by eqn [13]:

$$K_p = A_p \exp\left(\frac{Q_p}{RT_0}\right)$$

where A_p is the Arrhenius constant, Q_p is the activation energy (in this case for oxidation), R is the gas constant, and T_0 is the absolute temperature of reaction. Thus

$$K_a = \frac{dA_p \exp(Q_p/RT_0)}{Vf^2\xi^2\rho^2} \quad [19]$$

Substituting into Archard's equation[31] gives a final expression for wear rate:

$$W = \frac{dAA_p \exp(Q_p/RT_0)}{Vf^2\xi^2\rho^2} \quad [20]$$

This expression relates directly to the oxidational properties of the materials, plus the critical environmental variables affecting the wear process, such as temperature at the interface at the time of contact and sliding speed relative to the opposing interface, as well as the critical thickness of the oxide. Knowing the critical thickness of the oxide[62] and the static oxidation properties of the wearing materials, wear rate prediction can be easily achieved.

However, there are many complications that can prevent the accurate prediction of the wear rate:

- The difficulty in estimating the wear interface temperature, particularly in the presence of oxides;
- The slower heat flow from the wear interface and thus higher interface temperature, caused by lower thermal conductivity of the oxides;
- The presence of multilayer scales (formed particularly at high temperature, e.g., with iron), preventing the calculation of the temperature based on the oxide type generated[33];
- The expected presence of increased levels of surface defects at the contacting surfaces, increasing the oxidation rate constant.
- The continued removal of oxides, leading to exposure of fresh surfaces and a decrease in oxide thickness (hence diffusion distance), thereby enhancing the tribooxidation rate; and
- The presence of defects such as cracks and grain boundaries, allowing ingress of oxygen (in ion and molecular form), leading to an enhanced oxidation rate.

A schematic presentation of Quinn's models[84] is shown in **Figure 6**.

1.15.2.3.3 Modification of Quinn's oxidational wear model for discontinuous contact

The validity of Quinn's model[1] is conditional upon the maintenance of contact between the two surfaces, which is clearly often not the case. Quinn's model was further modified by Garcia *et al.*[83] to take into account discontinuous contacts between the contacting surfaces.

For this modified model, it is assumed that $1/K_a$ contact events are required for ξ, the critical oxide

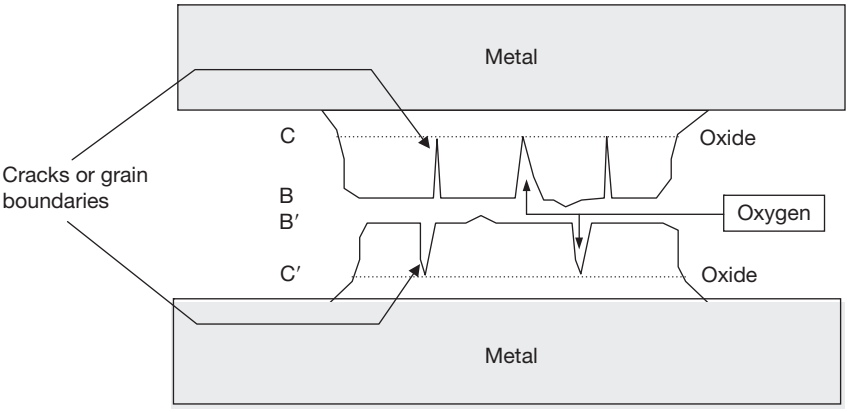

Figure 6 Oxygen transport between oxide plateaux and cracks in the oxides.[84] Quinn's oxidation model supposes that any oxygen species would have to diffuse right from the surface of the oxide (B or B′) to the metal. The presence of cracks and grain boundaries act as points of ingress for oxygen ions and in the case of cracks, molecular oxygen. This means that the distance for diffusion is significantly less where cracks in the outer layers of oxide are prevalent. Diffusion need only take place across the underlying oxide from the crack tips (C and C′) to the metal and thus the rate of oxidation is greater.

thickness, to be achieved; this is the same as for Quinn's model. However, in this case, the time required to reach this critical thickness depends on the contact frequency F, which is the inverse of the elapsed time between two contacts at a given point between the contacting surfaces; while this can clearly be related to the sliding speed, the frequency of contact can also be changed by varying the length of the wear track without any need to vary the sliding speed. It is clear that each asperity will not make contact each time the disk rotates; however, Garcia[83] comments that the probability of a contact (and hence a wear particle being generated) is included in the statistical meaning of the wear coefficient, K_a.

Therefore

$$t = \frac{1/K_a}{F} = \frac{1}{FK_a} \quad [21]$$

The constant of proportionality K_a in Archard and Hirst's model[31] is thus defined by

$$K_a = \frac{K_p}{Ff^2\xi^2\rho^2} \quad [22]$$

and substituting the rate constant as defined by eqn [11] gives

$$K_a = \frac{A_p \exp\left(Q_p/RT_0\right)}{Ff^2\xi^2\rho^2} \quad [23]$$

Substituting into Archard's equation [5]

$$W = \frac{K_a PL}{H} \text{ or } W = K_a AL\left(A = \frac{P}{H}\right)$$

gives a final expression for wear rate (again as the sliding distance L is assumed to be 1, the wear volume W can be taken to represent the wear rate), the frequency of contact events being the determining parameter for the input of energy for oxide growth, rather than the sliding speed:

$$W = \frac{AA_p \exp\left(Q_p/RT_0\right)}{Ff^2\xi^2\rho^2} \quad [24]$$

The validity of Garcia's model[83] is dependent upon a wear particle being generated on any given contact. For this to work, it is necessary for a wear particle to be generated each time a contact is made; this in itself is highly improbable. However, the lower level of data scatter achieved by Garcia's discontinuous contact model indicates that this alternative frequency-based approach provides a good approximation in circumstances where Quinn's model is less effective in predicting wear rates (i.e., where contact is not maintained).

1.15.2.4 Effect of Load and Sliding Speed

1.15.2.4.1 Early work

A significant contribution to the effects of load and sliding speed came from Welsh's work[27,28] on low-carbon steels using a pin-on-rotating-ring (cylinder) configuration with applied loads of up to 2 kgf and sliding speeds of up to 2.66 m s^{-1}. The wear process was characterized by two transitions: T_1, which is mild-to-severe at low load and sliding speed, and T_2, which is severe-to-mild at high load and sliding speed. Increasing the sliding speed decreased the critical load at which these transitions occurred (**Figure 7**), the lower transition being eliminated in some cases, leaving only the severe wear to mild wear transition. In extreme cases, these transitions could be decreased enough to be eliminated from the experimental data – mild wear could be observed over the whole range. The variation in the upper transition from the intermediate severe wear back to higher speed mild wear was observed to be the more sensitive to the sliding speed.

Low-speed, low-load mild wear was attributed to the presence of loose oxide debris at the sliding interface and intermediate severe wear to direct metal-to-metal wear. The mild wear encountered at high speed and high load was attributed to hardening, accompanied by the development of an adherent oxide film, as a result of frictional heating. The hardening came about as a result of the low-carbon steels undergoing phase changes, due to high localized temperatures around points of contact being sufficient to produce a transformation to austenite, followed by rapid cooling by conduction of heat into the bulk metal producing a structure at the surface not too dissimilar to martensite.

A critical hardness had to be exceeded by these phase changes for mild wear to be reestablished under high-speed, high-load conditions; the transition back from severe wear to mild wear is in fact a two part transition, with T_2 referring to the point where sufficient phase hardening occurs to suppress severe wear without the intervention of an oxide film (the development of which further acts to protect the wear surface) and a T_3 transition approximately matching the point where permanent phase change hardening occurs.

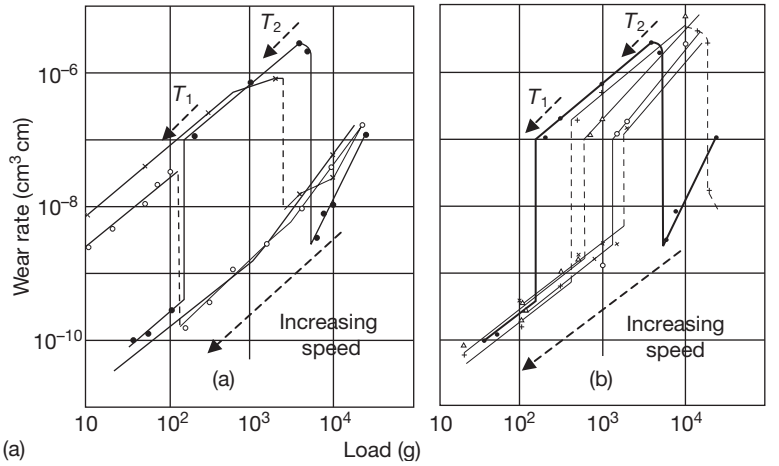

Figure 7 Effect of sliding speed on wear rate/load – 0.52% carbon steel.[27] (a) 1.00–2.66 m s^{-1} (● – 1.00 m s^{-1}; × – 1.33 m s^{-1}; ○ – 2.00 m s^{-1}; + – 2.66 m s^{-1}), (b) 0.17–1.00 m s^{-1} (× – 0.017 m s^{-1}; ○ – 0.067 m s^{-1}; ▽ – 0.33 m s^{-1}; + – 0.66 m s^{-1}; ● – 1.00 m s^{-1}). T_1 – Transition from low speed, low load mild wear to severe wear. T_2 – Transition from severe wear to high speed, high load mild wear. (Arrows show movement of transitions with increasing sliding speed).

Subramanian[85] conducted a series of sliding tests of an Al–12.3 wt% Si alloy in pin form against various rotating 'ring' counterfaces, including mild steel in the rolled condition, quenched and tempered die steel and copper with varying levels of aluminum, during which the sliding speed was increased at various times. The wear rate of the Al–12.3 wt% Si alloy pin (**Figure 8**) decreased with increased sliding speed up to a critical value of usually 1 m s^{-1}, regardless of counterface material or applied pressure used. Further increases in speed above this critical value led to progressive increases in wear.

Subramanian explains the decrease in wear with increasing sliding speed is due to increasing strain rates and due to increased hardness and flow strength of the wear surface. The true area of contact is thus and with a lower level of contacts between the wearing surfaces, a lower wear rate results. In competition with this is the effect of increased temperature because of frictional heating (which was observed to occur), softening the material at the wear interface. This results in an increase in the true area of contact and thus an increase in the wear rate. Subramanian does not go into detail with his reasoning; however, the softening of the material must allow for deformation and 'spreading' of asperities and also increased contact at other points.

Changes in wear mechanism were observed at Subramanian's '1 m s^{-1}' transition, with equiaxed particles produced below this critical or 'transition' speed, compaction of these particles and delamination of the compacted particles around the transition speed, and delamination or plastically deformed material at higher speeds. It is not stated whether the particles produced at any particular speed are metallic or oxide.

The critical speed was observed to be dependent on counterface material and a higher transition was noted for harder, more thermally conductive alloys. Decreased mutual solubility also led to a higher transition speed.

Welsh[27,28] discusses the existence of lower limits of load and speed, marking the transition from mild to severe wear and also an upper limit, marking the transition back to mild wear. So,[86] on the other hand, discusses only a single limit or critical value for both load and speed for the transition from mild wear at low speeds and loads, to severe wear at high speeds and loads. Comparison with the work of Welsh would make So's transition equivalent to the lower transition, with no mention of an upper transition despite the use of higher sliding speeds. So quotes values of 400 °C and 5 MPa contact pressure as being limiting conditions for mild wear for many steels. In one test of note, a high carbon steel sample underwent a mild-to-severe wear transition at a contact pressure of 4.43 MPa, on raising the sliding speed from 3 to 4 m s^{-1}. A Stellite sample remained in the mild wear state at a contact pressure of 8.85 MPa (just under twice as much pressure) under similar conditions. As So used a pin-on-disk configuration, compared to the pin-on-rotating-cylinder configuration of Welsh, this may account for the differences in results; the pin-on-disk configuration may not have generated sufficiently severe conditions for the upper transition to occur.

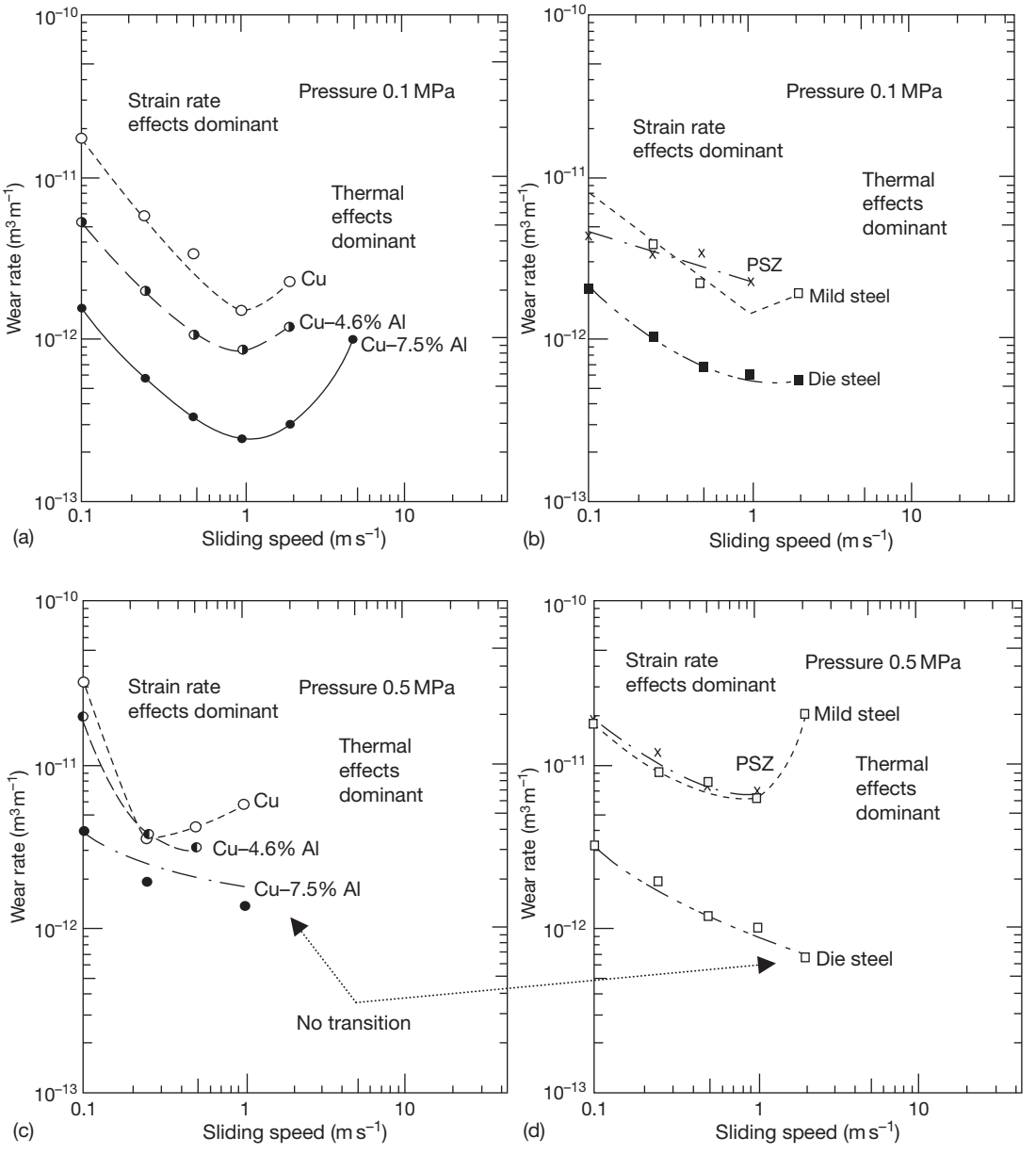

Figure 8 Effect of sliding speed on wear rate of Al–12.3 wt% Si versus various counterface materials.[85] (a) Cu, Cu–4.6 wt% Al, and Cu–7.5 wt% Al counterfaces, applied pressure 0.1 MPa, (b) mild steel, die steel, and partially stabilized zircona counterfaces, applied pressure 0.1 MPa, (c) Cu, Cu–4.6 wt% Al, and Cu–7.5 wt% Al counterfaces, applied pressure 0.5 MPa, (d) mild steel, die steel, and partially stabilized zircona counterfaces, applied pressure 0.5 MPa.

Most load and sliding speed work done to date has concentrated on what happens at room temperature, with little work at elevated temperature. One example is the work of Rose,[4] where a series of experiments were conducted at 750 °C with loads between 7 and 25 N, during which an apparent transition from mild-to-severe wear was noted at 15 N, when Nimonic 80A was worn against Incoloy 800HT. Also, when Incoloy MA956 was worn against Stellite 6 or Incoloy 800HT, at 25 N, the 'glaze' layer formed on the Incoloy MA956 was beginning to show signs of breaking away (as described later).

1.15.2.4.2 Wear of cobalt-based alloys

Valuable information can be gleaned from work on cobalt-based alloys. The most comprehensive work

carried out on the sliding wear of cobalt was that by Buckley,[87] who compared the sliding wear of cobalt with that of copper in vacuum. Lower friction and adhesion levels noted for cobalt were attributed to its hexagonal close-packed structure, compared to copper's face-centered cubic structure.

The observed increase in friction and cohesion for cobalt tested at temperatures $\geq$300 °C, with complete welding at 450 °C, was considered to result from a phase change from hexagonal close-packed to face-centered cubic because of increased temperature (to above 417 °C; the phase change temperature for cobalt), caused by frictional heating.

The differences between the sliding behavior of metals in hexagonal close-packed phase and face-centered cubic phase are due to the greater number of active slip systems available in face-centered cubic structures. There are 12 primary slip systems within a typical face-centered cubic metal (4 slip planes each with 3 slip directions), which are all crystallographically similar, compared to only three primary slip systems in cobalt, these being based on the basal plane with the highest atomic density (i.e., 1 slip plane with 3 slip directions). Cross slip is also more difficult, as with hexagonal close-packed structures such as cobalt, screw dislocations are required to move out of the primary basal glide plane onto planes that, unlike face-centered cubic structures, are crystallographically different. Hexagonal close-packed materials are thus less deformable.

The effect of these hexagonal close-packed structures on wear was further elaborated on by Persson[88,89] on studying the low friction tribological properties of Stellite 21 and Stellite 6. Persson comments that although a metastable face-centered cubic structure may be retained in both Stellite alloys down to room temperature, transformation to a hexagonal close-packed structure can be induced by application of sufficiently high shear stresses (i.e., during sliding). A thin, easily sheared layer can develop at the sliding surface due to the shear-induced alignment of the hexagonal close-packed basal plane parallel to the direction of sliding.[89] This alignment significantly reduces friction and improves galling resistance, with shear and adhesive transfer restricted to this layer. This sliding regime persists even as this layer is removed, as it is easily regenerated. Also, the removal of material in such thin sections may at least in part explain the ready generation of fine Stellite 6-sourced Co-based oxide debris observed elsewhere.[3–5,20–25] These sections may be more easily commutable to a small size and oxidized, providing a ready supply of material for 'glaze' formation.

The formation of compacted oxide layers during like-on-like fretting wear tests of cobalt-based Stellite 31, between room temperature and 800 °C (293–1074 K), was observed by Stott *et al.*[90] The formation of these oxides was by a similar route to that observed for iron-based and nickel-based alloys, with alloying components present in the oxides to roughly the same proportions as the original alloy.

At temperatures between room temperature and 300 °C, Stellite 31 undergoes a much lower level of wear than do various nickel- and iron-based alloys, which Stott also attributes to the smaller number of slip planes in the hexagonal close-packed structure of cobalt. He specifies an initial period of low wear for up to an hour, followed by the production of a bright, rough metallic wear scars showing characteristics of abrasion and evidence of material transfer. This he attributes to a probable change in phase from hexagonal close-packed to face-centered cubic and thus a loss in wear resistance. Later, the bright worn surface is lost with increasing amounts of oxide being produced, although the load-bearing areas remain metallic.

Both the 'phase changes' and oxide production have been attributed to temperature increases at the wear interface. However, the phase transformation temperature for cobalt is 417 °C; Stellite 31 contains 26% chromium, which has the effect of significantly raising the hexagonal close-packed to face-centered cubic transition temperature; 20% Cr is estimated to raise the transition temperature to 847 °C (expressing uncertainty as to the effects of the other alloying components). This suggests a far greater influence due to frictional heating and localized flash temperatures due to asperity interactions; for a phase change to readily occur, the temperature at the immediate interface would have to reach 500 °C above ambient. In a fretting wear situation, it is difficult to see how this could occur.

However, the level of alteration of temperature for any phase transitions will also depend on the effects of other alloying components in cobalt-based alloys. As already stated, chromium will raise the transition temperature quite dramatically. Other works[68,87–89] suggest that tungsten and molybdenum also raise this transition, while nickel and iron (also, magnesium and carbon[88,89]) have the effect of stabilizing the higher temperature face-centered cubic structure (due to increases in stacking fault energy[88,89]) and suppressing this transition. It is possible that the presence of nickel to 10.5% and iron to 2% may be sufficient to retard the effect of the chromium and

7.5% tungsten to a much lower level. Thus, a much smaller increment in temperature due to frictional heating and flash temperatures may be needed to effect any phase transition, confirming the conclusion that the damage observed can be attributed to phase changes, and hence, a decrease in resistance to deformation.

Stott *et al.*[90] observed that compacted oxide formation was not accompanied by any decreases in friction observed during similar experimentation with nickel-based alloys at elevated temperatures. With friction levels already low due to the hexagonal close-packed structure, it is possible that no significant difference between the friction levels before and after elimination of metallic contact by higher temperature 'glaze' formation may be discerned.

The face-centered cubic to hexagonal close-packed transformation observed in Co-based alloys is considered a martensitic transformation.[91] Attempts to utilize Co-free hard wearing alternatives making similar use of the austenite–martensite transition in Fe-based alloys have been limited by typical upper useful temperatures of ~180 °C[88,89] (not discussed in the current work).

1.15.2.4.3 The effect of load and sliding speed – Stellite 6

Following on from previously discussed work (Section 1.15.2.4.1) with a Stellite material,[86] So *et al.* went on to test Stellite 6 clad mild steel against AISI 4140 and 4340 steels in the martensitic phase, first as the pin material (4.75 mm in diameter) and then the disk material.[30] Measured hardness values were 580 Vickers hardness number (VHN) for the Stellite 6 layer and 750 VHN for the steels, increasing to 970 VHN after an unspecified heat treatment followed by water quenching, with test loads of up to 156.8 N and sliding speeds of up to 4 m s^{-1} used. After sliding for up to 10 000 m, the Stellite 6 layer was observed to be mostly covered by an oxide layer reported to consist of W_3O, CrO, and Co_2O_3. Where this oxide layer spalled, a new oxide film was observed to replace it readily. This applied for all combinations of loads (19.6, 39.2, 78.4, and 156.8 N) and sliding speeds (1, 2, 3, and 4 m s^{-1}), with the exception of the most severe tested combination, 156.8 N and 4 m s^{-1}, when severe wear was observed for the Stellite 6 as the pin material. The experimental data obtained from these tests are presented in Figure 9.

The steels underwent increased wear compared to the Stellite 6, despite being of much greater hardness, and So *et al.* concluded that the oxide layer formed on the Stellite 6 must be tougher than that formed on the steels. When used as a disk material, only a thin layer of oxide material was formed on the AISI 4340, compared to the thicker layer formed on the Stellite 6; the wear rate of the steel was seven times that of the Stellite 6 laser-clad pin. As the pin material, severe wear was observed for the AISI 4140 steel, the rate of wear being 10 times higher than that of the Stellite 6 laser-clad disk. For all but the highest load, the wear rate of the Stellite 6 pin actually decreased when the sliding speed was increased from 1 to 2 m s^{-1}, with only a slight increase at intermediate loads on raising the sliding speed to 4 m s^{-1} (Figure 9). At the lowest load used, the decrease in wear continued up to 4 m s^{-1}.

The increasing wear rate for specimens under a load of 156.8 N was ascribed to softening of material due to the higher flash temperatures encountered, especially at higher sliding speed. The higher flash temperatures also led to changes in the oxide phases that were reported to form on the respective wear surfaces. A shift was noted from Fe_2O_3 to FeO on the steels and from W_3O, through Co_2O_3, CrO, Cr_2O_3,

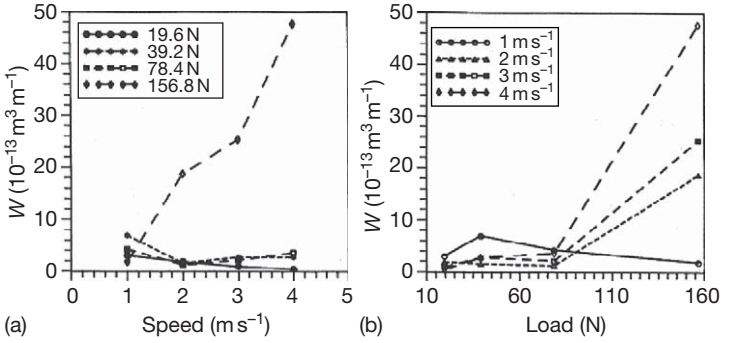

Figure 9 Variation in wear rate (*W*) with sliding speed (a) and load (b) for the rubbing of laser-clad Stellite 6 pins with AISI 4340 steel disks. Reproduced from So, H. *Wear* **1996**, *192*, 78–84.

to Cr_5O_{12} on the laser-clad Stellite 6 layer with increasing temperature; this was accompanied by a decrease in friction. So does not offer an explanation for the change in oxide with temperature, though as for the oxidation of iron, it appears that this can be attributed to changes in oxidation state of the chromium in Stellite 6, with preferential oxidation of tungsten and cobalt respectively at lower temperatures. It is curious to note here that, in the work of Wood[3] and Rose,[4] no such shift was observed for Stellite 6, with Cr_2O_3, Co_3O_4, or a combined oxide of the two being consistently observed from XRD results. No evidence of tungsten phases was found, although this could be attributed to the sensitivity of the measurement and characterization equipment.

Also of note was the fact that the oxide layers formed in So's work were more reminiscent of those created at higher ambient temperature in the work of Wood and Rose (>510 °C), indicating extremely high temperatures at the points of contact. So's measurements indicate a rapid rise in temperature with increasing load and speed (speed having less of an effect than load). So comments that, under the most severe conditions (156.8 N and 4 m s^{-1}), the mean surface temperature at the point of contact reaches over 700 °C and, because of this, wear becomes severe due to softening. This may be more to do with the load and speed conditions than to temperature (even accounting for phase transitions), as Wood and Rose tested Incoloy MA956 and Nimonic 80A against Stellite 6 at an ambient temperature of 750 °C, with oxide layers being obtained in both cases on the Stellite 6 counterface.

This implies that So has underestimated the temperature at the sliding interface in this case. The softening may again be attributable to phase changes from hexagonal close-packed to face-centered cubic. In the case of Stellite 6, there are far fewer alloying additions to offset the effects of chromium (present at 27%) and tungsten (5%) on this transition. The transition between the two phases for 27% chromium is ~880–900 °C,[5,92] almost 200 °C higher than So's 700 °C estimate.

Crook and Li[69] carried out a comparative 'like-on-like' sliding study of Stellite 6 and a number of other hard-facing alloys of various cobalt contents, including Stellite 1 (with higher levels of carbon, chromium, and tungsten than Stellite 6), Stellite 2006 (a 33% cobalt–iron–chromium alloy), Haynes No. 716 (a nickel–iron–chromium alloy with 11% cobalt), and Haynes No. 6 (a nickel–chromium alloy with no cobalt). They observed that in general the higher the cobalt content, the better was the resistance to metal–metal wear at temperatures up to 750 °C. Where no cobalt was present within the alloy, wear rates were observed to be highest. Above this temperature (at 1000 °C), all alloys exhibited low wear with a protective oxide layer forming across the wear surface. Increases in wear were observed for all combinations with increased contact pressure, though at high load, increases became less severe for cobalt–chromium and cobalt–iron–chromium alloys. Of particular note is the response to increasing the sliding speed by an order of 10 from the 7.06×10^{-4} m s^{-1} used for all their other tests, to 7.88×10^{-3} m s^{-1}, carried out at 500 °C and 20.69 MPa. For the high cobalt–chromium alloys, including Stellite 1 and Stellite 6, there was a slight decrease in the observed wear rate. Where cobalt levels were low or nonexistent, the converse was true and increases in wear were observed.

Crook and Li[69] attributed the superior wear resistance of the cobalt–chromium alloys, first, to the superior galling resistance, and second, to the tendency of alloys when in the face-centered cubic form to undergo phase changes and become hexagonal close-packed, which as discussed earlier is less prone to deformation, due to a smaller number of available slip planes. Conversely, they point out that high nickel alloys have a poor galling resistance, yet specifically quote the work of Stott *et al.*[55,56,58] as examples of nickel–chromium alloys, in particular, exhibiting low levels of wear and developing 'glaze' during the wear process at high temperature.

In both experimental programs, a low amplitude 'button-on-disk' system suitable for fretting wear studies was used. However, Stott *et al.* concentrated solely on one material (Nimonic 80A), whereas Crook and Li's comparative work on a range of alloys showed that, although wear was still low for nickel–chromium alloys, the wear resistances were inferior to those of cobalt-containing alloys. In both cases, it is not possible to say that in an extreme high wear environment (e.g., high speed, high load) similar observations of low wear would be made. In the case of Stellite 6, So's work[30] does indicate continued low wear rates during moderately high speed, high load unidirectional sliding wear (up to 156.8 N and 4 m s^{-1}, with frictional temperatures of up to 700 °C being generated); however, if the works of Wood[3] and Rose[4] are considered, high rates of wear are observed with Nimonic 80A at elevated temperature (750 °C, 0.654 m s^{-1}, 7 N, 9418 m sliding distance) when

undergoing unidirectional wear against a Stellite 6 counterface. Even in a like-on-like situation, wear properties of Nimonic 80A are inferior to those of Stellite 6.[4,93]

The presence of carbides in Stellite 6

In both the work of Stott[90] and So,[86] no mention was made of the effect of carbides that would have formed with both Stellite 31 and especially Stellite 6, carbon being present to 0.5% and 1.1%, respectively. In the cast form, carbon combines with chromium to form a chromium carbide phase at the grain boundaries; in Stellite alloys, these are of the form M_7C_3 and $M_{23}C_6$.[30] In the wrought and hot isostatically pressed forms, these carbides instead form discrete particles dispersed evenly in the microstructure (the effect of Stellite processing or carbide position on sliding wear has not, to the knowledge of the authors, been investigated).

The presence of these hard, difficult-to-deform carbides may have had a number of effects on both sets of experimental work. First, they may have further inhibited deformation of the mainly cobalt matrix during sliding wear, over and above the effect expected from the hexagonal close-packed structure, blocking the operation of the fewer slip planes present. Second, the removal of material from the Stellite alloys may have released some of these carbides into the sliding interface, increasing the levels of wear observed due to increased abrasion effects. The enhanced wear of the AISI 4140 and 4340 steels, when worn against Stellite 6 clad mild steel in So's work[30] may have in addition been partially attributable to this.

There is also the possibility that the carbides (up to 30 μm in size) within the Stellite 6 may affect the formation of 'glaze' (only a few micrometers thick) on opposing wear surfaces[4] as the Stellite 6 is worn down and the carbides are exposed; Inman,[5] however, suggested that the exposed carbides are not hard enough to do this. The possible effects of carbides are discussed in more detail in **Sections 1.15.2.5** and **1.15.3.3.2**.

1.15.2.5 Effect of a Second Phase on Wear

The role of second phases in the wear process is often neglected in wear studies. In many studies, experimentation has concentrated only on single-phase alloys. However, second phases are used in many alloys for various reasons, including enhancement of strength and creep resistance, especially in high temperature systems where the properties of the metallic matrix can become less robust.

During the wear process, where second phases are harder than the matrix material, it is not sufficient to assume that their presence will have no effect on the wear process and that they will simply be 'worn away' with the matrix as sliding proceeds; this only occurs if the second phase is of similar or lesser hardness. Vardavoulias[94] studied a number of steels into which hard ceramic phases of various sizes were introduced; these included titanium carbide (modified to a much finer carbon nitride phase by nitrogen annealing), copper phosphide, and alumina. It is assumed following that the substrate metal is oxidized and is the main source of compacted oxide or oxide debris and, thus, the oxide–metal interface is effectively moving into the metal.

If the sizes of the second phase particles are less than the critical oxide thickness (ξ from Quinn's oxidational wear theory[62]), then these particles pass into the oxide layer as the metal is oxidized. They may not protrude above the surface of the oxide layer and thus cannot directly protect the matrix or impinge on the counterface material. The particles are lost as the oxide layer breaks up at the critical thickness to form debris. The only contribution may be to enhance the load-carrying capacity of the metallic matrix in supporting the oxide film.

Where the second phase particle size is only slightly greater than the critical oxide thickness (between ξ and 3ξ), there is a transition in the wear mechanism – this is referred to as the 'first stage' – while a small quantity of the second phase may be removed with the oxide, as it breaks up, most will remain embedded in the substrate or matrix. These particles protrude above the nominal surface of the interface and the counterface slides over them. This continues until the oxide layer can reform and during this stage of wear, the matrix cannot influence the wear process; this is the 'second stage.'

The mechanical properties of the second phase particles influence what happens next during the 'second stage.' If the particles are able to resist the sliding action, then the matrix will be protected for a prolonged period and the 'second stage' is extended. Enhanced wear of the counterface material by abrasion may occur in this stage. If they are unable to resist the sliding process and fail under the load from the counterface, then contact between matrix and counterface is quickly restored and the 'first stage' of wear will be repeated. A further possibility is detachment of second phase particles as the oxide

breaks up, with these particles acting as third body abrasives; this occurs where cohesion between matrix and second phase is poor.

If the mean particle size is much greater than the critical oxide thickness, the particles show increased efficiency in providing oxidational wear protection to the material subject to wear. After break up of the oxide layer (end of the 'first stage'), the harder second phase particles remain embedded in the matrix. Again, the main interaction is between the particles and the counterface, and this process controls the wear mechanism; the matrix plays no direct part. The majority of the particles are surrounded by the matrix; thus, break up is more difficult and detachment is almost impossible. While this means that the matrix is well protected against wear, the counterface may undergo high rates of wear and thus become the main source of debris. The inference here is that the first stage cannot resume until these larger particles wear to near the level of the rest of the sample surface; as other particles will continue to be exposed elsewhere on the surface, first stage wear with protective oxide layer formation cannot readily happen and severe wear will continue.

On the basis of the apparent failure of carbides in Stellite 6 to disrupt 'glaze' formation for certain wear combinations, Inman[5] suggested that the second phase particles must also be harder than the generated 'glaze' on the opposing sliding surface (Section 1.15.3.3.2). If this is not so, the second phase particles may wear in preference to the 'glaze' layer and not promote its break-up. This may prove beneficial, with a harder second phase conferring wear resistance but allowing protective 'glazes' to form. Tribaloy alloys, consisting of a hard Laves intermetallic second phase in a Ni-based or more notably a Co-based matrix,[95] are possible examples (not discussed in the current work).

1.15.3 High Temperature Wear Behavior of Advanced Materials

1.15.3.1 Oxide Dispersion Strengthened (ODS) Alloys

1.15.3.1.1 Introduction

This section discusses the HT wear behavior of ferritic ODS alloys, Incoloy MA956, and its variants. The section starts with a brief introduction to ODS alloys to provide a context and facilitate interpretation of the experimental observations on their HT wear characteristics.

Ni-base-Inconel alloys MA 6000, MA754, MA758, and MA760, and Fe-base Incoloy MA956, PM2000, and PM2000SD are well-known examples of ODS superalloys. Such ODS alloys possess good high temperature strength and resistance to HT corrosion and oxidation. They derive their strength from the insoluble, deformation resistant and thermally stable dispersoids such as Y_2O_3 (as used in Incoloy MA956)[96] introduced during fabrication by mechanical alloying. This process offers great opportunities in the selection of dispersoids–matrix combination. Strengthening by insoluble, deformation resistant and inert dispersoids is far more effective than other methods such as solid solution and precipitation hardening, as thermodynamics imposes limitation on their continued effectiveness. At certain critical temperatures, solubility limits may be exceeded, leading to the onset of precipitation and eventually Oswald ripening of the precipitates.

During high temperature deformation, most ODS alloys exhibit a threshold stress σ_0 below which creep becomes negligible; the threshold stress σ_0 is less than Orwan stress σ_{or}. Several models, such as dislocation climb and dislocation detachment (local climb), have been advanced to explain the existence of the threshold stress. None of these models have been universally accepted.

To increase the temperature capability of ODS alloys, the powder produced by mechanical alloying is subjected to hot extrusion and the fine grained extruded structure is then subjected to a high temperature secondary recrystallization anneal.

The overall enhancement of HT capability may be associated with:

- large grain size produced by secondary recrystallization;
- high GAR (grain aspect ratio) produced by recrystallization under a high temperature gradient and minimizing the detrimental effect of transverse grain boundary effect;
- formation of serrated grain boundaries allowing grain interlocking; and
- minimum grain boundary hardening.

1.15.3.1.2 Observations on high temperature wear behavior of some ODS alloys

There is no evidence to suggest any improved wear resistance conferred by alloy pretreatment for the three near-identical ODS alloys, Incoloy MA956, PM2000, and PM2000SD[3] (Figure 10). Testing against various counterfaces (Stellite 6 and Si_3N_4)

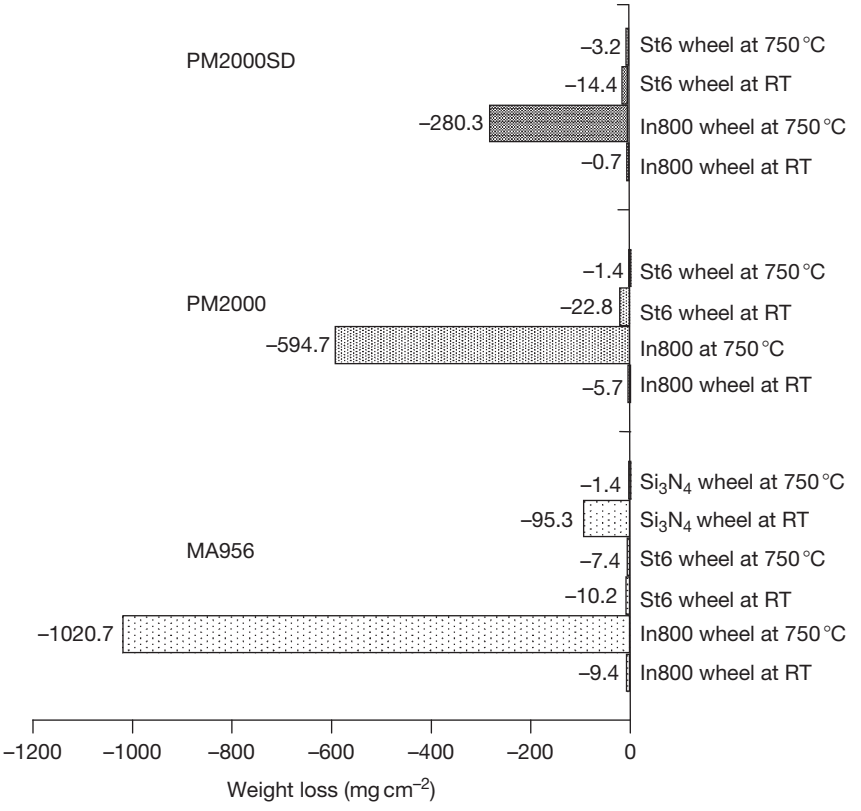

Figure 10 Weight change of the ODS alloys worn against various counterfaces at room temperature and 750 °C[3] (sliding speed 0.654 m s^{-1}, load 7 N).

and at various temperatures (room temperature to 750 °C) does not indicate a definitive trend in relation to grain size and hardness.

Incoloy 800HT counterface

Only on sliding against Incoloy 800HT there is an apparently strong preference towards lower grain size and increased hardness (**Table 2**) favoring higher wear.[3] The severity of wear was of the order PM2000SD, PM2000, and Incoloy MA956.

Poor wear resistance and high friction coefficient characterize the wear behavior of the ODS alloys worn against Incoloy 800HT at 750 °C (reciprocating rig, 0.314, 0.654, and 0.905 m s^{-1} sliding speed, 7 N load) as indicated by higher weight losses compared to that at room temperature (**Figure 10** – 0.654 m s^{-1}).[3] The apparent improved wear resistance observed at room temperature is attributable to transfer[3–5] and work hardening of a layer of Incoloy 800HT or back-transferred Incoloy MA956,[5] protecting the ODS alloy surface from sustained wear (**Figure 11(a)** – 0.654 m s^{-1}).

Table 2 Description and properties of the ODS alloys investigated

Alloy	*Description*	*Hv 500g*	*Av. grain size (μm)*
Ma956	ODS alloy strengthened through a yttria dispersion in Fe–Cr–Al matrix	303	3000
PM2000	ODS alloy strengthened through a yttria dispersion in Fe–Cr–Al matrix	311	500
PM2000SD	ODS alloy strengthened through a yttria dispersion in Fe–Cr–Al matrix. Rolled at higher temperature than PM2000 imparting greater ductility	363	80

Reproduced from Wood, P. D. Ph.D. Thesis, Northumbria University, UK, 1997.

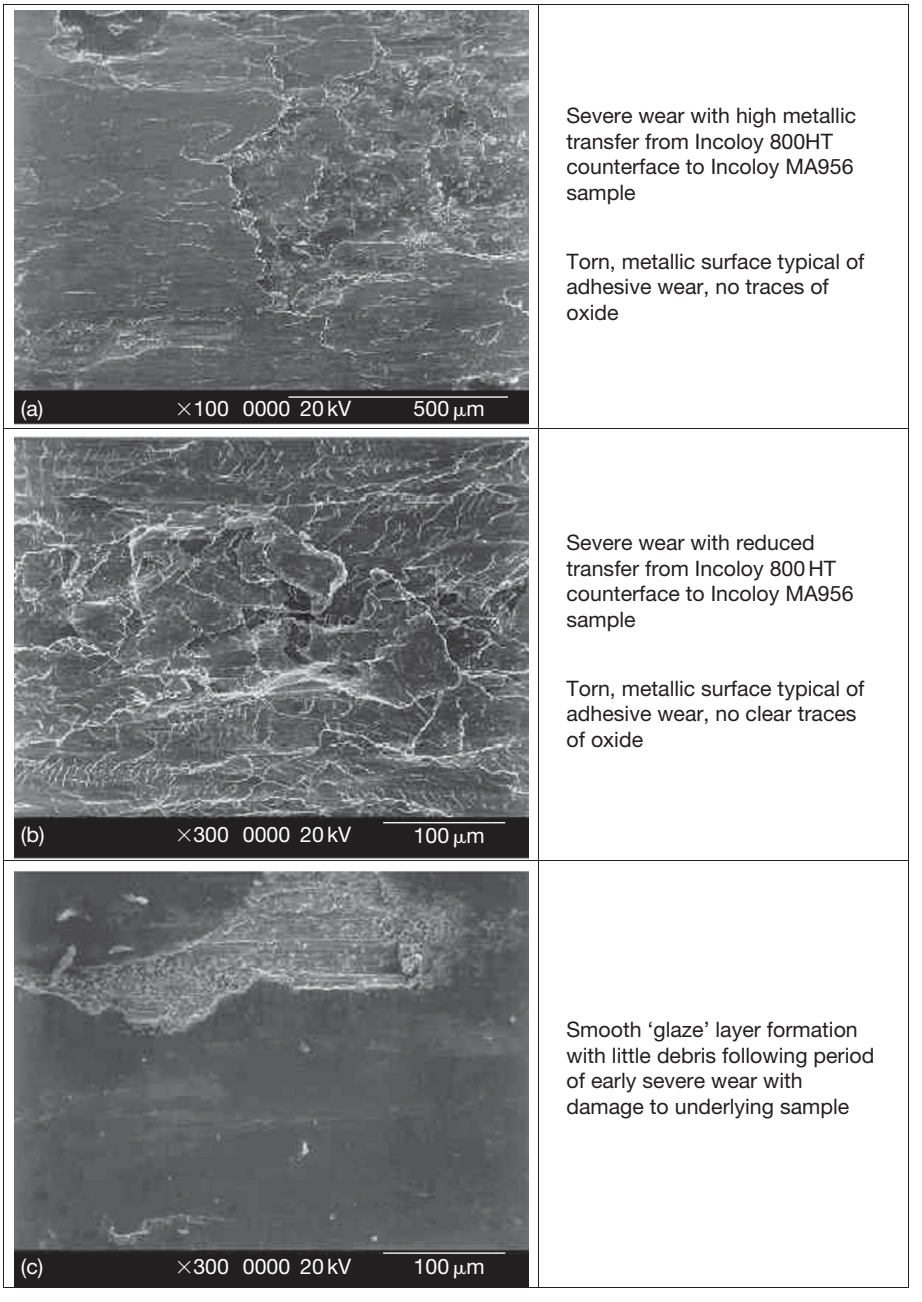

Figure 11 SEM micrographs of Incoloy MA956 wear surfaces after sliding at 0.654 m s^{-1} against an Incoloy 800HT counterface at room temperature, 510 and 750 °C (sliding distance 9418 m).[4] (a) Room temperature (shown), also typical of 270 °C, (b) 510 °C (also typical of 390, 450, 570, and 630 °C), (c) 750 °C (shown), also typical of 690 °C.

The loss of strength and hardness suffered by the ODS alloys at higher temperatures[10–12] (**Figure 12**) probably undermines the ability of the alloy to support the process of 'glaze' development. Severe wear continues (**Figure 11(b)** – 0.654 m s^{-1}) and the low levels of oxide produced act only to inhibit metallic adhesion, preventing the formation of the protective metallic transfer layer seen at room temperature[5] and wear thus increases with temperature. Some transfer of Incoloy 800HT material still occurs at high temperature; however, continued sliding removes this layer.[3,5] Such transfer tends to be greater at higher sliding speeds, and hence, the weight loss is lower at 0.905 m s^{-1} than at

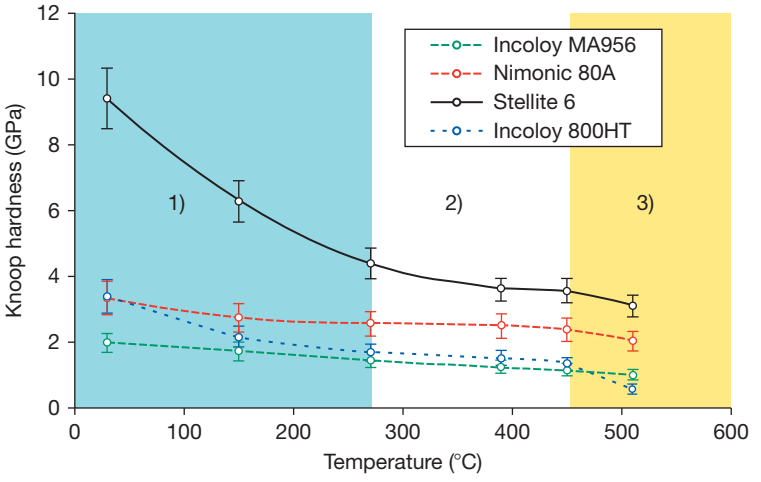

	Mean Knoop hardness (GPa)			
Temperature (°C)	Stellite 6	Nimonic 80A	MA956	Incoloy 800
30	9.39	3.33	1.99	3.38
150	6.28	2.75	1.71	2.16
270	4.37	2.58	1.45	1.68
390	3.61	2.50	1.24	1.52
450	3.55	2.37	1.16	1.34
510	3.08	2.01	0.97	0.55

Figure 12 Mean Knoop hardness (hot hardness, 50 g load, 12 s dwell time) from room temperature to 510 °C,[4] with wear regimes with respect to temperature identified for the Nimonic 80A/Stellite 6 and Incoloy MA956/Stellite 6 systems.[4,5] 1. Low-temperature oxidational wear, moderate falls (large for Stellite 6) in hardness. 2. Low-temperature oxidational wear at 0.314 m s^{-1}, metallic severe wear only at 0.905 m s^{-1}, little change in hardness. 3. 'Glaze' formation for Nimonic 80A vs. Stellite 6 at 0.314 m s^{-1} with high oxidational wear replacing metallic severe wear at 0.905 m s^{-1}. Also, early 'glaze' formation for Incoloy MA956 versus Stellite 6, with extended early severe wear at 0.905 m s^{-1}.

0.314 m s^{-1}[5] Only at 690 and 750 °C (**Figure 11(c)** – 0.654 m s^{-1} example shown) is an oxide[3] or 'glaze'[4,5] layer able to develop on the Incoloy MA956 surface (sourced from the Incoloy MA956) after an initial period of severe wear.[5]

Stellite 6 counterface

The improved wear resistance of ODS alloys when worn against Stellite 6 coincides with rapid oxide development; such oxide is sourced from both sample and counterface. At low temperature, this debris remains loose and does not readily form 'glaze' (**Figures 13(a) and 14(a)**). At high temperature, it sinters rapidly to form more extensive 'glaze' layers (**Figures 13(c) and 14(c)**).[3–5] The relative contributions of sample- and counterface-sourced debris (at least for Incoloy MA956 versus Stellite 6) have been observed to depend on sliding speed.[5,23] A slow sliding speed (0.314 m s^{-1})[5] favors greater Stellite 6 wear and thus higher levels of Co-based oxide debris. Faster sliding speeds (0.654 m s^{-1} [4]and especially, 0.905 m s^{-1})[5] encourage greater Incoloy MA956 wear and thus higher levels of Fe and Cr oxide contribution (**Figure 15**). At 750 °C, the presence of Co in the debris promotes more rapid 'glaze' formation[23] and prevents continued early wear.

Only at intermediate temperatures (390 and 450 °C)[4,5] and at 0.654 and 0.905 m s^{-1} does the oxide fail to separate wear surfaces and allow severe wear to occur (**Figure 14(b)**). Below these temperatures, the oxide separates the surfaces even in the

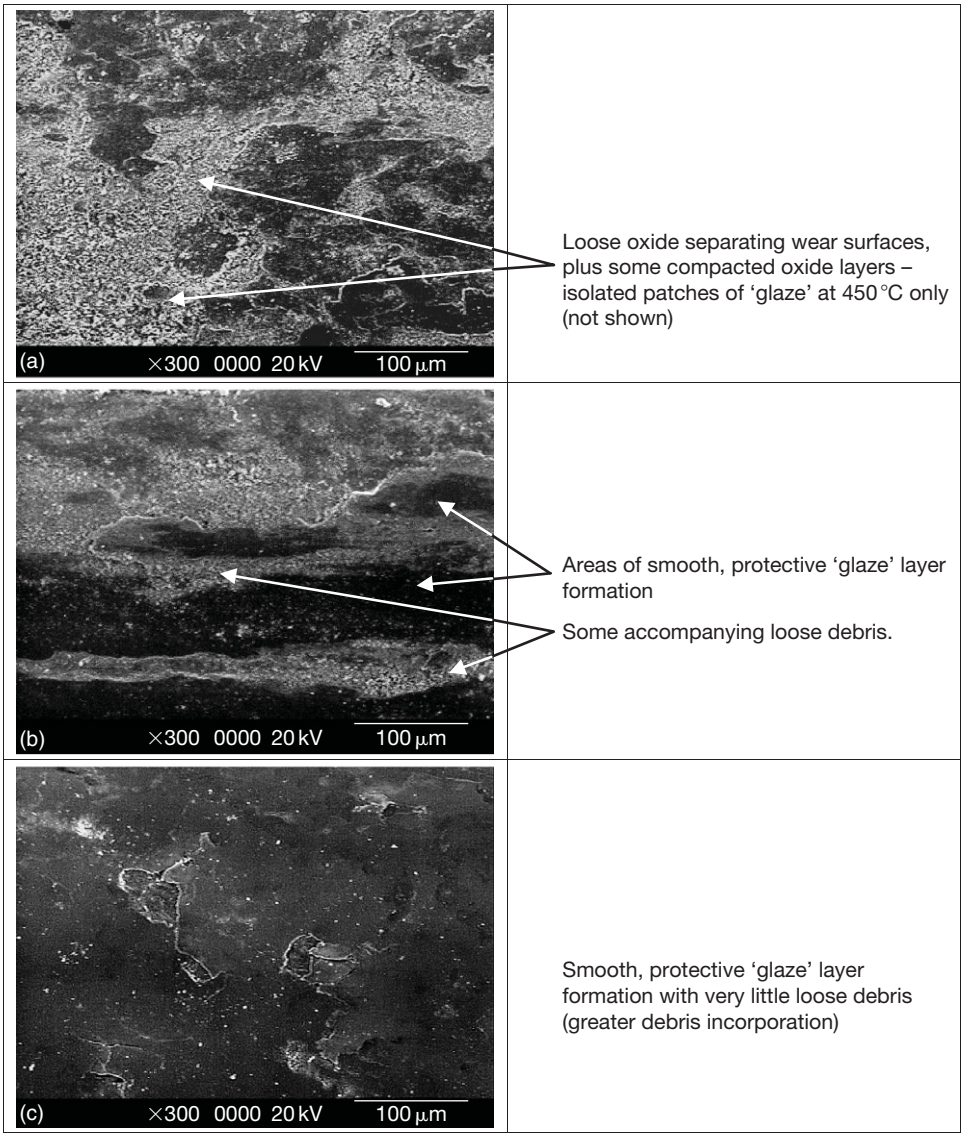

Figure 13 SEM micrographs of Incoloy MA956 wear surfaces after sliding at 0.314 m s^{-1} against a Stellite 6 counterface at room temperature, 510, and 750 °C.[23] (a) Room temperature (shown), also typical of 270, 390, and 450 °C, (b) 510 °C, and (c) 750 °C (shown), also typical of 570, 630, and 690 °C.

form of the aforementioned loose debris. At progressively higher temperatures, severe wear is increasingly restricted to only the initial sliding period as continued sliding promotes debris sintering and 'glaze' formation. Above 630 °C, 'glaze' development is so rapid that severe wear is all but eliminated. No severe wear is observed at 0.314 m s^{-1}, with the loose debris progressively developing into 'glaze' as sliding temperature is increased[5] (**Figure 13** shows the debris (a) loose at room temperature, (b) partially forming a 'glaze' layer at 510 °C, and (c) forming a comprehensive 'glaze' layer at 750 °C).

1.15.3.1.3 Effects of load

Rose[4] also examined the effect of load (7–25 N, 0.654 m s^{-1} only) on the sliding behavior of Incoloy MA956 when slid against Incoloy 800HT and Stellite 6 counterfaces at 750 °C (**Figure 16**). 'Glaze' layers were observed for all loads up to 20 N for both counterfaces and no change in oxide behavior was observed with increasing load (although greater material working was reported as being necessary to provide material for 'glaze' when an Incoloy 800HT counterface was used). No significant increases in weight loss were observed with increasing load up to 20 N (**Figure 17**). These

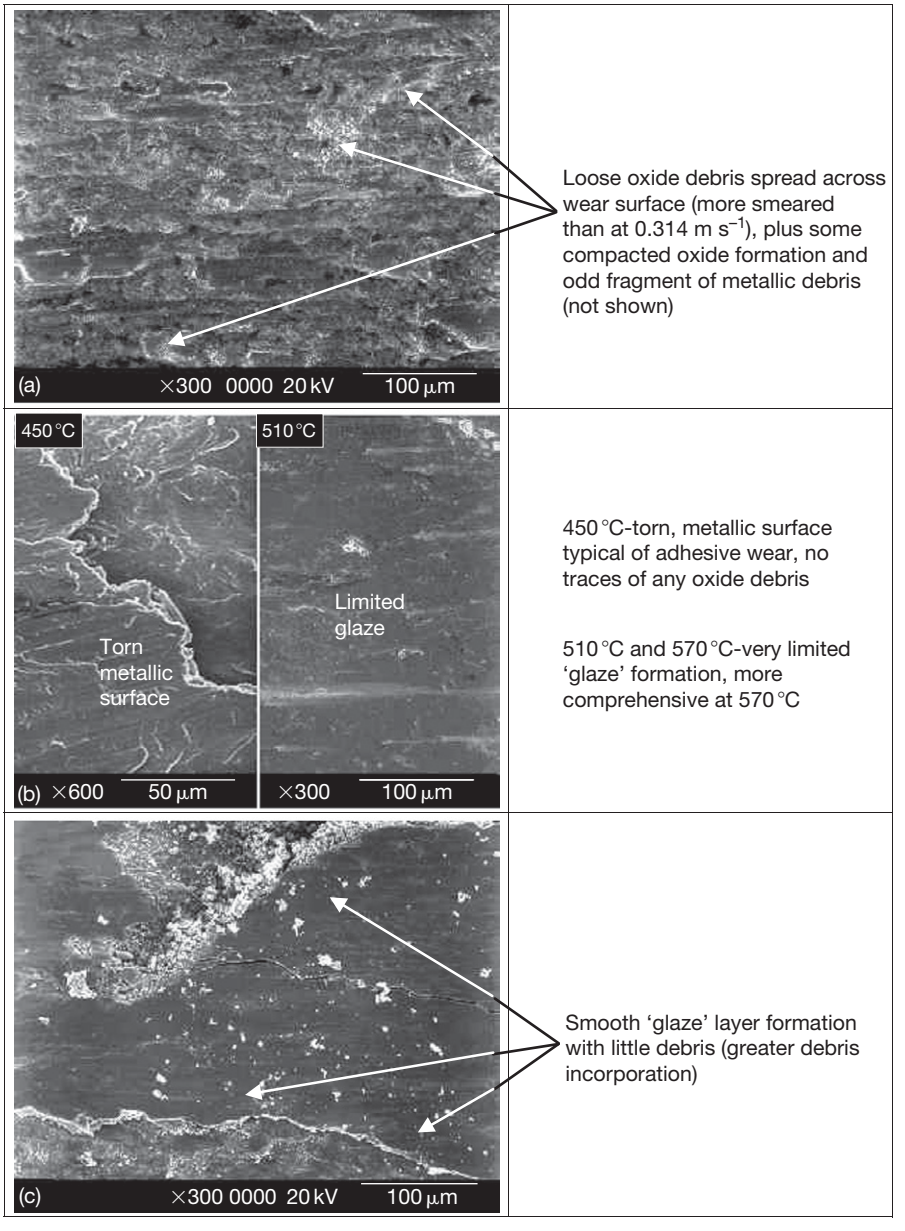

Figure 14 SEM micrographs of Incoloy MA956 wear surfaces after sliding at 0.654 m s^{-1} against a Stellite 6 counterface at room temperature, 450, 510, and 750 °C[4] (also representative of 0.905 m s^{-1}).[23] (a) Room temperature (shown), also typical of 270 and 390 °C, (b) 450 °C (left) and 510 °C (right – also typical of 570 °C), (c) 750 °C (shown), also typical of 630 and 690 °C.

observations were irrespective of whether the 'glaze' was primarily Stellite 6-counterface sourced or Incoloy MA956-sample sourced (when the counterface was Incoloy 800HT). Higher losses were reported at 25 N (most noticeably with an Incoloy 800HT counterface – Figure 17) and, although 'glaze' layers still formed, the Incoloy MA956 sample substrate was unable to provide sufficient support for the 'glaze' layer to remain protective.

1.15.3.2 Intermetallics

1.15.3.2.1 Introduction

Strong, predominantly metallic bonding between unlike atoms leads to the formation of intermetallics and intermetallic compound phases. From such bonding comes crystal structure, ordering, high strength at low and high temperature, low ductility, and low K_{1c}, particularly at low temperature.

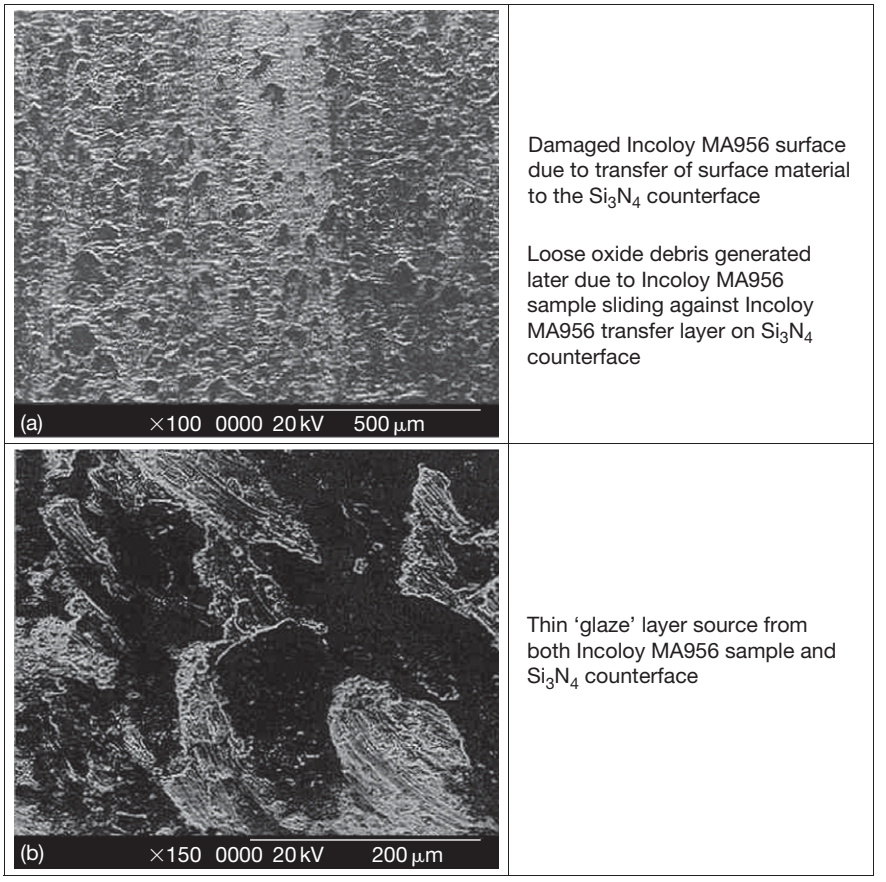

Figure 15 SEM micrographs of Incoloy MA956 wear surfaces after sliding at 0.654 m s^{-1} against a Si_3N_4 counterface at (a) room temperature and (b) 750 °C (load 7 N, sliding distance 9418 m). Reproduced from Wood, P. D. Ph.D. Thesis, Northumbria University, UK, 1997.

The low ductility, low K_{1c}, and high strength of intermetallics stem from such critical factors as complex crystal structures, the large Burgers Vector, high lattice stress, the inadequate slip systems and the inability to cross slip. The complex interplay between these parameters makes the prediction of intermetallic wear behavior difficult.

The expected improvement in wear resistance from high strength, ordering and an adequate slip system may be off-set by low K_{1c} and low fracture strain. The advantage in providing high wear resistance due to ordering may eventually be lost by the destruction of this ordering due to elemental diffusion from the counterface into the intermetallic lattice. At elevated temperature, increased K_{1c} and fracture strain are likely to improve the wear resistance; however, some of the effects of these parameters may be masked by the formation of wear resistance surface 'glaze' layers.

1.15.3.2.2 Wear of TiAl – Metallic counterfaces

In discussing intermetallic wear resistance, attention is focused on TiAl and TiAl-based intermetallics because of increasing interest in using these materials in many industrial applications, including automotive, aerospace, and power generation.

TiAl when worn against Incoloy 800HT at room temperature ('reciprocating-block-on-rotating-cylinder' rig, load 7 N, sliding speed 0.654 m s^{-1}) shows a similar wear pattern to the ODS and Nimonic alloys, and involves a similar mechanism[3]; the transfer of Incoloy 800 to the TiAl surface, followed by work hardening of the transferred layer, and formation of a wear-resistant oxide layer ($NiCr_2O_4/Fe_2O_3$). The development of this hardened, wear-resistant layer causes some improvement in wear resistance without any observable 'glaze' formation (**Figure 18(a)**).

In contrast, 'glaze' formation has been observed in the same system at 750 °C (7 N, 0.654 m s^{-1}), the 'glaze'

Incoloy 800HT counterface		Stellite 6 counterface	
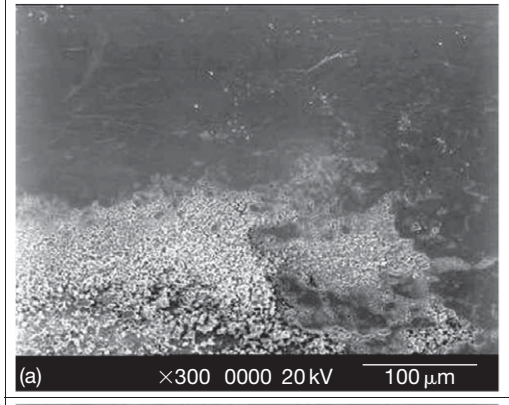	Smooth compacted oxide / 'glaze' layers with a little loose debris (underlying sample damaged due to early severe wear)	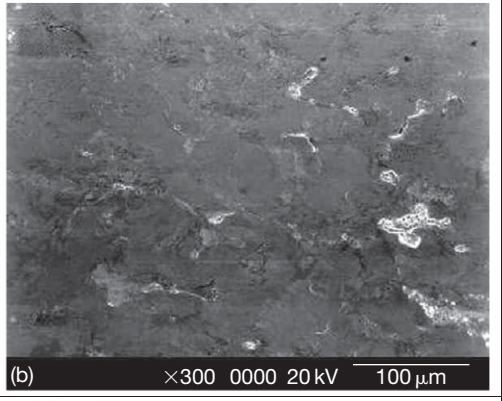	Smooth compacted oxide / 'glaze' layers
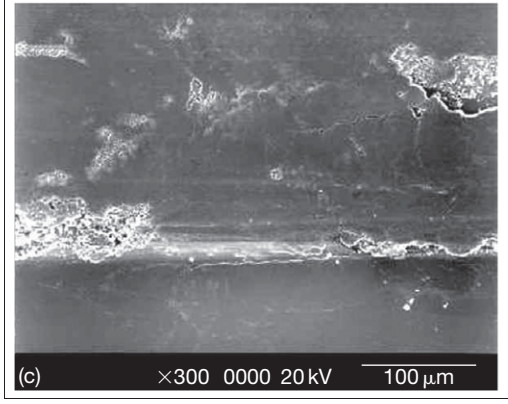	Smooth compacted oxide / 'glaze' layers and a little loose debris, with some cracking due to high load (underlying sample damaged due to early severe wear)	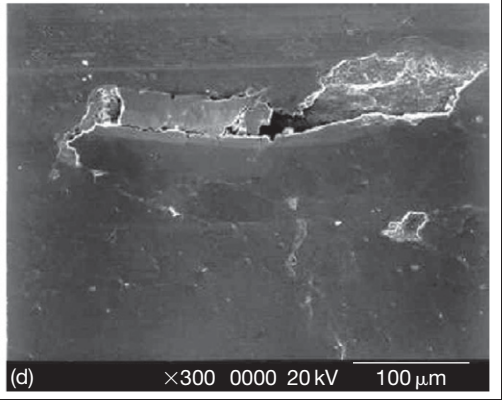	Smooth compacted oxide / 'glaze' layers, with some cracking due to high load

Figure 16 SEM micrographs of Incoloy MA956 worn against an Incoloy 800HT counterface at applied loads of (a) 7 N and (b) 25 N, and against a Stellite 6 counterface at applied loads of (c) 7 N and (d) 25 N (750 °C, sliding speed 0.654 m s^{-1}, sliding distance 9418 m). Reproduced from Rose, S. R. Ph.D. Thesis, Northumbria University, UK, 2000.

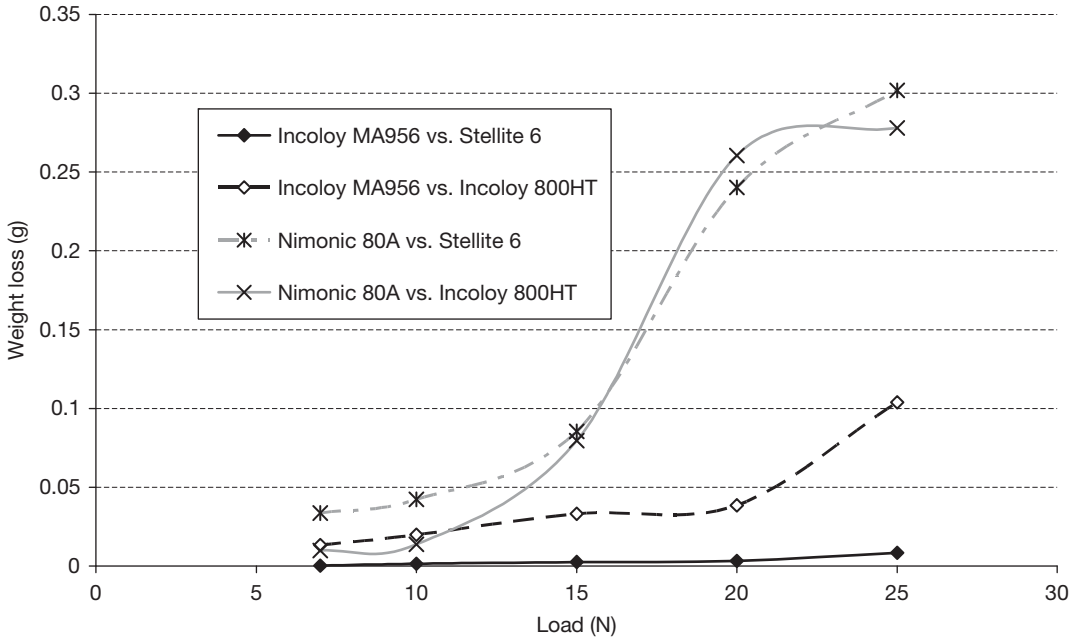

Figure 17 Weight losses for Incoloy MA956 and Nimonic 80A worn against Incoloy 800HT and Stellite 6 counterface at applied loads of between 7 and 25 N (750 °C, sliding speed 0.654 m s^{-1}, sliding distance 9418 m). Reproduced from Rose, S. R. Ph.D. Thesis, Northumbria University, UK, 2000.

(Figure 18(b)) containing mainly oxidized Fe/Ni/Cr material from Incoloy 800 with little Ti and Al.[3] These observations are in conflict with other work where the 'glaze' contained the elements of TiAl. It is believed that the use of a different test system ('pin-on-disk' rather than 'block-on-cylinder') in the latter work accounts for this difference. The role of TiAl is considered to provide a deformation and wear-resistant substrate for the 'glaze' to develop, to reside, and to be sustained.

When worn against Stellite 6 (7 N, 0.654 m s^{-1})[3], initial transfer of Stellite 6-based material on the TiAl surface results initially in a like-on-like sliding regime, with the Stellite 6 counterface sliding against this transferred layer. At room temperature (Figure 18(c)), instability of this layer leads to a continual process of transfer and removal from both surfaces and a loose oxide containing Ti and Al from the TiAl, and Co and Cr from the Stellite 6 is generated. Only at 750 °C (at 0.314 m s^{-1},[97] as well as 0.654 m s^{-1})[3] does the transferred Stellite 6 material form a primarily Co–Cr-oxide 'glaze' layer on the TiAl surface (Figures 18(d) and 19(a)), this layer being thinner than that created when sliding against Incoloy 800HT.

1.15.3.2.3 Wear of TiAl – Ceramic counterfaces

TiAl suffers moderate wear when slid against a silicon nitride interface at room temperature (0.654 m s^{-1}). While the debris generated (sourced from both sample and counterface) forms loose oxide platforms (or 'plateaux' – Figure 20(a)), these are formed and removed as sliding continues and do not form a wear protective layer. The high TiAl wear has been attributed to the elements of the counterface material interfering with the ordered structure of the intermetallic, as small atomic radii Si and N enter the lattice and increase its susceptibility to wear. A mixture of abrasive and adhesive wear with some evidence of stick-slip, possibly due to high mutual chemical compatibility between the Si_3N_4 and the TiAl, has been reported[98] (Si_3N_4 has been previously observed to have high mutual chemical compatibility with both Ti and Al[99]), leading to moderate wear of the TiAl and high wear of the Si_3N_4. In contrast, TiAl undergoes lower wear when slid against silicon nitride at 750 °C (at 0.314[97] and 0.654 m s^{-1}),[3] due to the rapid formation of a thin wear-resistant oxide layer (Figures 19(b) and 20(b)). The formation of this layer, sourced from both the TiAl and Si_3N_4, prevents substantial wear. It is suggested that any high mutual compatibility enhances the very early stages of wear, providing the necessary material for the wear-resistant layer.

TiAl undergoes higher wear when worn against Al_2O_3 at room temperature[97] with enhanced material removal by abrasion, the debris from which does not form a protective layer. The material generated from

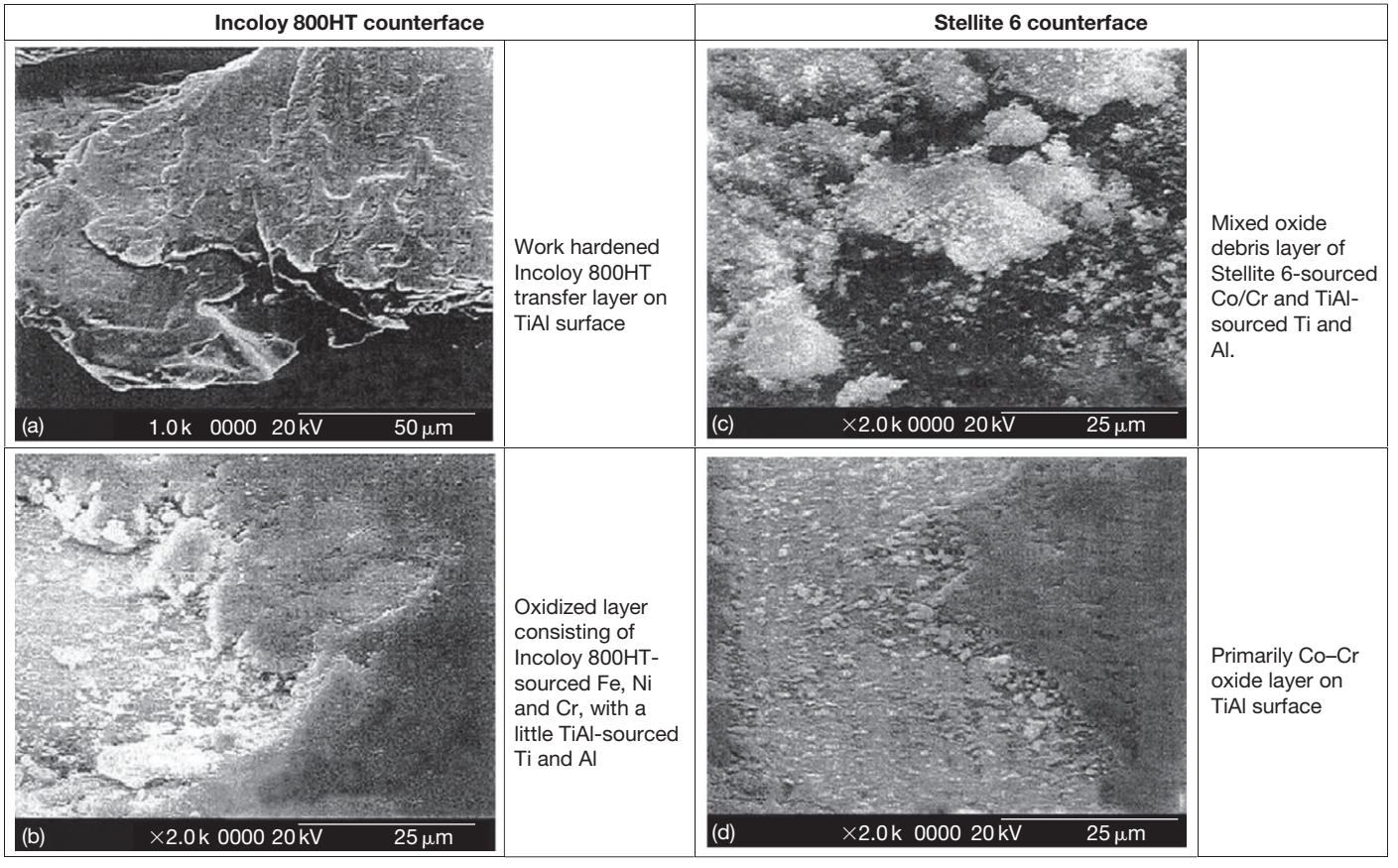

Figure 18 SEM micrographs of TiAl worn against an Incoloy 800HT counterface at (a) room temperature and (b) 750 °C, and against a Stellite 6 counterface at (c) room temperature and (d) 750 °C, sliding speed 0.654 m s^{-1} (load 7 N, sliding distance 9418 m). Reproduced from Wood, P. D. Ph.D. Thesis, Northumbria University, UK, 1997.

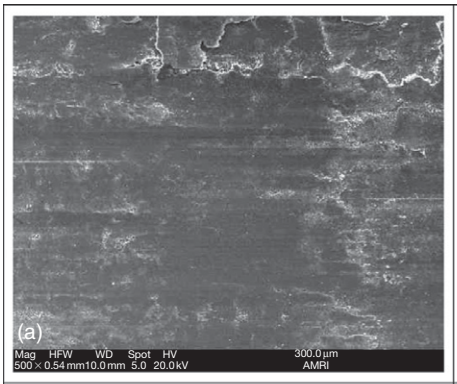

'Glaze' layer up to 3 µm thickness with limited fragmentation and break-away, most evident near top and top right

Also some loose debris evident (lighter areas to left and right)

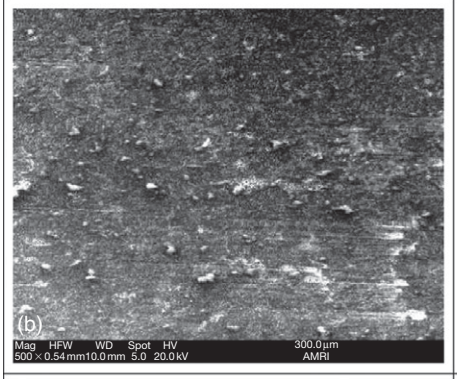

'Glaze' layer up to 3 µm thickness overlaid by a few fragements of broken-away 'glaze' of between 1 and 15 µm

Also some loose debris and very limited break-away (streaks in bottom right hand corner)

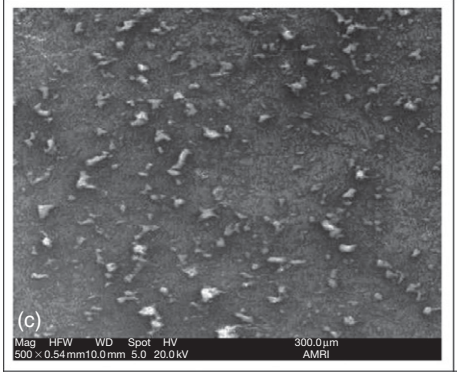

Smooth 'glaze' layer up to 3 µm overlaid by fragments of broken-awy 'glaze' of between 1 and 20 µm in size

Little evidence of loose debris

Figure 19 SEM micrographs of γ-TiAl wear scar surfaces after wear against Stellite 6, Si_3N_4 and Al_2O_3 counterfaces at 750 °C, sliding speed 0.314 m s^{-1} (load 7 N, sliding distance 4522 m).[97] (a) Stellite 6 counterface, (b) Si_3N_4 counterface, and (c) Al_2O_3 counterface.

an initial period of high TiAl-wear against Al_2O_3 at 750 °C,[97] however, readily forms a 'glaze' layer (Figure 19(c)) which provides some protection for the TiAl surface and prevents excessive wear. However, despite the 'glaze' layer, the abrasive nature of the oxide generated (a mixture of Ti and Al oxides) still promotes continued material removal. In contrast, the Al_2O_3 undergoes little wear at both room temperature[99] and 750 °C,[97] with it having no potential chemical compatibility with TiAl; hence, no adhesive mechanism can occur.

1.15.3.3 Nimonic Alloys

1.15.3.3.1 Incoloy 800HT counterface

Wood[3] reported a correlation between Nimonic 80A cast, Nimonic 80A HIPped, and Nimonic 90 when tested against different counterfaces at various temperatures (0.654 m s^{-1}, 7 N load and reciprocating-block/sample-on-rotating cylinder/counterface configuration). The results of room temperature tests seemed to be greatly influenced by the degree of material transfer to the Nimonic surface, this transfer

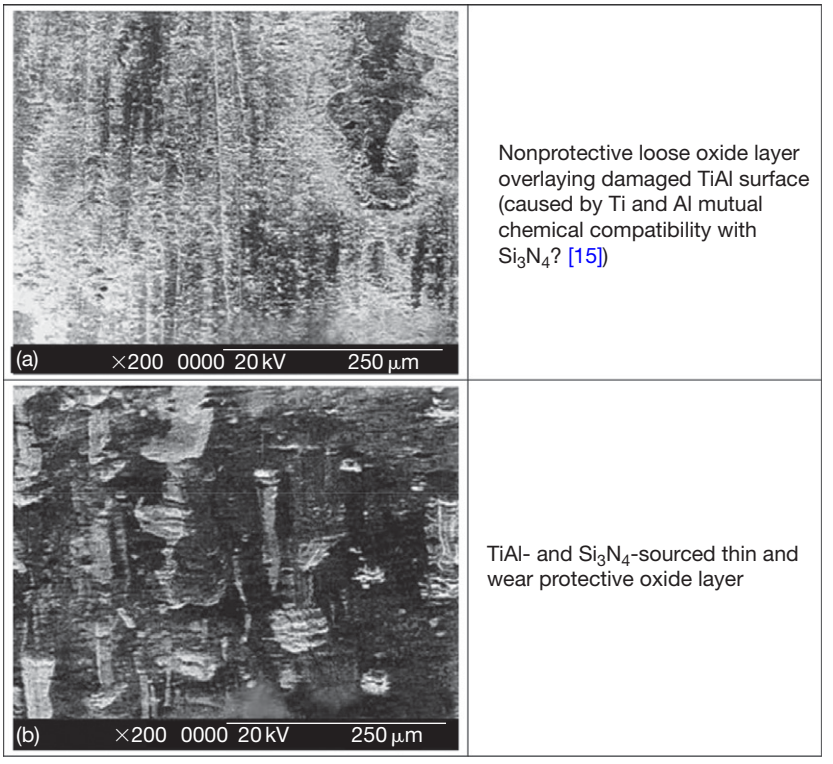

Figure 20 SEM micrographs of TiAl worn against a Si_3N_4 counterface at (a) room temperature and (b) 750 °C, sliding speed 0.654 m s^{-1} (load 7 N, sliding distance 9418 m). Reproduced from Wood, P. D. Ph.D. Thesis, Northumbria University, UK, 1997.

itself being influenced by counterface hardness; the softer the counterface the higher the amount of transfer.

Metallic transfer readily occurred from the relatively soft Incoloy 800HT counterface onto the surfaces of each of the Nimonic materials at room temperature. The transferred material formed a wear-resistant layer which protected the Nimonic material surfaces and led to very small weight changes. Inman[5] later reported the development of metallic transfer layers at 0.314 and 0.905 m s^{-1} (**Figures 21 and 22** – greater transfer was observed at 0.905 m s^{-1}) when Nimonic 80A was slid against Incoloy 800HT; these layers were work hardened.

At 750 °C, the Nimonic alloys showed a large range of behaviors when tested against the same three counterfaces.[3] When slid against Incoloy 800HT, mainly Incoloy 800HT-sourced layers that protected the Nimonic alloys against wear, together with low weight changes, were observed. Rose[4] and Inman[5] additionally reported 'glaze' overlying any transferred material when Nimonic 80A was worn against Incoloy 800HT at this temperature.

Rose (0.654 m s^{-1})[4] and Inman (0.314 and 0.905 m s^{-1})[5] examined temperatures between room temperature and 750 °C (**Figures 21 and 22**), with Rose[4] noting that Incoloy 800HT-sourced transfer layers continued to be observed up to 570 °C. Inman[5] reported the development of transfer layers up to 750 °C, observing an increase in transfer with sliding speed. At 0.314 m s^{-1}, transfer was less, due to increased amounts of oxide that interfered with metallic adhesion, but did not form 'glaze.' At 0.905 m s^{-1}, transfer was greater than at either 0.314 or 0.654 m s^{-1}; any surface oxidation was more readily removed, allowing greater adhesion of transferred material.

'Glaze' layers were observed only between 630 and 750 °C,[4,5] with its formation being favored by increased test temperature[4,5] and lower sliding speed (due to decreased material removal).[5] These 'glaze' layers were reported to form after transfer from the Incoloy 800HT counterface to the Nimonic 80A surface[5]; effectively, the 'glaze' was generated by 'like-on-like' sliding of the transfer layer against the Incoloy 800HT counterface.

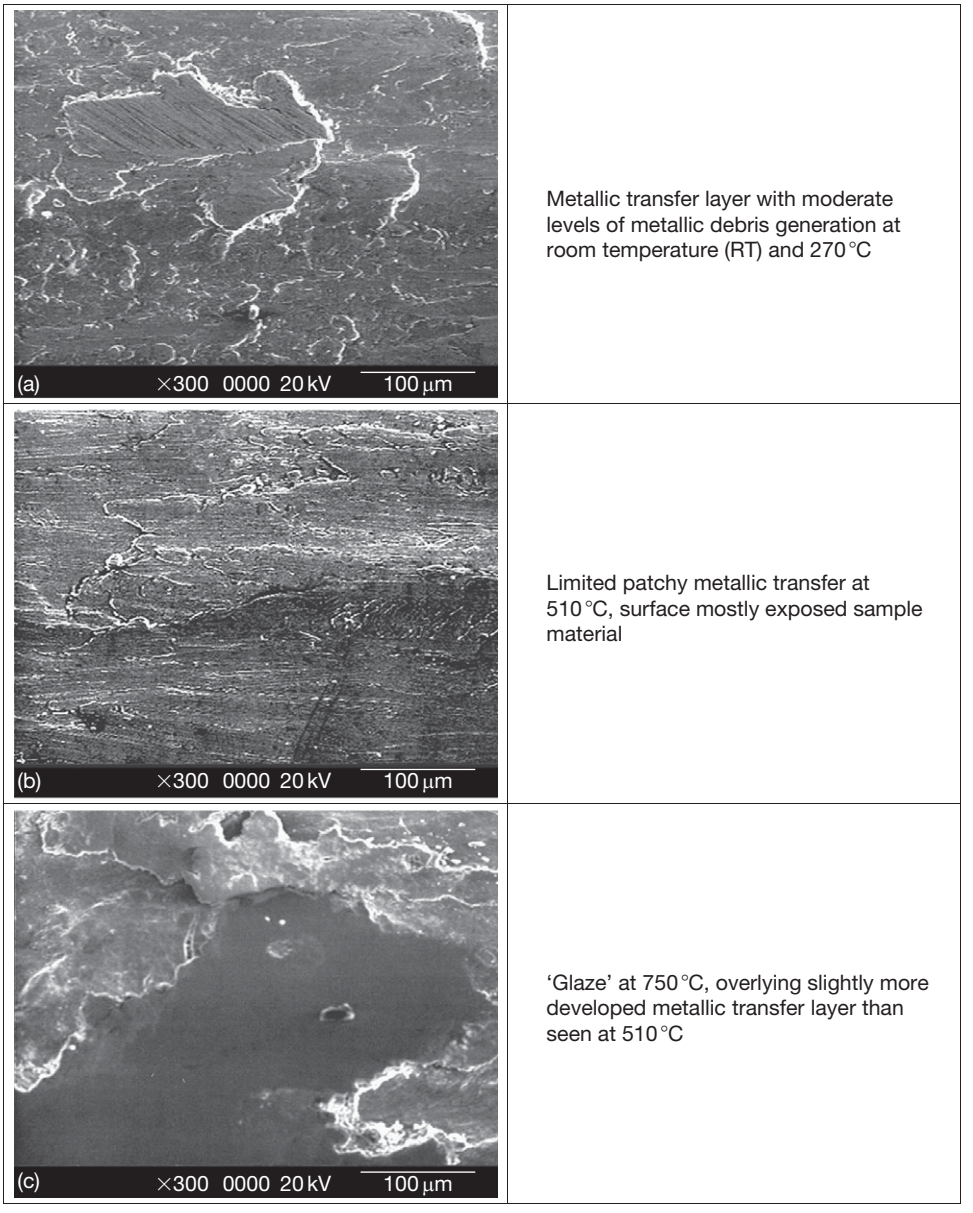

Figure 21 SEM micrographs of Nimonic 80A wear surfaces after sliding at 0.314 m s^{-1} (load 7 N, sliding distance 4522 m) against an Incoloy 800HT counterface at room temperature, 270, 570, and 750 °C.[5] (a) Room temperature (shown), also typical of 270 °C, (b) 510 °C (shown), also typical of 390, 450, 570, and 630 °C, and (c) 750 °C (shown), also typical of 690 °C.

Effects of load

Rose[4] also examined the effect of load (7–25 N, 0.654 m s^{-1} only) on sliding behavior for Nimonic 80A when slid against Incoloy 800HT at 750 °C. Limited compacted oxide layers formed at 7 N (**Figure 23(a)**) and 10 N load, protecting the Nimonic 80A surface. At loads between 15 and 25 N (**Figure 23(b)**), an abrasive, oxidational wear regime dominated, with no debris build-up or layer formation; the behavior of the oxide changed from protective to abrasive due to the increased load. This was reflected by a rapid increase in weight loss above 15 N (**Figure 17**).

1.15.3.3.2 Stellite 6 counterface

Wood (0.654 m s^{-1}, 7 N load)[3] reported only limited material transfer from the harder Stellite 6 counterface to the Nimonic material surfaces at room temperature. Thin mixed oxide layers were formed on the Nimonic

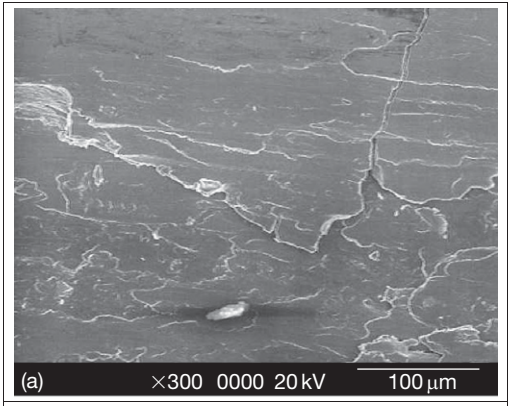

Metallic transfer layer with moderate levels of metallic debris generation at room temperature (RT) and 270 °C, greater transfer of metal onto sample surface than at 0.314 m s^{-1} (Fig. A1)

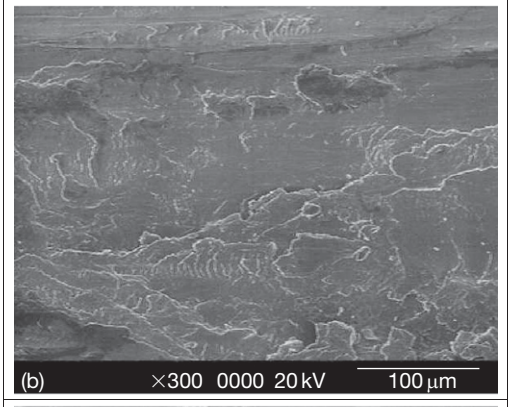

Comprehensive metallic transfer continuing at 510 °C (greater than at 0.314 m s^{-1} – Fig. A1) – metallic debris generation from both sample and counterface

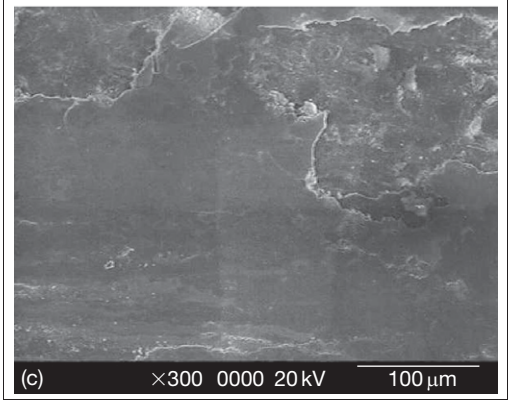

'Glaze' at 750 °C, overlying more limited metallic transfer layer

Figure 22 SEM micrographs of Nimonic 80A wear surfaces after sliding at 0.905 m s^{-1} (load 7 N, sliding distance 4522 m) against an Incoloy 800HT counterface at room temperature, 270, 570, and 750 °C.[5] (a) Room temperature and 270 °C (shown), also typical of 390 °C, (b) 570 °C (shown), also typical of 450, 510, and 630 °C, and (c) 750 °C (shown), also typical of 690 °C.

surfaces; these contained material from both the Nimonic and Stellite 6 wear surfaces and provided only limited protection. Testing of Nimonic 80A against a Stellite 6 counterface at 0.654 m s^{-1}[4] and at 0.314 and 0.905 m s^{-1}[5,21,22] (**Figures 24(a) and 25(a)**) resulted in preferential wear of the Stellite 6 counterface, generating loose Co–Cr-based oxides. This debris separated the wear surfaces, preventing metallic contact; a low temperature mild wear regime resulted.

Behavior at intermediate and high temperature depended significantly on sliding speed. At 0.314 m s^{-1}[5,21,22] the loose debris mild wear regime (**Figure 24(a)**) continued up to 450 °C. Increased sintering was observed at 390 °C, isolated 'glaze' at

Incoloy 800HT counterface		Stellite 6 counterface	
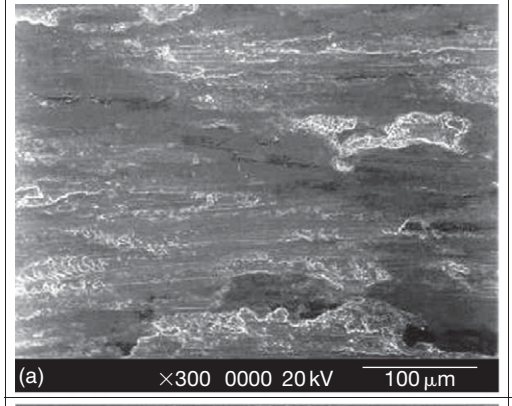	Limited compacted oxide layers overlying Nimonic 80 A surface	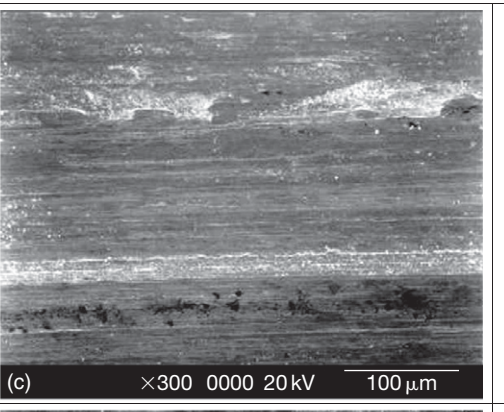	Grooved, worn surface due to abrasive action
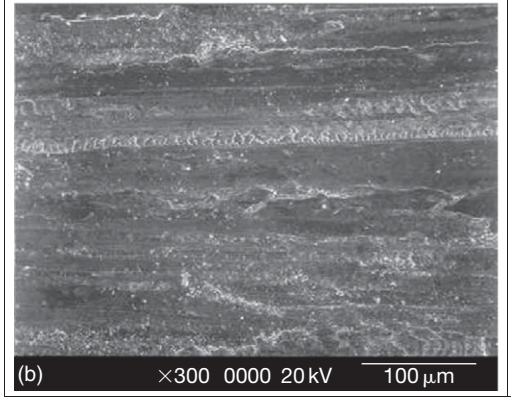	Grooved, worn surface due to abrasive action	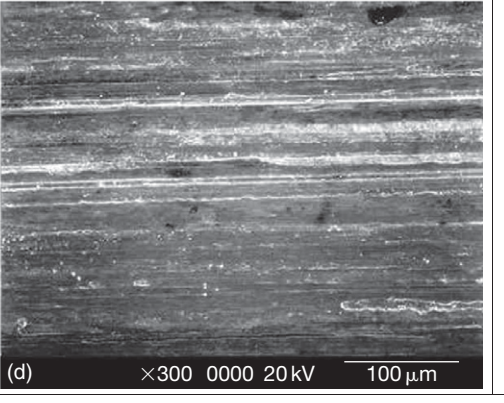	Damage (grooves) more pronounced at higher load

Figure 23 SEM micrographs of Nimonic 80A worn against an Incoloy 800HT counterface at applied loads of (a) 7 N and (b) 25 N, also against a Stellite 6 counterface at applied loads of (c) 7 N and (d) 25 N (750 °C, sliding speed 0.654 m s^{-1}, sliding distance 9418 m). Reproduced from Rose, S. R. Ph.D. Thesis, Northumbria University, UK, 2000.

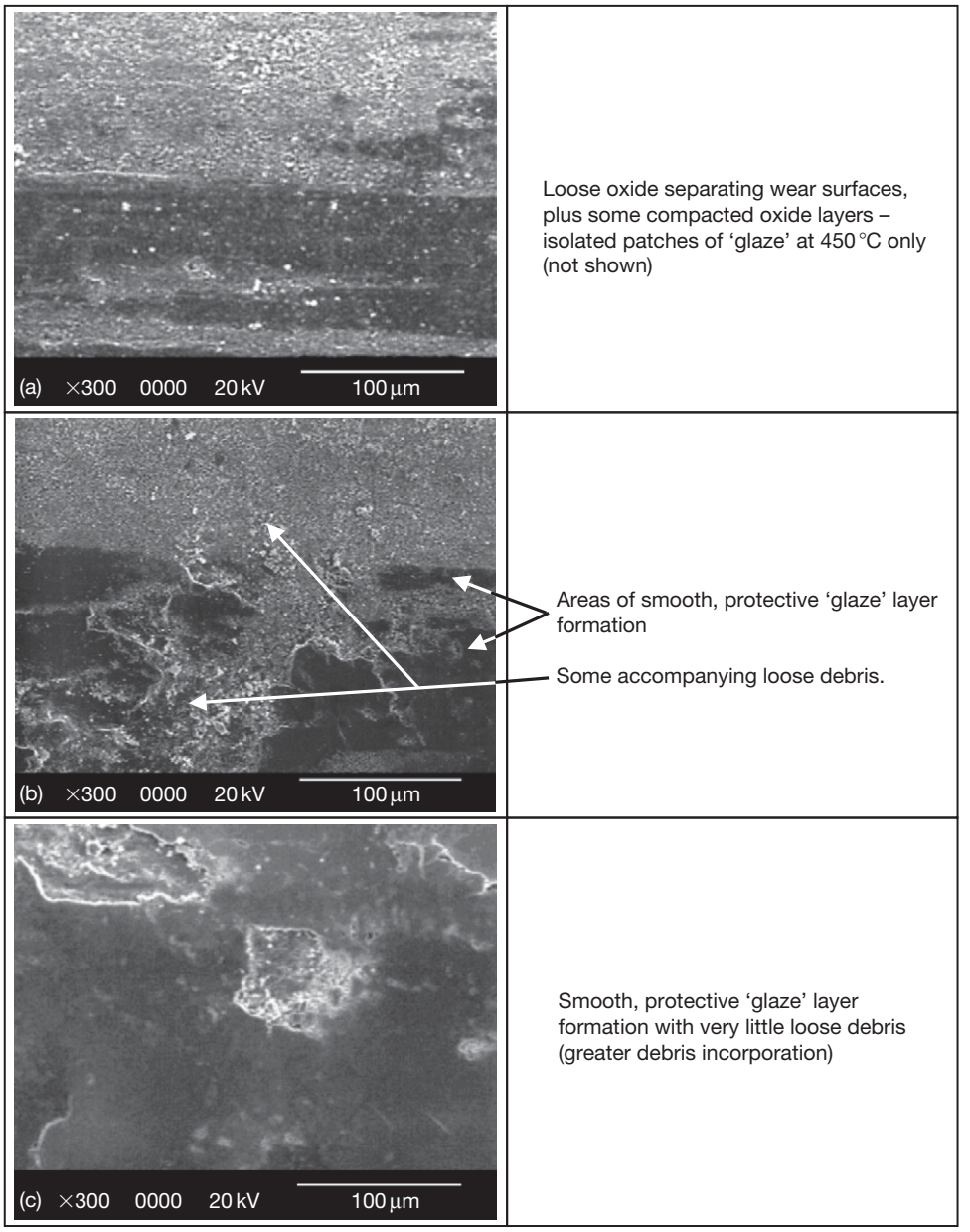

Figure 24 SEM micrographs of Nimonic 80A wear surfaces after sliding at 0.314 m s^{-1} (load 7 N, sliding distance 4522 m) against a Stellite 6 counterface at room temperature, 510 and 750 °C.[22] (a) Room temperature (shown), also typical of 270, 390, and 450 °C and (b) 510 °C, (c) 750 °C (shown), also typical of 570, 630, and 690 °C.

450 °C, with increasingly comprehensive 'glaze' formation above 510 °C (**Figure 24(b)**) and most notably between 630 and 750 °C (**Figure 24(c)**).[5,21,22,24]

The loose debris mild wear regime was observed up to 390 °C at 0.654 m s^{-1}[(4)] and 270 °C at 0.905 m s^{-1}[(5,21,22)]; at higher temperatures, there was a transition to intermediate severe wear. Such severe wear was observed at 0.654 m s^{-1} up to 570 °C,[4] without any evidence of oxide (**Figure 25(b)**); only metallic debris sourced from the Nimonic 80A was generated by delamination wear. At 630 °C, however, oxide was observed and this assisted severe wear by abrasion.[5,21,22,24] A similar pattern was observed at 0.905 m s^{-1}[(5,21,22)] though enhanced frictional heating led to oxide generation at 570 °C as well as 630 °C.

On increasing temperature to 690 and 750 °C, further increases in oxide production were sufficient to separate completely the Nimonic 80A sample and

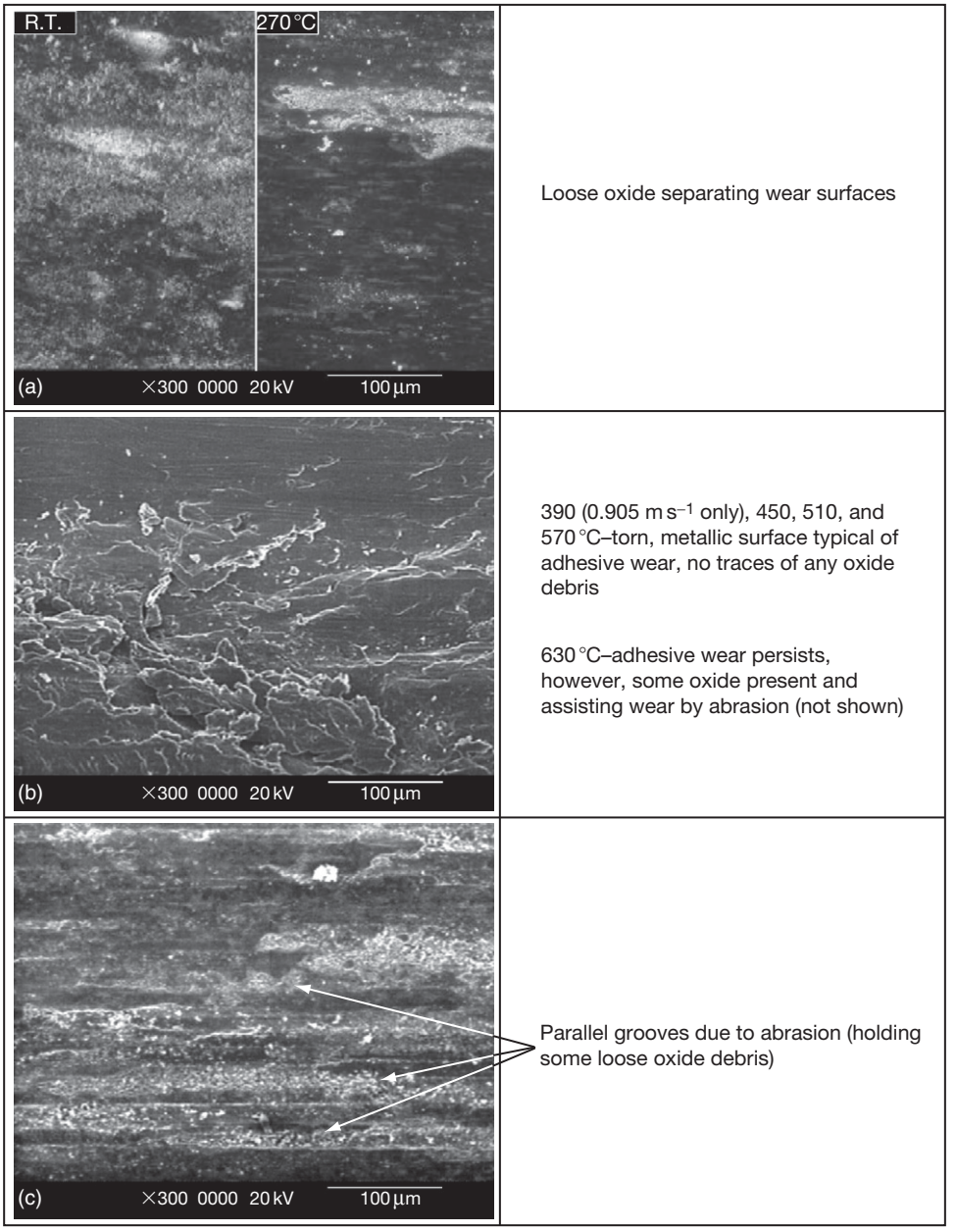

Figure 25 SEM micrographs of Nimonic 80A wear surfaces after sliding at 0.654 m s^{-1} (load 7 N, sliding distance 4522 m) against a Stellite 6 counterface at room temperature, 270, 570, and 750 °C (also typical of 0.905 m s^{-1}).[22] (a) Room temperature and 270 °C (shown), also typical of 390 °C (0.654 m s^{-1} only), (b) 570 °C (shown), also typical of 390 (0.905 m s^{-1} only) 450, 510, and 630 °C, and (c) 750 °C (shown), also typical of 690 °C.

Stellite 6 counterface; a mild wear regime was thus established. However, high wear rates continued; although technically a mild wear regime, the high wear rates indicates that the oxide was not protective. Two slightly different forms of oxidational behavior were observed, depending on researcher. At 0.654 m s^{-1}, Wood[3] reported the formation of a poorly adherent 'glaze' that was continuously removed. In contrast, Rose[4] reported no 'glaze' formation on Nimonic 80A and the generation of only loose oxides that acted abrasively (NiO and Cr_2O_3), thereby enhancing removal from the Nimonic 80A surface. These latter observations were confirmed by Inman[5,22,24] at both 0.654 m s^{-1} (**Figure 25(c)**) and 0.905 m s^{-1}, who

observed greater oxide generation at 0.905 m s^{-1} but still without 'glaze' layer formation.

Rose[4] stated that layers were unable to form due to insufficient debris adhesion to the Nimonic 80A sample surfaces and lack of debris cohesion, caused by the ploughing of sample surfaces by hard carbide particles in the Stellite 6 counterface. However, Inman[5] argued that the carbides were not hard enough to have this ploughing effect and inhibit the development of oxide layers; it was possible that the carbides were softer than the 'glaze' layers and wore in preference to them. This inability of the Nimonic 80A-sourced NiO and Cr_2O_3 oxides to form a 'glaze' was instead attributed to their relatively poor sinterability. If this failure to form 'glaze' layers had been due to carbide ploughing, then these layers would not have formed in other systems involving Stellite 6. For example, Stellite 6-sourced Co–Cr layers formed in the Nimonic 80A/Stellite 6 (counterface) system at 0.314 m s^{-1}.[5,22,24] Also, Incoloy MA956-sourced Fe–Cr-based layers formed at 0.905 m s^{-1} in the Incoloy MA956/Stellite 6 (counterface) system.[5,23]

Inman *et al.*[22] collated the available data to create a temperature versus sliding speed wear map for the Nimonic 80A versus Stellite 6 (counterface) system (later further developed by Inman and Datta[24]), covering a variety of different modes of wear behavior that are dependant on load–sliding speed combination. This is discussed further in **Section 1.15.5.3**.

Effects of load

Rose also studied the effect of load on sliding behavior for Nimonic 80A worn against Stellite 6 at 750 °C.[4] At all loads (7–25 N), the wear mechanism remained predominantly oxidational, with elements of abrasive wear, regardless of applied load (**Figures 23(c) and 23(d)**); no compacted debris layers were formed across the range of loads (7–25 N) at 750 °C. There was no evidence that changing load had any significant effect on wear regime in this case; however, the grooves on the damaged surface became more pronounced at high load. This was reflected by increased weight loss at high load (**Figure 17**).

1.15.3.3.3 Effect of Nimonic material processing route on wear

Very similar wear properties were observed for Nimonic 80A (cast) and Nimonic 80A (HIPped)[3] and it was not possible to conclude that processing route affected wear resistance. Wear behavior was also similar for Nimonic 90, the only exception being the enhanced wear resistance of Nimonic 90 over Nimonic 80A (cast) at 750 °C (**Figure 26**).

1.15.3.3.4 Nimonic 80A sliding wear – Comparisons between various wear rig configurations

The apparently poor sintering and 'glaze' forming characteristics of NiO and Cr_2O_3 generated from Nimonic 80A (at 0.654 and 0.905 m s^{-1})[4,5,21,22,24] at first seems to contradict the extensive studies carried out into 'glaze' formation with Nimonic 80A-based systems by Jiang *et al.*[2,16–19] However, the last group used lower sliding speeds with a like-on-like reciprocating 'pin-on-disk' configuration (mean sliding speed 83 mm s^{-1}); such systems have a higher degree of debris retention, providing greater opportunity for the oxide debris to sinter together to form 'glaze' layers. The 'block-on-cylinder' configuration used by Rose[4] and Inman *et al.*[5,21,22,24] is a unidirectional sliding wear system that promotes debris mobility and ejection over retention, especially at higher sliding speeds. The decreased residency and greater mobility of the debris do not allow sufficient contact time between debris particles for sintering and welding processes to occur, as is necessary for 'glaze' formation.

1.15.3.3.5 Si_3N_4 counterface

Wood (0.654 m s^{-1}, 7 N load)[3] reported limited material transfer from the harder Si_3N_4 counterface to the Nimonic material surfaces at room temperature. Thin mixed oxide layers were formed on the Nimonic surfaces; these contained material from both wear surfaces that provided only limited protection.

Wood[3] observed a very different wear resistance when Nimonic 80A (cast) and Nimonic 90 were worn against Si_3N_4 at 750 °C. Nimonic 80A (cast) showed very poor resistance, with no 'glaze' formation in contrast to Nimonic 90 where 'glaze' formation and very low weight losses were observed. Wood attributed the difference to the presence of Co in the Nimonic 90, which somehow improved 'glaze' adhesion and/or strength on the Nimonic 90 surface.

1.15.3.4 Effects of Environmental Variables

1.15.3.4.1 Oxygen levels and partial pressure

Even in environments with low oxygen partial pressure[19,100] (effectively removing much of the oxygen from the system), stable oxide layers are still able to form. Under vacuum, increasing pressure from high vacuum conditions to 10^{-2} Pa was enough to result in a decrease in friction in sliding of an iron–chromium alloy. Buckley[101] noted during the like-on-like sliding of clean iron that a pressure of 400 Pa (or 3 Torr) was

sufficient to prevent seizure. Lancaster[26] noted that, at 300 °C, the range of sliding speeds over which severe wear was observed when a 60/40 brass was slid against tool steel was greatly in an oxygen atmosphere compared to the level of wear observed in air (**Figure 2**).

Barnes *et al.*[100,102,103] investigated the effects of partial pressure on iron–chromium alloys, ranging from pure iron to iron–40% chromium (**Figure 27**). Initial work in a normal atmosphere indicated high friction and seizure at 450 °C for iron and between 500 and 600 °C (rising slightly with

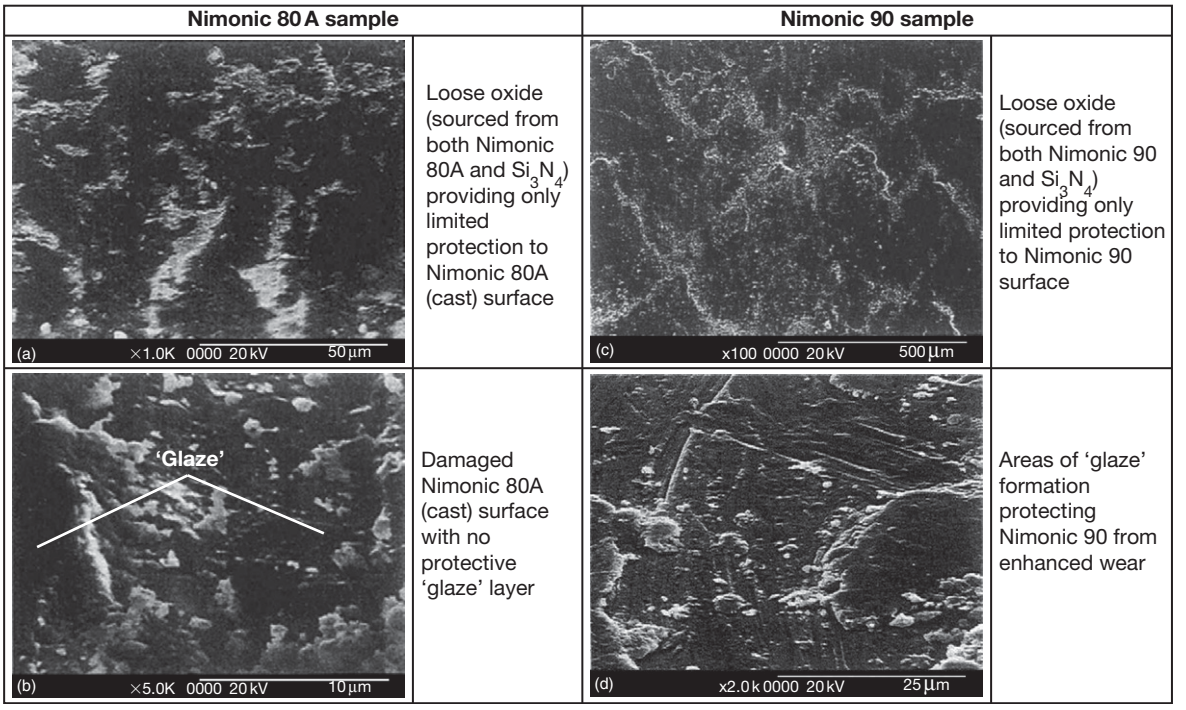

Figure 26 SEM micrographs of Nimonic 80A (cast) at (a) room temperature and (b) 750 °C, also Nimonic 90 at (c) room temperature and (d) 750 °C, worn against a Si_3N_4 counterface, sliding speed 0.654 m s^{-1} (load 7 N, sliding distance 9418 m). Reproduced from Wood, P. D. Ph.D. Thesis, Northumbria University, UK, 1997.

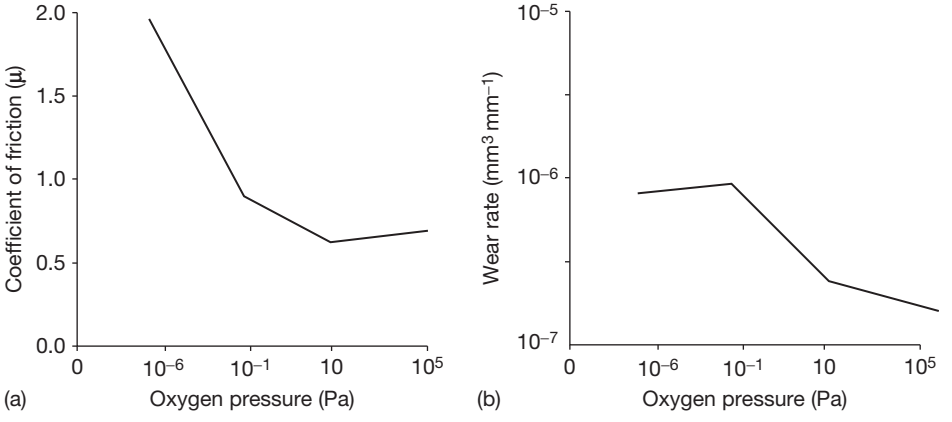

Figure 27 Variation of coefficient of friction (a) and wear rate (b) of Fe–4.9% Cr with oxygen partial pressure during like-on-like sliding at 20 °C. Reproduced from Barnes, D. J.; Wilson, J. E.; Stott, F. H.; Wood, G. C. *Wear* **1977**, *45*, 634–640.

chromium content) for various iron–chromium alloys; the only exception to this was Fe–40% Cr where there was no seizure up to the maximum test temperature of 850 °C.

Adhesive wear and seizure (here defined as the coefficient of friction rising above a nominal value of 3.5) were dominant at oxygen partial pressures of 10^{-6} and 10^{-5} Pa, despite there apparently being sufficient oxygen present to prevent this. On raising the partial pressure to 10^{-4} Pa, however, significant amounts of oxide were observed and areas of compacted debris had developed. These 'islands' were specified as the reason for the switch from severe to mild wear, with even more rapid development of these oxides on raising the partial pressure to 10^{-1} Pa. The compacted debris was either completely oxidized or oxide-covered metallic debris; its formation was accompanied by decreases in friction (**Figure 27**). However, despite the presence of this oxide debris, the wear rate remained high until the oxygen partial pressure reached 1 Pa or above.

Changes in partial pressure were also made during sliding tests,[100] with oxygen in some cases being removed from the wear system (the pressure was from 10^{-1} to 10^{-6} Pa). When this occurred, the oxide debris and the compacted oxide layers remained at the wear interface, showing continued stability and wear resistance even without a continued supply of oxygen.

1.15.3.4.2 Effect of water vapor and relative humidity

The presence of water vapor in the atmosphere can have a positive or negative effect on oxide development, depending on relative humidity levels and materials. For mild steel a decrease in wear was observed with increasing relative humidity under fretting conditions[104,105] and similarly with carbon steel under sliding wear conditions.[17] It has been suggested that adsorbed moisture might have a dual effect,[106] in that on the debris surface, it might act as a lubricant, promoting speedier debris dispersal and, thus, less abrasive wear. From this, it was proposed that the hydrated form of the iron oxide that develops in the presence of the moisture might be a less abrasive medium. Such debris does, however, have the potential to enhance interface contact and bring about adhesive wear.

Experimental work by Bill[107] demonstrated that this could be the case, with the relationship between relative humidity and wear rates becoming quite complex. Iron showed a significant increase in wear rate on raising the relative humidity from 0 to 10%, followed by a rapid decrease and minimum values in the region of 50–70%, then by a small increase towards atmospheric saturation. Increasing wear was demonstrated for titanium at up to 30% relative humidity, followed by an erratic decline in wear values up to saturation levels. Nickel showed a sharp decrease in wear levels between 0 and 10% relative humidity, followed by increasing wear with relative humidity up to saturation.

Oh *et al.*[17] suggested a transition from severe to mild wear with increasing relative humidity for carbon steels. At low relative humidity, severe wear was encountered, with total losses amounting to between 0.130 and 0.190 g. This remained the case up to 50% relative humidity. The level of wear dropped rapidly after this 'transition point,' with mild wear being observed at relative humidity levels of 70% and losses totaling no more than 0.002 g. The amounts of carbon in the steel were observed to affect this transition, which occurred at higher values with increasing carbon content. Friction was also observed to fall rapidly, from between 0.62 and 0.68 at 35% relative humidity to between 0.44 and 0.48 at 70% relative humidity.

1.15.3.4.3 Other atmospheres

The wear process in atmospheres other than air or oxygen will depend on whether the atmosphere is oxidizing or reducing. In most practical situations, corrosion product will not form in a reducing (non-oxidizing) atmosphere and, thus, the formation of wear protective layers is not possible. Only the presence of adsorbed gases or other volatiles will act to separate the wear surfaces, adhesion, and therefore, levels of wear and friction.[108]

In other oxidizing atmospheres, only carbon dioxide has been examined to any significant extent. Sullivan and Granville[51] showed that a compacted oxide layer was formed when a Fe–9% Cr steel was tested in a pin-on-disk rig in carbon dioxide, between 200 and 550 °C. Smith[109] observed the formation of compacted oxides on wear testing of 316 stainless steel in carbon dioxide at temperatures between 20 and 600 °C. The carbon dioxide acted as the oxidizing agent in each case:

$$n\mathrm{CO_2} + \mathrm{M} \rightarrow n\mathrm{CO} + \mathrm{MO}_n \qquad [\mathrm{I}]$$

with the wear mechanisms being very similar to those in air.

Research in other environments is extremely limited. Bill[107] obtained 'prodigious amounts of black debris' on testing titanium in supposedly pure dry

nitrogen. It may be that this is removed oxide that was present prior to sliding (or formed during sliding by reaction with the trace oxygen invariably present in bottled gases) or even a mixture of metallic titanium and oxide. The possibility of titanium nitride is extremely unlikely, if not impossible, due to the tests being carried out at room temperature. However, no attempt was made to analyze the debris or explain the result.

1.15.3.5 Effects of Pretreatment of Sliding Surfaces

1.15.3.5.1 Preoxidation

Stott and Mitchell[52] carried out preoxidation (oxidation prior to commencement of sliding) on Jethete M152 (a high chromium steel) and 321 stainless steel. Elimination of metal-to-metal contact was observed immediately on commencement of sliding in the case of Jethete M152 and also the immediate establishment of compacted oxide in the case of the 321 stainless steel. They concluded that the preoxidation provided an extra supply of oxide debris that led to the more rapid establishment of 'glaze' surfaces.

Iwabuchi *et al.*[65] studied the effects of preoxidation of a number of samples of S45C carbon steel; for each sliding test, a moving disk specimen was rotated against a fixed ring specimen, with both preoxidized samples and nonoxidized samples undergoing unidirectional sliding for 1000 m at room temperature. The preoxidation treatment was carried out at 300 °C for 5 min, 1 h, or 3 h. Times of 5 min and 1 h did result in progressive decreases in wear (**Figure 28**); however, increasing the time to 3 h produced no further improvement. The observed decreases in wear occurred because of break-down of the oxide layer to form debris, the presence of which prevented metal contact and adhesion.

Iwabuchi *et al.* conducted similar experiments with 304 stainless steel specimens,[65] with specimen configurations identical to those for S45C plain carbon steel. Preoxidation was carried out at 300 °C for times of up to 10 h. Although there was some scatter in the data after 300 m of sliding, there was no evidence of any effect of preoxidation on overall wear, regardless of the time of preoxidation and it was concluded that preoxidation had no effect under the prescribed test conditions. This was due to 'selective oxidation' of chromium at the surface;

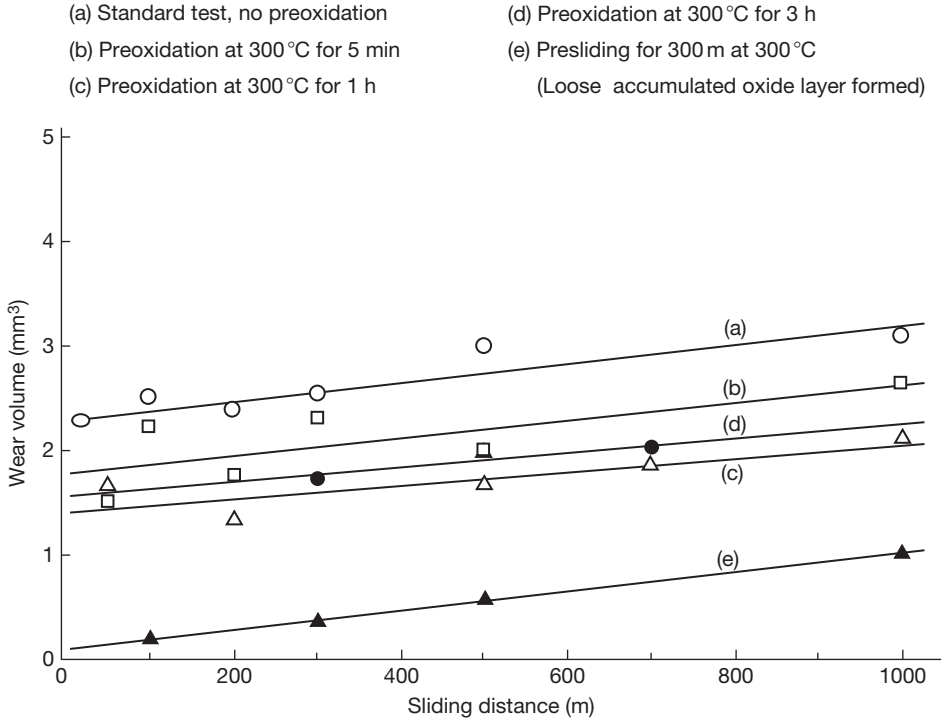

Figure 28 Effects of preoxidation and presliding on wear of S45C at 20 °C.[34] (a) Standard test, no preoxidation, (b) preoxidation at 300 °C for 5 min, (c) preoxidation at 300 °C for 1 h (loose accumulated oxide layer formed), (d) preoxidation at 300 °C for 3 h, and (e) presliding for 300 m at 300 °C.

this decreased the level of oxidation of the stainless steel, with the result that there was insufficient oxide to decrease the severe wear rate by debris generation from this layer.

Thus, although preoxidation can decrease or eliminate early metal–metal contact, this cannot be guaranteed. Under certain circumstances, possibly due to the effects of variations in alloy composition on the nature of the surface oxidation, the production of suitable surface oxide required for the promotion of early 'glaze' formation may not occur.

1.15.3.5.2 Presliding

Iwabuchi *et al.*[65] additionally looked at samples of S45C carbon steel that had undergone presliding for 300 m at 300 °C; this was sufficient to create an accumulated loose oxide layer. Subsequent tests indicated the complete elimination of the severe wear regime (Figure 28), with only mild wear being observed, regardless of test temperature. In the case of preoxidation, the oxide layer served at best only to reduce (dependent on combination) the severe wear 'run-in' period (Section 1.15.3.5.1).

A decrease in severe wear was also observed when 304 stainless steel underwent presliding for 100 m at room temperature, due again to the presence of an accumulated loose oxide layer. In both cases, the availability of preexisting oxide debris acted to prevent contact between the metallic interfaces.

Presliding was additionally carried out for 304 stainless steel over a distance of 300 m at room temperature, 200, and 400 °C (at which temperature the oxide layer formed was a 'glaze'), with the severe wear stage being eliminated in each case during subsequent sliding. The presence of accumulated oxide from presliding did not, however, lead to a decrease in the rate of wear during mild wear.

1.15.3.5.3 Ion implantation

Langguth *et al.*[66] carried out oxygen ion implantation on a series of chromium and carbon steels (AISI 52100, AISI 440B, AISI M2) and 321 stainless steel, followed by a series of sliding experiments using a pin-on-disk rig. A sliding speed of 28×10^{-3} m s^{-1} was used over a sliding distance of 400 m, with relative humidity at 30% or 80%.

In general, recorded levels of wear for the ion-implanted samples were much lower than for their untreated equivalents (Table 3). This was due to the oxygen in the surface layers assisting the formation of oxidized debris and, thus, decreasing the initial severe wear period. Certain aspects of heat treatment of the alloys and the sliding conditions were observed to affect this. For example, in the case of the chromium and carbon steels, the improvement in wear resulting from oxygen ion implantation was noticeably less for AISI 52100 and AISI 440B in the annealed form compared to the martensitic form; this can be seen from the data in Tables 3 and 4. Relative humidity has a marked effect, as in the case of AISI 52100 steel, where the oxygen ion implanted material actually undergoes a higher level of wear than the untreated material. These observations were attributed to the higher plasticity of the annealed samples.

Table 3 Wear rates of case-hardened steels before and after implantation of oxygen ions, 400 m sliding distance

	Wear rate (10^{-16} m^3 m^{-1})			
	Steel ball		*Tungsten carbide ball*	
	30% RH	*80% RH*	*30% RH*	*80% RH*
AISI 52100				
Untreated	1000	100	17.5	17.5
Implanted	1	3.4	1.8	0.3
AISI 440B				
Untreated	19	25	34	85
Implanted	1.4	2.5	2.8	1.8
AISI M2				
Untreated	11.5	2.9	11.2	20
Implanted	3.3	1.9	1.6	3.3

Ion implantation conditions 5×10^{17} cm^{-2}, 50 keV; test conditions in air at 30% or 80% relative humidity RH, 28×10^{-3} m s^{-1}. Reproduced from Stott, F. H.; Wood, G. C.*Tribol. Int.* **1978**, *11*, 211–218.

A change in the form of the debris was also observed, from a smooth oxide layer for the martensitic samples to loose debris for the annealed samples. The one exception was for AISI 440B steel, where the decrease was greater in the annealed state and sliding was accompanied by a change in the state of the oxide debris from the loose form to the oxide layer form.

In comparison to standard preoxidation treatment (Table 4), wear tended to be less, with the exception of annealed AISI 52100, where the preoxidized samples produced superior results, regardless of the levels of relative humidity.

Langguth *et al.* note also that implantation has been tried using different ions, including nitrogen, carbon, and boron, with varying degrees of success, though not to the same extent as oxygen, as these alternatives do not promote wear track oxidation.

Table 4 Wear rates of case-hardened steels before and after implantation of oxygen ions, 100 m sliding distance

	Wear rate (10^{-16} m^3 m^{-1})			
	Steel ball		*Tungsten carbide ball*	
	30% RH	*80% RH*	*30% RH*	*80% RH*
AISI 52100				
Untreated	611	7.7	38	1.5
Implanted	68	11.2	38	2.2
Oxidized	1.1	0	0.8	0.8
AISI 321				
Untreated	1400	72	4000	32
Implanted	215	72	2000	16
Oxidized	140	72	0	32
AISI 440B				
Untreated	98	9.1	42	42
Implanted	33	0.2	84	42

Ion implantation conditions 5×10^{17} cm^{-2}, 50–100 keV in case of AISI 52100; test conditions in air at 30% or 80% relative humidity RH, 28×10^{-3} $m\,s^{-1}$. Reproduced from Stott, F. H.; Wood, G. C. *Tribol. Int.* **1978**, *11*, 211–218.

1.15.4 'Glaze' Formation – Microscale and Nanoscale Investigations

1.15.4.1 Introduction

It is clearly recognized that 'glaze' formation on the contacting surfaces affords significant protection against wear damage and degradation. The generation of HT wear-resistant surfaces *in situ* overcomes the serious limitations on materials and coatings imposed by HT wear conditions. 'Glaze' formation is very useful as it takes advantage of important events that accompany the processes of HT wear, such as oxidation, debris generation, and elemental transfer between the contacting surfaces.[3–6,14,110] These events, under certain conditions of temperature, pressure, and speed[3–6,14,20–22,24,25,111] lead to the formation of surfaces with self-functionalized HT wear resistance. Although the phenomenon of 'glaze' formation and related general issues of HT wear have been extensively studied, it is still not possible to predict the precise conditions which promote 'glazed' surfaces.

Here, it has been recognized that a step forward would be to gain detailed knowledge of 'glaze' layer microstructure and nanoscale structure evolution so that the precise mechanisms of 'glaze' formation can be established. This section summarizes and updates the studies carried out on 'glaze' formation during wear of various systems. It has been written with emphasis on generic principles and wear systems have been selected that facilitate the mechanistic understanding of the 'glaze' formation process.

1.15.4.2 Microscale Studies of 'Glaze' Formation

From a study of mainly nickel- or nickel–iron-based alloys containing significant quantities of chromium in like-on-like sliding, and in some cases, cobalt, it was established by Stott *et al.*[6] that the oxides formed have elemental ratios that differ little from the original base alloys. It was thus concluded that the observed low wear and friction arise from the physical properties and condition of the glaze, rather than their chemical compositions.

Further research[6,50,55–59] allowed the identification of the following modes of compacted layer formation.

- The first mode is characterized by the formation of transient oxides, followed by the oxide thickening by continued oxidation by oxygen diffusion to the substrate–oxide interface and through physical defects.
- The second mode of formation is characterized by two stages. Stage one involves the formation of an insufficiently thick layer due to unfavorable temperature and low alloy strength, possibly involving an extended preglaze or severe run-in period. Stage two involves the formation of a sufficiently thick oxide layer through continued break-up and consolidation of 'glaze' debris produced in stage one.
- In the third mode, the 'glaze' does not remain stable during sliding and areas of compacted oxide continually break down and reform.

Stott *et al.*[10,50,55,61,112] later produced a further set of three modified mechanisms, based on their studies of the elevated temperature (200–600 °C) fretting wear of iron-based alloys. These mechanisms[50] were seen as limiting cases for oxide debris generation, after which the build-up of oxide to form compacted layers continued:

- *Oxidation–scrape–reoxidation*: This involves a two-stage process. In the first step, oxide generation takes place in the areas of contact between the two sliding surfaces, with general oxidation over the apparent sliding area of contact and, also, at asperity contacts where temperatures exceed the general temperature in the region of the sliding area of contact. In the second stage, this oxide is removed by subsequent traversals of the sliding interfaces, exposing fresh

metal for further oxidation. The debris formed may then be either completely removed from the interface, act as a third body abrasive, thereby contributing to the wear process or be compacted to form a wear-protective oxide layer.

- *Total oxidation*: Under certain conditions, particularly high ambient temperatures, oxide generated during sliding or even present prior to the commencement of sliding, is not completely removed by subsequent traversals of the sliding interfaces, allowing the oxide to thicken with time. Provided this layer is coherent and adherent to the metal substrate and can withstand the stresses of sliding, a plastically deformed wear-protective oxide layer can develop.
- *Metal debris*: Debris particles generated during the early stages of wear are broken up by the sliding action, with any fresh areas of exposed metal being subject to further oxidation. There may be a high level of oxidation of the debris surfaces, due to the relatively large exposed surface area of metal.

Enhanced oxidation is promoted by heat of deformation and increased energy of the particles due to increased defect density and surface energy (the exposed surface area of debris material will increase as particle size decreases). There is also an input due to the heat of oxidation, promoting oxidation of the metallic particles, the finer particles undergoing complete and spontaneous oxidation. The resulting oxide can later develop into a wear-protective layer.

The formation of compacted layers has also been observed by Wood *et al.*,[3,12] Rose,[4] Inman *et al.*,[5,21–25] Datta *et al.*,[20] and Du *et al.*[110]

The third mechanism proposed in Stott's original work is similar to that of Lin and Wood,[6] both depending on the generation of larger debris from the wear substrate and the comminutation of this debris to fine oxide particles as the wear process continues to develop.

The one major difficulty with these mechanisms is that they were developed from work on low speed reciprocating sliding wear, where frictional heating is not such an important factor.[61] At sliding speeds of greater that 1 m s^{-1},[104] frictional heating increasingly becomes an issue.

1.15.4.3 Third Body Interaction in Relation to Compact Oxide Formation

In Section 1.15.2.2.3, a brief discussion was made of four mechanisms of particle behavior at the sliding interface, as proposed by Jiang *et al.*[19] – these included (1) rotation, (2) skidding, (3) rolling, and (4) adhesion/sintering affected rolling (Figure 5). Jiang *et al.* observed that the friction levels for mechanism (4) are highly dependent on the adhesion force between particles in the sliding system. While this adhesion force is weak, friction levels for mechanism (4) are lower than those for mechanism (2); however, increasing this adhesion force above a critical level results in a situation where the reverse is the case. Skidding then becomes the dominant mechanism, with no relative movement between neighboring particles – an increase in adhesion force locks them in place. A stable compact layer can result and, at higher temperatures, a wear-resistant 'glaze type' layer is possible (with the particles locked together, there is sufficient time for sintering). Stott's later modification of this approach[111] (the inclusion of adhesion and sintering effects in rotation, skidding and rolling mechanisms) better recognizes the fact that adhesion and sintering has a more general effect on the various particles making up the particle layer, regardless of whether they are entrapped or in relative motion.

Adhesive forces and sintering tend to take effect at more elevated temperatures, as demonstrated by experimental work carried out by Jiang *et al.*[17] on the sliding wear of Nimonic 80A at 20, 150, and 250 °C. At 20 °C, a thick layer of compacted, fine wear debris was formed, with some evidence of solidification and sintering in some areas; however, these layers were found to be predominantly particulate in nature. There is a transition from metal–metal wear to contact between these primarily oxide particle layers, at which point increases in contact resistance and decreases in levels of wear are coincident. At 250 °C, sintering becomes a significant factor and there is a tendency to form smooth 'glaze' layers on top of these compacted oxide layers. The 150 °C case was intermediate, with some development of smooth load-bearing areas between the particulate layers. Removal of this more loosely compacted material by ultrasonic cleaning in acetone left behind the more compacted debris, load-bearing areas.

These observations clearly indicate that temperature is a major driving force for adhesion between particles and formation of load-bearing compacted debris layers. This was demonstrated further[17] by a heat treatment for 90 min at 600 °C, for samples preslid at 20 °C. The compacted layers formed during the sliding phase of the test became solidly sintered together as a result of the subsequent

heating of the samples. The effect of a very small particle size would be to increase the available surface energy, due to the resultant increase in relative surface area. This would act to drive the adhesion and sintering processes and allow for observable sintering at temperatures where sintering of the larger particles used in powder technology applications would not be noticeable. As adhesion itself is temperature-dependent, increases in temperature due to ambient or frictional heating would accelerate the adhesion and, therefore, the sintering process. An Arrhenius relationship[1] influences the process ($K_p = A_p \exp(Q_p/RT_0)$). Shrinkage and thermal stress-induced cracks were, however, observed on layers sintered at 600 °C.

From experimental observations, Jiang *et al.* proposed a descriptive model of the sliding wear process.[2,112] **Figure 29** shows this diagrammatically, with possible modifications to it for the reincorporation of debris for broken-down compacted oxide and 'glaze' layers:

1. Generation of wear particles due to the relative movement of the metal surfaces;

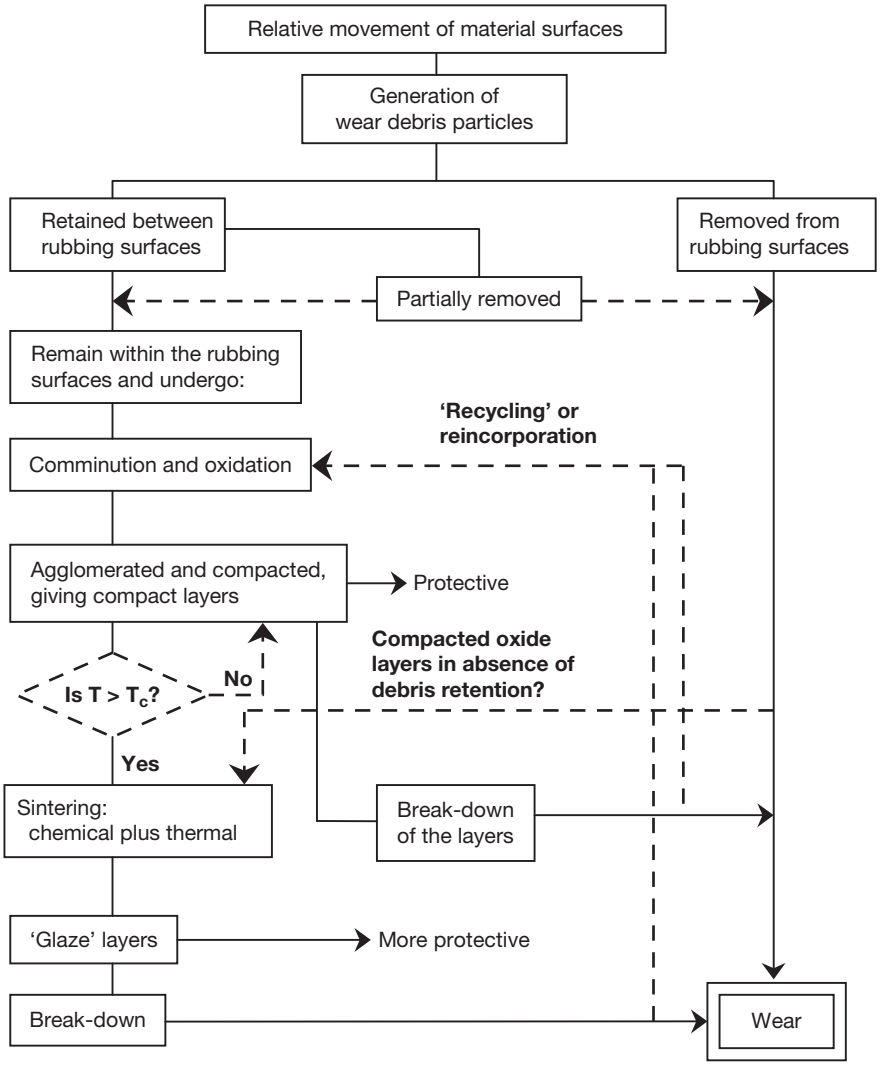

Figure 29 'Modified' version of Jiang's diagrammatic representation of sliding wear processes at various temperatures.[2,5] The original diagrammatic representation[2] does not contain any 'feedback' loops to account for recycling of broken down 'glaze' layers and debris. A decision box is inserted to describe what happens with the actual contact temperature T in relation to Jiang's critical temperature T_c. Also, what happens in the case of partial retention, plus the formation of compact layers when there is no significant debris retention, are not covered. Suggested modifications are indicated in bold. Reproduced from Inman, I. A. Ph.D. Thesis, Northumbria University, UK, 2003; published by 'Dissertation.com', 2006.

2. Removal of some particles from the wear tracks to form loose wear particles;
3. Retention of other particles within the wear track;
4. Comminution of the retained particles by repeated plastic deformation and fracture, with particles freely moving between the rubbing surfaces and undergoing partial or even complete oxidation, due to continued exposure of fresh metallic surfaces during comminutation;
5. Continued fragmentation and agglomeration at various sites on the wear surfaces, due to adhesion forces between solid surfaces originating from surface energy and the formation of relatively stable compact layers.

This has two effects, that is:

1. First, material loss is reduced by a material recycling effect of the wear debris particles. Material breaking away from the compacted debris may rejoin it.
2. Second, due to heavy deformation and oxidation of the wear debris particles, the layers formed are hard and wear-protective.

Two competitive processes then occur during subsequent sliding, that is:

(a) The compacted layers are continually broken down, the debris generated promoting wear (though, again, reincorporation may occur).
(b) Continuing sintering and cold welding between particles within the layers, leading to further consolidation.

For the latter case to predominate, the temperature must be high enough (in excess of a critical temperature) to encourage the sintering processes required to ensure the formation of a solid wear-protective layer on top of the compacted particle layers before the layers are broken down. The effects of this can be seen in the experimental work of Jiang *et al.* – at 20 °C, this critical temperature was not reached and the debris, although undergoing compaction, did not sinter to form a 'glaze' layer. At 250 °C, 'glaze' was clearly visible, while at 150 °C, closer to and possibly just above the critical temperature, more limited sintering meant; although some 'glaze' areas were formed, there were also substantial areas of loose debris still present.

Also of note is the formation of compacted debris layers close to the center of the wear scars, the location of highest debris retention,[18] where coverage by high resistance compacted layers was estimated to be 20–50%.

Jiang estimated also that, to cause a transition from severe to mild wear, only 20% of the surface needed to be covered by 'glaze'-type layers, compared to a value of greater than 30% for nonglaze compacted layers, demonstrating that 'glaze' layers offer more physical protection.

Jiang's model is based on experimental work done on fretting wear systems and Rose[4] questioned the applicability of Jiang's model in a low debris retention system. However, Jiang does account for debris removal from the system leading to wear as would occur in, for example, high-speed unidirectional sliding[3–5,20–25,110] or debris removed by introduced interfacial airflow.[46] Also, in Rose's own 'reciprocating-block-on-rotating-cylinder' experimental work (a higher speed unidirectional sliding configuration), examples of debris retention with 'glaze' formation and compacted layers do occur (i.e., Incoloy MA956 vs. Stellite 6), despite the more adverse sliding conditions. However, as Rose points out, there are examples where compacted oxide layers do form and there is no significant third body debris retention,[3–5,23,58] thus suggesting that Jiang's model requires further modification to account for this; **Figure 29** includes some suggestions by Inman[5] to cover these points.

1.15.4.4 Nanoscale Investigations of 'Glaze' Formation

This section reports recent findings on the evolution of structures and substructures of 'glaze' layers at the nanoscale level,[20,25,113] from extensive research carried out in the authors' laboratory. Data relating to transmission electron microscopy (TEM) and scanning tunneling microscopy (STM) studies are presented in **Figures 30–44**. Scanning tunneling spectroscopy (STS) and current imaging tunneling spectroscopy (CITS) data are not shown here.

The work presented here is generic in nature, but refers to a particular system in order to facilitate understanding of the underlying mechanisms for nanostructure evolution in the surface 'glaze' layers and their improved HT wear resistance. In this case, the 'Nimonic 80A (sample) versus Stellite 6 (counterface)' system is considered, using a counterface surface sliding speed of 0.314 m s^{-1}, with a 7 N applied load and total sliding distance of 4522 m.[5,23–25] The sample also underwent a reciprocating action against the counterface for a distance of 12 mm, three times a minute, thereby limiting debris retention to between 20 and 30% (most of the debris was allowed to escape).

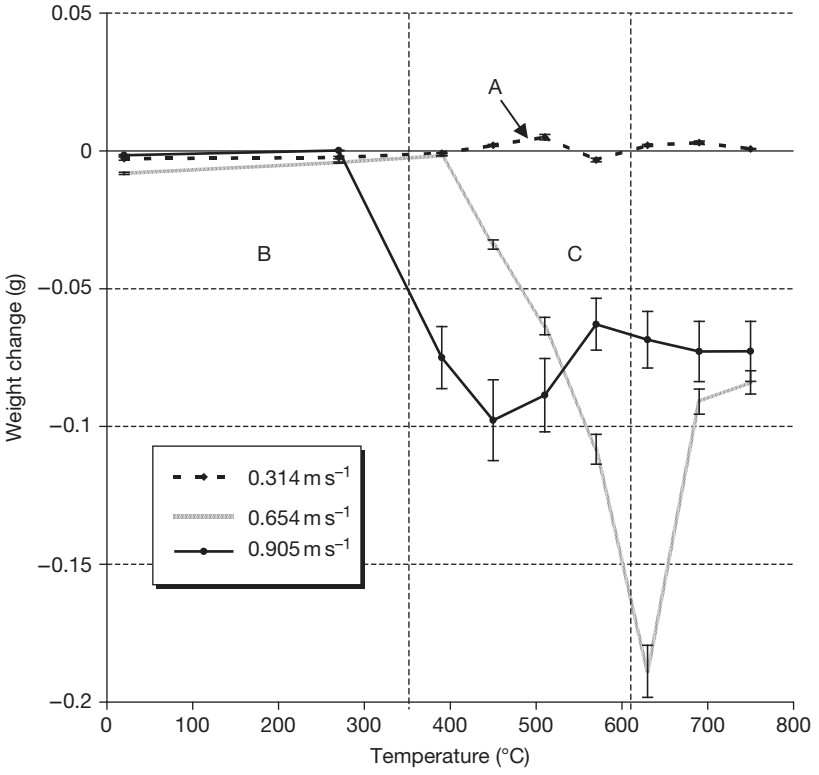

Figure 30 Weight change versus temperature for Nimonic 80A slid against Stellite 6 at 0.314, 0.654, and 0.905 m s^{-1} (load 7 N, sliding distance 4522 m).[22] At 0.314 m s^{-1}: (A) Loose oxide debris spread across wear surface, plus some compacted oxide formation, room temperature to 390 °C; smooth 'glaze' layers with only a little loose debris (450 °C to 750 °C). At 0.654 and 0.905 m s^{-1}: (B). Loose oxide debris spread across wear surface, plus some compacted oxide formation (room temperature and 270 °C at both 0.654 m s^{-1} and 0.905 m s^{-1}, also 390 °C at 0.654 m s^{-1}). (C) Torn, metallic surface typical of adhesive wear, no traces of any oxide debris (390 °C to 510 °C) or only very limited oxide debris formation (at 0.905 m s^{-1} – 570 °C; at 0.654 m s^{-1} and 0.905 m s^{-1} – 630 °C). (D) Loose oxide but with no compact oxide layers at 0.654 m s^{-1} and only isolated build-ups of oxide at 0.905 m s^{-1}; fine parallel grooves in direction of sliding on Nimonic 80A surface (690–750 °C).

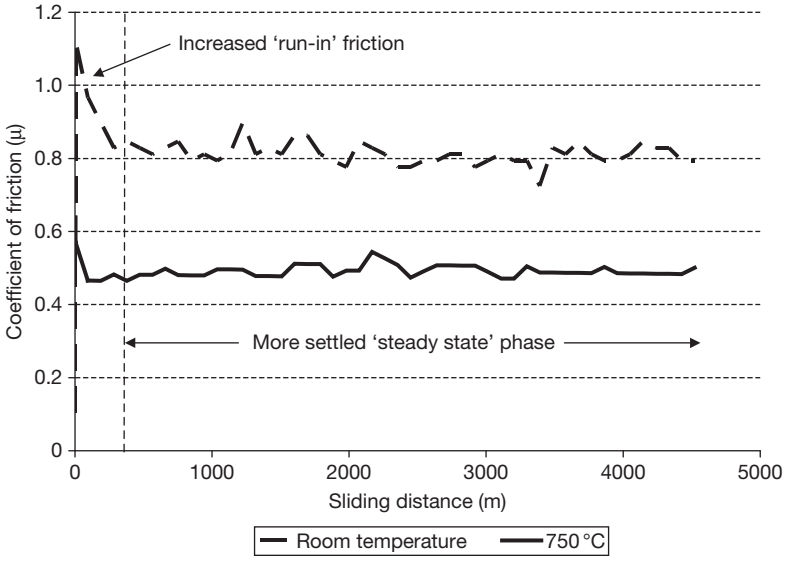

Figure 31 Coefficient of friction versus time for Nimonic 80A versus Stellite 6 at 0.314 m s^{-1}, room temperature and 750 °C.[5,21,25]

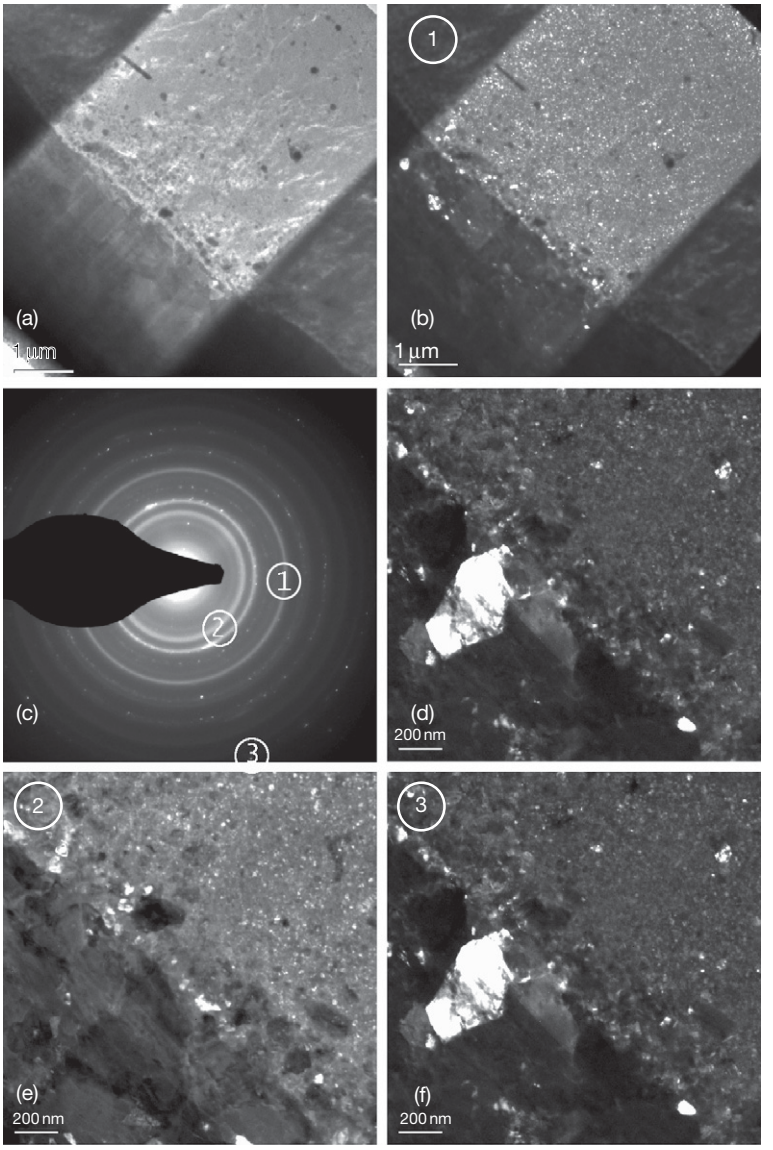

Figure 32 TEM overview of a cross-section of the wear affected surface (Nimonic 80A vs. Stellite 6, 0.314 m s^{-1}, 20 °C, load 7 N, sliding distance 4522 m): (a) bright-field overview image of the Nimonic 80A and the 'glaze' layer; (b) dark-field image of the nanocrystalline 'glaze' layer (obtained with a 10 μm objective aperture as indicated in the SAD pattern by ①); (c) selected area diffraction (SAD) pattern of the cross-section; (d) bright-field image of the interface; (e) dark-field image of the nano-crystalline 'glaze' layer close to the interface (as indicated in the SAD pattern by ②); (f) dark-field image of a larger crystal in the Nimonic 80A close to the interface (as indicated in the SAD pattern by ③). Reproduced from Du, H. L.; Datta, P. K.; Inman, I.; Geurts, R.; Kübel, C. *Mater. Sci. Eng. A* **2003**, *357*, 412–422.

1.15.4.4.1 Wear data

Figure 30 displays the wear data for the Nimonic 80A/Stellite 6 system as a function of temperature at 0.314 m s^{-1}. Weight changes after 4522 m of sliding were extremely low for all temperatures, with the largest mean change being 0.002(4) g at 270 °C. Slight gains were observed for all test temperatures between 450 and 750 °C, with maxima in the mean values at 510 and 630 °C of 0.001(1) and 0.001(4) g respectively. It should be noted that the wear data at 570 °C show a departure from the general trend and repeated experiments indicate the 570 °C situation needs further attention. The following discussion focuses on the situation at room temperature and 750 °C.

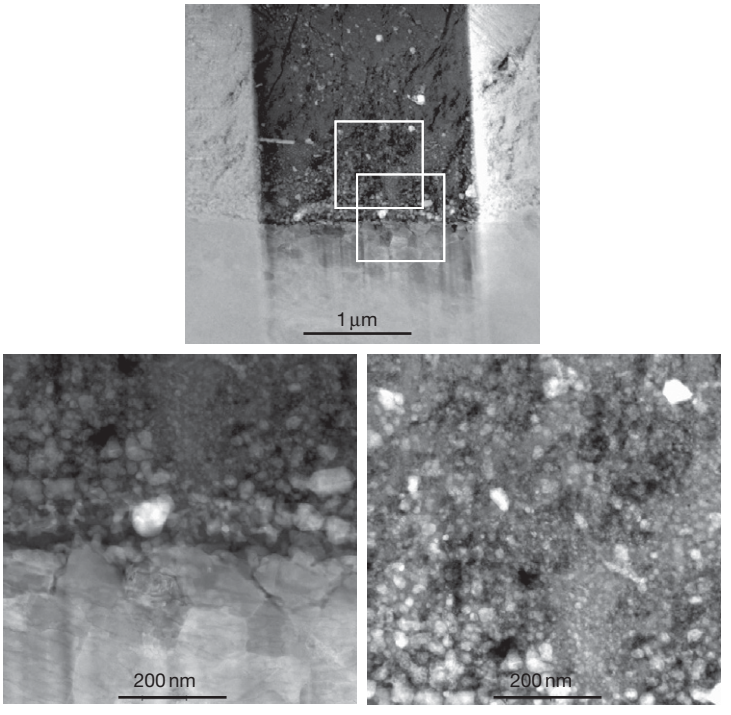

Figure 33 HAADF-STEM (200 mm camera length) overview image and close-up of the interface and the nanocrystalline 'glaze' layer (Nimonic 80A vs. Stellite 6, 0.314 m s^{-1}, 20 °C, load 7 N, sliding distance 4522 m). Reproduced from Du, H. L.; Datta, P. K.; Inman, I.; Geurts, R.; Kübel, C. *Mater. Sci. Eng. A* **2003**, *357*, 412–422.

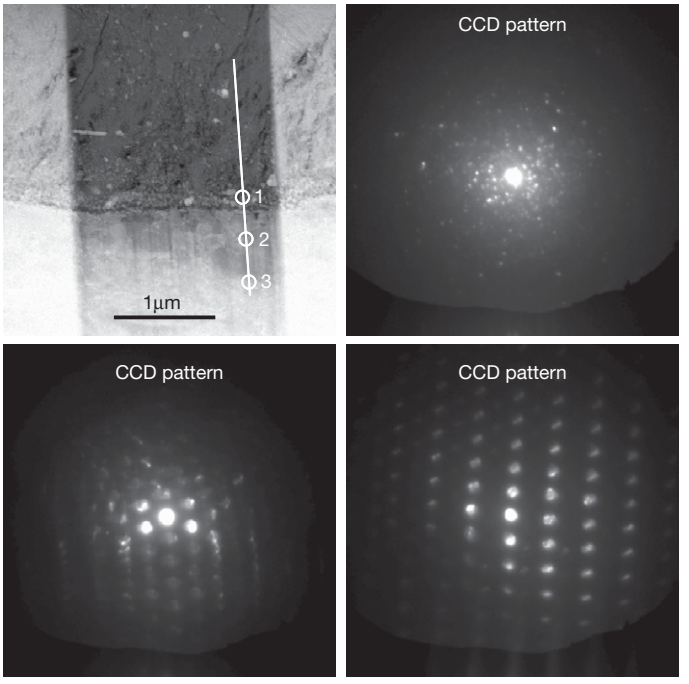

Figure 34 HAADF-STEM overview image with examples from a CCD line trace (Nimonic 80A vs. Stellite 6, 0.314 m s^{-1}, 20 °C, load 7 N, sliding distance 4522 m). Reproduced from Du, H. L.; Datta, P. K.; Inman, I.; Geurts, R.; Kübel, C. *Mater. Sci. Eng. A* **2003**, *357*, 412–422.

The coefficient of friction values measured during the tests showed an initial period of rapid change, before, in many cases, settling down into a 'steady state' situation with less variation. The data in Figure 31 show no significant changes with time after an initial peak at the very beginning of the test. This indicates the rapid onset of debris generation (up to 450 °C) or 'glaze' layer formation (~450 °C and above, almost immediate at 750 °C), with the lack of frictional variation during the 'steady state' stage being due to the continued presence of debris or 'glaze' on the worn surfaces (Figure 24). Coefficient of friction levels (Figure 31) are significantly lower for 'glaze' covered surfaces (i.e., 750 °C) than for loose debris covered surfaces (i.e., room temperature).

1.15.4.4.2 Studies of wear-affected surfaces produced during sliding of Nimonic 80A against Stellite 6 at 20 °C

Scanning electron microscopy (SEM)

The top layer of the wear surface after sliding at 20 °C (Figure 24) consisted of a loosely bound noncompacted oxide that was easily detachable by brushing or light polishing. Underneath this layer, there was a more compacted layer that was not clearly apparent using optical and scanning electron microscopy.[113]

Analysis of the surfaces reveals the presence of oxygen and elements from Nimonic 80A (typically Ni/Cr) and Stellite 6 (Co/Cr). The results indicate elemental transfer from the counterface to the specimen and mixing of the transferred and host element oxides. In this section, attention is focussed on the surface layers produced at 20 °C.[113]

Transmission electron microscopy (TEM)

Figure 32(a) shows a cross-sectional TEM image of the wear-affected Nimonic 80A surface, revealing the interface between the Nimonic 80A substrate and the compact 'glaze' layer (the loosely bound uncompacted oxide debris layer was not visible in this area).[113] The associated selected area diffraction (SAD) pattern (Figure 32(c)) is dominated by Debye rings and some well-defined Bragg reflections. Dark-field images (Figures 32(e) and 32(f)) reveal that the latter correspond to irregular shaped Nimonic 80A crystals of several hundred nanometres diameter, in a layer up to 1 μm from the 'glaze' layer/substrate interface. The 'glaze' layer shows a very different morphology, consisting of small and misoriented crystals produced by fragmentation (Figures 32(b) and 32(e)), of typical diameter of 5–20 nm. Although the adhesion between the 'glaze' layer and Nimonic 80A substrate was generally good, cracks were visible in some areas.

Figure 33 shows a HAADF-STEM overview image of the FIB prepared cross-section described in the previous paragraph.[113] This is consistent with the structural variations observed by TEM. Two different areas are revealed for the substrate: a uniform 'bulk' area and a large grained structure about one micron below the interface with the 'glaze' layer. The latter exhibits a fine-grained structure (5–20 nm) with irregular shaped grain boundaries. The particles are larger close to the interface (up to about 50 nm). Furthermore, the strong Z-dependence of the HAADF-STEM image reveals several metal particles in the (oxidized) 'glaze' layer as well as low-density material at the interface.

Figure 34 shows examples from a STEM line trace of nano-diffraction patterns, taken using a ~30 nm probe.[113] As previously, only small randomly oriented crystals are observed in the 'glaze' layer and at the interface. The larger grains in the alloy exhibit various crystallographic orientations; some of them well defined and similar to those expected for Nimonic 80A.

Figure 35 shows EDX analyses of the 'glaze' layers, together with their reference areas.[113] The quantification is based on theoretical k-factors and uses a thickness correction for an estimated 150 nm sample thickness (EELS thickness measurements indicate a thickness of 2–3 nm mean free path). Quantitative analysis of the Nimonic 80A layer (Area 1) gives the characteristic composition of the bulk alloy (Table 5), apart from a slightly higher silicon concentration and a small amount of cobalt.

Analysis of the 'glaze' layer shows that it is essentially oxidized Stellite 6, with a significant contribution of between 15–20% Ni from the Nimonic 80A.

The interface layer consists of a mixture of Nimonic 80A and Stellite 6, with a higher than average titanium concentration.[113] HAADF-STEM EELS/EDX line traces across the interface (Figure 36) show the transition between the 'glaze' layer and the Nimonic 80A substrate, based on the cobalt and nickel concentrations; the composition of the 'glaze' layer is locally inhomogeneous (Figures 36 and 37). There are some variations in the chromium, cobalt and oxygen concentrations as well as a few distinct particles with a high nickel concentration. Nevertheless, the overall concentrations are relatively uniform throughout the 'glaze' layer, for example, no nickel

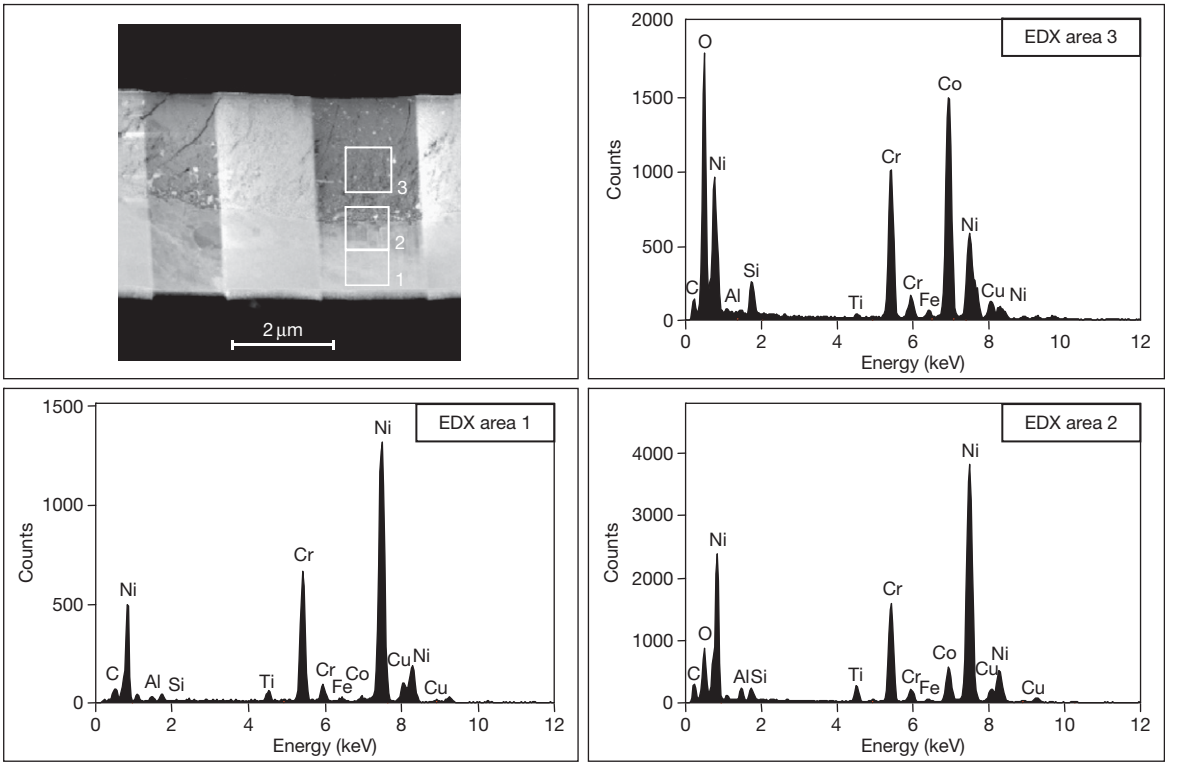

Figure 35 HAADF-STEM (200 mm camera length) overview image and local EDX analysis (Nimonic 80A vs. Stellite 6, 0.314 m s^{-1}, 20 °C, load 7 N, sliding distance 4522 m). Reproduced from Du, H. L.; Datta, P. K.; Inman, I.; Geurts, R.; Kübel, C. *Mater. Sci. Eng. A* **2003**, *357*, 412–422.

concentration gradient was observed. The line traces further reveal the preferential formation of titanium and aluminum oxides in a ~100 nm thick layer at the interface. Slight chromium depletion is observed in the substrate close to the interface, with a corresponding chromium enrichment in the first ~300 nm of the 'glaze' layer.

Similar areas of enrichment/depletion have been found at other locations along the interface; an example is given at a higher spatial resolution in **Figure 37**.[113] Furthermore, this line trace also confirms aluminum enrichment at the interface; moreover, this Al_2O_3 layer is between the TiO_2 layer and the Nimonic 80A substrate. Aluminum (in Al_2O_3) enrichment is further responsible for the dark areas in the HAADF-STEM image, leading from the interface into the substrate (**Figure 26**).

The atomic numbers of chromium (24), cobalt (27) and nickel (28) are similar and compositional variations of these main elements do not explain the strong contrast observed in the HAADF-STEM image (**Figure 38**).[113] However, the EDX/EELS line traces reveal a low oxygen concentration for the bright areas, indicating that the image mostly reflects the oxidation state. Furthermore, a low oxygen concentration coincides with a low chromium concentration; local EDX analysis shows a low chromium and oxygen concentration for the particles that appear bright in the image. This implies that some of the nickel and cobalt particles are not completely oxidized.

EDX line traces in an area up to about one micron below the interface reveal the preferential segregation of light elements, especially aluminum and in some cases titanium (**Figure 39**).[113] This segregation is also visible in the HAADF-STEM images as thin lines (<10 nm diameter) oriented parallel to the interface (**Figures 33–39**). It is noted that the peaks of Ti and Al are overlapped away from the interface, which indicates the presence of sub-microscopic γ'-phase, Ni_3Al or $Ni_3(TiAl)$ particles, as expected following ageing.[113]

These results clearly indicate the formation of a wear-resistant nanostructured surface during sliding wear of Nimonic 80A against Stellite 6 at 20 °C using

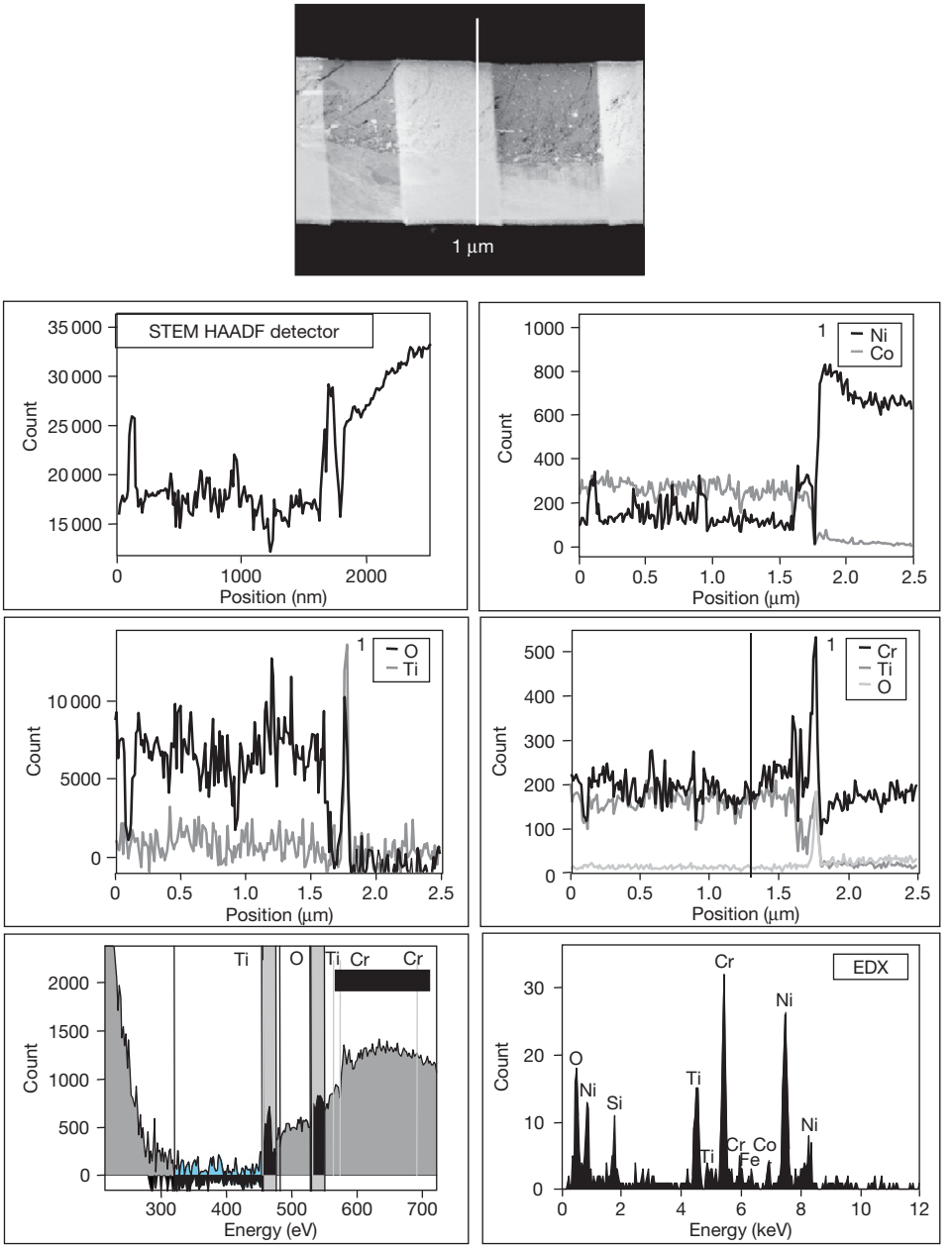

Figure 36 HAADF-STEM EELS/EDX line trace revealing the compositional variations of the wear affected surface (Nimonic 80A vs. Stellite 6, 0.314 m s^{-1}, 20 °C, load 7 N, sliding distance 4522 m); line trace performed with 1 nm probe size and spectra collected every 10 nm. Reproduced from Du, H. L.; Datta, P. K.; Inman, I.; Geurts, R.; Kübel, C. *Mater. Sci. Eng. A* **2003**, *357*, 412–422.

a speed of 0.314 m s^{-1} under a load of 7 N.[113] The analyses reveal the complex structure of this surface, which consists of multiple layers:

1. A loose, uncompacted, highly oxidized layer.
2. A nano-crystalline (5–20 nm grain diameter) compacted layer mostly consisting of oxides of elements originating both from Stellite 6 and Nimonic 80A. The nickel concentration (from the Nimonic 80A) is uniform throughout the whole layer, except for the presence of several larger nonoxidized particles that were randomly dispersed in the glaze.
3. Larger particles with a diameter of up to 50 nm were observed in a layer of about 300 nm at the base of the 'glaze' layer. The compositions indicate

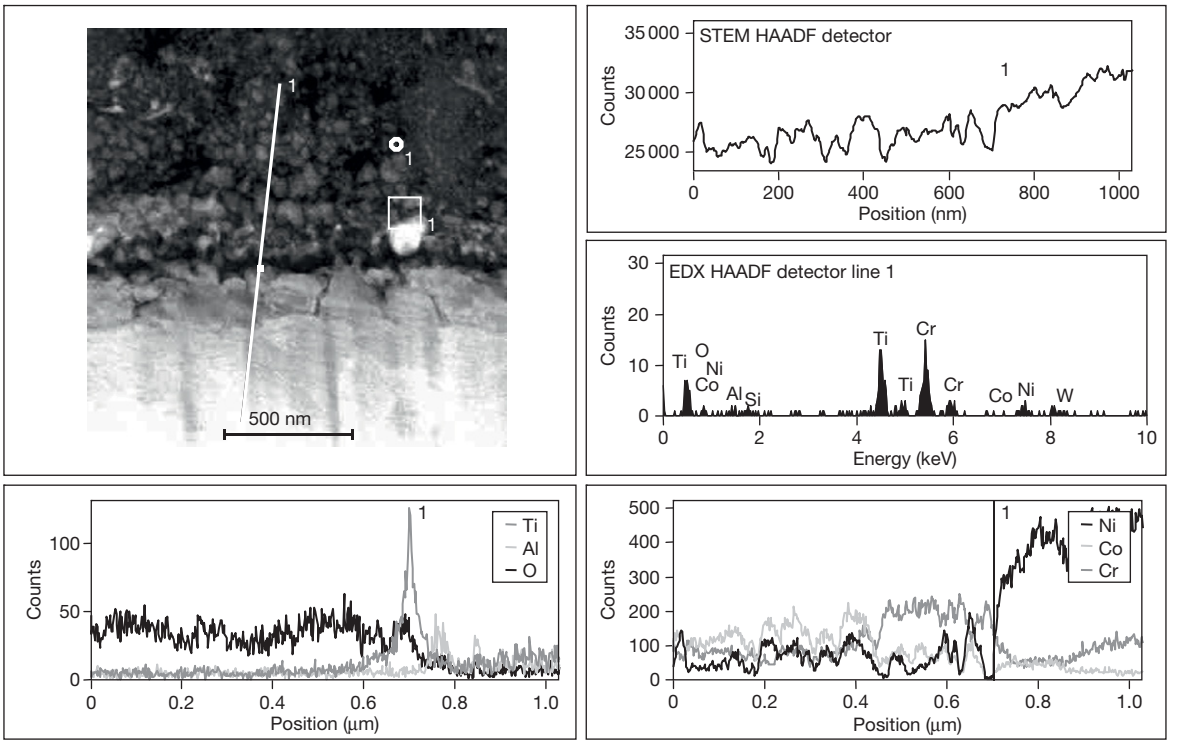

Figure 37 HAADF-STEM (200 mm camera length) overview and EDX line trace revealing the compositional variations of the wear interface structure (Nimonic 80A vs. Stellite 6, 0.314 m s^{-1}, 20 °C, load 7 N, sliding distance 4522 m); the line trace was performed with a 1 nm probe size and spectra collected every 2 nm. Reproduced from Du, H. L.; Datta, P. K.; Inman, I.; Geurts, R.; Kübel, C. *Mater. Sci. Eng. A* **2003**, *357*, 412–422.

the presence of elements from both Stellite 6 and Nimonic 80A, but chromium enriched.

4. The chromium-rich phase gradually gave way to a titanium (oxide)-rich phase of about 100 nm thickness, followed by an aluminum (oxide)-rich phase of about 50 nm thickness, at the interface with the Nimonic 80A substrate.
5. Adjacent to the interface with the 'glaze' layer, the Nimonic 80A substrate exhibited a large-grained structure (of diameter of several hundred nanometres). Slight chromium depletion was observed. The precipitation lines (diameter < 10 nm) indicated that aluminum-, and in some cases titanium-, enriched phases formed near the large-grained structures. The larger dark areas perpendicular to the interface were also due to aluminum enrichment.
6. A uniform 'bulk' Nimonic 80A composition was observed at depths greater than one micron below the interface.

The first key process in the development of nanostructured 'glaze' layers involves oxidation of the contacting surface/particles subjected to high mechanical stress due to rotation of the counterface. The 'glaze' layer, consisting mainly of the oxides of the elements originating from the contacting surfaces, acted as a barrier that separated the substrate from the environment. Although the mechanical effect would continue to influence the 'glaze' layer and subsurface deformation, the subsequent oxidation process is controlled by oxygen species and substrate element diffusion, and the thermodynamic nature of the relevant oxides. The observed sequential existence of the oxides Cr_2O_3/TiO_2/Al_2O_3/substrate at the interface can be understood in terms of thermodynamics. **Figure 40(a)** indicates the oxidation tendencies of relevant elements.[113] The dissociation partial pressures for Al_2O_3, TiO_2, Cr_2O_3, NiO, and Co_3O_4 follow the same trend in the range of temperatures 25–1000 °C. Al_2O_3, TiO_2 and Cr_2O_3 are more likely to develop with increasing temperatures. Although the temperature generated was not measured, the relatively fast kinetics of oxidation, as evidenced by the rapid formation of the 'glaze' layer, indicates the generation of relatively high temperatures, sufficient for such oxidation to occur.

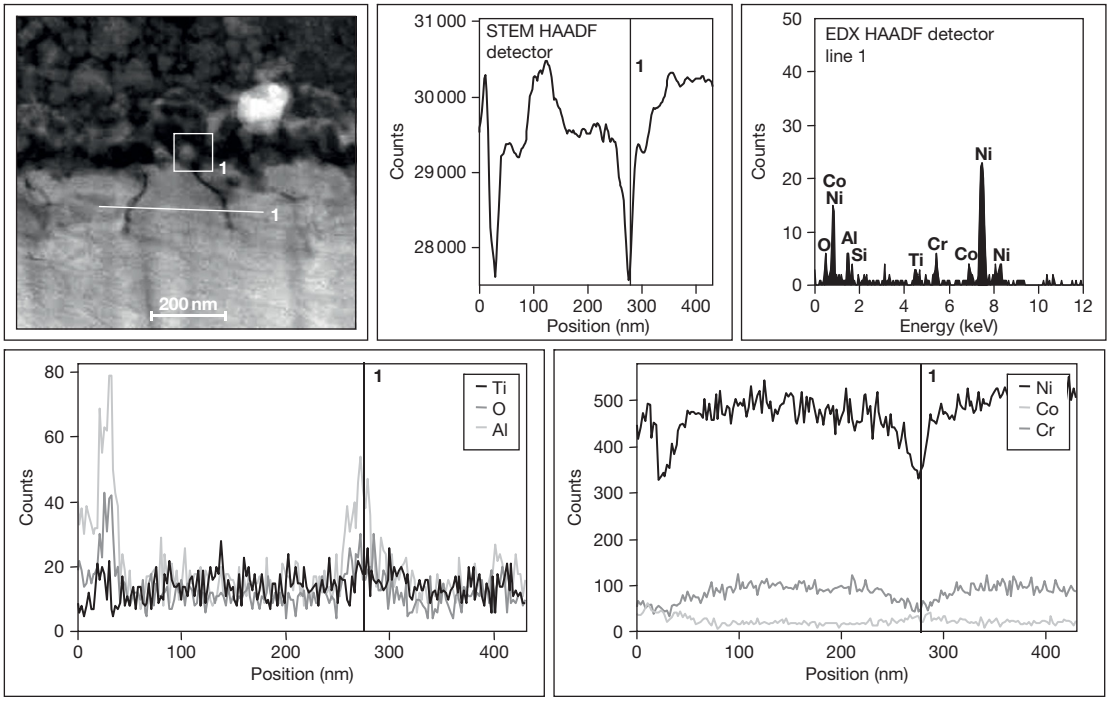

Figure 38 HAADF-STEM (50 mm camera length) overview and EDX line trace revealing the aluminum (oxide) segregation at the top of the Nimonic 80A phase (Nimonic 80A vs. Stellite 6, 0.314 m s^{-1}, 20 °C, load 7 N, sliding distance 4522 m); the line trace was performed with a 1 nm probe size and spectra collected every 2 nm. Reproduced from Du, H. L.; Datta, P. K.; Inman, I.; Geurts, R.; Kübel, C. *Mater. Sci. Eng. A* **2003**, *357*, 412–422.

Additionally, it is apparent that the high Cr activity in both counterface and sample materials leads to the formation of Cr_2O_3 preferentially in the early stages of the process. When oxygen diffuses inwards, Ti in the γ' phase is favorably oxidized. The formation of TiO_2 gives rise to a decrease in Ti activity and, correspondingly, the Al activity in the γ' phase increases and Al_2O_3 becomes a favorable product, as described for oxidation of TiAl in air.[115,116] NiO and Co_3O_4 are much less stable than TiO_2 and Al_2O_3, which is the reason why some particles of Ni and Co have not been oxidized in the wear process. These oxides (TiO_2 and Al_2O_3) formed beneath the 'glaze' layer, play an important role in providing support additional to that provided by the substrate, to sustain the 'glaze' layer and prevent it from collapsing.[4]

1.15.4.4.3 Nano-scale microscopy of 'glazed' layers formed during high temperature sliding wear at 750 °C

The spectrum from EDX analysis of the surface generated under sliding wear at 0.314 m s^{-1} and 750 °C for 4522 m, **Figure 40(b)**, reveals the dominant presence of Co, Ni, Cr and O on the 'glaze' surface.[20,25] Quantification of the results on average gives 34.2% Co, 36.2% Cr, 16.7% Ni, 3.8% Si, and 1.3% Fe (all at%). However, analysis by TEM-EDS showed some location-to-location variation. The dominant phases identified by XRD included $CoCr_2O_4$ and $Ni_{2.9}Cr_{0.7}Fe_{0.36}$.

Figure 41(a) is a cross-sectional composite TEM micrograph of the surface formed during wear.[20,25] It reveals the surface layer (glazed surface), the deformed substrate and the 'glazed' layer/substrate interface. The wear-affected region (total thickness ~3 μm) consists of three layers; the top-most layer (the 'glaze' layer) has a uniform grain structure of size 5–15 nm, some of the grains displaying contrast, while the dislocation density in this area is low. The interfacial layer consists of grains of 10–20 nm and has a higher dislocation density. The layer just beneath the interfacial layer shows subsurface deformation and elongated grains. The SAD pattern from the 'glaze' layer (**Figure 42**) consists of spots arranged in concentric circles, indicating the presence of small grains with high angle boundaries, multiple boundaries and large misorientations

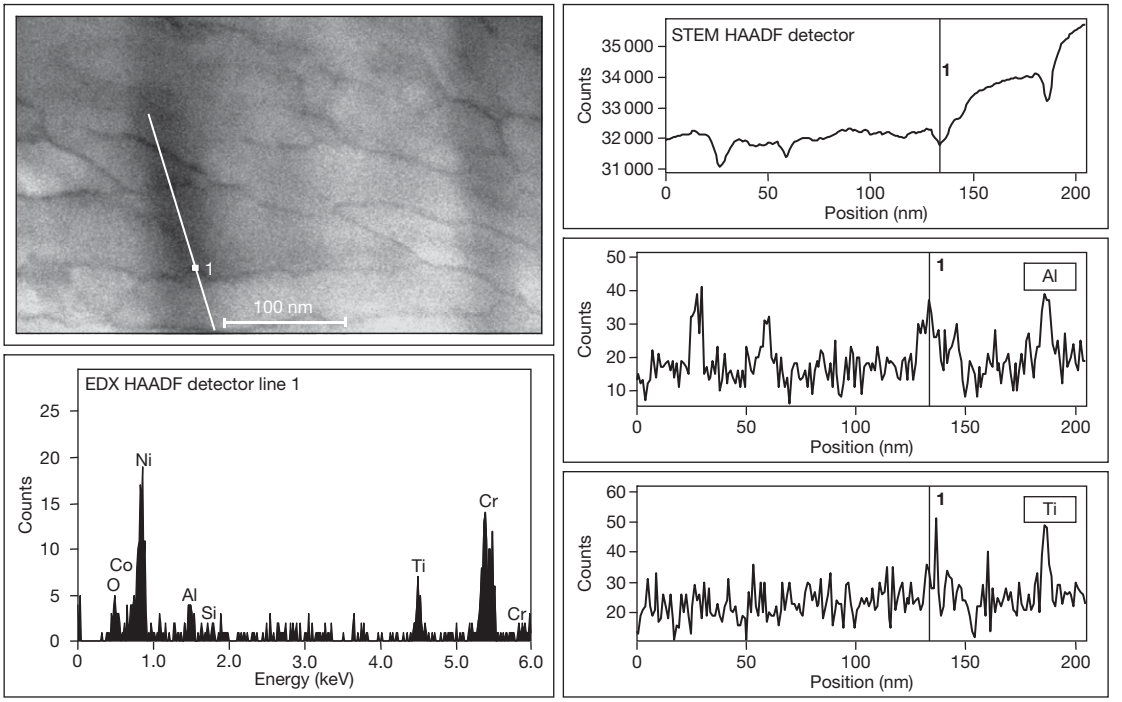

Figure 39 HAADF-STEM (50 mm camera length) overview and EDX line trace revealing the precipitation of light elements (aluminum and titanium) in the Nimonic 80A close to the wear interface (Nimonic 80A vs. Stellite 6, 0.314 m s^{-1}, 20 °C, load 7 N, sliding distance 4522 m). Reproduced from Du, H. L.; Datta, P. K.; Inman, I.; Geurts, R.; Kübel, C. *Mater. Sci. Eng. A* **2003**, *357*, 412–422.

(formation of misorientated lattice-fragmentation). The poorly-defined irregular boundaries indicate nonequilibrium high-energy configuration. The indexed SAD pattern also revealed the presence of oxides of Ni, Cr, and Co (indexing not shown here).

Sub-surface deformation is illustrated in **Figure 41(b)**.[20,25] Dislocations, present as networks inside the deformed (elongated) grains, have been observed in the deformed substrate. Shearing deformation took place in the substrate as a response to the sliding process.

The present results clearly indicate the formation of a nano-structured 'glaze' oxide layer during high temperature sliding wear under the specified conditions. The creation of nano-structures is confirmed by the STM topography, indicating grains of between 5 and 10 nm (**Figure 43**).[5,20,21,25] These results again demonstrate that such a nano-structured surface is extremely effective in conferring high resistance to wear.

It has been indicated by various authors[5,20,21,110] that, in many systems, surfaces with ultra-fine structure are generated during high temperature sliding wear. Mechanical mixing involving repeated welding, fracture and re-welding of the debris generated from both contacting surfaces is responsible for the generation of the ultrafine structured surfaces. Moreover, the detailed TEM studies presented here has enabled understanding of the formation mechanisms of wear-resistant nano-structured surfaces.

It is clear that the initial processes responsible for generating the 'glazed' layer at both 20 and 750 °C are 'deformation of the surface,' 'intermixing of the debris generated from the wear and the counterface surfaces,' 'oxidation,' 'further mixing,' and 'repeated welding and fracture.' These processes are aided by high temperature oxidation and diffusion. The positron annihilation studies confirmed the presence of vacancy clusters consisting of five vacancies.[110]

The next stage in the process involves deformation of oxides and generation of dislocations, leading to the formation of sub-grains. These sub-grains are then further refined, with increasing misorientation resulting in nano-structured grains with high angle boundaries (a process called 'fragmentation'), a non-equilibrium state indicated by poorly defined and irregular grain boundaries. High internal stress is created inside the grains; the dislocation density and arrangement depend on the grain size, with smaller

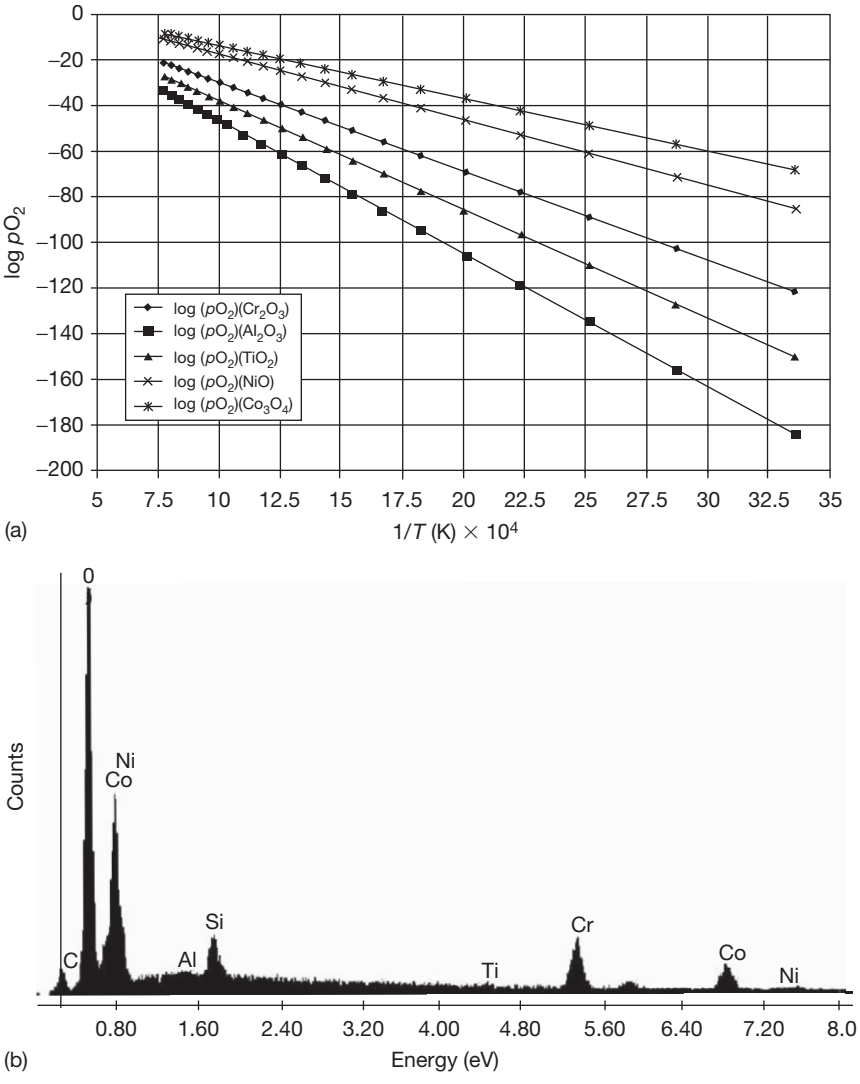

Figure 40 Plots showing (a) dissociation partial pressures of Al_2O_3, TiO_2, Cr_2O_3, NiO, and Co_3O_4 versus reciprocals of temperatures[20] and (b) EDX surface spectrum for Nimonic 80A vs. Stellite 6 (0.314 m s^{-1}, 750 °C, load 7 N, sliding distance 4522 m).[20, 25]

grains containing fewer dislocations. The process leads to the formation of high energy grain boundaries with a high defect density.[117–123]

1.15.4.4.4 Other systems

Such nanostructured 'glaze' layers are not unique to Nimonic 80A when slid against Stellite 6 (0.314 m s^{-1}, 7 N load, 4522 m sliding distance). For example, using AFM, Incoloy MA956 has also been shown to form nanostructured 'glaze' layers when slid against Stellite 6[23] and Incoloy 800HT at 750 °C (**Figure 44**).[114] In the case of the Incoloy MA956/Stellite 6 system, this nanostructured 'glaze' formed has been found to originate from both Co–Cr-dominated oxide debris at 0.314 m s^{-1} and Fe–Cr-dominated debris at 0.905 m s^{-1}; the sliding speed and composition having no noticeable affect on 'glaze' structure with this latter system.

1.15.5 Wear Maps: A Useful Design Aid for Selecting Wear-Resistant Materials and Surfaces

1.15.5.1 Introduction

Lancaster,[26] Welsh,[27,28] So,[29,30] Rose,[4] Inman,[5,21–24] and others[42,85] have shown that various combinations of load, temperature and sliding speed can

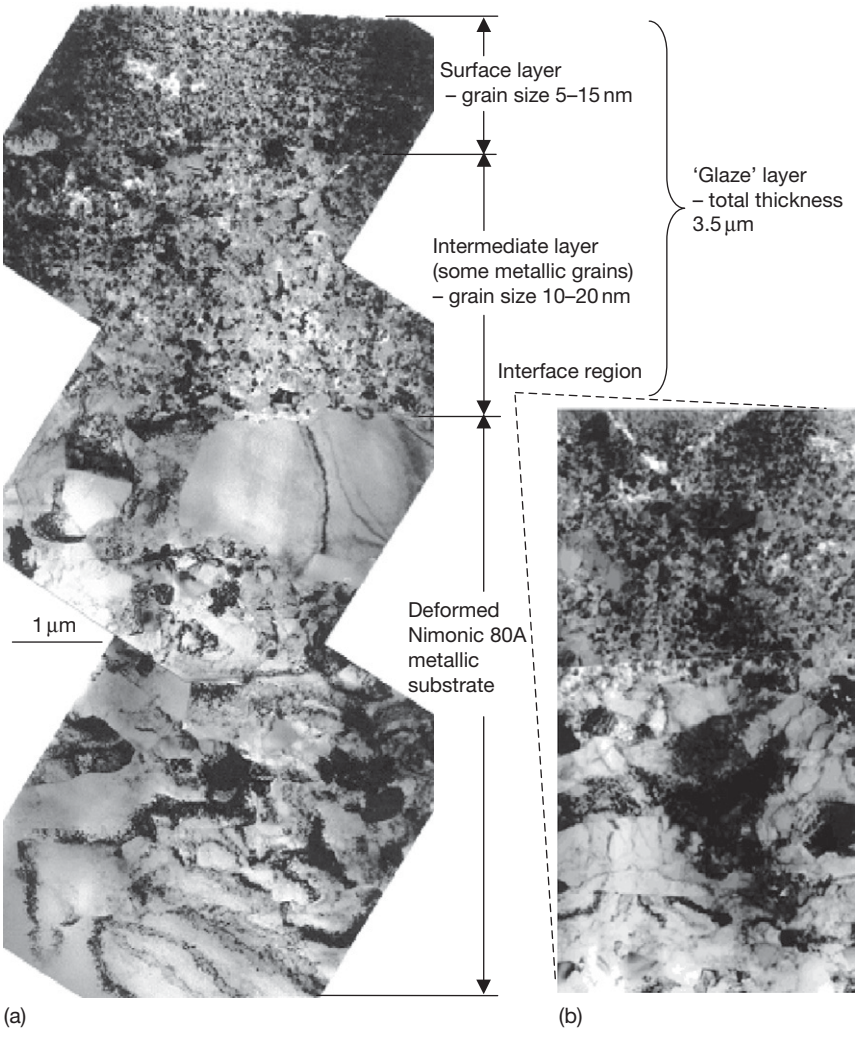

Figure 41 Nanoscale characterization of 'glaze' layers formed (Nimonic 80A vs. Stellite 6, 0.314 m s^{-1}, 750 °C, load 7 N, sliding distance 4522 m) showing TEM bright field images of (a) a wear-induced polycrystalline 'glaze' layer plus substrate deformation and (b) the interface of the 'glaze' layer and deformed substrate.[5,20,21,25]

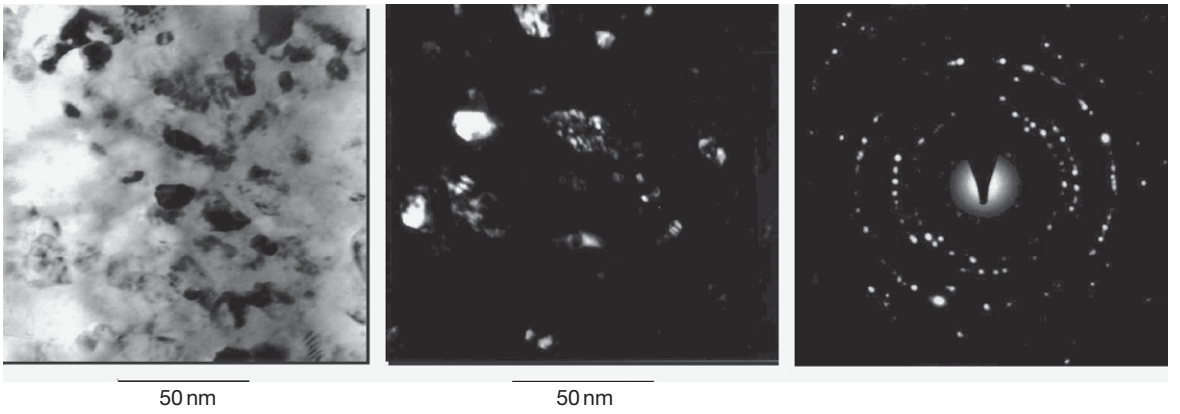

Figure 42 TEM morphological and structural details of the 'glaze' layer formed (Nimonic 80A vs. Stellite 6, 0.314 m s^{-1}, 750 °C, load 7 N, sliding distance 4522 m).[20,25]

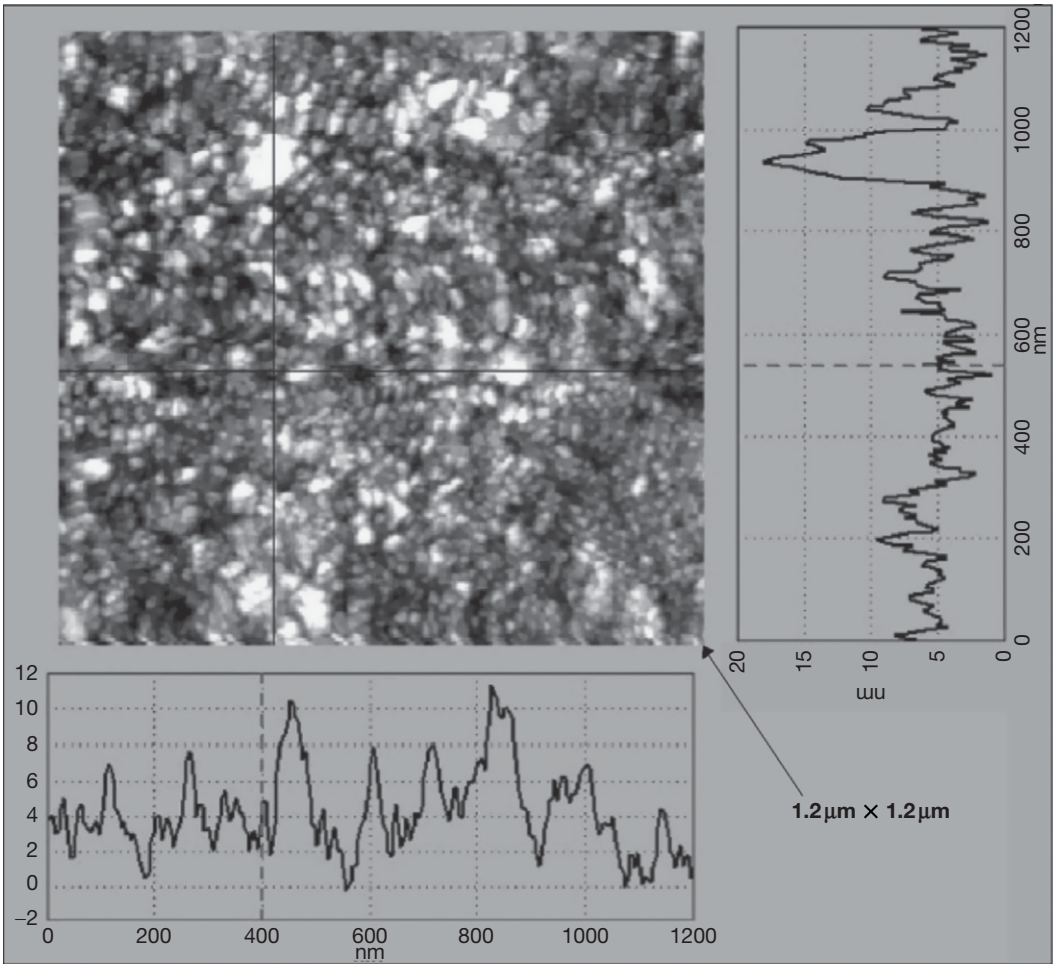

Figure 43 STM surface line profile results on the 'glaze' layer formed on Nimonic 80A (Stellite 6 counterface, 0.314 m s^{-1}, 750 °C, load 7 N, sliding distance 4522 m).[5,20,21,25]

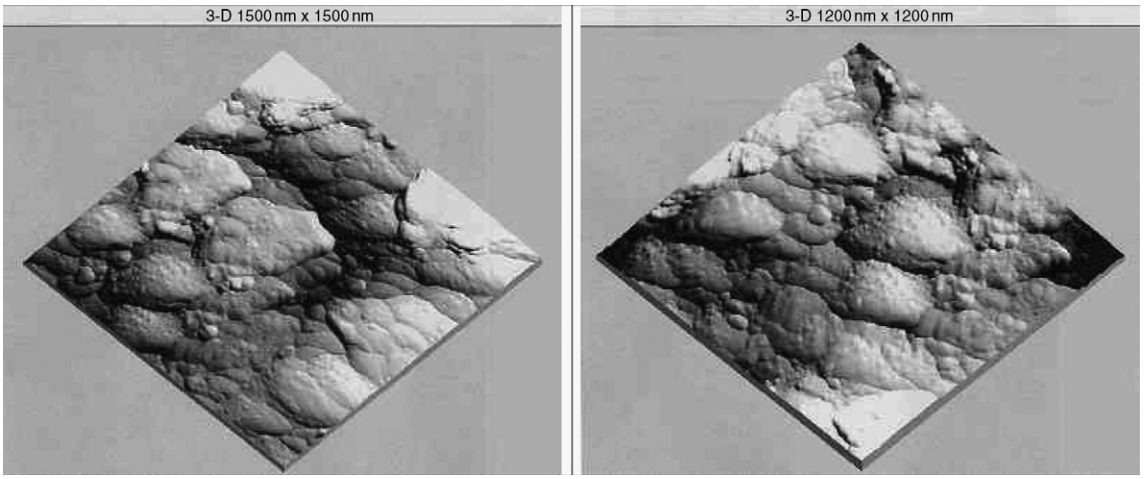

Figure 44 AFM image of 'glaze' layer surfaces produced on Incoloy MA956 (slid against Incoloy 800HT) at 750 °C and sliding speeds of (a) 0.314 m s^{-1} and (b) 0.905 m s^{-1}. Reproduced from Inman, I. A. Nano-scale studies of 'glaze' layers formed on Incoloy MA956 when slid against Incoloy 800HT at 750°C, Northumbria University, 2003, Unpublished work.

significantly affect wear behavior, regardless of whether or not a protective 'glaze' can form.

Several authors have also constructed wear maps in an attempt to present wear data in a more easily understood format, allowing prediction of likely wear mode under specified sliding conditions. Lim[124,125] (**Figure 45**), Childs[126] (**Figure 46(a)**), and more recently, Riahi and Alpas,[128] Chen and Alpas,[129] Yang *et al.*,[130] Grimanelis and Eyre,[131,132] and Elleuch *et al.*[133] have constructed wear maps for various sliding systems based on load/pressure and sliding speed. Other wear-related parameters have also been used and Kato and Hokkirigawa[127] developed an abrasive wear map using 'degree of penetration (of asperities)' and 'shear strength at the contact interface' as key parameters (**Figure 46(b)**). Adachi *et al.*[134] used 'severity of contact' and 'thermal severity of contact' for ceramic wear.

The following section discusses recent developments in high temperature wear maps made by the present authors, following a brief review of earlier work by Lim.

Table 5 Quantification of the EDX spectra in **Figure 35**

Element	*Area 1 (Nimonic 80 A substrate)*		*Area 3 (Glaze layer)*	
	wt.%	*at.%*	*wt.%*	*at.%*
Al	0.7	1.4	0.4	0.9
Si	0.7	1.3	1.1	2.3
Ti	1.8	2.1	0.4	0.5
Cr	18.7	20.2	25.0	27.4
Fe	0.7	0.7	1.4	1.4
Co	1.0	0.9	49.8	48.2
Ni	76.6	73.4	19.0	18.4
W	–	–	2.9	0.9

1.15.5.2 Work by Lim

Lim[124] attempted to collate the available data for mild steels into a single comprehensive wear map (**Figure 45**) using dimensionless parameters of normalized velocity versus normalized load. This showed that the selection of sliding conditions and configuration can greatly affect the wear behavior and transitions observed, with load, sliding speed, and temperature potentially having a large influence on the boundaries between the different modes of wear.

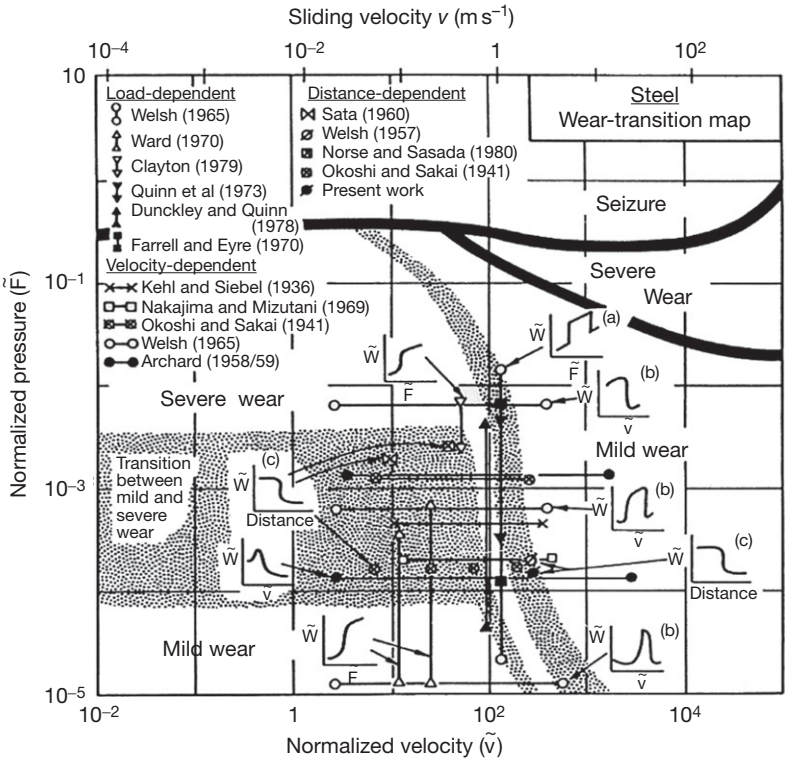

Figure 45 Wear transition map for steels showing regions of mild and severe wear – sliding conditions corresponding to different types of wear transitions observed are also indicated. Reproduced from Lim, S. C. *Tribol. Int.* **1998**, *31*(1–3), 87–97.

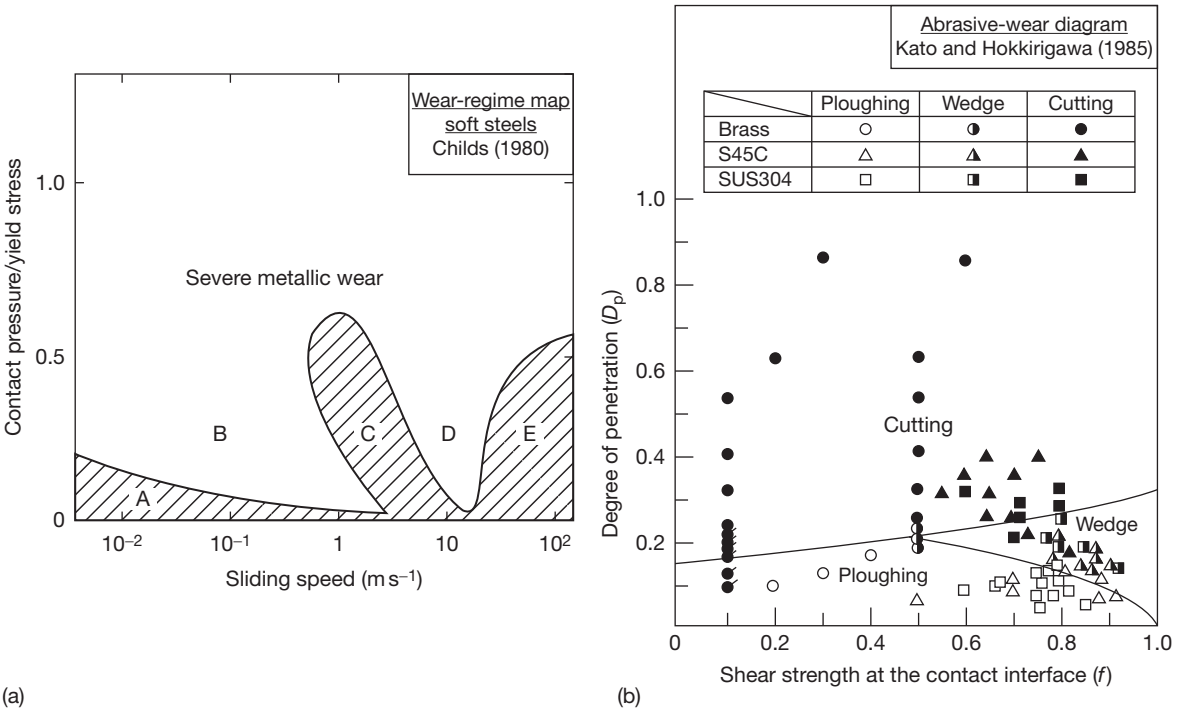

Figure 46 Examples of 'alternative parameter' wear maps: (a) Childs soft steels wear-regime map[126]; and (b) Kato and Hokkirigawa's abrasive-wear diagram for brass, S45C medium carbon steel and SUS304 stainless steel. Reproduced from Kato, K.; Hokkirigawa, K. In *Proceedings of the Eurotrib'85*; Elsevier: Amsterdam, 1985; Vol. 4, Section 5.3, pp 1–5.

For example, it can be seen that, if a relatively high fixed load is used, with increasing sliding speed, a transition from severe-to-mild wear is observed.[27] More complex forms result at lower loads when sliding speeds are at much higher values.[27,32] Similarly, if speed is fixed at an arbitrarily low value, increasing load may see a switch from mild to severe wear[124] while a higher speed can result in a more complex curve.[27] To summarize, when two surfaces are worn against each other, the outcome can be a variety of apparently contradictory results. Thus, mapping is necessary to understand the relative behaviors in different tests and the potential outcome under a given set of sliding conditions.

1.15.5.3 Dissimilar Interfaces

As discussed previously, Inman *et al.*[5,22,23] studied the effects of temperature and sliding speed on several superalloys using dissimilar interfaces. This section refers specifically to Nimonic 80A[22] and Incoloy MA 956[23] worn against Stellite 6. For both systems, the data have been used to create simple 'temperature versus sliding speed' wear maps[22,23] (**Figures 47** and **48**). The weight change data are presented in **Figures 30** and **49**.

For both systems,[23] mild wear with low weight loss dominates at $0.314\,m\,s^{-1}$ regardless of temperature (**Figures 47** and **48**). Up to 450 °C, a low temperature mild wear regime occurs, with the wear surfaces separated by a layer of Co–Cr oxide particles (i.e., loose debris – **Figures 13(a)** and **24(a)** – potentially underlain by a more compacted layer – **Section 1.15.4.3.2**), primarily sourced from the Stellite 6. Increased agglomeration and sintering of the debris has been observed at 390 °C, with isolated patches of 'glaze' at 450 °C (although most of the oxide remained as loose debris). Mild wear persists between 510 °C (**Figures 13(b)** and **24(b)**) and 750 °C (**Figures 13(c)** and **24(c)**), with the still Stellite 6-sourced oxide sintering to form comprehensive 'glaze' layers with nanostructured surfaces[5,20,21,23,25] (discussed in **Section 1.15.4.4**); with extremely low weight change with some very slight weight gains due to oxide development (**Figures 47** and **48**). At all temperatures, there was virtually no initial severe wear period, with sufficient Co–Cr oxide debris forming extremely rapidly.

The Nimonic 80A versus Stellite 6 system[22] is characterized by three distinct wear regimes at $0.654\,m\,s^{-1}$ (**Figure 47**); up to 390 °C, a low temperature 'low weight loss' mild wear regime (**Figure 30**) was observed, with a

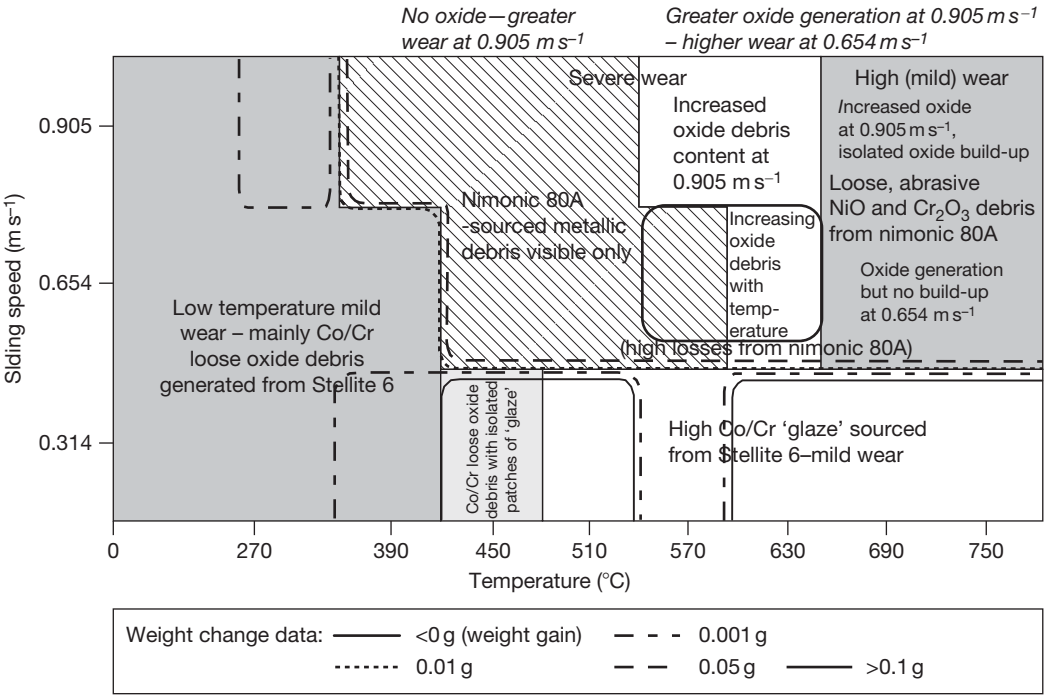

Figure 47 Wear map for Nimonic 80A versus Stellite 6 (load 7 N, sliding distance 4522 m), with weight loss (contour) data superimposed. Reproduced from Inman, I. A.; Rose, S. R.; Datta, P. K. *Wear* **2006**, *260*, 919–932.

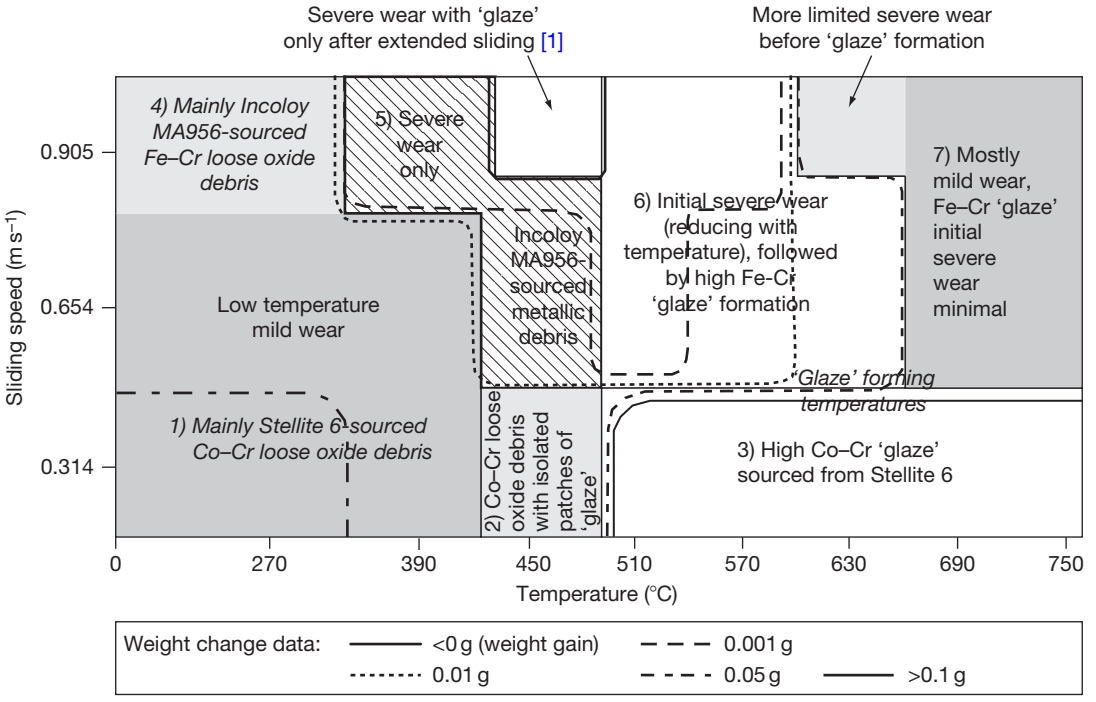

Figure 48 Wear map for Incoloy MA956 slid against a Stellite 6 counterface (load 7 N), with weight loss (contour) data superimposed. Reproduced from Inman, I. A.; Rose, S. R.; Datta, P. K. *Tribol. Int.* **2006**, *39*, 1361–1375.

layer of Stellite 6-sourced Co–Cr oxide particles separating the wear surfaces (Figure 41(a)). A metallic severe wear (especially of the Nimonic 80A) regime dominated between 450 and 630 °C (Figure 25(b)) with no visible oxide between 450 and 570 °C. This severe wear regime was also observed at 630 °C, now accompanied by a small amount of NiO and Cr_2O_3 generated by thermal and frictional heating; however, this oxide was insufficient to impede metal-to-metal contact and may instead have assisted wear by abrasion.

A mild oxidational wear regime was evident at 690 and 750 °C, although Nimonic 80A weight losses (Figure 30) remained high due to abrasion. This abrasion was caused by large amounts of Nimonic 80A-sourced NiO and Cr_2O_3, which (unlike Co–Cr oxides generated at 0.314 m s^{-1}) showed little tendency to sinter and form 'glaze.'

The sliding behavior at 0.905 m s^{-1} exhibited the same three sliding regimes observed at 0.654 m s^{-1}.[22] However, greater frictional heating resulted in a downward shift in the low-temperature-mild-wear-to-severe-wear transition from 390–450 to 270–390 °C. Increased amounts of loose NiO and Cr_2O_3 debris occurred at 570 °C upwards, but not sufficient to lower the severe-wear-to-abrasive-mild-wear transition from 690 °C.

The behavior for the Incoloy MA956 versus Stellite 6 system follows the same general pattern at 0.654 and 0.905 m s^{-1} as that of Nimonic 80A versus Stellite 6[23] (Figure 48). However, in this case, the high temperature mild wear regime confers protection, with the mixed Fe–Cr and Co–Cr oxides at 0.654 m s^{-1} or the largely Fe–Cr oxides at 0.905 m s^{-1} readily sintering to form 'glaze' layers. Such 'glaze' is observed from 510 °C upwards (450 °C after extended sliding at 0.905 m s^{-1}), after a period of early serve wear (Figure 14(b)) that decreases in length with increasing temperature. At and above 630 °C, rapid 'glaze' formation (Figure 14(c)) almost completely eliminates early severe wear (Figure 49).

A later study by Inman and Datta[24] looked to improve Nimonic 80A versus Stellite 6 wear map resolution between 630 and 750 °C by adding extra test sliding speeds. Rudimentary wear maps were also developed separately for Nimonic 80A and Incoloy MA956 as sample materials versus an Incoloy 800HT counterface.[5]

Such sliding studies indicate the potential for complex behavior during sliding of dissimilar

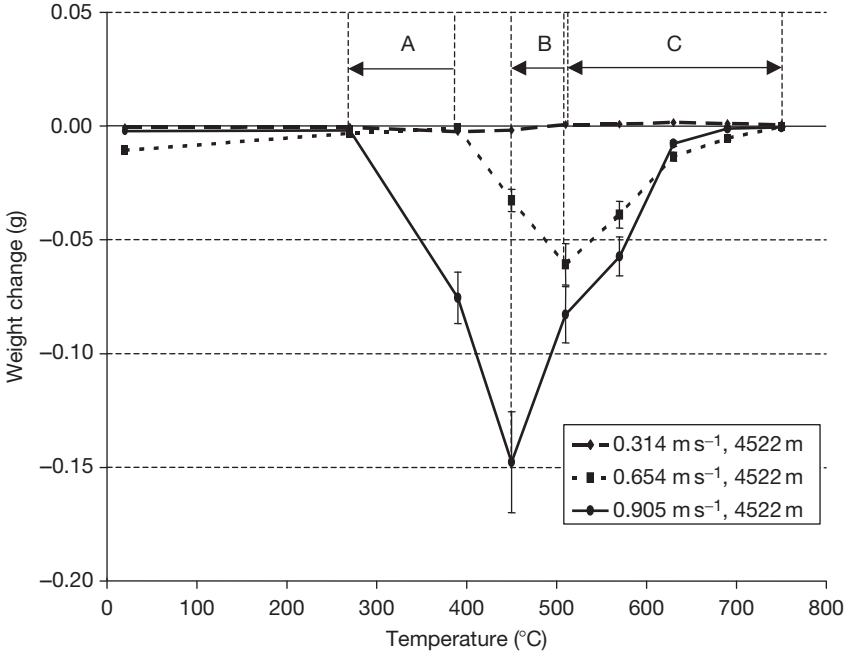

Figure 49 Weight change versus temperature for Incoloy MA956 slid against Stellite 6 at 0.314, 0.654, and 0.905 m s^{-1} (load 7 N, sliding distance 4522 m) – effect on transition temperatures on increasing sliding speed from 0.654 to 0.905 m s^{-1} are indicated.[23] (a) Decrease in low temperature mild to severe wear transition from 390 °C at 0.654 m s^{-1} to 270 °C at 0.905 m s^{-1}, (b) Decrease in temperature of first appearance of 'glaze' from 510 °C at 0.654 m s^{-1} to 450 °C after extended sliding at 0.905 m s^{-1}, and (c) More rapid 'glaze' formation at 0.905 m s^{-1}.

materials. In such cases, the necessity for mapping wear behavior to assist prediction of mild or severe wear is important, if potentially catastrophic material failure is to be avoided.

1.15.5.3.1 Oxide chemistry

These studies also indicate that the readiness for a wear-generated oxide to form 'glaze' layers depends not just upon the sliding conditions, but also on the chemical composition of the oxide. For example, Co–Cr-based oxides readily form wear protective 'glaze' layers at high temperature,[3,20–25] while Fe–Cr-based oxides[3,23] can also form fairly robust wear protective layers under adverse sliding conditions. NiO and Cr_2O_3 oxides produced from Nimonic 80A do not too readily sinter together to develop into 'glaze' and can actually enhance wear by abrasion[3,6,7]; however, NiO (produced from Nickel 200)[3] has been shown to easily form a 'glaze' in the absence of Cr_2O_3.

1.15.6 Summary

In writing this chapter strong emphasis has been placed on scientific principles underpinning the phenomenon of high temperature wear. At the outset a review of some of the well-known and relevant wear theories and models, supported by experimental findings on conventional and advanced materials, has been presented. This background information has provided a framework to discuss new areas of high temperature wear. In this context the high temperature wear behavior of those materials which have provided new information has been considered. Particular attention has been focused on high temperature wear behavior of oxide dispersion strengthened and Nimonic alloys, and intermetallic materials involving like-on-like and unlike-on-unlike combinations. The most significant part of this chapter includes the exposition of the phenomena of glaze formation at fundamental levels. Here the novel aspect is the inclusion of nanoscale elaboration of the processes of glaze formation underpinned by fundamental information gathered from TEM and STM/STS investigations. In this area significant reliance has been placed on the authors' own research.

References

1. Quinn, T. F. J. *Wear* **1992**, *153*, 179–200.
2. Jiang, J.; Stott, F. H.; Stack, M. M. *Wear* **1995**, *181–183*, 20–31.
3. Wood, P. D. Ph.D. Thesis, Northumbria University, UK, 1997.
4. Rose, S. R. Ph.D. Thesis, Northumbria University, UK, 2000.
5. Inman, I. A. Ph.D. Thesis, Northumbria University, UK, 2003; published by 'Dissertation.com', 2006.
6. Stott, F. H.; Lin, D. S.; Wood, G. C. *Corros. Sci.* **1973**, *13*, 449–469.
7. Johnson, M.; Moorhouse, P.; Nicholls, J. R. DTI Industry Valve Project 1990; pp 61–68.
8. Aoh, J.-N.; Chen, J.-C. *Wear* **2001**, *250–251*, 611.
9. Singh, J.; Alpas, A. T. *Metall. Mater. Trans. A* **1996**, *27*, 3135–3148.
10. Stott, F. H.; Glascott, J.; Wood, G. C. *Wear* **1984**, *97*, 93–106.
11. Gee, M. G.; Jennett, N. M. *Wear* **1995**, *193*, 133–145.
12. Wood, P. D.; Datta, P. K.; Burnell-Gray, J. S.; Wood, N. *Mater. Sci. Forum* **1997**, *251–254*, 467–474.
13. Wisbey, A.; Ward-Close, C. M. *Mater. Sci. Technol.* **1997**, *13*, 349–355.
14. Jiang, J.; Stott, F. H.; Stack, M. M. *Wear* **1997**, *203–204*, 615–625.
15. Li, X. Y.; Tandon, K. N. *Wear* **2000**, *245*, 148–161.
16. Jiang, J.; Stott, F. H.; Stack, M. M. *Wear* **2004**, *256*, 973–985.
17. Jiang, J.; Stott, F. H.; Stack, M. M. *Tribol. Int.* **1998**, *31–5*, 245–256.
18. Jiang, J.; Stott, F. H.; Stack, M. M. *Tribol. Int.* **1997**, *30–7*, 517–526.
19. Jiang, J.; Stott, F. H.; Stack, M. M. *Wear* **1994**, *176*, 185–194.
20. Datta, S.; Inman, I.; Du, H. L.; Luo, Q. Microscopy of 'glazed' layers formed during high temperature wear, Invited Talk at the Institute of Materials, Tribology Meeting, London, November 2001.
21. Inman, I. A.; Datta, S.; Du, H. L.; Burnell-Gray, J. S.; Pierzgalski, S.; Luo, Q. *Tribol. Int.* **2005**, *38*, 812–823.
22. Inman, I. A.; Rose, S. R.; Datta, P. K. *Wear* **2006**, *260*, 919–932.
23. Inman, I. A.; Rose, S. R.; Datta, P. K. *Tribol. Int.* **2006**, *39*, 1361–1375.
24. Inman, I. A.; Datta, P. S. *Wear* **2008**, *265*, 1592–1605.
25. Inman, I. A.; Datta, S.; Du, H. L.; Burnell-Gray, J. S.; Pierzgalski, S.; Luo, Q. *Wear* 2003, *254*, 461–467.
26. Lancaster, J. K. *Proc. Royal Soc. London A* **1962**, *273*, 466–483.
27. Welsh, N. C. *Philos. Trans. A* **1965**, *257*, 31–50.
28. Welsh, N. C. *Philos. Trans. A* **1965**, *257*, 51–70.
29. So, H. *Tribol. Int.* **1996**, *25*(5), 415–423.
30. So, H. *Wear* **1996**, *192*, 78–84.
31. Archard, J. F.; Hirst, W. *Proc. Royal Soc. London A* **1956**, *236*, 397–410.
32. Archard, J. F.; Hirst, W. *Proc. Royal Soc. London A* **1957**, *238*, 515–528.
33. Quinn, T. F. J. *Tribol. Int.* **1983**, *16*, 257–270.
34. Oh, H.-K.; Yeon, K.-H.; Kim, H. Y. *J. Mater. Process. Technol.* **1999**, *95*, 10–16.
35. Stott, F. H.; Wood, G. C. *Tribol. Int.* **1978**, *11*, 211–218.
36. Bowden, F. P.; Tabor, D. Friction, *An Introduction to Tribology;* Heinemann: London, 1973.
37. Eyre, T. S.; Maynard, D. *Wear* **1971**, *18*, 301–310.
38. Burwell, J. T.; Strang, C. D. *J. Appl. Phys.* **1952**, *23*, 18–28.
39. Ludema, K. Scuffing, run-in and the function of surface films, particularly oxides; Review Paper for Interdisciplinary Collaboration in Tribology Project, NASA-Lewis, 1981.
40. Tabor, D. Proceedings of the International Conference on Wear of Materials, St. Louis, Missouri in April 1977; ASME, 1978; pp 1–10.
41. Rabinowicz, E. C. *Friction and Wear of Materials;* Wiley: New York, 1965.

42. Blau, P. J. *Wear* **1981**, *72*, 55–66.
43. Iwabuchi, A. *Wear* **1990**, *151*, 301–311.
44. Iwabuchi, A.; Kubosawa, H.; Hori, K. *Wear* **1988**, *128*, 123–137.
45. Iwabuchi, A.; Kubosawa, H.; Hori, K. *Wear* **1990**, *139*, 319–333.
46. Leheup, E. R.; Pendlebury, R. E. *Wear* **1991**, *142*, 351–372.
47. Colombie, C.; Berthier, Y.; Floquet, A.; Vincent, L. *Trans. ASME* **1984**, *106F*, 194–201.
48. Hiratsukam, K.; Sasada, T.; Norose, S. *Wear* **1986**, *110*, 251–261.
49. Rigney, D. A. *Wear* **2000**, *245*, 1–9.
50. Stott, F. H.; Glascott, J.; Wood, G. C. *Proc. Royal Soc. London A* **1985**, *402*, 167–186.
51. Sullivan, J. L.; Granville, N. W. *Tribol. Int.* **1984**, *17*, 63–71.
52. Stott, F. H.; Mitchell, D. R. G. In *Surface Engineering*; Datta, P. K., Gray, J. S., Eds.; Vol. 1: Fundamentals of Coatings; Royal Society of Chemistry, 1993; pp 141–150.
53. Halliday, J. S.; Hirst, W. *Proc. Royal Soc. London A* **1956**, *236*, 411–425.
54. Stott, F. H. *Tribol. Int.* **2002**, *35*, 489–495.
55. Lin, D. S.; Stott, F. H.; Wood, G. C.; Wright, K. W.; Allen, J. H. *Wear* **1973**, *24*, 261–278.
56. Lin, D. S.; Stott, F. H.; Wood, G. C. *Trans. ASLE* **1973**, *17* (4), 251–262.
57. Stott, F. H.; Lin, D. S.; Wood, G. C. Proceedings of the 5th European Congress on Corrosion, 1973; pp 452–455.
58. Stott, F. H.; Lin, D. S.; Wood, G. C. *Nat. Phys. Sci.* **1973**, *242*, 75–77.
59. Stott, F. H.; Lin, D. S.; Wood, G. C.; Stevenson, C. W. *Wear* **1976**, *36*, 147–174.
60. Stott, F. H.; Glascott, J.; Wood, G. C. *Wear* **1984**, *97*, 155–178.
61. Stott, F. H. *Tribol. Int.* **1998**, *31*, 61–71.
62. Quinn, T. F. J. *Wear* **1971**, *18*, 413–419.
63. Quinn, T. F. J. *Wear* **1996**, *199*, 169–180.
64. Quinn, T. F. J. *Wear* **1994**, *175*, 199–208.
65. Iwabuchi, A.; Hori, K.; Kudo, H. Proceedings of the International Conference on Wear of Materials, New York 1987; pp 211–220.
66. Langgath, K.; Kluge, A.; Ryssel, H. *Wear* **1992**, *155*, 343–351.
67. Mølgaard, J. *Wear* **1976**, *40*, 277–291.
68. Kuzucu, V.; Ceylan, M.; Çelik, H.; Aksoy, I. *J. Mater. Process. Technol.* **1997**, *69*, 257–263.
69. Crook, P.; Li, C. C. *Wear of Materials*; ASME, 1983; pp 272–279, Pub. No. 110254.
70. Bartsch, M.; Wasilkowska, A.; Czyrska-Filemonowicz, A.; Messerschmidt, U. *Mater. Sci. Eng. A* **1999**, *272*, 152–162.
71. Fujita, A.; Shinohara, M.; Kamada, M.; Yokota, H. *Isij Int.* **1998**, *38*, 291–299.
72. Soda, N.; Sasada, T. *ASME Trans. J. Lubr. Technol.* **1978**, *100*(4), 492–499.
73. Wu, W.-Z.; Xing, J.-D.; Su, J.-Y. *Wear* **1997**, *210*, 299–303.
74. Suh, N. P.; Sin, H. C. *Wear* **1981**, *69*, 91–114.
75. Rice, S. L.; Moslehy, F. A.; Zhang, J. In *Proceedings of the 18th Leeds-Lyon Symposium on Tribology,* 3–6 September 1991, Lyon, France; Dowson, D., Ed.; Elsevier, 1991; pp 463–467.
76. Hesmat, H. *Tribol. Trans.* **1991**, *34*(3), 433–439.
77. Ludema, K. C. In *Proceedings of the 18th Leeds-Lyon Symposium on Tribology,* 3–6 September 1991, Lyon, France; Dowson, D., Ed.; Elsevier, 1991; pp 155–160.
78. Shaw, D. J. *Colloid and Surface Chemistry, 4th ed.;* Butterworth Heinemann, 1992.
79. Zhou, Y. H.; Harmelin, M.; Bigot, J. *Scr. Metall.* **1989**, *23*, 1391–1396.
80. Datta, P. K.; Du, H. L.; Kuzmann, E.; Inman, I. A. Near surface structural changes of 'glaze' layers formed during high temperature sliding wear, to be published in *Wear*.
81. Bhansali, K. J. *Wear* **1980**, *160*, 95–110.
82. Razavizadeh, K.; Eyre, T. S. *Wear* **1982**, *79*, 325–333.
83. Garcia, I.; Ramil, A.; Celis, J. P. *Wear* **2003**, *254*, 429–440.
84. Mølgaard, J.; Srivastava, V. K. *Tribol. Int.* **1983**, *16*, 305–314.
85. Subramanium, C. *Scr. Metall.* **1991**, *25*, 1369–1374.
86. So, H. *Tribol. Int.* **1996**, *25*(5), 415–423.
87. Buckley, D. H. *Cobalt* **1968**, *38*, 20–28.
88. Persson, D. H. E. Licentiate of Philosophy Dissertation, Uppsala University, 2003.
89. Persson, D. H. E. Ph.D. Thesis, Uppsala University, 2003.
90. Stott, F. H.; Stevenson, C. W.; Wood, G. C. *Met. Technol.* **1977**, *4*, 66–74.
91. Antony, K. C. *J. Met.* **1983**, *35*(2), 52–60.
92. Brandes, E. A.; Brook, G. B. *Smithells Metals Reference Book,* Butterworth Heinemann, 1992.
93. Inman, I. A. High temperature 'like-on-like' sliding of Nimonic 80A under conditions of limited debris retention, Northumbria University, 2003, Unpublished work.
94. Vardavoulias, M. *Wear* **1994**, *173*, 105–114.
95. Wood, P. D. Unpublished work.
96. Incoloy Alloy MA956; Special Metals Corporation, Publ. No. SMC-008.
97. Inman, I. A. The effects of pre-oxidation on the high temperature wear of γ-TiAl, Internal report, Northumbria University/University of Birmingham, 2005.
98. Li, C. X.; Xia, J.; Dong, H. *Wear* **2006**, *261*, 693–701.
99. Takadoum, J.; Houmid-Bennani, H.; Mairey, D. *J. Eur. Ceram. Soc.* **1998**, *18*, 553–556.
100. Barnes, D. J.; Wilson, J. E.; Stott, F. H.; Wood, G. C. *Wear* **1977**, *45*, 634–640.
101. Buckley, D. H. Influence of chemisorbed films on adhesion and friction of clean iron, NASA Center for Aerospace Information, NASA-TN-D-4775, 1968.
102. Barnes, D. J.; Stott, F. H.; Wood, G. C. *Wear* **1977**, *45*, 199–209.
103. Barnes, D. J.; Wilson, J. E.; Stott, F. H.; Wood, G. C. *Wear* **1977**, *45*, 97–111.
104. Feng, J.-M.; Uhlig, H. H. *J. Appl. Mech.* **1954**, *21*(4), 395–400.
105. Wright, K. H. R. *Proc. Inst. Mech. Eng.* **1952–1953**, *1B* (11), 556–574.
106. Waterhouse, R. B. *Fretting Corrosion;* Pergamon Press: New York, 1972.
107. Bill, R. C. *Wear of Materials*; ASME: New York, 1979; pp 356–370.
108. Hutchings, I. M. *Tribology: Friction and Wear of Engineering Materials;* Edward Arnold, 1992.
109. Smith, A. F. *Tribol. Int.* **1986**, *19*, 65–71.
110. Du, H. L.; Datta, P. K.; Inman, I. A.; Kuzmann, E.; Suvegh, K.; Marek, T.; Vértes, A. *Tribol. Lett.* **2005**, *18*(3), 393–402.
111. Chattopadhyay, B.; Wood, G. C. *Oxidat. Met.* **1970**, *2*, 373–399.
112. Stott, F. H. *Tribol. Int.* **2002**, *35*, 489–495.
113. Du, H. L.; Datta, P. K.; Inman, I.; Geurts, R.; Kübel, C. *Mater. Sci. Eng. A* **2003**, *357*, 412–422.
114. Inman, I. A. Nano-scale studies of 'glaze' layers formed on Incoloy MA956 when slid against Incoloy 800HT at 750°C, Northumbria University, 2003, Unpublished work.

115. Du, H. L.; Aljarany, A.; Datta, P. K.; Burnell-Gray, J. S. *Corros. Sci.* **2005**, *47*, 1706–1723.
116. Aljarany, A. A. Ph.D. Thesis University of Northumbria, UK, 2002.
117. Gleiter, H. *Prog. Mater. Sci.* **1989**, *33*, 223–315.
118. Valiev, R. Z.; Islamgalier, R. K.; Alexandrov, I. V. *Prog. Mater. Sci.* **2000**, *45*, 103–189.
119. Lowe, T. C.; Valiev, R. Z. *JOM* **2000**, *52*, 27–28.
120. Ghosh, A. K.; Huang, W. In *Investigations and Applications of Severe Plastic Deformation*; Lowe, T. C., Valiev, R. Z., Eds.; Kluwer Academic, 2000; pp 29–36.
121. Mishra, R. S.; McFadden, S. X.; Mukherjee, A. K. *Mater. Sci. Forum* **1999**, *304–306*, 31–38.
122. Mishra, R. S.; Mukherjee, A. K. In *Superplasticity and Superplastic Forming*; Ghosh, A. K., Bieler, T. R., Eds.; TMS Warrendale, 1998; pp 109–116.
123. Mishra, R. S.; McFadden, S. X.; Mukherjee, A. K. In *Investigations and Applications of Severe Plastic Deformation*; Lowe, T. C., Valiev, R. Z., Eds.; Kluwer Academic, 2000; pp 231–240.
124. Lim, S. C. *Tribol. Int.* **1998**, *31*(1–3), 87–97.
125. Lim, S. C. *Tribol. Int.* **2002**, *35*(11), 717–723.
126. Childs, T. H. C. *Tribol. Int.* **1980**, *13*, 285–293.
127. Kato, K.; Hokkirigawa, K. In *Proceedings of the Eurotrib'85;* Elsevier: Amsterdam, 1985; Vol. 4, Section 5.3, pp 1–5.
128. Riahi, A. R.; Alpas, A. T. *Wear* **2003**, *255*, 401–409.
129. Chen, H.; Alpas, A. T. *Wear* **2000**, *246*, 106–116.
130. Yang, S. H.; Kong, H.; Yoon, E.-S.; Kim, D. E. *Wear* **2003**, *255*, 883–892.
131. Grimanelis, D.; Eyre, T. S. *Wear* **2007**, *262*, 93–103.
132. Grimanelis, D.; Eyre, T. S. *Surf. Coat. Technol.* **2006**, *201–6*, 3260–3268.
133. Elleuch, K.; Elleuch, R.; Mnif, R.; Fridrici, V.; Kapsa, P. *Tribol. Int.* **2006**, *39–4*, 290–296.
134. Adachi, K.; Kato, K.; Chen, N. *Wear* **1997**, *203–204*, 291–301.

1.20 Gas Turbine Oxidation and Corrosion

J. R. Nicholls and N. J. Simms
Cranfield University, Cranfield, Bedfordshire MK43 0AL, UK

Abbreviations

APS Air plasma spray
CVD Chemical vapor deposition
EBPVD Electron beam physical vapor deposition
EFC European Federation of Corrosion
EPSRC Engineering and Physical Sciences Research Council (United Kingdom)
EU European Union
FOD Foreign object damage
HP High pressure
HRSG Heat recovery steam generator
HVOF High velocity oxy-fired
IGCC Integrated gasification combined cycle
ISO International Organization for Standardisation
LPPS Low pressure plasma spray
NGV Nozzle guide vane
NMAB National Materials Advisory Board (USA)
NRC National Research Council (USA)
PLPS Photoluminescence piezospectroscopy
TBC Thermal barrier coating
TGO Thermally grown oxide

Symbols

y Reciprocal value of the C to H ratio in mol
A/F Air to fuel mass flow ratio
MO Metal oxide
S/F Steam (water) to fuel mass flow ratio
X_A Contaminant concentration in inlet air (ppm) by weight
X_F Contaminant concentration in fuel (ppm) by weight
X_S Contaminant concentration in injected steam or water (ppm) by weight
X_T Total contamination in fuel equivalent (ppm) by weight
λ Amount of excess air: actual mass flow divided by the air mass flow for stoichiometric combustion

1.20.1 Introduction

Gas turbines have been developed rapidly over the last 60 years, with applications currently ranging from aeroengines to marine propulsion to industrial mechanical power to utility scale electrical power generation.[1,2] Whatever be the intended application

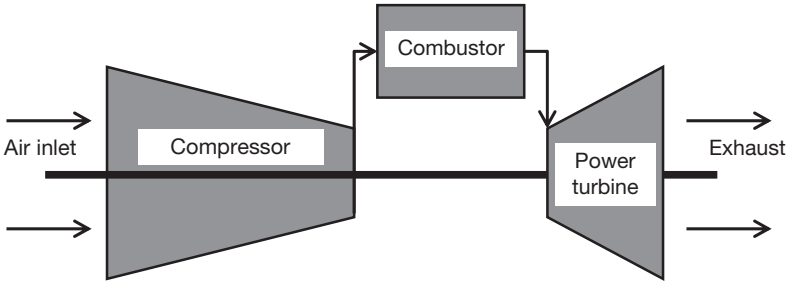

Figure 1 Schematic diagram of simple cycle gas turbine showing fundamental components.

of the gas turbine, the basic features and principles of operation are common. Figure 1 illustrates the fundamental parts of a gas turbine.

Details of the operation of gas turbines (which use the Brayton cycle) are available from numerous sources[1,2] but can be summarized as follows for the purposes of this chapter:

- air enters the gas turbine through the compressor;
- the air is compressed (and heated adiabatically) as it passes through a series of vane/rotor stages of the compressor;
- this air is passed into combustion chamber(s) where fuel is introduced and burnt raising the temperature of the gas stream;
- this hot, high pressure gas stream is then passed through the power turbine where its temperature and pressure are reduced as it passes through a series of vane/rotor stages which drive both the compressor and mechanical/electrical power conversion unit.

The Carnot efficiency of the gas turbine (as with any heat engine) is related to the difference between the maximum and minimum absolute temperatures of the working fluid (in which case, the inlet and outlet temperatures of the power turbine are divided by the inlet temperature). For a current gas turbine with an inlet temperature of 1400 °C (1673 K) and an exit temperature of 600 °C (873 K), this would give a Carnot efficiency of ~48%. Real cycle efficiencies are always lower than Carnot efficiencies, and in this case, for a simple cycle gas turbine, the efficiency would be closer to ~38–40%.[3] If the inlet temperature is to be raised to ~2100 °C or ~2373 K (just below stoichiometric combustion for maximum flame temperature[1] – a near impossible achievement) and the exit temperature remains at 600 °C (~873 K), then the maximum thermal efficiency will be ~63%, without dropping the exit temperature to extract energy from this lower grade heat source.

Thus, within these constraints, there are several routes to improve the efficiency of gas turbines:

- increasing the power turbine inlet temperature; this is the traditional route with limitations being set by the materials of construction for the hot gas path, but now also being set by cooling technologies and thermal barrier coating (TBC) performance;
- lower the exit temperature;
- using the heat in the exit gases in another way; for example, by passing the gases through a heat recovery steam generator (HRSG) to generate steam which is then passed through steam turbine to generate power (i.e., using a conventional Rankine cycle); the overall system is known as a combined cycle, and overall efficiencies for such systems have been reported to exceed 60%.

In addition, there are several other variations of gas turbine cycles that continue to be investigated:

- Indirect firing; where the compressed air is heated by an external heat source via heat exchangers before passing through the power turbine;
- Oxy-firing; where the fuel is burnt with oxygen to generate a combusted gas stream of mostly CO_2 and steam, from which the steam can be condensed to produce a CO_2 rich gas stream for recycling into the compressor or for storage (after further cleanup).

In terms of the sizes of gas turbines:

- the largest utility power turbines are rated at ~340 MWe in simple cycle mode and 530 MWe in combined cycle mode[4];
- jet engines are rated in terms of their thrust, with the largest generating up to 100 000 lbs.[1]

From the foregoing, it is evident that materials in gas turbines need to be capable of operating at high bulk temperatures with high static and fluctuating stresses, while by also withstanding the surrounding environments. The environments generated within

the hot gas paths of gas turbines can be both physically and chemically aggressive, with particles producing erosion or deposition while gaseous and vapor-phase species may produce different forms of deposition, as well as oxidation and hot corrosion. The balance between these various degradation mechanisms is component and turbine dependent (as are the temperatures and stresses involved).

Thus, from a generic materials point of view, issues of concern for gas turbine hot gas path components include:

- creep,
- fatigue (thermal, low cycle, and high cycle),
- thermal cycling,
- oxidation,
- hot corrosion,
- erosion/foreign object damage (FOD),
- synergistic oxidation/corrosion/mechanical property interactions.

This chapter focuses on the oxidation and hot corrosion performance of materials in a range of different gas turbines and on how thermal cycling, erosion, and mechanical loading affect this performance.

1.20.2 Gas Turbine Operating Conditions

Gas turbines have conventionally been fired using hydrocarbon fuels (such as diesels, jet fuels, and natural gases) burnt using air as the oxidant. More recent fuels have included syngases produced by coal or biomass gasification processes. In addition, use of oxygen as the oxidant is now being actively investigated for utility gas turbines as one potential route to enable CO_2 capture technologies to be introduced.

In all cases, the basic reaction of the fuels with the oxidant can be summarized as:

$$\text{Fuel} + \text{air} \rightarrow \text{Combusted gases}$$

or

$$\begin{aligned} &C + yH + \lambda(1 + y/4)(O_2 + 3.719N_2 + 0.043Ar) \\ &\rightarrow CO_2 + (y/2)H_2O + \lambda(1 + y/4)(3.719N_2 \\ &+ 0.043Ar) + (\lambda - 1)(1 + y/4)O_2 \end{aligned}$$

where y is the reciprocal value of the C to H ratio in mol, λ is the amount of excess air actual mass flow divided by the air mass flow for stoichiometric combustion.

Excess air is always used in the process to ensure that the fuel is completely consumed, to reduce the temperature of the combusted gas stream, and to increase the mass flow through the power turbine. This produces a high temperature combusted gas stream that is oxidizing. For some industrial gas turbines, water/steam is also added to increase the mass flow through the power turbine and/or reduce NO_X emissions[5–9] (in some cases, steam-cooled components also exhaust into the main combusted gas flow).

However, unwanted products of combustion processes can be produced:

- CO from incomplete combustion of the fuel;
- NO_X from thermal deposition of air or fuel-derived nitrogen species;
- SO_X from oxidation of fuel borne impurities.

Various approaches have been developed to control these unwanted combustion products, such as improved combustor design, staged combustion, water injection, etc. Not all are appropriate (or feasible) for every gas turbine application, so their use varies. However, increasingly stringent environmental regulations are being developed and applied in various countries; especially to utility scale gas turbines.

Unfortunately, the combusted fuel gas stream also includes species derived from minor and trace elements in the fuels and oxidant streams: these elements commonly include sulfur, alkali metals, chlorine, magnesium, calcium, lead, vanadium, etc. However, when gasification processes are considered, even more elements can be involved, including cadmium and arsenic.[10] These various elements can combine to cause hot corrosion damage to the hot gas path of the gas turbine. The reactions involved, their effects, and methods to limit them (including fuel specifications) are described in detail in **Section 1.20.5**.

During the last 60 years, there has been a continuous drive to increase the efficiencies of all types of gas turbine, but they still fall short of the Carnot theoretical optimum, which would be achieved at stoichiometric combustion combined with no mechanical losses. As a result, the firing temperatures and pressures of gas turbines have increased steadily (**Figure 2**). Current industrial gas turbines for power generation applications have firing temperatures of up to ~1430 °C and pressures of up to ~34 bar, while for jet engine applications, firing temperatures are up to ~1550 °C and pressures up to ~45 bar.[1]

Figure 3 illustrates the temperature and pressure variations expected through a generic gas turbine. There are wide variations in the actual

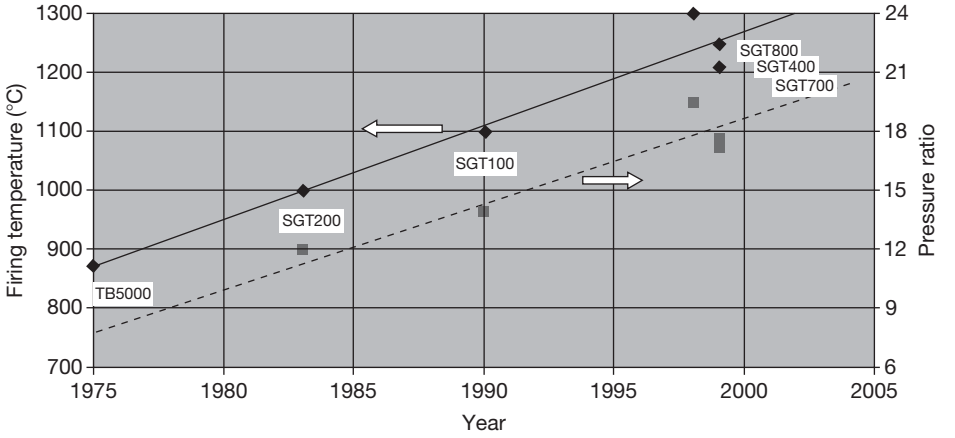

Figure 2 Increase in turbine entry temperatures and pressure ratios over time for Siemens industrial gas turbines (4–50 MW). Reproduced from Hannis, J. M. In *Power Generation in an Era of Climate Change*; Proceedings of the 7th International Charles Parsons Turbine Conference; Strang, A. *et al*. Eds.; IOM Communications, 2007; pp 37–49.

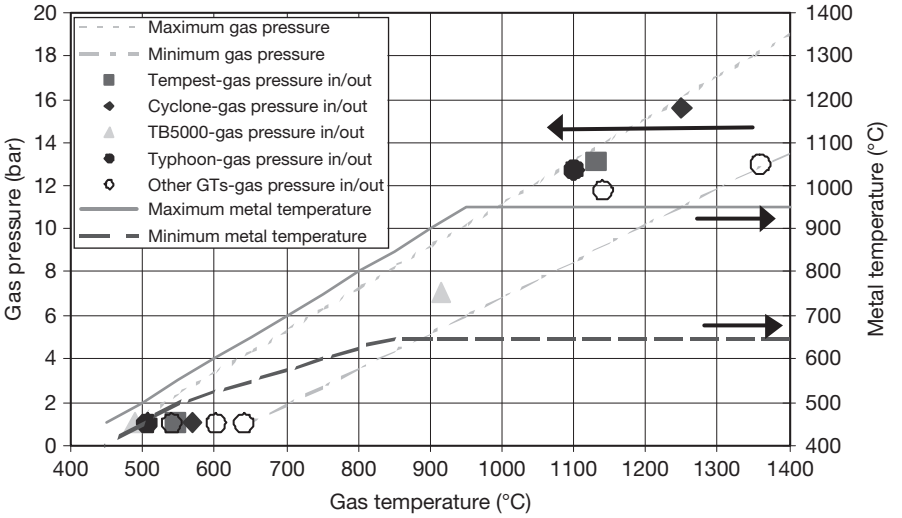

Figure 3 Variation in temperature and pressure of the gas stream passing through typical industrial gas turbines. Reproduced from Simms, N. J.; Nicholls, J. R.; Oakey, J. E. In *Lifetime Modelling of High Temperature Corrosion Processes*; Schütze, M. *et al*. Eds.; Maney, 2001; pp 379–397, EFC No. 34.

temperatures and pressures that are produced by different gas turbines. This results from a number of factors such as:

- power requirement of the turbine,
- design approach,
- duty and cycle required,
- materials/lifting restrictions.

The gas turbines used for the different applications outlined in the introduction, while obviously related by their basic principles of operation, have different detailed requirements. For example (**Figure 4**), civil aeroengines go through a routine cycle on every flight (with flight times of up to ~12 h), with peak operating temperatures for short periods during takeoff and landing. In contrast, industrial gas turbines designed for utility scale electrical power generation should be ramped slowly to their optimum operating temperature and then ideally remain there for hundreds if not thousands of hours. Other differences include weight limitations and the various contaminants that can enter the gas turbines during their operation. Thus the gas turbine usage defines the maximum gas temperature and pressure, duty cycle, operating time at temperature, number of shut-down cycles, and material operating environment.

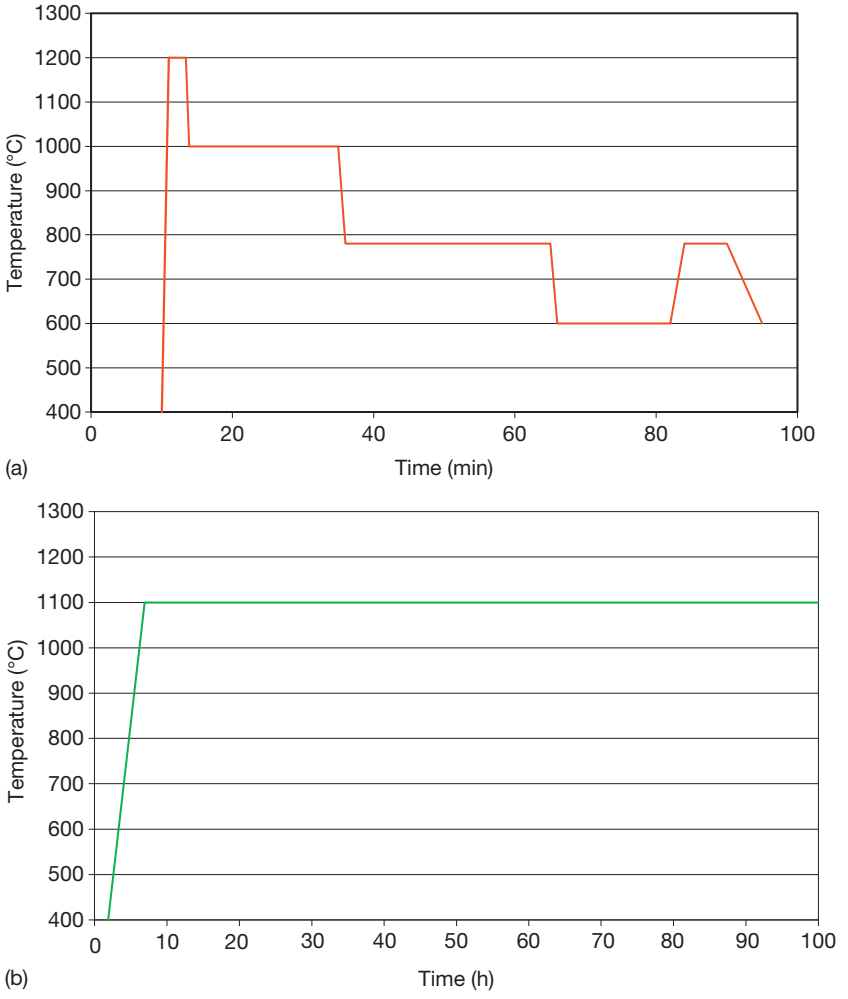

Figure 4 Examples of gas temperature cycles for an aeroengine flight and an industrial gas turbine.[12] (a) Example of short duration aeroengine cycle (Note: 4000–7500 cycles between overhauls, depending on cycle duration). (b) Example of industrial gas turbine cycle (Note: desired component lives of >24 000 h).

1.20.3 Gas Turbine Hot Gas Path Components and Materials

As efficiencies of all types of gas turbines increase with firing temperature and pressure, there has always been a drive for the hot gas paths to use materials close to their mechanical and environmental operating limits.[1,2] However, viable component lives for the hot gas path of the gas turbines have only been achieved as a result of significant materials developments coupled with improved manufacturing methods and engine designs (specifically efficient cooling). Originally steel parts were used, but as the severity of operating conditions was increased, it was necessary to invent and develop whole series of nickel-based and cobalt-based superalloys with improved mechanical properties and thermal stabilities. As these compositions have been progressively optimized, new materials have been developed with improved high temperature mechanical properties (**Figure 5**). Until the 1970s, such improvements in high temperature mechanical properties could be coupled to improved oxidation and hot corrosion resistance,[2,14] with alloys being designed to have sufficient chromium and aluminum contents to form self-protective oxide scales. However, more recent alloy developments, targeted at improved mechanical properties, could only be achieved to the detriment of oxidation and hot corrosion resistance of these alloys. Thus there is now a requirement for many hot gas path components to be coated to enable them to resist the surrounding environments and

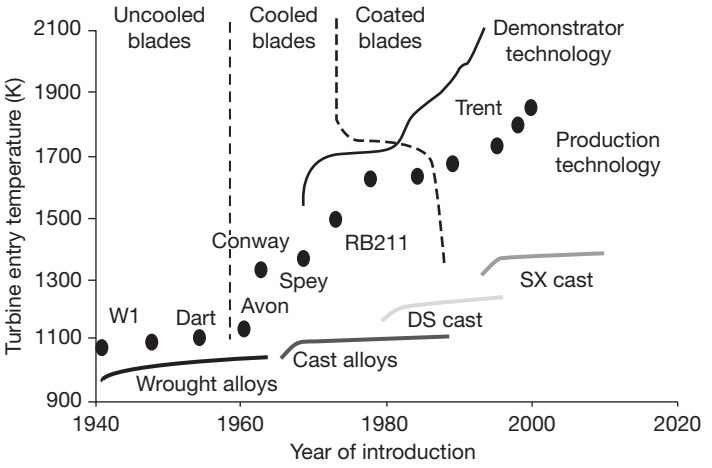

Figure 5 Improvements in materials strength with time and new alloy development. Reproduced from Rickerby, D. S.; Hicks, M. A. In *Power Generation in an Era of Climate Change*, Proceedings of the 7th International Charles Parsons Turbine Conference; Strang, A. *et al*. Eds.; IOM Communications, 2007; pp 229–240.

to permit economically viable component lives. Higher temperature alloy mechanical performance, as well as associated engine capability, has also been enhanced through improvements in casting technologies. These have permitted a change in the microstructure of nickel-based superalloys from equiaxed to directionally solidified and single-crystal blade materials (eliminating the grain boundaries that partly dictate high temperature creep damage). Originally these casting technologies were developed for small aero-engine blades, but now larger industrial gas turbine blades/vanes can also be processed.[3]

The development of a range of increasingly sophisticated component cooling technologies (including air impingement, film cooling, etc. **Figure 6**) has enabled gas stream temperatures to be decoupled from metal temperatures along the gas turbine hot gas path. Most of the cooling systems rely on air diverted from selected locations in the air compressor, but there are some land-based gas turbines that use steam cooling. The use of such cooling technologies has enabled gas temperatures to be progressively increased, much further than would be expected from alloy developments.

The introduction of cooled components has allowed the adoption and development of TBCs as part of the turbine thermal management system. These low conductivity ceramic coatings protect the underlying metallic materials from the surrounding high temperature gas streams and allow a balance between component life, component operating temperature, and cooling air requirements to be addressed. The principal of TBCs is illustrated in **Figure 7**. The use of advanced air cooling technologies coupled with TBCs means that first stage blades/vanes can now be operated at gas temperatures in excess of the melting points of the alloys used for these components.[3,4]

Critical components within the hot gas path of gas turbines include:

- combustor can/tiles/transitions ducts,
- vanes and blades (both in multiple stages),
- seals,
- discs.

Examples of alloys used for these components are given in **Table 1**.

A wide range of coatings have been developed and used for protection along the gas turbines hot gas path. The different routes for coating application that have developed are favored by different gas turbine manufacturers. Thus, the situation of using a 'standard' coating for protection against hot corrosion damage has not developed. Instead, there are several coatings from the different classes of coating materials available that are currently being used (**Table 2**):

- Overlay coatings:
  - typically Ni–Co–15–23% Cr–8–12% Al–0.1–0.9% Y,
  - applied by high velocity oxy-fuel (HVOF) or low pressure plasma spray (LPPS) coating processes,
  - some newer coatings also include Re, Hf, Ta, or Si in some combination.

- Diffusion coatings:
  - Aluminizing, chromizing, or chrome-aluminizing;

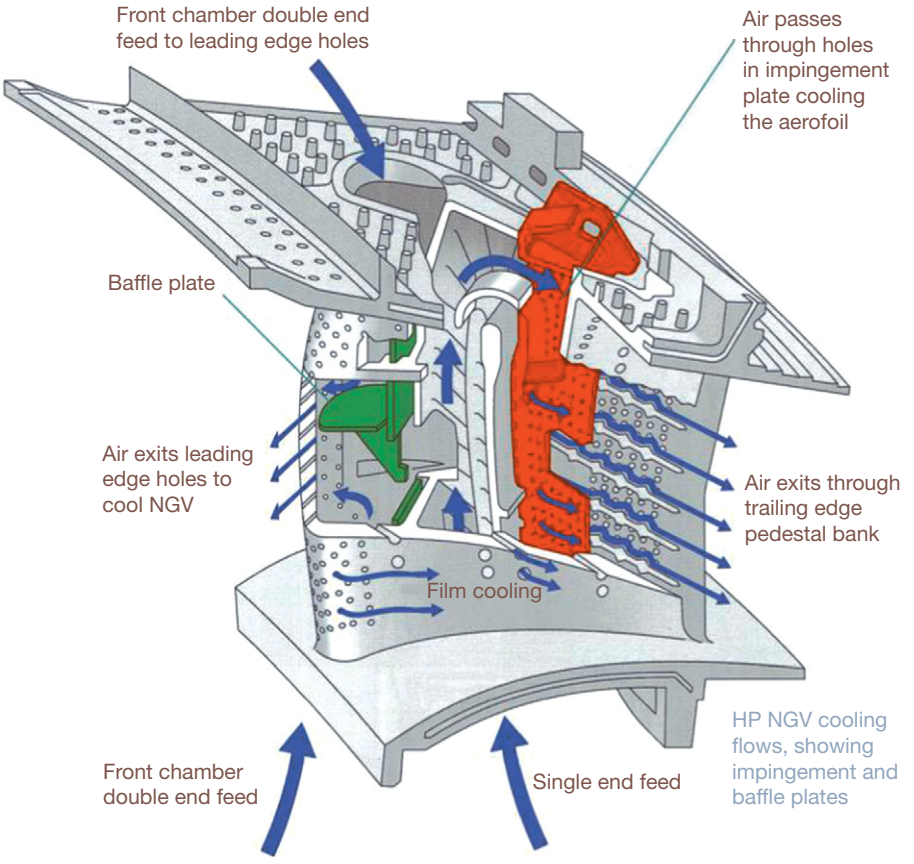

Figure 6 Example of air cooling systems in advanced gas turbine aerofoil.[1] Courtesy of Rolls Royce.

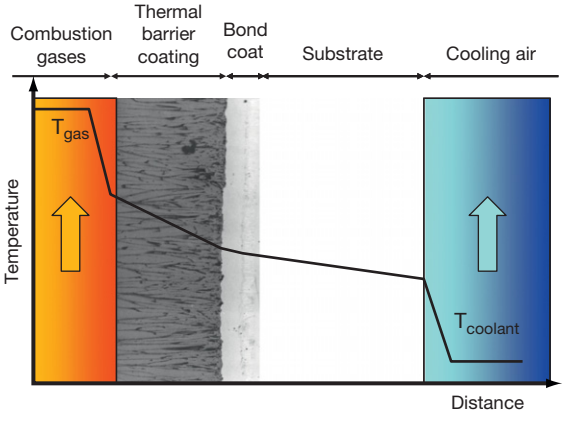

Figure 7 Principal of operation of thermal barrier coatings (TBCs).

- Chemical vapor deposition (CVD) processes applied by in-pack, above pack or gaseous routes;
- Gaseous routes enable coating of internal cooling passages in advanced aero-foil designs;
- Platinum-aluminizing;
  - Electroplate of platinum followed by CVD aluminizing process.
- Slurry coatings;
  - Silicon-aluminizing.
- Coating performance varies with base alloy compositions, which have a notable effect in terms of hot corrosion resistance, with such coatings on lower Cr-based alloys performing significantly worse than on higher Cr substrates.

1.20.4 Oxidation and Thermal Cycling

1.20.4.1 Oxide Formation and Spallation

1.20.4.1.1 Oxidation processes

Gas turbine materials will oxidize in the combustion gases produced in all gas turbine systems. The earlier superalloys were relatively rich in chromium and so formed slow growing protective Cr_2O_3 scales at their temperatures of use. However, as component

Table 1 Examples of materials used in gas turbine hot gas path components (in wt%)

	Ni	Co	Fe	Cr	Al	Ti	Mo	W	Others
CMSX-4	Bal	9.0		6.5	5	1	0.6		0.1 Hf
IN738LC	Bal	8.5		16	3.4	3.4	1.7	2.6	1.7 Ta, 0.9 Nb
GTD111	Bal	9.5		14	3	4.9	1.5	3.8	2.8 Ta
IN939	Bal	19		22.5	1.9	3.7		2.0	1.4 Ta, 1.0 Nb
IN6203	Bal	19		22	2.3	3.5		2.0	1.1 Ta, 0.8 Nb, 0.8 Hf
GTD222	Bal	14		22.5	1.2	2.3		2.0	1.0 Ta, 0.8 Nb
IN792	Bal	9.0		12.4	3.1	4.5	1.9	3.8	3.9 Ta
FSX-414	10	Bal	1	29				7.5	
MarM 247	Bal			8.3	5.5	1	0.7	10	1.5 Hf
Hastelloy X	Bal								
Haynes 230	Bal		<3	22	0.3		2	14	
RR1000	Bal	18.5		15	3	3.6	5		2 Ta, 0.5 Hf
IN718	Bal		18.5	19	0.5	0.9	3		5.1 Nb
Astroloy	Bal	15		15	4.4	3.5	5.2		
Waspalloy	Bal	13.5	<2	19.5	1.4	3	4.3		
U500	Bal	19	4	19	3	3	4		
U720Li	Bal	15		16	2.5	5	3	1.2	
Haynes 214	Bal		3	16	4.5				0.1 Zr, 0.01 Y
PM2000			Bal	20	5.5	0.5			0.5 Y as Y_2O_3
Aluchrom YHf	0.2		Bal	20	5.8				0.5 Y, 0.05 Hf, 0.05 Zr

Table 2 Examples of gas turbine coating compositions (wt%)

Overlays	Ni	Co	Cr	Al	Y	Other
Amdry 963	Bal	–	25	6	0.4	
Amdry 995	32	Bal	21	8	0.5	
Amdry 997	Bal	23	20	8.5	0.6	4 Ta
LCO22	32	Bal	21	8	0.5	
CT102	32	Bal	21	8	0.6	
CT103	Bal	22	17	12	0.6	
CT104	Bal	23	22	11	0.4	4 Hf, 0.4 Si
GT29	–	Bal.	29.0	6.0	0.3	
SV20	Bal	–	25	5.5	0.7	1 Ta, 2.7 Si
SV30	Bal.	–	25.0	5.0	0.7	0.1 Ta, 0.35 Ti
SC2231	30	Bal	28	8	0.5	0.5 Si
SC2453	Bal	10	28	12	0.6	3 Re

Diffusion	Description
Aluminized	Applied in-pack, above pack or by gas phase CVD
Chromized	Applied in-pack, above pack or by gas phase CVD
RT22 CN91 MDC150	Variations on platinum electro-plate followed by aluminizing
SermaLoy 1515	Slurry application

temperatures rose, so did the rate of Cr_2O_3 formation, and other oxidation mechanisms, such as formation of volatile oxide and oxyhydroxide species in the fast flowing combustion gases, also became signifcant.[2,15]

The development of superalloys for high metal temperatures resulted in materials with progressively less chromium and more aluminum. This resulted in alloys that formed slower growing Al_2O_3 scales at high temperatures that were not volatile in the surrounding gas streams.[2]

At temperatures higher than ~950–1000 °C, α-Al_2O_3 scales are the preferred scale to be formed. Considerable research targeted at a range of base alloys and different applications has been carried out on the growth of these scales over the year.[2,16] However, at lower metal temperatures, more complex oxides may form on the surfaces of superalloys: various transition aluminas (e.g., θ- or γ-Al_2O_3) as well as mixed $(Cr, Al)_2O_3$ oxides, spinel oxides of Cr and/or Al with base metal oxides, and oxides of other minor alloying elements that are present in these complex superalloy materials may form.

In general, the combination of metal temperature and a 'clean' oxidizing environment (i.e., a combustion gas stream with trace metal contaminants at too low a level to cause any hot corrosion) will result in the formation of slow-growing stable oxide scales for the appropriate blade and vane materials, plus any coating system, in the gas turbine hot gas path (but it should be noted that such materials will vary between gas turbine manufacturers, and with the intended use of gas turbine).

There will, therefore, be a difference between gas turbines: the higher peak temperatures of

aeroengines will encourage α-Al_2O_3 scale formation, compared to industrial machines operating close to oxide transition temperature. Another important difference in the exposure conditions will be number and severity of thermal cycles. Aeroengine temperatures are cycled much more frequently and rapidly than industrial gas turbines. As a result, the slow-growing scales may spall from the component surfaces and a new oxide will form during the next period of operation: whether this is the same oxide or not will depend on the composition of the underlying alloy/coating.

The coating of superalloys with most overlay and diffusion coatings (**Table 2**) results in a surface relatively rich in aluminum, which assists in the formation, retention, and reformation of a slow-growing Al_2O_3-based (or at least alumina rich) oxide scale. Overlay coatings traditionally include 'reactive elements' such as Y or Hf that are well known to enhance the adhesion of alumina scales (see **Chapter 1.23, High Temperature Corrosion of Chromia-forming Iron, Nickel and Cobalt-base Alloys**). Scales can develop through transient oxides (i.e., various Al_2O_3) and other oxides (e.g., NiO, spinels) and multiple oxide layer developments (e.g., undergrowths of Cr_2O_3 and α-Al_2O_3) before reaching a slow growing stable structure (e.g., **Figure 8**). This development depends on the exposure temperature and coating–base alloy composition.

Diffusion coatings have also progressively developed to assist in the growth and retention of alumina scales, in this case, using metals such as Pt and Pd. These coatings will also develop scales through the formation of transient oxides (i.e., various Al_2O_3) and other oxides (e.g., NiO) and multiple oxide layer developments (i.e., undergrowth of α-Al_2O_3) before reaching a slow growing stable structure. As for overlay coatings, this development depends on the exposure temperature and coating–base alloy composition.

At high temperatures, coatings will degrade by interdiffusion with the substrate as well as surface oxidation; this can be particularly important for aluminum which tends to diffuse inwards as well as being consumed due to oxidation. The development of diffusion barriers to reduce or prevent such inwards diffusion is an active research topic.

1.20.4.1.2 Modeling oxide growth and spallation

Oxide growth and spallation models have been developed for alumina type oxide scales by several research groups around the world, most notably: NASA,[18] Jülich–Cranfield[19,20] and Toulouse.[21] These models are essentially all empirical, but are based on the mathematical understanding of oxidation processes:

- The NASA cyclic oxidation and spallation (COSP) model is based on rate constants determined from mass change data and uses these combined with idealized parameters that describe the spallation process to predict the damage to a metal in terms of mass change or metal loss for different time periods, cycle durations, etc.
- The Toulouse p–k_p model uses a spalling proability (p) and parabolic rate constant (k_p) to predict the mass change of materials as a function of time and temperature.
- The Jülich–Cranfield model uses the concept of an aluminum reservoir to calculate the metal loss due to alumina growth and spallation. Spallation processes are assumed to commence after some critical mass gain (or oxide thickness) which is influenced by thermal cycling.

Continuous oxide growth and coating interdiffusion models are being developed by several research groups, most notably NASA,[22] DTU,[23] and Toulouse.[24,25] These use various finite difference or finite element methods, in some cases combined

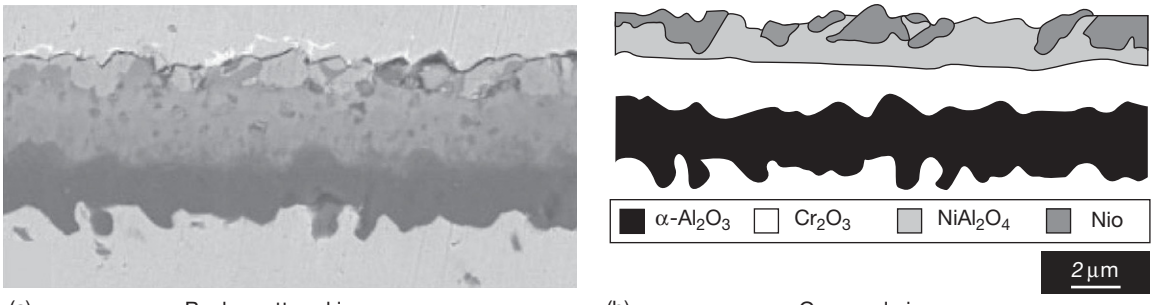

Figure 8 Scale grown on Ni–27Cr–8Al at 1353 K.[17] (a) Back-scattered image and (b) grey scale image.

with thermodynamic phase predictions, to calculate elemental profiles throughout the oxide–coating–substrate system as a function of time and temperature, again using the ideal α-Al_2O_3 scale formation.

1.20.4.2 Thermal Barrier Coating Systems

1.20.4.2.1 Damage mechanisms

Two types of TBCs are now frequently found in gas turbines. These are generally classified by their application routes: air plasma sprayed (APS) and electron beam physical vapor deposition (EB PVD) (**Figure 9**). However, currently their compositions are generally the same: ~7 wt% Y_2O_3 – balance ZrO_2. New thermal barrier ceramics are also being researched,[27] but a review of these is beyond the scope of this chapter.

Both types of TBCs are applied to gas turbine components after they have had a bond coating applied. The purpose of this bond coating is to encourage and maintain the formation of a stable α-Al_2O_3 scale at the interface between metal and ceramic, as well as to provide a transition zone between the metal and the ceramic layer. Thus bond coat materials are often classically established environmental protection coatings, for example, a platinum aluminide diffusion coating system or an MCrAlY overlay coating. However, bond coatings for APS and EB PVD TBCs require different initial characteristics to enable the coatings to be successfully applied. APS TBCs generally need to be applied to deliberately roughened bond coat surfaces to provide mechanical keying, whereas EBPVD TBCs are usually applied to smoother, polished, or media finished bond coat surfaces.

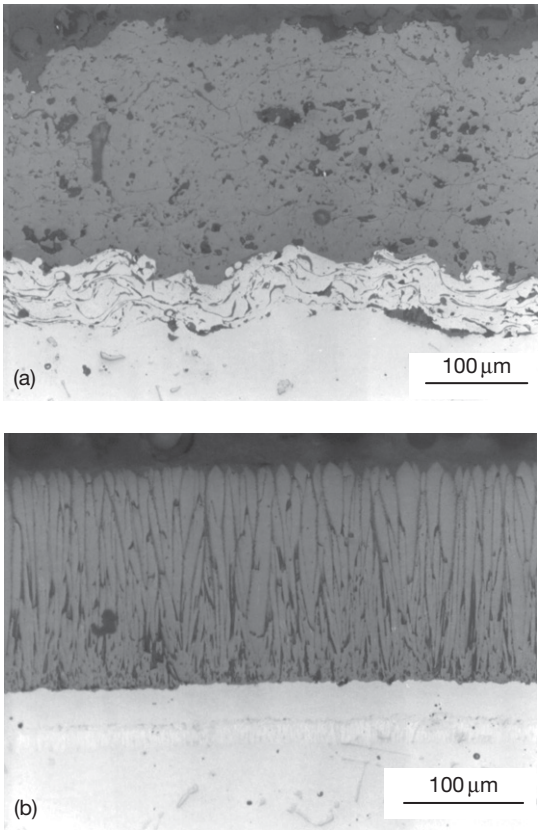

Figure 9 Two main types of TBCs.[26] (a) Air plasma sprayed thermal barrier coating (APS TBC) and (b) electron beam physical vapor deposition thermal barrier coating (EB PVD TBC).

The spallation of TBCs after exposure at high temperature is now well recognized as the life-limiting factor dictating TBC performance and has been frequently reported.[28] However, the causes of this spallation remain controversial (e.g., **Figure 10**). Features reported include[28]:

- spallation is usually observed on samples/components after the growth of ~5–10 μm of oxide scale;
- cracks grow roughly parallel to the bond coat/thermally grown oxide/TBC interfaces, before large areas of TBC spall;
- cracks may grow:
  - in TBC near TGO interface (between bondcoat peaks, or not),
  - within the TGO,
  - along bond coat/TGO interface, depending on the system;
- bondcoat/TGO/interfaces may roughen with exposure (for EBPVD TBCs on Pt–Al bond coats);
- mixed oxides $(Cr,Al)_2O_3$ or spinels (e.g., $(Ni,Co)Cr_2O_4$) may form above or below the stable alumina scales in areas close to crack growth.

Both academic and industrial research is actively continuing in this area, but has moved from characterization towards methods of finding damaged TBCs nondestructively and also developing predictive models for TBC spallation (see below). But it is worth noting that there are many significant differences between the preparation and processes used for applying bond coatings, initiating the growth of thermally grown oxide and applying the TBC layer that are used by different coating companies, all of which may interact and therefore influence susceptibility to TBC spallation.

Particular interest has been taken in finding ways of detecting the cracks in/close to TGO using nondestructive inspection methods, before the cracks have a chance to coalesce and cause TBC spallation

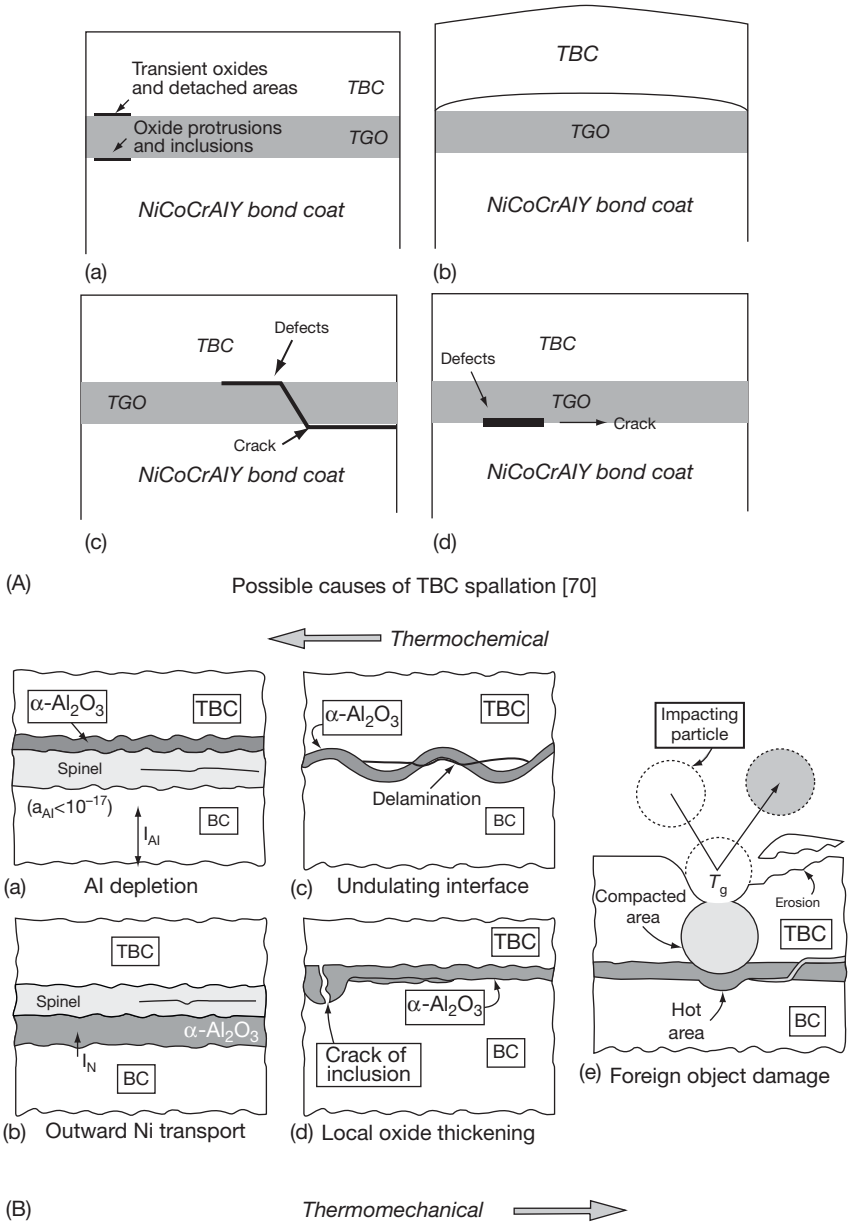

Figure 10 Schematic diagrams of alternative views of the causes of TBC spallation. (A) Possible causes of TBC spallation[29] and (B) possible causes of TBC spallation. Reproduced from Simms, N. J.; Kilgallon, P. J.; Roach, C.; Oakey, J. E. In *Microscopy of Oxidation*, Proceedings of 5th International Conference, Newcomb, S. and Tatlock, G. Eds.; Science Reviews, 2003; pp 273–280.

to occur. Promising nondestructive techniques currently include[30]:

- images produced by differential heat conduction (using lasers or other heat sources) – essentially relying on cracked regions of the coating system not allowing heat to pass through as readily as fully adherent coated regions;
- photoluminescence piezospectroscopy (PLPS) – this uses lasers to excite the Cr^{3+} contaminant ions that are always present in Al_2O_3 oxide scales in these material systems and detects the shift in the characteristic peaks produced: the greater the shift the more stressed the TGO. This technique can be used to examine a coated TBC component and to detect variations in stresses in the TGO (cracked areas

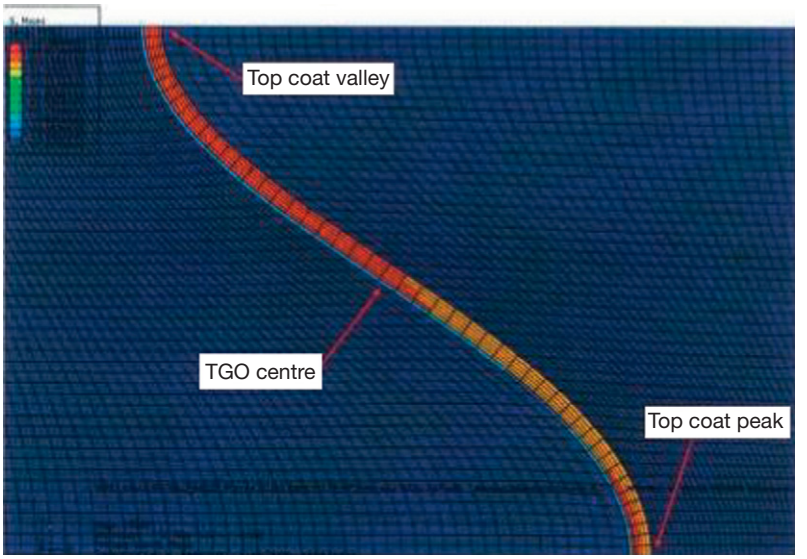

Figure 11 Finite element approach to TBC spallation modeling as a function of TGO growth. Reproduced from Hermosilla, U. PhD Thesis, Nottingham University 2008; UK EPSRC Supergen Plant Life Extension Consortium.

showing up as low stressed TGO). This technique works better on EB-PVD TBCs than APS TBCs due to the columnar microstructure of the former that allows light signals to pass through more easily.

1.20.4.2.2 Modeling TBC spallation

Several industrial and academic research groups are working on the development of models to predict spallation of TBCs.[31–37] There are essentially two distinct approaches:

- Finite element modeling of a selected area of an idealized TBC system to predict development of stresses around TGO as it grows (e.g., **Figure 11**); these models are being developed by several EU and US research groups.[32–34,36,37]
- Phenomenological approaches based on observation of the performance of many TBC-coated samples under a range of conditions to identify the most important variables and their effects as a function of exposure time and temperature (e.g., **Figure 12**); these types of models are being developed particularly by Dechema and Cranfield in Europe[31,35] and Pittsburg in USA.[29]

1.20.5 Hot Corrosion

Although oxidation of gas turbine hot gas path materials is rarely life-limiting, unless localized overheating has occurred (e.g., following TBC spallation), the hot corrosion of these materials can occur much more rapidly and can be life limiting for all components. As a result, hot corrosion of gas turbine hot gas path materials has been the subject of active research and industrial experience for more than 50 years.[2] The potential problems that may be encountered in gas turbines fired on conventional natural gas, diesel, and jet fuels have been well characterized,[2,15,38–45] and fuel standards derived (**Table 3**). In recent years, the ranges of fuels that need to be considered have widened in response to changes in availability and price. In addition, investigations have also been carried out into the potential effects on gas turbines from using fuel gases derived from solid fuels (e.g., gasification of coal and/or biomass).[47]

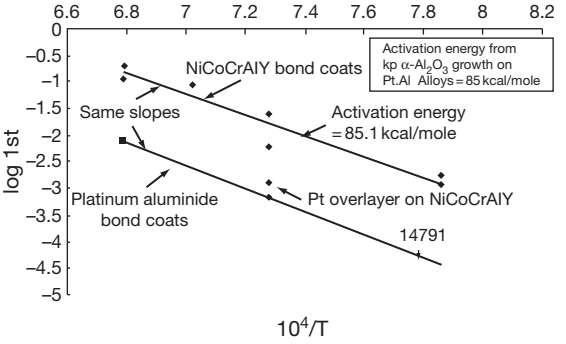

Figure 12 Observations of TBC spallation that form a basis for analytical approaches to life modeling. Reproduced from Yanar, N. M.; Kim, G.; Hamano, S.; Petit, F. S.; Meier, G. H. In *Microscopy of Oxidation*, Proceedings of 5th International Conference, Newcomb, S. and Tatlock, G., Eds.; Science Reviews, 2003; pp 249–260.

Table 3 Fuel specifications[46]

Fuel type	*True distillates*		*Ash-forming fuels*	
	Kerosene	*No.2 Distillate*	*Blended residuals and crude*	*Heavy residuals*
Sulfur (%)	0.01/0.1	0.1/0.8	0.2/3	0.5/4
Ash (as delivered) (ppm)	1/5	2/50	25/200	100/1000
Ash (inhibited) (ppm)	–	–	25/250	100/7000
Trace metal contaminants (untreated) (ppm)				
Sodium + potassium	0/0.5	0/1	1/100	1/350
Vanadium	0/0.1	0/0.1	0.1/80	5/400
Lead	0/0.5	0/1	0/1	0/25
Calcium	0/1	0/2	0/10	0/50

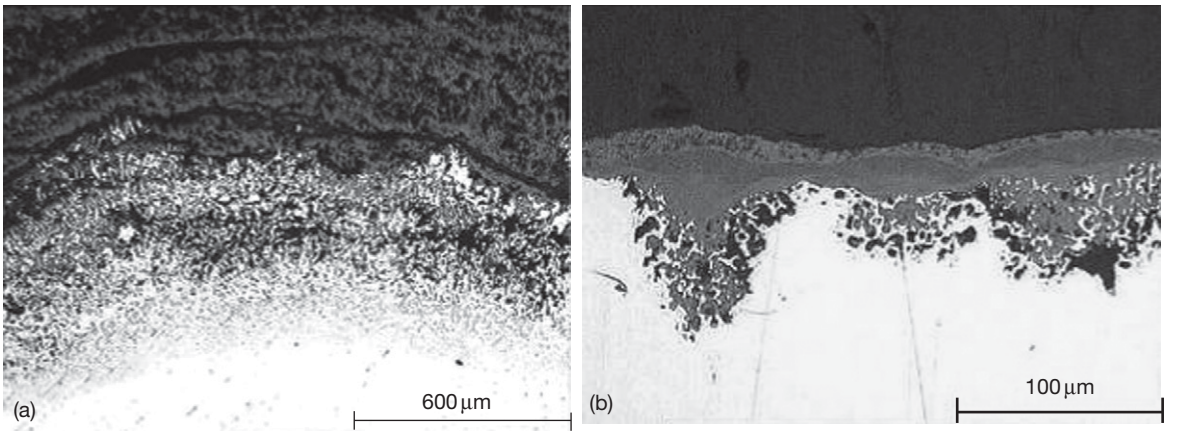

Figure 13 Typical appearance of type I and type II hot corrosion during their propagation stages.[50] (a) Type I hot corrosion and (b) type II hot corrosion.

These studies have successfully identified the causes of hot corrosion and some methods to limit the damage caused. A considerable amount of data on hot corrosion damage for a wide range of materials, under different exposure conditions, has been generated during the course of research projects and industrial usage.[2,42] This dataset has permitted, experimentally determined, safe operating conditions to be produced. However, the development of quantitative predictive models for hot corrosion damage to materials of current interest in gas turbines is an on-going activity,[48,49] with some embryonic models produced for these complex corrosion phenomena.

1.20.5.1 Hot Corrosion Mechanisms

Hot corrosion of materials in a power turbine occurs when a liquid deposit forms on the surface of a component. After a period of incubation as the deposit forms on the surface and reacts with the initially protective oxide, hot corrosion reactions move into their more rapid propagation stages. There are two widely recognized forms of hot corrosion, distinguished by their propagation modes in gas turbines (**Figure 13**)[2,15,38–45]:

- Type I hot corrosion has traditionally been observed in a temperature band between the melting point of the surface deposit and vapor deposition dew point for the deposit (above this dew point deposit is unstable and will evaporate). An example of this could be the formation of sodium sulfate deposits. This form of corrosion damage is characterized by the appearance of internal sulfide phases in a zone of selective alloy depletion beneath a fairly smooth scale–metal interface. The typical temperature ranges quoted for this type of attack are typically 750–900 °C. This form of attack has been called high temperature hot corrosion.
- Type II hot corrosion occurs at a lower range of temperatures (typically quoted as 600–750 °C). This form of attack relies on the formation of a complex mixed metal sulfate deposit: an example of this could be the formation of a mixed nickel

sulfate–sodium sulfate deposit. Such deposits are not very stable and require the presence of significant levels of SO_3 to stabilize them (hence the term 'gas phase induced acidic fluxing'). The corrosion occurs over the stability range of the liquid deposit from its melting point to its dissociation temperature. The attack is characterized by the formation of pitted or uneven surfaces with layers of corrosion products/deposits on the surface and no subsurface depletion zones or internal sulfide formations (although a layer of sulfides may be observed at the metal–scale interface). This form of attack has been called low temperature hot corrosion.

The mechanisms of hot corrosion are generally believed to be a result of the interaction of the surface oxide scales at first and then of the underlying alloys with molten surface deposits.[2,15,38,39,42] These are commonly described as fluxing mechanisms. Both acidic and basic fluxing reactions are possible depending on the deposit composition and the composition of oxide/underlying coating/alloy.

In basic fluxing, oxide ions are produced in a deposit of Na_2SO_4 by removal of oxygen and sulfur from the deposit by reaction with underlying coating/alloy. Then, the oxide scales (e.g., MO) that form can react with the oxide ions via reactions such as[2,15,38]:

$$MO + O^{2-} = MO_2^{2-}$$

In acidic fluxing, the oxide scale dissolves to donate oxide ions to the deposit melt[2,15,38]:

$$MO = M^{2+} + O^{2-}$$

Acidic conditions can be developed in a molten deposit by at least two different processes, leading to the terminology gas phase acidic fluxing and alloy-induced acidic fluxing.

As a result of these different possible hot corrosion mechanisms, the solubility of commonly formed oxides in molten deposits by acidic and basic reactions has been the subject of several studies (e.g., **Figure 14**).

In practice, the temperature ranges of type I and type II hot corrosion are affected by the composition of deposits formed. For example, the presence of potassium in a deposit can significantly lower the melting point of the deposit and lower the temperature range for type I when compared to sodium sulfate alone (**Figure 15**). Similarly, NaCl may also lower deposit melting points[51] and also assist the breakdown of any protective oxide scales.

Other elements can also affect the melting ranges of these deposits: these may be contaminants from

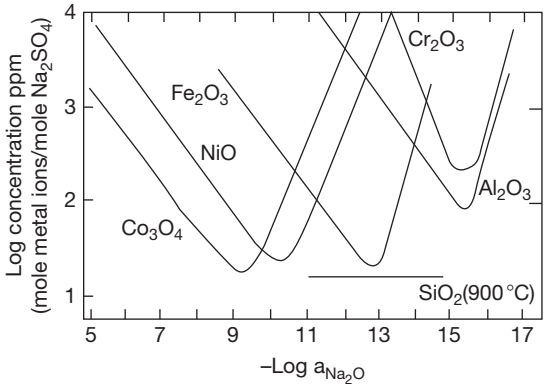

Figure 14 Oxide solubility in molten Na_2SO_4 at 927 °C. Reproduced from Sims, C. T.; Stoloff, N. S.; Hagel, W. C. Eds. *Superalloys*; Wiley: New York, USA, 1987; Vol. II.

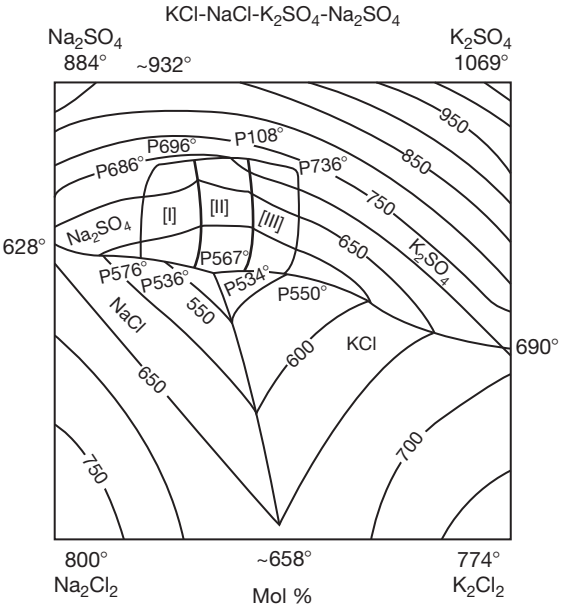

Figure 15 Na_2SO_4–K_2SO_4–NaCl–KCl phase diagram. Reproduced from *Phase Diagrams for Ceramists*; American Ceramic Society, 1964.

combustion gas stream (e.g., calcium, magnesium, lead, or chlorine) or elements from the components being corroded (e.g., molybdenum or tungsten). Some of these elements may also participate in the hot corrosion reactions between the deposit and the component materials.

Along with the distinctive propagation morphologies of types I and II hot corrosion, it is also possible for an intermediate form of attack to develop which has some of the features of both. This has been described as mixed mode attack or a transition-type

attack. It is characterized by the formation of layered corrosion products/deposit on the component surface and intermittent areas of internal sulfides/depletion zones and an uneven scale/metal interface. This form of attack has been observed at temperatures between traditional type I and type II corrosion regimes.

An alternative mode of hot corrosion attack is seen in turbines in which the combustion gas stream contains vanadium (usually a contaminant that arrives via a fuel oil). This form of hot corrosion also depends on the formation of liquid deposits on the surfaces of components, but these low-melting-point deposits do not require the presence of high levels of SO_3. In the presence of sodium-containing deposits, mixed deposits, for example, sodium vanadyl vanadate may form with melting points as low as 535 °C.[51] These sodium vanadate compounds can flux the protective oxide from component surfaces and then continue with a fluxing reaction with the metallic substrates below. It has been found that this form of hot corrosion can be suppressed by deliberately adding dopants (such as magnesium or chromium compounds) to the fuel; these are designed to react with the vanadium species as they pass through the combustion process and deposit onto component surfaces as solid deposits with high melting points that remain stable and unreactive.

1.20.5.2 Deposit Formation and Fuel Specifications

For hot corrosion to occur, a liquid or partially molten deposit must be created on the surface of components. Such deposits can be formed by a number of different mechanisms,[52,53] but all require the combusted gas streams passing through the gas turbine hot gas path to contain both trace metal species (such as alkali metals) and reactive gas species (such as SO_2/SO_3). The source of the contaminants may be either the fuel or the oxidant (usually air) or component coolant (usually air, but sometimes steam in large land based gas turbines) or a mixture of all three. For example:

- Sea salt contains a mixture of metal chlorides and lower levels of sulfates: these contaminants may enter a turbine through its air inlet, pass through the compressor and the combustor before entering the power turbine. The salts may build up as deposits on the compressor vanes/blades before shedding and passing further into the turbine as particles, or may pass through as vapor or aerosols.
- Gas turbine fuels usually contain sulfur compounds together with a number of trace metal species; in the combustor, these contaminants can join those exiting in the compressor and react as they pass through the combustor and power turbine.
- Salts entering the compressor can be diverted from the main air flow into smaller flows that are used to cool components in the power turbine; these salts do not get the chance to react with the fuel derived contaminants as they pass through the combustor, so different compositions of deposits can form from this contaminant routing.

For gas turbines that operate under steady conditions (i.e., some larger land-based gas turbines), it is possible to use knowledge of these conditions to calculate the total contaminants entering the system (whether from fuel or oxidant or coolant) giving rise to an equivalent fuel contaminant level[49,54,55]:

$$X_T = (A/F)X_A + (S/F)X_S + X_F$$

where X_T is the total contamination in fuel equivalent (ppm) by weight; A/F is the air to fuel mass flow ratio; S/F is the steam (water) to fuel mass flow ratio; X_A is the contaminant concentration in inlet air (ppm) by weight; X_S is the contaminant concentration in injected steam or water (ppm) by weight; X_F is the contaminant concentration in fuel (ppm) by weight.

This approach provides a method of assessing potential corrosiveness of gas streams within the gas turbine and is one route to setting specifications for safe operation of such turbines.

It is also possible to consider how the various contaminant species that enter the power turbine can deposit out onto components. There are several well-known deposition processes (and associated models[52,53,56–62]) that can occur within a gas turbine hot gas path (illustrated schematically in **Figure 16** for an aerofoil):

- Direct inertial impact ion; larger particles ($>\sim$5 μm) from the gas stream impact on components instead of following the gas flows around them; depending on their properties and the surface condition of the components, these particles may stick to the component surface, bounce off (or partially stick).
- Eddy diffusion; smaller particles may become entrained in the turbulent eddies that can form in certain locations in the gas paths (e.g., towards the trailing edge of aerofoil suction surfaces, or around blade platforms, disc edges, seals, etc.); these particles can then impact on component surfaces, and again depending on their properties and the surface

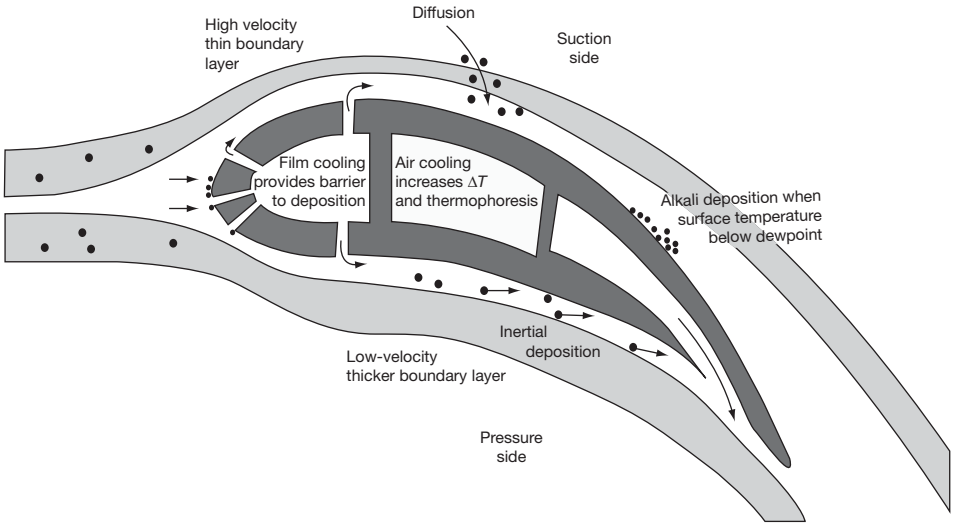

Figure 16 Potential deposition around a gas turbine aerofoil surface. Reproduced from Grimethorpe Topping Cycle Project, UK DTI Clean Coal Programme, Summary Report 1995.

condition of the components, these particles may stick to the component surface, bounce off (or partially stick). It is quite likely that the composition of the particles will vary with size, so this may cause the behavior of larger and smaller particles to differ, as well as the differences in impact conditions.

- Vapor deposition; this transfers trace elements from the bulk gas stream to the surface of components; however, there are several variations of this type of process which include:
  - condensation of a vapor of a particular species from a hot gas stream onto a cooler metal surface (e.g., gaseous sodium sulfate condensing out as solid or liquid sodium sulfate);
  - condensation of a vapor of a particular species from a hot gas stream into a solid or liquid of another species on a cooler surface (e.g., gaseous sodium hydroxide or sodium chloride condensing out as solid or liquid sodium sulfate); reaction with SO_2/SO_3 could happen during the condensation process or on the component surface after condensation;
  - these can be complex processes that depend on the activities and relative stabilities of all the contaminants involved in the gas stream and at the surface of the components, as well as the temperature differences between the bulk gas stream and component surface, system pressure, boundary layer thickness, and other flow related parameters.

Other deposition processes such as Brownian diffusion or thermophoresis (i.e., diffusion along a temperature gradient) are well known but are believed to be less probable in the environments present within a gas turbine.

It is clear from the brief descriptions of the different types of deposition processes above that the deposition mechanisms that will operate will depend on a large number of potential variables that include ones resulting from (a) the composition of the combusted gas flow and (b) gas turbine component operations/geometry.

Combusted gas stream factors (local to area of deposit formation):

- trace metal contaminant levels,
- SO_2/SO_3 levels,
- particle sizes,
- particle composition.

Gas turbine component operations and geometrical factors (local to area of deposit formation):

- bulk gas temperatures,
- component temperatures,
- difference between bulk gas and metal temperatures,
- gas pressure,
- component shape and size, affecting:
  - gas flows around component,
  - development of eddy flows,
  - development and thickness surface boundary layers.

The source of the contaminant can alter the form in which it enters the gas turbine, passes through it and deposits onto components in the power turbine.

For example, sodium chloride can enter the system from the fuel or combustion air, pass through the combustor as a vapor or as particles (or both), and then deposit via direct inertial impaction, eddy impaction, and/or vapor condensation on different areas of an aerofoil.

For a given gas turbine design, only factors related to the combusted gas stream composition may be open to an operator to control (and so minimize deposition and hot corrosion). Gas turbine manufacturers, some gas turbine operators, and standards bodies have all considered the potential damage that can be caused to gas turbines by fuel contaminants. As a result, a number of fuel specifications have been produced that include limitations on elements related to hot corrosion (the fuel standards also include limitations on many other fuel properties for other purposes). Examples of such fuel specifications are given in **Table 3**. All these specifications have the aim of reducing the damage caused by contaminants to levels acceptable to gas turbine manufacturers or users.

Along with controlling the contaminants entering the gas turbine hot gas path via the fuel, for many gas turbines (land and marine based systems), it is also possible to limit the contaminants entering the system via the combustion air (using air filters to remove particles and aerosols). For aeroengines, the contaminants entering the system via the air intakes depend on the types of flight path, its height, and location in the world: for example, for civil jet engines, island hopping with short flights at low altitudes over the sea versus long haul flights with long periods at high altitudes.[63]

In addition, it should also be recognized that contaminants can be accidentally put onto gas turbine components via cleaning fluids, greases, and other lubricants used during component manufacturing, inspection and/or assembly. However, every effort should obviously be made to avoid this deposit formation route wherever possible.

Fuel specifications have been derived mainly from experience with traditional gas turbine fuels such as diesels, jet fuels, heavy fuel oils and natural gas. However, in recent years, economic and environmental/regulatory pressures have encouraged the development of power systems that use a wider range of fuels, as well as new types of power systems[3,14,60,64–66]:

- Integrated gasification combined cycles (IGCC) in which solid fuels such as coal, biomass, and waste products are gasified, and then the fuel gases (or syngases) produced cleaned up and passed into a gas turbine for combustion and power generation;
- Pressurized combustion systems (such as pressurized fluidized bed combustion) in which solid fuels are burnt, and then the hot pressurized gas stream produced cleaned and passed through the power turbine part of the gas turbine (in some cases, the compression part could be used to produce the pressurized air stream needed for the combustion process);
- Use of natural gases with increasingly high H_2S levels (beyond the range of previously acceptable gas compositions);
- Natural gases or syngases are processed to reduce their carbon contents and enhance their hydrogen contents;
- Bio-oil fuels;
- Gas turbines fired using oxygen and any of the other potential fuels to produce a combusted gas stream of mostly CO_2 and steam, from which the steam can be condensed to produce a CO_2 rich gas stream for recycling into the compressor or for storage (after further cleanup).

All these systems can be expected to have similar contaminants (e.g., S, Cl, alkali metals, Ca, Pb, V) to those traditionally found in the various oil or natural gas systems fired on air. However, both the absolute and relative levels of these contaminants will be different in each of the different systems, as a result of different fuels being used in them. In addition, other trace metals (e.g., Cd, Sb, Zn), which may give rise to vapor phase species when different fuels are gasified, may affect the deposition and hot corrosion processes in the gas turbines that use the fuel gases produced.[49,50,60,64] Coal, biomass, and waste products have significantly different compositions to each other, and these variations persist to differing degrees for each element/fuel utilization process by the time the fuel gas streams reach the gas turbine.

Thus, new gas turbine fuel specifications will be needed for new types of fuels that are being considered. These are currently under active consideration and in some cases research.[14,49,50,60,62] However, in considering the use of gas turbines for new applications, it is necessary to consider both the composition of the combusted gas stream expected in the power turbine and detailed design of gas turbine as both should be optimized for the new gas turbine applications, to minimize deposition and subsequent hot corrosion (as well as allowing for new bulk gas compositions in some of the novel power generating cycles).

1.20.5.3 Damage Locations

The potential locations for hot corrosion along the gas turbine hot gas path are controlled by deposition processes (outlined in Section 1.20.4) and the heat transfer processes between bulk gas stream and various components that enclose it. Heat transfer processes (via radiation, convection, and conduction mechanisms) cause unique distributions of metal temperatures to be set up on each type of component; for example, the vanes and blades at each stage of any turbine will have different temperature distributions. The air-cooled vanes/blades in the higher pressure stages may have wider temperature distributions than the 'uncooled' vanes/blades in lower pressure stages. However, the temperature profiles on cooled vanes/blades depend on the cooling methods used (e.g., convection cooling, film cooling), details of the blade designs, and whether TBCs are used. Thus, the surface temperature distributions on all components along a gas turbine hot gas path are unique (and are often commercially sensitive). Figure 17 gives examples of predicted temperature distributions on a cooled and an uncooled turbine aerofoil surface.

It is quite possible for cooled blades or vanes in the higher pressure stages to have the combination of surface temperature and deposition conditions to cause oxidation as well as type I and type II hot corrosion in different areas of components. It should be noted that as operating temperatures are slowly being raised, potential areas for damage are not restricted to aerofoil surfaces traditionally considered. In addition, platforms, shrouds, roots, and shanks may also develop hot corrosion damage as may internal cooling air passages. In future advanced gas turbines, one may expect that even outer parts of discs and seals may also suffer from oxidation or corrosion damage as the gas temperatures and component operating temperatures are raised further.

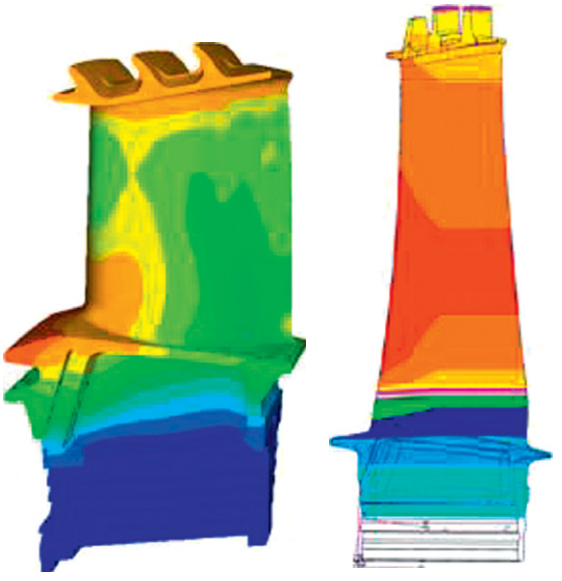

(a) Cooled aero-foil (b) Uncooled aero-foil

Figure 17 Examples of temperature distributions on (a) cooled and (b) uncooled gas turbine aerofoil surfaces. Courtesy of Siemens Industrial Turbo-Machinery Ltd.

1.20.5.4 Rates of Hot Corrosion Attack and Modeling Hot Corrosion Processes

The rates of hot corrosion attack on a component depend on the alloy and coating used as well as on exposure conditions (including local environment). As a result of the potential for hot corrosion to be a life-limiting failure mechanism for some hot gas path components within gas turbines, there have been many studies of the mechanisms of hot corrosion damage in gas turbines over the years.[2,15,38–45] Failed or damaged components from operating gas turbines have confirmed that the various potential hot corrosion mechanisms are all possible in practice and have enabled these potential problems to be well characterized. Thus, operating experience and research studies have identified the main factors that will influence the rates of hot corrosion; in no particular order, these are[2,15,38–45]:

- metal temperature,
- gas temperature,
- gas pressure,
- rate of deposit formation (or deposition flux),
- deposit composition,
- gas composition,
- component geometry,
- alloy composition,
- coating composition,
- exposure time (hot corrosion damage goes through an incubation stage before reaching the characteristic propagation stage).

Some of these factors relate more to deposition processes than hot corrosion processes, but are necessary to set up conditions needed for hot corrosion to proceed.

Unfortunately, each type of component in every gas turbine operating with different fuels provides a different combination of exposure conditions. Thus carrying out systematic studies on all the different

potential variables is not a viable option. However, information is available from:

- manufacturers and operators of fleets of gas turbines, that use fuels from different sources and turbines sited or operated in different locations;
- rainbow trials of components in operating gas turbines;
- burner rigs:
  - high velocity,
  - low velocity,
- laboratory tests:
  - deposit recoat methods,
  - dean rig,
  - buried in ash methods.

Moving down the above list, control over some of the exposure variables generally increases and their cost decreases, but their relevance to gas turbine service also decreases unless care is taken to match exposure conditions to particular in-service conditions. In addition it is necessary to ensure that materials performance data is produced in a form that is useful for comparison with component performance determined from use in real environments (i.e., metal loss data rather than weight change data).

Figure 18 illustrates hot corrosion damage found for two example gas turbine materials in burner rig studies carried out to compare the performance of base alloys and coatings under well-characterized operating conditions.

Such studies have confirmed that base alloys containing higher chromium (e.g., IN939, IN6203DS, IN738LC, and FSX-414) tend to perform well under hot corrosion conditions. Such materials are still used for components in many turbines. However, gas turbines that use high component operating temperatures have moved to using single crystal superalloys for blades and vanes in the higher pressure stages. These lower chromium materials (e.g., CMSX-4) do not have good hot corrosion resistance, so they require coating to provide them with the required surface protection.[14,49,50]

Figure 19 gives a qualitative indication of the relative performance of different coating types (dating from the late 1980s).[69,70] The introduction of single crystal materials with poor hot corrosion performance and the differences between type I and type II hot corrosion mechanisms, that are now known, have complicated this picture.

Quantitative data on hot corrosion of gas turbine substrate materials and coatings under well-characterized conditions are not frequently reported due to the difficulties of carrying out such experimental programs and the commercial sensitivities of the results if they are targeted at particular operating conditions or materials systems.[14]

However, over the last 15 years, a series of experimental programs have been carried out at Cranfield University with the aim of generating systematic data sets of the performance of generic gas turbine materials (e.g., IN738LC and CMSX-4) under ranges of

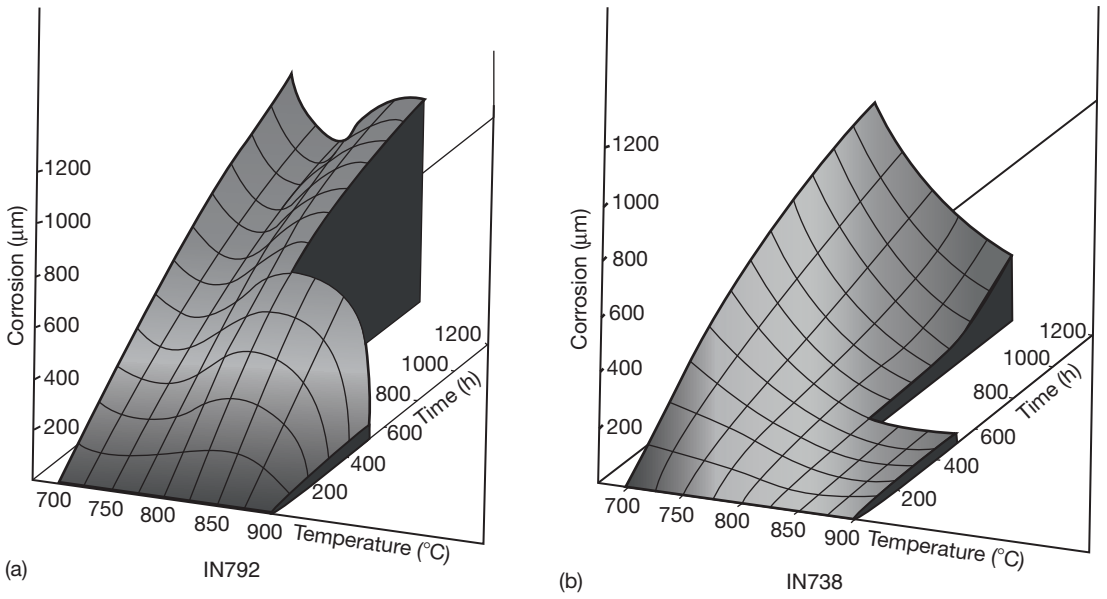

Figure 18 Examples of hot corrosion performance of two example materials in burner rig tests as a function of metal temperature and exposure time.[67] (a) IN792 and (b) IN738.

exposure conditions that reflect hot corrosion conditions in industrial and aeroengines that have been accelerated to differing degrees. These datasets are in the form of metal losses determined at a number of locations to give a cumulative probability distribution for the damage observed under specific exposure conditions. The methods being used for this work have been included in EU guidelines for hot corrosion testing that now form parts of draft ISO standards. The datasets generated illustrate some of the features of hot corrosion damage in gas turbine environments (**Figures 20** and **21**).

Figure 20 illustrates three different regimes for hot corrosion damage[11,47,48,50]:

- At low deposition fluxes; accelerated oxidation processes are observed and the hot corrosion is still in an incubation phase after this exposure time (500 h);

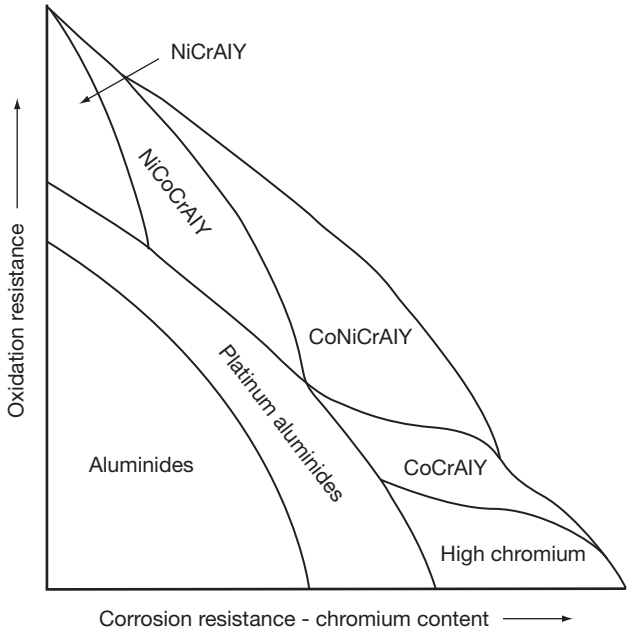

Figure 19 Qualitative indication of the relative performance of different coating types.[27,68–70]

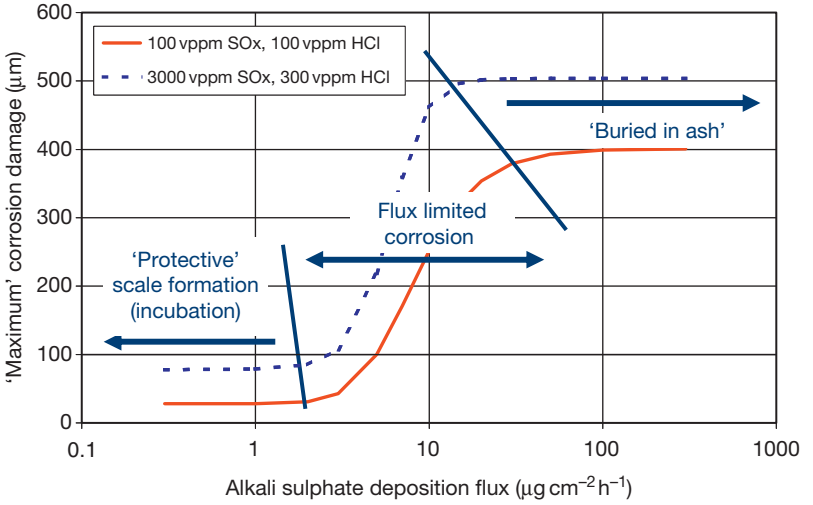

Figure 20 Dependency of type II hot corrosion damage as a function of deposition flux for IN738LC. Reproduced from Simms, N. J.; Nicholls, J. R.; Oakey, J. E. In *Lifetime Modelling of High Temperature Corrosion Processes*; Schütze, M. *et al*. Eds.; Maney, 2001; pp 379–397, EFC No. 34.

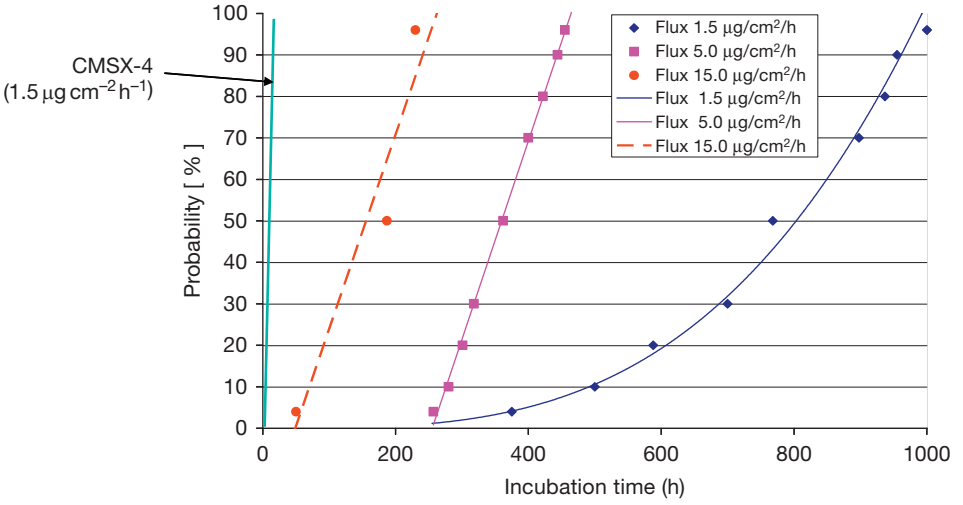

Figure 21 Dependence of type II hot corrosion incubation times on deposition flux for CMSX-4 and IN738LC. Reproduced from Nicholls, J. R.; Simms, N. J.; Encinas-Oropesa, A. In *Materials Issues Governing the Performance of Advanced 21st Century Energy Systems*; Levi, T. *et al*. Eds.; Science Reviews, 2008; pp 35–48.

- At intermediate deposition fluxes; corrosion rates are proportional to deposition fluxes;
- At high deposition fluxes; corrosion rates are not sensitive to deposition flux as it is no longer the rate limiting process in hot corrosion reactions (this is equivalent to previous and older 'buried in ash' test methods).

Figure 21 illustrates the much shorter incubation times found for the single crystal material CMSX-4 when compared to that of the older alloy IN738LC.[48] In addition, the effect of increasing deposition flux on the reduction of incubation times for the IN738LC is shown.

In such laboratory tests, the exposure conditions have been adjusted to accelerate the hot corrosion damage relative to that expected in operating gas turbines. However, by determining the sensitivity of the damage to changes in exposure conditions, it is possible to determine the expected degree of acceleration linked to specific operating conditions and then compare the data generated to that observed in practice under service conditions.

The overall data set being generated by this work is being used to produce empirical-mechanistic based models of hot corrosion damage to assist with the assessment and prediction of component lives within the hot gas paths of gas turbines.

1.20.6 Current/Future Issues

The development of gas turbine technologies for many different potential applications is a continuing process. In terms of hot corrosion, there are several issues that are believed to be of increasing interest in the near future[3,14,60,64–66]:

- Corrosion of internal blade cooling passages (from contaminants in the cooling air);
- Deposit-induced corrosion damage below blade platforms/on disc rims (due to increasing component temperatures);
- Much higher SO_x levels than traditionally considered (from dirtier/cheaper fuels) modifying type I and type II hot corrosion reactions;
- Gasifier fuel gas derived deposits with calcium, magnesia, alumina, silica, and iron compounds;
- Effects of novel environments (e.g., high steam levels from H_2 firing, or high CO_2/steam mixtures from oxy-fired systems) combined with traditional gas turbine degradation issues;
- Interaction between mechanical properties (e.g., fatigue) and hot corrosion;
- Development of single crystal alloys with compositions that produce higher hot corrosion resistance.

1.20.7 Summary

Gas turbines are currently used in a wide variety of applications: from jet engines to large-scale power generation. Each of these applications presents its own particular set of challenges for the use of specific gas turbine designs. However, many of these systems experience damage related to oxidation and hot

corrosion in the hot gas paths of gas turbines. These various forms of damage are related to a combination of operating conditions of the particular gas turbine and its components together with contaminants entering hot gas paths via air or fuel streams. The various forms of oxidation and hot corrosion that are expected under such exposure conditions are well known and are characterized with qualitative description of the potential mechanisms developed mostly during the 1970s. However, quantitative data on the various damaging reactions are less readily available, and models to enable the prediction of such damage are subjects of current research activity. The use of new materials designed for strength rather than corrosion resistance is proving to be problematic for some gas turbine applications. The on-going wish to increase gas turbine efficiencies and at the same time widening the range of potential fuels and including new types of power generation system, to meet environmental and regulatory wishes, is presenting a new series of challenges in terms of the oxidation and hot corrosion performance of components in various gas turbine hot gas paths.

References

1. Rolls Royce: The jet engine. Rolls Royce, 2005.
2. Sims, C. T.; Stoloff, N. S.; Hagel, W. C. Eds. *Superalloys;* Wiley: New York, USA, 1987; Vol. II.
3. Hannis, J. M. In *Power Generation in an Era of Climate Change*; Proceedings of the 7th International Charles Parsons Turbine Conference; Strang, A. *et al.* Eds.; IOM Communications, 2007; pp 37–49.
4. Data sheet for SGT5-8000H; Siemens AG, 2007.
5. Pavri, R.; Moore, G. D. *General Electric Reference Document, GER-4211*, 2001.
6. De Backer, W.; Bopp, C. In Proceedings of ASME TURBOEXPO 2000, Munich, Germany 2000; Paper 2000-GT-0307.
7. Ingistov, S. Proceedings of ASME TURBOEXPO 2000, Munich, Germany, 2000; Paper 2000-GT-305.
8. Horlock, J. H. Proceedings of ASME TURBOEXPO 2001, New Orleans, Louisiana, 2001; Paper 2001-GT-0343.
9. Bhargava, R.; Meher-Homji, C. B. In Proceedings of ASME TURBOEXPO 2001, Amsterdam, The Netherlands 2002; Paper 2002–30560.
10. Bradshaw, A.; Simms, N. J.; Nicholls, J. R. *Fuel* **2008**, *87*, 3529–3536.
11. Simms, N. J.; Nicholls, J. R.; Oakey, J. E. In *Lifetime Modelling of High Temperature Corrosion Processes*; Schütze, M. *et al.* Eds.; Maney, 2001; pp 379–397, EFC No. 34.
12. ADSEALS – Investigation in advanced high temperature seals, European Union FP5 project, G4RD-CT-2000-00185, 2004
13. Rickerby, D. S.; Hicks, M. A. In *Power Generation in an Era of Climate Change*, Proceedings of the 7th International Charles Parsons Turbine Conference; Strang, A. *et al.* Eds.; IOM Communications, 2007; pp 229–240.
14. Simms, N. J.; Bale, D. W.; Baxter, D.; Oakey, J. E. In *Materials for Advanced Power Engineering 2002*, Lecomte-Beckers, J. *et al.* Eds.; Jülich, 2002; p 73, 675–690.
15. Birks, N.; Meier, G. H.; Petit, F. S. *Introduction to the High Temperature Oxidation of Metals*; Cambridge University Press: Cambridge, 2006.
16. Schütze, M. *et al.* Eds. *Lifetime Modelling of High Temperature Corrosion Processes*; Maney, 2001, EFC No. 34.
17. Nijdam, T. J.; van der Pers, N. M.; Sloof, W. G. In *Novel Approaches to Improving High Temperature Corrosion Resistance*; Schütze, M. and Quadakkers, W. J., Eds.; Woodhead, 2008; pp 582–598, EFC No. 47.
18. Smialek, J. L.; Nesbitt, J. A.; Barrett, C. A.; Lowell, C. E. In *Cyclic Oxidation of High Temperature Materials*; Schütze, M. *et al.* Eds.; IOM Communicvations, 1999, Chapter 9, EFC No. 27.
19. Nicholls, J. R.; Newton, R.; Bennett, M. J.; Evans, H. E.; Al-Badairy, H.; Tatlock, G. J.; Naumenko, D.; Quadakkers, W. J.; Strehl, G.; Borchardt, G. In *Lifetime Modelling of High Temperature Corrosion Processes*; Schütze, M. *et al.* Eds.; Maney, 2001; pp 83–106, EFC No. 34.
20. Nicholls, J. R. In *Life Assessment of Hot Section Gas Turbine Components*; Townsend, R. *et al.* Eds.; IOM Communications, 2000; pp 135–154.
21. Poquillon, D.; Monceau, D. *Oxid. Met.* **2003**, *59*, 409.
22. Nesbitt, J. A. In *Lifetime Modelling of High Temperature Corrosion Processes*; Schütze, M. *et al.* Eds.; Maney, 2001; pp 359–378, EFC No. 34.
23. Dahl, K. V.; Hald, J. In *Materials for Advanced Power Engineering 2006*; Lecomte-Beckers, J. *et al.* Eds.; Jülich, 2006; pp 675–690.
24. Bertrand, N.; Desgranges, C.; Nastar, M.; Girardin, G; Poquillon, D.; Monceau, D. *Mater. Sci. Forum* **2008**, *595–598*, 463–472.
25. Bacos, M. P.; Josso, P.; Vialas, N.; Poquillon, D.; Pieraggi, B.; Monceau, D.; Nicholls, J. R.; Simms, N.; Encinas-Oropesa, A.; Ericsson, T.; *et al. Appl. Therm. Eng.* **2004**, *24*, 1745–1753.
26. Simms, N. J.; Kilgallon, P. J.; Roach, C.; Oakey, J. E. In *Microscopy of Oxidation*, Proceedings of 5th International Conference, Newcomb, S. and Tatlock, G. Eds.; Science Reviews, 2003; pp 273–280.
27. Nicholls, J. R. *Mater. Res. Soc. Bull.* **2003**, *28*(9), 659–670.
28. Newcomb, S. and Tatlock, G. Eds.; *Microscopy of Oxidation*; Proceedings of 5th International Conference Science Reviews, 2003.
29. Yanar, N. M.; Kim, G.; Hamano, S.; Petit, F. S.; Meier, G. H. In *Microscopy of Oxidation*, Proceedings of 5th International Conference, Newcomb, S. and Tatlock, G., Eds.; Science Reviews, 2003; pp 249–260.
30. Osgerby, S.; Rinaldi, C.; De Maria, L. In *Materials for Advanced Power Engineering 2006*; Lecomte-Beckers, J. *et al.* Eds.; Jülich, 2006; pp 217–232.
31. Renusch, D.; Schütze, M. *Mater. Sci. Forum* **2008**, *595–598*, 151–158.
32. Busso, E. P.; Lin, J.; Sakurai, S.; Nakayama, M. *Acta Mater.* **2001**, *49*, 1515.
33. Busso, E. P.; Evans, H. E.; Wright, L.; McCartney, L. N.; Nunn, J. E.; Osgerby, S. *Mater. Corros.* **2008**, *59*(7), 556–565.
34. Hermosilla, U. PhD Thesis, Nottingham University 2008; UK EPSRC Supergen Plant Life Extension Consortium.
35. Nicholls, J. R. *DARP: Advanced Aero-engine Materials (ADAM) – Next Generation Single Crystal and Lifing Methodologies*; GR/S26149/01, Final Report, EPSRC, 2007.
36. Padture, N. P.; Gell, M.; Jordan, E. H. *Science* **2002**, *296*, 280–284.

37. He, M. Y.; Hutchinson, J. W.; Evans, A. G. *Mater. Sci. Eng. A* **2003**, *345*, 172–178.
38. Kofstad, P. *High Temperature Corrosion;* Springer, 1988.
39. Giggins, C. S.; Pettit, F. S. Hot Corrosion of Metals and Alloys – A unified Theory, PWA Report No. FR-11545, 1979.
40. *Corrosion*, 9th ed.; ASM International: Ohio, USA, 1987; Vol. 13, ISBN 0-87170-007-7.
41. Stringer, J.; Wright, I. G. *Oxidation Metals* **1995**; *44*(1/2), 265–308.
42. Special Issue on Hot-salt corrosion standards, test procedures and performance, *High Temp. Technol.* **1989**, *7*(4).
43. Rapp, R. A. *Corros. Sci.* **2002**, *44*, 209–221.
44. Rapp, R. A.; Goto, K. S. In *Symposium on Fused Salts*; Braunstein, J., Selman, J. R., Eds.; The Electrochemical Society, 1979; p 159.
45. Shores, D. A. In *High Temperature Corrosion*; Rapp, R. A., Ed.; NACE, 1983; p 493.
46. Foster, A. D.; von Doering, H. E.; Hilt, M. B. *Fuels Flexibility in Heavy Duty Gas Turbines*; GE: Schenectady, NY, 1983; GER3428a.
47. Simms, N. J.; Nicholls, J. R.; Oakey, J. E. *Mater. Sci. Forum* **2001**, *369–372*, 833–840.
48. Nicholls, J. R.; Simms, N. J.; Encinas-Oropesa, A. In *Materials Issues Governing the Performance of Advanced 21st Century Energy Systems*; Levi, T. *et al.* Eds.; Science Reviews, 2008; pp 35–48.
49. Bordenet, B.; Bossman, H. P. *Mater. Sci. Forum* **2004**, *461–464*, 907–916.
50. Simms, N. J.; Encinas-Oropesa, A.; Nicholls, J. R. *Mater. Sci. Forum* **2004**, *461–464*, 941–948.
51. *Phase Diagrams for Ceramists*; American Ceramic Society, 1964.
52. Hamed, A.; Tabakoff, W.; Wenglarz, R. *J. Propul. Power* **2006**, *22*(2), 350–360.
53. Young, J. B.; Wu, Z. Particulate and vapour deposition in gas turbines fired on coal-derived gases, Final report DTI Cleaner Coal R&D Programme. Project 142, 2004.
54. Foster, A. D.; *et al.* Fuels flexibility in heavy-duty gas turbines, General Electric Reference Document, GER-3428a; GE: Schenectady, NY, 1983.
55. Wolf, J.; Werning, H. J. Proceedings of VGB Conference on 'Corrosion and Corrosion Protection in Power Plant Technology 1995 (VGB, 1995), paper 27.
56. Fackrell, J. E.; Tabberer, R. J.; Young, J. B.; Fantom, I. R. ASME International Gas Turbine & Aeroengine Congress, The Hague, 1994; Paper 94-GT-177.
57. Fackrell, J. E.; Tabberer, R. J.; Young, J. B. In *The Impact of Ash Deposition in Coal Fired Plants*; Williamson, J. *et al.* Eds.; Taylor and Francis, 1994; pp 123–134.
58. Hepworth, J. K.; Fackrell, J. E.; Pinder, L. W.; Wilson, J. D. In *Life Assessment of Hot Section Gas Turbine Components*, Townsend, R. *et al.* Eds.; IOM Communications, 2000; pp 281–292.
59. Simms, N. J.; Oakey, J. E.; Stephenson, D. J.; Smith, P. J.; Nicholls, J. R. In Proceedings 8th International Conference on Erosion by Liquid and Solid Impact; *Wear* **1995**; *186–187*(Part 1), 247–255.
60. DeCorso, M.; Newby, R.; Anson, D.; Wenglarz, R.; Wright, I. Coal/biomass fuels and the gas turbine: Utilization of solid fuels and their derivatives; ASME, Paper 96-AT-76, 1996.
61. Fackrell, J. E.; Tabberer, R. J.; Young, J. B.; Wu, Z. Gas turbines fired on coal-derived gases – Modelling of particulate and vapour deposition, UK DTI Report No. COAL R280, DTI/Pub URN 05/661, March 2005.
62. Grimethorpe Topping Cycle Project, UK DTI Clean Coal Programme, Summary Report 1995.
63. Leggett, A. J.; Simms, N. J.; Rickerby, D. S. In *Power Generation in an Era of Climate Change*, Proceedings of the 7th International Charles Parsons Turbine Conference; Strang, A. *et al.* Eds.; IOM Communications, 2007; pp 241–251.
64. Wenglarz, R.; Oakey, J. E. In *Materials for Advanced Power Engineering 2006*, Lecomte-Beckers, J. *et al.* Eds.; Jülich, 2006; pp 233–244.
65. Ruth, L. A. In *Life Cycle Issues in Advanced Energy Systems*, Norton, J. F. *et al.* Eds.; Science Reviews, 2003; pp 7–14.
66. Paisley, M. A.; Welch, M. J. In ASME Turbo Expo 2003; ASME, 2003; GT2003-38294.
67. High Temperature Corrosion of Aerospace Alloys, AGARD-AG-200, 1975.
68. *Coatings for High Temperature Structural Materials*, NMAB report of the NRC; National Academic Press: Washington DC, 1996.
69. Mom, J. A. NLR Report MP 81003U, Amsterdam, 1981.
70. Novak, R. C. Coating development and use: Case studies. *Presentation to the Committee on Coating for High-Temperature Structural Materials*; National Materials Adisory Board; National Research Council: Irvine; California, April 18–19, 1944. Cited in references [27] and [68].

1.21 Design of High Temperature Alloys

P. F. Tortorelli and M. P. Brady
Oak Ridge National Laboratory, Oak Ridge, TN 37831-6115, USA

Abbreviations

AA Accelerated attack
AAS Accelerated attack with spallation
POS Protective oxide scale

Symbols

d Specimen thickness
$\boldsymbol{D_{AB}}$ The alloy interdiffusion coefficient in binary alloy A–B where B is the metal that forms the protective oxide B_xO_y
$\boldsymbol{D_O}$ Diffusion coefficient of oxygen in alloy A–B
k Rate constant where $(kt)^n$ is the rate equation for B consumption by oxidation
M Mass conversion factor for metal and oxide
N_B^* Concentration of B needed to form protective B_xO_y
$\boldsymbol{N_{B,c}}$ Critical concentration below which a protective B_xO_y cannot be maintained
$\boldsymbol{N_B}$ Concentration of B in the bulk alloy A–B
$\boldsymbol{N_{O,s}}$ Solubility of oxygen in alloy A–B
t Time of exposure
$\boldsymbol{t_b}$ Time to breakaway
x Depth of internal oxidation
$\boldsymbol{\rho}$ Alloy density

1.21.1 Introduction

The design of alloys for corrosion resistance at high temperatures involves specification and manipulation of alloy composition and microstructures that assure preferential formation and long-term stability of a protective surface layer. Such surface layer formation involves a complex interplay of reactive and diffusive processes, mediated by both material and environmental factors. There are well known principles to overcome this design problem, particularly for the simpler alloy systems that exhibit behaviors that are a close match to the assumptions made to produce analytical expressions of reaction rates and species fluxes.[1] However, designing of alloys for maximal corrosion resistance at high temperatures is often a qualitative endeavor, due to the large set of possible alloy and environmental permutations that make quantification and prediction difficult. Therefore, material specifications for corrosion resistance are often based on empirical databases and experiences that lack the quantification needed for directly linking materials selection to the component design lifetime. Nevertheless, there are a number of cases where alloy composition can be manipulated, based on an underlying understanding of corrosion principles and their verification, to derive good or excellent corrosion behavior in appropriate high temperature environments. In this chapter, certain approaches based on some of these basic principles and empirical findings will be reviewed with selected alloy systems and environments used as examples. Many more specific examples of alloy design or optimization for high temperature corrosion resistance can be found in other chapters of this book.

The essence of the alloy design effort for high temperature corrosion resistance is to achieve a continuous and protective surface layer or scale. Once a layer of this type is established, the access of the alloy to the environment is effectively isolated and, thereafter, is controlled by the transport properties and

stability of the surface scale as long as its integrity is maintained. This type of scale is most often an oxide because virtually all high temperature, technically relevant environments contain reactive oxygen. Further, at equivalent gas activities and, frequently at very small concentrations of O_2 in many mixed-gas environments, oxides are more thermodynamically stable than their equivalent carbides, nitrides, sulfides, etc. It is important to note, though, that the approaches to alloy design for protective scale formation described here, while typically discussed in terms of oxides, are also applicable to situations where other reactive species are present, that is, the formation of surface or internal carbides, nitrides, sulfides, etc. by 'oxidation,' a chemical process by which the valence state of the metal species is increased. Such product formation can be of interest as a synthesis route to functional surface structures[2] but, at elevated temperatures in most technically-relevant environments, these nonoxide phases are less stable than their equivalent oxides and hence, can subsequently be converted to oxides. Even if thermodynamic stability is achieved, most nonoxides, and many oxides, cannot meet the other key criterion of protective scale formation: the kinetic standard of a slowly thickening layer that, by itself, is an effective permeation barrier between the reactive environmental species and the alloy on which it is growing. For temperatures in excess of 600 °C, the protective oxides relevant for alloys in service applications are Cr_2O_3, Al_2O_3, and, to a lesser extent, SiO_2 (as evidenced by the fact that most 'heat-resistant' alloys rely on these surface oxides for corrosion resistance). At lower temperatures, iron, nickel, cobalt, and zirconium oxides can be considered protective, but in this chapter, design examples focus on the former three types. Under certain conditions, protective oxides can also serve as efficient barriers to environmental species other than oxygen (such as water vapor, carbon, or sulfur), thus alloys designed to form these surface layers may have attractive applications in high temperature mixed-gas environments (see **Section 1.21.6** on alloy selection for specific environments).

1.21.2 Protective Oxidation

For this study, binary alloys, generally denoted as A–B, will be considered with other major alloying elements being treated as minor additions to the binary system, and with oxides as the exclusive form of protective scales for the reasons discussed above. In this hypothetical A–B alloy notation scheme, element A is typically a base metal such as Fe, Ni, or Co, while B forms the desired protective oxide:

$$xB + (y/2)O_2 = B_xO_y, \qquad [1]$$

with possible modification of the oxide by other major and minor alloying elements. Principal examples of B would be Al, Cr, and Si for Al_2O_3, Cr_2O_3, and SiO_2, respectively. The desired design goal is to formulate an alloy composition and microstructure that will produce a continuous layer of B_xO_y at the expense of less protective base metal A oxides. To assure this, B_xO_y must be thermodynamically stable in the subject environment, and, typically, have significantly greater stability than the oxide(s) of A. This thermodynamic tendency can be readily assessed qualitatively in terms of the (negative) free energies of formation (ΔGs) as a function of temperature. Such an Ellingham diagram is schematically shown in **Figure 1** for representative metal oxides. From an empirical alloy design experience, preferential formation of B_xO_y is found to be easier in alloy systems for which the difference between ΔGs of the A and B oxides is large. Hence, it is much easier to assure Al_2O_3 formation on Ni–Al than on Ti–Al. However, kinetic factors rather than thermodynamic factors are often more important in determining whether a continuous protective scale can be established.

In the present context, 'protective' has several attributes. First, B_xO_y must form preferentially, and

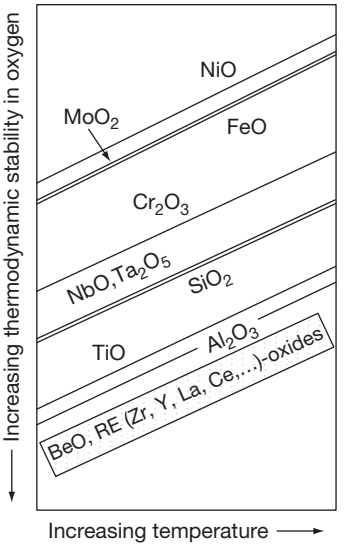

Figure 1 Schematic representation of free energies of formation of oxides of interest. Increasing stability means larger negative energies.

reduce the permeation between the reactive species in the environment and in the alloying elements – that is, both the solubility and diffusivity of anionic species (from the environment) and cationic species (from the alloy substrate) in the oxide scale must be low. Therefore, the product must be continuous across the alloy surface and exhibit long-term stability in the environment. Note that this does not necessarily mean that no other products can grow or exist. Rather, the protective layer must form in a way that it rapidly controls the transport across the entire surface of the alloy – see, for example, **Figure 2**, which shows the development of a continuous Al_2O_3 scale on a Nb–33Ti–40Al (wt%) alloy under the fast-growing Nb-rich transient (nonprotective) oxides. The protective scale should also be dense (no interconnected porosity or large pores), mechanically sound (no through cracks), and adherent to the alloy substrate on which it grows. This last attribute, strong adhesion to the alloy, is often problematic even when other chemical and physical characteristics are met; these oxides tend to have coefficients of thermal expansion (CTEs) that are quite different from those of the alloy and, thus, large stresses (typically compressive) are encountered upon cooling from high temperature such that spallation of the scale eventually occurs.[3] This is a disruptive event; the protective scale regrows during the next heating cycle (hopefully) and accelerates the metal wastage (as well as the attendant subsurface depletion of B) due to reinitiation of the product growth process.[4] Stresses can also develop in the scale due to the growth process itself[5] but, typically, these are not of the same order of magnitude as the thermal stresses on cooling, at least at a steady state.

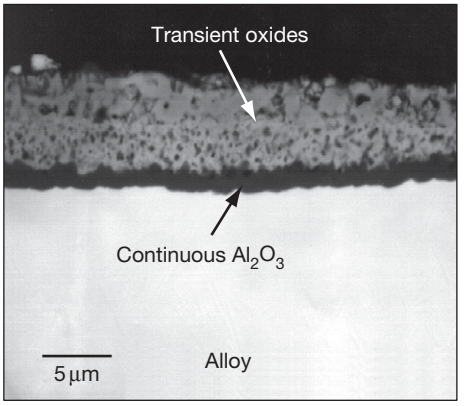

Figure 2 Scanning electron micrograph of cross-section of Nb–33Ti–40Al (at.%) exposed at 1400 °C in air for 15 min. Reproduced from Brady, M. P.; Gleeson, B.; Wright, I. G. *JOM* **2000**, *52*, 16–21.

1.21.3 Selective Oxidation and Establishment of a Protective Scale on an Alloy

Managing the inherent instability of a metallic material in a reactive environment so as to limit the amount of metal wastage through control of thermodynamic and kinetic factors is the goal of alloy design for high temperature applications. This is first attempted by the application of well founded, although somewhat idealized, fundamental principles of selective oxidation of alloys that effect preferential formation of a continuous protective scale (B_xO_y) on alloy A–B. (Some guidelines for choosing B_xO_y for a given set of environmental factors are discussed below.) For a single-phase alloy, A–B, the formalism is based on pioneering work of Wagner,[6] further studied and elaborated by a host of others.[7,8] For multiphase alloys, the development of relevant principles is more recent[9–11] and takes advantage of analytical advances originating from more extensive work on single-phase alloy oxidation. The treatment in this section follows the outline of a recent description of principles for protective scale formation on alloys by Brady *et al.*[12] Specific application of these approaches to intermetallics can be found in Brady and Tortorelli.[13]

As an illustration and reference to the discussion that follows, it is appropriate to consider the schematic descriptions of the two limiting cases, namely, fully nonprotective behavior (**Figure 3**, left side) and the best possible outcome for the alloy design process being addressed here (**Figure 3**, right side) under conditions where O_2 is the reactive species, A and B oxides are mutually insoluble, and the oxygen partial pressure is sufficiently high to oxidize either both A and B or just B. In the former (nonprotective) limiting case, internal oxidation of B occurs, with the possible formation of rapidly growing A oxides while, in the latter limiting case, a slowly growing, exclusive, continuous, adherent B_xO_y layer develops.

In the former case, the depth of internal oxidation, x, at time t can be described functionally as[14]

$$x^2 \propto \left(N_{O,s}/N_B D_{AB}\right)^2 D_O t \qquad [2]$$

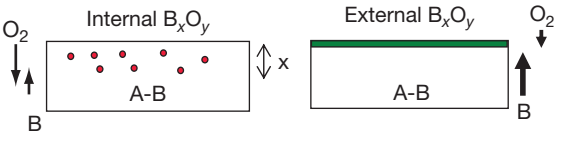

Figure 3 Schematic illustration of internal oxidation and external scale formation by selective oxidation.

where D_O is the diffusion coefficient of oxygen in A–B, $N_{O,s}$ is the solubility of oxygen in A–B, N_B is the concentration of B in the bulk alloy, and D_{AB} is the alloy interdiffusion coefficient. From a practical alloy design viewpoint, the extent of internal oxidation can be decreased most directly by increasing the concentration of B. Internal oxidation can also be decreased by decreasing the permeability of oxygen in A–B ($N_{O,s}D_O$) via ternary and higher-order alloying additions. Microstructure can impact the extent of internal oxidation if the morphology of these internal oxides enhances the transport of oxygen along their interfaces with the alloy matrix (increased D_O).[15] It is this type of mechanism that can explain the presence of stable (essentially inert) Al_2O_3 reinforcements in a Ni_3Al matrix composite structure that compromises the otherwise good oxidation resistance of the aluminide.[16]

From the Wagner perspective, as N_B is increased, the volume fraction of internal B_xO_y precipitates increases to the point where an external layer of B_xO_y forms (**Figure 3**, right side). Under this assumption, the critical concentration needed for external formation of B_xO_y, N_B^*, is a function of metal and oxygen diffusivities in the alloy, and the solubility of oxygen[6] such that

$$N_B^* \propto N_{O,s}(D_O/D_{AB})^{1/2} \quad [3]$$

Therefore, external B_xO_y formation is favored (that is, the critical concentration of B is decreased) by compositional and microstructural conditions that decrease the solubility and inherent diffusivity of the oxidizing species in the alloy and/or increase the mobility of the metallic elements (cf. **Figure 3**). One way to preferentially increase the effective value of D_{AB} and, thus, decrease the value of N_B^*, is to provide a greater density of short-circuit diffusion paths – for example, by decreasing the grain size[17] or increasing the dislocation density at the alloy surface.[18] Although such structural pathways may not be stable over long periods of time at elevated temperature, their existence during the period when the B_xO_y layer is being established is critical and effective.

In theory, ternary and higher order alloying additions that decrease the solubility of the environmental species in the alloy should, using eqns [2] and [3], decrease the value of N_B^* and promote protective scale formation. Obviously, the opposite is also true: compositional modifications that increase reactant solubility in the alloy can increase N_B^* to a value greater than N_B such that an exclusive protective scale does not form. Therefore, it is important from an alloy design viewpoint to be aware of how alloying (for whatever purpose) affects this solubility term to avoid unintended deleterious effects on the ability of an alloy to develop a protective surface product.

It is well known that protective scale development can be promoted by the 'third-element effect,' defined generically as an alloying addition that decreases the amount of B needed to form a protective layer of B_xO_y (N_B^*). This can be an important design principle if it is necessary to minimize the concentration of B to achieve other desirable properties of the alloy (for example, decreasing the aluminum concentration to avoid brittleness). For example, such an effect has been observed for (Ni,Co,Fe)–Al–Cr alloys, where the addition of Cr lowers the N_{Al}^* value for protective Al_2O_3 formation, and is, in fact, the basis for the design of commercial heat-resistant alloys.[19]

There are several mechanistic variants to the third-element effect. The 'classic' version is generally associated with a secondary gettering mechanism,[1,20] whereby X is added to A–B such that its oxide is of intermediate stability compared to that of the oxides of A and B, and decreases the effective partial pressure at the metal–oxide scale interface such that continuous B_xO_y layer formation can occur. A second type of third-element effect can be considered to be the influence of an alloying addition on early-stage oxidation, such that a transient oxide can preferentially nucleate the growth of B_xO_y.[21,22] Additionally, just as microstructure can enhance metal diffusivity in the alloy lattice (see above discussion), a third element can be used to influence diffusional effects so that protective oxide layer formation is promoted (D_{AB} is increased and/or $N_{O,s}$ and D_O are decreased).[23]

The activity(ies) of the reactant(s) in the subject environment must be a part of alloy design considerations for protective scale development.[12] For example, an alloy with $N_B > N_B^*$ at a given reactant (oxygen) partial pressure may not be able to form a protective B_xO_y layer at higher pressures where the oxygen solubility in A–B increases in accordance with Sievert's law and possibly raises the value of N_B^* above that of N_B (eqn [3]) or where the higher pressures result in altering the nature and/or stability of the competing A oxides. Similar considerations must be given to service temperature, which not only affects the reactant solubility in the alloy, but also other factors that influence the value of N_B^*.

Despite the importance of multiphase alloys to real-world applications, relatively little work in high temperature corrosion has been dedicated to comprehensive studies of such materials.[9–11,24–28] Nevertheless, some important and intriguing implications of alloy design have begun to emerge from developments in the understanding of how multiphase alloys oxidize. In this regard, two limiting cases of high temperature oxidation of a multiphase alloy[9] are shown in **Figure 4**. In (a), the component phases react independent of each other, and this can result in corrosion behavior that is worse than that displayed by either phase singly, and is certainly inferior to the other limiting case where the phases act together to form a continuous, exclusive protective layer, as depicted in (b) of **Figure 4**. In the latter case, a solute-rich phase acts as an efficient source or 'reservoir' of B, resulting in a subscale zone that is depleted of this component. The important factors include size, shape, distribution, volume fraction, and composition(s) of the minority phase(s). Normally, a finer dispersion of such phases is more efficient in promoting protective scale formation.[24,29] A striking example of this is shown in **Figure 5**, where the as-cast version of an alloy of Fe–15Cr–0.5C (wt%) composition did not form a protective Cr_2O_3, but a version of the same alloy with a refined dispersion of carbides did.[29]

A second approach using alloys to form a reservoir phase is best exemplified by the addition of Cr to γ-TiAl, facilitating the formation of a protective layer of Al_2O_3. Without a minimum of 8–10 at.% Cr in place of Ti, 60–70 at.% Al was needed for a protective alumina scale to form.[30] Because Cr is significantly more noble in oxygen than Ti or Al, this alloying benefit was not the traditional third-element secondary-gettering mechanism described earlier. Rather, the addition of Cr introduced a second (Laves) phase, $Ti(Cr,Al)_2$, which promoted the formation of a protective Al_2O_3 layer by equilibrating with, and stabilizing, the γ-TiAl phase that acted as an effective Al reservoir and did not transform to the less oxidation-resistant α_2-Ti_3Al phase due to Al depletion.[31,32] Such an example highlights the variety of phase stability relationships in multiphase alloys that can be exploited as design routes to protective scale formation. Similar approaches based on thermodynamic and kinetic pathway factors are currently being exploited, for example, in the design of multiphase coatings used as bond coats in thermal barrier systems[33] or as alloy templates for synthesizing composite structures by controlling gas–metal reactions.[2,13]

This section has briefly described the underlying principles for the promotion of a protective scale via alloying or microstructural manipulation. These serve as a qualitative guide in assuring that the selective oxidation process produces the desired surface layer, as opposed to internal oxidation or a mixed external scale that is not truly protective. For an A–B alloy, this is achieved by considering conditions that minimize the solubility and diffusion of environmental reactants in the alloy and maximize the flux of B to the reacting surface – by increasing its initial concentration, its availability, or its mobility. Once a protective scale is formed, there are other considerations for maximizing the corrosion resistance and component lifetime; these are discussed below in terms of alloying for minimizing the scale growth and spallation as well as for materials selection for specific environments.

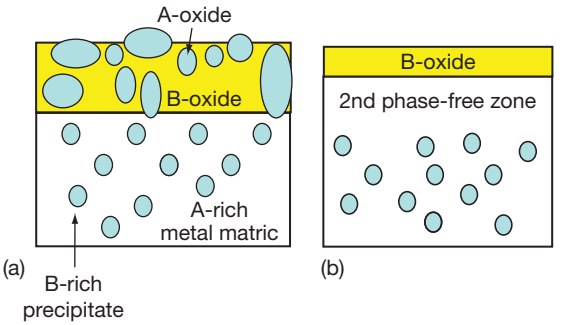

Figure 4 Schematic depiction of (a) independent and (b) cooperative oxidation based on concepts presented in Gesmundo, F.; Gleeson, B. *Oxid. Met.* **1995**, *44*, 211–238.

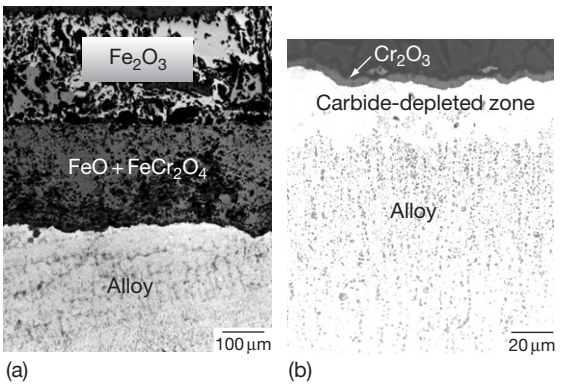

Figure 5 Cross-sectional micrographs of Fe–15Cr–0.5C (wt%) steel exposed at 850 °C for 72 h in 1 atm O_2 (a) as-cast and (b) hot-forged. Reproduced from Durham, R. N.; Gleeson, B.; Young, D. J. *Oxid. Met.* **1998**, *50*, 139–165.

1.21.4 Minimizing Oxide Growth and Improving Scale Adhesion by Alloying

It is now a known fact that dilute additions of reactive, or rare-earth elements (REs) can substantially decrease the oxide scale growth rate and improve the scale adhesion of alloys that form protective layers of chromia or alumina.[34–38] Oxides of REs are highly stable (see **Figure 1**) and are readily taken up into the protective oxide layer, where they can help decrease the steady-state growth rate.[35] These active elements can also improve the scale adhesion, in many cases by offsetting the detrimental effects of indigenous impurities, such as sulfur.[35,39] Therefore, the most oxidation-resistant commercial alloys contain minor (<0.1 wt%) concentrations of REs. As an example, **Figure 6** illustrates the beneficial effects of certain RE additions on cyclic oxidation lifetime for two Al_2O_3-forming alloy systems.

While all these active elements qualitatively respond in a similar manner upon exposure to an oxidizing environment, there are differences in the effectiveness of specific REs. Different effects on oxidation behavior are observed depending on the RE chosen, the way it is added to or incorporated into the alloy, and its concentration (see **Figure 6**), as well as how it is dispersed in the alloy matrix.[35–38] These additions can add significant costs to alloy production and, because of their reactivity, REs can be difficult to control to specified levels during processing, especially for coatings,[40,41] where laboratory-scale benefits have not yet been scaled up for commercialization. It is, therefore, particularly important to weigh all factors affecting the RE concentration and incorporation into the alloy, some of which (such as the use of multiple REs and the effects of other minor alloy constituents – see below) have only been widely discussed relatively recently.

The choice of a particular RE can be guided by empirical findings or rules. For example, as single additions, Hf and Zr are preferable for aluminides, while Y is superior in Ni–Cr–Al and Fe–Cr–Al alloys.[37] For chromia-forming alloys, La seems to be preferred based on its large ion size and its higher solubility, particularly in ferritic alloys.[42] In this regard, the low solubility of Y in many alumina-forming alloys limits its effectiveness.[37,43] When a RE exceeds its solubility limit, it can be more readily internally oxidized given

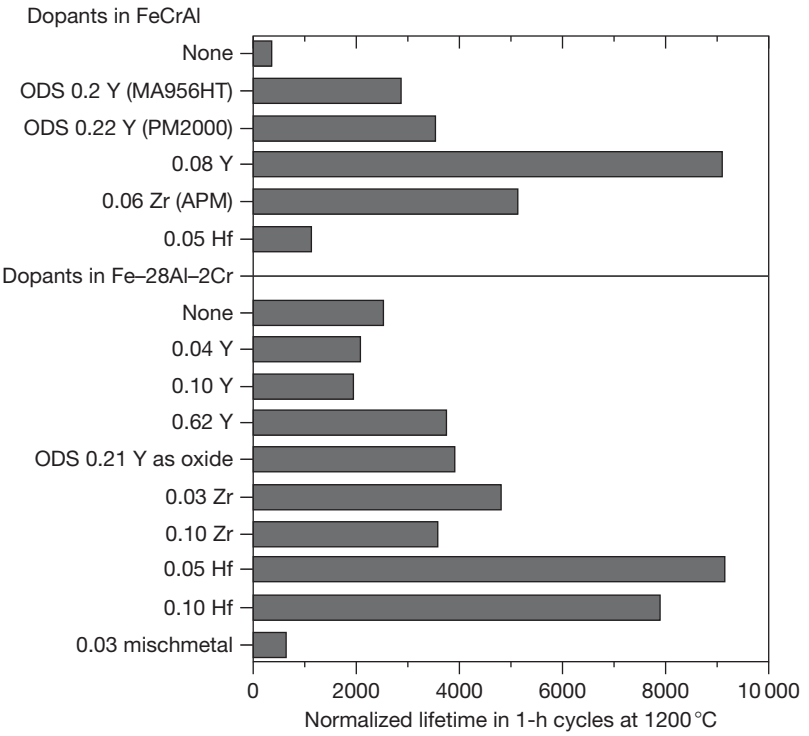

Figure 6 Effect of various RE additions to a base Fe–20Cr–10Al or Fe–28Al–2Cr (at.%) alloy in terms of normalized oxidation lifetime for 1-h thermal cycles at 1200 °C. Reproduced from Pint, B. A. In *Proceedings of John Stringer Symposium*; Tortorelli, P. F., Hou, P. Y., Wright, I. G., Eds.; ASM International: Materials Park, OH, 2003; pp 9–19.

the active nature of these elements (Figure 1). This can compromise the oxidation resistance and/or mechanical integrity (if extreme). The effective use of a RE requires optimization of its concentration.[38] Figure 6 clearly indicates that the oxidation resistance is quite sensitive to RE concentrations.

The use of two reactive elements (so-called 'co-doping') is often more effective than the use of a single RE,[38,43–45] at least for alumina-forming alloys. Several commercial alumina-forming alloys and coatings contain multiple REs.[43,44] It is thought (at least for Fe–Cr–Al alloys) that co-doping allows Y to be fully effective by keeping it below its solubility limit and then supplementing it with a more soluble RE, such as Hf or Zr. Thus, in general, it appears that co-doping allows the total RE concentration to be decreased while maintaining good scale adhesion, and low oxide growth rates. In many cases, this then decreases the amount of internal oxidation relative to the single dopant case.[43]

It is clear that attention to microalloying additions and/or impurity control is important in maximizing the oxidation resistance of alloys using REs. Sulfur (and possibly other) impurities can have a detrimental effect on scale adhesion.[4,46–48] Further, such indigenous impurities, as well as purposeful additions for microstructural tailoring and properties enhancement (such as carbon, nitrogen, boron, etc.), can mitigate the positive effects of REs on oxidation resistance.[38,45,49,50] For example, in Hf-doped NiAl, the Hf/C ratio has been found to be important in optimizing scale adhesion.[49,50] Figure 7 shows that NiAl suffered greater scale spallation with decreasing Hf/C ratios. It has been suggested that, if the Y:S and/or Hf:C ratios are <1, the alloy will have less than optimal performance.[38] Therefore, the active nature of REs makes alloy design with these elements a delicate optimization process.

It should be emphasized that, while effective when concentrations are optimized for given levels of impurities or microalloying additions, REs generally do not promote protective scale formation, that is, they do not make marginal Al_2O_3 or Cr_2O_3-forming compositions into robust ones.[37] Other approaches, as outlined in the previous sections, must be used. In this regard, however, any indirect effects of RE additions need to be evaluated and separated from the direct influence of RE's on scale growth and adherence. For example, a sufficient concentration of RE-rich precipitates in the alloy matrix can result in a finer grain size and, this in itself, can promote protective scale development (as discussed in a preceding section).[37]

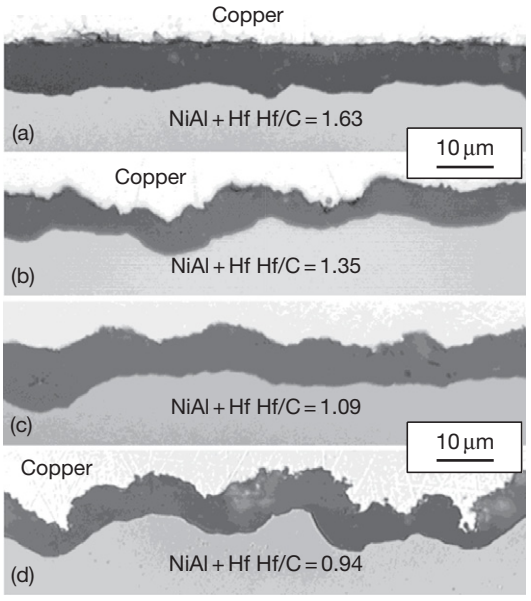

Figure 7 Polished cross-sections of the Al_2O_3 scale formed on coatings of NiAl+Hf with differing Hf/C ratios, after 10 100-h thermal cycles at 1200 °C. Reproduced from Pint, B. A. In *Proceedings of John Stringer Symposium*; Tortorelli, P. F., Hou, P. Y., Wright, I. G., Eds.; ASM International: Materials Park, OH, 2003; pp 9–19.

There are potential detrimental effects of other alloying elements on oxidation resistance if they are sufficiently active. For example, single additions of 1 at.% Re, Ti, Ta, or Cr (commonly present in coatings and Ni-base superalloys) were found to degrade the oxidation resistance of Hf-doped NiAl.[50] The Re and Cr additions formed precipitates in the alloy and negatively affected the oxide–metal adhesion, while the Ti and Ta were oxidized and incorporated into the scale as potential sites for scale breakdown.[51,52] On the contrary, certain precious metal additions to NiAl can improve the oxidation resistance by improving the scale adhesion,[53,54] presumably by mitigating the detrimental effect of sulfur, and promoting alumina formation on low-Al ($\gamma+\gamma'$) substrates.[33]

1.21.5 Maximizing Oxidation Lifetime

There has been an increasing focus on oxidation lifetime, particularly in terms of approaches used for predicting it accurately for a given material and exposure condition.[55] The primary reason for this trend is that lifetime values can lead to quantification of oxidation behavior in a way that can be better used by researchers, engineers, systems designers, plant

operators, etc. As the most corrosion-resistant materials have very long lifetimes, verified life prediction models provide a way to predict end of life without necessarily having to conduct extensive, extended exposures. Also, lifetime models can provide guidance to the alloy design process by quantifying the effect of specific approaches taken to improve high temperature corrosion resistance. Some trends based on these are discussed in this section.

Usually, lifetime is defined as the time-to-breakaway (t_b) – the time at which the protective scale fails and cannot be reformed, thereby resulting in the growth of faster-growing, nonprotective products. The cross-sectional image in **Figure 8** captures the process at t_b, that is, the transition from protective to nonprotective behavior, and illustrates the radical difference in the nature of the respective aluminum and iron oxides. After 1101 h, the protective Al_2O_3 layer on the right-hand side of the image in **Figure 8** reached the point where it could no longer be maintained by the supply of remaining Al from the alloy.[56] Therefore, iron oxides formed and rapidly consumed the remaining metal. Following Quadakkers *et al.*,[57,58] the time-to-breakaway for alloy A–B that forms a protective B_xO_y layer can be expressed as:

$$t_b = \left[\left(N_B - N_{B,c}\right)/100 \bullet d/2 \bullet \rho \bullet M^{-1} \bullet k^{-1}\right]^{1/n} \quad [4]$$

where N_B is the initial B concentration, $N_{B,c}$ is the critical concentration below which a protective B_xO_y layer cannot be maintained (different from N_B^*), d is the thickness of the specimen, ρ is the alloy density, M is the mass conversion factor for metal and oxide, and k is the rate constant, where $(kt)^n$ is the rate for consumption of B by oxidation. This k represents the total consumption of B by oxide growth as well as spallation. It can also be dependent (inversely) on d for thin cross-sections.[59]

From an alloy design viewpoint, oxidation lifetime can be increased by any approach (discussed above or elsewhere in this book), that slows the rate of scale growth or spallation (decreases k^n) or enhances the promotion of a protective layer (decreases $N_{B,c}$). In addition, t_b can be increased by increasing the concentration of B, assuming no alteration of other factors (e.g., solubilities or D_{AB}) that would destabilize the stability of the protective B_xO_y layer. However, increasing B can affect physical or mechanical properties that, in turn, can influence the lifetime through effects on k. For example, for Fe–Al systems, simply increasing the concentration of Al can actually decrease the lifetime. This is because the ordered structures at higher Al levels result in significantly higher values of alloy CTE than those of other iron-based alumina-forming alloys (see **Figure 9**).[60] Therefore, greater compressive stresses are experienced by the scales on cooling, leading to higher spallation rates and, thus, higher values of k. Hence, iron aluminides do not necessarily show substantially greater lifetimes than Fe–Cr–Al alloys despite much greater values of N_B.[56]

The critical concentration for maintaining the ability to reform a protective layer, $N_{B,c}$, is dependent on the failure mode of the B_xO_y layer (intrinsic chemical failure or mechanically-induced chemical failure).[61] Intrinsic failure is when the actual level of B falls below the equilibrium value for formation of the protective oxide by continued selective oxidation; here, $N_{B,c}$ can be quite low and only achieved under very limited circumstances when the alloy is very

Figure 8 Cross-sectional image of an Fe–28Al–5Cr–0.2Zr (at.%) alloy exposed in air for 1101 h at 1300 °C. Other data from these exposures reported in Bennett, M. J.; DeVan, J. H.; Tortorelli, P. F. The Oxidation Behavior of Iron Aluminides in Air at 1300°C. In *Microscopy of Oxidation 3*; Newcomb, S. B., Little, J. A., Eds.; The Institute of Materials: London, 1997; pp 233–245.

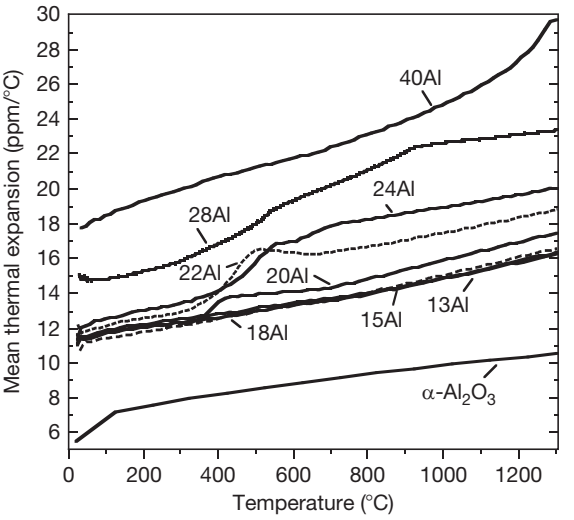

Figure 9 Mean thermal expansion coefficient versus temperature for α-Al_2O_3 and various Fe–Al alloys. Reproduced from Pint, B. A.; Porter, W. D.; Wright, I. G. *Mater. Sci. Forum* **2008**, *595–598*, 1083–1092.

thin (to relieve stresses readily by creep) and temperatures very high.[61–63] The mechanically induced chemical failure mode is the more typical one and occurs when the concentration of B becomes lower than the value needed for kinetically controlled scale rehealing, and the accumulated strain energy is sufficient for scale cracking and/or decohesion.[3] It may, therefore, be possible to use alloying additions to control this process and lower $N_{B,c}$ (raise t_b). For alumina forming alloys, Cr can increase the lifetime by allowing Cr_2O_3 scales to extend protection after Al_2O_3 scales can no longer form (intrinsic failure mode)[61] or to promote reestablishment of the latter by a type of third-element effect (mechanically induced chemical failure mode).[63] In this regard, alloying additions or heat treatments that affect the mechanical strength of the substrate can also influence oxidation lifetime by modifying the effective strain energy available for protective scale breakdown[37,64] as reflected by k (and n) in eqn [4]. This is another example of unintended, or secondary, consequences of alloy manipulation via effects on chemical, physical, or mechanical factors that affect either the ability to form a protective scale or to reform it after a failed event.

There are additional concerns about the lifetime of corrosion-resistant coatings designed for use at high temperatures. Because of the dependence of t_b on the total amount of B available for protective oxide scale (POS) formation (manifested through d in eqn [4]), coatings, particularly thin ones, have limited reservoirs of B. Additionally, the depletion of B by oxidation (k) is accompanied by loss of B by back-diffusion from the coating into the substrate on which it is deposited.[65] Alloy manipulation can be used to control this process to a certain extent.[33] Barrier layers at the coating–substrate interface may also have to be considered to prevent undesirable (from an oxidation perspective) alloying of the coating by elements diffusing from the substrate.[66] As discussed above, it is often difficult to synthesize coatings in a controlled manner with appropriate levels and distributions of REs; so attempts to minimize k in order to maximize lifetime are rather more limited in these cases.

1.21.6 Alloy Selection for Specific Environments

Most high temperature environments involve more than one potential reactant. In many mixed reactants involving O_2, N_2, H_2O, S_2, CO, etc., the reaction of alloys can be quite complex, with multiple types of internal precipitates and limited means to predict and control their formation.[67,68] However, in other cases of multiple reactive species, reactions with oxygen still predominate and can be used constructively to promote the formation of a POS that is an effective barrier to other reactive species in the environment. This is usually enabled, at least in part, by the greater stability of oxides relative to other products so that oxide formation is possible even at very low oxygen partial pressures. A good example in this regard is the preferential establishment of a protective Al_2O_3 layer even under the so-called 'reducing' sulfidizing environments, where the partial pressure of oxygen (p_{O_2}) is of the order of 10^{-20} atm while p_{S_2} is ~12–14 orders of magnitude greater.[69] Under these conditions, approaches to promote the stability, exclusiveness, integrity, and maintenance of POSs can still have a role in alloy design and selection for mixed-oxidant environments. Some examples of alloy selection for specific environments are given below. Further details of the relevant corrosion processes are described in other chapters of this book.

Air/Nitridation. Because of the typically greater stability of the oxides, the alloys that form protective Al_2O_3, SiO_2, and/or Cr_2O_3 scales often perform well in air with little interference from nitrogen. However, subscale nitride formation is possible if there is a way for the nitrogen to penetrate the oxide scale or disrupt its ability to form a continuous surface layer, or if the scale is mechanically breached and cannot heal. (This is true, of course, for many oxygen-second oxidant systems.) For example, Fe-based Al_2O_3-forming alloys usually perform similarly in oxygen and air but, recently, Pint *et al.* reported (nonclassical) internal oxidation and nitridation of Fe–Al alloys upon air exposure.[70] This accelerated attack was eliminated by additions of REs or Ti to the Fe–Al alloy, by promoting a less defective scale. For TiAl intermetallics, TiN formation during the initial stages of oxidation in air has been shown to disrupt the continuity of the Al_2O_3 layer, resulting in less protective (alumina + titania)-based mixed-oxide scales.[71] The addition of Ag or Cr to TiAl helps promote continuous Al_2O_3 layer formation and ameliorates this problem in part by modifying the nature of the compositional changes at the alloy–scale interface during the initial stages of oxidation which can otherwise trigger local TiN formation, and prevent the development of continuous alumina layers.[32,72]

The participation of nitrogen as a reactant for air exposures can also be triggered by the presence of

ambient water vapor in the environment. As an example, while Cr_2O_3 formed on a Cr–Nb alloy in both dry and humid air, subsurface nitridation only occurred in the latter case (**Figure 10**).[73] Similar behavior was also observed for a gamma-based Ti–Al–Cr alloy, with a borderline Cr content to promote alumina scale formation; protective Al_2O_3 formed in dry air at 1000 °C, but subscale nitridation was observed after exposure to humid air.[32] For Cr–Nb at 950 °C, little difference between dry and humid air was observed, but significant subscale nitridation was observed when the oxygen and sulfur impurities in the alloy were decreased, with possible synergistic effects between S and water vapor.[73] Experience suggests that such complicated effects tend to occur in alloy composition ranges which fall near the kinetic boundary for continuous, POS formation.

As already noted, internal nitridation can occur in air environments if a continuous, protective oxide layer cannot form or is breached. It can also be observed in nitrogen-rich environments that are reducing with respect to even the most stable oxides. Under such conditions, alloys with elements that minimize nitrogen solubility and diffusivity are less susceptible to attack (eqn [2]). In this regard, nickel and cobalt have strong beneficial effects, with the added advantage that neither Ni nor Co tend to form thermodynamically stable nitrides under most technologically relevant nitrogen-containing environments.[74,75] This impact of low nitrogen permeability is illustrated in **Figure 11**, which shows nitrogen update as a function of the sum of Ni and Co concentrations in Fe–Ni–Co alloys and in **Figure 12**, where reaction rates of internal nitridation are shown

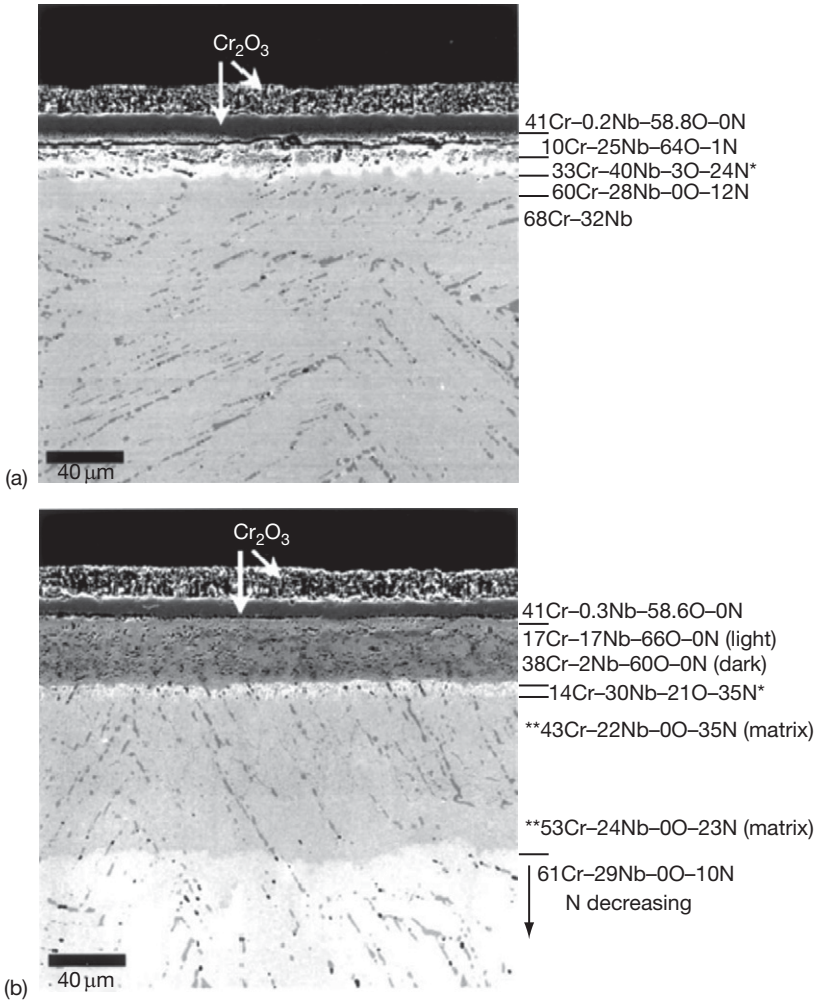

Figure 10 Cross-sectional micrographs of Cr–31Nb (at.%) oxidized for 24 h at 1100 °C. (a) filtered dry air (b) humid air. Reproduced from Brady, M. P.; Tortorelli, P. F.; Walker, L. R. *Oxid. Met.* **2002**, *58*, 297–318.

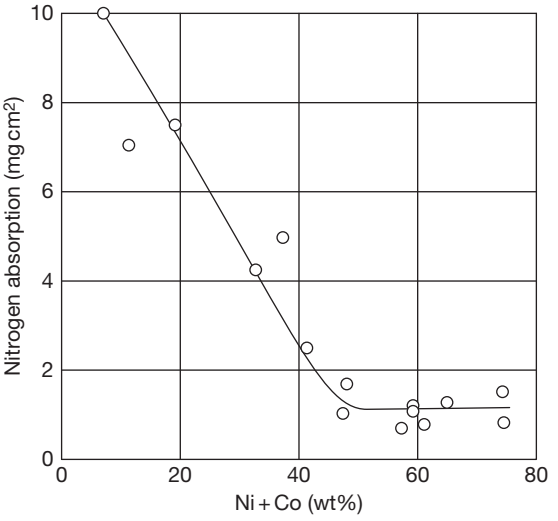

Figure 11 Effect of Ni + Co content in Fe–Ni–Co alloys on nitridation at 650 °C for 168 h (NH_3). Data of Barnes and Lai as shown in Lai, G. Y. *High Temperature Corrosion of Engineering Alloys*; ASM International: Materials Park, OH, 1990.

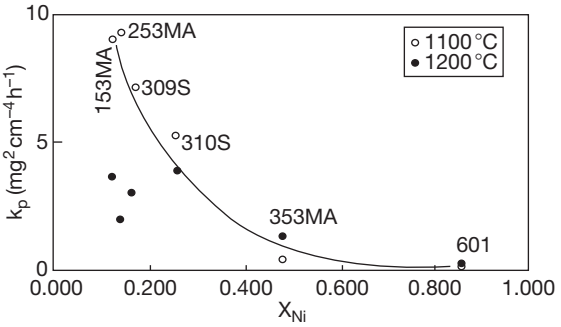

Figure 12 Parabolic rate constants for nitridation in NH_3 as a function of Ni concentration in various alloys. Reproduced from Tjokro, K.; Young, D. J. *Oxid. Met.* **1995**, *44*, 453–474.

to decrease strongly with nickel concentration of the alloy. Under these special circumstances, alloying additions of Cr, Al, or Ti will lead to internal precipitation of their respective nitrides and, therefore, will compromise the nitridation resistance of the nickel or cobalt. In particular, the introduction of Cr in Ni–Al or Ni–Ti base alloys strongly increased the amount of internal attack due to increased nitrogen permeability.[76]

Carburization and Metal Dusting. Like many cases of nitridation, carburization is manifested as an internal precipitate formation (of carbides), ahead of the alloy–scale interface. Chromia-forming materials are often used for service where carburization can occur due to the many options available among such alloys to combine good oxidation resistance with attractive high temperature mechanical properties at relatively low alloy cost. Resistance to attack derives from the development and maintenance of a continuous Cr_2O_3 scale. Consequently, alloy design approaches that generally promote chromia formation are also a benefit in carburizing environments. Alloying that leads to the development of an Al_2O_3 or SiO_2 layer or sublayer can proffer greater protection under carburization conditions that are too severe for chromia-forming alloys.[77,78] Recently, it was shown that increasing the nickel content of Fe–Cr–Ni alloys from 30–35 wt% to 45% or greater, significantly decreased the carburization rate due to decreased carbon solubility and diffusivity in the alloy (eqn [2]).[78] Furthermore, the addition of a few % Al to 60% Ni alloy increased the carburization resistance substantially due to alumina scale formation at higher temperatures.[78]

Metal dusting is a catastrophic form of metal degradation in carbonaceous environments that occurs over a lower temperature range (typically 400–800 °C), but accompanied by higher carbon activities than the carburization phenomenon described above.[79,80] It can result in the disintegration of alloy into powder, and occurs for nickel- as well as iron-based alloys (although it is less severe in the former case). As indicated above, alloying or microstructural approaches that promote the exclusive formation of a robust protective chromia scale improve the resistance to metal dusting, including the use of cold work or surface deformation to increase outward Cr diffusivity in the alloy.[81] Alloys with ≥26 wt% Cr and a few % of Si or Al should show improved resistance to metal dusting.[77] It is expected that silica or alumina scales should resist the uptake of carbon more than chromia scales and, therefore, be suitable for metal dusting resistance. Indeed, any alloy improvements that extend the time for localized oxide scale breakdown, and the initiation of metal dusting at such locations, will also confer a benefit from any processes that can be used to reoxidize a component during operational shutdowns.[82] Alloying Ni with Cu has been found to improve the resistance to metal dusting.[83] Rates of reaction of Ni–Cu alloys decreased significantly with increasing Cu up to 10 wt% with virtually no metal dusting at 20% Cu. Because Cu appears to be noncatalytic towards carbon deposition and has virtually no solubility for C, its positive effect on dusting of Ni–Cu alloys probably relates to a dilution effect.[83]

Sulfidation. Pure sulfidation, that is gas–metal reaction in an environment completely devoid of oxygen,

poses a challenge for the design of traditional heat-resistant high temperature alloys that normally depend on the development of Cr_2O_3, Al_2O_3, or SiO_2 scales[84] This is because the growth rates of many metal sulfides are quite high (due to their highly defective structures) and they cannot function as protective scales. On the contrary, refractory metal sulfides based on Mo or Nb are slow growing,[84] but little success in alloying Fe–Al with Mo or Nb has been reported.[77] The most promising system is Fe–Al–Mo, due to the formation of a protective layer of $Al_{0.55}Mo_2S_4$.[85]

As mentioned earlier in this section, there are applications in which the environment is highly sulfidizing, but there is a presence of oxygen (p_{O_2} of the order of 10^{-18}–10^{-24} atm or perhaps even lower). Under these circumstances, there are greater opportunities for design of more practical alloy systems. This is because Al_2O_3 and SiO_2 are thermodynamically/kinetically stable at these oxygen partial pressures, while Cr_2O_3 may or may not be.[86] At 700 °C with $p_{S_2} \sim 10^{-8}$ atm and $p_{O_2} \sim 10^{-20}$–10^{-24} atm, chromia scales can form on Fe–Cr(–Ni) alloys, at least at the highest oxygen pressures, with scales formed on Fe–Cr (M_2O_3 type with low Fe levels, M = metallic element) being significantly more protective that those on Fe–Cr–Ni (M_3O_4, with higher Fe contents).[86] Consequently, minor alloying elements that promote exclusive formation of M_2O_3-type scales (Si, Al) also improved sulfidation resistance.[86]

Work over a number of years has consistently shown that alumina-forming materials have significantly better resistance to corrosion under highly sulfidizing conditions than chromia-forming alloys,[69,87–89] particularly for iron-based systems. **Figure 13** compares mass change data at 800 °C for model Fe–Cr–Ni (stainless steel) and FeCrAl alloys with that of an Fe–28Al (at.%) alloy in a H_2S–H_2–H_2O gas mixture, where p_{O_2} was $\sim 10^{-22}$ and $p_{S_2} \sim 10^{-6}$ atm. The exceptionally low rate of reaction in this very aggressive environment is due to the formation of a protective Al_2O_3 scale for the iron aluminide while sulfides formed on the other alloys. Additions of Cr to the base Fe–28Al composition increased the rate of reaction at a concentration level of 4% and above.[69] The presence of REs in alumina-forming alloys was reported to have a beneficial effect on sulfidation resistance by improving the scale integrity.[90] In contrast, no influence of REs on sulfidation behavior of chromia-forming systems, where scale breakdown was not by mechanical disruption of the oxide scale, was found.[90]

Recent work with TiAlCr alloys in H_2S–H_2–H_2O environments indicated that, in contrast to Fe–Cr–Al

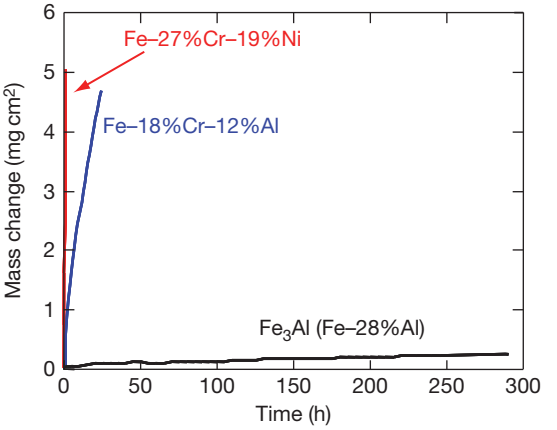

Figure 13 Mass change of Fe-based alloys in H_2–H_2S–H_2O at 800 °C ($p_{O_2} \sim 10^{-22}$ and $p_{S_2} \sim 10^{-6}$ atm). Concentrations are in at.%. Reproduced from DeVan, J. H. In *Oxidation of Intermetallics*; Grobstein, T., Doychak, J., Eds.; TMS: Warrendale, PA, 1989; pp 107–115.

alloy systems, alloying approaches that promote exclusive formation of protective Al_2O_3 layers in this system result in good sulfidation resistance.[91] This is speculated to result, in part, from the unusual mechanism of the third-element effect in the Ti–Al–Cr system, mechanistically based on sub-scale alloying depletion effects during reaction rather than the more classical gettering type behavior for Fe–Cr–Al.[25] There have been other reports of good sulfidation resistance for coatings based on Ti–Al,[92] and a low reaction rate for Ti–6Al–4V.[93]

Alloys that form SiO_2 scales also show some promise for the highly sulfidizing-oxidizing environments described above. Good resistance of $MoSi_2$ to Ar–H_2–H_2S has been reported,[92] presumably due to the slow reaction rate of Mo in sulfur[84] and the lack of a stable sulfide of Si. More recently, work with multiphase Mo–Si–B alloys in the same mixed sulfidizing-oxidizing gas as used for the data in **Figure 13** showed low reaction rates at 800 °C, with the formation of $MoSi_2$ and SiO_2 scales.[94] Despite the susceptibility of nickel to reaction with sulfur or SO_2, silica scales seemed to proffer good sulfidation resistance to iron and nickel silicides.[95]

As p_{S_2} is decreased and p_{O_2} increased, SO_2 becomes the dominant reactive species. Such environments are typically found in combustion of sulfur-bearing fuels. Under these conditions, chromia is often stable, although its range of stability is usually determined by kinetic factors.[96] However, the overall corrosion resistance still involves approaches for manipulating alloy composition and microstructure

to promote the formation and maintenance of a protective Cr_2O_3(-rich) scale, as discussed above. Many studies of sulfidation and POS breakdown under such oxidizing–sulfidizing conditions have been conducted.[74,77,96] Alloys that form protective Al_2O_3 and SiO_2 scales can, in theory, show good resistance to corrosion by SO_2. On the other hand, nickel aluminides were not particularly resistant to corrosion in the presence of SO_2,[97] although iron aluminides should be.[89] If conditions are such that sulfate salts deposit on alloys, chromia scales are most resistant compared to Al_2O_3 and SiO_2 scales under the so-called type II hot corrosion conditions (lower temperature mode), while alumina scales can be preferable for resistance to type-I attack.[98]

Water vapor. The effects of water vapor (H_2O) on high temperature oxidation have received increasingly greater attention. In large part, this is because most power-generation applications (gas turbines, combustion and steam-generation systems, solid oxide fuel cells, etc.) involve environments with relatively high levels of H_2O. As such, there is a critical need for materials that are relatively nonreactive with water vapor under the aggressive conditions imposed by the increased operating temperatures and pressures needed to achieve high power-generation efficiencies and decreased emissions. As described elsewhere in this book, the presence of water vapor in the environment typically leads to higher oxidation rates, particularly for chromia- or silica-forming alloys where H_2O can dramatically enhance oxide volatilization and/or impact oxide structure/stability and solid-state transport properties.[99,100] In particular, water vapor results in the formation of volatile oxyhydroxides, which can significantly compromise the formation of POS by constant thinning of the oxide surface layer due to volatilization.[99] Because chromia has the highest volatilization susceptibility of the major high temperature protective oxides,[100] Mn is added to chromia-forming steels to decrease the rate of volatilization substantially by promoting the development of $(Cr,Mn)_3O_4$ surface layers.[101] In contrast to Cr_2O_3 and SiO_2 scales, Al_2O_3 scales are far more stable in H_2O-containing environments (see **Table 1**)[100] and, as discussed below, are generally less susceptible to accelerated oxidation in the presence of water vapor.

Accelerated oxide scale growth rates, decreased time-to-breakaway (associated with formation of iron oxide nodules), and increased spallation susceptibility under thermal-cycling conditions have been widely reported for water vapor effects on chromia-forming

Table 1 Approximate upper use temperature (°C) for oxides based on partial pressure of all volatile species equal to 1×10^{-7}MPa

	Air: 0.1 MPa total 2.1 × 10^{-2} MPa O_2 10^{-3} MPa H_2O	*0.1 MPa total 10^{-2} MPa O_2 10^{-2} MPa H_2O*	*1 MPa total 0.1 MPa O_2 0.1 MPa H_2O*
Cr_2O_3	1122	1042	499
SiO_2	1575	1370	967
Al_2O_3	*	1864	1345

*limited by melting point of oxide rather than volatility.
Source: Adapted from Opila, E. J.; Jacobson, N. S.; Myers, D. L.; Copland, E. H. *JOM* **2006**, *58*, 22–28.

ferritic and austenitic steels, which are extensively used in the ~500–800 °C range (see other chapters in this book).[102–110] However, proper alloying can improve oxidation resistance of these chromia-forming alloys in the presence of water vapor. This is shown schematically for Cr and Ni in **Figure 14**, which indicates the compositional regions where behavior associated with development of a POS consisting of Cr-rich $(Cr,Fe)_2O_3$ was observed at 650 and 800°C.[106] As expected normally (cf. eqn [2]), increasing Cr has a beneficial effect on promoting POS formation in water vapor-containing environments. At levels above ~16 wt% Cr, increasing the Ni level in the alloy also provides some improvement in oxidation resistance in the presence of water vapor.[106] While increasing the Cr levels above those shown in **Figure 14** may improve the oxidation resistance even more, the onset of brittle sigma phase formation in the alloy and its detrimental effect on the mechanical properties must be considered.[109] As discussed in the previous sections, a finer alloy grain size can help promote POS formation on an alloy.[17] This has been observed in water vapor-containing environments for chromia-forming alloys.[111]

Minor individual alloying additions of Mn (0.1–3.5 wt%), Si (0.2%), Ti, and B to form TiB_2 (≤1%), and Nb and C to form NbC (≤1%) in model Fe–16 wt% Cr base alloys have been reported to have a beneficial effect on oxidation resistance in air +10% H_2O.[111] The effects of Ti and Nb may result, in part, by decreasing the alloy grain size by formation of TiB_2 and NbC, which retard the grain growth during alloy processing. No beneficial effect of RE-type additions (0.3% La, 0.1% Y, 0.03% Zr) on oxidation resistance in water vapor was noted.[111] As mentioned previously, Mn additions to Fe–Cr alloys in sufficient concentrations to promote a Cr–Mn spinel layer can be beneficial by decreasing oxide volatilization.[101] Additions of Mn and Si to Fe–20Cr–20Ni (wt%)

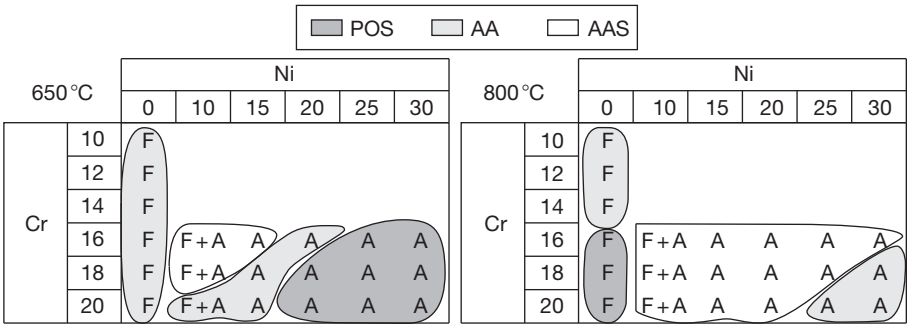

Figure 14 Maps of three behaviors (POS – protective oxide scale, AA – accelerated attack, AAS – accelerated attack with spallation) as a function of Ni and Cr concentrations (wt%) in Fe-based alloys (F – ferritic, A-austenitic). Based on observations for 100 1-h thermal cycles in air + 10 vol. %H_2O at indicated temperatures. Reproduced from Peraldi, R.; Pint, B. A. *Oxid. Met.* **2004**, *61*, 463–483.

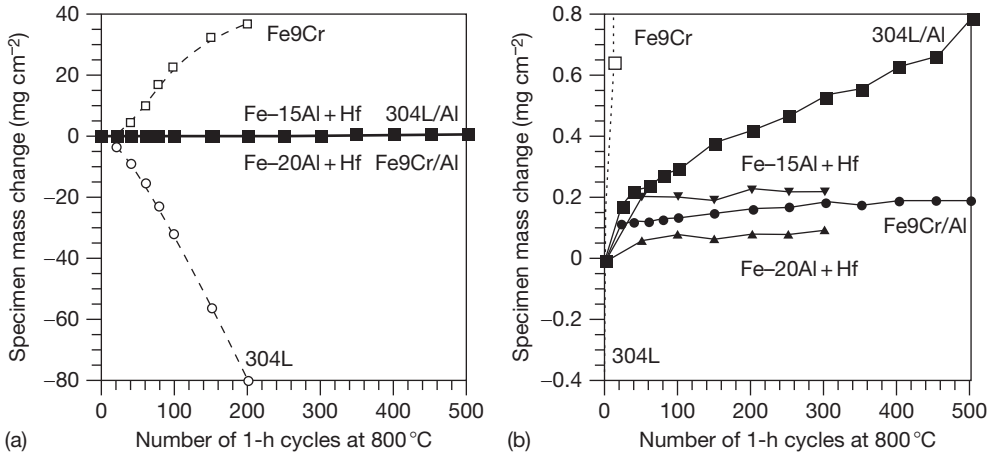

Figure 15 Mass changes for 1-h thermal cycles at 800 °C in air + 10 vol. % H_2O. Selected data from (a) are shown in (b) over a smaller ordinate range. 'Fe9Cr/Al' and '304/Al' denote data for aluminized Fe–9Cr–1Mo steel and type 304L stainless steel, respectively. Concentrations are in wt%. Reproduced from Zhang, Y.; Pint, B. A.; Haynes, J. A.; Tortorelli, P. F. *Oxid. Met.* **2004** *62*, 103–120.

have been reported to have a positive effect on oxidation in air+10% H_2O, with the best performance observed when both elements were present.[111] Henry *et al.* have also indicated a positive effect of Si on oxidation resistance in water vapor.[105] However, recent work of Hammer *et al.* indicates an opposite effect for Si because of the presence of SiO_2 at the oxide–metal interface,[109] a reason suggested by Pint *et al.* for its beneficial effect.[111] These observations illustrate the need to balance the effect of Si as an alloying addition to chromia-forming alloys (for water vapor-containing environments as well for oxidizing conditions, in general). The formation of a silica layer beneath the chromia scales can decrease the overall scale growth rate relative to that of chromia, but only if the Si concentration is insufficient to form a brittle continuous subscale that promotes scale spallation.[112,113]

Kvernes *et al.* found that additions of Al to a Fe–13Cr alloy eliminated the detrimental influence of water vapor in the oxidizing environment (studied up to 2.3% H_2O) if present in sufficient concentration to form a continuous protective layer of Al_2O_3 (1% Al was needed at 680 °C and 4 at.% 980 °C).[102] While there are some reported detrimental effects of H_2O on Al_2O_3-forming alloys,[114] these are relatively minor compared to those reported for chromia- and silica-forming alloys, and protective alumina scales provide substantially improved resistance for alloys in water vapor-containing environments.[115,116] For example, **Figure 15** shows the mass changes of an Fe–Al alloy and ferritic, and austenitic steels (Fe–9Cr and type 304L stainless steel) with and without an aluminized coating in air + 10% H_2O under cyclic oxidation exposures at 800 °C. Both the Fe–Al alloy

and the aluminized specimens (which developed Fe–Al-based surface compositions) showed excellent oxidation resistance despite the presence of H_2O, whereas the uncoated chromia-forming steels oxidized rapidly.

Given the attractiveness of alumina-forming alloys for water vapor (and other) applications, the alloy design problem, therefore, becomes one of assuring the development and maintenance of protective Al_2O_3 scales and devising routes to achieving adequate strength and ductility, particularly under creep conditions, at higher temperatures and H_2O pressures envisioned for advanced uses of such materials. In this system, increasing the Al content (that is, increasing N_B) is limited because aluminum stabilizes the body-centered cubic form of Fe, which inherently exhibits poor high temperature creep strength. (Austenitic Ni-base alumina-forming alloys are available, but their high cost limits their use to a small subset of higher performance applications.) To this end, there has been some recent progress in the design of creep-resistant, alumina-forming austenitic stainless steels based on Fe–(20–25)Ni–(12–15)Cr–(2–4)Al (wt%) with fine dispersions of MC (M = Nb, V, Ti) and intermetallic B2–NiAl and Fe_2Nb Laves precipitates.[117–119] At ~600–800 °C, Nb was found to promote Al_2O_3 layer development, while both Ti and V had the reverse effect for the range of compositions with good creep resistance.[118] In order to maintain a single-phase austenitic matrix microstructure, these compositions contain lean levels of Al and Cr (via a third-element effect) for protective Al_2O_3 scale formation. Therefore, under certain conditions, enhanced internal oxidation and a transition to nonprotective Fe-based oxide nodule formation were observed in water vapor-containing environments compared to exposures in dry air.[119] Enhanced internal oxidation of chromia-forming alloys in the presence of water vapor has also been reported.[110] This effect has been speculated to be the result of hydrogen ingress into the alloy from decomposition of the water vapor, possibly shifting the balance of internal/external oxidation by increasing the oxygen solubility (cf. eqns [2] and [3]).[110]

1.21.7 Conclusions

Given the vast number of possible alloy and environmental combinations, this chapter has focused on general principles and illustrative (but far from exhaustive) examples related to the formation of the most protective scales needed for corrosion resistance of alloys used at high temperatures, Cr_2O_3, Al_2O_3, and SiO_2, with emphasis on the first two. At its essence, alloy design for high temperature corrosion resistance relates to the tailoring of composition and microstructure to promote the preferential formation of the desired POS by selective oxidation, and its subsequent stability and integrity, while balancing the effects on other properties. The attractiveness of alumina as a protective scale for higher temperatures as well as in a variety of aggressive multireactant environments (e.g., water vapor, sulfur) is evident, but widespread applications of appropriate compositions await further alloy and/or coating development that must optimize high temperature corrosion resistance, desired mechanical performance, and/or physical properties.

The goal of the alloy design or materials selection processes should, in most cases, be to maximize the overall oxidation lifetime by accounting for all factors (thermodynamic, kinetic, mechanical, physical, metallurgical, etc.) that influence it. Looking into the future, it is hoped that understanding and control of these factors can be developed to the point that improved lifetime prediction will enable quantification of the effectiveness of various alloying schemes for given application environments and component designs. To this end, it is anticipated that the ability to describe adequately and manipulate reaction product development and kinetic pathways for complex, multiphase alloys and material systems in multireactant, high temperature environments will provide the foundation for approaches to be successful and efficient in alloy design, and selection for a variety of future applications.

This research was sponsored by the U.S. Department of Energy under Contract No. DE-AC05–00OR22725. By accepting the article for publication, the publisher acknowledges that the United States Government retains a nonexclusive, paid-up, irrevocable, worldwide license to publish or reproduce the published form of this work, or allow others to do so, for United States Government purposes.

References

1. Stott, F. H.; Wood, G. C.; Stringer, J. *Oxid. Met.* **1995**, *44*, 113–145.
2. Brady, M. P.; Tortorelli, P. F.; More, K. L.; Payzant, E. A.; Armstrong, B. L.; Lin, H. T.; Lance, M. J.; Huang, F.; Weaver, M. L. *Mater. Corros.* **2005**, *56*, 748–755.
3. Schütze, M. *Protective Oxide Scales and their Breakdown;* John Wiley and Sons: Chichester, 1997.

4. Smialek, J. *JOM* **2000**, *52*, 22–25.
5. Stott, F. H.; Atkinson, A. *Mater. High Temp.* **1994**, *12*, 195–207.
6. Wagner, C. *Z. Elektrochem.* **1959**, *63*, 772–790.
7. Whittle, D. P. In *High Temperature Corrosion*; Rapp, R. A., Ed.; National Association of Corrosion Engineers: Houston, TX, 1981; pp 171–183.
8. Stott, F. H. *Rep. Prog. Phys.* **1987**, *50*, 861–913.
9. Gesmundo, F.; Gleeson, B. *Oxid. Met.* **1995**, *44*, 211–238.
10. Gesmundo, F.; Castello, P.; Viani, F. *Oxid. Met.* **1996**, *46*, 383–398.
11. Gesmundo, F.; Niu, Y. *Oxid. Met.* **1998**, *50*, 1–26.
12. Brady, M. P.; Gleeson, B.; Wright, I. G. *JOM* **2000**, *52*, 16–21.
13. Brady, M. P.; Tortorelli, P. F. *Intermetallics* **2004**, *12*, 779–789.
14. Rapp, R. A. *Corrision* **1965**, *21*, 382–401.
15. Stott, F. H. *Mater. Charact.* **1992**, *28*, 311–325.
16. Tortorelli, P. F.; DeVan, J. H.; McKamey, C. G.; Howell, M. *Ceram. Trans.* **1991**, *19*, 961–968.
17. Yurek, G. J.; Eisen, D.; Garratt-Reed, A. *Metall. Trans. A* **1982**, *13*, 473–485.
18. Caplan, D. *Corros. Sci.* **1966**, *6*, 509–515.
19. Wright, I. G. Oxidation of Iron-, Nickel-, and Cobalt-Base Alloys, Metals and Ceramics Information Center Report MCIC-72–07 (Columbus, OH, Battelle Columbus Laboratories, 1972).
20. Wagner, C. *Corros. Sci* **1965**, *5*, 751–764.
21. Renusch, D.; Veal, B.; Natesan, K.; Grimsditch, M. *Oxid. Met.* **1996**, *46*, 365–381.
22. Niu, Y.; Wang, S.; Gao, F.; Zhang, Z. G.; Gesmundo, F. *Corros. Sci.* **2008**, *50*, 345–356.
23. Guan, S. W.; Smelzer, W. W. *Oxid. Met.* **1994**, *42*, 375–391.
24. Wang, Ge; Gleeson, B.; Douglass, D. L. *Oxid. Met.* **1991**, *35*, 333–348.
25. Gesmundo, F.; Viani, F.; Niu, Y. *Oxid. Met.* 1994, *42*, 409–429.
26. Gesmundo, F.; Niu, Y.; Douglass, D. L. *Oxid. Met.* **1994**, *42*, 465–484.
27. Gesmundo, F.; Viani, F.; Niu, Y. *Oxid. Met.* **1996**, *45*, 51–76.
28. Carter, P.; Gleeson, B.; Young, D. *Acta Mater.* **1996**, *44*, 4033–4038.
29. Durham, R. N.; Gleeson, B.; Young, D. J. *Oxid. Met.* **1998**, *50*, 139–165.
30. Perkins, R. A.; Meier, G. H. In *Proceedings of the Industry-University Advanced Materials Conference II*; Smith, F. W., Ed.; Advanced Materials Institute: Denver, 1989; pp 92–99.
31. Brady, M. P.; Smialek, J. L.; Terepka, F. *Scripta Met.* **1995**, *32*, 1659–1664.
32. Brady, M. P.; Smialek, J. L.; Smith, J.; Humphrey, D. L. *Acta Mater.* **1997**, *45*, 2357–2369.
33. Gleeson, B.; Mu, N.; Hayashi, S. *J. Mater. Sci.* **2009**, *44*, 1704–1710.
34. Whittle, D. P.; Stringer, J. *Philos. Trans. Royal Soc. London* **1980**, *295*(A), 309–329.
35. Pint, B. A. *Oxid. Met.* **1996**, *45*, 1–37.
36. Quadakkers, J.; Singheiser, L. *Mater. Sci. Forum* **2001**, *369–372*, 77–92.
37. Pint, B. A. In *Proceedings of John Stringer Symposium*; Tortorelli, P. F., Hou, P. Y., Wright, I. G., Eds.; ASM International: Materials Park, OH, 2003; pp 9–19.
38. Pint, B. A. *J. Am. Ceram. Soc.* **2003**, *86*, 686–695.
39. Sigler, D. R. *Oxid. Met.* **1993**, *40*, 555–583.
40. Warnes, B. M. *Surf. Coat. Technol.* **2001**, *146–147*, 7–12.
41. Naveos, S.; Oberlaender, G.; Cadoret, Y.; Josso, P.; Bacos, M. P. *Mater. Sci. Forum* **2004**, *461–464*, 375–382.
42. Quadakkers, W. J.; Malkow, T.; Phon-Abellan, J.; Flesch, U.; Shemet, V.; Singheiser, L.; McEvoy, A. J., Ed.; In *Proceedings of the 4th European Solid Oxide Fuel cell Forum;* Elsevier: Amsterdam, 2000; Vol. 2, pp 827–836.
43. Pint, B. A.; More, K. L.; Wright, I. G. *Mater. High Temp.* **2003**, *20*, 375–386.
44. Gupta, D. K.; Duvall, D. S. In *Superalloys*; Gell, M., *et al.* Eds.; TMS: Warrendale, PA, 1984; pp 711–720.
45. Kochubey, V.; Al-Badairy, H.; Tatlock, G.; Le-Coze, J.; Naumenko, D.; Quadakkers, W. J. *Mater. Corros.* **2005**, *56*, 848–853.
46. Funkenbush, A. W.; Smeggil, J. G.; Bornstein, N. S. *Met. Trans.* **1985**, *16A*, 1164–1166.
47. Sigler, D. R. *Metals* **1989**, *32*, 337–355.
48. Smialek, J. L.; Jayne, D. T.; Schaeffer, J. C.; Murphy, W. H. *Thin Solid Films* **1994**, *253*, 285–292.
49. Wright, I. G.; Pint, B. A. In *Proceedings of SF2M*; Journees d'automne, Soc. Francaise de Metallurgie et de Materiaux: Paris, 2000; pp 86–87.
50. Pint, B. A.; More, K. L.; Wright, I. G. *Oxid. Mat.* **2003**, *59*, 257–283.
51. Pint, B. A.; Wright, I. G.; Lee, W. Y.; Zhang, Y.; Prüßner, K.; Alexander, K. B. *Mater. Sci. Eng.* **1998**, *A245*, 201–211.
52. Wright, I. G.; Pint, B. A.; Lee, W. Y.; Alexander, K. B.; Prüßner, K. In *High Temperature Surface Engineering*; Nicholls, J., Rickergy, D., Eds.; Institute of Materials: London, 2000; pp 95–113.
53. Haynes, J. A.; More, K. L.; Pint, B. A.; Wright, I. G.; Cooley, K.; Zhang, Y. *Mater. Sci. Forum* **2001**, *369–372*, 679–686.
54. Cadoret, Y.; Bacos, M. P.; Josso, P.; Maurice, V.; Marcus, P.; Zanna, S. *Mater. Sci. Forum* **2004**, *461–464*, 247–254.
55. Schütze, M. Quadakkers, W. J.; Nicholls, J. R. Eds. *Lifetime Modeling of High Temperature Corrosion Processes*; Maney Publishing: London, 2001.
56. Bennett, M. J.; DeVan, J. H.; Tortorelli, P. F. The Oxidation Behavior of Iron Aluminides in Air at 1300°C In *Microscopy of Oxidation 3*; Newcomb, S. B., Little, J. A., Eds.; The Institute of Materials: London, 1997; pp 233–245.
57. Quadakkers, W. J.; Bongartz, K. *Mater. Corros.* **1994**, *45*, 232–241.
58. Guruppa, I.; Weinbruch, S.; Naumenko, D.; Quadakkers, W. J. *Mater. Corros.* **2000**, *51*, 101–108.
59. Huczkowski, P.; Shemet, V.; Piron-Abellan, J.; Singheiser, L.; Quadakkers, W. J.; Christiansen, N. *Mater. Corros.* **2004**, *55*, 825–830.
60. Pint, B. A.; Porter, W. D.; Wright, I. G. *Mater. Sci. Forum* **2008**, *595–598*, 1083–1092.
61. Evans, H. E.; Donaldson, A. T.; Gilmour, T. C. *Oxid. Met.* **1999**, *52*, 379–402.
62. Newton, R.; *et al.* In *Modeling of High Temperature Corrosion Processes*; Schütze, M., Quadakkers, W. J., Nicholls, J. R., Eds.; Maney Publishing: London, 2001; pp 15–36.
63. Nicholls, J. R.; Newton, R.; Bennett, M. J.; Evans, H. E.; Al-Badairy, H.; Tatlock, G. J.; Naumenko, D.; Quadakkers, W. J.; Strehl, G.; Borchadt, G. In *Modeling of High Temperature Corrosion Processes*; Schütze, M., Quadakkers, W. J., Nicholls, J. R., Eds.; Maney Publishing: London, 2001; pp 83–106.
64. Evans, H. E. *Inter. Mater. Rev.* **1995**, *40*, 1–40.
65. Nesbitt, J. A. *Oxid. Met.* **1995**, *44*, 309–338.
66. Haynes, J. A.; Zhang, Y.; Cooley, K. M.; Walker, L.; Reeves, K. S.; Pint, B. A. *Surf. Coat. Technol.* **2004**, *188–189*, 153–157.
67. Giggins, C. S.; Pettit, F. S. *Oxid. Met.* **1980**, *14*, 363–413.
68. Young, D. J.; Watson, S. *Oxid. Met.* **1995**, *44*, 239–264.

69. DeVan, J. H. In *Oxidation of Intermetallics*; Grobstein, T., Doychak, J., Eds.; TMS: Warrendale, PA, 1989; pp 107–115.
70. Pint, B. A.; Dwyer, M. J.; Deacon, R. M. *Oxid. Met.* **2008**, 211–231.
71. Dettenwanger, F.; Schumann, E.; Rühle, M.; Rakowski, J. M.; Meier, G. H. *Oxid. Met.* **1998**, *50*, 269–307.
72. Shemet, V.; Tyagi, A. K.; Becker, J. S.; Lersch, P.; Singheiser, L.; Quadakkers, W. J. *Oxid. Met.* **2000**, *54*, 211–235.
73. Brady, M. P.; Tortorelli, P. F.; Walker, L. R. *Oxid. Met.* **2002**, *58*, 297–318.
74. Lai, G. Y. *High Temperature Corrosion of Engineering Alloys;* ASM International: Materials Park, OH, 1990.
75. Tjokro, K.; Young, D. J. *Oxid. Met.* **1995**, *44*, 453–474.
76. Krupp, U.; Christ, H.-J. *Oxid. Met.* **1999**, *52*, 277–298.
77. Gleeson, B. In *Materials Science and Technology: Corrosion and Environmental Degradation*; Shütze, M., Ed.; Wiley-VCH: Weinheim, 2000; Vol. 2, Chapter 5.
78. Becker, P.; Young, D. J. *Oxid. Met.* **2007**, *67*, 267–277.
79. Hochman, R. F. In *Properties of High Temperature Alloys*; Foroulis, Z. A., Pettit, F. S., Eds.; The Electrochemical Society: Pennington, NJ, 1976; pp 715–732.
80. Nava Paz, J. C.; Grabke, H. J. *Oxid. Met.* **1993**, *39*, 437–456.
81. Grabke, H. J.; Müller-Lorenz, E. M.; Strauss, S.; Pippel, E.; Woltersdorf, J. *Oxid. Met.* **1998**, *50*, 241–254.
82. Zeng, Z.; Natesan, K. *Oxid. Met.* **2006**, *66*, 1–20.
83. Zhang, J.; Cole, D. M. I.; Young, D. J. *Mater. Corros.* **2005**, *56*, 756–764.
84. Mrowec, S. *Oxid. Met.* **1995**, *44*, 177–209.
85. Gleeson, B.; Douglass, D. L.; Gesmundo, F. *Oxid. Met.* **1990**, *34*, 123–150.
86. Wright, I. G.; Srinivasan, V.; Vedula, K. M. *Mater. High Temp.* **1993**, *11*, 159–166.
87. Green, S. W.; Stott, F. H. *Oxid. Met.* **1991**, *36*, 239–252.
88. Stott, F. H.; Chuah, K. T.; Bradley, L. B. *Mater. Corros.* **1996**, *47*, 695–700.
89. Tortorelli, P. F.; Natesan, K. *Mater. Sci. Eng. A* **1998**, *258*, 115–125.
90. Stott, F. H.; Chong, F. M. F.; Stirling, C. A. *Mater. Sci. Forum* **1989**, *43*, 327–362.
91. Brady, M. P.; Tortorelli, P. F.; More, K. L.; Walker, L. R. Oak Ridge National Laboratory, *Oxid. Met*. 2009 (in press).
92. Schütze, M.; Nöth, M. NACE Paper 517, Proceedings of Corrosion/98; NACE International: Houston, TX, 1998.
93. Du, H. L.; Datta, P. K.; Lewis, D. B.; Burnell-Gray, J. S. *Oxid. Met.* **1996**, *45*, 507–527.
94. Tortorelli, P. F.; Schneibel, J. H.; More, K. L.; Pint, B. A. *Mater. Sci. Forum* **2004**, *461–464*, 1063–1070.
95. Kim, G. M.; Meier, G. H. Breakdown Mechanisms of Al_2O_3, Cr_2O_3, and SiO_2 Scales in $H_2/H_2O/H_2S$ Environments, Oak Ridge National Laboratory report, ORNL/Sub-83–43346/02, 1989.
96. Baxter, D. J.; Natesan, K. *Oxid. Met.* **1989**, *31*, 305–313.
97. Natesan, K. *Oxid. Met.* **1988**, *30*, 53–83.
98. Nicholls, J. R. *JOM* **2000**, *52*, 28–35.
99. Opila, E. J. *J. Am. Ceram. Soc.* **1994**, *77*, 730–736.
100. Opila, E. J.; Jacobson, N. S.; Myers, D. L.; Copland, E. H. *JOM* **2006**, *58*, 22–28.
101. Stanislowski, M.; Wessel, E.; Hilpert, K.; Markus, T.; Singheiser, L. *J. Electrochem. Soc.* **2007**, *154*, A295–A306.
102. Kvernes, I.; Oleveira, M.; Kofstad, P. *Corros. Sci.* **1977**, *17*, 237–252.
103. Asteman, H.; Svensson, J.-E.; Norell, M.; Johansson, L.-G. *Oxid. Met.* **2000**, *54*, 11–26.
104. Rakowski, J. M.; Pint, B. A. NACE Paper 00–517, Proceedings of Corrosion 2000; NACE International: Houston TX, 2000.
105. Henry, S.; Galerie, A.; Antoni, L. *Mater. Sci. Forum* **2001**, *369–372*, 353–360.
106. Peraldi, R.; Pint, B. A. *Oxid. Met.* **2004**, *61*, 463–483.
107. Pint, B. A. Paper GT2005–68495, Proceedings of ASME Turbo Expo 2005; ASME International: New York, 2005.
108. Ehlers, J.; Young, D. J.; Smaardijk, E. J.; Tyagi, A. K.; Penkalla, H. J.; Singheiser, L.; Quadakkers, W. J. *Corros. Sci.* **2006**, 3428–3454.
109. Hammer, J. E.; Laney, S. J.; Jackson, R. W.; Coyne, K.; Pettit, F. S.; Meier, G. H. *Oxid. Met.* **2007**, *67*, 1–38.
110. Essuman, E.; Meier, G. H.; Zurek, J.; Hänsel, M.; Quadakkers, W. J. *Oxid. Met.* **2008**, *69*, 143–162.
111. Pint, B. A.; Peraldi, R.; Maziasz, P. J. *Mater. Sci. Forum* **2004**, *461–464*, 815–822.
112. Bennett, M. J.; Desport, J. A.; Labun, P. A. *Oxid. Met.* **1984**, *22*, 291–306.
113. Hoelzer, D. T.; Pint, B. A.; Wright, I. G. *J. Nucl. Mater.* **2000**, *283–287*, 1306–1310.
114. Maris-Sida, M. C.; Meier, G. H.; Pettit, F. S. *Metall. Mater. Trans. A* **2003**, *34A*, 2609–2619.
115. Zhang, Y.; Pint, B. A.; Haynes, J. A.; Tortorelli, P. F. *Oxid. Met.* **2004**, *62*, 103–120.
116. Pint, B. A.; Shingledecker, J. P.; Brady, M. P.; Maziasz, P. J. paper GT2007–27916, Proceedings of the ASME Turbo Expo 2007l; ASME International: New York, 2007.
117. Yamamoto, Y.; Brady, M. P.; Lu, Z. P.; Maziasz, P. J.; Liu, C. T.; Pint, B. A.; More, K. L.; Meyer, H. M.; Payzant, E. A. *Science* **2007**, *316*, 433–436.
118. Brady, M. P.; Yamamoto, Y.; Santella, M. L.; Pint, B. A. *Scripta Mater.* **2007**, *57*, 1117–1120.
119. Brady, M. P.; Yamamoto, Y.; Santella, M. L.; Maziasz, P. J.; Pint, B. A.; Liu, C. T.; Lu, Z. P.; Bei, H. *JOM* **2008**, *60*, 12–18.

1.19 High Temperature Corrosion Issues for Metallic Materials in Solid Oxide Fuel Cells

L. Singheiser, P. Huczkowski, T. Markus, and W. J. Quadakkers
Forschungszentrum Jülich, IEF2, Jülich, Germany

Symbols

a Activity
C_B Critical chromium concentration in the component (wt%)
ΔV^F Volume change associated with the formation of the relevant point defect (cm^3)
C_v Vacancy concentration ((z) cm^{-3})
C_v^o Equilibrium concentration of vacancies in the unstressed state ((z) cm^{-3})
C_0 Initial chromium concentration in the component (wt%)
d Component thickness (mm)
D Diffusivity ($m^2\ s^{-1}$)
D Interdiffusion coefficient of volatile species in laminar boundary layer ($cm^2\ s^{-1}$)
D_o Oxygen grain boundary diffusion coefficient ($m^2\ s^{-1}$)
J Mass flux (mg $cm^{-2}\ h^{-1}$)
k Oxidation rate constant (mg $cm^{-2}\ h^{-n}$)
k' Parabolic oxidation rate constant ($cm^2\ s^{-1}$)
K Equilibrium constant of the reaction
K_P Parabolic oxidation rate constant ($mg^2\ cm^{-4}\ s^{-1}$)
K_p' Apparent oxidation rate constant ($g^2\ cm^{-4}\ s^{-1}$)
L Characteristic length (cm)
M Molecular weight of volatile species (g mol^{-1})
n Oxidation rate exponent
p Vapor pressure bar (Pa)
P Partial pressure of volatile species (atm)
r Grain size (μm)
R Gas constant ($(cm^3\ atm)\ K^{-1}\ mol^{-1}$)
Re Reynold's number
Sc Schmidt number
t Time (h, s)
t_B Time to breakaway (h)
T Temperature (K, °C)
x Oxide scale thickness (cm, μm)
δ Grain boundary width (nm)
ρ Alloy density (mg cm^{-3})
σ Electrical conductivity (S cm^{-1})
σ_h Hydrostatic component of the stress tensor (Pa)
σ_{xx} Biaxial compressive stress (Pa)
Δm Oxygen uptake per unit area (Weight change) (mg cm^{-2})
Δm^* Critical weight change at which the onset of scale spallation occurs (mg cm^{-2})

ΔH Enthalpy (kJ mol^{-1})
ΔH^* Activation enthalpy (kJ mol^{-1})
ΔS^* Activation entropy (kJ mol^{-1} K^{-1})
ΔV^* Activation volume (m^3 mol^{-1})
$\Delta \mu_o$ Oxygen – potential gradient across the scale (J mol^{-1})

1.19.1 Introduction

A solid oxide fuel cell (SOFC) is an electrochemical device that converts the chemical energy in fuels into electrical energy by utilizing the natural tendency of oxygen and hydrogen to react.[1] Fuel cells are able to convert hydrogen-based fuels with higher efficiency compared to engines and thermal power plants. Compared with other fuel cell systems, the main advantage of the SOFC is its ability to use not only hydrogen but also the currently available fossil fuels (such as methane, butane, or even gasoline and diesel), thus reducing operating costs and flexibility. SOFCs possess no moving parts, so the cells are free of vibration, and therefore, the noise pollution commonly associated with power generation is eliminated.

In an SOFC system, the single cell is constructed with an electrolyte arranged between two porous electrodes (Figure 1). When the oxygen in the flowing air at the cathode side contacts the cathode–electrolyte interface, it catalytically acquires electrons from the cathode and splits into oxygen ions. The oxygen ions diffuse into the electrolyte material and migrate to the anode side of the cell where they react with the fuel at the anode–electrolyte interface thereby giving off water (and/or carbon dioxide if a CO-containing fuel is used), heat, and electrons. The electrons are transported through the anode to the external circuit and back to the cathode, providing a source of useful electrical energy in an external circuit.[1]

Two possible design configurations for SOFCs have been considered, they are: the tubular and the planar design, the latter drawing more attention because it allows higher power densities than the tubular configuration. In the planar design, the components are assembled in flat stacks, with air and fuel flowing through channels, in most cases built into the

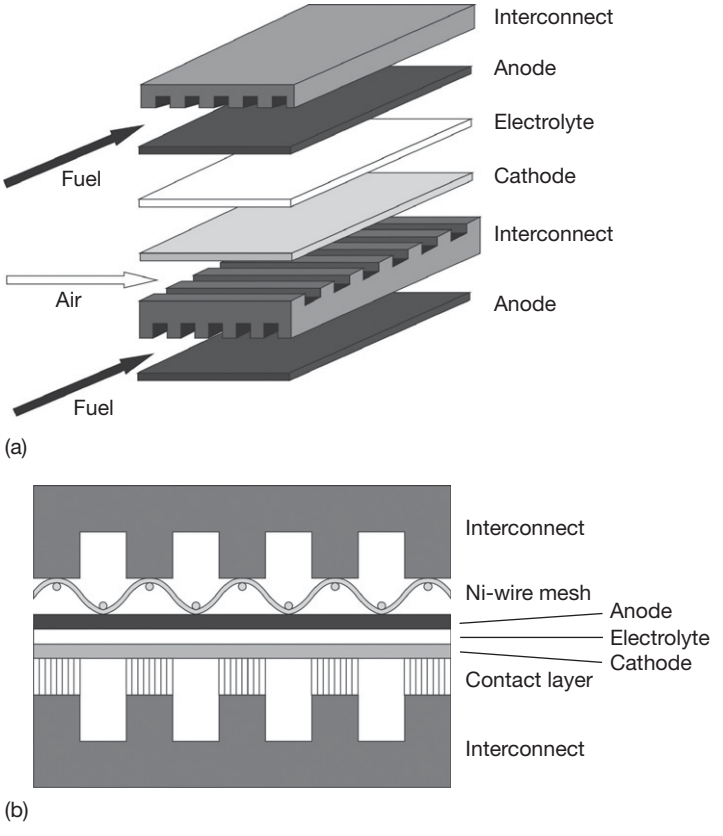

Figure 1 Schematic configuration of a planar SOFC stack (a) and schematic cross-section showing means of contacting between interconnect and electrodes (b).

interconnect (Figure 1). In an SOFC stack, the interconnect thus provides the separation of the gas atmospheres, acts as current collector, and provides the electrical connection between the various single cells.[1] In most planar designs, two additional components are present to improve the electrical contact between the interconnect and the anode and cathode, respectively (Figure 1):

- a Ni-wire mesh at the anode side,
- a ceramic contact layer with high electronic conductivity at the cathode side.

The most important properties required for the interconnector material are high electronic conductivity, thermal stability in the cathode and anode side gas at the high-service temperatures (650–1000 °C), and a thermal expansion coefficient (Table 1) similar to that of the ceramic, electro-active components. Most designs use yttria-stabilized zirconia (YSZ) as electrolyte, $(La,Sr)MnO_3$ as cathode, and Ni/ZrO_2-cermet as anode.[2,3] Ceramic, perowskite type materials on the basis of La-chromite have been shown to possess the property combination required for SOFC interconnects.[3–5] However, in planar cell designs, the interconnector also acts as the mechanical support for the thin electroactive ceramic parts and it is the gas-proof separation between fuel gas and oxidant. Besides, it distributes the gases in co-, cross, and/or counter flow and acts as the constructional connection to the external inlets and outlets. Therefore, the use of metals has a number of significant advantages over La-chromite-based ceramics,[6–9] because they are easier, and therefore cheaper to fabricate than ceramics, they are less brittle, easier to machine, and they can be joined with a number of standard welding and brazing techniques. Additionally, they possess higher electrical and thermal conductivities than most ceramics.

Table 1 Thermal expansion coefficients (between RT and 1000 °C) of ceramic materials used in SOFCs compared with that of a Cr-based alloy and a high-Cr ferritic steel

Material	*TEC ($10^{-6}K^{-1}$)*
8YSZ-	10.5
Ni-YSZ-Cermet	11–12
$(La,Sr)MnO_3$	11–14
$LaCrO_3$	9.5
$(La,Sr)CrO_3$	11
$LaCoO_3$	20–23
$(La,Sr)CoO_3$	18–23
$(La,Ca)(Cr,Co)O_3$	9.5–23
Cr-based ODS alloy	9–10
Ferritic steel Crofer 22 APU	12

Source: Minh, N. Q. *J. Am. Ceram. Soc.* **1993**, *176*(3), 563–588.
Steele, B. C. H. *Solid State Ionics* **2000**, *134*, 3–20.
Singhal, S. C. In *Solid Oxide Fuel Cell (SOFC-V)*; Stimming, U., Singhal, S. C., Tagawa, H., Lehnert, W., Eds.; The Electrochemical Society Proceedings Series, Pennington, NJ, 1997; p 88, PV 97-40.
Stolten, D.; Späh, R.; Schamm, R.; In *Solid Oxide Fuel Cell (SOFC-V)*; Stimming, U., Singhal, S. C., Tagawa, H., Lehnert, W., Eds.; The Electrochemical Society Proceedings Series, Pennington, NJ, 1997; p 88, PV 97-40.
Quadakkers, W. J.; Piron-Abellan, J.; Shemet, V.; Singheiser, L. *Mater. High Temp.* **2003**, *20*(2), 115–127.

1.19.2 Metallic Materials for High Temperature Applications

When using metallic interconnect materials, it has to be considered that the reaction with the anode and cathode side service environments at the high operating temperatures may not only lead to dimensional changes and loss in load-bearing cross sections of the components but also to the formation of oxide scales on the component surface[10,11] which mostly possess low electrical conductivities. The use of noble metals could avoid these problems, however, because of the limited availability and high cost, this solution has been abandoned for large scale application, and conventional high temperature alloys[12,13] have received by far the most attention as possible candidate metallic interconnector materials.

From the viewpoint of oxidation resistance, alloys of the type NiCrAl, CoCrAl, and especially FeCrAl would be the materials to be chosen as construction materials for interconnects.[10] These types of high temperature alloys are able to form extremely slowly growing alumina scales on the material surface upon high temperature exposure. Alumina-forming intermetallics on the basis of NiAl have been considered as interconnector materials[14] because they not only possess superior oxidation resistance but also the required low thermal expansion coefficient. However, like all alumina-forming metallic materials, they have a major drawback; that is, the surface oxide scales possess an extremely low electronic conductivity[15–17] and the use of such materials would thus require measures to overcome this problem by developing special stack designs to assure suitable, long-term stable electrical connections of the interconnector with anode and cathode.

The second type of surface oxide scale which is potentially suitable to provide oxidation/corrosion protection to high temperature alloys is silica.

However, the formation and long-term stability of a protective silica scale requires quite a large amount of silicon additions in nickel-, cobalt-, or iron-based alloys. This leads, in nearly all cases, to substantial embrittlement, thus making the alloys unsuitable as construction materials. Besides, silica has a very low electronic conductivity, leading to similar problems in SOFC application as mentioned above for alumina surface scales.

Most commercially available high temperature alloys rely on the formation of chromia-based surface scales for their oxidation resistance during the high temperature service. Chromia provides less oxidation/corrosion protection than alumina or silica,[11] however, its electronic conductivity in the envisaged SOFC operation temperature range of ~600–1000 °C is orders of magnitude larger than that of alumina or silica. Due to the required similarity of the thermal expansion coefficient with that of the commonly used electroactive ceramic cell materials,[18,19] the chromia-forming alloys, most frequently studied for SOFC interconnector application, are based on the binary alloy system Fe–Cr. The thermal expansion coefficient in Fe–Cr alloys decreases with increasing chromium content[20] and consequently, chromium-based materials have in most cases been considered for application in zirconia electrolyte-based SOFC concepts.[6,21–23] If a slightly higher thermal expansion coefficient is tolerable (typically $12 \times 10^{-6}\,K^{-1}$), for example, the case in Ni-cermet anode-based cell concepts or in cells using ceria as electrolyte, high-chromium ferritic steels are commonly considered as construction material for the interconnect.[20]

1.19.3 Chromium-Base Metallic Interconnectors

The chromia scales forming on pure chromium and chromium-based alloys at high temperatures exhibit slow growth rates. However, when formed during exposure in air or oxygen, the scales tend to buckle and possess poor adherence to the metallic substrate. The buckling is related to substantial compressive growth stresses in combination with vacancy condensation at the scale–metal interface. Tracer studies using ^{18}O isotopes revealed that the latter is related to outward chromium diffusion being the dominating transport mechanism in chromia scales whereas the contribution of oxygen transport is substantially smaller.[24–27] The buckling that occurs at oxidation temperature as a result of lateral growth[24] has frequently been attributed to oxide formation within the scale resulting from the parallel diffusion of chromium and oxygen along chromia grain boundaries.[11,25]

An improvement in scale adherence and reduction in scale growth rate can be obtained by the addition of the so-called reactive elements (REs) such as Y, La, Ce, and Zr, either in metallic form or in the form of an oxide dispersion.[28–31] This RE-imparted change of the most important oxide scale properties is frequently claimed to be related to a suppression of the outward transport of chromium ions.[27–31]

A major drawback of metallic chromium is its high ductile to brittle transition temperature (DBTT) which is known to be significantly affected by interstitially dissolved gaseous impurities such as oxygen and nitrogen.[23] Extensive research work at Plansee led to the development of oxide dispersion strengthened (ODS) chromium which showed substantially improved mechanical properties compared to conventional chromium alloys.[6,7] The ODS materials are manufactured by elemental mixing of the starting powders (abbreviated as MIX alloy) or by mechanical alloying (MA), that is, by high-energy ball milling of chromium and oxide powders in a nonoxidizing environment.[23,32] The latter process can produce a very finely distributed oxide dispersion (typical size ≈ 15 nm) embedded in the chromium matrix, compared to the coarser dispersions in MIX materials, as shown in **Figure 2**.[6,7] The alloys manufactured from the compacted powders possess superior mechanical properties, especially with respect to creep resistance (**Figure 3**). The improvement in ductility depends on a number of factors, for example, dispersion type and distribution. A substantial ductility increase of Cr was obtained by using MgO dispersions,[33] however, no further data on other mechanical properties have yet been reported. The commercial dispersion strengthened Cr alloys especially developed for SOFC application mostly contain a few percent of iron to adjust the thermal expansion coefficient as close as possible to that of the yttria-stabilized zirconia electrolyte.[6,7] As mentioned above, the RE-oxide dispersion not only improves the mechanical properties but also decreases the oxide growth rate and improves the adherence of the oxide to the metallic substrate.[28–32]

1.19.4 Volatile Cr Species

During the operation of planar SOFCs with Cr-based interconnects, rapid degradation of the cell performance has frequently been found and was claimed to

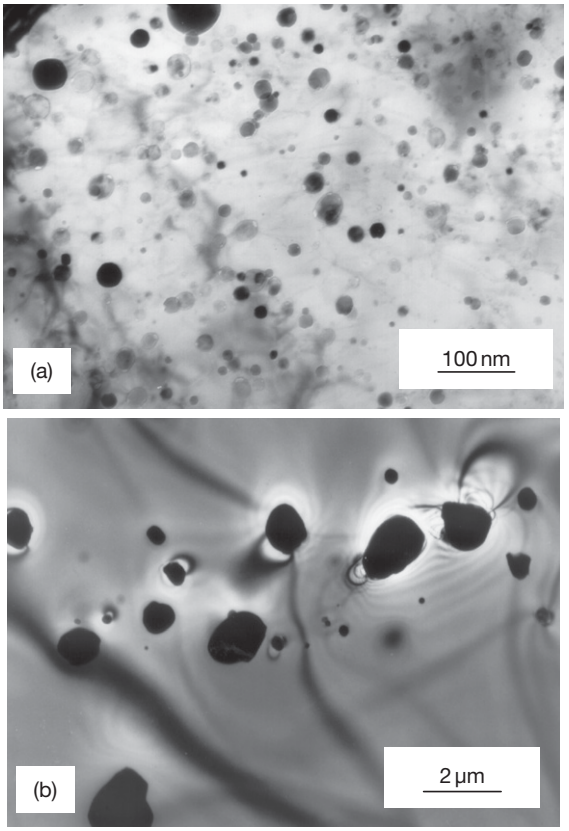

Figure 2 TEM pictures showing distribution of Y_2O_3 dispersions in Cr-based ODS alloys, manufactured by (a) mechanical alloying (MA) and (b) elemental mixing (MIX) of the metal and oxide powders. Reproduced from Quadakkers *et al. Mater. High Temp.* **2003**, *20*(2), 115–127.

be caused by the release of gaseous Cr species, designated in the following sections as 'Cr vaporization,'[34] from the metallic materials. The volatile Cr species are reduced at the triple-phase boundaries between cathode, electrolyte, and air thereby forming solid Cr_2O_3 and other Cr-rich phases which inhibit the electrochemical processes of the cell. This effect is often called 'poisoning' of the cathode and/or the cathode–electrolyte interface. A detailed description of the degradation mechanisms was given by Hilpert *et al.*[35] and Jiang *et al.*[36]

The gas on the cathode side of the SOFC is in most cases normal air which contains the usual minor amounts of water vapor. Several authors have shown that even small amounts of water vapor may substantially increase the 'Cr vaporization' in the high temperature environment. Chromia are known to react with water vapor at elevated temperatures to form volatile (oxy-) hydroxide species, however, the published data on the actual thermodynamic stability of these vapor species still show major differences. The rate of material loss by volatilization is highly dependent on the partial pressures of the volatile species as well as the gas flow rate. It is known that under laminar flow conditions, which are representative of many power generation and propulsion environments, the rate of material loss, $\mathcal{J}$ (in $mg\,cm^{-2}\,h^{-1}$) by evaporation, is given by the following expression[37]:

$$\mathcal{J} = 0.664\ \mathrm{Re}^{1/2}\,\mathrm{Sc}^{1/3}\frac{DPM}{LRT} \qquad [1]$$

where the terms are: $\mathcal{J}$ is the mass flux ($mg\,cm^{-2}\,h^{-1}$); Re, the Reynold's number; Sc, the Schmidt number; D, the interdiffusion coefficient of volatile species in laminar boundary layer ($cm^2\,s^{-1}$); P, the partial pressure of volatile species (atm); M, the molecular weight of volatile species ($g\,mol^{-1}$); L, the characteristic length (cm); R, the gas constant (cm^3 atm) $K^{-1}\,mol^{-1}$; T is the absolute temperature (K).

At high temperatures in dry air, the Cr_2O_3 surface scale present on Cr or Cr-based alloys evaporates according to the following reactions, forming volatile CrO, CrO_2, and CrO_3:

$$Cr_2O_3(s) + \frac{1}{2}O_2(g) \leftrightarrow 2CrO_2(g) \qquad [2]$$

$$Cr_2O_3(s) \leftrightarrow 2CrO(g) + \frac{1}{2}O_2(g) \qquad [3]$$

$$Cr_2O_3(s) + \frac{3}{2}O_2(g) \leftrightarrow 2CrO_3(g) \qquad [4]$$

Ebbinghaus *et al.*[38] summarized and evaluated the available literature data and found $CrO_3(g)$ to be the most abundant vapor species formed upon vaporization in dry air.

In the development of SOFCs that use chromia-forming alloys or conductive chromia-containing ceramics as interconnect, the loss of chromium in the presence of air and water vapor has frequently been identified as a major cause for cell degradation. Therefore, a detailed knowledge on the vaporization behavior and equilibria of chromia in the cathode side environments, especially in the presence of water vapor, is of great importance.

It has been experimentally proven that in wet air the volatile $CrO_2(OH)_2$ is formed by the reaction[35,39]:

$$\frac{1}{2}Cr_2O_3(s) + \frac{3}{4}O_2(g) + H_2O(g) \leftrightarrow CrO_2(OH)_2(g) \qquad [5]$$

At the cathode–electrolyte interface, the

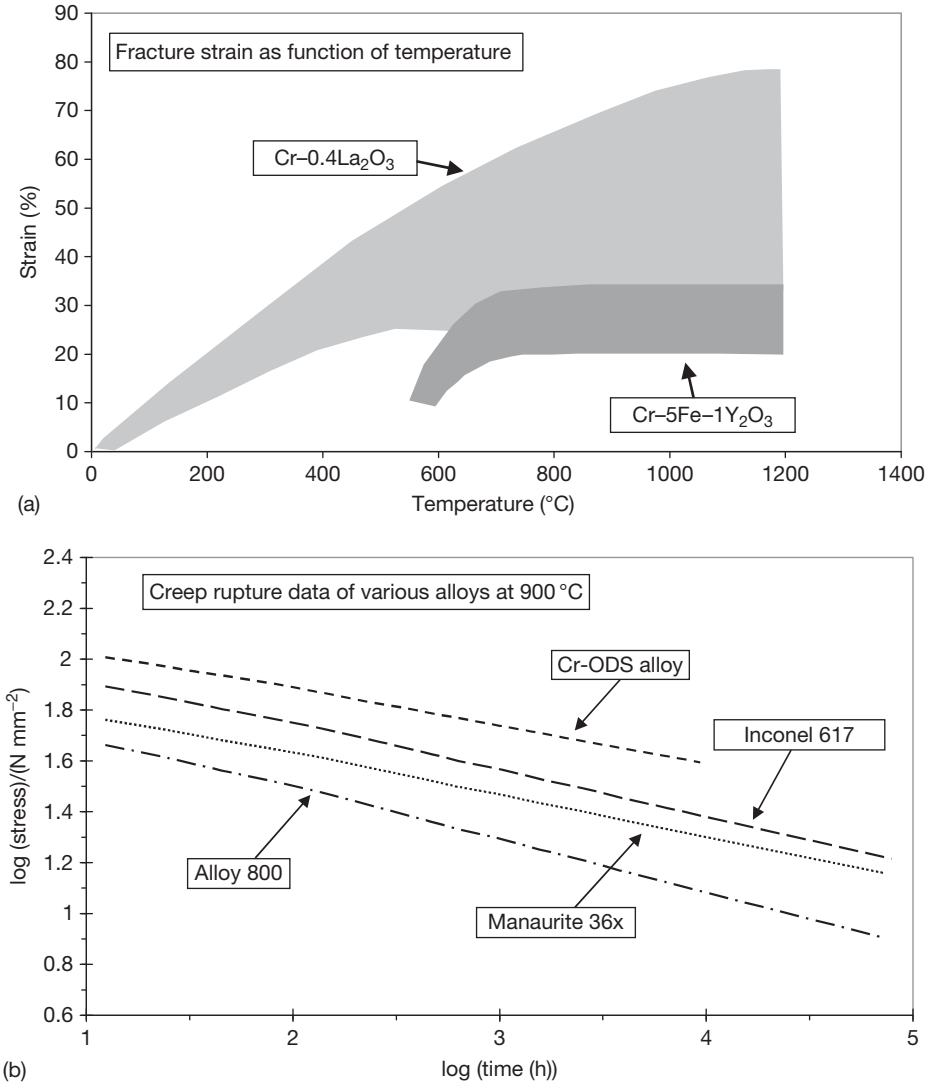

Figure 3 Typical mechanical properties of Cr-based ODS alloys. Reproduced from Quadakkers, W. J.; Greiner, H.; Köck, W. In *Proceedings of the First European Solid Oxide Fuel Cell Forum*, Bossel, U., Ed.; European SOFC Forum, Dr. Ulf Bossel, Morgenacher Str. 2F, CH-5452: Oberrohrdorf, Switzerland, 1994; Vol. 2, p 525.

oxyhydroxide reacts according to:

$$2CrO_2(OH)_2^{(g)} + 6e^- \rightarrow Cr_2O_3^{(s)} + 2H_2O^{(g)} + 3O^{2-} \quad [6]$$

Ebbinghaus[38] derived thermodynamic data for a large number of volatile chromium oxyhydroxides in 1993 using the limited available experimental data at that time, in combination with the molecular constant method. Empirical relationships were employed, where needed, to estimate unknown molecular properties, which in some cases resulted in large uncertainties of the derived thermodynamic data. Assuming the validity of eqn [5], the equilibrium constant K_p of the reaction can be calculated from experiments using the vapor transpiration method. Stanislowski *et al.*[40] have carried out equilibrium vaporization experiments with Cr_2O_3(s) in humid air under SOFC-relevant conditions. The data derived are confirmed by the work of Opila *et al.*[41] The results are shown in **Figure 4**. For comparison, the calculated equilibrium constants according to the thermodynamic database IVTANTHERMO,[42] as well as the data from Ebbinghaus[38] and the experimental results from Gindorf *et al.*[43] are shown. From those results, the

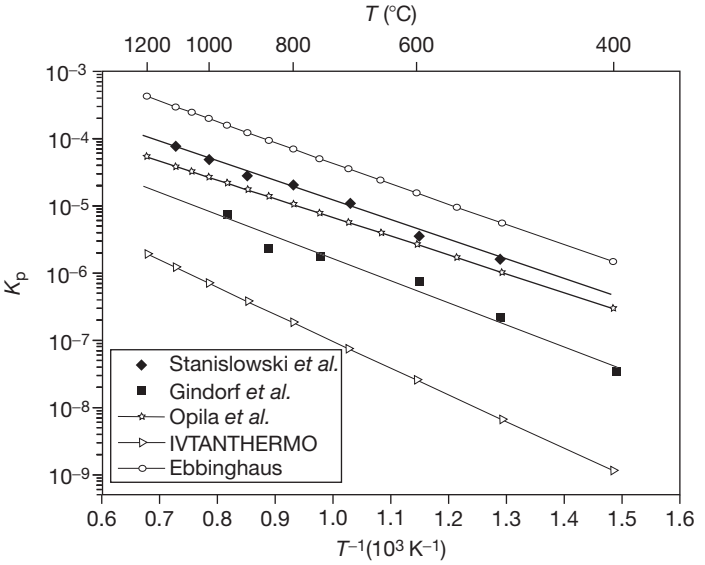

Figure 4 Equilibrium constant for reaction [5], comparing the data of various authors. Reproduced from Stanislowski, M.; Wessel, E.; Hilpert, K.; Markus, T.; Singheiser L. *JES* **2007**, *154*(4), A295–A306.

enthalpy and entropy of formation for the volatile species $CrO_2(OH)_2(g)$ can be calculated. The recommended value resulting from the aforementioned comparison is $\Delta H^0_{f,298} = -767.7 \pm 11\ kJ\ mol^{-1}$.

In technical systems, the actually occurring chromium evaporation also depends on a number of other factors such as the morphology of the outer oxide layer as well as its growth mechanism and its adherence to the metallic material. Therefore, the actual chromium release from Cr-based alloys under operating conditions may quantitatively differ from that measured for pure chromia samples.

Although the significance of reaction [6] occurring at the triple-phase boundaries has been identified in a number of studies, several authors have claimed that the driving force for cell degradation is related to spinel formation in the cathode. This occurs by the reaction of volatile Cr species with elements such as Mn, Co, and Fe present in the perowskite type cathode and/or contact layer. The extent of degradation thus depends on the cathode composition.[36] Several protection methods have been proposed to minimize evaporation of volatile Cr-species, such as coating of the interconnector with La-chromite[44] or -manganite,[45] metallic layers,[46] oxide layers,[46] or aluminum surface enrichment to promote alumina surface scale formation on interconnector areas, where electrical conductivity is not a major issue.[46,47] This subject will be extensively treated in **Section 1.19.16**.

1.19.5 Behavior of Cr-Based Alloys in H_2/H_2O-Based Gases

Several reviews on oxidation of chromium in oxygen or air have been published and substantial information can be found in text books.[10,11,48,49] Far less information is available on behavior of Cr and Cr alloys in SOFC-relevant anode side H_2/H_2O-based gases. Hänsel *et al.*[50] found the oxidation rate of Cr-based ODS alloys at 950–1050 °C in an $Ar/H_2/H_2O$-mixture (equilibrium oxygen partial pressure $\sim 10^{-15}$ bar at 1000 °C) to be higher than in high-pO_2 environments (air, Ar/O_2), whereby the difference could only partly be explained by formation of volatile oxides and hydroxides in the high-pO_2 gases (**Figure 5**). In the $Ar/H_2/H_2O$-environment, where the formation of volatile Cr species is negligible, the alloys tended to form whisker type oxide morphologies, the extent of whisker formation being decreased by an 'optimum' addition of a reactive element (oxide dispersion).

Chromia scales formed on Cr-based ODS alloys in $Ar/H_2O/H_2$ are far less voided and exhibit substantially better adherence to the metallic substrate than those formed in air or oxygen.[24,50] This effect of atmosphere composition on scale adhesion is even more dramatic in the case of non-RE-doped alloys and elemental chromium. Water vapor can eliminate or at least decrease oxide porosity by providing rapid gas phase transport of oxygen within the void space. As proposed earlier,[51] the oxygen transport is facilitated

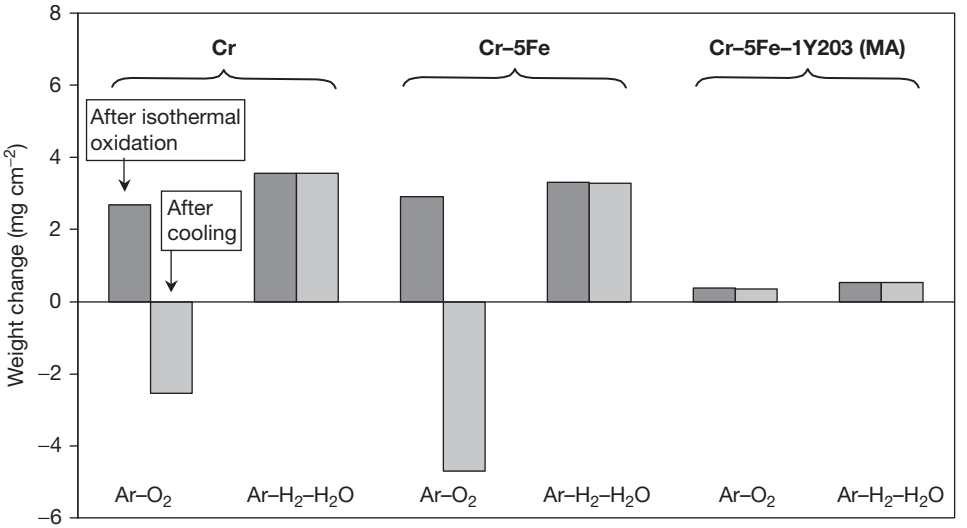

Figure 5 Weight changes of Cr, Cr–5Fe, and the ODS alloy Cr–5Fe–Y_2O_3 after isothermal oxidation in Ar–20% O_2 and Ar–4% H_2–2% H_2O at 1000 °C and after subsequent cooling to room temperature. The results illustrate, especially for the RE-free materials, the importance of the test atmosphere for oxide adherence. Reproduced from Hänsel, M.; Quadakkers, W. J.; Singheiser, L.; Nickel, H. *Report Forschungszentrum Jülich, Jülich FRG, Jül-3583*, 1998; ISSN 0944-2952.

by the reaction between $H_2O^{(g)}$ and oxide. Water vapor reacts with the oxide on the side of the cavity nearest to the metal, whereas the formed hydrogen reacts with the outer surface of the void. These redox reactions are coupled with gas phase mass transfer, and the inward oxygen transport through the scale via this mechanism leads to new oxide formation at the scale–metal interface, reducing the probability of void formation and subsequent scale detachment.[52] Enhanced inward oxygen transport, which was proven by two-stage oxidation tests using Ar–H_2–$H_2^{18}O$,[53] accounts satisfactorily for the observed decrease in the scale porosity and improved scale adhesion. The change in the dominating growth mechanism of chromia in the high- and low-pO_2 environments is accompanied by a substantial change in oxide grain size, the grains being much smaller when formed in the low pO_2 environment. More detailed information on the differences in chromia scale formation in low- and high-pO_2 gases can be found in the chapter 'Oxidation in Steam and Steam/Hydrogen Environments.'

1.19.6 Mixed Gas Corrosion of Cr-Based Alloys

During service in the SOFC cathode side environment, the reaction of oxygen with the surface of the Cr-based interconnect may be affected by the presence of nitrogen and/or water vapor. Especially, for non-RE-doped chromium and chromium alloys, reaction with nitrogen is of major concern because it leads to environmentally induced embrittlement during high temperature exposure.[23] This is caused by nitrogen dissolution in the metal or the alloy as well as by nitride formation beneath the chromia scale (**Figure 6**). The sensitivity for nitrogen uptake depends on the gas tightness of the chromia layer because nitrogen transport between gas atmosphere and metal or alloy is known to occur via gas molecules rather than via solid state diffusion through the scale. Generally, it can be said that the thick chromia scales formed on non-RE-doped Cr and Cr alloys are more permeable for nitrogen than the thinner, that is, more protective, scales on RE- or RE-oxide-doped metals or alloys. This observation in fact indicates that also in a purely oxidizing environment, the protective properties of the chromium oxide layer are to a large extent determined by its ability to prevent molecular transport of oxidizing species rather than by the exact concentration of point defects in the chromia lattice.

The second reactive gaseous species which is of importance during air oxidation of Cr-based materials is water vapor. As extensively described in the previous section, the first well-known effect of water vapor is that it promotes the formation of volatile chromium oxyhydroxides.[35,38,39,54] A second, less apparent effect was observed by Hänsel *et al.*[50] The authors found the scale growth rate in the temperature range 950–1050 °C to be enhanced if water vapor was

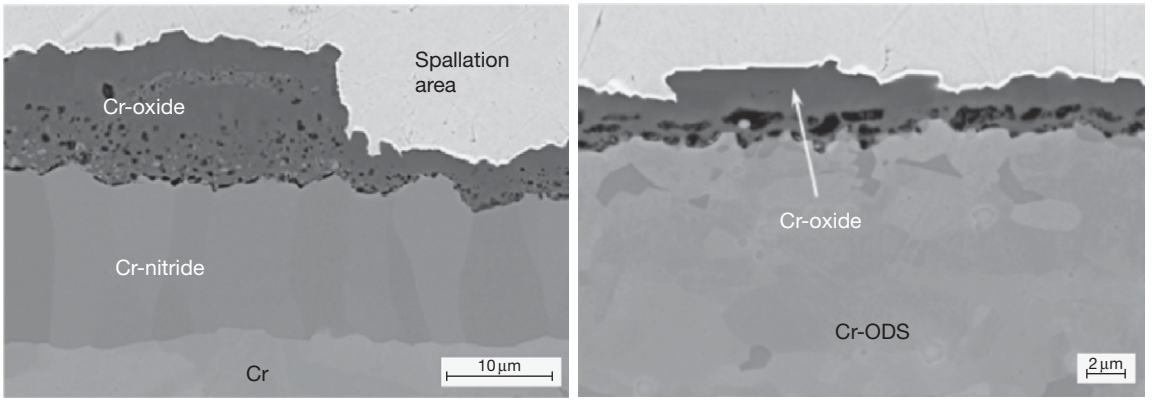

Figure 6 Metallographic cross-sections (SEM images) of Cr and Cr ODS alloy after 1000 h oxidation at 800 °C in air.

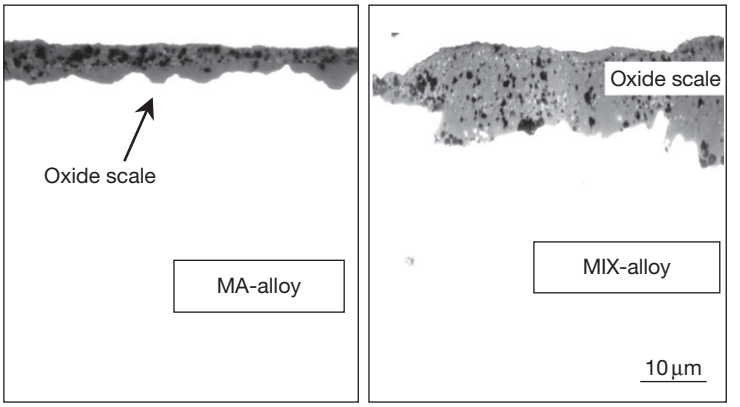

Figure 7 Oxide scales on Cr-based ODS alloys, manufactured by different processes (cf. **Figure 2**) after 1000 h exposure in a H_2O–H_2 mixture at 950 °C. Reproduced from Hänsel, M.; Quadakkers, W. J.; Singheiser, L.; Nickel, H. *Report Forschungszentrum Jülich, Jülich FRG, Jül-3583*, 1998; ISSN 0944-2952.

present in air or Ar–O_2, and this effect was related to the enhanced oxidation of cracks which formed in the chromia layers as a result of growth stresses even during the isothermal oxidation. The enhanced oxidation may therefore be related to a dissociation mechanism occurring in voids and cracks,[51] similar to that described in the previous section.

Depending on the cell operating conditions and the actually used fuel, the mixed gas corrosion of Cr-based alloys also has to be considered in the anode side gas. If carbon-containing gas species such as CO and/or CH_4 are present, all Cr-based alloys tend to form a subscale layer containing Cr-carbide, that is, mainly $Cr_{23}C_6$, sometimes in combination with Cr_7C_3.[21,55] In the case of a CH_4-based test gas, the carbides exist as a near-continuous layer,[21] whereas in the case of a CO-based gas, the subscale layer mainly consists of an oxide–carbide mixture.[55] The extent of carbon attack, which occurs by molecular transport of the carbon-containing gas species through the oxide scale, decreases with the decreasing growth rate of the oxide layer.[55] This again is a strong indication that in the case of chromia scales, protectiveness means to a large extent resistance against molecular transport from the gaseous atmosphere to the metal or alloy. In the case of Cr-ODS alloys, the protective scale properties depend on the dispersion type, and even more on the dispersion distribution[50,55,56] and thus on the alloy manufacturing process (**Figures 7** and **8**).

1.19.7 Oxidation Rates of Chromium-Based Alloys

If chromia growth proceeds by diffusion of point defects in the oxygen and/or chromium sublattice,

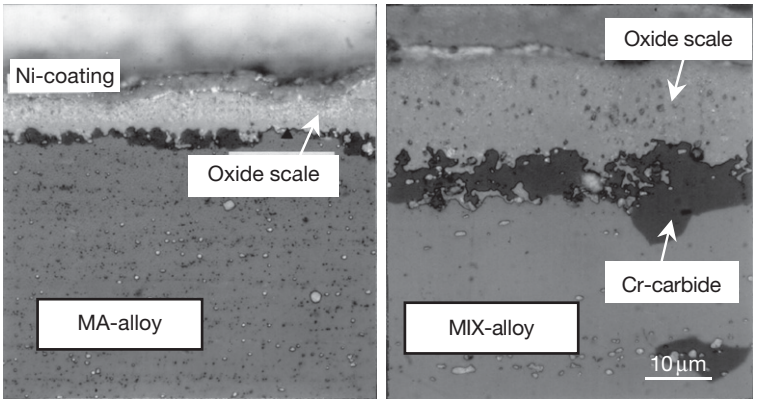

Figure 8 Oxide scales on Cr-based ODS alloys, manufactured by different processes (cf. **Figure 2**) after 1000 h exposure in a CO-containing H_2O–H_2 mixture at 950 °C. Reproduced from Hänsel, M.; Quadakkers, W. J.; Singheiser, L.; Nickel, H. *Report Forschungszentrum Jülich, Jülich FRG, Jül-3583*, 1998; ISSN 0944-2952.

scaling rates could be calculated by Wagner theory,[11] if the self-diffusion coefficients of chromium and oxygen were known. Lattice self-diffusion coefficients of both chromium and oxygen in chromia are reported to be extremely small, whereby the literature data show considerable scatter. At 1100 °C, the self-diffusion coefficients are in the range 10^{-17} to 10^{-18} $cm^2\,s^{-1}$.[57–59] These low values indicate that it is extremely difficult to achieve true equilibrium, and this might be an important reason for the discrepancies in the literature diffusion data.

The oxidation rate of Cr-based ODS alloys is substantially slower than that of pure Cr or Cr alloys without addition of a RE (oxide).[48–50] It is difficult to give a quantitative figure of this reduction in oxidation rate by the RE addition because Cr as well as Cr-based alloys frequently do not exhibit the classical parabolic time dependence for oxide scale growth. Classical Wagner's oxidation theory[11] predicts the scale growth to obey a parabolic time dependence, if oxidation is controlled by diffusion of metal and/or oxygen ions through the oxide lattice:

$$x^2 = K't \qquad [7]$$

in which x is the scale thickness, t the time, and k the parabolic oxidation rate constant. Expressed as oxygen uptake per unit area (Δm), eqn [7] is mostly written in the following form:

$$(\Delta m)^2 = K_p t \qquad [8]$$

For Cr, Cr alloys, and especially Cr-based ODS alloys, eqn [8] is not often followed[50,51,60] because the assumptions made to describe scale growth by eqn [8] are mostly not completely fulfilled.[61–63] Chromia growth proceeds to a large extent via rapid diffusion paths, such as oxide grain boundaries,[26,27,58] the density of which is in most cases not time-independent. For ODS alloys, the parabolic rate constant K' (in $cm^2\,s^{-1}$) for such cases can be written as[62]:

$$K' \sim \frac{D_o \delta}{r}\frac{\Delta\mu_o}{RT} \qquad [9]$$

in which D_o is the oxygen grain boundary diffusion coefficient; δ, the grain boundary width; r, the grain size; and $\Delta\mu_o$, the oxygen-potential gradient across the scale. In many cases, r increases in scale growth direction, and/or with oxidation time.[62,63] This frequently leads to a K'-value which decreases with increasing oxidation time (**Figure 9**).

Another factor which has to be considered in evaluating oxide growth rates is that the scales are not completely gas-tight due to the formation of micro voids and micro cracks and consequently, molecular gas transport contributes to the growth process. Furthermore, the above-mentioned formation of volatile oxides and/or hydroxides can affect chromia growth, especially, at high temperatures in oxygen-rich environments (see previous sections).

In the case of ODS alloys, it has to be considered that the desired low oxide growth rate of the scales requires the RE to become incorporated in the surface oxide layer.[31,64] This occurs by embedding the dispersions in the inwardly growing oxide scale and subsequent diffusion of the RE to the oxide grain boundaries.[60] Consequently, the beneficial effect does not immediately become apparent but appears only after a certain oxidation time, with the consequence that a rapid oxide growth rate occurs which then subsequently decreases to very low values.[50,60,62,63]

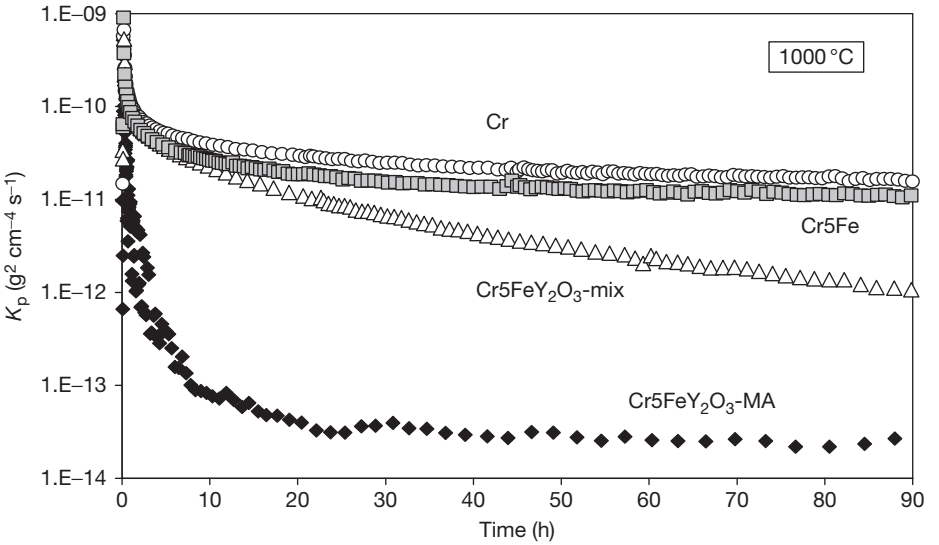

Figure 9 Typical time dependence of the apparent oxidation rate K_p' during isothermal oxidation of Cr and Cr alloys in Ar/H_2/H_2O at 1000 °C. Reproduced from Hänsel, M.; Quadakkers, W. J.; Singheiser, L.; Nickel, H. *Report Forschungszentrum Jülich, Jülich FRG, Jül-3583*, 1998; ISSN 0944-2952.

As a reduction in scale growth rate in a RE (oxide) containing Cr alloy requires the RE to become incorporated into the scale,[64,65] the RE-imparted reduction in chromia growth rate is strongly affected by size and distribution of the oxide dispersion.[50] Small dispersoid sizes and small distances between the dispersoids are required to obtain an optimum growth rate reduction. The oxidation rates of the ODS alloys thus depend on the manufacturing process.[50] In fact, tracer studies using $^{18}O_2$ revealed that even by the optimum dispersion distribution, which can be achieved in commercial alloys, the resulting RE distribution in the growing scale does not completely block outward chromium transport. A virtually complete suppression of outward growth can be obtained by a strong surface enrichment of the RE, for example, by applying a RE-oxide coating or by RE-ion implantation.[65,66]

1.19.8 Electronic Conductivity of Chromia-Based Scales

Chromia is an electronic conductor and at high temperatures (>1000 °C) the electrical conductivity is found to be independent of the oxygen partial pressure.[67–69] At lower temperatures, the concentration of electronic defects due to the intrinsic electronic equilibrium becomes so small that the chromia changes into an extrinsic electronic conductor, the electronic conductivity being dominated by the presence of impurities or dopants.[68–73] The electrical conductivity of bulk chromia samples at 800–1000 °C (**Figure 10**) has been reported to be in the range 1×10^{-2} to 5×10^{-2} S cm^{-1},[68–71,74] although lower values have also been found.[75–77] Below 1000 °C Mg, doped chromia is a p-type conductor, whereby the electronic conductivity only marginally depends on oxygen partial pressure.[68] In H_2–H_2O mixtures, the conductivity is affected by dissolved protons,[68,70] whereas in TiO_2-doped chromia, no effect of hydrogen on conductivity is detected.[69] In the temperature range 400–1000 °C, the Ti-doped chromia is an n-type conductor at low oxygen partial pressures and a p-type conductor at near atmospheric oxygen partial pressure. Nagai *et al.*[75,78,79] found the electronic conductivity to increase by Y_2O_3 or La_2O_3 doping and decrease with increasing oxygen partial pressure, although this effect is not very pronounced, especially at high temperatures (**Figure 11**). The highest increase of the conductivity was observed for doping by NiO, whereby in this case no oxygen partial pressure dependence was found. Also doping by CeO_2 or Fe_2O_3 increased the conductivity, however, the effect was much smaller than that observed for NiO-doping.

1.19.9 High-Chromium Ferritic Steels

High-chromium ferritic steels are to be preferred over Cr-based (ODS) alloys if lower SOFC service

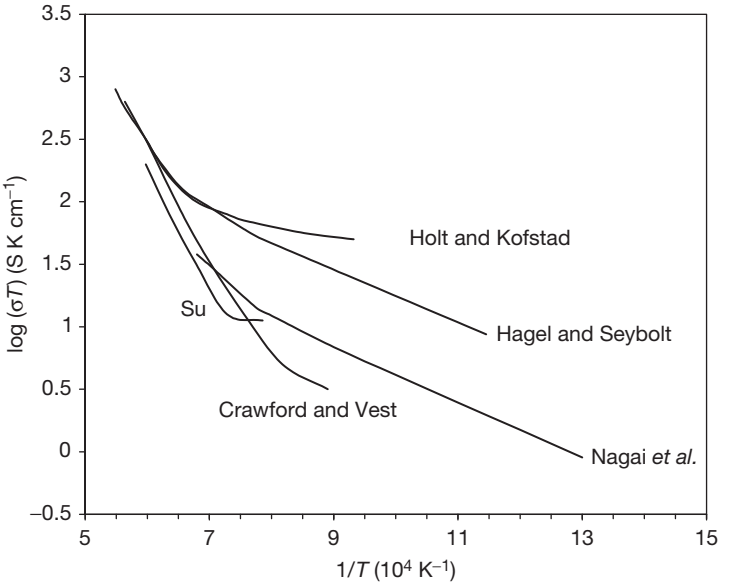

Figure 10 Electrical conductivity of Cr_2O_3 as function of reciprocal temperature in air (derived from Holt,[68–71] Hagel and Seybolt,[74] Nagai and Fujikawa,[75] Su,[76] and Crawford and Vest[77]).

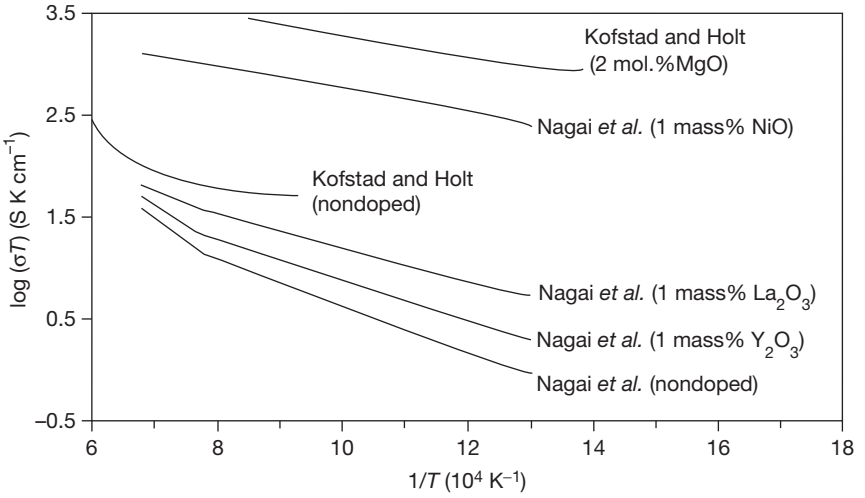

Figure 11 Effect of dopants on electrical conductivity of Cr_2O_3 as a function of reciprocal temperature (derived from Nagai and Fujikawa,[75] Nagai and Ohbayashi,[78] Nagai *et al.*[79]).

temperatures (<900 °C) prevail, especially in the case of anode-supported cell designs, in which the CTE is mainly governed by the anode rather than the electrolyte. In commercially available ferritic steels, for high temperature application, the Cr content varies between ~7 and 28 mass% (**Table 2**). During air exposure, for example, in the temperature range 700–1000 °C, the oxide scale composition strongly varies with Cr concentration and the oxidation resistance generally increases with increasing Cr content.[80] On low-Cr steels (<5% Cr), the scales consist of nearly pure Fe-oxide accompanied by internal oxide precipitates of Cr_2O_3 and/or $FeCr_2O_4$-spinels. With increasing Cr content, the scales become richer in spinel and chromia, which is accompanied by a decrease of the scale growth rate. Formation of a highly protective, single-phase chromia layer requires a chromium content of ~17–20%, the

Table 2 Main alloying elements in selected commercially available, high-Cr ferritic steels

Material	*Commercial name*	*DIN-Nr.*	*Composition of Cr, Al, Si, Mn, and others (mass%)*				
X10CrAl7	Ferrotherm 4713	1.4713	6–8	0.5–1	0.5–1	–	
X10Cr13	Nirosta 4006	1.4006	11.9	<0.02	0.49	0.30	
	–	1.4509	15–16	<1.25	<0.5	<1	Ti/Nb
X10CrAl18	Ferrotherm 4742	1.4742	17.3	1.04	0.93	0.31	
X10CrAl24	Ferrotherm 4762	1.4762	23.5	1.82	1.01	0.38	
			24.4	1.38	1.14	0.54	
Fe-25Cr-Mn	RA 446	–	24.2	–	0.43	0.67	
Fe-26Cr-1Mo	E Brite	–	25.8	–	0.24	0.02	
X18CrN28	Sandvik 4C54	1.4749	26.5	<0.01	0.47	0.70	
Fe-29Cr-4Mo-Ti	Al29–4C	–	27.3	–	0.26	0.28	Ti

exact concentration depending on surface treatment, minor alloying additions, environment, and impurities (e.g., C, S, P). The critical Cr content for obtaining protective chromia scale formation on ferritic steels increases with increasing temperature.

Minor alloying additions of Mn, Ti, Si, and Al may substantially alter the oxidation behavior of commercial ferritic steels (**Figure 12**). During high temperature exposure, the two first mentioned elements tend to become incorporated in the scale,[81] although titanium can also be present in the form of internal titania precipitates in the subsurface region. Titanium can become dissolved in chromia at low oxygen partial pressures, that is, in the inner part of the scale, whereas at higher oxygen partial pressures, that is in the outer part of the scale, it tends to become reprecipitated. It is therefore frequently found in the form of titania crystals at the scale–gas interface.[81] The incorporation of Ti into the oxide scale tends to increase the chromia growth rate, especially at higher temperatures. Mn possesses only a small solubility in chromia and it is frequently found in the form of a Cr–Mn-spinel layer in the outer part of the oxide scale.

Oxides of Si and Al mostly prevail as internal oxides rather than being incorporated into the external scale. This is related to the higher thermodynamic stability of those oxides compared to that of chromia. If the Al and/or Si contents in the steel are increased to ~1%, the internal silica and/or alumina precipitation can change into protective, external scale formation, which is accompanied by a strong decrease in oxidation rate.[80] The exact Si and/or Al levels, at which this effect occurs, depend on temperature, Cr content, concentrations of minor alloying additions, and component surface treatment. The latter effect was, for example, clearly demonstrated during air oxidation at 800 °C of an 18Cr, 1Al steel (DIN designation 1.4742) which formed poorly protective Fe- and Cr-rich heterogeneous oxide mixtures accompanied by internal oxidation and nitridation of aluminum on coarse ground surfaces but tended to form a protective alumina scale on polished surfaces.[80,82,83]

This finding illustrates that only slight changes in alloy composition, service temperature, or design-related parameters can fundamentally change the oxidation properties of high-chromium ferritic steels (**Figure 12**). Additionally, a change from one oxide scale type into another may occur during long-term service due to the depletion of minor alloying elements such as Al, Si, Mn, and/or Ti in the alloy matrix because of their low concentrations.

External silica scale formation is rarely observed during oxidation of commercial ferritic steels. Sometimes silica, mostly in the amorphous state, locally forms relatively dense subscales at the interface between alloy and chromia-based external layer (**Figure 13**). This effect is frequently accompanied by an increased tendency of the oxide scales to spallation during thermal cycling, probably due to the extremely small thermal expansion coefficient (CTE) of the silica compared to that of the alloy and/or due to the transformation, for example, into crystoballite.

As already mentioned before, the formation of alumina or silica in the form of a closed (sub-) layer is generally not desired in SOFC application, because it can dramatically increase the contact resistance between the interconnector and the electrodes or contact materials.

1.19.10 Behavior of High-Cr Ferritic Steels in Anode Gas

A change of the test atmosphere from air to an anode gas simulating H_2O–H_2 mixture for high-Cr ferritic

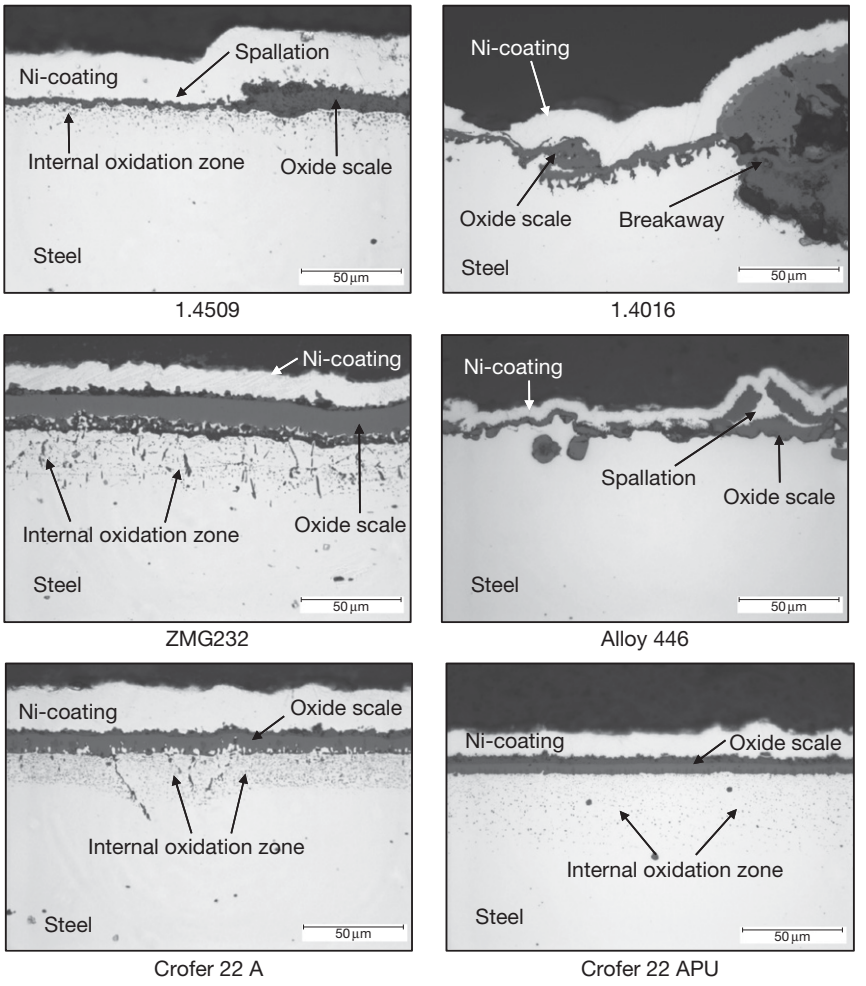

Figure 12 Different types of oxide scale formation on high-Cr ferritic steels after 1000 h oxidation at 900 °C in air.

steels has similar effects as described for the Cr-based alloys. The morphology of the chromia and spinel-rich surface layers is slightly modified[84] and the adherence of the scale is improved.[80] The oxide growth rates of ferritic steels with Cr contents above about 20% in H_2O–H_2 mixtures are generally similar or slightly smaller than those in air. This observation seems at first sight to be surprising because chromia scales on Cr-based alloys showed an opposite gas composition dependence of the oxidation rates, as described in **Section 1.19.5**. The behavior of the high-chromium ferritic steels in anode and cathode side gases was shown[85] to be governed by the differences in growth mechanisms of a Cr–Mn-spinel layer which forms on top of the inner chromia scale. In anode gas, the spinel tends to be stoichiometric $MnCr_2O_4$, whereas in air it is $Mn_{1+x}Cr_{2-x}O_4$. The latter grows by the outward lattice diffusion of cations whereas the spinel in simulated anode gas grows via grain boundary diffusion[86] resulting in plate and whisker type oxide morphologies and microvoids at the chromia–spinel interface (**Figures 14** and **15**). Further details can be found in the section on 'Oxidation in Steam and Steam/Hydrogen Environments.'

Due to the substantially lower equilibrium oxygen partial of the anode gas compared to that of the cathode side environment, the thermodynamic driving force for oxide formation in anode gas is in fact substantially smaller than that in the cathode gas. In ferritic steels with Cr contents which are lower than ~20%, the anode side environment can, for instance during the transient stages of oxidation, suppress formation of oxides with low thermodynamic stability.[80] This may for such steels result in a type and morphology of external and internal oxide formation which completely differs from that occurring during air or oxygen

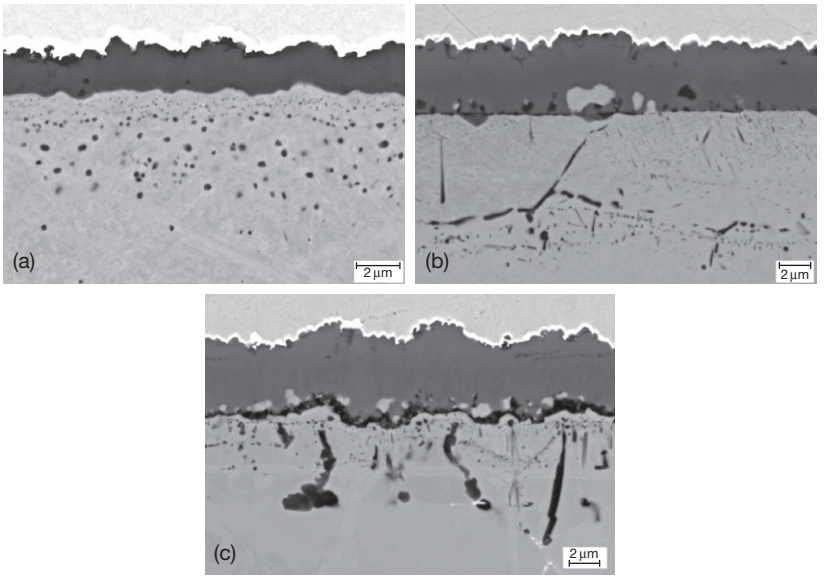

Figure 13 Oxide scale formation on ferritic steels with 22% Cr after 1000 h exposure at 800 °C in air showing effect of Si/Al content: (a) 0.01% Si/Al, (b) 0.1% Si/Al, and (c) 0.4% Si/0.2% Al. Reproduced from Quadakkers *et al*. *Mater. High Temp*. **2003**, *20*(2), 115–127.

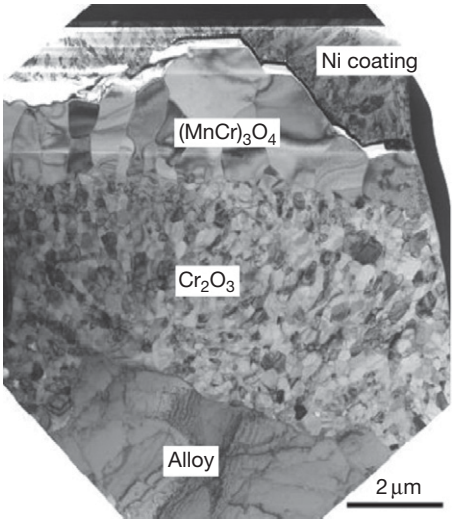

Figure 14 TEM bright field image of oxide scale (spinel + chromia) on high-Cr ferritic steel after exposure in air at 900 °C for 1000 h. Reproduced from Essuman *et al. Corros. Sci*. **2008**, *50*, 1753–1760.

exposure.[80] This, however, does not mean that the oxidation rates are generally smaller in anode than in cathode gas. An example of higher growth rates in anode gas was already illustrated for the case of pure chromia scales formed on chromium-based alloys (**Section 1.19.5**) and was also found to occur in the case of Mn-free, high-purity Fe–Cr and Ni–Cr model alloys with Cr contents well above 20%.

A more dramatic effect of atmosphere dependence of oxidation rates can be found for ferritic steels with intermediate Cr contents of 10–20%. In atmospheres in which water vapor is the main oxidizing species, the tendency to form a protective external chromia-based scale is substantially suppressed compared to that during air or oxygen exposure.[88,89] Presence of high amount of water vapor thus shifts the critical Cr content for obtaining protective chromia scale formation towards higher concentrations. This has as a result, that a steel with an intermediate Cr content, which may form a protective chromia-based scale during air or oxygen exposure, may form a poorly protective, Fe-base oxide scale during exposure in a high water vapor-containing environment. The tendency to nonprotective scale formation is suppressed by the small size of alloy grain and surface deformation of the steel. Details on the mechanisms of nonprotective scale formation in wet gases can be found in the chapter on 'Oxidation in Steam and Steam/Hydrogen Environments.'

The formation of poorly protective, Fe-rich oxides will, of course, occur only if the equilibrium oxygen partial pressure in the gas is higher than the dissociation pressures of the Fe oxides. In an H_2–H_2O gas mixture at typical SOFC temperatures in the range 600–900 °C, this is the case if the H_2/H_2O ratio is lesser than ~1. Thus, if pure hydrogen is used as fuel in an SOFC stack with an intermediate Cr content,

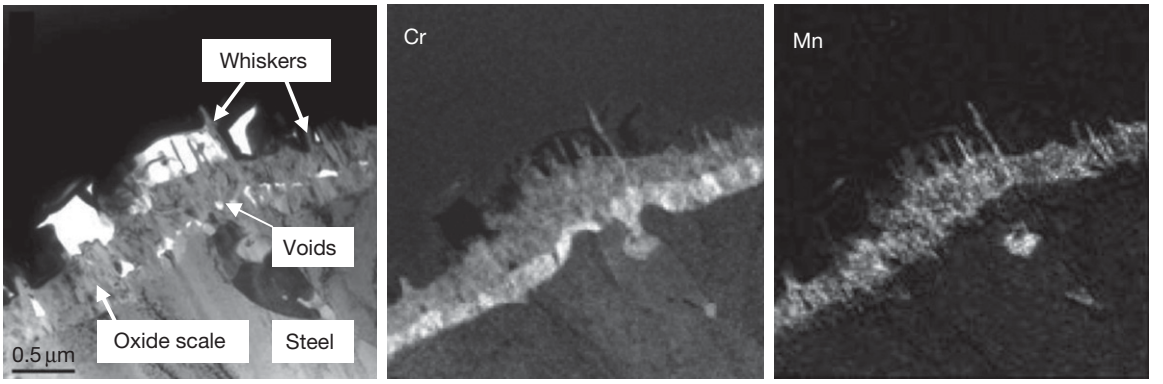

Figure 15 TEM bright field image and EELS maps for Mn and Cr of the oxide scale on high-Cr ferritic steel during 15 h exposure at 800 °C in Ar–4%H_2–2% H_2O. Reproduced from Essuman *et al. Corros. Sci.* **2008**, *50*, 1753–1760.

ferritic interconnect, the poorly protective oxides will not form in areas near the gas entrance of the stack but only in gas flow direction nearer to the gas outlet, the critical areas being determined by the actually applied fuel utilization.

1.19.11 Ferritic Steels in Anode Gases Containing Carbonaceous Gas Species

Applying internal or external reforming, SOFCs can handle a variety of fuels containing carbon-containing gas species. The simulated anode gas will then contain gas species such as CO, CO_2, and/or CH_4 in addition to H_2 and H_2O.

The carbon transfer which may occur from the service environment to the alloy can, depending on the prevailing gas composition, the temperature, and the properties of the interconnect material, result in a number of material degradation mechanisms, that is, carburization, metal dusting, and C deposition. The latter two effects occur only if the C activity of the environment is larger than unity. Thereby C deposition may hamper the cell performance, for example, by blocking narrow gas passages, but it does not necessarily affect the properties of the interconnect adversely. Metal dusting, however, is a process which commonly results in a very rapid damage of metallic materials. The mechanisms of the metal dusting process are still a subject of scientific debate and a detailed description of it falls outside the scope of this chapter. The reader is referred to a number of references[90,91] in which the various steps in the degradation process are described.

Table 3 Typical gas composition at SOFC gas inlet and gas outlet (assuming 80% fuel utilization) when using reformed gasoline as fuel

Gas species	*Gas composition (vol.%)*	
	Stack inlet	*Stack outlet*
H_2	20	4
CO	22	4.4
N_2	52	52
CO_2	3	20.6
H_2O	2.5	18.5
CH_4	0.5	0.2

When using carbonaceous fuels, the interconnect may be subjected to environments in which the oxygen partial pressure and the carbon activity substantially change as a function of time. For illustration, we use the application of an SOFC stack in mobile application using reformed gasoline as fuel (**Table 3**).

During the heating process of the stack to the operation temperature, the interconnect is subjected to a gas with a high-carbon activity and thus a substantial danger for occurrence of metal dusting exists, especially in the temperature range 400–650 °C (**Figure 16**). When reaching the SOFC operation temperature of 800 °C, the carbon activity is lower than unity and metal dusting attack is no longer possible. Due to the electrochemical reactions occurring at the anode side of the cell, the concentrations of CO, CH_4, and H_2 decrease in gas flow direction, whereas the concentrations of CO_2 and H_2O increase. As shown in the Cr–O–C stability diagram in **Figure 17**, chromia is the stable phase in equilibrium with the gas atmospheres at 800 °C. However, it is well established[55,90] that under such conditions, formation of internal Cr carbide, for example, $Cr_{23}C_6$, may occur even if the equilibrium

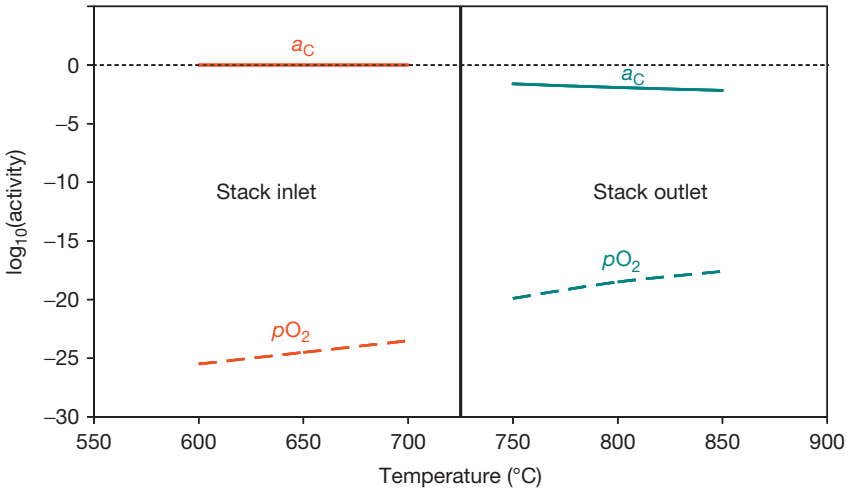

Figure 16 C activities and oxygen partial pressures of gases in **Table 3** as a function of temperature.

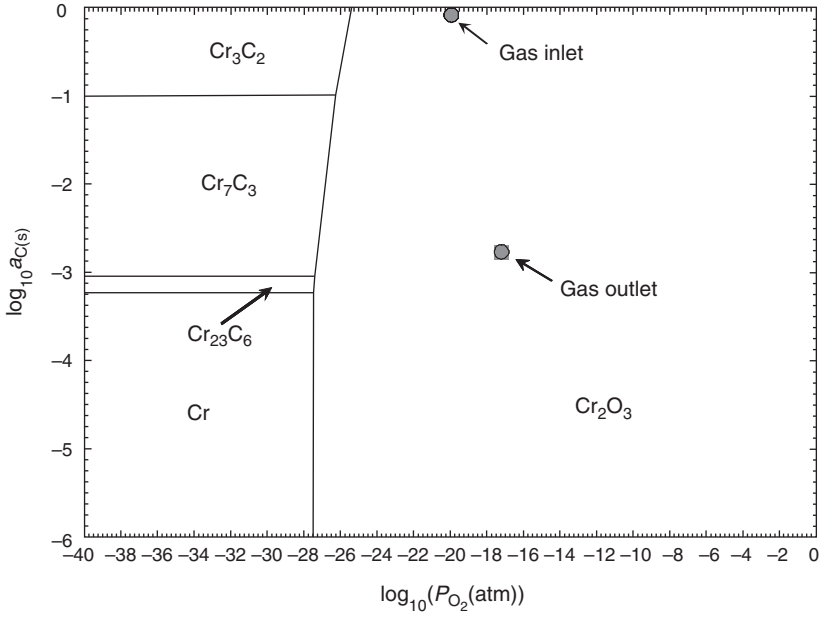

Figure 17 Cr–O–C stability diagram at 800 °C and the location of the equilibrium oxygen partial pressures and carbon activities of the atmospheres in **Table 3**.

carbon activity in the gas is smaller than the activity required to form the carbide. This is related to a decrease in oxygen partial pressure and a parallel increase in carbon activity upon molecular transport of the gaseous carbonaceous species through the surface oxide layer.[90]

Internal carburization in the case of ferritic steels does not generally result in formation of a continuous subscale carbide layer, but in formation of finely distributed carbide precipitates in the alloy matrix. The formation of these Cr-rich carbides ($Cr_{23}C_6$ and/or Cr_7C_3) leads to material embrittlement and additionally depletes Cr from the ferritic matrix in the surface-near region of the alloy. The latter may result in a reduced Cr availability for transport to the surface required for protective scale formation and thus in a deterioration of the steel oxidation resistance.

During stack operation, the steel interconnect may thus be subjected to service environments

which, from the viewpoint of thermodynamic driving forces, cycle between metal dusting and oxidizing/carburizing conditions. It is generally accepted that metal dusting as well as internal carburization can be prevented by the presence of a protective surface oxide layer which prohibits molecular transport of carbonaceous species to the metal surface. The resistance against metal dusting and carburization thus increases with increasing protective properties of the surface oxide layer. Ferritic steels with Cr contents well above 20% showed higher metal dusting and carburization resistance under SOFC conditions than lower Cr steels and, for example, 18–20% Cr austenitics.[92]

1.19.12 Ferritic Steels Designed for SOFC Application

The optimum steel composition for an SOFC interconnector will depend on the used cell design (e.g., electrolyte or anode supported concept) and the service conditions (temperature, thermal cycling, fuel gas composition, and required service life).[93] If a YS–ZrO_2 electrolyte-supported design is considered, a low thermal expansion coefficient of $\sim 10 \times 10^{-6}\,K^{-1}$ is a crucial requirement for the interconnector. Using binary Fe–Cr alloys with Cr contents commonly present in ferritic steels (see **Table 2**), such a low value cannot be achieved.[20] Some authors, therefore, alloyed steels on the basis of Fe–20% Cr with large amounts of refractory elements such as Mo or W[94,95] to decrease the CTE. The oxidation resistance could be improved by adding small amounts of REs. However, it has to be demonstrated whether the scaling rates are sufficiently small for the materials to be used in SOFCs with the required high-application temperature of 1000 °C in electrolyte-supported designs.

Substantially lower service temperatures between 600 and 800 °C seem to be more appropriate if ferritic steels are to be used as interconnectors. In this temperature range, for example, ceria should be used as electrolyte[3] or an anode-supported cell design allowing an extremely thin YS–ZrO_2 electrolyte should be applied.[82,83] The choice of such concepts would require interconnectors with CTEs similar to that of the Ni/ZrO_2-anode, that is, in the range $11–12 \times 10^{-6}\,K^{-1}$. Such CTE values can be achieved by ferritic steels with Cr contents of ~20%.

Quadakkers *et al.*[96,97] studied the suitability of model steels with Cr contents of 16–25% and evaluated the effect of various RE additions to achieve an optimum combination of low scale growth rate and excellent scale adherence. La appeared to be the preferred RE addition, mainly because it does not, contrary to other commonly used REs, form intermetallic compounds with iron. This allows La to become evenly distributed in the alloy rather than being precipitated in the form of intermetallics on the alloy grain boundaries, for example, observed if Y or Ce additions[98] are being used. The actual scale growth rate strongly depends on commonly present minor alloying additions/impurities such as Mn and Ti (**Figures 18** and **19**). Although in RE-doped steels, very protective behavior can be obtained if the Cr content is just 16–18%, a substantially higher level was chosen to obtain a larger 'Cr reservoir' to counteract the danger for the occurrence of breakaway oxidation due to the presence of high water vapor contents in the anode gas,[99] Cr loss due to interaction with contacting materials[100] or rapid exhaustion of the Cr reservoir in very thin interconnects. Small amounts of Mn and Ti were added to obtain external spinel formation which is known to decrease the formation of volatile Cr species.[43,97,101] Minor Ti additions were added to obtain fine internal oxide precipitates of titania (**Figure 20**) which results in strengthening of the surface-near alloy region thus reducing the tendency for occurrence of surface wrinkling caused by relaxation of oxidation-induced stresses during thermal cycling. By defining low Al and Si contents (**Table 4**), formation of oxide scales with a very low electrical resistance was obtained for alloys of the type FeCrMn(La/Ti) (**Figures 21** and **22**). The low Al/Si content also prevents extensive internal oxide formation which was found to affect not only the mechanical properties of the surface-near regions but also the growth rate of the external chromia scale. The latter is related to a volume increase imparted by the internal oxide formation resulting in outward metal flow and inclusions of metallic nodules in the scale.[86,102]

Further indications for development of steels which are especially designed for SOFC application are described elsewhere,[103–105] however, no detailed information in respect to steel composition prevail. Recently, developments on the basis of 22% Cr-containing ferritic steels with systematic variations of minor alloying additions were described.[106] Honnegger *et al.*[107] developed high-Cr ferritic materials for SOFC application that were produced by powder metallurgical techniques, thus allowing incorporation of oxide dispersions to achieve dispersion strengthening. The mechanical alloying

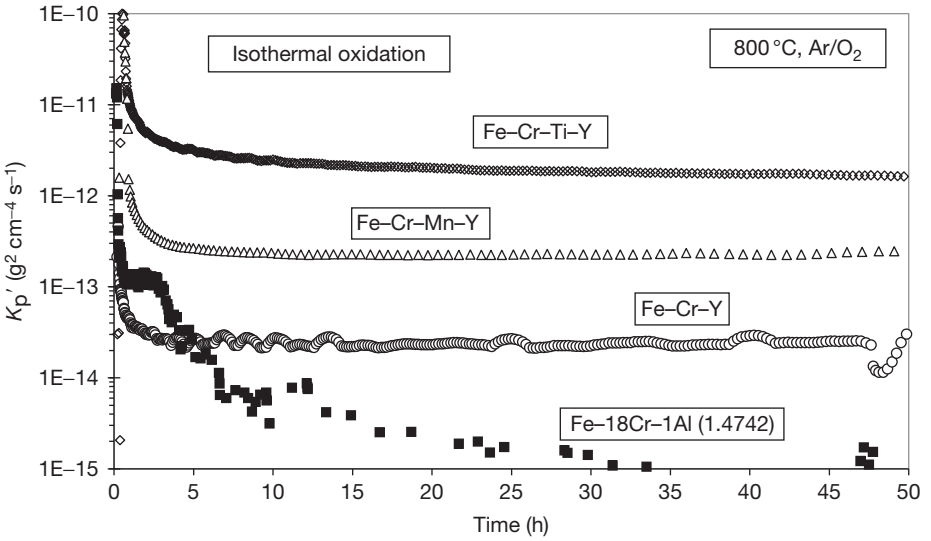

Figure 18 Apparent oxidation rate K_p' as function of time for various types of FeCr alloys during isothermal oxidation at 800 °C in Ar/oxygen. Reproduced from Piron-Abellan, J.; Quadakkers, W. J. Development of ferritic steels for application as interconnect materials for intermediate temperature solid oxide fuel cells (SOFCs), Report Forschungszentrum Jülich, Jül-4170, March 2005; ISSN 0944-2952.

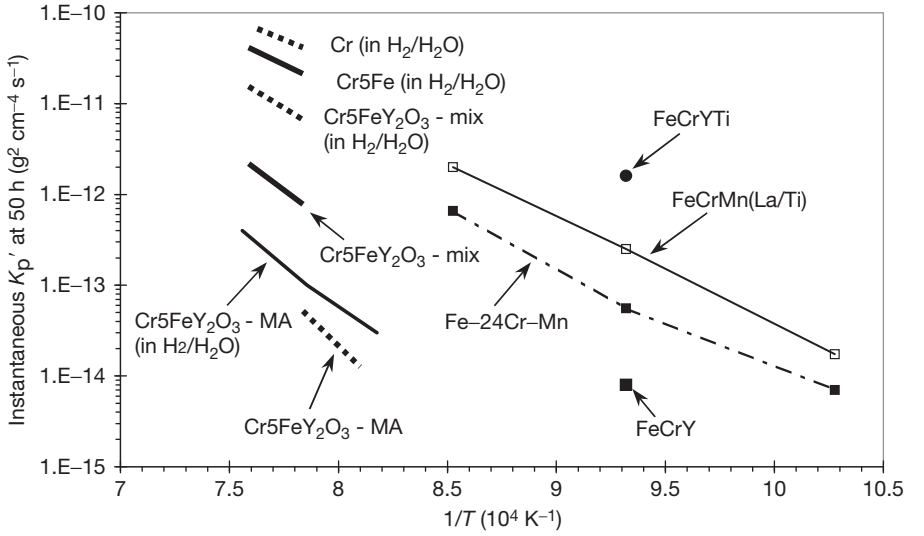

Figure 19 Instantaneous apparent oxidation rates at 50 h of FeCr-RE and FeCrMn(La/Ti) alloys during isothermal oxidation at various temperatures compared with data of various Cr alloys. If not indicated, data relate to exposures in Ar/20% O_2 (compiled from Refs. 24, 50, 85).

process allows to produce materials with substantially higher concentrations of REs (here Y) than can be obtained by conventional alloy manufacturing methods (**Table 4**). Therefore, the ferritic ODS steels generally exhibit lower oxidation rates than RE containing wrought alloys produced by conventional methods. A high RE content in the surface regions can also be obtained by applying a RE-containing coating. In this way, the oxidation rate of a commercial, ferritic 18% Cr steels can substantially be decreased.

A major disadvantage of high-Cr ferritic steels is their tendency to form σ-phase and α′ precipitates at lower temperatures. As both processes lead to

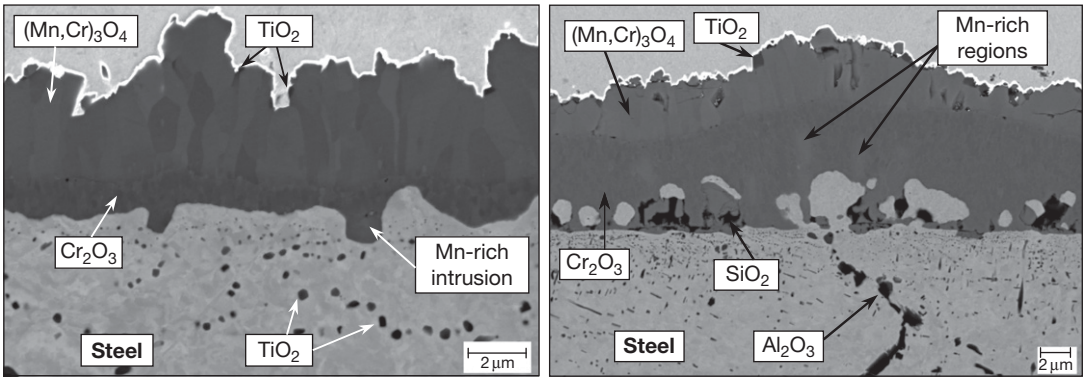

Figure 20 Cross sections of oxide scales on type FeCrMn(La/Ti) steels after 6000 h exposure in air at 800 °C showing effect of minor Al/Si additions. Left: Crofer 22APU, right: Crofer 22A. (Mark the differences in magnification). Reproduced from Huczkowski, P.; Christiansen, N.; Shemet, V.; Niewolak, L.; Piron-Abellan, J.; Singheiser, L.; Quadakkers, W. J. *Fuel Cells* **2006**, *2*, 93–99.

Table 4 Compositions of selected ferritic steels specially developed for SOFC application

Steel	*Composition (mass%)*									
	Fe	*Cr*	*Mn*	*Ti*	*La*	*Si*	*Al*	*Ni*	*Zr*	*Others*
Crofer 22A	Bal.	22	0.4	0.05	0.09	<0.01	<0.01	<0.002	–	
Crofer 22APU	Bal.	22	0.4	0.06	0.07	0.11	0.12	0.16	–	
Crofer 22H	Bal	22	0.4	0.06	0.09	0.3	0.01	0.1	–	Nb, W
ZMG232	Bal.	22	0.5	–	–	0.36	0.19	0.31	0.13	
Sanergy HT	Bal.	22	<0.5	–	–	<0.3	–	–	–	Nb, Mo, Ce
IT11	Bal.	26	0.04	0.2	–	–	0.03	–	–	Mo; Y_2O_3

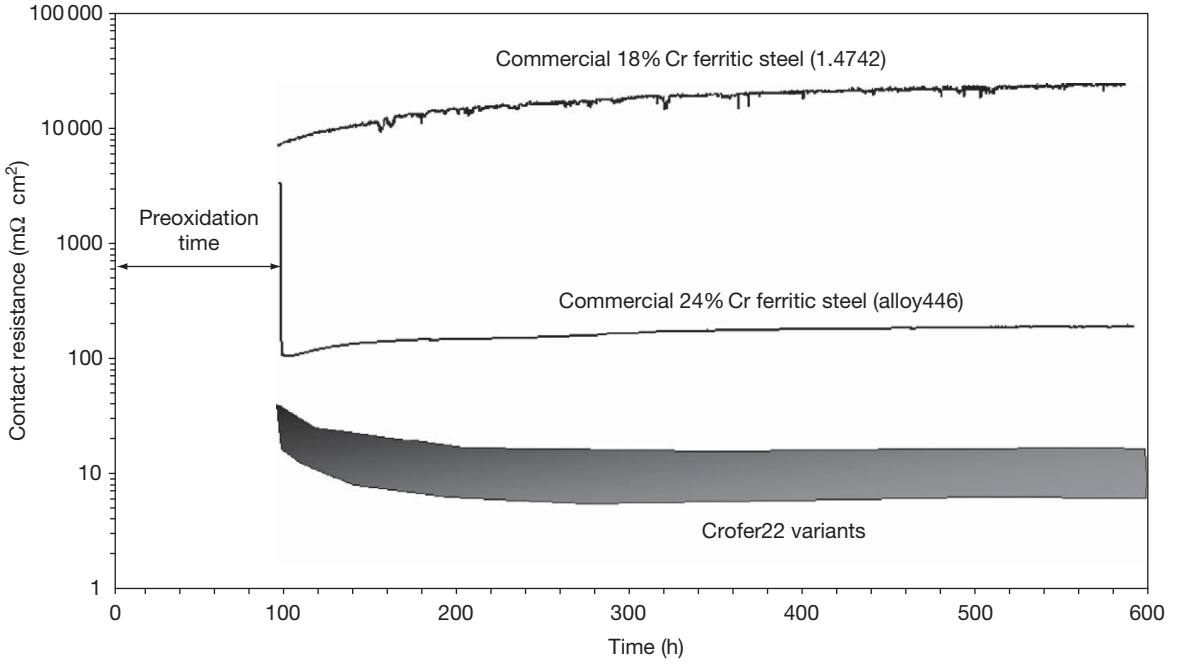

Figure 21 Contact resistance of various steels during isothermal exposure at 800 °C in air. Reproduced from Piron-Abellan, J.; Quadakkers, W. J. Development of ferritic steels for application as interconnect materials for intermediate temperature solid oxide fuel cells (SOFCs), Report Forschungszentrum Jülich, Jül-4170, March 2005; ISSN 0944-2952.

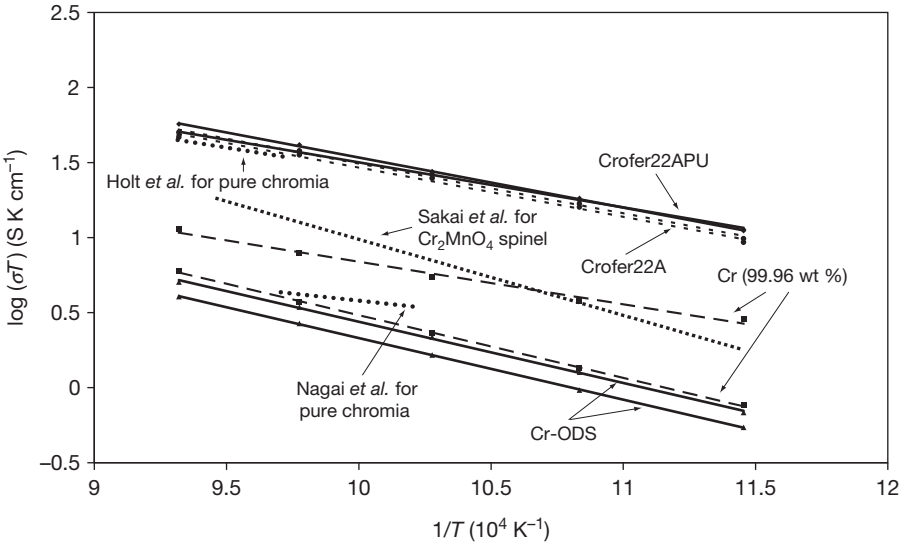

Figure 22 Temperature dependence of 'apparent' conductivity for various steels during exposure at 800 °C in air. Reproduced from Huczkowski, P.; Christiansen, N.; Shemet, V.; Niewolak, L.; Piron-Abellan, J.; Singheiser, L.; Quadakkers, W. J. *Fuel Cells* **2006**, *2*, 93–99.

embrittlement of the steels, the exact alloy composition has to be carefully adapted to the actual envisaged application temperature. For instance, steels with a Cr content of more than 25% are prone to σ-phase formation even at temperatures as high as 800 °C, whereby the σ-phase formation is known to be promoted, for example, by alloying additions of Mo and Si. Hammer *et al.*[102] illustrated that the σ-phase nucleation is not only affected by the alloy purity but also by the actual prevailing service environment. Steels with Cr contents substantially lower than 20% behave more 'forgiving' in respect to embritteling precipitate formation. However, they are prone to breakaway oxidation in high water vapor-containing anode side gases.[108] They also may easily run into breakaway oxidation in cathode side gases in the case of thin components, as will be illustrated in the next section.

1.19.13 Effect of Component Thickness on Oxidation Behavior

Especially in mobile applications of SOFCs, a reduction in weight of the fuel cell stack is a major design requirement. Weight reduction can be achieved by reducing the interconnect thickness from the common few millimeters to a few tenths of a millimeter. When using such thin components of high-chromium ferritic steels, it has to be considered that the long-term formation of protective chromia-based oxide scales is not only governed by the alloy chromium content but also by the chromium reservoir in the prevailing interconnect. The growth of the chromia-based surface scale consumes chromium from the metallic material with the result that after long-term service, the initial chromium concentration in the component (C_0) may decrease to such a low level (C_B) that the growth of the protective scale can no longer be sustained. The time until depletion of the chromium content down to this critical concentration will be shorter in thin than in thick components. Huczkowski *et al.*[109] used a simplified expression derived from studies on breakaway oxidation of alumina-forming FeCrAl alloys to predict the time (t_B) until the occurrence of breakdown of the protective chromia scale for selected high-chromium ferritic steels as a function of temperature and component thickness (**Figure 23**)

$$t_B = \left[2.3 \times 10^{-3}(C_0 - C_B)\frac{\rho d}{k}\right]^{1/n} \qquad [10]$$

Here k and n are the oxidation parameters; d, the component thickness; and ρ, the alloy density. In deriving this expression, it was assumed that the chromium depletion profiles beneath the oxide scales are virtually ideally flat. Experimental data showed that in the temperature range 800–900 °C, this assumption was a close description of the actual

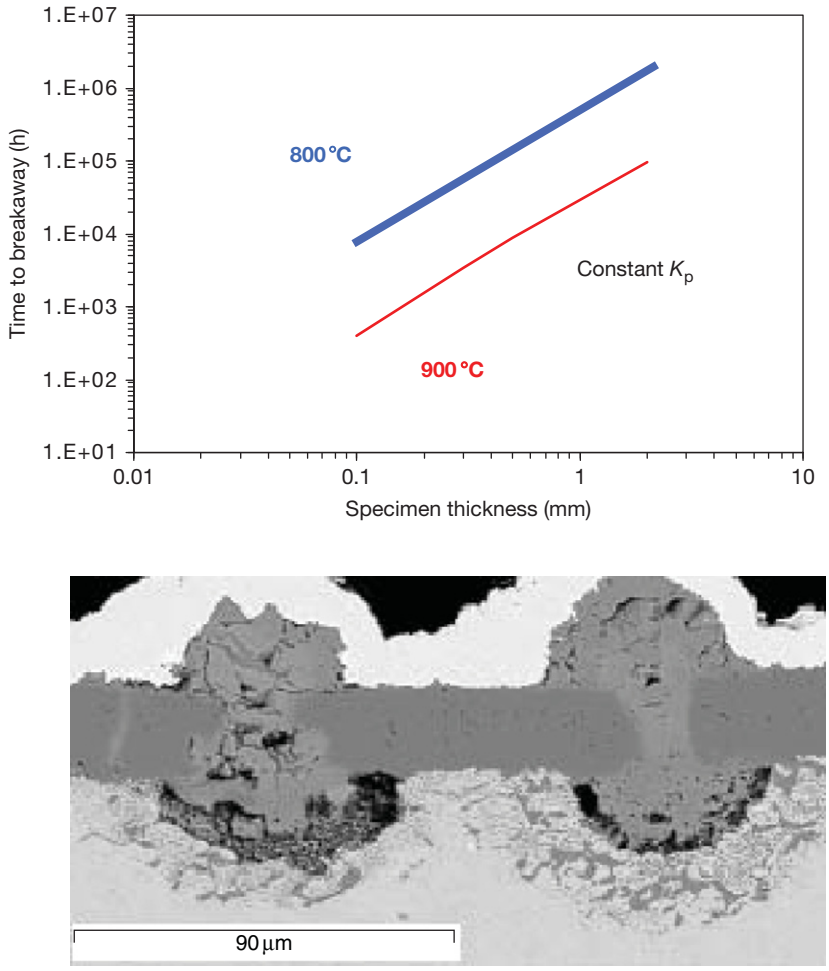

Figure 23 Upper figure shows calculated life time for plate material of Crofer 22A in air at 800 and 900 °C (ignoring scale spalling and thickness dependence of K_p). Lower figure shows example for loss of protective scale properties for 0.2 mm specimen after 1000 h at 900 °C. Reproduced from Huczkowski, P.; Quadakkers, W. J. Effect of geometry and composition of Cr steels on oxide scale properties relevant for interconnector applications in solid oxide fuel cells (SOFCs), Report Forschungszentrum Jülich, Energy Technology; 2007; Vol. 65, ISBN 978-3-89336-484-8.

occurring profiles because the ratio between oxidation rate k (in $cm^2\ s^{-1}$) and diffusion coefficient (D) of chromium in the ferritic steel is quite small.[109]

For cases in which oxide scale spallation occurred, a modified expression based on observations for FeCrAl alloys[110,111] may be derived:

$$t_B = 2.3 \times 10^{-3}(C_0 - C_B)\rho d(k)^{-1/n}(\Delta m^*)^{(1/n)-1} \quad [11]$$

Here, Δm^* is the critical weight change at which the onset of scale spallation occurs.

A major finding of Huczkowski *et al.*[112] was that, in these life time calculations, it had to be taken into account that not only the time until occurrence of breakaway oxidation depended on component thickness but also the intrinsic oxidation rates of the alloys. **Figure 24** shows mass change data for the high-Cr ferritic steel Crofer 22 A[109,112] during cyclic oxidation at 900 °C for specimens of different thickness. The thickening rate of the two-phase oxide layer consisting of Cr_2O_3 and $MnCr_2O_4$ appears to increase with decreasing specimen thickness. This is confirmed by the metallographic cross sections in **Figure 25** which shows that the difference in overall scale thickness on high-chromium ferritic steels is mainly related to the difference in thickness of the inner chromia layer, whereas the thickness of the outer spinel layer differs only marginally.[109,112] A second effect of specimen thickness is that the extent of internal oxidation may become limited by the reservoir of the minor elements Ti and Al in the

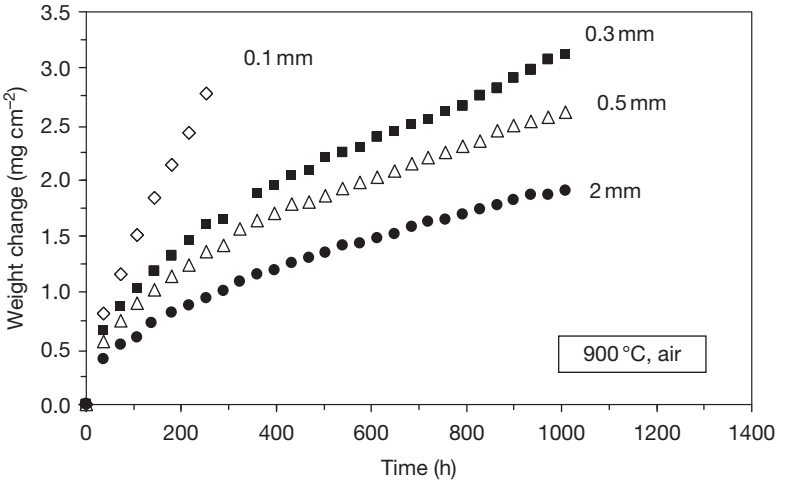

Figure 24 Weight change during cyclic air oxidation of ferritic steel Crofer 22 A at 900 °C showing effect of specimen thickness on oxidation rate. Reproduced from Huczkowski, P.; Quadakkers, W. J. Effect of geometry and composition of Cr steels on oxide scale properties relevant for interconnector applications in solid oxide fuel cells (SOFCs), Report Forschungszentrum Jülich, Energy Technology; 2007; Vol. 65, ISBN 978-3-89336-484-8.

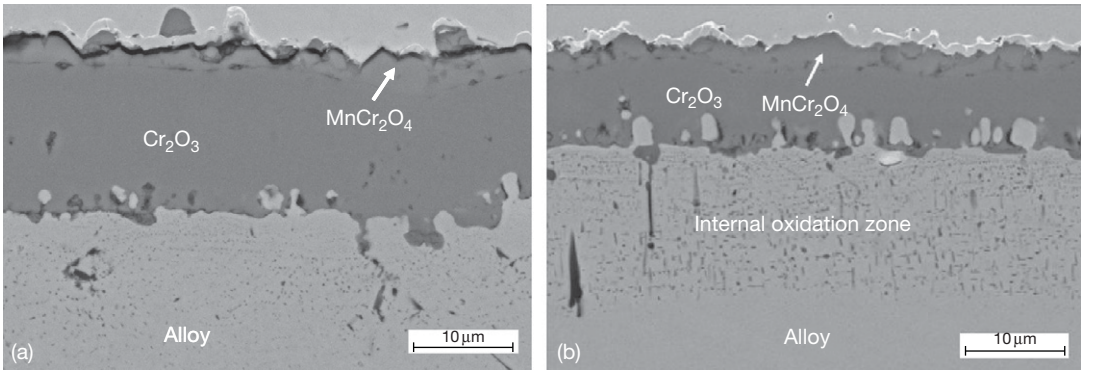

Figure 25 Metallographic cross sections (SEM images) of Crofer 22 A after 1000 h cyclic oxidation at 900 °C in air: (a) 0.3 mm thick specimen and (b) 2 mm thick specimen. Reproduced from Huczkowski, P.; Quadakkers, W. J. Effect of geometry and composition of Cr steels on oxide scale properties relevant for interconnector applications in solid oxide fuel cells (SOFCs), Report Forschungszentrum Jülich, Energy Technology; 2007; Vol. 65, ISBN 978-3-89336-484-8.

component (**Figure 25**). At 800 °C, the thickness dependence of the oxidation rate is less pronounced than at 900 °C, but is still clearly seen and of technical importance (**Figure 26**).

First attempts to explain the specimen thickness dependence of the oxidation rates related to depletion of major (Cr) and minor alloying elements (Al, Si, La, Ti, and/or Mn) as well as scale microcracking occurring during thermal cycling.[109,112] However, more recent experimental results for the ferritic steels[113] in combination with data for Ni-base alloys[114] indicate that all these factors quantitatively affect the oxidation rates, however, they do not seem to be the main reason for the oxidation rate dependence on specimen thickness. Strong indications were found that the difference in growth rate of the chromia-based scales on thick and thin specimens is the result of compressive growth stresses in the scales which can relax by plastic deformation of the substrate for thin specimens but are maintained at significant levels for thick specimens.

For an oxide under a biaxial compressive stress σ_{xx}, the diffusivity may be written as[114,115]:

$$D = A\exp\left(\frac{\Delta S^*}{R}\right)\exp\left(\frac{-\Delta H^*}{RT}\right)\exp\left(\frac{\frac{2}{3}\Delta V^*\sigma_{xx}}{RT}\right) \quad [12]$$

in which ΔH^* and ΔS^* are the *activation enthalpy* and *entropy*, respectively, ΔV^* is the *activation volume*, and A is a pre-exponential constant. Additionally, there is

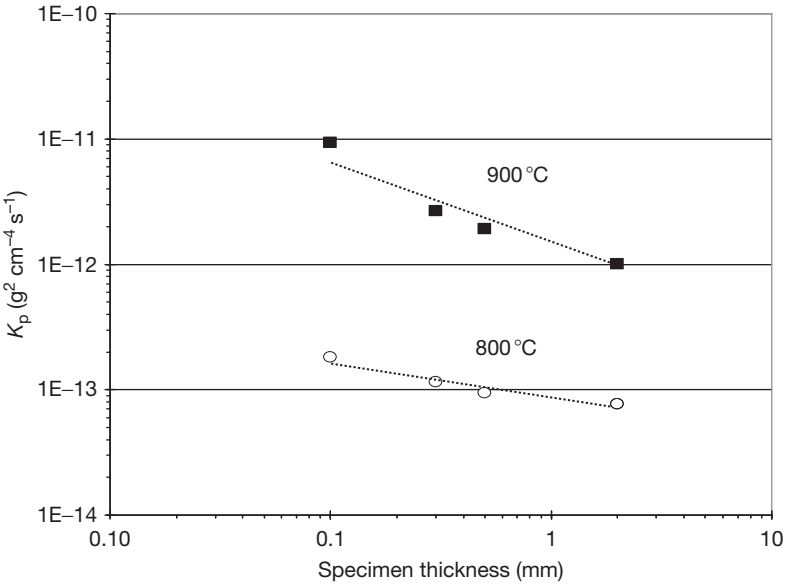

Figure 26 Measured K_p values as a function of specimen thickness during cyclic oxidation of high-Cr ferritic steel Crofer 22 A in air. Reproduced from Huczkowski, P.; Quadakkers, W. J. Effect of geometry and composition of Cr steels on oxide scale properties relevant for interconnector applications in solid oxide fuel cells (SOFCs), Report Forschungszentrum Jülich, Energy Technology; 2007; Vol. 65, ISBN 978-3-89336-484-8.

the possibility of a stress gradient over the oxide scale whereby both cations and anions are transported from regions where the stress is compressive to regions where the stress is tensile resulting in a net transport of oxide into the tensile regions. The vacancy concentration can be written as

$$C_V = C_V^0 \exp\left(\frac{\sigma_h \Delta V^F}{RT}\right) \quad [13]$$

where C_v^0 is the equilibrium concentration of vacancies in the unstressed state and ΔV^F is the volume change associated with the formation of the relevant point defect. Of course, in the case of oxidation, the rate is controlled by the faster diffusing ion. An estimate of the reduction caused by the effect of an assumed compressive stress[116–118] revealed for chromia that the effect of stress on the defect concentrations may be more significant than the direct effect on diffusivity.[114]

This explanation for the effect of specimen thickness on oxidation rate implies that occurrence of the effect depends on the extent of growth stress development in the scale. This explains the observation that the specimen thickness dependence differs from environment to environment and is, for instance, far less pronounced in anode than in cathode gas.[86] The explanation also implies that an increase in creep strength of the ferritic steel would decrease the tendency for the oxidation rates to increase with decreasing component thickness. Studies on steel compositions such as Crofer 22H which were modified by adding the solid solution strengthening element tungsten in combination with the Laves phase forming element niobium, indeed showed that, especially the oxidation rates of thin components of a few tenths of a millimeter at 800 °C were markedly reduced compared to corresponding specimens made of high-purity, high-chromium ferritics (**Figure 27(a)**).

A further beneficial property of this type of creep-resistant steels of the type Crofer22H (**Table 4**),[119,120] is that the Laves phase was found to dissolve substantial amounts of silicon,[121] an element which is commonly added in minor amounts as deoxidant of the alloy melt. As explained above, these minor additions (commonly a few tenths of a percent) of silicon in conventional alloys result, during high temperature exposure, in undesired internal oxidation and/or formation of a silica sublayer beneath the chromia scale. The incorporation of silicon in the Laves phase leads to a decreased activity of this element in the steel matrix with the result that no internal oxidation of silicon occurs (**Figure 27(b)**) if the niobium/silicon ratio is carefully adjusted.[119] In parallel, the incorporation of silicon stabilizes the Laves phase with the result that the adverse effect of niobium on the chromia growth rate is suppressed. This finding allowed the definition of ferritic steel compositions that contained a minor

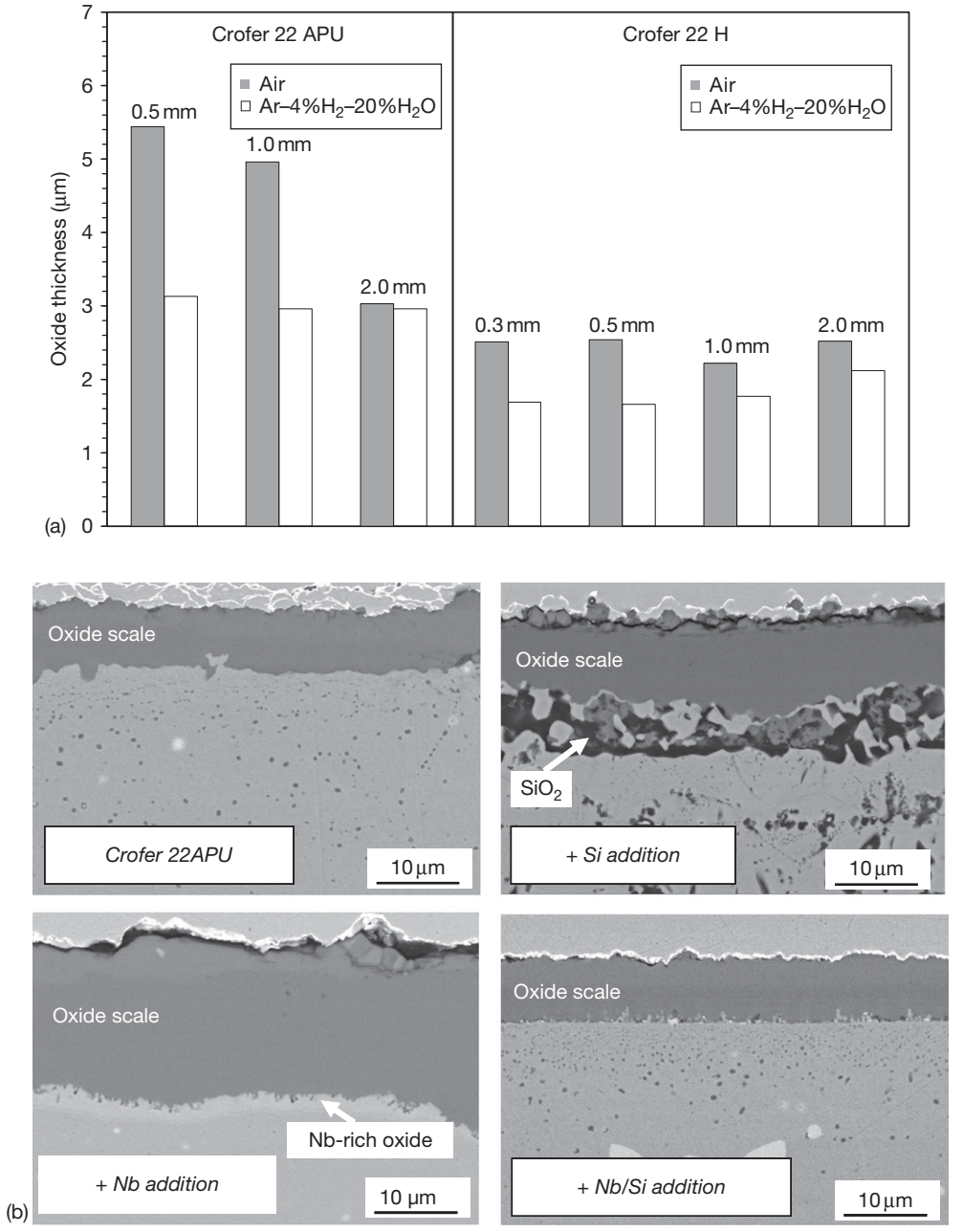

Figure 27 (a) Oxide thicknesses on Crofer 22 APU and Crofer 22 H after 1000 h discontinuous oxidation at 800 °C (100 h cycles) in different gases. (b) Effect of Si, Nb, and combined Si/Nb addition on oxide scale formation (1000 h, 900 °C, air) on Crofer22 type materials. Alloy designated as 'Nb/Si addition' corresponds to Crofer 22H in **Table 4**. Reproduced from Froitzheim, J. Ferritic steel interconnectors and their interactions with Ni base anodes in solid oxide fuel cells (SOFC), RWTH Aachen, Report Forschungszentrum Jülich, Energy and Environment, Vol. 16, 2008; ISBN 978-3-89336-540-1.

amount of silicon which are desired from the viewpoint of alloy manufacturing by conventional methods, but did not exhibit the disadvantageous effect of silicon on the oxide scale formation mechanisms. In this way, oxidation properties could be obtained for components of a few millimeter thickness which were similar to those of the high-purity steels thus allowing to decrease the alloy manufacturing costs compared to

those of the high-purity, single-phase ferritic steels.[122] For components with a thickness of a few tenths of a millimeter, this creep resistant steel showed lower oxidation rates than the high-purity steel.

1.19.14 Oxidation Behavior of Ferritic Steels Under Dual Atmosphere Conditions

Most laboratory oxidation testing of candidate materials for interconnect application is based on short- or long-term exposures in cathode gas and various types of anode gases. However, in reality, the metallic interconnect is simultaneously exposed to air at the cathode side and fuel at the anode side and thus experiences a chemical potential gradient from the fuel side to the air side. A number of investigations have shown that under such conditions, the oxidation behavior of metallic interconnects on the cathode side may differ from that observed during normal air oxidation.[123,124] Especially, ferritic stainless steels with relatively low Cr contents of less than ~20%, under dual atmosphere conditions, show a tendency to form oxide scales with less protective properties than formed during normal air oxidation. The 17% Cr ferritic steel AISI 430 exhibited hematite nodules on the air side of an air–hydrogen sample during isothermal exposure at 800 °C, whereas no hematite formation was seen on the air–air sample. The oxidation behavior on the hydrogen side of the air–hydrogen sample was similar to that on the hydrogen–hydrogen sample. The detrimental effects of the dual exposures are far less pronounced in the case of steels with higher Cr contents, such as Crofer 22APU or E-brite, although a modification of the outer spinel layer was observed[125,126] and some Fe-oxide formation was found at higher exposure temperatures. Dual atmosphere effects were observed for austenitic stainless steels,[127] Ni–Cr-base alloys,[128] alumina-forming alloys[125] as well as pure metals such as nickel or silver.[125,129] The observations are in qualitative agreement with observations of Nakagawa *et al.*[130] when studying the oxidation behavior of martensitic steels under conditions in which the inner surface of a tube was exposed to steam and the other side to air.

The poorer oxidation resistance of ferritic steels with relatively low Cr contents under dual atmosphere conditions is commonly attributed to the transport of hydrogen through the metal substrate from the fuel side to the air side. Hydrogen permeation through metallic materials at high temperatures is known to be very fast[131] but may be substantially reduced by presence of protective, perfectly gas-tight surface oxide layers of chromia.[131] The modified air side oxidation behavior of ferritic steels under dual atmosphere conditions is similar to that found when such steels are exposed to wet air[88,132] or wet oxygen.[133] The extent of enhanced attack depends on steel composition, interconnect thickness as well as exact composition of the anode gas environment and tends to be reduced by a preoxidation treatment.

1.19.15 Interaction of Chromia-Forming Interconnects with Cathode Side Materials

In evaluating the growth rates and the electronic properties of the surface scales of metallic interconnectors, it has to be borne in mind that parts of the interconnects are at the cathode side in direct contact with the cathode or with ceramic contact materials.

The cathode and contact materials are in most cases La-based perowskites. Due to interaction between these compounds and the interconnect, two important processes can occur: a change of the oxide composition on the interconnect surface and/or a change in the alloy composition in the surface-near region of the interconnect, mainly due to Cr transport into the perowskite.[106,134] These processes can change the contact resistance as well as the oxidation resistance of the interconnect.[134,135] With perowskite type contact materials commonly used in SOFCs, formation of spinel layers (e.g., $CoCr_2O_4$, $MnCr_2O_4$) is frequently observed at the interface between the surface oxide film and the perowskite.[134–138]

The changes in interface composition can affect the contact resistance in a positive as well as negative way. The relatively pure chromia layers formed on Cr-based (ODS) alloys are frequently reported to exhibit high contact resistances which can even be at 1000 °C in the range $\Omega\,cm^2$.[139] Larring and Norby[140] observed, for contact layers of Sr-doped La-manganite and La-cobaltite on a Cr-ODS alloy at 900 °C, an extrapolated contact resistance of $24\,m\Omega\,cm^2$ after 10 000 h. It was claimed that the formation of CoMn-spinel at the interface reduced the transport of Cr from the interconnector into the perowskite. This chromium transport has been shown to at least partly occur via volatile species,[141] as already discussed in **Section 1.19.4**. Due to the significance of this effect for cell performance, some authors

tried to select the composition of the perowskite-based contact layer in such a way that it not only acted as contacting material but also as 'gettering agent' for the evaporating chromium species. Other authors proposed that a dense and gas-tight Cr-free spinel layer can be formed on top of a protective chromia scale by reaction of manganese, which outwardly diffuses through the chromia scale on the ferritic steel, with contact layers containing large amounts of spinel-forming elements such as Co or Ni (**Figure 28**). The dense, Cr-free spinel layer, formed by interdiffusion, acts as barrier against vapor-phase transport of volatile chromium oxides and hydroxides.[101,140,142]

Several authors found that Sr or Ca dopants added to increase the electrical conductivity of conact layers on the basis of La-manganite, -chromite, and -cobaltite are easily transported from the cathode or contact layer in the direction of the Cr-based or ferritic steel interconnect surface.[141,143] This not only alters the initial electrical conductivity of the perowskite contact layer but also that of the chromia surface scale (**Figure 29**) due to formation of compounds such as $SrCrO_4$ and/or $Sr_3Cr_2O_8$.

In the case of ferritic steels, the chemical compatibility between alloy and perowskite mainly depends on the relative thermodynamic stability of the mixed

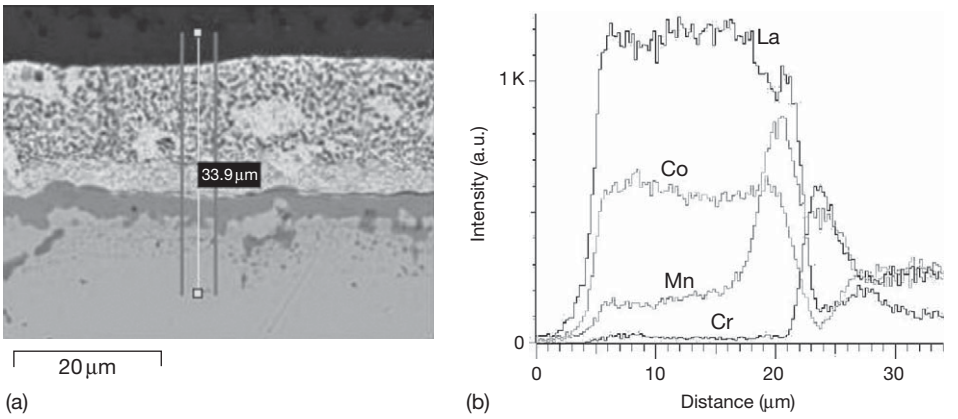

Figure 28 Interface between steel of the type FeCrMn(La/Ti) and $LaCoO_3$ contact layer after 1000 h exposure at 800 °C in air. (a) SEM cross section and (b) element profiles measured along trace indicated in (a). Reproduced from Quadakkers, W. J.; Piron-Abellan, J.; Shemet, V.; Singheiser, L. *Mater. High Temp.* **2003**, *20*(2), 115–127.

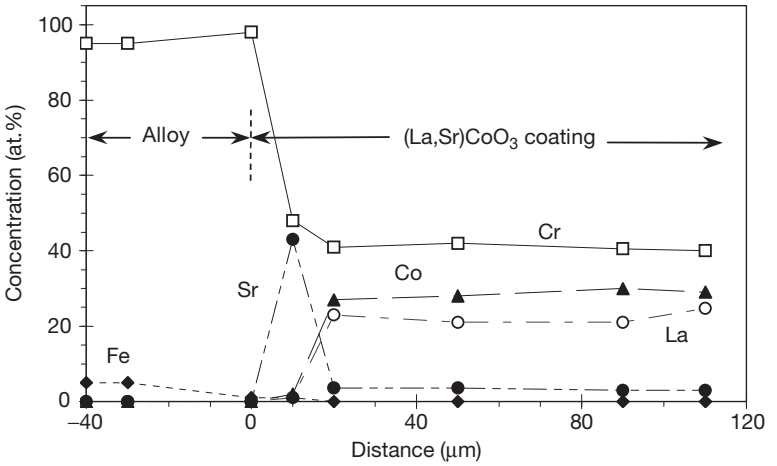

Figure 29 Element profiles measured near interface between Cr-ODS alloy and $(La,Sr)CoO_3$ contact layer after 500 h exposure at 950 °C in air. Reproduced from Quadakkers, W. J.; Piron-Abellan, J.; Shemet, V.; Singheiser, L. *Mater. High Temp.* **2003**, *20*(2), 115–127.

oxides (e.g., spinels) which can form due to reaction of Cr from the alloy with the B-type elements (Co, Mn, Cr, Fe, Cu, etc.) in the perowskite contact layer.[80,134–136] From this viewpoint, it seems obvious that manganites and especially chromites provide the best compatibility with the ferritic steels, whereas cobaltites and ferrites tend to result in extensive reaction with the ferritic steel, thereby decreasing its oxidation resistance.[80,144–148] Also, the presence of Cu in the perowskite substantially enhances the oxidation rates of interconnector steels.[149]

The effect of these interface reactions on the contact resistance cannot simply be correlated with the thickness of the reaction layer. The resistance depends on the type of perowskite used and also on perowskite and oxide layer morphology. The results are also affected by the way in which the perowskite is applied, that is, to a bare or to a preoxidized metal. Indications were found that the dense inner chromia layer frequently present at the interface with the alloy possesses a higher specific resistivity than the outer mixed oxide layers (e.g., of the spinel type) formed either due to oxidation of steel alloying elements or due to reaction of the chromia layer with perowskite constituents. Several surface modifications were therefore proposed to decrease the scale growth rate or to modify the composition of the inner chromia layer. To achieve this goal, a number of methods such as RE implantation or application of RE-nitrate solutions have been used, sometimes in combination with Ni deposition to increase chromia conductivity.[66,150–153]

From the viewpoint of long-term stack performance, it has to be considered that the electronic conductivity of actually formed reaction products alone does not govern the relevant contact resistance of the interface between interconnector and contact layer. The reaction between the perowskite and the chromia-based surface scales may also lead to morphological changes of the perowskite layer near the interface with the surface oxide. These morphological changes sometimes, for example, result in substantial void formation which increases the overall contact resistance. Therefore, a number of authors[154] considered the use of Co–Mn or Co–Mn–Fe-spinels as possible contact layer materials. These spinels were found to exhibit less extensive reactions with the steel surfaces than most perowskites, thus ensuring a slower increase in contact resistance during long-term cell operation. Yang *et al.*[155] used a combination of Co-based spinels and RE-oxides, the latter being added to improve the adherence of the oxide scale to the steel surface.

1.19.16 Protection Methods to Minimize Cr Vaporization

Different strategies are used to minimize the cell degradation as a result of the Cr release from metallic interconnector materials in SOFCs. They include a decrease in the operation temperature of the SOFC, the application of less Cr-sensitive cathode materials, the design of alternative multilayer interconnects, the development of interconnect alloys with a lower Cr release, and the use of barrier coatings against Cr release.

It has been observed that the Cr vaporization can be reduced by the formation of outer spinel layers formed on the inner protective chromia scale on high temperature alloys[97] and therefore, ferritic interconnect steels such as Crofer 22APU, with defined additions of Mn and Ti in combination with reactive elements (REs) such as Y, Ce, Zr, or La, have been developed (**Table 4**). A number of studies on Cr vaporization of a number of these steels are available.[40,43] The potential of the Cr retention capability of alloys with different types of oxide layers on the outer surface, such as for example $(Cr,Mn)_3O_4$ layers or other oxide scales, is described elsewhere.[156] The Cr vaporization rates of ferritic stainless steels, specifically developed for application as interconnector materials in SOFCs such as Crofer 22 APU, ZMG 232, and IT-10 and IT-11, are very similar. These alloys form a well-adhering outer $(Cr,Mn)_3O_4$-spinel layer that reduces Cr vaporization rates in humid air at 800 °C by 61–75% compared to alloys which form pure chromia scales such as Cr-based ODS alloys or E-Brite. Substantially lower oxidation rates were found for Fe-, Ni-, or Co-base alloys with relatively low Cr contents. This type of alloys formed thicker oxides of the base material (e.g., Co-oxide on Co-based alloy) on top of the inner chromia layer, however, with the disadvantage of high oxidation rates.

For electrically insulating SOFC components, alumina-forming alloys are sometimes considered. At high temperatures, these alloys at their surfaces form slow-growing alumina scales which possess far better protective properties and resistance against Cr evaporation than chromia-forming materials. However, due to the low electronic conductivity of alumina, these materials do not seem to be suitable as construction materials for interconnectors.

Numerous authors aimed to reduce the Cr vaporization from ferritic steels by development of coating systems which possess sufficient electronic conductivity at the SOFC operating temperature.[43,137,141,148,157,158]

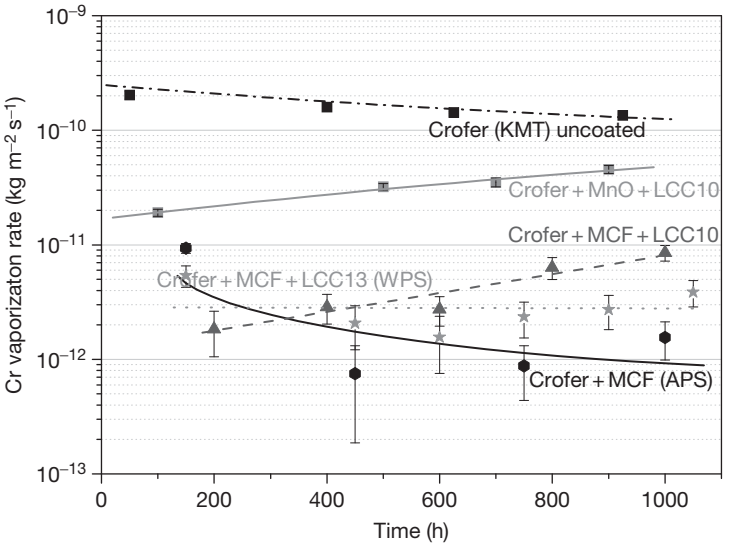

Figure 30 Cr evaporation rate of Crofer 22 APU with and without various types of coatings during exposure in wet air at 800 °C.[158] LCC: La-base perowskite; MCF: Mn/Co/Fe-spinel.

The coatings mostly are perowskites layers on the basis of $(La,Sr)MnO_3$, $(La,Sr)CoO_3$, and $(La,Sr)CrO_3$ or combinations of these (**Figure 30**). There were also attempts to use reactive coatings of La_2O_3 and SrO, that is, compounds which form protective $(La,Sr)CrO_3$ layers by reaction with Cr in the steel.[48] The most common coating techniques used to apply such protection layers are vacuum plasma spraying (VPS), air plasma spraying (APS), and wet powder spraying.[43,48,140,141]

Sputtered ceramic Cr barrier coatings of $La_{0.8}Sr_{0.2}CrO_3$, $La_{0.99}(Cr_{0.77}Mg_{0.05}Al_{0.18})O_3$, $La_{0.80}Sr_{0.20}MnO_3$, and $La_{0.65}Sr_{0.30}MnO_3$ on substrates of Crofer 22 APU showed only a minor reduction of the Cr release. This is mainly related to the formation of pores due to crystallization of the amorphous sputter coatings during high temperatures exposure. The LSM coatings showed a high tendency to spallation after thermal cycling, which might be prevented by a proper adjustment of the manufacturing parameters such as the thickness of the coating. In general, the practical application of perowskite type Cr retention layers seems to be questionable due to high costs and difficulties with the fabrication of dense coatings.

Promising results have been obtained with coatings on the basis of spinel type oxides, for example, on the basis of Co and/or Ni. The coatings were either directly applied in the form of respective oxides or as metallic coatings of Co or Ni with a thickness of about 10 µm. The metallic layers are transformed into oxides during high temperature exposure and form the spinel layers by reactions with the chromia-based surface scales present on the ferritic steels. With such coatings, Cr retentions of more than 99% up to the maximum test time of 1200 h at 800 °C in humid air could be achieved. The coatings seem to be applicable for a wide range of stainless steels and fulfill the requirements for mobile and stationary long-term applications. These types of coatings were found to possess electronic conductivities which are 1–2 orders of magnitude larger than that of Cr_2O_3 and even tend to reduce the oxidation of the ferritic substrate.

Figure 31 shows a comparison of the chromium release during 1000 h exposure in wet air at 800 °C for different types of ferritic steels with and without various types of coatings. It is obvious that suitable coating compositions can effectively reduce the chromium release by approximately two orders of magnitude provided that they can be applied in the form of a dense layer with suitable adhesion to the metallic substrate.

1.19.17 Interaction of Chromia-Forming Interconnects with Anode Side Materials

At the anode side, the interconnect is in direct contact with the Ni/ZrO_2 cermet anode or, in most cases, with a Ni wire mesh which provides the electrical contact between the interconnect and the anode. If, for instance, the Ni net is spot welded to the

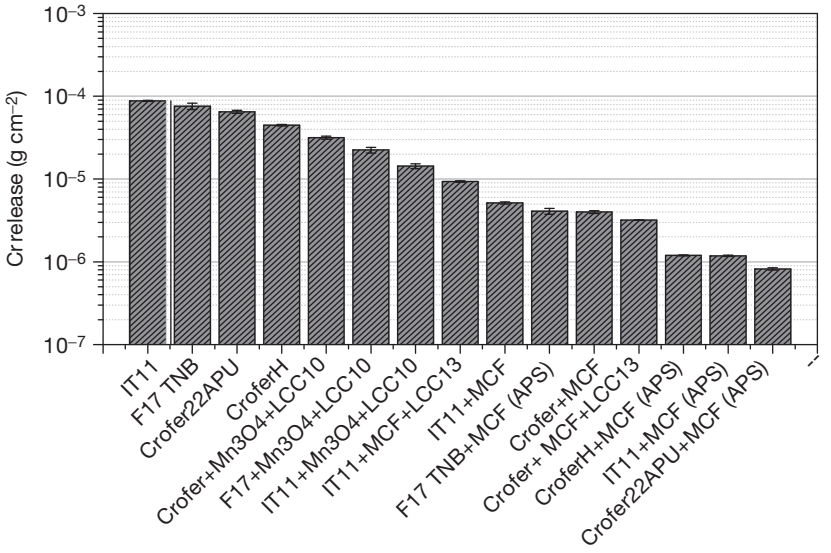

Figure 31 Total Cr release during 1000 h exposure in air with standard humidity of 60% rel. at 25 °C. LCC: Perowskite type coating; MCF: Mn/Co/Fe-spinel coating. Reproduced from Trebbels, R. Ph.D. Thesis, RWTH Aachen, 2009.

interconnector, excellent contact resistance values are initially observed. In the case of a Cr-based interconnector, however, interdiffusion can result in excessive Kirkendall-void formation at the Cr–Ni interface, eventually resulting in deterioration of the contact. Ni plating of the interconnector has been applied to reduce this problem,[135] however, extensive outward diffusion of Cr into the Ni with subsequent chromia formation on the Ni layer has been found to occur after long-term exposure.

Interdiffusion between a ferritic steel interconnect and the spot-welded nickel wire mesh will lead to Ni transport into the steel resulting in local austenite formation (**Figure 32**), thereby changing the steel oxidation resistance as well as the thermal expansion coefficient. As a result of interdiffusion these property changes will be of special concern if very thin interconnects are being used.

Vice versa, transport of Fe, Cr, and other steel constituents into the wire mesh renders the latter as an alloy which will tend to form surface oxide layers in the anode side environment resulting in a decreased catalytic activity.[159]

Preoxidation layers have been examined as possible barriers to minimize interdiffusion processes between the ferritic steel and the Ni wire mesh or the Ni/ZrO_2-anode. However, the preformed oxide scales tended to become dissociated at the Ni–steel interfaces,[160,161] so after longer exposure time, the unwanted interdiffusion processes appeared again

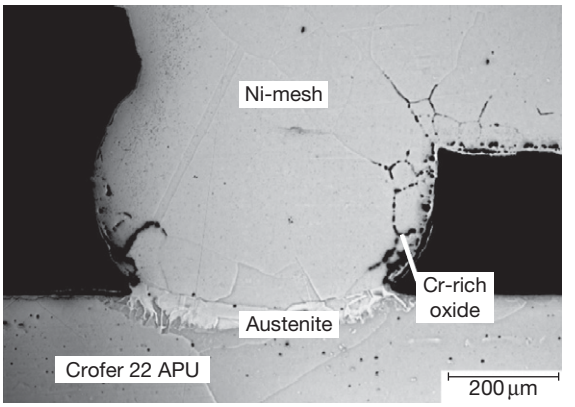

Figure 32 Ni mesh in direct contact with the interconnect plate of an SOFC stack after 3000 h at 800 °C. Reproduced from Brandner, M.; Bram, M.; Froitzheim, J.; Buchkremer, H.P.; Stover, D. *Solid State Ionics* **2008**, *179*(27–32), 1501–1504.

(**Figure 33**). A number of externally applied diffusion barrier layers have been proposed and quite promising results were obtained with sputtered ceria layers.[162,163] The intrinsic electronic conductivity of ceria in the low-pO_2 anode gas is substantially smaller than that of Ni, but it is sufficiently high to obtain low contact resistance values because layers of only a few micrometer thickness appeared to be sufficient to virtually completely suppress the interdiffusion phenomena.[87] During long-term operation, however, the outward growing Cr–Mn-spinel oxide

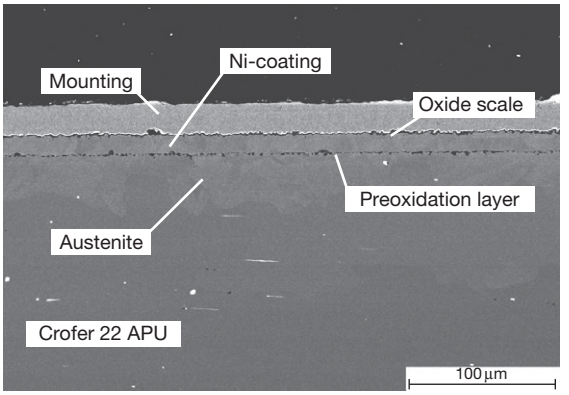

Figure 33 Cross section of sample with a Ni coating on (100 h) preoxidized Crofer 22 APU after 1000 h exposure in Ar–4H_2–2H_2O at 800 °C showing austenite formation, dissociation of the preformed oxide layer, and chromia formation on top of the Ni coating. Reproduced from Froitzheim, J.; Niewolak, L.; Brandner, M.; Singheiser, L.; Quadakkers, W. J. *J. Fuel Cell Sci. Technol.* in press *6*(4).

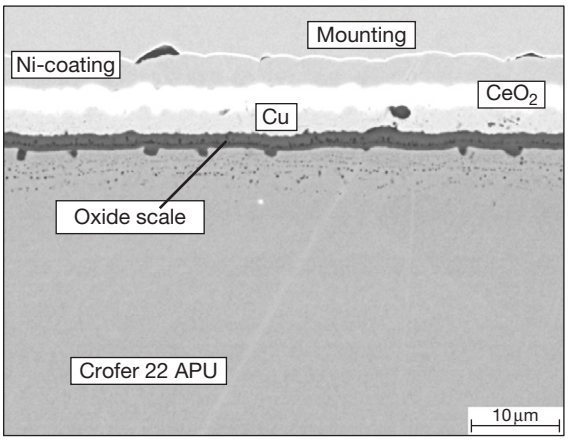

Figure 34 Cross section of multilayer ceria/Cu coating between preoxidized Crofer 22 APU and Ni layer after 1000 h of exposure in Ar–4H_2–2H_2O at 800 °C. Reproduced from Froitzheim, J.; Niewolak, L.; Brandner, M.; Singheiser, L.; Quadakkers, W. J. *J. Fuel Cell Sci. Technol.* in press *6*(4).

on the steel deteriorated the chemical contact between oxide scale and ceria layer. An improvement of the electrical contact could be obtained by applying a duplex layer of ceria and copper on a preoxidized ferritic steel (**Figure 34**). The high oxygen solubility in Cu prevented the dissociation of the oxide layer and the geometrical deterioration of the contact was reduced because the geometrical irregularities were compensated by plastic deformation of the Cu layer.[87]

1.19.18 Interaction of Metallic Interconnects with Glass Sealants

Most glass sealants used in solid oxide fuel cells are based on the system, barium-calcium-aluminosilicate (BCAS).[164–167] The glasses frequently contain further minor amounts of other oxides, for instance, to increase the wetting properties. The extent of the reaction of high-chromium ferritic steels with the glass ceramics depends on the exposure conditions and the distance of the interface of sealing glass and ferritic steel to the ambient air.[168–170] Near the triple-phase boundary, steel/glass/air volatile chromium species react with BaO, thereby forming $BaCrO_4$ (**Figure 35**). In the interior seal regions, hardly any access of oxygen from the air is possible and thus only a very minor reaction with the steel surface occurs and the chromium tends to slightly dissolve into the glass. The extent of reaction depends on the steel composition. Crofer 22 APU was found to exhibit better chemical compatibility and bonding with the BCAS-based glass-ceramics than most other ferritic steels due to the growth of its specific oxide scale on the alloy during high temperature exposure.[170] A further suppression of interface reactions and $BaCrO_4$ formation was obtained when an alumina-forming alloy was used.[169] Thus, one approach to improve the sealing effectiveness is to engineer the alloy surface, for example, by local aluminizing[171] in places where electrical conductivity is not required.

More severe reactions may occur if the glass contains minor amounts of wetting agents in the form of thermodynamically less stable oxides such as PbO or ZnO. Depending on the ferritic steel composition, the use of such glasses may result in rapid short circuiting of SOFC stacks by excessive iron oxide formation on the ferritic steels near the triple-phase boundary air/glass/metal.[172–175] It was however found that the trigger of this detrimental effect occurred near the triple-phase boundary at the anode side of the stack. Here, the less stable oxides were reduced to, for example, metallic Pb, which possesses a substantial vapor pressure ($\sim 10^{-4}$ bar at 800 °C) at the prevailing high service temperature of 800–900 °C. As confirmed by laboratory tests,[159] the presence of Pb vapor resulted in severe grain boundary attack in the high-chromium ferritic steels accompanied by excessive internal oxidation of chromium (**Figure 36**). Due to the low pO_2 in the anode side gas, no external iron oxide formation occurred. However, the internal oxidation resulted in a large volume increase and thus in a local bulging of the steel. In the actual SOFC stack,

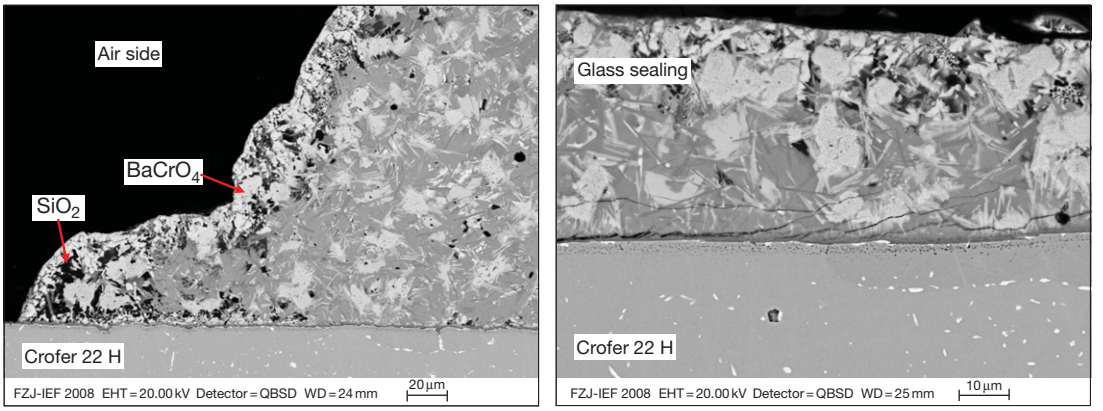

Figure 35 SEM/BSE pictures of glass/metal microstructure on cathode side (left) and interseal region (right) of SOFC stack after 1000 h operation at 800 °C. Reproduced from Shemet, V.; Quadakkers, W. J. Unpublished results.

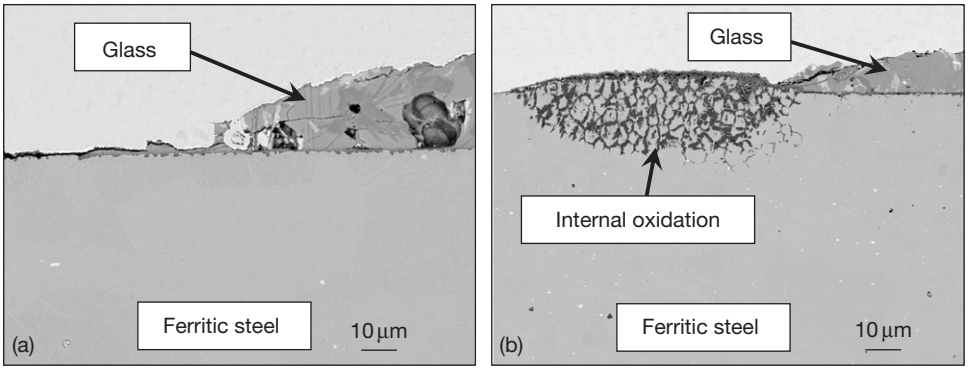

Figure 36 Interaction of ferritic steel with PbO-containing BCAS glass at 800 °C in (a) air and (b) Ar–H_2–H_2O. Reproduced from Shemet, V.; Quadakkers, W. J. Unpublished results.

this initiated a cracking at/near the steel–glass interface which allowed the Pb vapor-triggered internal oxidation to propagate in the direction of the triple-phase boundary glass/steel/air. When reaching this point, the chromium-depleted steel matrix started to form rapidly growing iron-base oxide which eventually 'bridged' the small distance between two interconnector plates. The high electronic conductivity of the Fe-base oxide in this way resulted in a short circuiting of the stack.

The rate at which this Pb vapor-induced reaction occurred, appeared to depend on the amount of the minor alloying additions Si and Al in the ferritic steel. Concentrations of a few tenths of a percent results, as explained in **Section 1.19.9**, in formation of internal silicon- and aluminum oxides. The minor volume increase imparted by this effect leads to outward metal flow, noticeable by formation of metallic nodules in the surface oxide scale[86,102] and is accompanied by formation of micro cracks. The latter can act as channels for transport of Pb vapor through the oxide scale towards the steel surface resulting in the above described enhanced oxidation attack. High-purity steels (for instance Crofer 22APU) with very low Al and Si contents in the range 0.01% were less prone to Pb vapor attack than steels (such as, e.g., Crofer 22A) with more common Al/Si contents of ~0.1%.

A further effect imparted by an indirect interaction of the steel with the ceramic sealant is related to the high silicon content of the glass. In dry and wet gases, silicon may form a number of volatile oxides and (oxy-)hydroxides

$$2SiO_2 = 2SiO^{(g)} + O_2 \quad [14]$$

$$SiO_2 + 2H_2O^{(g)} = Si(OH)_4^{(g)} \quad [15]$$

$$SiO_2 + H_2O^{(g)} = SiO(OH)_2^{(g)} \quad [16]$$

It is apparent that reaction [14] is only significant in low-pO_2 environments. Reactions [15] and [16] are independent of pO_2 and the vapor pressure of the volatile species is proportional to $p^2(H_2O)$ and $p(H_2O)$,

respectively.[176] Due to these volatile species, silicon-containing oxides are frequently found at the external surface at the anode side of ferritic steel interconnects after long-term stack operation, mainly in the form of Mn-silicate.[177] For further details on the formation of volatile silicon-containing species, see the chapter on 'Oxidation in Steam and Steam/Hydrogen Environments.'

References

1. Singhal, S. C. *MRS Bull.* **2000**, *25*(3), 16–21.
2. Minh, N. Q. *J. Am. Ceram. Soc.* **1993**, *176*(3), 563–588.
3. Steele, B. C. H. *Solid State Ionics* **2000**, *134*, 3–20.
4. Singhal, S. C. In *Solid Oxide Fuel Cell (SOFC-V)*; Stimming, U., Singhal, S. C., Tagawa, H., Lehnert, W., Eds.; The Electrochemical Society Proceedings Series: Pennington, NJ, 1997; p 88, PV 97-40.
5. Stolten, D.; Späh, R.; Schamm, R. In *Solid Oxide Fuel Cell (SOFC-V)*; Stimming, U., Singhal, S. C., Tagawa, H., Lehnert, W., Eds.; The Electrochemical Society Proceedings Series: Pennington, NJ, 1997; p 88, PV 97-40.
6. Quadakkers, W. J.; Piron-Abellan, J.; Shemet, V.; Singheiser, L. *Mater. High Temp.* **2003**, *20*(2), 115–127.
7. Köck, W.; Martinz, H.; Greiner, H.; Janousek, M. In *Solid Oxide Fuel Cells (SOFC IV)*; Dokiya, M., Yamamoto, O., Tagawa, H., Singhal, S. C., Eds.; The Electrochemical Society Proceedings Series: Pennington, NJ, 1995; p 841, PV 95-1.
8. Yang, Z. *Int. Mater. Rev.* **2008**, *53*(1), 39–54.
9. Stöver, D.; Diekmann, U.; Flesch, U.; Kabs, H.; Quadakkers, W. J.; Tietz, F.; Vinke, I. In *Solid Oxide Fuel Cells (SOFC VI)*; Singhal, S. C., Dokiya, M., Eds.; The Electrochemical Society Proceedings Series: Pennington, NJ, 1999; p 812, PV 99-19.
10. Lai, G. *High Temperature Corrosion of Engineering Alloys*; ASM International: Materials Park, OH, 1990.
11. Kofstad, P. *High Temperature Corrosion*; Elsevier Applied Sciences/Chapman and Hall: London, 1988.
12. England, D.; Virkar, A. V. *J. Electrochem. Soc.* **1999**, *146*(9), 3196.
13. Wersing, W.; Ivers-Tiffee, E.; Schiessl, M.; Greiner, H. In Proceedings of the International Symposium on Solid Oxide Fuel Cells; Nagoya, Japan, 13–14 November 1989; Yamamoto, O., Dokiya, M., Tagawa, H., Eds.; Scince House: Tokyo, Japan, 1989; p 33.
14. Yamamoto, O. *Electrochim. Acta* **2000**, *45*, 2423.
15. Kofstad, P. In *Proceedings of the 2nd European Solid Oxide Fuel Cell Forum*; Thorstensen, B., Ed.; European SOFC Forum: Switzerland, 1996; Vol. 2, p 479.
16. Kofstad, P. In *Proceedings of the 17th Risø International Symposium on Materials Science: High Temperature Electrochemistry, Ceramics and Metals*; Poulsen, F., Bonanos, N., Linderoth, S., Mogenson, M., Zachau-Christiansen, B., Eds.; Riso National Laboratory: Roskilde, Denmark, 1996; p 55.
17. Kofstad, P.; Bredesen, R. *Solid State Ionics* **1992**, *52*, 69.
18. Matsuzaki, Y.; Yasuda, I. *Solid State Ionics* **2000**, *132*, 271.
19. Yasuda, I.; Baba, Y.; Ogiwara, T.; Yakabe, H.; Matsuzaki, Y. In *Solid Oxide Fuel Cells (SOFC VII)*; Yokokawa, H., Singhal, S. C., Eds.; The Electrochemical Society Proceedings Series: Pennington, NJ, 2001; p 130, PV 2001-16.
20. Malkow, T.; Crone, U. v. d.; Laptev, A. M.; Koppitz, T.; Breuer, U.; Quadakkers, W. J. In *Solid Oxide Fuel Cells (SOFC V)*; Stimming, U., Singhal, S. C., Tagawa, H., Lehnert, W., Eds.; The Electrochemical Society Proceedings Series: Pennington, NJ, 1997; p 1245, PV 97-40.
21. Thierfelder, W.; Greiner, H.; Köck, W. In *Solid Oxide Fuel Cells (SOFC V)*; Stimming, U., Singhal, S. C., Tagawa, H., Lehnert, W., Eds.; The Electrochemical Society Proceedings Series: Pennington, NJ, 1997; p 1306, PV 97-40.
22. Schmidt, H.; Brückner, B.; Fischer, K. In *Solid Oxide Fuel Cells (SOFC IV)*; Dokiya, M., Yamamoto, O., Tagawa, H., Singhal, S. C., Eds.; The Electrochemical Society Proceedings Series: Pennington, NJ, 1995; p 869, PV 95-1.
23. Quadakkers, W. J.; Greiner, H.; Köck, W. In *Proceedings of the First European Solid Oxide Fuel Cell Forum* Bossel, U., Ed.; European SOFC Forum, Dr. Ulf Bossel, Morgenacher Str. 2F, CH-5452: Oberrohrdorf, Switzerland, 1994; Vol. 2, p 525.
24. Quadakkers, W. J.; Norton, J. F.; Penkalla, H. J.; Breuer, U.; Gil, A.; Rieck, T.; Hänsel, M. In *Proceedings of the 3rd International Conference on Microscopy of Oxidation, Cambridge, 16–18 September 1996*; Newcomb, S. B., Little, J. A., Eds.; The Institute of Materials, 1996; p 221.
25. Graham, M.; Hussey, R. *Oxid. Met.* **1995**, *44*, 339–374.
26. Cotell, C.; Yurek, G.; Hussey, R.; Mitchel, D.; Graham, M. *J. Electrochem. Soc.* **1987**, *134*, 1871.
27. Quadakkers, W. J.; Holzbrecher, H.; Briefs, K. G.; Beske, H. In *Proceedings of the Europ. Coll. on the Role of Active Elements in the Oxidation Behaviour of High Temperature Alloys, 12–13 December 88*; Petten, N. L., Lang, E., Ed.; European Communities, 1988; p 155.
28. Hou, P.; Stringer, J. *Oxid. Met.* **1992**, *38*, 323.
29. Whittle, D.; Stringer, J. *Philos. Trans. Roy. Soc. London A* **1980**, *295*, 309.
30. Golightly, F.; Stott, H.; Wood, G. *Oxid. Met.* **1976**, *10*(3), 163.
31. Pint, B. *Oxid. Met.* **1996**, *45*, 1.
32. Quadakkers, W. J.; Greiner, H.; Köck, W.; Buchkremer, H. P.; Hilpert, K.; Stöver, D. In *Proceedings of the 2nd European Solid Oxide Fuel Cell Forum*; Thorstensen, B., Ed.; European SOFC Forum, Dr. Ulf Bossel, Morgenacher Str. 2F, CH-5452: Oberrohrdorf, Switzerland, 1996; Vol. 2, p 297.
33. Brady, M. P.; Wright, I. G.; Anderson, I. M.; Sikka, V. K.; Ohriner, E. K.; Walls, C.; Westmoreland, G.; Weaver, M. L. In *Ductilization of Cr via Oxide Dispersions*; Proceedings of the 15th International Plansee Symposium; Plansee, AG, Reutte, Kneringer, G., Rodhammer, P., Wildner, H., Eds.; 2001; pp 108-1–108-13.
34. Badwal, S. P. S.; Deller, R.; Foger, K.; Ramprakash, Y.; Zhang, J. P. *Solid State Ionics* **1997**, *99*, 297.
35. Hilpert, K.; Das, D.; Miller, M.; Peck, D. H.; Weiß, R. *J. Electrochem. Soc.* **1996**, *143*, 3642.
36. Jiang, S. P.; Zhang, J. P.; Apateanu, L.; Froger, K. *J. Electrochem. Soc.* **2001**, *148*, 447.
37. Odell, S. P.; Ding, G. L.; Tewari, S. N. *Metall. Mater. Trans. A* **1999**, *30A*, 2159–2165.
38. Ebbinhaus, B. B. *Comb. Flame* **1993**, *93*, 119.
39. Das, D.; Miller, M.; Nickel, H.; Hilpert, K. In *Proceedings of the First European Solid Oxide Fuel Cell Forum*; Bossel, U., Ed.; European SOFC Forum, Dr. Ulf Bossel, Morgenacher Str. 2F, CH-5452: Oberrohrdorf, Switzerland, 1994; Vol. 2, p 703.

40. Stanislowski, M.; Wessel, E.; Hilpert, K.; Markus, T.; Singheiser, L. *JES* **2007**, *154*(4), A295–A306.
41. Opila, E. J.; Myers, D. L.; Jacobson, N. S.; *et al. J. Phys. Chem. A* **2007**, *111*, 1971–1980.
42. Yungman, V. S.; Medvedev, V. A.; Veits, I. V. and Bergman, G. A.; Eds. *IVTANTHERMO – A Thermodynamic Database and Software System for the Personal Computer*; CRC Press/Begell House: Boca Raton, FL, 1993.
43. Gindorf, C.; Singheiser, L.; Hilpert, K. *Steel Res.* **2001**, *72*, 528.
44. Gindorf, C.; Hilpert, K.; Nabielek, H.; Singheiser, L.; Ruckdäschel, R.; Schiller, G. In *Proceedings of the Fourth European Solid Oxide Fuel Cell Forum*; McEvoy, J., Ed.; European SOFC Forum, Dr. Ulf Bossel, Morgenacher Str. 2F, CH-5452: Oberrohrdorf, Switzerland, 2000; Vol. 2, p 845.
45. Batawi, E.; Plas, A.; Straub, W.; Honegger, K.; Diethelm, R. In *Solid Oxide Fuel Cells (SOFC VI)*; Singhal, S. C., Dokiya, M., Eds.; The Electrochemical Society Proceedings Series: Pennington, NJ, 1999; p 767, PV 99-19.
46. Quadakkers, W. J. *German Patent DE 195 47 699 C2*; 1995.
47. Quadakkers, W. J.; Baumanns, F.; Nickel, H. *German Patent DE 44 10 711*; 1995.
48. Linderoth, S. *Mater. Processes* **1998**, *17*, 217.
49. Linderoth, S.; Hendriksen, P.; Mogensen, M.; Langvad, N. *J. Mater. Sci.* **1996**, *31*(9), 5077.
50. Hänsel, M.; Quadakkers, W. J.; Singheiser, L.; Nickel, H. *Report Forschungszentrum Jülich, Jülich FRG, Jül-3583*, 1998; ISSN 0944-2952.
51. Rahmel, A.; Tobolski, J. *Corros. Sci.* **1965**, *5*, 333.
52. Young, D. J. *Mater. Sci. Forum* **2008**, *595–598*, 1189–1197.
53. Zurek, J.; Young, D. J.; Essuman, E.; Hänsel, M.; Penkalla, H. J.; Niewolak, L.; Quadakkers, W. J. *Mater. Sci. Eng. A* **2008**, *477*, 259–270.
54. Miyake, Y.; Yasuo, T.; Taniguichi, Y.; Kadowaki, M.; Kawamura, H.; Saitoh, T. In *Proceedings of the 4th International Symposium on Solid Oxide Fuel Cells (SOFC IV)*; Dokiya, M., Yamamoto, O., Tagawa, H., Singhal, S. C., Eds.; The Electrochemical Society Proceedings Series: Pennington, NJ, 1995; p 100, PV 95-1.
55. Quadakkers, W. J.; Hänsel, M.; Rieck, T. *Mater. Corros.* **1998**, *49*, 252.
56. Crone, U. v. d.; Hänsel, M.; Quadakkers, W. J.; Vaßen, R. *Fresenius J. Anal. Chem.* **1997**, *358*, 230.
57. Atkinson, A.; Taylor, R. In *Transport in Non-Stoichiometric Compounds*; Simkovich, G., Stubican, G., Eds.; *NATO ASI Series, Series B: Physics Col.* Vol. 129, Plenum Press: New York, 1984; p 285.
58. Sabioni, A.; Huntz, A.; Millot, F.; Monty, C. *Philos. Mag. A* **1992**, *66*, 351.
59. Sockel, H.; Saal, B.; Heilmayer, M. *Surf. Interf. Anal.* **1988**, *12*, 531.
60. Gil, A.; Penkalla, H. J.; Hänsel, M.; Norton, J.; Köck, W.; Quadakkers, W. J. *IX Conference on Electron Microscopy of Solids, 6–9 May 1996*, Krakow-Zakopane, Poland 1996, Fotobit: Krakow, Poland; p 441.
61. Quadakkers, W. J. *J. Phys. IV* **1993**, *3*(part I), 177.
62. Quadakkers, W. J. *Werkst. Korros.* **1990**, *41*, 659.
63. Bongartz, K.; Quadakkers, W. J.; Pfeifer, J. P.; Becker, J. S. *Surf. Sci.* **1993**, *292*, 196.
64. Quadakkers, W. J. *Mater. Sci. Forum* **2001**, *369–372*, 77.
65. Hou, P.; Brown, I.; Stringer, J. *Nucl. Instrum. Meth. B* **1991**, *59/60*, 1345.
66. Quadakkers, W. J.; Breuer, U.; Tyagi, A.; Gil, A.; Stroosnijder, M. F.; Becker, S.; Hänsel, M. Report, Forschungszentrum Jülich, Jülich, FRG, Jül-1372, p. 97, ISSN 0944–2952.
67. Park, J. H.; Natesan, K. *Oxid. Met.* **1990**, *33*(1/2), 31.
68. Holt, A.; Kofstadt, P. *Solid State Ionics* **1994**, *69*, 137.
69. Holt, A.; Kofstadt, P. *Solid State Ionics* **1999**, *117*, 21.
70. Holt, A.; Kofstadt, P. *Solid State Ionics* **1997**, *100*, 201.
71. Holt, A.; Kofstad, P. *Solid State Ionics* **1994**, *69*, 127.
72. Liu, H.; Stack, M.; Lyon, S. *Solid State Ionics* **1998**, *109*, 247.
73. Huczkowski, P.; Christiansen, N.; Shemet, V.; Niewolak, L.; Piron-Abellan, J.; Singheiser, L.; Quadakkers, W. J. *Fuel Cells* **2006**, *2*, 93–99.
74. Hagel, W. C.; Seybolt, A. U. *J. Electrochem. Soc.* **1961**, *108*(12), 1146–1152.
75. Nagai, H.; Fujikawa, T. *Trans. JIM* **1983**, *24*(8), 581.
76. Su, M. Y. *Diss. Abstr. Int.* **1988**, *48*, 3049.
77. Crawford, J. A.; Vest, R. W. *J. Appl. Phys.* **1964**, *35*(8), 2413–2418.
78. Nagai, H.; Ohbayashi, K. *J. Am. Ceram. Soc.* **1989**, *72*, 400.
79. Nagai, H.; Ishikawa, S.; Amano, N. *Trans. JIM* **1985**, *26*(10), 753.
80. Malkow, Th.; Quadakkers, W. J.; Singheiser, L.; Nickel, H. Report Forschungszentrum, Jülich, Jülich, FRG, Jül-3589,1998; ISSN 0944-2952.
81. Ennis, P. J.; Quadakkers, W. J. In *Proceedings of the Conference High Temperature Alloys – Their Exploitable Potential*, JRC Petten, NL, 15–17 October 1985; Marriot, J. B., Merz, M., Nihoul, J., Ward, J. O., Eds.; Elsevier Applied Science: London, 1987; p 465.
82. Buchkremer, H. P.; Diekmann, U.; Stöver, D. In *Proceedings of the 2nd European Solid Oxide Fuel Cell Forum*, Thorstensen, B., Ed.; European SOFC Forum, Dr. Ulf Bossel, Morgenacher Str. 2F, CH-5452: Oberrohrdorf, Switzerland, 1996; Vol. 2, p 221.
83. De Haart, L.; Vinke, I. C.; Janke, A.; Ringel, H.; Tietz, F. In *Solid Oxide Fuel Cells (SOFC VII)*; Yokokawa, H., Singhal, S. C., Eds.; The Electrochemical Society Proceedings Series: Pennington, NJ, 2001; p 111, PV 2001-16.
84. Horita, T.; Xiong, Y.; Yamaji, K.; Sakai, N.; Yokokawa, H. In *Proceedings of the 5th European Solid Oxide Fuel Cell Forum*, Huijsmans, J., Ed.; European SOFC Forum, Dr. Ulf Bossel, Morgenacher Str 2F, CH-5452: Oberrohrdorf, Switzerland, 2002; Vol. 1, p 401.
85. Piron-Abellan, J.; Quadakkers, W. J. Development of ferritic steels for application as interconnect materials for intermediate temperature solid oxide fuel cells (SOFCs), Report Forschungszentrum Jülich, Jül-4170, March 2005; ISSN 0944-2952.
86. Huczkowski, P.; Ertl, S.; Piron-Abellan, J.; Christiansen, N.; Hoefler, T.; Shemet, V.; Singheiser, L.; Quadakkers, W.J. *Mater. High Temp*. **2005**, *22*(3/4), 253–262.
87. Froitzheim, J. Ferritic steel interconnectors and their interactions with Ni base anodes in solid oxide fuel cells (SOFC), RWTH Aachen, Report Forschungszentrum Jülich, Energy and Environment, Vol. 16, 2008; ISBN 978-3-89336-540-1.
88. Fujii, C. T.; Meussner, R. A. *Corros. Iron & Steel* **1964**, *111*, 1215–1221.
89. Essuman, E.; Meier, G. H.; Zurek, J.; Hänsel, M.; Quadakkers, W. J. *Oxid. Met.* **2008**, *69*, 143–162.
90. Grabke, H. J. *Mater. Corros.* **2003**, *54*(10), 736–746.
91. Young, D. J. *Mater. High Temp.* **2007**, *24*(3), 225–232.
92. Huczkowski, P.; Quadakkers, W. J. Unpublished results.
93. Dulieu, D.; Cotton, J.; Greiner, H.; Honegger, K.; Scholten, A.; Christie, M.; Seguelong, T. In *3rd European*

SOFC Forum; Stevens, P., Ed.; European Fuel Cell Forum: Oberrohrdorf, Switzerland, CH-5452, 1998; p 447.
94. Ueda, M.; Taimatsu, H. In *Proceedings of the Fourth European Solid Oxide Fuel Cell Forum*, McEvoy, J., Ed.; European SOFC Forum, Dr. Ulf Bossel, Morgenacher Str. 2F, CH-5452: Oberrohrdorf, Switzerland, 2000; Vol. 2, p 837.
95. Ueda, M.; Kadowaki, M.; Taimatsu, H. *Mat. Trans. JIM* **2000**, *41*(2), 317–322.
96. Quadakkers, W. J.; Malkow, T.; Piron-Abellan, J.; Flesch, U.; Shemet, V.; Singheiser, L. In *Proceedings of the Fourth European Solid Oxide Fuel Cell Forum*, McEvoy, J., Ed.; European SOFC Forum, Dr. Ulf Bossel, Morgenacher Str. 2F, CH-5452: Oberrohrdorf, Switzerland, 2000; Vol. 2, p 827.
97. Piron-Abellan, J.; Shemet, V.; Tietz, F.; Singheiser, L.; Quadakkers, W. J. In *Solid Oxide Fuel Cells (SOFC VII)*; Yokokawa, H., Singhal, S. C., Eds.; The Electrochemical Society Proceedings Series: Pennington, NJ, 2001; p 811, PV 2001-16.
98. Bredesen, R.; Kofstad, P. In *Proceedings of the 17th Risø International Symposium on Materials Science: High Temperature Electrochemistry*, Ceramics and Metals; Poulsen, F., Bonanos, N., Linderoth, S., Mogenson, M., Zachau-Christiansen, B., Eds.; Risø National Laboratory: Ros Rilde, Denmark. 1996; p 187.
99. Quadakkers, W. J.; Thiele, M.; Ennis, P. J.; Teichmann, H.; Schwarz, W. In *Proceedings of the EUROCORR 97, Trondheim, Norway, 22–25 September 1997*, European Federation of Corrosion, 1997; Vol. II, p 35.
100. Huang, K.; Hou, P.; Goodenough, J. *Solid State Ionics* **2000**, *129*, 237.
101. Pirón-Abellán, J.; Tietz, F.; Shemet, V.; Gil, A.; Ladwein, T.; Singheiser, L.; Quadakkers, W. J. In *Proceedings of the 5th European Solid Oxide Fuel Cell Forum*, Huijsmans, J., Ed.; European SOFC Forum, Dr. Ulf Bossel, Morgenacher Str 2F, CH-5452: Oberrohrdorf, Switzerland, 2002; Vol. 1, p 248.
102. Hammer, J. E.; Laney, S. J.; Jackson, R. W.; Coyne, K.; Pettit, F. S.; Meier, G. H. *Oxid. Met.* **2007**, *67*(1/2), 1–38.
103. Ghosh, D.; Tang, E.; Perry, M.; Prediger, D.; Pastula, M.; Boersma, R. In *Solid Oxide Fuel Cells (SOFC VII)*; Yokokawa, H., Singhal, S. C., Eds.; The Electrochemical Society Proceedings Series: Pennington, NJ, 2001; p 101, PV 2001-16.
104. Kung, S.; Cal, T.; Moris, T.; Barringer, E.; Elangovan, S.; Hartvigsen, J. In Proceedings of the 2000 Fuel Cell Seminar, Portland OR, 30 October–2 November 2000; **2000**; p 585.
105. Krumpelt, M.; Ralph, J.; Cruse, T.; Bae, J.-M. In *Proceedings of the 5th European Solid Oxide Fuel Cell Forum*, Huijsmans, J., Ed.; European SOFC Forum, Dr. Ulf Bossel, Morgenacher Str 2F, CH-5452: Oberrohrdorf, Switzerland, 2002; Vol. 1, p 215.
106. Uehara, T.; Ohno, T.; Toji, A. In *Proceedings of the 5th European Solid Oxide Fuel Cell Forum*, Huijsmans, J., Ed.; European SOFC Forum, Dr. Ulf Bossel, Morgenacher Str 2F, CH-5452: Oberrohrdorf, Switzerland, 2002; Vol. 1, p 281.
107. Honegger, K.; Plas, A.; Diethelm, R.; Glatz, W. In *Solid Oxide Fuel Cells (SOFC VII)*; Yokokawa, H., Singhal, S. C., Eds.; The Electrochemical Society Proceedings Series: Pennington, NJ, 2001; p 803, PV 2001-16.
108. Ehlers, J.; Quadakkers, W. J. Oxidation von 9–12% Cr-Stählen in wasserdampfhaltigen Atmosphären bei 550 bis 650°C, Report Forschungszentrum Jülich, Jülich, FRG, Jül-3883, ISSN 0944–2952, June 2001.
109. Huczkowski, P.; Christiansen, N.; Shemet, V.; Piron Abellan, J.; Singheiser, L.; Quadakkers, W. J. *Mater. Corros.* **2004**, *55*(11), 825–830.
110. Quadakkers, W. J.; Bongartz, K. *Werkst. Korros.* **1994**, *45*, 232–241.
111. Gurrappa, I.; Weinbruch, S.; Naumenko, D.; Quadakkers, W. J. *Mater. Corros.* **2000**, *51*, 224–235.
112. Huczkowski, P.; Christiansen, N.; Shemet, V.; Piron Abellan, J.; Singheiser, L.; Quadakkers, W. J. *J. Fuel Cell Sci. Technol.* **2004**, *1*, 30.
113. Huczkowski, P.; Quadakkers, W. J. Effect of geometry and composition of Cr steels on oxide scale properties relevant for interconnector applications in solid oxide fuel cells (SOFCs), Report Forschungszentrum Jülich, Energy Technology; 2007; Vol. 65, ISBN 978-3-89336-484-8.
114. Zurek, J.; Meier, G. H.; Essuman, E.; Hänsel, M.; Singheiser, L.; Quadakkers, W. J. *J. Alloys Comp.* 467 (2009) 450–458.
115. Mehrer, H. *Defect Diffus. Forum* **1996**, *57*, 129–130.
116. Huntz, A.-M.; Daghigh, S.; Piant, A.; Lebrun, J. L. *Mater. Sci. Eng. A* **1998**, *248*, 44.
117. Galerie, A.; Toscan, F.; Dupeux, M.; Mougin, J.; Lucazeau, G.; Valot, C.; Huntz, A.-M.; Antoni, L. *Mater. Res.* **2004**, *7*, 81.
118. Gray, S.; Berriche-Bouhanek, K.; Evans, H. E. *Mater. Sci. Forum* **2004**, *755*, 461–464.
119. Froitzheim, J.; Meier, G. H.; Niewolak, L.; Ennis, P. J.; Hattendorf, H.; Singheiser, L.; Quadakkers, W. J. *J. Power Sources* **2008**, *178*, 163–173.
120. Quadakkers, W. J.; Niewolak, L.; Ennis, P. J. Patent number(s): WO2007093148-A1; DE102006007598-A1. Application date, 18 February 2006 (DE), PCT/DE2007/000166.
121. Niewolak, L.; Huczkowski, P.; Froitzheim, J.; Ennis, P. J.; Singheiser, L.; Quadakkers, W. J. In Proceedings of the 7th European SOFC Forum, 3–7 July 2006, Lucerne, CH, CD-ROM, Paper B084.
122. Niewolak, L.; Quadakkers, W. J. Unpublished results.
123. Yang, Z.; Walker, M. S.; Singh, P.; Stevenson, J. W. *Electrochem. Solid State Lett.* **2003**, *6*, B35–B37.
124. Nakagawa, K.; Matsunaga, Y.; Yanagisawa, T. *Mater. High Temp.* **2003**, *20*, 67–73.
125. Yang, Z.; Xia, G.-G.; Walker, M. P.; Wang, C.-M.; Stevenson, J. W.; Singh, P. *Int. J. Hydrogen Energy* **2007**, *32*, 3770.
126. Yang, Z.; Walker, M. S.; Singh, P.; Stevenson, J. W.; Norby, T. *J. Electrochem. Soc.* **2004**, *151*, B669–B678.
127. Ziomek-Moroz, M.; Cramer, S. D.; Holcomb, G. R.; Covino, B. S., Jr.; Bullard, S. J.; Singh, P. In *Corrosion 2005*; NACE International: Houston, TX, 2005; Paper no. 10.
128. Yang, Z.; Xia, G.-G.; Singh, P.; Stevenson, J. W. *J. Power Sources* **2006**, *160*, 1104–1110.
129. Jackson, R. W.; Pettit, F. S.; Meier, G. H. *Journal of Power Sources* **2008**, *185*(2), 1030–1039.
130. Nakagawa, K.; Matsunaga, Y.; Yanagisawa, T. *Mater. High Temp.* **2001**, *18*, 51–56.
131. Hecker, R.; Stover, D.; Jonas, H.; Buchkremer, H. P. *J. Nucl. Mater.* **1990**, *171*(1), 84–93.
132. Wood, G. C.; Wright, I. G.; Hodgkiess, T.; Whittle, D. P. *Werkst. Korros.* **1970**, *21*, 900–910.
133. Ehlers, J.; Young, D. J.; Smaardijk, E. J.; Tyagi, A. K.; Penkalla, H. J.; Singheiser, L.; Quadakkers, W. J. *Corros. Sci.* **2006**, *48*, 3428–3454.
134. Tietz, F.; Simwonis, D.; Batfalsky, P.; Diekmann, U.; Stöver, D. In *Degradation Phenomena during Operation of Solid Oxide Fuel Cells*, Proceedings of the 12th IEA Workshop on SOFCs: Materials and Mechanisms;

Nisancioglu, K., Ed.; International Energy Agency, 1999; p 3.
135. Teller, O.; Meulenberg, W.; Tietz, F.; Wessel, E.; Quadakkers, W. J. In *Solid Oxide Fuel Cells (SOFC VII)*; Yokokawa, H., Singhal, S. C., Eds.; The Electrochemical Society Proceedings Series: Pennington, NJ, 2001; p 895, PV 2001-16.
136. Batfalsky, P.; Buchkremer, H.-P.; Froning, D.; Meschke, F.; Nabielek, H.; Steinbrech, R. W.; Tietz, F. In *Proceedings of the 3rd International Fuel Cell Conference*; New Energy and Industrial Technology Development Organization (NEDO) and Fuel Cell Development Information Center (FCDIC), Japan, 1999; p 349.
137. Urbanek, J.; Miller, M.; Schmidt, H.; Hilpert, K. In *Proceedings of the 2nd European Solid Oxide Fuel Cell Forum*, Thorstensen, B., Ed.; European SOFC Forum, Dr. Ulf Bossel, Morgenacher Str. 2F, CH-5452: Oberrohrdorf, Switzerland, 1996; Vol. 2, p 503.
138. Quadakkers, W. J.; Mallener, W.; Grübmeier, H.; Wallura, E. In Proceedings of the 5th IEA Workshop on SOFC; Materials, Process Engineering and Electrochemistry, Jülich Germany, 2–4 March 1993, Forschungszentrum Jülich, Jülich, FRG **1993**; p 87; ISBN 3-89336-127-8.
139. Badwal, S.; Deller, R.; Foger, K.; Ramprakash, Y.; Zhang, J. *Solid State Ionics* **1997**, *99*, 297.
140. Larring, Y.; Norby, T. *J. Electrochem. Soc.* **2000**, *147*, 3251.
141. Quadakkers, W. J.; Greiner, H.; Hänsel, M.; Pattaniak, A.; Khanna, A. S.; Mallener, W. *Solid State Ionics* **1996**, *91*, 55.
142. Tietz, F.; Mohsine, Z.; Quadakkers, W. J.; Shemet, V. U.S. Patent, US 7,407,717, B2, PCT/DE2004/000024, Application Data 18 February 2003.
143. Kadowaki, T.; Shiomitsu, T.; Matsuda, E.; Nakagawa, H.; Tsuneizumi, H.; Maruyanama, T. *Solid State Ionics* **1993**, *67*, 65.
144. Maruyama, T.; Ioue, T.; Nagata, K. In *Solid Oxide Fuel Cells (SOFC IV)*; Dokiya, M., Yamamoto, O., Tagawa, H., Singhal, S. C., Eds.; The Electrochemical Society Proceedings Series: Pennington, NJ, 1995; p 889, PV 95-1.
145. Oishi, N.; Namikawa, T.; Yamazaki, Y. *Surf. Coatings Technol.* **2000**, *132*, 58.
146. Yoo, Y.; Dauga, M. In *Solid Oxide Fuel Cells (SOFC VII)*; Yokokawa, H., Singhal, S. C., Eds.; The Electrochemical Society Proceedings Series: Pennington, NJ, 2001; p 837, PV 2001-16.
147. Godfrey, B.; Föger, K.; Gillespie, R.; Bolden, R.; Badwal, S. *J. Power Sources* **2000**, *86*, 68.
148. Hou, P.; Huang, K.; Bakker, W. In *Solid Oxide Fuel Cells (SOFC VI)*; Singhal, S. C., Dokiya, M., Eds.; The Electrochemical Society Proceedings Series: Pennington, NJ, 1999; p 737, PV 99-19.
149. Tietz, F.; Sebold, D. *Mater. Sci. Eng. B* **2008**, *150*(2), 135–140.
150. Ager, F. J.; Respaldiza, M.; Botella, J.; Soares, J.; Da Silva, M.; Benitez, J.; Adriozola, J. *Acta Mater.* **1996**, *44*, 675.
151. Ruiz, M.; Heredia, A.; Botella, J.; Adriozola, J. *J. Mater. Sci.* **1995**, *30*(20), 5146.
152. Brylewski, T.; Nanko, M.; Maruyama, T.; Przybylski, K. *Solid State Ionics* **2001**, *143*, 131.
153. Quadakkers, W. J. German Patent DE 19 54 66 14, 1995; Quadakkers, W. J.; Hänsel, M. German Patent DE 19 60 98 13, 1996.
154. Montero, X.; Jordan, N.; Piron-Abellan, J.; Tietz, F.; Stover, D.; Cassir, M.; Villarreal, I. *J. Electrochem. Soc.* **2009**, *156*(1), B188–B196.
155. Yang, Z. G.; Xia, G. G.; Nie, Z. M.; *et al. Electrochem. Solid State Lett.* **2008**, *11*(8), B140–B143.
156. Stanislowski, M.; Froitzheim, J.; Niewolak, L.; Quadakkers, W. J.; Hilpert, K.; Markus, T.; Singheiser, L. *J. Power Sources* **2007**, *164*, 578–589.
157. Batawi, E.; Honegger, K.; Diethelm, R. In Proceedings of the 6th IEA Workshop on Advanced SOFC, published by ENEA, Energy Department, 22–29 February 1994; Rome, Italy, p 175.
158. Trebbels, R. Ph.D. Thesis, RWTH Aachen, 2009.
159. Shemet, V.; Quadakkers, W. J. Unpublished results.
160. Ertl, S. T. Ph.D. Thesis, RWTH Aachen, 2006.
161. Froitzheim, J.; Niewolak, L.; Brandner, M.; Singheiser, L.; Quadakkers, W. J. *J. Fuel Cell Sci. Technol.* in press *6*(4).
162. Brandner, M.; Bram, M.; Froitzheim, J.; Buchkremer, H. P.; Stover, D. *Solid State Ionics* **2008**, *179*(27–32), 1501–1504.
163. Brandner, M.; Niewolak, L.; Froitzheim, J.; Quadakkers, W. J.; Bram, M. Patent number(s): DE102006056251-A1; WO2008064938-A1.
164. Menzler, N. H.; Sebold, D.; Zahid, M.; Gross, S. M.; Koppitz, T. *J. Power Sources* **2005**, *152*(1), 156–167.
165. Weil, K. S. *JOM* **2006**, *58*, 37–44.
166. Eichler, K.; Solow, G.; Otschik, P.; Schafferath, W. *J. Eur. Ceram. Soc.* **1999**, *19*, 101–104.
167. Sohn, S.-B.; Choi, S.-Y.; Kim, G.-H.; Song, H.-S.; Kim, G.-D. *J. Amer. Ceram. Soc.* **2004**, *87*, 254–260.
168. Yang, Z.; Meinhardt, K. D.; Stevenson, J. W. *J. Electrochem. Soc.* **2003**, *150*, A1095–A1101.
169. Yang, Z.; Stevenson, J. W.; Meinhardt, K. D. *Solid State Ionics* **2003**, *160*, 213–225.
170. Yang, Z.; Xia, G.-G.; Meihardt, K. D.; Weil, K. S.; Stevenson, J. W. *J. Mater. Eng. Perform.* **2004**, *13*, 327–334.
171. Yang, Z.; Coyle, C. A.; Baskaran, S.; Chick, L. A. US Patent, 6,843,406, 2005.
172. Haanappel, V. A. C.; Shemet, V.; Vinke, I. C.; Quadakkers, W. J. *J. Power Sources* **2005**, *141*, 102–107.
173. Haanappel, V. A. C.; Shemet, V.; Vinke, I. C.; Gross, S. M.; Koppitz, Th.; Menzler, N. H.; Zahid, M.; Quadakkers, W. J. *J. Mater. Sci.* **2005**, *40*, 1583–1592.
174. Haanappel, V. A. C.; Shemet, V.; Gross, S. M.; Koppitz, Th.; Menzler, N. H.; Zahid, M.; Quadakkers, W. J. *J. Power Sources* **2005**, *150*, 86–100.
175. Menzler, N. H.; Batfalsky, P.; Blum, L.; Bram, M.; Gross, S. M.; Haanappel, V. A. C.; Malzbender, J.; Shemet, V.; Steinbrech, R. W.; Vinke, I. *Fuel Cells* **2007**, *7*(5), 356–363.
176. Opila, E. J.; Jacobson, N. S.; Myers, D. L.; Copland, E. H. *JOM* **2006**, *58*, 22–28.
177. Niewolak, L.; Shemet, V. Forschungszentrum Jülich, 2008, Unpublished results.

1.22 High Temperature Corrosion of Low Alloy Steels

L. W. Pinder
E.ON Engineering Limited Technology Centre, Ratcliffe on Soar, Nottingham, NG11 OEE
K. Dawson and G. J. Tatlock
Department of Engineering, University of Liverpool, Liverpool, L69 3GH

This article is a revision of the Third Edition article 7.2 by L. W. Pinder, volume 1, pp 7:16–7:52, © 2010 Elsevier B.V.

1.22.1 Introduction

Low alloy steels are generally considered to comprise plain carbon steels and steels with a total alloying content of up to 12 wt%. This group of steels is exploited for many applications, including those in the heavy engineering industries. While these materials are often selected based on mechanical properties, extensive use in high temperature applications often involving harsh environments including power generation and the petrochemical industries demands a degree of oxidation resistance. Emerging industries creating energy from waste and biofuels have introduced more varied and complex environments to which steels may be exposed. Novel manufacturing techniques such as mechanically alloyed steels produced via powder metallurgy techniques are also offering new groups of steels designed for utilization in high temperature applications.

The drive for increased efficiency in power generation requires higher operating temperatures. Low alloy ferritic steels with attractive mechanical properties, including low coefficients of thermal expansion, have been optimized for high temperature performance. Since they possess adequate creep strength for their designed capability, the service life of these Fe–Cr alloys is now often limited by their steam-side oxidation resistance.

Alloying additions of Si, Al, and Cr which form stable, slow growing, protective scales on steels are extensively used; however, these additions can be financially inhibitive and/or detrimental to mechanical properties. In terms of low alloy steels in general, the restricted quantities (12 wt%) of alloying additions may not enable the most protective form of oxide to grow.

The extent to which low alloy steels react to high temperature corrosive environments is the subject of this chapter. In view of the commercial importance of these steels, the published literature on this topic is extensive and being continually enlarged. The reader is encouraged to refer to many excellent papers and current issues of journals, referenced at the end of the chapter, for more detailed and contemporary information on the topic.

1.22.2 Factors Governing Oxidation Behavior

In the absence of stress, the survival of a given component is largely determined by the extent to which the material of construction reacts with the environment in which it resides. This can largely be categorized by the extent to which the following two criteria are satisfied:

1. Is the material thermodynamically stable in the environment?
2. If not, will the reaction rate between the environment and the material be slow enough to give an acceptable life?

In the vast majority of cases at elevated temperatures, the answer to the first question is 'no.' With the exception of gold and platinum, which are generally too expensive for large-scale industrial use, are in short supply, and do not have the required mechanical properties, most materials will react to some degree with their environment. Most highly alloyed steels and superalloys satisfy the second criterion for a wide range of high temperature environments. However, these materials may be far too expensive for large-scale industrial applications. The oxidation behavior of most metals and alloys in a high temperature environment is, therefore, governed by the degree of protection afforded by any oxide scale that forms.[1] This depends upon the oxide melting point, its mechanical integrity, and the rate of diffusion of elemental species present within both the environment and the alloy, through the oxide scale.

In certain cases (e.g., Cr above 1000 °C), the CrO_3 oxide that forms is volatile, and clearly affords no protection to the substrate.[1] In other cases, a solid oxide scale forms that may, or may not, be continuous. The extent to which a solid surface scale protects the metal depends upon the extent of surface coverage. This behavior can largely be categorized according to whether the volume of oxide produced is less or greater than the volume of metal consumed during the oxidation reaction. This principle was originally advanced by Pilling and Bedworth,[2] with the oxide: metal volume ratio being known as the Pilling Bedworth Ratio (PBR), where

$$\text{PBR} = \frac{\text{Volume of oxide produced}}{\text{Volume of metal consumed}}$$

If the PBR is less than unity, the oxide will be nonprotective and oxidation will follow a linear rate law, governed by surface reaction kinetics. However, if the PBR is greater than unity, then a protective oxide scale may form and oxidation will follow a reaction rate law governed by the speed of transport of metal or environmental species through the scale. Then the degree of conversion of metal to oxide will be dependent upon the time for which the reaction is allowed to proceed. For a diffusion-controlled process, integration of Fick's First Law of Diffusion with respect to time yields the classic Tammann relationship,[3] commonly referred to as the Parabolic Rate Law:

$$x^2 = Kt \qquad [1]$$

where x is a measure parameter, K is the rate constant, and t is time. The progress of oxidation (x) is generally measured by weight gain, weight loss, scale thickness, or retreat of the metal surface. However, other parameters, such as loss of oxidant in the environment, may be used. The time interval may be measured in seconds, hours, thousands of hours and years. As a consequence, many different units of the measured oxidation parameter and the time period have been reported in the literature, leading to many differing units for the quoted rate constant.

In some circumstances, the reaction rates may not be exactly parabolic, and even initially parabolic rates may be influenced by changes within the oxide scale with time. As an oxide scale grows, the build-up of inherent growth stresses, externally applied strains, and chemical changes to either the oxide scale or the metal may all compromise the initial protection offered by the scale, leading to scale breakdown and ultimately to a partial or complete loss of protection; paralinear or linear kinetics may ensue. In other circumstances, as will be seen later in this chapter, very small additions of contaminants to the

environment may radically modify the oxidation response, by either favoring nonprotective scales from the outset or causing rapid breakaway corrosion following an initially protective period. Hence, there are many hidden dangers in extrapolating short-term oxidation kinetic data to long periods, and great care is required when utilizing published oxidation data to assess potential corrosion rates and component lives in industrial environments.

The temperature dependence of a diffusion-controlled reaction is typically described by the Arrhenius relationship:

$$K = a \exp \frac{(-Q)}{RT} \qquad [2]$$

where a is a constant, Q is the activation energy, R is the gas constant, and T is the temperature (K). Hence the rate constant (K) will be influenced by the temperature of exposure because of the increased ion mobility at higher temperatures, via the activation energy term. Again, great care is required when extrapolating data beyond the temperature range of the initial experimental data. Sharp changes in the Arrhenius slope may occur with the appearance of a new, thermodynamically favored, species within the scale. In addition, an Arrhenius plot of the temperature dependence of the reaction rate may reveal curvature because of the progressive change from one rate determining process to another. Both the features are observed in the Arrhenius plot for low-alloy steels (**Figure 1**).

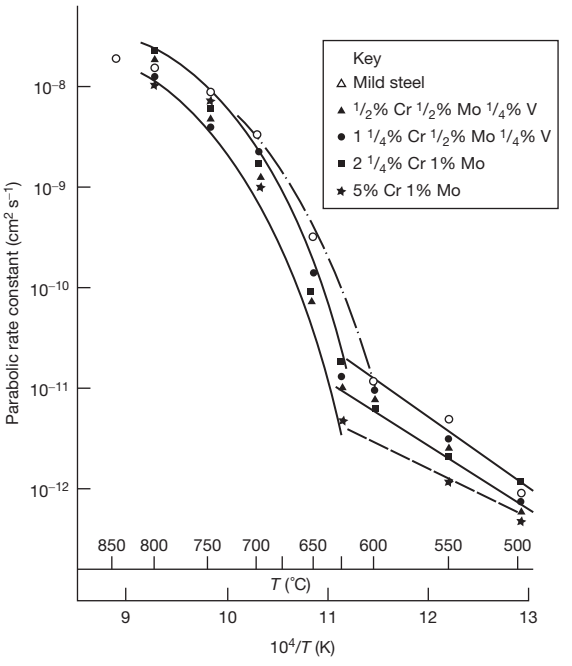

Figure 1 Arrhenius plot for the oxidation of mild steel and low-alloy steels in air showing a sharp break in the slope and curvature due to the appearance of FeO in the scale above 570 °C.

1.22.3 The Oxidation of Iron

For iron in most oxidizing environments, the PBR is approximately 2.2 and the scale formed is protective. The oxidation reaction forms a compact, adherent scale, the inner and outer surfaces of which are in thermodynamic equilibrium with the metal substrate and the environment respectively, and ion mobility through the scale is diffusion controlled.

The rate of oxidation of iron is then governed by the stabilities of the various phases, which are in turn a function of the temperature and oxygen partial pressure of the environment. Examination of the Fe–O_2 phase diagram (**Figure 2**) reveals that the principal solid oxide phases below 570 °C will be Fe_3O_4 (magnetite) and Fe_2O_3 (haematite). Above 570 °C, FeO (wüstite) appears as a third phase within the scale. These phases are present within the scale as individual layers, with the layer sequence dictated by the equilibrium oxygen partial pressure (pO_2) for phase stability

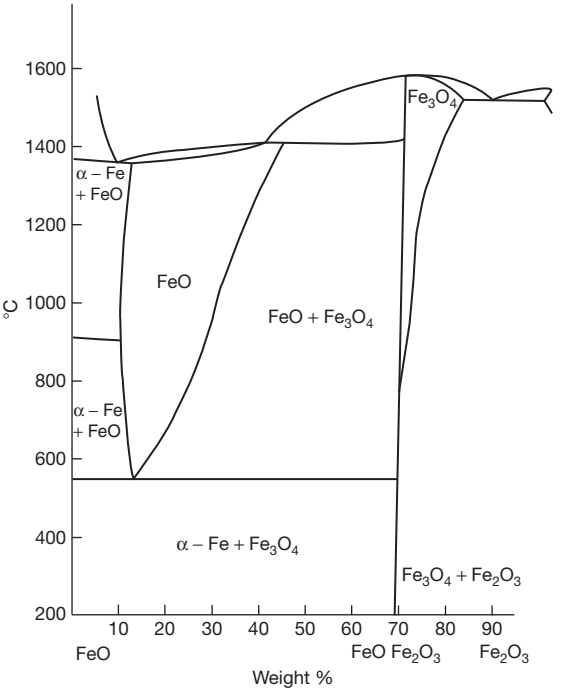

Figure 2 Fe–O phase diagram showing the principal solid phases stable on iron and wide stoichiometry limits of FeO. Adapted from White, J. CEGB Private Communication.

prevailing at the given temperature. Hence, the oxide phase stable at the lowest pO_2 (FeO at >570 °C) is found closest to the metal substrate, whereas the phase stable at the highest pO_2 (Fe_2O_3) is found closest to the oxidizing environment. If, however, the pO_2 of the environment is low enough, only FeO will be formed. At intermediate values of the pO_2, Fe_3O_4 will also form, and for most industrial environments, the pO_2 is sufficient for the formation of an outer layer of Fe_2O_3. While these observations are true for bulk scales, FeO has also been found to be stable in very thin films at temperatures down to 400 °C[4] and within narrow cracks at 500 °C.[5]

In the initial stages of oxidation, nucleation of oxide occurs at favored crystallographic sites, followed by preferential lateral spread from these nuclei to form a continuous thin film over the iron surface. At low temperatures (<200 °C), thin films, tens of nanometers thick, form exceedingly rapidly. Ion mobility is driven by space charges between gas–oxide and oxide–metal interfaces. As the scale thickens, the initial rapid growth rate is superseded by an extremely slow, logarithmic or inverse logarithmic growth law.

For iron oxidizing at temperatures between 350 and 500 °C, Fe_3O_4 nucleates first and grows laterally over the surface.[6] Once complete coverage is achieved, the Fe_3O_4 thickens parabolically. Ultimately, nucleation and lateral overgrowth by Fe_2O_3 occur, slowing the growth rate of the Fe_3O_4 appreciably, because of the lower effective pO_2 at the Fe_3O_4 surface, that is, the pO_2 falls from that of the environment to that governed by the equilibrium between Fe_3O_4 and Fe_2O_3 at the prevailing temperature. Both FeO and Fe_3O_4 nucleate first and grow out of the surface of pure Fe and Fe–3%Cr alloy at 700–800 °C in low pressure O_2 (10^{-3} Pa).[7,8] While Fe_2O_3 is thermodynamically stable, it can form only when the oxygen available for Fe_2O_3 growth has increased sufficiently. Initially, the available oxygen is continually depleted by the formation of Fe_3O_4. The length of this induction period prior to Fe_2O_3 growth is a direct function of the prevailing pO_2, being 3 h at 40 Pa, but only 1 min at 101 kPa.[7]

Above 570 °C, a distinct break occurs in the Arrhenius plot for iron, corresponding to the appearance of FeO in the scale. The Arrhenius plot is then nonlinear at higher temperatures. This curvature is due to the wide stoichiometry limits of FeO: limits that diverge progressively with increasing temperature. Diffraction studies have shown that complex clusters of vacancies exist in $Fe_{(1-x)}O$.[9,10] Such defect clustering is more prevalent in oxides that demonstrate a high degree of nonstoichiometry; with vacancy–hole complexes possibly being present at the higher deviations.[11] Single defects occur only when these oxides are closest to their stoichiometric composition. These considerations lead to a complex dependence of the cation diffusion coefficient on the oxide stoichiometry,[12] and hence on temperature.

Mass transport measurements have shown that cation transport predominates in FeO (Fe^{2+}) and Fe_3O_4 (Fe^{2+}, Fe^{3+}), whereas anion transport predominates in Fe_2O_3 (O^{2-}). This leads to the well-accepted growth scheme for multilayered scale growth on iron as shown in **Figure 3**, the governing equations for individual layer growth being

$$Fe_3O_4 + Fe = 4FeO \text{ above } 570\,^{\circ}C$$
$$4Fe_2O_3 + Fe = 3Fe_3O_4$$
$$2Fe_3O_4 + O = 3Fe_2O_3$$

It was originally considered that the growth of these layers was largely controlled by lattice diffusion, following the theories expounded by Wagner.[13,14] However, experimental work has shown that, for Fe_3O_4 below 600 °C and Fe_2O_3 at all temperatures, theoretical calculations of oxide growth, using lattice diffusion coefficients are unable to predict the growth rates observed in practice.[15,16] Tracer studies during the growth of Fe_3O_4 on Fe at 500 °C have shown that Fe_3O_4 growth is dominated by outward diffusion of Fe ions along short-circuit paths in the oxide.[17] These short-circuit paths are largely considered to be the oxide grain boundaries.[15] For Fe_3O_4 above 600 °C, the observed parabolic growth rate constants are within

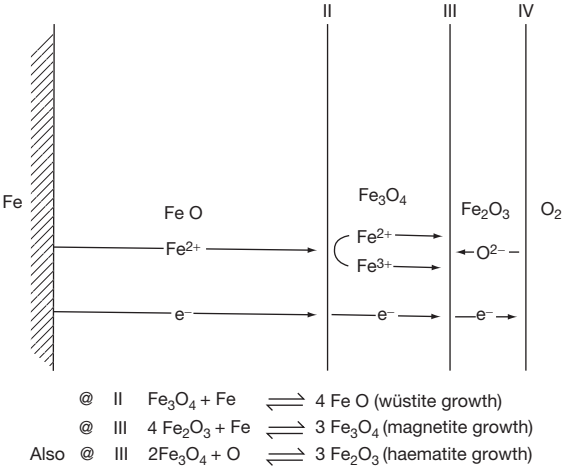

Figure 3 Simplified scheme for the diffusion-controlled growth of multilayered scales on pure iron and mild steel above 570 °C.

an order of magnitude of those calculated from tracer diffusion of Fe in Fe_3O_4.[18] A similar correspondence between theory and practice has been found for the growth of Fe_3O_4 by the solid state reactions from FeO and Fe_2O_3 between 600 and 1200 °C.[18] The growth rate of FeO is within 10% of the theoretical rate expected from Fe lattice diffusion, calculated according to the Wagner theory.[19]

The measured activation energy for Fe_2O_3 growth is of the order of 169–222 kJ mol^{-1}.[20] This activation energy is much lower than that expected from measurements of the tracer diffusion of Fe or O[21] and the measured rate constant for Fe_2O_3 growth is approximately ten times greater than that calculated according to Wagner.[13] O^{18} tracer diffusion studies of the growth of Fe_2O_3 during the oxidation of Fe at 823 K have shown that, although the primary diffusion species through the crystal lattice is Fe ions, fast, inward O_2 diffusion occurs down cracks in the scale.[22]

The oxidation rate of pure Fe in O_2 has been shown to be affected by the specimen shape and the original surface profile.[23] For iron oxidizing in O_2, 50:50 $O_2 + H_2O$ and $O_2 + CO_2$ rough surfaces have been found to oxidize more slowly than smooth surfaces, since surface irregularities hinder the oxide flow.[23,24] The oxide is unable to deform sufficiently to maintain intimate contact with the metal surface such that porous scales are formed.[25]

For the oxidation of pure Fe at 500 °C, the early reaction rate is more rapid on cold-rolled than annealed surfaces. On cold-worked surfaces, the scale tends to be rough and poorly adherent and contains less Fe_3O_4.[26] Cold-work enhances the oxidation rate by mopping up vacancies so that pore-free scales are formed which maintain contact with the substrate.[27–31] One of the authors[32] has found an effect of stored cold-work during the oxidation of fracture surfaces at 600 °C, which disappears with increasing oxidation because of the effect of surface annealing and consumption of the cold-worked layer by oxidation. At long oxidation times (>200 h), the oxidation rate of a fracture surface becomes indistinguishable from that of an annealed emery-ground surface.[32] At temperatures above approximately 625 °C, there is no effect of cold-work.[23]

1.22.4 General Alloying Effects on Oxidation

The general requirements for higher temperature alloys is that they should be cheap, should possess adequate mechanical strength, should be resistant to chemical degradation by the environment, and should be easily fabricated. These requirements are often conflicting, and a compromise is required for alloy design. Simple iron alloys form oxides that are not normally protective enough at temperatures above about 550 °C.[33] Therefore, the addition of other elements is needed to form a more protective scale. These elements usually comprise chromium, aluminum, and/or silicon. For these elements to confer adequate protection, the scale that they develop should be stoichiometric (to minimize ionic transport rates), free of gross defects, stress free at temperature, should resist spalling, and should not be volatile by further reaction with the environment.[34]

It has already been shown that bulk lattice diffusion is not generally considered to be the rate-controlling process for the oxidation of iron in most real situations. Hence, the classical Wagner treatment, whereby the valency of the alloying element increases or decreases the number of lattice defects, provides little clue as to the overall effects of alloying elements on the oxidation of iron alloys. Rather, studies have shown that the effects of alloying elements on the oxidation of iron alloys are largely brought about by their mobility (or lack of mobility) in the iron oxide lattice, and the effect this has on scale morphology, phase structure, and oxide plasticity. The addition of even small quantities of alloying elements can profoundly influence the scale morphology produced and hence the subsequent oxidation behavior.

The Fe_3O_4 unit cell comprises an inverse spinel structure, with Fe^{2+} and Fe^{3+} cations occupying octahedral and tetrahedral interstitial sites within a close-packed oxygen lattice. The occupation of an interstitial site is accompanied by a specific site energy and particular cations show a preference for occupation of that site in which they sit most comfortably, that is, the lowest-energy site (**Figure 4**). The difference between the potential energy of a cation in a preferred site to that in a nonpreferred site is termed the crystal field preference energy[35] (CFPE) and is principally determined by the number of electrons on the d-shell. The direction of travel of a cation through the magnetite lattice is via alternate octahedral–tetrahedral–octahedral site transfers.[36] These interstitial sites are interconnected by saddle points within the lattice, and in order to transfer from one interstitial site to another, the diffusing ion must acquire enough energy to surmount this energy barrier and pass through the saddle point. If the direction of movement of the cation is from a favored to a nonfavored site, additional energy is required to overcome the CFPE. If, however, the direction of cation

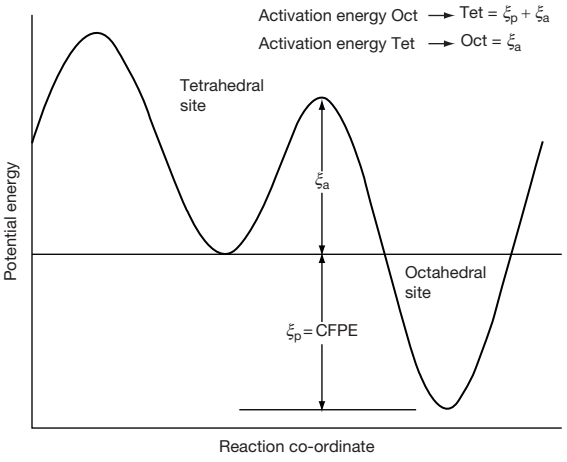

Figure 4 Potential energy/lattice position diagram for occupation of interstitial sites in Fe_3O_4 lattice alloying element cations.

movement is in the opposite direction, there is a net reduction in the total lattice energy equivalent to the CFPE. It is apparent that, if the cation shows a high CFPE between interstitial sites, then cation transfer is much easier in one direction than the other and diffusion of the cation through the lattice will be severely hindered. The CFPE for Cr, Mo, and V in octahedral sites in magnetite is high, whereas that for Mn is virtually identical to that of Fe, both of which are very low. Hence Cr, Mo, and V are virtually immobile in the magnetite lattice, while Mn is found throughout the scale at atom ratios to the iron similar to those found in the original metal.[37,38]

As a result of this lack of mobility of certain alloying elements, a new phase layer appears in the scale. This new layer grows inward from the original metal surface, is in intimate contact with the substrate alloy,[39] and has an alloying element composition approximately 1.5 times that of the original metal.[37] Moreau[40] identified this inward growing layer on Fe–Cr steels as $FeCr_2O_4$ globules within a wüstite matrix. Further, Rahmel[39] determined that the inner layer of four-layered scales grown on iron alloys containing Cr, Mo, V, and Si consisted of FeO containing $(Fe, X)_3O_4$, where X is Cr, Mo, V, or Si. The oxygen transport through the inner layer is thought to take place via pores within the inner layer, since solid-state diffusion of oxygen through the magnetite lattice is five orders of magnitude too low,[41] and grain boundary diffusion is also too low, to account for the observed growth rates.[42] The oxygen pathways are now thought to comprise grain boundary triple points and transient microvoids, continuously created and rearranged by creep.[43]

At temperatures below approximately 600 °C, numerous studies have shown that the thickness of the inward growing layer approximates to that of the outwardly growing magnetite + hematite scale, with the location of the spinel–magnetite interface approximately located at the original metal surface.[34,37,44–46] Hence, the new spinel formed approximately balances the volume of metal consumed, implying equal amounts of oxygen and cation transport in duplex film growth[34] and also implying that the rate of growth of the two scales are linked to one another. Moreover, it is now considered that the overall growth rate is mainly determined by the rate of cation diffusion outward through the outer layer, since the cations must first diffuse out to provide space for inner layer growth. Hence, the extent of inner layer growth is dictated by the recession of the oxide–metal interface.

These observations have been rationalized by Robertson and Manning,[43] who suggest that, for single-layer growth, the metal ions are transported as metal vacancies to the scale–metal interface. This interface consists of incomplete planes of metal atoms, or ledges, on which there are incomplete rows or jogs, analogous to interfacial edge dislocations. A metal vacancy in the oxide, on arrival at the interface, aligns with a jog atom on the metal surface. Oxidation then occurs when the jog atom moves into the oxide and annihilates the vacancy. Repetition of this process causes continual stripping of the metal ledge and allows oxide to fall into the space created (analogous to the climb of an edge dislocation). The surrounding oxide lattice then relaxes, maintaining adhesion. Since Cr is much less mobile in Fe_3O_4 than Fe, a Cr ion tends to remain at the site where it first enters the oxide and inhibits dislocation movement.[47] This prevents the scale falling into the space created by the outward diffusion of Fe ions and microvoids (a few atom sites) are formed at the scale–metal interface. This initiates duplex growth by creating the space required for inner layer growth, without compromising adhesion.

For many low-alloy steels, therefore, the scale phase sequence is as shown in **Figure 5** and the governing equations for individual layer growth are similar to those for pure iron, with the addition of

$$Fe_3O_4 = Fe^{2+} + 2Fe^{3+} + 4O^{2-}$$

at the spinel–magnetite interface and

$$3(FeX) + 4O^{2-} = (FeX)_3O_4$$

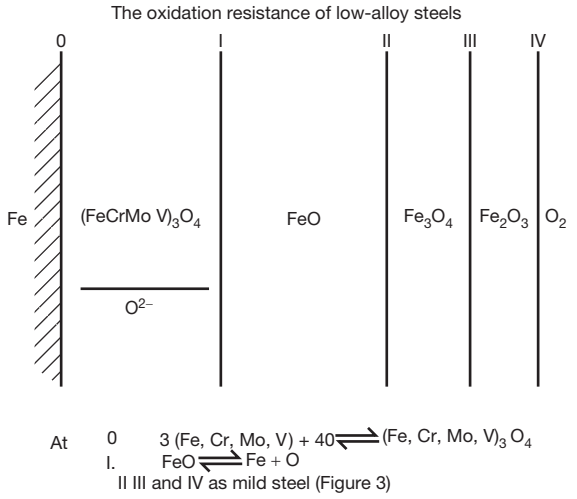

Figure 5 Simplified scheme for the diffusion-controlled growth of multilayered scales containing spinel layers on low-alloy steels.

at the metal–spinel interface. The Fe^{2+} and Fe^{3+} ions diffuse through the overlying magnetite (or wüstite) to promote higher oxide reduction as before. The O^{2-} ions percolate through pores and microfissures in the underlaying spinel to promote growth of the spinel layer.

With some alloying elements, for example, Si and Al, the concentration of element required in the lattice to form their own oxide is so low that preferential formation of pure Al_2O_3 or SiO_2, which are both highly protective, may occur. For the reaction

$$A\mathrm{O} + B(\text{in alloy}) = A(\text{in alloy}) + B\mathrm{O}$$

the limiting mole fraction (N_A) of A required for protection is given by

$$\frac{N_A}{1 - N_A} = \exp \frac{1}{RT}(\Delta G_{A\mathrm{O}} - \Delta G_{B\mathrm{O}}) \qquad [3]$$

where $\Delta G_{A\mathrm{O}}$ and $\Delta G_{B\mathrm{O}}$ are the free energies of formation of the oxides AO and BO, respectively.

Provided the mole fraction of A does not fall below N_A, the oxide AO will be formed exclusively. The important criterion is the ratio of the oxidation parabolic rate constant to that of the diffusion coefficient of A.[48] For Al in Fe, the parabolic rate constant is very low, while the diffusion coefficient is relatively high, whereas the diffusion coefficient of Cr is much lower. Hence, the bulk alloy composition of Al in iron required for the exclusive formation of Al_2O_3 at any given temperature is lower than the Cr concentration required for the exclusive formation of Cr_2O_3.

By adding a third element (C), it is possible to increase the likelihood of forming compound BO, at a lower concentration than would be required in the pure binary alloy A–B, provided that the third element C has an affinity for O intermediate between that of A and B.[49] If the mobility of B in the ternary alloy is high enough and element C has sufficient thermodynamic activity in the alloy to form CO, then the potential of O may be lowered to such an extent that BO forms more readily, that is, element C acts as a getter for element B. Such behavior is characteristic of, for instance, Fe–Al–Si and Fe–Cr–Si alloys.

1.22.5 Effects of Specific Alloying Elements on the Oxidation of Iron

Although in reality, binary low alloy steels are rarely used in industry, the effects of single element additions to iron will be discussed. However, the effects of further additions whether intentional or as impurities to form ternary, quaternary or multi-element alloys can be large and may alter the behavior of the previous system to which they were added to a great extent.

1.22.5.1 Carbon

The addition of carbon to iron principally affects the subsequent oxidation response via the oxidation of the carbon in the steel to form CO and CO_2. Runk and Kim[50,51] and latterly Nosek and Werber[52] have all reported similar observations on the oxidation of Fe–C alloys at temperatures up to 400 °C. It appears that magnetite nucleates first over the ferrite, the growth reaction obeying two-stage logarithmic kinetics with electron transfer through the scale being the rate-controlling process. Due to the formation of a kinetic barrier of CO and CO_2 at the carbide–oxide interface, only a thin film (15 nm) of randomly oriented crystallites of γ-Fe_2O_3 of approximately 7 nm mean grain diameter form over the cementite. Continued oxidation results in grain growth in the γ-Fe_2O_3 due to strain-induced grain boundary migration and a transition from γ- to α-Fe_2O_3. This latter transformation is accompanied by a 2.3% volume decrease, which causes cracking and allows the carbon oxides to escape. Ultimately, lateral magnetite overgrowth of the cementite occurs, and once Fe_3O_4 has spread over the whole surface, protective kinetics prevail, since the magnetite is impermeable to the carbon oxides.

Bohnenkamp and Engell[53] and Caplan *et al.*[54,55] have also reported rapid carbon loss from the steel during the initial stage of oxidation at higher

temperatures (~850 °C) followed by a much lower, or zero, loss of carbon later. Caplan *et al.* measured the CO_2 evolution by infrared gas analysis and reported that the percentage of carbon loss from 0.1% C, 0.4% C, 0.8% C, and 1.2% C steels was overall very small and may be redistributed in the metal. There was no carbon loss detected at 700 °C. The overall oxidation rates were all found to be parabolic at 850 °C and less than the oxidation rate of pure Fe. In the Fe–C alloys, the individual phases of FeO, Fe_3O_4, and Fe_2O_3 were found to be less regular than those of pure Fe and were often highly porous.

Malik[56] reported that, at temperatures between 600 and 850 °C, in 101 kPa oxygen, the oxidation rate of Fe–5% *M*–C steels (where *M* was Si, Ti, V, Nb, Ta, Cr, W, or Ni) fell as the carbide stability increased. The oxidation of all of the alloys obeyed parabolic kinetics, although some breakaway occurred following an incubation period. This breakaway was attributed to scale disruption, as a result of CO_2 evolution, with the carbon loss being most rapid during the first 5 min. Although the amount of carbon loss increased with the carbon content of the alloy, as did the oxidation rate constant, the total carbon loss was very much lower than that available. Those alloys forming a pure carbide phase were found to have a lower oxidation rate than those alloys comprising a solid solution phase or cementite. All of the binary Fe–5% *M* alloys displayed a similar reaction rate, which was approximately one order of magnitude lower than that of pure Fe, because of the formation of mixed oxides or spinels in the scale. The Fe–5% *M*–C alloys always showed two-layered scales, with an inner mixed oxide or spinel overlaid with Fe_2O_3. The scales formed on the high-carbon alloys were generally more compact and adherent (following initial scale disruption by C loss) because of carbide dispersion improving scale integrity. Malik[56] argued that the carbide-forming elements retard the diffusion of carbon in austenite, reducing the overall scaling rate. In non-carbide-forming alloys, such as Ni and Si, the oxidation rate was greater because of a higher carbon mobility in the steel.

At 850 °C and 1.2% C, the oxidation rate was found to be in the order Fe–Cr–C > Fe–C > Fe–Ni–C > Fe–Ti–C > Fe–Ta–C > Fe–Nb–C > Fe–V–C > Fe–W–C, which is nearly, but not exactly, the sequence of carbide stabilities.

1.22.5.2 Aluminum

On oxidation, aluminum forms the highly refractory, and hence protective, Al_2O_3. However, the addition of aluminium to steels produces a dramatic change in their mechanical properties with a reduction in toughness and an increase in ductile-to-brittle transition temperature (DBTT), which is detrimental in many circumstances. There is a need, therefore, to realize the protective benefit of aluminum at as low a concentration as possible within the steel. Al compositions of 8 wt% results in severe embrittlement at room temperature, and the oxidation of iron–aluminum alloys has been reviewed in detail by Prescott and Graham.[57] At aluminum concentrations below 2.4 wt%, bulky stratified scales, comprising Fe_2O_3 and Fe_3O_4, with an inner layer of Al_2O_3 or $FeAl_2O_4$ are formed at 800 °C.[58] At 2.5% aluminum, large areas of Al_2O_3 were always observed with iron oxide nodules. Formation of these iron oxide nodules is suppressed only when the aluminum content exceeds approximately 7 wt%.[58–60]

Ahmed and Smeltzer,[61] Pons *et al.*,[62] and Smith *et al.*[63] have all found that, at 1173 K, iron alloys containing around 5–6% aluminum initially form a rapidly growing duplex scale comprising an outer α-Fe_2O_3 layer overlaying an inner $(FeAl)_3O_4$ layer. However, with prolonged oxidation, an Al_2O_3 layer eventually forms at the oxide–metal interface and precipitates within the alloy. The reaction rate gradually decreases as the Al_2O_3 at, or near, the surface coalesces eventually to form a continuous film that virtually stops the outward diffusion of Fe ions. Electron backscattered Mössbauer spectroscopy studies have shown that the outer Fe_2O_3 contains approximately 10% Al^{3+} and the inner layer comprises Al_2O_3 with some Fe^{3+}.[(64)] The benefits afforded by alumina scale formation are well documented: slow growth as a result of low defect concentrations and stability at high temperature. A disadvantage associated with alumina scales on iron is the relatively poor scale adherence which can result in spallation of the protective layer.[65]

Alumina generally develops as either α-Al_2O_3 or γ-Al_2O_3 during the oxidation of Fe-Al alloys. α-Al_2O_3 forms, and is stable at higher temperatures and is more desirable for conferring oxidation resistance.[57] Initial transient stages of alloy oxidation show scale compositions controlled by kinetics rather than those predicted by thermodynamics. The growth of convoluted transient scales containing all of the alloying elements is quickly replaced by a slow growing protective alumina scale dependent on composition and temperature. The critical Al content for the exclusive formation of Al_2O_3 has been found to be raised by the presence of Ti and B.[66]

The beneficial effects of adding both aluminum and chromium to steels has been demonstrated by Tomaszewicz and Wallwork[66] during oxidation studies of Fe–Al–Cr alloys at 800 °C in pure oxygen at 26.6 kPa. They showed that Al acts as a primary getter for oxygen, nucleating Al_2O_3, with Cr acting as a secondary getter, nucleating Cr_2O_3. If there had been sufficient Cr and Al in the alloy, no iron oxides would have been formed. The total Al + Cr content to suppress nodule formation was found to be in the range of 7–8%, with 7% Al required at 0% Cr, but only 3% Al required at 5% Cr.

The diffusion coefficient for S in Al_2O_3[67] at 950 °C is approximately 100 times lower than that in Cr_2O_3.[68] Hence, for high temperature applications in S environments, aluminum confers a much greater degree of protection than that afforded by chromium.

1.22.5.3 Silicon

The addition of silicon to iron has been reported by many authors to confer significant corrosion protection. Rahmel and Tobolski[69] found that binary alloys containing up to 4% Si displayed a limiting corrosion rate due to the formation of an iron-silicate layer when exposed to pure oxygen, $O_2 + H_2O$ or CO_2 in the temperature range 750–1050 °C. However, Robertson and Manning[70] indicate that Fe–Si oxides are generally immiscible. Several authors[71–74] have reported that the corrosion protection apparent in Fe-Si alloys arises from the formation of a SiO_2 healing layer, beneath the magnetite, which acts as a barrier to outward transport of metal ions. At the low oxygen potentials at the base of the scale, and for very thin films, charged effects in the amorphous SiO_2 network and electronic carriers control the growth of the SiO_2.[42,75]

Adachi and Meier[76] studied the oxidation of Fe–Si alloys under isothermal and cyclic oxidation conditions, in air, between 900 and 1000 °C. They found that oxidation rates in air decreased with the silicon content, such that at 10 wt% Si the oxidation rate was lower than that conferred by Cr, because of the formation of a continuous film of SiO_2. The oxidation kinetics of these steels was found to be linear because of the diffusion of Fe through a film of SiO_2 of constant thickness. Outward diffusing Fe subsequently dilutes the SiO_2 to form Fe_2SiO_4 and produced the Fe_2O_3 as an outer layer. At greater than 10% Si, SiO_2, overlaid with Fe_2O_3, comprised the total scale.

At the low oxygen potentials found in CO/CO_2 environments, the critical concentration of Si for the selective formation of a continuous film of SiO_2 is only approximately 0.05%.[77] However, at higher oxygen potentials, the higher growth rate of transient iron oxides suppresses the growth of this continuous SiO_2 scale. Even at 5% Si in the steel, no continuous SiO_2 layer formed during oxidation in air, whereas such a film was seen to form during oxidation in Ar at a pO_2 of 10^{-4}.

Logani and Smeltzer[78–80] have observed that, for Fe–1.5% Si at 1000 °C in CO/CO_2, the initial slow reaction rate was followed by regions of linear behavior because of the amorphous SiO_2 film being consumed by the growth of wüstite–fayelite nodules during the early stages. These wüstite–fayelite nodules were nucleated at alloy grain boundaries and then grew laterally to inundate the SiO_2 films over alloy grains.

During the oxidation of high Si content steels in high-pressure CO_2, the oxidation reaction can suddenly switch to a highly protective mode that proceeds extremely slowly after an initial incubation period.[70] This follows the formation of a healing layer, comprising a line of amorphous silicon-rich oxide along the oxide–metal interface with Cr enrichment to 30–40 at% just above the healing layer and Cr depletion in adjacent metal sites. Slowing of the oxidation reaction by the SiO_2 permits selective oxidation of Cr. Cr and Si are then synergistic, with less Si being required in Cr-containing steels than in straight Fe–Si steels, because of secondary gettering. For Fe–Si, then, 2.5–3% Si is required for healing layer formation, irrespective of the temperature. For Fe–Cr–Si, however, the critical Si content decreases with increasing Cr content and temperature.

Silicon has a major effect on the rate of oxidation of iron. Yang *et al.*[81] found that small additions (less than 2 wt% Si) result in a marked decrease in the rate of oxidation up to 1000 °C in dry moving air, however, at 1200 °C the formation of a liquid phase resulting from the melt of FeO and SiO_2 substantially increased the oxidation rate. Adachi and Meier[76] showed that the addition of 5 wt% Si is observed to decrease the oxidation rate of iron by more than two orders of magnitude and additions of 10 wt% Si or more results in oxidation rates slower than Fe-26 wt% Cr. Lashin *et al.*[82] studied Fe – 6 at.%Si steels at 500 °C – 540 °C in ambient air of various pressures. The tests were designed to show the oxidation behavior of steels intended for use in electro-magnetic applications.

Ishitsuka *et al.*[83] report a reduction in the steam side oxidation rate of 9Cr- 0.5Mo 1.8W (P92) with increasing Si content. Improved oxidation resistance

was apparent at all temperatures investigated (500 °C, 550 °C, 600 °C, 650 °C and 700 °C). The largest reduction in corrosion rate was observed at 700 °C, oxidation rates at all other temperatures showed similar rate reductions. At 700 °C the remarkable reduction in oxidation rate was attributed to the formation of a protective amorphous SiO_2 film grown at the scale metal interface. At temperatures of 600 °C, or less, only dissolved silicon in the Fe–Cr spinel lattice contributes to the effect of silicon on oxidation rates.

1.22.5.4 Manganese

Since Mn is both soluble in iron oxides and mobile to the same extent as Fe, the addition of Mn to steels has little effect on the overall scaling rate in air or oxygen. Jackson and Wallwork[84] have shown that between 20% and 40% manganese must be added to steel before the iron oxides are replaced by manganese oxides. However, Mn suppresses breakaway oxidation in CO/CO_2 possibly by reducing the coalescence of pores in the oxide scale. It also appears to be important in the healing of microcracks in protective chromia/spinel oxide scales formed on highly alloyed steels.[85]

The addition of up to 15% Mn to pure Fe, under sulfidizing conditions at 1073 K, leads to a small increase in the scaling rate.[86] At 2% Mn, MnS forms as stringers in the subscale, but these do not form a coherent layer even at a concentration of 15% Mn. The increase in scaling rate is possibly due to increased short-circuit diffusion, since metal diffusion in MnS is much slower than in FeS.[87]

1.22.5.5 Sulfur

The presence of small quantities of S in steels has little effect on the initial scaling rates in air, but may be detrimental to long-term scale adhesion. Sulfur has, however, been shown to be detrimental to breakaway oxidation in CO/CO_2 environments.[88] However, it has been shown to reduce the total uptake of carbon in the steel under CO/CO_2[89] and reduce the scale thickening rate. In this context, free-cutting steels were found to oxidize at a significantly lower rate, as did steels subjected to pretreatment in H_2S.

Modern steel making techniques are capable of routinely producing alloys of sulfur contents < 50 ppmw;[90] however, recent research by a number of groups[91–93] indicates that removing sulfur to extremely low levels may have a detrimental effect on the oxidation resistance of 9–12Cr steels in steam and it may, therefore, be necessary to intentionally add sulfur to these alloys.

1.22.5.6 Phosphorus

Like sulfur, phosphorus appears to have only a small effect on the overall scaling of iron alloys in air. For example, minor editions (<0.1 wt%) have been shown to increase the oxidation resistance of iron at 500 °C, but above this amount the oxide layers begin to break and become nonprotective.[94] However, phosphorus may play a role in suppressing breakaway oxidation in carbon steels in CO/CO_2 environments. Donati and Garaud[95] found that the tendency for breakaway was lower over ferrite, where P segregates. To confirm this, the authors doped pure Fe with P and found that the breakaway rate slowed down at 350 ppm phosphorus and was totally suppressed at 900 ppm phosphorus. A similar benefit has been reported by Dewanckel *et al.*[88]

1.22.5.7 Nickel

The addition of Ni to Fe dramatically reduces the oxidation rate due to the virtual insolubility of NiO in FeO.[96] The oxidation of iron nickel alloys in general was reviewed by Foley in 1962.[97] During the oxidation of Fe–Ni alloys, and in the absence of nickel oxide formation, Ni concentrates at the FeO-substrate interface as a result of Fe depletion. Oxidation rates decrease due to the reduced Fe activity at the base of the FeO scale and thus the stability of the FeO layer is diminished. Menzies and Lubkiewicz[98] found that the oxidation of an Fe-12%Ni alloy in O_2 obeyed parabolic kinetics at all temperatures between 700 °C and 1000 °C. At 700 °C, the Ni suppressed the formation of FeO, with the scale comprising only Fe_3O_4 and Fe_2O_3. Progressive enrichment of Ni occurred in the alloy as the substrate was consumed by oxidation. When the concentration of Ni reached 50–60%, the Ni entered the spinel phase, leading to the formation of $Ni_{(x)}\ Fe_{(3-x)}O_4$ with x approximately equal to 0.24 near the alloy surface and less than 0.01 near the Fe_2O_3. At 900 °C – 1000 °C, the Ni entered the spinel in the early stages of oxidation, with x values of 0.4 at 900 °C. This led to a reduction in the parabolic rate constant. At 1000 °C FeO is the stable oxide phase formed on Fe–Ni alloys, even up to 80% Ni, since FeO is more stable than NiO.[99]

1.22.5.8 Chromium

Of all of the alloying elements added to steels, Cr has been the most used for improving the corrosion properties. In terms of high temperature oxidation, steels

containing approximately 10% Cr are capable of forming a continuous, highly protective film of Cr_2O_3.[33] Rhys-Jones *et al.*[100] reported that the isothermal oxidation kinetics of Fe10Cr at 1000 °C were parabolic. However, significant reductions in the oxidation rate are also realized at lower Cr concentrations because of the formation of FeCr spinels[101] and the suppression of FeO formation to temperatures in excess of 570 °C.[102] At 700 °C, FeO exhibits a very narrow stability range on the Fe–Cr–O phase diagram (**Figure 6**) for Cr up to 6%.[103] The wüstite stability range is almost negligible on Fe–0.5% Cr because of the high reactivity of Cr toward O_2 at 1000 °C. However, while Cr_2O_3 is normally protective on steels in air or O_2 up to approximately 900 °C, volatile CrO_3 may form at higher temperatures.[33] Dewanckel *et al.*[88] found that although the addition of Cr to steels is normally considered beneficial, low quantities (<500 ppm Cr) were detrimental to the breakaway performance of low-alloy and carbon steels.

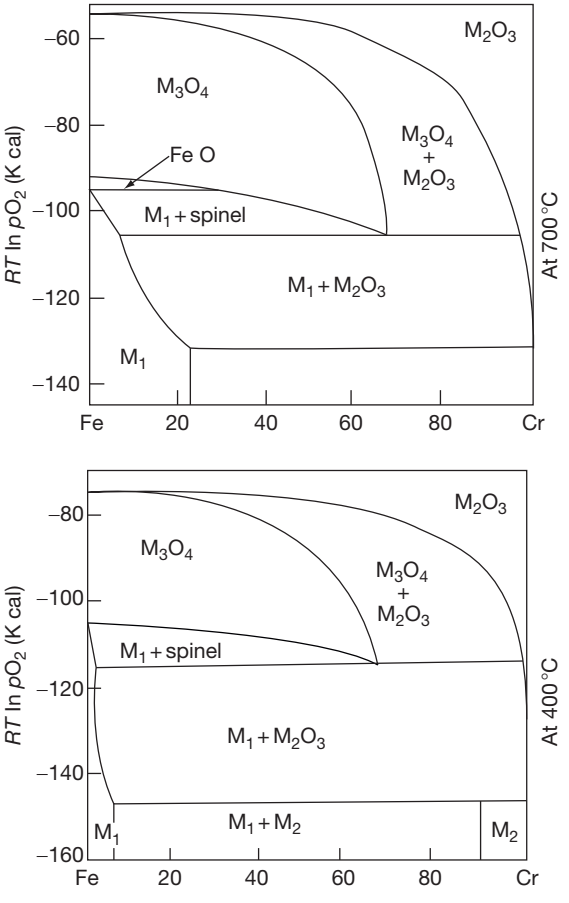

Figure 6 Fe–Cr–O phase diagram for Fe–Cr alloys at 400 °C and 700 °C.

Many studies have shown that surface pretreatment of Fe–Cr alloys has a strong effect on the scale morphology and subsequent oxidation rate.[27,104–106] For instance, Caplan[27] indicated that several Fe–Cr alloys showed improvements in corrosion resistance because of cold work, with greater than 16% Cr required to show the optimum benefit. Khanna and Gnanamoorthy[104] examined the effect of cold work on 2.25% Cr–1% Mo steels at temperatures between 400 and 950 °C over 4 h in 1 atm O_2. They found that up to 90% reduction by cold rolling had a negligible effect on the oxidation rate up to 700 °C. However, above 700 °C there was a general reduction in the kinetics because of enhanced Cr diffusion in the alloy, leading to the formation of a Cr-rich spinel. In addition, they found that breakaway corrosion occurred at 900 °C on annealed samples, but this did not occur on samples that had been cold-worked. For Fe–10% Cr at 600 °C in air, Hossain found that the oxidation resistance increased with the degree of cold work.[105]

1.22.5.9 Molybdenum

In the temperature range 500–1000 °C, additions of between 0.5% and 5.6% of Mo decreases the oxidation rate of iron by a factor of almost 10, with the maximum benefit being obtained at a concentration of approximately 2%.[107] Like many alloying elements, Mo promotes the formation of a duplex spinel–magnetite scale, with the Mo retained within the inner spinel layer.[105]

1.22.5.10 Boron

Tsipas and Rus[108] and Suwattananont and Petrova[109] found that thermally diffusing boron into the surface of steel gave a boride layer with enhanced oxidation resistance at temperatures up to 900 °C by acting as a barrier to inward diffusing oxygen. Rowley *et al.*[110] also found that adding small amounts of boron to Fe–Cr alloys strongly affects the materials oxidation characteristics in super-heater steam. Enhanced manganese and/or chromium content of the oxide films in comparison to those seen in undoped 9Cr steels provides greater protection and hence a reduction in oxidation rates. Rowley proposes two likely models for boron doped oxide growth:

1. The possibility that Schottky electron emission from the metal substrate into the conduction band of the oxide layer and/or subsequent electron diffusion may control oxide growth kinetics.

These processes are governed by the space charge in the oxide film which is due to the electric field produced by an ionic defect gradient through the layer. Existing theories indicate that this mechanism is applicable for oxide thicknesses ranging from 5–100 nm in the temperature region 300–600 °C, both of these conditions are satisfied in the case of boron doped oxide films.

2. It is possible that a boron containing phase of low ionic conductivity is formed at grain boundaries. This may lead to a progressive reduction in ionic mobilities via a mechanism similar to that postulated for the reactive elements effect[111] (cited by Rowley *et al.*). Although boron does show a tendency to migrate to grain boundaries, it is experimentally observed that the limiting oxide thickness is reached extremely rapidly indicating an almost instantaneous formation of a blocking phase. Furthermore, the ultrafine grain size exhibited by boron doped oxides would provide a much larger number of short-circuit diffusion pathways than in control oxides. This suggests that ionic blocking must be extremely effective for this mechanism to be tenable.

1.22.5.11 Others

Small additions of Ce have been shown to have a favorable influence on the oxide growth of several Fe–Cr alloys by improving scale adherence and acting as nucleation sites for Cr_2O_3.[112] In a $H_2{\cdot}H_2O{\cdot}CO{\cdot}CO_2$ atmosphere at 700 °C cerium levels as low as 0.024% reduce the carbon uptake of steels in carbonaceous atmospheres by several orders of magnitude. However, Sroda *et al.*[113] found additions of Ce to low alloy steels to have a negative effect on corrosion resistance at 500 °C, especially, in HCl containing atmospheres. The techniques used in the study did not enable the author to detect Ce in the oxide scale and thus it was not possible to determine the role of cerium in the corrosion process (although thermodynamic calculations show that the formation of cerium oxides is possible). Trace concentrations of As and Sn have been found to improve the breakaway properties of scales formed on mild and low-alloy steels in CO/CO_2, whereas Cu has been found to be detrimental.[88]

1.22.5.12 Effects of Heat Flux and Cold Work

Another factor which has been largely ignored in earlier work is any influence of heat flux on the oxidation behavior of boiler steels, for example. Most industrial components in service will be subjected to a thermal gradient across them, and the effect of this has been investigated recently by Fry *et al.*[114,115] They showed that the oxide grain size and morphology could change in subtle ways when subjected to a heat flux, and that this could have important implications under some conditions. Trindade *et al.*[116] have also shown that surface finish and cold work can influence the substrate grain size and hence the high temperature oxidation of pure Fe and 2.25Cr–1Mo steel. Decreasing grain size increases oxidation rates by facilitating oxygen diffusion down grain boundaries. Internal oxidation including the formation of $FeCr_2O_4$ and Cr_2O_3 along grain boundaries was observed. Oxidation kinetics decreased strongly with an increase in grain size as a result of the reduction of grain boundary density leading to less internal oxidation per unit volume. Fluctuation in grain size did not appear to affect the rate or structure of external oxide scales.

The effect of cold working on high temperature oxidation was also investigated. In agreement with Ostwald,[117] Trindade[116] suggests the increased dislocation density associated with cold working allows greater diffusion rates of chromium in bcc steel; this increased mobility enables Cr enrichment of the spinel layer in comparison to non-cold worked specimens. The increased Cr content within the spinel scale affords improved oxidation resistance. Recrystallization/recovery of specimens subjected to greater than 42% cold work resulted in low dislocation densities and polygonization; the ensuing fine grained low dislocation density microstructure led to an overall increase in oxidation rates.

Samples of pure iron were heat treated to establish microstructures of two different grain sizes and then oxidised in laboratory air at 550 °C for 72 h. Gold markers were used to indicate the position of the original metal surface and to define the mass transport direction. Studies reveal that the oxide scale in pure iron also grows by outward Fe migration and inward oxygen diffusion and that, similarly to 2.25Cr–1Mo steels, oxidation kinetics of pure iron also decrease with an increase in substrate grain size.

However, Caplan and Cohen[30] studied the effects of cold work on the oxidation rates of pure iron, where in contrast to the findings of cold worked 2.25Cr–1Mo steels, oxidation rates of cold worked pure Fe were observed to increase as a result of cold work. It was proposed that as iron diffused outwards, vacancies are annihilated at dislocations or lattice steps on the cold

worked Fe surface. As a result, the oxide layer remains in good contact with the Fe substrate in the absence of pore formation and rapid oxide growth ensues.

1.22.6 Stress Effects

While alloying elements may initially determine the protective nature of an oxide scale, the response of this oxide scale to stress is often crucial in determining the long-term oxidation performance of an alloy in an industrial environment.[118] The stresses in an oxide scale may arise both internally (because of growth stresses) and externally (because of applied stresses).[119] In general, oxide scales do not possess sufficient slip systems for plasticity and thus rely upon diffusion-controlled creep for plastic deformation and stress relief.[120] At temperatures below approximately 600 °C, only elastic deformation is possible and stress relief by cracking is likely to occur. If the scale–metal interface is strong, and the bulk oxide is weak, through-scale cracking results when the combined stresses exceed a critical value.[121] If the interface has a lower strength than the oxide bulk strength, decohesion occurs first. A minimum energy is required for cracking or decohesion.[122,123] Evans and Lobb[121] have calculated that cracking occurs when the strain energy per unit volume (w^*) of oxide contained in layer thickness (t) equals the work required for internal cracking (G_c) or decohesion (G_d). For internal cracking,

$$w^* = \frac{8PG_c}{fL} \sim \frac{4G_c}{fL} \qquad [4]$$

where L is the side length of unit volume; f, the fraction of stored energy in the oxide; G_c, the energy for unit area of cracked oxide surface; and P is the geometric parameter (~0.5). For decohesion,

$$tw^* = \frac{G_d}{f} \qquad [5]$$

where f is the energy/unit area of fresh metal at the oxide–metal interface.

Through-scale cracking may not necessarily be detrimental to an alloy if rapid scale healing can occur,[124] and scale delamination can reduce the total scaling rate if the scale remains adjacent to the alloy surface.[119,125] In this instance, scale separation confounds the transport of metal ions across the interface into the oxide. However, if through-scale cracking occurs in conjunction with delamination, scale spalling may follow,[121] with an attendant loss of protection. For pure metals which oxidize in a parabolic manner, repetitive scale spalling may produce a much increased total metal loss over time, since the reaction kinetics continually revert to the initial rapid period of the oxidation curve and paralinear kinetics ensue.

The majority of heat-resisting alloys contain at least one element that is selectively oxidized (e.g., Cr, Si, Al). The resulting scale is highly protective, but depletion of the secondary element may occur if the diffusion rate of this element in the alloy is low. Then repetitious loss of the scale can be profoundly detrimental to long-term performance, since depletion of the alloying element near the surface may occur to such an extent that its concentration falls below the critical level for the exclusive reformation of the highly protective scale.[126,127]

1.22.6.1 Growth Stresses

As indicated earlier, protective oxide scales typically have a PBR greater than unity and are, therefore, less dense than the metal from which they have formed. As a result, the formation of protective oxides invariably results in a local volume increase or a stress-free oxidation strain.[128,129] If lateral growth occurs, then compressive stresses can build up, and these are intensified at convex and reduced at concave interfaces by the radial displacement of the scale due to outward cation diffusion (**Figure 7**).[48,129,130]

The reduced oxidation near sample corners is related to these stress effects, either by retarded diffusion or by modified interfacial reactions.[128] Manning[131] described these stresses in terms of the conformational strain and distinguished between anion and cation diffusion, and concave and convex surfaces. He defined a radial vector M, describing the direction and extent of displacement of the oxide layer in order to remain in contact with the retreating metal surface, where

$$M = \frac{V_{ox}}{V_{me}}(1-a)1(1-\upsilon) \qquad [6]$$

and V_{ox}/V_{me} is the PBR, a is the amount of oxide formed at the surface, and υ is the volume gain due to vacancy injection into the metal. If υ is zero, the sign of M depends upon the predominance of anion ($a = 0$) or cation ($a = 1$) diffusion. The enforced radial displacement (δy) of the oxide layer results in a tangential or radial reaction stress in both the oxide and the metal. The strain rate ($\delta\epsilon/\delta t$) of the oxide layer

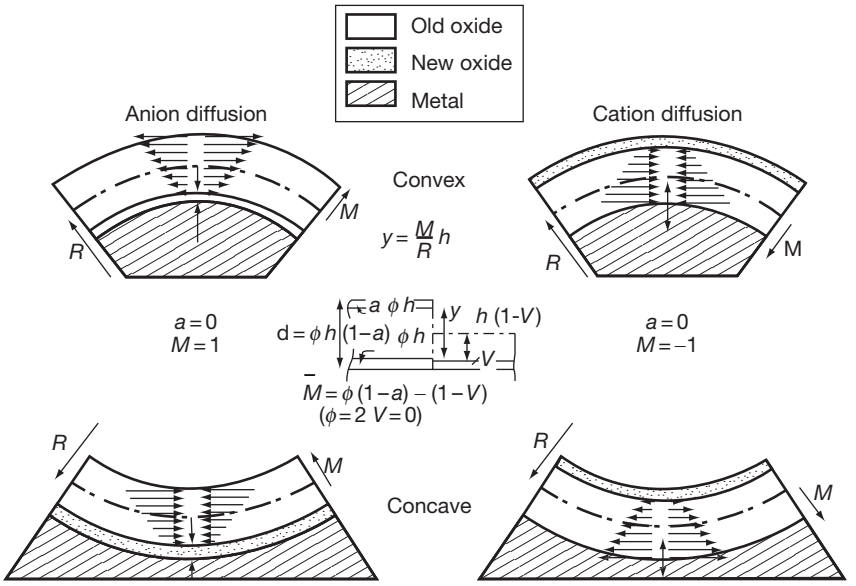

Figure 7 Oxide growth stresses on curved surfaces. Reproduced from Hsueh, C. H.; Evans, A. G. *J. Appl. Phys.* **1983**, *54*, 6672.

then depends upon the radius of curvature (R) and the rate of metal loss ($\delta h/\delta t$) as

$$\frac{\delta e}{\delta t} = \frac{M(\delta h)}{R(\delta t)} \qquad [7]$$

This leads to high strains on regions of high curvature and zero strain on a flat surface. If new growth occurs stress free, then the oldest region of oxide will be the most highly stressed, this being located at the oxide surface for anion-controlled growth and at the oxide–metal interface for cation-controlled growth. Hsueh and Evans[128] carried out a similar analysis and calculated the distribution of radial and tangential stress within the oxide scale as a function of scale thickness and specimen geometry.

Whisker growth is a process often reported for the relief of compressive growth stresses during oxidation.[132–134] This whisker formation and scale buckling of thin hematite layers have been linked to the stresses arising from oxide formation at the magnetite–hematite interface as a result of the countercurrent of cation and anion diffusion in both oxides.[130] Acoustic emission studies of 2.25% Cr–1% Mo steel at 900 °C have shown that, as the oxide thickness increases, growth stress builds up in the scale and is relieved by scale cracking.[135]

1.22.6.2 System-Applied Stresses

The tensile failure strain of oxides grown on EN2 steel between 600 and 900 °C lies in the range 1×10^{-4} to 2.5×10^{-4}.[(136)] Components in service may be stressed beyond these failure strains, leading to scale cracking.

Ward *et al.*[137] have shown that, under cyclical loading, the oxidation rate of steels is similar to that under unstressed isothermal conditions, provided the fatigue stress is below the stress required to exceed the scale failure strain. If, however, the failure strain is exceeded, the oxidation rate is accelerated because of repetitive scale failure, and linear kinetics are observed.

Low-cycle fatigue loading of 9.5% Cr steel at 650 °C in air has been shown to enhance uniform scale formation as well as promote nodular scale formation at cracks.[124] However, no cracks were found in the scale after exposure, indicating that any cracks that form must heal very quickly. This healing of cracks was attributed to the overgrowth of the chromium-rich oxide by an iron-rich oxide.

1.22.6.3 Thermal Stresses

Under thermal cycling conditions, the principal source of stress within the oxide scale is the temperature change.[121] Christl *et al.*[125] have noted that, when cooling 2.25% Cr–1% Mo steel from 600 °C in air, compressive stresses build up in the hematite, while tensile stresses build up in the magnetite and spinel layers. This arises because the thermal expansion coefficients of the individual oxide layers increase in the order α metal $< \alpha$ spinel $< \alpha$ magnetite $< \alpha$ hematite.[119]

Multilaminated scales have been reported following thermal cycling,[138] and Rolls and Nematollahi[139]

have studied the influence of thermal cycling on the oxidation of 1% Cr–0.5% Mo low-carbon steel. The oxidation kinetics were found to be mostly parabolic, with thin scales (10 μm) more prone to spalling than thick scales (20 μm). The authors reported that the higher the temperature drop on cycling, the greater the degree of scale disruption. They derived a qualitative relationship to describe this behavior:

$$Y = \frac{f(NO)}{x} \qquad [8]$$

where Y is the degree of scale detachment, N is the number of cycles, x is the thickness, and O is the cooling rate. This implies that thicker scales cooled slowly show less detachment than thinner scales cooled rapidly. The oxide scale comprised spinel, magnetite, and wüstite, with only the spinel layer remaining adherent during thermal cycling. From this, the authors concluded that the bulk scale cohesive strength was less than the inner spinel adhesive strength. Scale detachment was observed at voids and microcracks produced at the outer–spinel interface during isothermal oxidation. Hence, the number of scale layers that became detached during thermal cycling was governed by the number of parallel rows of voids in the scale and not by the number of thermal cycles.

1.22.7 Commercial Low-Alloy Steels in Air or Oxygen

Simms and Little[140] have examined the early stages of scale growth on 2.25% Cr–1% Mo steel at 600 °C in dry flowing oxygen. Between 1 and 22 h, they found that a thick oxide layer spreads laterally over a thin oxide layer. After 50 h, no thin areas of oxide layer were left. Whiskers gradually developed on the outer surface and these were well defined after 100 h. Fracture sections of the oxide revealed that the thin scales were duplex, whereas the thicker scale was triplex, with a middle layer of Fe_3O_4 which spread laterally with time. The authors concluded that the first phases to develop were fine equiaxed α-Fe_2O_3 overlying a doped spinel. Later, nucleation and lateral spread of coarse columnar grains of Fe_3O_4 occurred between the two first-formed layers. The Fe_2O_3 appears to reach a limiting thickness at which time Fe_3O_4 nucleates.

One of the authors[141] has carried out exposures of a range of low-alloy steels (up to 5% Cr) in laboratory air between 500 and 850 °C. Plain carbon steel displayed a duplex scale, comprising 75% Fe_3O_4 and 25% Fe_2O_3 at all temperatures below 600 °C (Figure 8). Above 600 °C, a coarse, columnar-grained layer of FeO occupying approximately 90% of the scale thickness was observed. For the Cr-containing steels, a distinct spinel phase was observed at temperatures in excess of around 615 °C, with all of the Cr, Mo, and V incorporated within this layer, beneath the Fe_3O_4 and Fe_2O_3. FeO was not observed in the scale until temperatures exceeded 650 °C, the FeO appearing as a fourth layer between the spinel and Fe_3O_4 layers. Parabolic oxidation kinetics were observed for all steels at all temperatures. Below 600 °C, there was little difference in the oxidation kinetics between the chromium steels until the Cr level reached around 5%, this difference mainly arising because of an increasing activation energy for Fe_3O_4 growth with increasing Cr content. There was no significant difference in the activation energy for Fe_2O_3 growth, irrespective of the Cr content of the steel (Figure 9).

1.22.8 Industrial Environments

1.22.8.1 Steam

Many low alloy steels are utilized as pressure vessels in high temperature applications in a number of

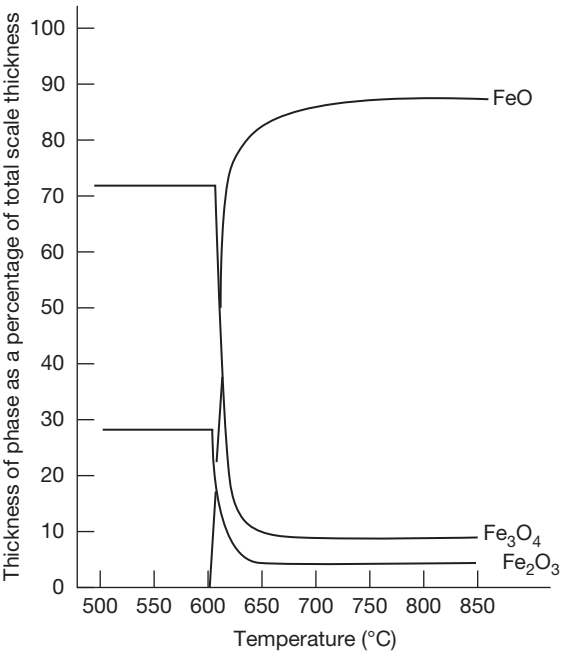

Figure 8 Relative thickness of wüstite, magnetite and hematite on mild steel as a function of formation temperature.

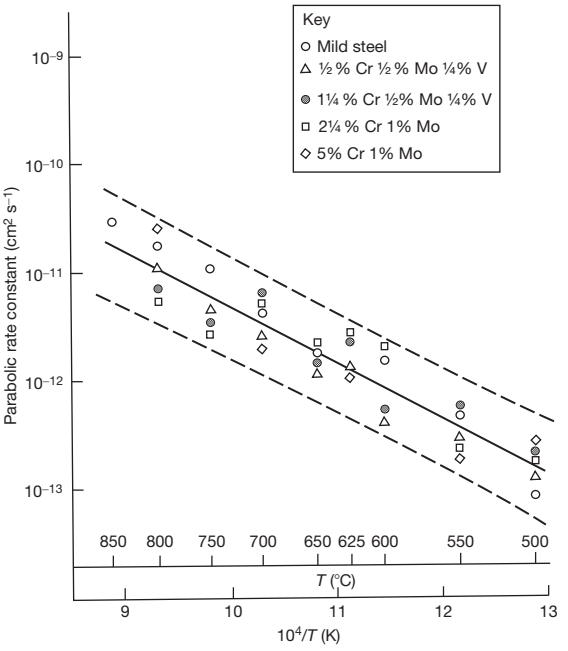

Figure 9 Arrhenius plot for the hematite thickening rate on mild steel and low-chromium alloy steels in air.

diverse and often aggressive environments. Metal wastage by oxidation and corrosion reduces the load bearing cross sectional area of a vessel wall and can have grave consequences in terms of creep rupture life, especially of thin walled components. Different environment parameters including temperature, gas/fluid composition, pressure, flow rates and alloy composition will define the oxidation mechanisms and rate of material wastage. It is therefore imperative that a material gains protection from the formation of a stable slow growing oxide scale. Wright and Pint[142] predict that in steam environments the protective behavior associated with the formation of a complete Cr_2O_3 layer is not necessarily observed in FeCr alloys with Cr contents below 20%.

Jonsson *et al.*[143] compared the oxidation of iron at 600 °C in dry O_2 and wet O_2 (40% H_2O) where a three layer scale is formed consisting of a haematite outer layer, a magnetite middle layer and a wüstite inner layer forming the metal–scale interface. All three layers grow with time, but with different growth rates, the overall rate being roughly parabolic in both environments. While the detrimental effects of water vapour on oxidation rates are well reported, there is no consensus regarding the causes of this effect, however, recent investigations into the effect of hydrogen-accelerated oxidation on scale growth and morphology has offered a possible insight into the increased steam side oxidation of low alloy steels.[144–146]

In recent years the group of modified 9%Cr steels has been developed for utilization in high temperature environments including power generation. Although the mechanical properties of these steels have been optimized, it is now appreciated that steam side oxidation of these alloys may be the factor that limits their maximum service temperature. Oxide growth rates have been shown to increase exponentially with temperature[142] up to 700 °C, where the isothermal oxidation rates are observed to be parabolic. However, investigations (COST-522, Europe's Thermie and the U.S. Vision 21 programs) aimed at improving thermodynamic efficiency by increasing service temperatures suggested that linear kinetics prevailed at temperatures above 700 °C for steels with Cr contents in the range 1–15 wt%.[142,147]

9% Cr ferritic martensitic steels show acceptable oxidation resistance in dry air at high temperatures due to the formation of a protective scale; between 400 °C and 600 °C the scale comprises of FeO, Fe_2O_3, and Cr_2O_3. However, operation atmospheres composed of water vapour or steam + oxygen are much more corrosive than dry air. Subsequent scales that grow are less protective than Fe_2O_3, or Cr_2O_3. Sanchez *et al.*[148] predicts the formation of Fe_3O_4, Fe_2O_3 and $(FeCr)_3O_4$ scales in 100% H_2O atmosphere at 650 °C on 9%Cr steels, in contrast, at 800 °C the scale is mainly composed of Fe_3O_4 and $(FeCr)_3O_4$.

Itagaki *et al.*[149] found that an addition of 3%Pd to steel NF616 (similar to modified 9Cr–1Mo) gave significant improvements in oxidation resistance in steam at 650 °C as the growth of a Cr rich $(Fe_2Cr)_2O_3$ rhombohedral structured oxide was observed in the absence of a magnetite layer. Czyrska-Filemonowicz *et al.*[150] state that oxidation (weight gain) of P91 steel can increase 30 fold in atmospheres containing water vapour compared to dry air.

Tuurna *et al.*[151] also studied the effects of water vapour on the high temperature oxidation of low alloy steels. Tests on 2.25Cr–1Mo steels at constant temperature (550 °C) with variable moisture content (5%–10%–15%) revealed an increasing linear relationship between moisture content and mass gain after 360 hours. Further tests at fixed moisture (15%) and variable temperature result in a steep increase in oxidation occurring at higher temperatures as the oxide scale becomes nonprotective; the use of 2.25Cr–1Mo steels is thus restricted to temperatures below 580 °C.

Nakai *et al.*[152] report the effects of preoxidation of Fe, 10%Cr, 0.08%C ternary alloy on subsequent steam

oxidation.[143] Cr_2O_3 scales containing a small amount of Fe_2O_3 are formed during preoxidation offering short term improvements in oxidation resistance. After long-term oxidation in steam nodular like oxides are formed on the preoxidised specimen showing a clear resemblance both chemically and structurally to the oxides formed on non-preoxidised specimens.

It is understood that hydrogen dissolves inward when steam oxidation takes place on the surface of steels.[145,146,152] Thus it appears that hydrogen plays an important role in the accelerated growth of the oxide scale when the steels are exposed to a wet gas atmosphere. Nakai *et al.*[152] proposes a model, where hydrogen dissolves as a proton (H^+ ion) in $(Fe, Cr)_3O_4$ modifying the point defect structure inducing significant changes in the ionic diffusivity in the oxide. For example, the dissolved hydrogen will decrease the diffusion rate of Cr ions in $(Fe, Cr)_3O_4$. The ensuing inhibited ionic Cr supply to the oxide layer results in the attendant decrease of the Cr concentration in $(Fe, Cr)_3O_4$. Subsequently an apparent increase in the diffusion rate of Fe ions in the oxide is observed. As the oxidation rate of Fe–Cr steels is determined mainly by the Fe diffusivity in the $(Fe, Cr)_3O_4$ layer,[153] hydrogen dissolution induces the accelerated growth of the oxide scale on the steels.

Low alloy steels containing a maximum Cr content of 9 wt% but excluding T/P91 display similar scale morphologies and tendency/mechanisms to spallation showing a laminated oxide scale. The initial formation of a magnetite outer layer and an inner spinel layer is followed by the formation of similar underlying duplex layers (**Figure 10**), possibly as a result of delamination of the original scale at the oxide–substrate interface.[90] Repetition of this process develops a multilayered scale consisting of repeated duplex magnetite and spinel layers, successive duplex layers becoming noticeably thinner. Exfoliation of these scales has a propensity to occur along a plane between one of the sets of duplex layers or at the scale–metal interface and is likely to be a mechanism of stress relief. There is evidence that there are conditions where the scales formed on ferritic steels in steam can remain perfectly adherent for long times; for instance, from tests in a side loop on an operating boiler, Griess and Maxwell[154] reported that alloy T22 formed adherent scales throughout exposures for 28kh in 105 bar steam at 482 °C; at 538 °C exfoliation initiated after approximately 12kh. Alloys 9Cr–1Mo (0.46Si), 9Cr–2Mo, and Sandvik HT9 (11.4Cr) followed essentially the same kinetic behavior (and rates) as T22, but exhibited no signs of exfoliation at 482 and 538 °C after exposures of 28kh, 19kh, and 28kh, respectively.

The laminated scales of low alloy steels are rarely observed on T/P91 steel, instead a largely duplex scale is observed with an incomplete outer layer of haematite. The duplex layer consists of an outer magnetite layer underlayed with a spinel layer rich in Cr, Si and Mo in comparison to the alloy composition.

12%Cr alloy steels display duplex oxide scale similar to those initially formed on the lower alloy ferritic steels. The outer scale is predominantly magnetite and the inner layer is a Cr rich spinel. The inner layer shows morphology similar to that often observed in P91 scales of incomplete Cr rich bands.

As quoted in the EPRI report on oxidation of alloys in steam[90] "There are five possible scenarios by which the scale morphologies observed on ferritic steels in steam might develop. Thus, it is suggested that the development of the (initial) double-layered scales on ferritic steels in steam (under isothermal conditions before the onset of any transition to multilayered scales) involves the following steps; note that, in order to reflect the uncertainty in the dominant transport modes in these scales, five possible pathways for oxide growth are suggested (**Figure 11**)":

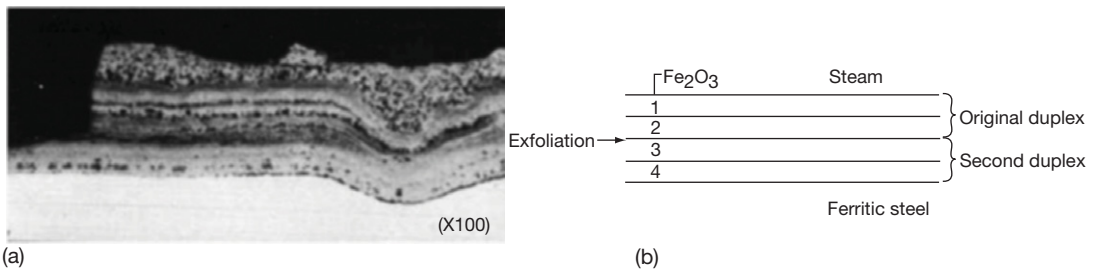

Figure 10 (a) A cross section from a 2.25Cr–1Mo steel tube oxidised in steam. (b) A schematic representation defining the duplex layered system.[155]

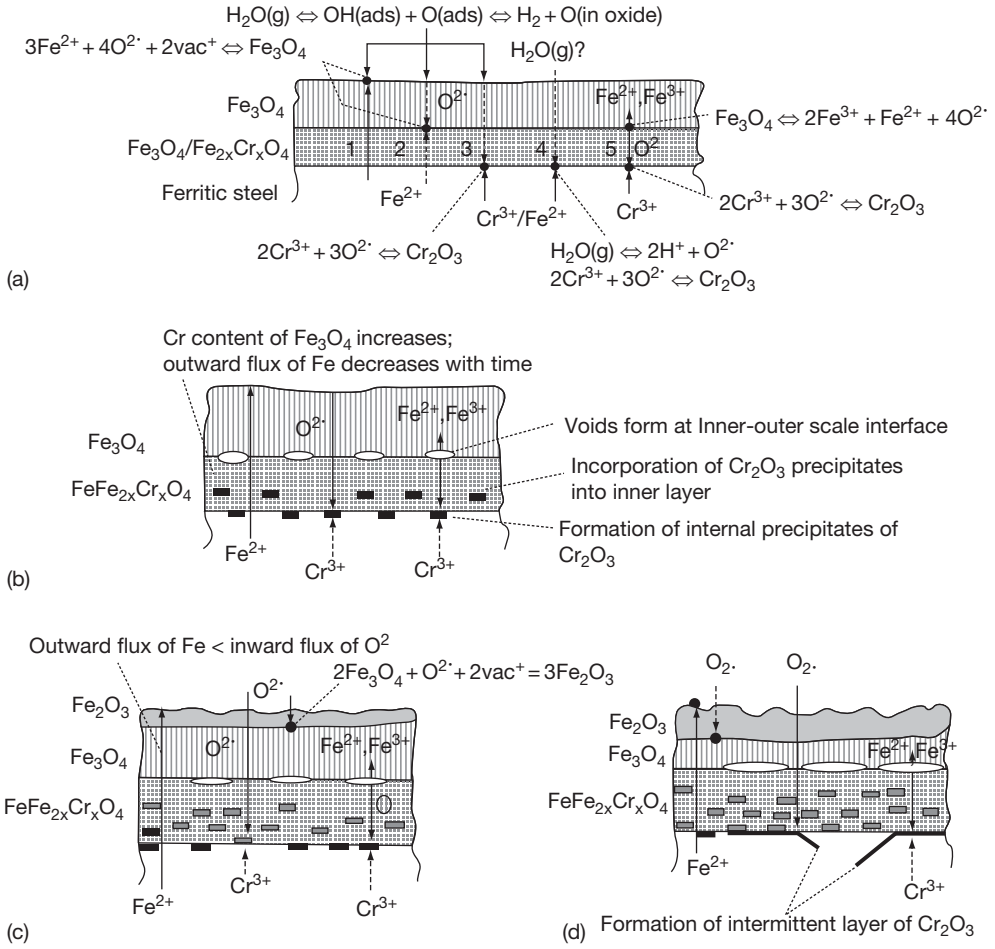

Figure 11 Schematic representation of the oxidation mechanisms observed in low alloy steels containing chromium.[158]

Path 1: outward diffusion of iron ions, which react at the oxide-steam interface with oxygen from the dissociation of steam to form fresh magnetite.[156,157]

Path 2: dissociation of steam at the oxide-steam interface, and diffusion of oxygen ions inwards via defects in the oxygen lattice, or "hydrogen defects"[159]; these react with iron ions diffusing from the alloy to form new oxide at the interface between the inner and outer oxide layers.

Path 3: dissociation of steam at the oxide-steam interface, and diffusion of oxygen ions inwards to the alloy-oxide interface, where they react with chromium in the alloy to form discrete internal particles of chromia.

Path 4: suggests that molecular steam is transported through the scale, dissociating in the scale (in this case at the alloy-oxide interface) to form iron or chromium oxides. This path is considered to be unlikely, unless the scale has significant, interconnected porosity.[160]

Path 5: which involves the dissociation of magnetite at the interface with the inner and outer layers,[160,161] with the iron ions released diffusing to the oxide-gas interface to react and form new oxide, and the released oxygen diffusing to the alloy-oxide interface to react with Cr in the alloy to form internal particles of Cr_2O_3 (or Fe–Cr spinel).[162]

This whole area of steam oxidation has been reviewed recently by Wright and Dooley.[162]

1.22.8.2 Combustion Gases

A considerable amount of work has been carried out investigating the corrosion of steels in the gases produced during the combustion of fossil fuel due to

extensive use of low-alloy steels as heat exchanger tubes in power generation. Combustion gases contain many species, such as CO, CO_2, SO_2, SO_3, H_2S, and HCl, arising from elements within the fuel. The different combinations of operating temperature and chemical stoichiometry of combustion reactions lead to many possible complex corrosion reactions.

In coal-fired power stations, severe corrosion of the steam-generating tubes in the furnace walls has been attributed to reducing conditions with high pCO, low pO_2, high pHCl, and high local heat fluxes and flame impingement.[163,164] In areas of high corrosion, large concentrations of CO are almost always present, and thick Fe_3O_4 scales, with islands and bands of FeS are observed.[163,164] Under the most severe reducing conditions, thick columnar scales of almost pure FeS have been observed.[164] The high corrosion rate areas are also subject to a significant flux of sulfur-bearing carbonaceous material in the flame envelope[163] which may locally exacerbate reducing conditions and raise the pH_2S.[164] Outside the high corrosion rate areas, the furnace atmospheres are found to be relatively O_2-rich and the corrosion scales comprise protective Fe_3O_4.[163]

The emergence in recent times of biomass fuels intended to reduce the reliance on fossil fuels for steam power generation has introduced new challenges to the corrosion engineer. The use of biomass fuels based on a wide range of agricultural waste products, such as straw, forestry waste, sawdust, and purpose grown crops including coppiced willow and miscanthus have been investigated.[165] Concerns over potential high rates of metal wastage have been raised as the fireside environment is known to be particularly aggressive since it often contains HCl and different alkali salts which condense on heat exchanger surfaces promoting corrosion. Presently, it is necessary to operate biomass and energy from waste plants at lower temperatures than traditional coal fired systems so that tolerable corrosion rates prevail.[166] However, proposed methods of modifying combustion gas chemistry where corrosive KCl is converted to the far less corrosive K_2SO_4 by the addition of sulphur may enable higher service temperatures to be attained.[167]

Similarily, refuse incineration plants are now based on the Waste-to-Energy concept, and it is necessary to optimize thermal transfer between combustion gases and water vapour. A significant problem with these installations concerns the fireside corrosion of the tubes. Combustion of waste generates highly corrosive flue gas often containing HCl, SO_2, NaCl, KCl, alkali and heavy metal chlorides and ashes containing chlorides and sulphates. *Wright and Krause*[168,169] predict corrosion by either combustion gases and/or molten deposits; erosion corrosion is also problematic due to flow rates and the presence of silica and alumina–silica particulates.

Fluidized-bed systems produce higher combustion intensities at lower temperatures than combustion of pulverized fuel in conventional fossil-fuel-fired boilers. The mineral matter for corrosion does not form fused salts and is not expected to release corrosive species. Fluidized bed combustors can, therefore, burn lower grade, cheaper fuel in smaller plant with better pollution control than traditional boilers.[170]

Minchener[171] reports that the bubble phase of atmospheric fluidized bed combustion has a pO_2 in the range 2×10^{-1} to 2×10^{-2}. Combustion in the dense phase is substoichiometric, with the pO_2 as low as 10^{-13}, and SO_2 and SO_3 present in the range 500–5000 ppm. Low Cr–Mo steels show heavy scaling in these conditions, whereas 9–12% Cr steels show good resistance to sulfidation up to 650 °C. Roberts *et al.*,[172] however, report that for pressurized fluidized-bed combustion, ferritic steels at or below 9% Cr show heavy general corrosion above 540–560 °C.

1.22.8.3 Chemical Environments

The oil industry frequently uses stainless steels or exotic bonded alloys for the processing of crude oil in the temperature range 200–600 °C. These materials are very expensive and there is a strong economic incentive for finding cheaper alloys that are resistant to H_2S and some gaseous organic sulfides arising from the S content of the crude oil.[173]

Metal sulfides show the same type of predominant defects as metal oxides, that is, cations in $Fe_{(1-x)}S$, $Cr_{(2+y)}S_3$. The defect concentration in most sulfides is much higher than those in the corresponding oxides, but the defect mobilities are only slightly higher. Thus, the higher diffusivities and growth rates are determined by the higher defect concentrations. Cr and Al only slightly reduce the corrosion rate, and much higher Al is needed than that required for oxidation protection. Very protective scales are formed only at a S pressure lower than that for the formation of the base-metal sulfide.[174]

Mrowec *et al.*[175] examined the resistance to high temperature corrosion of Fe alloys with Cr contents between 0.35 and 74 at% Cr in 101 kPa S vapor. They found that the corrosion was parabolic, irrespective of the temperature or alloy composition, and noted

that sulfidation takes place at a rate five orders of magnitude greater than oxidation at equivalent temperatures. At less than 2% Cr, the alloys formed $Fe_{(1-x)}S$ growing by outward diffusion of Fe ions, with traces of $FeCr_2S_4$ near the metal core.

Narita and Nishida[176] examined the sulfidation of low Cr–Fe alloys at 700–900 °C in 101 kPa of pure S. They found that the addition of small quantities of Cr significantly decreased the corrosion rate because of the formation of $FeCr_2S_4$ in the inner reaches of the scale. The scale comprised an outer FeS layer, with an inner layer of FeS, $FeCr_2S_4$, and Cr_3S_4 in varying amounts depending upon the Cr content. The corners of specimens corroded more rapidly than flat faces because of breakaway conditions. At low Cr contents, the rate was increased, but above 4–6% Cr the parabolic rate constant decreased. Above 7.4% Cr, an intermediate layer containing $FeCr_2S_4$ and varying amounts of Cr_3S_4, the proportion of the latter increasing with increasing Cr content, formed between the inner and outer layers.

In view of this potentially rapid degradation of Cr-containing steels by high temperature sulfidation in petrochemical and coal gasification reactors, Al is much used in the Fe alloys for these applications.[177–180] Al in Fe reduces the sulfidation rate in S_2 vapor by up to two orders of magnitude[181] because of the high thermodynamic stability of aluminum sulfide relative to iron sulfide, the low rate of sulfidation of Al compared with pure Fe and the large PB ratio of Al_2S_3 (3.7). The addition of 5% Al in Fe in 101 kPa S_2 vapor between 500 and 700 °C resulted in the rate of reaction decreasing by a factor of 10. Paralinear kinetics were observed, with the inner layer of a duplex FeS scale containing a finely dispersed Al_2S_3 phase which acts as a diffusion barrier to Fe^{2+} migration. Increasing the temperature to 800 °C resulted in a rapid take off of the corrosion rate, with catastrophic corrosion rates above 800 °C due to the large volume of Al_2S_3 causing an increase in scale porosity.

Condit *et al.*[182] examined the sulfidation of several Fe–Cr–Al alloys under a variety of sulfidizing conditions. They noted that, in the early stages of sulfidation, a thin compact inner layer forms that is high in Cr and Al. Subsequently, a thicker microcrystalline outer layer forms with a uniform Fe, Cr, and Al composition. Formation of the outer compact layer was favored by increasing pS_2 and decreasing temperature, with the layer forming much more rapidly in H_2S than in pure S_2. The sublayer disappeared more or less rapidly depending upon the alloy composition. The authors propose three stages for scale development. First, a thin compact layer forms because of the penetration of S into the alloy with preferential formation of sulfide from those metals with the highest affinity for S. $Fe_{(1-x)}S$ also forms because of the abundance of Fe in the alloy.

The outer layer then dissociates to release sulfur, which dissolves in the grain boundaries of the alloy to form Cr and Al sulfides. The Fe released by this dissociation sulfidizes again at the interface between the two layers. The volume increase associated with the conversion of metal to sulfide generates a mechanical stress that causes the outer layer to break up and permits permeation of S. This initiates a second stage, where growth of the scale is linear and comprises a porous outer layer, with FeS, Cr_2S_3, and Al_2S_3 evenly distributed, possibly as $FeCr_2S_4$, $FeAl_2S_4$, and $FeCr_{(x)}Al_{(2-x)}S_4$. S then diffuses through the pores to the scale–metal interface. The third stage comprises the formation of an outer compact layer of $Fe_{(1-x)}S$ and continued thickening of the inner layer.

Addition of Cr to Fe–Al alloys aids the formation of Cr sulfides and Al_2S_3, which together markedly reduce the sulfidation rate.[173] Between 2% and 5% Cr then, more than 3% Al is required to obtain protection. At 9% Cr, however, only 1% Al is needed to give protection, since the Cr is sufficiently active to lower the S potential seen by Al (secondary gettering). Thus, all Fe–Cr–Al alloys initially form FeS, Cr sulfides, and Al_2S_3. The Cr and Al are then exposed to a much lower pS_2 at the scale–metal interface and Cr sulfides and Al_2S_3 grow preferentially if their activity is high enough. Ultimately, a protective layer of Al_2S_3 or Al_2S_3 + Cr sulfides develops at the scale–metal interface and the reaction rate decreases substantially.

Karlson *et al.*[183] found, from on-site experience of cement-producing plant, that corrosion of Fe surfaces may occur in gases containing O_2, SO_2, and alkali chlorides such as NaCl and KCl between 300 and 500 °C. They reported that the corrosion rates may be extraordinarily high (5–10 mm month^{-1}) implying liquid-phase corrosion. Laboratory simulation of the plant conditions demonstrated the need for both SO_2 and the alkali chloride in the environment. The principal corrosion reaction was found to be

$$2Fe_2O_3 + 12[K,Na]Cl(s,l) + 12SO_2(g) + 9O_2(g) \rightarrow 4[K,Na]_3Fe(SO_4)_3(s,l) + 6Cl_2(g)$$

A thermodynamic evaluation of this equation indicated that the reaction could proceed with SO_2 levels as low as 100 ppm.

1.22.8.4 CO/CO_2

Failures of mild steel components in Magnox reactors in the United Kingdom and Italy after approximately 5 years of operation alerted the world to the potential for breakaway oxidation of low-alloy steels in CO/CO_2 environments.[95] The CO_2, 1% CO, 300 vppm CH_4, 250 vppm H_2O, 100 vppm H_2 environment used in CAGRs was selected on the need to minimize oxidation of the graphite reactor core and deposition of C from the coolant gas.[184] Corrosion rate tests of 15 000–20 000 h, in the limited range of conditions anticipated by the designers, showed that the maximum reduction in corrosion rate of ferritic steels in CO_2 at 600 °C is realized at around the 9% Cr level.[185–187] Therefore, 9Cr1Mo steel was chosen for the evaporator and primary superheater sections of the CAGR.[185] However, in the late 1960s, Taylor (reported in Holmes *et al.*) identified evidence for a significant change in the corrosion mechanism for 9% Cr steels at around 550 °C. This change could lead to rate inversion with increasing temperature in steels containing 0.7–0.8% Si, or breakaway in 0.4–0.5% Si steels.

Because of their importance to the nuclear power generation industry, these observations initiated a vast amount of research into the oxidation of low-alloy steels in CO/CO_2 environments. It is now clear that low-alloy steels exhibit three types of behavior when exposed to CO/CO_2, that is, protective, transitional, and linear-breakaway (**Figure 12**), with the time to breakaway and the breakaway rate being of crucial importance in determining component life.

For mild and low-alloy steels in CO_2, the first scale to form is a compact coarse columnar layer of Fe_3O_4.[188–190] Growth of this layer is controlled by outward grain boundary diffusion of Fe ions.[190–192] The inward counter-current of vacancies is initially annihilated at the metal surface, but eventually vacancy condensation at the scale–metal interface gives decohesion, the scale develops microporosity, an inner layer grows within the space created by the departing metal ions and a duplex scale forms.[193–195] Then for Cr-containing steels, the protective scale comprises an outer, coarse columnar-grained magnetite layer and an inner, slightly porous, Cr-rich spinel of fine (0.1 μm) equiaxed grains.[70,194,196] As with low-alloy steels in other environments, the Cr is not mobile in the scale, but is oxidized *in situ*.[195,196] Studies have shown that the M_3O_4 spinel nucleates at asperities on the surface and duplex growth is also known to be favored in the vicinity of inclusions and specimen corners.[197] Once initiated, the inner layer grows by inward diffusion of O, probably as CO_2, down microfissures and micropores,[17,136,196] in both the lateral and vertical directions, until a complete layer is obtained.[197] The growth of this layer subsequently follows the parabolic rate law.

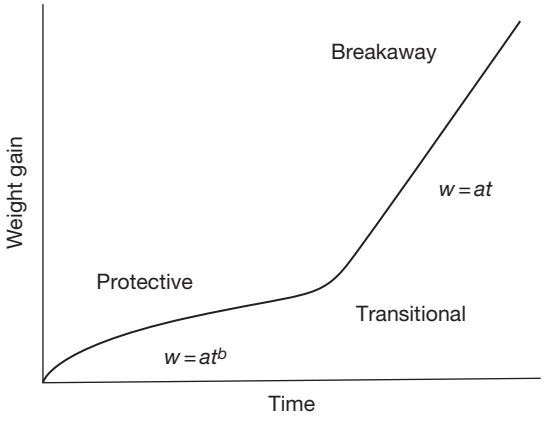

Figure 12 Schematic diagram of stages of low-alloy steel oxidation in CO/CO_2.

During this protective stage, decreasing the water and CO content of the gas appears to decrease the rate constant of Cr-containing steels,[184] but has little effect on the rate constant of carbon steels.[193,198] The rate constant of all steels has been found to decrease with decreasing temperature and increasing Si content.[184,185,195,199] Ferguson *et al.*[198] have also reported that increasing the S content of carbon steels reduces the parabolic rate constant.

An increase in the Si content of the steel has been reported to give a significant increase in the duration of the protective regime for carbon steel.[188,200,201] A similar benefit has also been reported for Cr-containing steels.[193,198,202] Increases in the duration of the protective regime are also realized with reductions in the CO and H_2O contents of the gas,[198] in the temperatures,[185,193,198] and for carbon steels, in the surface roughness,[193] or for 9Cr steels, with increased surface cold work. Robertson and Manning[43] found that breakaway may also be delayed by some S-containing gases.

Following the initial protective period, under certain conditions of temperature, alloy and gas composition,[185] the oxidation goes through a transitional stage into breakaway. Several authors have reported that breakaway oxidation is initiated once the scale reaches a critical thickness[184,185] or weight gain[70] and only occurs below an initially protective duplex layer.[43,195] Both single-layer protective and duplex-layer

protective scales have a PBR of 2.1, whereas breakaway scales show a PBR of approximately 2.7, containing around 23% porosity,[195] and graphitic carbon grains (up to 6% by weight) between the oxide grains.[193,198]

During this transitional period, and once full breakaway is established, growth occurs throughout the oxide and close to the scale–metal interface.[203] Growth below the oxidant surface requires oxidant transport through the scale, but solid-state lattice diffusion is much too slow to account for the rates observed.[17] Therefore, a porous scale is required. Mechanisms for pore growth have been postulated by several authors[204–207] who have suggested that the transition from single-layer to duplex growth is due to the initiation of pores within the scale. Then breakaway was thought to be caused by increased porosity giving unlimited access of oxidant to metal surface. However Atkinson[47] has shown single layer scales to be slightly porous. Robertson and Manning[43] have proposed that oxidant access is always available and the type of scale that develops is dependent upon conditions at the scale–metal interface. Breakaway occurs if space is created by continuous scale deformation or creep.[208]

The inward penetration of CO_2 via cracks and micropores gives

$$3Fe + 4CO_2 = Fe_3O_4 + 4CO$$
$$2CO = O_2 + 2C \text{ via the Boudouard reaction}$$

at the scale–metal interface.[136,196]

The carbon initially diffuses into the steel, but ultimately, the steel may become saturated with C.[208] There is no detectable solubility of C in FeO, Fe_3O_4, MnO, or Cr_2O_3,[209] and C can only permeate through pores or faulty scales.[112] Thus, the C then deposits at the scale–metal interface and prevents the formation of a coherent protective layer once it reaches a critical activity.[208] Carbides in the steel have been found to be the preferred sites for breakaway. These are either pre-existing carbides or carbides precipitated by C injection during oxidation.[190] Precarburized or graphite-painted steel breaks away rapidly, as do thin foils, because of the smaller C sink available.[190] Pritchard *et al.*[89] reported that the proportion of C in the scale increased with scale thickness and water content of the gas and was higher in breakaway oxide. For 9% Cr steel, breakaway oxidation is associated with heavy carburization of the metal and C deposition within the oxide, with preferential breakaway occurring at corners and edges.[196]

For Fe in CO/CO_2 at atmospheric pressure, Surman[210] found that if

$$10^{-3} < \frac{pCO}{pCO + pCO_2} < 0.3$$

then the oxidation is parabolic and very little C deposition occurs. He concluded that magnetite is not sufficiently catalytic to promote the Boudouard reaction unless CO > 10% and moisture is present and surmised that H_2O promotes the formation of a Boudouard catalyst. If the CO is greater than 0.4 in this expression, oxidation and carbon deposition occur simultaneously at a linear rate.[211]

German and Littlejohn[193] have observed that increasing the Si content of carbon steel reduces the linear rate constant during breakaway and Banks and Lorimer[208] have shown that Cr and Si reduce the creep rate of Fe_3O_4, thus reducing the postbreakaway rate of Cr-containing steels. However, Si has been reported as having no effect on the postbreakaway rate on 9Cr steels.[184,199] Small changes to the CO and H_2O content of the environment and the temperature have no significant effect on the breakaway rate constant, but a large reduction in the CO can cause reversion to protective kinetics,[211] as does reducing the CO_2 pressure to atmospheric.[212] Increasing the CO switches breakaway on again.[211]

References

1. Holmes, D. R.; Stringer, J. In *Corrosion of Steels in CO_2*; Holmes, D. R., Hill, R. B., Wyatt, L. M., Eds.; British Nuclear Energy Society: London, 1974; p 165.
2. Pilling, N. B.; Bedworth, R. E. *J. Inst. Met.* **1923**, *29*, 529.
3. Tammann, G. *Z. Anorg. Allgem. Chem.* **1920**, *111*, 78.
4. Gulbransen, E. A.; Ruka, R. *Trans. AIME* **1950**, *188*, 1500.
5. Pinder, L. W. C.E.G.B Unclassified Report, MID/SSD/80/0050/R *August* 1980.
6. Howe, C. I.; McEnany, B.; Scott, V. D. *Corr. Sci.* **1985**, *25*(3), 195.
7. Goursat, A. G.; Smeltzer, W. W. *Oxid. Met.* **1973**, *6*(2), 101.
8. Kuroda, K.; Labun, P. A.; Welsch, G.; Mitchell, T. E. *Oxid. Met.* **1983**, *19*(3/4), 117.
9. Koch, F.; Cohen, J. B. *Acta Crystallogr.* **1969**, *B 25*, 275.
10. Cheetham, A. K.; Fender, B. E. G.; Taylor, R. I. *J. Phys. C.* **1971**, *V*, 2160.
11. Catlow, C. R. A.; Mackrodt, W. C.; Norgett, M. J.; Stoneham, A. M. *Philos. Mag. A.* **1979**, *40*(2), 161.
12. Chen, W. K.; Peterson, N. L. *J. Phys. Chem. Solids* **1975**, *36*, 1097.
13. Wagner, C. *Z. Phys. Chem.* **1933**, *B621*, 25.
14. Wagner, C. *Atom Movements,* ASM: Cleavland, **1951**, p 153.
15. Atkinson, A. *Rev. Mod. Phys.* **1985**, *57*, 437.
16. Atkinson, A.; Taylor, R. I. *J. Phys. Chem. Solids* **1985**, *46*, 469.
17. Atkinson, A.; Taylor, R. I. *High Temperature – High Pressure* **1982**, *14*, 571.

18. Dieckmann, R.; Kohne, M. *Phys Chem.* **1983**, *87*, 495.
19. Garnaud, G.; Rapp, R. A. *Oxid. Met.* **1977**, *11*, 193.
20. Channing, D. A.; Graham, M. J. *Corr. Sci.* **1972**, *12*, 271.
21. Channing, D. A.; Dickerson, S. M.; Graham, M. J. *Corr. Sci.* **1973**, *13*, 933.
22. Francis, R.; Lees, D. G. *Corr. Sci.* **1976**, *16*, 847.
23. Rahmel, A. *Werkst. Korros.* **1965**, *16*(10), 837.
24. Rahmel, A. *Korrosion* **1966**, *18*, 41.
25. Eubanks, K. G.; Moore, D. G.; Pennington, W. A. *J. Electochem. Soc.* **1962**, *109*, 382.
26. Svedung, I.; Hammar, B.; Vannerberg, N. G. *OXid. Met.* **1973**, *6*(1), 21.
27. Caplan, D. *Corr.Sci.* **1966**, *6*, 509.
28. von Fraunhofer, J. A.; Pickup, G. A. *Corr. Sci.* **1970**, *10*, 253.
29. Janssen, S.; Lehtinen, B. *Metallurgie* **1967**, *7*, 61.
30. Caplan, D.; Cohen, M. *Corr. Sci.* **1966**, *6*, 321.
31. Price, W. R. *Corr. Sci.* **1967**, *7*, 473.
32. Pinder, L. W. C.E.G.B Unclassified Report, MID/SSD/80/0057/R *August* 1980.
33. Stott, F. H. *Mat. Sci. Tech.* **1989**, *5*(8), 743.
34. Atkinson, A. *Mat. Sci. Tech.* **1988**, *4*(12), 1046.
35. Dunitz, J. D.; Orgel, L. E. *J. Phys. Chem. Solids* **1957**, *3*, 318.
36. Azaroff, L. V. *J. Phys.* **1969**, *32*, Part 9, 1658.
37. Cox, M. G. C.; MacEnany, B.; Scott, V. D. *Phil. Mag.* **1972**, *26*, 839.
38. Hodge, J. D. *Electrochem. Soc.* **1978**, *125*(2), 55c.
39. Rahmel, A. Z. *Electrochem.* **1962**, *66*(4), 363.
40. Moreau, J. *Compte. Rendu.* **1953**, *236*, 85.
41. Surman, P. L.; Castle, J. E. *Corr. Sci.* **1969**, *9*, 771.
42. Atkinson, A. In *Oxidation of Metals and Associated Mass Transport*; Dayananda, M. A., *et al.* Ed.; The Metallurgical Society of the AIME: Warrendale, PA, 1987; p 29.
43. Robertson, J.; Manning, M. I. *Mat. Sci. Tech.* **1988**, *4*, 1064.
44. Bruckman, A.; Emmerich, R.; Mrowec, S. *Oxid. Met.* **1972**, *5*(2), 137.
45. Fromhold, A., Jr.; Sato, N. *Oxid. Met.* **1981**, *16*(3/4), 203.
46. Harrison, P. L. *Oxid. Met.* **1984**, *22*(1/2), 35.
47. Atkinson, A. *Philos. Mag. B* **1987**, *55*, 637.
48. Whittle, D. P. *Acta Met.* **1967**, *15*, 1421.
49. Wagner, C. *Corr. Sci.* **1965**, *5*, 751.
50. Runk, R. B.; Kim, H. J. *Oxid. Met.* **1970**, *2*(3), 285.
51. Kim, H. J.; Runk, R. B. *Oxid. Met.* **1970**, *2*(3), 307.
52. Nosek, E.; Werber, T. *Oxid. Met.* **1986**, *25*(3/4), 121.
53. Bohnenkamp, V. J.; Engell, H. J. *Arch. Eisenhuettenw.* **1962**, *33*, 359.
54. Caplan, D.; Sproule, G. I.; Hussey, R. J.; Graham, M. J. *Oxid. Met.* **1979**, *13*, 255.
55. Caplan, D.; Sproule, G. I.; Hussey, R. J.; Graham, M. J. *Oxid. Met.* **1978**, *12*, 67.
56. Malik, A. U. *Oxid. Met.* **1985**, *25*(5/6), 223.
57. Prescott, R.; Graham, M. J. *Oxid. Met.* **1992**, *38*(1–2), 73–87.
58. Tomaszewicz, P.; Wallwork, G. R. *Oxid. Met.* **1983**, *19*(5–6), 165–185.
59. Tomaszewicz, P.; Wallwork, G. R. *International Corrosion Conference Series*; 1983.
60. Boggs, W. E. *J. Electrochem. Soc.: Solid State Sci.* **1971**, *118*, 906.
61. Ahmed, H. A.; Smeltzer, W. W. *J. Electrochem. Soc.* **1986**, *133*(1), 212–216.
62. Pons, M.; Caillet, M.; Galerie, A. *Corros. Sci.* **1982**, *22*(3), 239–249.
63. Smith, P. J.; Beauprie, R. M.; Smeltzer, W. W.; Stevanovic, D. V.; Thompson, D. A. *Oxid. Met.* **1987**, *28*(5–6), 259–276.
64. Ahmed, H. A.; Underbill, R. P.; Smeltzer, W. W.; Brett, M. E.; Graham, M. J. *Oxid. Met.* **1987**, *28*(5–6), 347–351.
65. Fox, P.; Tatlock, G. J. *Mater. Sci. Technol.* **1988**, *4*, 439.
66. Tomaszewicz, P.; Wallwork, G. R. *Oxid. Met.* **1983**, *20*(3–4), 75–109.
67. Wagner, J. B. In *Defects and Transport in Oxides*; Smeltzer, M. S., Jaffe, R. I., Eds.; Plenum Press: New York, 1974; p 283.
68. Seybolt, A. U. *Trans. Met. Soc. AIME* **1968**, *242*, 752.
69. Rahmel, A.; Tobolski, J. *Werkst. Korros.* **1965**, *16*(8), 662.
70. Robertson, J.; Manning, M. I. *Mater. Sci. Technol.* **1989**, *5*(8), 741–753.
71. Darken, L. S. *Trans. AIME* **1942**, *150*, 157–171.
72. Tuck, C. W. *Corros. Sci.* **1965**, *5*(9), 631–634, IN3–IN7, 635–643.
73. Svedung, I.; Vannerberg, N. G. *Corros. Sci.* **1974**, *14*(6), 391–399.
74. Wood, G. C.; Richardson, J. A.; Hobby, M. G.; Boustead, J. *Corros. Sci.* **1969**, *9*(9), 659–668, IN7–IN12, 669–671.
75. Rochet, F.; Rigo, S.; Froment, M.; D'Anterroches, C.; Maillot, C.; Roulet, H.; Dufour, G. *Philos. Mag. B.* **1986**, *55*(2), 309.
76. Adachi, T.; Meier, G. H. *Oxid. Met.* **1987**, *27*(5–6), 347–366.
77. Atkinson, A. *Corros. Sci.* **1982**, *22*(2), 87–102.
78. Logani, R. C.; Smeltzer, W. W. *Oxid. Met.* **1971**, *3*(3), 279–290.
79. Logani, R.; Smeltzer, W. W. *Oxid. Met.* **1969**, *1*(1), 3–21.
80. Logani, R. C.; Smeltzer, W. W. *Oxid. Met.* **1971**, *3*(1), 15–32.
81. Yang, C.-H.; Lin, S.-N.; Chen, C.-H.; Tsai, W.-T. *Oxid. Met.* **2009**, *72*(3), 145–157.
82. Lashin, A.-R.; Schneeweiss, O.; Houbaert, Y. *Corros. Sci.* **2008**, *50*(9), 2580–2587.
83. Ishitsuka, T.; Inoue, Y.; Ogawa, H. *Oxid. Met.* **2004**, *61*(1–2), 125–142.
84. Jackson, P. R. S.; Wallwork, G. R. *Oxid. Met.* **1983**, *20*(1–2), 1–17.
85. Huczkowski, P.; Ertl, S.; Piron-Abellan, J.; Christiansen, N.; Höfler, T.; Shemet, V.; Singheiser, L.; Quadakkers, W. J. *Mater. High Temp.* **2005**, *22*(3–4), 253–262.
86. McAdam, G.; Young, D. J. *Oxid. Met.* **1987**, *28*(3–4), 165–181.
87. Nishida, K.; Narita, T.; Tani, T.; Sasaki, G. *Oxid. Met.* **1980**, *14*(1), 65–83.
88. Dewanckel, B.; Leclercq, D.; Dixmier, J.; Holmes, D. R. *Corrosion of unalloyed or low-alloyed steels in pressurized carbon dioxide,* 1974; p 3.
89. Pritchard, A. M.; Antill, J. E.; Cottell, K. R. J.; Peakall, K. A.; Truswell, A. E. In *Corrosion of Steels in CO_2*; Holmes, D. R., Hill, R. B., Wyatt, L. M., Eds.; British Nuclear Energy Society: London, 1974; p 73.
90. *Program on Technology Innovation: Oxide Growth and Exfoliation on Alloys Exposed to Steam*; EPRI, Palo Alto, CA: 2007. 1013666.
91. Morinaga, M.; Murata, Y.; Hashizume, R.; Sawaragi, Y. *ISIJ Int.* **2001**, *41*(3), 314–316.
92. Kutsumi, H.; Itagaki, T.; Abe, F. *Tetsu-To-Hagane/J. Iron Steel Inst. Jpn.* **2002**, *88*(9), 520–525.
93. Greeff, A. P.; Louw, C. W.; Terblans, J. J.; Swart, H. C. *Corros. Sci.* **2000**, *42*(6), 991–1004.
94. Vannerberg, N. G.; Svedung, I. *Corros. Sci.* **1971**, *11*(12), 915–927.
95. Donati; Garaud. In *Corrosion of Steels in CO_2* Holmes, D. R., Hill, R. B., Wyatt, L. M., Eds.; British Nuclear Energy Society: London, 1974; p 28.
96. Menzies, L. A.; Tomlinson, W. J. *JISI* **1958**, *204*, 1239.
97. Foley, R. T. *J. Electrochem. Soc.* **1962**, *109*(4), 278–284.
98. Menzies, I. A.; Lubkiewicz, J. *Oxid. Met.* **1971**, *3*(1), 41–58.
99. Dalvi, A. D.; Coates, D. E. *Oxid. Met.* **1972**, *5*(2), 113–135.

100. Rhys-Jones, T. N.; Grabke, H. J.; Kudielka, H. *Corros. Sci.* **1987**, *27*(1), 49–63, 65–73.
101. Wood, G. C. *Oxid. Met.* **1970**, *2*(1), 11–57.
102. Yearian, H. J.; Randell, E. C.; Longo, T. A. *Corrosion* **1956**, *12*, 515t–525t.
103. Douglass, D. L.; Gesmundo, F.; de Asmundis, C. *Oxid. Met.* **1986**, *25*(3–4), 235–268.
104. Khanna, A. S.; Gnanamoorthy, J. B. *Oxid. Met.* **1985**, *23*(1–2), 17–33.
105. Hossain, M. K. *Corros. Sci.* **1979**, *19*(7), 1031–1045.
106. Caplan, D.; Sproule, G. I. *Oxid. Met.* **1975**, *9*(5), 459–472.
107. Rahmel, A.; Jarger, W.; Becker, K. *Arch. Eisenhuttenwes* **1959**, *30*, 351–359.
108. Tsipas, D. N.; Noguera, H.; Rus, J. *Mater. Chem. Phys.* **1987**, *18*(3), 295–303.
109. Suwattananont, N.; Petrova, R. *Oxid. Met.* **2008**, *70*(5), 307–315.
110. Rowley, P. N.; Brydson, R.; Little, J.; Saunders, S. R. J.; Sauer, H.; Engel, W. *Oxid. Met.* **1991**, *35*(5), 375–395.
111. Hussey, R. J.; Mitchell, D. F.; Graham, M. J. *Werkst. Korros.* **1987**, *38*(10), 575–583.
112. Wolf, I.; Grabke, H. J.; Schmidt, P. *Oxid. Met.* **1988**, *29*(3–4), 289–306.
113. Sroda, S.; Baxter, D.; Arponen, M. *Mater. Corros.* **2005**, *56*(11), 791–795.
114. Fry, A.; Banks, J.; Osgerby, S. The influence of heat flux on the oxidation of boiler steels. *Parson Conference*; 2007.
115. Fry, A. T.; Roberts, S.; Chapman, L. Measuring heat transfer through steam grown oxide scales. *NPL Measurement Note - DEPC(MN)043,* **2007**; p 9.
116. Trindade, V. B.; Borin, R.; Hanjari, B. Z.; Yang, S.; Krupp, U.; Christ, H. J. *Mater. Res.* **2005**, *8*(4), 365–369.
117. Ostwald, C.; Grabke, H. J. *Corros. Sci.* **2004**, *46*(5), 1113–1127.
118. Baxter, D. J.; Natesan, K. *Rev. High Temp. Mater.* **1983**, *5*(3–4), 149–250.
119. Schutze, M. *Mater. Sci. Technol.* **1988**, *4*, 407–414.
120. Stringer, J. *Corros. Sci.* **1970**, *10*(7), 513–543.
121. Evans, H. E.; Lobb, R. C. *Corros. Sci.* **1984**, *24*(3), 209–222.
122. Kubaschewski, O.; Hopkins, B. E. *Oxidation of Metals and Alloys* Butterworths: London, 1967; Vol. 50, pp 83–249.
123. Manning, M. I.; Metcalfe, E. In *EROCOR '77, Eur Congr on Met Corros, 92nd Event of the Eur Fed of Corros.* **1977**; pp 121–127.
124. Barbehön, J.; Rahmel, A.; Schütze, M. *Oxid. Met.* **1988**, *30*(1–2), 85–94.
125. Christi, W.; Rahmel, A.; Schütze, M. *Oxid. Met.* **1989**, *31*(1–2), 1–34.
126. Whittle, D. P. *Oxid. Met.* **1972**, *4*(3), 171–179.
127. Deadmore, D. L.; Lowell, C. E. *Oxid. Met.* **1977**, *11*(2), 91–106.
128. Hsueh, C. H.; Evans, A. G. *J. Appl. Phys.* **1983**, *54*(11), 6672–6686.
129. Douglass, D. L. *Oxidation of Metals and Alloys*; American Society of Metals: Metals Park, OH, 1971; p 1137.
130. Mitchell, T. E.; Voss, D. A.; Butler, E. P. *J. Mater. Sci.* **1982**, *17*(6), 1825–1833.
131. Manning, M. I. *Corros. Sci.* **1981**, *21*(4), 301–316.
132. Evans, A. G.; Crumley, G. B.; Demaray, R. E. *Oxid. Met.* **1983**, *20*(5–6), 193–216.
133. Norin, A. *Oxid. Met.* **1975**, *9*(3), 259–274.
134. Appleby, W. K.; Tylecote, R. F. *Corros. Sci.* **1970**, *10*(5), 325–341.
135. Jha, B. B.; Raj, B.; Khanna, A. S. *Oxid. Met.* **1986**, *26*(3–4), 263–273.
136. Hancock, P.; Hurst, R. C. In *Corrosion of Steels in CO_2*; Holmes, D. R., Hill, R. B., Wyatt, L. M., Eds.; British Nuclear Energy Society: London, 1974; p 320.
137. Ward, G.; Hockenhull, B. S.; Hancock, P. *Metall. Trans.* **1974**, *5*(6), 1451–1455.
138. Forrest, J. E.; Bell, P. S. Relationship between the deformation of substrate and scale in the mechanism of multilayer oxide formation on low alloy ferritic steels; Commission of the European Communities, (Report) EUR, 1981.
139. Rolls, R.; Nematollahi, M. *Oxid. Met.* **1983**, *20*(1–2), 19–35.
140. Simms, N. J.; Little, J. A. *Mater. Sci. Technol.* **1988**, *4*(12), 1133–1139.
141. Pinder, L. W. C.E.G.B. Unclassified Report SSD/MID/R58/77, November 1977.
142. Wright, I. G.; Pint, B. A. In *NACE 2002*; 2002. Paper no. 02377.
143. Jonsson, T.; Pujilaksono, B.; Fuchs, A.; Svensson, J. E.; Johansson, L. G.; Halvarsson, M. In *7th International Symposium on High Temperature Corrosion and Protection of Materials*; Trans Tech Publications Ltd.: Les Embiez, France, 2008.
144. Yang, Z.; Xia, G.-G.; Walker, M. S.; Wang, C.-M.; Stevenson, J. W.; Singh, P. *Int. J. Hydrogen Energy* **2007**, *32*(16), 3770–3777.
145. Nakagawa, K.; Matsunaga, Y.; Yanagisawa, T. *Mater. High Temp.* **2001**, *18*, 51–56.
146. Nakagawa, K.; Matsunaga, Y.; Yanagisawa, T. *Mater. High Temp.* **2003**, *20*, 67–73.
147. Fujii, C. T.; Meussner, R. A. *J. Electrochem. Soc.* **1964**, *111*(11), 1215–1221.
148. Sánchez, L.; Hierro, M.; Pérez, F. *Oxid. Met.* **2009**, *71*(3), 173–186.
149. Itagaki, T.; Kutsumi, H.; Haruyama, H.; Igarashi, M.; Abe, F. *Corrosion* **2005**, *61*(4), 307–316.
150. Czyrska-Filemonowicz, A.; Zielińska-Lipiec, A.; Ennis, P. J. *J. Achiev. Mater. Manufact. Eng.* **2006**, *19*(2), 43–48.
151. Tuurna, S.; Yli-Olli, S. Heikinheimo, L. *Mater. Sci. Forum.*; 2008.
152. Nakai, M.; Nagai, K.; Murata, Y.; Morinaga, M. *Corros. Sci.* **2006**, *48*(11), 3869–3885.
153. Fujikawa, H.; Otsuka, N. *Nippon Kagaku Kaishi/Chemical Society of Japan – Chem. Indust. Chemis. J.* **1998**, *1*, 51–52.
154. Griess, J. C.; Maxwell, W. A. *The long-term oxidation of selected alloys in superheated steam at 482 and 538°C.*; 1981.
155. Dooley, R. B.; Paterson, S. J.; Wright, I. *G.* Presented at a EPRI-NPL Workshop on Scale Growth and Exfoliation in Steam Plant.; National Physical Lab, 2003.
156. Gala, A.; Grabke, H. J. *Archiv. Fur. Das. Eisenhuttenwesen* **1972**, *43*(6), 463.
157. Grabke, H. J.; Viefhaus, H. *Berichte Der Bunsen-Gesellschaft – Phys. Chem. Chem. Phys.* **1980**, *84*(2), 152–159.
158. Wright, I. G.; Wood, G. C. *Dilute Fe–Cr alloys*; 1969.
159. Norby, T. In *3rd International Symposium on High Temperature Corrosion and Protection of Materials*; Editions Physique: Les Embiez, France, 1992.
160. Mayer, P.; Manolescu, A. V. In *International Corrosion Conference Series;* 1983.
161. Stott, F. H.; Wright, I. G.; Hodgkiess, T.; Wood, G. C. *Oxid. Met.* **1977**, *11*(3), 141–150.
162. Wright, I. G.; Dooley, R. B. A review of the oxidation behaviour of structural alloys in steam; in press.
163. Clarke, F.; Morris, C. W. In *Corrosion Resistant Materials for Coal Combustion Systems*; Meadowcroft, D. B., Manning, M. I., Eds.; Applied Science Publishers: London, 1983; p 47.

164. Lees, D. G.; Whitehead, M. E. In *Corrosion Resistant Materials for Coal Combustion Systems*; Meadowcroft, D. B., Manning, M. I., Eds.; Applied Science Publishers: London, 1983; p 63.
165. Coleman, K. E.; Simms, N. J.; Kilgallon, P. J.; Oakey, J. E. *7th International Symposium on High Temperature Corrosion and Protection of Materials*; Trans Tech Publications Ltd.: Les Embiez, France, 2008.
166. Johansson, L. G.; Svensson, J. E.; Skog, E.; Pettersson, J.; Pettersson, C.; Folkeson, N.; Asteman, H.; Jonsson, T.; Halvarsson, M. *J. Iron Steel Res. Int.* **2007**, *14*(5 Suppl. 1), 35–39.
167. Henderson, P.; Szakálos, P.; Pettersson, R.; Andersson, C.; Högberg, J. *Mater. Corros.* **2006**, *57*(2), 128–134.
168. Krause, H. H. *Mater. Perform.* **1994**, *33*(3), 63–69.
169. Krause, H. H.; Wright, L. G. *Mater. Perform.* **1996**, *35*(1), 46–53.
170. Perkins, R. A. In *Corrosion Resistant Materials for Coal Combustion Systems*; Meadowcroft, D. B., Manning, M. I., Eds.; Applied Science Publishers: London, 1983; p 219.
171. Minchener, A. J. In *Corrosion Resistant Materials for Coal Combustion Systems*; Meadowcroft, D. B., Manning, M. I., Eds.; Applied Science Publishers: London, 1983; p 299.
172. Roberts, A. G.; Raven, P.; Lane, G.; Stringer, J. In *Corrosion Resistant Materials for Coal Combustion Systems*; Meadowcroft, D. B., Manning, M. I., Eds.; Applied Science Publishers: London, 1983; p 323.
173. Zelankof, P. D.; Simkovich, G. *Oxid. Met.* **1974**, *8*(5), 343–360.
174. Mrowec, S.; Przybylski, K. *Oxid. Met.* **1985**, *23*(3–4), 107–139.
175. Mrowec, S.; Walec, T.; Werber, T. *Oxid. Met.* **1969**, *1*(1), 93–120.
176. Narita, T.; Nishida, K. *Oxid. Met.* **1973**, *6*(3), 181–196.
177. Setterlund, R. B.; Prescott, G. R. *Corrosion* **1961**, *17*(6), 277–282.
178. Backensto, E.; Prior, B.; Sjoberg, J. E. *Corros. Sci.* **1962**, *18*, 253–258.
179. Malinowski, E. *Metal* **1962**, *94*(4).
180. Burns, F. J. *Corrosion* **1969**, *25*, 119.
181. Strafford, K. N.; Manifold, R. *Oxid. Met.* **1969**, *1*(2), 221–240.
182. Condit, R. H.; Hobbins, R. R.; Birchenall, C. E. *Oxid. Met.* **1974**, *8*(6), 409–455.
183. Karlsson, A.; Mäller, P. J.; Johansen, V. *Corros. Sci.* **1990**, *30*(2–3), 153–158.
184. Rowlands, P. C.; Garrett, J. C. P.; Garrett, F.; Hicks, F. G.; Lister, B. K.; Lloyd, B.; Twelves, J. A. In *Corrosion of Steels in CO_2*; Holmes, D. R., Hill, R. B., Wyatt, L. M., Eds.; British Nuclear Energy Society: London, 1974; p 193.
185. Holmes, D. R.; Mortimer, D.; Newell, J. *Proc. BNES* **1974**, p 151.
186. Newell, J. E. *Nucl. Energy Int.* **1972**, *17*, 637.
187. Taylor, J. W.; Trotsenberg, P. V. In *Corrosion of Steels in CO_2*; Holmes, D. R., Hill, R. B., Wyatt, L. M., Eds.; British Nuclear Energy Society: London, 1974; p 180.
188. German, P. A.; Littlejohn, A. C. In *Corrosion of Steels in CO_2*; Holmes, D. R., Hill, R. B., Wyatt,, L. M., Eds.; British Nuclear Energy Society: London, 1974; p 1.
189. Hussey, R. J.; Sproule, G. I.; Caplan, D.; Graham, M. J. *Oxid. Met.* **1977**, *11*, 65.
190. Gibbs, G. B.; Pendlebury, R. E.; Wooton, M. R. In *Corrosion of Steels in CO_2*; Holmes, D. R., Hill, R. B., Wyatt, L. M., Eds.; British Nuclear Energy Society: London, 1974; p 59.
191. Atkinson, A.; Taylor, R. I. *High Temp. High Pressure* **1982**, *14*, 571.
192. Cox, M. G. C.; McEnaney, B.; Scott, V. D. *High Temp. High Pressure* **1982**, *14*, 247.
193. German, P. A.; Littlejohn, A. C. In *Corrosion of Steels in CO_2*; Holmes, D. R., Hill, R. B., Wyatt, L. M., Eds.; British Nuclear Energy Society: London, 1974; p 1.
194. Hussey, R. J.; Sproule, G. I.; Caplan, D.; Graham, M. J. *Oxid. Met.* **1977**, *11*(2), 65–79.
195. Gibbs, G. B.; Pendlebury, R. E.; Wooton, M. R. In *Corrosion of Steels in CO_2*; Holmes, D. R., Hill, R. B., Wyatt, L. M., Eds.; British Nuclear Energy Society: London, 1974; p 59.
196. Harrison, P. L.; Dooley, R. B.; Lister, S. K.; Meadowcroft, D. B.; Nolan, P. J.; Pendlebury, R. E.; Surman, P. L.; Wooton, M. R. In *Corrosion of Steels in CO_2*; Holmes, D. R., Hill, R. B., Wyatt, L. M., Eds.; British Nuclear Energy Society: London, 1974; p 220.
197. Cox, M. G. C.; McEnaney, B.; Scott, V. C. In *Corrosion of Steels in CO_2*; Holmes, D. R., Hill, R. B., Wyatt, L. M., Eds.; British Nuclear Energy Society: London, 1974; p 247.
198. Ferguson, J. M.; Garrett, F.; Lloyd, B. In *Corrosion of Steels in CO_2*; Holmes, D. R., Hill, R. B., Wyatt, L. M., Eds.; British Nuclear Energy Society: London, 1974; p 15.
199. Grandison, N. O.; Facer, R. I. In *Corrosion of Steels in CO_2*; Holmes, D. R., Hill, R. B., Wyatt, L. M., Eds.; British Nuclear Energy Society: London, 1974; p 208.
200. Ferguson, J. M.; Garrett, J. C. P.; Lloyd, B. In *Corrosion of Steels in CO_2*; Holmes, D. R., Hill, R. B., Wyatt, L. M., Eds.; British Nuclear Energy Society: London, 1974; p 15.
201. Rowlands, P. C.; Garrett, J. C. P.; Popple, L. A.; Whittaker, A.; Hoaksey, A. *Nucl. Energy* **1986**, *25*(5), 267.
202. Rowlands, P. C.; Garrett, J. C. P.; Popple, L. A.; Whittaker, A.; Hoaksey, A. *Nucl. Energy* **1986**, *25*(5), 267–275.
203. Gleave, C.; Calvert, J. M.; Lees, D. G.; Rowlands, P. C. *Proc. R. Soc. London Ser. A.* **1982**, *379*, 409.
204. Gibbs, G. B. *Oxid. Met.* **1973**, *7*(3), 173–184.
205. Gibbs, G. B.; Hales, R. *Corros. Sci.* **1977**, *17*(6), 487–497, 499–507.
206. Kofstad, P. *Oxid. Met.* **1985**, *24*(5–6), 265–276.
207. Mrowec, S. *Corros. Sci.* **1967**, *7*(9), 563–578.
208. Banks, P.; Lorimer, G. W. In *Materials to Supply the Energy Demand*; Hawbolt, E. B., Mitchell, A., Eds.; American Institute of mechanical Engineers: New York, 1982; p 231.
209. Wolf, I.; Grabke, H. J. *Solid State Commun.* **1985**, *54*(1), 5–10.
210. Surman, P. L. *Corros. Sci.* **1973**, *13*(11), 825–830, IN1–IN5, 831–832.
211. Surman, P. L.; Brown, A. M. In *Corrosion of Steels in CO_2*; Holmes, D. R., Hill, R. B., Wyatt, L. M., Eds.; British Nuclear Energy Society: London, 1974; p 85.
212. Goodison, D.; Harris, R. J.; Goldenbaum, P. In *British Joint Corrosion Group Symposium on Metal–Gas Reactions in Atmospheres Containing CO_2*; London, March 1967.

1.23 High Temperature Corrosion of Chromia-forming Iron, Nickel and Cobalt-base Alloys

A. Galerie
SIMaP, Grenoble INP/CNRS/UJF, Domaine Universitaire, BP 75, 39402 Saint Martin d'Héres, France

Abbreviations

bcc body-centered cubic
fcc face-centered cubic
AISI American Iron and Steel Institute
CTE coefficient of thermal expansion
DIN Deutsches Institut für Normung
EN European norms
MICF mechanically-induced chemical failure
REE reactive element effect
SOFC solid oxide fuel cell
UNS Unified Numbering System

Symbols

α bcc ferritic solid solution
γ fcc austenitic solid solution σ
σ brittle intermetallic sigma phase

1.23.1 Introduction

In industrial applications where high temperatures are required or produced, chromium-containing alloys are widely used. Based on iron and/or nickel, and less often on cobalt, they can offer mechanical properties which can be adjusted to the situations they will encounter, with additional resistance to chemical attack by the various gaseous atmospheres.

Over the years, there have been arguments about who invented stainless steels, the first chromium-containing alloys. It seems that Pierre Berthier in France was the first to report ~1820 that addition of sufficient chromium to iron suppressed attack by water and acids. However, he could not, at that time, produce mechanically resistant steels. Harry Brearley of Sheffield was the first to produce a 13% Cr–0.24% C martensitic stainless steel in 1913 and to observe its excellent resistance to corrosion. It is amazing to note that this discovery was made as Brearley looked for better erosion (and not corrosion) resistance of gun barrels. More interesting is that his work was made in a technical laboratory cofinanced by two main Sheffield steel companies of the day. It seems however that the Krupp German company in Essen (first austenitic stainless steel patent: 1912) as well as Swedish steelmakers produced stainless steels at this time. In fact, all industrial countries could produce such materials after World War I. In 1924, grade 304 (18Cr–8Ni) was produced at Sheffield by W. H. Hatfield.

Concerning nickel based alloys, they were developed a decade later, for example, by Haynes International, USA. The term Superalloy appeared just after World War II for designing new alloys for aircraft engine applications.

Cobalt based alloys were also first produced at the beginning of the twentieth century, for example, by Stellite in 1907 in Canada.

The first published systematic comparative study of the behavior of numerous chromium-containing alloys by Hatfield appeared in the *Journal of the Iron and Steel Institute* in 1927.[1]

The same author published the first quantified values in 1928, using a 'scaling index' (SI) defined as the temperature giving a certain weight gain (in g m^{-2}) at the end of a seven 6-h cycle oxidation run.[2] The higher the SI, the better the behavior of the alloys. His results for SI_{10} (10 g m^{-2}), SI_{20} (20 g m^{-2}), and SI_{100} (100 g m^{-2}) are presented in **Table 1**.

Nowadays, many results can be found either in the scientific literature or in technical notes provided by the steelmakers, giving the maximum service temperature acceptable for all commercial alloys. **Figure 1** presents such data for isothermal oxidation in air; it is generally considered that this maximum service temperature must be reduced by at least 25 °C in cycling conditions, sometimes by larger values in more aggressive atmospheres (metal dusting or sulfidizing environments).

At present, simple scientific principles can explain the results of Hatfield; they are recalled in the following section.

1.23.2 Underlying Principles of High Temperature Corrosion Protection by Chromium

High temperature alloys must be protected in service by an external slow-growing oxide scale. In the case of chromium-containing alloys, this protective scale is based on chromia Cr_2O_3.

1.23.2.1 Various Types of Chromium-Containing Alloys

As may be observed on Fe–Cr, Ni–Cr, and Co–Cr binary system phase diagrams (**Figures 2–4**),

Table 1 Scaling indexes (°C) for a series of chromium-containing alloys

Cr	*Ni*	*Si*	*Mn*	*Others*	SI_{10} (°C)	SI_{20} (°C)	SI_{100}(°C)
0.1	0.1	0.25	0.82		<400	600	620
3.1	0.3	0.26	0.55	Mo	<500	600	640
3.1	0.9	0.22	0.61	Mo, V	<500	600	615
8.5	0.3	3.37	0.50		950	960	1010
9.0	0.4	0.19	0.48	Mo	<500	640	695
12.9	0.3	0.21	0.37		800	820	835
12.8	0.5	0.31	0.31		790	800	825
16.6	2.5	0.29	0.41		750	790	850
12.3	0.3	0.19	0.46	Mo	800	810	820
10.9	0.6	0.42	0.86	Mo, V	800	805	820
10.6	0.8	0.43	1.06	Mo, V, Nb	800	810	815
11.4	2.6	0.48	0.73	Mo, V, Nb	750	760	770
10.7	0.6	0.48	0.89	Mo, V, Nb, Co	800	810	825
15.9	4.0	0.55	0.26	Nb, Cu,	780	807	818
13.9	5.5	0.32	0.78	Mo, Nb, Cu	750	770	830
16.0	0.3	0.42	0.37		850	860	875
20.5	0.2	0.39	0.73		900	1000	1075
28.9	1.8	1.49	1.34	N	900	1120	1160
13.1	0.1	0.55	0.85	Al	1060	1100	1125
18.7	10.0	0.51	1.04		860	880	915
18.3	9.0	0.76	0.80	Ti	820	860	890
18.3	10.0	0.40	0.76	Nb	820	860	890
16.4	10.5	0.19	1.69	Mo	700	820	845
22.0	14.4	0.47	1.17		980	1060	1070
25.2	20.2	0.48	1.49		1030	1090	1180
20.3	33.5	0.60	1.12	Ti, Al	970	1010	1140

Oxidizing atmosphere: combustion gas with 50% excess air.

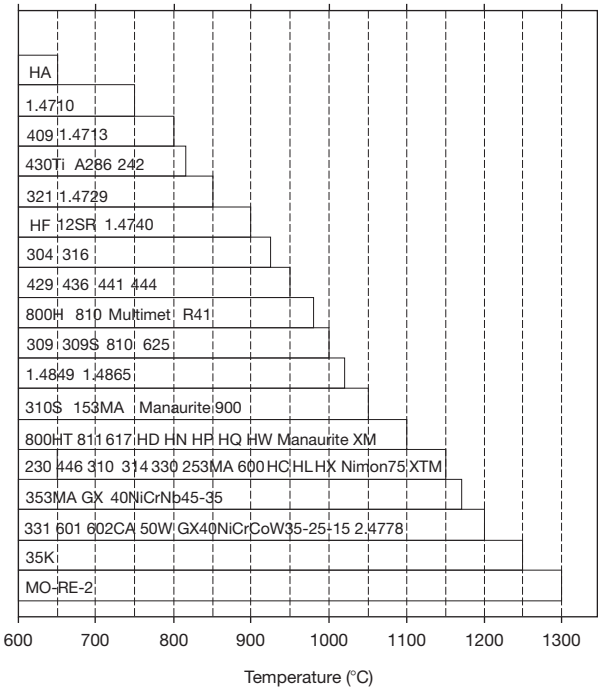

Figure 1 Maximum isothermal service temperature for various chromia-forming alloys, estimated from literature and producer data.

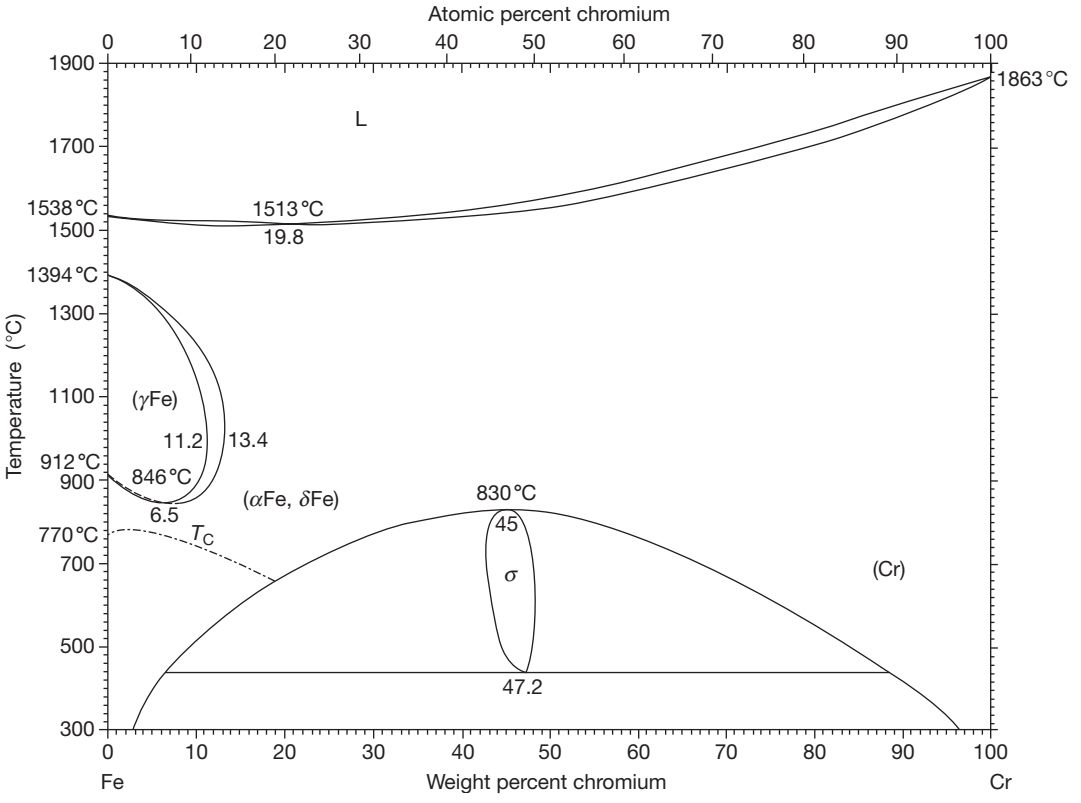

Figure 2 Fe–Cr phase diagram.

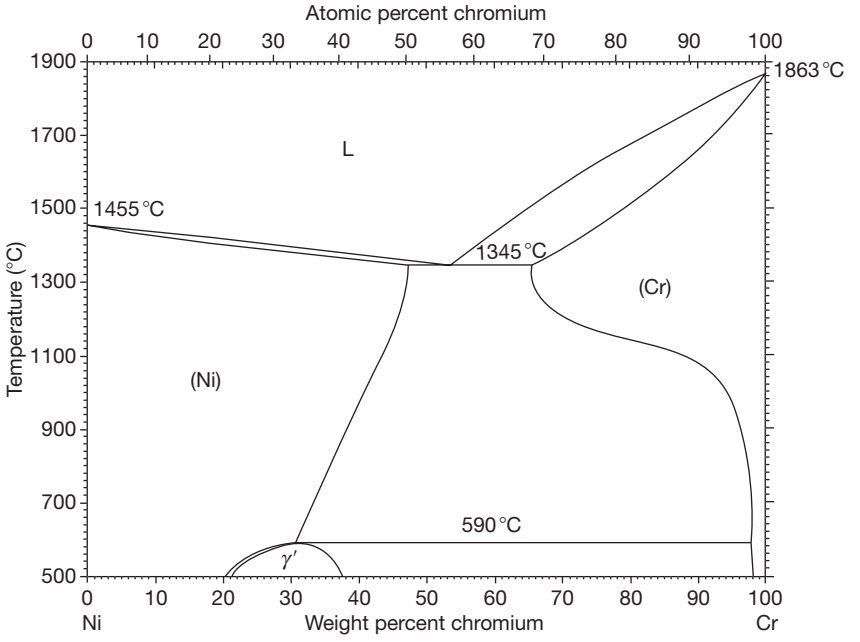

Figure 3 Ni–Cr phase diagram.

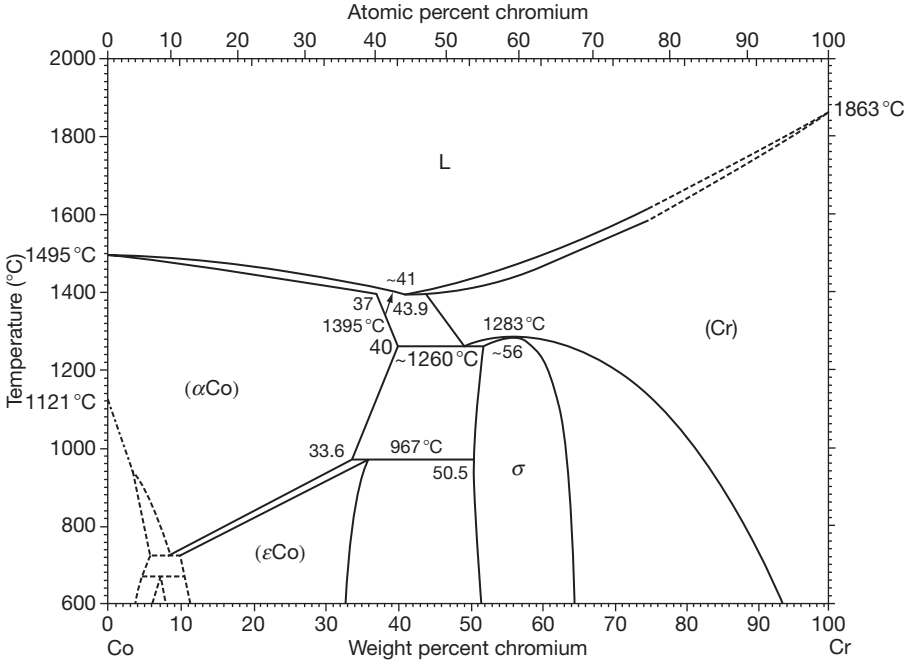

Figure 4 Co–Cr phase diagram.

chromium is a highly soluble element in iron, nickel, and cobalt.[3] However, the intermetallic sigma phase may appear during long time anneal of iron–chromium alloys at medium temperatures (700–1100 K), with very bad mechanical properties (high brittleness) and its formation must be avoided. Ternary or quaternary Fe–Ni–Co–Cr solid solutions are also stable.

The particular situation of iron, where bcc–fcc allotropic transformation occurs at 912 °C, has to be considered. Increasing chromium content of bcc Fe–Cr alloys to 5 wt% first reduces this value to ~850 °C before increasing it to ~1050 °C for 15 wt%. For higher Cr contents, the steels retain the bcc structure up to the melting temperature. Fe–Cr ferritic stainless steels with a chromium content falling in the $\gamma + \alpha$ loop, if not 'stabilized,' undergo phase transformation on heating, leading to a biphasic structure. As described in the following, the appearance of the fcc γ phase significantly modifies two main properties of the alloy: diffusion coefficient of chromium and coefficient of thermal expansion (CTE).

Nickel is used as γ-promoter in chromium alloys, giving better mechanical properties than the ferritic structure. Considering not only the high price of nickel, but also the instability of its market, efforts have been made to replace it by other gamma-stabilizing elements. Manganese-containing austenitic stainless steels, such as 204Cu grade, have been produced and tested in high temperature situations.[4]

Carbon and nitrogen minor elements in Fe–Cr alloys are γ-stabilizers. Their concentration is therefore not strictly limited in austenitic alloys and can be adjusted according to the destination of the materials. Conversely, their amounts must be controlled in ferritic steels.

Metallic elements such as Ti, Nb, Mo, intrinsically ferrite promoters, have the additional property to strongly fix carbon and nitrogen as carbides, nitrides, and carbonitrides. Due to this fact, they increase the stability domain of ferrite and are largely used in 'stabilized' ferritic stainless steels.

Regarding these considerations, high temperature chromium-rich alloys are generally described as martensitic steels (iron based, with ferritic structure), stainless steels (iron based, with ferritic or austenitic structure) and refractory alloys (iron, nickel, or cobalt based, with austenitic structure).

Martensitic low chromium steel grades are first hardened by rapid cooling, and then tempered at a temperature in excess of the proposed service temperature. They are largely used for pressurized water or steam tubes, vessels and heat exchangers. Initially, based on the composition Fe–2.25Cr–1Mo (T22 steel), these grades had to follow the regular increase in temperature and pressure of processes to fit the required decrease in CO_2 emissions; they now include 9% Cr (T9 steel) and several similar grades with minor additions that increase their creep resistance in service (steels T91, T92, T911).

Chromium steels containing 12% Cr and more are usually qualified as stainless steels. Commercial grades are 12% and 17% Cr, with a new composition recently appeared at 14%. Higher chromium is also available, up to 30%. These alloys are ferritic or austenitic depending on the fraction of γ-stabilizing element (Ni or Mn). Both ferritic and austenitic stainless steels are protected in high temperature service by a chromia scale. However, that does not mean they can be used indifferently in any industrial situation. Austenitic stainless steels are preferably used when mechanical resistance at high temperatures is required, despite their higher price. Conversely, ferritic grades are used in situations where permanent or cyclic mechanical loading in service remains low. However, a careful design of parts made of ferritic grades may authorize their use in various industrial situations.

Due to their difference in crystallographic structure, ferritics, and austenitics do not allow identical chromium diffusion rates; the more open bcc ferritic structure allow quicker chromium diffusion than the compact fcc austenitic structure. As a result, alloy chromium depletion under chromia scales will be more marked, but to shorter depths, in austenitics.

A second property which makes ferritics and austenitics different is their CTE, which lies in the range $(12–13) \times 10^{-6}\,K^{-1}$ for the bcc grades and $(19–20) \times 10^{-6}\,K^{-1}$ for the fcc grades. Due to the lower CTE of chromia ($(8–12) \times 10^{-6}\,K^{-1}$ according to various authors), chromia scales grown on austenitic stainless steels are subjected to more intense compressive stresses on cooling than the same scales on ferritics.

A particular phenomenon occurring during temperature increase (decrease) of the nonstabilized ferritic grades is the volume increase (decrease) associated with the ferrite–austenite transformation which can be deleterious for the integrity of the oxide scale, producing early breakaway corrosion in thermal cycling conditions.

Refractory alloys contain high chromium levels and strengthening elements to increase their mechanical properties at high temperatures. Based on the austenitic structure, they are mainly Fe or Ni-rich, and less often Co-rich.

1.23.2.2 Growth of Cr-Containing Oxides

To discuss the behavior of the various chromia-forming alloys used in high temperature industrial applications, several physical, chemical, and

mechanical mechanisms are of importance. Although they have been mostly described in other chapters, they are briefly recalled here for an efficient reading of this chapter.

1.23.2.2.1 Chromia growth

Regarding M–Cr–O systems (M = Fe, Ni, Co) subjected to oxidizing atmospheres, chromia Cr_2O_3 is the most stable oxide. It is therefore expected to inhibit M oxidation by creating a chromia barrier to oxygen, lowering the oxygen chemical potential in contact with the alloy to a value too low for oxidation of the major element M. In fact, the minimum chromium content for effectively growing a chromia scale is ~14% for iron, 20% for nickel, and 25% for cobalt.[5] Chromia is regarded as an amphoteric semiconductor, with predominant chromium interstitials at low oxygen potentials (i.e., near the metal–oxide interface) and predominant chromium vacancies at higher oxygen potentials (i.e., near the oxide–gas interface).[6] In all situations where chromium alloys are oxidized in air, chromia growth takes place by chromium transport through the scale. Inversion of transport may occur by blocking cation diffusion using yttrium or rare earth trace additions to the alloys, resulting in slower growth by oxygen transport (reactive element effect, REE). Water vapor or steam atmospheres also produce chromia scales where inward transport of H-assisted oxygen is predominant.[7]

Due to the high compactness of chromia, and also due to the necessity for less oxidizable Fe and Ni elements to enter it in the atomic state (atomic radius ~ 125 pm compared to ionic (+II) radius ~ 77 pm), this oxide is a good diffusion barrier for these major elements of stainless steels and refractory alloys. Conversely, Mn, Ti and, to a lesser extent, Nb, which are more oxidizable than chromium, rapidly diffuse through chromia scales as small cations ($r_{Mn^{2+}} = 80$ pm, $r_{Ti^{4+}} = 68$ pm).

The behavior of iron also has to be considered, as Fe^{3+} and Cr^{3+} ions are completely exchangeable in the rhombohedral chromia structure. All range of solid solutions between Fe_2O_3 (hematite) and Cr_2O_3 (chromia) are known, with the general formula $Cr_{2-x}Fe_xO_3$. In high temperature processes, it is of importance to limit the values of x to the minimum by rapidly heating the steels to 800 °C or using a reducing atmosphere for hematite during heating. This is of particular importance when iron-free surfaces are needed, for example, in the petrochemical industry where iron catalyzes graphite deposition (catalytic coking).

Maintaining protection against oxidation necessitates that chromia scales remain compact and adherent to the alloy substrates. Understanding the mechanisms of scale spallation was the subject of much work in the past decades.[8,9] Many results of stress measurements appear in the literature, showing mean values of 1–3 GPa compressive stresses in chromia scales, counterbalanced by tensile MPa values in the alloy substrates. However, it was experienced that oxide stress is not the key parameter in scale spallation, but that scale adhesion energy, defined as the metal–oxide interfacial fracture energy, was of greater importance.[10]

1.23.2.2.2 Growth of spinel phases

In any situation where a chromia scale cannot grow or be maintained on any Fe-containing alloy surface, magnetite enriched in chromium becomes the major oxidation product. This compound exhibits less protective properties than chromia, allowing outward transport of iron and inward transport of oxygen. That results in a typical duplex morphology where the external subscale is chromium free (hematite or magnetite) and the internal one has the limit stoichiometry of $FeCr_2O_4$ (chromite spinel phase).

Iron chromite affords lower protection against oxidation compared to chromia, with larger mobility of oxide ions leading to more internal oxide growth.

Nickel–chromium spinel (nickel chromite $NiCr_2O_4$) formation may occur concurrently with chromia on nickel based low chromium alloys, leading to some loss of protection. Increasing chromium content in the alloy tends to suppress this formation.

Manganese–chromium spinel (manganese chromite, $Mn_{3-x}Cr_xO_4$, with x generally between 1.5 and 2) is known to constitute the external part of the scale grown on high temperature alloys containing fractions of manganese, as low as 0.5%. This oxide overlays the internal chromia part of the scale and is the result of manganese diffusion from the alloy through this chromia part. The formation of this oxide is not considered as deleterious as it remains generally compact and adherent and it was even claimed that it is better resistant than chromia to chromium carbide transformation in high carbon activity atmospheres.[11] It also decreases chromia activity and consequently inhibits chromium (VI) vaporization.[12,13]

Competition between chromia and iron–nickel chromite is sometimes a key factor for long lasting use of high temperature alloys. Catastrophic break away oxidation occurs generally by local than by

generalized transformation of chromia to a spinel phase.[14,15] Factors that promote spinel appearance are

- high temperatures,
- low chromium and/or subsurface dechromization,
- thermal cycling, and
- water vapor atmospheres.

Promoting chromia growth may be obtained by increasing the chromium content of alloy or by any chemical or mechanical operation that enhances the number of fast diffusion paths for chromium from the alloy to the metal–oxide interface: laser glazing induced microcrystallization or work hardening generating high concentration of dislocations.

1.23.2.3 Influence of Alloy Minor Elements

Properties of today's industrial chromia-forming alloys are tailored to their exact application by adjusting the amount of minor metallic (Mn, Ti, Nb, Mo, Y, La, Ce, Zr) or nonmetallic (C, S, Si, B) elements.

The effect of manganese was described above. Titanium, in the form of carbide, nitride, carbonitride, and eventually excess solid solution Ti, slightly increases the parabolic rate constant of oxidation, but concurrently promotes scale adhesion,[16] due to TiO_2 precipitation at the alloy–scale interface. External diffusion of titanium through chromia may also occur, forming titania and/or Cr_2TiO_5 surface nodules. Niobium in the form of carbide, nitride, carbonitride, but also of Fe_2Nb intergranular intermetallic precipitates, may slowly oxidize to NbO at the alloy–scale interface and also slowly diffuse to the scale surface, forming NbO_2 (in solid solution with TiO_2 when this latter element is present). Molybdenum is not oxidized at the alloy–chromia interface, remaining as an intermetallic phase. Silicon and boron, more oxidizable than chromium, enrich as oxides at the metal–scale interface. Sulfur also segregates at this interface in the elementary form, strongly reducing scale adhesion.[17] Reactive elements (Y, La, Ce, Zr) decrease oxidation rates and promote scale adhesion. Mechanisms for that have been discussed at length. Interface sulfur removing and scale growth inversion are probably of major importance in these beneficial phenomena.

1.23.3 High Temperature Oxidation Behavior of Chromium Alloys

Oxidation, in its original meaning of oxygen fixation, is the most frequently encountered mode of high temperature corrosion. All furnace elements working in air or combustion atmospheres are subject to oxide scale growth. It should be noted that oxidation, generally considered as a degradation mechanism, may be used as a beneficial phenomenon, as in stainless steel processing where iron–chromium thick scales formed during reheating before hot rolling consume surface defects and form a ductile lubricating coating preventing sticking between the metal and the roller.

1.23.3.1 Oxidation of Martensitic and Ferritic Stainless Steels

Martensitic grades are possibly chromia-formers in oxygen or air in low aggressive conditions, but exhibit rapid chromia destabilization with increases in temperature and time. This destabilization, leading to the so-called breakaway corrosion, is also accelerated by thermal cycling. Post-breakaway scales exhibit classical duplex morphology, with internal Cr-containing magnetite subscale and external hematite. In water vapor or steam, chromia destabilization is easier and these grades can no longer be considered as chromia-formers. Duplex iron-rich scales are observed, as in air, generally with external magnetite instead of hematite due to low values of the oxygen chemical potential in the steam environment. For such a steam situation, an empirical law was proposed by Gabrel *et al.*[18] for the parabolic increase of scale thickness ζ

$$\zeta^2 = (8.099)^2 \times 2.35.10^{10} \exp\left[-\frac{16200}{8.32T}\right] (1 - \mathrm{Si})^{187} (1 - \mathrm{Cr})^{36.7} t$$

High chromium ($\geq$18%) ferritic stainless steels (AISI 4XX grades) oxidize with near-parabolic slow growth of chromia-rich scales. The Fe/Cr ratio of the rhombohedral oxide increases with increasing temperature and oxidation time. For these grades, passive chromia scales can form for long periods, giving excellent oxidation resistance. As a consequence, increasing chromium concentration confers better oxidation resistance in isothermal conditions, as observed in Figure 5. It is noted that small aluminum additions to ferritic stainless steels generate internal precipitation of alumina between the steel substrate and the chromia scale, leading to strong improvements in the oxidation behavior, as shown for the 12SR (12Cr–1Al) and 18SR (18Cr–2Al) in Figure 5. Such alloys

are chromia-formers in air, but may become exclusively alumina-formers in high temperature situations of decreased oxygen chemical potential where chromia becomes unstable. Ferritic FeCrAls, exclusively alumina-formers need a minimum composition of 20Cr–4Al.

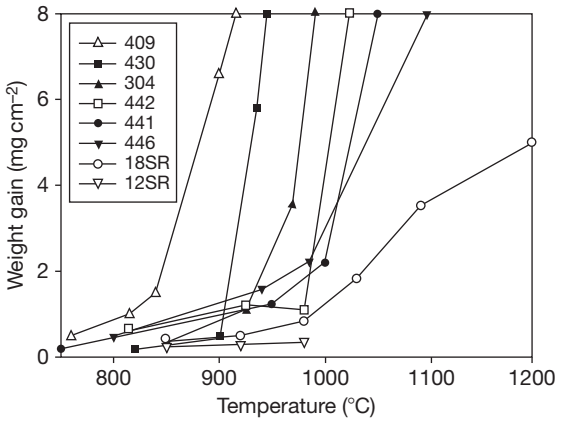

Figure 5 Weight gains of various stainless steel grades after 100 h isothermal oxidation in air (data from producers).

Table 2 Time to breakaway for cyclic oxidation of ferritic stainless steels (in and out 20 min cycles in laboratory air at 950 °C)

Steel grade	*409*	*439*	*441*	*436*
Composition	12 Cr	18 Cr	18 Cr–Ti, Nb	18 Cr–1 Mo
Time to breakaway (h)	150	900	>1200	>1200

In thermal cycling situations, good protection is obtained up to MICF (mechanically induced chemical failure), as proposed by Evans,[19] where breakaway oxidation occurs by forming nonprotective iron-rich oxides. In such thermal cycling situations, the same beneficial influence of chromium was noted, with also clear improvement by the ferrite stabilizers Ti and Nb (**Table 2**).[20] The 441 grade is commonly proposed for exhaust parts in the automotive industry.

High temperatures or water vapor in the gas may promote chromium (VI) oxide or oxohydroxide volatilization, strongly impeded by manganese additions which form an external $MnCr_2O_4$ spinel phase, decreasing chromium (III) oxide activity and therefore the gaseous chromium (VI) compound's partial pressure as seen in **Table 3**.

The growing interest in solid oxide fuel cells (SOFCs) working at intermediate temperatures (<800 °C) has led to increasing work on ferritic stainless steels which are possibly used as interconnectors, separating the cathode side (air) from the anode side (wet hydrogen) of the cell. Good technical solutions need decreased chromium (VI) poisoning of the cathode and manganese additions help by lowering the partial pressure of undesired gas species. Another important parameter for this application is the low contact resistance between scale and metal and elements forming internal oxide enrichment at the metal–scale interface (mainly Si and Al) must be avoided. Following these observations, special grades to be used in SOFCs have been produced and are now available in the market (**Table 4**).

Table 3 Calculated partial pressures of gaseous chromium (VI) oxide or oxyhydroxide in equilibrium with solid Cr_2O_3 or $MnCr_2O_4$

Atmosphere	*Solid compound*	*Predominant gas*	*900 (K)*	*1200 (K)*	*1500 (K)*
N_2 + 20% O_2	Cr_2O_3	CrO_3	1.5×10^{-8}	1.4×10^{-6}	3.3×10^{-5}
N_2 + 20% O_2	$MnCr_2O_4$	CrO_3	5.0×10^{-10}	1.1×10^{-7}	4.3×10^{-6}
N_2 + 20% O_2 + 15% H_2O	Cr_2O_3	$CrO_2(OH)_2$	1.6×10^{-7}	9.4×10^{-7}	3.7×10^{-6}
N_2 + 20% O_2 + 15% H_2O	$MnCr_2O_4$	$CrO_2(OH)_2$	5.2×10^{-9}	7.3×10^{-8}	3.5×10^{-7}

Data for CrO_3 from Barin,[21] for $CrO_2(OH)_2$ from Opila *et al.*[22] for $MnCr_2O_4$ from Jung.[23] It is reminded that volatilization is assumed to be negligible for gas pressure <1 nbar and catastrophic for gas pressure >0.1 mbar.

Table 4 Composition of ferritic grades specially adjusted to be used as SOFC interconnectors

Name	*Cr*	*C*	*Si*	*Mn*	*Cu*	*Al*	*Ti*	*Ni*	*Others*
CROFER22APU ThyssenKrupp	22	<0.03	<0.5	0.3–0.8	0.5	0.5	0.03–0.2		La 0.04–0.2
ZMG232	22	0.02	0.4	0.5		0.05		0.26	0.04 La, 0.22 Zr
Hitachi metals									
Fe–Cr–W	20		0.3			0.5			0.3 Zr
Sumitomo metals									7 W

1.23.3.2 Oxidation of Austenitic Stainless Steels (AISI 3XX Grades)

For temperatures lower than 800 °C, 18Cr–8Ni stainless steels 304 and 321 are commonly used. Increasing service temperature needs increased chromium up to 20–25%, with larger silicon additions up to 2–2.5% producing silica enrichment at the alloy–chromia interface, decreasing chromium incorporation into the scale. With such compositions, grades 309, 310, and 314 are known as 'refractory stainless steels.' All these grades are more mechanically resistant than ferritics and can be further strengthened by increasing carbon and/or nitrogen contents.

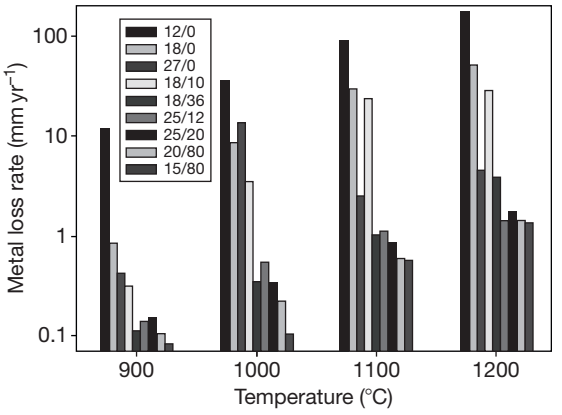

Figure 6 Isothermal air behavior of various austenitic grades compared to three ferritics with equivalent chromium contents; legend: Cr/Ni in wt%. Redrawn from Brasunas, A. de S.; Gow, J. T.; Harder, O. E. *Proc. ASTM* **1946**, *46*, 870.

Care must be taken when using high chromium austenitic grades at intermediate temperatures where σ-FeCr may precipitate (310, 314, 253 MA grades, for example), leading to brittleness. Possible formation of this phase can be roughly predicted from the Fe–Ni–Cr phase diagram, with additional influence of minor elements by using empirical relations.[24]

In **Figure 6**, it is shown that the austenitic grades are more scaling resistant in isothermal conditions than the ferritic ones for equivalent chromium content.

In cyclic conditions, heavy spallation is observed clearly due to strong differential contraction on cooling. Here also, increasing nickel content leads to better behavior (**Figure 7**).

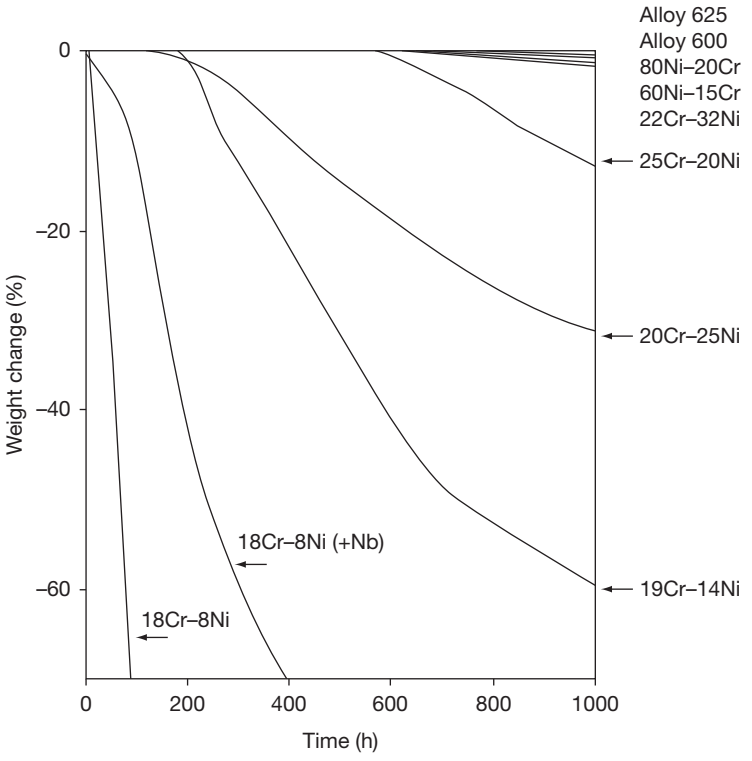

Figure 7 Weight loss in cyclic conditions (15 min heating at 980 °C, 5 min cooling) of austenitic grades with different chromium and nickel contents. Adapted from Lai, G. A. *High Temperature Corrosion of Engineering Alloys*; ASM International: Metals Park, OH, 1990.

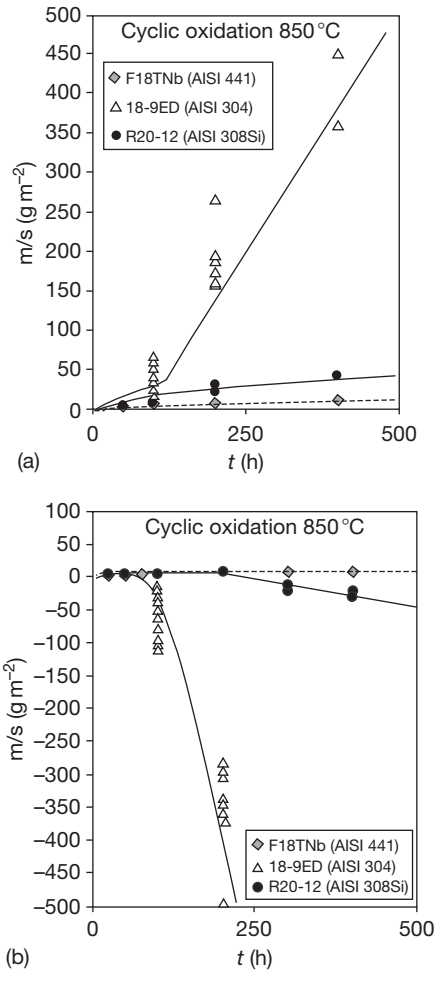

Figure 8 Comparative air cyclic oxidation of ferritic and austenitic grades (20 min cycles). (a) gross mass gain; (b) mass change after descaling.

An influence of steel structure on spallation appears also in the recent results from a study by Ugine & ALZ (today ArcelorMittal Stainless Europe) for exhaust systems (**Figure 8**),[25] confirming older results (**Table 5** and **Figure 9**) showing that ferritic stainless steels are better resistant in short cycle situations than austenitic ones. This is due to a lower thermal expansion coefficient which prevents high stress states from appearing during cooling. Ferritic materials also relax by high temperature creep, further decreasing oxide stress. However, the good behavior of ferritic stainless steels in cyclic conditions is lost as soon as they are used at temperatures entering the $(\alpha + \gamma)$ domain.

Internal alumina precipitation for the 18SR grade is also beneficial as seen in **Table 5**.

1.23.3.3 High Temperature Oxidation of Ni- and Co-Containing Alloys

1.23.3.3.1 Ni–Cr alloys

Binary nickel–chromium alloys have been recognized very early as high temperature oxidation resistant. **Table 6** summarizes results published in 1957 showing the ability of Cr to drastically decrease the parabolic rate constant of nickel oxidation.[28] It can be noted that higher chromium is necessary when the temperature increases. Commercial alloys mainly contain 20–30% Cr to stabilize a protective chromia scale and always contain several minor additions to improve their mechanical and/or chemical properties: typical 'Nichrome' (UNS N06003, EN/DIN 2.4869) contains 1% Si and

Table 5 Weight changes of austenitic and (stabilized) ferritic grades of equivalent composition in air thermal cycling conditions

Alloy	*Average composition*	*Cycling between 870 and 930 (°C)*				*Cycling between 980 and 1040 (°C)*				
		288 cycles	480 cycles	750 cycles	958 cycles	130 cycles	368 cycles	561 cycles	753 cycles	1029 cycles
309	20 Cr, 12 Ni, 2 Si	0.3	−4.6	−23.7	−32.6	−24.2	−77.5	−178	−242	−358
310	25 Cr, 20 Ni, 2 Si	n.t.[a]	n.t.	n.t.	n.t.	1.5	−11.3	−29.3	−62.8	−107
442	20 Cr, 1 Mo, 1 Si	0.7	1.2	1.5	1.5	n.t.	n.t.	n.t.	n.t.	n.t.
446	25 Cr, 0.5 Si	0.3	0.4	0.3	0.1	0.4	0.5	−0.2	7.0	−19.4
18SR	18 Cr, 1 Si, 0.4 Ti, 2 Al	0.3	0.4	0.5	0.6	0.7	1.1	1.5	2.2	3.0

[a]n.t.: not tested.

Source: Reproduced from Lasday, S. B. *Ind. Heating* **1979**, 12. Reproduced from Lai, G. A. *High Temperature Corrosion of Engineering Alloys*; ASM International: Metals Park, OH, 1990.

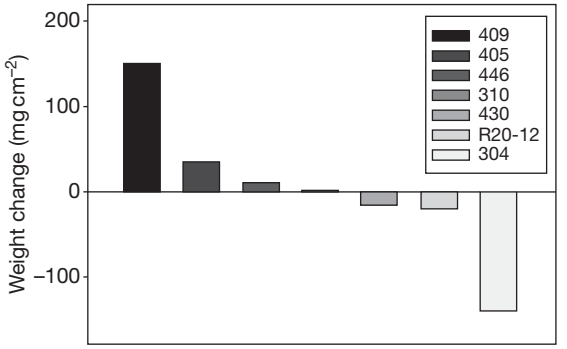

Figure 9 Cyclic oxidation weight change of several ferritic and austenitic stainless steels after 400 cycles in air at 1000 °C (30 min in furnace, 30 min out). Reproduced from Kado, S., Yamazaki, T., Yoshida, K., Yabe, K., Kobayashi, H., *Trans. Iron Steel Inst. Jpn.* **1978**, *18*, 387.

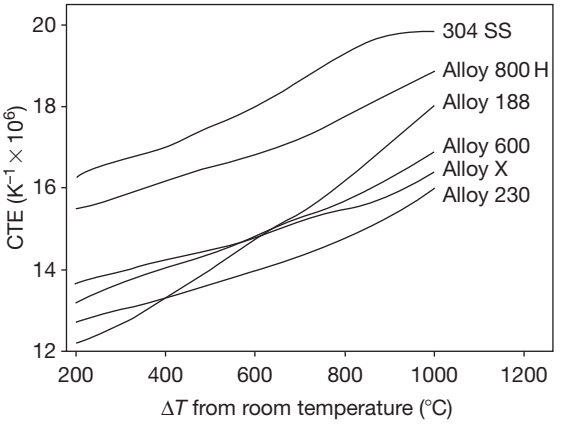

Figure 10 Reduction of the coefficient of thermal expansion (CTE) by minor element additions for several chromia-forming alloys. Data from Haynes International.

Table 6 Parabolic rate constant of oxidation in air or in pure oxygen (atmospheric pressure) of pure nickel and various nickel–chromium alloys

Chromium content (wt%)	*Atmosphere*	*Temperature (°C)*	*Parabolic rate constant × 100 ($g^2\ cm^{-4}\ s^{-1}$)*
0.0	Air	900	0.28
1.97	Air	900	4.9
4.12	Air	900	5.8
5.89	Air	900	8.2
8.0	Air	900	0.0
0.0	Oxygen	1000	3.48
0.3	Oxygen	1000	15.0
1.0	Oxygen	1000	25.8
3.0	Oxygen	1000	28.3
10.0	Oxygen	1000	5.55
0.0	Oxygen	1096	5.48
0.32	Oxygen	1096	23.6
0.92	Oxygen	1096	29.7
2.0	Oxygen	1096	39.6
3.45	Oxygen	1096	46.8
5.67	Oxygen	1096	58.5
7.64	Oxygen	1096	67.8
8.71	Oxygen	1096	30.8
11.1	Oxygen	1096	3.79
14.9	Oxygen	1096	0.35
20.0	Oxygen	1096	0.07

Source: Zima, G. E., *Trans. Am. Soc. Met.* **1957**, *49*, 924.

0.01–0.04 reactive element, whereas Nimonic 75 contains 0.5% Ti.

Nickel–chromium alloys are mainly used in the form of wires for electrical heating and for making heat resistant parts in situations where mechanical considerations are low.

1.23.3.3.2 Ni–Fe–Cr alloys

Increasing nickel content from stainless steels stabilizes the gamma phase and prevents sigma phase formation. High mechanical resistance, particularly to creep in service, is realized by adding interstitial nonmetallic elements (C, N, B) and/or substitutional refractory elements (Mo, W, Ta, Nb) in solid solution in the γ phase. Carbide or intermetallic precipitation also participates in alloy strengthening.

Other effects of minor element additions are to slow down grain growth in service, to inhibit sigma phase formation and to lower the thermal expansion coefficient. Figure 10 shows that Ni-base alloys (600, X, and 230) have naturally lower CTE than Fe-based (304, 800H) and also that the strongly-charged 230 alloy (14% W, 2% Mo) has lower CTE than Alloy X (9% Mo) and alloy 600 (no W, Mo). Decreasing CTE enhances resistance to scale spallation in thermal cycling service.

Scaling resistance of nickel-based alloys in oxidizing atmospheres is far better compared to stainless steels (Figure 11) and these grades are of major importance in all very high temperature processes using furnaces or combustion chambers for energy transformation and chemical or metallurgical reactions.

1.23.3.3.3 Co–Cr alloys

Industrial cobalt–chromium alloys are strengthened by solid solution and carbide formation. They present very good resistance to high temperature creep, even for temperatures above 1000 °C. Due to their high

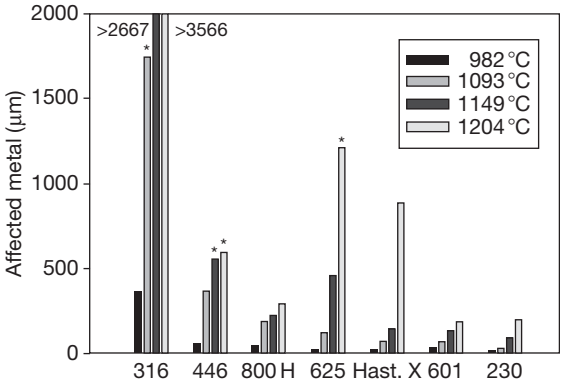

Figure 11 Metal loss plus average internal penetration measured on various iron- and nickel-base alloys after 1008 h under flowing air (213.4 cm min^{-1}). Metal loss from weight gain, penetration from cross-section observations. Samples cycled to room temperature once a week. Asterisk: actual value larger. Data from Haynes International.

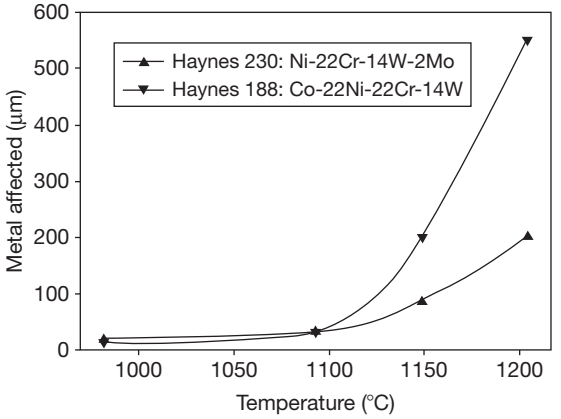

Figure 12 Comparative oxidation damage of one nickel- and one cobalt-based alloy of approximate identical composition showing better performance of the nickel alloy at the highest temperatures.

chromium contents, they also resist oxidation well, but it was reported that alloy 188 is sensitive to water vapor in the oxidizing atmosphere which reduces its life time. They are of interesting use when nickel is prohibited, for example in sulfidizing situations where Ni-containing low melting temperature eutectics can form.

The drawback is that their market price is high. When no particular situation imposes the choice of cobalt, it seems preferable to use nickel alloys as shown in **Figure 12**.

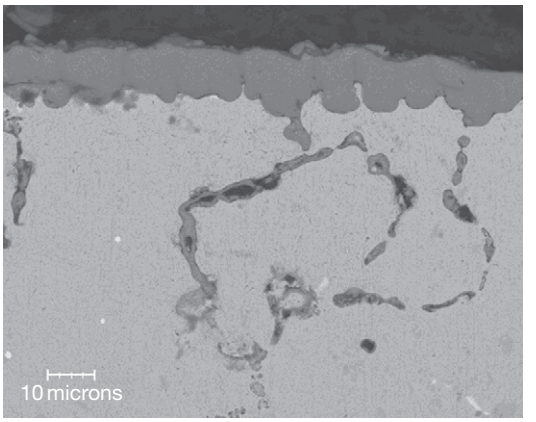

Figure 13 Cross section of alloy HK40 oxidized at 1100 °C in air for 50 h, showing large internal penetrations.

1.23.3.3.4 Various comparisons between alloy grades

One point which may be emphasized concerns the high concentrations of minor oxidizable elements, particularly for Ni(Co)–Cr grades, which lead to internal inter- and intragranular oxidation to depths often much larger than the chromia scale thickness (**Figure 13**). This may be deleterious for the mechanical resistance of these alloys in situations where the total weight gain seems to be not catastrophic. For engineering comparison between different grades, figures concerning metal loss or scale thickness must necessarily be discussed together with the depth of the affected metal (**Table 7**).

As seen earlier, it is difficult to compare the resistance to high temperature oxidation of various industrial grades using only one parameter. Trying to overcome this difficulty, an important work done at NASA was presented by Barrett where not only kinetics were taken into account but also the visual aspect of the samples.[27] Many industrial alloys were submitted to 10 cycles of 1000 h each at 982 °C in air. Kinetics were evaluated by determining linear (k_l) and parabolic (k_p) rate constants from weight change measurements according to

$$\Delta m/A = k_l t + k_p t^{1/2}$$

The attack parameter, called KB_3, was defined by

$$KB_3 = k_p + 100|k_l|$$

for positive values of k_p, or by

$$KB_3 = 250|k_l|$$

for negligible or negative values of k_p.

Table 7 Comparative metal loss and depth of affected metal for Fe–Ni–Co grades after six 1-week cycles (data from Haynes International)

Alloy	*T (°C)*							
	980		*1095*		*1150*		*1205*	
	Metal loss (mm)	Affected metal (mm)	Metal loss (mm)	Affected metal (mm)	Metal loss (mm)	Affected metal (mm)	Metal loss (mm)	Affected metal (mm)
Iron base alloys								
253MA	0.033	0.074	0.018	0.210	0.210	0.41	0.465	0.73
310	0.009	0.029	0.023	0.033	0.075	0.113	0.2	0.26
316	0.315	0.365	>1.75	>1.74	>2.7	>2.67	>3.57	>3.57
330	0.010	0.109	0.02	0.170	0.041	0.221	0.096	–
446	0.035	0.060	0.335	0.370	>0.55	>0.551	>0.59	>0.592
556	0.010	0.027	0.027	0.065	0.237	0.296	>3.8	>3.8
800H	0.024	0.045	0.137	0.188	0.191	0.225	0.29	0.35
Multimet	0.100	0.033	0.226	0.295	>1.2	>1.2	>3.7	>1.7
RA 85H	0.013	0.210	0.074	0.660	0.092	>1.47	0.097	>1.47
Nickel base alloys								
214	0.002	0.005	0.002	0.003	0.004	0.008	0.005	0.018
230	0.006	0.018	0.011	0.032	0.058	0.087	0.11	0.201
263	0.018	0.145	0.089	0.361	0.18	0.409	>0.91	>0.91
600	0.008	0.023	0.027	0.041	0.044	0.073	0.13	0.213
601	0.013	0.033	0.031	0.066	0.061	0.135	0.11	0.191[a]
617	0.080	0.033	0.015	0.046	0.028	0.086	0.27	0.32
625	0.008	0.018	0.083	0.122	0.405	0.462	>1.2	>1.21
HR-120	0.008	0.094	0.030	0.190				
HR-160	0.015	0.147	0.042	0.257	0.068	0.325	0.102	0.605
R-41	0.018	0.122	0.086	0.295	0.210	0.442	>0.73	>0.73
S	0.005	0.012	0.011	0.033	0.026	0.042	>0.81	>0.81
Waspaloy	0.015	0.079	0.036	0.137	0.079	0.231	>0.4	>0.4
X	0.009	0.024	0.038	0.069	0.114	0.148	>0.9	>0.89
Cobalt base alloys								
25	0.010	0.018	0.234	0.259	0.430	0.490	>0.96	>0.96
188	0.005	0.015	0.010	0.033	0.184	0.204	>0.55	>0.55

[a]Porosity formation in the metallic substrate.

In addition to KB_3, the post-test appearance of samples was ranked from 1 to 5:

rank 1: excellent,
rank 2: good,
rank 3: fair,
rank 4: poor,
rank 5: catastrophic

and the global rating parameter (KB_4) was defined by

$$KB_4 = KB_3[1 + 0.1(\text{rank} - 1)]$$

Using this global parameter, the behavior of alloys in long term thermal cycling situations was ranked according to the following rule:

- $KB_4 > 0.2$: excellent
- $0.2 < KB_4 < 0.5$: good
- $0.5 < KB_4 < 1$: fair
- $1 < KB_4 < 5$: poor
- $KB_4 > 5$: catastrophic.

The results for Fe-, Ni-, and Co-chromium containing alloys appear in **Figures 14–16** respectively.

None of the iron-base alloys were 'excellent,' with only four in the 'good' range. A minimum of 20% Cr seemed necessary for this 'good' ranking. Nickel-base alloys behave better, with four grades in the 'excellent' family and nine in the 'good' one. It should be observed that Hasteloy-S, which behaved the best, contains the reactive element (La) that improves scale adhesion, but Chromel-A, having a quite similar KB_4, does not. In fact, this test exhibiting very long isothermal periods and only a few thermal cycles was probably not discriminating in terms of scale spallation. Cobalt-base alloys presented the best behavior, with five alloys out of

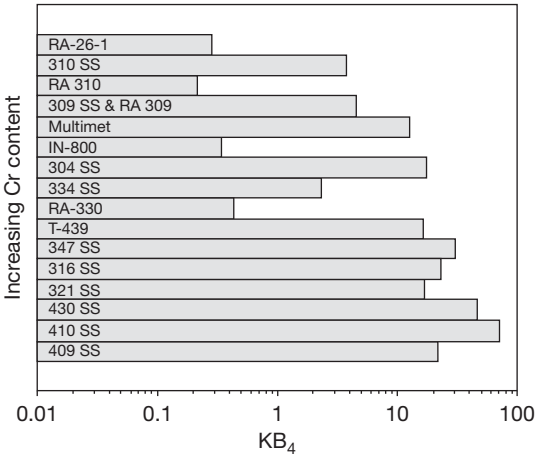

Figure 14 KB_4 parameter for various iron-base chromia-forming alloys.

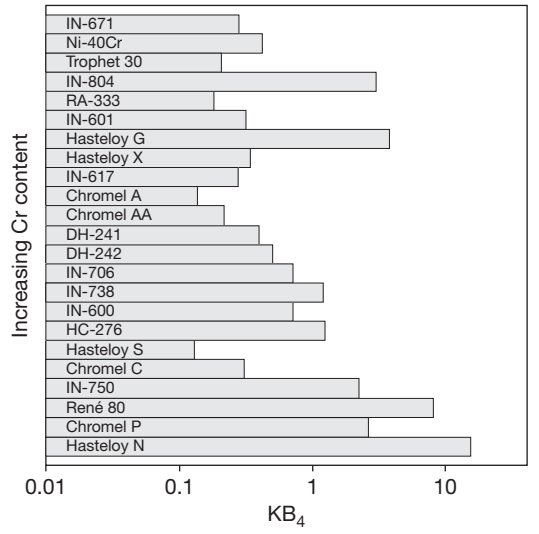

Figure 15 KB_4 parameter for various nickel-base chromia-forming alloys.

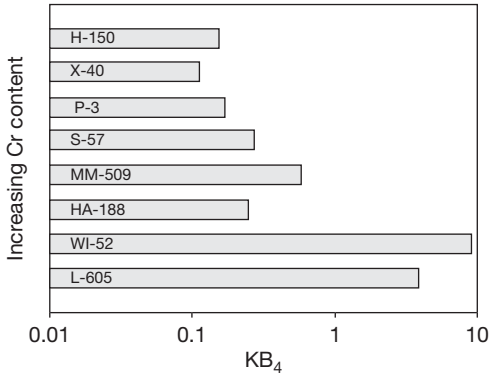

Figure 16 KB_4 parameter for several cobalt-base chromia-forming alloys.

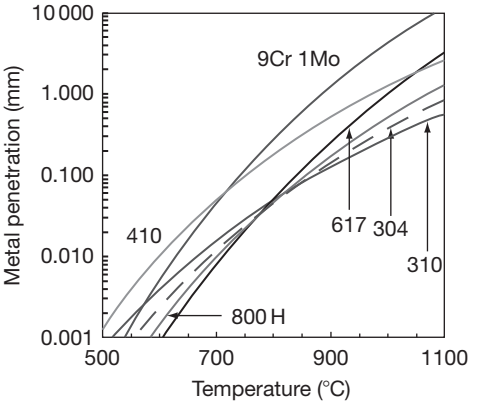

Figure 17 Comparative metal penetration (metal loss + internal oxidation) of various alloys after 1 year oxidation in air as proposed by the ASSET system. Reproduced from John, R. C.; Pelton, A. D.; Thomson, W. T.; Young, A. L.; Wright, I. G. *High Temperature Corrosion Materials Chemistry III.* Electrochemical Society Meeting, March 25–30, 2001, Washington, DC, USA.

eight tested ranking 'good' to 'excellent.' They all have high chromium content (25–28%). MAR-M-509 alloy, with 23.5% Cr has a 'fair' behavior probably due to 7% W and both alloys with lower chromium and higher W (WI-52 and L-605, 21Cr–11W and 20Cr–15W respectively) behaved 'catastrophic' and 'poor.'

It has to be reminded that the proposed test was performed at 982 °C, a temperature where chromia volatilization was not detrimental. The observation of the complete set of results also showed that alumina-forming alloys behaved much better than chromia-forming alloys, with 10 grades showing $KB_4 < 0.1$.

Another attempt to present comparative sets of results was initiated by SHELL under the name 'ASSET' (Alloy Selection System for Elevated Temperatures), in collaboration with several industrial and academic organizations in five countries.[28] This information system proposes a compilation of high temperature corrosion data, from literature and from specific testing, arranged so that engineering decisions can be made on lifetime, maximum temperature and influence of gas composition. In Figure 17 is presented the oxidation behavior of six common alloys exposed to air for 1 year. It is remarkable that, except the two ferritics (9Cr, 1Mo, and 410), all alloys behave similarly at 800 °C. Major differences are found at the lower and higher test temperatures,

with the worst alloys at 500 °C behaving the best at 1100 °C.

Attention has to be paid to transposition of oxidation data from laboratory tests to industrial practice. Alloys exposed in service to combustion atmospheres are better tested in burner rigs, a procedure really aggressive due to high rates of gas flow and possible particle impact. Figure 18 shows comparative data from burner and furnace testing for various Fe-, Ni-, and Co-base alloys. It is clear that burner oxidation is more severe than still air by a factor extending from 3–5 for the best alloys to 15–40 for the worst ones. However, the general ranking of alloys established by furnace testing is not strongly modified.

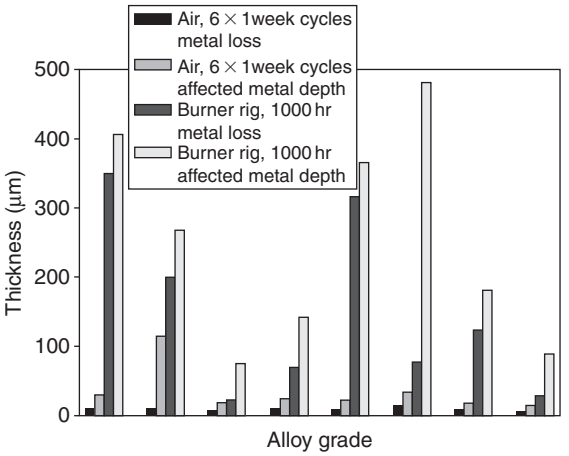

Figure 18 Metal loss and average metal penetration for various alloys exposed to still air oxidation (980 °C, six 1-week cycles, conditions of Table 7) and burner test rig at 980 °C for 1000 h. Data from Haynes International.

1.23.4 Concluding Remarks

The number of technical chromia-forming alloys proposed on the market is very large (see Appendices 1–6) and the choice of the right material is generally very difficult. The first step to a right choice is the careful observation of the service conditions which will be supported by the alloy, with clear definition of the possible accidental situations. To select the best grade, laboratory tests have to be performed at a temperature and in an atmosphere as close as possible to the real ones, taking into account possible thermal cycling. Comparison with specimens exposed to the real industrial situations may validate the laboratory tests.

Attention has also to be paid to the desired shape, as all alloys are not available in all shapes, and sometimes, the shape influences the corrosion resistance.

The cost of the material is also an important parameter, and the technical engineers must always decide whether they want to use an expensive alloy which will function for a long time or a cheaper one which will have to be replaced after limited service.

A last criterion to have in mind is the availability of the chosen grade, which must be rapidly delivered and possibly by several suppliers to avoid a monopoly situation.

Appendix 1 Denomination and composition of refractory ferritic stainless steels

Alloy	*EN*	*UNS*	*Fe*	*Cr*	*Mo*	*Si*	*C*	*Ti*	*Others*
409	1.4512	S40900	Bal	10.5–12.5					
430	1.4016	S43000	Bal	16–18	1	<1	<0.08	6(C+N)<Ti <0.65	
430Ti	1.4510	S43036	Bal	16–18	1	<1	<0.05	4(C+N) + 0.15–0.8	
436	1.4526	S43600	Bal	16–18	0.8–1.4	<1	<0.08		7(C+N) + 0.1–1 Nb
439	1.4510	S43035	Bal	17.5		0.35	0.02	0.4	
441	1.4509	S44100	Bal	17.5–18.5		<1	<0.03	0.1–0.6	3 C+0.3–1 Nb
442		S44200	Bal	18–23	1	1	0.2		
444	1.4521	S44400	Bal	17–20	1.8–2.5	<1	<0.025	4(C+N) + 0.15–0.8	0.45 (Ti+Nb)
446	1.4763	S44600	Bal	23–26	1.5	<1	<0.1		
CROFER 22APU	1.4760	S44535	Bal	20–24		<0.5	<0.03	0.03–0.2	0.04–0.2 La
ZMG232			Bal	22		0.4	0.02		0.04 La, 0.02 Zr
12SR				12		0.6	0.02	0.3	1.2 Al 0.6 Nb
18SR	1.4736		Bal	18		1	0.02	0.4	2 Al
R2012		S482800	Bal	20		2			

Appendix 2 Denomination and composition of refractory austenitic stainless steels

Alloy	*EN*	*UNS*	*Fe*	*Ni*	*Cr*	*Mo*	*Si*	*C*	*Others*
302B/309	1.4828	S30900	Bal	8–10	19–21		1.5–2.5	<0.2	
308		S30800	Bal	10–12	19–21		1	0.08	
347	1.4550	S34700	Bal	9–13	17–19			<0.08	10 C<Nb+Ta<1
310/314	1.4841	S31400/S31000	Bal	19–22	24–26		1.5–2.5	<0.2	
25–20	1.4843			19–21	23–25		1.5–2.5	<0.1	<0.1 RE 0.3 Al
31	1.4562	N08031	Bal	30–32	26–28	6–7	<0.3	<0.015	1–1.4 Cu 0.15–0.25 N
33	1.4591	R20033	Bal	30–33	31–35	0.5–2	<0.5	<0.015	0.3–1.2 Cu 0.35–0.6 N
153MA	1.4818	S30415	Bal	9–11	18–20		1–2	0.04–0.08	0.03–0.08 Ce 0.12–0.2 N
204Cu		S20430	Bal	1.5–3	16–18	<1	<1	<0.15	0.05–0.25 N 2–4 Cu; 6.5–9 Mn
253MA	1.4835	S30815	Bal	10–12	20–22		1.4–2.5	0.05–0.12	0.03–0.08 Ce 0.12–0.2 N
304	1.4301	S30400	Bal	8–11	18–20		0.75	0.08	
309S	1.4833	S30908	Bal	12–14	22–24		<1	<0.15	
310S	1.4845	S31008	Bal	19–22	24–26		<1.5	<0.1	
316	1.4401	S31600	Bal	10–14	16–18	2–3	0.75	<0.08	
321	1.4878	S32100	Bal	9–12	17–19		<1	<0.1	0.5×(C–0.8)Ti
353MA	1.4854	S35315	Bal	34–36	24–26		1.2–2	0.04–0.08	0.053–0.08 Ce 0.12–0.2 N; 1.5 Mn
RA85H		S30615	Bal	14.5	18.5		3.5	0.2	1 Al

Appendix 3 Denomination and composition of wrought refractory Fe–Ni–Cr alloys (balance: Fe)

Alloy	*EN*	*UNS*	*Ni*	*Co*	*Cr*	*Al*	*Mo*	*Si*	*C*	*Ti*	*Others*
	1.4872		6–8		24–26			<1	0.2–0.3		0.2–0.4 N; 8–10 Mn
	1.4877		31–33		26–28			<0.3	0.04–0.08		0.05–0.1 Ce; 0.6–1 Nb
	1.4887		33–37		20–23			1–2	<0.15		1–1.5 Nb; <0.11 N
30–20	1.4860		30–31		19.5–21.5	<0.3		1.8–3	<0.1		<0.1 RE
330	1.4886	N08330	33–37		17–20			1–2	<0.15		1.5 Mn; <0.11 N
556	1.4971 1.4833	R30556	20	18	22	0.2	3	0.4	0.1		2.5 W; 0.02 La; 0.6 Ta
800	1.4958	N08800	30–35		19–23	0.15–0.6		<1	<0.1	0.15–0.6	0.3–1.2 Ti+Al; 0.8 Mn
800H	1.4876	N08810	30–35		19–23	0.15–0.6		<1	0.05–0.1	0.15–0.6	0.3–1.2 Ti+Al; 0.9 Mn
800HT	1.4876	N08811	30–35		19–23	0.25–0.6		<1	0.06–0.1	0.25–0.6	0.85–1.2 Ti+Al; 0.9 Mn
803		S35045	32–37		25–29	0.15–0.6		<1	0.06–0.1	0.15–0.6	0.9 Mn
864		S35135	30–38		20–25	0.3	4–4.8	0.8	<0.08	0.6	0.4 Mn
903		N19903	38	15		0.7				1.4	3 Nb
907		N19907	38.4	13		0.03		0.15		1.5	4.7 Nb
A-286	1.4980	S66286	24–27		13.5–16	<0.35	1–1.5	<1	<0.08	1.9–2.35	<0.01 B; 1.3 Mn; 0.1–0.5 V
DS	1.4864	N08332	34.5–41		17–19			1.9–2.6	0.1	0.2	0.8–1.5 Mn; 0.5 Cu
Multimet		R30155	20	20	21		3	1	0.08		2.5 W; 1Nb+Ta
Nitronic 50		S20910	12.5		22		2.25				5 Mn; 0.3 N; 0.2 Nb; 0.2 V
Nitronic 60		S21800	8.5		17			4			8 Mn; 0.15 N

Appendix 4 Denominations and composition of wrought refractory Ni–(Fe)–Cr alloys (balance: Ni)

Alloy	*EN*	*UNS*	*Fe*	*Co*	*Cr*	*Al*	*Mo*	*Si*	*C*	*Ti*	*Others*
Waspaloy	2.4654	N07001	<2	12–15	18–21	1.2–1.6		<0.75	0.02–0.1	2.75–3.25	Zr, B
X	2.4665	N06002	17–20	0.5–2.5	20.5–23.5	<0.25		<1	0.05–0.15		0.2–1 W
S		N06635	2		15.5	0.3		0.4	0.02		0.2 Mn; 0.05 La; 0.01 B; 0.8 W
Chromel A			0.5		20			1.4	0.03		0.2 Mn
Chromel AA			10		20			2	0.03		0.2 Mn
Chromel C			24		15			1.4	0.06		0.2 Mn
Chromel P			0.2		10			0.4	0.01		
G		N06007	20		22			0.4	0.03		1 Nb; 1 Ta; 1.3 Mn; 2 Cu; 0.5 W
N		N10003	<5		7			1	0.06		0.3 Cu
N4				7.5	9.8	4.2			0.06	3.5	0.5 Nb; 5 Ta; 0.15 Hf; 6 W
N6				12.5	4.2	5.75					5.4 RE; 7.2 Ta; 0.15 Hf; 6 W
Astroloy				17	15	4			0.06	3.5	0.03 B
X-750	2.4669	N07750	5–9		14–17	0.4–1		<0.5	<0.08	2.25–2.75	1(Nb+Ta); 0.5 Mn
HR-160	2.4880	N12160	2	30	2828			2.8	0.05	0.5	0.5 Mn
HR-120	2.4854	N08120	35		25	0.1		0.6	0.05	0.1	0.7 Nb; 0.7 Mn; 0.004 B
R-95				8	14	3.5			0.15	2.5	0.01 B; 0.05 Zr; 3.5 Nb; 3.5 W
R-41	2.4973	N07041	5	10	18	1.5		0.5	0.09	3.1	0.005 B
G-30		N06030	15	5	29.5			0.4	0.03		2 Cu; 2.5 W
G-3	2.4619	N06985	18–21	<5	21–23.5			<1	<0.015		<0.5(Nb+Ta); 2 Cu; <1.5 W
70–30	2.4658	N06003	<1		29–31	<0.2		1–1.5	<0.07		0.01–0.04 RE
45-TM	2.4889	N06045	21–25		26–29			2.5–3	0.05–0.12		0.03 Zr; Ce
59	2.4605	N06059	<1.5		22–24	0.1–0.4		<0.1	<0.01		
60–16	2.4867	N06004	Bal		14–17	<0.3		1–1.75	<0.1		<0.04 RE
80–20	2.4869	N06003	<1		19–21	<0.2		1–1.5	<0.08		0.01–0.04 RE
Nimonic 75	2.4951	N06075	<5		18–21			<1	0.08–0.15	0.2–0.6	0.3 Mn
Nimonic 80A	2.4952	N07080	<3	<2	18–21	1–1.8		<1	<0.1	1.8–2.7	0.3 Mn; 0.06 Zr; 0.003 B
Nimonic 90	2.4632	N07090	<1.5	15–21	18–21	1.2		<1	<0.13	2–3	0.3 Mn; 0.06 Zr; 0.003 B

Nimonic 105	2.4634		<1	18–22	14–15.7	4.5–9	4.5–5.5	<1	<0.12	0.9–1.5	0.3 Mn; 0.1 Zr; 0.005 B
Nimonic 115	2.4636		<1	13–15.5	14–16	4.5–5.5	3–5	<1	0.12–0.2	3.5–4.5	0.016 B; 0.04 Zr
214	2.4646	N07214	3.5		16	4.5			0.04		0.05 Y; 0.03 Zr
230	2.4633	N06230	<3		22	0.3	2	0.4	0.1		14 W; 0.02 La; 0.5 Mn; 0.004 B
242					8		25		0.03		14 W
Nimonic 263	2.4650	N07263	<0.7	19–21	19–21	<0.6	5.6–6.1	<0.4	0.04–0.08	1.9–2.4	0.4 Mn; 0.02 Zr; 0.001 B
333	2.4608	N06333	18	3	25		3	1.25	0.05		3 W
Udimet 400				14	17.5	1.5	4		0.06	2.5	0.5 Nb; 0.06 Zr; 0.008 B
Monel 400	2.4360	N04400	<2.5		0.1	0.02		<0.5	<0.3	0.4	28–34 Cu; 0.8 Mn
Udimet 500				18.5	18	2.9	4		0.08	2.9	0.05 Zr; 0.006 B
Udimet 520				12	19	2	6		0.05	3	1 W; 0.005 B
600	2.4816	N06600	6–10		14–17	<0.3		<0.5	<0.08	0.2–0.6	<1 Mn
601	2.4851	N06601	Bal		21–25	1–17		<0.5	<0.1	0.4	0.5 Mn
602CA	2.4633	N06025	8–11		24–26	1.8–2.4		<0.5	0.15–0.25	0.1–0.2	0.1 Zr; 0.001–0.1 Y
617	2.4663	N06617	<2	10–13	20–23	0.5–1.5	8–10	<0.7	0.05–0.1	0.2–0.6	
625	2.4856	N06625	<5	<1	20–23	<0.4	8–10	<0.5	<0.1	<0.4	3.5–4.15(Nb+Ta)
625LCF		N06626	<5	<1	20–23	<0.4	8–10	<0.15	<0.03	<0.4	3.5–4.15(Nb+Ta); <0.02 N
Udimet 630			18		18	0.5	3		0.03	1	6.5 Nb; 3 W
671					46	0.3			0.05	0.3	
686	2.4606	N06686	<5		19–23		15–17	<0.08	<0.01	0.02–0.25	3–4.4 W
690	2.4642	N06690	7–11		27–31			<0.5	<0.05		
693		N06693	2.5–6		27–31	2.5–4		<0.5	<0.15	<1	0.5–2.5 Nb
Udimet 700				17	15	4.3	5		0.06	3.5	0.08 Zr; 0.03 B
702		N09702	0.5		15.4	3.1			0.04	0.4	
706		N09706	39–44		14.5–17.5	<0.4		<0.35	<0.06	1.5–2	2.5–3.3(Nb+Ta)
Udimet 710				15	18	2.5	3		0.07	5	1.5 W; 0.02 B
718	2.4668	N07718	20–24	<1	17–21	0.2–0.8	2.8–3.3	<0.35	<0.08	0.65–1.15	4.75–5.5(Nb+Ta)
Udimet 720				15	16	2.5	3		0.03	5	1.3 W; 0.033 B; 0.03 Zr
751		N07751	5–9		14–17	0.9–1.5		<0.5	0.04	2–2.6	0.5 Mn; 0.7–1.2(Nb+Ta)
825	2.4858	N08825	<22		19.5–23.5	<0.2	2.5–3.5	<0.5	<0.05	0.6–1.2	1.5–3 Cu; 0.4 Mn

Appendix 5 Denomination and composition of wrought refractory Co–Cr alloys (balance: Co)

Alloy	*EN*	*UNS*	*Fe*	*Ni*	*Co*	*Cr*	*Al*	*Mo*	*Si*	*C*	*Ti*	*Others*
25/L605	2.4964	R30605	<0.3	9–11	Bal	19–21			<0.3	0.05–0.15		14–16 W; 1–2 Mn
Belgian S-57					Bal	25	3					5 Ta; 0.5 Y
Belgian P-3			29.5	12	Bal	25				0.05		
6B			3	3	Bal	30		<1.5	2	1.2		4.5 W; 2 Mn
150			20	1	Bal	28			0.7	0.08		0.6 Mn; 0.02 P; 0.002 S
188	2.4683	R30188	<0.3	20–24	Bal	20–24			0.2–0.4	<0.15		13–16 W; <0.12 La; 0.004 B
MAR-M-918				20	Bal	20				0.05		7.5 Ta; 0.1 Zr
1233		R31231	3		Bal	26		5				2 W
S-816		R30816	4		Bal	20		4				4 Nb; 4 W
MP-35N		R30035			Bal	20		10				
Ultimet		R31233	3	9	Bal	25		5	0.3	0.06		2 W; 0.6 Mn

Appendix 6 Denomination and composition of cast refractory Fe-, Ni-, and Co-base alloys

EN	*UNS*	*Alloy*	*Fe*	*Ni*	*Co*	*Cr*	*Al*	*Mo*	*Si*	*C*	*Others*
Iron-base											
1.4729			Bal			12–14			1–2.5	0.3–0.5	
1.4740			Bal			16–19			1–2.5	0.3–0.5	
1.4745			Bal			23–26			1–2.5	0.3–0.5	
1.4777			Bal			27–30			1–2.5	1.2–1.5	0.5–1 Mn
1.4743			Bal			17–19			1–2.5	1.4–1.8	
		HA	Bal			8–10		0.9–1.2	<1	<0.2	
1.4776	J92605	HC	Bal	<4		27–30			1–2.5	0.3–0.5	
1.4823	J93005	HD	Bal	3–6		25–28			1–2.5	0.3–0.5	
	J93403	HE	Bal	8–11		26–30			0.5–2	0.2–0.5	
1.4825	J92603	HF	Bal	8–10		17–19			0.5–2	0.15–0.35	
1.4826			Bal	9–11		21–23			1–2.5	0.3–0.5	
1.4832			Bal	13–15		19–21			0.5–2.5	0.15–0.35	
1.4855			Bal	23–25		23–25			1–2.5	0.3–0.5	0.8–1.8 Nb
1.4837	J93503	HH	Bal	11–14		24–27			1–2	0.3–0.5	
	J93503	HH1	Bal	12		26			1–2	0.4	0.5 Mn
	J94003	HI	Bal	14–18		26–30			0.5–2	0.2–0.5	
1.4848	J94224	HK	Bal	19–22		24–27			1–2.5	0.4–0.5	
	J94204	HK40	Bal	20		26			1.4	0.4	0.6 Mn
	J94604	HL	Bal	18–22		28–32			0.5–2	0.2–0.6	
	J94213	HN	Bal	23–27		19–23			1–2	0.2–0.5	
1.4852	J95705	HP	Bal	33–36		24–27			1–2.5	0.3–0.5	0.8–1.8 Nb
	J94605	HT	Bal	33–37		13–17			1.7	0.35–0.75	0.9 Mn
1.4865			Bal	36–39		18–21			1–2.5	0.3–0.5	
	N08004	HU	Bal	37–41		17–21			1–2.5	0.35–0.75	
1.4849			Bal	36–39		18–21			1–2.5	0.3–0.5	1.2–1.8 Nb
1.4859			Bal	31–33		19–21			0.5–1.5	0.05–0.15	0.5–1.5 Nb
1.4857			Bal	33–36		24–27			1–2.5	0.3–0.5	1.2–1.8 Nb
		GX40NiCrCo 20–20–20	Bal	18–22	18.5–22	19–22			<1	0.35–0.65	2–3 W; 0.75–1.25 Nb
Nickel-base											
			13–23-	Bal	14–16	24–26			1–2	0.45–0.55	4–6 W
			11–21	Bal		32.5–37.5			1.5–2	0.35–0.45	
	N08001	HW	12–28	Bal		12–18			1–2.5	0.35–0.65	1–1.5 Mn; 1.5–2 Nb
	N08006	HX	10–20	Bal		15–19			1–2.5	0.35–0.75	
		NA22H	24.4	Bal		25				0.55	
		GX40CrNiSiNb35–17	38–50	Bal		17–20			1–2.5	0.3–0.5	0.8–1.8 Nb
		GX40CrNiSi 35–17	40–45	Bal		16–18			1–2.5	0.3–0.5	0.8–1.8 Nb
1.4865		GX40CrNiSi 38–19	37–45	Bal		18–21			1–2.5	0.3–0.5	

Continued

Appendix 6 Continued

EN	*UNS*	*Alloy*	*Fe*	*Ni*	*Co*	*Cr*	*Al*	*Mo*	*Si*	*C*	*Others*
		GX40NiCrCoW35–25–15	22–33	Bal	14–16	24–26			1–2	0.45–0.55	4–6 W
		GX40NiCrNb 45–35	10–20	Bal		32.5–37.5			1.5–2	0.35–0.45	1–1.5 Mn 1.5–2 Nb
		B-1900		Bal	10	8	6	6		0.1	4.3 Ta; 1 Ti; 0.1 Nb; 0.08 Zr; 0.15 B
		1N-100		Bal	15	10	5.5	3		0.18	5.5 Ti; 1 V; 0.05 Zr; 0.015 B
		IN-713 LC		Bal		12	6	4.5		0.05	2 Nb; 0.6 Ti; 0.1 Zr; 0.01 B
		IN-738		Bal	8.5	16	3.4	1.7		0.17	3.4 Ti; 1.7 Ta; 0.9 Nb; 0.1 Zr; 0.01 B
		MAR-M-200		Bal	10	9	5			0.15	2 Ti; 1 Nb; 0.05 Zr; 0.015 B
		Rene´ 120		Bal	10	9	4.3	2			4 Ta; 4 Ti; 0.07 Zr; 0.015 B
		Rene´ 80		Bal	9.5	14	3	4		0.17	5 Ti; 0.03 Zr; 0.015 B
		TAZ-8A		Bal		6	6	4		0.13	8 Ta; 2.5 Nb; 1 Zr; 0.004 B
		TRW-VIA		Bal	7.5	6	5.4	2		0.13	9 Ta; 1 Ti; 0.5 Nb; 0.4 Hf; 0.13 Zr; 0.02 B
		WAZ-20		Bal			6.5			0.15	0.15 Zr
	N07765	IN-657		Bal		50				0.03	1.5 Mn
Cobalt-base											
		X-40		10.5	Bal	26				0.5	
		WI-52			Bal	21				0.45	2 Nb
		MAR-M-509		10	Bal	24				0.6	3.5 Ta; 0.5 Zr; 0.2 Ti

References

1. Hatfield, W. H. *J. Iron Steel Inst.* **1927**, *115*, 517.
2. Hatfield, W. H. *J. Inst. Fuel* **1938**, *11*, 245.
3. Massalski, T. B. *Binary Alloys Phase Diagrams;* ASM International: Materials Park, OH, USA, 1990.
4. Antoni, L. *Mater. Sci. Forum* **2001**, *369–373*, 345–352.
5. Gleeson, B. In *Corrosion and Environmental Degradation*; Schütze, M., Ed.; Wiley-VCH: Weinheim, Germany, 2000; Vol. 2, pp 173–228.
6. Kofstad, P. *High Temperature Corrosion;* Elsevier, 1988.
7. Bamba, G.; Wouters, Y.; Galerie, A.; Borchardt, G.; Shimada, S.; Heintz, O.; Chevalier, S. *Scripta Mater.* **2007**, *57*(8), 671–674.
8. Evans, H. E. *Int. Mater. Rev.* **1995**, *40*(1), 1–40.
9. Schütze, M. In Series on Corrosion and Protection; Holmes, D. R., Ed.; John Wiley: Chichester, UK, 1997; Vol. 1.
10. Galerie, A.; Dupeux, M.; Wouters, Y.; Toscan, F. *Mater. Sci. Forum* **2006**, *522–523*, 441–450.
11. European Patent 1,325,166 B1, 2006.
12. Holcomb, G. R.; Alman, D. E. *Scripta Mater.* **2006**, *54*(10), 1821–1825.
13. Stanilowski, M.; Wessel, E.; Hilpert, K.; Markus, T.; Singheiser, L. J. *Electrochem. Soc.* **2007**, *154*(4), A295–A306.
14. Essuman, E.; Meier, G. H.; Zurek, J.; Haensel, M.; Norby, T.; Singheiser, L.; Quadakkers, W. J. *Corros. Sci.* **2008**, *50*(6), 1753–1760.
15. Halvarsson, M.; Tang, J. E.; Asteman, H.; Svensson, J. E.; Johansson, L. G. *Corros. Sci.* **2006**, *48*, 2014–2035.
16. Toscan, F.; Antoni, L.; Wouters, Y.; Dupeux, M.; Galerie, A. *Mater. Sci. Forum* **2004**, *461–464*, 705–712.
17. Belogolowsky, I.; Hou, P. Y.; Jacobson, C. P.; Visco, S. J. *J. Power Sources* **2008**, *182*, 259–264.
18. Gabrel, J.; Coussement, C.; Verest, L.; Blum, R.; Chen, Q.; Testani, C. *Mater. Sci. Forum* **2001**, *369–372*, 931–938.
19. Evans, H. E.; Donaldson, A. T.; Gilmour, T. C. *Oxid. Met.* **1999**, *52*(5/6), 379–402.
20. Antoni, L.; Baroux, B. *La Revue de Métallurgie-CIT/ Science et Génie des Matériaux* **2002**, 177–188.
21. Barin, I. *Thermochemical Data of Pure Substances;* VCH: Weinheim, Germany, 1989.
22. Opila, E. J.; Myers, D. L.; Jacobson, N. S.; Nielsen, I. M. B.; Olminsky, J. K.; Allendorf, M. D. *J. Phys. Chem.* **2007**, *111*, 1971–1980.
23. Jung, I. H. *Solid State Ionics* **2006**, *177*, 765–777.
24. Sourmail, T. *Mater. Sci. Technol.* **2001**, *17*, 1–12.
25. Santacreu, P. O. *ArcelorMittal Stainless Europe;* personal communication, 2007.
26. Lai, G. A. *High Temperature Corrosion of Engineering Alloys;* ASM International: Metals Park, OH, 1990.
27. Barrett, C. A. 10 000 hour cyclic oxidation behavior at 982 °C (1800 °F) of 68 Co-, Fe- and Ni-base alloys; NASA Technical Memorandum 107394, 1997.
28. John, R. C.; Pelton, A. D.; Thomson, W. T.; Young, A. L.; Wright, I. G. *High Temperature Corrosion Materials Chemistry III.* Electrochemical Society Meeting, March 25–30, 2001, Washington, DC, USA.

1.25 High Temperature Corrosion of Intermetallic Alloys

J. W. Fergus
Materials Research and Education Center, 275 Wilmore Laboratories, Auburn University, Auburn, AL 36849, USA

Glossary

B2 Crystal structure formed by NiAl and FeAl (see Figure 1(a)).

Corundum Crystal structure formed by α-Al_2O_3.

$D0_3$ Crystal structure formed by Fe_3Al (see Figure 1(d)).

$D0_{19}$ Crystal structure formed by Ti_3Al (see Figure 1(e)).

Hot corrosion Corrosion in a high temperature environment where molten salts are present.

Kirkendall effect Vacancy formation in a diffusion couple because of differences in the interdiffusion coefficients of the two atoms.

Laves phase Intermetallic crystal structure.

$L1_0$ Crystal structure formed by TiAl (see Figure 1(b)).

$L1_2$ Crystal structure formed by Ni_3Al (see Figure 1(c)).

Pack cementation Chemical vapor deposition process performed in a packed bed.

Rutile Crystal structure formed by TiO_2.
Spinel Crystal structure formed by $NiAl_2O_4$ and other mixed oxides.
X-phase Mixed titanium–aluminum oxide phase.
Z-phase Mixed titanium–aluminum oxide phase.

Abbreviations

CVD Chemical vapor deposition
NCP New cubic phase (formed in Ti–Al–O system)
TBC Thermal barrier coating
TCP Topographically close packed (phases)
TGO Thermally grown oxide

1.25.1 Introduction

Metal alloys, such as those discussed in the chapter on **High Temperature Corrosion of Alumina-forming Iron, Nickel and Cobalt-base Alloys** can be strengthened by the formation of intermetallic compounds, but alloys consisting entirely of intermetallic compounds are stronger. These intermetallic compounds typically have higher melting temperatures compared with their constituent metals, and are thus attractive materials for high temperature applications. The most widely used intermetallic compounds for high temperature applications are aluminides, because of their low densities and their ability, or at least potential, to form a protective alumina scale. Silicides are also used for some high temperature applications, but their oxidation behavior is similar to that of nonoxide ceramics, such as silicon carbide and silicon nitride, so they are discussed in the chapter on **High Temperature Corrosion of Ceramics and Refractory Materials**. Thus, the focus of this chapter is on the high temperature corrosion behavior of aluminide intermetallic alloys.

1.25.1.1 General Uses of Intermetallic Alloys

The low density of intermetallic aluminides is primarily due to their high aluminum content, which also promotes the formation of an aluminum scale for good high temperature corrosion resistance. Intermetallic compounds also have good high temperature strength and creep resistance, but the mechanical properties at low temperatures (including ambient room temperature) are inferior to those of metal alloys. In particular, intermetallic compounds tend to have low ductility because of the difficulty of slip in their ordered structures, which leads to low fracture toughness and creates challenges in the fabrication of intermetallic alloys and their implementation in engineering structures. The synthesis of intermetallic alloys is complicated because of the larger differences in melting temperature among the constituent elements, which limits the available fabrication processes. In addition, the properties of intermetallic alloys depend strongly on small changes in composition, so compositional control during synthesis and processing is particularly important.

Despite these significant engineering challenges, the attractive high temperature properties of intermetallic alloys have led to their use in a variety of high temperature applications.[1–3] One of the most promising applications of intermetallic alloys is for components in aeroturbine engines, where increases in operating temperature and decreases in weight improve engine efficiency and performance. Although low density is particularly important in aerospace applications, intermetallic alloys have also been used in other applications, such as valves and turbocharger rotors in high-performance internal combustion engines for automotive applications.

1.25.1.2 Common Intermetallic Alloys

Many of the promising intermetallic aluminide alloys have been developed from the nickel- and iron-based high temperature alloys described in the chapter on **High Temperature Corrosion of Alumina-forming Iron, Nickel and Cobalt-base Alloys**. Intermetallic alloys have also been developed in the titanium–aluminum system. In all cases, the intermetallic compounds form ordered crystal structures, some examples of which are shown in Figure 1. Plastic deformation by dislocation movement in such ordered structures is more difficult than in disordered metallic structures, so these compounds have high strength and low ductility. Some of the characteristics of these widely used systems are described in the following sections.

1.25.1.2.1 Nickel aluminides

Alloys based on both NiAl and Ni_3Al have been developed. As shown in Figure 2, NiAl, which forms the cubic B2 structure (Figure 1(a)), has a much wider range of stoichiometry than Ni_3Al, which forms the cubic $L1_2$ structure (Figure 1(c)). Ni_3Al-based alloys exhibit an anomalous temperature dependence of flow stress, in which the strength

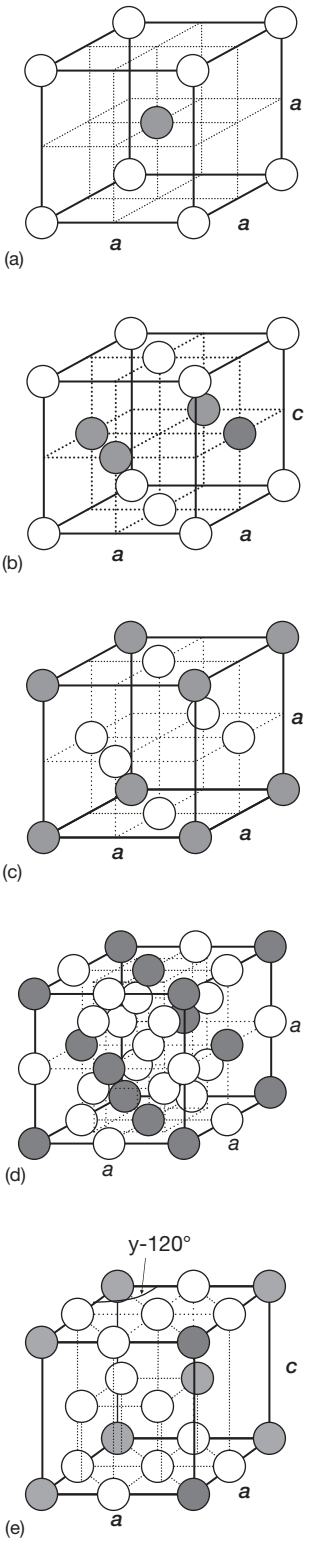

Figure 1 Crystal structures of selected intermetallic compounds in the Ni–Al, Fe–Al, and Ti–Al systems. (a) B2 (NiAl, FeAl), Pearson symbol *cP*2, structure type CsCl, space group $Pm\bar{3}m$. (b) $L1_0$ (TiAl), Pearson symbol *tP*4, structure type AuCu, space Group P_4/mmm. (c) $L1_2$ (Ni_3Al), Pearson symbol *cP*4, structure type Cu_3Al, space group $Pm\bar{3}m$. (d) $D0_3$ (Fe_3Al), Pearson symbol *cF*16, structure type BiF_3, space group $Fm\bar{3}m$. (e) $D0_{19}$ (Ti_3Al) Pearson symbol *hP*8, structure type Ni_3Sn, space group $P63/mmc$. Reproduced from Villars P., Calvert L.D. (Eds.), *Pearson's Handbook of Crystallographic Data for Intermetallic Phases*, 2nd ed., ASM International, Materials Park, OH, 1991, with permission from ASM International.

increases with increasing temperature up to about 700 °C and then decreases at higher temperatures. Polycrystalline Ni_3Al is difficult to fabricate because of its low deformability. Although their ductility can be improved with boron, Ni_3Al-based alloys have relatively large densities and do not offer significant advantages over nickel-based superalloys. NiAl-based alloys, however, have a higher aluminum content, which decreases density and also improves oxidation resistance. NiAl-based alloys have a higher melting temperature and better creep resistance compared to nickel-based superalloys. The strength can be improved with the addition of niobium or tantalum, which leads to the formation of Laves phases, and the ductility can be improved with alloying additions such as chromium, molybdenum, rhenium, and iron. However, the creep resistance of NiAl above 1000 °C is not good.

1.25.1.2.2 Iron aluminides

The iron–aluminum system is similar to the nickel–aluminum system, in that both Fe_3Al and FeAl compounds are formed. Like NiAl, FeAl forms the cubic B2 structure (**Figure 1(a)**), but Fe_3Al forms the $D0_3$ structure (**Figure 1(d)**). The tendency towards ordering in the iron–aluminum system is not as strong as that in the nickel–aluminum system, as indicated by the large disordered ferrite region shown in the phase diagram in **Figure 3**. As in the nickel–aluminum system, the strengths of Fe_3Al-based alloys increase with increasing temperature to about 500 °C and then decrease at higher temperatures. However, FeAl offers more advantages over superalloys than NiAl. In particular, the fracture toughness and specific properties of FeAl-based alloys are better than those of NiAl-based alloys, but ductility is low compared to metal alloys. The ductility can be improved with alloying additions such as zirconium. Another difference between the iron–aluminum and nickel–aluminum systems is that carbon is often used in the iron–aluminum system to improve strength through carbide strengthening.

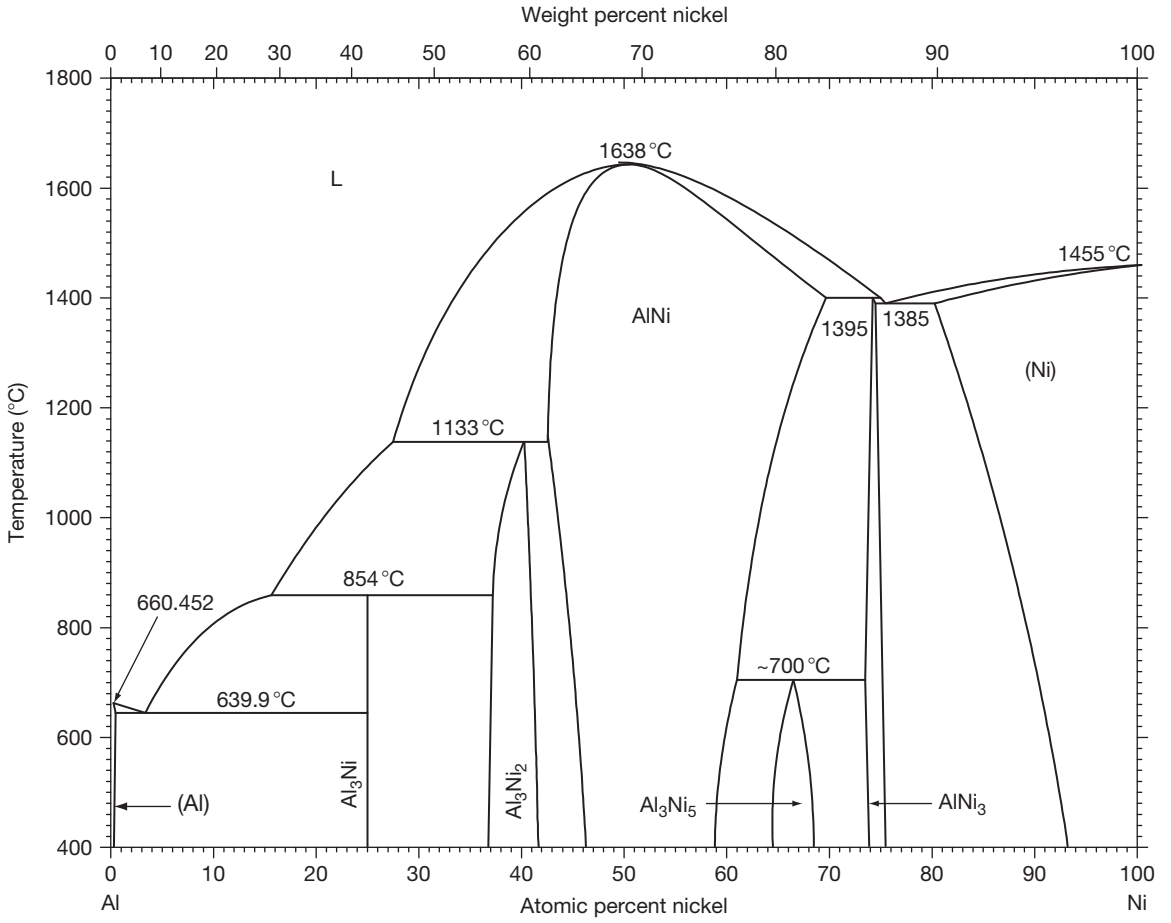

Figure 2 NiAl phase diagram. Reproduced from *Binary Alloy Phase Diagrams*, 2nd ed., ASM International, Materials Park OH, 1996, with permission from ASM International.

1.25.1.2.3 Titanium aluminides

Titanium aluminide alloys have the lowest densities among the three common aluminide systems and thus offer the best specific properties. The phase diagram in **Figure 4** shows that Ti_3Al and TiAl have similar ranges of stoichiometry. TiAl forms the tetragonal $L1_0$ structure (**Figure 1(b)**), while Ti_3Al forms the hexagonal $D0_{19}$ structure (**Figure 1(e)**). Both Ti_3Al- and TiAl-based alloys have been developed, but the best ductility is achieved with two-phase (Ti_3Al + TiAl) alloys. Production of the desirable two-phase microstructure requires careful control of both the chemical composition and the heat treatment process. The aluminum content in Ti_3Al is typically not sufficient for good oxidation resistance, so the most promising alloys consist entirely or mostly of the γ-phase (TiAl in the $L1_0$ structure). The mechanical properties can be improved by adding substitutional elements such as chromium, as well as interstitial elements such as carbon and boron. The high reactivity of titanium creates challenges in attaining corrosion resistance, as will be discussed later, as well as in reliable alloy production.

1.25.2 Oxidation

A major difference between titanium aluminides and the other two common aluminide systems (nickel and iron) is that titanium is much more active than either iron or nickel. This is illustrated in the Ellingham diagram shown in **Figure 5**. Titanium can change valence from Ti^{2+} to Ti^{4+}, so there are several titanium oxides, a few of which are included in **Figure 5**. The two important titanium oxides are TiO, which is in equilibrium with titanium metal, and TiO_2, which is stable in air. The free energy of TiO (per mole of oxygen) is about the same as that of Al_2O_3, indicating there is a strong competition between the formation of titanium and aluminum oxides on TiAl. In comparison,

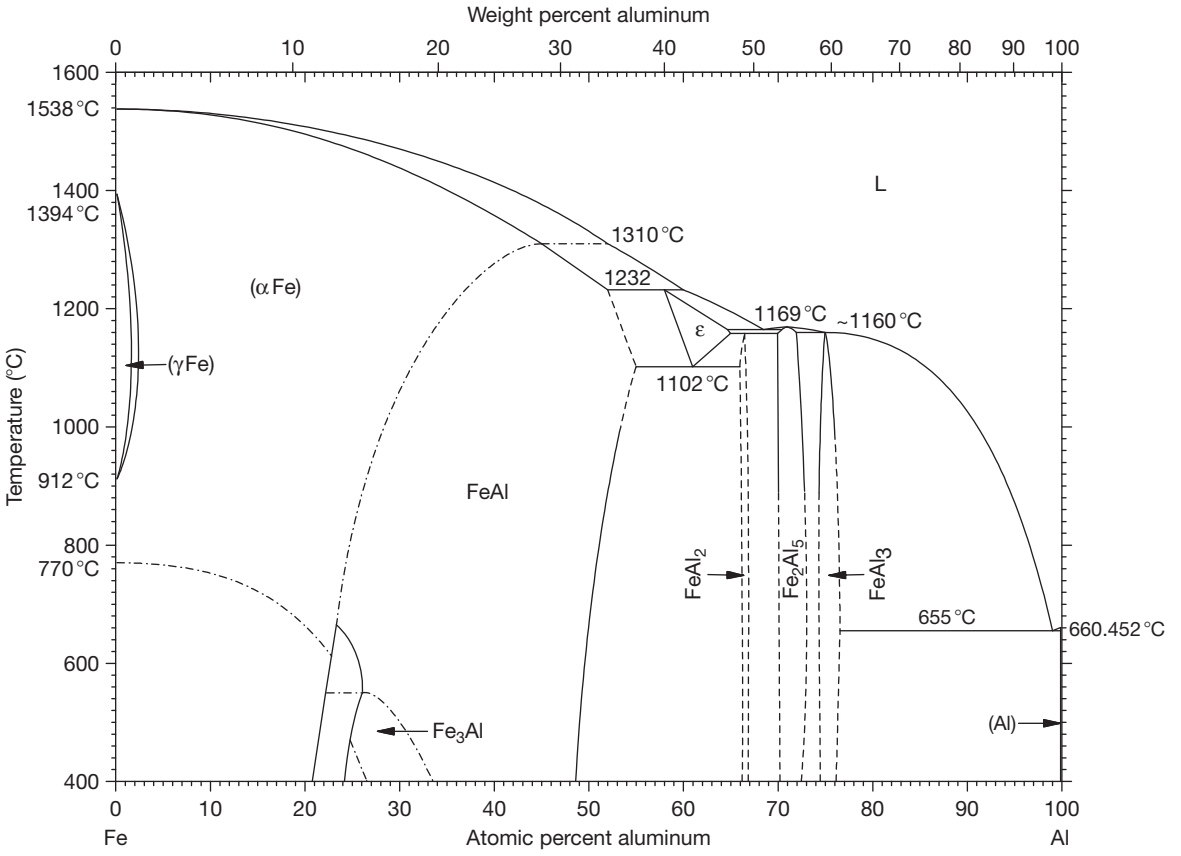

Figure 3 FeAl phase diagram. Reproduced from *Binary Alloy Phase Diagrams*, 2nd ed., ASM International, Materials Park OH, 1996, with permission from ASM International.

nickel and iron oxides are much less stable than Al_2O_3, so the amount of aluminum in the alloy required for the formation of an Al_2O_3 scale is much less in nickel and iron aluminides than in titanium aluminides. Because of this significant difference in oxide stabilities, nickel and iron aluminides have, in many ways, similar oxidation behavior and will be discussed together in the next section. This will be followed by a section on titanium aluminides, and then a section on some less commonly used aluminide alloys.

1.25.2.1 Nickel and Iron Aluminides

There are several general reviews of the oxidation of intermetallic alloys[4–6] as well as reviews that focus on either the nickel–aluminum[7,8] or iron–aluminum[9] system.

1.25.2.1.1 Scale properties/structure

As a result of the large differences in oxide stability (**Figure 5**), Ni_3Al, NiAl, Fe_3Al, and FeAl are in equilibrium with Al_2O_3, so Al_2O_3 is always present in the scale formed during oxidation. However, nickel and iron oxides can also exist in the scale, either as pure oxides (e.g., NiO, Fe_2O_3) or mixed oxides (e.g., $NiAl_2O_4$ spinel). In addition, with long-time exposure, the growth of an Al_2O_3 scale depletes the alloy of aluminum, so the amount of aluminum required to maintain a protective scale is higher than the minimum for thermodynamic stability or initial alumina formation. Pettit[10] characterized the oxidation behavior of nickel–aluminum alloys and found that Ni_3Al alloys form a scale with alumina and NiO or the $NiAl_2O_4$ spinel, whereas NiAl alloys form a protective alumina scale. Once the critical aluminum content for a protective alumina scale is reached, additional aluminum has little effect on the oxidation rate for short-term exposures. However, with longer exposures, the aluminum content of the alloy beneath the scale can decrease, which leads to an increase in the oxidation rate. Changes in the aluminum content can also affect the microstructure. For example, the decrease in the aluminum content in FeAl can lead to a disordered structure (i.e., FeAl

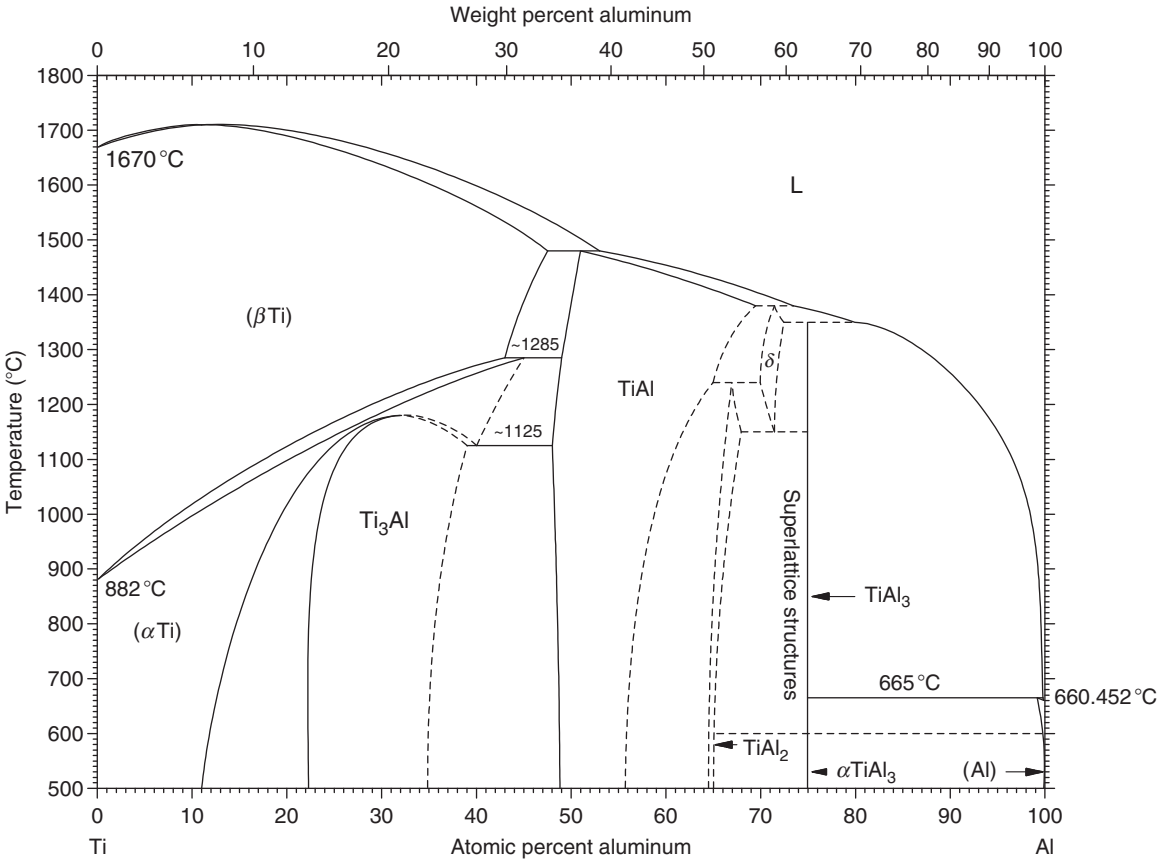

Figure 4 TiAl phase diagram. Reproduced from *Binary Alloy Phase Diagrams*, 2nd ed., ASM International, Materials Park OH, 1996, with permission from ASM International.

to α-Fe in **Figure 3**) below the oxide scale. Such changes can affect the oxidation behavior, as diffusion rates in the alloy will determine the magnitude of any changes in alloy composition at the alloy–scale interface, which determines the oxide phases formed in the scale.

In addition to alloy composition, microstructure also affects the oxidation behavior. For example, a finer alloy grain size can lead to reduced oxidation rates, because the diffusion of aluminum to replenish the aluminum used to form the alumina scale can reach the scale faster by grain boundary diffusion. A fine-grained microstructure has also been shown to improve the adherence of an alumina scale on NiAl.[11] Scale adherence is particularly important during thermal cycling, as thermal stresses are generated in the scale due to differences between the coefficients of thermal expansion of the scale and the alloy. However, stresses can be generated in the scale even in isothermal oxidation due to growth or transformation stresses in the oxides. In addition, porosity or segregation of particular elements to the alloy–scale interface can lead to weakening of the interface.

Porosity is often formed beneath the scale formed on nickel and iron aluminide alloys. The formation of porosity is generally attributed to the coalescence of vacancies formed during the growth of alumina. **Figure 6** shows the transport processes that occur during the growth of an alumina scale on an aluminide alloy. Bulk alumina grows by the outward diffusion of aluminum through the inward diffusion of aluminum vacancies, which are created at the oxide surface from oxygen in the gas phase. The vacancies are filled by aluminum from the existing oxide, so that the new oxide is formed on the outer surface. The aluminum vacancies migrate to the alloy and are filled with aluminum from the alloy, which creates vacancies in the alloy. Once the concentration of these vacancies exceeds the maximum concentration in the alloy, pores will form.

The growth process at grain boundaries is generally attributed to the inward migration of oxygen rather than to the outward migration of aluminum.

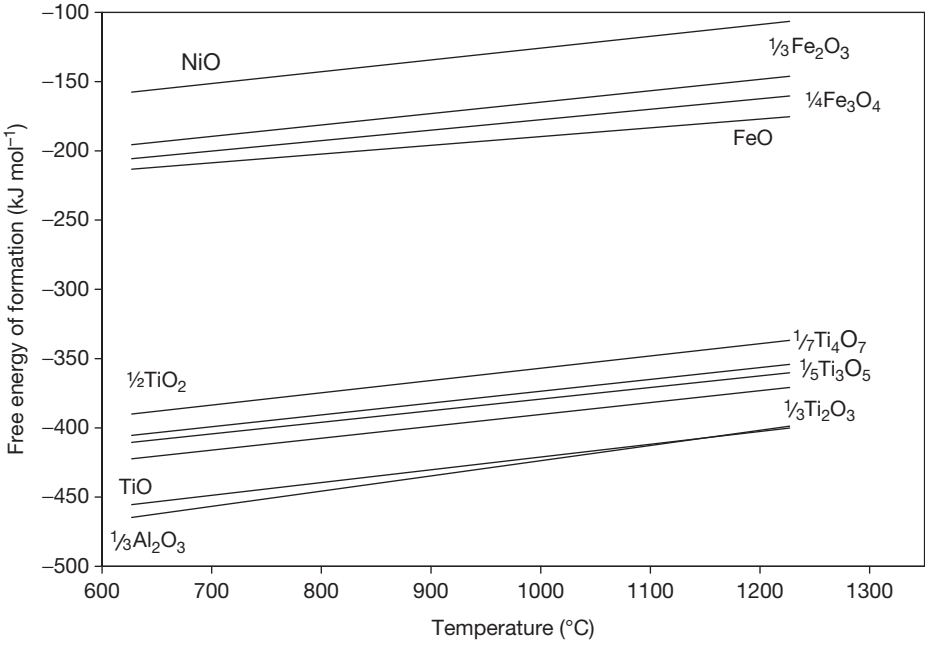

Figure 5 Ellingham diagram for nickel, iron, titanium, and aluminum oxides. Data from Kubaschewski, O., Alcock, C. B. *Metallurgical Thermochemistry*, 5th ed., Pergamon Press, 1979; Chase M.W., Jr. (Ed.), NIST-JANAF Thermochemical Tables, 4th ed., *J. Phys. Chem. Ref. Data, Monograph No. 9*, 1998.

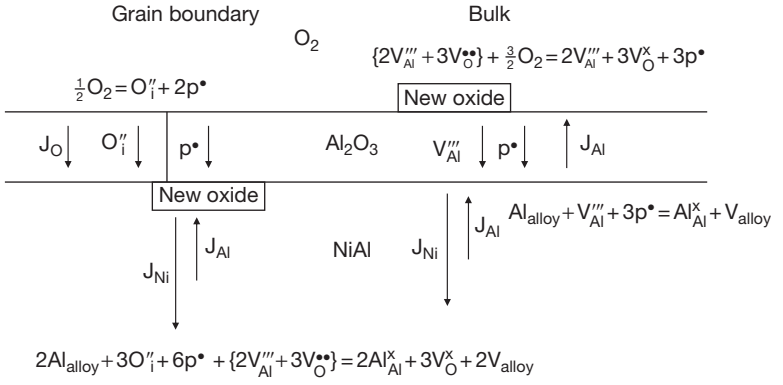

Figure 6 Transport during growth of alumina scale on nickel aluminide alloys. The predominant inward diffusing oxygen species has not been determined, so oxygen interstitials are used as an example.

Although the specific oxygen defect by which oxygen is transported is not well established, for illustrative purposes, oxygen interstitials are shown in **Figure 6**. Regardless of the specific predominant oxygen defect, however, inward migration of oxygen will lead to the forming of new oxide at the alloy–scale interface. Inward-growing scales generally contain less porosity at the alloy–scale interface as compared to outward-growing scales. However, in the Ni–Al system, porosity can still form within the inward-growing scale. The formation of porosity is generally attributed to the Kirkendall effect, as, for nickel-rich compositions, the diffusion constant for aluminum in NiAl is smaller than that for nickel in NiAl.[12] Thus, the diffusion of nickel away from the scale into the alloy is faster than the diffusion of aluminum from the bulk toward the scale, which leads to a net movement of mass away from the scale and the formation of vacancies in the metal beneath the scale. The concentration of vacancies continues to increase with increasing oxidation and eventually leads to the formation of pores. The Kirkendall effect can occur regardless of where

the new oxide forms. However, the Kirkendall effect does not occur for aluminum-rich compositions of NiAl, because, in this case, the diffusion of aluminum is not slower than that of nickel. This mechanism is supported by the observation that the number of voids formed decreases with decreasing grain size, as the larger amount of grain boundary diffusion in the finer grained material would reduce the amount of vacancies formed.[13]

The most important effect of the formation of porosity at the alloy–scale interface is that it weakens scale adhesion. The voids can act as stress concentrators and detachment of the oxide has been observed at the pores.[14] Pore formation does not, however, appear to significantly affect the oxidation rate. Although the loss of contact between the alloy and the scale at pores or voids might be expected to affect the scale growth, the AlO_x vapor pressure is large enough for vapor-phase transport of aluminum across the void to occur. The number and size of voids increase with oxidation time and the growth of voids in directions parallel to the surface is faster than that perpendicular to the surface.[15] Void formation has been attributed to the growth of the oxide around perturbations at the alloy–scale interface.[16]

Corundum (α-Al_2O_3) is the most stable form of alumina and the scale formed on nickel- and iron aluminide alloys is predominantly α-Al_2O_3. However, the first alumina phase to form is generally one of the metastable alumina phases – usually θ or γ, but occasionally δ. These transient phases form on nickel and iron aluminide alloys, but are especially prevalent on NiAl. The crystallographic orientation of the θ- or γ-Al_2O_3 phases is typically aligned with that of the alloy, and the oxides can grow epitaxially, as observed by transmission electron microscopy[17] and low energy electron diffraction.[18] Epitaxial growth is maintained for a longer time on NiAl crystals with the (001) and (012) orientations as compared to those with (011) and (111) orientations.[19] The transient phases grow by outward diffusion of aluminum, but at a higher growth rate (with lower activation energy) as compared with α-Al_2O_3.[20,21] The transport of aluminum in θ-Al_2O_3 is sufficiently high for the overall growth rate of the scale to be controlled in some cases by diffusion of aluminum from the bulk of the alloy to the alloy–scale interface, rather than the diffusion of aluminum through the scale to the surface.[22] As expected for meta-stable phases, the transient alumina phases are more prevalent at lower temperatures.[23] They are also more prevalent at low oxygen partial pressures and high humidity. The transient alumina phases eventually transform to the more stable α-Al_2O_3 phase, which leads to a reduction in the oxidation rate, but volumetric changes associated with the phase transformation can generate stresses that can affect the morphology of the oxide scale.

The stresses generated in the α-Al_2O_3 are tensile, but relax with time.[24] Relaxation can occur by deformation in either the alloy or the oxide, and thus depends on the microstructure. Fine grains in either phase will enhance this deformation (i.e., creep of the oxide or grain-boundary sliding in the alloy), and thus accelerate relaxation of the stresses. The stresses can also lead to convolution of the alloy–scale interface, which is commonly referred to as rumpling.[25] Although the interface of the rumpled scale is irregular, contact is maintained between the alloy and the scale. The rumpling is associated with swelling of the scale, which is attributed to the different diffusion rates of nickel and aluminum in NiAl (i.e., the same Kirkendall effect that leads to void formation beneath the scale).[26] This has led to the suggestion that rumpling is initiated by swelling of individual grains in the alloy.

The α-Al_2O_3 forming from the transient oxides has been reported to nucleate at both the scale–gas interface[27] and at the alloy–scale interface.[28] After nucleation, the transformation progresses in directions both perpendicular to the surface (inward or outward) and parallel to the alloy surface (lateral) and can lead to the formation of ridges as illustrated in **Figure 7**.[6] The lateral growth of α-Al_2O_3 from the nucleation site results in low-angle grain boundaries, which are oriented radially from the nucleation site. The transformation of the transient alumina phase creates tensile stresses in the α-Al_2O_3 that can lead to the formation of radial cracks with associated accelerated growth, which can result in 'spokes' along the radial cracks (not shown in **Figure 7**). The outer ridges form because the transient phases in this region are the last to transform to α-Al_2O_3 and the higher growth rate of the transient oxides leads to a thicker scale in the region. The ridges do eventually transform to α-Al_2O_3 and high-angle grain boundaries are formed in the ridges at the boundaries between α-Al_2O_3 grown from adjacent nuclei. The high angle boundaries allow for more short-circuit migration of oxygen (as shown in **Figure 6**), so the growth rate of the ridges can continue to be higher than that inside the ridge, where only low-angle boundaries are present. The transformation stresses are relaxed with time and the scale eventually consists of columnar α-Al_2O_3 grains.

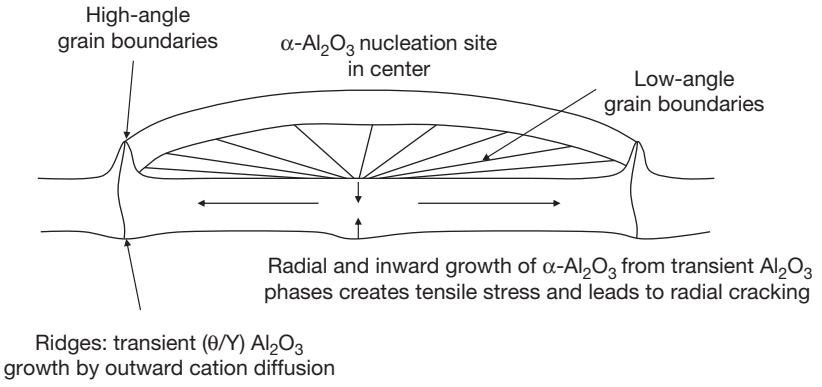

Figure 7 Ridge formation in alumina scale formed on nickel aluminide alloys.[6]

In iron aluminides, the nucleation of α-Al_2O_3 can be enhanced by Fe_2O_3, which can be present in the oxide scale and act as a template or nucleation site for the α-Al_2O_3. This transformation of the transient oxides to α-Al_2O_3 enhances rumpling or wrinkling of the scale. The degree of wrinkling increases with increasing temperature and aluminum content and also depends on the crystallographic structure (ordered or disordered) and orientation. Another difference between iron- and nickel aluminide alloys is that the Fe_2O_3 formed on iron aluminides is often mixed with the alumina, whereas the NiO or spinel formed on nickel aluminides is usually located on the outer scale surface.

1.25.2.1.2 Effect of atmospheres/impurities

In systems in which the active component provides the oxide for good corrosion resistance, such as nickel and iron aluminides, a reduced oxygen partial pressure is typically beneficial to the corrosion resistance, because it promotes the formation of the protective scale. If the oxygen pressure is sufficiently low, the oxide of the base metal could become unstable. However, even if the oxide of the base metal is stable, the dissolution of oxygen into the alloy is reduced at lower oxygen partial pressures, which reduces the formation of internal oxidation and promotes the formation of an external protective scale. Because the low oxygen partial pressure can promote a protective scale, preoxidation in low oxygen partial pressures is often used to improve the oxidation resistance. These trends apply to the nickel– and iron–aluminum systems as the amount of alumina in the scale is typically larger for oxidation in lower oxygen partial pressures, but there are exceptions. For example, the lower oxygen partial pressure stabilizes the transient oxides, which, as discussed earlier, leads to higher growth rates. Nickel dissolves more readily in the transient oxides, so the outward diffusion of nickel is more prevalent in low oxygen partial pressures.[29] The dissolution of nickel has been postulated to increase the ionic transport number, but the effect on the parabolic rate constant is not significant.[30] At very low oxygen partial pressures, the formation of nickel oxide can be completely eliminated. Although this would seem to be beneficial, since alumina, rather than NiO, provides the good oxidation resistance, the absence of NiO can lead to higher stresses in the oxide scale.[31]

The presence of water vapor has less effect on the oxidation of alumina-forming alloys compared with its effect on chromia-forming alloys. Although water vapor often does not significantly affect the oxidation rate of aluminides, it can lead to increased spallation and oxidation rates for NiAl.[32,33] The increased spallation has been attributed to the hydration of the alumina scale. Hydrate phases are not stable at oxidation temperatures, but they can form during cooling and generate stresses in the scale, which promote scale spallation.[32] Although water vapor generally has little effect on the oxidation rate of iron aluminides, increased rates have been observed in some experiments.[34] Such variable results suggest that water vapor may influence transient phase transformations, which can be affected by minor changes in scale microstructure or morphology.

The most important impurity for the oxidation of alumina-forming oxides is sulfur, which can increase porosity at the alloy–scale interface and enhance crack propagation.[35,36] Sulfur diffuses to the scale and initially adsorbs to the surface of pores. Once a continuous alumina scale is formed, the sulfur segregation

expands to the alloy–scale interface. As increased porosity and sulfur segregation weaken the scale adherence, sulfur is detrimental to oxidation resistance. The diffusion rate of sulfur in NiAl decreases with increasing aluminum content; therefore the amount of segregation, and thus the associated detrimental effects, are greater for lower aluminum contents. In iron aluminides, sulfur initially adsorbs to the pore surface and subsequently cosegregates with aluminum. The presence of sulfur increases the scale convolution, which, as discussed earlier, results from growth and transformation stresses.

1.25.2.1.3 Effect of alloying additions

The oxidation resistance of aluminide alloys can be improved with alloying additions. Reactive elements have been shown to be beneficial to the oxidation of aluminide alloys by reducing the amount of porosity that forms at the alloy–scale interface.[37,38] One of the mechanisms proposed for this beneficial effect of reactive elements is that the reactive elements segregate to the grain boundaries in the oxide scale and form oxides that block the outward diffusion of cations.[36,38,39] Decreasing the outward diffusion of cations leads to an increase in the proportion of growth by inward diffusion of oxygen, which, as discussed earlier, reduces the amount of porosity formed at the alloy–scale interface and thus improves scale adherence. This mechanism appears to be more prevalent in nickel aluminides compared to iron aluminides.

The reactive element most commonly added to aluminide alloys is yttrium, which can be added as a metallic alloy or as an oxide in oxide dispersion strengthened (ODS) alloys. In nickel aluminide alloys, the addition of yttrium can lead to the formation of a NiY_x phase, which promotes spinel formation and thus is detrimental to oxidation behavior. The formation of NiY_x is more likely when yttrium is added as a metallic alloy than when added as an oxide phase.[40] As too large an addition of yttrium can increase stresses in the oxide,[41] yttrium is most effective when added in small amounts as an oxide phase. At low temperatures, yttrium additions promote α-Al_2O_3 formation and thus decrease the oxidation rate. However, at high temperatures, where α-Al_2O_3 forms easily with or without yttrium additions, yttrium is detrimental by decreasing the grain size of the oxide scale, which increases the amount of short-circuit grain-boundary diffusion and thus increases the oxidation rate.[42]

Another common reactive element used with aluminide alloys is hafnium, which improves the adhesion of the oxide scale.[43] The improvement is observed at temperatures lower than those at which the general reactive element effects are observed, and is attributed to the formation of hafnium oxides that protrude into the scale and provide anchors, which improve adhesion.[44] Hafnium also improves the plasticity of the scale, which increases the magnitude of stresses that can be accommodated without spallation. The addition of hafnium can significantly extend the lifetime of aluminide alloys, particularly when exposed to cyclic oxidation.[45]

Zirconium is also a commonly added alloy, and, like yttrium, can lead to the formation of an additional intermetallic compound, $NiZr_5$, which can lead to the formation of ZrO_2 in the scale; therefore, the amount of zirconium added must be limited. Small amounts of zirconium can improve adherence and reduce oxide scale growth rate by increasing grain size. However, zirconium can also be detrimental by impeding the formation of α-Al_2O_3 and promoting outward scale growth, which increases growth rates. Zirconium is a strong carbide former, so if zirconium is added with carbon, which is commonly added to iron aluminides, the ratio of zirconium to carbon must be controlled, so that the appropriate amount of zirconium is available to beneficially affect the oxidation behavior.

Other reactive elements, such as titanium and cerium, have also been shown to decrease the oxidation rate, either by decreasing the outward diffusion of aluminum or by increasing the grain size of the oxide. However, not all reactive elements are beneficial to oxidation behavior; e.g., lanthanum leads to both a higher oxidation rate and lower scale adherence.

Transition metals are often used as alloying additions for aluminide alloys. Chromium is commonly added to intermetallic alloys to improve ductility and minimize environmentally assisted crack embrittlement. Chromium is beneficial to the alumina-forming nickel- and iron-based alloys, because it reduces the amount of aluminum required to avoid internal oxidation and form a protective scale. Chromium has a similar effect in Ni_3Al as it reduces the amount of aluminum required to maintain an effectively rehealing scale for long oxidation exposures. Chromium affects the transformation of θ-Al_2O_3 to α-Al_2O_3, although the reported effects are mixed as chromium has been reported to both inhibit[42] and promote[21] α-Al_2O_3 formation. Chromium dissolves in θ-Al_2O_3, which would explain the inhibitive effect, as the chromium diffusion may be required for α-Al_2O_3 formation.[46] At the same time, chromium appears to accelerate

nucleation of α-Al_2O_3. The effects of chromium on the oxidation rate are likewise mixed as it has been reported to both increase and decrease the oxidation rate. Chromium can segregate to the alloy–scale interface and lead to additional phase formation, which decreases adherence and is therefore detrimental to oxidation resistance.

The effects of niobium and tantalum are more consistent than those of chromium. Like chromium, niobium and tantalum are added to improve the mechanical properties. In both cases, a mixed oxide, $NiTa_2O_6$ or $NiNb_2O_6$, forms and is detrimental to oxidation resistance. However, if added in small amounts, niobium and tantalum improve the mechanical properties with an acceptably minimal effect on oxidation resistance. Although increasing the niobium content is detrimental to the oxidation resistance, very large niobium contents (i.e., NiAl + $NbAl_3$ alloys) can lead to the formation of Laves phases, which promote the formation of a protective alumina scale during oxidation.

Refractory metals, such as molybdenum, tungsten, and vanadium, are generally detrimental because of the formation of liquid or gaseous oxides. For example, although molybdenum does not significantly affect short-term oxidation behavior, for longer exposures, the formation of molybdenum oxide vapor phases is detrimental.

Noble metals, such as Pt, Re, and Rh, can be beneficial to the adherence of the oxide scale.[6] For example, the beneficial effect of platinum to the oxidation behavior of NiAl is generally attributed to its interaction with sulfur.[47] Platinum, like sulfur, segregates to the pore surfaces and alloy–scale interfaces. Any platinum present at these locations displaces sulfur, and thus decreases the detrimental effects associated with sulfur segregation. Platinum can also be detrimental by stabilizing θ-Al_2O_3, which inhibits the formation of α-Al_2O_3, thus increasing the oxidation rate.[23] However, because of the catastrophic effects of scale spallation, the beneficial effects of improved adherence can often outweigh the detrimental effects of increased growth rates. Scale spallation is particularly critical when the aluminide is used as a bond for thermal barrier coatings, which will be discussed in a later section. Large amounts of platinum additions can lead to the formation of a platinum aluminide phase ($PtAl_2$), which minimizes depletion of aluminum from the alloy–scale interface. Maintenance of a sufficient aluminum level at the alloy–scale interface prevents the formation of Ni_3Al, which can lead to local stresses at the interface, and improves the long-term oxidation resistance of the alloy.

As mentioned earlier, carbon is used to strengthen iron aluminide alloys. Carbon is generally detrimental to oxidation resistance. The oxide scale formed on the carbide phase (Fe_3AlC_x) that strengthens the alloy is thicker than, but has the same morphology as, the scale formed on the metal phase. As mentioned earlier, when used with strong carbide formers (e.g., zirconium), the effects of carbide formation must be considered in optimizing the alloy composition.[45] Boron, another interstitial additional alloy, is also generally detrimental to oxidation behavior, but can be beneficial when added with others, such as zirconium or hafnium.

1.25.2.2 Titanium Aluminides

The high reactivity of titanium, relative to iron and nickel, creates additional challenges for the formation and maintenance of an alumina scale, because of the competition between aluminum and titanium for oxide formation. However, as mentioned earlier, titanium aluminides have excellent specific properties and so have been developed for aerospace application. There are several reviews of their oxidation behavior.[48–51]

1.25.2.2.1 Scale properties/structure

The minimum aluminum content required for alumina formation on titanium aluminide alloys is much higher than that for alumina formation on nickel or iron aluminide alloys. TiAl is in equilibrium with TiO and Al_2O_3, but any lower compositions are not in equilibrium with Al_2O_3; so, even before any aluminum depletion occurs, TiAl is at the borderline aluminum composition for Al_2O_3 formation. Thus, scales formed on titanium aluminides generally contain both aluminum and titanium oxides.

The typical scale morphology of the scale formed on TiAl is shown schematically in **Figure 8**.

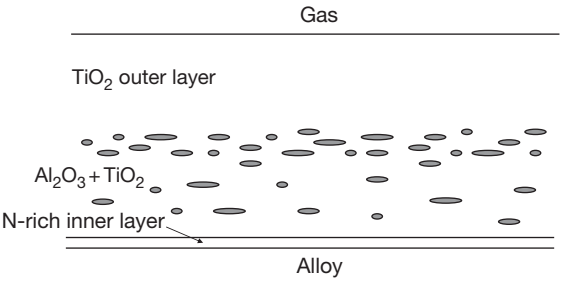

Figure 8 Schematic of scale formed during oxidation of titanium aluminide alloys.

Although TiO is the titanium oxide in equilibrium with the alloy, TiO_2 is stable in air. While there may be some titanium oxides with valence lower than +4 at the alloy–scale interface, the major portion of the titanium oxide is rutile TiO_2. Rutile is an oxygen-deficient oxide, for which the predominant ionic point defects are oxygen vacancies at high oxygen partial pressures and titanium interstitials at low oxygen partial pressures. Platinum marker experiments on the oxidation of pure titanium have shown that the new oxide forms in the middle of the oxide, indicating that the oxygen vacancies are predominant in the outer scale and titanium interstitials are predominant in the inner scale. The oxidation of titanium aluminide is further complicated, as the scale also contains aluminum oxides. As shown in **Figure 8**, the aluminum oxide is often dispersed in the rutile in the inner portion of the scale. The outer portion of the scale is usually TiO_2. Sometimes, as shown in **Figure 8**, there is a layer in the middle of the scale where the amount of alumina is higher than that in the inner portion of the scale. These layers could be in part due to the oxygen partial pressure dependence of the ionic point defects in rutile as described earlier. Although the defect chemistry has not been well established, platinum marker experiments have shown that, as in the case of pure titanium, the new oxide forms in the middle of the scale. There is typically an inner layer, which contains nitrogen if the oxidation is performed in air. This inner layer may also contain titanium in a lower valence and/or mixed oxides. The mixed titanium–aluminum oxide phases (X-phase, Z-phase, NCP) are not thermodynamically stable at the oxidation temperature, but can form at the interface and affect the oxidation behavior.

The growth rate of rutile is much higher than that of alumina, so an alumina scale is desired for oxidation resistance. A continuous alumina layer would provide the lowest oxidation rate and has been achieved on some titanium aluminide alloys. However, a mixed scale, as shown in **Figure 8**, is more typical and the growth rate of such a scale is between the rates for alumina and titania growth. Although increasing the amount of alumina is beneficial for oxidation resistance, the morphology is also important. For example, the more continuous the aluminum-rich layer in the middle of the scale (**Figure 8**), the slower is the growth rate. Thus, control of the oxidation rate of titanium aluminum alloys depends critically on the scale morphology. Because of the mixed scale that grows at a rate higher than pure alumina, the oxidation resistances of titanium aluminide alloys are generally inferior to those of nickel and iron aluminides, so titanium aluminide alloys are usually considered for lower temperature applications.

1.25.2.2.2 Effect of atmosphere and pretreatment

The presence of a nitrogen-containing layer suggests that nitrogen may influence oxidation behavior. Nitrogen is often considered essentially inert for many oxidation processes. However, titanium, in particular, and aluminum to a lesser extent, are nitride formers, so nitrogen does affect oxidation behavior. The oxidation behavior of titanium aluminide alloys in air is different from that in argon–oxygen mixtures.[49,50] Although the results are somewhat varied, the oxygen rates in air are typically higher than those in oxygen without nitrogen for the same oxygen partial pressure. The detrimental effect of nitrogen is attributed to the nitrogen-containing layer promoting the formation of TiO_2. Although the nitride layer contains aluminum and titanium, the amount of titanium is typically higher than that of aluminum. Nitrogen has also been shown to be beneficial to the oxidation behavior of some alloys – particularly alloys with lower aluminum content. The beneficial effect of nitrogen is attributed to nitrogen doping the rutile and decreasing the concentration of the mobile defect, which decreases transport through the scale. Nitrogen may also promote the formation of alumina in the scale by reducing the titanium activity in the alloy.

Because of the delicate balance between alumina and titania formation, small changes can determine which phase nucleates and grows; subtle differences can therefore affect oxidation behavior. For example, surface finish has been shown to significantly affect the oxidation rate in oxygen, but not in air.[52] The surface finish most likely affects nucleation, which implies that the superior performance in oxygen is due to the formation of a phase that is inhibited by either the presence of nitrogen or the surface roughness. Such phenomena are difficult to characterize because they likely depend on transient phases and microstructures, which are not present when the sample characterization is performed after the oxidation experiment is completed.

The alloy microstructure also affects oxidation behavior. For the same alloy composition, the oxidation rate with a lamellar microstructure is lower than that for a duplex microstructure.[53] One of the challenges in the application of titanium aluminide alloys is control of the microstructure, as the microstructure also affects the mechanical properties. Production of

parts with the same microstructure throughout the sample, as well as between samples, is a significant engineering challenge. Microstructural inhomogeneities can lead to locally high corrosion rates or local mechanical weaknesses.

Water vapor in the atmosphere can increase the oxidation rate. This increase is generally attributed to increasing water vapor transport in the scale. Although water vapor does not significantly affect the growth of alumina, it does affect transport in rutile, which is generally the continuous phase in the oxidation scale and thus dominates the overall scale growth rate.

Preoxidation and presulfidation have been used to improve the oxidation resistance of titanium aluminide alloys. There are often conditions in which a protective scale would not form, but could be maintained if it had already formed. Under such conditions, a pretreatment in carefully controlled conditions can be used to form a protective scale, which subsequently grows at a slow rate.

1.25.2.2.3 Effect of alloying additions

The aluminum content in titanium aluminide alloys is more critical than in nickel and iron aluminide alloys. The oxidation resistance of Ti_3Al is generally poor, and in binary titanium–aluminum alloys, at least 48–50 at% aluminum is generally required for good oxidation resistance. The amount of aluminum required, however, can be reduced with alloying additions.

The alloying addition most widely used for improving the oxidation resistance of titanium aluminide alloys is niobium. During oxidation, the alloy beneath the scale is enriched with niobium, but niobium is also incorporated in the scale. Several explanations for the beneficial effects of niobium additions have been proposed. One explanation is that niobium increases the activity of aluminum in the alloy, but this has not been supported by subsequent thermodynamic measurements of the aluminum activity.[49] Another explanation is that niobium increases the diffusion of aluminum and/or decreases the diffusion of oxygen in the alloy, which reduces the amount of internal oxidation of aluminum and promotes a more continuous alumina scale. The beneficial effect of niobium has also been attributed to niobium doping the rutile scale and decreasing the concentration of oxygen vacancies and/or titanium interstitials. Niobium has also been reported to improve the mechanical integrity of the scale, which improves the resistance to cyclic oxidation. Large amounts of niobium, however, can be detrimental if a Nb_2O_5 phase forms in the oxide scale.

Another common alloying addition for titanium aluminide alloys is chromium, which is added primarily to improve the mechanical properties of the alloy. Small amounts of chromium lead to an increase in the oxidation rate. This increase is typically attributed to the chromium doping the rutile scale and increasing the concentration of oxygen vacancies and/or titanium interstitials. Larger amounts of chromium, however, are beneficial to oxidation resistance. The beneficial effect has been attributed to chromium increasing the aluminum activity in the alloy. While increases in the aluminum activity have been measured, the magnitude of the increase is not sufficient to explain the observed improvements. Another explanation is related to the formation of Laves phases, which form in alloys with high chromium content. The Laves phases have low oxygen solubility and lower titanium activity, both of which promote a more protective alumina scale.

Niobium and chromium are sometimes added together and, fortunately, the oxidation behavior appears to be dominated by niobium rather than by chromium. The oxidation rates of alloys with a combination of niobium and other alloying additions such as manganese, zirconia, and hafnium are also similar to those of alloys with niobium as the only alloying addition.

Like chromium, other transition metals, such as iron, nickel, manganese, and vanadium, are generally detrimental to the oxidation of titanium aluminide alloys, while refractory metals, such as tungsten and molybdenum, are beneficial. The beneficial effects of tungsten, like those of niobium, are attributed to decreasing the oxygen solubility in the alloy (to inhibit internal oxidation) and doping of the rutile (to reduce oxygen vacancies and/or titanium interstitial concentrations).

Silicon additions can be beneficial to the oxidation resistance of titanium aluminide alloys. If silicon is present in the alloy, silica will usually form in the scale. However, silica is often dispersed so that is it is not effective for reducing the oxidation rate. In some cases, silicon additions lead to a continuous silica layer, which provides a barrier to oxygen diffusion and thus improves the oxidation resistance. However, this layer leads to stresses during thermal cycling and is thus detrimental to the cyclic oxidation resistance.

Noble metals have mixed effects on the oxidation of titanium aluminide alloys. Platinum and gold are detrimental to oxidation resistance, but silver is beneficial.[54] Silver promotes the formation of θ-Al_2O_3, which, as discussed earlier, grows at a faster rate than α-Al_2O_3 and thus would seem to be detrimental. However, the α-Al_2O_3 formed from transient alumina

is continuous and the oxidation rate of the alloy is the same as that for the growth of an alumina scale. The beneficial effect of silver decreases with increasing temperature, presumably because it results from the transient formation of θ-Al_2O_3, which is metastable and thus becomes less prevalent with increasing temperature. The addition of small amounts (1–3%) of chromium to silver-doped alloys is detrimental to oxidation resistance, but with larger amounts (5–7%) the oxidation rate is reduced to that of an alumina-forming alloy.[55] The excellent oxidation resistance of these alloys, like the high-chromium-content alloys described earlier, is attributed to the presence of Laves phases in the alloy microstructure.

Reactive elements are used as alloying additions in titanium aluminide alloys, but not to the extent, or to the same beneficial effect, as in nickel and iron aluminide. Small amounts of reactive elements, such as zirconium, hafnium, and yttrium, are beneficial to oxidation resistance. Hafnium has been shown to improve scale adherence. Zirconium, while beneficial for short oxidation exposures, eventually leads to the formation of zirconia, the transformation of which creates stresses in the oxide scale.

One of the most successful recent approaches for improving the oxidation resistance of TiAl-based alloys is the addition of halogen elements, such as fluorine, chlorine, or bromine. The addition of the appropriate amount of a halogen element can lead to a continuous alumina scale and kinetics following the growth of an alumina scale. Various explanations have been proposed for the beneficial effect of halogen additions. One explanation is that chlorine doping of the scale decreases the oxygen vacancy and/or titanium interstitial concentration (i.e., the same as that of niobium and tungsten doping).[56] Other explanations are that the formation of TiO_2 is inhibited by the presence of the halogen element[57] or by a reduction in titanium activity due to volatilization of titanium. The explanation that best illustrates the long-term effect is shown in **Figure 9**.[58,59] In this model, aluminum is transported from the alloy to the scale–gas interface in a gas phase that diffuses through pores or microcracks in the scale. Once the aluminum-containing vapor reaches the scale surface, it reacts with oxygen to form alumina and evolves chlorine, which can diffuse back to the alloy and form more of the aluminum-containing species. The chlorine that evolves is thus recycled and provides a mechanism for the transport of aluminum to heal pores and/or cracks in the scale. For this mechanism to work, chlorine partial pressure must be in a critical

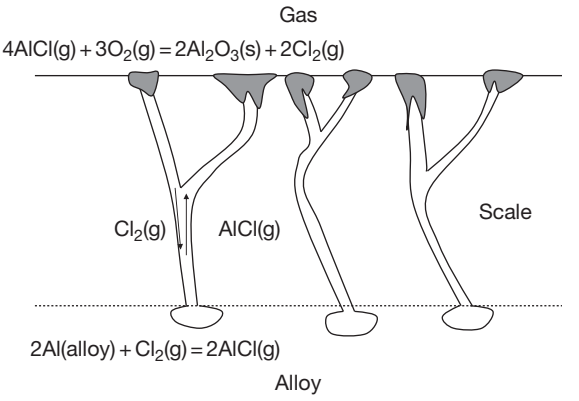

Figure 9 Vapor transport mechanism for beneficial effect of halogen additions on the oxidation of titanium aluminide alloys.[58,59]

range: it must be high enough to transport sufficient aluminum to maintain the protective scale, but if it is too high, the partial pressure of a titanium chloride species may exceed that of the aluminum-containing species. When the pressure of the titanium species is too high the alumina forms in a whisker-like morphology, which does not provide adequate protection.

To impart its beneficial effect on oxidation resistance, the halogen element is needed only at the surface, so ion implantation is often used to add halogen elements to titanium aluminide alloys. The same is true for other alloying elements added for improved corrosion resistance, especially those which may have detrimental properties on the mechanical properties of the alloy. Thus, ion implantation is used to alloy titanium aluminide alloys with other metallic elements, as well as nonmetallic elements, such as phosphorous.[60] This technique minimizes the amount of alloying elements used by localizing the addition to the location at which the element is needed. This technique would not be effective for an element that is consumed during oxidation, as there is a limited source, which could become depleted after long exposures. However, in the case of halogen additions, the halogen element appears to be recycled, and ion implantation has been shown to improve oxidation resistance for long periods of time.

1.25.2.3 Other Aluminides

Most of the aluminide alloys used are from the nickel–, iron–, or titanium–aluminum system. However, there are a few other systems that have been developed, including aluminides of noble and active metals.

As described earlier, the beneficial effect of platinum additions to NiAl is due, in part, to the formation

of a platinum aluminide phase at the alloy–scale interface. Since platinum does not form a stable solid oxide, the only oxide that can form on a platinum aluminide alloy is alumina. The microstructure of the alumina scale is similar to that formed on NiAl, but the adhesion is better on platinum aluminide alloys.[61] The scale growth occurs predominately through short-circuit grain boundary diffusion, so the grain size of the oxide scale affects the oxidation rate. The adhesion can be further improved with zirconia additions, which segregate to the alloy–scale interface and lead to a convoluted, but strong, interface between the alloy and the scale.[62] A platinum aluminide coating is clearly expensive and thus is used in applications where a small amount of material is required, such as in a bond coat, which will be discussed in a later section.

Other noble metal aluminides include those of ruthenium and iridium. Ruthenium aluminide has better ductility than most aluminide alloys and has good oxidation resistance. The scale morphology suggests that the scale grows by outward diffusion of aluminum, although voids are not formed beneath the scale.[63] Two-phase Ru(Al) + RuAl are particularly attractive because of their good ductility. However, the oxidation resistance decreases as the amount of the metal phase increases, because the high oxygen diffusivity of the metallic phase leads to internal oxidation.[64] The oxidation resistance can be improved with platinum additions, but weight loss still occurs during cyclic oxidation.[65] Iridium aluminide is used because iridium has very low oxygen permeability and thus is an excellent oxygen barrier. The oxidation rates of iridium–aluminum alloys are representative of pure alumina scale growth.[66]

An aluminide alloy system that has been investigated because of its high melting point and low density is niobium aluminide.[6] However, niobium aluminides, even with large aluminum concentrations (e.g., $NbAl_3$), form mixed oxide scales rather than alumina scales. In particular, the scales contain $AlNbO_4$ and Nb_2O_5 and are thus not protective. Zirconium aluminide has been investigated but has poor oxidation resistance because of the formation of ZrO_2. ZrO_2 not only has high oxygen permeability, but also undergoes phase transitions, which generate stresses in the oxide scale.

1.25.3 Hot Corrosion

The presence of other reactive species, such as sulfur and chlorine, in the environment can accelerate the corrosion of intermetallic alloys. The corrosion can be enhanced if the additional species is in the gas phase, but corrosion is further accelerated if a condensed molten salt phase is formed.

1.25.3.1 Sulfur-Containing Environments

The sulfidation behavior of intermetallic alloys has recently been reviewed.[67] The effects of sulfur on the corrosion rate depend on the oxygen partial pressure and whether a condensed phase is formed.

1.25.3.1.1 Gaseous

The addition of SO_2 to an oxidizing environment does not significantly affect corrosion behavior. While the scale formed in SO_2 contains oxides and sulfides, scales formed in oxygen with SO_2 contain mostly oxides with little or no sulfides.[68] One notable difference between oxidation with and without sulfur is that silver, which as discussed earlier, is beneficial to the oxidation behavior of TiAl, is detrimental to the corrosion of TiAl in sulfur-containing atmospheres.

The corrosion behavior changes as the oxygen partial pressure is reduced. In H_2–H_2S–H_2O mixtures, the oxygen partial pressure is typically sufficiently high for alumina to form and alumina is present in the outer portion of the scale. However, the inner portion of the scale consists of sulfides, which can be mixed, but usually contain little or no aluminum (e.g., TiS for TiAl[69] or FeS for FeAl[70]). As expected from the low aluminum content in the sulfides, increasing the aluminum content in the alloy increases the amount of alumina in the scale. For the corrosion of TiAl, TiO_2 is also formed in the scale. In addition, the rapid transport of titanium in the inner TiS layer leads to depletion of titanium in the alloy, so phases with higher aluminum content, such as $TiAl_2$ and $TiAl_3$, form beneath the scale. The addition of niobium improves the sulfidation resistance of both FeAl and TiAl. Niobium oxides and sulfides form in the scale and the scale adherence is improved with niobium additions.[71]

With further decrease in the oxygen partial pressure in H_2–H_2S environments, the oxides become less stable and the scale consists almost entirely of sulfides. For FeAl alloys, FeS and mixed (Fe,Al)S phases are formed in sulfidizing environments. The predominant phase formed during sulfidation of NiAl is Ni_3S_2, which can also contain Al_2S_3 or $NiAl_2S_4$ inclusions. For low H_2S levels the sulfidation rate is reasonably low, but as the H_2S content increases a Ni–Ni_3S_2 eutectic forms and leads to large (~4 orders of magnitude) increases in corrosion

rates. The addition of chromium leads to the formation of $(Cr,Al)_3S_4$ and further degrades the sulfidation resistance.[72] Similarly, zirconium additions increase the amount of internal corrosion and increase the sulfidation rate. In general, nickel aluminides have poor sulfidation resistance.

TiAl forms a layered sulfide structure in low oxygen-partial-pressure sulfidizing atmospheres.[73] The scale typically contains Ti_3S_4, TiS, and Al_2S_3. The sulfide scale typically contains more titanium than aluminum, so the alloy beneath the scale is depleted in titanium, and aluminum-rich phases, such as $TiAl_2$ and $TiAl_3$, form. Alloying addition affect the specific sulfide phases formed, but in most cases do not significantly affect the overall sulfidation rate. Silver and copper additions, however, increase the amount of sulfidation.

1.25.3.1.2 Molten salts

The corrosion behavior changes when sulfur is present in a condensed salt on the alloy surface. An oxide scale that is relatively stable in a gaseous environment may dissolve in the salt and lead to increased corrosion rates.

The reaction between FeAl and Na_2SO_4 produces a complex mixture of oxygen- and sulfur-containing compounds (e.g., $NaAlO_2$, $NaAl(SO_4)_2$, Fe_2O_3, Al_2O_3). The corrosion of the alloy occurs by dissolution of the oxide in the molten salt and internal sulfidation of the alloy. Corrosion resistance can improve with increasing temperature as the more rapid growth of the alumina results in a more protective scale.[74] Similarly, the addition of dispersed Al_2O_3 to the alloy improves the corrosion resistance by stabilizing the Al_2O_3 in the scale. Carbon additions have been shown to improve the corrosion resistance of FeAl by forming carbides that inhibit sulfur diffusion into the alloy. Boron additions, however, have mixed effects as they have been shown to be both beneficial and detrimental to hot corrosion resistance.

Aluminization of nickel-based superalloys has been used to improve hot corrosion resistance. The oxide scale formed on nickel aluminide alloys during hot corrosion in molten sulfates contains an outer layer of NiO or $NiAl_2O_4$. The latter has better hot corrosion resistance because of the lower solubility of the spinel, as compared to NiO, in the molten salt.[75] The resistance to molten sulfate corrosion can be improved with the addition of platinum, palladium, or chromium.

The oxide formed during the corrosion of titanium aluminide alloys in molten sulfates contains TiO_2 and Al_2O_3 with an inner layer of sulfides as shown schematically in Figure 10.[76] As with sulfidation in a gaseous environment, the scale contains more titanium than aluminum, so the alloy beneath the scale is depleted in titanium and a layer of $TiAl_3$ is formed. Also, as with other sulfidation and oxidation processes, increasing the amount of aluminum in the alloy increases the amount of alumina in the scale and improves corrosion resistance. Niobium is beneficial to the oxidation resistance as it improves scale adherence.[76] Chromium aids the hot corrosion resistance, and, as will be discussed later, is often added to protect aluminide coatings. Vanadium additions, however, increase the amount of scale spallation and are thus detrimental.

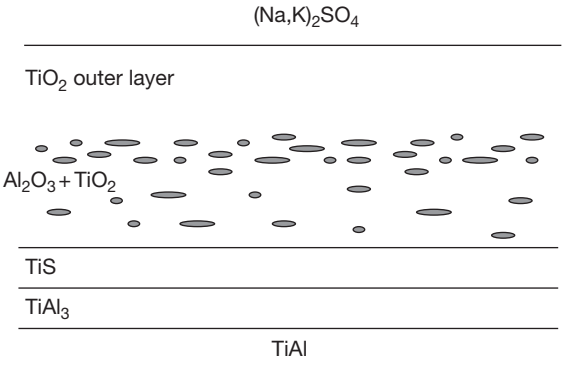

Figure 10 Schematic of scale formed during corrosion of Ti–50Al in $(Na,K)_2SO_4$ at 900 °C.[76]

1.25.3.2 Chlorine-Containing Environments

Chlorine enhances the corrosion rate of most materials and intermetallic alloys are no exception. Chlorine can be present in the gas phase or in a molten salt – either a chloride or mixed salt.

1.25.3.2.1 Gaseous

The primary effect of chlorine in the gas-phase corrosion of aluminide alloys is the formation of volatile chloride species.[77] In particular, the vapor pressure of $AlCl_3$ is relatively high and can lead to loss of aluminum and/or void formation in the scale, both of which are detrimental, as loss of aluminum decreases the amount of alumina in the scale, and void formation degrades scale adherence. The addition of zirconium has been shown to reduce the loss of aluminum and thus improve corrosion resistance. In some cases, the liquid chlorides can form from reaction with the chlorine in the gas and can enhance the corrosion rate.

1.25.3.2.2 Molten salts

Molten chlorides can also be formed from salts deposited on the alloy surface. For example, the reaction of titanium aluminides with sodium chloride results in the formation of TiO_2, Al_2O_3, and $NaTiO_2$. The increase in corrosion rate due to the presence of sodium chloride is generally attributed to vapor phase transport via chloride gas species.[78] As discussed earlier, controlled amounts of chlorine, or other halogens, can improve the oxidation of titanium aluminide alloys, but for this beneficial effect to occur, the chlorine content must be limited so that transport of aluminum, but not titanium, occurs. The chlorine levels present during hot corrosion in NaCl are high enough for the transport of both titanium and aluminum from the alloy to the scale surface. Under these conditions, the alumina forms as whiskers, rather than as a protective layer, so the corrosion rate is increased.

Hot corrosion in lithium-containing chloride salts, such as LiCl–Li_2O or KCl–Li_2O, results in the formation of multiple mixed oxides. For TiAl, in addition to TiO_2 and Al_2O_3, $LiAlO_2$ forms in the outer portion of the scale, while Li_2TiO_3 forms in the inner portion of the scale. $LiAlO_2$ also forms during corrosion of NiAl and FeAl in lithium-containing salts, but NiAl is more resistant than FeAl to chloride attack.[79]

The corrosion of titanium aluminide alloys in mixed sulfide–chloride molten salts is similar to that in chloride salts, although in some cases the corrosion in a molten chloride is faster than that in a mixed salt. The chloride vapor transport mechanism described above is active in the corrosion of TiAl in a mixed chloride–sulfide salt. Chromium and silver additions to TiAl improve the hot corrosion resistance by improving the adherence of the mixed oxide phase (Z-phase) formed at the alloy–scale interface.[76,80] The morphology of the scale formed on titanium aluminide containing 1–3% silver is shown in **Figure 11**.[80] Niobium, which, as discussed earlier, is generally beneficial to the corrosion of TiAl, can be detrimental when added in large amounts because of sulfide phase formation.

The corrosion of nickel aluminide alloys in mixed sulfide–chloride molten salts is similar to that in sulfide melts, presumably due to the absence of significant partial pressures of nickel chloride gas species to provide vapor phase transport analogous to that which occurs in titanium aluminide alloys. The oxide scale formed on nickel aluminide alloys consists of a layer of NiO and Al_2O_3 above an inner layer of sulfides. The alloy beneath the scale is depleted in aluminum and the scale is generally not protective. Silicon additions increase the amount of alumina, and thus improve the oxidation resistance. Oxide (Y_2O_3) dispersions can also improve the corrosion resistance by improving scale adherence.[81]

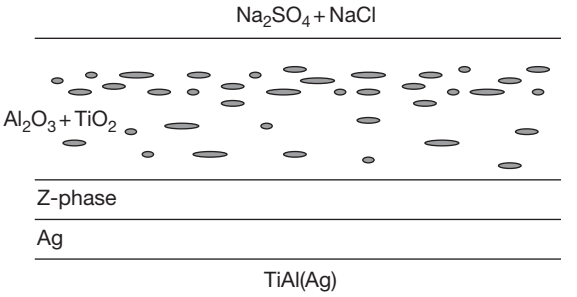

Figure 11 Schematic of scale formed during corrosion of Ti–48Al–(1–3)Ag in Na_2SO_4 + NaCl at 800 °C.[80]

1.25.3.3 Others

Molten carbonates can also lead to enhanced corrosion of aluminide alloys. Corrosion in lithium-containing carbonates is similar to that in other lithium-containing salts in that $LiAlO_2$ is present in the corrosion scale. Because of their high aluminum content, NiAl and FeAl, are used as replacements or coatings on stainless steels and superalloys in molten carbonate environments.

As mentioned earlier, vanadium is detrimental to the corrosion of TiAl in sulfate salts. Vanadium is also detrimental when present in a corrosive salt. Vanadium-containing salts are more corrosive than sodium chloride to iron aluminides. The scale formed in V_2O_5-containing salts consists of several mixed oxides and can be quite complex. For example, the weight loss of FeAl in a V_2O_5–Na_2SO_4 mixture increases with increasing temperature up to about 700 °C and then decreases at higher temperatures due to the formation of a more protective scale. The addition of Al_2O_3 to the alloy provides some improvement in scale adherence.[82]

1.25.4 Coatings

Aluminide alloys are attractive as oxidation resistant coatings, because ductility, while desirable, is less critical in a coating than it is in a structural load-bearing member. Aluminide coatings can be used as coatings for other aluminide alloys with inferior oxidation resistance, but superior mechanical properties.

In addition, aluminide coatings can be applied to metallic alloys that have high ductility, but contain little or no aluminum and thus may have poor oxidation resistance. Coatings can be applied by a variety of techniques, some of which will be discussed in the chapter on **High Temperature Coatings: Protection and Breakdown**. However, diffusion coatings are widely used for aluminide intermetallic alloys and will be discussed in this chapter. Aluminum is typically supplied in a gaseous or liquid phase, but solid-state diffusion is required for the growth of the coating. For aluminide coatings of the same base alloy (e.g., NiAl on nickel-based alloys), only aluminum need be added to form an aluminide phase, although other elements are often added for improved properties. However, for aluminide coatings with a different base than the substrate (e.g., NiAl on steel), both elements of the aluminide phase (e.g., nickel and aluminum for NiAl on steel), must be provided, which complicates the coating process.

1.25.4.1 Aluminide Coatings with Same Base as Substrate

Increasing the aluminum concentration at the surface is especially useful in the titanium–aluminum system, since, as discussed earlier, TiAl is a borderline alumina-former. The formation of $TiAl_3$ coatings on TiAl-based alloys can improve oxidation resistance.[83] A similar approach can be used in the nickel or iron systems, but an increase in the aluminum content of NiAl- or FeAl-based alloys is less critical, because, with the lower stability of the nickel- and iron-oxide phases, the alumina phase is more stable and the additional aluminum content only provides significant benefit for long exposure times when aluminum depletion occurs. However, aluminide coatings can significantly improve the oxidation resistance of metallic alloys with little or no aluminum. For example, aluminide coatings have been used for more than 30 years to improve the oxidation resistance of superalloys.[84] Such alloys contain several alloying additions, the concentrations of which can change during the diffusion process, and can lead to undesired microstructural changes, such as the formation of topographically close packed (TCP) phases.[85] Similarly, the corrosion resistance of steel can be improved by aluminization to form an iron aluminide coating. In this case, the presence of carbon, which can lead to undesired carbide precipitation, places restrictions on the coating process.[86] In the following sections, the application of aluminide coating processes to simple and complicated alloy systems will be discussed. While alloying additions from the substrate alloy can complicate the coating process, the coating process can also be used to introduce desired alloying additions for improved coating performance.

1.25.4.1.1 Simple aluminide coatings

The aluminum for growth of the aluminide coating can be introduced through several different methods. One method is to sputter an aluminum, or aluminum-containing, layer on the surface of the alloy. The sputtering process is typically followed by a high temperature anneal for diffusion of the aluminum into the alloy. Another method is to place the substrate in molten aluminum, which provides good contact with the alloy as well as protection from oxidation. The most common method for producing aluminide coatings, however, is pack cementation.

The pack in the pack cementation process consists of 10–30% of an aluminum source (aluminum metal or aluminum-containing alloy) and a few percent of an activator (typically a halide species), which are dispersed in an inert filler (typically alumina). Upon heating, aluminum halide gaseous species are formed and transport aluminum to the substrate material. Pure aluminum can be used as the aluminum source for process temperatures below the melting point of aluminum, while aluminum-containing alloys must be used for higher temperature deposition. Pack cementation processes are referred to as high activity or low activity, based on the aluminum activity in the aluminum source. Coatings formed in a high-activity process are inward-growing as aluminum diffuses into the alloy. Low-activity processes (e.g., $Al/Ni < 1$), however, result in the outward growth as both elements (e.g., Ni and Al) are deposited. The low-activity process is commonly referred to as chemical vapor deposition (CVD), as both, or all, components of the coating are deposited. One of the advantages of a low-activity process is that impurity elements, such as sulfur and phosphorus, are removed during the process, so that high-quality coatings are produced. The low-activity CVD process is more complicated, but provides flexibility to deposit a variety of coatings.[87]

1.25.4.1.2 Alloyed aluminide coatings

As with bulk materials, the corrosion resistance of aluminide coatings can be improved with alloying additions, so the coating processes are often modified to incorporate other elements in the coating. One example is the introduction of chromium to improve

the resistance to corrosion in chlorine-containing environments. Chromium, as well as reactive element additions, can be deposited simultaneously with aluminum in a pack cementation process by using an alloy containing the desired elements as the source.[88] This process is complicated when steel is used as the substrate, because carbon in the steel reacts with chromium to form chromium carbides. For low carbon contents, the carbide particles form separate precipitates, but for higher carbon contents, even as low as 0.2%, a chromium carbide layer forms and disrupts the coating process. This problem can be overcome by using a two-step process, which is illustrated in **Figure 12**.[89] In the first step, the pack is heated to a relatively low temperature where there is a significant partial pressure of the aluminum chloride vapor species, but the vapor species of the chromium chloride species is low, so that aluminum, but not chromium, is deposited. Aluminum stabilizes the ferrite structure, so dissolution of aluminum causes a phase change in the iron from austenite to ferrite. Because of the low carbon solubility of ferrite, carbon is rejected into the austenite layer below the ferrite. In the second step, the pack is heated to a higher temperature where the partial pressure of the chromium vapor species increases, so chromium is now deposited and diffuses in the ferrite. Because of the low concentration of carbon in the ferrite, chromium carbides do not form and a high-quality coating is produced. A similar process has been used with a nickel-based superalloy to produce a coating with an outer high-chromium layer, which provides good hot corrosion resistance.[90] Chromium, in larger amounts, can also improve the oxidation resistance of titanium aluminide alloys and is often incorporated in titanium aluminide coatings.

Another element that is commonly added to aluminide coatings is silicon. Silicon additions result in the formation of silica, which provides excellent oxidation resistance because of its low oxygen permeability and is particularly resistant to acidic melts. Like chromium, silicon can be added in the pack cementation process, and, also like chromium, a two-step process can be used to produce a coating with the desired composition distribution.[91] Although silicon can be introduced through the vapor phase, the eutectic in the aluminum–silicon system provides an opportunity for the introduction of silicon and aluminum through liquid-phase processes. This includes simple dipping processes as well as surface melting processes, such as laser surface melting. Siliconizing is most widely used for titanium aluminide alloys. Although such processes can result in an outer titanium silicide layer, the scale formed during oxidation is similar to that formed on uncoated titanium aluminide alloys. The outer scales consist of titanium and aluminum oxides, but a silica layer is formed in the inner portion of the scale and improves the oxidation resistance.[92]

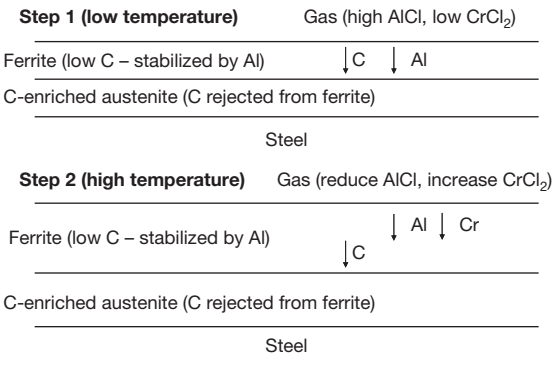

Figure 12 Two-step process for codeposition of aluminum and chromium on steel.[89]

Aluminide coatings can also be used as the bond coating between superalloys and thermal barrier coatings (TBC). In this application, in addition to the inherent oxidation behavior, the interface between the thermally grown oxide (TGO) on the bond coating and the TBC must be strong, so that the TBC remains attached to the alloy during use (particularly during thermal cycling). Thus, the adherence of the scale is of greater importance than the growth rate, because a thicker TGO is less of a problem than the loss of the TBC. Because of the importance of adherence, one of the common additions to NiAl bond coating is platinum.[93,94] Platinum-containing coatings maintain good scale adherence even with significant amounts of sulfur, which, as discussed earlier, generally degrades scale adherence. Platinum is typically added as a coating prior to aluminization. There are several commercial pack cementation processes for producing platinum-containing coatings, including high-activity inward-growing coating with the substrate in the pack (e.g., Chromalloy RT22), high-activity inward-growing coating with the substrate above the pack (e.g., Howmet SS82A), and low-activity outward-growing coating (e.g., Thermatech MDC150L).[95] The addition of platinum eliminates void formation at the coating–TGO interface, but voids are observed at the alloy–coating interface, as shown schematically in **Figure 13**.[96] Void formation beneath the scale can lead to spallation of the scale during thermal cycling, which is especially critical if the coating is used as a bond coat, since such spallation will lead to loss of the TBC. Void formation at the coating–scale interface has been

attributed to both the Kirkendall effect and stresses associated with the transformation of β-NiAl to γ′-Ni_3Al.[97] The void formation at the alloy–coating interface is less critical than that at the coating–scale interface; as both NiAl and Ni_3Al are more ductile than alumina, crack propagation is less likely.

As mentioned earlier, large amounts of platinum additions can lead to the formation of $PtAl_2$, which in addition to improving the supply of aluminum needed to maintain an α-Al_2O_3 layer, also limits the transport of transition metal impurities outward from the aluminide coating into the scale. This is particularly important in coatings for superalloys, which contain elements that can degrade the corrosion protection provided by the coating.

Other noble metals used in NiAl bond coatings include rhenium and palladium. Rhenium acts like platinum in that it promotes the formation of an α-Al_2O_3 layer and forms a compound that acts as a diffusion barrier. Palladium helps to stabilize the NiAl phase and maintain sufficient aluminum in the scale. Noble metals can also be used with reactive elements. For example, hafnium and platinum have been used together, where, in addition to improving the oxidation resistance, the formation of a Hf–Pt layer provides a diffusion barrier to prevent loss of aluminum and incorporation of transition metals in the coating and scale.

Titanium aluminide alloys can also be used with TBCs. The TBC has relatively good adherence to the alloy, which is attributed to the better match in the coefficients of thermal expansion as compared to nickel-based superalloys. However, a bond coat, such as TiAlCr or $TiAl_3$, is needed for long lifetimes.[98]

1.25.4.2 Aluminide Coatings with Different Base as Substrate

Deposition of an aluminide phase of an element not in the substrate can provide useful properties, but is more complicated than simply increasing the aluminum content of the surface. For example, as discussed earlier, alumina is more stable on NiAl than on TiAl, so NiAl can provide improved long-term corrosion protection, but TiAl is less dense and has better specific strength. Titanium aluminide coated with NiAl combines the advantages of the two materials and can be produced by first electroplating the TiAl with nickel and then aluminizing the nickel layer by pack cementation.[99] The same process can be used for applying a NiAl coating to steel and allows for a reduction in the processing temperature to avoid grain growth or carbide formation in the steel substrate.[100] Similarly, steel, and other non-titanium alloys, can be coated with titanium aluminide by first depositing a layer of titanium and then aluminizing the titanium to form the corrosion resistant titanium aluminide coating.

An analogous process can be used to produce a ruthenium aluminide coating on a nickel-base superalloy.[101] In this case, the coating microstructure depends on whether the ruthenium layer is aluminized using a high-activity pack cementation process or a low-activity CVD process. As shown schematically in **Figure 14**, in a high-activity process, the coating grows by inward diffusion of aluminum, which results in an outer layer of RuAl and an inner layer of NiAl that are separated by a zone containing Ru(Al,Ta) precipitates. In a low-activity process, the coating grows by outward diffusion of aluminum, which results in an outer layer of NiAl. The coating with the outer NiAl layer has superior oxidation resistance. However, the presence of the inner RuAl layer is beneficial as it acts as a diffusion barrier, which can prevent undesired elements from the substrate from entering the outer coating and oxidation scale.

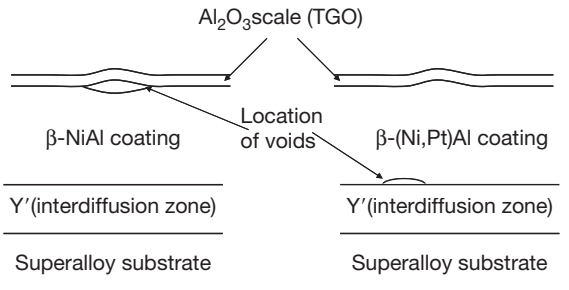

Figure 13 Effect of platinum additions on pore formation in β-nickel aluminide coating after oxidation at 1150 °C.[96]

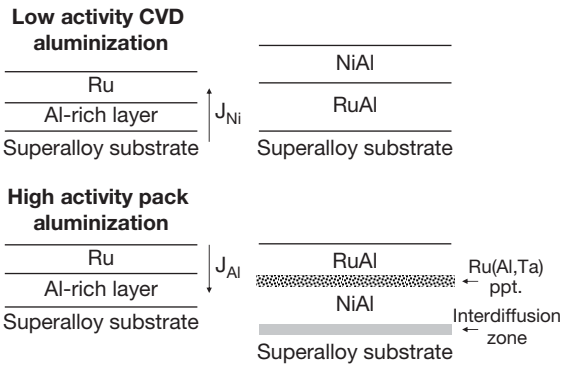

Figure 14 Ruthenium-modified coatings by low-activity CVD aluminization and high-activity pack aluminization.[101]

1.25.5 Summary and Conclusions

Intermetallic aluminide alloys are attractive for high temperature applications. The corrosion resistance of aluminide alloys is achieved by the formation and maintenance of a protective alumina, or alumina-containing, scale. Of the three common aluminide systems, nickel, iron, and titanium, the formation of an alumina scale is most challenging on titanium aluminide alloys because of the thermodynamic stability of titanium oxide. However, titanium aluminide alloys also offer the greatest benefit in terms of improvements in specific properties. In addition to the initial thermodynamic stability of the oxides, long-term corrosion resistance requires maintenance of the protective scale in the presence of stresses (thermal and transformation) and changes in alloy composition with time. In applications where the intermetallic alloys have inadequate mechanical properties for use as structural components, they can be applied as coatings to provide corrosion resistance for structural alloys. Improvements in corrosion resistance can be achieved with alloying additions, but the effects of these elements on other factors, such as mechanical properties, cost, and manufacturability, must also be considered.

References

1. Lasalmonie, A. *Intermetallics* **2006**, *14*, 1126–1129.
2. Dimiduk, D. M. *Mater. Sci. Eng.* **1999**, *A263*, 281–288.
3. Stoloff, N. S.; Sikka, V. A. *Physical Metallurgy and Processing of Intermetallic Compounds*; Chapman & Hall: New York, NY, 1996.
4. Brady, M. P.; Gleeson, B.; Wright, I. G. *JOM* **2000**, *52*(1), 16–21.
5. Meier, G. H.; Pettit, F. S. *Mater. Sci. Eng. A* **1992**, *153*, 548–560.
6. Doychak, J. In *Intermetallics Compounds Principles and Practice. Vol. 1. Principles*; Westbook, J. H., Fleischer, R. L., Eds.; John Wiley, 1995; pp 977–1016.
7. Cathcart, J. V. *Mater. Res. Soc. Proc.* **1985**, *39* (High-Temperature Ordered Intermetallic Alloys), 445–459.
8. Grabke, H. J. *Intermetallics* **1999**, *7*, 1153–1158.
9. Tottorelli, P. F.; Natesan, K. *Mater. Sci. Eng. A* **1998**, *258*, 115–125.
10. Pettit, F. S. *Trans. Metall. Soc. AIME* **1967**, *239*, 2196–1305.
11. Godlewska, E. *Electrochem. Soc. Proc.* **2003**, *16* (High Temperature Corrosion and Materials Chemistry IV), 51–61.
12. Katsman, A.; Grabke, H. J.; Levin, L. *Oxidation of Metals* **1996**, *46*, 313–331.
13. Liu, Z.; Gao, W. *Intermetallics* **2000**, *8*, 1385–1391.
14. Choi, S. C.; Cho, H. J.; Kim, Y. J.; Lee, D. B. *Oxidation Metals* **1996**, *46*, 51–72.
15. Hou, P. Y.; Niu, Y.; Van Lienden, C. *Oxidation Metals* **2003**, *59*, 41–61.
16. Pint, B. A. *Oxidation Metals* **1997**, *47*, 303–328.
17. Yang, J. C.; Nadarzinski, K.; Schumann, E.; Rühle, M. *Scripta Metall. Mater.* **1995**, *33*, 1043–1048.
18. McCarty, K. F. *Surf. Sci.* **2001**, *474*, L165–L172.
19. Doychak, J.; Smialek, J. L.; Mitchell, T. E. *Metall. Trans. A* **1989**, *20A*, 499–518.
20. González-Carrasco, J. L.; Pérez, P.; Adeva, P.; Chao, J. *Intermetallics* **1999**, *7*, 69–78.
21. Grabke, H. J.; Brumm, M.; Steinhorst, M. *Mater. Sci. Technol.* **1992**, *8*, 339–344.
22. Rivoaland, L.; Maurice, V.; Josso, P.; Bacos, M. P.; Marcus, P. *Oxidation Metals* **2003**, *60*, 159–178.
23. Cadoret, Y.; Monceau, D.; Bacos, M. P.; Josso, P.; Maurice, V.; Marcus, P. *Oxidation Metals* **2005**, *64*, 185–205.
24. Heuer, A. H.; Reddy, A.; Hovis, D. B.; Veal, B.; Paulikas, A.; Vlad, A.; Rühle, M. *Scripta Mater.* **2006**, *54*, 1907–1912.
25. Zhang, Z. G.; Hou, P. Y. *Mater. Sci. Eng. A* **2005**, *391*, 1–9.
26. Tolpygo, V. K.; Clarke, D. R. *Acta Mater.* **2004**, *52*, 5129–5141.
27. Doychak, J.; Rühle, M. *Oxidation Metals* **1989**, *31*, 431–452.
28. Yang, J. C.; Schumann, E.; Levin, I.; Rühle, M. *Acta Mater.* **1998**, *46*, 2195–2201.
29. Bobeth, M.; Pompe, W.; Schumann, E.; Rühle, M. *Acta Metall. Mater.* **1992**, *40*, 2669–2676.
30. Balmain, J.; Huntz, A. M. *Oxidation Metals* **1996**, *45*, 183–196.
31. Yi, H. C.; Smeltzer, W. W.; Petric, A. *Oxidation Metals* **1996**, *45*, 281–299.
32. Kartono, R.; Young, D. J. *Electrochem. Soc. Proc.* **2004**, *16*(High Temperatures Corrosion and Materials Chemistry V), 43–55.
33. Pint, B. A.; Haynes, J. A.; Zhang, Y.; More, K. L.; Wright, I. G. *Surf. Coatings Tech.* **2006**, *201*, 3882–3886.
34. Pint, B. A.; Regina, J. R.; Prussner, K.; Chitwood, L. D.; Alexander, K. B.; Tortorelli, P. F. *Intermetallics* **2001**, *9*, 735–739.
35. Zhang, Z. F.; Thaidigsmann, K.; Ager, J.; Hou, P. Y. *J. Mater. Res.* **2006**, *21*, 1409–1419.
36. Hou, P. Y. *J. Am. Ceram. Soc.* **2003**, *86*, 660–668.
37. Kuenzly, J. D.; Douglass, D. L. *Oxidation Metals* **1974**, *8*, 139–178.
38. Pint, B. A. *Oxidation Metals* **1996**, *45*, 1–37.
39. Schumann, E.; Yang, J. C.; Rühle, M.; Graham, M. J. *Oxidation Metals* **1996**, *46*, 37–49.
40. Pint, B. A.; Hobbs, L. W. *Oxidation Metals* **2004**, *61*, 273–292.
41. Berlanga, M.; González-Carrasco, J. L.; Montealegre, M. A.; Muñoz-Morris, M. A. *Intermetallics* **2004**, *13*, 205–212.
42. Montealegre, M. A.; Strehl, G.; González-Carrasco, J. L.; Borchardt, G. *Intermetallics* **2005**, *13*, 896–906.
43. Taniguchi, S.; Shibata, T. In *Oxidation of High-Temperature Intermetallics*; Grobstein, T., Doychak, J., Eds.; The Minerals, Metals & Materials Society: Warrendale, PA, **1989**; pp 17–29.
44. Pint, B. A.; Wright, I. G. *Materials Science Forum* **2004**, *461–464*(High Temperature Corrosion and Protection of Materials 6, Part 2), 799–806.
45. Pint, B. A.; Schneibel, J. H. *Scripta Mater.* **2005**, *52*, 1199–1204.
46. Pérez, P.; Adeva, P. *Oxidation Metals* **2006**, *65*, 15–38.
47. Hou, P. Y.; McCarty, K. F. *Scripta Mater.* **2006**, *54*, 937–941.

48. Fergus, J. W. *Mater. Sci. Eng. A* **2002**, *338*, 108–125.
49. Brady, M. P.; Pint, B. A.; Tortorelli, P. F.; Wright, I. G.; Hanrahan, R. J., Jr. In *Corrosion and Environmental Degradation, Vol. II*; Schütze, M., Ed.; Wiley-VCH Verlag GmbH, Weinheim, Germany, 2000; pp 229–326.
50. Rahmel, A.; Quadakkers, W. J.; Schütze, M. *Mater. Corros.* **1995**, *46*, 271–285.
51. Leyens, C. In *Titanium and Titanium Alloys*; Leyens, C., Peters, M., Eds.; Wiley-VCH, 2003; pp 187, 230.
52. Haanappel, A. C.; Hofman, R.; Sunderkötter, J. D.; Glatz, W.; Clemens, H.; Stroosnijder, M. F. *Oxidation Metals* **1997**, *48*, 263–287.
53. Dettenwanger, F.; Schumann, E.; Rühle, M.; Rakowski, J.; Meier, G. H. *Oxidation Metals* **1998**, *50*, 269–307.
54. Shemet, V.; Tyagi, A. K.; Becker, J. S.; Lersch, P.; Singheiser, L.; Quadakkers, W. J. *Oxidation Metals* **2000**, *54*, 211–235.
55. Tang, Z.; Shemet, V.; Niewolak, L.; Singheiser, L.; Quadakkers, W. J. *Intermetallics* **2003**, *11*, 1–8.
56. Kumagai, M.; Shibue, K.; Kim, M. S.; Yonemitsum, M. *Intermetallics* **1996**, *4*, 557–566.
57. Kim, Y. J.; Kim, I. B.; Kim, M. S.; You, B. D.; Han, W.; Hwang, W. S. *Metals Mater.* **2000**, *6*, 455–459.
58. Donchev, A.; Richter, E.; Schütze, M.; Yankov, R. *Intermetallics* **2006**, *14*, 1136–1142.
59. Donchev, A.; Gleeson, B.; Schütze, M. *Intermetallics* **2003**, *11*, 387–398.
60. Yoshihara, M.; Taniguchi, S.; Zhu, Y. C. *Metall. Mater. Trans. A* **2003**, *34A*, 2253–2261.
61. Felten, E. J.; Pettit, F. S. *Oxidation of Metals* **1976**, *10*, 189–223.
62. Dickey, E. C.; Pint, B. A.; Alexander, K. B.; Wright, I. G. *J. Mater. Res.* **1999**, *14*, 4531–4540.
63. Soldera, F.; Ilić, N.; Brännström, S.; Barrientos, I.; Gobran, H.; Mücklich, F. *Oxidation Metals* **2003**, *59*, 529–542.
64. Ilić, N.; Soldera, F.; Mücklich, F. *Intermetallics* **2005**, *13*, 444–453.
65. Cao, F.; Nandy, T. K.; Stobbe, D.; Pollock, T. M. *Intermetallics* **2004**, *15*, 34–43.
66. Kuppusami, P.; Murakami, H. *Surf. Coatings Technol.* **2004**, *186*, 377–388.
67. Natesan, K.; Datta, P. K. In *Intermetallic Compounds, Principles and Practice, Vol. 3, Progress*; Westbrook, J. H., Fleischer, R. L., Eds.; Wiley, 2002; pp 707–719.
68. Natesan, K. *Oxidation Metals* **1988**, *30*, 53–83.
69. Kai, W.; Chang, M. T.; Bai, C. Y. *Oxidation Metals* **2001**, *56*, 191–214.
70. Kai, W.; Huang, R. T. *Oxidation Metals* **1997**, *47*, 59–86.
71. Kai, W.; Lee, S. H.; Chiang, D. L.; Chu, J. P. *Mater. Sci. Eng. A* **1998**, *258*, 146–152.
72. Godlewska, E. *Mater. Corros.* **1997**, *48*, 687–699.
73. Izumi, T.; Yoshioka, T.; Hayashi, S.; Narita, T. *Intermetallics* **2000**, *8*, 891–901.
74. González-Rodríguez, J. G.; Luna-Ramírez, A.; Salazar, M.; Porcayo-Calderon, J.; Rosas, G.; Martínez-Villafañe, A. *Mater. Sci. Eng. A* **2005**, *399*, 344–350.
75. Lee, W. H.; Lin, R. Y. *Mater. Chem. Phys.* **2003**, *77*, 86–96.
76. Tang, Z.; Wang, F.; Wu, W. *Oxidation Metals* **1999**, *51*, 235–250.
77. Kim, I.; Cho, W. D. *Mater. Sci. Eng. A* **1999**, *264*, 269–278.
78. Nicholls, J. R.; Leggett, J.; Andrews, P. In *Oxidation of Intermetallics*; Grabke, H. J., Schütze, M., Eds.; Wiley-VCH Verlag GmbH: Weinheim, Germany, 1998; pp 329–344.
79. Li, Y. S.; Spiegel, M. *Corrosion Sci.* **2004**, *46*, 2009–2023.
80. Zhang, K.; Gao, W.; Liang, J. *Intermetallics* **2004**, *12*, 539–544.
81. Liang, J.; Gao, W.; Li, Z.; He, Y. *Mater. Lett.* **2004**, *58*, 3280–3284.
82. Amaya, M.; Espinosa-Medina, M. A.; Porcayo-Calderon, J.; Martinez, L.; González-Rodriguez, J. G. *Mater. Sci. Eng. A* **2003**, *349*, 12–19.
83. Gauthier, V.; Dettenwanger, F.; Schütze, M.; Quadakkers, W. J. *Oxidation Metals* **2003**, *59*, 233–255.
84. Lindblad, N. R. *Oxidation Metals* **1969**, *1*, 143–170.
85. Rae, C. M. F.; Hook, M. S.; Reed, R. C. *Mater. Sci. Eng. A* **2005**, *396*, 231–239.
86. Xiang, Z. D.; Datta, P. K. *Metall. Mater. Trans. A* **2006**, *37A*, 3347–3358.
87. Warnes, B. M. *Surf. Coatings Tech.* **2003**, *163–164*, 106–111.
88. Bianco, R.; Rapp, R. A. *J. Electrochem. Soc.* **1993**, *140*, 1181–1190.
89. Zheng, M.; Rapp, R. A. *Oxidation Metals* **1998**, *49*, 19–31.
90. Bai, C.-Y.; Luo, Y.-J.; Koo, C.-H. *Surf. Coatings Technol.* **2004**, *183*, 74–88.
91. Brossard, J. M.; Hierro, M. P.; Trilleros, J. A.; Carpintero, M. C.; Sánchez, L.; Bolívar, F. J.; Pérez, F. J. *Surf. Coating Technol.* **2006**, *201*, 5743–5750.
92. Xiong, H. P.; Mao, W.; Xie, Y.-H.; Ma, W.-L.; Chen, Y.-F.; Li, X.-H.; Li, J.-P.; Cheng, Y.-Y. *Acta Mater.* **2004**, *52*, 2605–2620.
93. Pint, B. A. *Surf. Coatings Technol.* **2004**, *188–189*, 71–78.
94. Pint, B. A.; Speakman, S. A.; Rawn, C. J.; Zhang, Y. *JOM* **2006**, *58*(1), 47–52.
95. Angenete, J.; Stiller, K.; Langer, V. *Oxidation Metals* **2003**, *60*, 47–82.
96. Zhang, Y.; Haynes, J. A.; Lee, W. Y.; Wright, I. G.; Pint, B. A.; Cooley, K. M.; Liaw, P. K. *Metall. Mater. Trans. A* **2001**, *32A*, 1727–1741.
97. Angenete, J.; Stiller, K.; Bakchinova, E. *Surf. Coatings Technol.* **2004**, *176*, 272–283.
98. Leyens, C.; Braun, R.; Fröhlich, M.; Hovsepian, P. Eh. *JOM* **2006**, *58*(1), 17–21.
99. Izumi, T.; Nishimoto, T.; Narita, T. *Intermetallics* **2005**, *13*, 727–732.
100. Xiang, Z. D.; Datta, P. K. *J. Mater. Sci.* **2005**, *40*, 1959–1966.
101. Tryon, B.; Feng, Q.; Wellman, R. G.; Murphy, K. S.; Yang, J.; Levi, C. G.; Nicholls, J. R.; Pollock, T. M. *Metall. Mater. Trans. A* **2006**, *37A*, 3347–3358.

1.17 Oxidation in Steam and Steam/Hydrogen Environments

W. J. Quadakkers and J. Żurek
Forschungszentrum Jülich, Institute of Energy Research (IEF-2), 52428 Jülich, Germany

Abbreviations

BC Bond coat
EDX Energy dispersive X-ray spectroscopy
IEP Isoelectric point
ODS Oxide dispersion strengthened
PSEs Protective scale forming elements
REs Reactive elements
SEM Scanning electron microscopy
SNMS Sputtered neutrals mass spectrometry
SOFC Solid oxide fuel cell
TBC Thermal barrier coating
TEM Transmission electron microscopy

XPS X-RAY photoelectron spectroscopy
XRD X-Ray diffraction

Symbols

$h^{\bullet}$ Positive hole
$k_p(K_p)$ Parabolic rate constant ($mg^2\,cm^{-4}\,s^{-1}$, $\mu m^2\,h^{-1}$)
n Oxidation rate exponent
p Vapor pressure (bar, Pa)
p_i Partial pressure of component (bar, Pa)
t Time (h, s)
x Material loss (cm, μm)
x Oxide scale thickness (cm, μm)
A Surface area (m^2, cm^2)
$\tilde{D}_{Fe-Cr}$ Alloy interdiffusion coefficient ($m^2\,s^{-1}$)
D_O Diffusivity of oxygen ($m^2\,s^{-1}$)
$H_i^{\bullet}$ Interstitial proton
J_{O_2} Oxygen flux ($mol\,cm^{-2}\,s^{-1}$)
K_{15} Equilibrium constant for reaction (15)
K Oxidation rate ($mm^2\,h^{-1}$)
K' Oxidation parameter
M Molecular mass ($g\,mol^{-1}$)
$N_{Cr}^{(1)}, N_{Cr}^{(2)}$ Critical Cr mole fraction for external scale formation
$N_O^{(s)}$ Oxygen solubility (mol/mol)
Q Activation energy ($J\,mol^{-1}$)
R Universal gas constant ($8.314\,J\,mol^{-1}\,K^{-1}$)
T Temperature (K, °C)
V_{Cr}''' Cr vacancy
V_m Molar volume of alloy ($cm^3\,mol^{-1}$)
$V_O^{\bullet\bullet}$ Oxygen vacancy
ΔG^o Standard free energy ($J\,mol^{-1}$)
Δm Weight change ($mg\,cm^{-2}$)

1.17.1 Introduction

In practical applications, metallic construction materials for high temperature components are subjected to a large variety of service environments. Stability and growth rate of the oxide scales that form on the component surfaces during exposure are commonly described on the basis of equilibrium oxygen partial pressures of the various environments. However in many of these applications, water vapor has been found to substantially alter the technologically relevant properties, mainly growth rate and adherence, of the surface oxides.[1] Thereby it has to be considered whether water vapor can be present in the service environment as the main oxidizing gas species or in addition to larger amounts of 'free oxygen.' From the viewpoint of equilibrium oxygen partial pressure and oxygen/water vapor ratio, the service environments may be divided into four groups:

A. Wet air or gases originating, for example, from combustion processes with a high oxygen (air) to fuel ratio. In such environments the oxygen content may be as high as 10–20%.[2]
B. Combustion or exhaust gases originating from combustion processes with low oxygen (air) to fuel ratio. In such gases, which, for example, prevail in car exhaust gas or in the combustion gas of lignite/coal fired power plants, the oxygen content may be as low as 1% or even smaller.[3]
C. Environments based on steam such as, for example, prevailing in chemical processes or in steam power plants.[4]
D. Service environments that contain hydrogen in addition to water vapor which may prevail in chemical plants, gasification plants and (solid oxide) fuel cells.[5]

In the first two types of environments (A and B), the equilibrium oxygen partial pressure is hardly affected by the presence of water vapor, whereas in environments C and D it is mainly governed by the absolute water vapor partial pressure or the H_2O/H_2 ratio. The equilibrium oxygen partial pressures in these environments are orders of magnitude smaller than in gases of type A and B. Consequently, oxide phases and vapor pressures of volatile species that form by reaction of metallic components with gases of group A and B may substantially differ from those formed in gases of groups C and D. When comparing the oxidation behavior of metallic materials in dry oxygen with that in water vapor-containing gases, it is therefore important to distinguish between the various types of water vapor-containing atmospheres.

The following sections deal with the oxidation properties of metallic construction materials in gases of type C and D. The main emphasis will be put on describing the oxidation mechanisms in these environments compared to the behavior in dry oxygen, oxygen–inert gas mixtures or air. The examples shown will mainly deal with alloy systems that are commonly used as construction materials in practical applications where typical application temperature ranges for the respective materials are being considered.

Nomenclature

In the following sections, the behavior of various materials in $(Ar/N_2-)H_2O$ and $(Ar/N_2-)H_2-H_2O$ is

compared with that in air, oxygen or various mixtures of oxygen and inert gases. The equilibrium oxygen partial pressures of the two mentioned H_2O-containing gas types at, for example, 800 °C are typically in the range 10^{-8} to 10^{-18} bar. This is obviously orders of magnitude lower than the p_{O_2} in the mentioned O_2-based gases. Therefore, in the following discussion the mentioned H_2-containing gases are frequently termed 'low-p_{O_2} gases,' and the O_2-based environments 'high-p_{O_2} gases.'

1.17.2 Thermodynamic Considerations

1.17.2.1 Thermodynamics of the Gas Atmosphere and Stability of Solid Oxides

In mixtures of hydrogen and water vapor, the oxygen partial pressure is substantially lower than in air where p_{O_2} is approximately 0.2 bar. The equilibrium oxygen partial pressure can be derived from:

$$2H_2O \Leftrightarrow 2H_2 + O_2 \qquad [1]$$

and

$$p_{O_2} = \left\{\exp\left(\frac{-\Delta G^\circ}{RT}\right)\right\} / \left(\frac{p_{H_2}}{p_{H_2O}}\right)^2 \qquad [2]$$

in which ΔG° is the standard free energy of formation.[6]

In pure steam or Ar–H_2O mixtures, the equilibrium hydrogen and oxygen partial pressures are similar, but in the calculations the change in water vapor content due to formation of H_2, O_2, and other gas species such as $HO_2^{(g)}$ and $OH^{(g)}$ has to be taken into account to calculate the oxygen partial pressure of the fully equilibrated gas or gas mixture. The equilibrium oxygen partial pressure in steam and in gases with various H_2/H_2O ratios in the temperature range 500–1100 °C is presented in Figure 1.

Figure 2 compares the equilibrium oxygen partial pressure of an Ar–50 vol.% H_2O mixture and an Ar–H_2O/H_2 mixture (H_2O/H_2 ratio = 1/1) with that of the dissociation pressures of selected oxides. It is apparent that oxides of Cr, Al, Si, and Ti are stable in both atmospheres in the temperature range 500–1100 °C. Fe will easily oxidize in Ar–H_2O but only at lower temperatures in the Ar–H_2–H_2O mixture. In the latter gas, Ni and Co will not oxidize.

Equation [2] reveals that the equilibrium oxygen partial pressure of an H_2O/H_2 mixture is governed by the H_2O/H_2 ratio and thus independent of the total gas pressure. This is not the case in pure steam or in mixtures of water vapor with an inert gas.[8] In these gases, the equilibrium oxygen partial pressure increases with increasing total pressure (Figure 3).

1.17.2.2 Volatile Reaction Products in H_2O-Containing Gases

The oxidation behavior of metallic materials may be substantially affected by the formation of volatile oxides. Well known examples are $CrO_3^{(g)}$, which

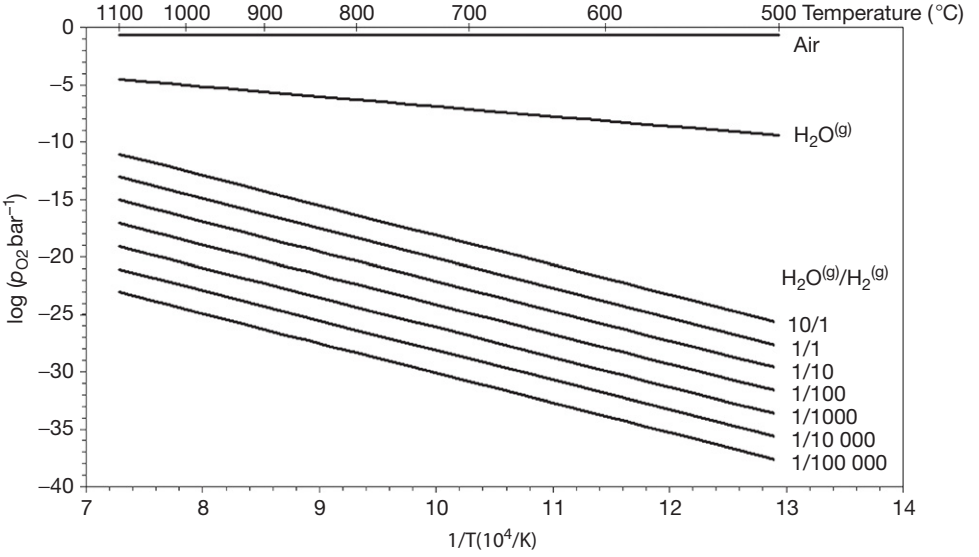

Figure 1 Equilibrium oxygen partial pressure as function of temperature in various gas atmospheres (calculations carried out with the Program Fact Sage[7]).

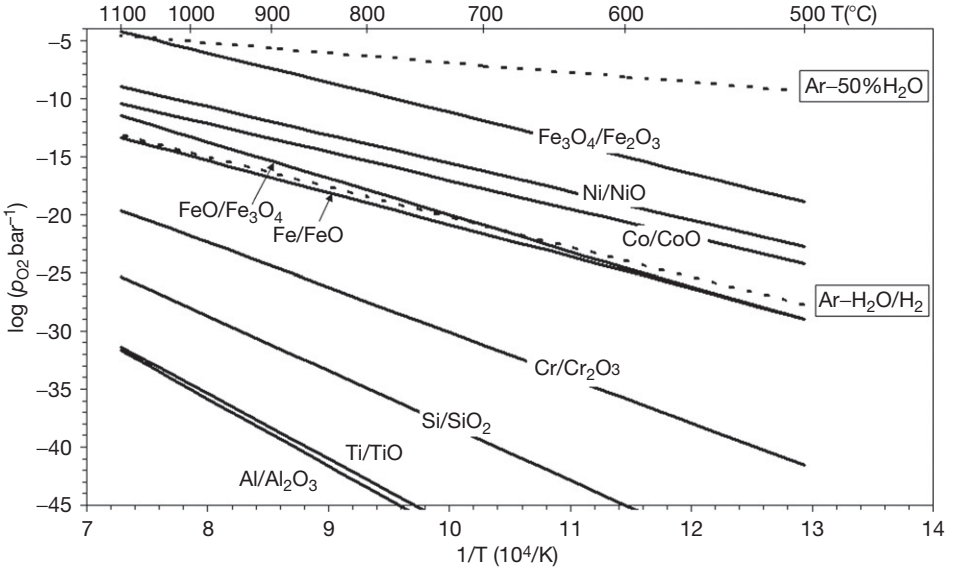

Figure 2 Comparison of the equilibrium oxygen partial pressure of an Ar–50 vol.% H_2O mixture and an Ar–H_2O/H_2 mixture (H_2O/H_2 ratio = 1:1) with that of the dissociation pressures of selected oxides (calculations carried out with the Program Fact Sage[7]).

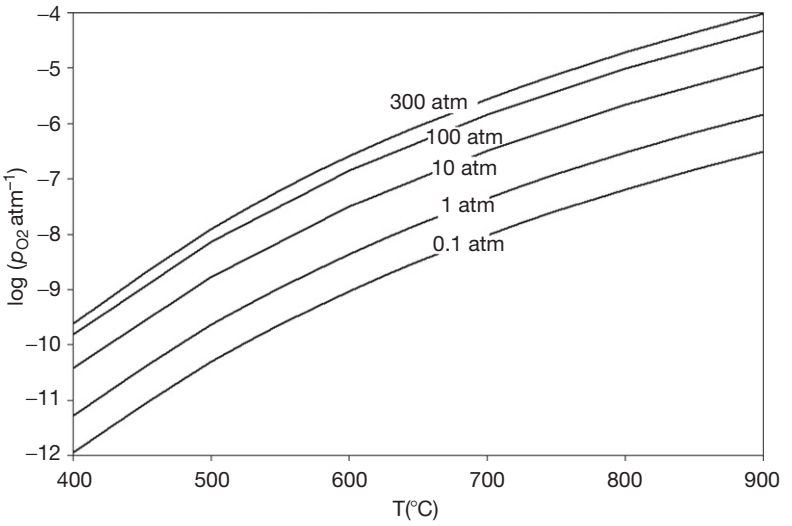

Figure 3 Calculated equilibrium oxygen partial pressure in steam at various total pressures. Calculations carried out with the Program Fact Sage [7].

forms in equilibrium with Cr_2O_3, and $SiO^{(g)}$ in equilibrium with Si or SiO_2. The vapor pressure of $SiO^{(g)}$ increases with decreasing p_{O_2}, whereas $CrO_3^{(g)}$ becomes more significant at high p_{O_2}. In case of competition between oxide scale growth and volatilization, a simple Tedmon model,[9] in which the overall rate of metal wastage is a function of the parabolic rate constant for oxide growth and the linear rate constant for volatilization, is frequently used to describe the observed kinetics. In the presence of water vapor, a number of additional volatile species may form. For the three most important protective surface oxides on metallic materials, alumina, chromia, and silica, the following reactions in equilibrium with the respective oxide phases seem to be the most important ones:[10]

$$1/2Cr_2O_3 + H_2O^{(g)} + 3/4O_2^{(g)} = CrO_2(OH)_2^{(g)} \quad [3]$$

$$SiO_2 + 2H_2O^{(g)} = Si(OH)_4^{(g)} \quad [4]$$

$$SiO_2 + H_2O^{(g)} = SiO(OH)_2^{(g)} \quad [5]$$

$$1/2Al_2O_3 + 3/2H_2O^{(g)} = Al(OH)_3^{(g)} \quad [6]$$

Various data sets[11] exist for vapor pressure data of these volatile oxyhydroxides, and in the case of $CrO_2(OH)_2$ this literature data substantially differ (**Figure 4**). More recent data show, for example, for the partial pressure of this oxyhydroxide at 850 °C in Air + 2% H_2O, a variation between 10^{-8} and 10^{-9} bar.[12] On the basis of own experimental data and an extensive evaluation of the various data sources, Opila[11] showed that the rates of evaporation increase in the following order: $Al(OH)_3^{(g)} < Si(OH)_4^{(g)} < CrO_2(OH)_2^{(g)}$, as shown in **Figure 5**. It is apparent from eqn. [3] that the loss of chromium by volatilization of $CrO_2(OH)_2^{(g)}$ should have a significant impact only on the oxidation process in gases in which partial pressures of both oxygen and water vapor are high,[13] and it should not be significant for the overall oxidation process in the low-p_{O_2} gases considered in the present paper. In such gases, in fact $Cr(OH)_3^{(g)}$ is the most volatile chromium compound over the entire considered temperature range but the vapor pressure at 700 °C, for example, is only about 10^{-13} atm. Galerie *et al.*,[14] Michalik *et al.*,[15] and Ehlers *et al.*[16] confirmed that at low-p_{O_2} $CrO_2(OH)_2$ does not possess sufficient volatility to be considered, for instance, as a possible cause of breakaway oxidation of ferritic steels in water vapor. Young and Pint[17] showed that the volatile Cr oxyhydroxide may become significant in high-pressure steam.

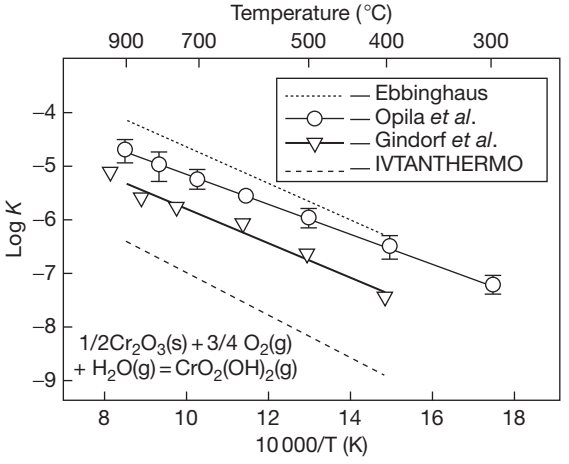

Figure 4 Temperature dependence of the equilibrium constant K for the reaction $1/2Cr_2O_3^{(s)} + H_2O^{(g)} + 3/4O_2^{(g)} = CrO_2(OH)_2^{(g)}$. Compiled by Opila[11] using data from various sources.

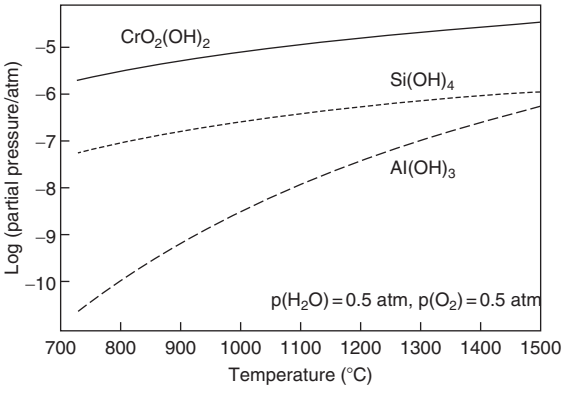

Figure 5 Partial pressures of primary volatile species calculated for each oxide at 1 atm total pressure: 0.5 atm O_2, 0.5 atm H_2O.[10]

The data of Opila[11] shows that the reaction products of water vapor with chromia and silica have significant volatility at temperatures above about 800 °C, whereas for alumina this is the case only at temperatures in excess of 1400 °C. It is important to note that the vapor pressures of the most important volatile Al- and Si-containing species are independent of p_{O_2} (eqns [4] and [6]) and they can therefore be equally important for oxidation processes in H_2O ($-H_2$)-based gas mixtures and, for example, in wet air.

Also, volatilization of other alloying elements has been considered to play a role in the oxidation process in wet environments. For reaction of the ferritic 9% Cr steel P92 in oxygen/water vapor gas mixtures at 650 °C, formation of volatile species was considered by Milewska *et al.*[18] as function of p_{O_2} but with a constant water vapor content of 10%. At a low p_{O_2} of 10^{-19} atm the most volatile species are $Fe(OH)_2^{(g)}$, $MoO_2(OH)_2^{(g)}$, and $WO_2(OH)_2^{(g)}$. With increasing p_{O_2} up to 10^{-1} atm, $MoO_2(OH)_2^{(g)}$ and $WO_2(OH)_2^{(g)}$ remain the most volatile compounds but $CrO_2(OH)_2^{(g)}$ and $Mo_3O_2^{(g)}$ also show significant volatility. The hydroxide $Fe(OH)_2^{(g)}$ as possible active volatile species in the oxidation of 9% Cr steels in presence of water vapor, especially at high total pressure, was also proposed by Thiele *et al.*,[19] Ehlers *et al.*,[16] and Davis and Dinsdale.[8] This was based on an evaluation by Surman and Castle,[20] but the authors indicated that better data was required to confirm its significance for oxidation processes.

1.17.2.3 Considerations for Material Testing in Steam Environments

When testing materials in water vapor-containing gases, impurities in the test gas may have an important effect on the equilibrium oxygen partial pressure

that establishes in the gas. If, for example, an inert gas such as Ar is bubbled through water at controlled temperature to establish a certain partial pressure of $H_2O^{(g)}$, the equilibrium oxygen partial pressure of the gas mixture at temperatures between 500 and 900 °C is in the range 10^{-9} to 10^{-6} bars (**Figure 6**). Therefore, traces of oxygen as low as, for example, 1 ppm in the Ar carrier gas may, in this temperature range, substantially affect the equilibrium values. This will not be the case in (Ar–)H_2–H_2O mixtures containing a few percent of H_2. Hydrogen will at high temperature react with the O_2 impurity such that the initial content of oxygen in the carrier gas will become insignificant for the overall equilibrium oxygen partial pressure. However, in pure steam or in Ar–H_2O mixtures, not only traces of oxygen but also hydrogen in the initial gas mixture can have a substantial effect on the p_{O_2} of the equilibrated gas. For example, the presence of 1 ppm H_2 in an Ar–4% H_2O gas mixture would, in a large temperature range, be sufficient to destabilize haematite, while traces of oxygen would have the opposite effect (**Figure 6**). It should be mentioned that traces of hydrogen may, for example, be present in the inert carrier gas, but may also originate from the reaction of the water vapor with the metallic material to be tested.[21,22] The latter effect was claimed to be responsible for differences in oxide scale composition and thickness in the gas flow direction when testing ferritic steel specimens in slow-flowing Ar–H_2O (**Figure 7**).[22] The effect did not occur if the test gas contained substantial amounts of hydrogen in addition to water vapor.[23]

The possible formation of volatile species due to reaction of oxides with water vapor has important implications for materials testing. Owing to its excellent thermal shock resistance, quartz is frequently used as construction material for reaction tubes and/or specimen holders in oxidation test facilities. In environments containing substantial amounts of water vapor, the formation of volatile Si-containing gas species such as, for example, $Si(OH)_4^{(g)}$ can, however, substantially affect the oxidation process, as illustrated in **Figure 8**. In such test gases, reaction tubes and specimen holders should therefore, for instance, be made of alumina, in spite of problems that might occur due to the poorer thermal shock resistance of this material.

A further consequence of the $Si(OH)_4^{(g)}$ formation is that materials or coatings that rely on formation of silica-based surface scales may not be suitable for material protection in steam environments. This is especially the case in high-pressure steam because eqn [4] shows that the vapor pressure of $Si(OH)_4^{(g)}$ is proportional to $[p_{H_2O}]^2$.

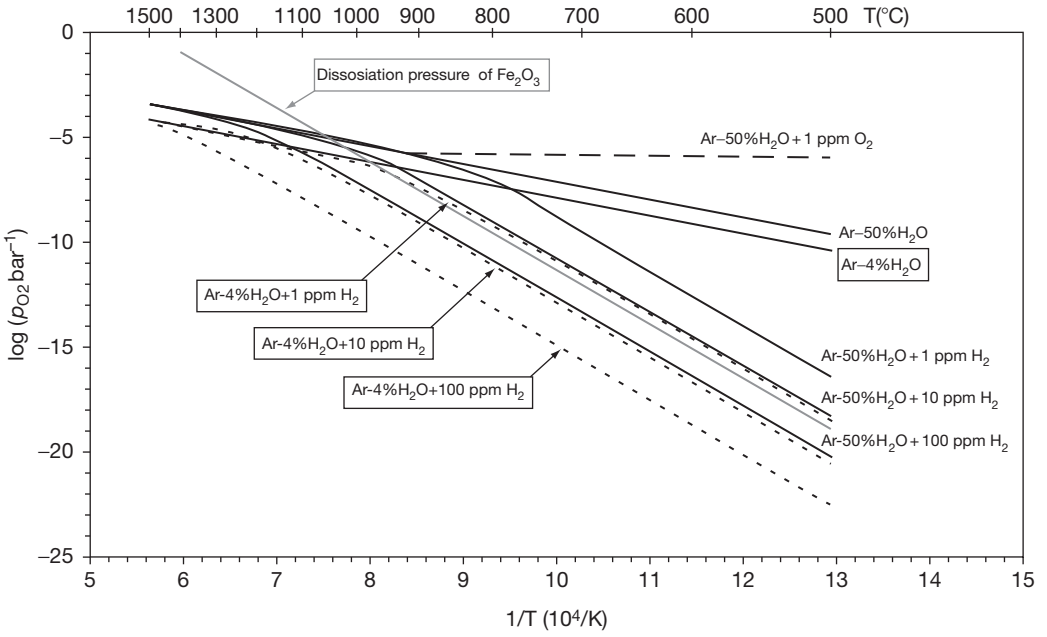

Figure 6 Calculated equilibrium oxygen partial pressures in various Ar–H_2O(–H_2) gas atmospheres compared with the dissociation pressure of Fe_2O_3, showing effect of trace amounts of O_2 and H_2. Reproduced from Żurek, J.; Michalik, M.; Schmitz, F.; Kern, T. U.; Singheiser, L.; Quadakkers, W. J. *Oxid. Met.* **2005**, *63*(5/6), 401–422, calculated using FactSage.

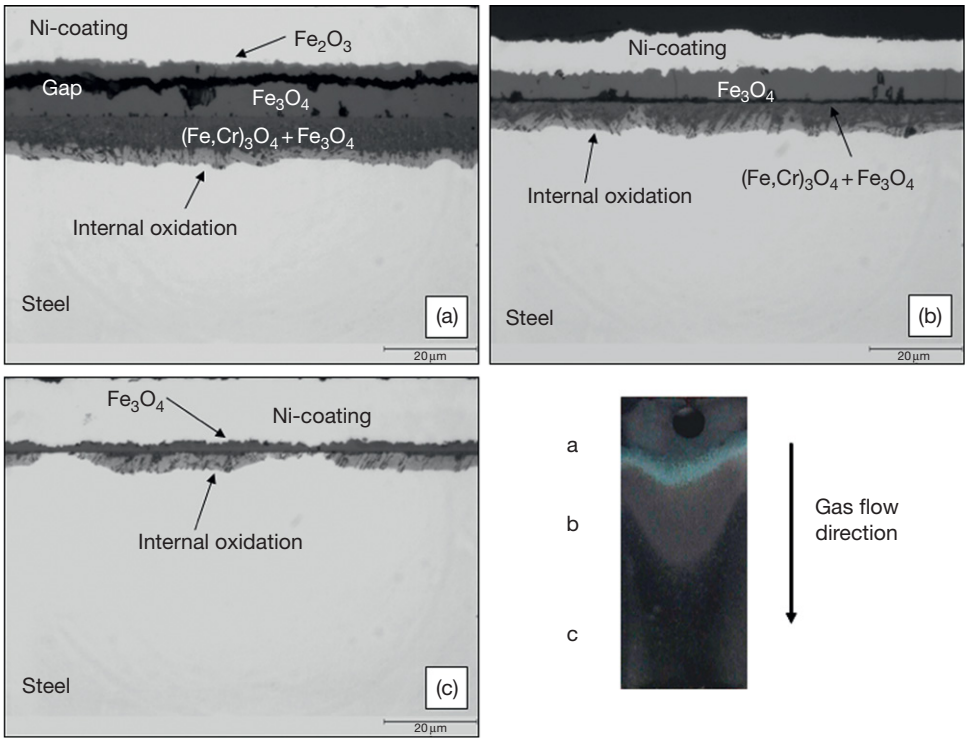

Figure 7 Cross sections in different locations of rectangular specimen (20 × 9 × 2 mm) oxidized for 5 h at 15 l h^{-1} gas flow in Ar–10% H_2O at 650 °C. Macropicture shows the flow patterns and analysis areas. The specimen was placed in a reaction tube with a diameter of 10 mm and the linear gas flow rate was 5.31 cm s^{-1}.[22]

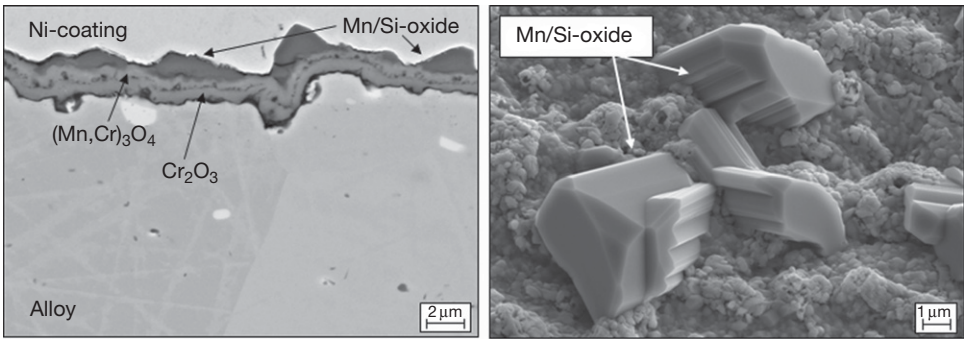

Figure 8 Formation of mixed Mn/Si oxide on high-Cr ferritic steel during exposure in Ar–H_2–H_2O mixture with 18.5% $H_2O^{(g)}$ at 800 °C using a quartz reaction chamber.

1.17.3 Growth Mechanisms of Oxide Scales

1.17.3.1 Kinetics of Surface Reactions

Upon long-term oxidation, the growth of oxide scales is frequently governed by solid-state transport processes within the scale. This results in an oxide thickening, which can, according to the classical oxidation theory developed by Wagner,[6] in many cases be described by an approximate parabolic time dependence. However, especially in the early stages of oxidation, the kinetics of the surface reactions may be the rate-limiting step in the oxidation process.

Michalik *et al.*[24] studied the early stages of oxidation of Cr at 1000 °C in an Ar–1% O_2–2% H_2O mixture using $H_2^{18}O$ as tracer (**Figure 9**). The authors found that the chromia scale formation for up to exposure times of 3 h virtually contained only ^{18}O, thus showing that in

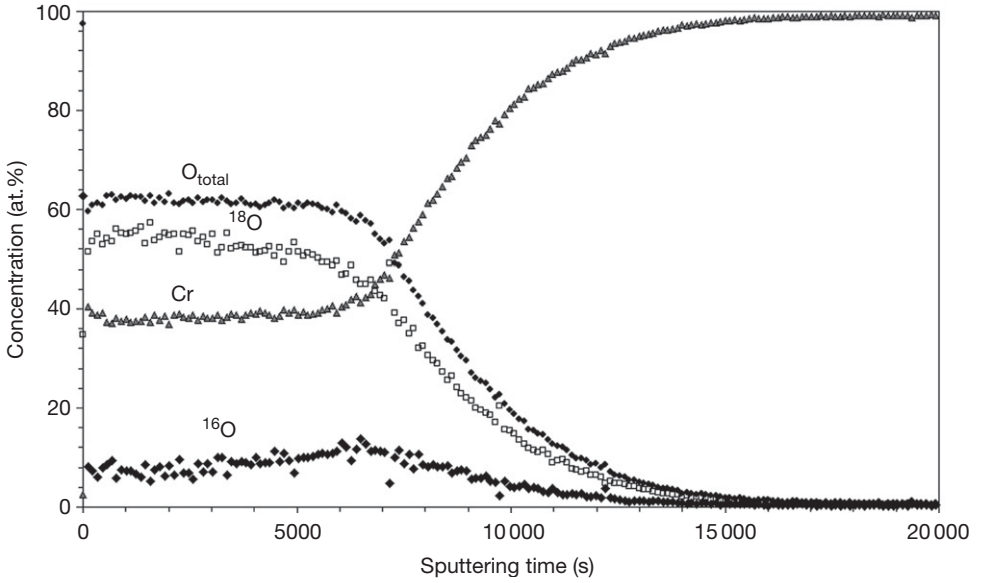

Figure 9 SNMS depth profile after oxidation of chromium for 3 h in Ar–1% $^{16}O_2$–2% $H_2^{18}O$ at 1000°C.[24]

this stage of the oxidation process oxygen transfer via $H_2O^{(g)}$ is much faster than that via $O_2^{(g)}$. Also, Jacob *et al.*[25] reported for chromium oxidized in $^{18}O_2/H_2^{16}O$ mixtures that oxygen derived from water vapor was the major component of the oxide even though the $p_{H_2O}^{(g)}/p_{O_2}^{(g)}$ ratio was only 0.05 in that case.

In several studies it was found that whisker formation was promoted by the presence of water vapor.[26,27] Whiskers are believed to be formed at dislocations in the oxide[28] and have hollow cores such that rapid surface diffusion within the whisker can take place and their growth is then limited by the availability of oxidant at the whisker tip.[28] It was proposed[26] that the faster growth of whiskers in moist atmospheres is related to the generally faster dissociation of water molecules than for most other oxidant molecules.

Anghel *et al.*[29] studied the adsorption of N_2, H_2, CO, and H_2O on oxidized Cr- and Zr-based materials in the temperature range 400–600 °C. When adding water vapor to CO gas, the dissociation rate of CO on Cr decreased, which can be interpreted as being the result of a blocking effect by water. On the basis of the results of these authors, the following ranking for the tendency of adsorption at high temperatures was made: $N_2 < H_2 < CO < H_2O$. This might explain the results of Michalik *et al.*,[24] who found pure Cr to form subscale nitrides during exposure at 1000 °C in N_2–O_2 but not in N_2–H_2–H_2O. Zheng and Young[30] found that for pure Cr at 900 °C subscale nitride formation occured in N_2–CO–CO_2 but not in N_2–H_2–H_2O atmosphere with the same equilibrium oxygen partial pressure. The authors explained the results in terms of competitive adsorption of the various gas species on oxide surfaces and grain boundaries. Thus, as p_{H_2O}/p_{O_2} increases, preferential adsorption of H_2O becomes favored. Evidently, nitrogen can enter and penetrate dry Cr_2O_3 grain boundaries, but cannot do so when large numbers of water molecules are present. This confirms the ability of $H_2O^{(g)}$ to interact with the interior of chromia scales modifying their transport properties.[30]

Akermark and Hultquist[31] showed that with an Fe–20% Cr–10% Al alloy oxidized at 920 °C, water dissociation rates decreased with decreasing oxidation rates, and they interpreted this as the result of fewer defects in the more mature alumina scale. In general, it appears that dissociation of a gas molecule such as $H_2O^{(g)}$ is favored by defects in the surface, and the stoichiometric oxides such as alumina may therefore be less active than, for example, FeO.

A number of authors have proposed that the relative acidity/basicity of oxides controls the reaction with water vapor,[32] where water vapor will react more strongly with more acidic oxides (**Figure 10**). The commonly used method of PZC (point of zero charge) or IEP (isoelectric point) is believed to yield a good relative assessment for oxide ranking, while use of chemical shift measurements by X-ray photoelectron spectroscopy (XPS) or heats of adsorption by calorimetry or gas chromatography yield better absolute values.[33]

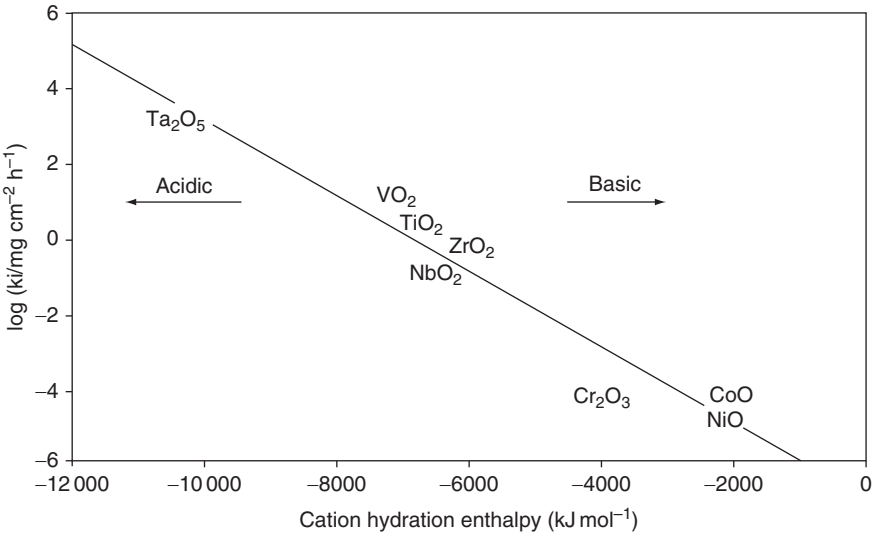

Figure 10 Correlation between the oxidation rate of metals by water vapor at 800 °C and the hydration enthalpy of the corresponding cation.[32]

1.17.3.2 Effect of Water Vapor and Hydrogen on Lattice Diffusion in Oxide Scales

The possible effects of hydrogen/water vapor incorporation in the transport properties of oxides were considered by several authors. Hydrogen dissolves in the oxide as protons and is bound to oxide ions to form the substitutional hydroxide $(OH)_O^{\bullet}$.[34] These defects may equivalently and more simply be described as interstitial protons $H_i^{\bullet}$. Generally it is found that the concentration of $H_i^{\bullet}$ increases with increasing p_{H_2O} and decreasing temperature. The dissolution of protons in an oxide can be written as:

$$\frac{1}{2}H_2^{(g)} = H_i^{\bullet} + e' \qquad [7]$$

or, by considering gas equilibria,

$$\frac{1}{2}H_2O^{(g)} = H_i^{\bullet} + e' + \frac{1}{4}O_2^{(g)} \qquad [8]$$

Thus, at sufficiently low p_{H_2O} or p_{H_2}, protons are minority defects. The concentrations of native defects are independent of p_{H_2O} or p_{H_2} (at constant p_{O_2}), while the concentrations of protons increase with p_{H_2O}½ or p_{H_2}½. At higher p_{H_2O} or p_{O_2}, protons may become the dominant defect, compensated for by defect electrons, metal vacancies, oxygen interstitials or acceptor dopants. Many investigations focus on the equilibrium between water vapor, oxygen vacancies and protons as being the most likely:

$$H_2O^{(g)} + O_O^x + V_O^{\bullet\bullet} = 2(OH)_O^{\bullet} \qquad [9]$$

which, in general, is exothermic so that protons are dominant at low temperatures and oxygen vacancies at high temperatures. It is also important to consider the parallel reaction of dissolution from the gas phase:

$$H_2O^{(gas)} = H_2O^{(diss)} \qquad [10]$$

Thus, different types of hydrogen-containing species may be present simultaneously, that is, molecular water and OH groups, as is frequently found in glasses.[35] In close-packed structures such as alumina and chromia, dissolution of molecular water would be less favored. Transport of 'water' in oxide scales is claimed to occur by a proton 'hopping' process in which protons localized at oxide ions move by transfer from one oxygen to another. Since oxygen is available everywhere, the net effect of proton diffusion is diffusion of water, and since proton diffusion rates are high compared with those of metal or oxygen, diffusion of 'water' is easy. Although the general principles of the effects of protons can be outlined, the uncertainties regarding transport in the oxides scales of interest are such that it is not possible to predict with any certainty the effects of water vapor on lattice transport.

1.17.3.3 Molecular Diffusion in Oxide Scales in Wet Gases

Already in earlier studies it was claimed that, depending on the scale type, the oxidation kinetics in H_2O-containing gases at least partially depends on the ingress of water molecules through the oxides scales. For this to happen, 'microchannels' must be present,

or, as in the case of silica, an open network structure allows the transport of large molecular species.

It is important to consider gaseous or volatile species that might be created during oxidation reactions involving water vapor and how these are transported within the scale. A well-accepted process for vapor or gaseous transport is the dissociative mechanism first proposed by Rahmel and Tobolski.[36] This mechanism is applicable only for scales grown by cation transport and involves interaction with void formed by vacancy condensation.[6] If a void contains both hydrogen and water vapor, oxidation of the surface nearest the metal will occur by reaction with water to form new oxide and the gaseous reaction product hydrogen (Figure 11). Adapting this suggestion to Cr_2O_3 and using the Kröger–Vink notation, one can write[37]

$$3H_2O^{(g)} = 3H_2^{(g)} + 3O_O^x + 2V_{Cr}''' + 6h^\bullet \qquad [11]$$

This process occurs in the forward direction, on the side of the cavity nearest the metal, and in the reverse direction at the outer surface of the cavity. It provides for rapid inward diffusion of oxygen while the void gradually moves outwards from the metal/oxide interface to the oxide/gas interface.

As mentioned in Section 1.17.2.2, Surman and Castle[20] and Ehlers *et al.*[16] have proposed that volatile $Fe(OH)_2^{(g)}$ might participate in the scale-formation process in wet gases and might be an important factor for pore generation in an oxide formed on a 9% Cr steel in wet gas. Using available thermodynamic data, however, Ehlers *et al.*[16] calculated that the vapor pressure of $Fe(OH)_2^{(g)}$ is too low to sustain the reaction, but pointed out that these data need verification. The process may be of more importance at high steam pressures.[17]

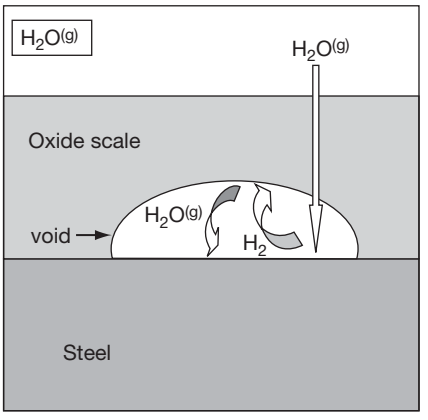

Figure 11 Schematic illustration showing oxygen transfer across in-scale voids in water vapor-containing gas. (From Ref. 16 based on the Rahmel–Tobolski mechanism[36]).

Void transport by the Rahmel–Tobolski mechanism or generation of volatile $Fe(OH)_2^{(g)}$ obviously requires water vapor to exist within the oxide scale. In addition to proton diffusion, the presence of cracks and fissures in the oxide is a possible mechanism to allow water ingress. Ehlers *et al.*[16] have found that scales grown in water vapor mixtures on the 9% Cr steel P91 are more permeable than those grown under dry conditions, which was demonstrated by $^{16}O_2/H_2^{18}O$ studies (Figure 12). A competitive adsorption between water and oxygen occurred at inner surfaces, with water being preferentially adsorbed if the p_{H_2O}/p_{O_2} ratio is ≥ 1.

1.17.4 Metallic High Temperature Components in Steam and Steam/Hydrogen Environments

1.17.4.1 General Remarks

Nearly all high temperature metallic construction materials rely for their oxidation protection on chromia or alumina scales that form on the component surface during high temperature service. Only in a few cases, silica, mostly found as sublayer beneath chromia base scales, is of importance for metallic materials protection. Pure silica scales are of far more importance for environmental protection of a number of ceramic materials, for example, of the type Si nitride or carbide.

When comparing the behavior of metallic high temperature components in steam and steam/hydrogen gases with that in oxygen or air, the literature data indicate that the service environment may affect the growth of the protective scale (chromia or alumina) as well as that of the less protective oxides of the base elements (Fe, Ni, Co). Therefore, the effect of the environment on the overall material behavior of alloys with high concentrations of protective scale-forming elements (PSEs) chromium and aluminum may differ from that of lower alloyed materials that form oxide scales of the base elements or alloys that can be considered as 'borderline' alloys between protective and nonprotective behavior.

Figure 13 shows the qualitative dependence of the oxidation behavior of Fe-, Ni-, and Co-based alloys as a function of the amount of PSEs, as frequently measured when exposing the alloys to oxygen or air.[6] With small additions of PSEs (group I alloys), the total oxygen uptake frequently tends to be slightly higher than in case of pure base metal oxidation because of doping effects and/or occurrence of internal oxidation.[6,38] With a further increase in concentration of PSEs, the

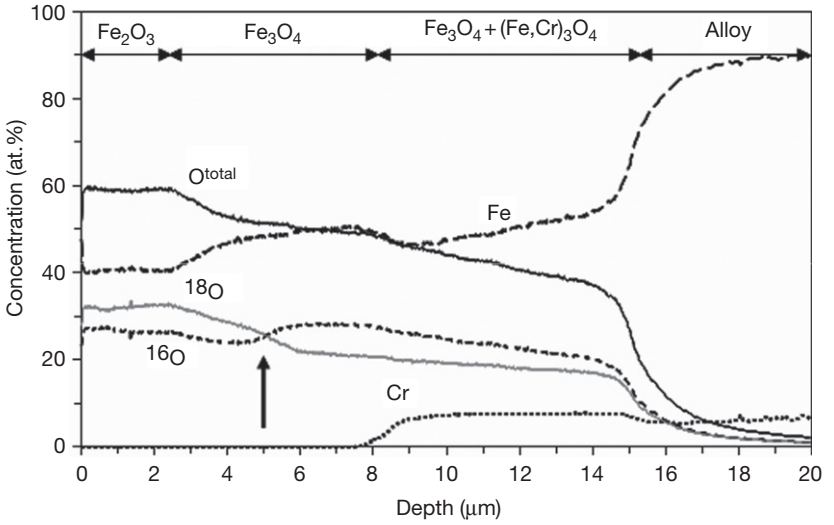

Figure 12 MCs^+ secondary ion mass spectrometry profile of P91 steel after 30 h oxidation at 650 °C in N_2–1% $^{16}O_2$–4% $H_2^{18}O$ showing differences in distribution of ^{18}O and ^{16}O in the Fe-based oxide scale. Arrow indicates location of gap in outer magnetite layer. Reproduced from Ehlers, J.; Young, D. J.; Smaardijk, E. J.; Tyagi, A. K.; Penkalla, H. J.; Singheiser, L.; Quadakkers, W. J. *Corros. Sci.* **2006**, *48*, 3428–3454.

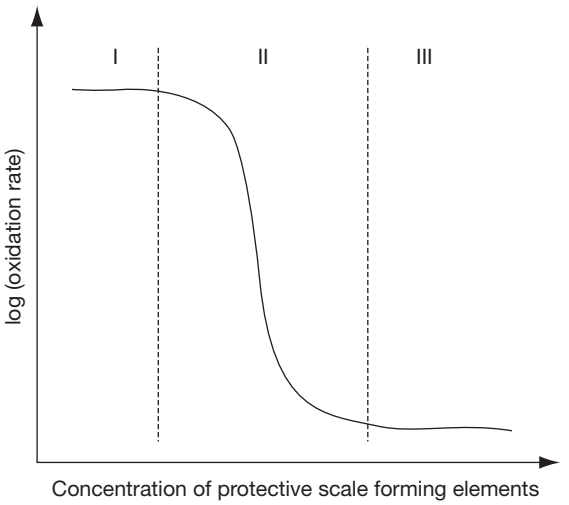

Figure 13 Schematic illustration showing qualitatively the effect of Cr and/or Al content on the oxidation rates of Ni-, Fe- and Co-based alloys during exposure in air or oxygen. (The oxidation rates of group I and group III alloys are not necessary independent of the concentration of PSEs, as explained, for example, by Birks *et al.*[6]).

oxidation rate decreases as a result of the formation of larger amounts of more protective oxides in the surface scale. Above a critical concentration of the PSEs, the alloy starts forming a slowly growing scale of chromia or alumina. The exact concentration at which this fundamental change in oxidation mechanism occurs depends on numerous parameters such as temperature, time, gas composition, minor alloying additions, and surface treatment. Alloys with a concentration of the PSE near the steep drop in oxidation rate (group II alloys) can thus be considered as 'borderline' alloys between protective and nonprotective scale formation.

The commercially available alloy systems for high temperature applications are mostly materials of group II and III in Figure 13. Therefore, in the following sections the effect of service environment on the behavior of these types of alloy systems will be described. First, chromia scale formation on pure Cr as well as high-Cr Fe- and Ni-based alloys (group III materials) will be discussed. Subsequently, the scale formation on corresponding 'borderline alloys' with intermediate Cr contents (group II) will be treated. Owing to its technological importance, special emphasis will be put on steam oxidation behavior of ferritic/martensitic and austenitic steels in the temperature range 550–650 °C. The final sections will deal with alumina-forming alloys and coatings, including the behavior of 'borderline' alumina formers.

Nomenclature

In the following discussion the chromia and alumina scales will be frequently termed as 'protective scales' whereas the oxides of the base elements Fe, Ni, and, for example, Ti will be termed 'nonprotective oxides.' This expression is strictly speaking not correct because oxides with relatively high growth rates still offer protection of the metal or alloy. The expressions will, however, be used for convenience.

1.17.4.2 Oxidation of Chromium and High-Chromium Alloys

1.17.4.2.1 Oxidation of chromium

In earlier studies, Quadakkers *et al.*[39] found the oxide scale on pure chromium in an $Ar/H_2/H_2O$ mixture to grow faster than that formed in air. During cyclic oxidation, however, the overall oxidation resistance of the material was far better in $Ar/H_2/H_2O$ because of the better adherence of the scales than that of the scales formed in air. The oxide scales formed in the low-p_{O_2} gas showed a smaller tendency to buckle, but a larger tendency to whisker formation, than found during air exposure.

The lower growth rate and/or poorer adherence might be related to the subscale nitride formation which is known to occur during air exposure of Cr. However, similar observations in respect to differences in adherence and growth rate were made by Hänsel *et al.*[40] when comparing the behavior in $Ar–H_2–H_2O$ with that in $Ar–O_2$. Hultquist *et al.*[41] found the chromia growth rates at 900 °C to be approximately doubled in 2% water vapor (20 mbar) compared with the rate in dry oxygen at the same total pressure. A similar acceleration was observed when the Cr contained dissolved hydrogen prior to exposure.[42] The adhesion of the scale was improved when it was formed in water vapor-containing atmospheres, and this was proposed to be related to a greater fraction of scale growth at the metal–oxide interface. The fact that adherence of chromia-based scales formed in $Ar/H_2/H_2O$ is better than those formed in air or oxygen was also observed by Malkow *et al.*[43] for a number of high-Cr ferritic steels.

At higher levels of water vapor ($Ar–15\%\ H_2O$), Henry *et al.*[44] observed that the growth rate of chromia on pure chromium at 900 °C was higher than in an Ar–15% oxygen gas mixture. The authors proposed that the increased rate of growth was due to enhanced inward scale growth as a result of the smaller ionic radius of OH^- (95 pm) compared with that of O^{2-} (140 pm). It was also found that scale adhesion was significantly improved when water vapor was present compared with the case for dry oxygen. Hänsel *et al.*[45] showed that for Cr oxidized at 1000 °C the oxidation rates in $Ar–H_2–H_2O$ mixtures were equal or greater than those in $Ar–O_2$ or $Ar–O_2/H_2O$ and the formation of blades was observed at the oxide surface. They proposed a model in which oxide growth in $Ar–H_2–H_2O$ was sustained by diffusion of chromium vacancies and adsorption of H_2O on oxide exposed to low oxygen-activity gas led to the formation of hydroxyl species. At high oxygen activities, molecular oxygen adsorbs preferentially on the entire surface, overwhelming any local variation due to catalysis of H_2O dissociation. This explained the absence of whiskers in high-oxygen-content atmospheres.

Figure 14 shows results of Michalik *et al.*[15] comparing weight-change data after isothermal exposures of Cr in various low- and high-p_{O_2} gases. Also shown are the weight changes after cooling to room temperature. The data confirm that samples oxidized in low-p_{O_2} gases ($Ar–H_2O$ and $Ar–H_2–H_2O$) generally showed, during cooling, far less extensive scale spalling than samples oxidized in high-p_{O_2} gas. The most pronounced spalling was found for the specimen oxidized in $Ar–20\%\ O_2$. **Figure 15** shows transmission electron microscopy (TEM) micrographs from cross sections of specimens oxidized in $Ar–20\%\ O_2$ and $Ar–2\%\ H_2O$ at 950 °C for 0.5 h. The oxide scale formed in the high-p_{O_2} gas exhibits pores and cracks, mainly at the alloy–oxide interface. The oxide formed during oxidation in the low-p_{O_2} gas appears to be very dense, the alloy–oxide interface is intact and the oxide adheres well to the metal (**Figure 15(b)**).

Michalik *et al.*[15,24] carried out two-stage oxidation tests with Cr at 1000 °C where the gas was, without intermediate cooling, changed from $Ar–O_2$ to $Ar–H_2–H_2O$. An oxide layer with a morphology typical for scales formed in $Ar–H_2–H_2O$ was found at the scale/metal interface, beneath the buckled layer grown in $Ar–O_2$.

The oxidation of Cr and chromia-forming alloys in dry, high-p_{O_2} gases is known to be influenced by reactive evaporation at the scale/gas interface which releases $CrO_3^{(g)}$ as the primary species,[6] whereas in the low-p_{O_2} gas the partial pressure of volatile Cr species should be extremely low.[11,12] The differences in oxide growth rates observed in the various environments might thus be related to differences in the formation of volatile species in $Ar–O_2$ and $Ar(–H_2)–H_2O$ (see **Section 1.17.2.2**). However, Michalik *et al.*[15] illustrated that, under the used experimental conditions, this effect could not explain the observed differences in scale growth rates.

1.17.4.2.2 Oxidation of chromia-forming Fe- and Ni-based alloys

Essuman *et al.*[46] studied the isothermal oxidation behavior of FeCr alloys at 900 °C in $Ar–O_2$ and $Ar–H_2–H_2O$. Energy dispersive X-ray (EDX) analysis showed that the surface oxide scales formed in both test gases on Fe–20% Cr consisted essentially of chromia, and no indication for the presence of Fe in the scale

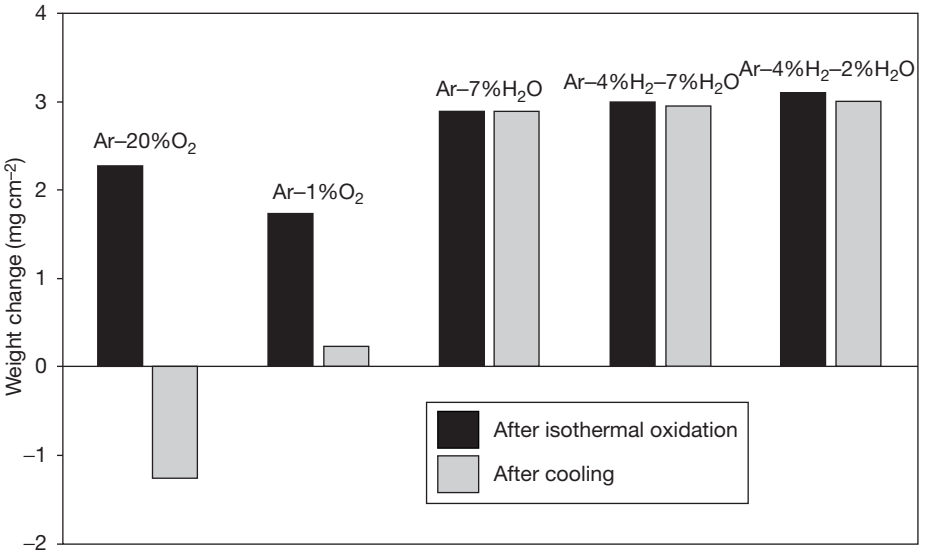

Figure 14 Weight changes after 72 h isothermal oxidation and after subsequent cooling to room temperature of pure Cr in different high- and low-p_{O_2} gases at 1000 °C. Reproduced from Michalik, M.; Hänsel, M.; Żurek, J.; Singheiser, L.; Quadakkers, W. J. *Mater. High Temp.* **2005**, *22*(3/4), 213–221.

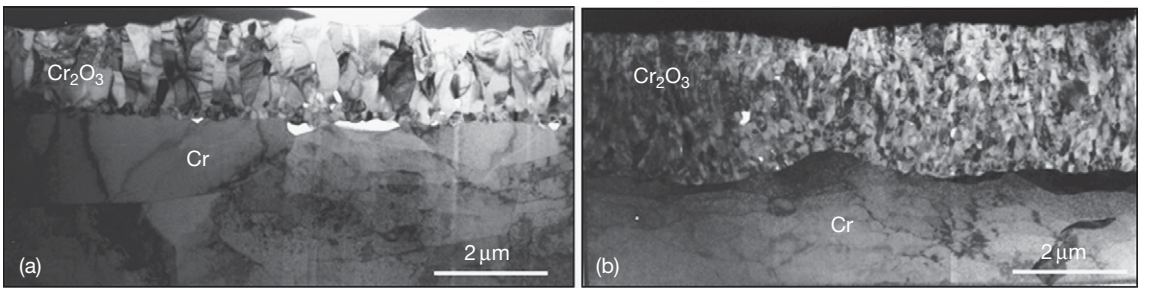

Figure 15 TEM cross sections of oxide scales formed on pure chromium after 0.5 h oxidation at 950 °C in (a) Ar–20% O_2 and (b) Ar–2% H_2O. Reproduced from Michalik, M.; Hänsel, M.; Quadakkers, W. J. Report Forschungszentrum Jülich, **67** (2007), ISBN 978-3-89336-486-2.

could be found. As described above for pure Cr, the chromia scale that formed in the Ar–H_2–H_2O gas exhibited a higher growth rate than that that formed in Ar–O_2.

Figure 16 shows gravimetric data during isothermal oxidation of a binary Ni–25Cr alloy in low-p_{O_2} gases Ar–(4% H_2–)7% H_2O and in Ar–20% O_2. The growth rate in the latter gas was smaller than that in the low-p_{O_2} gases and the scale was found to have developed voids and internal pores at and near the oxide–alloy interface. In contrast, the oxide grown on this alloy in Ar–4% H_2–7% H_2O was compact and closely adherent to the substrate.[47] The latter phenomenon had already been found in the earlier studies of Wood *et al.*[48] for scales grown on Fe–28% Cr in Ar–10% H_2O compared to scales grown in oxygen.

1.17.4.2.3 Mechanisms of chromia scale growth

The differences in chromia growth in the various gases appear to be similar for all three discussed materials, that is, Cr as well as high-Cr Ni- and Fe-based alloys. The scales exhibit higher growth rates but are more compact, show better adherence and frequently exhibit a flatter metal/scale interface when formed in low-p_{O_2} gas.

The better adherence of the oxide in the low-p_{O_2} gases might be related to the H_2O/H_2 bridges in voids described by Rahmel and Tobolski (see Section 1.17.3.3). In Ar–O_2 the outward-growing scale will result in vacancy condensation, preferentially at the alloy/oxide interface, resulting in poor

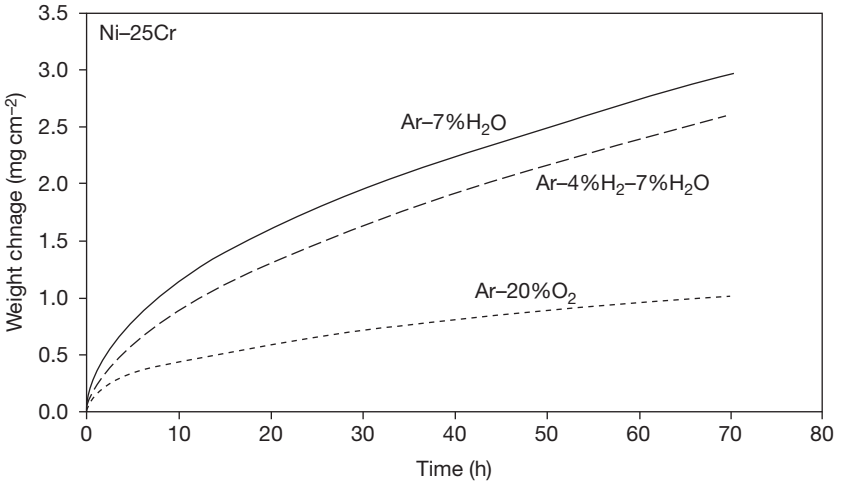

Figure 16 Weight change versus time during isothermal oxidation of Ni–25Cr model alloy at 1050 °C in Ar–20% O_2, Ar–7% H_2O and Ar–4% H_2–7% H_2O. Reproduced from Essuman, E.; Meier, G. H.; Żurek, J.; Hänsel, M.; Norby, T.; Singheiser, L.; Quadakkers, W. J. *Corros. Sci.* **2008**, *50*(6), 1753–1760.

adherence. The Rahmel–Tobolski mechanism provides an inward oxygen transport resulting in void healing and a net transport of the void away from the metal scale interface, which increases scale adherence. However, the mechanism cannot explain why, in fact, less voidage is seen in the scales formed in the low-p_{O_2} gases (**Figures 15** and **17**).

The growth of chromia scales is generally believed to be controlled by boundary diffusion rather than lattice diffusion.[37] Nonetheless, if the mobile species are ionic and at local equilibrium with the surrounding oxide, then Wagner's description[6,49] of the dependence on p_{O_2} of scale growth rate can be applied, providing that a suitable effective diffusion coefficient is used. If the predominant defects are fully charged vacancies, then it is predicted for the parabolic rate constant k_p.[49]

$$k_p \approx \text{const}(p_{O_2})^{\frac{1}{16}} \qquad [12]$$

However, if the principal defects are interstitials and the ambient p_{O_2} value is significantly above the Cr/Cr_2O_3 equilibrium value, then k_p is independent of p_{O_2}. Both predictions are not in agreement with the experimental observations.

From the TEM cross sections of the oxidized Cr (**Figure 15**) and Ni–25Cr specimens (**Figure 17**), it is apparent that the oxide scales formed in the high-p_{O_2} gas show large grains with a columnar morphology which is typical, as frequently described by several authors,[50] for scales that mainly grow by outward cation diffusion. The oxides formed in the two low-p_{O_2} gases are, however, extremely fine grained with a small tendency for the grain size to increase towards the scale/alloy interface.

Figure 18 shows the distribution of oxygen isotopes in the scale formed on alloy Ni–25Cr during the two-stage oxidation in $Ar–H_2–H_2^{16}O/H_2^{18}O$ at 1050 °C. The small ^{18}O peak at the scale/alloy interface is a clear proof of inward transport of oxygen-bearing species along rapid diffusion paths, likely grain boundaries.[51] The continuously decreasing ^{18}O concentration in the outer part of the scale is, at least partly, related to extensive isotope exchange between ^{18}O at the grain boundaries and ^{16}O within the grains due to the extremely fine size of the chromia grains.[51] A similar difference in growth mechanism in a low- and high-p_{O_2} environment was also found by Bamba *et al.*[52] for the alloy Fe–15Cr–0.5 Si at 850 °C.

In earlier studies it was proposed that the better adherence of chromia scales on pure chromium formed in water vapor-containing atmosphere may be related to enhanced scale plasticity.[53,54] It would seem that in terms of defect concentration the main effect of water vapor is to increase the concentration of the majority species so that one might not expect to see an effect on creep rates.[27] The improved plasticity in the low p_{O_2} gas could be related to the smaller chromia grain size compared to that formed on chromia in dry atmospheres. However, on the basis of the newer results, a more likely explanation is that the observed differences in adherence as well as growth rate of the scales found in the high- and low-p_{O_2} gases are just a result of the difference in scale growth mechanisms. By the substantial inward

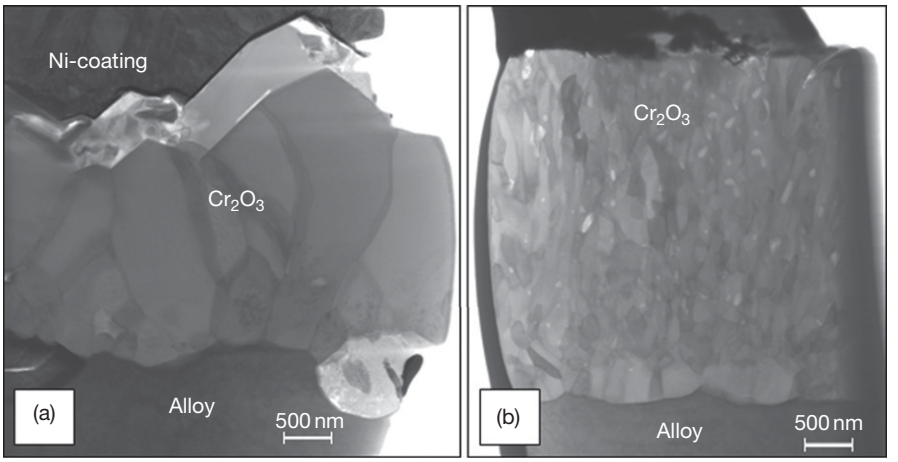

Figure 17 TEM cross sections of oxide scales formed on Ni–25Cr model alloy during 4 h oxidation in (a) Ar–20% O_2 and (b) Ar–4% H_2–2% H_2O at 1050 °C.

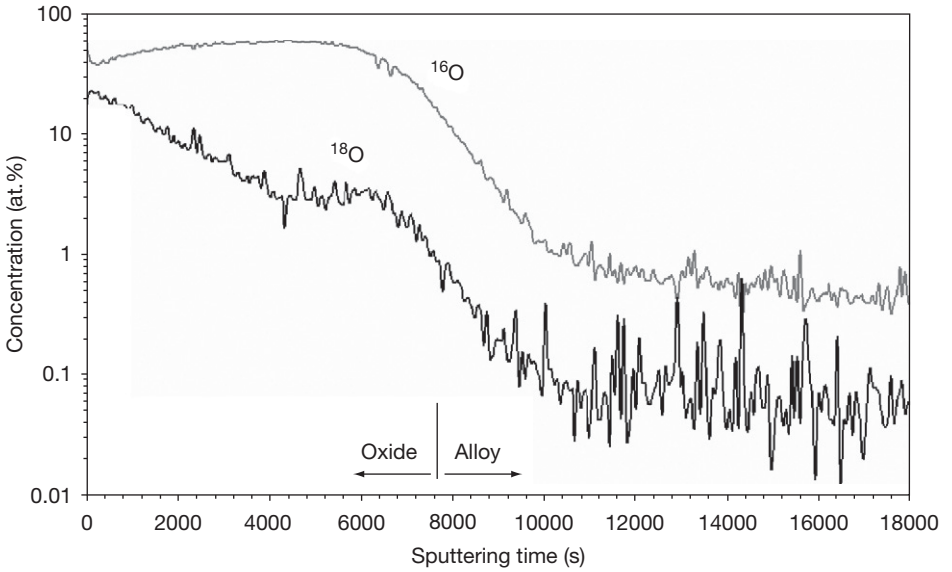

Figure 18 Semi-logarithmic plot of the ^{18}O and ^{16}O profiles in the oxide scale on a Ni–25Cr model alloy after two-stage oxidation at 1050 °C: first stage 0.5 h in Ar–4% H_2–2% $H_2^{16}O$; second stage 2 h in Ar–4% H_2–2% $H_2^{18}O$. Reproduced from Żurek, J.; Young, D. J.; Essuman, E.; Hänsel, M.; Penkalla, H. J.; Niewolak, L.; Quadakkers, W. J. *Mater. Sci. Eng. A* **2008**, *477*, 259–270.

oxygen transport in the low-p_{O_2} gas, growth of voids as a result of vacancy condensation at the scale–metal interface is suppressed, resulting in better scale adherence. The extremely high grain boundary density favors inward oxygen transport, resulting in a higher oxide growth rate in the low-p_{O_2} gas.

The remaining questions concern the mechanism whereby $H_2O^{(g)}$ alters the grain size in the low-p_{O_2} gas and the way in which inward oxygen transport occurs.[37] One possibility is that the presence of H_2O adsorbed at the oxide grain boundaries hinders their movement and thus grain growth. This would explain the extremely fine oxide grains formed in Ar(–H_2)–H_2O.[51] However, it could also be argued that the stronger contribution of inward scale growth might not be the result of the finer grain size: rather, the finer grain size could result from the modified scale growth process induced by $H_2O^{(g)}$. The available results do not allow a distinction to be drawn between the two possibilities. Nonetheless, it is clear that the effect of water vapor during oxidation in Ar–(H_2–)H_2O environments is twofold: water molecules

incorporated into the scale provide accelerated mass transport while simultaneously promoting the formation of a fine-grained, inwardly growing, and therefore better adhering, oxide scale.

1.17.4.2.4 Commercial chromia-forming Fe- and Ni-based alloys

Nearly all commercially available chromia-forming alloys contain intentionally added alloying elements and impurities which may substantially affect the oxidation mechanisms and thus also differences in oxidation behavior in the mentioned low and high-p_{O2} gases. The alloying elements and impurities may, for example, lead to doping of the chromia layer and/or result in formation of other mixed oxides, for example, of the spinel type. Only a few systematic studies that deal with the effect of such impurities and minor alloying additions on the differences in the oxidation behavior in low- and high-p_{O_2} gases are available.

England and Virkar[55,56] studied the oxidation of a series of thin-foil nickel-based alloys (Inconel 625, Inconel 718, Hastelloy X, and Haynes 230) in air and wet hydrogen ($p_{O_2} = 10^{-21}$ to 10^{-16} atm, $p_{H_2O} = 0.07$ atm) at 700–1100 °C. At 800 °C the oxidation rate in wet hydrogen was increased by factors ranging between 8 and 30, but at 1100 °C the effect of wet hydrogen was to decrease the oxidation rate compared to that in air by factors ranging between 1.5 and 13. Hussain *et al.*[57,58] reported that Hastelloy C-4 formed a protective scale in 100% steam at all temperatures in the range 600–1200 °C, whereas the scale spalled when formed in air.

Extensive studies concerning the behavior of chromia forming-alloys, especially high-Cr ferritic steels, in low- and high-p_{O_2} gases have been carried out in the development of solid oxide fuel cells (SOFCs), as in these devices metallic interconnects are exposed on one side to the oxidant gas (mostly air) and on the other side to moist hydrogen-based environments. **Figure 19** shows the oxide scales on a high-Cr ferritic steel Crofer APU (nominal composition in mass%, 22Cr–0.5Mn–Ti–La) after exposure for 1000 h at 800 °C in air and Ar–H_2–H_2O. In both cases a two-layered scale is formed consisting of Cr_2O_3 and an outer Cr/Mn-spinel. During air exposure the spinel is present in the form of well-developed crystals, whereas in Ar–H_2–H_2O it possesses a blade-like morphology (**Figure 20**). The scale formed in the low-p_{O_2} gas tends to form voids at/near the interface between the chromia and the spinel layer (**Figure 19**). Traces of Ti are frequently present in the scales: that is, dissolved in the Cr_2O_3 near the scale–alloy interface and in form of TiO_2 particles near the scale–gas interface.[59,60] Presence of minor concentrations of Al and Si (a few tenths of a percent) results in internal oxide precipitates of those elements in the subsurface layer. In some cases the oxides contain traces of reactive elements (REs), for example, La or Y, which are added to the ferritic steels in metallic form or in the form of an oxide dispersion to lower the oxidation rates and/or improve the scale adherence.[53,54]

Contrary to the cases described in the previous section, the Cr-rich surface scales on the ferritic steel show a slightly slower growth rate in low-than in high-p_{O_2} gas (**Figure 19**). This is in agreement with findings of other authors,[60,61] who observed that the growth rates of Cr-rich oxide scales on high-Cr ferritic steels at 800–900 °C in the H_2/H_2O-based gases are similar to, or smaller than, in air. The reason why these ferritic steels behave, in respect to gas composition dependence of the oxidation rate,

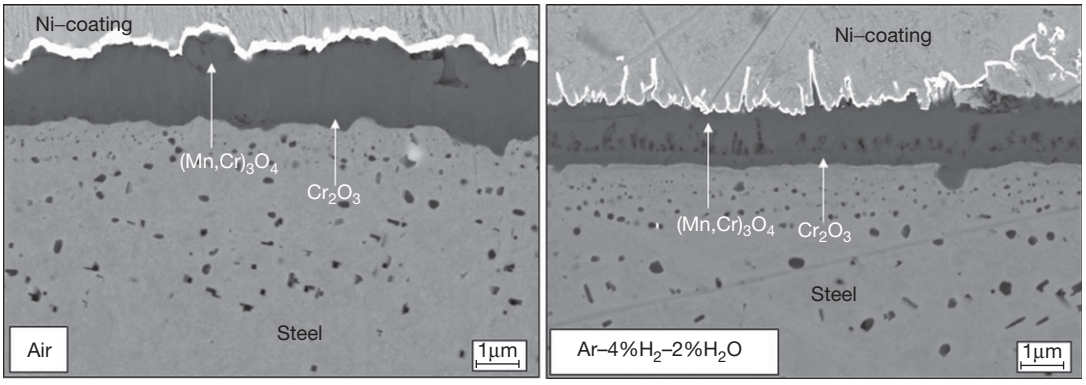

Figure 19 SEM cross sections of high-Cr ferritic steel Crofer 22 APU after 1000 h oxidation at 800 °C in air and Ar–H_2–H_2O.[59,60]

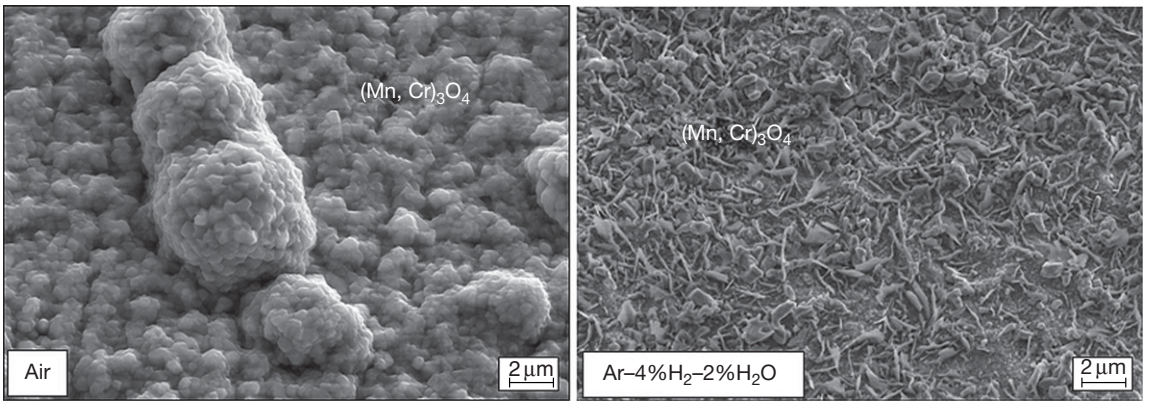

Figure 20 Surface scale morphologies of high-Cr ferritic steel Crofer 22 APU after 1000 h exposure at 800 °C in air and Ar–H_2–H_2O. Adapted from Piron-Abellan, J.; Quadakkers, W. J. Report Forschungszentrum Jülich, Jül-4170, 2005; ISSN 0944-2952.

differently from that of Cr and model alloys of the type NiCr and FeCr (see Sections 1.17.4.2.1 and 1.17.4.2.2) cannot be unequivocally derived from the mentioned SOFC-related studies. Also, the differences in behavior mentioned above for the commercial Ni-based alloys are not immediately apparent from the respective papers. A likely explanation is that a change in scale growth mechanism imparted by one or more of the mentioned minor alloying additions (Mn, Ti, Si, Al, rare earths) results in a change of the gas composition dependence of the oxidation rate. Therefore, possible effects of some common minor alloying additions on the scale formation of chromia-forming alloys in low- and high-p_{O_2} gases will be discussed in the following section.

1.17.4.2.5 Effect of common minor alloying additions

Figure 21 shows weight change data of a number of ternary Ni–25Cr-based model alloys in low- and high-p_{O_2} gas after isothermal exposure at 1050 °C. Also presented are the weight changes after subsequent cooling to room temperature. The data shows that Y reduces, as frequently demonstrated,[53,54] the scale growth rate and spallation from the NiCr alloy during oxidation in Ar–O_2. However, the Y addition has hardly any effect on the growth rate in the low-p_{O_2} gas. The measured weight changes in this gas are even slightly higher than those of the corresponding Y-free alloy, which was found to be related to an additional oxygen uptake due to internal Y oxidation.[51] Like Ni–25Cr, the Ni–25CrY alloy showed a substantially higher oxide growth rate in Ar–H_2O–H_2 than in Ar–O_2. Apparently, the reactive element addition does not fundamentally alter the atmosphere dependence observed for Cr, NiCr, and FeCr. This is in agreement with recent results from Essuman *et al.*,[46] who found for an Y_2O_3 dispersion strengthened Ni–Cr-based alloy a similar atmosphere dependence of the oxidation rate as observed for Ni–25Cr.

The decreased growth rate and improved adherence of chromia scales grown in air and other oxygen-rich environments due to the Y addition is commonly explained by a reduction of outward cation diffusion as a result of Y segregation to the oxide grain boundaries.[54] The predominant inward grain boundary oxygen transport in combination with the high grain boundary density of the scales formed in Ar–4% H_2–7% H_2O (Section 1.17.4.2.3) has the result that Y-addition to the Ni–Cr alloy does not substantially alter the scale growth rate, unlike the effect observed during oxidation in O_2-rich environments.

Mn addition apparently enhances the oxidation rate and decreases the scale adherence during Ar–O_2 exposure, but it decreases the growth rate in Ar–H_2–H_2O (Figure 21).[51] Similar low oxidation rates of the Mn-containing alloys were found during exposure in Ar–CO–CO_2,[62] thereby indicating that the underlying mechanism is related to the low-p_{O_2} rather than the presence of water vapor and/or hydrogen. The ternary NiCrMn alloy formed a double-layered oxide scale consisting of Cr_2O_3 and a thin layer of Cr/Mn spinel in the outer part of the scale. In the case of Ar–20% O_2 exposure, the spinel layer was slightly thinner than that formed in Ar–4% H_2–7% H_2O; additionally, NiO was locally observed. The oxide scale formed on alloy NiCrMnY had a morphology similar to that on alloy NiCrMn; however, no clear indication of Ni-containing oxide was found during Ar–O_2 exposure, and the scale adherence was dramatically improved.

These results strongly indicate that the atmosphere dependence of the oxidation rate of the NiCrMn alloy and also that described in the previous section for the high-Cr ferritic steels are related to the formation of the Cr/Mn spinel on top of the chromia scale. Manganese has a higher solubility in Cr_2O_3 at high oxygen potentials than at low p_{O_2} values.[63] One might speculate that in the low-p_{O_2} gas Mn hinders inward oxygen transport by segregating at oxide grain boundaries. As far as known to the authors, this effect has not been studied extensively and no unequivocal evidence could be derived from previous work. Grain boundary segregation of Mn in the scale formed in the low-p_{O_2} gas is not unlikely, considering the large size of the Mn^{+2} ion compared to that of Cr^{+3}.

On the basis of the phase diagrams (**Figure 22**) of Naoumidis *et al.*,[63] the spinel phase formed in the low-p_{O_2} gas is stoichiometric $MnCr_2O_4$, whereas in high-p_{O_2} gas it is $Mn_{1+x}Cr_{2-x}O_4$. This is confirmed by the secondary neutral mass spectrometry (SNMS) results in **Figure 23** showing a nearly constant Cr/Mn ratio in the outer part of the oxide scale after exposure of a Mn-containing, high-Cr ferritic steel in Ar–H_2–H_2O but a changing ratio as function of depth, and thus as function of p_{O_2}, when formed in air. Retaining the double-layered oxide structure during longer time exposure in Ar–H_2–H_2O would require a balanced flux of Cr and Mn ions through the oxide scale. If, because of the low Mn concentration in the alloy the flux of Mn is reduced after longer

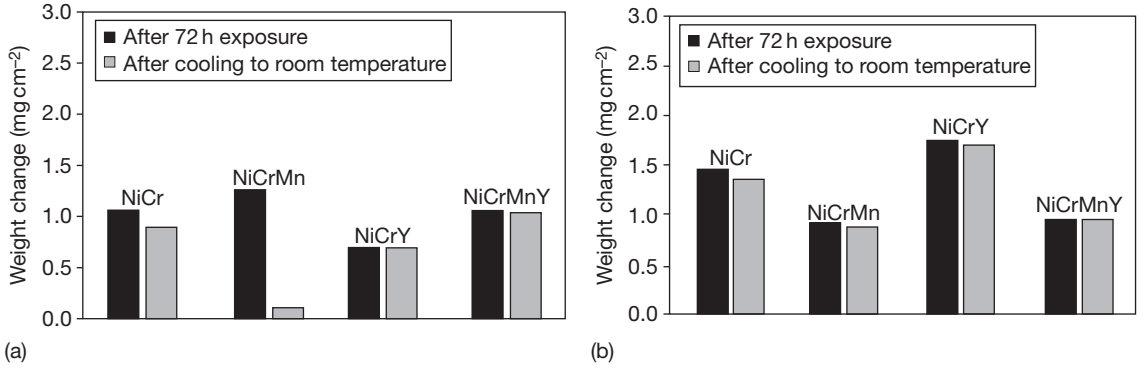

Figure 21 Weight changes of Ni–25Cr-based model alloys after isothermal exposure at 1050 °C and after subsequent cooling to room temperature in (a) Ar–20% O_2 and (b) Ar–4% H_2–7% H_2O. Mn and/or Y addition were 0.50 and 0.15% respectively. Reproduced from Żurek, J.; Young, D. J.; Essuman, E.; Hänsel, M.; Penkalla, H. J.; Niewolak, L.; Quadakkers, W. J. *Mater. Sci. Eng. A* **2008**, *477*, 259–270.

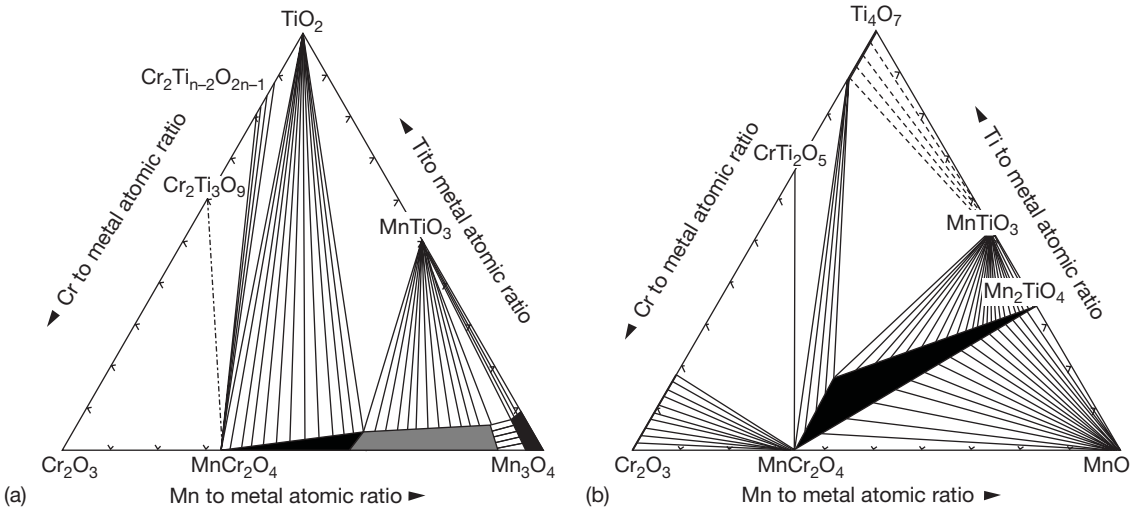

Figure 22 Phase equilibria in the quasi-ternary system: (a) Cr_2O_3–Mn_3O_4–TiO_2, after annealing at 1000 °C in air; (b) Cr_2O_3–MnO–Ti_4O_7 after annealing at 1000 °C in a gas with an equilibrium oxygen partial pressure of 10^{-21} bar. Reproduced from Naoumidis, A.; Schulze, H. A.; Jungen, W.; Lersch, P. *J. Eur. Ceram. Soc.* **1991**, *7*, 55–63.

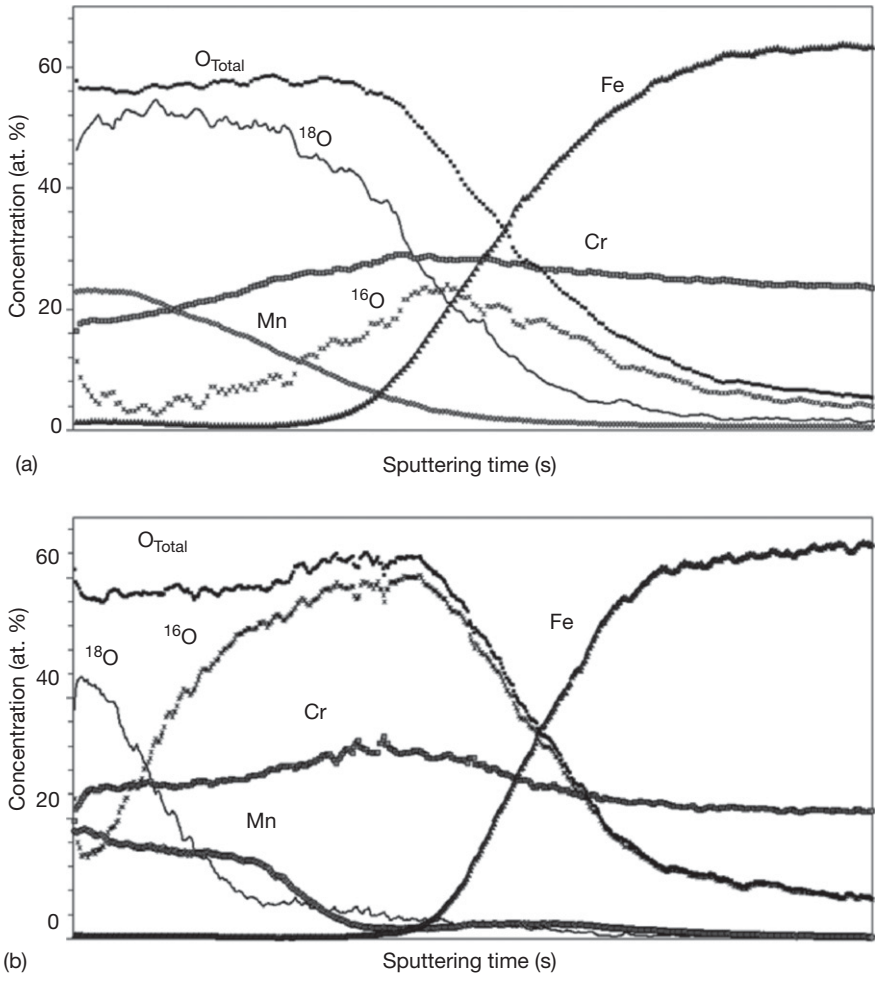

Figure 23 SNMS profiles of high-Cr ferritic steel Crofer 22 APU after two-stage oxidation at 900 °C for (a) 2 h in Ar–20% $^{16}O_2$, 4 h in Ar–20% $^{18}O_2$; (b) 2 h in Ar–4% H_2–2% $H_2^{16}O$, 4 h in Ar–4% H_2–2% $H_2^{18}O$. Reproduced from Ertl, S. T. Diss. RWTH Aachen, 2006.

exposure times,[61] a Mn deficit will occur in the spinel layer. In the p_{O_2} gradient existing in the scale, this will result in a vacancy flux from the spinel surface towards the spinel–chromia interface. Here these vacancies tend to condense and result in void formation, as illustrated in **Figure 19**. In air, the Mn deficit in the spinel may be compensated by Cr cations from the inner chromia layer. This would result in an enhanced outward flux of Cr, which could explain why during air exposure the presence of Mn in the alloy increases not only the overall thickness of the oxide but also that of the inner chromia scale.[51]

It should be mentioned that the rapid incorporation of Mn into the oxide layer may easily lead to complete exhaustion of the Mn reservoir in the test specimen. This effect, which will be especially pronounced at high oxidation temperatures and/or when using thin components,[61] will obviously alter the described effect of Mn additions on the gas composition dependence of the oxide growth kinetics.

Figure 24 shows metallographic cross sections of a high-Cr ferritic steel with a very similar composition as that shown in **Figure 19** but with minor additions of Si and Al, after exposure in air and H_2/H_2O at 800 °C. The volume increase accompanied by the internal oxide formation leads to outward metal flow[61,64] resulting in formation of metallic nodules in the scale and damage of the oxide scale.[61] In spite of this difference in scale morphology compared to that shown in **Figure 19**, both steels exhibit a double-layered surface oxide of Cr_2O_3 and Cr/Mn spinel that exhibits a slightly higher growth rate in high – than in low – p_{O_2} gas. Apparently, the atmosphere dependence is mainly governed by presence of the Cr/Mn spinel and is not

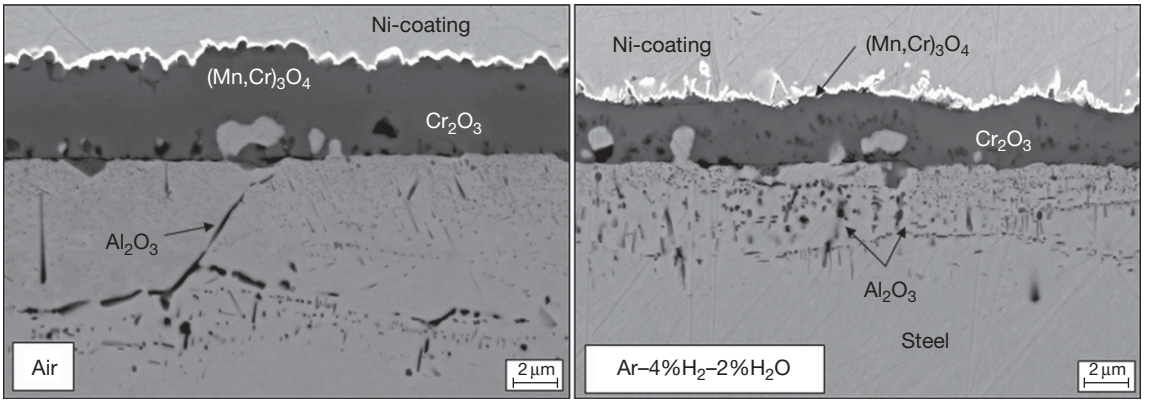

Figure 24 Metallographic cross sections of high-Cr ferritic steel Crofer 22 A after 1000 h exposure in Air and in Ar–4% H_2–2% H_2O at 800 °C. The steel had a very similar composition as that shown in **Figure 19**; however, it contained 0.1% Al and 0.1% Si.

fundamentally affected by presence of the minor alloying additions (0.1%) of Al and Si. This may be different if higher amounts (e.g., a few tenths of a percent) of Si/Al are present. In that case, a more extensive internal oxidation and formation of metallic protrusions result in a more severe damage of the external scale with the result that molecular transport substantially contributes to the scale growth process.[61] It is obvious that then a substantially different atmosphere dependence may occur. This can be derived from results of Hammer *et al.*,[65] who studied the behavior of high-Cr ferritic steels containing Al and/or Si up to 1 wt% in low- and high-p_{O_2} gas between 700 and 900 °C. For such alloys the gas composition dependence described earlier for alloys forming 'ideal' gas-tight two-layered spinel/chromia layers is not clearly observed.

Further studies on the effect of minor alloying additions on the oxidation behavior in low- and high-p_{O_2} gases were carried out by Galerie *et al.*[14] The authors investigated the behavior of 18% Cr ferritic steels containing minor additions of Nb or Ti. Both elements affected the growth rate of the protective scale but did not fundamentally alter the relative differences between Ar–O_2 and Ar–H_2O exposure.

1.17.4.3 Effect of Environment on Scale Formation in Case of 'Borderline Alloys'

1.17.4.3.1 Nonprotective oxidation in water vapor

For iron–chromium alloys with intermediate Cr content in the range 8–20%, it has frequently been found that oxidation rates in water vapor may be several orders of magnitude higher than those found under dry conditions.[6,16,22,49,66–68] These high rates are related to a change in oxide composition from a chromia base to an Fe-oxide base scale. They are sometimes preceded by an initial period of protection after which breakaway oxidation occurs as a consequence of failure of the protective chromium-rich oxide layer. Referring to **Figure 13**, the critical Cr content required for obtaining protective chromia scale formation in water vapor is thus higher than that required during O_2 or air exposure.

Ehlers *et al.*[4] suggested that during exposure of 9% Cr steels, in Ar–50% H_2O at 600–650 °C, volatile $Fe(OH)_2^{(g)}$ may form in the inner layers of the scale which is then converted to hematite or magnetite in the outer layers of the scale thereby contributing to the deterioration of the protective Cr-rich oxide. However, based on the available thermodynamic data, the vapor pressure of the hydroxide may be too low to provide sufficient mass transport by the volatile species.[16] Galerie *et al.*[14] showed that the first stage of breakaway of Fe–15% Cr at 800–1000 °C in Ar–15% H_2O corresponds to a separation of the chromia scale from the alloy and consequently scale equilibration, allowing the formation of hematite at the metal–oxide interface. Then rapid growth of hematite at this interface disrupts the chromia scale and breakaway is initiated. The authors propose that the more acidic nature of hematite compared to chromia encourages more rapid dissociation of water and therefore continued hematite growth is favored, whereas in the absence of water vapor chromia would continue to form and protection is maintained. Fujii and Meussner[68] oxidized a range of FeCr alloys with up to 25% Cr at temperatures between 700 and 1100 °C in Ar–10% water vapor and observed a period of protective oxidation before occurrence of high

oxidation rates for the alloys with a Cr content greater than 20%. They proposed that the high rates of oxidation were related to hydrogen/water dissociation in pores (see Section 1.17.3.3) within the wüstite layer. Mikkelsen and Linderoth[67] explained the breakaway oxidation of Fe–22% Cr at 800 °C in a H_2/Ar gas mixture (7:93) with addition of 12% water vapor to be the consequence of the stability of fast-growing wüstite, whereas with 1% water vapor wüstite is not stable. Hayashi *et al.*[69] observed for diluted Fe–Al alloys a very similar gas composition dependence as observed for Fe–Cr alloys by other authors.

Summarizing, it can be said that the breakaway type oxidation of 'borderline' FeCr-based alloys with intermediate contents of protective scale-forming elements exhibits a number of common features which strongly indicates that the responsible process is independent of the type of oxide formed. The mechanisms occurring at high temperatures (700–1000 °C) seem to be not fundamentally different from those at lower temperature (500–650 °C). Modified transport processes in, for example, wüstite due to presence of water vapor have clearly been verified, but are unlikely to be responsible for the initiation of breakaway because it also occurs at temperatures at which wüstite is unstable. A mechanism that explains the breakaway oxidation at higher as well as lower temperature will be discussed in the following sections.

1.17.4.3.2 Internal oxidation of Cr as trigger for breakaway oxidation

Figure 25 shows SEM cross sections of an Fe–10Cr model alloy after isothermal oxidation for 72 h at 900 °C in Ar–20% O_2, Ar–4% H_2–2% H_2O and Ar–7% H_2O. In Ar–O_2 the scale contains substantial amounts of Fe and consists of Fe_2O_3 near the scale–gas interface, an intermediate layer of spinel, and a thin chromia layer in contact with the alloy. Apparently, significant transient oxidation occurred before the chromia became continuous, and thus Fe–10Cr can be considered as a 'borderline alloy' when exposed to Ar–O_2.[70] In Ar–H_2–H_2O, only internal oxides, mainly of Fe/Cr spinel, have formed.[62] Very rapid oxidation occurred in Ar–H_2O because the oxide scale consisted mainly of Fe-rich oxides. Similar observations were made at 1050 °C.[46]

These results clearly show that internal oxidation of Cr is promoted in the gases containing water vapor. In the gas with the highest oxygen potential (Ar–20% O_2), a continuous external chromia layer develops despite the presence of transient oxides. In the gas with the lowest oxygen potential (Ar–H_2–H_2O), the Cr is oxidized internally and no external Fe oxide scale is formed because of the low oxygen activity in the gas (Figure 2). This in contrary to Ar–H_2O in which the alloy matrix, which is Cr-depleted due to the internal oxidation, oxidized because of the higher p_{O_2}, resulting in non-protective scale formation. A similar effect of water vapor on internal oxidation was found by Ani *et al.*[71] These authors studied the behavior of FeCr alloys at 800 °C in dry and wet gas ($pH_2O = 3 \times 10^{-3}$ bar) at a fixed low p_{O_2} of 1.1×10^{-9} bar. The transition from internal to external oxidation was shifted from 8% Cr in the dry gas to 12% Cr in the wet gas. In low Cr alloys, the depth of internal oxidation in the wet gas was substantially larger than in the dry gas.

These results thus indicate that the inward flux of oxygen in the FeCr alloys is greater in the water vapor-containing gases than in the dry gases. It is well known that hydrogen from water vapor readily permeates ferritic steels at high temperatures. Rahmel and Tobolski[36] observed hydrogen uptake in the samples oxidized in wet gases. Also a 'dual atmosphere' effect has been observed for ferritic steel interconnects in SOFCs where the oxidation on the cathode (air) side is influenced by the presence of a hydrogen/water vapor mixture on the anode (fuel) side.[72] Furthermore, the intrinsic diffusivity of hydrogen in bcc iron at 900 °C is approximately 4×10^{-3} cm^2 s^{-1},[73] which is 3 orders of magnitude larger than that of oxygen, which is 2×10^{-6} cm^2 s^{-1}.[74] The values in fcc iron are 7×10^{-5} cm^2 s^{-1} for hydrogen[75] and 1.8×10^{-7} cm^2 s^{-1} for oxygen.[74]

The reasons for the enhanced internal Cr oxidation by hydrogen incorporation into the alloy will now be discussed.

1.17.4.3.3 Conditions for external chromia formation in dry and wet gases

The development and maintenance of a continuous external chromia scale require that two criteria are satisfied. First, the Cr concentration in the alloy must exceed that necessary for outward diffusion to prevent internal oxidation.[76] This criterion for the case of Fe–Cr alloys is:

$$N_{Cr}^{(1)} > \left[\frac{\pi g^*}{3} N_O^{(S)} \frac{D_O V_m}{\tilde{D}_{Fe-Cr} V_{CrO_{1.5}}}\right]^{1/2} \quad [13]$$

where $N_O^{(S)}$ is the oxygen solubility in the alloy, D_O is the diffusivity of oxygen in the alloy, $\tilde{D}_{Fe\text{-}Cr}$ is the alloy

interdiffusion coefficient, and V_m and $V_{CrO_{1.5}}$ are the molar volumes of the alloy and oxide, respectively. It was assumed here that the internal oxide was chromia. The factor g^* is generally approximated as about 0.3.[77] Equation [13] was derived under conditions where only Cr could oxidize. Under conditions where both Fe and Cr can oxidize, the transient oxidation of Fe must also be considered. Gesmundo and Viani[78] showed that the critical solute concentration increases as the rate constant for the growth of the transient, nonprotective oxide increases.

The second criterion is that, once a continuous external scale is formed, diffusion in the alloy must be rapid enough to supply the solute at least at the rate it is being consumed by scale growth.[79] This criterion may be expressed as:

$$N_{Cr}^{(2)} = \frac{V_m}{32v}\left(\frac{\pi k_p}{\tilde{D}_{Fe-Cr}}\right)^{1/2} \qquad [14]$$

where k_p is the parabolic rate constant for growth of the external scale, measured in terms of scale thickness. Based on data Essuman *et al.*[46], it was derived that, for example, at 900 °C $N_{Cr}^{(1)}$ for FeCr alloys is ~0.03. Comparison of the results in **Figures 25–27** shows that for the FeCr alloys the critical Cr content for external scale formation in Ar–20% O_2 at 900 °C is near 10 mass% ($N_{Cr}^{(1)} \approx 0.11$). In Ar–H_2–H_2O, that is, a gas in which Fe oxide can hardly form, it is apparently between 10 and 20 mass% ($N_{Cr}^{(1)}$ between 0.11 and 0.21). In the wet gas Ar–H_2O, in which Fe can easily oxidize, it is larger than 20 mass% ($N_{Cr}^{(1)} > 0.21$).

Essuman *et al.*[80] have shown that for FeCr alloys the parameter regarding internal oxidation $N_{Cr}^{(1)}$ (eqn [13]) moves to higher values as the temperature is increased (see **Figure 27**). **Figure 27** shows that this is indeed the case for exposure in Ar–O_2 as well as in Ar–H_2O. Thus, for Fe–20Cr, non-protective oxidation occurs in both gases at 1050 °C, only in Ar–H_2O at 900 °C and in none of the gases at 800 °C.

Consideration of eqn [13] indicates that promoting internal oxidation by dissolution of hydrogen could result from a reduction of $\tilde{D}_{Fe\text{-}Cr}$; however, based on data of Park *et al.*[81], this seems to be unlikely. The second possibility is that water vapor is increasing the effective value of $N_O^{(S)}$. The rapid diffusion of hydrogen into the specimen may shift the H–O–H_2O equilibrium such that a metastably high concentration of oxygen exists at the specimen surface and results in an increased inward flux of oxygen.[46] Considering the equilibration of water vapor at the specimen surface

$$H_2O^{(g)} = 2\underline{H} + \underline{O} \qquad [15]$$

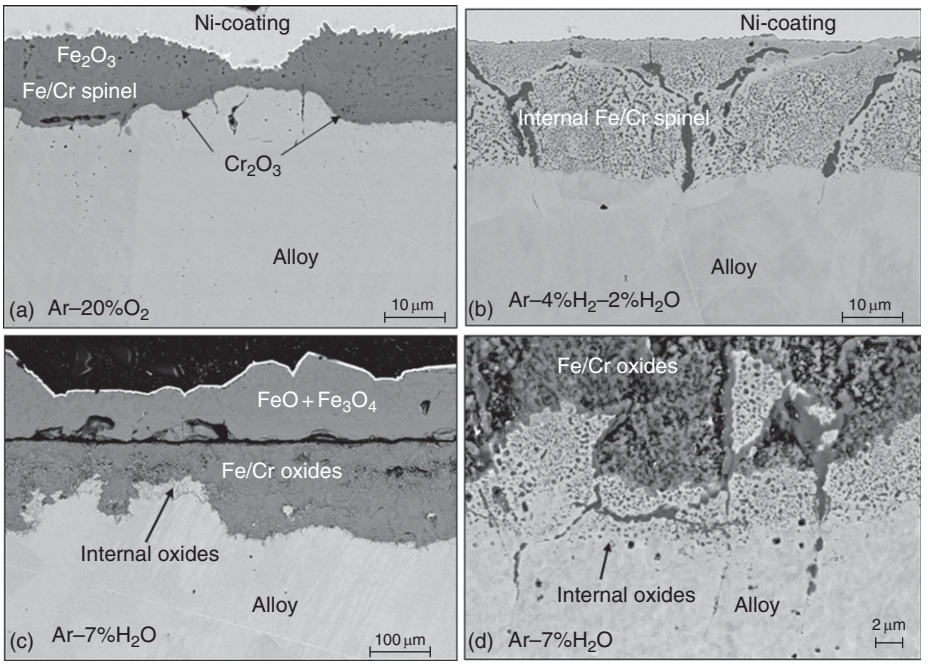

Figure 25 Cross-section SEM micrographs of Fe–10Cr model alloy after isothermal oxidation for 72 h at 900 °C in various atmospheres: (a) Ar–20% O_2; (b) Ar–4% H_2–2% H_2O: (c) Ar–7% H_2O; (d) Ar–7% H_2O high magnification of the internal oxidation zone in Fig. (c). Note the differences in magnification.[46,62]

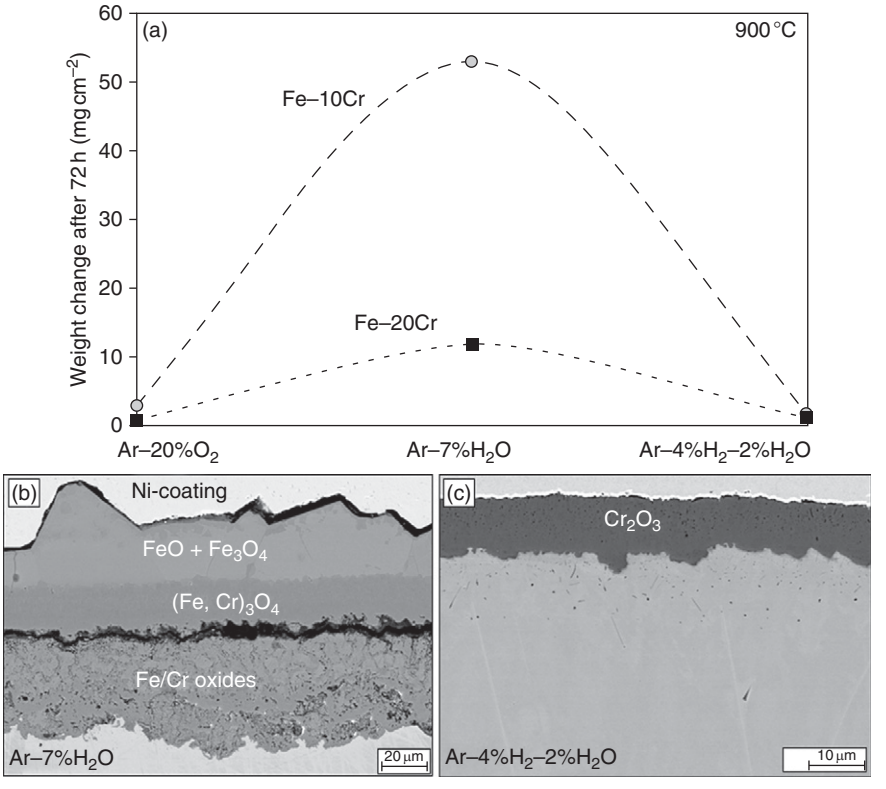

Figure 26 (a) Weight change of Fe–10Cr and Fe–20Cr model alloys after 72 h isothermal exposure in different test environments at 900 °C. The dotted/dashed lines do not show the real dependence of the gas composition but are just inserted for easier visibility of the data points. SEM cross sections of the Fe–20Cr model alloy showing oxide scales formed during 72 h isothermal oxidation in (b) Ar–7% H_2O, and (c) Ar–4% H_2–2% H_2O at 900 °C.[46,62]

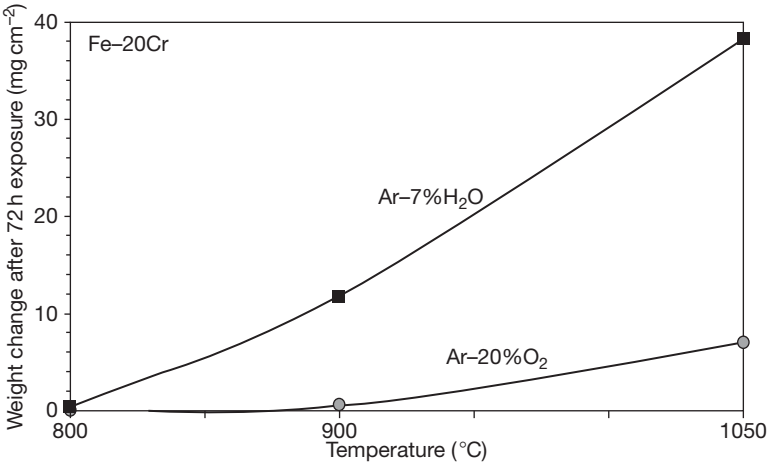

Figure 27 Weight changes after 72 h isothermal oxidation of a binary Fe–20Cr model alloy in Ar–O_2 and Ar–H_2O at different temperatures. Reproduced from Essuman, E.; Meier, G. H.; Żurek, J.; Hänsel, M.; Singheiser, L.; Quadakkers, W. J. *Mater. Sci. Forum* **2008**, *595–598*, 699–706.

the concentration of oxygen at the metal surface may be expressed as:

$$N_O = K_{15} \frac{p_{H_2O}}{N_H^2} \quad [16]$$

If the hydrogen concentration is reduced by rapid inward diffusion, the gas phase will establish an increased concentration of dissolved oxygen, resulting in a concomitantly higher inward oxygen flux.

The final possibility is that the dissolved hydrogen increases the diffusivity of oxygen. It is known from studies on austenitic iron that lattice distortion produced by interstitials can affect diffusivities. For example, the intrinsic diffusivity of carbon increases with increasing carbon content, which is usually interpreted in terms of carbon interstitials expanding the Fe lattice and thus increasing their own mobility.[82] It is conceivable that the rapidly diffusing hydrogen interstitials expand the iron lattice sufficiently so that the diffusivity of the larger oxygen interstitials is increased.

1.17.4.3.4 Breakaway oxidation mechanisms of FeCr alloys in water vapor

As stated in Section 1.17.4.3.1, enhanced, breakaway type oxidation of 'borderline' Fe(Ni)Cr-based alloys in water vapor-containing environments has been described in a large number of publications as well as in textbooks.[1,6] If enhanced internal oxidation of Cr due to dissolution of hydrogen in the alloy is the main reason for the occurrence of breakaway oxidation in steam or Ar–H_2O, then this process will be promoted if molecules of water vapor or hydrogen have direct access to the steel surface. The significance of molecular transport of water vapor was identified by several authors as an important factor for the occurrence of breakaway in O_2/H_2O mixtures.[16] Ikeda *et al.*[83] proposed molecular transport as a major pre-requisite for the breakdown of initially protective scales on 5–30% Cr steels in O_2–10 vol.% H_2O at 750 and 900 °C. Similar conclusions were derived by Ehlers *et al.*[16] from thermogravimetry studies of a 9% Cr steel, where the gas was in situ changed from dry Ar–1% O_2 to an Ar–1% O_2–7% H_2O mixture at 650 °C. Galerie *et al.*[14,32] proposed that the change from a protective oxide scale formed in dry gas into breakaway-type oxidation of an Fe–15% Cr alloy at 800–1000 °C during subsequent exposure in wet gas was initiated by molecular transport of water vapor via microcracks.

In many of the studies in which Fe-rich, breakaway-type oxide scales were observed during exposure of Fe–Cr alloys in water vapor, a zone with internal precipitates of Cr-rich oxide was found (see Figure 25 and, e.g., Ueda *et al.*[84]). In classical oxidation theory, the presence of this zone can be described as a logical consequence of the formation of the nonprotective Fe-based oxide scale; that is, the oxygen partial pressure below that scale at the scale–alloy interface is sufficiently high for Cr to become oxidized internally. Ehlers *et al.*[4,16] showed that an internal oxidation zone was present after 250 h oxidation of a 9% Cr steel in Ar–50% H_2O at 650 °C. After subsequent exposure of the specimen in air, this internal oxidation zone vanished and a thin, protective, Cr-rich layer was formed at the scale–alloy interface and the scale growth rate in this second oxidation stage was extremely small. This change in composition and morphology of the inner interface upon changing from water vapor to a high-p_{O_2} atmosphere or vice versa can be explained by changes in transport processes in the scale by one or more of the mechanisms described in Section 1.17.3. However, based on the discussions in the previous sections, the main change in oxidation mechanism that occurs when changing from water vapor to a high-p_{O_2} gas is the decreased tendency of Cr to become internally oxidized. The formation of the rapid, breakaway-type, Fe-rich oxide scales when exposing 'borderline alloys' in water vapor is just a result of Cr depletion in the alloy matrix because Cr oxidizes internally rather than in the form of a protective external scale. This mechanism would be promoted by a direct reaction of $H_2O^{(g)}$ molecules with the metal surface, thus explaining the observations described above that transport of $H_2O^{(g)}$ through a preexisting scale is required to initiate breakaway oxidation. In $H_2O^{(g)}$/$O_2^{(g)}$ mixtures, competitive adsorption of oxygen and water vapor molecules at external and internal surfaces of the oxide scale was found to govern the growth of the Fe-rich oxide scales at high H_2O/O_2 ratios. It would therefore be expected that occurrence of breakaway oxidation is determined by the $H_2O^{(g)}/O_2^{(g)}$ ratio in the gas, as was indeed experimentally observed for a 9% Cr steel at 600 °C.[16] Also, the oxidation behavior of Fe-Al alloys with Al contents of 5 wt% was found to depend on the $H_2O^{(g)}/O_2^{(g)}$ ratio.[85]

1.17.4.3.5 Borderline NiCr alloys in water vapor

Essuman *et al.*[47] studied the oxidation behavior of Ni–25Cr and Ni–20Cr as well as the 'borderline alloy' Ni–10Cr in various dry and wet Ar-based gas mixtures. Decreasing the oxygen content in dry gas from 20% to 1% was found to promote the selective oxidation of Cr in the 'borderline alloy' Ni–10Cr. It could be shown that this is related to a decrease of the NiO growth rate with decreasing oxygen partial pressure (Figure 28), which, according to Gesmundo

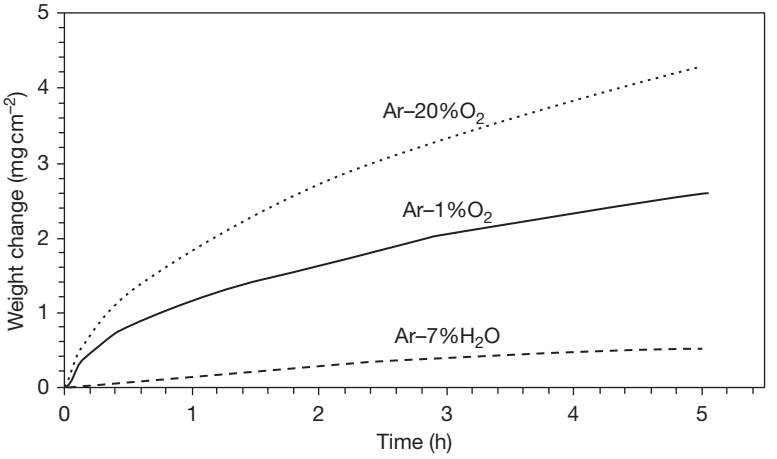

Figure 28 Weight change versus time during isothermal oxidation of pure Ni at 1050 °C in Ar–20% O_2, Ar–1% O_2 and Ar–7% H_2O.

et al.,[78] promotes selective oxidation of Cr. Exposure in Ar–H_2O would then be expected to result in a further improvement in selective oxidation due to the very slow growth rate of NiO in this low-p_{O_2} gas.[32] However, the Cr-rich surface scale formed in Ar–H_2O contained Ni-rich oxide. Also, internal oxides of Cr could be found. These results clearly indicated that, like in FeCr alloys, hydrogen promotes internal oxidation of Cr also in NiCr alloys.

In spite of this similarity in mechanism, the gas composition dependence of borderline NiCr alloys substantially differs from that of corresponding FeCr alloys, the most obvious difference being that the high oxidation rates observed for Fe–10Cr and Fe–20Cr in Ar–H_2O[46] are not found for Ni-based alloys with the same Cr content (**Figure 29**). The reason is that the growth rate of NiO strongly decreases with decreasing p_{O_2}, with the result that in Ar–H_2O the NiO growth rate is extremely small,[32] that is, in fact similar to that of chromia. Even if the Cr content was so low that a protective chromia scale could not form, the overall oxidation rate would still be quite low because of the very slow growth rate of NiO in Ar–H_2O (**Figure 28**), and, obviously, in Ar–H_2–H_2O the NiO will not form at all.

Fe oxide exhibits quite high growth rates in Ar–H_2O mixtures,[14,16,36] and for an Fe–10Cr alloy in Ar–H_2O the enhanced internal oxidation of Cr will, thus, in contrary to Ni–10Cr, result in formation of rapidly growing Fe-rich oxide scales. The behavior of borderline FeCr alloys in Ar–H_2O–H_2 mixtures strongly depends on the exact gas composition because the equilibrium oxygen partial pressure in a gas with a H_2O/H_2 ratio of 1 is very near to the dissociation pressure of Fe oxide (**Figure 2**).

1.17.4.4 Oxidation of Ferritic and Austenitic Steels in Steam

1.17.4.4.1 General remarks

A technologically important example in which 'borderline' FeCr- and FeNiCr-based alloys are subjected to steam at relatively high temperatures is encountered in many power generation systems. In conventional power plants, steam-carrying components are commonly designed using low-Cr (e.g., 2¼% Cr) steels. The behavior of this type of materials at steam temperatures up to ≈ 530 °C has frequently been described[86,87] and will not extensively be treated here. Increasing the steam temperature to 600 °C and even higher for obtaining higher energy conversion efficiencies requires construction materials that possess a higher creep strength than that of the low-Cr steels. This led to introduction of martensitic steels with Cr contents of 9–10% for tubing in heat exchanging components (e.g., T91, T92) as well as for various components in steam turbines.[88] Depending on the actual application, steels with higher Cr contents (e.g., 12% Cr in X20CrMoV12 1 or HCM 12) are considered (**Table 1**); however, these generally possess a lower creep strength than the 9% Cr steels.[89] Based on the results in the previous section, martensitic 9–12% Cr steels may, from the viewpoint of oxidation resistance, be considered as

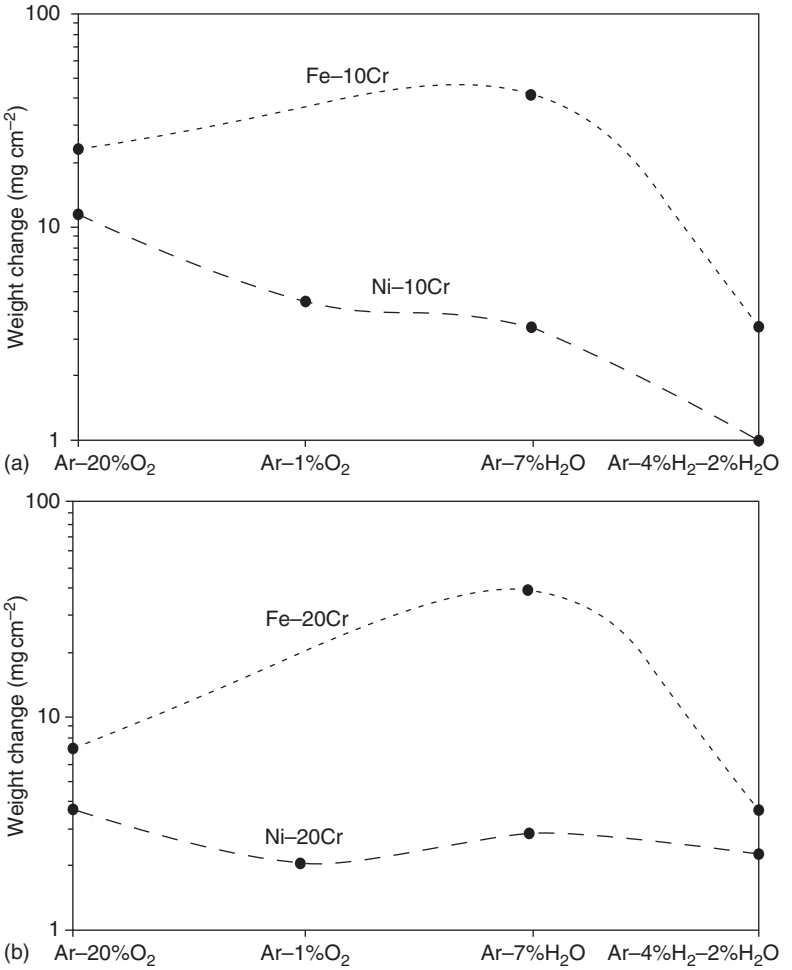

Figure 29 Weight change of Ni–10Cr and Fe–10Cr (a), as well as Ni–20Cr and Fe–20Cr (b) after 72 h isothermal oxidation at 1050 °C in different test environments. Dotted/dashed lines do not present a real pO_2 dependence of the oxidation rate; they are just inserted for clearer visibility of the data points.

Table 1 Typical examples of ferritic, martensitic, and austenitic steels as well as Ni-based alloys presently considered as construction materials for steam-carrying components in fossil fuel-fired power plants

Steel designation	*Nominal composition*	*Steel designation*	*Nominal composition*
Ferritic and martensitic steels		*Austenitic steels*	
30CrMoNiV5–11	1Cr–1Mo	1.4910	17Cr–13Ni–Mo–N
HCM2S (T23)	2¼Cr–1.5W–V	Super 304H	18Cr–10Ni
NF616 (P92)	9Cr–2W–Mo–V–Nb–N	TP347HFG	18Cr–10Ni–Nb
P91	9Cr–1W–Mo–V–Nb–N	NF709	20Cr–25Ni
E911	9Cr–1Mo–1W–V–Nb–N	Save 25	23Cr–18Ni–3Cu–1.5W–Nb-N
X7CrCoNiMo10–6	10Cr–6Co–1Mo	HR3C	25Cr–20Ni–Nb–N
VM 12	11Cr–0.5Si–Mn	AC66	28Cr–32Ni–Ce–Nb
HCM 12	12Cr–1Mo–1W–V–Nb	*Ni-based alloys*	
HCM12A (P-122)	12Cr–1.5W–Mo–V–Nb–Cu-N	Alloy 617	22Cr–12Co–9Mo
X20CrMoV12–1	12Cr–1Mo–V	Alloy 740	24Cr–20Co–0.5Mo
AISI 430	17Cr–0.5Mn–0.5Si	Alloy 263	22Cr–20Co–0.6Al

Nominal concentrations of alloying additions given in mass%.

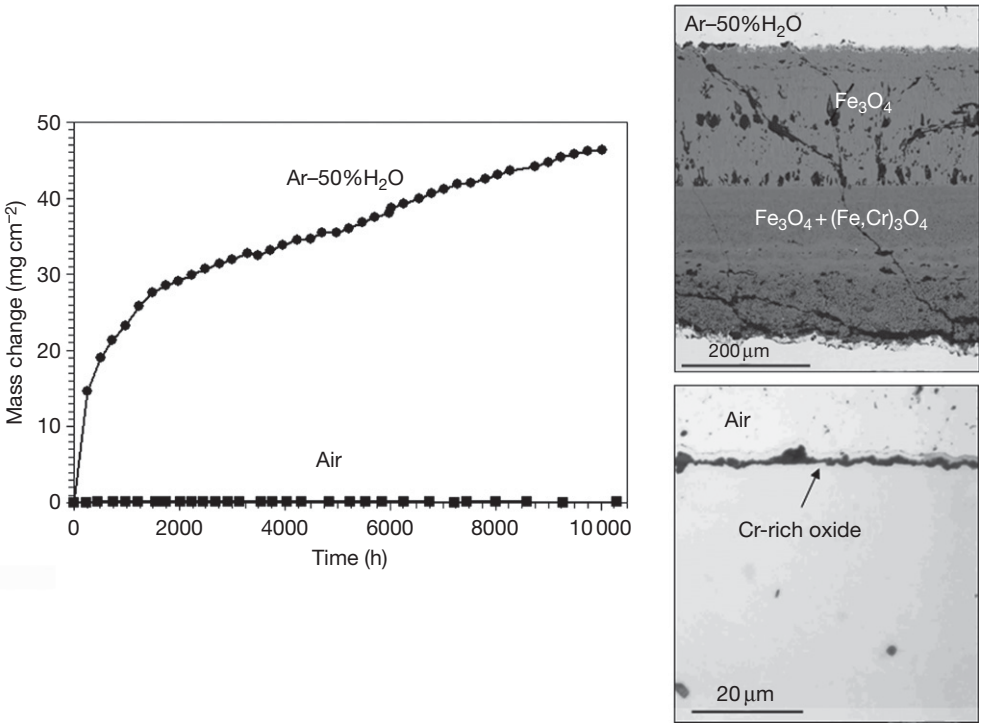

Figure 30 Weight change versus time for oxidation of 9% Cr steel P92 during exposure at 650 °C in air and Ar–50% H_2O. Metallographic cross sections show differences in scale morphology after 10 000 h exposure. Adapted from Ehlers, J.; Quadakkers, W. J. Report Forschungszentrum Jülich, Jül-3883, 2001; ISSN 0944-2952.

'borderline' alloys. This is confirmed by the results in Figure 30, which shows the weight change data of the 9% Cr steel P92 during exposure at 650 °C in air and in Ar–50% H_2O.

1.17.4.4.2 Steam oxidation mechanisms of 9–12% Cr steels

During exposure in (simulated) steam in the temperature range 550–650 °C, all ferritic 9–12% Cr steels tend to exhibit an incubation period in which the oxidation rates are very low (Figure 31). This incubation period can range from minutes to several hundreds of hours and it increases with increasing amount of protective scale-forming elements (e.g., Cr, Si) and the extent of cold work. In this oxidation stage, oxide layers of the type $(Fe,Cr)_2O_3$ and/or Cr-rich $(Fe,Cr)_3O_4$ covered by a hematite layer are formed.[4,19,90]

After longer exposure times, breakdown of this protective scale occurs, which is accompanied by formation of rapidly growing magnetite and a zone with internal Cr_2O_3 precipitates (Figure 31).[46] At temperatures above approximately 580 °C, wüstite may be present near the scale–steel interface.[16,84,87] The inner and outer layers are separated by a gap, probably caused by vacancy condensation resulting from the rapid outward growth of the outer magnetite layer (Figure 31). Further growth of the scale depends to a large extent on transport processes within this gap, likely by the so-called H_2/H_2O bridges (see Section 1.17.3.3). This explains why there is a relative movement of the 'transient gap' towards the magnetite layer in the outer part of the scale during prolonged exposure. As the overall scale thickness increases, the Fe activity at the scale–gas interface gradually decreases because of the increasingly difficult transport of Fe cations to the oxide surface as a result of the presence of the in-scale gap (Figures 31 and 32). This decrease in Fe activity in the outer scale eventually results in formation of hematite, that is, the oxide in equilibrium with the gas atmosphere (Figure 32), on top of the scale. The formation of hematite starts at the grain boundaries of the magnetite layer (Figure 32(b)). Additionally, molecular gas transport occurs through the outer scale.[83]

For a 10% Cr steel at 650 °C, time t_1 in Figure 31 is ~10–15 min and t_5 ~5 h[91]. Exact times, however, differ with the water vapor content, exact steel composition and surface deformation, for example,

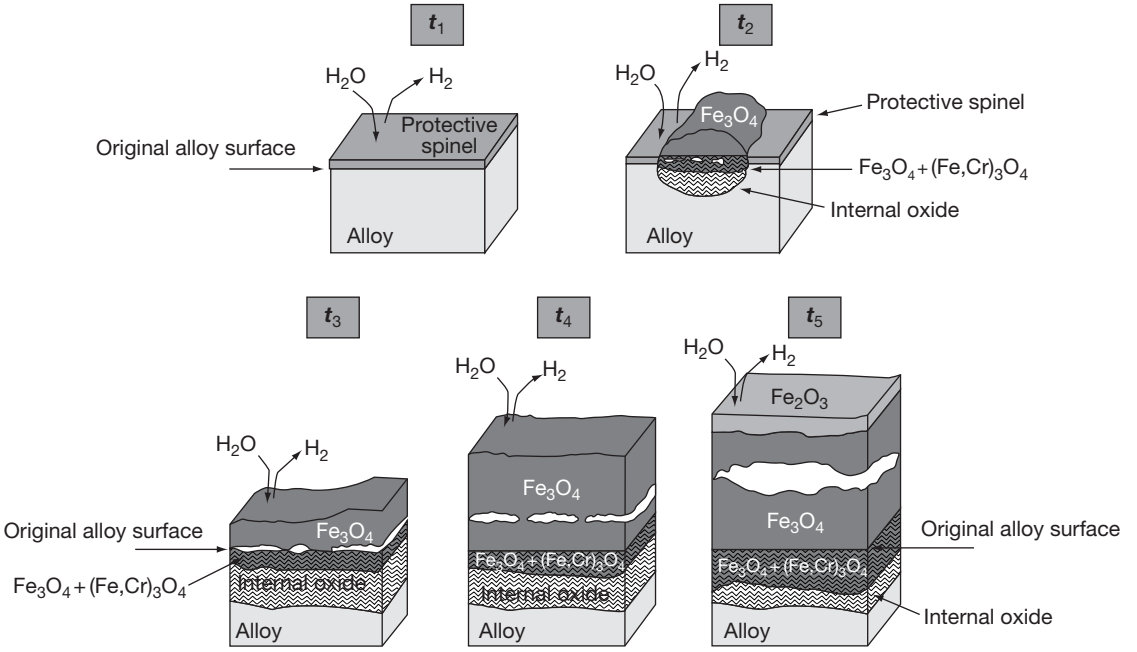

Figure 31 Proposed mechanism for the oxide scale formation on ferritic 10% Cr steel in Ar-H_2O mixtures. Times t_1, t_2, t_3, t_4, t_5 represent subsequent time steps during the oxidation process. Reproduced from Quadakkers, W. J.; Ennis, P. J.; Żurek, J.; Michalik, M. *Mater. High Temp.* **2004**, *22*(1/2), 37–47.

introduced by grinding or cold work. The depth of the internal oxidation zone tends to decrease with increasing temperature, as will be more extensively discussed later.

The change from protective to non-protective oxidation ($t_1 \rightarrow t_2$ in **Figure 31**) can be explained by the enhanced oxygen transport in voids by H_2/H_2O as proposed by Fujii and Meussner.[92] During exposure in oxygen or air, and during the incubation period in wet gas (t_1, Figure **31**), voids may be formed at the interface between steel and the protective Cr-rich oxide as result of vacancy condensation. In the case of Cr_2O_3, p_{O_2} at the scale–alloy interface at 650 °C is $\sim 10^{-34}$ atm and the flux of oxygen ($\mathcal{J}_{O_2}$) across a void can be calculated using the Hertz–Langmuir equation:[93]

$$\mathcal{J}_{O_2} = \frac{p}{(2\pi MRT)^{0.5}} \quad [17]$$

where p is the vapor pressure and M the mass of the gas molecules. The flux is found to be extremely low (in the range 8×10^{-34} g cm^{-2} s^{-1}), thus giving Cr sufficient time to diffuse from the bulk alloy towards the inner surface of the void, which can, therefore, heal by again forming a Cr-rich scale. Such a healing process could be illustrated by the TEM cross sections of an oxide scale on a 9% Cr steel after air exposure at 650 °C.[16] If, however, $H_2O^{(g)}$ is present in the void, its partial pressure will be determined by the equilibrium:

$$H_2O^{(g)} = H_2^{(g)} + \frac{1}{2}O_2^{(g)} \quad [18]$$

Calculating the equilibrium gas composition at a total pressure of 1 atm, assuming the gas Ar–50% H_2O to be in equilibrium with the dissociation pressure of the oxide (10^{-34} atm), reveals for p_{H_2O} a value of 10^{-6} atm. Putting this value in the Langmuir equation, it is found that an oxygen flux of 5×10^{-6} g cm^{-2} s^{-1} can be sustained. This is substantially larger than the actually observed oxidation rate in the wet gas. Thus, oxygen transport via the H_2/H_2O bridges[36] in voids within the scale can in principle explain the breakdown of the protective Cr-rich oxide and can account for the high oxidation rates in Ar–H_2O.

However, based on the considerations in the previous sections, the change from protective to nonprotective oxidation will likely be triggered by enhanced internal oxidation of Cr due to hydrogen dissolution in the alloy. Water vapor and hydrogen can be transported through the oxide layer, for example, via microcracks formed as a result of growth stresses.[66] Nakagawa *et al.*[94] considered the case where different oxidation processes were occurring on two sides of

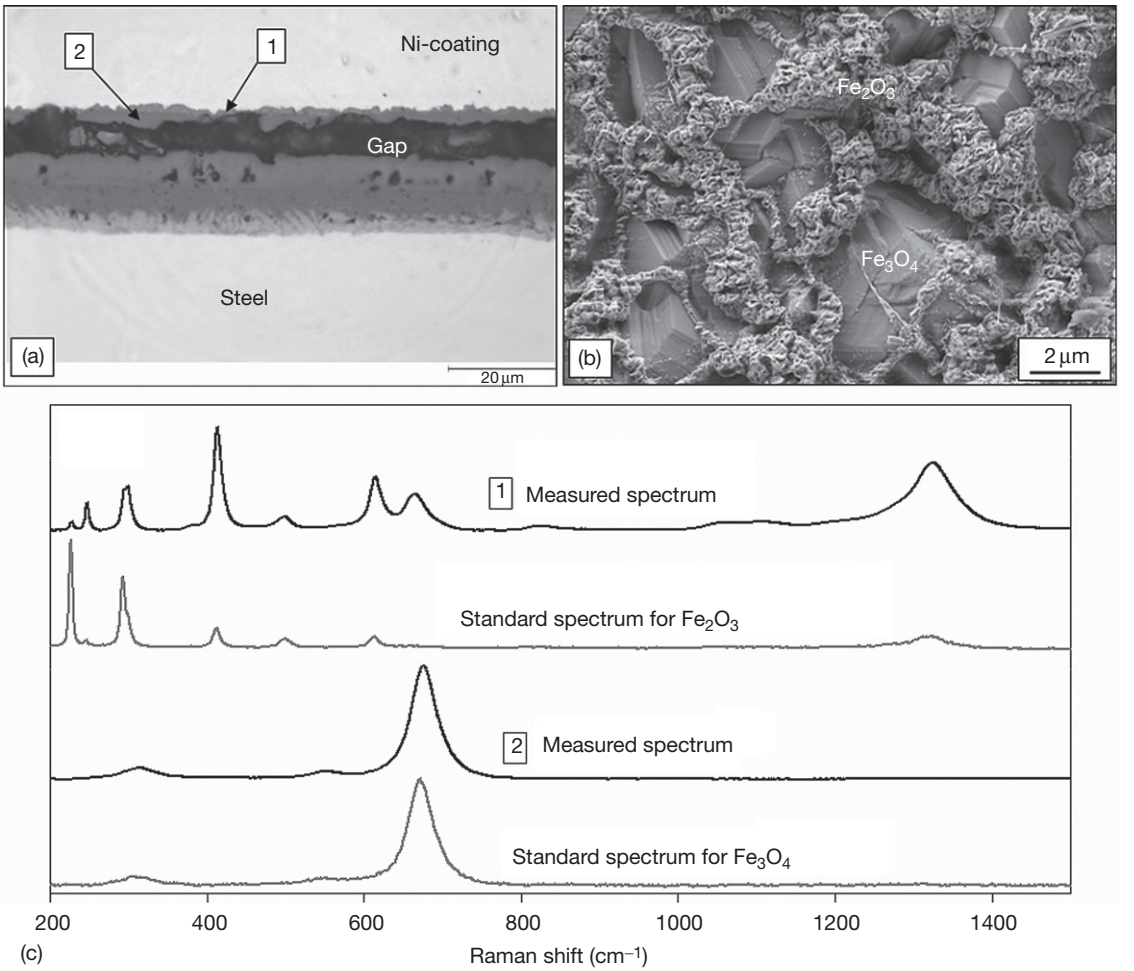

Figure 32 Metallographic cross section (a) and SEM picture (b) of oxide surface of 10Cr–1Mo–1W (low Si) steel after 5 h oxidation in Ar–4% H_2O at 650 °C. Point 1 and 2 in (a) relate to Raman analyses in (c). Reproduced from Żurek, J.; Michalik, M.; Schmitz, F.; Kern, T. U.; Singheiser, L.; Quadakkers, W. J. *Oxid. Met.* **2005**, *63*(5/6), 401–422.

ferritic steels when used as a boiler tube material for power stations. It was proposed that hydrogen generated on one side of the tube wall diffuses to the side with the higher p_{O_2} and deteriorates the protective properties of the air-formed chromia base scale. In many cases cited above, hydrogen diffusion into the metal was observed, a clear sign of direct reaction of the water vapor in the oxidation process.

1.17.4.4.3 Void and gap formation

The oxide scales after oxidation of 9–10% Cr steels in water vapor contain nearly always a substantial amount of pores and/or microvoids (**Figure 33**), finally resulting in the formation of gaps that may promote spallation of the scales during thermal cycling. The main reason for void formation in the oxide scale given in the literature is vacancy condensation as a result of the fast outward migration of metal ions through the scale.[6,49]

During long-term exposure, void formation seems to occur at different locations in the scale. First voids ('transient gap') start to form already after very short oxidation times as shown in **Figure 31**. If the isothermal exposure is continued, the 'transient' gap may heal by growth of the inner oxide scale as water vapor molecules gain access through the outer layer, and the gap may eventually completely close which results in a more or less compact scale. Transport of Fe cations to the surface then becomes again possible and thus the Fe activity at the oxide surface increases. At a sufficiently large flux of Fe cations, the outer hematite transforms into magnetite, and after longer times (at 650 °C, for example, a few hundred hours)

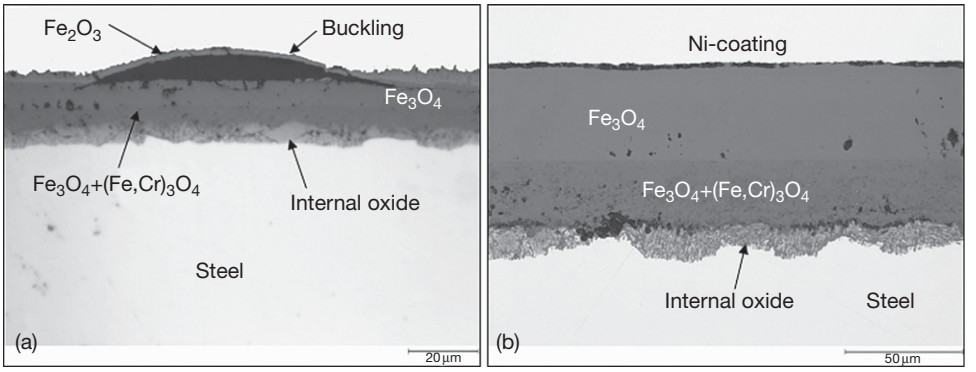

Figure 33 (a) Isothermal oxidation of a 10Cr–Mo–W–Si steel at 625 °C in Ar–7% H_2O showing buckling of oxide separation at hematite–magnetite interface, (b) oxidation of 10Cr–Mo–W–Si steel at 600 °C in Ar–50% H_2O (intermediate cooling every 250 h) showing formation of compact oxide layer. No evidence of spalling was found up to the total exposure time of 1000 h. Reproduced from Quadakkers, W. J.; Ennis, P. J.; Żurek, J.; Michalik, M. *Mater. High Temp.* **2004**, *22*(1/2), 37–47.

the scale appearance is then similar to that shown in Figure 33(b).

If a thermal cycle is introduced in the early stages of the oxidation process, that is, before healing of the 'transient gap,' scale spallation occurs. Further exposure then results in growth of the freely exposed magnetite layer eventually leading to a scale morphology similar to that shown in Figure 33(b). The question of whether spallation or healing of the outer layer above the gap occurs thus depends on the time at which, for a given temperature, the thermal cycle is introduced. This could be shown for a 10Cr–Mo–W–Si steel after exposures at 600 and 625 °C in Ar–H_2O.[91] If the specimen was cooled after 70 h exposure, spallation of the top layer occurred because of the presence of the in-scale gap. If the first temperature cycle was introduced after 250 h, sufficient time was available for healing of the gap and thus excellent oxide adherence was found even after extended exposure for several thousand hours.

As long as the scale contains an outer hematite layer, local buckling by a separation at the magnetite–hematite interface is sometimes observed (Figure 33(a)). This might be related to a mechanism which is similar to that frequently described for oxide films on, for example, pure chromium,[39] that is, lateral growth of the scale due to in-scale oxide formation at scale grain boundaries. The cation and anion diffusion in the Fe_2O_3 lattice are known to be much smaller than in magnetite and wüstite. Therefore, scale growth is likely to occur to a large extent via and at the oxide grain boundaries, and thus in-scale growth can occur by reaction of inwardly and outwardly moving species.

The time required for complete healing of the 'transient' gap tends to increase with decreasing temperature. After 550 °C exposure, remnants of the gap within the magnetite can sometimes be found up to quite long exposure times of more than 1000 h (Figure 34(a)), whereas after the same exposure time at higher temperatures only a dense magnetite layer, sometimes with isolated voids in the outer scale, is found (Figure 34(b)).

1.17.4.4.4 Long-term behavior

The long-term behavior of the various types of commercially available martensitic Cr steels in steam in the temperature range 550–650 °C can be rationalized on the basis of a graph similar to that shown in Figure 13. The borderline between the various oxidation regimes is substantially affected by alloying additions, as seen by the data in Figure 35, with the result that a large variation in oxidation rates for group II alloys with the same Cr contents may be observed. As will be shown later, the exact location of the borderline between the various types of oxide scales depends on temperature. Taking these restrictions into account, it can be said that ferritic steels with a Cr content of less than approximately 8% (group I) exhibit at 600–650 °C high oxidation rates and the main oxide phases present in the surface scales are magnetite and (Fe,Cr) spinel. Steels of group III exhibit very low oxidation rates and the oxide scales mainly consist of Cr_2O_3 and $(Cr,Fe)_2O_3$. The steels of group II are 'intermediate cases' because the oxidation rates and scale morphologies may substantially differ as a function of time, temperature, minor alloying additions, and surface treatment.

There is general consensus that steam-side oxidation of ferritic and martensitic boiler tubes occurs at a rate given by:

$$x = K' t^n \qquad [19]$$

where x is the oxide scale thickness, t is the exposure time, n is the rate exponent, and K' is the proportionality coefficient, which is a function of temperature, alloy composition, oxygen partial pressure, stress level, and radius of curvature of the tubing. For tubing of ferritic/martensitic steels from groups I and II, n has been found to vary from 1/2 to 1/3, and is believed to be a function of time and temperature.[88]

During exposure of the ferritic steels of group I or II (Figure 35) for longer times of, for example, 1000 h in the temperature range 600–650 °C, the outer magnetite layer is mostly compact and no hematite can be found (Figure 36). The magnetite frequently contains cracks perpendicular to the oxide surface, which are caused by tensile cracking during cooling due to the high thermal expansion coefficient of the magnetite.[95]

Upon prolonged exposure, the scales start to develop more and more microvoidage. This first occurs in the inner scale (Figure 36). Here the largest extent of void formation seems to develop at the interface between the internal oxidation zone, if present, and the inner oxide layer (Figure 36). The eventual pore morphology and distribution in the inner scale depend on the way in which the vacancies within the scale and/or at the scale–alloy interface

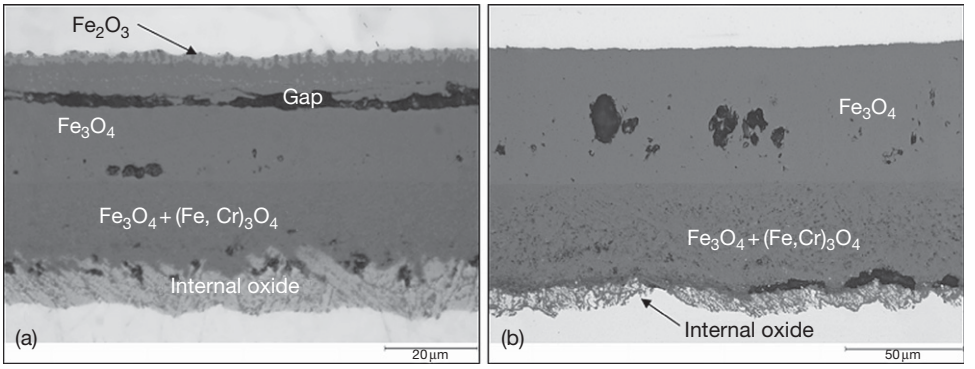

Figure 34 Effect of temperature on morphology and void/gap formation of scale on 10Cr–1Mo–1W (low Si) steel during exposure in Ar–50% H_2O for 1000 h: (left) 550 °C; (right) 600 °C. Note the differences in magnification. Reproduced from Quadakkers, W. J.; Ennis, P. J.; Żurek, J.; Michalik, M. *Mater. High Temp.* **2004**, *22*(1/2), 37–47.

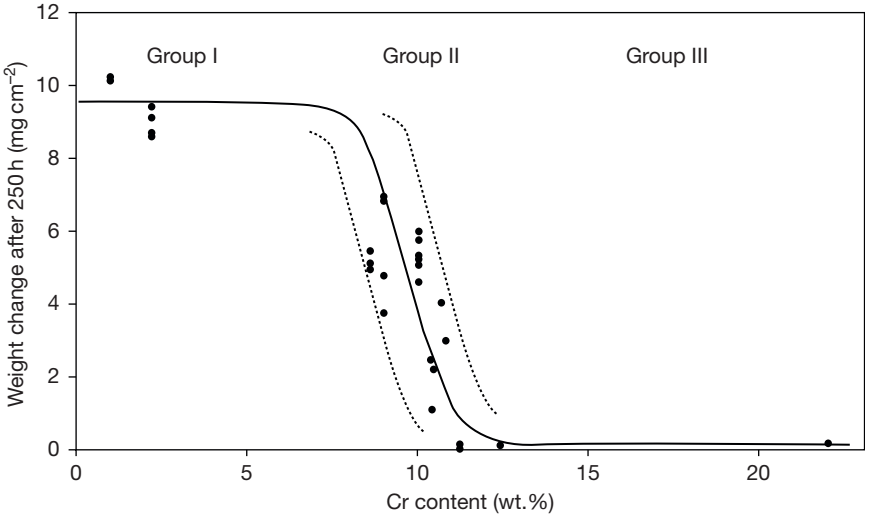

Figure 35 Weight change of various ferritic and martensitic steels after 250 h oxidation in Ar–50% H_2O at 600 °C, derived from data in Ehlers and Quadakkers.[4] Designations 'Group I–III' are explained in the text.

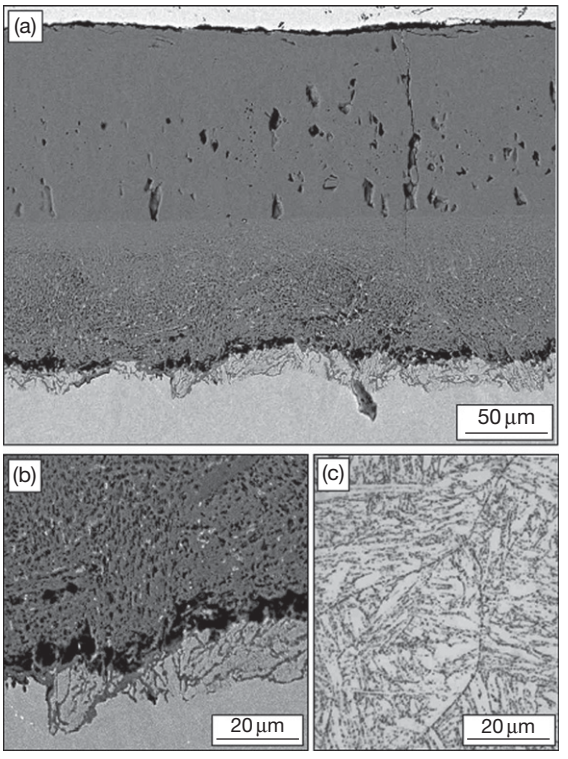

Figure 36 Oxide scale formed on 10Cr–1Mo–1W steel during exposure for 1000 h in Ar–50% H_2O at 650 °C: (a) overview; (b) higher magnification of scale–steel interface; (c) steel microstructure. Reproduced from Ehlers, R. J.; Ennis, P. J.; Singheiser, L.; Quadakkers, W. J.; Link, T. In EFC Workshop 2001; Schütze, M.; Quadakkers, W. J., Nicholls, J. R., Eds.; The European Federation of Corrosion Publications, 2001; Vol. 34, Paper 12, pp 178–193.

coalesce to voids. **Figure 36** shows a clear difference in pore morphology in the outer pure Fe_3O_4 layer and in the inner two-phase layer consisting of Fe_3O_4 + $(Fe,Cr,Mn)_3O_4$ and in the internal oxidation zone adjacent to the alloy. Numerous tiny voids are present in the inner two-phase layer (**Figure 36**) which seem to be correlated with the $(Fe,Cr,Mn)_3O_4$ bands embedded in the Fe_3O_4 matrix.[4] Apparently, the interfaces between these bands and the magnetite act as nucleation sites for the voids. For a given alloy, the morphology and distribution of the 'bands' depend on temperature, as will be illustrated later.

This type of void formation, as well as the morphologies of the inner spinel layers and the zone of internal oxidation, is affected by the underlying steel microstructure (**Figure 37**), including carbides preferentially formed at steel grain boundaries and/or martensitic laths.[96] **Figure 38** compares the scale cross sections of a 10Cr–Mo–W steel with that of a Fe–9% Cr model alloy manufactured from high-purity elements after 1000 h exposure in Ar–50% H_2O. Although the thicknesses of the scales on the two materials do not substantially differ, the void and crack morphologies exhibit tremendous differences. The most striking difference is the large gap occurring in the case of the model alloy near the alloy–steel interface, but not in case of the commercial steel. This is likely related to differences in the mechanisms of vacancy condensation, due to the absence of carbide precipitates in the model alloy. This results in a concentration of the voidage at the scale–steel interface, whereas in case of the commercial steel the voids at first tend to be evenly distributed in the whole inner layer.

During long exposure of the commercial steels of group II, voidage also starts to occur in the outer magnetite layer (**Figure 36**). These voids can be unevenly distributed or they can coalesce to a gap at the interface between the inner and outer layers (**Figure 39(a)**). Indications have been found that the latter is caused by limitations of the cation transport in the inner scale. Here three possible reasons may be mentioned[97]:

1. The continuing formation of voids in the inner scale decreases the transport area available for cation diffusion.
2. The two-phase mixture of FeCr spinel and magnetite in the inner scale changes, near the interface between outer and inner scale, to a single-phase layer. Magnetite, which acts as 'rapid diffusion path' for Fe cations, vanishes with the result that the transport of Fe cations from the inner to the outer scale decreases.
3. The formation of a protective, Cr-rich spinel layer at the oxide–alloy interface.

The limitation of cation transport has the result that the growth rate of the outer magnetite in the existing oxygen activity gradient can no longer be sustained. Consequently, inwardly moving vacancies in the magnetite tend to condense at the interface between the inner and the outer layer resulting in void and gap formation (**Figure 39(a)**).

The formation of a Cr-rich layer at the oxide–alloy interface (No. 3 above) preferentially occurs at higher temperatures (at and above 600 °C) because then diffusion of Cr in the alloy and/or the rate of spinel formation are sufficiently fast. It is also favored by increasing the amounts of protective scale-forming elements (Cr, Si), and, therefore, the tendency for extensive void formation in the outer magnetite layer and/or at the interface between inner and outer scale

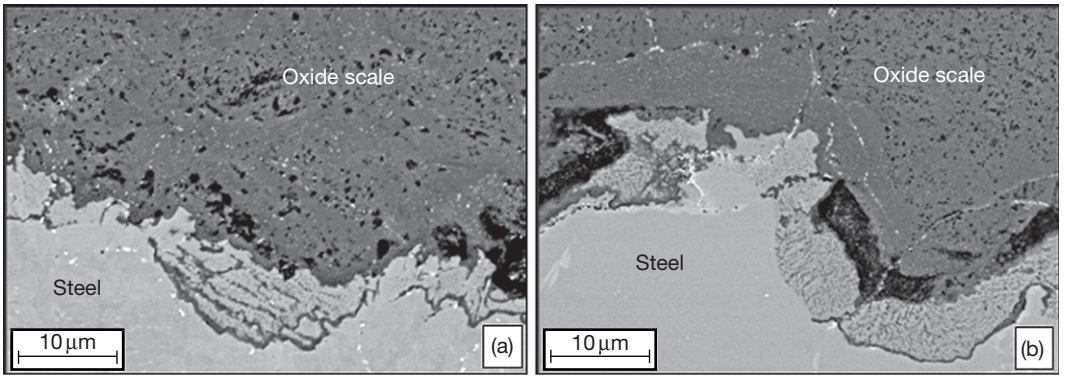

Figure 37 Cross-sections of oxide scales on specimens of 9% Cr steel P92 after oxidation for 1250 h at 650 °C in Ar–50% H_2O. Prior to exposure the specimens were heat-treated so that they had a martensitic (a) or ferritic (b) microstructure. Reproduced from Ehlers, R. J.; Ennis, P. J.; Singheiser, L.; Quadakkers, W. J.; Link, T. In EFC Workshop 2001; Schütze, M.; Quadakkers, W. J., Nicholls, J. R., Eds.; The European Federation of Corrosion Publications, 2001; Vol. 34, Paper 12, pp 178–193.

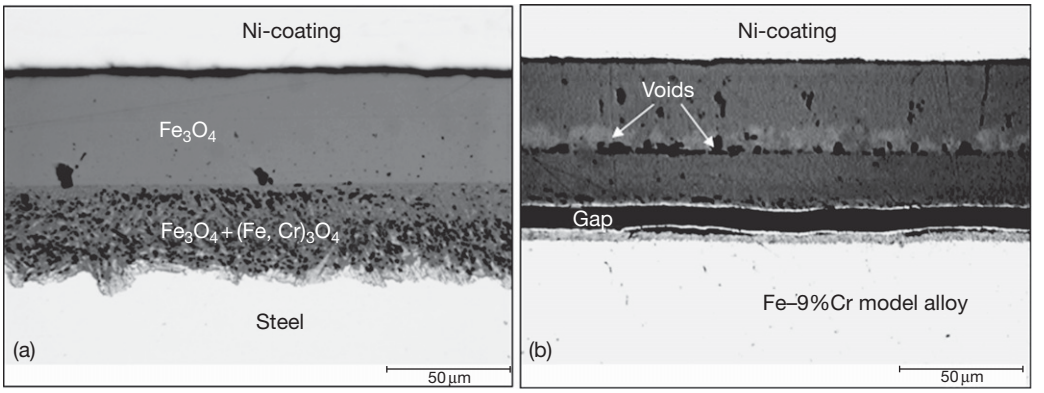

Figure 38 Metallographic cross sections of oxide scales on (a) commercial 10Cr–Mo–W steel and (b) Fe–9% Cr model alloy (manufactured from high-purity materials) after 1000 h isothermal exposure in Ar–50% H_2O at 625 °C, showing differences in void/gap formation in the scale. Reproduced from Quadakkers, W. J.; Ennis, P. J.; Żurek, J.; Michalik, M. *Mater. High Temp.* **2004**, *22*(1/2), 37–47.

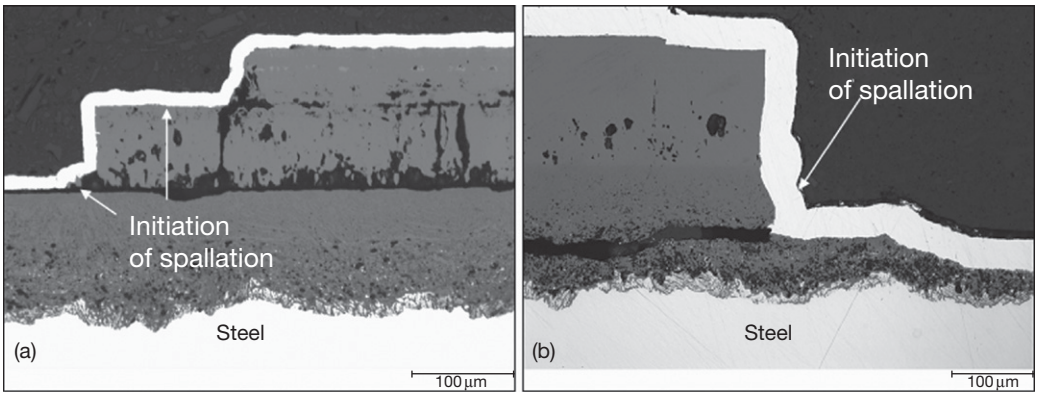

Figure 39 Different types of scale spallation during oxidation on 10Cr–1Mo–1W low Si steel after long-term exposure in Ar–50% H_2O at (a) 625 °C and (b) 650 °C.

will in principle be larger for steels of group II in Figure 13 than for lower Cr steels (group I).

As explained in Section 1.17.4.4.2, extensive void/gap formation will eventually result in the formation of hematite on top of the outer magnetite layer. Macroscopic observation of hematite is thus frequently a strong indication for the formation of a heavily voided/cracked magnetite layer, which is expected to be prone to spallation. Nishimura *et al.*[98] described a similar mechanism for the hematite formation and claimed that the transformation of magnetite into hematite plays a role in oxide spalling. An interesting feature is that the outer surface of the hematite is in some cases flat; in other cases it exhibits a whisker type morphology, possibly related to a mechanism described in Section 1.17.3.1 for whisker formation on chromia scales. The reasons for these differences in morphology of the hematite are, as far as known to the authors, not fully clarified.

On the basis of the described mechanisms of void/gap formation, it can generally be said that the crack initiation/propagation modes occurring can result in three different types of scale spallation: that is, spalling occurring in the outer magnetite layer (Figure 39(a)); near the interface between the oxide and the alloy or the internal oxidation zone (Figure 39(b)); or at the interface between inner and outer scale (Figure 39(a)). The latter mode preferentially occurs in case of group II alloys with higher Cr (and Si) contents and is similar to that frequently found for austenitic steels (see Section 1.17.4.4.6).

1.17.4.4.5 Temperature dependence of oxidation during long-term exposure

Watanabe *et al.*[99] investigated the oxidation behavior of various steels in steam in an autoclave in the range 560–700 °C. Low alloy steels (group I) showed the same activation energy (Q) for the oxidation rate constant, that is, 350–400 kJ mol^{-1}, over the entire temperature range (Figure 40). On the other hand, the 9% Cr and 12% Cr steels (group II) showed a bilinear behavior. Below 600 °C they had the same Q but exhibited much lower values in the range 600–700 °C; the higher the Cr content, the lower the Q values. HCM12A had a Q value of 40 kJ mol^{-1}.

The data show that the oxidation behavior of steels with Cr concentrations between 2 and 8% in superheated steam at temperatures below 600 °C is virtually independent of the Cr content.[100] The difference between 9% Cr steels and 12% Cr steels is also small at 600 °C but becomes marked at 650 °C.

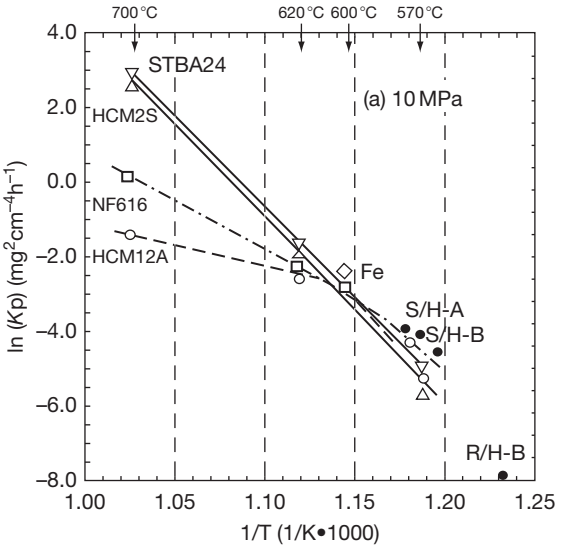

Figure 40 Arrhenius-type plots of oxidation rate constant K_p measured at 10 MPa. Reproduced from Yi, Y. S.; Watanabe, Y.; Kondo, T.; Kimura, H.; Sato, M. *J. Pressure Vessel Technol.* **2001**, *123*, 391–397.

A similar difference in temperature dependence of various steel types was found by Ehlers *et al.*[4] after exposure in Ar–50% H_2O at 1 bar pressure. Also, the data from Husemann,[101] derived from service exposed tubes, show that at low temperatures (~550 °C) the oxidation rates of the 9% Cr steels are not substantially lower than those of the low alloy steels (Figure 41). These data also show that large differences in oxidation rates may occur between different batches of one steel, here shown for X20 'low Cr' and 'high Cr.' This was also found by other authors during laboratory tests of 10.5% Cr and 11.3% Cr batches of this steel type (Figure 41(c)). The results in Refs. 4 and 101 indicate that at 550 °C a clear difference exists between low alloy steels and 12% Cr steel. This contradicts the results of Yi *et al.*[100]

The differences in temperature dependence of the oxidation rates for various steel types (Figure 40) are mainly related to the enhanced incorporation of chromium and other protective scale-forming elements into the scale upon temperature increase. The tendency to form surface scales which are richer in Cr upon increasing the temperature from, say, 550–650 °C is in some steels even more pronounced if the temperature is even further increased. This then has as result that the oxidation rate of, for example, P91 at 700 °C is, at least during short-term oxidation, smaller than at 600 °C.[102]

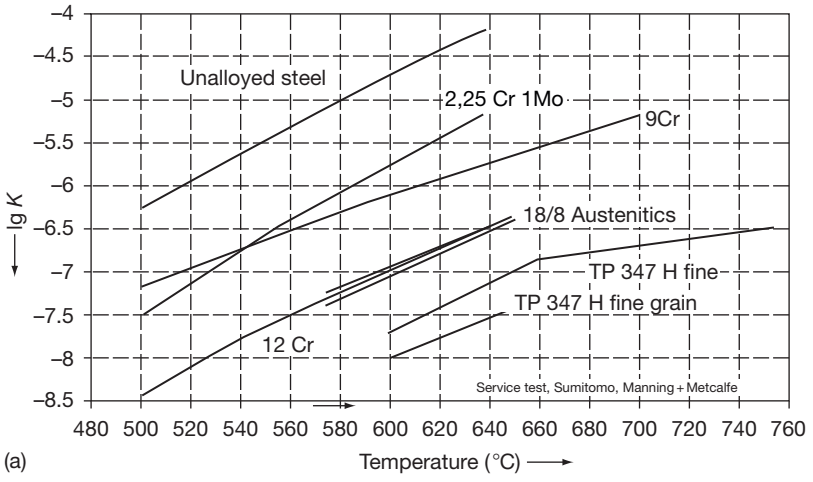

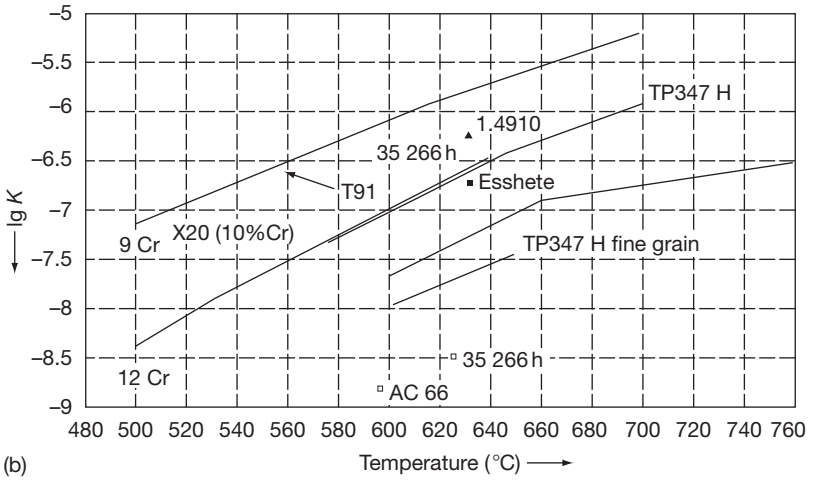

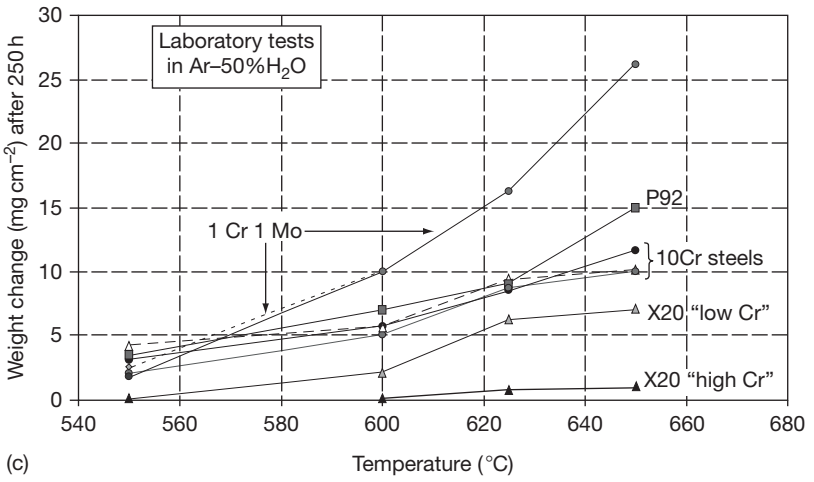

Figure 41 (a, b) Oxidation rates for various steels derived from literature data and service-exposed tubes. The rate constant K here refers to the material loss x in mm defined as $x^2 = Kt$ whereby t is the time in hours.[101] (c) Weight changes for various steels after laboratory tests of 250 h in Ar–50% H_2O.[4] Designation 'X20' relates to X20CrMoV12–1 (see **Table 1**).

Depending on the exact steel composition, a decreasing oxidation rate with increasing temperature can already occur at lower temperatures. Figure 42 shows the mass change data after 1000 h exposure of different steels at different temperatures in Ar–50% H_2O. Samples of 1Cr–Mo–V and 10Cr–Mo–W steels clearly exhibit increasing oxidation rates with increasing temperature (Figure 42). However, the 12% Cr steel exhibits lower oxidation rates at 625 °C than at 550 °C, whereas the Co-containing 11% Cr steel shows a quite complex temperature dependence (Figure 42). After 1000 h exposure at 625 °C, the weight changes are clearly lower than those observed after the 550 °C exposure, whereas at 600 °C the value is only slightly smaller than that at 550 °C. It is important to note that the high value at 600 °C was already reached after 250 h; in other words, the oxidation rate between 250 and 1000 h is as small as that observed at 625 °C.

Figure 43 shows the oxide scales formed on the Co-containing steel after 1000 h of exposure at 550 and 600 °C. In agreement with the mass change data in Figure 42, the thicknesses of the scales formed at 550 and 600 °C are quite similar. However, the scale

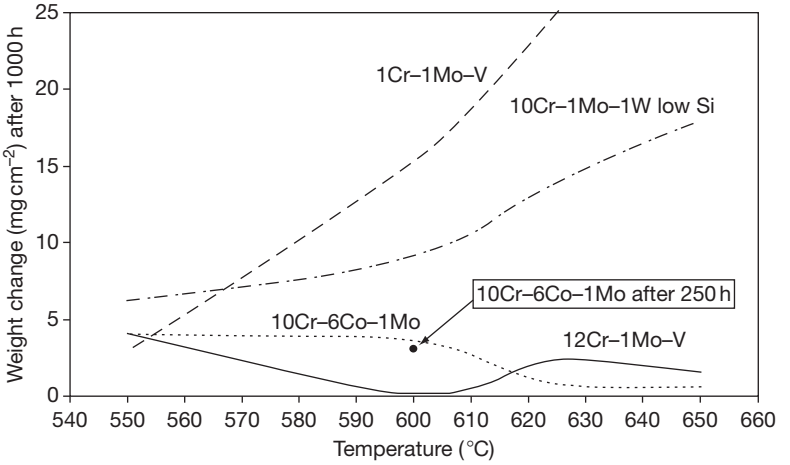

Figure 42 Weight changes of four different ferritic steels after exposure for 1000 h in Ar–50% H_2O showing different types of temperature dependence of the oxidation rates. Also inserted is the weight change of the 10Cr–6Co–1Mo steel after 250 h, showing that between 250 and 1000 h hardly any weight gain occurred. Reproduced from Żurek, J.; Wessel, E.; Niewolak, L.; Schmitz, F.; Kern, T. U.; Singheiser, L.; Quadakkers, W. J. *Corros. Sci.* **2004**, *46*(9), 2301–2317.

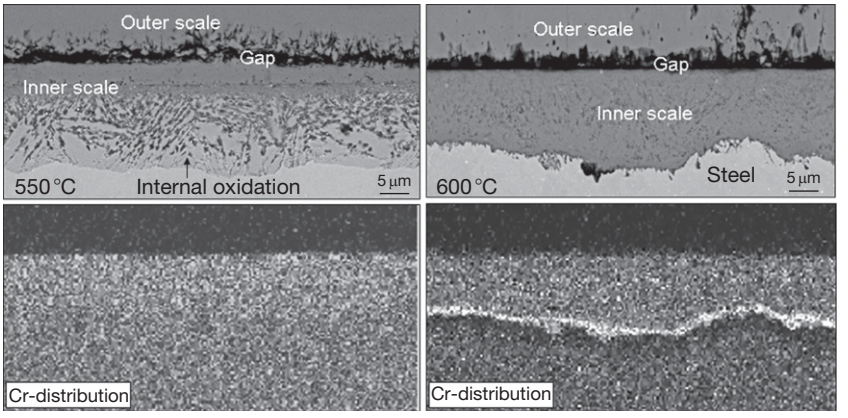

Figure 43 Backscattered electron images and Cr distribution in scales formed on 10Cr–Co–Mo steel after 1000 h exposure in Ar–50% H_2O at 550 and 600 °C showing the temperature dependence of Cr distribution in the inner scale. Reproduced from Żurek, J.; Wessel, E.; Niewolak, L.; Schmitz, F.; Kern, T. U.; Singheiser, L.; Quadakkers, W. J. *Corros. Sci.* **2004**, *46*(9), 2301–2317.

morphologies show substantial differences. At 550 °C, the inner part of the scale exhibits a wide zone of internal oxide precipitates which are embedded in a Co-rich alloy matrix. After exposure at 600 °C, the internal oxidation zone is absent.

At 550 °C, chromium diffusion in the alloy and in the oxide is so slow that Cr can be considered as being virtually immobile. It becomes preferentially incorporated in the inner part of the scale as a result of oxidation of the Cr-rich carbides at the steel grain boundaries and/or martensite laths prevailing in the alloy.[97] The Cr-rich internal oxides become subsequently embedded in the scale by the inwardly moving oxidation front.[96] The Cr-rich bands in the inner scale thus exhibit a sort of 'fingerprint' of the typical microstructure in this type of steel (**Figures 36(b)** and **36(c)**).

On the basis of the initial rapid mass change (**Figure 42**), the scale formation mechanism at 600 °C is more similar to that at 550 °C than that at 625 °C. However, after longer times the oxidation rate resembles that found at the higher temperatures, which means that somewhere in the scale a protective Cr-rich oxide becomes stabilized after about 250 h of exposure. The element mapping in **Figure 43** shows that the overall Cr enrichment in the inner part of the scale is not very pronounced, but a strong enrichment is visible in a narrow band near the scale–alloy interface. Beneath this, a Cr depletion in the alloy as a result of the selective oxidation of Cr is clearly visible. The enhanced diffusion and the associated increase in the selective oxidation of Cr become more pronounced if the temperature is increased to 625 °C. The Cr-rich oxide then becomes stabilized already in the very early stages of oxidation, resulting in an extremely slow oxidation rate during the whole 1000 h of exposure (**Figure 42**).

Qualitatively, these features in respect to the adverse temperature dependence of the oxidation behavior can also be observed in the case of the 12% Cr steel (**Figure 42**), in agreement with earlier findings of Haarmann *et al.*[103] for this type of steels. At 550 °C, the Cr-enriched regions almost exclusively consist of oxides initially formed on grain boundaries and martensite laths, thus expressing the original microstructure in the steel. After exposure at 625 °C, the alloy exhibits Cr-rich stringers in the inner oxide layer, arranged parallel to the initial steel surface, indicating more rapid Cr diffusion from the bulk alloy in the direction of the scale.[104] This preferential oxidation of Cr results in a Cr depletion beneath the Cr-rich spinel layer in the alloy. After continued Cr depletion, the growth of the Cr-rich spinel can eventually no longer be

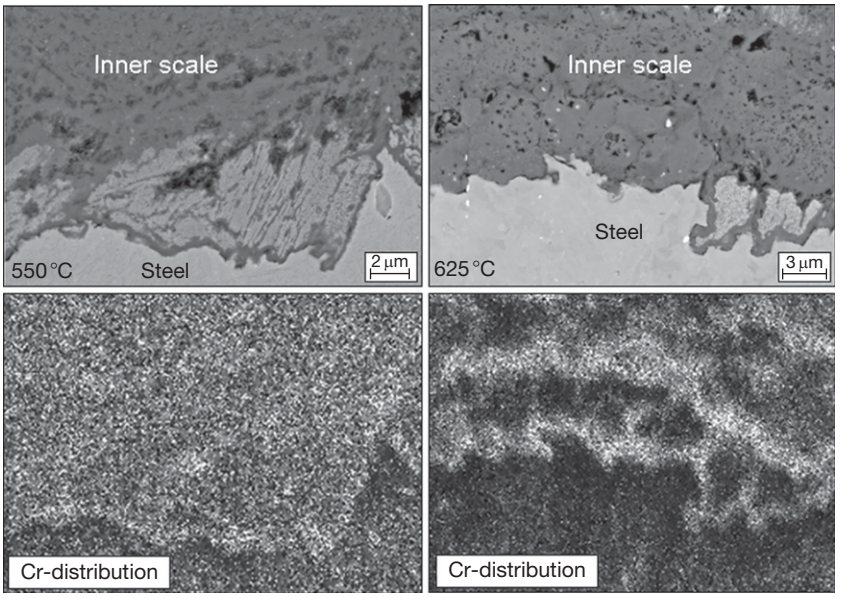

Figure 44 Backscattered electron images and Cr distributions in inner scale formed on 12Cr–Mo–V steel after 1000 h exposure at 550 and 625 °C showing temperature dependence of Cr incorporation and distribution in inner scale. Reproduced from Z˙urek, J.; Wessel, E.; Niewolak, L.; Schmitz, F.; Kern, T. U.; Singheiser, L.; Quadakkers, W. J. *Corros. Sci.* **2004**, *46*(9), 2301–2317.

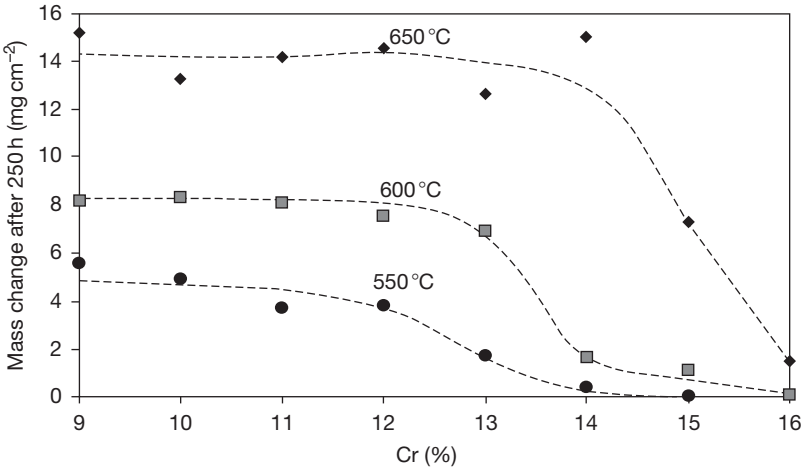

Figure 45 Weight changes of binary Fe–Cr model alloys after 250 h exposure in Ar–50% H_2O in the temperature range 550–650 °C. Adapted from Nieto-Hierro, L.; Quadakkers, W. J. Unpublished results, Forschungszentrum Jülich, FRG, 2006.

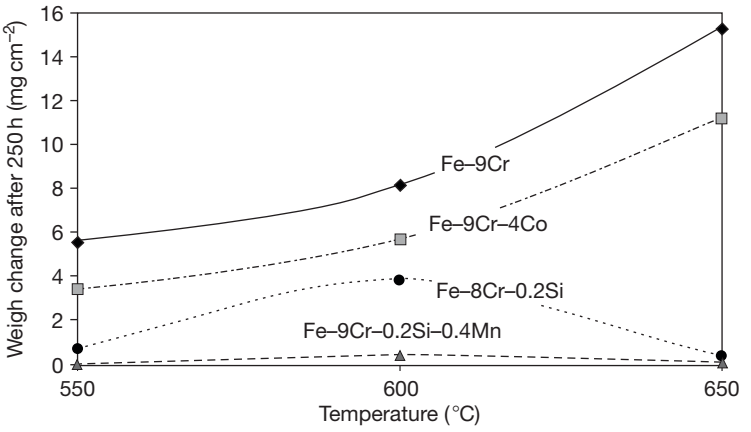

Figure 46 Weight changes of Fe–Cr model alloys with various additions of minor elements, after 250 h exposure in Ar–50% H_2O in the temperature range 550–650 °C. Derived from Nieto-Hierro and Quadakkers.[105]

sustained, and as a result Fe-rich oxides are subsequently formed. Repetition of this process leads to the microstructure in the inner part of the scale shown in **Figure 44**.

The adverse temperature dependence (**Figure 42**) can thus be expected in steels that exhibit a higher tendency to form protective Cr-rich scales (group II, **Figure 13**), that is, it increases with increasing amounts of elements (Cr, Si, etc.) that participate in the formation of protective scales.

The adverse temperature dependence, shown for two steels in **Figure 42**, in fact seems to contradict the results and considerations in **Section 1.17.4.3.3** which showed that for binary FeCr alloys in the temperature range 800–1050 °C the tendency to form protective scales decreases with increasing temperature. The results obtained for high-purity Fe–Cr model alloys in **Figure 45** illustrate that this is also the case for steam oxidation in the temperature range 550–600 °C.[105] If a different temperature dependence is sometimes observed for the commercial ferritic steels, then apparently factors other than just temperature dependence of Cr and oxygen diffusion in the alloy affect protective scale formation. On the basis of studies with a number of ternary and quaternary model alloys, parameters that affect this process are alloying elements such as Si and Mn which participate in the oxidation process, C content in the alloy which apparently affects the Cr-distribution and activity, as well as enhanced dissolution of carbides with increasing temperature thereby 'releasing' Cr for diffusion. The results in **Figure 46** confirm the significance of minor additions of Si and Mn for decreasing oxidation rates upon temperature increase.

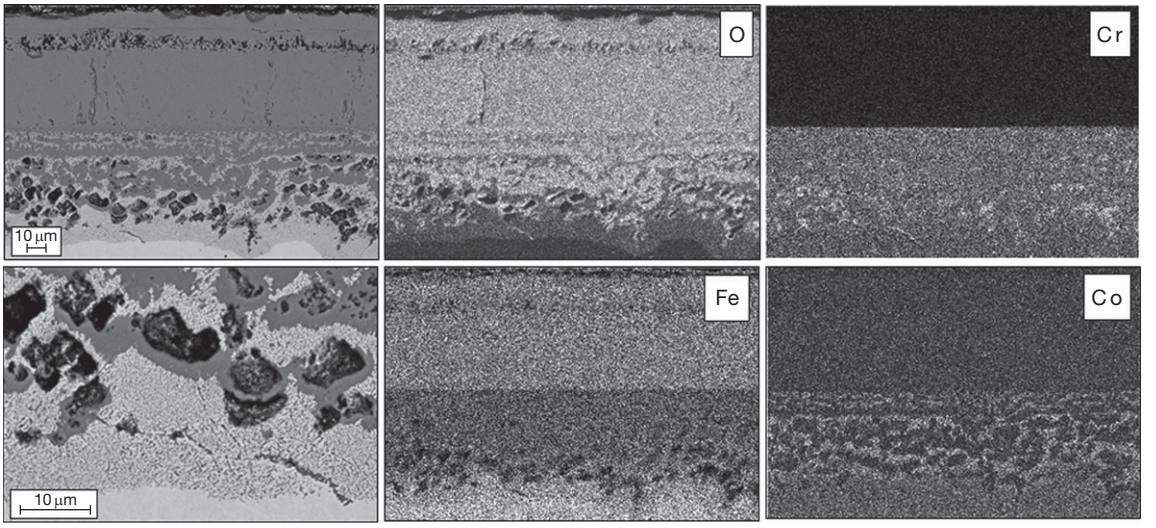

Figure 47 Backscattered electron images (left) and X-ray mappings of oxide scale formed on model alloy Fe–9Cr–4Co after 1000 h of exposure at 650°C in Ar–50% H_2O. Pictures on left side show an overview of oxide scale and higher magnification of scale–steel interface, respectively. Adapted from Nieto-Hierro, L.; Quadakkers, W. J. Unpublished results, Forschungszentrum Jülich, FRG, 2006.

For Si-containing steels, the occurrence of the adverse temperature dependence was also found by other researchers,[106,107] and a detailed description concerning the effect of Si for disappearance of the internal oxidation zone and the resulting formation of barrier layers was given by Ueda *et al.*[84] Single additions of other common alloying elements such as W, Co, and Nb did not fundamentally alter the *T*-dependence of the oxidation rates.[4,105] However, Co contents of more than 4% appeared to substantially affect the oxidation behavior of the Fe–Cr model as illustrated in **Figure 46**.

An Fe–9% Cr–4% Co model alloy forms at 650 °C an inner and outer scale (**Figure 47**), as shown for other steels before. However, here, the selective oxidation of Cr, and subsequently Fe, leads in the inner part of the scale to an apparent enrichment of Co in the remaining metallic regions due to the high dissociation pressure of Co oxide (**Figure 47**). X-ray diffraction (XRD) revealed even the presence of pure cobalt near the interface between inner and outer scale.[105] This results in a microstructure in which the transport of Fe cations is strongly hampered. In this way, sufficiently large additions of Co (e.g., 4%) substantially decrease the Cr content required to form protective Cr-rich oxide scales (**Figure 46**); however, no adverse temperature dependence is found.

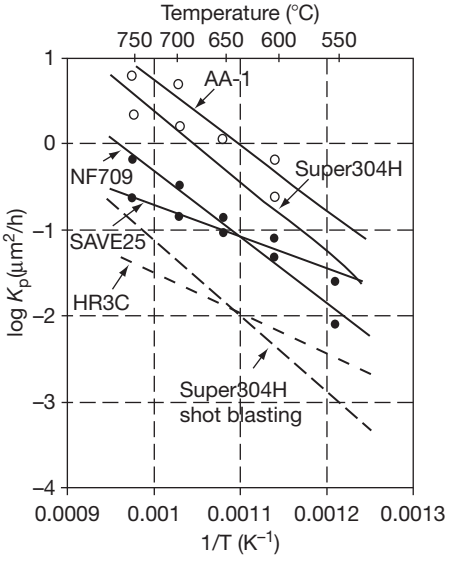

Figure 48 Scale growth rate K_p of various austenitic steels versus reciprocal temperature during steam oxidation. Here K_p is defined as $K_p = x^2/t$ with x the scale thickness and t the time. Reproduced from Muramatsu, K. In *Development of Ultrasupercritical Plant in Japan, Advanced Heat Resistant Steel for Power Generation*; Viswanathan, R., Nutting, J. W., Eds.; IOM Communications: London, UK, 1999; Book 708, pp 543–559.

1.17.4.4.6 Austenitic steels

Attempts to further increase the steam temperature in power generation systems frequently requires the highest temperature components to be designed using austenitic materials, sometimes from the viewpoint of mechanical properties and in other cases for obtaining improved steam oxidation resistance.

The various austenitic steels that are potentially suitable as construction materials for heat-exchanging components widely differ in composition, for example, in respect to Cr and Ni content (**Table 1**), and consequently steam oxidation resistance may substantially differ between various materials.

Depending on the composition, the commercially available austenitics may, in respect to steam oxidation resistance, be described as group II or group III alloys in **Figure 13**. Steels with Cr contents in the range 17–20% may be considered as group II alloys and thus show oxide scales that exhibit many features similar to those described for the high-Cr ferritics of group II. Muramatsu[108] found that the oxidation rates of the austenitic steels are characterized by a single activation energy over the entire temperature range between 550 and 750 °C, whereas the activation energy Q decreases as Cr concentration increases (**Figure 48**).

Oxide scales formed on austenitic steels are sometimes more prone to spallation than those on ferritic or martensitic steels. **Figure 49** shows the gross and net mass changes of an austenitic 25Ni–15Cr–Ti steel as a function of time during exposure in Ar–50% H_2O in the temperature range 550–650 °C. As described for some of the high-Cr group II ferritics (**Section 1.17.4.4.5**), different from the materials studied by Muramatsu[108] this austenitic steel shows an 'adverse temperature dependence': the growth rate of the initially formed surface scale at 650 °C is

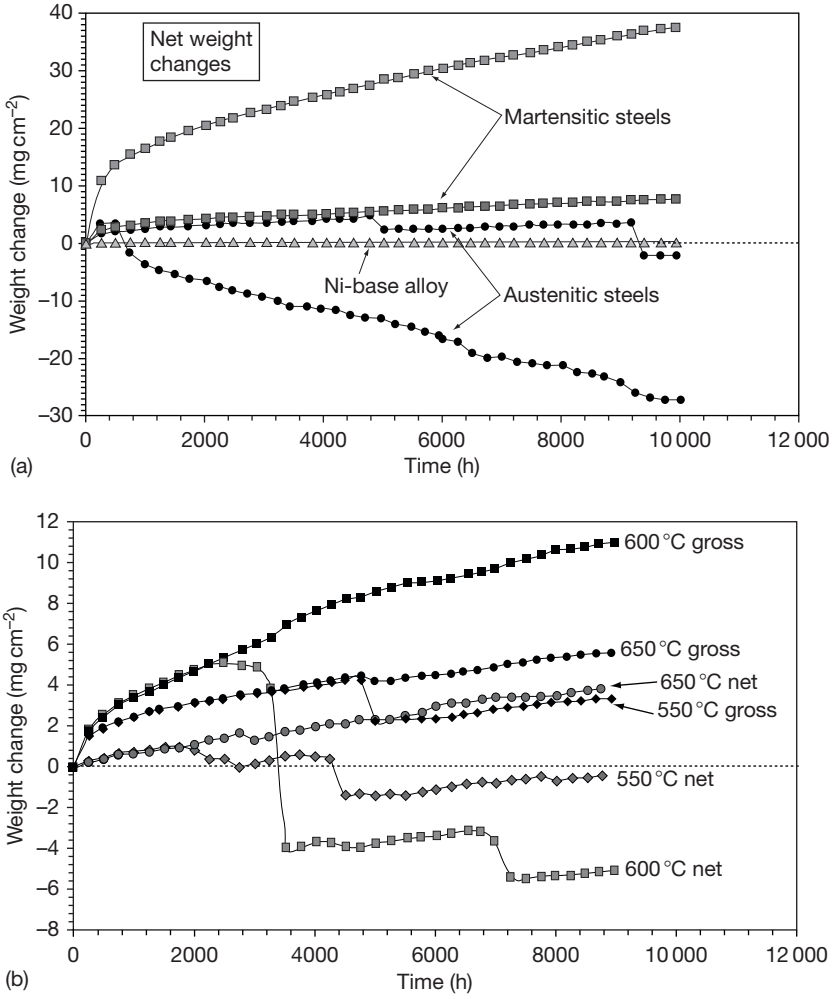

Figure 49 Mass changes as function of time during oxidation in the temperature range 550–650 °C in Ar–50% H_2O: (a) Typical examples showing differences in behavior of martensitic 9–10% Cr steels, austenitics and Ni-base alloy; (b) Temperature dependence for onset of scale spallation for austenitic steel 25Ni–15Cr–Ti. 'Net' and 'gross' weight changes correspond to specimen mass changes without and with spalled oxide, respectively.

smaller than that at 600 °C. The data illustrates that no clear correlation exists between the oxidation rate and the time for the onset of scale spallation. For example, at 600 °C, the first spallation occurs after 3000 h where the net mass change is ~5 mg cm^{-2}, while at 650 °C spallation occurs after 5000 h, that is, when the mass change equals ~3.5 mg cm^{-2}. At 550 °C, spallation starts to occur after 2000 h exposure, where the mass change exceeds ~1 mg cm^{-2}. The onset of spallation can thus not easily be correlated with a critical thickness of the oxide scale.

The metallographic cross sections presented in **Figure 50** illustrate the typical scale morphologies on austenitic steels. Spallation generally occurs at the interface between the inner and the outer scale, that is, near the original metal surface. After the total outer scale has spalled, the scale regrowth is determined by transport processes in the thick inner scale and thus occurs at a rate similar to that prevailing just before the occurrence of spalling. Owing to the high Cr content, Fe diffusion in the inner scale is slow, and thus the regrown oxide exhibits features as described in the previous sections, which means that it mainly consists of hematite on top of a gap. The spalling rate is thus governed by an initial smaller weight loss, a slow scale re-growth and consequently a smaller weight loss during the following spalling steps. This is, for example, clearly illustrated by the 600 °C curve in **Figure 49**.

There are, however, a number of major differences in oxide scale formation between 17% and 20% Cr austenitic steels and most of the commercially available 9–12% Cr martensitic steels. The effect of carbide formation on martensite laths for the inner scale morphology does obviously not occur in the austenitic steels. Also, chromium diffusion in austenite is slower by approximately a factor 10 than in ferrite.[104,109] Therefore, the critical Cr content to obtain protective chromia base scale formation will generally be higher for austenitic than for ferritic steels. In coarse-grained austenitics, the change from formation of Fe/Cr spinel to pure Cr_2O_3 was reported to require a Cr content of 25% such as prevailing in HR3C.[88] Owing to the slow diffusion, Cr transport along grain boundaries in the alloy plays a more important role in austenitics for the overall scale formation than in case of ferritic steels. This has the result that the steam oxidation behavior can be strongly affected by the steel grain size or by 'imperfections' introduced by surface deformation (**Figure 51**). An interesting feature sometimes found in austenitic steels is that the depletion of Cr beneath a Cr-rich surface scale may differ from grain to grain (**Figure 52**).

Beneficial effects due to grain refining have been pursued as a proven method for improving oxidation resistance of austenitic steels. A typical example is TP347HFG, which has been applied widely in the grain-refined condition, and favorable service experience up to 50 000 h is available. Currently, the technique is being extended to other stainless steels such as SUPER304H. Sato *et al.*[110] have described substantial beneficial effects on oxidation resistance of austenitic stainless steels due to shot-blasting. This technique has been applied to conventional austenitic steels in Japan for more than 20 years. The effect of cold work pretreatment on the corrosion rate[111] is explained by the improved diffusivity of Cr in the defect structure, preferential oxidation, and formation of Cr-rich solid solution ($FeFe_{2-x}Cr_xO_4$) spinel-type oxide scales.[112]

Another important feature is the role of Ni in the overall oxidation process. The thermodynamic driving force for oxidation of Ni in the steam environment is much smaller than that for Cr or Fe.

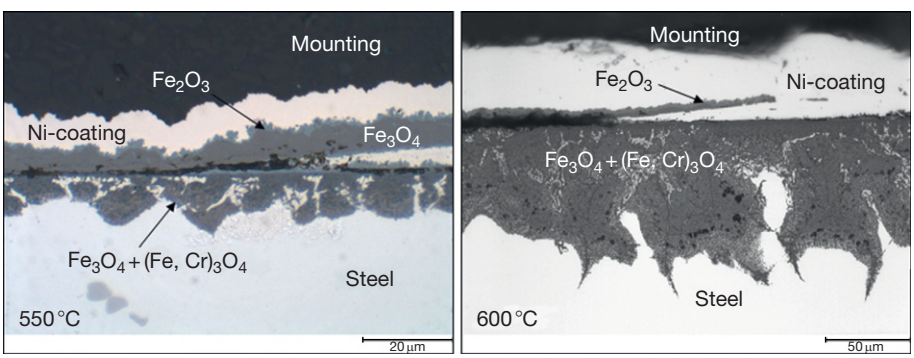

Figure 50 Metallographic cross sections of 25Ni–15Cr–Ti after oxidation in Ar–50% H_2O at 550 °C after 3000 h and 600 °C after 10 000 h.

Therefore, Ni is generally not present in the outer magnetite–hematite scale. As described for Co in Co-containing martensitic steels in Section 1.17.4.4.5, Ni is frequently found in the inner scale where it sometimes prevails in metallic form (Figure 53) because in that area of the scale the oxygen partial pressure is apparently lower than the dissociation pressure of NiO or Ni/Fe/Cr spinel. The chromium and oxygen distribution clearly show that the steel initially formed a Cr-rich surface layer, remnants of

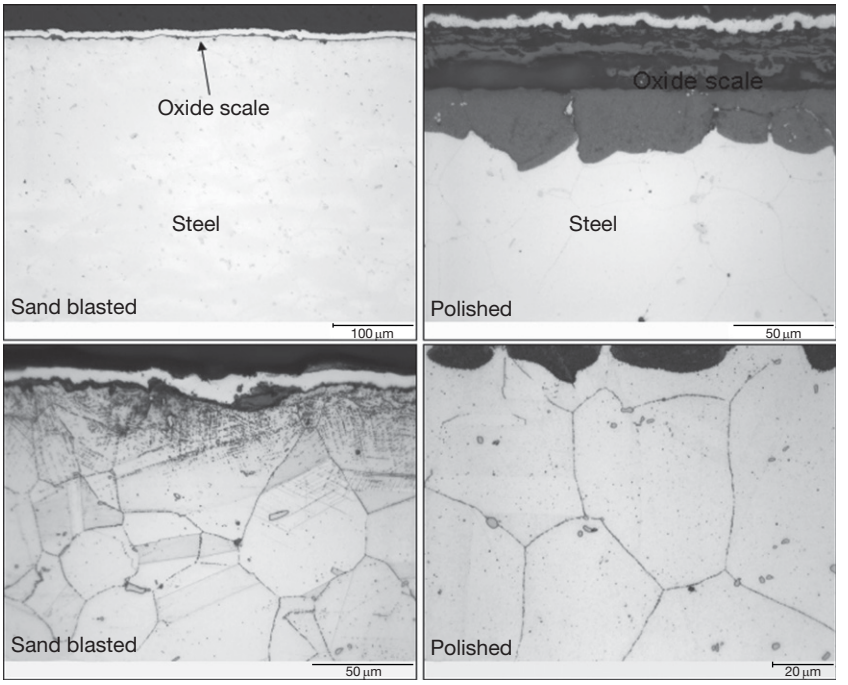

Figure 51 Metallographic cross sections showing effect of surface treatment on oxide scale formation of austenitic steel TP347HFG during exposure in Ar–50% H_2O for 1000 h at 625 °C. Adapted from Piron-Abellan, J.; Quadakkers, W. J. Unpublished results, Forschungszentrum Jülich, FRG, 2007.

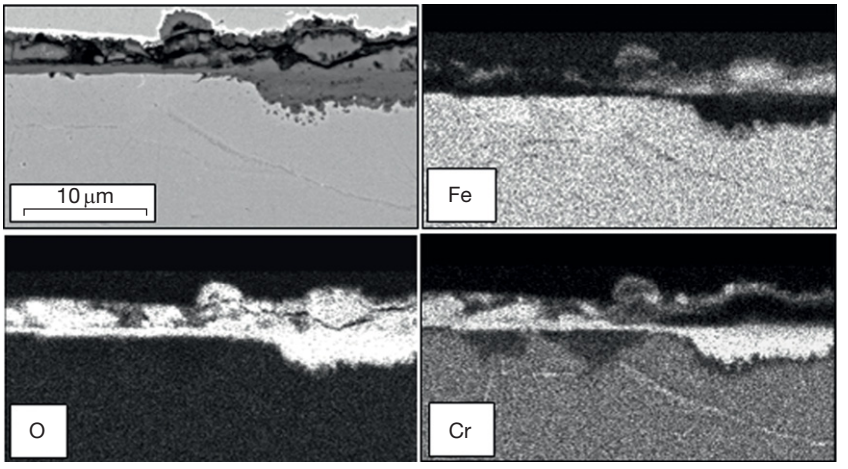

Figure 52 Backscattered electron image and X-ray mappings of oxide scale on steel 310N (HR3C) after exposure at 600 °C for 10 000 h in Ar–50% H_2O. Adapted from Piron-Abellan, J.; Quadakkers, W. J. Unpublished results, Forschungszentrum Jülich, FRG, 2007.

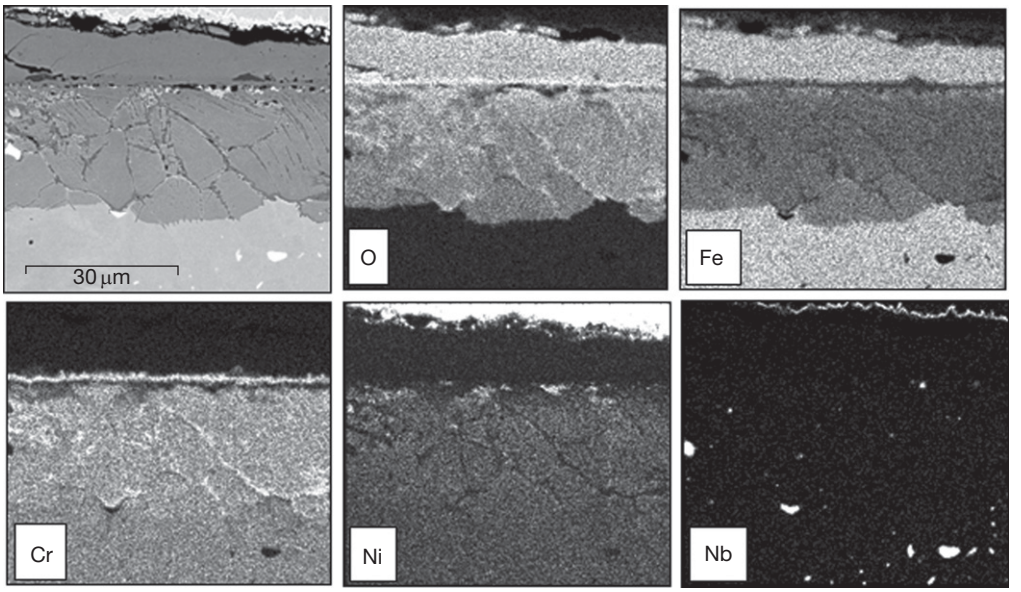

Figure 53 Backscattered electron image and X-ray mappings of oxide scale on steel Super304H after exposure at 625 °C for 10 000 h in Ar–50% H_2O. Adapted from Piron-Abellan, J.; Quadakkers, W. J. Unpublished results, Forschungszentru Jülich, FRG, 2007.

which can be seen between the inner and outer layer. In the inner scale, Cr-rich oxide is present as continuous bands at the alloy grain boundaries and as internal oxides within the grains. Areas with Ni-rich alloy matrix prevail in the inner scale especially near the initial steel surface.

1.17.4.4.7 Effect of pressure on steam oxidation

Data regarding the influence of pressure on steam oxidation behavior show a considerable amount of variation.[113] Otoguro *et al.*[114] measured the maximum scale thickness on four austenitic alloys (SUS347 HTB, 17/14CuMo, 20Cr/25Ni and 22Cr/35Ni) after exposure to steam for 500 h at 650 and 700 °C and pressures up to 35 MPa. On increasing the pressure at 650 °C, two of the alloys (SUS347 HTB, 17/14CuMo) investigated showed a decrease in scale growth rate of ~20%, one of the alloys (22Cr/35Ni) showed no influence of pressure on the scale thickness and one alloy (20Cr/25Ni) showed an increase in scale thickness by a factor of 4. The same trend in results was observed at 700 °C. Montgomery and Karlsson[115] have summarized the data on the influence of pressure on scale growth kinetics during exposure of martensitic steels to steam environments. The high-pressure data for HCM12 indicated a decrease in scale growth rate with increasing pressure, whereas the high-pressure data for P92 revealed either no effect of pressure or a change in the pressure effect with temperature depending on interpretation.

An apparent influence of steam pressure on the scale morphology is illustrated in **Figure 54** for a ferritic 12Cr–1Mo–V steel oxidized for 250 h at 650 °C. When exposed to Ar–50% H_2O at ambient pressure, hematite was formed at the outer surface, whereas only magnetite was present after the high-pressure oxidation. However, the high-pressure exposure was carried out in an autoclave in stagnant gas, and the observed effect is probably due to a build-up of hydrogen in the sealed system. This leads to a decrease in oxygen partial pressure, thus inhibiting hematite formation, as explained in **Section 1.17.2.3**. The build-up of H_2 may also have affected the high-pressure results of Yi *et al.*,[100] which were carried out in stagnant gas.

1.17.4.5 Alumina-Forming Alloys and Coatings

1.17.4.5.1 α-Alumina scales

There are conflicting reports about the behavior of alumina-forming alloys and coatings in water vapor-containing gases. In an extensive review of the effects of water vapor on the oxidation of metals,[1] it was concluded that water vapor had little effect on the oxidation behavior of alumina-forming alloys, although some evidence was cited that hydrogen defects were

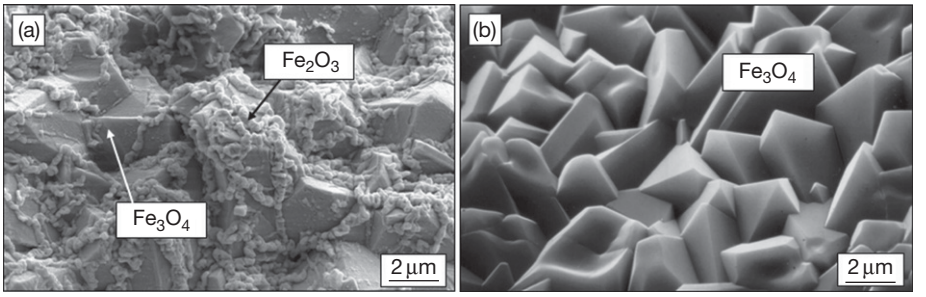

Figure 54 Surface scale morphology of 12Cr–1Mo–V steel after 250 h exposure at 650 °C: (a) flowing Ar–50% H_2O at 1 bar total pressure; (b) static steam at 300 bar total pressure. Adapted from Ehlers, J.; Quadakkers, W. J. Report Forschungszentrum Jülich, Jül-3883, 2001.

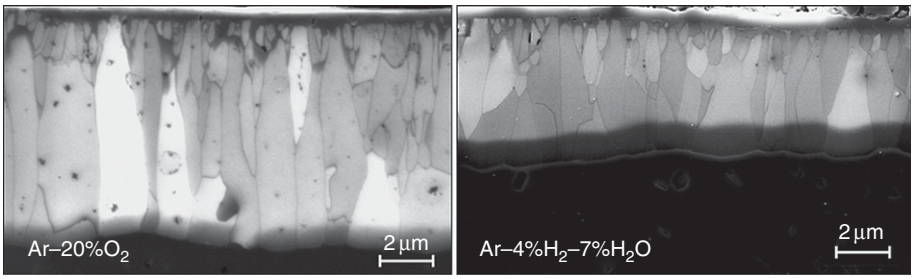

Figure 55 In-lens SEM images of oxide scales formed on an FeCrAlY model alloy after 100 h isothermal oxidation in low- and high-p_{O_2} gas at 1250 °C. Reproduced from Naumenko, D.; Quadakkers, W. J. Unpublished results, Forschungszentrum Jülich, FRG, 2007.

present in Mg-doped alumina and that scale adhesion was reduced by water vapor. It should be noted that the mentioned studies mainly relate to wet air or wet oxygen rather than low-p_{O_2} gases.

Kolb-Telieps *et al.*[116] showed the α-alumina scale on an FeCrAlY alloy in the temperature range 1200–1300 °C to grow more slowly in Ar–H_2–H_2O mixtures than in Ar–O_2 or air (**Figure 55**). Kochubey *et al.*[117] found a p_{O_2} dependence of the sub-parabolic oxidation rates assuming oxygen grain boundary diffusion to be the dominating scale growth process whereby the oxide grains size increased in scale growth direction.[118] Also in a low-p_{O_2} exhaust gas[116] and in H_2/H_2O-based shield gases,[119] the growth rate of α-alumina on an Y-doped FeCrAl alloy was found to be smaller than that in air. In the low-p_{O_2} exhaust gas, Naumenko *et al.*[120] found, however, the adherence of the scales to be worse than that of the scales formed in air or Ar–O_2. Poorer scale adherence of alumina scales due to presence of water vapor therefore seems to be a feature which is independent of the p_{O_2} of the test gas. It was also observed by Janakiraman *et al.*[121] during oxidation of Ni-based superalloys and MCrAl coatings in wet air. Dieckmann[35] proposed hydrogen segregation at the oxide–metal interface to be a possible reason for poor scale adherence. Kirchheim[122–124] actually observed hydrogen to segregate at metal–oxide interfaces during internal oxidation of Pd-based alloys. In recent studies, Smialek[125] attributed the poor alumina scale adherence in wet gases to hydrogen embrittlement of the scale–alloy interface.

Toscano *et al.*[126] studied the thermal cycling behavior of a thermal barrier coated (TBC) coated Ni-based alloy where the bond coat (BC) was a NiCoCrAlY alloy containing 10 mass% Al. The α-alumina scale that formed during cyclic oxidation at the BC surface beneath the TBC appeared to grow faster in air than in Ar–H_2–H_2O. As a result, the life time of the TBC at 1100 °C, which was governed by spallation of the α-alumina scale at the BC surface, was substantially longer in Ar–H_2–H_2O than in air.

This gas composition dependence was found only in case of optimized reactive element (RE) doped alloys or coatings which formed a scale that does not allow molecular gas transport. FeCrAl alloys that contained Zr (300 ppm) as a second RE in addition to Y developed in Ar–O_2 as well as in Ar–H_2–H_2O alumina scales, which exhibited substantial porosity. This was related to internal oxide particles of zirconia that became incorporated into the inwardly growing

α-alumina scale during long-term exposure.[127] Porosity appeared to develop at the interfaces between the alumina scale and the zirconia particles. Therefore the scale did not develop the ideal columnar, large-grained microstructure shown in **Figure 55**, and probably molecular transport participated in the scale growth process. This had the result that the p_{O_2} dependence of the oxidation rate was far less obvious than in case of the Zr-free alloy (**Figure 56**). At higher temperature (1300 °C) in low-pO_2 gas, variations in oxide thickness over the specimen were found and locally the scale was even thicker than after Ar–O_2 oxidation (**Figure 57**). Indications were found that the Ar–H_2–H_2O exposure modified the internal oxidation of the Zr in a manner similar to that described for FeCr alloys in **Section 1.17.4.3.2**, and in this way the Ar–H_2–H_2O indirectly changed the alumina growth rate. The strong dependence of the α-alumina growth rate on scale morphology may be the reason for the fact that Ramanarayanan *et al.*[128] found in the oxidation of an FeCrAl-based oxide dispersion strengthened (ODS) alloy at 1000–1200 °C no clear effect of oxygen partial pressure on scale growth kinetics.

1.17.4.5.2 Metastable alumina

Naumenko *et al.*[129] also studied the effect of gas composition on the oxidation of Y-doped FeCrAl alloys at lower temperatures. The authors found that the dependence of the oxidation behavior on gas composition in the temperature range 800–950 °C was completely different from that at temperatures well above 1000 °C. At the lower temperatures, the Ar–H_2–H_2O mixture tended to promote the formation of rapidly growing, metastable aluminum oxide phases (e.g., γ, Θ) compared to Ar–O_2

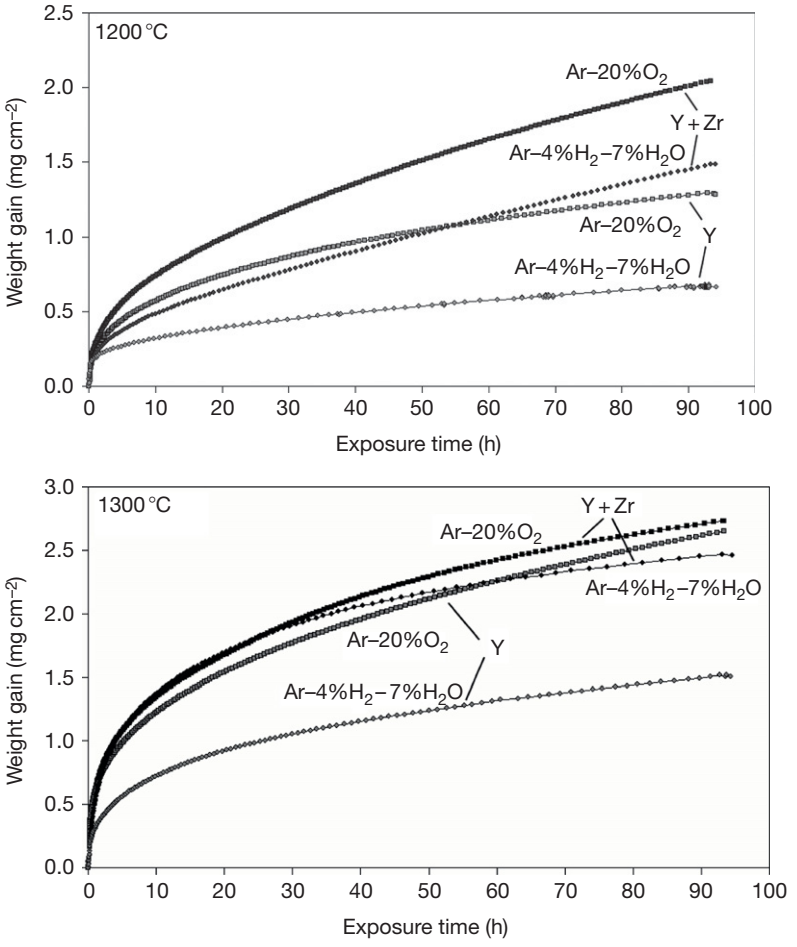

Figure 56 Weight changes during isothermal oxidation of FeCrAlY alloy (Y content 500 ppm) without or with 300 ppm Zr in high and low-p_{O_2} gas at 1200 and 1300 °C. Reproduced from Naumenko, D.; Quadakkers, W. J. Unpublished results, Forschungszentrum Jülich, FRG, 2007.

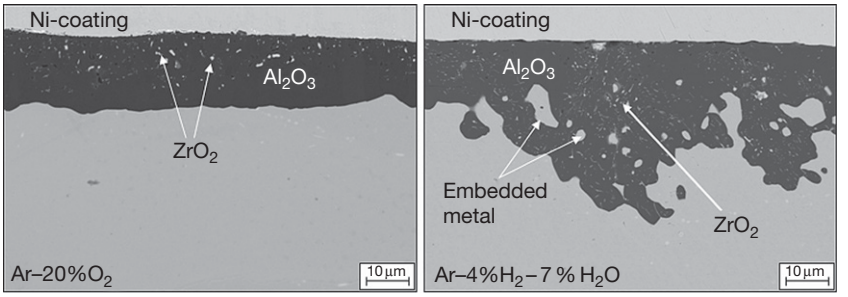

Figure 57 SEM images of oxide scales on FeCrAlY + Zr alloy (compare **Figure 56**) after 100 h oxidation at 1300 °C in various atmospheres.[117] Reproduced from Kochubey, V. Ph.D. Thesis, Bochum University, 2005.

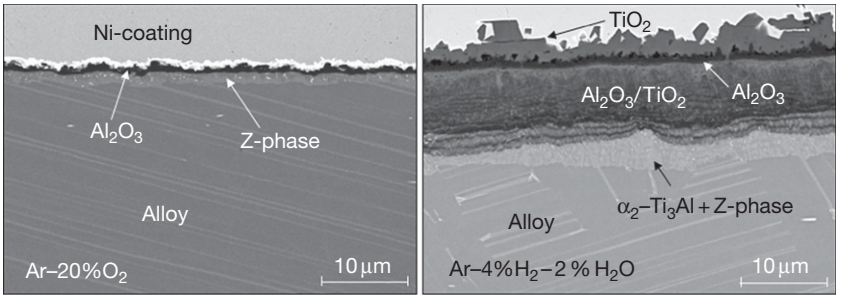

Figure 58 Oxide scales on Ti–46.5Al–4(Cr, Nb, Ta, B) alloy after 96 h oxidation at 800 °C in Ar–20% O_2 and Ar–4% H_2–2% H_2O. Reproduced from Niewolak, L. Unpublished results, Forschungszentrum Jülich, FRG, 2003.

exposure. This effect was also found by Götlind *et al.*[130] when comparing the behavior of a commercial FeCrAl alloy in O_2 with that in O_2–H_2O, thereby indicating that presence of water vapor promotes metastable alumina growth, independent of the oxygen partial pressure in the gas. In a recent study, Lodziana *et al.*[131] demonstrated that strongly bonded hydroxide groups form on Θ-Al_2O_3 in the presence of water vapor. It was suggested that γ-Al_2O_3, when formed on FeCrAl alloys at 900 °C, can generate a strongly bonded surface hydroxide similar to Θ-Al_2O_3. This is supported by the observation that γ-Al_2O_3 powders can absorb significant amounts of water vapor (~3% by weight) at 900 °C.[132]

1.17.4.5.3 Borderline alumina forming alloys

In earlier studies, Boggs[133] showed that the oxidation rate of Fe–5% Al was significantly increased at 800 °C when about 3% water vapor was present either alone or with oxygen. γ-Alumina formed initially in dry oxygen which later transformed to α-alumina, with about 1% Fe-rich nodules. Hayashi *et al.*[69] found for an Fe–5% Al alloy at 800 °C a substantially lower growth rate in N_2–20 vol.% O_2 than in N_2–12.2 vol. % H_2O. Malkow *et al.*[43] observed for an 18% Cr ferritic steel containing 1.2% Al protective alumina scale formation after 1000 h exposure at 800 °C in air. However, in simulated SOFC anode gas (Ar–H_2–H_2O–(CO)), the alloy tended to form a Cr-rich surface oxide and internal oxidation of Al. The results for these borderline alloys might be related to enhanced internal oxidation of the protective scale-forming element Al due to hydrogen incorporation in the alloy, in a similar manner as described for FeCr alloys in **Section 1.17.4.3.2**.

Another alloy system for which retarded protective alumina scale formation due to the presence of water vapor was described is the intermetallic phase γ-TiAl. On the basis of numerous studies, γ-TiAl can be considered as 'borderline alloy' because protective alumina scale formation in the temperature 700–900 °C has been shown to depend, for example, on the exact Al content, microstructure, surface treatment, alloying additions of, for example, Cr or Ag, and presence of microdopants such as halogens, etc.[134–136] Also, for this alloy system most of the studies in respect to the effect of water vapor relate to wet oxygen or wet air and only a few studies are available in low-p_{O_2} gases.

Niewolak[137] found protective alumina scale formation on a Ti–46.5Al–4(Cr, Nb, Ta, B) alloy after

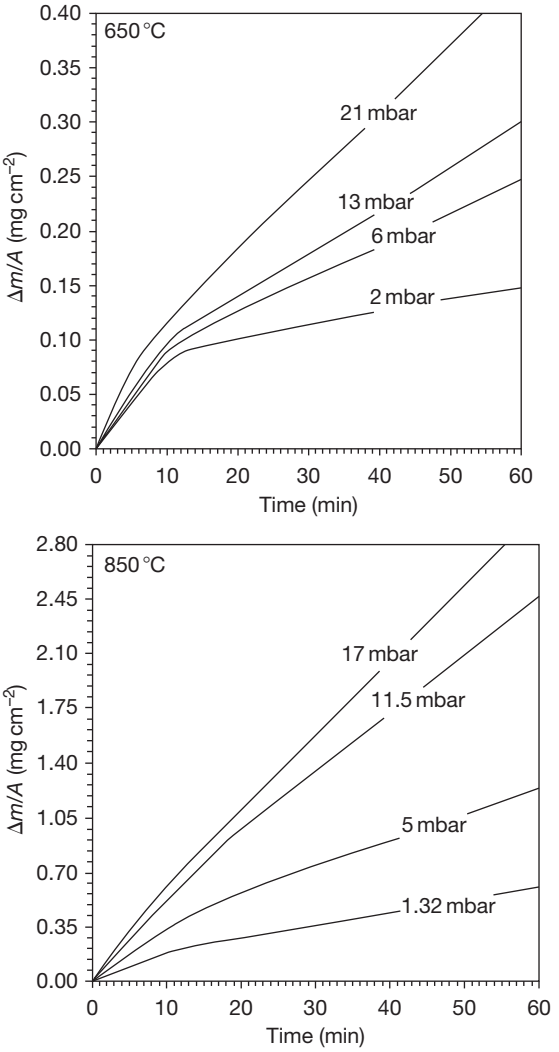

Figure 59 Weight changes during isothermal oxidation of Ti in Ar–H_2O showing influence of temperature and water vapor pressure. Reproduced from Wouters, Y.; Galerie, A.; Petit, J. P. *Solid State Ionics* **1997**, *104*, 89–96.

96 h of isothermal exposure at 800 °C in Ar–20% O_2 (**Figure 58**). However, when oxidized in Ar–4% H_2–2% H_2O, rapidly growing, mixed Al_2O_3/TiO_2 base scales were formed (**Figure 58**). As above, this effect might have been be caused by an enhanced internal oxidation of Al due to hydrogen incorporation in the alloy. Considering the morphology of the mixed Al_2O_3/TiO_2 scales, also H_2O/H_2 bridges (**Section 1.17.3.3**) in voids could principally explain this effect, although in this alloy system this mechanism seems unlikely. The oxygen partial pressure in a void at the scale–alloy interface will be extremely low, for instance, at 800 °C in the range 10^{-43} atm. Therefore, the equilibrium water vapor partial pressure in that void would only be 10^{-14} atm. This would, using the Langmuir equation (**Section 1.17.4.4.2**), result in a maximum rate of oxygen transfer of 5×10^{-13} g cm^{-2} s^{-1}, which is far too low to sustain the oxidation rates observed by Niewolak[137] in the wet gas.

Another possible explanation for the nonprotective scale formation in Ar–H_2–H_2O would be that water vapor increases the growth rate of the nonprotective oxide, here TiO_2, thereby, according to Gesmundo *et al.* (**Section 1.17.4.3.3**), increasing the critical Al content required for protective scale formation. Such an explanation may be derived from the results of Wouters *et al.*,[138] who reviewed the oxidation behavior of Ti in H_2O containing gas. For example, after 25 h oxidation of Ti at 850 °C, the mass gain was higher by about a factor of 3 in 20 mbar H_2O compared with the rate in 20 mbar O_2. In the temperature range 650–850 °C, the rate of oxidation was directly proportional to the water vapor content, and approximately parabolic kinetics were observed (**Figure 59**). Hydrogen was found in the metal after exposure and there was no change in the conductivity of the oxide, which remained n-type. Wouters *et al.*[138] proposed that the increased rate of oxidation results from incorporation of OH^- in the titania lattice and the more rapid diffusion associated with the smaller ionic radius than the oxide ion.

Niewolak[137] investigated the oxidation kinetics of γ-TiAl alloys in a number of dry and wet, high- and low-p_{O_2} gases. He found, that the change from a protective alumina base scale to a poorly protective TiO_2-rich oxide layer (**Figure 58**) also occurred when decreasing the oxygen content in dry Ar–O_2 gases from 20% to less than 5%. The results thus indicate that the gas composition dependence shown in **Figure 59** is at least to certain extent related to the differences in oxygen partial pressures of the test gases. Several authors[139–141] have shown that the dominating point defects in TiO_2 are oxygen vacancies at high oxygen partial pressure, whereas titanium interstitials dominate at low p_{O_2}. At 800 °C the oxygen partial pressure at which this change from one dominating defect type to another occurs is $\sim 10^{-3}$ bar.[142] It has also been shown[143–145] that the solubility of Al in TiO_2 increases with decreasing oxygen partial pressure, a factor frequently illustrated to be of great importance for oxide scale formation on γ-TiAl-based alloys. Decreasing the oxygen partial pressure of the gas thus not only changes the growth rate of the 'nonprotective' oxide TiO_2 but also the competition between formation of the alumina scale and its dissolution in TiO_2.

References

1. Douglass, D. L.; Kofstad, P.; Rahmel, A.; Wood, G. C. *Oxid. Met.* **1996**, *45*(5/6), 529–620.
2. Asteman, H.; Svensson, J. E.; Johansson, L. G.; Norell, M. *Oxid. Met.* **1999**, *52*(1), 95–111.
3. Thiele, M.; Quadakkers, W. J.; Schubert, F.; Nickel, H. Report Forschungszentrum Jülich, Jül-3712,1999; ISSN 0944-2952.
4. Ehlers, J.; Quadakkers, W. J. Report Forschungszentrum Jülich, Jül-3883, 2001; ISSN 0944-2952.
5. Quadakkers, W. J.; Piron-Abellan, J.; Shemet, V.; Singheiser, L. *Mater. High Temp.* **2003**, *20*(2), 115–127.
6. Birks, N.; Meier, G. H.; Pettit, F. S. *Introduction to the High Temperature Oxidation of Metals*; Cambridge University Press: Cambridge, UK, 2006.
7. Bale, C. W.; Pelton, A. D.; Thompson,, W. J.; Eriksson, G.; Hack, K.; Chartrand, P.; Degterov, S.; Melancon, J.; Petersen, S. FactSage 5.3, Thermfact, 1976–2004.
8. Davies, H.; Dinsdale, A. *Mater. High Temp.* **2005**, *22*, 15–25.
9. Tedmon, C. S. *J. Electrochem. Soc.* **1966**, *113*(8), 766–768.
10. Opila, E. J. *Mater. Sci. Forum* **2004**, *461–464*, 765–774.
11. Opila, E. J.; Jacobson, N. S.; Myers, D. L.; Copland, E. H. *JOM*, **2006**, 22–28.
12. Stanislowski, M. Report Forschungszentrum Jülich, **54** (2006), ISBN 3-89336-432-2.
13. Segerdahl, K.; Svensson, J. E.; Halvarsson, M.; Panas, I.; Johansson, L. G. *Mater. High Temp.* **2005**, *22*, 69–78.
14. Galerie, A.; Henry, S.; Wouters, Y.; Mermoux, M.; Petit, J. P.; Antoni, L. *Mater. High Temp.* **2005**, *21*(4), 105–112.
15. Michalik, M.; Hänsel, M.; Żurek, J.; Singheiser, L.; Quadakkers, W. J. *Mater. High Temp.* **2005**, *22*(3/4), 213–221.
16. Ehlers, J.; Young, D. J.; Smaardijk, E. J.; Tyagi, A. K.; Penkalla, H. J.; Singheiser, L.; Quadakkers, W. J. *Corros. Sci.* **2006**, *48*, 3428–3454.
17. Young, D. J.; Pint, B. A. *Oxid. Met.* **2006**, *66*(3/4), 137–153.
18. Milewska, A.; Hierro, M. P.; Trilleros, J. A.; Bolivar, F. J.; Pérez, F. J. *Mater. Sci. Forum* **2004**, *461–464*, 321–326.
19. Thiele, M.; Teichmann, H.; Schwarz, W.; Quadakkers, W. J. *VGB Kraftwerkstechnik* **1997**, *77*(Heft 2), 135–140.
20. Surman, P. L.; Castle, J. E. *Corros. Sci.* **1969**, *9*, 771–777.
21. Tomlinson, L.; Cory, N. J. *Corros. Sci.* **1989**, *29*(8), 939–965.
22. Żurek, J.; Michalik, M.; Schmitz, F.; Kern, T. U.; Singheiser, L.; Quadakkers, W. J. *Oxid. Met.* **2005**, *63*(5/6), 401–422.
23. Żurek, J.; Michalik, M.; Singheiser, L.; Quadakkers, W. J. *Mater. Sci. Forum* **2006**, *522–523*, 155–162.
24. Michalik, M.; Hänsel, M.; Quadakkers, W. J. Report Forschungszentrum Jülich, **67**(2007), ISBN 978-3-89336-486-2.
25. Jacob, Y. P.; Haanappel, V. A. C.; Stroosnijder, M. F.; Buscail, H.; Fielitz, P.; Borchardt, G. *Corros. Sci.* **2002**, *44*, 2027–2039.
26. Raynaud, G. M.; Rapp, R. A. *Oxid. Met.* **1984**, *21*(1/2), 89–102.
27. Saunders, S. R. J.; Monteiro, M.; Rizzo, F. *Prog. Mater. Sci.* **2008**, *53*(5), 775–837.
28. Tallman, R. L.; Gulbransen, E. A. *J. Electrochem. Soc.* **1967**, *114*(12), 1227–1230.
29. Anghel, C.; Hörnlund, E.; Hultquist, G.; Limbäck, M. *Appl. Surf. Sci.* **2004**, *233*, 392–401.
30. Zheng, X. G.; Young, D. J. *Oxid. Met.* **1994**, *42*(3/4), 163–190.
31. Åkermark, T.; Hultquist, G. *Oxid. Met.* **1997**, *47*(1), 117–137.
32. Galerie, A.; Wouters, Y.; Caillet, M. *Mater. Sci. Forum* **2001**, *369–372*, 231–238.
33. Sun, C.; Berg, J. C. *Adv. Colloid Interf. Sci.* **2003**, *105*(1–3), 151–175.
34. Norby, T. *J. Phys. IV* **1993**, *3*(C9), 99–106.
35. Dieckmann, R. *Mater. High Temp.* **2005**, *22*(172), 93–103.
36. Rahmel, A.; Tobolski, J. *Corros. Sci.* **1965**, *5*, 333–346.
37. Young, D. J. *Mater. Sci. Forum* **2008**, *595–598*, 1189–1197.
38. Wood, G. C. *Oxid. Met.* **1970**, *2*(1), 11–57.
39. Quadakkers, W. J.; Norton, J. F.; Canetoli, S.; Schuster, K.; Gil, A. In 3rd International Conference on Microscopy of Oxidation; Newcomb, S. B., Little, J. A., Eds.; The Institute of Materials: Cambridge, 1996; pp 609–619.
40. Hänsel, M.; Quadakkers, W. J.; Singheiser, L.; Nickel, H. Report Forschungszentrum Jülich, Jül-3583,1998; ISSN 0944-2952.
41. Hultquist, G.; Tventen, B.; Hörnlund, E. *Oxid. Met.* **2000**, *54*(1/2), 1–10.
42. Tveten, B.; Hultquist, G.; Norby, T. *Oxid. Met.* **1999**, *51*(3), 221–233.
43. Malkow, T.; Quadakkers, W. J.; Singheiser, L.; Nickel, H. Report Forschungszentrum Jülich, Jül-3589,1998; ISSN 0944-2952.
44. Henry, S.; Mougin, J.; Wouters, Y.; Petit, J. P.; Galerie, A. *Mater. High Temp.* **2000**, *17*(2), 231–235.
45. Hänsel, M.; Quadakkers, W. J.; Young, D. J. *Oxid. Met.* **2003**, *59*(3/4), 285–301.
46. Essuman, E.; Meier, G.; Żurek, J.; Hänsel, M.; Quadakkers, W. J. *Oxid. Met.* **2008**, *69*(3), 143–162.
47. Essuman, E.; Meier, G. H.; Żurek, J.; Hänsel, M.; Norby, T.; Singheiser, L.; Quadakkers, W. J. *Corros. Sci.* **2008**, *50*(6), 1753–1760.
48. Wood, G. C.; Wright, I. G.; Hodgkiess, T.; Whittle, D. P. *Werkstoffe Korrosion*, **1970**, *21*(11), 900–910.
49. Kofstad, P. *High Temperature Corrosion*; Elsevier Applied Science: London, 1988.
50. Przybylski, K.; Yurek, G. J. *J. Electrochem. Soc.* **1988**, *135*(2), 517–523.
51. Żurek, J.; Young, D. J.; Essuman, E.; Hänsel, M.; Penkalla, H. J.; Niewolak, L.; Quadakkers, W. J. *Mater. Sci. Eng. A* **2008**, *477*, 259–270.
52. Bamba, G.; Wouters, Y.; Galerie, A.; Borchardt, G.; Shimada, S.; Heintz, O.; Chevalier, S. *Scr. Mater.* **2007**, *57*(8), 671–674.
53. Whittle, D. P.; Stringer, J. *Philos. Trans. R. Soc. A* **1980**, *295*, 309–329.
54. Pint, B. A. In *John Stringer Symposium on High Temperature Corrosion*; Tortorelli, P. F., Wright, I. G., Eds.; ASM International: USA, 2003; pp 1–10.
55. England, D. M.; Virkar, A. V. *J. Electrochem. Soc.* **1999**, *146*(9), 3196–3202.
56. England, D. M.; Virkar, A. V. *J. Electrochem. Soc.* **2001**, *148*(4), A330–A338.
57. Hussain, N.; Qureshi, A. H.; Shahid, K. A.; Chughtai, N. A.; Khalid, F. A. *Oxid. Met.* **2004**, *61*(5), 355–364.
58. Hussain, N.; Shahid, K. A.; Khan, I. H.; Rahman, S. *Oxid. Met.* **1994**, *41*(3), 251–269.

59. Piron-Abellan, J.; Quadakkers, W. J. Report Forschungszentrum Jülich, Jül-4170, 2005; ISSN 0944-2952.
60. Huczkowski, P.; Quadakkers, W. J. Report Forschungszentrum Jülich, 65, 2005; ISBN 978-3-89336-484-8.
61. Huczkowski, P.; Ertl, S.; Pirón-Abellán, J.; Christiansen, N.; Höfler, T.; Shemet, V.; Singheiser, L.; Quadakkers, W. J. *Mater. High Temp.* **2006**, *22*, 253–262.
62. Żurek, J.; Quadakkers, W. J. Unpublished results, Forschungszentrum Jülich, FRG, 2007.
63. Naoumidis, A.; Schulze, H. A.; Jungen, W.; Lersch, P. *J. Eur. Ceram. Soc.* **1991**, *7*, 55–63.
64. Krupp, U.; Christ, H. J. *Oxid. Met.* **1999**, *52*(3), 277–298.
65. Hammer, J.; Laney, S.; Jackson, R.; Coyne, K.; Pettit, F.; Meier, G. *Oxid. Met.* **2007**, *67*(1), 1–38.
66. Schütze, M.; Renusch, D.; Schorr, M. *Mater. High Temp.* **2005**, *22*(1/2), 113–120.
67. Mikkelsen, L.; Linderoth, S. *Mater. Sci. Eng. A* **2003**, *361*(1–2), 198–212.
68. Fujii, C. T.; Meussner, R. A. *J. Electrochem. Soc.* **1964**, *111*(11), 1215–1221.
69. Hayashi, S.; Narita, T. *Oxid. Met.* **2001**, *56*(3), 251–270.
70. Essuman, E.; Meier, G. H.; Żurek, J.; Hänsel, M.; Singheiser, L.; Quadakkers, W. J. *Scr. Mater.* **2007**, *57*(9), 845–848.
71. Ani, M. H. B.; Ueda, M.; Kawamura, K.; Maruyama, T. In Proceedings of the European Corrosion Congress, Paper 183, Eurocorr 2007, 2007.
72. Yang, Z.; Xia, G.; Singh, P.; Stevenson, J. W. *Solid State Ionics* **2005**, *176*, 1495–1503.
73. Eichenauer, W.; Künzig, H.; Pebler, A. *Z. Metallk.* **1958**, *49*, 220.
74. Swisher, J. H.; Turkdogan, E. T. *Trans. Metall. Soc. AIME* **1967**, *239*, 426–431.
75. Fromm, E.; Gebhardt, E. *Gase und Kohlenstoff in Metallen*; Springer: Berlin, 1976.
76. Wagner, C. *J. Electrochem. Soc.* **1952**, *99*(10), 369–380.
77. Rapp, R. A. *Acta Metall.* **1961**, *9*(8), 730–741.
78. Gesmundo, F.; Viani, F. *Oxid. Met.* **1986**, *25*(5), 269–282.
79. Wagner, C. *Z. Elektrochem.* **1959**, *63*, 772.
80. Essuman, E.; Meier, G. H.; Żurek, J.; Hänsel, M.; Singheiser, L.; Quadakkers, W. J. *Mater. Sci. Forum* **2008**, *595–598*, 699–706.
81. Park, E.; Hüning, B.; Grabke, H. J.; Spiegel, M. *Defect Diffusion Forum* **2005**, *237–240*, 928–933.
82. Ågren, J. *Scr. Metall.* **1986**, *20*(11), 1507–1510.
83. Ikeda, Y.; Nii, K. *Trans. Nat. Res. Inst. Met.* **1984**, *26*(1), 52–62.
84. Ueda, M.; Nanko, M.; Kawamura, K.; Maruyama, T. *Mater. High Temp.* **2003**, *20*(2), 109.
85. Hayashi, S.; Narita, T. *Oxid. Met.* **2002**, *58*(3), 319–330.
86. Griess, J. C.; De Van, J. H. *Mater. Perform.* **1980**, *19*(6), 46–52.
87. Cory, N. J.; Herrington, T. M. *Oxid. Met.* **1987**, *28*(5), 237–258.
88. Viswanathan, R.; Sarver, J.; Tanzosh, J. M. *J. Mater. Eng. Perform.* **2006**, *15*(3), 255–274.
89. Ennis, P. J.; Quadakkers, W. J. *VGB PowerTech* **2001**, *8*, 87–90.
90. Mayer, P.; Manolescu, A. V. In *High Temperature Corrosion*; Rapp, R. A., Ed.; National Association of Corrosion Engineers, 1983; pp 368–379.
91. Quadakkers, W. J.; Ennis, P. J.; Żurek, J.; Michalik, M. *Mater. High Temp.* **2004**, *22*(1/2), 37–47.
92. Fujii, C. T.; Meussner, R. A. *J. Electrochem. Soc.* **1963**, *110*(12), 1195–1204.
93. Langmuir, I. *Phys. Rev.* **1913**, *5*(2), 329–342.
94. Nakagawa, K.; Matsunaga, Y.; Yanagisawa, T. *Mater. High Temp.* **2001**, *18*(1), 51–56.
95. Armitt, I.; Holmes, D. P. The spalling of steam grown oxide from superheater and reheater tube steels, Technical Planning Study 76-655, Final Report, EPRI, USA,1978.
96. Ehlers, R. J.; Ennis, P. J.; Singheiser, L.; Quadakkers, W. J.; Link, T. In EFC Workshop 2001; Schütze, M., Quadakkers, W. J., Nicholls, J. R., Eds.; The European Federation of Corrosion Publications, 2001; Vol 34, Paper 12, pp 178–193.
97. Żurek, J.; Wessel, E.; Niewolak, L.; Schmitz, F.; Kern, T. U.; Singheiser, L.; Quadakkers, W. J. *Corros. Sci.* **2004**, *46*(9), 2301–2317.
98. Nishimura, N.; Komai, N.; Hirayama, Y.; Masuyama, F. *Mater. High Temp.* **2005**, *22*(1/2), 3–10.
99. Watanabe, Y.; Yi, Y. S.; Kondo, T.; Inui, K.; Kishinami, T.; Kimura, H.; Sato, M. In Proceedings of the 9th International Conference on Pressure Vessel Technology, ICPVT-9, Sydney, Australia; Price, J., Ed.; **2000**; pp 545–552.
100. Yi, Y. S.; Watanabe, Y.; Kondo, T.; Kimura, H.; Sato, M. *J. Pressure Vessel Technol.* **2001**, *123*, 391–397.
101. Husemann, R. U. *VGB Kraftwerkstechnik* **1999**, *10*, 146–149.
102. Ehlers, J.; Smaardijk, E. J.; Penkalla, H. J.; Tyagi, A. K.; Singheiser, L.; Quadakkers, W. J. In Proceedings of International Corrosion Congress, Cape Town, South Africa, 1999; Vol. 3, Paper 336.
103. Haarmann, K.; Vaillant, J. C.; Bendick, W.; Arbab, A. *The T91/P91 Book*; Vallourec & Mannesmann Tubes, 1999.
104. Piehl, C.; Tökei, Z.; Grabke, H. J. *Defect Diffusion Forum* **2001**, *194–199*, 1689–1694.
105. Nieto-Hierro, L.; Quadakkers, W. J. Unpublished results, Forschungszentrum Jülich, FRG, 2006.
106. Khanna, A. S.; Rodriguez, P.; Gnanamoorthy, J. B. *Oxid. Met.* **1986**, *26*(3), 171–200.
107. Ishitsuka, T.; Inoue, Y.; Ogawa, H. *Oxid. Met.* **2004**, *61*(1), 125–142.
108. Muramatsu, K. *In Development of Ultrasupercritical Plant in Japan, Advanced Heat Resistant Steel for Power Generation;* Viswanathan, R., Nutting, J. W., Eds.; IOM Communications: London, UK, 1999; Book 708, pp 543–559.
109. Peraldi, R.; Pint, B. A. *Oxid. Met.* **2004**, *61*(5), 463–483.
110. Sato, T.; Fukuda, Y.; Mitsuhara, K.; Sakai, K. In *Advances in Materials Technology for Fossil Power Plants*; Viswanathan, R., Gandy, D., Coleman, K., Eds.; ASM International, 2005.
111. Piron-Abellan, J.; Quadakkers, W. J. Unpublished results, Forschungszenrum Jülich, FRG, 2007.
112. Leistikow, S.; Wolf, I.; Grabke, H. J. *Werkstoffe Korrosion* **1987**, *38*, 556–562.
113. Osgerby, S.; Quadakkers, W. J. *Mater. High Temp.* **2005**, *22*(1/2), 27–33.
114. Otoguro, Y.; Sakakibara, M.; Saito, T.; Ito, H.; Inoue, Y. *Trans. Iron Steel Inst. Jpn.* **1988**, *28*, 761–768.
115. Montgomery, M.; Karlsson, A. *VGB Kraftwerkstechnik* **1995**, *75*(3), 258–264.
116. Kolb-Telieps, A.; Strehl, G.; Naumenko, D.; Quadakkers, W. J.; Newton, R. *High Temperature Corrosion of FeCrAlY/Aluchrom YHf in environments relevant to exhaust gas systems, Materials Aspects in Automotive Catalytic Converters*; Wiley-VCH: Weinheim, Germany, 2001.
117. Kochubey, V. PhD thesis, Bochum University, 2005.

118. Naumenko, D.; Gleeson, B.; Wessel, E.; Singheiser, L.; Quadakkers, W. J. *Metall. Mater. Trans.* **2007**, *38A*, 2974–2983.
119. Bennett, M. J.; Newton, R.; Nicholls, J. R. *Mater. High Temp.* **2003**, *20*(3), 347–356.
120. Naumenko, D.; Quadakkers, W. J. Unpublished results, Forschungszentrum Jülich, FRG,2007.
121. Janakiraman, R.; Meier, G. H.; Pettit, F. S. *Metall. Mater. Trans. A* **1999**, *30A*, 2905–2913.
122. Kirchheim, R. *Acta Metall.* **1981**, *29*(5), 835–843.
123. Kirchheim, R. *Acta Metall.* **1981**, *29*(5), 845–853.
124. Kirchheim, R.; Hirth, J. P. *Scr. Metall.* **1982**, *16*(4), 475–478.
125. Smialek, J. L. *JOM* **2006**, 29–35.
126. Toscano, J.; Naumenko, D.; Gil, A.; Singheiser, L.; Quadakkers, W. J. *Mater. Corros.* **2008**, *59*(6), 501–507.
127. Wessel, E.; Kochubey, V.; Naumenko, D.; Niewolak, L.; Singheiser, L.; Quadakkers, W. J. *Scr. Mater.* **2004**, *51* (10), 987–992.
128. Ramanarayanan, T. A.; Ayer, R.; Petkovic-Luton, R.; Leta, D. P. *Oxid. Met.* **1988**, *29*(5), 445–472.
129. Naumenko, D.; Quadakkers, W. J.; Galerie, A.; Wouters, Y.; Jourdain, S. *Mater. High Temp.* **2003**, *20*(3), 287–293.
130. Götlind, H.; Liu, F.; Svensson, J. E.; Halvarsson, M.; Johansson, L. G. *Oxid. Met.* **2007**, *67*(5), 251–266.
131. Lodziana, Z.; Topsoe, N. Y.; Norskov, J. K. *Nat. Mater.* **2004**, *3*, 289–293.
132. Götlind, H. Thesis for the degree of doctor of engineering. Chalmers University of Technology: Göteborg, Sweden, 2614, 2007, ISBN 978-91-7291-933-4.
133. Boggs, W. E. *J. Electrochem. Soc.* **1971**, *118*(6), 906–913.
134. Niewolak, L.; Shemet, V.; Thomas, C.; Lersch, P.; Singheiser, L.; Quadakkers, W. J. *Intermetallics* **2004**, *12* (12), 1387–1396.
135. Donchev, A.; Richter, E.; Schütze, M.; Yankov, R. *Intermetallics* **2006**, *14*(10–11), 1168–1174.
136. Rakowski, J. M.; Meier, G. H.; Pettit, F. S.; Dettenwanger, F.; Schumann, E.; Rühle, M. *Scr. Mater.* **1996**, *35*(12), 1417–1422.
137. Niewolak, L. Unpublished results, Forschungszentrum Jülich, FRG,2003.
138. Wouters, Y.; Galerie, A.; Petit, J. P. *Solid State Ionics* **1997**, *104*, 89–96.
139. Bak, T.; Nowotny, J.; Rekas, M.; Sorrell, C. C. *J. Phys. Chem. Solids* **2003**, *64*(7), 1043–1056.
140. Nowotny, J.; Bak, T.; Nowotny, M. K.; Sheppard, L. R. *Int. J. Hydrogen Energy* **2007**, *32*(14), 2630–2643.
141. Kofstad, P. *Nonstoichiometry, Diffusion and Electrical Conductivity in Binary Metal Oxides*; Wiley Interscience: New York, 1972.
142. Nowotny, J.; Radecka, M.; Rekas, M.; Sugihara, S.; Vance, E. R.; Weppner, W. *Ceram. Int.* **1998**, *24*(8), 571–577.
143. Rahmel, A.; Schütze, M.; Quadakkers, W. J. *Mater. Corros.* **1995**, *46*(5), 271–285.
144. Rahmel, A.; Spencer, P. J. *Oxid. Met.* **1991**, *35*(1), 53–68.
145. Becker, S.; Rahmel, A.; Schorr, M.; Schütze, M. *Oxid. Met.* **1992**, *38*(5), 425–464.

1.26 High Temperature Corrosion of Ceramics and Refractory Materials

K. G. Nickel
Applied Mineralogy, Institute for Geosciences, University Tübingen, Wilhelmstr. 56, D-72074 Tübingen, Germany
P. Quirmbach and J. Pötschke
Deutsches Institut für Feuerfest und Keramik GmbH, An der Elisabethenkirche 27, D-53113 Bonn, Germany

Glossary

Converter The containment for the industrial conversion of ore to metal and its purification by slag formation.

Ellipsometry Measurement of the change of light polarization upon reflection or transmission. In corrosion, it is usually done in reflection and used to infer the thickness of a very thin layer (down to the angstrom-level) of reaction product.

Flue gas Exhaust gases from a fireplace, oven, furnace, or other production process.

Hot corrosion Historically evolved name for the attack of a material by or involving salt melts. A typical representative is a Na_2SO_4 melt.

Hydrothermal Conditions which involve a water fluid at elevated temperatures. Commonly used for conditions above 100 °C at pressures above the atmospheric pressure.

Ladle Container for transport and pouring of (metal) melts.

Rate constant Constant which relates the quantitative progress of a process, example, a growth of a layer on an infinite plate, to time.

Slag By-product of ore smelting or refining. It usually consists mainly of oxides, with or without other constituents like sulfides, phosphates, and metals.

Steady-state conditions Conditions in which a system has a constant behavior with time. In corrosion, this often implies that external conditions such as the atmospheric partial pressure of the attacking medium are kept constant and a dynamic equilibrium is established, where two or more reversible processes occur at one rate.

Thermogravimetry Continuous instrumental determination of mass changes of a sample as a function of time, with or without regular changes in temperature, pressure, or gas composition during the observed time.

Wetting angle Contact angle at which the liquid–vapor interface of a fluid and the solid–vapor interface of a contacting solid meet. Describes the tendency of the fluid to form a film (perfectly at 0 °C) or a ball resting on the surface (perfectly above 150 °C).

Abbreviations

SEN Submerged entry nozzle

SSiC Pressureless sintered silicon carbide

Symbols

$\boldsymbol{A}$ Surface area (m^2)

$\boldsymbol{a}$ Thermal diffusivity ($m^2\,s^{-1}$)

$\boldsymbol{C_0}$ Concentration of carbon in liquid iron (wt %)

$\boldsymbol{C_S}$ Saturation concentration of carbon in liquid iron (wt %)

$\boldsymbol{D_i}$ Diffusion coefficient of component i ($m^2\,s^{-1}$)

$\boldsymbol{D_p}$ Pore-diffusion coefficient ($m^2\,s^{-1}$)

$\boldsymbol{E}$ Modulus of elasticity (GPa)

$\boldsymbol{G_F}$ Crack energy ($J\,m^{-2}$)

$\Delta\boldsymbol{G^0}$ Free enthalpy in the standard state ($J\,mol^{-1}$)

$\boldsymbol{g}$ Acceleration of gravity ($m\,s^{-2}$)

$\boldsymbol{h}$ Height (m)

$\boldsymbol{h_l}$ Diameter of the convection loop (m)

$\mathbf{h_g}$ Characteristic length of the corrosion groove (m)

$\boldsymbol{K}$ Equilibrium constant

$\boldsymbol{k_{linear}}$ Linear rate constant ($m\,s^{-1}$ or $kg\,m^{-2}\,s^{-1}$)

$\boldsymbol{k_{log}}$ Logarithmic rate constant

$\boldsymbol{k_p}$ Parabolic rate constant ($m^2\,s^{-1}$ or $kg^2\,m^{-4}\,s^{-1}$)

$\boldsymbol{l}$ Length (m)

$\boldsymbol{P_i}$ Partial pressure of species i

$\boldsymbol{R}$ Universal gas constant ($8314\,J\,mol^{-1}\,K^{-1}$)

$\boldsymbol{T}$ Temperature (K)

$\boldsymbol{t}$ Time (s)

$\boldsymbol{u}$ Stoichiometry factor

$\boldsymbol{V_l}$ Molar volume of phase l ($m^3\,mol^{-1}$)

$\boldsymbol{v}$ Flow velocity ($m\,s^{-1}$)

$\Delta\boldsymbol{w}$ Mass change ($kg\,m^{-2}$)

$\boldsymbol{x}$ Mass change per unit area ($kg\,m^{-2}$) or scale thickness (m)

$\boldsymbol{\alpha}$ Thermal expansion coefficient (K^{-1})

$\boldsymbol{\beta}$ Mass transfer coefficients ($m\,s^{-1}$)

$\boldsymbol{\gamma}$ Labyrinth factor, tortuosity

$\boldsymbol{\delta}$ Boundary layer of diffusion (m)

$\boldsymbol{\delta_{Pr}}$ Prandtl's boundary layer thickness (m)

$\boldsymbol{\delta_N}$ Nernst's diffusion-boundary-layer thickness (m)

$\boldsymbol{p_c}$ Open porosity of the decarburized zone (%)

$\boldsymbol{\varepsilon_c}$ Critical elongation

$\boldsymbol{\rho}$ Density ($kg\,m^{-3}$)

η Dynamic viscosity ($kg\,m\,s^{-1}$)

$\boldsymbol{\mu}$ Poisson ratio

ν Kinematic viscosity ($m^2 s^{-1}$)
σ Interfacial tension ($N m^{-1}$)
σ_c Critical stress (MPa)
θ Wetting angle (°)
τ Correction time (s)

1.26.1 Introduction

Ceramics are nonmetallic–inorganic materials, which are usually made by forming from a mass or a powder and firing at high temperature, upon which the material becomes consolidated and obtains its properties. This implies that ceramics have thermal and chemical stability at the firing temperature in the firing environment. 'High temperature' is a very blurred term, but most people would accept temperatures above 800 °C as high temperature. An exception is the behavior in hydrothermal conditions. Hot, pressurized water is very reactive and many compounds have a high level of solubility in it. For this reason, we will describe the hydrothermal behavior of ceramics at lower temperatures.

A classical division of ceramics is silicate, oxide, and nonoxide ceramics. Textbooks and handbooks on their properties and manufacture have been published[1–4] and contain chapters on their corrosion resistance.

Metals and intermetallics do survive at high temperatures in many environments only because they form phases, commonly oxides, which protect them from further attack. In this respect, many chapters in this book deal with ceramics. In order not to repeat too many issues, readers are referred to appropriate chapters, in particular the ones on **Oxidation of Metals and Alloys** and **High Temperature Coatings: Protection and Breakdown**. In this chapter, we will deal with bulk materials.

There are many applications of ceramics at high temperatures: one deals with materials that contain and protect from melts in the metal or glass industry, another is the function to transport or contain heat in predominantly gaseous environments. For some tasks, structural loads under adverse conditions have to be met, whereas for others, several forms of attack may occur, e.g., waste incineration. A rather new application is the use of SiC as an electronic material, commonly in the form of single crystal wafers. Although the use is at low or moderate temperatures, a high temperature treatment to produce insulating silica is a common step in the production of these new functional materials.

A refractory material is firstly a ceramic that has not reached the softening point, at which a special pyramid (Seger-cone SK17) would bend when heated to 1500 °C. However, the material has to fulfill other criteria at high temperatures to be called refractory, namely, it has to keep its shape, survive thermal fluctuations, and withstand attack by slags or melts for a sufficiently long time.[5,6] Refractories are in most cases porous composites, making the behavior complex.

There is an overlap in materials chemistry between refractories and technical ceramics. For example, alumina and silicon carbide are manufactured both as refractories and as dense, advanced engineering ceramics. For this reason, refractories are dealt with in the form of typical examples from the steel- and iron-making industries. Other applications have similar principal problems and, from a chemical point of view, are contained within the ceramics section.

1.26.2 Differences between Metals and Ceramics

In the corrosion of metals, we usually find oxidation of the metal to form some phase, which is then lost to the environment by spallation, dissolution, or some other mechanisms, resulting in mass loss or the formation of a surface layer, which can have protective characteristics. Basic cases like the oxidation of iron are well known[7] and may be described by simple laws such as a parabolic weight gain in certain regimes.

The complexities of scale evolution often necessitate a more complex modeling of the transport in oxide scales, and finite difference calculations are used to predict the process progression.[8]

The importance of the oxide development in silicon-based semiconductors has led to the development of sophisticated detailed models for high temperature oxidation, whether related to initial periods[9] or general laws.[10]

Ceramics are often oxides, carbides, or nitrides. In general, nonmetals have a higher electronegativity than metals. The bonding is mostly a mixed ionic–covalent one, but formally the electrons have to be assigned to the nonmetal. High temperature oxidation of these carbides and nitrides thus oxidizes the carbon or the nitrogen and leaves the metal or semiconductor in its oxidation state. Also, in contrast to metals, where often the metal is transported as an ion to the surface to become oxidized, in ceramics we usually have the transport of the corroding agent to

the scale–substrate interface where reaction occurs. The oxidation process is therefore better compared with semiconductors rather than with ordinary metals.

Oxide ceramics are stable in environments having sufficient oxygen; their corrosion is based on reactions that form other phases, becoming dissolved or evaporated.

1.26.3 Corrosion Modes and Kinetics

To understand the principles, we first assume the material to be single phased, isotropic, dense, and to have perfect surfaces. Just like metals, ceramics can show both active and passive corrosion behaviors. Unless retarding phases are formed, steady-state processes in active corrosion have simple and constant mass loss rates for a given set of physical boundary conditions. It does not matter whether the chemical reaction rate, the dissolution kinetics, or the diffusion from or into the corrosive medium is rate determining. The constancy of boundary conditions such as constant gradients in the attacking agent necessitates linear kinetics following eqn. [1], in which x denotes either the thickness of the layer lost or the mass of material loss per unit area, t the time, and k_{linear} is the linear rate constant:

$$x(\text{m or kg m}^{-2}) = k_{\text{linear}}(\text{ms}^{-1} \text{or kg m}^{-2}\,\text{s}^{-1}) \cdot t(\text{s}) \quad [1]$$

The time to reach those steady-state conditions is not covered by the model, so initial periods with differing rates are possible. In the initial period, transport-related problems are less likely to dominate, so formation or removal of surface adlayers may lead to incubation periods. Alternatively, the buildup of a gradient may be fast in the beginning and turn into a steady-state rate later.

The ease of this formulation hides the problems associated with it. Everything rests on the constancy of external conditions, and therefore the measured rates depend on a large number of boundary conditions. Laminar or turbulent flows of the attacking medium, convection or still conditions, and flow velocity of the attacking gas or fluid are only a few obvious parameters.

For polyphasic materials, the resistance against attack is usually different for the different phases. Here, eqn. [1] is only valid for each phase individually and only as long as the processes do not influence each other. The example of a preferential grain boundary phase attack is easy to understand. Here, boundary phase removal concurrent with a more or less inert matrix material gives us the picture of increasing pathway lengths for the attacking agent with time. This is very likely to slow down the corrosion progress. In such cases, eqn. [1] is correct for neither the bulk material nor the individual phase.

Porous materials have another prominent problem: establishing contact with the medium so that the development of transport pathways becomes complex. Wetting behavior is of utmost importance, as it governs the penetration and hence the true contact surface. Wetting depends on surface energies and these are likely to change with time due to gradient developments, saturation effects, etc. Such problems are dealt with in detail in **Section 1.26.14** on refractory corrosion in the form of typical examples and equations.

Although the chemical removal of phases is a corrosive process, it may well be influenced by erosive or mechanical stresses accompanying the attack. This is also described in the refractory section of this chapter (**Section 1.26.10**). At this point, we only want to hint that the formation of a solid reaction product during corrosion may not always retard the corrosion progress. Such a special form of active corrosion, which is particular to nonoxide ceramics, has been described for silicon carbide at very high temperatures,[11] where a high pressure of CO can create bubbles, which are easily removed by spallation and erosion.

The formation of solid phases during corrosion can often result in scales or layers. It depends on their physical nature whether they hamper the corrosion process or not. Oxide scales on nonoxide ceramics often do not have such a high mismatch in thermal expansion coefficients as oxidized metals. Hence, stresses in the scale can be lower and spallation is a less common phenomenon. Nonetheless, the oxides can undergo phase transitions with volume changes large enough to cause stresses and cracking during thermal cycling. Multiphase scales likewise can develop stresses that induce cracks. Bubbles are another way of potentially short-circuiting the scale.

In all such cases, eqn. [1] is also valid for passive corrosion, because the scale that develops is not protective. The equation has then positive constants for mass gain. Also in any real process where a scale becomes protective, there is an initial period, in which it is not thick enough to be rate determining. This has been established for the oxidation of silicon by Deal and Grove,[10] where the linear character of the initial period has been shown.

In both metals and ceramics, corrosion in which the transport of the reacting agent through a growing layer is governed by the diffusion of this agent or the reaction product through the scale, we have long-time behavior approximated by a simple parabolic law

$$x(\mathrm{m\ or\ kgm^{-2}}) = \sqrt{k_p(\mathrm{m^2\,s^{-1}\ or\ kg^2\,m^{-4}\,s^{-1}}) \cdot t(\mathrm{s})} \quad [2]$$

In eqns. [2]–[5], x now denotes either the thickness of the layer formed or the mass of material gained per unit area, t is the time, and k_p is the parabolic rate constant. Following the reasoning above, both parts of the process can be joined with the linear–parabolic model[10] to give

$$x^2 + Ax = B(t + \tau) \quad [3]$$

in which several physical parameter are contained in the factors A and B and a correction time τ is introduced, which accounts for an initial scale thickness. By setting reasonable boundary conditions, it is found that B equals k_p for long times and thus eqn. [3] is approximated by eqn. [2], B/A equals k_{linear} and thus eqn. [3] is approximated by eqn. [1] for short times. Note that 'short times' is an expression relating to corrosion progress and can last, for example, for days at 700 °C in the oxidation of silicon.

It was claimed that the oxidation data for silicon can equally well be fitted by a simple power law[12]

$$x = at^b \quad [4]$$

This method has not been used extensively in the literature for oxidation of semiconductors or ceramics. The lack of a good physical explanation for the parameters of eqn. [4] is probably the main reason.

For easy fitting, a variant of eqn. [3] may be preferred:

$$\frac{x^2}{k_p} + \frac{x}{k_l} - \tau = t \quad [5]$$

A difference to be noted between ceramics and metals is that the corrosion progress x is not directly transferred from thickness to weight change units via densities ρ, because in nonoxides there is a loss of the accompanying light element. As described elsewhere,[13] a stoichiometry factor relating to the reaction equation

$$u = \frac{(n \cdot M)_{\text{Condensed product}}}{(n \cdot M)_{\text{Condensed product}} - (n \cdot M)_{\text{Material}}} \quad [6]$$

where n is the number of moles in the chemical reaction equation and M the molecular weight, has to be calculated to relate rate constants to each other by eqn. [7]:

$$k_p(\mathrm{m\,s^{-1}})\frac{\rho^2_{\text{Product}}(\mathrm{kg\,m^{-3}})^2}{u^2} = k_p(\mathrm{kg^2\,m^{-2}\,s^{-1}}) \quad [7]$$

A third basic law is the logarithmic or asymptotic law

$$x = c + k_{\log}\,\log(t) \quad [8]$$

This may be used for corrosion processes, which are effectively stopped by the formation of a material barrier during corrosion. It basically describes the decrease in the effective exposed surface area. The barrier may be a crystalline phase with a much lower diffusion coefficient.

Kinetic breaks are observed in cases where a physical effect interferes with the corrosion process. An example is the repeated cracking of the scale. If a critical thickness is responsible for the critical stress, which initiates the cracking process, pseudolinear behavior with a succession of periods of parabolic growth and intervening periods of renewal of short-circuiting paths follows.

Internal oxidation is observed in multiphase ceramics. A grain boundary phase is often the weakest material in terms of corrosion resistance and provides a transport path for the exchange of matter between the inside and the outside of the structure. The production of selectively corroded phases in the interior induces internal stresses because of volume increases. After a critical stress level is reached, mechanical failure of parts of the component near the surface may follow. If this cannot be healed during the process, a large new surface area is opened and a 'break-away' situation is likely, i.e., a change to fast linear corrosion.

Another typical break situation is observed in porous materials. The closure of pore openings by the formed scale diminishes the exposed surface markedly and almost instantaneously. A much slower progress follows after closure.

Simple basic laws of passive processes are only true for constant diffusion coefficients. In all cases, where extrinsic or intrinsic impurities, additives, etc., are present and enter the scale forming material, an influence on the diffusion coefficient must be envisaged. An increase or decrease in the coefficient causes the mass change curve to become steeper or flatter relative to parabolic behavior. Simulations show that for strong effects of this kind linear [1] or asymptotic behavior [7] is approximated.

Therefore, we have good reasons to envisage complex kinetic behavior during corrosion to be possible.

Complex strictly physical models are a matter of model calculations still and hard to generalize. Attempts to model complex situations by semi- or purely empirical curve fitting procedures, e.g., by using a multiple linear approach in the form

$$x = k_0 + k_{\text{lin}}t + k''_{\text{p}}\sqrt{t} + k_{\log}\,\log(t) \qquad [9]$$

have been proposed[14, 15] and shown to be quite successful. Attempts to introduce an even higher degree of sophistication made the equations less robust to the errors inherited from the uncertainties of measurement.[16]

A special case of complex kinetics arises from situations in which active and passive processes occur simultaneously. This has been discussed extensively because it is of great importance to applications such as gas turbines.[17] Corrosion in which a scale is formed and evaporated at the same time has a typical pattern in plots of mass change against time, because the initial gain will turn into a linear loss after longer times. Opila[18] has shown that the equation for metal oxidation with evaporation reported by Tedmon[19] in the form

$$t = \left[\frac{u_1^2 k_p}{2k_l^2}\left[-\frac{2k_l\,\Delta w_1}{u_1 k_p} - \ln\left(1 - \frac{2k_l\,\Delta w_1}{u_1 k_p}\right)\right]\right] - \frac{\Delta w_2}{u_2 k_l} \qquad [10]$$

where u_1 and u_2 are stoichiometric factors, which account for the mass balance of the appropriate reactions, Δw_1 and Δw_2 are weight gain and weight loss by scale growth and volatilization, respectively, is successful in describing this steady-state situation, leading to the establishment of a steady-state scale thickness and progressing corrosion of the material. The engineering basis for the loss function was also explored and simulated with parameters for the flow of fluids.[20]

1.26.4 Corrosion Measurement

In situ experiments of ceramic corrosion can only be done for simple cases. Simple oxidation of a nonoxide in a defined atmosphere can be followed continuously by thermogravimetry (TGA), which allows proper kinetic modeling. Resolution, accuracy, precision, and long-time stability of the apparatus have to be controlled. Other problems, e.g., contamination or the creation of local atmospheres, are identical to those discussed below.

Scale growth monitoring measurements, e.g., by ellipsometry, which are common for oxidation of silicon, have rarely been used in ceramics. Only in recent years, with SiC wafers for electronic applications becoming available, have such data been produced in greater numbers.

The most common experiments in ceramics corrosion are still exposures in special environments, followed by weighing and inspecting with microscopic and other available analytical techniques.

Melt corrosion is often studied by ordinary drop, crucible, and finger tests; these should only be used to rank materials, because they give qualitative data inside a narrow frame set by the standardized experimental setup.

Burner rigs are used to test for salt melt corrosion ('hot corrosion').[21] Salts are injected into the flame of a burner and deposited at constant rates onto samples, which are positioned and agitated in front of the apparatus exhaust.

Post-inspection of samples from furnace tests is most common for the investigation of interactions with gases. As a typical example for the contamination problems associated with the method, we can look at protective tubes made from alumina. Most gases, even expensive high-purity types, do contain water at the ppm-level. Unless the alumina tube was fired and flushed at high temperatures for times in the order of 1000 h, it may contaminate the sample with sodium, and as long as extreme measures have not been taken to dry the atmosphere (e.g., by P_2O_5), there may be substantial contamination by alumina in the form of transfer as hydroxide.[22] In deliberately moistened atmospheres, the effect is quite high.[23] The effect on oxidation rates for silica formers has been shown to be extensive even for low contamination levels,[24] because the contaminants are good glass formers, and may change the properties of growing scales. Apart from contamination, local atmospheres may play a role, which may explain the observed influences of furnace size on experimental oxidation rates.[25]

High temperature experiments have always an extended level of contamination possibilities. An increased level of uncertainty in corrosion data comes also from sample inhomogeneities. Preferential corrosion of secondary or grain boundary phases is often calculated directly relative to the total sample surface and yields a corresponding bias in parameter evaluation. Adding the increased uncertainty levels of temperature measurement and physical side effects such as the relative large areas in the vicinity of an edge in the usually small

samples, it is plain that one has to allow for some systematic and statistical error in the experimental data.

1.26.5 Oxides

A number of oxides with high melting points could qualify as high temperature materials. Out of these only a small number is used as bulk engineering material, and therefore only alumina and zirconia are dealt with here in detail. The other oxides are either covered by the chapter on "Oxidation of Metals and Alloys" or are covered by the chapter on **Oxidation of Metals and Alloys** or are contained within the refractory sections of this chapter.

1.26.5.1 Alumina

The only form of alumina that is stable at high temperature is corundum or α-Al_2O_3. It is well known for its excellent chemical resistance, even at high temperatures. For this reason, it is a common tube material in high temperature furnace systems with oxidizing atmospheres. The applications at high temperature are often limited by other properties rather than corrosion, namely creep and poor mechanical properties.

Nonetheless, there are some restrictions for the use of alumina based on its chemical behavior. At temperatures of 1700 °C in Ar/H_2O mixtures, evaporation of alumina was reported and excessive grain growth may have enhanced the problems.[26] Reducing environments can also foster carbothermic reduction of alumina, e.g., in the presence of SiC,[27] but in general a good resistance to flue gases of the aluminum-remelting industry has been reported.[28] The attack by alkali metal vapors is impurity dependent.

Corrosion by aggressive gases can be estimated via calculation of the partial pressures of volatile species over alumina.[29] This has been shown for halogens[30] and is certainly true for other such agents. The vaporization in water containing systems is mainly in the form of $Al(OH)_3$. Therefore, in high-velocity gas streams containing water, there is a limitation for long-time applications.

Solid-state reactions for silica are not restricted to phase equilibria with mullite, because the system is complicated and characterized by metastable immiscibility gaps at temperatures significantly below the eutectic value close to 1600 °C. Alumina is a common component in, and therefore can be dissolved by, silicate slags. For the details of the process dependencies, the reader is referred to example references.[31]

The corrosion resistance of alumina ceramics is strongly influenced by impurities because some of these are incorporated as grain boundary phases with accordingly selective preferential damage. In particular, silica and alkalis are typical impurities for alumina in engineering ceramics and even small amounts have been shown to be responsible for the corrosion in hydrothermal conditions.[32] Similarly corrosion by salt melts is related to impurities and grain boundary phases.[33]

1.26.5.2 Zirconia

Zirconia (ZrO_2) is a high temperature phase with a melting point above 2500 °C. Extremely high values even for the lowest eutectic temperatures in the binary systems with alumina and silica make it a prime material for refractory systems by itself or with those oxides. For many conditions, it will behave in an almost inert manner in contact with silica or alumina.

The section on thermal barrier coatings in this book discusses the corrosion aspects in those high temperature applications.

As a pure monolithic material, it is more problematic, because martensitic phase transformations with volume changes occur and tend to embrittle the material during thermal cycling. The addition of Mg, Ca, Y, and Ce stabilizes the higher temperature modifications (for a review on the basic science of these transformations see Hannink *et al.*[34]), and with appropriately high concentrations the cubic modification is stable down to room temperature.

In a stabilized modification, the use of zirconia as a refractory material is possible. Such refractories are susceptible to corrosion by slags, because slags with low basicity leach MgO, and highly basic slags can dissolve the material completely. Applications in remelting furnaces showed a good resistance to flue gases.

The stabilization can have deleterious effects on Ce-doped materials because the variation of external oxygen fugacity can induce corrosion due to a change in the oxidation state. Corrosion by water is a serious problem because even at low temperatures it can enter the structure of zirconia and destabilize the modifications. Appropriate phase transformations have been observed under hydrothermal conditions.[35]

1.26.5.3 Cordierite

Cordierite ($Al_3Mg_2(Si_5AlO_{18})$) is a rock-forming mineral, and the pure Mg-end member of the solid solution with Fe melts incongruently at 1460 °C to yield mullite and liquid. It is a widely applied ceramic for soot filters or heat exchanger, because it

has a low thermal expansion coefficient and therefore is very tolerant to thermal shocks and cycling.

High temperature corrosion of cordierite is known from treatments with molten salts (hot corrosion).

1.26.6 Carbides

1.26.6.1 Boron Carbide

Hydrothermal corrosion of B_4C proceeds at low pressures and C:H-ratios according to reactions of the type

$$B_4C + 8H_2O \Leftrightarrow 2B_2O_3 + CO_2 + 8H_2 \quad [11]$$

in which CO_2 is replaced by methane or carbon monoxide under appropriate carbide/water ratios. In analogy with water vapor systems, reactions start at temperatures as low as 250 °C because no carbon layer is produced.

Experiments on the attack by oxygen on powders,[36] coatings, and sintered materials confirm that at low and moderate temperatures the oxidation yields boric acid

$$B_4C + 4O_2 \Leftrightarrow 2B_2O_3 + CO_2 \quad [12]$$

and the kinetics are governed by oxygen diffusion through it. In the high temperature regime, starting at about 800 °C, boric acid evaporates and the process becomes paralinear with an overall loss at longer times. Evaporation is stronger in wet atmospheres, because the reaction

$$B_2O_3 + 3H_2O \Leftrightarrow 2H_3BO_3 \quad [13]$$

dominates at temperatures below about 1000 °C with high partial pressures. Boron carbide was investigated in steam because it is an important material in the nuclear industry. The dependence of the kinetics on partial pressures of water and flow speed was confirmed and modeled.[37] It should be noted that many commercial bulk boron carbides contain impurities or additives, which strongly influence the process.[38]

1.26.6.2 Silicon Carbide

Corrosion data collections for SiC-based materials are found in a number of handbooks and textbooks,[39–42] are contained in specific conference proceedings[14,43,44] and a vast number of publications. The interest in the high temperature behavior of this material comes historically from its use as a refractory material, later from the structural engineering advanced ceramics, and in recent times, increasingly from the need to understand the behavior to obtain insulating parts within a semiconductor.

Hydrothermal corrosion is significant only at temperatures exceeding 500 °C, even though initial reactions may occur at 300 °C. The hydrothermal oxidation yields silica along with CH_4, $CO_x \pm C$. The attack is commonly an active corrosion, because silica is dissolved in H_2O. The dissolution rate of silica is the key to the kinetics of the process and can be modified by increasing the pH of the water. The onset of hydrothermal oxidation in silicon nitride, likewise forming silica, is at much lower temperatures. The difference indicates protection by the formation of carbon layers at temperatures below about 500 °C, which has been observed for SiC-based fibers[45] and in halogen containing environments.[46]

Silicides are thermodynamically often more stable than SiC and a number of low-temperature eutectics exist with SiC. Therefore, metals can corrode SiC and a compilation[41] gives indications for reactions with Al (750 °C), Au (950 °C), Bi (600 °C), Cr (1000 °C), Cu (950 °C), Co (1150 °C), Fe (1000 °C), Li (815 °C), Mg (800 °C), Ti (575 °C), Mo (1200 °C), Nb (1300 °C), Ni (500 °C), Pd (600 °C), Ta (1200 °C), and W (1500 °C). Resistance to the attack was noted for Ag (962 °C), Ca (1180 °C), Cd (500 °C), Na (350 °C), Pb (815 °C), and Sn (600 °C).

Most of those data were obtained in vacuum, where the wetting behavior, which is essential for the form and strength of attack, is different from oxidizing conditions. It should also be noted that SiC containing free Si reacts more readily than SiC. Temperatures of possible reactions may be evaluated with the aid of phase diagrams of the appropriate Si–metal system. In appropriate wear conditions, a reaction of SiC with a metal is therefore feasible.

For attack by salt melts (hot corrosion), the reviews by Jacobson and coworkers[47–49] are still fundamental. As explained in the appropriate chapter in this book, the attacking salts are best represented by Na_2SO_4, which forms in combustion environments by

$$2NaCl + SO_2 + 0.5O_2 + H_2O \Leftrightarrow Na_2SO_4 + 2HCl \quad [14]$$

A first condition for a window of effective hot corrosion is given by the melting and dew points of Na_2SO_4. The melting point is 884 °C, the dew point varies with pressure, S content of the fuel, and NaCl concentration in the atmosphere. In gases with NaCl > 1 ppm and combustion pressures of 100 bar, the dew point ranges between 1100 and 1200 °C (from eqn.[14]).

The corrosive effect is not a reaction with the sulfate. It is due to the activity of Na_2O from the decomposition

$$Na_2SO_4 \Leftrightarrow Na_2O + SO_3 \quad [15]$$

and reaction with the protective SiO_2 scale

$$xSiO_2 + Na_2O \Leftrightarrow Na_2O \cdot (SiO_2)_x \quad [16]$$

Therefore, other compounds releasing alkali oxide on decomposition, e.g., Na_2CO_3, also cause hot corrosion.

Reaction [15] shows that a low $P(SO_3)$ value drives reaction [16] to the right side, typical for the external $P(SO_3)$ from the combustion of low-S fuels (<0.5%, a condition met by many modern fuels) at temperatures of about 1000 °C.

However, corrosion starts at the melting point of Na_2SO_4. Free carbon is often present in commercial SSiC (=pressureless sintered silicon carbide) and promotes the dissociation of Na_2SO_4 by making the silicate melt more basic. Accordingly, very strong hot corrosion of SiC with free carbon is known.[50]

Even without free carbon hot corrosion of SiC should occur as an internally governed process analogous to studies[51] on Si_3N_4, because SiC may act as the reducing agent to promote sulfate dissociation directly or by establishing an oxygen gradient in the silica scale consumed by reaction [16].

Hot corrosion tests are often only qualitative. Even burner-rig methods have problems for quantifying the attack. In terms of degradation of the mechanical properties, it should be noted that hot corrosion commonly causes pitting with a change in exposed surface and nonuniform attack. Pitting may not in all cases be a secondary phase problem, because it can be initiated by the immiscibility of two liquids.[51] It seems to be fairly difficult to model the damage by hot corrosion in a general way. One approach is to relate the pit diameter to strength data, i.e., to treat them as critical flaw sizes in the Griffith equation.

Hot corrosion protection has been investigated using mullite coatings.[17] Some temporary protection may even come from simple silica coatings.[52]

The corrosion of SiC by hot gases has been the subject of many studies. Active corrosion is a form of attack by gases, which do not form condensed species with Si at the temperatures of interest. Thus, halogens induce active corrosion, and calculated pressures of species such as SiF_4 or $SiCl_4$ over SiC will be as high as the concentration of F and Cl in the gas.

These pressures will be significantly decreased and the damage is less severe in the presence of oxygen, as evidenced by a study on Cl_2 corrosion.[53]

Corrosion of pure SiC by H_2 starts at temperatures above 1300 °C, while grain boundaries and secondary phases in sintered SiC are attacked at temperatures as low as 1000 °C.

The formation of silica is therefore essential for the stability of SiC. The boundary for active-to-passive oxidation is described in **Figure 1**. Wagner-type models predict the transition for diffusion-related situations and are relatively successful. From experimental evidence at temperatures of ~1760 °C,[54]

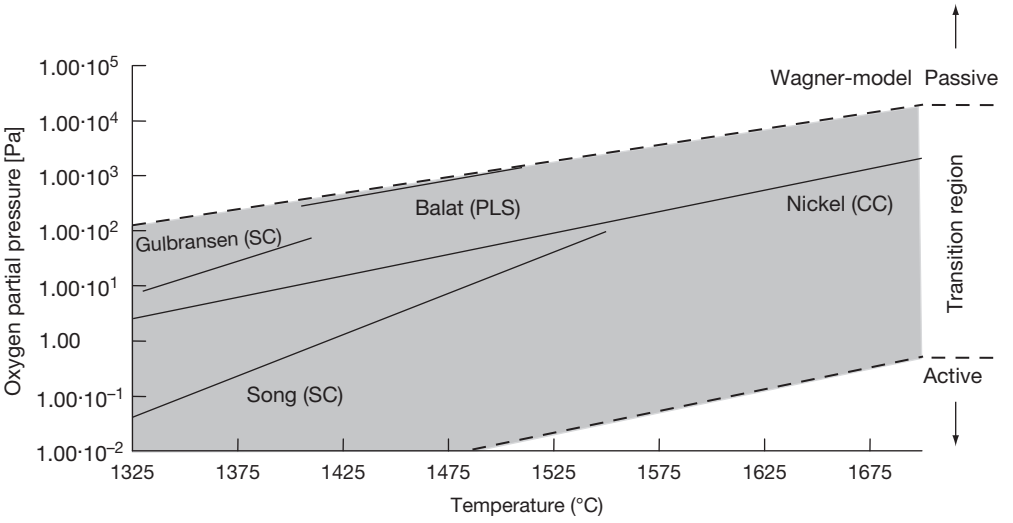

Figure 1 Active-to-passive transition of SiC thermal oxidation calculated (CC) from Wagner-type models and volatility diagrams and experimental values on single crystals (SC) and SSiC (PLS), see Presser and Nickel.[56]

a secondary active-to-passive transition was formulated, at which the formed silica spalled because of a CO interface pressure exceeding ambient pressures.

Oxygen pressures in **Figure 1** should not be confused with data from CO_x experiments, because CO is a reactive and an oxidizing gas species for SiC[41] despite a low oxygen partial pressure. Therefore, active oxidation in CO is only observed at very high temperatures.[55]

The silica formation in the passive regime at high temperatures is in detail a complex process, which includes several stages of amorphous silica formation and its crystallization. A review will be given elsewhere.[56] At temperatures below about 1200 °C a linear–parabolic model in the sense of Deal and Grove[10] is necessary to explain the oxidation data, whereas at higher temperatures a simple parabolic law is usually sufficient.

The process is still not well understood, because the rate constants are clearly dependent on the exposed crystallographic face of SiC,[57] and at the same time it is believed that it depends on the diffusion of oxygen through silica, because the kinetics are parabolic and activation energies fit this process.[58] However, at temperatures above about 1300 °C, there are data sets indicating a high activation energy, compatible with network oxygen diffusion in amorphous silica rather than molecular diffusion. It has been argued that this is related to extrinsic impurities from the experimental setups.[59]

In a plot compiling rate constants from a large number of data for fairly pure SiC (CVD, single crystals), including differing crystallographic faces, the situation is not so straight-forward,[56] but a fairly high spread of parabolic rates is evident (**Figure 2**).

Commercial qualities of sintered SiC often have low impurity or additive contents and have rates as low as pure materials, indicating extremely good oxidation resistance up to very high temperatures. This is certainly not really true for T above 1600 °C, because at very high temperatures the long-time kinetics are not adequately described by the parabolic law, the problem of active II oxidation is important and in addition bubble-and-pit formation, which is usually attributed to additives containing boron and/or aluminum, is likely to endanger applications (**Figure 3**). It should also be noted that bubble-and-pit formation can occur after an 'incubation period' of several 100 h at $T > 1600$ °C, while oxidation studies run usually only for times <100 h. Therefore long-time studies may be necessary for a true qualification of SiC at extremely high temperatures.

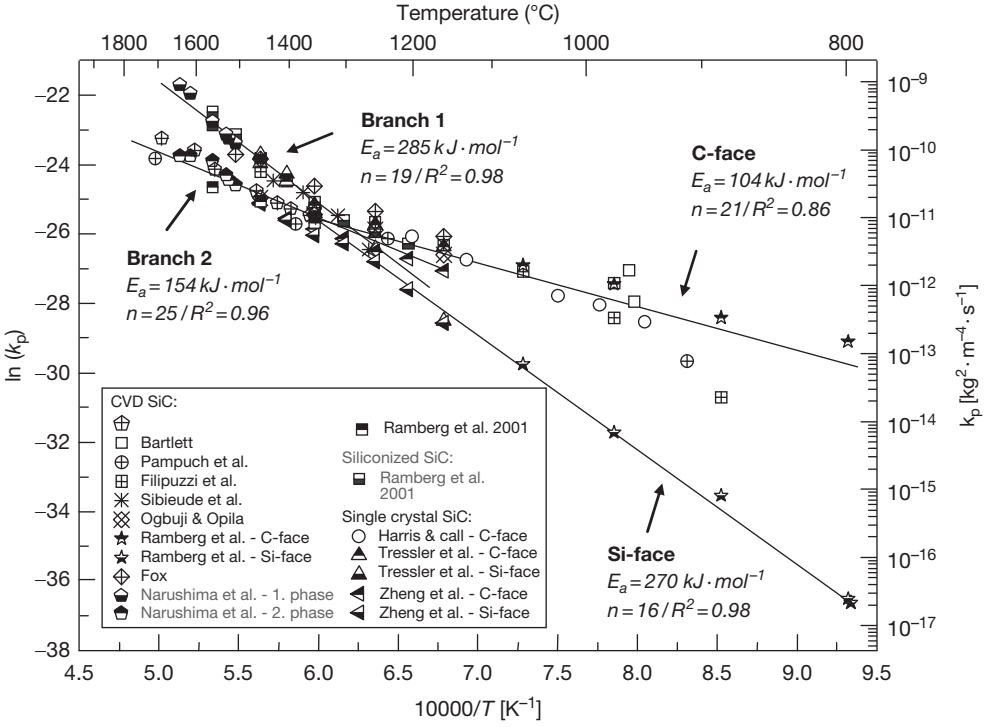

Figure 2 Comparative plot of parabolic rate constants. The plot comes from Presser and Nickel[56] where the data sources are referenced.

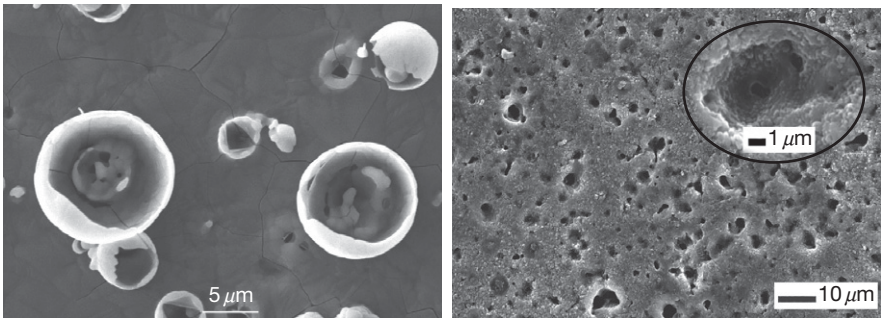

Figure 3 Bubbles at the surface of SSiC oxidized at 1500 °C for 24 h under humid conditions and pits beneath (1500°C, 50 h) revealed by HF-etching of oxidized SSiC from Ref. 100.

Furthermore, good resistance to oxidation by O_2 or air does not guarantee equally good behavior in complex industrial environments. Other components of the atmosphere or extrinsic impurities can change the behavior markedly and make a prediction difficult in cases of strong variations in temperature and gas composition, even though resistance of SiC-based materials to other aggressive environments, e.g., such as SO_2 or H_2S, has been reported.[14]

For such environments, case studies give an indication but are not unambiguous.[14] SSiC was reported to resist flue gases of aluminum-remelting furnaces up to 1000 h without much change in strength in one study but had problems in others. The strength of SSiC was unchanged in nitrogen-based gases of the system N_2–H_2–CO, but decreased up to 50% in endothermic gases at 1200–1300 °C in long-time experiments.

Water enhances the oxidation of SiC only slightly, but the transport of extrinsic impurities because of water can strongly enhance oxidation and the limitations in applications with high gas flow rates because of vaporization of the silica scale inducing paralinear behavior are known.[60]

1.26.7 Nitrides

1.26.7.1 Silicon Nitride

Silicon nitrides are often discussed together with silicon carbides, because both materials are silica formers. For this reason, data collections and textbook sections are identical to those already cited for carbides.[13,14,39,40,42–44] For an additional, detailed study see Ref. 61. A typical difference from the silicon carbides is the much higher additive content of almost all commercial sintered silicon nitrides. Only liquid-phase sintered SiC types ('LP-SiC') have comparably high amounts.

Hydrothermal corrosion of silicon nitride starts at about 130 °C because of the high solubility of silica in water under high pressure. The reaction

$$Si_3N_4 + 6H_2O \Leftrightarrow 3SiO_2 + 4NH_3 \qquad [17]$$

does not passivate because the dissolution of NH_3 makes the solution caustic, which strongly enhances silica solubility. Therefore, reaction kinetics are linear and active corrosion prevails.

The hydrothermal corrosion of the grain boundary phase of Si_3N_4 ceramics can be very strong and pit formation was observed at 300 °C and 8.6 MPa.[62] From experiments on hot isostatically pressed silicon nitride (HIPSN), which were free of additives other than silica, we know that preferential hydrothermal leaching of silica as the grain boundary phase can cause grain dislodgment.[63]

A compilation of data for the reactions of Si_3N_4 with metals and alloys has been given in Ref. 64. The interaction is important for bonding to metals; often silicides or other ternary compounds are formed. The interaction of the related SiAlONs (silicon nitrides, which incorporate alumina and yttria in their lattice) and alloys was found to be similar. In inert gas atmosphere or under vacuum, Si_3N_4 reacts readily with most transition elements below 1000 °C and with many other metals at various temperatures, while protection by silica in oxidizing conditions is effective for some conditions.[64]

Hot corrosion of Si_3N_4 attacks the silica scale and the behavior is therefore similar to that of SiC, as confirmed by studies at NASA labs.[48,65] However, the initial process may be governed by intrinsic factors, because surface tension differences between sulfate and silicate melts result in a fractal pattern of hillocks of silicate melt beneath the sulfate. This was reported to enhance local corrosion and induce pit formation. The process slows down with time and

therefore Si_3N_4-based ceramics can serve well under hot corrosion conditions. Even though there is a degradation in mechanical properties similar to that of SiC,[21,66] the remaining strength after hot corrosion of the nitride is higher than that of SiC.

Active corrosion of Si_3N_4 ceramics by hot gases is often stronger than comparable attack on SiC, because the grain boundary phase removal causes grain dislodgment and inhomogeneous internal corrosion. In particular, halogens create high partial pressures of Si-bearing species and accordingly strong active corrosion, but small amounts of oxygen or water can significantly decrease the effect of Cl_2 or sulfidizing environments by silica formation. The active-to-passive transition occurs at similar conditions as the one for SiC (**Figure 1**).

From thermodynamic considerations[67] the passive oxidation of pure Si_3N_4 should involve a two-step oxidation

$$2Si_3N_4 + 1\tfrac{1}{2}O_2 \Leftrightarrow 3Si_2N_2O + N_2 \quad [18]$$

$$Si_2N_2O + 1\tfrac{1}{2}O_2 \Leftrightarrow 2SiO_2 + N_2 \quad [19]$$

forming a duplex layer in an oxygen potential gradient. A definitive proof for a sublayer of Si_2N_2O was only provided for pure nitrides,[68] but a superior oxidation resistance for pure Si_3N_4 compared with that for SiC at temperatures of about 1500 °C is evident and contrasts with the behavior of sintered Si_3N_4. This is plain from **Figure 4**, which shows calculated critical times t_c for 100 μm penetration on pure and sintered nitride and carbides, assuming parabolic growth and using the data compiled earlier.[13]

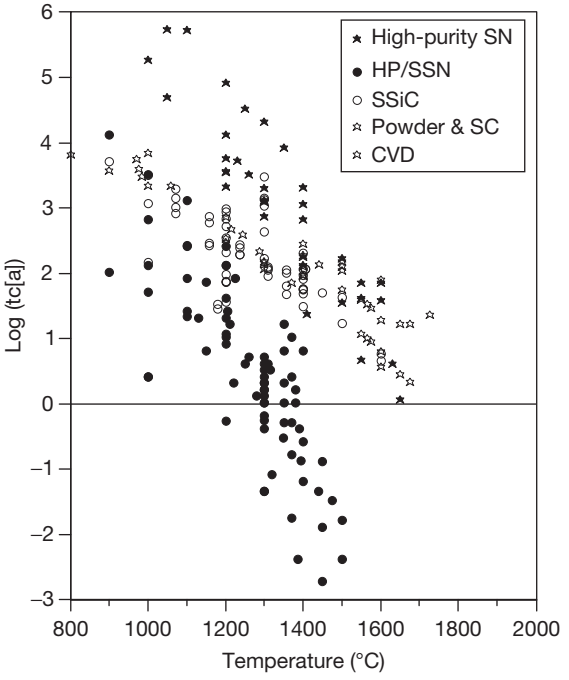

Figure 4 Logarithm of calculated critical times in years for 100 μm penetration for silicon nitrides (full symbols) and silicon carbides (open symbols) vs. temperature from compiled parabolic rate constants.[13]

The presence of grain boundary phases is the main reason for the pronounced decrease in oxidation resistance. In detail, a number of processes, including the leaching of grain boundary constituents to the scale, crystallization, internal oxidation, bubble formation, and scale cracking, occur and vary with amount and exact composition of the additives. The discussion of such processes is referenced in the textbooks cited at the beginning of this chapter.

Again, it must be noted that the data in **Figure 4** should serve as an indication only, because the values were calculated assuming a truly simple parabolic behavior, which is often not really fulfilled.

1.26.7.2 Boron Nitride

In hydrothermal conditions, BN is attacked at temperatures as low as 150 °C, following linear kinetics.[69] Hexagonal BN is often applied in the production of the metal and for thermocouples in Fe alloy melts, which is ample evidence for a good corrosion resistance against metal melts and slags at much higher temperatures, namely alkali halides, lithium borate, and cryolite. This is due to the poor wetting behavior of such melts on BN.

Only molten alkali carbonates and hydroxides decompose boron nitride by the reactions of the type

$$BN + K_2CO_3 \Leftrightarrow KBO_2 + KOCN \quad [20]$$

The product of the oxidation of boron nitride at atmospheric and low pressures is boric acid

$$4BN + 3O_2 \Leftrightarrow 2B_2O_3 + 2N_2 \quad [21]$$

and therefore the material has a similarity to boron carbide. The melting point of boric acid at 410–450 °C keeps the formed oxide liquid at high temperatures. Accordingly, at temperatures exceeding 700 °C, there is paralinear oxidation with the loss of boria by evaporation.[70] Water enhances the evaporation process, because the partial pressure of hydrogen-bearing species is high[71] and the oxidation can be described as

$$BN + 3H_2O \Leftrightarrow H_3BO_3 + NH_3 \quad [22]$$

1.26.7.3 Silico-Carbonitrides

The precursor-derived amorphous silico-carbonitrides have high thermal stabilities, a boron-containing type reportedly up to 2000 °C.[72]

Crystallization may induce detrimental reactions as was shown for pure carbontirides at ≈1400–1500 °C.[73] Their nominal stoichiometry has C in addition to Si_3N_4 and SiC and therefore the reaction

$$Si_3N_4 + 3C \Leftrightarrow 3SiC + 2N_2 \qquad [23]$$

takes place at about the thermodynamically predicted temperature (≈1405 °C at 1 bar N_2). Oxidized samples without such a reaction[74] were observed to survive because of an internal pressure buildup of several bars.

As suggested earlier,[75] carbonitrides are susceptible to hot corrosion because the excess carbon will tend to make a melt basic. In terms of oxidation resistance, the data[76–78] suggest that they have very low oxidation rates at temperatures up to 1600 °C. The problem of bubble formation seems to be avoidable by Al incorporation in the ceramic. However, the penetration rates are probably not much better than those for pure silicon nitrides, and the problem of paralinear behavior in fast-flowing gases is valid for these materials as well.

1.26.8 Titanium Compounds

TiC and TiN show a very wide range of stoichiometry and form solid solutions in the Ti–C–N system. Thermodynamic equilibria in water–carbide systems[79] indicated that carbon, corresponding oxides, CH_4, CO_2, CO, and H_2 are the main products of hydrothermal corrosion of metal carbides in the temperature range 300–1000 °C. No protective oxide layers were formed upon hydrothermal corrosion of carbides of transition metals, but Raman spectra from hydrothermally treated TiC powders demonstrated the presence of graphite.

Oxidation of TiN powders, films, and sintered bodies[80,81] showed that oxidation occurs at very low temperatures and becomes significant at about 500 °C, with the formation of TiO_2. Scales from titania are usually not protective at temperatures above 800 °C, which limits the use of monolithic titanium compounds at high temperature.

TiB_2 forms titania and boria and is known primarily for coatings and composites. Oxidation of TiB_2 is significant above 700 °C and shows parabolic kinetics at those temperatures.[82] In powder experiments, an onset of oxidation was found at 400 °C and $TiBO_3$ was an oxidation product at low temperatures.[83] At 950 °C, the evaporation of B_2O_3 becomes significant and paralinear oxidation occurs. However, unlike for boron carbide and nitride, the kinetics become parabolic again at higher temperatures (>1200 °C). This is explained by the fact that, when B_2O_3 is completely evaporated, the process is controlled by diffusion through the titanium dioxide film.

Impurities and metal binders were found to improve the oxidation resistance of TiB_2, because the rutile scale sinters and becomes dense.[84]

The use of TiB_2 as a component of composites and their oxidation and corrosion behaviors are the subject of a large number of papers. The behavior can be fairly complex because other phases such as aluminum borates become stable and influence the behavior.

1.26.9 Ultrahigh Temperature Ceramics

With the realization of the limits of silica-forming ceramics in fast-flowing wet atmospheres, the search for so-called 'ultrahigh temperature ceramics' was started. The classes looked at were either the polymer-derived ceramics[85,86] or those forming very refractory oxides, particularly ZrO_2 or HfO_2. However, the precursor-derived ceramics are silica formers, and therefore at least at temperatures above 1650 °C the problems of silica are inherent. The zirconia and hafnia formers have the problem of fast ionic oxygen transport and thus materials such as ZrB_2 or HfB_2 oxidize extremely fast[87] and are only candidates for very short-lived applications.

Together with the fact of decreasing mechanical properties for all metallic materials at very high temperatures, the only current vision is the development of composites, which are protected from oxidation by some sort of coating. Therefore, environmental barrier systems are a subject of current investigation. The old dream of a carbon-based system with its high temperature properties protected by coatings is still alive and investigated repeatedly with new approaches and systems. It must still be regarded as one of the most promising ways to maintain a strong system at very high temperatures!

1.26.10 Refractories

Formed and unformed refractory products have a wide process engineering spectrum of applicability and therefore satisfy various demands and reciprocal actions. The following text will present the corrosion of refractory materials with typical examples of the iron and steel industries. The effecting part-mechanisms can be compared with other industrial sectors and can be divided as follows.

1.26.10.1 Chemical Dissolution

The driving force is the existing thermochemical nonequilibrium between the two involved phases (liquid steel/slag/atmosphere – refractory lining) of a system. The thermodynamic stability of a phase (refractory material) is described by the free enthalpy of formation ΔG and is heavily affected by the variables of temperature, pressure, and concentration. Besides the dissolution itself, reduction and oxidation processes as well as vaporization and evaporation play essential roles.

1.26.10.2 Erosion

The driving force is the flow of melts by gas flushing, vacuum treatment, tapping, and filling the metallurgical reactor respectively, and continuous casting and gases charged with solids. During the first process, a mostly predamaged structure is washed out. During the latter, the damage is affected by solid particles impacting onto the refractory lining because of their inertia, and which break off the material because of surface disruption.

1.26.10.3 Mechanical Wear

Thermal shocks and steep temperature gradients (e.g., during heating up, change of temperature when filling a ladle, etc.) cause thermal stresses and sometimes structure changes. Furthermore, the handling in steel plants (e.g., filling a converter with scrap, the cleaning process with skull breakout and removal of slag, the filling and transport of a ladle, etc.) cause wear by mechanical contacts.

These three mechanisms are superimposed and accelerated by infiltration, i.e., weakening the structure of the refractory materials by the 'inner' dissolution of the matrix. In practice, chemical dissolution, erosion, mechanical wear, and infiltration appear together with varying degrees of importance.

1.26.11 Chemical Dissolution

1.26.11.1 Diffusion/Blast Furnace

In a shaft-shaped, double conic built blast furnace, iron ore is constantly reduced to pig iron by carbon and carbon monoxide, respectively. The liquid iron drips into the hearth of the blast furnace, gathers on the ground, and is tapped periodically and in a batch wise manner into transport ladles. The fluid slag in the hearth floating on top of the pig iron fixes the impurities contained in the ore and is extracted continuously.

The hearth, which is water cooled via its outer wall, is lined with carbon and graphite containing bricks. The furnace lifetime is typically 10 years or more with a wall thickness of up to 2 m. In addition to high heat conductivity, another advantage of this lining is the nonwettability of the graphite by slag. No infiltration takes place.

Furthermore, the iron melt approaching from above is saturated with carbon, which strongly decreases attack of the lining. The saturation with carbon is also due to the presence of a bed of coke in the hearth, which is highly porous and filled with slag and pig iron. In addition elements such as Si and Mn accompanying the pig iron decrease the saturation concentration of carbon.[88]

Any iron melt not saturated in carbon causes a linear dissolution rate for a unidirectional water-cooled carbon plate described by the equation:

$$\frac{\Delta x}{\Delta t} = \beta \frac{\rho_{Fe}}{\rho_C} \cdot \frac{C_S - C_0}{100} \quad (\mathrm{cm\,s^{-1}}) \qquad [24]$$

where β is the mass transfer coefficient ($\mathrm{cm\,s^{-1}}$); ρ_{Fe}, the density of liquid iron ($6.67\,\mathrm{g\,cm^{-3}}$), ρ_C, the density of carbon/graphite ($2.25\,\mathrm{g\,cm^{-3}}$); C_S, the saturation concentration of carbon in liquid iron (1500 °C: 5.16 wt %); C_0 is the concentration of carbon in liquid iron.

The mass transfer coefficient β is given by

$$\beta = \frac{D_C}{\delta} = \left(\frac{4 D_C v}{\pi h_l}\right)^{1/2} \left(\frac{D_C}{\upsilon}\right)^{1/6} \quad (\mathrm{cm\,s^{-1}}) \qquad [25]$$

where D_C is the diffusion coefficient of carbon in liquid iron ($10^{-4}\,\mathrm{cm^2\,s^{-1}}$); δ, the boundary layer of diffusion (cm); v, the flow velocity of the melt ($\mathrm{cm \cdot s^{-1}}$); h_l, the diameter of the convection loop (assumption: 1 cm); υ is the kinematic viscosity of liquid iron ($10^{-3}\,\mathrm{cm^2\,s^{-1}}$).

A laminar flow is predominant (free convection, $Re \leq 2100$) because of low temperature differences at

the phase interface ($\Delta T < 1$ K). The speed of the convection loop moving at the phase interface can be estimated by using the Reynolds number *Re*:

$$v \leq \frac{Re \cdot \upsilon}{h_l} \quad (\mathrm{cm\,s^{-1}}) \qquad [26]$$

Using the above values, the flow velocity is $u \leq 21\ \mathrm{cm\,s^{-1}}$. Inserting this upper limit in eqn. [25], a mass transfer coefficient β of $0.035\ \mathrm{cm\,s^{-1}}$ is obtained. For a temperature of 1500 °C, the carbon concentration in the liquid iron will be 5.15 wt %.[89] Then, eqn. [24] yields the linear dissolution rate:

$$\frac{\Delta x}{\Delta t} = 0.035 \frac{6.67}{2.25} \frac{5.16 - 5.15}{100} = 10^{-5}\ \mathrm{cm\,s^{-1}}\ \text{or}\ 0.04\ \mathrm{cm\,h^{-1}} \qquad [27]$$

At such a rate, the lining in the hearth of the blast furnace would be fully worn out within a few hours of operation. However, because of the above-described mechanisms, the presence of a coke bed and the decrease in the carbon saturation by the additional elements present in the pig iron, a long service life of up to 2 years is achievable.

1.26.11.2 Marangoni Convection/SEN

Preferential wear along the three-phase steel/slag/refractory material interface, such as at a submerged entry nozzle (SEN) used in a mould or in a ladle, can be explained by the temperature and particularly by the concentration-dependent interface phenomenon of Marangoni convection (**Figure 5**). The refractory material reacts with the steel and the slag. If it contains carbon, it dissolves in the steel which is constrained by the oxide in the refractory material. In turn, the dissolution of the oxide in the refractory material into the slag is constrained by the graphite. Nonetheless, ~0.1 wt % of carbon dissolves into the slag. Because of this reaction, a local concentration gradient develops at the steel/slag interface. For carbon-containing refractory material, there is a slightly increased carbon concentration in the region close to the three-phase interface, which makes the interfacial tension σ_{II} (**Figure 5**) higher than σ_I. A part of the carbon dissolved in the slag reacts with the steel, thereby forming carbon monoxide (CO) and this causes a locally decreased oxygen content at point II. The corresponding increase in the interfacial tension decreases the capillary activity of the slag and the steel tends to convect from point I to point II in order to decrease the interfacial tension there.

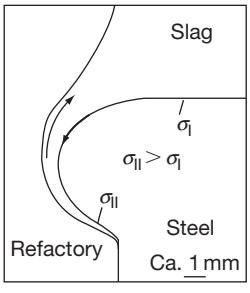

Figure 5 Advanced wear by Marangoni convection.

In a lot of cases, no infiltration occurs, because the corrosion progress is faster than the speed of infiltration. To estimate the extent of corrosive wear, one may use the approximation of eqn. [24]. The mass transfer coefficient β is estimated well by eqn. [25]. The flow velocity of the steel and slag along the phase interface is then[90]:

$$v_M = -\frac{h_g}{4\eta_S}\left(\frac{d\sigma}{dC}\mathrm{grad}\ C + \frac{d\sigma}{dT}\mathrm{grad}\ T\right) \quad (\mathrm{cm\,s^{-1}}) \qquad [28]$$

where h_g is the characteristic length of the corrosion groove (assumption: 1 cm) and η_S is the dynamic viscosity of steel (1600 °C: $0.04\ \mathrm{g\,cm^{-1}\,s^{-1}}$).

In this equation, the change in the interfacial energy of the steel/slag interface in relation to the oxygen content in the liquid steel is estimated as

$$\frac{d\sigma}{dC} = -\frac{200}{C^I_{[O]}}\ [\mathrm{mN\,m^{-1}\ wt\%^{-1}}] \qquad [29]$$

the approximated concentration gradient of the oxygen along the phase interface is

$$\mathrm{grad}\ C = \frac{C^I_{[O]} - C^{II}_{[O]}}{h_g} = 0.001\ \mathrm{wt\%\ cm^{-1}} \qquad [30]$$

the change in the interfacial energy in relation to the temperature is[91]

$$\frac{d\sigma}{dT} = \sigma_T = -0.2\ \mathrm{mN\,m^{-1}K^{-1}} \qquad [31]$$

and the approximated temperature gradient because of the heat removal to the refractory material is

$$\mathrm{grad}\,T = \frac{T^I - T^{II}}{h} = 10\ \mathrm{K\,cm^{-1}} \qquad [32]$$

With an assumed oxygen content $C^I_{[O]} = 0.004$ wt % (40 ppm) in eqn. [19], the insertion of the values from eqns. [30]–[32] into eqn. [28] yields a flow velocity v_M of $325\ \mathrm{cm\,s^{-1}}$.

Assuming that the back-flow velocity along the refractory material/slag interface is about the same

as v_M, the thickness of Prandtl's flow-boundary-layer δ_{Pr} can be easily calculated:

$$\delta_{BL} = \left(\frac{\eta_{Sl} \cdot h}{\rho_{Sl} \cdot u_M}\right)^{1/2} \quad (cm) \qquad [33]$$

where η_{Sl} is the dynamic viscosity of the slag ($2\,g\,cm^{-1}\,s^{-1}$, $0.2\,Pa\,s^{-1}$) and ρ_{Sl} is the density of the slag ($2.7\,g\,cm^{-3}$).

The thickness of the Nernst's diffusion-boundary-layer δ_N is then

$$\delta_N = \left(\frac{\eta_{Sl}}{\rho_{Sl} D_{Sl}}\right)^{-1/3} \delta_{Pr} \quad (cm) \qquad [34]$$

where D_{Sl} is the diffusion coefficient of the corrosion determining component (1650 °C: $1 \times 10^{-7}\,cm^2\,s^{-1}$)

With these material values, we get $\delta_{Pr} = 1.51 \times 10^{-2}$ cm and $\delta_N i = 1.67 \times 10^{-4}$ cm. Accordingly, the mass transfer coefficient β is calculated by

$$\beta = \frac{D_{Sl}}{\delta_N} \quad (cm\,s^{-1}) \qquad [35]$$

The result is $\beta = 6 \times 10^{-4}$ cm s. Assuming a slag whose starting content of Al_2O_3 is ~13 wt %, and whose saturation concentration at 1650 °C is in the range of 60 wt % $A1_2O_3$, the wear of a corundum-enriched, graphite-containing refractory material ($\rho_R = 3.3\,g\,cm^{-3}$) due to Marangoni convection approximately amounts to

$$v_{corr} = 360 \times 6 \times 10^{-4} \frac{2.7}{3.3}(60 - 12) = 8.5\,mm\,h^{-1} \qquad [36]$$

which is in accordance with laboratory experiments. The question is how to decrease this extremely severe corrosion. The process cannot be influenced easily. In the case of the continuous casting process, the concentration gradient and the temperature gradient are nearly fixed. The temperature and concentration dependency of the interfacial energy are natural values, and the same applies for the dynamic viscosity of the steel. Therefore, the only way left is to use a refractory material that is as chemically inert as possible.

This is, for instance, achieved by the implementation of a sleeve made of ZrO_2 at the three-phase interface of a SEN. According to eqn. [24], the slag and the mould powder, respectively, can be enriched with Al_2O_3 up to a certain amount, in order to maintain the difference in the saturation concentration as small as possible.

1.26.11.3 Oxidation/Ladle

The crude steel coming from the melting aggregates (converter or electric arc furnace) is partially already post-treated during tapping into the ladle and then again within the ladle. This treatment, which is referred to as secondary metallurgy, includes the process steps[92] of degassing, decarburization, desulphurization, dephosphorization as well as removal of trace elements, fine adjustment of alloying contents, deoxidization, inclusion transformation, improvement in the purity levels as well as the solidifying structure, adjustment and homogenization of temperature and chemical composition.

To minimize the thermal stresses and the corresponding wear because of the actual temperature gradient when filling with crude steel (T up to 1800 °C), the cold ladle lined with MgO–C bricks is preheated for 2 hours in the steel mill. A newly lined ladle does not have a slag layer protecting the bricks against oxidation of the binding carbon (graphite, 5–15 wt %). As an instantaneous result of this preheating procedure, the graphite oxidizes. The carbon bonding and its advantageous properties such as the good thermal shock resistance and the nonwettability by slag are lost. At the same time, an enormous pore volume (about 35 vol %) is opened. Steel and slag can easily infiltrate into the microstructure and therewith lead to 'inner' dissolution.

The temporal progress of the reaction

$$2C + O_2 \rightarrow 2CO \qquad [37]$$

in a MgO–C brick can be described by the following differential equation:

$$\frac{dx_i}{dt} = -2 V_C D_P \frac{n_0 - n_i}{x_0 - x_i} \qquad [38]$$

The sharp transition from the bright, decarburized outer zone to the black core suggests a topochemical reaction which is controlled by diffusion ($\sqrt{t}$-law). The determining factor is the pore-diffusion coefficient D_P[93]

$$D_P = D_{O_2} \gamma p_c \quad (cm^2\,h^{-1}) \qquad [39]$$

with

$$D_{O_2} = 2.7 \times 10^{-2}\, T^{1.79} \quad (cm^2\,h^{-1}) \qquad [40]$$

and

$$\gamma = 1.84 \times \sqrt{p_c} - 0.3 \qquad [41]$$

where D_{O2} is the diffusion coefficient of oxygen; T, the temperature (≈1373 K); γ, the labyrinth factor; and p_c is the open porosity of the decarburized zone (≈0.35).

The insertion of these values results in $D_P = 3081\ \mathrm{cm^2\,h^{-1}}$. The solution of the differential equation [38] for an infinite plate is given by[14]

$$(1-\phi)^2 = \tau \qquad [42]$$

with

$$\phi = \frac{x_i}{x_0}\,(x_i = x_0 \text{ at } t = 0) \qquad [43]$$

where x_i is the position of the reaction front in the plate (cm) and x_0 is the total thickness of the plate (cm).

$$\tau = \frac{t}{t_0} \qquad [44]$$

where t is the time (h) and t_0 is the time for total decarburization of a plate with x_0 (h) and

$$t_0 = \frac{x_0^2}{2zV_C D_P (n_0 - n_i)}\ \text{(h)} \qquad [45]$$

where V_C is the mole volume of graphite ($5\ \mathrm{cm^3\,mol^{-1}}$), z, the geometry factor (infinite plate: $z = 2$); n_0, the oxygen content at the plate surface (20 vol %; $2 \times 10^{-6}\ \mathrm{mol\,cm^{-3}}$); and n_i is the oxygen content at the reaction front ($n_i \ll n_0$, $n_i \to 0$).

A MgO–C brick with $x_0 = 10$ cm would be totally decarburized within $t_0 = 1014$ h. The time t required to decarburize 1 cm ($x_i = 9$ cm) of the brick results as follows:

$$\tau = \left(1 - \frac{9}{10}\right)^2 = 0.01 \qquad [46]$$

with $t = \tau\ t_0 = 0.01 \times 1014\ \mathrm{h} = 10.14\ \mathrm{h}$

Numerous experiments demonstrated that the process is in fact controlled by diffusion and is extensively blocked by specific additives, such as >10 wt % ZrB_2. However, the addition of 3 wt % metallic aluminum as an antioxidant has hardly any effect, since the porosity of the decarburized refractory material is high, and during the coke reaction at $T \geq 800\,^\circ\mathrm{C}$, the metallic aluminum is consumed by the formation of Al_3C_4, and above 1200 °C by spinel formation.

1.26.12 Erosion

1.26.12.1 Blast Wear/Pipes

Pneumatic conveying systems and pipes in thermotechnical aggregates are subject to severe wear because of erosion. The reason for this is the segregation of a solid loaded gas flow because of the mass inertia of its solid particles. These particles impact mostly in areas of flow redirection (elbow) onto the refractory lining, whereby a cyclic mechanical stress occurs at permanently changing surface areas. For brittle materials, such as refractories, these alternating local impacts and corresponding multiaxial tensile and compression loads finally cause material removal by surface disruption. It should be noted that the resulting wear is always a system characteristic and is influenced by numerous factors.

At room temperature, the testing of refractory materials with respect to their wear by perpendicular impacting solid particles is performed according to ASTM C 704. For this purpose, 1000 g of SiC particles of predefined granularity are accelerated by a pressurized air flow within 450 ± 15 s and shot over a distance of 203 mm perpendicular onto a surface of a test sample. The resulting wear volume (in $\mathrm{cm^3}$) is determined by weighing the geometrically well-defined sample.

However, the results thus achieved can hardly be transferred to the temperatures applied in operation. That is why a special experimental setup was developed, which is as far as possible in accordance with ASTM C 704 and whereby the wear by impacting particles can be determined at temperatures of up to 1400 °C. The main item of this experimental setup is a ring burner by which the pressurized air flow, the blasting abrasive (SiC particles), and the test sample are heated to the relevant test temperature. It has been shown that the wear volume of heterogenic refractory materials decreases with an increase in temperature, which correlates quite well with the change in thermomechanical properties.

While brittle–elastic deformation behavior occurs at room temperature, viscoplastic deformation behavior is dominant at high temperatures, where molten phases from the binder phase are present. The local stress peaks, which are generated by the impacting SiC particles, are decreased by plastic deformation and by stress relaxation of the binder phase, respectively. In this context, particularly wear-resistant grains (SiC, corundum) incorporated inside the microstructure show no wear-reducing action.[94] Moreover, these grains break upon impact of a SiC particle because of their poor ductility.

1.26.12.2 Flowing Melts/Converter

During filling of a torpedo ladle or a converter with pig iron, or of a ladle with crude steel, the melt often 'falls' at about 2 m. Because of the high flow speed, the lining in the collision area of the melt

stream, which is possibly predamaged by chemical dissolution, thermal shock stress, or infiltration, is washed out. However, a quantitative prognosis is not possible. The same applies for the circulation current generated during gas stirring treatment within a converter or in a ladle. In connection with the high flow velocities of the melt, cavitation erosion might play a significant role, but this has not been examined further in the field of steel production.

1.26.13 Mechanical Wear

1.26.13.1 Thermal Shock Resistance/Ladle

In practice, mechanical wear as an instantaneous result of a poor thermal shock resistance is commonly found. During the filling of a ladle with crude steel, the lining is heated up rapidly from 1000 to 1800 °C within a few minutes. High tensile stresses develop in the surface, which frequently results in a single incipient crack, which can grow catastrophically. Offbursts occur in the surface region of the lining, which is also referred to as 'spalling.' This mechanism is promoted by a modified structure of surface areas containing slag infiltrations.

An assessment of various refractory materials concerning their thermal shock resistance can be performed by the quick quenching of a 950 °C test sample by blowing pressurized air (DIN EN V 993-11) onto its surface, or by dipping the test sample into water (DIN 51068-1). Then tensile stresses occur, starting from the surface, which result in a large amount of incipient cracking. Usually, a catastrophic break does not occur.

No isothermal boundary conditions can be found in these cases and therefore a theoretical treatment becomes difficult. Modeling of 'quasistationary' crack propagation is possible, but during rapid heating up of a ladle lining, unstable crack propagation occurs. Therefore, characterization of the thermal shock resistance of refractory materials uses the resistance parameter R during unstable crack propagation and R_{st} during stationary crack propagation[95]:

$$R''''' = \frac{G_F E}{\sigma_c^2} \approx L \ (\text{mm}) \qquad [47]$$

$$R_{st} = \sqrt{\frac{G_F}{\alpha^2 E}} \quad (\text{m}^{1/2}\,\text{K}) \qquad [48]$$

where G_F is the crack energy (J m^{-2}); E, the modulus of elasticity (GPa); σ_c, the critical stress (MPa); α, the thermal expansion coefficient (K^{-1}); and L is the characteristic length (mm).

Both equations were derived from nonlinear fracture mechanics, which is necessary when dealing with refractory materials, since they have a very heterogeneous structure (grains, binder phase, pores). Together, both crack resistance parameters describe the so-called structure flexibility. From eqns. [47] and [48], it is plain that an increase in the required crack energy and the crack propagation work G_F with both unstable as well as 'quasistationary' crack propagation is advantageous in order to reach a high value for the respective resistance parameter and, therefore, to achieve a high thermal shock resistance.

This can be obtained in structures with coarse grains in a fine-grained matrix, where entanglement of the grains increases the crack length. The modulus of elasticity, however, has the opposite effect, which is dependent on the mechanism of the crack propagation alone. With unstable crack propagation, the crack itself and the incipient crack arising must be as big as possible to reach the area of the 'quasistationary' crack propagation without reaching the catastrophic breakpoint. In the area of the stationary crack propagation, the modulus of elasticity should be as small as possible, which calls for an optimization of the structure concerning both crack propagation mechanisms. A crack then gradually propagates with every higher and more critical temperature difference.

In spite of great experimental endeavor, no definite connection between the resistance parameters and the standard tests for judging the thermal shock resistance has been found.[96] At the moment, values must be inserted into the aforementioned equations, which have been measured isothermally.

Critical heating rates may be calculated according to the example of a hot plate made out of sintered corundum (99% Al_2O_3) at 1000 °C:

$$\dot{T} = \frac{\varepsilon_c(1-2\mu)}{3\alpha}\frac{16a}{x^2} \quad (\text{K s}^{-1}) \qquad [49]$$

where ε_c is the critical elongation (0.001); μ, the Poisson ratio (0.21); α, the thermal expansion coefficient ($1 \times 10^{-5}\,\text{K}^{-1}$); a, the thermal diffusivity ($1 \times 10^{-6}\,\text{m}^2\,\text{s}^{-1}$); and x is the thickness of the plate (0.02 m).

Inserting the values results in $\dot{T} = 0.77\ \text{K s}^{-1}$. If the sample cools down/warms up faster, a breakage (crack) occurs.

1.26.13.2 Carbon Bursting/Blast Furnace

In industrial processes (chemical plants, blast furnace shaft) in the temperature range from 400 to 800 °C,

carbon bursting of refractory material in atmospheres containing CO is known. This phenomenon is due to the temperature dependence of the Boudouard equilibrium:

$$2CO \leftrightarrow CO_2 + C \qquad [50]$$

When crystalline graphite precipitates in refractory materials, it can create an enormous crystallization pressure, capable of bursting the structure. This precipitation is said to be catalytically promoted by metallic iron, hematite (Fe_2O_3), and magnetite (Fe_3O_4). In examination of the resistance to CO according to ASTM C 288, refractory materials are exposed to a pure CO atmosphere after a thermal pretreatment at 500 °C for 200 h.

A small amount of hydrogen (~3%) accelerates the carbon precipitation and thus we assume a catalytic effect of hydrogen. After the test, a visual evaluation of the refractory material leading to a classification concerning its resistance to CO is performed. The resulting crystallization pressure ($\pi - 1$) can be calculated using the following equation:

$$\pi - 1 = \frac{-\Delta G^0 - RT \ln K_C}{\Delta V_C \frac{R}{R*}} \qquad [51]$$

where ΔG^0 is the free enthalpy in the standard state (J/mol); R, the universal gas constant (8.314 J mol^{-1} K^{-1}); R^*, the gas constant (84.8 atm cm^3 mol^{-1} K^{-1}); T, the temperature (K); K_C, the equilibrium constant; and ΔV_C is the mole volume of graphite (5 cm^3 mol^{-1}).

At 500 °C (773 K), magnetite is reduced to metallic iron, if the volumetric contents of CO and CO_2 are equal; the formation of graphite results for the earlier stated reaction [50] with

$$K = \frac{P_{CO_2}}{P_{CO}^2} = 2 \quad \text{with } a_C = 1 \qquad [52]$$

$$\Delta G^0 = 169452 - 172.6T,$$
$$\Delta G^0(773K) = -35522 \text{ Jmol}^{-1} \qquad [53]$$

Inserting all values in eqn. [51] results in a crystallization pressure of 63 375.3 atm, corresponding to 62 150 bars, thereby destroying the structure of the refractory material.

1.26.13.3 Destruction due to Impact/ Converter

In the converter, crude steel is produced by blowing oxygen onto and/or into the molten pig iron. In this process, the dissolved carbon is oxidized to a certain amount. Iron and those elements accompanying the pig iron such as P, Si, and Mn are oxidized and form a slag. Temperatures of above 2000 °C are reached by strong exothermal reactions. It is, therefore, preferable that a large part of the crude steel charge is replaced by scrap steel, whose melting offers a cooling effect for the melt.

The lining of an emptied converter is ~1200 °C at the hot bottom and is therefore under both thermal and mechanical stresses upon refilling with scrap steel.

To estimate the procedures during charging, the transmitted mechanical energy of a falling scrap piece mgh onto an impact area A is equated with the required crack energy AnG_F for a number of n cracks. The prevailing impact area and the number of produced cracks are unknown, since the position of the scrap piece at the moment of impact is incidental and the shock wave spreads into the floor. It is assumed that a scrap piece falling from a height $h = 4$ m with a mass $m = 100$ kg influences a surface area $A = 0.1$ m^2. The measured crack energy of the MgO–C material at 1200 °C is $G_F = 500$ J m^{-2}. The number of emerging cracks is

$$n = \frac{mgh}{AG_F} = \frac{100 \times 9.81 \times 4}{0.1 \times 500} \approx 80 \qquad [54]$$

and accordingly MgO–C material may break out of the surface. In the following refining process, temperatures of above 1800 °C develop, so there is also a good chance that cracks will heal again. To improve the structural flexibility of such stressed components, metallic aluminum powder and steel needles are added to the MgO–C material.[97]

1.26.14 Infiltration by Steel and Slag

1.26.14.1 Basic Equations

The contact of a pure oxide and a graphite-containing refractory material with liquid steel or slag in a thermodynamic equilibrium is described by wetting theory. The vectors of the surface tensions of the three involved phases acting at the point of contact of all three phases are in a mechanical equilibrium state:

$$\sigma_R - \sigma_S \cos\theta - \sigma_{R/S} = 0 \qquad [55]$$

where σ_R is the surface tension of the refractory material (mN m^{-1}); σ_S, the surface tension of the

steel or slag ($mN\,m^{-1}$); $\sigma_{R/S}$, the interfacial tension between refractory material/steel or refractory material/slag ($mN\,m^{-1}$); and θ is the wetting angle (°).

The interactions of the three phases involved are characterized by the wetting angle of contact:

$$\cos\theta = \frac{\sigma_R - \sigma_{R/S}}{\sigma_S} \qquad [56]$$

and

$\theta > 90$, if $\sigma_R - \sigma_{R/S} < 0$ (non-wettability)
$\theta = 90$, if $\sigma_R - \sigma_{R/S} = 0$
$\theta < 90$, if $\sigma_R - \sigma_{R/S} > 0$ (wettability)

The wetting angle of contact θ and the surface tension σ_s are the decisive values for the infiltration of a capillary or pore by steel or slag, which can be determined experimentally. The equilibrium of forces in a partly filled pore is then:

$$\rho_S g h = -\frac{4\sigma_S \cos\theta}{d} \qquad [57]$$

where ρ_S is the density steel/slag ($kg\,m^{-3}$); g, the acceleration of gravity ($m\,s^{-2}$); h, the height of steel-/slag-column above the pore entry (m); d is the pore diameter (m).

If the wetting angle of contact θ is smaller than 90°, capillary ascension is present. For instance, a liquid slag penetrates the pore or capillary system of an oxidic refractory material without the effect of any external force. In the case of liquid steel and oxide refractory material, capillary depression is present, since the wetting angle of contact is $\theta > 90°$. Thus, an external (ferrostatic) pressure is necessary to allow the liquid steel to penetrate into the pore or capillary system. The same is true for a slag that does not wet the graphite binder phase of the oxide refractory material.

The infiltration speed of the slag or steel into the structure results from the Hagen–Poiseuille equation[98]:

$$\frac{dl}{dt} = \frac{d^2}{32\eta l}\left(\frac{4\sigma_S \cos\theta}{d} + \rho g h\right) \qquad [58]$$

Integration leads to the penetration depth l, in relation to the time t:

$$l = \sqrt{\left(\frac{d\sigma_S \cos\theta}{4\eta_S} + \frac{d^2 \rho_S g h}{16\eta_S}\right) t} \qquad [59]$$

where l is the penetration depth (m); η_S, the dynamic viscosity of steel/slag (Pa s); and t is the time (s).

1.26.15 Examples

1.26.15.1 Slag/MgO

A MgO brick in contact with a slag with a minimal surface energy at 1600 °C ($\sigma_S = 0.51\,N\,m^{-1}$, $\eta_S = 1$ Pa s) will show a penetration depth of 1 cm within a pore $d = 50\,\mu m$ according to eqn. [59] after an interaction period of 10 min. The dependence on the wetting angle disregarding a slag-column above the pore entry is outlined in Table 1. Note that this estimation is obtained with simplifications, namely that there is neither chemical interaction between the slag and the refractory material nor a temperature gradient within the inner structure.

1.26.15.2 Steel/MgO

Liquid steel (1600 °C: $\sigma_S = 1.5\,N\,m^{-1}$, $\eta_S = 6.8 \times 10^{-3}$ Pa s, $\rho_S = 7.700\,kg\,m^{-3}$) and a MgO brick show completely different infiltration because of the wetting angle of $\theta = 120°$. According to eqn. [57], steel can only penetrate into open pores, if their diameter is sufficiently large. For this, Table 2 gives the infiltration

Table 1 Penetration depth of a slag in relation to the wetting angle of contact ($d = 50\,\mu m$ and $t = 600$ s)

(°)	l (cm)
0	1.96
10	1.94
20	1.90
30	1.82
40	1.71
50	1.57
60	1.38
70	1.14
80	0.81
89	0.26
90	0

Table 2 Infiltratable pore diameter d and penetration depth l in relation to the steel pool depth h

h (m)	d (m)	l (m). d = 200 m
0.25	172	0.73
0.50	86	2.10
0.75	57	2.80
1.00	43	3.48
1.25	34	4.00
1.50	29	4.46
1.75	25	4.87
2.00	22	5.25
2.25	19	5.61
2.50	17	5.94
2.75	16	6.26
3.00	14	6.56

pore diameter d in relation to the depth of the steel pool, h (ferrostatic pressure). As we can see, the greater the depth, the higher the risk of infiltration of smaller pores.

Considering a depth, h, the penetration depth of the steel into a pore having a diameter of $d = 200\,\mu m$ after 10 min is calculated according to eqn. [59]. The penetration depth increases with a growing pool depth h and amounts to a about 2 m (see **Table 2**).

1.26.15.3 Steel/MgO–C

The graphitic binder phase of MgO–C bricks is resistant to slag because graphite is not wetted and only minimally dissolved. In contact with liquid steel, the situation is different. For example, carbon is soluble in iron at a temperature of 1600 °C, up to 5.41 wt %. Therefore MgO–C should not be useful in practice and the question arises: 'Why can MgO–C be used?'

1. From the Vatcher–Hamilton equilibrium between dissolved oxygen in iron and carbon[88]:

$$\underline{C} + \underline{O} \rightarrow \{CO\} \qquad [60]$$

At 1600 °C the partial pressure P_{CO} is

$$\underline{C} \cdot \underline{O} = 0.0024 P_{CO} \qquad [61]$$

If a steel melt with a dissolved oxygen content of 30 ppm tries to enter into a pore and therefore comes into contact with the graphitic binder phase, the carbon activity a_C at this specific point is, thus, 1. Inserted into eqn. [45]

$$P_{CO} = \frac{1 \times 0.003}{0.0024} = 1.25 \text{ bar} \qquad [62]$$

At the contact point, therefore, CO gas is produced, which separates the reaction partners from each other and retards the dissolution and the infiltration kinetically.

2. If steel would enter into the pore despite the CO cushion, the solubility of the carbon would be strongly decreased. The partial pressure P_{CO} inside the structure is only 0.05 bar. From eqn. [61], we have $\underline{C} = 0.04$ wt % for the dissolved carbon, which can be supported by experimental data.[99]

3. Furthermore, the formation of a MgO protective layer may take place because of the carbothermal reaction inside the structure:

$$MgO + C \rightarrow \{Mg\} + \{CO\} \qquad [63]$$

Gaseous magnesium dissolves in the steel and reacts with the oxygen also dissolved in the steel in order to form secondary MgO that precipitates at the interface (heterogeneous nucleation) and, thus, restrains further infiltration into the structure.

4. The carbon solubility in liquid iron is also affected by higher aluminum levels and the reaction thereof with oxygen. If the MgO–C material contains, for instance, metallic aluminum as an antioxidant, this metallic aluminum melts on contact with the steel and dissolves into the steel, infiltrating the open pores. During this process, an oxidation reaction according to the following equation occurs:

$$2\underline{Al} + 3\underline{O} \rightarrow Al_2O_3 \quad \text{with} \quad \Delta G^0 = -460 \text{ kJ mol}^{-1} \qquad [64]$$

The equilibrium constant K of this reaction at 1600 °C is

$$K = \frac{\underline{Al}^2 \cdot \underline{O}^3}{1} = e^{-\Delta G^0/RT} = 3 \times 10^{-13} \qquad [65]$$

In general, the steel penetrating the pores contains 0.1 wt % of dissolved aluminum. The content of dissolved oxygen then in the equilibrium state is, according to eqn. [65], ~3 ppm. As a consequence, the oxygen potential is decreased so that the bumping effect of the CO gas and the formation of a MgO protective layer are suspended. The infiltration and dissolution of the graphitic binder material are promoted. Accordingly, the content of carbon dissolved in the infiltrate, from eqn. [61], is

$$\underline{C} = \frac{0.0024 \times 0.05}{0.0003} = 0.4 \text{ wt\%} \qquad [66]$$

which is much less than 5.4%.

In summary, infiltration influences the corrosion profoundly. It may have beneficial effects, if the reaction with the refractory material leads to a surface compaction (formation of an MgO protective layer) or to stiffening of the infiltrate (slag), but it also can have detrimental effects, if chipping (spalling) occurs.

1.26.16 Concluding Remarks

As can be seen from this chapter about ceramics and refractories, the subject is fairly complex, because often the interplay of physical boundary conditions and chemical interaction is governing corrosion processes. Furthermore, the microstructure of the materials, particularly when it comes to refractories, is likewise adding complexity, because several phases interact simultaneously and the ubiquitous porosity is

also causing problems in investigating the processes. Thus, despite its industrial importance there are a lot of things to be learned and certainly there are good possibilities to improve the corrosion resistance.

We are sure that the progress, which was made in the investigations of the technical ceramics and is described in the first parts of this chapter, will help both to extend the use of those materials in high temperature processes and to find economic viable solutions for the refractory world. Doing so could become a key issue in helping us to work more efficiently and less harmfully for our environment in many processes. The efforts to protect our climate could have a significant input from the work on corrosion resistant ceramics and refractories.

References

1. Kingery, W. D.; Bowen, H. K.; Uhlmann, D. R. *Introduction to Ceramics*, 2nd ed.; John Wiley: New York, 1976; 1038.
2. Barsoum, M. W. *Fundamentals of Ceramics*; Drexel University: Philadelphia, 2002; 600.
3. Richerson, D. W. *Modern Ceramic Engineering*, 3rd ed.; CRC Press, 2006; 707.
4. Carter, C. B.; Norton, M. G. *Ceramic Materials Science and Engineering*; Springer: Berlin, 2007; 740.
5. Carniglia, S. C.; Barna, G. L. *Handbook of Industrial Refractories Technology – Principles, Types, Properties and Applications* William Andrew Publishing: Noyes, USA, 1992.
6. Schacht, C. *Refractories Handbook*; CRC, 2004; 520.
7. Goursat, A. G.; Smeltzer, W. W. Oxidation of iron *Rev. High-Temp. Mater.* **1973**, *1*(4), 351–395.
8. Nesbitt, J. A. *Oxid. Metals* **1995**, *44*(1/2), 309–338.
9. Irene, E. A. *CRC Crit. Rev. Solid State Mater. Sci.* **1988**, *14*(2), 175–223.
10. Deal, B. E.; Grove, A. S. *J. Appl. Phys.* **1965**, *36*(12), 3770–3778.
11. Nickel, K. G. *J. Eur. Ceram. Soc.* **1992**, *9*, 3–8.
12. Reisman, A.; Nicollian, E. H.; Williams, C. K.; Merz, C. J. *J. Electron. Mater.* **1987**, *16*(1), 45–55.
13. Nickel, K. G.; Gogotsi, Y. G. In Handbook of Ceramic Hard Materials; Riedel, R., Ed.; VCH-Wiley: Weinheim, 2000; Vol. 1; pp 140–182.
14. Nickel, K. G. *Corrosion of Advanced Ceramics – Measurement and Modelling*; Kluwer Academic Publisher: Dordrecht, NL, 1994; Vol. 267; 467.
15. Nickel, K. G. *J. Eur. Ceram. Soc.* **2005**, *25*(10), 1699–1704.
16. Ogbuji, L. U. J. T. *J. Electrochem. Soc.* **1998**, *145*(8), 2876–2882.
17. Jacobson, N. S.; Fox, D. S.; Smialek, J. L.; Opila, E. J.; Tottorelli, P. F.; More, K. L.; Nickel, K. G.; Hirata, T.; Yoshida, M.; Yuri, I. In *Ceramic Gas Turbine Component Development and Characterisation*; Van Roode, M., Ferber, M. K., Richerson, D. W., Eds.; ASME Press: New York, 2003; pp 607–640.
18. Opila, E. J.; Hann, R. E., Jr. *J. Am. Ceram. Soc.* **1997**, *80*(1), 197–205.
19. Tedmon, C. S. J. *J. Electrochem. Soc.* **1966**, *142*(3), 925–930.
20. Opila, E. J. *J. Am. Ceram. Soc.* **2003**, *86*(8), 1238–1248.
21. Baxter, D. J. In *Corrosion of Advanced Ceramics – Measurement and Modelling*; Nickel, K. G., Ed.; Kluwer Academic Publishers: Dordrecht, NL, 1994; Vol. NATO ASI E 267; pp 249–260.
22. Opila, E. J. *J. Am. Ceram. Soc.* **1994**, *77*(3), 730–736.
23. Maier, N.; Nickel, K. G. *Key Eng. Mater.* **2006**, 326–328, 1780–1783.
24. Opila, E. *J. Am. Ceram. Soc.* **1995**, *78*(4), 1107–1110.
25. Maeda, M.; Nakamura, K.; Tsuge, A. *J. Mater. Sci. Lett.* **1989**, *8*, 195–197.
26. Tai, W.-P.; Watanabe, T.; Jacobson, N. *J. Am. Ceram. Soc.* **1999**, *82*(1), 245–248.
27. Mah, T.; Keller, K. A.; Sambasivan, S.; Kerans, R. J. *J. Am. Ceram. Soc.* **1997**, *80*(4), 874–878.
28. Federer, J. I. In *Corrosion and Corrosive Degradation of Ceramics*; Tressler, R. E., McNallan, M., Eds.; Martinus Nijhoff: Boston, MA, 1990; pp 425–443.
29. Jacobson, N.; Myers, D.; Opila, E.; Copland, E. *J. Phys. Chem. Solids* **2005**, *66*(2–4), 471–478.
30. Readey, D. W. *J. Eur. Ceram. Soc.* **1998**, *18*, 2383–2387.
31. Sarpoolaky, H.; Zhang, S.; Lee, W. E. *J. Eur. Ceram. Soc.* **2003**, *23*, 293–300.
32. Oda, K.; Yoshio, T. *J. Am. Ceram. Soc.* **1997**, *80*(12), 3233–3236.
33. Hirata, T.; Ota, S.; Morimoto, T. *J. Eur. Ceram. Soc.* **2003**, *23*, 91–97.
34. Hannink, R. H. J.; Kelly, P. M.; Muddle, B. C. *J. Am. Ceram. Soc.* **2000**, *83*(3), 461–487.
35. Herrmann, M.; Schilm, J.; Michael, G.; Seipel, B.; Nickel, K. G. *J. Eur. Ceram. Soc.* **2005**, *25*(10), 1805–1812.
36. Li, Y. Q. *Mater. Sci. Eng. A* **2007**, *444*, 184–191.
37. Steinbruck, M.; Veshchunov, M. S.; Boldyrev, A. V.; Shestak, V. E. *Nucl. Eng. Des.* **2007**, *237*(2), 161–181.
38. Gogotsi, Y. G.; Yaroshenko, V. P.; Porz, F. *J. Mater. Sci. Lett.* **1992**, *11*, 308–310.
39. Gogotsi, Y. G.; Lavrenko, V. A. *Corrosion of High-Performance Ceramics*; Springer Verlag: Berlin, F.R.G., 1992; 181.
40. Morell, R. *Handbook of Properties of Technical & Engineering Ceramics* HMSO Books: London, 1987.
41. Haase, V. In *Gmelins Handbuch der Anorganischen Chemie*; Schröder, F., Ed.; Springer: Berlin, 1986; Vol. B3; pp 325–395.
42. Nickel, K. G.; Quirmbach, P. In *Technische Keramische Werkstoffe*; Kriegesmann, J., Ed.; Deutscher Wirtschaftsdienst: Köln 1991; pp 1–76.
43. Tressler, R. E.; McNallan, M. *Corrosion and Corrosive Degradation of Ceramics* American Ceramic Society: Westerville, OH, 1990. Vol. 10; 493.
44. Blachere, J. R.; Pettit, F. S. *High Temperature Corrosion of Ceramics*. Noyes Data Corporation: Park Ridge, NJ, 1989; 188.
45. Gogotsi, Y. G.; Yoshimura, M. *J. Mater. Sci. Lett.* **1994**, *13*, 395–399.
46. Gogotsi, Y. G.; In-Deok, J.; McNallan, M. J. *J. Mater. Chem.* **1997**, *7*(9), 1841–1848.
47. Jacobson, N. S.; Smialek, J. L.; Fox, D. S. In *Handbook of Ceramics and Composites*; Cheremisinoff, N. P., Ed.; Marcel Dekker: New York, 1990; pp 99–136.
48. Jacobson, N. S. *J. Am. Ceram. Soc.* **1993**, *76*(1), 3–28.
49. Jacobson, N. S.; Smialek, J. L.; Fox, D. S. In *Corrosion of Advanced Ceramics – Measurement and Modelling*; Nickel, K. G., Ed.; Kluwer Academic Publishers: Dordrecht, 1994; Vol. NATO ASI Series E 267; pp 205–222.
50. Jacobson, N. S. *J. Am. Ceram. Soc.* **1985**, *68*(8), 432–439.

51. Berthold, C.; Nickel, K. G. *J. Eur. Ceram. Soc.* **1998**, *5*, 2365–2372.
52. Nickel, K. G.; Berthold, C. In *High Temperature Corrosion and Materials Chemistry*; McNallan, M. J., Opila, E. J., Maruyama, T., Narita, T., Eds.; Electrochemical Society: Pennington, NJ, 2000; Vol. PV 99–38; pp 429–438.
53. Ip, S. Y.; McNallan, M. J.; Park, D. S. *J. Am. Ceram. Soc.* **1992**, *75*(7), 1942–1948.
54. Schneider, G. A.; Nickel, K. G.; Petzow, G. In *Physics and Chemistry of Carbides, Nitrides and Borides, NATO ASI Series E: 185*; Freer, R., Ed.; Kluwer Academic: Dordrecht, NL, 1990; pp 387–401.
55. Narushima, T.; Goto, T.; Yokoyama, Y.; Iguchi, Y. *J. Am. Ceram. Soc.* **1993**, *76*(10), 2521–2524.
56. Presser, V.; Nickel, K. G. *CRC Crit. Rev. Solid State Mater. Sci.* **2008**, *33*(1), 1–99.
57. Costello, J. A.; Tressler, R. E. *J. Am. Ceram. Soc.* **1986**, *69*(9), 674–681.
58. Ogbuji, L. U. J. T.; Opila, E. J. *J. Electrochem. Soc.* **1995**, *142*(3), 925–930.
59. Ramberg, C. E.; Worrell, W. L. *J. Am. Ceram. Soc.* **2001**, *84*, 2607–2716.
60. Opila, E. J. *J. Am. Ceram. Soc.* **1999**, *82*(3), 625–636.
61. Sangster, R. C.; Kämpf, P.; Nohl, U. *Silicon Suppl. B 5d2;* Springer-Verlag: Berlin, 1995; Vol. 15; 304.
62. Yoshio, T.; Oda, K. In *Corrosion and Corrosive Degradation of Ceramics*; Tressler, R. E., McNallan, M., Eds.; American Ceramic Society, 1990; pp 367, 386.
63. Oda, K.; Yoshio, T.; Miyamoto, Y.; Koizumi, M. *J. Am. Ceram. Soc.* **1993**, *76*(5), 1365–1368.
64. Sangster, R. C.; Bär, G. In *Gmelin Handbook of Inorganic and Organometallic Chemistry*; Schröder, F., Ed.; 8th ed.; Springer-Verlag: Berlin, 1995; Vol. Suppl. B 5d1; p 255.
65. Fox, D. S.; Smialek, J. L. *J. Am. Ceram. Soc.* **1990**, *73*(2), 303–311.
66. Fox, D. S.; Jacobson, N. S.; Smialek, J. L. In *Corrosion and Corrosive Degradation of Ceramics*; Tressler, R. E., McNallan, M., Eds.; Martinus Nijhoff: Boston, MA, 1990; pp 227–249.
67. Singhal, S. C. *Ceramurgia Int.* **1976**, *2*(3), 123–129.
68. Ogbuji, L.; Smialek, J. *J. Electrochem. Soc.* **1991**, *138* (10), 51–53.
69. Oda, K.; Yoshio, T. *J. Ceram. Soc. Jpn.* **1993**, *101*(8), 855–859.
70. Jacobson, N.; Farmer, S.; Moore, A.; Sayir, H. *J. Am. Ceram. Soc.* **1999**, *82*(2), 393–398.
71. Jacobson, N. S.; Eckel, A. J.; Misra, A. K.; Humphrey, D. L. *J. Am. Ceram. Soc.* **1990**, *73*(8), 2330–2332.
72. Riedel, R.; Kienzle, A.; Dreßler, W.; Ruwisch, L.; Bill, J.; Aldinger, F. *Nature* **1996**, *382*, 796–798.
73. Friess, M.; Bill, J.; Aldinger, F.; Szabo, D. V.; Riedel, R. *Key Eng. Mater.* **1994**, 89–9195–100..
74. Riedel, R.; Kleebe, H.-J.; Schönfelder, H.; Aldinger, F. *Nature* **1995**, *374*(6), 526–528.
75. Nickel, K. G. In *Precursor-Derived Ceramics*; Bill, J., Wakai, F., Aldinger, F., Eds.; VCH-Wiley: Weinheim, 1999.
76. Butchereit, E.; Nickel, K. G.; Müller, A. *J. Am. Ceram. Soc.* **2001**, *84*(10), 2184–2188.
77. Müller, A.; Gerstel, P.; Butchereit, E.; Nickel, K. G.; Aldinger, F. *J. Eur. Ceram. Soc.* **2004**, *24*, 3409–3417.
78. Wang, Y.; Fei, W.; An, L. *J. Am. Ceram. Soc.* **2006**, *89*(3), 1079–1082.
79. Jacobson, N. S.; Gogotsi, Y. G.; Yoshimura, M. *J. Mater. Chem.* **1995**, *5*(4), 595–601.
80. Gogotsi, Y. G.; Dransfield, G.; Porz, F. In *Microscopy of Oxidation*; Newcomb, S. B., Bennett, M. J., Eds.; The Institute of Materials: Cambridge, 1993; Vol. 2; pp 509.
81. Shimada, S.; Takada, Y.; Tsujino, J. *J. Eur. Ceram. Soc.* **2005**, *25*, 1765–1770.
82. Basu, B.; Raju, G. B.; Suri, A. K. *Int. Mater. Rev.* **2006**, *51* (6), 352–374.
83. Kulpa, A.; Troczynski, T. *J. Am. Ceram. Soc.* **1996**, *79*(2), 518–520.
84. Voitovich, V. B.; Lavrenko, V. A.; Adejev, V. M. *Oxid. Metals* **1994**, *42*(1), 145–161.
85. Raj, R.; Riedel, R.; Sorarù, G. D. *J. Am. Ceram. Soc.* **2001**, *84*(10), 2158–2159.
86. Wang, Z. C.; Gerstel, P.; Kaiser, G.; Bill, J.; Aldinger, F. *J. Am. Ceram. Soc.* **2005**, *88*(10), 2709–2712.
87. Nguyen, Q. N.; Opila, E. J.; Robinson, R. C. *J. Electrochem. Soc.* **2004**, *151*(10), B558–B562.
88. Czichos, H. *HÜTTE - Die Grundlagen der Ingenieurwissenschaften*, 29th ed.; Springer-Verlag: Berlin, 1991; 1417.
89. Markert, J. Gravimetrische und elektrochemische Untersuchung der Reaktion zwischen Kieselsäure und Korund in desoxidierten Eisenschmelzen. RWTH Aachen, Aachen, 1977.
90. Levich, V. G. *Physiochemical Hydrodynamics*; Prentice Hall: Englewood Cliffs, NJ, 1962; pp 373–390.
91. Turkdogan, E. T. *Physiochemical Properties of Molten Slags and Glasses*; Metals Society: London, 1983; pp 163–174.
92. Eisenhüttenleute, V. D. *Stahlfibel*; Verlag Stahleisen mbH: Düsseldorf, 1989.
93. von Bogdandy, L. *Die Reduktion der Eisenerze*; Verlag Stahleisen mbH: Düsseldorf, 1967.
94. Brüggmann, C.; Krause, O.; Pötschke, J.; Simmat, R. In *High Temperature Abrasion Resistance of Cement-Based Refractories* 48th International Colloquium on Refractories, Aachen; 2005, pp 35–39.
95. Harmuth, H.; Tschegg, E. K. *Veitsch-Radex Rundschau* **1994**, *1–2*, 465–480.
96. Alapin, B.; Ollig, M.; Pötschke, J. In *Thermomechanical Properties of Selected Refractory Materials up to 1500°C* 46th International Colloquium on Refractories, Aachen, D, 2003, pp 107–112.
97. Jansen, H. *Stahl und Eisen* **2005**, *125*(11), 43–49.
98. Lee, W. E.; Zhang, S. *Int. Mater. Rev.* **1999**, *44*(3), 77–104.
99. Ollig, M. Reaktionen kohlenstoffhaltiger MgO-Werkstoffe mit flüssigem Eisen. RWTH Aachen, Aachen, 2000.
100. Schumacher, C.; Nickel, K. G. *Ceram. Eng. Sci. Proc.*; **2000.**

1.24 High Temperature Corrosion of Alumina-forming Iron, Nickel and Cobalt-base Alloys

B. A. Pint
Materials Science and Technology Division, Oak Ridge National Laboratory, Oak Ridge, TN 37831-6156, USA

Abbreviations

COSIM Coating oxidation and substrate interdiffusion model
COSP Cyclic oxidation simulation program, NASA computer model
CTE Coefficient of thermal expansion
EPMA Electron probe microanalysis using wavelength dispersive spectroscopy
NASA National Air and Space Administration
ORNL Oak Ridge National Laboratory
PM Powder metallurgy
RE Reactive element
SIMS Secondary ion mass spectroscopy

Symbols

C_b Critical Al content of metal at breakaway oxidation, nominal or average
C_{bi} Critical Al content at breakaway oxidation at the metal-oxide interface
C_{min} Minimum initial Al content needed for alumina formation
C_o Initial Al content
d Specimen thickness
D_{Al} Self-diffusion coefficient of aluminum
D_O Self-diffusion coefficient of oxygen
E_{ox} Elastic modulus of oxide
M Metal: Fe, Ni or Co
p'_{O_2} Partial pressure of oxygen at the metal-oxide interface, Al/Al_2O_3 equilibrium
p''_{O_2} Partial pressure of oxygen at the oxide-gas interface
t_b Exposure time to breakaway oxidation
t_z Exposure time to zero mass gain
W^* Strain energy
W_{ad} Work of adhesion
$[X]$ Concentration of element X, atom percent
α Coefficient of thermal expansion
γ_{int} Surface energy of the metal-oxide interface
γ_{met} Surface energy of the metal substrate
γ_{ox} Surface energy of the oxide scale
ρ Alloy density
ν Poisson's ratio
ξ Scale thickness
ξ_f Critical scale thickness at scale spallation
$\Delta\alpha$ Change in coefficient of thermal expansion
ΔT Change in temperature

1.24.1 Introduction

This chapter will discuss the oxidation behavior of alumina-forming alloys, particularly MCrAl and M(Al) where M is Fe, Ni and to a lesser extent, Co. (Information on intermetallic aluminides, such as NiAl, TiAl, or Fe_3Al is included in **Chapter 1.25, High Temperature Corrosion of Intermetallic Alloys**) For the most part, these alloys owe their high temperature oxidation resistance to the formation of a dense, protective, external alumina scale; although some portion of the discussion will concern alloys that benefit from Al additions but do not exclusively form alumina scales. Compositions generally will be discussed in atomic percentage, with Al contents typically $\leq$22% in the binary alloys. However, in Table 1, commercial alloy compositions are given in weight or mass percentage, which is the common convention, while Table 2 provides compositions in atomic percentage. The oxidation behavior of alumina-forming alloys will be discussed in a general sense in Sections 1.24.2–1.24.5 for air or oxygen environments. Section 1.24.6 covers the behavior of these materials in different oxidants, for example, H_2O, S, C, or N. This discussion assumes some basic knowledge of the high temperature oxidation concepts that were discussed in **Chapter 1.10, Oxidation of Metals and Alloys**. The terminology is defined in the Glossary. It is almost impossible to discuss the oxidation behavior of alumina-forming alloys without discussing the reactive element (RE) effect.[1–11] Low levels (~0.1 at.%) of RE dopants have a dramatic effect on oxidation performance and most commercial alloys contain one or more additions. The examples given will rely heavily on the oxidation database of the Corrosion Science and Technology Group in the Materials Science and Technology Division at Oak Ridge National Laboratory (ORNL) in Oak Ridge, TN.[12]

1.24.1.1 Functionality of Alumina-Forming Alloys

In a general sense, applications for alumina-forming alloys are only for the highest temperatures (>900 °C) or most aggressive conditions. At lower temperatures, chromia-forming alloys, such as stainless steels, usually have sufficient high temperature oxidation resistance for most applications. In fact, Ni–Cr alloys are often discussed for applications as high as 1200 °C.[13] However, metal consumption rates for Fe- and Ni-based chromia forming alloys become significant at temperatures above 1000 °C.[14] These differences are not apparent at short intervals, but become more important after long intervals. Figure 1 shows the total mass gain and the spalled mass of alloy coupons after 15 kh at 1000 °C in laboratory air. (Total mass gain (i.e., specimen mass gain + spalled oxide) will be frequently used in this chapter as it is directly proportional to metal wastage and gives more information than just the specimen mass change which is typically lower than the total mass. Total mass is obtained by conducting the exposure in a preannealed alumina crucible.[15] The spalled mass can be larger than the total mass because the spalled mass includes the metal cations while the total mass reflects only O uptake.) One of the most

Table 1 Alloy chemical compositions (mass or wt%) determined by inductively coupled plasma analysis and combustion analysis (interstitials)

Material	*Fe*	*Ni*	*Al*	*Cr*	*Si*	*Ti*	*C*	*S*	*Other*
Commercial chromia-forming alloys									
800H	43.2	33.8	0.7	19.7	0.3	0.5	0.08	<3	0.2 Mo, 1 Mn
330RA	42.6	35.9	0.1	19.0	0.1[a]	0.1	0.06	<3	0.1 Mo, 1.5 Mn
45TM	23.7	47.8	0.1	27.4	0.2[a]	0.1	0.08	<3	0.04 Ce, 0.02 La
X	17.9	46.8	0.1	22.1	0.3	0.01	0.07	<3	9.5 Mo, 1.8 Co, 0.6 W, 0.7 Mn
617	0.6	53.5	1.1	22.4	0.2	0.3	0.06	<3	12.5 Co, 9.2 Mo
556	31.3	22.2	0.1	21.6	0.3	0.03	0.11	3	18.5 Co, 3 Mo, 1 W, 0.3 Ta, 0.03 La
353MA	36.6	35.7	0.02	25.1	0.2	0.01	0.06	<3	0.05 Ce, 0.02La, 0.01 Nd
625	3.3	63.8	0.2	23.1	0.2	0.2	0.02	<10	8.9 Mo, 0.2 Nb
230	1.5	63.4	0.3	22.6	0.4	0.01	0.10	9	12.3 W, 1.4 Mo, 0.5 Mn, 0.01 La
602CA	9.5	62.3	2.4	24.9	0.08	0.15	0.19	<10	0.1 Zr, 0.1 Y
ODS Ni–25Cr (lab.)	0.5	74.2	0.01	24.3	0.06	<	0.04	220	0.08 Y, 0.6 O
Commercial alumina-forming alloys									
214	3.5	75.9	4.3	16.0	0.08	0.01	0.05	3	0.02 Zr, 0.004 Y
693	4.8	62.1	3.1	28.6	0.05	0.4	0.03	<3	0.6 Nb, 0.2 Mn, 0.05 Zr
702	0.04	81.9	2.9	14.7	0.01	0.3	<	<1	0.04 Mg, 0.02 Zr
René N5	0.07	63.5	6.3	6.8	0.07	0.01	0.05	4	7 Co, 6 Ta, 5 W, 3 Re, 0.2 Hf, 0.005 Y
Nimonic 105	0.8	53.0	4.9	15.5	0.13	1.36	0.14	20	19 Co, 4.7 Mo, 0.12 Zr
MA956	74.2	0.08	4.5	20.0	0.07	0.4	0.01	25	0.4 Y (oxide)
MA956HT	71.2	0.05	5.6	21.9	0.06	0.4	0.04	44	0.4 Y (oxide)
PM2000	73.2	0.02	5.5	20.1	0.02	0.4	0.01	31	0.4 Y (oxide)
ODM751	75.8	0.02	5.0	16.1	0.04	0.56	0.01	57	1.5 Mo, 0.4 Y
APM	73.3		5.5	20.4	0.2	0.03	0.03	10	0.1 Zr
APMT	69.2	0.2	5.0	21.1	0.6	0.02	0.03	<10	2.8 Mo, 0.2 Hf, 0.25 Y, 0.1 Zr
Ohmalloy 30	82.8	0.6	2.6	12.6	0.3	0.3	0.02	<3	0.4 Mn, 0.012 Mg
Ohmalloy 40	81.7	0.5	3.6	12.7	0.2	0.3	0.02	<3	0.4 Mn, 0.012 Mg
SUH21	78.6	0.1	3.0	17.7	0.3	0.1	0.01	<3	0.1 Mn, 0.01 Ce
Aluchrom YHf	72.9	0.1	6.1	20.3	0.2	<	0.02	<10	0.2 Mn, 0.06 Y, 0.05 Zr, 0.03 Hf

[a]Higher value in product literature.
<Below the detectability limit of <0.01% or <0.001% for interstitials.

oxidation-resistant, commercial, chromia-forming alloys is the Ni-based, alloy 230, Table 1. Even after 15 kh at 1000 °C (although there were only scale spallation-inducing, thermal cycles every 500 h, see Section 1.24.4.4.6), the mass gain for alumina-forming alloys (e.g., 214, MA956, PM2000, see Table 1) is not significantly lower than that for alloy 230. However, the amount of spalled oxide for the alumina-forming alloys is typically much lower (Figure 1). This has significant implications for extrapolations of oxidation-limited lifetimes for real applications where 40 kh is often considered a short interval between equipment overhauls and fossil or nuclear energy plant life can be 300 kh.[16] Also, alloy 230 was one of the best commercial alloys tested in the study. A number of chromia-forming alloys, particularly those without a RE addition (e.g., 330RA and 800H, while 230 contains La, Table 1) showed significantly more metal wastage in the study and a few had to be stopped early because of the degree of attack.

Above 1000 °C, the benefit of alumina-forming alloys becomes much more evident. Instead of just comparing the mass change of various alloys, consider the example of designing a heat exchanger where the wall thickness will determine the lifetime of the component. Figure 2 shows the time to reach 20–40 mg cm^{-2} total mass gains as a function of specimen thickness for alloy 230 (Ni–Cr, Table 1) at 1100 °C in laboratory air (exposed with 100 h per cycle). These times are compared with the times to breakaway oxidation (t_b, see Section 1.24.5) for oxide dispersed FeCrAl alloy MA956. As will be discussed in Section 1.24.5, Ni-based alloys do not have such a definitive, binary-like, transition time and instead show an increase in the rates of mass gain and spallation. Thus, for a 2 mm thick alloy 230 specimen, almost 7 kh of exposure at 1100 °C was needed to reach 20 mg cm^{-2} of total mass gain but in less than 1000 h more exposure, the mass gain increased to 40 mg cm^{-2} (Figure 2). These times were not significantly different

Table 2 Alloy chemical compositions (at.%) determined by inductively coupled plasma analysis and combustion analysis (interstitials)

Material	*Fe*	*Ni*	*Al*	*Cr*	*Si*	*Ti*	*C*	*S*	*Other*
Commercial alumina-forming commercial alloys									
214	3.4	70.5	8.7	16.7	0.16	0.01	0.23	5	0.012 Zr, 0.003 Y
693	4.7	57.7	6.2	30.0	0.10	0.47	0.12	<4	0.4 Nb, 0.2 Mn, 0.03 Zr
702	0.04	77.7	6.1	15.7	0.02	0.38	<	<1	0.09 Mg, 0.012 Zr
René N5	0.1	64.9	13.9	7.8	0.15	0.01	0.25	7	7 Co, 2 Ta, 2 W, 1 Re, 0.05 Hf, 0.003 Y
Nimonic105	0.8	49.6	10.0	16.4	0.25	1.56	0.64	34	17.8 Co, 2.7 Mo, 0.07 Zr
MA956	69.4	0.07	8.8	20.1	0.13	0.40	0.06	41	0.24 Y
MA956HT	65.7	0.04	10.7	21.7	0.11	0.43	0.17	71	0.23 Y
PM2000	67.8	0.02	10.6	20.0	0.04	0.44	0.03	50	0.23 Y
APM	68.1		10.7	20.4	0.43	0.03	0.13	16	0.06 Zr
APMT	65.2	0.1	9.7	21.3	1.11	0.02	0.13	<10	1.6 Mo, 0.15 Y, 0.07 Hf, 0.06 Zr
Ohmalloy 30	79.6	0.5	5.2	13.0	0.50	0.38	0.077	<4	0.03 Mg, 0.4 Mn
Ohmalloy 40	77.8	0.5	7.1	12.9	0.42	0.38	0.095	<4	0.03 Mg, 0.4 Mn
SUH21	75.0	0.1	5.9	18.1	0.55	0.12	0.04	<4	0.1 Mn, <0.01 Ce
Aluchrom YHf	67.3	0.1	11.7	20.1	0.35	<	0.09	<10	0.2 Mn, 0.036 Y, 0.028 Zr, 0.008 Hf
Model alumina-forming alloys									
NiAl + Hf	<	51.6	48.3	<	<	<	0.034	<4	0.056 Hf
Ni_3Al + Hf	<	75.1	24.8	<	<	<	0.041	<4	0.057 Hf
Ni–22Al–5Pt + Hf	0.02	72.8	22.1	<	0.02	<	0.024	<10	5.0 Pt, 0.016 Hf
Ni–22Al–10Pt + Hf	0.02	68.1	21.7	0.01	<	<	0.012	<4	9.7 Pt, 0.39 Hf
NiCrAl + Hf	0.01	61.8	19.2	18.9	<	<	0.043	8	0.058 Hf
NiCrAl + Y	0.01	60.9	19.0	20.0	<	<	0.043	8	0.052 Y
NiCrAl + Y,Hf	0.01	61.4	18.9	19.5	0.02	<	0.042	5	0.046 Hf, 0.006 Y
NiCoCrAlY	0.02	40.4	23.5	17.4	<	<	0.042	8	0.147 Y
FeNiCrAl	56.5	18.7	5.1	15.0	0.29		0.39		2 Mn, 1.4 Mo, 0.6 Nb
FeCrAl	70.3	<	9.6	20.1	<	<	<	85	
FeCrAl–0.04Y	69.1	<	10.2	20.6	<	<	0.01	<10	0.041 Y
FeCrAl–0.08Y	69.8	<	9.9	20.2	<	<	<	16	0.082 Y
FeCrAl + Hf	70.1	<	10.0	19.8	<	<	0.044	41	0.053 Hf
FeCrAl + Mm	70.3	<	10.0	19.6	<	<	0.043	20	0.19 Ce, 0.007 Nd, 0.004 La, 0.006 Hf
FeCrAl + 0.04Hf,Y	70.1	0.01	9.8	20.1	<	<	0.037	16	0.035 Hf, 0.003 Y
FeCrAl + 0.02Hf,Y	69.6	0.01	10.1	20.3	<	<	0.010	16	0.018 Hf, 0.002 Y
FeCrAl + Al_2O_3	69.2	0.04	9.6	19.6	0.17	0.01	0.17	44	0.84 O
FeCrAl + Ho_2O_3	67.9	0.04	9.4	19.4	0.11	<	0.086	45	1.7 O, 0.9 N, 0.15 Ho
Fe–13Al + Hf	86.5	0.01	13.4	0.01	<	<	0.004	37	0.044 Hf
Fe–17Al + Hf	83.1	<	16.7	<	0.05	<	0.005	67	0.057 Hf
Fe–17Al + Y,Hf	82.8	<	17.1	<	0.02	<	0.009	8	0.023 Hf, 0.010 Y
Fe–17Al + Y,Ti	82.6	<	16.9	<	<	0.44	0.012	<	0.069 Y
Fe–17Al–10Cr + Y	72.5	<	17.4	10.0	0.05	<	0.014	<4	0.062 Y
Fe–18Al + Y	81.9	<	18.0	0.02	0.02	<	0.013	<15	0.057 Y
Fe–20Al + Hf	79.7	<	20.1	<	0.02	<	0.003	39	0.056 Hf
Fe–20Al + Y_2O_3	76.9	0.06	19.8	0.11	0.09	0.01	0.08	41	0.13 Y, 2.5 O, 0.4 N
Fe–40Al + Hf	60.5	<	39.5	<	<	<	0.007	21	0.047 Hf

<Below the detectability limit of <0.01% or <0.001% for interstitials.

for alloy 230 specimens that were <1 mm thick. In contrast, a drastic increase in the time to breakaway oxidation was observed for MA956 coupons in this exposure. The example of MA956 is given because a number of other alloys (typically with higher Al contents) have such high values for t_b that it is difficult to put them on the same plot with alloy 230.[14] It is easy to see that if one were designing a 1100 °C heat exchanger with a minimum lifetime service of 25 kh it would be extremely difficult to predict any wall thickness of alloy 230 that would be applicable but an extrapolation of the MA956 data would suggest a minimum wall thickness of ~3 mm. Oxidation-limited lifetime predictions are further discussed in **Section 1.24.5**.

The upper temperature limit for alumina-forming alloys is, of course, application dependent.

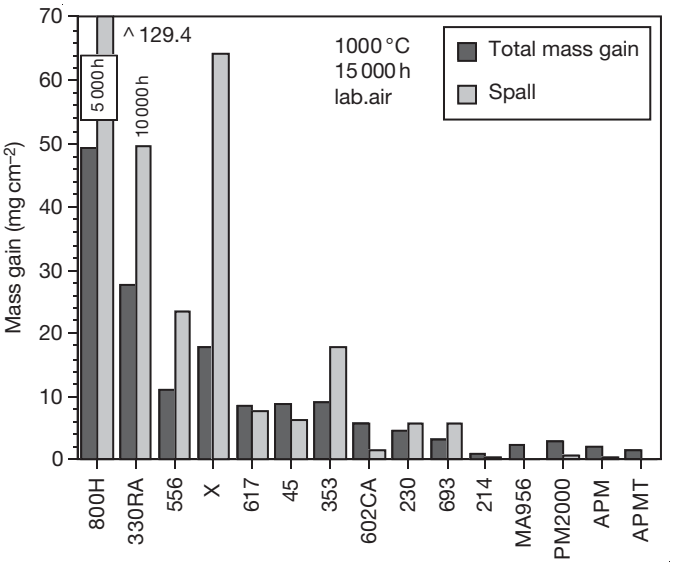

Figure 1 Bar graph of the total mass gain (specimen mass gain + spalled oxide) and spalled oxide mass per unit area for various commercial alloy specimens (compositions in **Table 1**) at 1000 °C in laboratory air after 30, 500 h cycles (15 kh total exposure). Data from Pint[12] and Pint and Keiser.[14]

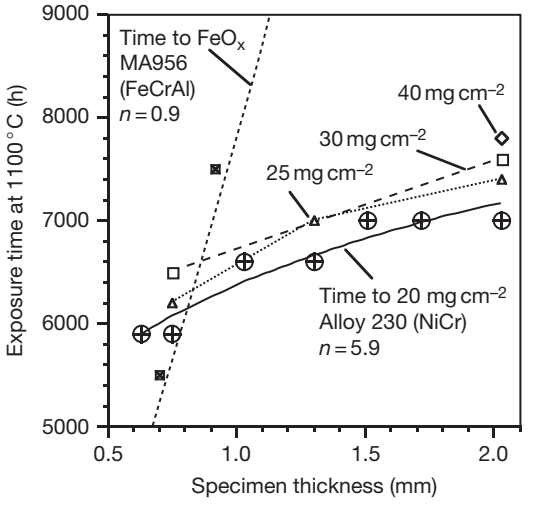

Figure 2 Time to accelerated attack as a function of specimen thickness for NiCr alloy 230 and alloy MA956 (see **Table 1** for compositions) for exposure in 100 h cycles at 1100 °C in laboratory air. For MA956, the time is for the onset of Fe-rich oxide formation and increases significantly with thickness. For NiCr, the times are to total mass gains of 20–40 mg cm^{-2} that do not change significantly with thickness. Values of n are given for eqn [5]. Data from Pint[12] and Pint and Keiser.[14]

However, the lifetime predictions made by NASA using modeling methods like Cyclic oxidation simulation program (COSP)[17] for β-NiAl and NiAl + Zr, usually with criteria of 250 μm metal consumption in <10 kh and 1 h thermal cycles, showed maximum temperatures of ~1250 °C for NiAl + Zr[18] which contains a substantially higher initial Al content (~50 at.%) than most alumina-forming alloys. Even with a longer cycle time between cooling to room temperature, the maximum temperature used to achieve respectable lifetimes will not be significantly higher. This is because scale spallation must also be considered. Specifically, the strain energy per unit volume (W^*) is defined[19] as

$$W^* = E_{ox}(\Delta T \Delta\alpha)^2(1-\nu) \quad [1]$$

(where E_{ox} is the elastic modulus of the oxide, ΔT is the temperature drop, $\Delta\alpha$ is the coefficient of thermal expansion (CTE) difference between metal and oxide, and ν is Poisson's ratio) in a thick alumina scale ($\xi > 10\,\mu m$) will exceed the work of adhesion (W_{ad}), that is, the work needed to form unit area of oxide and metal interfaces from unit area of interface of the metal–oxide interface[20]:

$$W_{ad} = \gamma_{ox} + \gamma_{met} - \gamma_{int} - \xi W^* \quad [2]$$

where the γ's are the surface energies of the oxide, metal and interface. This leads to spallation and the Al consumed to regrow the spalled oxide significantly increases the Al consumption rate, after spallation begins. For example, the time needed to form a 10 μm thick alumina scale is ~200 h at 1200 °C but ~10 kh at 1050 °C. Thus, the prime temperature range of interest for commercial applications of alumina-forming alloys is ~1050–1250 °C.

Because of the high temperatures involved, applications for alumina-forming alloys are often limited by their creep strength. For ferritic alumina-formers such as FeCrAl, some of the primary applications are as heating elements (e.g., Kanthal alloys) and in foil (30–70 μm) form as catalyst supports in automotive applications[21] as well as catalytic combustion to lower emissions from turbine engines.[22] Some of the less discussed applications are: (1) dissipative resistor banks, which are used to eliminate excess electricity for regenerative braking of diesel electric locomotives,[23] (2) reinforcement for molded refractory products, and (3) thermal protection shields.

Oxide dispersion strengthened (ODS) FeCrAl alloys have been the subject of considerable research and will be discussed throughout this chapter. The use of yttria dispersions increases the creep strength of these materials but the drawback is that the powder metallurgy (PM) processing[24] increases their cost significantly. These alloys have been investigated for a variety of high temperature applications including heat exchangers running at ~1100 °C.[25] **Figure 3** gives the creep rupture life for 125 μm thick PM2000 foil compared to 100 μm thick Ni-based alloys. The higher creep strength of this material allows a wider range of applications to be considered. However, manufacturers (e.g., Plansee and Special Metals) are discontinuing production because of the limited market. Less expensive dispersion strengthened alloys such as Kanthal alloys APM® and APMT® also have been developed and are more widely available. Because of their higher strength, dispersion strengthened alloys have better dimensional stability at high temperature and APMT is available in tube form. Because of its strength and oxidation resistance, APMT was selected as a heat shield material in the heat exchanger of a biomass gasifier.[14]

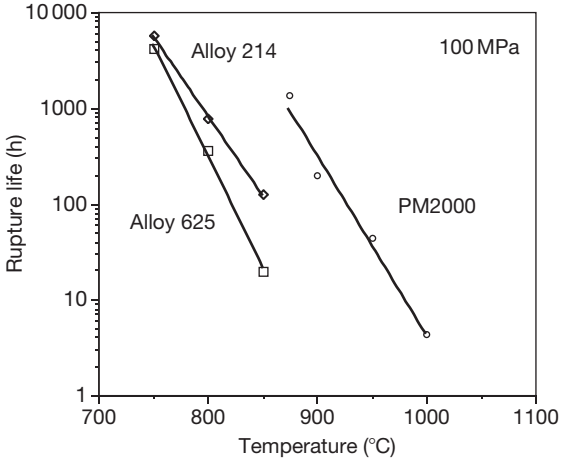

Figure 3 Creep rupture life at 100 MPa for 100 μm thick foil of Ni-base alloys 214 and 625 and for 125 μm thick alloy PM2000 foil (alloy compositions in **Table 1**). Adapted from Pint, B. A.; Swindeman, R. W.; More, K. L.; Tortorelli, P. F. Materials selection for high temperature (750–1000°C) metallic recuperators for improved efficiency microturbines, ASME Paper #2001-GT-445, Presented at the International Gas Turbine and Aeroengine Congress and Exhibition, New Orleans, LA, June 4–7, 2001.

Nickel-based alumina-forming alloys generally have better high temperature strength than wrought ferritic alloys and can be considered for a broader range of applications. Alloys such as 214 have similar oxidation resistance as FeCrAl alloys and are available in foil form, as in **Figure 3**. The second-generation of single crystal (SX) and dispersion strengthened Ni-based super alloys contain ~11–13 Al and have fairly good oxidation resistance, even without a coating.[16,27,28] To further improve their oxidation resistance, Ni-based superalloys are often coated with a higher Al content NiAl or NiCoCrAl composition (dealt elsewhere in **Chapter 1.27, High Temperature Coatings: Protection and Breakdown**). When sufficient Al is added to an alloy for alumina scale formation, other properties such as strength, phase stability, and weldability may be adversely affected Nevertheless, cast NiCrAlY alloys have been developed for steam reforming applications where the formation of a chemically inert alumina scale has an additional benefit of reducing surface coke formation.[29]

Cobalt-based alumina-forming alloys are also primarily used as coatings, especially for hot corrosion (see **Section 1.24.6.2**) or high temperature wear resistance applications. The addition of Co in MCrAlY coatings is known to change the phase composition and mechanical behavior.[30,31] Minimal research has been reported on Co-based alumina-forming alloys in the last 20 years and their application seems somewhat specialized and limited at present.

1.24.1.2 Other Applications for Thermally-Grown Alumina Layers

One of the more interesting aspects of alumina-forming alloys is the usage of the alumina layer in other applications besides for oxidation resistance. After forming a dense-adherent alumina layer at high temperature, this layer could be used at lower temperatures where further alumina formation would be limited. Some of the properties of interest are electrical (insulating),

chemical inertness (for chemical processing applications) and wear resistance. Besides microelectronics, one application where alumina is attractive for its electrical resistance is, as a coating to decrease the magneto-hydrodynamic force in magnetic confinement fusion reactors. Alumina could be used as a coating or inside a flow channel insert.[32] Another property of interest is hydrogen or tritium permeability.[33] Alumina has a hydrogen permeability several orders of magnitude lower than most metals (**Figure 4**). Because of the recent interest in the use of hydrogen as a clean-burning fuel and in the use of more traditional weapons and nuclear energy applications (e.g., hydride fuels), permeation barriers are widely desired but frequently ineffective.[35] Also nuclear-related, alumina can be a corrosion barrier in liquid Pb (or Pb eutectics like Pb–Li or Pb–Bi) systems[36] but not liquid Li, which dissolves alumina[37] because of the thermodynamic stability of LiO_2.[38,39] Even with a decreased Li activity in Pb–Li eutectic, the Li can transform a preformed α-Al_2O_3 scale on alloy PM2000 to $LiAlO_2$ after exposure to Pb–Li at 600–800 °C.[40]

1.24.2 Selective Oxidation

The first issue to consider as far as alumina-forming alloys are concerned is the need for selective oxidation of Al in the alloy to form alumina and the minimum alloy Al content, C_{min}, needed to form alumina in the alloy. This minimum value is not necessarily equal to the minimum concentration needed to reform Al after an alumina scale had already been established, C_b.[41,42] The basic concept of selective oxidation was discussed in **Chapter 1.09, Thermodynamics and Theory of External and Internal Oxidation of Alloys**. For alumina-forming alloys, the general interest is the behavior of M–Al and M–X–Al, where X is normally Cr but can also be another element, such as Mn, with nobility between M and Al, the so-called third element.[43]

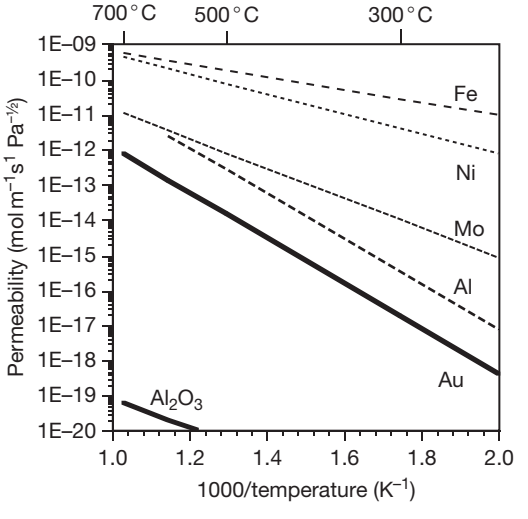

Figure 4 Hydrogen permeability as a function of reciprocal temperature for various pure metals and alumina. Data from Fowler *et al.*[33] and Steward.[34]

1.24.2.1 M–Al Alloys

For Ni–Al alloys, an early work by Pettit[44] considered the thermodynamics of the system as well as experimental evidence which indicated that kinetic issues dominate C_{min}. The thermodynamic calculations indicated <1 ppm Al at the alloy surface was needed for NiO or $NiAl_2O_4$ (spinel) to be stable. However, experimental work, summarized in **Figure 5** showed that much higher Al contents were needed for transition from Al internal oxidation with an external NiO scale (Region I) to an external alumina formation (Region III) in 0.1 atm O_2. (An over-lying spinel layer is formed at up to ~40 at.% in the β-NiAl phase field.[45]) The effect of temperature was to slightly lower C_{min} at higher temperatures. Even in a CO/CO_2 mixture (2:1) where NiO was not stable, the

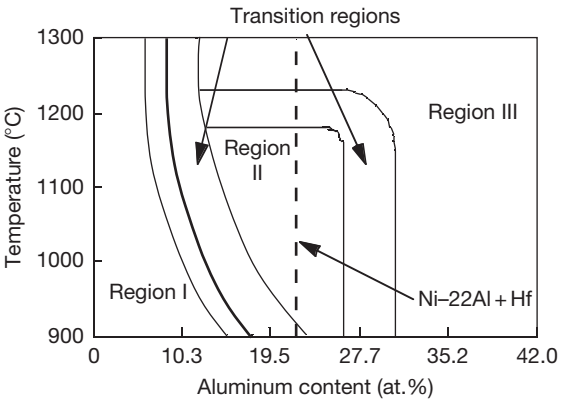

Figure 5 Relationship between oxidation temperature and Al content on the reaction products formed on Ni–Al alloys oxidized in 0.1 atm O_2. The various regions are: I – primarily NiO + Al internal oxidation, II – initial spinel ($NiAl_2O_4$) + Al_2O_3 formation, but eventual NiO, III – primarily Al_2O_3. The bold line indicates the transition between internal and external oxidation in CO–CO_2 mixtures where Al_2O_3 was the only stable oxide. Adapted from Pettit[44] with the Al content changed to atomic%. The dashed line is an observation for Ni–22Al + Hf where the initial $NiAl_2O_4$ + Al_2O_3 scale was stable for 1000 h at 1000–1200 °C. Pint, B. A. Unpublished oxidation data, ORNL, Oak Ridge, TN, 1994–2008.

solid bold line in **Figure 5** shows a fairly high Al content needed for transition from internal to external alumina formation. Thus, kinetic factors such as the scale growth rate and diffusivities in the metal and oxide dominate the selective oxidation process.

Values of C_{min} for Fe–Al alloys have been reviewed[46] and **Figure 6** shows a summary of C_{min} values found during oxidation in air or O_2.[47–52] As discussed by Pint *et al.*,[51] a distinct difference between complete alumina scale formation and Fe-rich oxide formation is clear at ≥1000 °C but can be more difficult to differentiate at lower temperatures, especially at 600–700 °C where an exclusive alumina scale is difficult to form on binary Fe–Al alloys and there is no significant difference in mass gain between high and low Al contents. One reason for the large range of values in **Figure 6** may be because of the interpretation. If the criterion is that no Fe-rich oxide formed using a visual assessment of scale color, then the contents of ~18–20%Al are typically needed. However, the same requirement for Ni–Al alloys in air would require $C_{min} > 35\%$. A more appropriate criterion is that a continuous alumina scale forms underneath the transient, base metal oxide. This is the criteria used in **Figure 5**. **Figure 7** gives an example for Y_2O_3-dispersed Fe–20Al where large faceted Fe-rich grains were observed at the gas interface after oxidation at 1100 °C but underneath is a fully-developed columnar alumina scale. Subsequent sections will discuss some of the other reasons for the scatter in **Figure 6**. Recent calculations by Zhang *et al.*[53] using relevant Fe–Al rate constants predicted much lower C_{min} values (0.5–4.5% depending on the assumptions) which does not agree with the experimental results summarized in **Figure 6**.

One issue that can affect C_{min} is time, that is, the length of exposure, and whether the alloy can maintain the alumina scale during extended exposures. Region II in **Figure 5** indicates where an initial external alumina scale was not sustained and a faster growing NiO formed. The likely explanation was Al depletion in the metal which did not allow the sustained formation of alumina.[44] This point might be more relevant to the discussion of lifetime, i.e., the amount of time an alloy can sustain the formation of an alumina scale (discussed in **Sections 1.24.4.4** and **1.24.5**). Nevertheless, the usefulness of C_{min} plots may be questionable if the specified level of Al cannot sustain alumina formation. For example, Hf-doped Fe–11Al at 1200 °C (**Figure 6**) only survived for 300 h before breakaway oxidation.[52] Thus, these plots provide a defined minimum Al level and not a target Al content for alloy development.

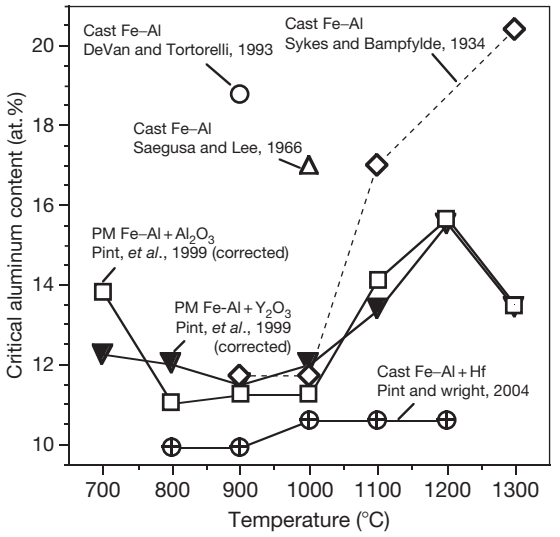

Figure 6 Summary of critical Al contents for Fe–Al alloys from various studies. The values for powder metallurgy (PM) alloys[51] were decreased by ~2% because this Al was tied up as oxides in these materials. Generally, these values were determined for exposures of ~100 h. Data from Sykes and Bampfylde,[47] Saegusa and Lee,[48] Devan and Tortorelli,[50] Pint *et al.*,[51] and Pint and Wright.[52]

1.24.2.2 MCrAl and M–X–Al Alloys

Most commercial alumina-forming alloys are based on MCrAl rather than M–Al compositions. The main

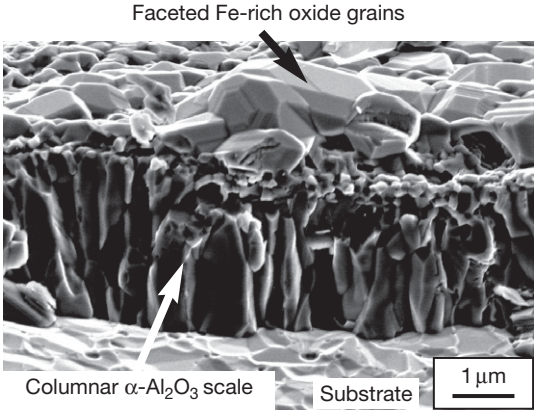

Figure 7 SEM secondary electron image of scale fracture cross section after 100 h at 1100 °C in air on Fe–20Al–Y_2O_3. An outer Fe-rich oxide formed over the inner α-Al_2O_3 layer because of the relatively low Al content in this alloy. Adapted from Pint, B. A.; Leibowitz, J.; DeVan, J. H. *Oxid. Met.* **1999**, *51*, 181–197.

reason is that the addition of Cr (typically 10–25%, see **Table 2**) allows alloys with much lower Al contents to form a continuous alumina-scale than observed in M–Al compositions. Since Al tends to have detrimental effects on mechanical and fabrication (i.e., rolling, joining) properties, minimizing the Al content is often a goal in alloy development. The effect of Cr is described as a third element effect.[43,53–55] There is still a disagreement as to whether the third element (1) acts as an oxygen 'getter,' (2) changes the Al activity, (3) increases the Al diffusivity, (4) increases the volume of internal oxides in the alloy, (5) simply decreases the concentration of base metal in the alloy, and/or (6) acts by some other mechanism. Most agree that the third element effect is more complex than the early explanation of Wagner.[54]

To illustrate the performance of Ni–Cr–Al alloys (**Figure 8**) shows examples of Ni–(17–30)Cr alloys with various Al additions oxidized in 100-h cycles at 1200 °C. Lower Al additions, 2.5–4.8% such as in alloys 617 and 602CA resulted in high mass gains similar to alloy 230 without Al. Alloy 602CA does not form an external alumina layer at 1200 °C; only internal Al oxidation is observed.[56] However, the ~6% Al addition in alloys 702 and 693 resulted in a significantly lower mass gain after the initial transient formation of Ni- and Cr-rich oxides. Further increases in Al content, for example, alloy 214, decreased the transient (i.e., Ni-rich) oxide formation and mass gain but did not decrease the long-term growth rate. With the presence of Cr in these alloys, the Al level needed for alumina formation, ~6%, is significantly lower than the Al levels discussed in binary Ni–Al alloys (**Figure 5**).

Composition effects can be summarized in so-called oxide maps.[57–59] **Figure 9** shows a Ni–Cr–Al oxide map with some of the data points from **Figure 8**. The three oxide regions, very similar in composition to the work of Giggins and Pettit[57] (and not at all like Wallwork and Hed[58]) are: I – Ni-rich scale with Al internal oxidation, II – Cr-rich scale with Al internal oxidation (e.g., alloys 602 and 617), and III – continuous Al_2O_3 scale. Obviously, the most oxidation-resistant alumina-forming alloys will be in region III.

A similar map was constructed for CoCrAl.[57] The main difference between CoCrAl and NiCrAl was that much higher Cr and Al contents were needed to achieve alumina scale formation, on the order of 20% Cr and 20% Al. The need for higher Cr and Al contents in Co-based alloys was also observed in a separate study.[60] Alloys based on TiCrAl are covered in a separate chapter.

Similarly to NiCrAl, in Fe-based alloys, as little as 13Cr is added to Ohmalloy® alloys combined with 5.2%Al to form alumina, **Table 2**.[23] In both Fe- and Ni-based alloys, a reasonable starting point for a standard alumina-forming MCrAl composition

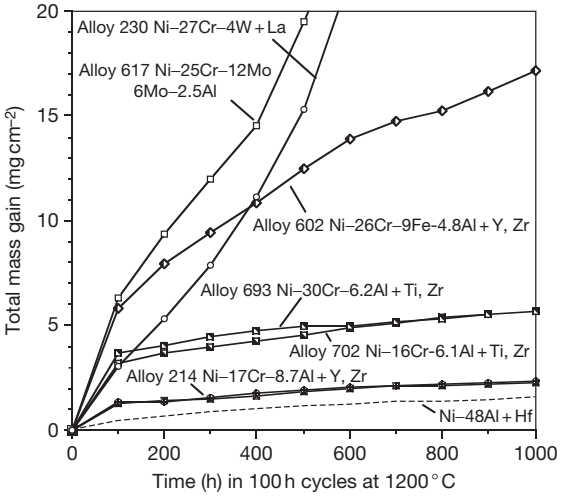

Figure 8 Total mass gain (specimen + spalled oxide) during 100 h cycles at 1200 °C in laboratory air for various Ni–Cr and Ni–Cr–Al alloys (see **Table 1**). Generally, the mass gain decreases with Al content due to the formation of a protective alumina scale with NiAl + Hf having one of the slowest growth rates of any alumina-former. Data from Pint.[12]

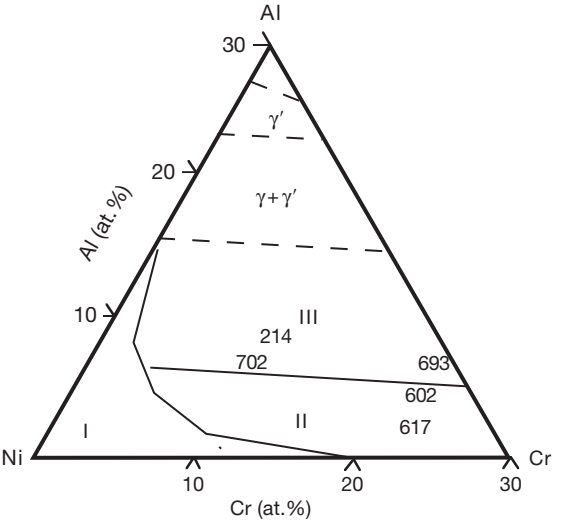

Figure 9 Schematic of the oxide map for Ni–Cr–Al and the location of the commercial alloys from **Figure 8**. Region I is for alloys which form Ni-rich oxide and Al internal oxide, Region II alloys form a Cr-rich oxide and Al internal oxide, and Region III alloys are able to form a continuous alumina scale. Map based on Giggins and Pettit,[57] alloy data from Pint.[12]

is ~20% Cr and ~10% Al (~5 wt%). Obviously, lower Cr and Al contents can form alumina, as demonstrated by both commercial and laboratory alloys (**Tables 1 and 2**). Higher Cr contents (>25%) lead to a decrease in workability and ductility and in FeCrAlY to a decrease in the incipient melting temperature of any Y-rich precipitate.[61]

While Cr is the most popular third element addition, other elements are used or have been investigated. To replace Cr, Mn additions have been investigated in Fe-based alloys by several authors.[62,63] These austenitic alloys have good wear properties but their oxidation resistance, particularly above 900 °C, is compromised of the formation of Mn-rich oxides. The addition of Si has been investigated in Fe–Al alloys[64] and has been shown to exhibit a third element effect in Ni–Si–Al alloys.[65] (Large Si additions are mainly an academic exercise as Si has detrimental effects on ductility and fabricability.) In Fe–Al–Si alloys, higher Si contents led to a decrease in oxidation rate. Also, Ni additions to Fe–Al alloys have been attempted.[66] However, the addition of Ni did not appear to improve the oxidation behavior at 600–800 °C compared to binary Fe–Al.

Quaternary additions on selective oxidation have been explored. In the case of alumina-forming austenitics (AFA, see example in **Table 2**), where low levels by Al are needed to retain a fully austenitic matrix (and retain creep-resistance[67,68]), additions of Nb have been found to influence whether the alloy forms an alumina scale at 800 °C (**Figure 10**).[69] At constant 5 or 6 at.% Al in Fe–15Cr–19Ni, increasing the Nb content decreased the mass gain after 500 h at 800 °C. At low levels of Nb, mass losses were observed due to the formation of a thick Fe- and Cr-rich oxide. The effect of Y on selective oxidation also has been investigated. Castello and coworkers[70] reported improved selective oxidation in Ni–12.9Al–11.9Cr–7.5C–0.11Y compared to the Ni–Al + Cr_3C_2 alloy without Y. They attributed the effect to Y reducing the growth rate of the initially-formed Cr-rich scale. **Figure 6** shows that Hf-additions to Fe–Al alloys decreased the critical Al content needed to form alumina.[52] Studies of Y_2O_3 additions in PM Fe–Al alloys did not find a benefit of Y on selective oxidation compared to PM alloys with an Al_2O_3 dispersion.[51] Rather, the fine-grain size of the PM Fe–Al alloys was thought to influence selective oxidation.

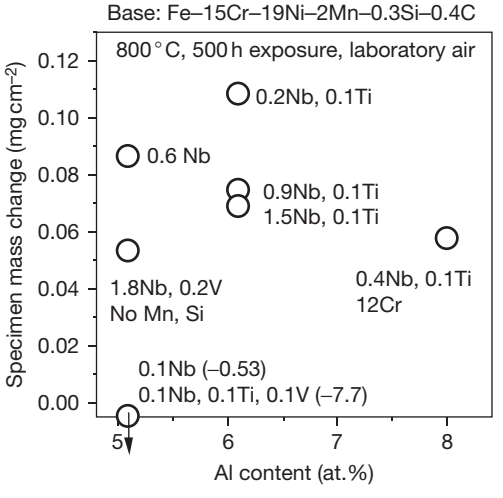

Figure 10 Specimen mass gain for Fe–15 at.% Cr–19Ni alloys with various Al and carbide forming elements (Nb, Ti, V) after 500 h (5, 100-h cycles) in laboratory air at 800 °C. Data from Brady *et al*.[69]

1.24.2.3 Alloy Grain Size Effect

Alloy grain size effects on selective oxidation are not widely appreciated in high temperature oxidation but are extremely important and often ignored as specimen alloy grain size is not always specified in literature papers. Early work on chromia-forming stainless steels showed that a fine-grained substrate was more oxidation resistant.[71–73] More grain boundaries increased the flux of Cr to the surface along these fast diffusion paths. This concept was used in alumina-forming alloys by Maloney and Yurek[74,75] where rapid solidification was used to achieve a fine grain size in Fe–2.8Cr–4.7Al alloys and TiB_2 dispersions were used to stabilize the fine grains. As discussed in the previous section, these low levels of Cr and Al are well below commercial FeCrAl alloys, **Table 2**. **Figure 11** shows the low mass gain at 600 °C and 700 °C for the fine-grained material compared to the conventionally-cast, coarse-grained Fe–2.8Cr–4.7Al specimens. While the TiB_2 additions may have contributed to the effect, **Figure 12** shows a thicker oxide formed over a large grain in the TiB_2-dispersed FeCrAl specimen. A thin Al-rich oxide (arrow) formed over the small grains in the substrate.

Goedjen and Shores[76] investigated the effect of grain size on NiCrAlY alloys. They found a decreased transient mass gain (i.e., less Ni-rich oxide formation) with finer grains but no change in the steady-state alumina scale growth rate. More recently, coating processes that produce fine-grained NiCrAl coatings have been found to have better selective oxidation.[77,78] Collectively, these results suggest that for low Al content alloys, reducing the grain size will improve

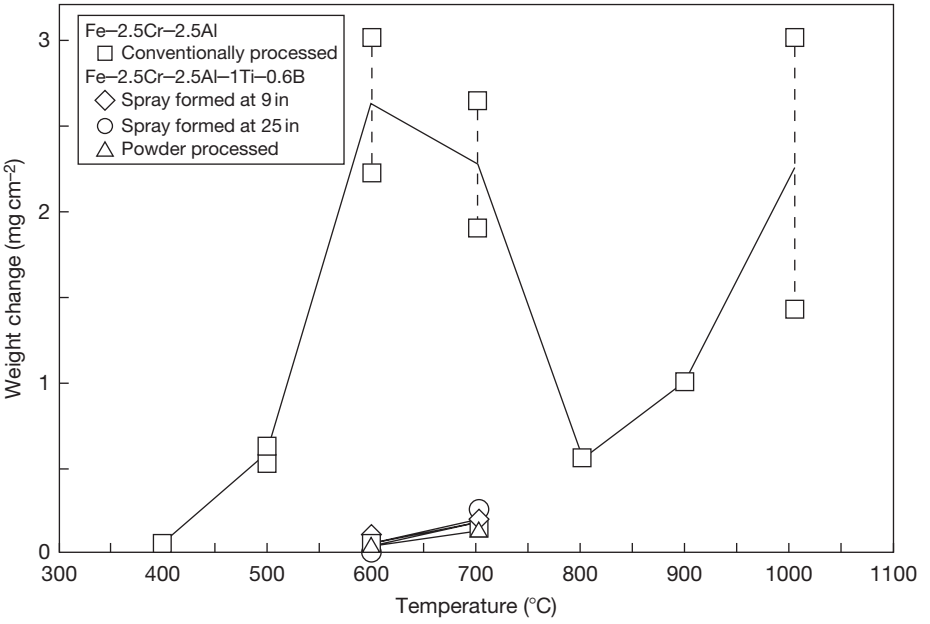

Figure 11 Mass change for conventional processed and fine-grained Fe–2.5 wt% Cr–2.5Al (2.8 at.% Cr–4.7Al) alloys made by several spray and powder processes. By using TiB_2 to keep a fine grain size, an Al-rich oxide was formed at 600–700 °C, thereby decreasing the mass gain of these alloys compared to conventional, coarse-grained material with the same Cr and Al content. Maloney, M. J. Ph.D. Thesis, Massachusetts Institute of Technology, Cambridge, MA, 1989, Maloney, M. J.; Yurek, G. J. In *Composites/Corrosion-Coatings of Advanced Materials*, Proceedings IMAM-4; Kimura, S., Kobayashi, A., Umekawa, S., Nii, K., Saito, Y., Yoshimura, M. Eds.; Materials Research Society: Pittsburgh, PA, 1989; Vol. 1, pp 383–388.

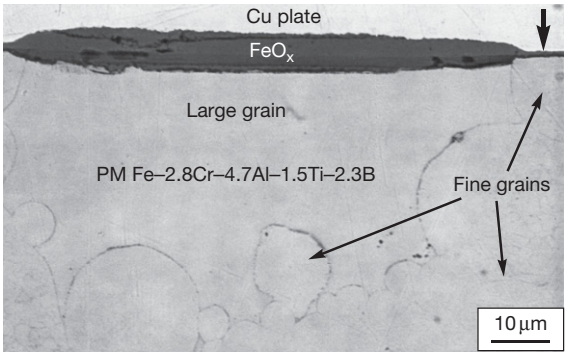

Figure 12 SEM secondary electron image of a polished cross-section of Fe–2.8 at.% Cr–4.7Al–1.5Ti–2.3B after 50 h at 700 °C. A thick Fe-rich oxide formed over a large grain in the substrate, elsewhere a thin Al-rich oxide formed over the finer-grained regions (arrow). Adapted from Maloney, M. J. Ph.D. Thesis, Massachusetts Institute of Technology, Cambridge, MA, 1989.

the possibility of forming an alumina scale. Furthermore, this effect will probably be most critical at lower temperatures 600–1000 °C where selective alumina formation is more difficult because of slow diffusion rates and less critical at higher temperature >1100 °C where diffusion in the alloy is much faster.

1.24.2.4 Precious or Platinum Group Metal (PGM) Effect

One of the more intriguing results of this decade in alumina-forming alloys is the work on γ–γ′ Ni–Pt–Al compositions.[79–81] The addition of a PGM such as Pt (or Ir, Pd, Rh, etc.)[81–83] to a base Ni–(16–22)Al alloy improves selective oxidation (i.e., decreases the formation of Ni-rich oxide) such that the alloy becomes a primary alumina former, similar to β-NiAl. However, TEM (or careful metallography) has found that a thin Ni-rich oxide layer does form on these alloys even with 30% Pt.[82,83] Improved selective oxidation had been previously observed in NiCrAl + Pt alloys by Felten,[84] Pt-containing superalloys by Tatlock and Hurd[85] and with Pt on the surface of MCrAl alloys.[86]

To illustrate the PGM effect on transient oxidation, **Figure 13** shows the mass gain after a 500 h isothermal exposure at 1000 °C as a function of PGM addition in cast Ni–22Al±Hf alloys.[82,83] The mass gain for Ni–48Al + Hf serves as a baseline for alumina formation with no Ni-rich oxide formation. The alloys without a PGM addition show a higher mass gain due to the formation of a Ni-rich scale with some contribution due to Hf internal oxidation.

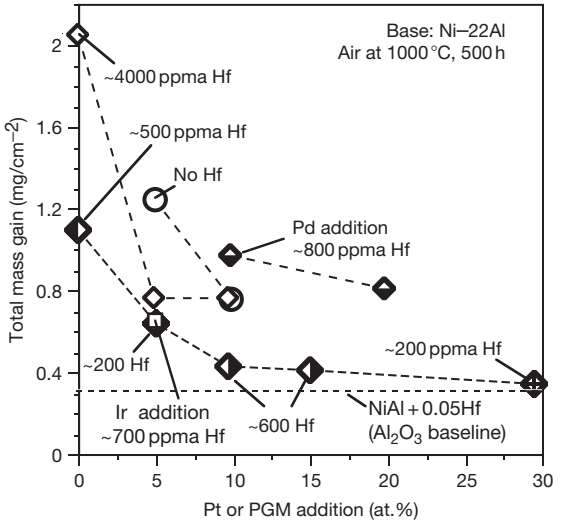

Figure 13 Total mass gain (specimen + spalled oxide) after a 500 h isothermal exposure at 1000 °C in laboratory air for various precious metal (PM) and Hf additions to Ni–22Al alloys. Data from Pint *et al*.[82,83]

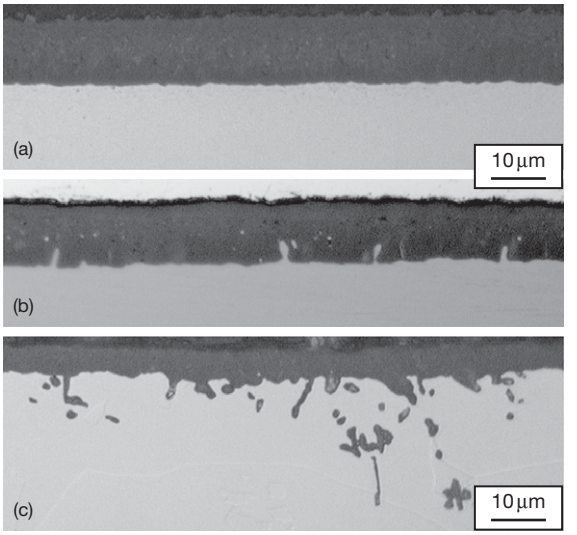

Figure 14 Light microscopy of polished cross-sections after 2000, 1 h cycles at 1100 °C in O_2 (a) Ni–22Al–10Pt, (b) Ni–50Al–5Pt, and (c) Ni–22Al–10Pt + 0.4Hf. Adapted from Pint, B. A.; More, K. L.; Wright, I. G. *Oxid. Met.* in preparation.

With increasing PGM content, the mass gain decreased. An Ir addition showed a similar benefit as Pt at the 5% level but 10–20% Pd, which is significantly less expensive than Pt, was not as effective due to formation of additional phases.[83] As an example of the alumina scale formed on these alloys, Figure 14 shows scale cross-sections after 2000, 1-h cycles at 1100 °C. Without a Hf addition, the alumina scale on Ni–22Al–10Pt is similar in thickness to that formed on β-Ni–50Al–5Pt (**Figures 14(a) and 14(b)**). The addition of 0.4 Hf to Ni–22Al–10Pt decreased the oxide thickness but some internal oxidation of Hf was evident (**Figure 14(c)**).

The γ–γ′ Ni–Pt–Al compositions are primarily considered for coatings on NiCrAl-based superalloys but some effort has been dedicated to alloy development.[87] By suppressing the formation of Ni-rich oxides with the associated weak Al_2O_3–$NiAl_2O_4$ interface,[88,89] these compositions can be used as bond coatings in thermal barrier coatings (TBCs). Such γ–γ′ coatings are attractive because (1) they can be formed simply by interdiffusing a plated Pt layer into the surface of the super alloy (i.e., a Pt diffusion coating rather than a Pt-modified β-phase aluminide), (2) Al interdiffusion is less of an issue because the phase composition of the coatings is the same as the super alloy substrate[79] and Pt appears to decrease the Al activity in the coating,[90] thereby creating a chemical potential gradient for Al to diffuse from the substrate into the coating (rather than out of an Al-rich coating), and (3) their high strength compared to β-NiAl and MCrAlY coatings[82] is thought to increase their resistance to thermal mechanical fatigue. When the γ–γ′ coating contains 5–10% Cr, either by interdiffusion from the substrate or by addition as a part of a secondary coating process, the hot corrosion resistance is improved.[91] One concern about these coatings is the depletion of Pt due to interdiffusion with the super alloy, which is significant at 1100 °C.[92]

1.24.3 Transient Oxidation

1.24.3.1 Base Metal Oxide Formation

As already discussed in the previous section on selective oxidation, during the initial or transient stage of oxidation, alumina-forming alloys will tend to form some base-metal oxide (e.g., NiO, FeO_x, or M–Al–O spinel, etc.), see **Figure 7**. This is illustrated in **Figure 15** for Fe–Al alloys oxidized at 900 °C. The decreasing mass gain with increasing Al content is due to a decrease in the initial transient Fe-rich oxide formation.[93] Because of the subsequent slow alumina scale growth, the mass gain after 5 kh is dominated by the mass gain after the first 500 h exposure (triangles in **Figure 15**). In addition to the alloy composition, the transient oxide thickness and phase composition are affected by many factors associated with the

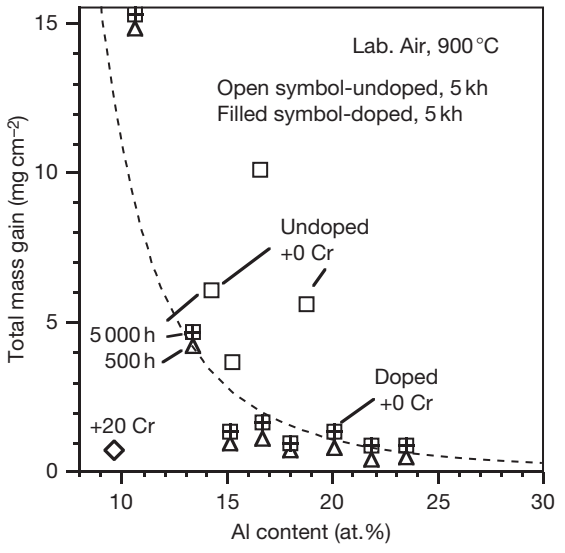

Figure 15 Total mass gain (specimen + spalled oxide) after 1 or 10, 500-h cycles at 900 °C in air for Fe(Al) alloys as a function of Al content. The doped alloys contained Ti, Hf, Zr, or Y and the Fe–20Cr–10Al specimen contained no dopant. For doped Fe–Al alloys (dashed line fit), the majority of the mass gain occurred during the first 500 h (triangle) when Fe-rich oxide formed. The higher mass gains for the undoped Fe–Al alloys (open squares) were due to an internal oxidation/nitridation with nearly linear kinetics. This internal oxidation was not observed for FeCrAl. Data from Pint[12] and Pint *et al*.[93]

thermodynamics and kinetics of oxide formation. Examples of thermodynamic factors are temperature and the partial pressure of the oxygen (e.g., H_2–H_2O or CO–CO_2 gas mixtures). Some of the kinetic factors are heating rate, alloy grain size (affecting the flux of Al in the alloy) and surface preparation which can affect the number of fast-diffusion paths in the near surface region (e.g., grinding versus acid etching).

Oxidation temperature is a critical factor for transient oxide because of the slow-formation of alumina below 800 °C. (A slow heating rate to a higher temperature can have a similar effect.) Alumina may be the thermodynamically stable phase but kinetics often dominate, allowing rapid base-metal oxidation. A simple strategy to enhance alumina formation is to preoxidize at a higher temperature where an alumina scale forms more readily. **Figure 16** gives an example of this strategy for alloy 214 foil (~50 μm thick) preoxidized for 2 h at 1100 °C. Because of the difficulty in forming alumina at low temperatures, the parabolic rate constant after 5000 h was higher at 700 °C (8×10^{-16} g^2 cm^{-4} s^{-1}) than at 800 °C (2×10^{-16} g^2 $\times 10^{-16}$ g^2 cm^{-4} s^{-1}) (**Figure 16(a)**). The observed mass gains reflect the formation of a Ni- and Cr-rich transient oxide which is nonuniform (e.g., **Figure 16(b)**). (Even at 1100 °C, a thin (0.5–1 μm) external layer of $Ni(Al,Cr)_2O_4$ formed on this alloy with only 8.7 at.% Al (see **Table 2**). But this exposure was sufficient to develop a continuous, underlying α-Al_2O_3 layer.[94]) With the preoxidation (<0.2 mg cm^{-2} mass gain), no further mass gain was measured during 10 kh exposures in air at 700 or 800 °C.[12]

The differences in oxidation behavior among Co-, Ni-, and Fe-based alumina-forming alloys were studied at 1000 and 1200 °C by Stott *et al*.[60] The critical factors identified were D_{Al} and O permeability in the alloy. With similar Cr and Al contents, Co-based alloys formed thicker transient oxides that were attributed to the fast growth rate of CoO and the relatively slow Al diffusivity in Co-based alloys. (Stated differently, higher Cr and Al contents were needed in Co-based alloys to quickly form alumina.) The growth rate of FeO is faster, which is important at breakaway (see **Section 1.24.5**), but faster Al diffusivity in ferritic FeCrAl alloys resulted in rapid alumina formation. A less comprehensive study of Fe, Ni, and Co–Al alloys by Hagel found similar results.[95]

The work of Kear *et al*.[96] was one of the earliest microstructure studies of the transient stage oxidation of NiCrAl. By reducing the oxygen partial pressure, NiO and Ni-rich spinel-type oxide formation was suppressed at 1000 °C resulting in a mixture of Cr_2O_3 and Al_2O_3. A subsequent characterization was reported by Smialek and Gibala.[97] On FeCrAl, there is typically very little transient base-metal oxidation. Quadakkers and coworkers[98] used the Fe and Cr in the outer scale to mark the original metal interface and study the alumina growth mechanism. **Figure 17** gives an example of the type of transient scale on ODS FeCrAl after 2 h at 1000 °C in O_2.[40] The Fe and Cr maps (**Figures 17(b) and 17(c)**) show that Cr and Fe were concentrated in a thin (~100 nm) outer layer after these conditions.

1.24.3.2 Cubic Alumina Phases

One of the most critical transient oxidation issues for alumina-forming alloys is the formation of metastable cubic Al_2O_3 phases (e.g., γ, δ, θ phases). Their formation can be considered as a transient phenomenon because, given time and temperature, these metastable phases generally transform to the stable α phase. However, because these cubic phases are more defective than α, they allow faster diffusion and grow at a faster rate.[95,99,100]

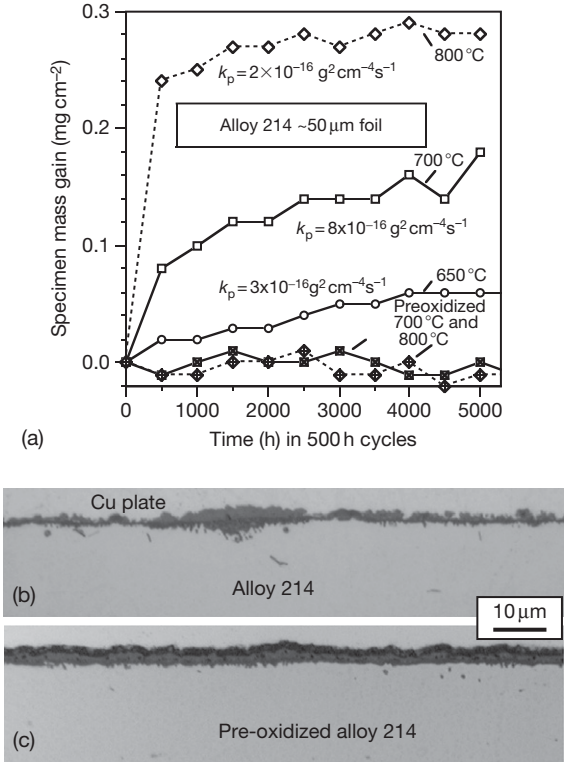

Figure 16 (a) Specimen mass gains for alloy 214 (NiCrAl, see **Table 2**) foil (~50 μm) with and without preoxidation exposed for 500 h cycles in laboratory air at 650 °C, 700 °C, and 800 °C. Polished cross-sections for the specimens shown in (a) after exposure in laboratory air at 800 °C, (b) as-received foil specimen oxidized for 5000 h, and (c) preoxidized (2 h at 1100 °C in dry O_2) foil after 10 000 h. Data from Pint.[12]

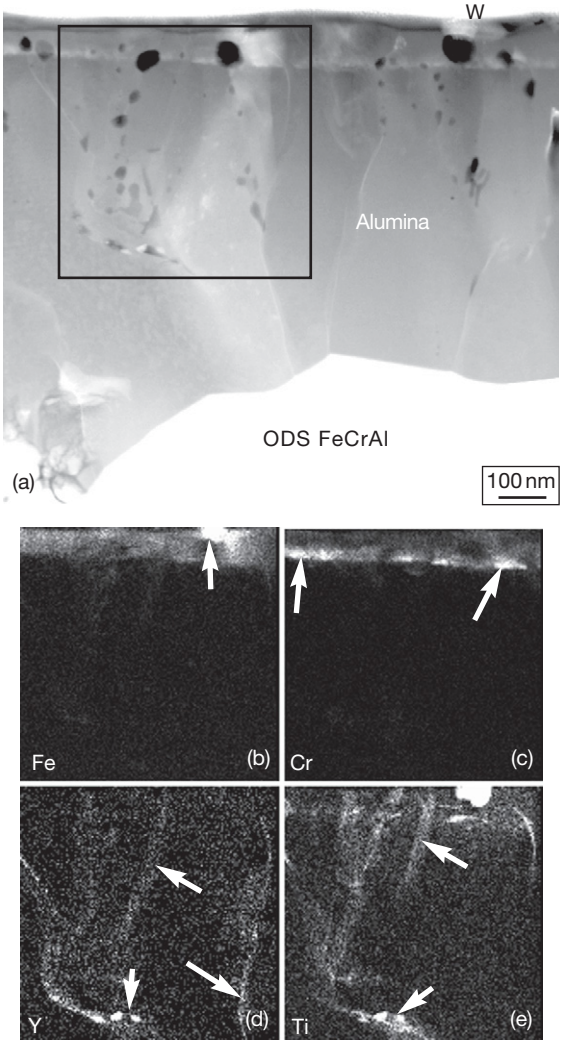

Figure 17 Cross-section of the α-Al_2O_3 scale formed on PM2000 (ODS FeCrAl, see **Table 1**)) after 2 h at 1000 °C in dry O_2 (a), STEM high angle annular dark field image and EDS X-ray maps from the box in (a): (b) Fe, (c) Cr, (d) Y, and (e) Ti. Adapted from Pint, B. A.; More, K. L. *J. Nucl. Mater.* 2008, 376, 108–113.

The formation of cubic alumina phases on alumina-forming alloys was discussed in the early literature.[95] However, the possibility of forming these metastable phases, rather than α, was not discussed for many years and probably led to the controversy regarding the growth mechanism of alumina scales in the 1980s. The observation of growth by outward Al transport was assumed to be for an α-Al_2O_3 scale but, based on the oxidation time and temperature, was likely θ-Al_2O_3.[101] This issue will be further discussed in **Section 1.24.4.2**.

The hallmark of cubic alumina phases is the gas-side blade or whisker morphology often observed. Much of the cubic alumina scale characterization work has been done on β-NiAl,[102–105] because of the cubic epitaxy with the β phase and because Fe and Cr in the substrate tend to help nucleate α phase.[100,106] However, at lower temperatures (<950 °C), cubic alumina scales form even on FeCrAl. Typical surface morphologies on commercial FeCrAl foil are shown in **Figure 18**. The outward growing features are minor at 700 °C but are very evident at 800 °C (**Figure 18(b)**). After long-term exposure at 900 °C, there is little evidence of outward transport and the scale has completely transformed to α-Al_2O_3 (**Figure 18(c)**). However, aluminized foils (aluminized to increase the Al reservoir) showed more distinct remnants of outward growth (**Figure 18(d)**). This is consistent with work on NiAl where surface enrichment of Al by ion implantation led to more cubic alumina formation.[107] Cubic alumina phases

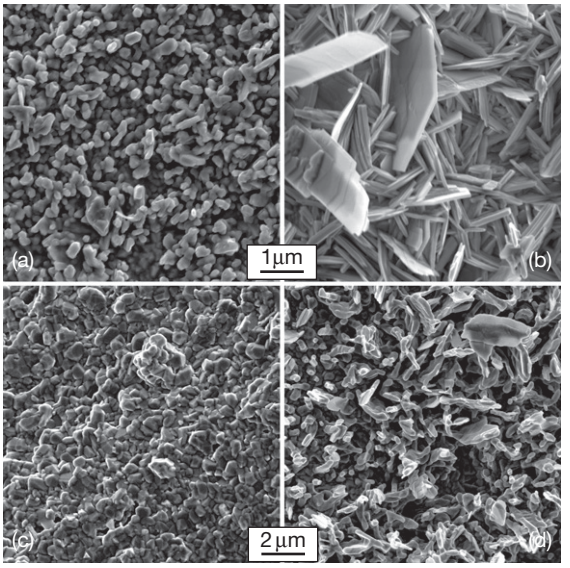

Figure 18 SEM secondary electron plan view images of the alumina scale morphology formed on ~50 μm commercial FeCrAl foils after exposure in laboratory air: (a) FeCrAl + Y,Hf, 700 °C 10 kh, (b) FeCrAl + Y,Hf, 800 °C, 10 kh, (c) FeCrAl + Mm (mischmetal), 900 °C, 50 kh, and (d) aluminized FeCrAl + Mm, 900 °C, 50 kh. Adapted from Pint, B. A. Unpublished oxidation data, ORNL, Oak Ridge, TN, 1994–2008.

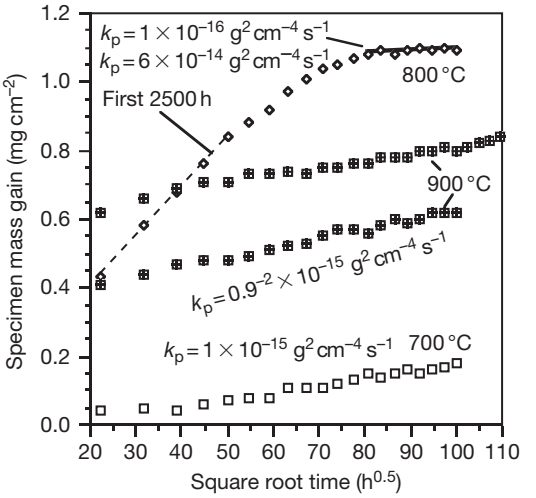

Figure 19 Specimen mass gains for aluminized FeCrAl + Mm foil (~50 μm) exposed for 500 h cycles in laboratory air at 700, 800, and 900 °C. The higher rate for cubic alumina phases is seen at 700 °C and initially at 800 °C. Data from Pint[12] and Dryepondt *et al.*[110]

such as θ also have been observed on bulk FeCrAl alloys at 900 °C.[104,108,109] For Ni-based alloys, cubic aluminas are less common because they tend to form Ni-rich oxides first and the nucleation of alumina beneath this layer apparently favors α-Al_2O_3 formation. The alloy 214 (NiCrAl) foils in **Figure 16** do not show the high parabolic rate constants observed on FeCrAl foils (**Figure 19**).

The study of the alumina phase may seem an academic exercise except that there is a strong effect on performance of commercial MCrAl foils in the 700–950 °C temperature range. **Figure 19** shows the kinetics for commercial aluminized FeCrAl foil oxidation in air at 700–900 °C. At 900 °C, the initial jump in mass gain is due to the initial formation of the cubic phase. Based on the mass gain, more Al was consumed during the first 500 h exposure than during the next 10 kh of exposure, after the cubic phase had transformed to a slower growing α-Al_2O_3 scale. Because of the faster growth of cubic-aluminas, the parabolic rate constant at 700 °C (1×10^{-15} g^2 cm^{-4} s^{-1}) is comparable to the rate at 900 °C (**Figure 19**). At 800 °C, where the blade structure was most evident (**Figure 18(b)**), the mass gain after 10 kh is higher than at 900 °C, although the rate decreased significantly during the last 2.5 kh. All of these mass gains are relatively low. However, with the foil there is a limited Al reservoir. **Figure 20** shows the starting and final Al contents in these foils.[110] The starting Al profile in the aluminized FeCrAl is not flat because of the aluminization step. As expected, the Al content drops with exposure time at 900 °C with very little Al remaining after 50 kh. However, because of the faster growth of the cubic alumina scale, the foil was almost completely depleted of Al after only 10 kh at 800 °C (**Figure 20**) is similar to other observations for FeCrAl foils in this temperature range.[111]

Because of the use of these foils in automotive catalytic converters and other applications operating in this temperature range, there is considerable concern about the increasing Al depletion due to transient oxide formation. Various treatments have been developed to speed the transformation to an α-Al_2O_3 scale.[112] Small ion dopants such as Ti are known to speed the transformation from θ to α-Al_2O_3.[113,114] Therefore, a TiO_2 slurry was an effective surface modification.[112] Studies have shown a faster transformation to α-Al_2O_3 in the presence of H_2O,[112,115] although an earlier study found the opposite effect.[116] Thus, a higher temperature pretreatment in H_2–H_2O is another strategy to quickly form an α-Al_2O_3 scale.

Once a continuous α-Al_2O_3 scale has formed, the transient stage of oxidation is completed and the steady-state period of oxidation begins.

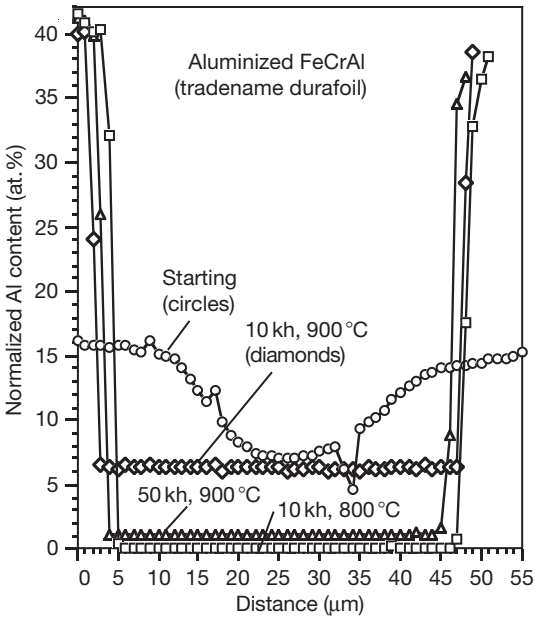

Figure 20 Electron probe microanalysis using wavelength dispersive spectroscopy Al profiles of the aluminized FeCrAl + RE foil after various exposures in laboratory air. The higher depletion after 10 kh at 800 °C compared to 10 kh at 900 °C is consistent with the mass gain data in **Figure 19** and is attributed to the formation of a faster-growing metastable cubic alumina scale. Data from Pint[12] and Dryepondt *et al*.[110]

1.24.4 Steady-State Oxidation

At the completion of the transient stage of oxidation, a complete alumina scale would have formed and subsequent oxidation should be controlled by the properties of this layer. This section will consider the performance of this layer and the factors that affect it. This will be a general discussion with examples given for various materials. The issues relevant to steady-state alumina formation have been reviewed several times.[9,46,117] Nominally, if the scale remains dense and adherent, steady-state oxidation should continue until the substrate is depleted in Al. This depletion will occur more rapidly if scale spallation occurs, requiring reformation of the oxide. Thus, adhesion of the oxide is also an important issue. Most commercial alumina-forming alloys contain a RE addition, for example, Y, Hf, Zr, La, Ce, etc. which strongly affects the steady state oxidation behavior. The role of RE additions will be discussed throughout. These dopants can be added as alloy additions, oxide dispersions or less effectively, as surface treatments or coatings such as slurries or ion implantation.[6,118] The amount of addition can vary from the ppm level to 0.5% and one of the significant issues is optimizing the RE benefit to achieve the longest alloy lifetime.

1.24.4.1 Scale Growth Rate

The previous section on transient cubic alumina formation began the discussion about growth rates. Starting with the derivation of Wagner,[119] the steady-state rate limiting step should be solid state diffusion through the alumina scale. Therefore, as the diffusion distance increases with time due to the formation of new oxide, the reaction kinetics are expected to be parabolic. Typically, parabolic rate constants have units in a form such as $g^2\,cm^{-4}\,s^{-1}$ for changes in mass data. The rate also could be expressed in terms of oxide thickness change or metal loss but mass change is the easiest parameter to quantify. For alumina in the temperature range of most interest (1050–1250 °C), the diffusion is along short-circuiting paths, likely the scale grain boundaries. As the oxide grain size increases with oxidation time, it has been argued that the kinetics are actually cubic.[120,121] The steady-state compressive growth stresses in an alumina scale[122–124] also could cause a change in the kinetics as Evans and coworkers argued for ZrO_2.[125] However, as will be shown for lifetime predictions of bulk alloys in the next section, the onset of scale spallation results in Al consumption kinetics which is nearly linear with time. Nevertheless, parabolic rate constants are a standard and conventional way to quantify and compare scale growth rates.

As a diffusion-controlled process, rate constants are expected to follow an Arrhenius-type relationship with temperature. **Figure 21** shows an Arrhenius plot of rate constants, mostly for RE-doped FeCrAl. As mentioned in the previous section, the rates are higher for cubic alumina scales such as θ-Al_2O_3. Since cubic alumina is metastable, these scales are only present at lower temperatures, <1000 °C. At higher temperatures, only α-Al_2O_3 scales are formed. **Table 3** gives some values for FeCrAl with and without RE dopants and the associated activation energies over the range 1000–1300 °C. The activation energies for undoped α-Al_2O_3 are lower than that for RE-doped α-Al_2O_3. The activation energy for θ-Al_2O_3 is also similar to undoped α-Al_2O_3, 235 kJ mol^{-1} for FeCrAl foils which is comparable to the ~200 kJ mol^{-1} found for the cubic alumina scales formed on β-NiAl.[99]

Table 3 Parabolic rate constants ($g^2\,cm^{-4}s$) and activation energy ($kJ\,mol^{-1}$) for several FeCrAl alloys. Data from Pint.[129]

Temperature	*Undoped FeCrAl*	*0.08Y*	*0.038Hf + Y*	*0.020 Hf + Y*
1000 °C	3.1×10^{-13}	$(1.1–2.0) \times 10^{-13}$	4.8×10^{-14}	2.5×10^{-14}
1100 °C	3.2×10^{-12}	$(4.2–4.4) \times 10^{-13}$	$1.4–3.7 \times 10^{-13}$	$0.98–1.5 \times 10^{-13}$
1200 °C	1.4×10^{-11}	7.5×10^{-12}	5.6×10^{-12}	3.5×10^{-12}
1300 °C	$(2.4–3.3) \times 10^{-11}$	$(3.6–4.4) \times 10^{-11}$	$2.2–2.3 \times 10^{-11}$	1.1×10^{-11}
Activation energy ($kJ\,mol^{-1}$)	244	352	367	366

As can be seen in **Table 3**, RE additions can decrease the scale growth rate. However, this RE effect was not widely accepted until the past decade, particularly when it was discovered by Doychak[126] that Hf-doping in aluminides decreased the parabolic rate constant by a factor of 10.[127–129] One of the complicating factors is the additional mass gain in RE-doped alloys due to the internal oxidation of the RE addition. **Figure 22** illustrates this issue comparing the mass gains for FeCrAl and FeCrAl–0.08Y at 1100 °C. Little difference was observed after a 200 h exposure. However, for Y_2O_3-dispersed FeCrAl (PM2000) a slower rate was measured. For PM2000, there was no mass gain associated with the oxidation of Y because the Y was added to the alloy as an oxide. By minimizing the RE addition to limit internal RE oxidation, the rate constant was further decreased (**Figure 22**). **Figure 23** illustrates the effect on the oxide thickness after 1000 h at 1200 °C by minimizing the RE addition.[94,129] In these backscattered SEM images, the bright phases in the α-Al_2O_3 scale are RE-rich oxides which are defects in the scale allowing fast O transport.[130] Minimizing the RE addition, minimizes the number of these particles as well as RE-rich oxide penetrations that penetrate deeper into the substrate, typically referred to as pegs. Note that the lowest RE addition resulted in the thinnest alumina scale on FeCrAl (**Figure 23**).

Several RE optimization studies[131–133] have been conducted to determine the minimum alumina growth rate possible, as in **Figure 24**. With very low RE additions, little benefit was observed. With very high additions, the internal oxidation and entrapped RE-oxides increase the rate. However, the optimal RE levels found in laboratory scale heats may not be viable in commercial alloys with standard impurity levels of interstitials such as S, C, and N.[10] For ODS alloys, the level of Y_2O_3 may be selected to optimize creep strength rather than a lower level that may minimize the oxidation rate.[109,134] The type of dopant can affect the oxidation rate. A clear effect of dopant ion size was found for chromia-forming alloys where larger ions decreased the rate more effectively

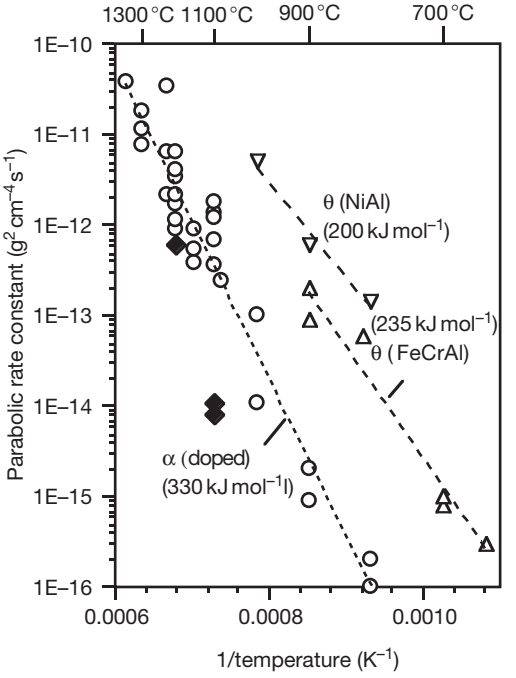

Figure 21 Summary of parabolic growth rates reported in the literature for RE-doped FeCrAl and calculated activation energies. Rates can be split into those for α-Al_2O_3 and θ-Al_2O_3. For comparison, the θ-Al_2O_3 rate data for NiAl is included.[99] The highlighted rates (diamonds) represent the lowest reported rates at 1100 °C and 1200 °C for Hf-doped NiAl. Other data points from Pint[12] and Pint.[129]

than smaller ions (**Figure 25**).[11] A similar relationship has not been established for alumina-forming alloys,[135] where ion size does not predict the strong beneficial effect of Hf. However, larger ions with high oxygen affinity, for example, Y, Zr, Hf, La, Ce, are all beneficial in reducing the scale growth rate. Smaller dopant ions such as Ti, Nb and Ta do not strongly affect the scale growth rate.[135]

As mentioned earlier, the parabolic rate constant is related to the rate of solid state ionic diffusion through the scale. However, there is no simple relationship and a number of authors have had difficulty relating the published α-Al_2O_3 diffusion data to alumina scale growth rates.[136] Using the derivation of

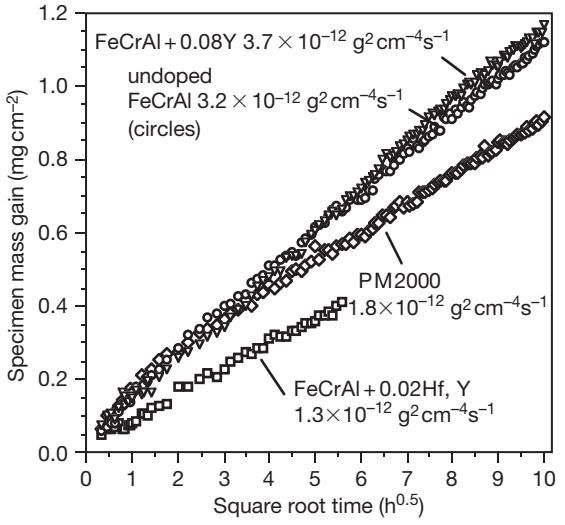

Figure 22 Specimen mass gain for various FeCrAl alloys (**Table 2**) during isothermal oxidation at 1100 °C in dry flowing O_2. The addition of Y did not decrease the reaction rate compared to undoped FeCrAl due to the additional mass gain associated with the internal oxidation of Y. When the addition is made as Y_2O_3 or lower alloy additions, lower oxidation rates were measured. Data from Pint.[12]

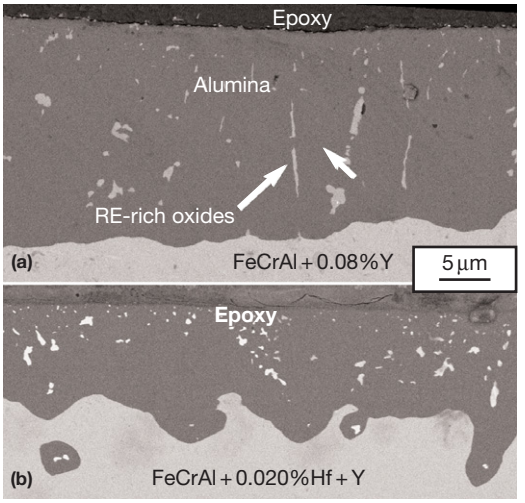

Figure 23 SEM backscattered electron images of the polished cross-section of the scale formed after 10, 100 h cycles at 1200 °C on FeCrAl with additions of (a) 0.08% Y and (b) 0.020% Hf/Y. Adapted from Pint, B. A.; More, K. L.; Wright, I. G. *Mater. High Temp.* **2003**, *20*, 375–386.

Wagner[119] and the interpretation of Yurek,[137] the parabolic oxidation rate constant for the formation of Al_2O_3 can be related to the solid state diffusion constant by the following equation for Al_2O_3:

$$k_p = \frac{1}{2}\int_{P''_{O_2}}^{P'_{O_2}} [3/2D_{Al} + D_O]\mathrm{d}\ \ln\ P_{O_2} \qquad [3]$$

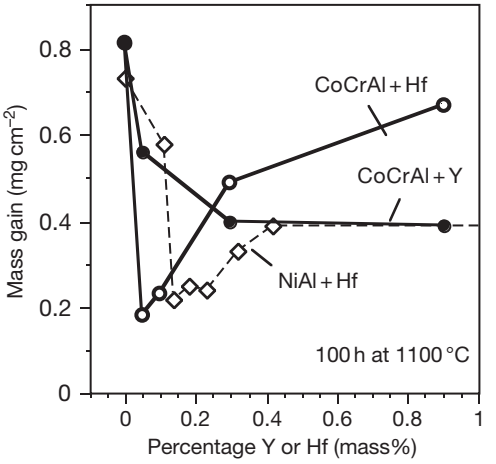

Figure 24 Mass gain for CoCrAl and NiAl after 100 h at 1100 °C with various reactive element additions. CoCrAl data are from **Figure 3** in Whittle and Stringer,[1] NiAl data are from Pint.[12]

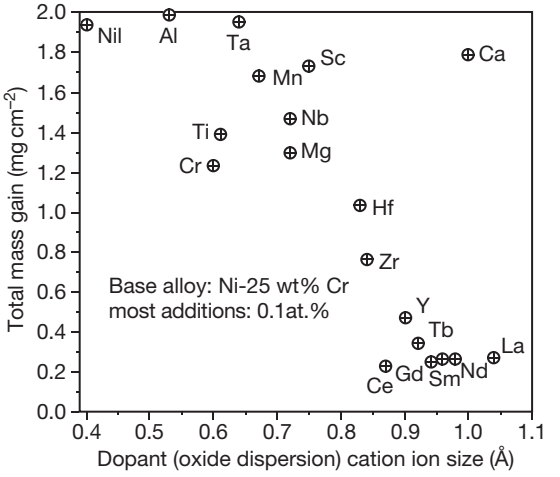

Figure 25 Total mass gain for Ni–25 wt% Cr alloys with various oxide dispersions added at a nominal level of 0.1 cation% after 100 h at 1000 °C. The mass gain decreased for larger cation additions. The addition of an Al_2O_3 dispersion had little effect on the scale growth rate. Data from Pint.[11]

where k_p is parabolic oxidation rate constant, P'_{O_2} is the decomposition pressure of Al_2O_3, P''_{O_2} is the ambient oxygen pressure, and D_{Al} and D_O are the respective self diffusion coefficients for aluminum and oxygen. This equation can be greatly simplified[137] given the observation that the alumina growth rate is independent of oxygen content in the environment, P''_{O_2}.[108] Extrapolating published diffusion rates for bulk α-Al_2O_3[138,139] to 1200 °C, **Table 4**

Table 4 Parabolic rate constants at 1200 °C calculated from diffusion data from the literature[138,139] and compared to measured values for RE-doped and undoped alumina-forming alloys[7,127,203]

Predominant diffusion pathway and species	*k_g ($g^2\,cm^{-4}\,s^{-1}$) at 1200 °C*
Calculated	
Grain boundary diffusion of O	1.4×10^{-12}
Grain boundary diffusion of Al	1.5×10^{-11}
Lattice diffusion of O	9.3×10^{-14}
Measured	
RE-doped FeCrAl	$(3.0–4.4) \times 10^{-12}$
Hf-doped NiAl	$(0.76–1.0) \times 10^{-12}$
Undoped FeCrAl, or NiAl	$(0.9–1.4) \times 10^{-11}$

shows that parabolic rate constants can be calculated which are of the same order of magnitude as those measured.[140] A recent literature review concluded that diffusion in α-Al_2O_3 is not fundamentally well understood, making it difficult to correlate diffusion data with oxidation data.[141]

1.24.4.2 Mechanism

While there was some confusion about the growth mechanism of Al_2O_3 scales in the 1980s, the issue seems to be largely settled today. There were several complicating issues. First, Pt does not wet the surface of α-Al_2O_3 (based on work with Pt photolithographic markers[142]). Thus, traditional inert Pt markers used to determine the scale growth mechanism floated on the alumina scale surface whether the scale grew inward or outward. In all cases, the markers showed inward growth.[61,143] For Cr_2O_3 scales, inert markers showed a predominant Cr outward growth without RE dopants and predominantly O inward growth with RE dopants and this was confirmed, without controversy, using ^{18}O tracer experiments.[144,145] Second, the transient, cubic Al_2O_3 phase formation confused some of the early ^{18}O studies.[101,146] The issue was later clarified, showing that θ-Al_2O_3 scales predominantly grow by an Al outward mechanism,[104] which is intuitive given their morphology[147] (**Figure 18(b)**). Third, unlike Cr_2O_3, there is no distinct difference between undoped and RE-doped α-Al_2O_3, both show some growth by inward O diffusion. With RE-doping, the outward Al transport is diminished and the scale grows predominantly by inward transport. This has been shown by several ^{18}O tracer studies.[134,148–153] An example of the tracer profiles is shown in **Figure 26**. The ^{18}O tracer was used first followed by ^{16}O. The first stage was 20 min at 1200 °C to ensure that the scale was 100% α-Al_2O_3.[150] In the undoped scale (**Figure 26(a)**), the ^{16}O is enriched in both the inner and outer scale indicating both Al and O transport. With the addition of Zr, only a minor ^{16}O peak was observed at the specimen surface. A stronger ^{16}O peak was observed underneath the outer ^{18}O peak indicating predominantly inward O boundary transport.

The explanation for the RE effect on transport has long been thought to be the segregation of RE ions to scale grain boundaries in both alumina and chromia scales.[8,154–157] Segregation of dopant ions is commonly observed in bulk alumina because of the low solubility of many cations in the closed-packed α lattice.[158] Examples of Y and Ti grain boundary segregation are shown in **Figure 17**. The mechanism by which RE ions inhibit cation transport could be blocking or site competition or a space charge effect.[159] However, the RE valence has not been shown to be an important variable.[135] A dynamic blocking mechanism was suggested, where large, slow-diffusing RE ions on the boundaries inhibit the diffusion of Al.[8] This mechanism is based on the observed outward transport of RE dopants during oxidation. **Figure 27(a)** shows a schematic of this phenomenon which is even observed on oxide-dispersed alloys like PM2000. After extended times at temperature, RE-rich oxide particles nucleate at the metal–oxide interface and grow during exposure.[8,135,160] **Figures 27(b)** and **27(c)** show an example at 1100 °C where the faceted $Y_3Al_5O_{12}$ particles at the gas interface increase in volume with time and do not just coarsen. This mechanism explains why smaller dopants, Ti, Nb, and Ta, segregate to α-Al_2O_3 grain boundaries but do not have the same effect on the scale growth rate as larger RE dopants.[135] These smaller ions rapidly diffuse outward and thus do not effectively inhibit Al boundary transport.

Recently, there has been renewed interest in studying the effect of RE dopants on diffusion and sintering in bulk ceramics[161,162] because of the observation that RE dopants like Y and La strongly improve the tensile creep strength of polycrystalline alumina.[163] The boundary electronic structure model proposed as an alternative to a simple dopant ion sized model to explain the behavior of various dopants[164] may be relevant to the effect of RE dopants on scales. Similar to results for bulk ceramics, an increase in the creep resistance of Hf-doped alumina scales has recently been demonstrated.[165]

As mentioned previously, the O and/or Al transport is likely along the scale grain boundaries because bulk diffusion rates in α-Al_2O_3 are too slow to

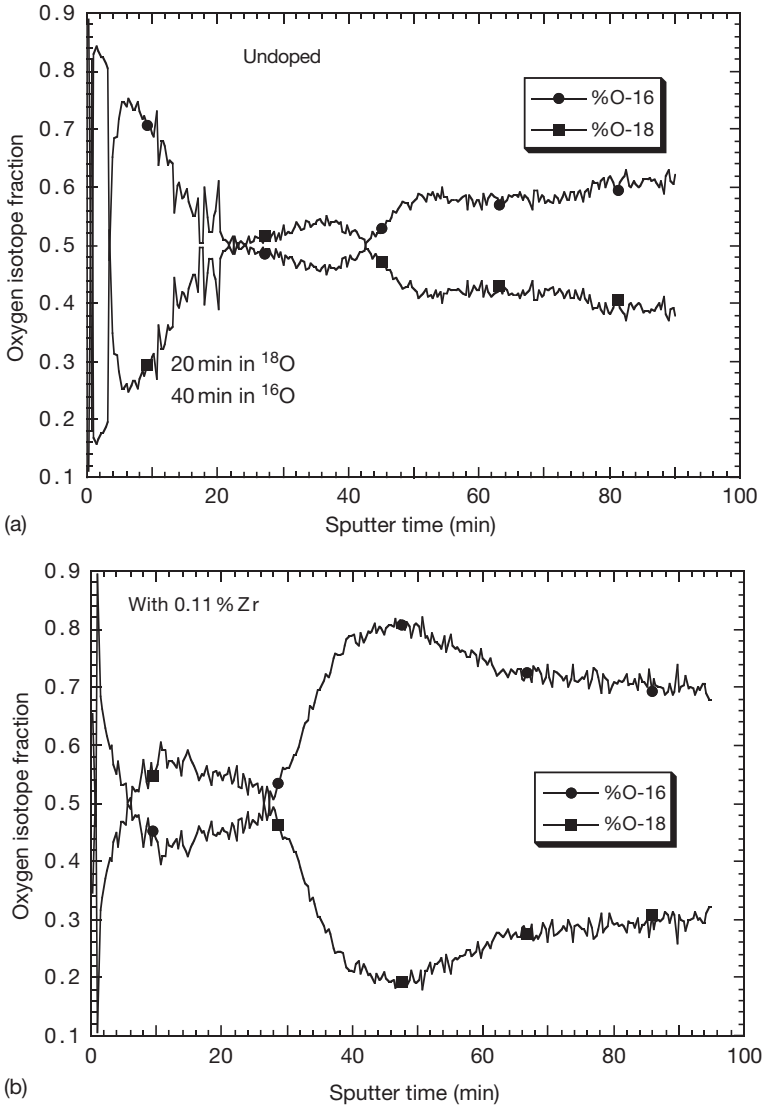

Figure 26 Secondary ion mass spectroscopy (SIMS) sputter depth profiles of 100% α-Al_2O_3 scales formed isothermally at 1200 °C after 20 min in ^{18}O and 40 min in ^{16}O on (a) undoped NiAl and (b) NiAl + 0.11%Zr. Data from Pint *et al.*[150]

account for the observed growth rates. **Figure 17** shows a typical cross-section of an alumina scale where very few dislocations or other defects were observed that might accommodate ionic transport. Atkinson and coworkers[166] calculated that a high dislocation density was needed for dislocation transport through the grains. It could be argued that the dislocations were present at a temperature but were annihilated during cooling.[141] However, the cooling rate for the thin scale is rapid which would not support this hypothesis. Experimental work has also indicated that, rather than neutral species, transport in alumina scales is via charged ions, that is, O^{-x} or Al^{+y}, as applied voltages have been shown to alter the scale growth rate[167–169] and electrical properties measurements indicate that x is ~2.[170]

A final point about scale growth is that there is now considerable interest in studying scale growth stresses, particularly with the advanced characterization techniques now available for *in situ* measurements.[124,165,171–174] These *in situ* results are considerably better than measuring the stress after cooling to room temperature by photostimulated luminescence and attempting to separate the growth stress from the thermal stress.[175,176] This recent *in situ* work has confirmed the observation that these growth stresses can be tensile,[171,172] rather than the common assumption of compressive growth stresses.[177]

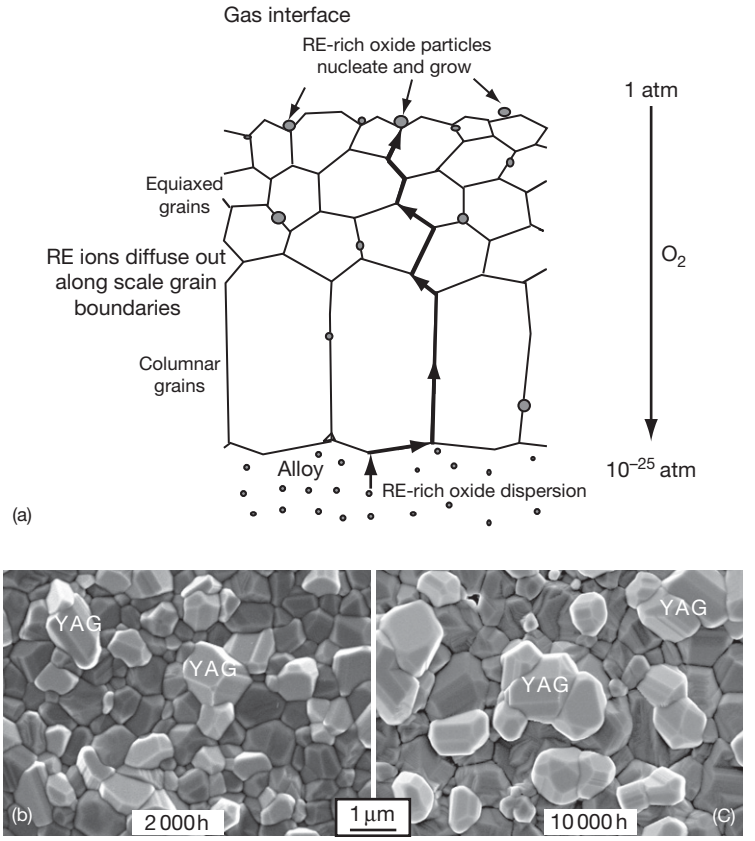

Figure 27 (a) Schematic representation of the outward diffusion of RE ions from oxide particles in the substrate to incorporation in the scale.[8] (b) and (c) show plan view SEM secondary electron images of the scale formed on PM2000 (ODS FeCrAl) after exposures in air at 1100 °C for (b) 2000 h and (c) 10 000 h.[12] The size and volume fraction of Y-rich oxide particles such as $Y_3Al_5O_{12}$ (YAG) has increased with exposure time. Titanium, also present in the alloy, is highly enriched at the gas interface.

The stresses can also decay with time as they are accommodated by substrate or scale creep.[165] Nevertheless, these stresses are generally <10% of the thermal stresses generated on cooling due to the CTE mismatch between metal and scale (see **Section 1.24.4.4.4**). Thus, they are often ignored when calculating the effect of stress on adhesion, eqn [1].[19]

1.24.4.3 Morphology

Figures 28 and **29** give some examples of typical scale morphologies on alumina-forming alloys that do not form a base metal transient oxide and are commonly observed in the literature.[7,135,178–181] The surface morphology of transient cubic aluminas was shown in **Figure 18**. Without a RE addition, undoped α-Al_2O_3 often shows a wrinkled morphology with oxide whiskers at the gas interface[7,117,143,178–181] which hint at the outward transport of Al. As alumina scales are usually thin, the original surface roughness (e.g., level of polishing for laboratory specimens) often affects the morphology.[181] At higher magnification, fine ridges can be seen that also suggest outward transport (**Figure 28(a)**). (These ridges are not the same as the ridges on β-NiAl formed by the θ–α phase transformation.[102]) Undulations of the undoped oxide scales also occur on FeCrAl and Fe(Al), sometimes accompanied by equivalent deformation of the underlying metal but also due to the formation of interfacial voids.[7,182–187] The undulations are not found when undoped FeCrAl substrates have low S contents[185] or an Al_2O_3 oxide dispersion is added (**Figure 29(a)**).[187,188] These differences suggest that the interfacial strength or mechanical properties of the oxide and scale may control this phenomenon.[188] In the cross-section, the scale typically has an equiaxed grain structure with or without wrinkles (**Figure 29(a)**).

With a RE addition, the surface ridges and whiskers are not present, indicative of the RE's role in

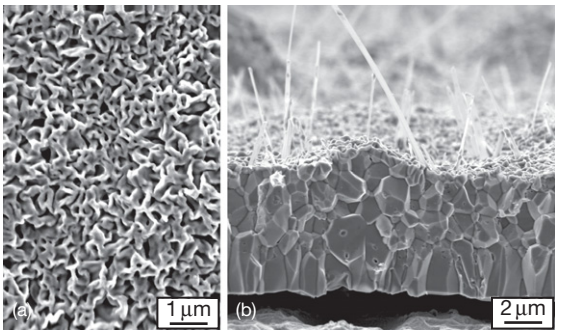

Figure 28 SEM secondary electron images of the α-Al_2O_3 scale formed on undoped FeCrAl at 1200 °C in dry flowing O_2. (a) Plan-view image of undoped FeCrAl after 2 h and (b) cross-section of the scale formed on Al_2O_3-dispersed FeCrAl after 100 h. In (a), the ridges can be referred to as intrinsic ridges to differentiate them from the extrinsic ridges formed on NiAl due to the alumina phase transformation. Adapted from Pint, B. A. Unpublished oxidation data, ORNL, Oak Ridge, TN, 1994–2008.

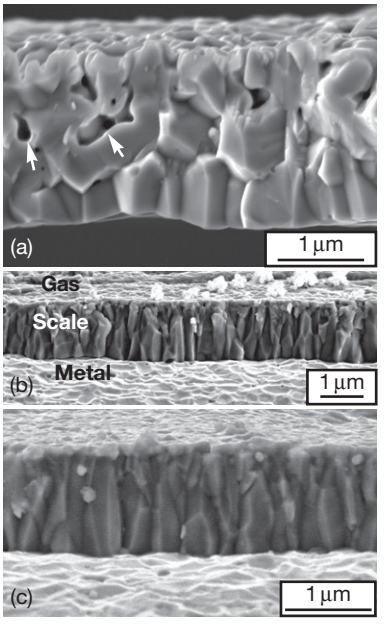

Figure 29 SEM secondary electron images of fracture cross-sections of scales formed on oxide dispersed FeCrAl after 2 h at 1200 °C in dry flowing O_2. (a) Al_2O_3, (b) Ho_2O_3, and (c) Er_2O_3. Adapted from Pint, B. A. Unpublished oxidation data, ORNL, Oak Ridge, TN, 1994–2008; Pint, B. A.; Alexander, K. B. *J. Electrochem. Soc.* **1998**, *145*, 1819–1829. Arrows in (a) indicate internal voids.[186]

suppressing outward Al transport.[148–153] As shown in Figure 27, instead of ridges, fine RE-rich oxide particles form on the surface. Additions such as Ti will tend to make the surface grains more rounded and less angular.[135,189] The most distinctive RE effect on morphology is on the grain structure where the change in growth mechanism results in a columnar grain structure with fine equiaxed grains near the gas interface.[178] In many alloys, the layer of equiaxed grains does increase in thickness with time because of the small amount of outward Al transport.[190] However, the scale thickening is predominantly due to an increase in the length of the columnar grains. Unlike some studies showing no texture, an x-ray pole figure on the scale formed on PM2000 at 1200 °C showed a preferred growth direction.[191] The grain structure of RE-doped α-Al_2O_3 is remarkably similar independent of the RE type and substrate, that is, M–Al or M–Cr–Al, likely because the scales on all these substrates grow by a similar mechanism. Some less common RE dopants are shown in Figure 29 to illustrate that a wide range of dopants produce similar effects. Varying the type and amount of dopant can alter the size and structure of the columnar grains.[192]

1.24.4.4 Adhesion

The most critical performance issue for alumina-forming alloys in long-term high temperature applications is scale adhesion. Adherent scales grow with parabolic (or even cubic) kinetics which results in very slow Al consumption rates from the substrate. However, when the scale spalls, the oxide must regrow or heal the spalled region, resulting in a significant increase in the rate of Al consumption due to the initial high rate of oxidation. As described in Section 1.24.1, the major cause of scale spallation is the thermal or cooling stress due to the CTE mismatch ($\Delta\alpha$) between the substrate and oxide, see eqn [1]. An additional issue is the formation of voids or other defects at the exposure temperature that lead to decohesion. Without defects, the scale will eventually reach a critical thickness, ξ_f, where the strain energy (W^*) is sufficient to cause spallation, eqn [2]. Defects will decrease the interfacial adhesion resulting in failure at a lower scale thickness.

For undoped alumina-formers, void formation at the metal–alumina interface is typically one of the critical issues that determines adhesion. Provenzano and coworkers[193] found in CoCrAl compositions that the interfacial void area increased with temperature from 700 to 1000 °C. Typically, these voids are thought to be formed by a Kirkendall-type mechanism either due to diffusion in the alloy or the oxide or both. Because of the outward transport of Al in the undoped scale, a counter current vacancy flux moves

towards the metal-scale interface. Also, because of the faster undoped scale growth rate, there is increased diffusion in the substrate with Al diffusing to the interface and other elements moving in the opposite direction. Contributing to the nucleation or growth of interfacial voids may be surface-active interstitial impurities such as S,[186,194] which will be discussed further in **Section 1.24.4.4.2**.

One problem with discussing scale adhesion is that it is difficult to quantify.[195,196] A well-formed scale is more tenacious than most epoxies used in quantifiable pull tests with an interface fracture toughness of >90 MPa.[197] Specimen mass gain curves can be used with a decrease in mass suggesting spallation. However, consider some NiCrAl alloy examples in **Figure 30**. The specimens that spall and rapidly lose mass are obvious but a higher specimen mass gain does not necessarily indicate a more adherent oxide. A higher mass gain could indicate a faster growing oxide coupled with minor spallation. The lower mass gain for NiAl + Hf is due to a thinner, adherent oxide. Furthermore, some oxides remain attached but are friable and therefore not protective,[198] resulting in a false indication of adhesion. Many early RE optimization studies relied on a relatively short term cyclic oxidation data to conclude that a certain composition was superior.[131,133]

A more absolute way of quantifying scale adhesion is cyclically testing specimens through the steady-state oxidation period until they reach breakaway oxidation (see **Section 1.24.5**). **Figure 31** shows the time to breakaway for various FeCrAl models and commercial alloys, all with ~10% Al. In order to accelerate the test, 1 h cycles were used at 1200 °C. The time has been normalized to a 1.5 mm thick specimen. Thus, all the specimens begin with a similar Al reservoir and the rate of scale growth and adhesion are thus key parameters in determining lifetime (see **Section 1.24.5**). An undoped wrought FeCrAl specimen, which spalls readily during thermal cycling, had a lifetime of only ~300, 1-h cycles. From **Figure 31**, it is obvious that RE additions play a critical role in increasing scale adhesion and thus increasing life.

1.24.4.4.1 Reactive elements

The main beneficial effect of RE additions (e.g., Y, Zr, Hf, La, Ce) on alumina-forming alloys is the improvement in scale adhesion. **Figure 31** shows that the addition of 0.08 Y increased the lifetime of FeCrAl by a factor of 30 compared to undoped FeCrAl. Most studies have observed a reduction in the interfacial void formation. A number of hypotheses have been proposed to explain the RE effect on void formation. Tien and Pettit[143] proposed that the RE dopants in the alloy formed a vacancy complex that prevented vacancies from coalescing at the metal scale interface. Using a similar logic, Kumar *et al.*[199] suggested that RE internal oxides in NiCrAl acted as a vacancy sink. However, there is no experimental evidence of these hypotheses. The formation of RE internal oxides or 'pegs' was thought to create a mechanical interlock that improved scale adhesion.[61,131,132,200] While a small number of

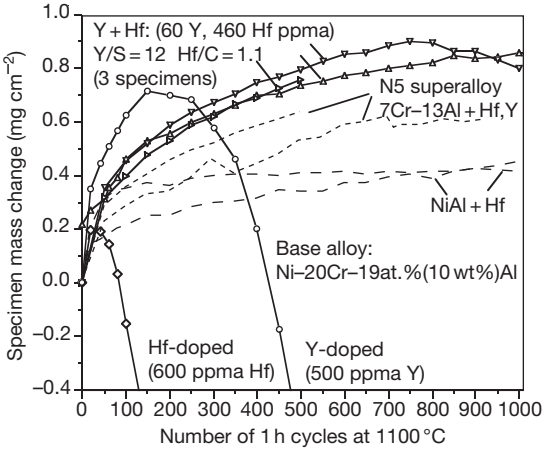

Figure 30 Specimen mass change of various Ni–20Cr–19Al alloys during 1 h cycles at 1100 °C in dry flowing O_2. The codoping of Y and Hf produced better scale adhesion compared to Hf or Y additions alone. Data from Pint[12] and Pint *et al.*[94]

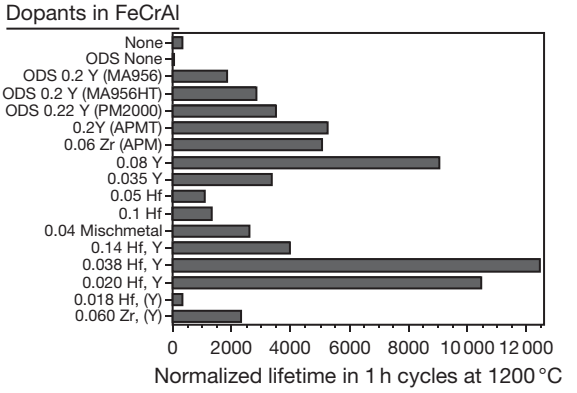

Figure 31 Normalized time to breakaway oxidation (as an indicator of scale adhesion) for various FeCrAl alloys (see **Table 2**) at 1200 °C in 1 h cycles. The lifetime is normalized to a 1.5 mm thick specimen. Model wrought alloys doped with Y and Hf showed the longest lifetime. Data from Pint.[12,129]

pegs is likely to be beneficial in preventing interfacial (metal–scale) crack propagation, pegs are not necessary as ODS alloys achieve good scale adhesion without forming pegs. For example, the lifetimes for several ODS alloys are shown in **Figure 31**.

Another hypothesis was that the finer grained RE-doped alumina scale resulted in a more plastic oxide that accommodated the strain better.[61,201] Ironically, the recent work on RE-doped bulk alumina[161,163,164] and scales[165] has shown that RE-doping actually increased the creep strength by several orders of magnitude. The change in mechanical response of the oxide scale with Y doping can explain the higher residual stresses measured in Y-doped alumina scales.[176] Weaker, undoped scales can wrinkle to accommodate the growth stress at temperature.

One of the issues that confounded potential hypotheses to explain the role of RE additions was the reported benefit of *any* oxide dispersion, including Al_2O_3 on scale adhesion.[143,202] This result could not be repeated in more recent work on Fe_3Al, NiAl, or FeCrAl.[135,188,203] No benefit on scale adhesion, growth rate, or scale morphology was observed with only an Al_2O_3 dispersion. In **Figure 31**, an Al_2O_3 dispersion reduced the lifetime from 300 h for wrought undoped FeCrAl to 70 h.

A current interpretation[8] of the role of RE additions on scale adhesion involves several issues: (1) the inhibition of outward Al transport decreases the counter vacancy flux to the interface, (2) the segregation of RE ions to the interface decreases the interfacial energy (γ_{int}), thereby increasing the critical scale thickness[7,8,204] (see eqn [2]), and (3) the RE addition prevents the interfacial segregation of S which has a detrimental effect on void growth. The observed outward flux of RE ions from the alloy into the scale results in RE ions segregated at the metal–scale interface.[7,8]

Mechanistically, the role of RE additions may be resolved, but, practically the issue of optimizing that benefit has not. The type of dopant, the amount, and the method of addition has still not been completely resolved. However, a few issues have been clarified. Surface doping with RE oxide coatings or ion implantation does not produce optimal benefits.[6,118,205] Alloy additions and oxide dispersions are clearly superior. Effective RE dopants have two qualities: large ion size and high oxygen affinity.[135] To avoid the issue of dopant solubility, which affects internal oxidation and other issues, a screening test was performed on various dopants added as oxide dispersions. **Figure 32** shows the 1200 °C, 1 h cycle

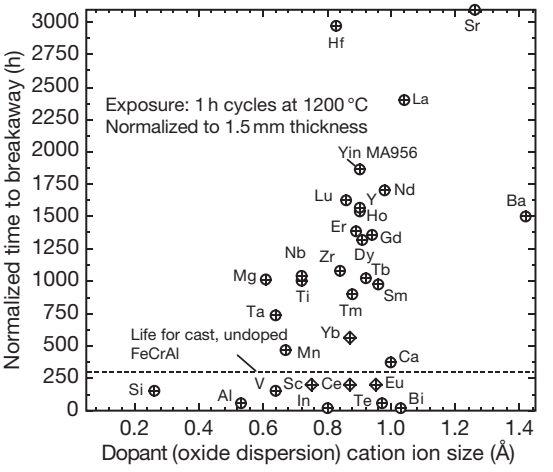

Figure 32 Normalized time to breakaway oxidation (as an indicator of scale adhesion) at 1200 °C in 1 h cycles for various oxide (VN for V, $BaTiO_3$ for Ba) dispersions (0.025–0.2 cation% additions) in Fe–20Cr–10Al. Lifetimes were normalized to a 1.5 mm specimen thickness. Low lifetimes for diamonds (Sc, Ce, Eu, and Yb) were attributed to overdoping with 0.2% additions. In general, all the lifetimes are somewhat lower than in commercial ODS alloys because of the laboratory processing. Data from Pint.[11,12] and Pint and Alexander.[135]

normalized lifetime for various dopants added as 0.2 cation% oxide dispersion additions to FeCrAl. (In general, the lifetimes for these laboratory-made alloys were not as good as that of the higher-quality commercial alloys (**Figure 31**).) There is a weak correlation between lifetime and larger ion size with many dopants not fitting this explanation. Several large ions, such as In, Te and Bi, have low oxygen affinity and never become incorporated into the oxide. Dopants such as Sc, Yb, Ce, Hf, La, and Eu produced negative effects with 0.2% additions associated with over-doping.[135] The data points for Hf and La, two of the highest lifetimes, were additions of 0.05%.

For alloy additions, **Figure 31** suggests that the best RE dopant is Y (compared to Hf, Zr, or mischmetal, a combination of Ce, La, and Nd). However, there was a considerable difference in lifetime between 0.08 and 0.035 Y additions. **Figure 33** shows lifetime as a function of specimen thickness for several Y additions. It is interesting to note that the lower Y contents, which would result in less internal oxidation, produced lower lifetimes than the specimens with 0.08% Y. A wider range of Y additions needs to be studied to resolve this issue and identify an optimum for lifetime. However, given the weak correlation with specimen thickness, these results suggest that the thicker specimens may become depleted in Y due to

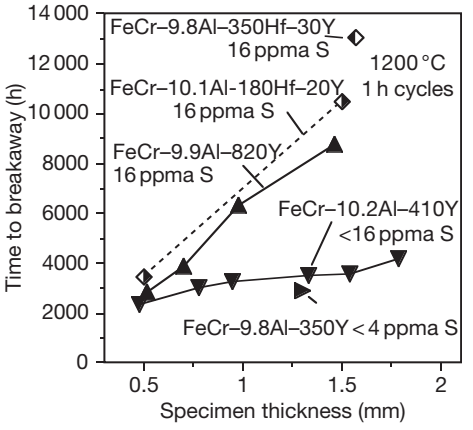

Figure 33 Time to breakaway oxidation (i.e., Fe-rich oxide formation) at 1200 °C using 1 h cycles for various RE-doped FeCrAl alloys (dopant contents in ppma) as a function of specimen thickness. For both Y-doped and co-doped (Y and Hf) alloys, there is a decrease in lifetime with very low RE additions. Data from Pint.[12]

spallation and not get as full a benefit as with higher Y additions. A similar result has been observed with RE doping in NiCrAl coatings.[206]

Figure 30 shows better spallation resistance for a NiCrAl with both Y and Hf compared to Y or Hf alone. **Figures 31** and **33** show the highest lifetimes for a combination of Y and Hf. This so-called co-doping results in low scale growth rates, minimal internal oxidation, and more optimal performance. Commercially, some alloys contain two or more dopants such as NiCrAl alloy 214 (Y and Zr), SX superalloys 1487 and N5+ (Hf and Y), and Aluchrom YHf (Y, Zr, Hf, and Ti) (Tables 1 and 2). A Pratt & Whitney NiCoCrAl coating (PWA286) also contains Y and Hf.[207] Co-doped alloys rely on a higher solubility dopant (Hf or Zr) along with lower levels of the low solubility Y dopant. Again, dopant depletion can be an issue because the lowest level of Y and Hf dopant did not produce the longest lifetime in a model FeCrAl alloy (**Figures 31** and **33**). Co-doping levels in model alloys were selected to match the alloy interstitial levels to achieve a [Y]/[S] >1 and a [Hf]/[C] >1.[129] This interstitial-dopant ratio strategy was originally proposed by Sigler.[208] In commercial alloys, the interstitial levels are higher than in the laboratory, which may require slightly different doping strategies.[10] Trying to target narrow composition windows is probably not realistic for commercial production, particularly considering that a co-doped alloy with a Y/S <1 will have very poor performance lifetime, for example, FeCrAl with 0.018Hf(+Y) in Figure 31.

1.24.4.4.2 Interstitials (S, C, etc.)

Identifying the detrimental role of S, and possibly other interstitials, has caused a major shift in the thought process on scale adhesion of alumina-forming alloys in the past 25 years.[28,185,204,208–216] The early work by Smeggil and Smialek on NiCrAl and later on FeCrAl has resulted in almost every commercial high temperature alloy being produced with <5 ppma S, Table 2. While an early hypothesis[217] suggesting that S could explain all RE effects was disproved,[8,204] the current mechanistic understanding is that S segregates to the metal–scale interface thereby increasing the interface energy, which in turn increases the formation of interfacial voids and weakens the interface.[186,194,218,219] Sulfur segregates to all free surfaces[220] and alloy grain boundaries; thus, it is not surprising that a high S content in nano-grained FeCrAl did not have a detrimental effect on alumina scale adhesion.[221] The large number of alloy grain boundaries provided alternative locations for S segregation besides the metal–scale interface.

An alternative explanation, that other interstitial elements besides S, such as Na and Ca, has been proposed.[222] However, a follow-up study by Smialek[223] which examined 41 elements in a Ni-based superalloy found that hydrogen annealing of superalloys, which improved alumina scale adhesion, primarily lowered the S and C contents. It has been suggested that La additions to superalloys was beneficial in countering a detrimental effect of P.[224] However, a study of Ni–7Cr–13Al + Y alloys with intentional P additions (70 ppma) showed no effect on scale adhesion during 1 h cyclic testing at 1100 °C.[12]

A common RE–S explanation is that RE dopants 'getter' S away from the metal–scale interface by forming RE–S compounds.[210] However, this mechanism has not been proven for ODS alloys (which contain high S levels, Table 2) where dispersoids did not contain S and S was not found segregated to the dispersoid–alloy interface.[8] The observation of a Y–S compound[225,226] is not proof of a gettering mechanism, only that Y forms a stable sulfide. A segregation-based RE mechanism suggests that RE ions segregate to the metal–scale interface and lowers the energy such that S segregation is no longer thermodynamically favorable.[8] Whether this involves site competition for segregation or another mechanism is not known. Nevertheless, there is a clear relationship where the Y/S ratio needs to be greater than unity for good scale adhesion in FeCrAl and NiCrAl.[28,129]

1.24.4.4.3 Precious metals

Alumina scale adhesion has been improved by Pt and other Pt group metals (PGMs).[79,84–86,227–229] The majority of observations have been for Ni-based alloys and coatings, especially β-NiAl. Pt additions also have been used to improve the performance of CoCrAlY coatings.[227] While the effect of Pt on adhesion is similar to RE additions as both are likely to lower the metal–scale interface energy, the mechanism is quite different as ~2 at.% Pt or Ir is needed as an alloy addition to improve adhesion. Also, Pt does not alter the scale growth rate and does not become incorporated into the alumina scale or segregate to scale grain boundaries, even on Pt–Al alloys.[230]

There is some disagreement about the effect of Pt additions in FeCrAl-based alloys. One study suggested that PGM additions benefited scale adhesion on FeCrAl.[229] However, that result could not be reproduced with 0.1 or 3 at.% Pt additions.[12] Unlike in Ni-based compositions, the formation of a Pt-rich phase in FeCrAl + 3Pt, likely due to limited solubility of Pt in ferrite, may explain the lack of benefit compared to Ni- and Co-based alloys and coatings.

1.24.4.4.4 Role of CTE

Thermal expansion mismatch between the metal and scale is a critical factor in understanding the oxidation resistance of various alumina-forming alloys. The effect is most evident in the Fe–Al system because of the very high CTE of the aluminide phases, particularly β-FeAl.[52,128,231–233] The difference in CTE can explain the scale spallation problems of RE-doped aluminides compared to ferritic FeCrAl and Fe(Al) alloys. The effect in RE-doped Fe–Al alloys can be quantified to a certain extent by using an approximation of the critical scale thickness, ξ_f, from eqns [1] and [2]:

$$\xi_f \propto (\Delta T \Delta\alpha)^{-2} \qquad [4]$$

Above this thickness, the strain energy in the scale exceeds the interface strength and spallation occurs. Assuming that the Al content does not affect the interface or oxide properties, if $\xi_f = 10\,\mu m$ for FeCrAl, then it is only 1 μm for β-phase Fe–40Al and 2 μm for Fe_3Al.[233]

Figure 34 gives some typical mean CTE values for alumina-forming alloys as a function of temperature. The values for NiAl, FeCrAl and Ni–22Al–5Pt are all remarkably similar at 1000–1200 °C and all these materials have the lowest CTE mismatch with

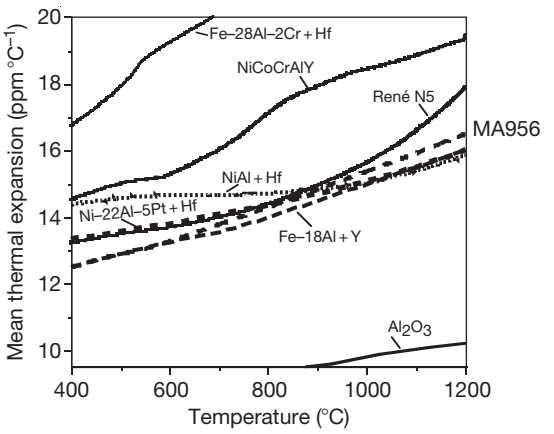

Figure 34 Mean coefficient of thermal expansion as a function of temperature for several Ni- and Fe-based alloys (see Table 2) showing the difference between these metals and alumina. Data from Haynes *et al.*,[30] Pint *et al.*,[82] Wright *et al.*,[232] and Pint *et al.*[233]

α-Al_2O_3. Alloys that have a phase transformation such as NiCoCrAlY or β-FeAl have much higher CTE than the materials that remain a single phase across the 25–1200 °C temperature range.

For Ni-based alloys, it is difficult to draw an exact correlation between CTE mismatch and scale adhesion, again because it is difficult to quantify scale adhesion. One criterion used previously for lifetime modeling was the time to zero specimen mass gain, t_z, in a cyclic oxidation test.[234] For example, in Figure 31 the t_z for Hf-doped NiCrAl would be ~85 h and ~425 h for Y-doped NiCrAl. In Figure 35, the CTE mismatch is plotted versus t_z at 1150 °C for several Ni-based alloys.[30] The general trend in the data is that a smaller $\Delta\alpha$ results in a longer t_z. The various NiCrAl and NiCoCrAlY compositions have a higher CTE and spall more readily. One complicating issue for this type of plot is that RE additions have a strong influence on scale adhesion (and thus t_z) but have no effect on CTE.[30] Therefore, the horizontal arrows show the increase associated with RE-doping or RE optimization (in the case of NiCrAlYHf). The dashed line represents an assumed optimum for RE doping. (Note that the 2 000 h value for Hf-doped NiAl was an approximation, the mass gain did not reach zero after 2000 1 h cycles at 1150 °C, although it was decreasing towards zero.[12])

1.24.4.4.5 Role of substrate strength

One of the alloys that does not fit the trend in Figure 35 is the single-crystal (SX) superalloy, N5, which contains both Y and Hf. There are two possible

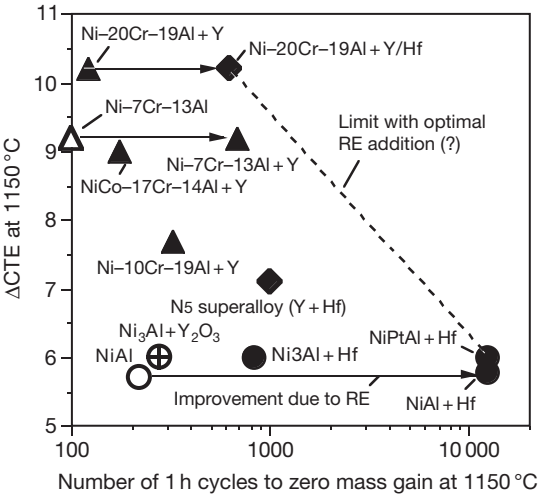

Figure 35 Difference in CTE between the alloy and alumina at 1150 °C for various Ni-based alloys (see **Table 2**) plotted versus the number of 1 h cycles to zero mass gain at 1150 °C. The number of cycles reflects the relative scale adhesion of these materials. Intermetallic alloys have much lower CTE values than the multiphase NiCrAl alloys that undergo phase transformations between RT and 1150 °C. Adapted from Haynes, J. A.; Pint, B. A.; Porter, W. D.; Wright, I. G. *Mater. High Temp.* **2004**, *21*, 87–94.

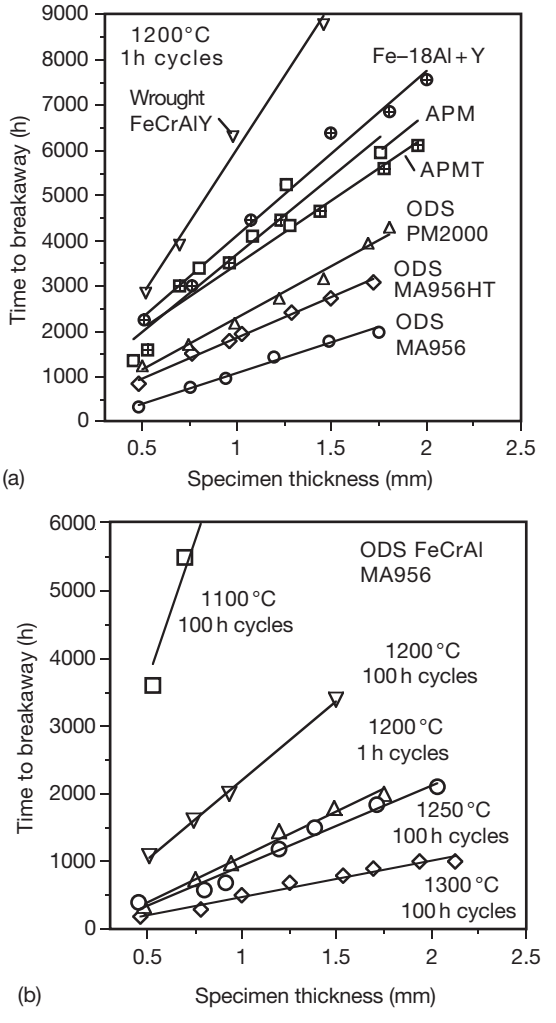

Figure 36 Time to breakaway oxidation (i.e., Fe-rich oxide formation) as a function of initial specimen thickness (a) at 1200 °C using 1 h cycles for various FeCrAl and Fe–Al alloys (b) for alloy MA956 under various cyclic conditions (see **Table 2** for compositions). Data from Pint[12] and Pint *et al*.[233]

reasons for this deviation, one is that the spallation of the transient oxide on this alloy increases the specimen mass loss but does not actually reflect the adhesion of the alumina scale. The other possible reason is that this very strong SX substrate does not accommodate the stresses in the scale (e.g., by creep) like a weaker substrate, such as NiAl, resulting in earlier scale spallation.[235,236]

A substrate creep strength hypothesis has been used to explain the decreased alloy lifetimes of ODS FeCrAl alloys compared to weaker wrought FeCrAlY or Fe(Al)Y (**Figures 31** and **36(a)**).[233] One exception to this negative effect of alloy strength is the commercial FeCrAl alloys APM and APMT.[233] With the addition of Mo and lower Cr content, APMT has a higher creep strength than APM[237] but essentially no decrease in lifetime (**Figure 36(a)**). However, APMT also contains Y and Zr so that RE optimization compared to APM may be responsible for maintaining the cyclic oxidation lifetime.

Substrate strength also affects the performance of foil specimens. In this case, the thin metal section deforms due to stresses in the oxide and little scale spallation occurs in most cases. The compressive stress generated in the growing oxide can cause the foil to lengthen due to the tensile stress in the adjacent metal. This increase in length has been characterized because it can be detrimental to the performance of FeCrAl catalyst supports.[238]

In general, it is difficult to quantify the mechanical effects of typical alumina-forming alloys because the tensile properties and creep (primary, as well as steady-state) rates are not commonly measured at the temperatures relevant for high temperature oxidation.[187]

1.24.4.4.6 Effect of cycle frequency

A final note about adhesion is that increasing the cycle frequency, that is, reducing the time per cycle usually decreases scale adhesion by increasing the number of

thermal cycles per time period.[15,198,234,239] Figure 36(b) gives examples of the time to breakaway oxidation for ODS alloy MA956 under various cyclic conditions. Of course increasing the temperature decreases the lifetime using 100 h cycles at 1200–1300 °C. However, increasing the cycle frequency from 100 to 1 h per cycle at 1200 °C, produced a reduction in lifetime similar to increasing the test temperature by 50 °C. Figure 37 gives an example for FeCrAlY where during 100 h cycles to a total time of 5000 h cycles, virtually no scale spallation occurred. However, in 1 or 2 h cycles, spallation began after a few hundred hours. One-hour cycles are used in lifetime testing to accelerate the experiment by inducing scale spallation more quickly.

Exceptions to the inverse relationship between cycle frequency and scale adhesion were observed for some Ni-based superalloys.[15] This behavior was attributed to the spallation of transient scale during longer cycles but could also be due to the time-dependent growth of defects such as interfacial voids. In short cycles, the defect may never reach the critical size necessary to cause spallation or only cause small areas to spall. Longer cycles, with long holds at temperature, may allow defects to grow to a sufficient size or accumulate such that scale spallation occurs over large areas.

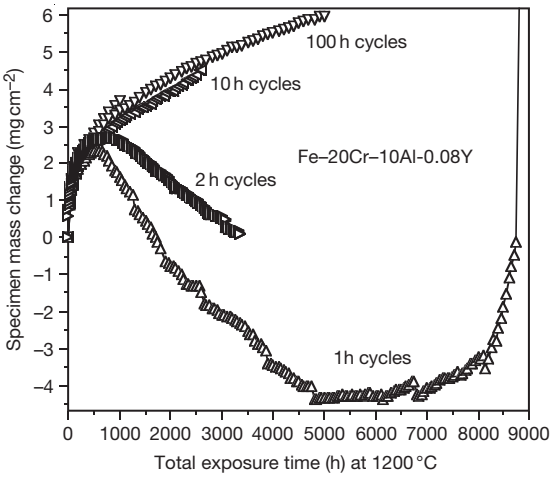

Figure 37 Specimen mass change for FeCrAl–0.08Y as a function of total exposure time for various cycle frequencies of 1–100 h per cycle. In 100 h cycles, very little spallation was observed but reducing the cycle time increases the number of thermal cycles and increases the amount of spallation, particularly for 1 and 2 h cycles. Data from Pint[12] and Pint *et al.*[15]

1.24.4.5 Internal Oxidation

The formation of oxide (or, more generally, any oxidation reaction product) within the alloy, beneath the external scale, is generally regarded as detrimental because it can degrade the mechanical properties of the substrate and interfere with the long-term chemical or mechanical stability of the protective external scale. For example, an internal oxide can help to nucleate a crack in the substrate. As also described previously (Section 1.24.4.1), internal oxidation generally increases the overall oxidation rate and can serve as fast transport paths for oxidants. The issue of internal oxidation of Al could be related to insufficient Al content to form an alumina scale, which essentially is a problem of low Al content alloys and/or alloys with poor selective oxidation.

Internal oxidation behavior has been studied on dilute M–Al alloys to understand the transition from internal to external oxidation. As oxidation is a diffusion controlled process, parabolic kinetics are generally observed.[240,241] The internal versus external oxidation condition given by Wagner[240] suggested that the oxidant solubility and diffusivity in the alloy were critical. Wolf and Evans[242] showed that the internal oxidation rate of Ni–Al alloys was nearly independent of the pO_2 in the environment. Whittle *et al.*[243] found that the internal formation of Al_2O_3 in dilute Ni–Al alloys accelerated O diffusion within the alloy, likely at the Al_2O_3 precipitate–metal interface. This could explain the faster oxidation kinetics of dilute Ni–Al alloys compared to unalloyed Ni.[244]

In alloys with sufficient Al to form an external alumina scale, internal oxidation of Al has been observed in Fe(Al) + 0–5Cr alloys at 800–1000 °C in air.[93] Internal oxides as well as nitrides were observed on undoped alloys with defective alumina scales. It was concluded that the defective scale allowed N permeation through the scale into the substrate. The less-stable AlN precipitates were displaced by more-stable oxides and nitride formation moved further (deeper or laterally) into the substrate with time. The high mass gains (with linear kinetics) for the undoped ferritic Fe(Al) alloys are shown in Figure 15. Figure 15 also shows that internal oxidation did not occur in air for undoped Fe–20Cr–10Al.

Internal oxidation of other alloy elements may occur, typically only those with a higher affinity for O than Al such that oxidation will occur below the Al/Al_2O_3 equilibrium pO_2 at the metal–scale interface. All RE additions fall into this category.[135] The issue of RE internal oxidation has already been

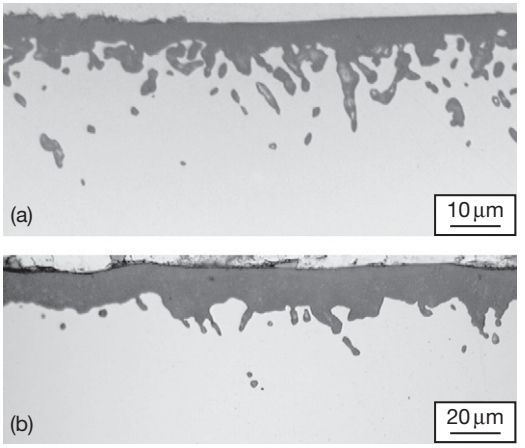

Figure 38 Light microscopy of polished cross-sections of FeCrAl + 0.038(Y,Hf) after oxidation in laboratory air for (a) 5000 h at 1000 °C and (b) 100 h at 1300 °C.[12] More internal oxidation occurred at low temperature than at high temperature where a much thicker external oxide formed.

discussed in terms of minimizing the internal oxidation by reducing the RE addition (e.g., **Figure 23**). The effect of oxidation temperature on internal oxidation is complicated by the effects of solubility and diffusivity.[240] The solubilities and diffusivities of both O and the RE increase with temperature but at different rates. An example of the effect of temperature on internal oxidation is shown for FeCrAlYHf in **Figure 38**. Over the range of 1000–1300 °C, it is difficult to make direct comparisons. However, relative to the external scale thickness, the internal attack at 1000 °C was deeper than at 1300 °C. The solubility of the particular RE addition in the alloy also could play a factor in the temperature effect.

For γ–γ′ NiPtAl alloys, the addition of Pt decreased the internal oxidation of Hf.[80] The effect was particularly strong with 10–15%Pt and Hf levels up to 0.4%. This Pt effect was attributed to Pt suppressing the Hf activity;[80] however, it could also be an effect of Pt on the O solubility.

1.24.4.6 Comparison of Fe-, Ni-, and Co-Based Alumina Forming Alloys

Only a few authors have explicitly examined the differences in oxidation behavior due to the base metal.[60,95] In general, FeCrAl alloys are the best alumina-formers because they are single-phase, have a lower CTE, faster diffusion in the alloy (due to their bcc structure) and lower O solubility. This combination of diffusivity and solubility results in lower Cr and Al additions needed to form alumina and better alumina adhesion. With two-phase alloys, the Al-poor phase will tend to form more base-metal oxide. Furthermore, alloy phase transformations typically increase the CTE. The low CTE of FeCrAl results in less thermal stress which drives scale spallation. Faster Al diffusion in the alloy minimizes Al concentration gradients in the alloy and decreases the critical Al content needed to form alumina. The rapid growth of FeO ($\sim 10^6$ times faster than Al_2O_3) results in more catastrophic failure at the end of life compared to NiCrAl (NiO forms $\sim 10^3$ times faster than Al_2O_3), however, the other factors tend to outweigh this problem.[60]

Several studies agree that the oxidation behavior of CoCrAl alloys are decidedly inferior to NiCrAl or FeCrAl.[60,245] For the formation of an alumina scale, Co-based alloys require higher Cr and Al contents because of the rapid growth of CoO ($\sim 10^5$ times faster than Al_2O_3) and the relatively low diffusivity in the alloy compared to Ni ($\sim 10^2$ slower) and Fe-based ($\sim 10^3$ slower) alloys.[60] In cyclic oxidation testing, CoCrAl alloys can be improved by RE additions.[132,245,246] However, their cyclic oxidation resistance is inferior to NiCrAl. The main interest for Co-based alumina-forming materials appears to be as coatings for Co-based alloys.

1.24.5 Breakaway Oxidation

The final stage of oxidation is breakaway which is characterized by rapid oxidation due to the depletion of Al from the substrate and the formation of faster-growing reaction products. **Figure 39** shows a failed specimen of FeCrAl alloy APMT cycled to failure at 1200 °C using 1 h cycles. One edge had been completely consumed by Fe-rich oxide formation. Typical of many dispersion strengthened alloys,[247] the center contains Kirkendall voids due to the depletion of Al. In stronger ODS FeCrAl, the voids are often perfectly round. In weaker wrought FeCrAlY, more deformation of the substrate occurs and center voids are not very evident.

The time to breakaway, t_b, is thus the useful lifetime of a component with thickness, d. It was used in several figures in the previous section (**Figures 31–33** and **36**). A common model for lifetime of Fe-based alloys is based on the Al reservoir in the component and the rate of consumption of that reservoir[41,42]:

$$d\rho(C_0 - C_b) = Akt_b^n \qquad [5]$$

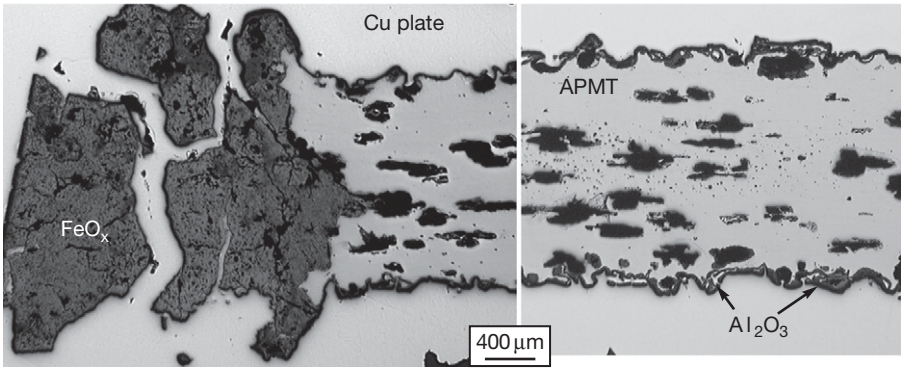

Figure 39 Light microscopy of polished cross-sections of alloy APMT after cycling to failure in 1 h cycles at 1200 °C.[12] One edge has been consumed and only Fe-rich oxide remains. In the center of the specimen, large Kirkendall voids remain from the depletion of Al.

where ρ is the alloy density, C_0 is the starting Al content in the alloy, C_b is the Al content where the material can no longer form a protective alumina scale, A is a constant, k is a rate constant, and $n = 0.5$ for parabolic kinetics and 1 for linear kinetics. For FeCrAl-type alloys with ~20% Cr, C_b is close to zero. With lower Cr contents, C_b increases to ~10% Al in Fe–Al binary alloys.[248,249] This type of equation allows the lifetime to be predicted as a function of component thickness or for a thickness to be selected to achieve a desired service lifetime.

One of the key assumptions of the reservoir model is that there are no Al gradients in the substrate; this greatly simplifies behavior. It is a reasonable assumption for foil (e.g., **Figure 20**) and thin (<1 mm) components.[248] However, for thicker components, Al gradients do occur and cause significant deviations in lifetime behavior.[249] For example, **Figure 40** shows the gradients in several MA956 specimens oxidized to failure at 1200, 1250, and 1300 °C. The center of the specimen contained >1%Al while the end of the specimen, near where the breakaway formation of Fe-rich oxide occurred, had ~0.1% Al. Earlier studies suggested that C_b was a function of thickness.[250] While C_b effectively increases with thickness because of Al gradients in thick substrates, mechanistically, in all cases, the value of C_b at the metal–scale interface, C_{bi}, at breakaway is close to zero.[249]

Gradients also drive early failures in some materials (**Figure 41**). For Fe–17Al + Hf and NiCrAlYZr (alloy 214), increasing the specimen thickness resulted in virtually no increase in t_b. It was shown that Al gradients formed in Fe–17Al + Hf resulted in early failures for the thicker specimens.[52,249] A similar failure mechanism may occur on alloy 214,[251] but less characterization work was performed

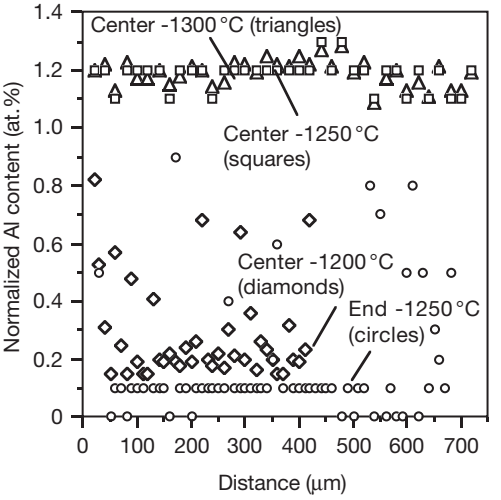

Figure 40 EPMA Al line scans from two different MA956 (ODS FeCrAl) specimens oxidized to breakaway at 1200—1300 °C and metallographically sectioned. The center scans are across the entire specimen thickness near the center of the specimen while the end scan is from an end of the specimen with distance from the edge towards the center of the specimen. Data from Pint *et al*.[249]

on this alloy after cyclic oxidation. Specimen geometry (e.g., corners on thin specimens) can also lead to early failure. Therefore the specimen surface area to volume also can affect lifetime and round versus flat specimens may behave differently.[252]

As shown for alloy 214 (**Figure 41**), the behavior of Ni-based alumina-forming alloys[12] may not be explained well by the Quadakkers reservoir model. The slower diffusion of Al in austenitic alloys and the formation of multiple phases (γ, γ′, β) in NiCrAl alloys may result in complications that are better modeled by a diffusion based model as suggested by Nesbitt and Heckel[253] or the spallation-based COSP

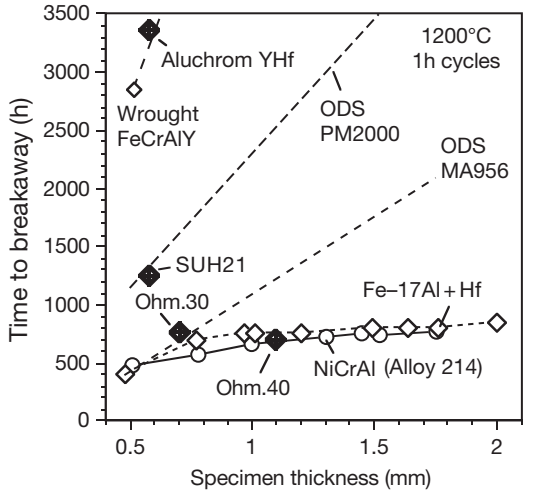

Figure 41 Time to breakaway in 1 h cycles at 1200 °C versus specimen thickness for various alumina-forming alloys (see **Tables 1** and **2**). For alloy 214 and Hf-doped Fe–17Al, there was little increase in lifetime with specimen thickness due to the formation of alumina gradients. Data from Pint[12] and Pint *et al.*[233]

model.[17] These models and Nesbitt's COSIM (Coating Oxidation and Substrate Interdiffusion Model)[254] are well suited for studying the behavior of NiCrAl coatings where the Al content decreases both due to oxidation and interdiffusion with the coating substrate.

As shown in eqn [5], the consumption side of the equality is very simplistic. Parabolic kinetics would only be observed for alloys where no spallation occurred. As shown in **Figure 41** and in previous figures, the nearly linear relationship between specimen thickness and t_b suggests that linear kinetics, that is, $n = 1$, are more relevant. However, this approximation would overestimate the Al loss at early times, when the scale is adherent and Al consumption follows parabolic kinetics. A more complicated consumption equation probably involves several time stages with different k and n values for each stage.[251] If a critical scale thickness could be identified to determine the change from the protective scale phase to the spallation phase (with higher Al consumption and higher n), such a model would be more mechanistic and accurate.

Other models are available to predict lifetime. The NASA-developed COSP model uses the scale growth and spallation rates to predict lifetime.[17] The spallation mass loss rate is attributed to an area fraction of spallation and regrowth. This model has been applied to an extensive oxidation database of typically Ni-based and ODS FeCrAl alloys that exhibit near-linear spallation rates. However, wrought Fe-based alloys that do not spall as orderly cannot be modeled in this manner (compare Ni-base spall behavior in **Figure 30** to Fe-based spallation in **Figure 37**). In general, measuring the residual Al content and determining the rate of Al loss in the alloy is the most accurate method of predicting lifetime.[255]

1.24.5.1 Failure Mechanisms

In practice, two types of oxidation-induced failure can be distinguished.[256] A chemical failure occurs when the substrate is sufficiently depleted in Al that it can no longer form alumina. The most extreme example of such a failure is for FeCrAl(+RE) foil where no scale spallation occurs because the foil can deform and accommodate strain energy from the scale. When the foil is depleted in Al, a chromia scale has been observed to form beneath the alumina scale.[257] As Cr_2O_3 is less stable than Al_2O_3, normally this would not be thermodynamically possible. It occurs when Al is removed from the metal and the interface oxygen potential increases allowing Cr_2O_3 to form.

Prior to a chemical failure, a mechanical failure can cause a premature failure by cracking the scale and requiring reformation of alumina at a bare interface.[256] The mechanical failure could be due to the typical thermal stress (which can induce scale spallation), an applied stress to the component in service or a one-time upset or impact which removes the surface oxide. In this case, the C_b at failure is higher, reducing t_b.

1.24.5.2 Unusual Failure Mechanisms

Some unusual circumstances can cause early failure of alumina scales. Additional oxidants (discussed in the next section) can cause early failure as will environments that can otherwise degrade the alumina scale. As mentioned previously, the formation of Al concentration gradients in the alloy will result in earlier failures. This is generally not a problem for Fe-based alloys with relatively rapid Al diffusion (e.g., flat Al profiles in **Figures 20** and **40**). However, it appeared to be a problem for Fe–17Al + Hf, Ni-based alloy 214 (see **Figure 41**) and is likely a problem for Co-based alloys. There is little data in the literature for Ni- and Co-based alloys on residual Al profiles or lifetime as a function of specimen thickness.

Another unusual failure mechanism for Fe-based alloys has been attributed to the internal oxidation of Cr carbides on alloy grain boundaries resulting in

accelerated Fe-rich oxide formation at alloy grain boundaries, sometimes called 'broccoli' failures because of the eruption of the voluminous Fe-rich oxide.[258] This type of failure is found in alloys with higher C contents but no strong carbide former, for example, Y-doped FeCrAl and Fe–Al. The problem can be eliminated by the addition of a strong carbide former such as Hf or Ti, which is a common addition in commercial alloys, **Table 2**. For example, **Figure 42** shows the mass gain of ferritic Fe–17Al alloys tested at 1250 °C to accelerate their failure. With only Y or Y and Cr additions, t_b was relatively short compared to the specimen with a Hf addition. The early failures showed broccoli failures. However, when a small amount of Ti or Hf was added, the lifetime increased dramatically.

1.24.5.3 Strategies for Extending Lifetime

One goal of alloy development is to design alloys with longer lifetimes. Despite shortcomings, eqn [5] does focus attention on some of the key lifetime variables: the Al reservoir ($C_0 - C_b$) and the Al consumption rate by oxidation (k and n). It suggests that lifetime could be increased by decreasing the rate of consumption, or by increasing the Al reservoir either by increasing C_0 or decreasing C_b. As discussed previously, the scale growth rate can be decreased by RE optimization. However, in commercial alloys, the possibility of achieving narrow composition targets may be an unrealistic goal. In terms of increasing C_0, alloy mechanical properties and the phase equilibria limit the amount of Al that can be added without significant negative consequences to other properties. **Figure 41** shows the relatively low lifetimes for some commercial alloys, Ohmalloy 30 and 40 and SUH21, all with lower Al contents (**Tables 1 and 2**). However, these alloys are easier to fabricate, process and join than alloys with higher Al content such as ODS alloys and Aluchrom YHf. Also, FeCrAl alloys become very brittle above 12 at.% Al.[61] Decreasing C_b is virtually impossible for FeCrAl alloys because C_b is already close to zero. For ferritic Fe(Al) alloys with higher Al contents (up to 19%), attempts to lower C_b from ~10% for binary alloys have been unsuccessful.[12] Additions of 'third elements' Mn and Cr were explored with little success.[12,233] Manganese appears to become quickly incorporated into the scale near the end of life and Cr additions appear to increase the CTE resulting in increased spallation. A general strategy of lowering the CTE, possibly with refractory metal additions, may be possible but has not been successful for Fe-based alloys to date.[233] A low CTE Ni-based bond coating has been developed.[259]

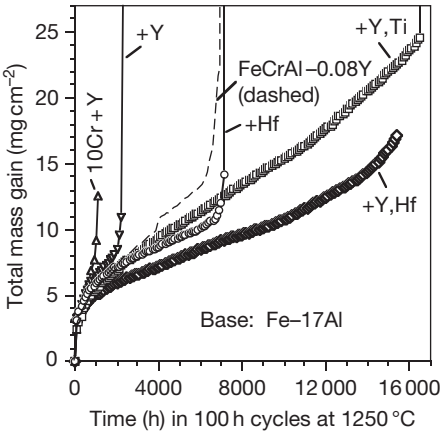

Figure 42 Total mass gain (specimen + spalled oxide) for ferritic Fe–17Al alloys (see **Table 2** examples) during 100 h cycles at 1250 °C in laboratory air. Specimens of alloys with only Y additions showed relatively short times to breakaway oxidation due to 'broccoli' formation.[258] Specimens with strong carbide-forming elements: Hf, Y + Hf or Y + Ti, prevent this form of attack associated with accelerated oxidation of grain boundary carbides. The co-doped alloy specimens had a much longer time to breakaway oxidation. Data from Pint.[12]

1.24.6 Effect of Environment

The previous sections discussed the oxidation behavior of alumina-forming alloys in O_2 or air with low levels of water vapor in the ambient laboratory environment. In practice, high temperature applications tend to involve more complex environments. However, because of the inherent chemical inertness (i.e., thermodynamic stability) of α-Al_2O_3, alumina-forming alloys tend to have an advantage over conventional chromia-forming alloys under these conditions.

1.24.6.1 Water Vapor

In actual applications, particularly those involving combustion, water vapor is commonly found in the environment. While Kofstad called the effect of water vapor on oxidation a 'forgotten' problem in 1991,[260] it has become a significant topic for research in the past decade because of increases in temperature application and the desire to use new materials. Also, combustion of hydrogen or synthetic natural gas from coal would increase the water content in the combustion product from 10 to 15% for natural gas or jet fuel to 60% for hydrogen, making water vapor more of a

concern.[261] As shown by Opila,[262] chromia and silica scales readily form oxy-hydroxides in the presence of H_2O and O_2 resulting in accelerated oxidation attack for chromia-forming alloys and silica-based ceramics.[263,264] For typical stainless steels at 650–800 °C, the Cr consumption becomes linear due to the evaporation.[265]

As α-Al_2O_3 is more stable than Cr_2O_3 or SiO_2, the reaction with water vapor is minimal until higher temperatures >1300 °C.[262] The effect of Al additions on resistance to water vapor is quite dramatic. Kvernes *et al.*[266] showed that small Al additions to Fe–Cr alloys were very effective in improving the oxidation resistance. Likewise, Pint *et al.*,[267] showed that additions of Al to austenitic Fe–15Cr–15Ni were very effective in reducing the detrimental role of water vapor. However, that study also showed that the addition of Al caused the formation of ferritic phases in the steel that decreased the 750 °C creep life by ~2 orders of magnitude, making the resulting alloy unacceptable for many applications. Recently, Brady and coworkers[67–69] showed that careful composition control and minor element additions could produce an Fe-based alumina-forming austenitic steel with very good creep strength and resistance to water vapor environments. This alloy is a potential solution to the problem of degradation of heat exchangers or recuperators for small turbines.[268] Compact, high-efficiency primary surface recuperators for these turbines require <100 µm thick foil with good creep and oxidation resistance.

The excellent resistance of alumina scales to water vapor has led to extensive work on alumina-forming coatings on Fe-based alloys for combustion and steam environments. Thin coatings can improve oxidation resistance to steam for Fe–9Cr alloys for >40 kh at 650 °C.[269] Ferritic Fe(Al,Cr) weld overlaid coatings have shown promising results for boiler applications at <600 °C.[270] Coatings are further addressed in a separate chapter.

Several studies have examined the effect of water vapor on Ni-based alloys.[261,271–274] The general conclusions focused on three effects of water vapor on alumina-scales are: (1) Water vapor increases the spallation rate of alumina scales, particularly for marginally adherent scales. Smialek[275] suggested that this could be due to water vapor increasing the crack growth rate at the metal–scale interface. **Figure 43** shows the specimen mass gain for NiAl + Hf and NiCrAlYHf specimens in dry O_2 and air with 10–90 vol.% H_2O. For NiCrAlYHf, the drop in mass gain suggests scale spallation which increases with

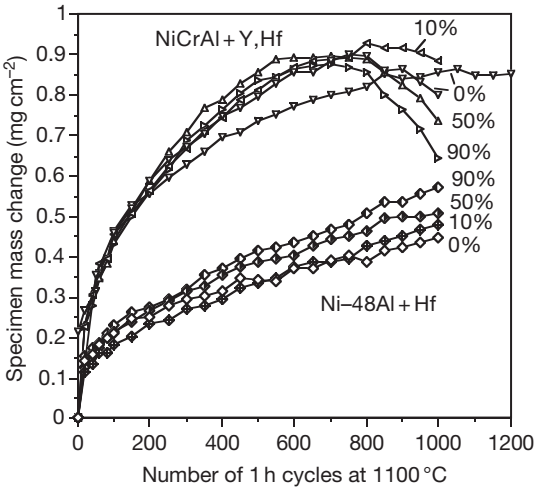

Figure 43 Specimen mass gain for cast Ni–20Cr–10Al + Y,Hf and Ni–48Al–0.05Hf specimens (see **Table 2**) exposed to 1 h cycles at 1100 °C in dry O_2 or air with various vol% of H_2O from 10 to 90%. The addition of water vapor caused a minor increase in the mass gain for Hf-doped NiAl and a slight increase in spallation (mass losses) after 800 cycles for NiCrAlYHf. Data from Pint[12] and Pint *et al.*[261]

H_2O content. (2) A small increase in the oxidation rate. The mass gain of NiAl + Hf increases with H_2O content suggesting a slight increase in the rate constant (**Figure 43**). This was also noted for Fe-based alloys.[276] (3) A decrease in selective oxidation. On low Al alloys, more Ni-rich spinel oxide was formed with the addition of water vapor. This is a particular concern for uncoated superalloys and γ–γ' NiPtAl coatings with low Al content.[82,261] An explanation for this decrease based on H injection into the substrate may apply to both alumina- and chromia-forming alloys.[277] Nevertheless, for adherent alumina-forming alloys with adequate Al, these effects are relatively minor as shown by the data in **Figure 43** where even 90% water vapor caused a minor effect at 1100 °C.

1.24.6.2 Sulfur and Hot Corrosion

A wide range of environments contain sulfur, sulfur-containing compounds (i.e., hot corrosion) or, more commonly, mixtures of S and O such as in coal-fired combustion (SO_x) or gasification (H_2S, low pO_2), which was extensively investigated in the 1980s. For purely sulfidizing and hot corrosion (salt) environments, alumina-forming alloys are only marginally effective since Al does not really form a selective, protective sulfide layer and can be fluxed away by sodium–sulfate salts. As a result, the sulfidation

reaction of the base metal is a key issue. Ni-based alumina-forming alloys will be catastrophically affected by the formation of a liquid Ni–S reaction product above 700 °C.[278,279] Cobalt-based alloys are thought to be more resistant to sulfidation. Therefore, CoCrAl alloys and coatings have been developed for their sulfidation and hot corrosion resistance.[280,281] For Fe-based alumina-formers, some improvement is associated with the addition of Al compared to FeCr alloys but the sulfidation rates are still relatively high.[282] For example, a 150 μm thick scale was formed in 7 h at 800 °C with a $pS_2 = 0.1$ Pa.

For oxidizing–sulfidizing environments, the performance of Fe-based alumina-forming alloys in petroleum environments has been investigated for more than 40 years.[283] Since then a great deal of work has been conducted on Fe(Al) and FeCrAl alloys in low oxygen, high sulfur pressure environments.[50,284–288] Under these conditions, binary (low Cr) Fe–Al alloys are generally superior to FeCrAl alloys because of the possible sulfidation reaction with Cr. However, ~19%Al is needed in Fe(Al) for this sulfidation resistance.[286] A similar level of Al was needed at the surface of Fe–Al coatings for a protective scale to form.[289] However, these experiments were typically performed at ~800 °C. At lower temperatures, 400–600 °C, where reaction rates are lower and it is more difficult to form alumina, the presence of Cr may be beneficial and work better than Fe–Al materials. This has been observed for Fe_3Al and FeCrAl porous metal filters used in sulfidizing environments.[12]

Several studies suggest that additions of Y and Zr are beneficial to corrosion resistance in sulfur-containing environments at 600–800 °C.[284,285] In some mixed O–S environments it is possible to form an alumina scale that could be protective. Another common strategy has been to preoxidize the alloy in an oxidizing environment prior to exposure to S-bearing gases, particularly for FeCrAl.[290–292] If metastable, cubic alumina phases form during preoxidation, the volume reduction and associated scale cracking during the transformation to α-Al_2O_3 will likely be detrimental to performance.[292] Thus, the preoxidation step must be controlled to assure an α-Al_2O_3 preoxidation scale. While preoxidation has been successful in laboratory tests, in practice it has been less effective. In some applications, the problem is probably due to the damage of the preoxidation scale during subsequent handling and joining.

Even when the alumina scale is adherent and dense, it has been shown that S will penetrate alumina scales and S was found segregated to α-Al_2O_3 grain boundaries using STEM after exposure to a H_2–H_2O–H_2S environment.[293] Cracks in the scale are another possible route for S penetration.

Hot corrosion, generally associated with Na_2SO_4 salts, can be decreased by the formation of an adherent alumina scale. For example, on γ–γ′ NiPtAl compositions, preoxidation was very effective in reducing hot corrosion attack.[91] Therefore, RE additions and Pt may be somewhat beneficial in hot corrosion.[294] However, because of the fundamental fluxing reaction controlling hot corrosion,[295] Cr is much more effective than Al or Pt in reducing hot corrosion attack.[296]

1.24.6.3 Carbon

For environments with high C activity where internal carburization and metal dusting occur,[297] alumina-forming alloys appear to be oxidation resistant. Compared to chromia-forming stainless steels, where the Cr_2O_3 scale appears to allow the ingress of C, alumina scales appear to prevent C penetration.[298,299] The addition of Al or alumina-forming coatings appears to solve many C-related oxidation problems.

Again, the issue of alloy strength and joining is a critical one for alloy selections in many relevant applications. Alumina-forming alloys may not have the necessary strength or can be difficult to fabricate or join for commercial applications where high carbon activities are a concern. Recently, cast NiCrAlY alloy tubes have been developed for steam reforming applications.[29] The authors reported no major drop in creep strength or weldability. In addition, the relatively inert alumina scale had an additional benefit of reducing surface coke formation.

1.24.6.4 Nitrogen

Nitrogen containing environments appear to be one condition that can cause problems for alumina-forming alloys. It appears that N can permeate through alumina scales and internally nitride alumina-forming alloys.[93,299] Most likely, the N permeation is not diffusion through dense alumina but penetration in the cracks in the scale. However, diffusion along α-Al_2O_3 grain boundaries, like S, cannot be ruled out. For Fe-based alumina-forming alloys, internal nitridation has been observed in atmospheres with predominantly N and low pO_2.[299–301] Both Al and Ti (when present) are internally nitride. Internal nitridation of Al is observed at higher pO_2 levels when the Al content is decreased

during extended exposure. As mentioned previously, internal nitridation has been observed for undoped Fe(Al) alloys in air but not for undoped FeCrAl.[93]

For Ni-based alloys, Han and Young[302] found that internal oxidation and nitridation of Ni–Al–Cr alloys was a result of heavy spallation which depleted the alloy in Al and caused a phase transformation. The internal nitridation of Ni-based superalloys is commonly observed[303] and was briefly reviewed by Krupp and Christ.[304] Their study of model NiCrAlTi alloys concluded that higher Cr contents increased the N solubility and diffusivity in NiCrAlTi alloys.

Bennett and coworkers[305] also found internal nitridation of FeCrAl by 'crevice corrosion.' In this case, it was proposed that in crevices in components, O could be locally depleted in the gas due to reaction with the surrounding metal and stagnant flow. The resulting high N and low O environment could cause internal attack.

1.24.7 Summary

Alumina-forming alloys are the most oxidation resistant alloys due to their low oxidation rates and thermodynamically stable scale. However, because of the negative effects of Al on alloy mechanical properties, fabrication, and joining, alumina-forming alloys are not widely used except when needed in very high temperature applications or in particular environments such as those with water vapor (or steam) and high C activities. As application temperatures increase in search of higher generation and production efficiencies, the use of alumina-forming alloys or coatings will inevitably increase.

Acknowledgments

The author would like to thank his colleagues at ORNL, acknowledge the discussions with I. G. Wright, appreciate the comments on the manuscript from M. P. Brady and P. F. Tortorelli, and gratefully acknowledge the assistance provided by the dedicated technical staff, L. D. Chitwood, G. W. Garner, J. L. Moser, H. F. Longmire and L. R. Walker for the experimental work. The manuscript preparation was sponsored by the U.S. Department of Energy, Fossil Energy Advanced Research Materials Program and work at the SHaRE User Facility by the Division of Scientific User Facilities, under contract DE-AC05-00OR22725 with UT-Battelle, LLC.

References

1. Whittle, D. P.; Stringer, J. *Philos. Trans. R. Soc. London, Ser. A* **1980**, *295*, 309–329.
2. Lang, E. Ed. *The Role of Active Elements in the Oxidation Behavior of High Temperature Metals and Alloys*; Elsevier Applied Science: London, 1989.
3. King, W. E. Ed. *Material Science Forum 43, The Reactive Element Effect on High Temperature Oxidation – After Fifty Years*; Trans Tech Publications: Switzerland, 1989.
4. Moon, D. P. *Mater. Sci. Technol.* **1989**, *5*, 754–764.
5. Strawbridge, A.; Hou, P. Y. *Mater. High Temp.* **1994**, *12*, 177–1781.
6. Pint, B. A. *Mater. Res. Bull.* **1994**, *19*(10), 26–30.
7. Pint, B. A.; Garratt-Reed, A. J.; Hobbs, L. W. *Mater. High Temp.* **1995**, *13*, 3–16.
8. Pint, B. A. *Oxid. Met.* **1996**, *45*, 1–37.
9. Stott, F. H. *Mater. Sci. Forum* **1997**, *251–254*, 19–32.
10. Quadakkers, J.; Singheiser, L. *Mater. Sci. Forum* **2001**, *369–372*, 77–92.
11. Pint, B. A. In *Progress in Understanding the Reactive Element Effect Since the Whittle and Stringer Literature Review*, Proceedings of John Stringer Symposium on High Temperature Corrosion; Tortorelli, P. F., Wright, I. G., Hou, P. Y., Eds.; ASM International: Materials Park, OH, 2003; pp 9–19.
12. Pint, B. A. Unpublished oxidation data, ORNL, Oak Ridge, TN, 1994–2008.
13. Agarwal, D. C.; Brill, U. Performance of Alloy 602CA (UNS N06025) in high temperature environments up to 1200°C (~2200°F), NACE Paper 00-521, Houston, TX, Presented at NACE Corrosion 2000, Orlando, FL, March 2000.
14. Pint, B. A.; Keiser, J. R. Alloy selection for high temperature heat exchangers, NACE Paper 06-469, Houston, TX, Presented at NACE Corrosion 2006, San Diego, CA, March 2006.
15. Pint, B. A.; Tortorelli, P. F.; Wright, I. G. *Oxid. Met.* **2002**, *58*, 73–101.
16. Pint, B. A.; DiStefano, J. R.; Wright, I. G. *Mater. Sci. Eng. A* **2006**, *415*, 255–263.
17. Lowell, C. E.; Barrett, C. A.; Palmer, R. W.; Auping, J. V.; Probst, H. B. *Oxid. Met.* **1991**, *36*, 81–112.
18. Nesbitt, J. A.; Vinarcik, E. J.; Barrett, C. A.; Doychak, J. *Mater. Sci. Eng. A* **1992**, *153*, 561–566.
19. Evans, H. E.; Lobb, R. C. *Corros. Sci.* **1984**, *24*, 209–222.
20. Przybylski, K.; Yurek, G. J. *Mater. Sci. Forum* **1989**, *43*, 1–74.
21. Heck, R. M.; Farrauto, R. J. *Appl. Catal. A* **2001**, *221*, 443–457.
22. Kajita, S.; Dalla Betta, R. *Catal. Today* **2003**, *83*, 279–288.
23. *Stainless Steel Ohmaloy® 30 and Ohmaloy® 40 Resistance Alloys*; ATI Allegheny Ludlum: Brackenridge, PA, 2007.
24. Benjamin, J. S. *Metall. Trans.* **1970**, *1*, 2943–2951.
25. Nicholls, J. R.; Newton, R.; Simms, N. J.; Norton, J. F. *Mater. High Temp.* **2003**, *20*, 93–108.
26. Pint, B. A.; Swindeman, R. W.; More, K. L.; Tortorelli, P. F. Materials selection for high temperature (750–1000°C) metallic recuperators for improved efficiency microturbines, ASME Paper #2001-GT-445, Presented at the International Gas Turbine and Aeroengine Congress and Exhibition, New Orleans, LA, June 4–7, 2001.
27. Wright, I. G.; Pint, B. A.; Lee, W. Y.; Alexander, K. B.; Prüßner, K. In *High Temperature Surface Engineering*; Nicholls, J., Rickerby, D., Eds.; Institute of Materials: London, UK, 2000; pp 95–113.

28. Smialek, J. L.; Pint, B. A. *Mater. Sci. Forum* **2001**, *369–372*, 459–466.
29. Kirchheiner, R. R.; Becker, P.; Young, D. J.; Durham, R. Improved oxidation and coking resistance of a new alumina forming Alloy 60 HT for the petrochemical industry, NACE Paper 05-428, Houston, TX, Presented at NACE Corrosion 2005, Houston, TX, April 2005.
30. Haynes, J. A.; Pint, B. A.; Porter, W. D.; Wright, I. G. *Mater. High Temp.* **2004**, *21*, 87–94.
31. Toscano, J.; Gil, A.; Huttel, T.; Wessel, E.; Naumenko, D.; Singheiser, L.; Quadakkers, W. J. *Surf. Coat. Technol.* **2007**, *202*, 603–607.
32. Malang, S.; Deckers, H.; Fischer, U.; John, H.; Meyder, R.; Norajitra, P.; Reimann, J. J.; Reiser, H.; Rust, K. *Fusion Eng. Des.* **1991**, *14*, 373–399.
33. Fowler, J. D.; Causey, R. A.; Chandra, D.; Elleman, T. S.; Verghese, K. *J. Vac. Sci. Technol.* **1976**, *13*, 401–402.
34. Steward, S. A. Review of hydrogen isotope permeability through materials, LLNL Report #UCRL-53441, Lawrence Livermore National Laboratory, Livermore, CA, 1983.
35. Konys, J.; Aiello, A.; Benamati, G.; Giancarli, L. *Fusion Sci. Technol.* **2005**, *47*, 844–850.
36. Müller, G.; Heinzel, A.; Konys, J.; Schumacher, G.; Weisenburger, A.; Zimmermann, F.; Engelko, V.; Rusanov, A.; Markov, V. *J. Nucl. Mater.* **2002**, *301*, 40–46.
37. Lauf, R. J.; DeVan, J. H. *J. Electrochem. Soc.* **1992**, *139*, 2087–2091.
38. Hubberstey, P.; Sample, T.; Terlain, A. *Fusion Technol.* **1995**, *28*, 1194–1199.
39. Hubberstey, P. *J. Nucl. Mater.* **1997**, *247*, 208–214.
40. Pint, B. A.; More, K. L. *J. Nucl. Mater.* **2008**, *376*, 108–113.
41. Quadakkers, W. J.; Bennett, M. J. *Mater. Sci. Technol.* **1994**, *10*, 126–131.
42. Quadakkers, W. J.; Bongartz, K. *Mater. Corros.* **1994**, *45*, 232–241.
43. Stott, F. H.; Wood, G. C.; Stringer, J. *Oxid. Met.* **1995**, *44*, 113–145.
44. Pettit, F. S. *Trans. Metall. Soc. AIME* **1967**, *239*, 1296–1305.
45. Pint, B. A. *Surf. Coat. Technol.* **2004**, *188–189*, 71–78.
46. Prescott, R.; Graham, M. J. *Oxid. Met.* **1992**, *38*, 233–254.
47. Sykes, C.; Bampfylde, J. W. *J. Iron Steel Inst. Adv. Copy* **1934**, *12*, 22.
48. Saegusa, F.; Lee, L. *Corrosion* **1966**, *22*, 168–177.
49. Boggs, W. E. *J. Electrochem. Soc.* **1971**, *118*, 906–913.
50. DeVan, J. H.; Tortorelli, P. F. *Corros. Sci.* **1993**, *35*, 1065–1071.
51. Pint, B. A.; Leibowitz, J.; DeVan, J. H. *Oxid. Met.* **1999**, *51*, 181–197.
52. Pint, B. A.; Wright, I. G. *Mater. Sci. Forum* **2004**, *461–464*, 799–806.
53. Zhang, Z. G.; Gesmundo, F.; Hou, P. Y.; Niu, Y. *Corros. Sci.* **2006**, *48*, 741–765.
54. Wagner, C. *Corros. Sci.* **1965**, *5*, 751–764.
55. Zhang, X. J.; Wang, S. Y.; Gesmundo, F.; Niu, Y. *Oxid. Met.* **2006**, *65*, 151–165.
56. Pint, B. A.; Paul, L. D. Oxidation behavior of welded and base metal UNS N06025, NACE Paper 07-470, Houston, TX, Presented at NACE Corrosion 2007, Nashville, TN, March 2007.
57. Giggins, C. S.; Pettit, F. S. *J. Electrochem. Soc.* **1971**, *118*, 1782–1790.
58. Wallwork, G. R.; Hed, A. Z. *Oxid. Met.* **1971**, *3*, 171–184.
59. Wallwork, G. R. *Rep. Prog. Phys.* **1976**, *39*, 401–485.
60. Stott, F. H.; Wood, G. C.; Hobby, M. G. *Oxid. Met.* **1971**, *3*, 103–113.
61. Wukusick, C. S.; Collins, J. F. *Mater. Res. Stand.* **1964**, *4*, 637–646.
62. Sauer, J. P.; Rapp, R. A.; Hirth, J. P. *Oxid. Met.* **1982**, *18*, 285–294.
63. De Freitas Cunha Lins, V.; Freitas, M. A.; De Paula e Silva, E. M. *Corros. Sci.* **2004**, *46*, 1895–1907.
64. Boggs, W. E. *Oxid. Met.* **1976**, *10*, 277–289.
65. Wu, Y.; Niu, Y. *Corros. Sci.* **2007**, *49*, 1656–1672.
66. Sakiyama, M.; Tomaszewicz, P.; Wallwork, G. R. *Oxid. Met.* **1979**, *13*, 311–330.
67. Yamamoto, Y.; Brady, M. P.; Lu, Z. P.; Maziasz, P. J.; Liu, C. T.; Pint, B. A.; More, K. L.; Meyer, H. M.; Payzant, E. A. *Science* **2007**, *316*, 433–436.
68. Brady, M. P.; Yamamoto, Y.; Santella, M. L.; Maziasz, P. J.; Pint, B. A.; Liu, C. T.; Lu, Z. P.; Bei, H. *JOM* **2008**, *60*(7), 12–18.
69. Brady, M. P.; Yamamoto, Y.; Santella, M. L.; Pint, B. A. *Scr. Mater.* **2007**, *57*, 1117–1120.
70. Castello, P.; Stott, F. H.; Gesmundo, F. *Corros. Sci.* **1999**, *41*, 901–918.
71. Merz, M. D. *Metall. Trans. A* **1979**, *10*, 71–77.
72. Baer, D. R.; Merz, M. D. *Metall. Trans. A* **1980**, *11*, 1973–1980.
73. Yurek, G. J.; Eisen, D.; Garratt-Reed, A. J. *Metall. Trans. A* **1982**, *13*, 473–485.
74. Maloney, M. J. Ph.D. Thesis, Massachusetts Institute of Technology, Cambridge, MA, 1989.
75. Maloney, M. J.; Yurek, G. J. In *Composites/Corrosion-Coatings of Advanced Materials*, Proceedings IMAM-4; Kimura, S., Kobayashi, A., Umekawa, S., Nii, K., Saito, Y., Yoshimura, M., Eds.; Materials Research Society: Pittsburgh, PA, 1989; Vol. 1, pp 383–388.
76. Goedjen, J. G.; Shores, D. A. *Oxid. Met.* **1992**, *37*, 125–142.
77. Wang, F. *Oxid. Met.* **1997**, *48*, 215–224.
78. Chen, G.; Lou, H. *Oxid. Met.* **2000**, *54*, 155–162.
79. Gleeson, B.; Wang, W.; Hayashi, S.; Sordelet, D. *Mater. Sci. Forum* **2004**, *461–464*, 213–222.
80. Izumi, T.; Gleeson, B. *Mater. Sci. Forum* **2005**, *522–523*, 221–228.
81. Kartono, R.; Young, D. J. *Mater. Corros.* **2008**, *59*, 455–462.
82. Pint, B. A.; Haynes, J. A.; More, K. L.; Schneibel, J. H.; Zhang, Y.; Wright, I. G. In *Superalloys 2008*; Reed, R. C., *et al.* Ed.; TMS: Warrendale, PA, 2008; pp 641–650.
83. Pint, B.A.; More, K.L.; Wright, I.G. *Oxid. Met.* in preparation.
84. Felten, E. J. *Oxid. Met.* **1976**, *10*, 23–28.
85. Tatlock, G. J.; Hurd, T. J. *Oxid. Met.* **1984**, *22*, 201–226.
86. Fountain, J. G.; Golightly, F. A.; Stott, F. H.; Wood, G. C. *Oxid. Met.* **1976**, *10*, 341–345.
87. Ballard, D. L.; Martin, P. L.; Gleeson, B.; Menon, S. Structure and oxidation behavior of PGM modified nickel-base alloys, Presentation at 18th AeroMat Conference and Expo, Baltimore, MD, ASM, June 2007.
88. Doychak, J.; Rühle, M. *Oxid. Met.* **1989**, *31*, 431–452.
89. Pint, B. A.; Garratt-Reed, A. J.; Hobbs, L. W. *Oxid. Met.* **2001**, *56*, 119–145.
90. Copland, E. *J. Phase Equilib. Diff.* **2007**, *28*, 38–48.
91. Deodeshmukh, V.; Mu, N.; Li, B.; Gleeson, B. *Surf. Coat. Technol.* **2006**, *201*, 3836–3840.
92. Zhang, Y.; Haynes, J. A.; Pint, B. A.; Wright, I. G. *Surf. Coat. Technol.* **2005**, *200*, 1259–1263.
93. Pint, B. A.; Dwyer, M. J.; Deacon, R. M. *Oxid. Met.* **2008**, *69*, 211–231.

94. Pint, B. A.; More, K. L.; Wright, I. G. *Mater. High Temp.* **2003**, *20*, 375–386.
95. Hagel, W. C. *Corrosion* **1965**, *21*, 316–326.
96. Kear, B. H.; Pettit, F. S.; Fornwalt, D. E.; Lemaire, L. P. *Oxid. Met.* **1971**, *3*, 557–569.
97. Smialek, J. L.; Gibala, R. *Metall. Trans. A* **1983**, *14*, 2143–2161.
98. Quadakkers, W. J.; Elschner, A.; Speier, W.; Nickel, H. *Appl. Surf. Sci.* **1991**, *52*, 271–287.
99. Rybicki, G. C.; Smialek, J. L. *Oxid. Met.* **1989**, *31*, 275–304.
100. Brumm, M. W.; Grabke, H. J. *Corros. Sci.* **1992**, *33*, 1677–1690.
101. Young, E. W. A.; de Wit, J. H. W. *Oxid. Met.* **1986**, *26*, 351–361.
102. Doychak, J.; Smialek, J. L.; Mitchell, T. E. *Metall. Trans. A* **1989**, *20*, 499–518.
103. Prüßner, K.; Bruley, J.; Salzberger, U.; Zweygart, H.; Schumann, E.; Rühle, M. In *Microscopy of Oxidation 2*; Newcomb, S. B., Bennett, M. J., Eds.; Institute of Metals: London, 1993; pp 435–444.
104. Pint, B. A.; Martin, J. R.; Hobbs, L. W. *Solid State Ionics* **1995**, *78*, 99–107.
105. Yang, J. C.; Schumann, E.; Levin, I.; Rühle, M. *Acta Mater.* **1998**, *46*, 2195–2201.
106. Bye, G. C.; Simpkin, G. T. *J. Am. Ceram. Soc.* **1974**, *57*, 367–371.
107. Pint, B. A.; Jain, A.; Hobbs, L. W. In *High Temperature Ordered Intermetallics V, Symposium Proceedings*; Baker, I., Darolia, R., Whittenberger, J. D., Yoo, M. H., Eds.; Materials Research Society: Pittsburgh, PA, 1993; Vol. 288, pp 1013–1018.
108. Ramanarayanan, T. A.; Raghavan, M.; Petkovic-Luton, R. In *Proceedings of JIMIS-3, High Temperature Corrosion Transactions Supplement* Japan Institute of Metals: Tokyo, Japan, 1983; Vol. 24, pp 199–206.
109. Quadakkers, W. J.; Schmidt, K.; Grubmeier, H.; Wallura, E. *Mater. High Temp.* **1992**, *10*, 23–32.
110. Dryepondt, S.; Pint, B. A.; Lara-Curzio, E. *Acta Mater*. in preparation.
111. Bennett, M. J.; Newton, R.; Nicholls, J. R.; Al-Badairy, H.; Tatlock, G. J. *Mater. Sci. Forum* **2004**, *461–464*, 463–472.
112. N'Dah, E.; Galerie, A.; Wouters, Y.; Goossens, D.; Naumenko, D.; Kochubey, V.; Quadakkers, W. J. *Mater. Corros.* **2005**, *56*, 843–847.
113. Burtin, P.; Brunelle, J. P.; Pijolat, M.; Soustelle, M. *Appl. Catal.* **1987**, *34*, 225–238.
114. Pint, B. A.; Treska, M.; Hobbs, L. W. *Oxid. Met.* **1997**, *47*, 1–20.
115. Pijolat, M.; Dauzat, M.; Soustelle, M. *Thermochim. Acta* **1987**, *122*, 71–77.
116. Moseley, P. T.; Hyde, K. R.; Bellamy, B. A.; Tappin, G. *Corros. Sci.* **1984**, *24*, 547–565.
117. Hindam, H. M.; Whittle, D. P. *Oxid. Met.* **1982**, *18*, 245–284.
118. Hou, P. Y.; Shui, Z. R.; Chuang, G. Y.; Stringer, J. *J. Electrochem. Soc.* **1992**, *139*, 1119–1126.
119. Wagner, C. *Atom Movements*; American Society of Metals: Cleveland, OH, 1951; pp 153–173.
120. Quadakkers, W. J. *Mater. Corros.* **1990**, *41*, 659–668.
121. Quadakkers, W. J.; Naumenko, D.; Wessel, E.; Kochubey, V.; Singheiser, L. *Oxid. Met.* **2004**, *61*, 17–37.
122. Saunders, S. R. J.; Evans, H. E.; Li, M.; Gohil, D. D.; Osgerby, S. *Oxid. Met.* **1997**, *48*, 189–200.
123. Tolpygo, V. K.; Dryden, J. R.; Clarke, D. R. *Acta Mater.* **1998**, *46*, 927–937.
124. Hou, P. Y.; Paulikas, A. P.; Veal, B. W. *Mater. Sci. Forum* **2004**, *461–464*, 671–680.
125. Evans, H. E.; Norfolk, D. J.; Swan, T. *J. Electrochem. Soc.* **1978**, *125*, 1180–1185.
126. Doychak, J. In *Intermetallic Compounds, Principles*; Westbrook, J. H., Fleischer, R. L., Eds.; John Wiley & Sons: New York, NY, 1994; Vol. 1, pp 977–1016.
127. Pint, B. A.; Wright, I. G.; Lee, W. Y.; Zhang, Y.; Prüßner, K.; Alexander, K. B. *Mater. Sci. Eng. A* **1998**, *245*, 201–211.
128. Pint, B. A.; More, K. L.; Tortorelli, P. F.; Porter, W. D.; Wright, I. G. *Mater. Sci. Forum* **2001**, *369–372*, 411–418.
129. Pint, B. A. *J. Am. Ceram. Soc.* **2003**, *86*, 686–695.
130. Hindam, H.; Whittle, D. P. *J. Electrochem. Soc.* **1982**, *129*, 1147–1149.
131. Kvernes, I. *Oxid. Met.* **1973**, *6*, 45–64.
132. Allam, I. M.; Whittle, D. P.; Stringer, J. *Oxid. Met.* **1978**, *12*, 35–66.
133. Pivin, J. C.; Delaunay, D.; Roques-Carmes, C.; Huntz, A. M.; Lacombe, P. *Corros. Sci.* **1980**, *20*, 351–373.
134. Clemens, D.; Bongartz, K.; Speier, W.; Hussey, R. J.; Quadakkers, W. J. *Fresenius J. Anal. Chem.* **1993**, *346*, 318–322.
135. Pint, B. A.; Alexander, K. B. *J. Electrochem. Soc.* **1998**, *145*, 1819–1829.
136. Balmain, J.; Loudjani, M. K.; Huntz, A. M. *Mater. Sci. Eng. A* **1997**, *224*, 87–100.
137. Yurek, G. J. In *Corrosion Mechanisms*; Mansfeld, F., Ed.; Marcel Dekker: New York, 1987; pp 397–446.
138. Oishi, Y.; Kingery, W. D. *J. Chem. Phys.* **1960**, *33*, 480–486.
139. Paladino, A. E.; Kingery, W. D. *J. Am. Ceram. Soc.* **1962**, *37*, 957–962.
140. Pint, B. A.; Deacon, R. M. *J. Appl. Phys.* **2005**, *97*(11), 116111.
141. Heuer, A. H. *J. Eur. Ceram. Soc.* **2008**, *28*, 1495–1507.
142. Kim, C. K. *Oxid. Met.* **1996**, *45*, 133–152.
143. Tien, J. K.; Pettit, F. S. *Metall. Trans. A* **1972**, *3*, 1587–1599.
144. Cotell, C. M.; Yurek, G. J.; Hussey, R. J.; Mitchell, D. F.; Graham, M. J. *J. Electrochem. Soc.* **1987**, *134*, 1871–1872.
145. Cotell, C. M.; Yurek, G. J.; Hussey, R. J.; Mitchell, D. F.; Graham, M. J. *Oxid. Met.* **1990**, *34*, 173–200.
146. Jedlinski, J.; Borchardt, G.; Mrowec, S. *Solid State Ionics* **1992**, *50*, 67–74.
147. Felten, E. J.; Pettit, F. S. *Oxid. Met.* **1976**, *10*, 189–223.
148. Reddy, K. P. R.; Smialek, J. L.; Cooper, A. R. *Oxid. Met.* **1982**, *17*, 429–449.
149. Quadakkers, W. J.; Holzbrecher, H.; Briefs, K. G.; Beske, H. *Oxid. Met.* **1989**, *32*, 67–88.
150. Pint, B. A.; Martin, J. R.; Hobbs, L. W. *Oxid. Met.* **1993**, *39*, 167–195.
151. Versaci, R. A.; Clemens, D.; Quadakkers, W. J.; Hussey, R. *Solid State Ionics* **1993**, *59*, 235–242.
152. Prescott, R.; Mitchell, D. F.; Graham, M. J.; Doychak, J. *Corros. Sci.* **1995**, *37*, 1341–1364.
153. Mennicke, C.; Schumann, E.; Rühle, M.; Hussey, R. J.; Sproule, G. I.; Graham, M. J. *Oxid. Met.* **1998**, *49*, 455–466.
154. Ecer, G. M.; Singh, R. B.; Meier, G. H. *Oxid. Met.* **1982**, *18*, 55–81.
155. Kofstad, P. *Oxid. Met.* **1985**, *24*, 265–276.
156. Ramanarayanan, T. A.; Raghavan, M.; Petkovic-Luton, R. *J. Electrochem. Soc.* **1984**, *131*, 923–931.
157. Przybylski, K.; Garratt-Reed, A. J.; Pint, B. A.; Katz, E. P.; Yurek, G. J. *J. Electrochem. Soc.* **1987**, *134*, 3207–3208.
158. Li, C. W.; Kingery, W. D. In *Structure and Properties of MgO and Al_2O_3 Ceramics, Advances in Ceramics;* American Ceramic Society: Columbus, OH, 1984; Vol. 10, pp 368–378.
159. Kingery, W. D. *Solid State Ionics* **1984**, *12*, 299–307.

160. Pint, B. A.; Garratt-Reed, A. J.; Hobbs, L. W. *J. Am. Ceram. Soc.* **1998**, *81*, 305–314.
161. Fang, J.; Thompson, A. M.; Harmer, M. P.; Chan, H. M. *J. Am. Ceram. Soc.* **1997**, *80*, 2005–2012.
162. Bedu-Amissah, K.; Rickman, J. M.; Chan, H. M.; Harmer, M. P. *J. Am. Ceram. Soc.* **2007**, *90*, 1551–1555.
163. Cho, J.; Harmer, M. P.; Chan, H. M.; Rickman, J. M.; Thompson, A. M. *J. Am. Ceram. Soc.* **1997**, *80*, 1013–1017.
164. Yoshida, H.; Ikuhara, Y.; Sakuma, T. *Acta Mater.* **2002**, *50*, 2955–2966.
165. Veal, B. W.; Paulikas, A. P.; Gleeson, B.; Hou, P. Y. *Surf. Coat. Technol.* **2007**, *202*, 608–612.
166. Atkinson, A.; Taylor, R. I.; Hughes, A. E. *Philos. Mag. A* **1982**, *45*, 979–998.
167. Sheasby, J. S.; Jory, D. B. *Oxid. Met.* **1977**, *12*, 527–539.
168. Huntz, A. M.; Moulin, G.; Lesage, B. *Contribution of Combined Techniques for Studying Oxidation Mechanisms*, Proceedings of the 9th International Congress on Metallic Corrosion; National Research Council of Canada: Ottawa, Canada, 1984; Vol. 2, pp 400–405.
169. Nicolas-Chaubet, D.; Huntz, A. M.; Millot, F. *Coll. Phys.* **1990**, *51*, 1015–1020.
170. Ben Abderrazik, G.; Millot, F.; Moulin, G.; Huntz, A. M. *J. Am. Ceram. Soc.* **1985**, *68*, 307–314.
171. Tortorelli, P. F.; More, K. L.; Specht, E. D.; Pint, B. A.; Zscack, P. *Mater. High Temp.* **2003**, *20*, 303–310.
172. Veal, B. W.; Paulikas, A. P.; Hou, P. Y. *Nat. Mater.* **2006**, *5*, 349–351.
173. Hou, P. Y.; Paulikas, A. P.; Veal, B. W. *Mater. Sci. Forum* **2006**, *522–523*, 433–440.
174. Reddy, A.; Hovis, D. B.; Heuer, A. H.; Paulikas, A. P.; Veal, B. W. *Oxid. Met.* **2007**, *67*, 153–177.
175. Lipkin, D. M.; Clarke, D. R. *Oxid. Met.* **1995**, *45*, 267–280.
176. Christensen, R. J.; Tolpygo, V. K.; Clarke, D. R. *Acta Mater.* **1997**, *45*, 1761–1766.
177. Rhines, F. N.; Wolf, J. S. *Metall. Trans.* **1970**, *1*, 1701–1710.
178. Golightly, F. A.; Stott, F. H.; Wood, G. C. *Oxid. Met.* **1976**, *10*, 163–187.
179. Golightly, F. A.; Stott, F. H.; Wood, G. C. *J. Electrochem. Soc.* **1979**, *126*, 1035–1042.
180. Tolpygo, V. K.; Grabke, H. J. *Oxid. Met.* **1994**, *41*, 343–364.
181. Tolpygo, V. K. *Oxid. Met.* **1999**, *51*, 449–477.
182. Stott, F. H.; Wood, G. C.; Golightly, F. A. *Corros. Sci.* **1979**, *19*, 869–887.
183. Fox, P.; Tatlock, G. J. *Mater. Sci. Technol.* **1988**, *4*, 439–445.
184. Tolpygo, V. K.; Clarke, D. R. *Acta Mater.* **1998**, *46*, 5153–5166.
185. Mennicke, C.; Schumann, E.; Ulrich, C.; Rühle, M. *Mater. Sci. Forum* **1997**, *251–254*, 389–396.
186. Pint, B. A. *Oxid. Met.* **1997**, *48*, 303–328.
187. Dryepondt, S.; Pint, B. A. *Mater. Sci. Eng. A* **2008**, *497*, 224–230.
188. Pint, B. A. *Mater. Sci. Forum* **1997**, *251–254*, 397–404.
189. Pint, B. A.; Garratt-Reed, A. J.; Hobbs, L. W. *J. Phys. IV* **1993**, *3*(C9), 247–255.
190. Nychka, J. A.; Clarke, D. R. *Oxid. Met.* **2005**, *63*, 325–352.
191. Lance, M. J.; Pint, B. A. Unpublished data; ORNL, Oak Ridge, TN, 1999.
192. Naumenko, D.; Kochubey, V.; Le Coze, J.; Wessel, E.; Singheiser, L.; Quadakkers, W. J. *Mater. Sci. Forum* **2004**, *461–464*, 489–495.
193. Provenzano, V.; Sadananda, K.; Louat, N. P.; Reed, J. R. *Surf. Coat. Technol.* **1988**, *36*, 61–74.
194. Grabke, H. J.; Weimer, D.; Viefhaus, H. *Appl. Surf. Sci.* **1991**, *47*, 243–250.
195. Jedlinski, J.; Bennett, M. J.; Evans, H. E. *Mater. High Temp.* **1994**, *12*, 169–175.
196. Hou, P. Y.; Saunders, S. R. J. *Mater. High Temp.* **2005**, *22*, 121–130.
197. Hou, P. Y.; Priimak, K. *Oxid. Met.* **2005**, *63*, 113–130.
198. Stott, F. H.; Golightly, F. A.; Wood, G. C. *Corros. Sci.* **1979**, *19*, 889–906.
199. Kumar, A.; Nasrallah, M.; Douglass, D. L. *Oxid. Met.* **1974**, *8*, 227–263.
200. Giggins, C. S.; Kear, B. H.; Pettit, F. S.; Tien, J. K. *Metall. Trans.* **1974**, *5*, 1685–1688.
201. Antill, J. E.; Peakall, K. A. *J. Iron Steel Inst. Adv. Copy* **1967**, *205*, 1136–1142.
202. Kingsley, L. M.; Stringer, J. *Oxid. Met.* **1989**, *32*, 371–378.
203. Pint, B. A. *Oxid. Met.* **1998**, *49*, 531–560.
204. Hou, P. Y. *Oxid. Met.* **1999**, *52*, 337–351.
205. Hou, P. Y.; Stringer, J. *J. Phys. IV* **1993**, *3*(C9), 231–240.
206. Quadakkers, W. J.; Huczkowski, P.; Naumenko, D.; Zurek, J.; Meier, G. H.; Niewolak, L.; Singheiser, L. *Mater. Sci. Forum* **2008**, *595–598*, 1111–1118.
207. Gupta, D. K.; Duvall, D. S. In *Superalloys*; Gell, M., *et al.* Eds.; TMS: Warrendale, PA, 1984; pp 711–720.
208. Sigler, D. R. *Oxid. Met.* **1989**, *32*, 337–355.
209. Ikeda, Y.; Nii, K.; Yoshihara, K. *Trans. Jpn. Inst. Met.* **1983**, *24*, 207–214.
210. Funkenbush, A. W.; Smeggil, J. G.; Bornstein, N. S. *Metall. Trans. A* **1985**, *16*, 1164–1166.
211. Smeggil, J. G.; Funkenbusch, A. W.; Bornstein, N. S. *Metall. Trans. A* **1986**, *17*, 923–932.
212. Smialek, J. L. *Metall. Trans. A* **1987**, *18*, 164–167.
213. Quadakkers, W. J.; Wasserfuhr, C.; Khanna, A. S.; Nickel, H. *Mater. Sci. Technol.* **1988**, *4*, 1119–1125.
214. Smialek, J. L.; Jayne, D. T.; Schaeffer, J. C.; Murphy, W. H. *Thin Solid Films* **1994**, *253*, 285–292.
215. Meier, G. H.; Pettit, F. S.; Smialek, J. L. *Mater. Corros.* **1995**, *46*, 232–240.
216. Sarioglu, C.; Stinner, C.; Blachere, J. R.; Birks, N.; Pettit, F. S.; Meier, G. H. In *Superalloys*; Kissinger, R. D., Deye, D. J., Anton, D. L., Cetel, A. D., Nathal, M. V., Pollack, T. M., Woodford, D. A., Eds.; TMS: Warrendale, PA, 1996; pp 71–80.
217. Lees, D. G. *Oxid. Met.* **1987**, *27*, 75–81.
218. Hou, P. Y.; Stringer, J. *Oxid. Met.* **1992**, *38*, 323–345.
219. Hou, P. Y. *Annu. Rev. Mater. Res.* **2008**, *38*, 275–298.
220. Briant, C. L.; Luthra, K. L. *Metall. Trans. A* **1988**, *19*, 2099–2108.
221. Yang, S.; Wang, F. *Oxid. Met.* **2006**, *65*, 195–205.
222. Tolpygo, V. K.; Grabke, H. J. *Scr. Mater.* **1997**, *38*, 123–129.
223. Smialek, J. L. *Oxid. Met.* **2001**, *55*, 75–86.
224. Harris, K.; Wahl, J. B. In *Superalloys*; Green, K. A., Pollock, T. M., Harada, H., Howson, T. E., Reed, R. C., Schirra, J., Walston, S., Eds.; TMS: Warrendale, PA, 2004; pp 45–52.
225. Schumann, E.; Yang, J. C.; Graham, M. J. *Scr. Mater.* **1996**, *34*, 1365–1370.
226. Mendis, B. G.; Livi, K. J. T.; Hemker, K. J. *Scr. Mater.* **2006**, *55*, 589–592.
227. Lowrie, D.; Boone, D. H. *Thin Solid Films* **1977**, *45*, 491–498.
228. Allam, I. M.; Akuezue, H. C.; Whittle, D. P. *Oxid. Met.* **1980**, *14*, 517–530.
229. Amano, T.; Takezawa, Y.; Shiino, A.; Shishido, T. *J. Alloys Compd.* **2008**, *452*, 16–22.
230. Dickey, E. C.; Pint, B. A.; Alexander, K. B.; Wright, I. G. *J. Mater. Res.* **1999**, *14*, 4531–4540.
231. Smialek, J. L.; Doychak, J.; Gaydosh, D. J. *Oxid. Met.* **1990**, *34*, 259–275.

232. Wright, I. G.; Pint, B. A.; Tortorelli, P. F. *Oxid. Met.* **2001**, *55*, 333–357.
233. Pint, B. A.; Porter, W. D.; Wright, I. G. *Mater. Sci. Forum* **2008**, *595–598*, 1083–1092.
234. Smialek, J. L.; A Nesbitt, J.; Barrett, C. A.; Lowell, C. E. In *Cyclic Oxidation of High Temperature Materials*; Schütze, M., Quadakkers, W. J., Eds.; Institute of Materials: London, UK, 1999; pp 148–168.
235. Evans, H. E. *Int. Mater. Rev.* **1995**, *40*, 1–40.
236. Nicholls, J. R.; Evans, H. E.; Saunders, S. R. J. *Mater. High Temp.* **1997**, *14*, 5–13.
237. Jönsson, B.; Berglund, R.; Magnusson, J.; Henning, P.; Hättestrand, M. *Mater. Sci. Forum* **2004**, *461–464*, 455–462.
238. Herbelin, J. M.; Mantel, M. *Mater. Sci. Forum* **1997**, *251–254*, 349–356.
239. Lowell, C. E.; Deadmore, D. L. *Oxid. Met.* **1980**, *14*, 325–336.
240. Wagner, C. *J. Electrochem. Soc.* **1952**, *99*, 369–380.
241. Douglass, D. L. *Oxid. Met.* **1995**, *44*, 81–111.
242. Wolf, J. S.; Evans, E. B. *Corrosion* **1962**, *18*, 129–136.
243. Whittle, D. P.; Shida, Y.; Wood, G. C.; Stott, F. H.; Bastow, B. D. *Philos. Mag. A* **1982**, *46*, 931–949.
244. Hindam, H. M.; Smeltzer, W. W. *J. Electrochem. Soc.* **1980**, *127*, 1622–1635.
245. Barrett, C. A.; Lowell, C. E. *Oxid. Met.* **1978**, *12*, 293–311.
246. Allam, I. M.; Whittle, D. P.; Stringer, J. *Oxid. Met.* **1979**, *13*, 381–401.
247. Bennett, M. J.; Romary, H.; Price, J. B. In *Heat Resistant Materials*; Natesan, K., Tillack, D. J., Eds.; ASM: Materials Park, OH, 1991; pp 95–103.
248. Gurrappa, I.; Weinbruch, S.; Naumenko, D.; Quadakkers, W. J. *Mater. Corros.* **2000**, *51*, 224–235.
249. Pint, B. A.; Walker, L. R.; Wright, I. G. *Mater. High Temp.* **2004**, *21*, 175–185.
250. Wilber, J. P.; Bennett, M. J.; Nicholls, J. R. *Mater. High Temp.* **2000**, *17*, 125–132.
251. Wright, I. G.; Pint, B. A.; Hall, L. M.; Tortorelli, P. F. In *Lifetime Modelling of High Temperature Corrosion Processes*; Schütze, M., Quadakkers, W. J., Nicholls, J. R., Eds.; Maney: London, 2001; pp 299–318.
252. Wright, I. G.; Peraldi, R.; Pint, B. A. *Mater. Sci. Forum* **2004**, *461–464*, 579–590.
253. Nesbitt, J. A.; Heckel, R. W. *Oxid. Met.* **1988**, *29*, 75–102.
254. Nesbitt, J. A. NASA Glenn Research Center: Cleveland, OH, 2000NASA/TM, 2000-209271.
255. Pint, B. A.; Walker, L. R.; Wright, I. G. *Mater. High Temp.* **2009**, in press.
256. Evans, H. E.; Donaldson, A. T.; Gilmour, T. C. *Oxid. Met.* **1999**, *52*, 379–402.
257. Hiramatsu, N.; Stott, F. H. *Oxid. Met.* **1999**, *51*, 479–494.
258. Kochubey, V.; Naumenko, D.; Wessel, E.; Le Coze, J.; Singheiser, L.; Al-Baidary, H.; Tatlock, G. J.; Quadakkers, W. J. *Mater. Lett.* **2006**, *60*, 1564–1568.
259. Fritscher, K.; Leyens, C.; Peters, M. *Mater. Sci. Eng. A* **1995**, *190*, 253–258.
260. Kofstad, P. In *Microscopy of Oxidation I*; Bennett, M. J., Lorimer, G. W., Eds.; Institute of Metals: London, 1991; pp 2–9.
261. Pint, B. A.; Haynes, J. A.; Zhang, Y.; More, K. L.; Wright, I. G. *Surf. Coat. Technol.* **2006**, *201*, 3852–3856.
262. Opila, E. J. *Mater. Sci. Forum* **2004**, *461–464*, 765–774.
263. Asteman, H.; Svensson, J.-E.; Johansson, L.-G.; Norell, M. *Oxid. Met.* **1999**, *52*, 95–111.
264. Opila, E. J.; Hann, R. E., Jr. *J. Am. Ceram. Soc.* **1997**, *80*, 197–205.
265. Young, D. J.; Pint, B. A. *Oxid. Met.* **2006**, *66*, 137–153.
266. Kvernes, I.; Olivera, M.; Kofstad, P. *Corros. Sci.* **1977**, *17*, 237–252.
267. Pint, B. A.; Peraldi, R.; Maziasz, P. J. *Mater. Sci. Forum* **2004**, *461–464*, 815–822.
268. Pint, B. A.; More, K. L.; Trejo, R.; Lara-Curzio, E. *J. Eng. Gas Turbines Power* **2008**, *130*, 012101.
269. Agüero, A.; Muelas, R.; Gutiérrez, M.; Van Vulpen, R.; Osgerby, S.; Banks, J. P. *Surf. Coat. Technol.* **2007**, *201*, 6253–6260.
270. Regina, J. R.; DuPont, J. N.; Marder, A. R. *Oxid. Met.* **2004**, *61*, 69–90.
271. Leyens, C.; Fritscher, K.; Gehrling, R.; Peters, M.; Kaysser, W. A. *Surf. Coat. Technol.* **1996**, *82*, 133–144.
272. Janakiraman, R.; Meier, G. H.; Pettit, F. S. *Metall. Mater. Trans. A* **1999**, *30*, 2905–2913.
273. Onal, K.; Maris-Sida, M. C.; Meier, G. H.; Pettit, F. S. *Mater. High Temp.* **2003**, *20*, 327–337.
274. Maris-Sida, M. C.; Meier, G. H.; Pettit, F. S. *Metall. Mater. Trans. A* **2003**, *34*, 2609–2619.
275. Smialek, J. L. *JOM* **2006**, *58*(1), 29–35.
276. Al-Badairy, H.; Tatlock, G. J. *Mater. High Temp.* **2000**, *17*, 133–137.
277. Essuman, E.; Meier, G. H.; Zurek, J.; Hänsel, M.; Quadakkers, W. J. *Oxid. Met.* **2008**, *69*, 143–162.
278. Alcock, C. B.; Hocking, M. G.; Zador, S. *Corros. Sci.* **1969**, *9*, 111–122.
279. Vineberg, E. J.; Douglass, D. L. *Oxid. Met.* **1986**, *25*, 1–28.
280. Wright, I. G. In *Proceedings of the 1974 Gas Turbine Materials in the Marine Environment Conference*; Fairbanks, J. W., Machlan, I., Eds.; Battelle: Columbus, OH, 1975; pp 357–377.
281. Nakamori, M.; Kayano, I.; Tsukuda, Y.; Takahashi, K.; Torigoe, T. *Mater. Sci. Forum* **1997**, *251–254*, 633–640.
282. Narita, T.; Przybylski, K.; Smeltzer, W. W. *Oxid. Met.* **1984**, *22*, 181–200.
283. Setterlund, R. B.; Prescott, G. R. *Corrosion* **1961**, *17*, 103–108.
284. Huang, T. T.; Lin, Y. C.; Shores, D. A.; Pfender, E. *J. Electrochem. Soc.* **1984**, *131*, 2191–2196.
285. Saxena, D.; Prakash, S.; Mehta, M. L.; Saraswat, I. P. *Oxid. Met.* **1987**, *28*, 127–153.
286. DeVan, J. H.; Tortorelli, P. F. *Mater. High Temp.* **1993**, *11*, 30–35.
287. Nyassi, A.; Larpin, J. P.; Bendriss, A. *Oxid. Met.* **1995**, *43*, 543–560.
288. Banovic, S. W.; Du Pont, J. N.; Marder, A. R. *Metall. Mater. Trans. A* **2000**, *31*, 1805–1817.
289. Pint, B. A.; Zhang, Y.; Tortorelli, P. F.; Haynes, J. A.; Wright, I. G. *Mater. High Temp.* **2001**, *18*, 185–192.
290. Mari, P. A.; Chaix, J. M.; Larpin, J. P. *Oxid. Met.* **1982**, *17*, 315–328.
291. Stott, F. H.; Chong, F. M. F.; Stirling, C. A. In *Proceedings of the 9th International Congress on Metallic Corrosion* National Research Council of Canada: Ottawa, Canada, 1984; Vol. 2, pp 1–16.
292. Taniguchi, S.; Shibata, T. *Oxid. Met.* **1989**, *32*, 391–404.
293. Kim, Y.-K.; Przybylski, K.; Yurek, G. J. In *Fundamental Aspects of High Temperature Corrosion*; Shores, D., Yurek, G. J., Eds.; Electrochemical Society: Pennington, NJ, 1986; Vol. II, pp 259–281.
294. Schaeffer, J.; Kim, G. M.; Meier, G. H.; Pettit, F. S. In Lang, E., Ed.; *The Role of Active Elements in the Oxidation Behavior of High Temperature Metals and Alloys;* Elsevier Applied Science: London, 1989; pp 231–267.
295. Rapp, R. A. *Mater. Sci. Eng.* **1987**, *87*, 319–327.
296. Leyens, C.; Wright, I. G.; Pint, B. A. *Mater. Sci. Forum* **2001**, *369–372*, 571–578.

297. Grabke, H. J. *Mater. Corros.* **1998**, *49*, 303–308.
298. Loudjani, M. K.; Pivin, J. C.; Huntz, A. M.; Davidson, J. H. *Corros. Sci.* **1988**, *28*, 1075–1088.
299. Jönsson, B.; Svedberg, C. *Mater. Sci. Forum* **1997**, *251–254*, 551–558.
300. Turker, M.; Hughes, T. A. In *Microscopy of Oxidation*; Newcomb, S. B., Bennett, M. J., Eds.; Institute of Metals: London, 1993; Vol. 2, pp 310–320.
301. Bennett, M. J.; Newton, R.; Nicholls, J. R. *Mater. High Temp.* **2003**, *20*, 347–356.
302. Han, S.; Young, D. J. *Oxid. Met.* **2001**, *55*, 223–242.
303. Stott, F. H.; Berg, S.; Sang, M.; Karim, N. In *High Temperature Materials for Power Engineering*; Bachelet, *et al.* Eds.; Kluwer Academic Publishers: Dordrecht, Netherlands, 1990; Vol. 1, pp 213–226.
304. Krupp, U.; Christ, H.-J. *Metall. Mater. Trans. A* **2000**, *31*, 47–56.
305. Bennett, M. J.; Nicholls, J. R.; Borchardt, G.; Strehl, G. *Mater. High Temp.* **2002**, *19*, 117–125.

1.27 High Temperature Coatings: Protection and Breakdown

H. E. Evans
School of Metallurgy and Materials, The University of Birmingham, Birmingham B15 2TT, UK

Symbols

a Amplitude of bond coat surface roughness (m)
b Wavelength of bond coat surface roughness (m)
C Concentration (at.%)
C_{Al} Concentration of aluminum (m^{-3})
C_b Bulk concentration (at.%)
D Interdiffusion coefficient ($m^2\ s^{-1}$)
D_{Al} Interdiffusion coefficient for aluminum ($m^2\ s^{-1}$)
E_m Young's modulus of the alloy or metallic coating (Pa or GPa)
E_{ox} Young's modulus of the oxide (Pa or GPa)
f_B Bulk fractional concentration of solute
f_I Fractional concentration of solute at oxide–coating interface
f(x) Fractional concentration at position *x*
h thickness of oxide layer (m)
h_o Preexisting oxide thickness (m)

J_{Al} Flux of aluminum ($m^{-2}\ s^{-1}$)
k_n Oxidation rate constant ($m^n\ s^{-1}$)
k_p Parabolic oxidation rate constant ($m^2\ s^{-1}$)
k'_p Mass gain parabolic rate constant ($g^2\ m^{-4}\ s^{-1}$ or $mg^2\ cm^{-4}\ s^{-1}$)
M_o Atomic weight of oxygen (kg)
M_{ox} Molecular weight of the oxide (kg)
n Dimensionless number
R Radius of decohesion zone (m)
t Exposure time (s)
T Temperature (K)
T_{ox} Oxidation temperature (K)
ΔT Amplitude of temperature change (K)
ΔT_b Critical temperature change for oxide buckling (K)
ΔT_c Critical temperature change for oxide spallation (K)
v Volume of oxide formed per aluminum atom (m^3)
w Half the specimen or cell thickness (m)
W^* Strain energy ($J\ m^{-3}$)
W_{Al} Atomic weight of aluminum (kg)
$W_{Al_2O_3}$ Molecular weight of alumina (kg)
x Spatial coordinate and distance from the oxide–metal interface (m)
x_h Section loss (m)
α_m Linear thermal expansion coefficient of alloy or coating (K^{-1})
α_{ox} Linear thermal expansion coefficient of oxide (K^{-1})
ε Strain
ϕ Pilling–Bedworth ratio
γ_F Effective fracture energy ($J\ m^{-2}$)
ν Poisson's ratio
$\rho_{Al_2O_3}$ Density of alumina ($kg\ m^{-3}$)
ρ_m Density of the alloy ($kg\ m^{-3}$)
ρ_{ox} Density of the oxide ($kg\ m^{-3}$)
σ_{ox} In-plane oxide stress (Pa or MPa)

1.27.1 The Need for Coatings

High temperature superalloys, usually based on iron-, cobalt-, or nickel-rich compositions,[1] are optimized for mechanical properties, such as creep and fatigue resistance, since they are used for highly-stressed components. In all cases, however, these alloys will be exposed to oxidizing or hot-corrosion environments during service and will undergo some form of degradation process resulting from this interaction. The composition optimization required to achieve good mechanical properties, however, often conflicts with the requirements for oxidation/hot-corrosion protection. As a result, the intrinsic protection capability of many superalloys is adequate only for short-term exposures and coatings are required to permit extended operation under service conditions. This point will be demonstrated in the later text for the particular case of Ni-based superalloys under oxidizing conditions.

High-strength nickel-based alloys are used extensively for components in gas turbines; an excellent account of their development and properties is provided by Reed.[1] Single crystal alloys, for example, CMSX4, are used for high-pressure blades in aeroengines and in small (~10 MW) land-based turbines, but, in larger machines, polycrystalline alloys (e.g., IN738LC) are used. Some compositions of nickel-based alloys are given in **Table 1**. These are given in 'weight percentage' as is customary, but, in assessing the ability to form and maintain a protective alumina layer at high temperatures, it is the atomic percentage of available aluminum which is a key factor. For alloys having high nickel, chromium, and cobalt contents, the atomic concentration of aluminum is roughly twice the weight percentage value. In more complex alloys containing appreciable amounts of heavy elements such as tungsten, rhenium, or ruthenium, this factor is nearer 2.5. Thus, even though in most of the alloys (shown in **Table 1**) the aluminum concentration is ~5.6 wt%, its atomic concentration increases from ~11 at.% in simpler alloys such as RR2000 to ~13 at.% in PWA1497. Much of this aluminum is associated with the strengthening γ' phase in these alloys.

The importance of both aluminum and chromium concentrations to the ability of a Ni-based alloy to form a protective alumina layer is summarized in **Figure 1**. This diagram is similar to that given by Evans and Taylor,[2] but has been modified to reflect the low-Cr compositions of the more recent alloys shown in **Table 1** and to include γ/γ' coatings. For convenience in comparing between alloys, concentrations in weight percentage are used. The experimentally based lines shown in **Figure 1** derive from the work of Giggins and Pettit[3] on NiCrAl alloys at temperatures within the range 1000–1200 °C. They show that in simple Ni–Al binary alloys, at least 6 wt % aluminum is required to form an alumina layer at these temperatures. This critical value decreases with increasing alloy chromium content to ~3 wt% aluminum at chromium contents ≥10 wt%. At low aluminum and chromium contents, that is, below the downward sloping line to the left-hand side of **Figure 1**, the principal surface oxide is expected to

Table 1 Compositions (wt%) of some representative nickel-based superalloys

Alloy	*Ni*	*Co*	*W*	*Cr*	*Al*	*Ta*	*Re*	*Hf*	*Ru*	*Ti*	*Mo*	*Nb*
RR2000	Balance	15.0	–	10.0	5.5	2.8	–	–	–	4.0	3.0	–
IN738LC	Balance	8.5	2.6	16.0	3.4	1.7	–	–	–	3.4	1.7	0.9
CM186	Balance	9.3	8.5	6.0	5.7	3.4	3.0	1.4	–	0.5	0.2	–
CMSX4	Balance	9.8	6.4	6.4	5.6	6.5	3.0	0.1	–	1.0	0.6	0.4
CMSX10	Balance	3.0	5.0	2.0	5.7	8.0	6.0	0.03	–	0.2	2.9	–
PWA1497	Balance	16.5	6.0	2.0	5.6	8.3	6.0	0.15	3.0	–	2.0	–
TMS162	Balance	5.8	5.8	2.9	5.8	5.6	4.9	0.1	6.0	–	3.9	–

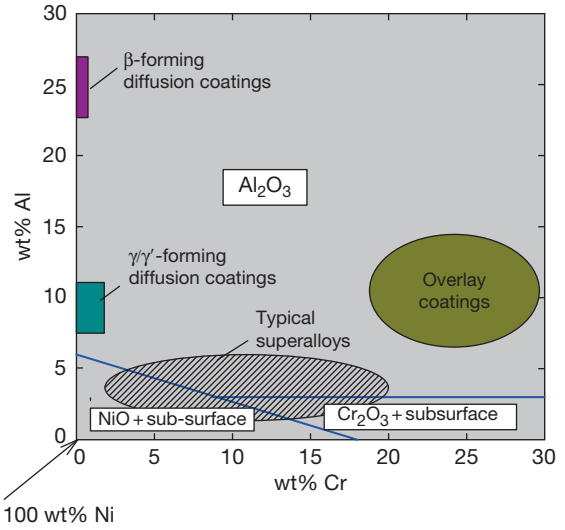

Figure 1 A schematic map derived from Evans and Taylor,[2] based on experimental data[3] showing the type of oxide formed in the NiCrAl system over the temperature range 1000–1200 °C. Superimposed are the composition ranges of typical superalloys and coatings.

be NiO (in NiCrAl alloys), with internal oxidation of aluminum and chromium. To the right-hand side of Figure 1, corresponding to alloys of high chromium and low aluminum content, chromia will be the expected surface oxide and aluminum will oxidize internally.

Also shown schematically, as the cross-hatched ellipse in Figure 1, is the approximate range of aluminum and chromium contents often used in Ni-based superalloys. It is immediately apparent that they tend to lie on or near the bounding lines for protective alumina formation. In some cases, alumina formation can be expected but not in others. As a group, these Ni-based superalloys can be considered to be borderline alumina formers and nonprotective oxidation has been reported in this temperature range for IN738LC[4,5] and CMSX10.[6] The situation is exacerbated with recent generations of alloys in which chromium levels have been decreased to ~2–2.5 wt% (Table 1), making it less favorable for a protective layer of alumina to form (see Figure 1). In addition, elements such as rhenium and ruthenium have been introduced, which have volatile oxides that can be released at high temperatures, at least in the absence of a protective surface oxide layer.

Another important consideration when assessing the oxidation resistance of an alloy is its ability to reform a protective alumina layer should that which formed initially spall or crack. This is an arduous requirement for borderline alloys, since the formation and growth of the original alumina layer is a process of selective oxidation and necessarily depletes the alloy of aluminum. Thus, even though an alumina layer may have formed initially on the superalloy, residual aluminum concentrations are unlikely to be able to maintain protective conditions when repeated spallation events occur.

It is for this combination of reasons that Ni-based superalloys operating at elevated temperatures, say ≥1000 °C, are coated with Al-rich layers. The composition ranges of two important classes of such coatings, overlays and diffusion coatings, are shown in Figure 1. These will be discussed shortly but, clearly, both types are designed to lie within the alumina-forming region in the diagram. It is the combination of high-strength superalloy and oxidation-resistant coating that permits component operation for extended periods at high temperatures.

1.27.2 Underlying Requirements of Coatings

1.27.2.1 The Protective Oxide Layer

High temperature coatings rely, for protection, on the formation of a dense and adherent surface oxide layer that is chemically stable, thickens slowly with time at temperature, and has good adherence to the coating.

These are, of course, the same requirements as are needed in the design of oxidation-resistant alloys in general, as discussed elsewhere in this book, and, as in that case, the choice is limited to chromia (Cr_2O_3), silica (SiO_2), and alumina (α-Al_2O_3).

Chromia layers are particularly useful in conferring protection against Type-II hot corrosion[7] and intermediate-temperature oxidation, say 600–800 °C, but can be converted to CrO_3 at higher temperatures. The rate of formation of this gaseous oxide can be significant in both dry and moist air at temperatures $\geq$950 °C and chromia-forming coatings have limited usage at high temperatures in such environments. Silica layers are capable of providing protection to very high temperatures, for example, *via* ceramic layers on carbon-based materials, to ~1800 °C.[8] They also suffer, however, from concerns with chemical stability in moist environments. Alumina layers do not suffer from such concerns and are the favored means of protection under Type-I hot-corrosion and high temperature oxidation conditions. The majority of coatings are now designed to form a continuous alumina layer under these conditions and to have sufficient aluminum content to provide a healing capability in the event of cracking or spallation of this layer. The majority of this chapter will place emphasis on the behavior of such alumina-forming coatings designed for use under high temperature oxidizing conditions, but interesting exceptions with commercial relevance are also included.

1.27.2.2 Coating Composition and Solute Supply

The initial priority of oxidation-resistant coatings is to form a protective layer that can be achieved simply by incorporating sufficient amount of the relevant element into the coating composition. However, this approach can impair physical and mechanical properties, for example, by decreasing melting temperatures or coating fracture toughness and ductility, and a balance must always be sought. The composition ranges of three types of alumina-forming coatings are shown in Figure 1, from which it is clear that all lie in the appropriate composition range for protective oxide formation. Detailed discussion of the coating types is provided later, but it is clear that aluminum concentrations of ~10 wt% are typical for both the MCrAlY overlays and γ/γ' diffusion coatings. These compare with the minimum requirements for alumina formation (solid lines) of ~3 and 6 wt% aluminum, respectively. The β-forming class of diffusion coating has substantially larger amounts of aluminum at ~25 wt%.

It must be borne in mind, though, that the formation of the protective layer is a process of selective oxidation in which the solute atom is preferentially removed from the coating, oxidized, and incorporated into the oxide layer. This removal necessarily depletes the coating of the solute and will generate a concentration profile as shown schematically in Figure 2 for the case of aluminum removal from, nominally, a NiCrAlY overlay coating. This is assumed to have had an initial aluminum concentration of 10 wt% and can be compared with the uncoated alloy having an initial concentration of 5.6 wt%.

The second requirement of a protective coating is that the residual solute concentration after initial formation of the surface layer is still sufficient to reform a protective layer in the event of cracking or spalling of this first-formed layer. As shown in Figure 2, the coating has sufficient aluminum, and hence even after alumina formation, there is still sufficient solute at the oxide–metal interface to reform this layer. By contrast, because the superalloy had barely sufficient aluminum to form the alumina layer initially, the interfacial concentration falls below the critical value after formation of the protective layer. Subsequent spallation of this layer would then mean that rapid oxidation of the alloy would take place until the local concentration had reached the critical value for reforming the alumina layer. The quantity of metal consumed is shown by the hatched area in Figure 2 as ~7 μm but it will be much larger if spallation occurs later in life when more pronounced depletion has occurred. Typically, the thickness of this at-risk zone will increase parabolically with exposure time up to the first spallation event.

The shapes of the depletion profiles shown in Figure 2 are determined by the need to maintain a mass balance at the oxide–metal interface, such that the flux of aluminum leaving the metal is equal to that required to produce the observed thickening rate of the oxide.[9] Considering the ideal case that the oxide thickness, h, increases parabolically with time, t, and forms at the start of the exposure period, the rate constant, k_p, is then defined as

$$k_p = h^2/t \qquad [1]$$

This means that the flux of aluminum atoms, $\mathcal{J}_{Al}$, arriving at the oxide–metal interface is

$$\mathcal{J}_{Al} = -D_{Al}\left(\frac{\partial C_{Al}}{\partial x}\right)_{x=0} = \frac{1}{V}\left(\frac{d\xi}{dt}\right) = \frac{1}{2}k_p^{0.5}t^{-0.5} \qquad [2]$$

where it is assumed, reasonably for protective conditions, that the recession of the oxide–metal interface is much smaller than the diffusion distances within

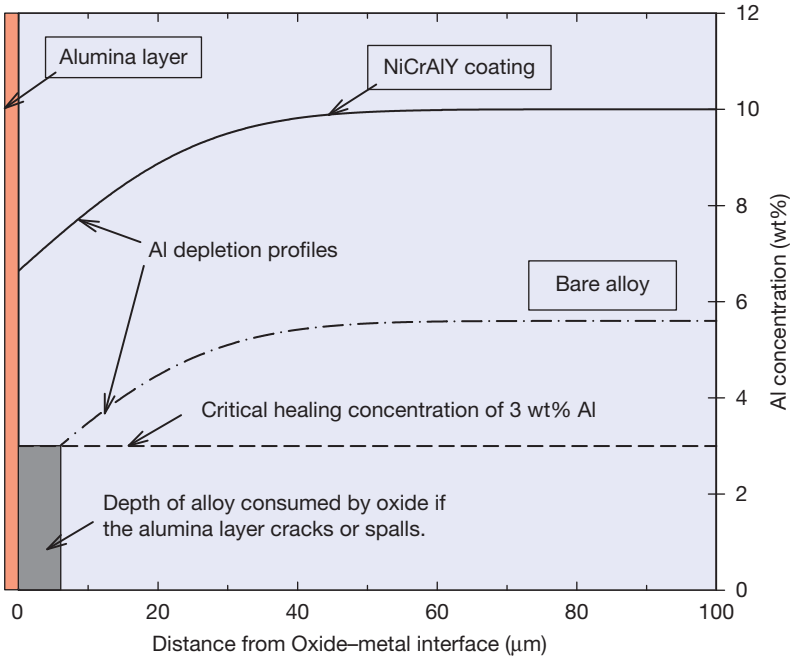

Figure 2 Selective oxidation of aluminum from a NiCrAlY coating and superalloy produces depletion profiles in that element. They result in interfacial aluminum concentrations insufficient to reform the alumina layer on the superalloy without the prior consumption of some of the underlying metal. The critical interfacial concentration for reforming an alumina layer is taken as 3 wt%, that is, of similar magnitude to those shown as solid lines in **Figure 1**.

the coating. In eqn. [2], D_{Al} is the interdiffusion coefficient for aluminum within the coating, C_{Al} is the aluminum concentration (number/unit volume), x is the spatial coordinate measured from the oxide–metal interface, and V is the volume of oxide formed per aluminum atom. The depletion profile within the metal can then be obtained from solution of Fick's second law

$$\frac{\partial C_{Al}}{\partial t} = D_{Al}\frac{\partial^2 C_{Al}}{\partial x^2} \qquad [3]$$

using eqn. [2] as a boundary condition, that is, the flux of aluminum at the oxide–metal interface varies as $t^{-1/2}$. At relatively short exposure times, the depletion distance will be small compared with the thickness of the coating so that the latter can then be considered as semiinfinite. Under these conditions, the depletion profile is obtained as[10]

$$\frac{f(x) - f_I}{f_B - f_I} = \text{erf}\left(\frac{x}{2(D_{Al}t)^{0.5}}\right) \qquad [4]$$

where the fs are consistent concentration parameters, for example, weight (mass) fractions, $f(x)$ is the value at distance x, f_I is the value in the metal at the oxide–metal interface, f_B is the bulk value, and erf is the error function. The interfacial concentration, f_I, is constant provided that parabolic oxidation and semiinfinite conditions apply, but its value is directly related to the rate constant k_p and can be determined from the need to conserve the aluminum flux at the oxide–metal interface. For simplicity, taking f as a weight fraction, the interfacial concentration during the growth of alumina is given as[11]

$$f_I = f_B - \left[\left(\frac{\pi k_p}{D_{Al}}\right)^{1/2}\left(\frac{\rho_{Al_2O_3} W_{Al}}{\rho_m W_{Al_2O_3}}\right)\right] \qquad [5]$$

Here, ρ is density, W is molecular or atomic weight, the suffix 'm' is the coating, and Al_2O_3 the oxide.

The concentration in the coating at its interface with the oxide will be maintained provided that there is sufficient aluminum reservoir and thickness of the coating to approximate to semiinfinite conditions. Protection should, thus, be provided by these generic coatings until end-of-life effects, initiated often by aluminum-reservoir depletion, intervene. At this stage, the interfacial concentration will begin to decrease and a level will eventually be reached where the protective alumina layer cannot be maintained. These issues will be discussed in detail in the following sections.

1.27.3 Examples of Main Coating Types

1.27.3.1 Overlay Coatings

1.27.3.1.1 MCrAlY coatings

Overlay coatings consist of a discrete coating layer deposited onto the surface of the component, with little interdiffusion and chemical reaction with the alloy substrate. These overlay coatings are often metallic alloys, 150–300 μm thick, based on MCrAlY compositions where M is Ni, Co, sometimes Fe, or a combination of these. Early development of these overlay coatings centered on cobalt-based materials containing 20–40 wt% Cr, 12–20 wt% Al, and 0.5 wt% Y.[12] On the basis of hot corrosion and mechanical property tests, an optimal composition of Co25Cr14Al0.5Y (wt%) was selected. This initial composition is similar to those of the more recent Co-based coatings, ATD 2B and ATD 5B, given in Table 2. Later trends, however, have been to replace some or all of the cobalt content with nickel in order to improve toughness and to limit interdiffusion effects when protecting high temperature Ni-based superalloys. There has also been a tendency to decrease aluminum content, again to improve coating toughness. A few examples of the composition of current MCrAlY overlay coatings are given in Table 2.

It is sometimes the case, as can be inferred from Table 2, that overlay coatings of the same or similar compositions have different designations, for example, LCO22 and CN122. This reflects the different possible deposition methods in commercial use. These include air plasma spraying (APS), argon-shrouded plasma spraying (ASPS), low-pressure plasma spraying (LPPS), high-velocity oxy-fuel (HVOF) spraying, electrodeposition, and physical vapor deposition (PVD) processes such as sputtering and electron beam (EB) PVD. Some of these methods relate to the coatings shown in the table. Details of these techniques and the historical development of protective coatings can be found elsewhere.[13–18]

Even though the details of the coating techniques will be covered elsewhere in this book, it is important to note that different application methods will produce different coating structures as can be appreciated from Figure 3. In both of the plasma sprayed coatings, (a) and (b), the sequential spray runs are evident in the lateral dark stringers of oxide formed around individual alloy particles during the deposition process. These stringers can be continuous in the APS coating in which extensive oxidation in the air environment can result. Some oxide formation is inevitable also under LPPS, as can be appreciated from Figure 3(b), but in this case, continuous stringers are not usually formed (e.g., see Figure 4). These differences affect the longevity of the coatings, even for a given nominal composition, as will be discussed later with reference to aluminum reservoir issues. The EB-PVD coating, by contrast, forms as vertical columns with negligible oxidation. These vertical features can be seen on closer inspection in Figure 3(c), and their presence provides sites of potential mechanical weakness, which can be removed by postprocessing, for example, peening, to improve lateral bonding.

The MCrAlY coatings (shown in Table 2) have a nominal β/γ structure, where β can be NiAl or CoAl and γ is face-centered cubic Ni- or Co-rich solid solution. In practice, however, the actual microstructure will depend on cooling rate and temperature as well as on the detailed composition. Ni-rich phases, for example, can undergo the following four-phase reaction at ~980 °C[19]:

$$\beta + \gamma \rightarrow \gamma' + \alpha \qquad [6]$$

where γ' is the Ni_3Al phase and α is the α-Cr solid solution. It can be appreciated that a given coating

Table 2 Compositions (wt%) of some MCrAlY overlay coatings

Coating or feedstock	*Al*	*Cr*	*Ni*	*Co*	*Fe*	*Y*	*Others*
ATD 2B	12	23	–	Balance	–	0.3	
ATD 5B	11	18	–	Balance	–	0.5	
LCO 22	8	22	32	Balance	–	0.5	–
CN 122	8	22	32	Balance	–	0.5	–
LN 34	11	20	Balance	–	–	0.5	0.5Mo
ATD 8	11	24	–	–	Balance	0.6	–
Amdry 963	6	25	Balance	–	–	0.4	–
Amdry 995	8	21	32	Balance	–	0.5	–
Amdry 997	8.5	20	Balance	23	–	0.6	4Ta

LN and LCO coatings deposited by argon-shrouded plasma spraying, ATD deposited by EB-PVD, CN deposited by low-pressure plasma spraying, Amdry are feedstock powders.

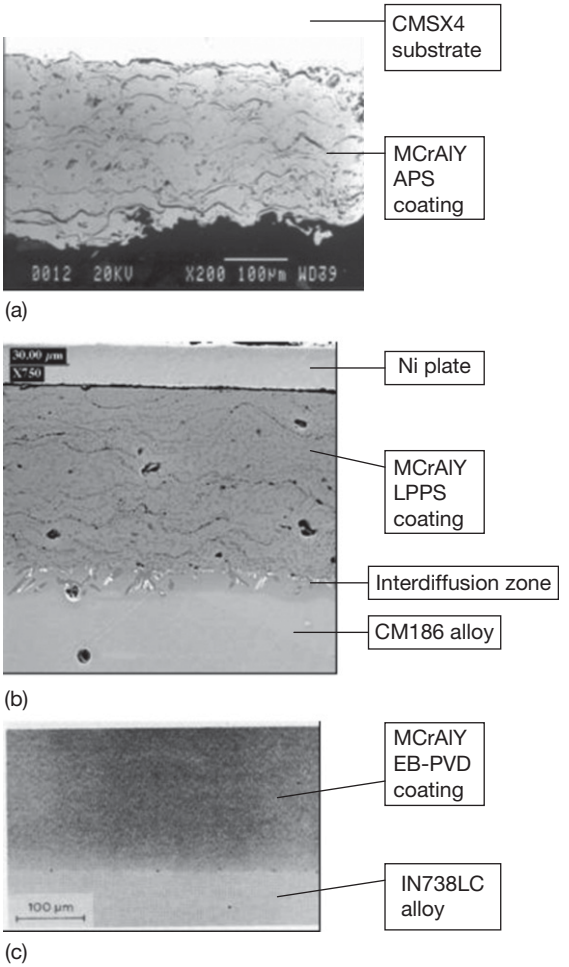

Figure 3 Examples of the structure of MCrAlY coatings deposited by (a) APS,[2] (b) LPPS,[2] and (c) EB-PVD [13] techniques.

composition can have a β/γ microstructure at higher temperatures, but at lower temperatures – often corresponding to service conditions – can be γ'/α. In reality, particularly if fairly rapid temperature changes take place, the microstructure may be non-equilibrium and contain a mixture of the various phases.[20] An example of a typical duplex microstructure is provided in **Figure 4**. Further complications may arise near the interface with the substrate alloy if γ'-stabilizing elements such as tantalum, titanium, and niobium have diffused into the coating; the γ' phase can then exist to temperatures above 980 °C at this location.

Reaction [6] is also accompanied by linear contraction strains of ~0.7% and there has been concern that this could prejudice the integrity of the coating. There is no particular evidence for any deleterious

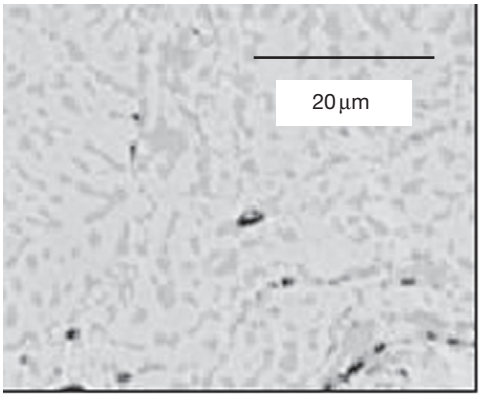

Figure 4 The duplex microstructure of a LPPS CoNiCrAlY overlay coating. Courtesy of Dr. M.P. Taylor.

effect, however, possibly because the strains arise at temperatures where the coating is ductile and stress relaxation rates are high.[21,22] Nevertheless, the concern has been one of the historic factors influencing the incorporation of cobalt into many coating compositions in order to decrease the stability of the γ' phase. Even so, γ' phases have been reported[20] in Ni-based MCrAlY coatings containing 20 wt% Co.

Minor alloying additions, in addition to yttrium, have also been made to MCrAlY coatings either in attempts to improve alumina formation or adherence or to improve mechanical properties. Some examples include silicon[23] and hafnium[24] and also tantalum (**Table 2**), titanium,[23] molybdenum (**Table 2**), niobium, rhenium, and zirconium. These are often used in combinations, but detailed compositions of current coatings tend to be proprietary. MCrAlY coatings have also been modified by means of surface enrichment with silicon[25] and aluminum (e.g., GE coatings 29+ and 33+) and, in lower-density air plasma sprayed structures, by inward percolation of liquid $NiAl_3$.[26]

1.27.3.1.2 Examples of other metallic coatings

Much effort has been made to deposit metallic coatings other than MCrAlYs in attempts to improve substrate properties[15]; some examples designed to confer oxidation resistance are given here.

Ti–Al alloys have considerable commercial potential because of their high specific creep strength, that is, the combination of good creep strength and low density. Their disadvantage lies in their poor oxidation resistance resulting from the competitive growth of alumina and rutile (TiO_2). Both of these oxides are very stable, but the latter has a much higher growth rate than alumina and the combination makes it difficult to form and sustain protective conditions.

The situation can be improved by the application of surface coatings of increased aluminum to titanium ratios having greater propensity to form alumina. Interesting examples are the use of a sputtered Ti–51Al–13Cr (at.%) overlay[27] to improve oxidation performance of a near-α titanium alloy at 750 °C in air. A similar principle has been adopted[28] through the use of either graded or discrete sequential layers of Ti_3Al, TiAl, and $TiAl_3$, again on a near-α alloy. In an alternative approach,[29] it is recognized that at typical operating temperatures for Ti–Al (say 700–750 °C), it is not necessary to use an alumina layer for oxidation protection, since a chromia layer will provide the necessary improvements. As a consequence, it is possible to use Al-free chromia-forming coatings of high fracture toughness and ductility to confer oxidation protection.[29]

Overlay coatings may also allow the potential of other reactive alloys with attractive mechanical properties to be realized. Important examples are those alloys based on niobium, which have good creep properties at high temperature but poor oxidation resistance. Alumina-forming FeCrAlY and silica-forming SiCrAlY overlays, deposited by APS, can produce oxidation protection to molybdenum for significant periods, 300 and 2000 h, respectively, at 1200 °C.[30] An advanced coating architecture for the protection of a Nb–5Mo–15W alloy has been developed by Narita and coworkers,[31] in which the outer Al-rich reservoir within the coating is protected from interdiffusion by underlying Re–Cr-rich layers.

1.27.3.1.3 Oxide overlay coatings

Directly depositing a surface coating of a protective oxide layer ought, in principle, to be an attractive option, since it bypasses the need for the metallic element to be present in significant quantities in the underlying alloy. This is particularly the case for aluminum and silicon, whose presence in large amounts can impair the mechanical properties of the alloy.

A low-cost method for the deposition of an oxide coating is through the use of sol–gels.[15,32] In this, the coating is formed by evaporation of a colloidal suspension of oxide or hydroxide particles and subsequent consolidation of the deposit to form a dense layer. A common feature, though, is the formation of cracks during the curing process, which necessitates the use of multilayers to confer reasonable oxidation protection. Even so, crack-like defects will exist within the layer thickness, which will lead to decreased coating ductility. A better approach is to produce the oxide layer from the vapor phase and this has had considerable success with the formation of silica coatings. An early evaluation of silica coatings, produced from silane onto a 9Cr ferritic steel, has been made by Crouch and Dooley.[33] Later developments have used plasma-assisted vapor deposition (PAVD) resulting from the decomposition of tetraethoxysilane. Very dense, uncracked, and adherent amorphous silica coatings up to 10 μm thick have been produced by this method on, for example, Incoloy 800H,[34] IN 738LC[35] and 20Cr25Ni, Nb-stabilized austenitic steel.[36] The improvements in oxidation resistance obtained from these coatings have been substantial, for example, decrease by a factor of 5 in mass gain for IN 738LC after 5000 h exposure in air at 900 °C.[35]

A striking demonstration of the improvement obtained on the 20Cr25Ni austenitic steel at 1300 °C is given in **Figure 5**.[37] In this figure, the top micrograph shows how the entire cross-section of the uncoated specimen has been oxidized after 1 h exposure at this temperature in a CO_2-based gas. In contrast, the silica-coated specimen (lower micrograph) is largely still intact. This example is particularly interesting, since the 20Cr25Ni, Nb-stabilized alloy is used as thin-walled (0.38 mm) tubes to contain UO_2 fuel in the UK's Advanced Gas-Cooled Reactors (AGRs). The test time and temperature used relate to postulated fault scenarios with restricted coolant flow.

These substantial improvements in oxidation resistance arise because the silica coating acts as a barrier both to the inward diffusion of oxygen and to

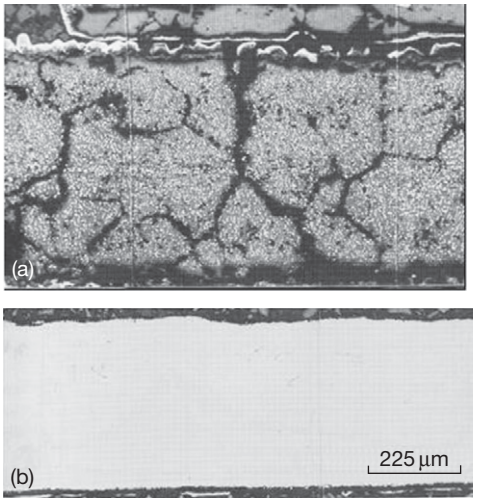

Figure 5 Optical micrographs of cross-sections of specimens of a 20Cr25Ni, Nb-stabilized alloy after oxidation for 1 h at 1300 °C in a CO_2/1% CO gas.[37] (a) Complete oxidation of the uncoated alloy and (b) relatively intact silica-coated specimen. The magnification is the same in each case.

the outward diffusion of the alloy constituents. A disadvantage, though, is that the coating offers no self-healing capability in the event that through-thickness cracks or localized spallation occurs. In other words, there is no reservoir of silicon available to reform the silica layer. Cracks in the layer will allow oxygen ingress to the underlying alloy and the continuing formation of nonprotective oxides.[32] The situation is aggravated in the case of amorphous silica because of its low linear thermal expansion coefficient of 0.5×10^{-6} K^{-1}. Because the coating layer is much thinner than the metal thickness, it is reasonable to assume that the planar dimensions of the coating will follow those of the underlying alloy during a temperature change, $\Delta T = (T - T_{ox})$, (where T is the new temperature and T_{ox} is the original oxidation temperature). The in-plane strain, ε, within the coating is then given as

$$\varepsilon = \Delta T(\alpha_{metal} - \alpha_{silica}) \quad [7]$$

where α is the respective thermal expansion coefficient. A detailed discussion of such mechanical issues has been given elsewhere,[38] but it is instructive here to calculate the thermal expansion strain in the silica coating of Figure 5(b). Assuming that the silica layer was deposited at 800 °C, $\Delta T = 500$ °C for the temperature rise to the test temperature of 1300 °C. Taking also $\alpha_{metal} = 17.5 \times 10^{-6}$ K^{-1} then gives a tensile in-plane strain within the silica coating of 0.85%. Interestingly, this is much higher than the fracture strain values at 500 °C of 0.27–0.45% found by Crouch and Dooley[33] for sol–gel-deposited silica. It can be surmised from Figure 5(b) that the silica layer formed by PAVD remains uncracked, however, even after the 500 °C temperature rise, since there is continued oxidation protection. It implies that the PAVD structure either contains fewer crack-like defects and, hence, has higher intrinsic ductility than the sol–gel equivalent or that creep processes at the oxidation temperature relax stresses at crack tips and, again, increase ductility.

Eventual degradation of the amorphous silica layer is associated both with its transformation to the crystalline state (α-cristobalite) and with reaction with cations from the alloy.[34]

1.27.3.2 SMART MCrAlY Overlay Coatings

The compositions of current MCrAlY coatings (Table 2) reflect a compromise between the need to provide protection against low-temperature Type-II hot corrosion and intermediate-temperature oxidation and the need to protect against Type-I hot corrosion and high temperature oxidation. In the former case, high chromium levels and chromia protective layers are optimum whereas, in the latter case, high aluminum concentrations and protective alumina layers are more effective.[7,39] These coatings respond reasonably but not as well as coatings designed for specific local conditions of temperature and environment within, say, a large land-based gas turbine. Furthermore, the range of protection afforded by these coatings is limited and hampers moves to a more flexible operating regime in which various alternative fuels could be employed, for example, ranging from natural gas through kerosene, diesel oils to gaseous fuels made from coal, biomass, or waste.

SMART MCrAlY overlay coatings have been designed[40,41] to address this problem of flexibility and also the need to increase fuel efficiency by higher-temperature operation. Under these aggressive conditions, high temperature oxidation and both Type-I and Type-II hot corrosion may be experienced across a single component. The intention is for *SMART* coatings to respond to the local environment and to generate the optimum protective system to it, that is, either a chromia or an alumina layer. The coatings are chemically graded to provide surface layers enriched in aluminum and chromium, respectively, overlying a MCrAlY overlay coating. The structure is shown schematically in Figure 6. The

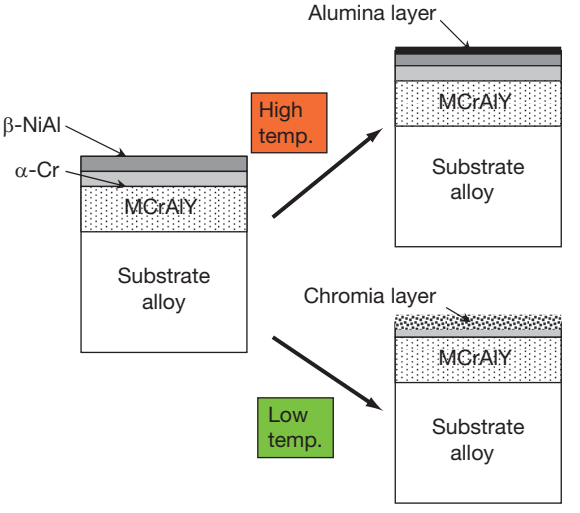

Figure 6 Schematic diagram of the chemically-graded *SMART* coating structure showing the outer β-NiAl layer and the intermediate Cr-rich zone overlying the base MCrAlY coating. The right-hand figures show the expected response under different oxidation and hot-corrosion regimes.

outer layer consists of β-NiAl produced by aluminizing but before this treatment, the base MCrAlY coating had been pretreated to form an intermediate layer rich in chromium. Manufacturing details of this process are currently proprietary,[41] but it is the presence of this intermediate Cr-rich layer that distinguishes *SMART* coatings from over-aluminized variants, for example, GT33+, currently available.

Under high temperature oxidation or Type-I hot corrosion conditions, the outer layer of the *SMART* coating reacts to form an alumina layer and provide optimum protection. The Cr-rich intermediate layer acts as a diffusion barrier limiting interdiffusion and, particularly, the loss of aluminum from the outer layer into the base coating. Under Type-II hot corrosion conditions, say at 600–800 °C, the outer region of the coating forms an alumina layer sluggishly and is intended to be sacrificed to allow the corrosion front to encounter the intermediate Cr-rich layer at which a chromia protective layer will form. The rate of pitting attack, associated with Type-II corrosion, will then be substantially decreased at this stage.

Extensive testing of these coatings[40,41] under hot corrosion conditions has demonstrated that these concepts do work, as can be appreciated from the montage of SEM micrographs of cross-sections of corroded specimens shown in **Figure 7**.[40,41] The test duration in all cases was 500 h in an air–400 vpm SO_2/SO_3 environment and were recoated every 20 h in an 80% Na_2SO_4/20% K_2SO_4 eutectic mix. **Figure 7** shows a comparison of a *SMART* coating variant (SmC 155H) with a Pt-aluminized diffusion coating (RT22) and an over-aluminized CoNiCrAlY overlay coating in the as-produced condition and after testing at 700 and 800 °C. It can be seen that both commercial coatings have been severely corroded at both temperatures whereas the *SMART* variant is relatively unaffected at 800 °C and shows penetration only through the outer aluminized layer at the lower temperature.

1.27.3.3 Diffusion Coatings

1.27.3.3.1 Basic types

Diffusion coatings are formed by direct interaction of the substrate alloy with elements, typically chromium, aluminum, and silicon, which are capable of forming protective oxide layers. Typically, coatings are produced through either immersion in a cementation-type pack or by vapor transfer of the

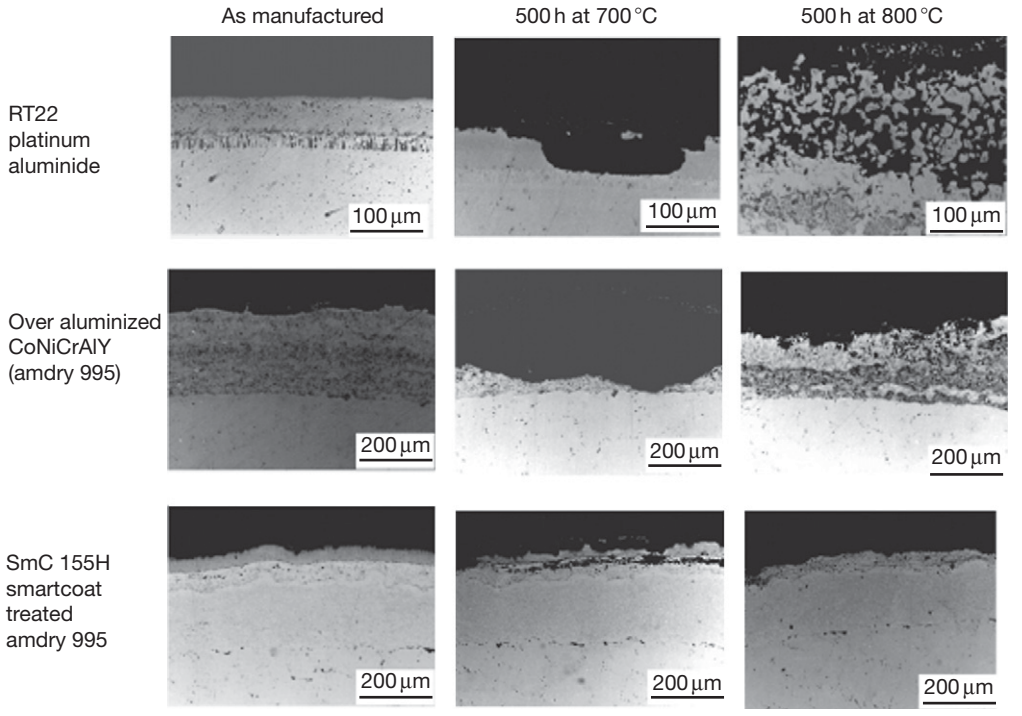

Figure 7 Comparison of the corrosion morphology of a *SMART* coating variant with a RT22 (platinum-aluminide) coating and an over-aluminized MCrAlY coating.[41] See text for further details.

active species to the component remote from the pack at temperatures where concurrent diffusion in the alloy develops the coating layer. Details can be found elsewhere.[13–18] Unlike overlays, diffusion coatings produced by these methods have limited flexibility to vary composition, although it is possible to codeposit more than one reactive species, for example, Al/Cr,[42] Al/Si,[43] and Cr/Si[44] and to use predeposited layers, for example, platinum, to vary coating structure.[45] More flexibility with regard to coating composition can be achieved through the use of a slurry of reactive species, which can be painted or sprayed onto a work piece and subsequently diffusion annealed. By repetition of this process, multilayered coatings can be produced.[46] Important examples include Cr–Si- and Al–Si-rich compositions, for example, Sermaloy J and Sermetel 1515.

Chromizing can be used with both iron- and nickel-based alloys to provide protection at moderate temperatures (700 °C) against Type-II hot corrosion and intermediate-temperature oxidation. The concentration of chromium in the alloy surface can be raised to 40–80 wt% and this is sufficient to form a protective chromia layer. Chrome–aluminizing is also used to improve protection, particularly at slightly higher temperatures. It has become the case, however, as temperatures increase in the pursuit of improved fuel efficiency, that more attention has been paid to the production of aluminide layers and the subsequent formation of alumina protective layers.

1.27.3.3.2 Aluminide coatings

Important applications of aluminide coatings arise in the protection of Co- and, particularly, Ni-based superalloys, since both form aluminide phases which fix high concentrations of aluminum as a surface layer, typically 30–70 μm thick. The coatings can be produced from packs of either high or low aluminum activity. The former is processed at lower temperatures and the latter at higher temperatures in the typical range 800–1100 °C. High-activity aluminizing results in the formation of a Ni_2Al_3 layer produced predominantly by inward diffusion of aluminum. Constituents of the alloy can become incorporated within this layer, which has relatively poor toughness. Improvements result in subsequent heat treatment to convert the higher aluminide to NiAl. Low-activity processing results directly in the formation of a NiAl layer, which forms principally by the outward diffusion of nickel. This layer is then relatively free of alloy constituents (but can contain pack residues unless formed by vapor deposition above pack) and exists over a wide range of stoichiometry[47] as shown schematically in Figure 1. These coatings provide good resistance to Type-I hot corrosion and to high temperature oxidation through the formation and maintenance of a protective alumina layer. Their disadvantage is that they are relatively thin and, although having higher aluminum contents than the thicker MCrAlY overlay coatings, have a smaller total reservoir of aluminum. Loss of aluminum through the oxidation process as well as by interdiffusion with the substrate alloy limits their effectiveness after extended periods at high temperatures, say >1050 °C.

A particularly successful modification to aluminide coatings has been the incorporation of platinum into the coating by deposition of a thin layer, ~10 μm thick, prior to the aluminizing stage. The β layer which is formed, again ~50 μm thick, has the composition (Ni, Pt)Al with platinum contents of ~8 at.%. This phase can also exist over a wide range of aluminum and platinum contents.[47] The microstructure of such a coating is shown in the as-received condition in Figure 8(a) as a bondcoat (BC) within a thermal

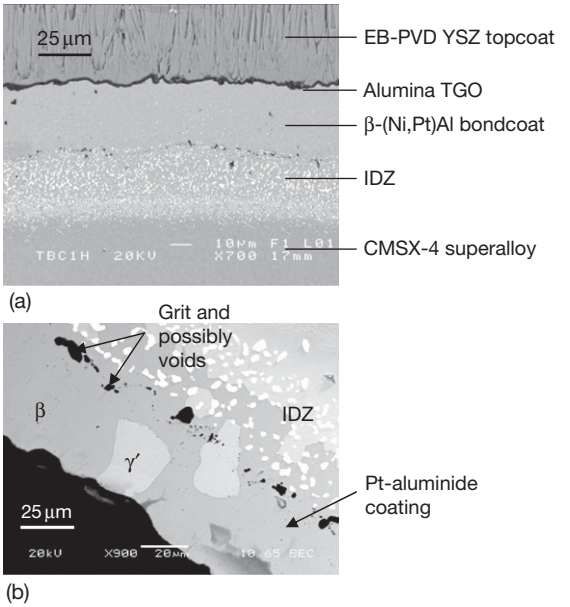

Figure 8 Cross-section of Pt-aluminide diffusion coatings. (a) In the as-received condition as a bondcoat (BC) in a TBC system showing the fully β-(Ni, Pt)Al layer and an extensive interdiffusion zone (IDZ) and (b) after 100 h oxidation at 1100 °C showing partial transformation of the original β phase to γ′ resulting from aluminum depletion. Courtesy of Miss F. Schenach.

barrier coating (TBC) system, which will be described later. It can be seen that there is also an extensive interdiffusion zone beneath the β layer. This contains a dispersion of phases rich in alloy constituents such as tantalum and titanium.

The addition of platinum to the β-phase appears to improve the oxide spallation resistance of the coatings, possibly by decreasing the segregation of sulfur to the oxide–metal interface.[48,49] It also decreases the chemical activity of aluminum[47] and then should be expected to decrease the extent of aluminum loss by interdiffusion with the substrate alloy. The experimental evidence is ambiguous, however, because platinum additions also seem to increase the principal diffusion coefficient of aluminum.[47] Continued exposures at high temperature will inevitably result in aluminum depletion as a consequence of both alumina formation and interdiffusion and this will cause phase transformation within the coating along the sequence

$$\beta \rightarrow \gamma' \rightarrow \gamma$$

An example of a Pt-aluminized coating with partial transformation to the γ′ phase after oxidation at 1000 °C for 100 h is shown in **Figure 8(b)**. It should be noted, though, that both phases have adequate aluminum contents to maintain a protective alumina layer.

1.27.3.3.3 Platinized coatings

An important variation on the conventional Pt-aluminized coatings described above is to omit the aluminizing stage in coating manufacture but to retain the step of platinum deposition and subsequent inward diffusion into the Ni-based superalloy. This approach was patented in 1999 by Rolls-Royce and Chromalloy UK[50] and has subsequently been developed to the stage of commercial deployment as BCs in TBCs – see later text for a description of these. Unfortunately, few of the results of the underlying research work supporting this development have appeared in the open literature.[51,52]

The key requirement of the coating is that it should be capable of forming and maintaining a protective alumina layer. It is not intuitively obvious, however, that this should be so because no aluminum is added and, as is recalled from **Section 1.27.1** and **1.27.2**, the Ni-based superalloy has borderline properties in this respect. Nevertheless, a 50-μm-thick γ/γ′ surface zone of enhanced aluminum concentration is formed indicating that there must be an outward flux of aluminum from the alloy into this zone. Concentrations of aluminum in the Ni–Al–Pt coating need to be ∼10 wt%, that is, approximately twice the base alloy concentration, to stabilize the γ/γ′ phase structure at 1100 °C.[47] The likely range of aluminum contents within the coating, shown schematically in **Figure 1**, is similar to that of MCrAlY coatings and will be sufficient both to form an initial alumina layer and to reheal this in the event of its failure (**Figure 2**). The apparent 'uphill' diffusion of aluminum out of the alloy into the coating, that is, its diffusion against its concentration gradient, can be explained again by the strong bonding between platinum and aluminum. It must mean that the chemical activity of aluminum within the coating is lower than that within the alloy so that the enrichment within the coating is simply a consequence of aluminum diffusing down its activity gradient. As recognized,[47] the coating has a replenishing capability by being able to transfer aluminum into itself from the alloy, as the continued growth of the alumina layer removes aluminum from its outer surface.

1.27.3.3.4 Silicide diffusion coatings

Silicide coatings have the potential of offering significant improvements in oxidation and hot corrosion resistance through the formation of a protective layer of silica. Siliconizing of iron and simple carbon steels was achieved by Fitzer in 1954[53] using pack cementation. These coatings were found to improve resistance to both Type-I and Type-II hot corrosion. They consist principally of an outer layer of ferrite containing up to ∼10 wt% Si and are susceptible to cracking during mechanical and thermal loading.[54] Silicon-rich coatings on Ni-based alloys have been achieved using chemical vapor deposition (CVD)[55] but there are concerns with the Ni–Si system over the presence of relatively low melting temperature eutectics. NiSi, in particular, forms an eutectic with Ni_2Si which melts at 943 °C. More attractive approaches for iron- and nickel-based alloys are likely to involve the incorporation of silicon into chromized or aluminized layers.[36,56]

Direct reaction of silicon with the alloy substrate to form a high melting-point surface layer is of particular interest with molybdenum-,[57] niobium-,[58] and titanium-based[57,59–62] alloys. The last, in particular, are of current relevance in aeroengines because of their good density-compensated creep properties but are handicapped by poor long-term oxidation resistance.

A wide range of titanium silicides can be produced in sequential layers on the alloy surface by using a

cementation pack, as shown by Cockeram and Rapp.[57,61] These coatings can be ~100 μm thick and substantially improve oxidation resistance, particularly when doped with germanium when oxidation rates in the temperature range 700–1000 °C are similar to those for the growth of silica itself (**Figure 9**). Protection is maintained even under thermal cycling but the layers are brittle and cracking should be expected. This is accentuated by the thickness of the coating which increases the probability of crack-like initiating defects being present.

Thinner coatings (~1–10 μm) can be produced by siliconizing, in which the test piece is buried in silicon powder, at temperatures between 800 and 1100 °C.[59,60] Higher temperatures in this range favor the formation of the Ti_5Si_3 phase rather than $TiSi_2$ as the outermost layer produced in the cementation pack.[57,61] These thin Ti_5Si_3 layers were uncracked and the layers again conferred significant improvements in oxidation resistance of the underlying Ti-rich alloy, as can be appreciated from **Figure 9**. A rather novel approach[62] to producing a thin, 1–2 μm, layer of Ti_5Si_3 is to use reaction (B) below to transport silicon to a Ti–Al test piece *via* gaseous SiO.

$$3SiO_2 \rightarrow 3SiO + 1½O_2 \quad [8]$$

The subsequent reaction [9] produces the silicide:

$$5Ti + 3SiO \rightarrow Ti_5Si_3 + 1½O_2 \quad [9]$$

The overall reaction is

$$5Ti + 3SiO_2 \rightarrow Ti_5Si_3 + 3O_2 \quad [10]$$

This reaction will only proceed in the direction shown at low oxygen partial pressures, calculated by Gray *et al.*[62] at 7.7×10^{-22}. This seems to have been achieved in a sealed silica capsule, evacuated from an argon atmosphere, without the use of extraneous oxygen getters, such as titanium chips, but by using the α_2 phase of the alloy as an intrinsic getter. As with the above, a substantial improvement in oxidation resistance, a factor 5 in weight gain in this case, was achieved over the uncoated Ti–Al control over the test duration of 500 h at 900 °C. The parabolic rate constants of the more protective coatings are plotted in **Figure 9** and compared with the behavior of unalloyed titanium[63] and pure silicon.[64] It can be seen that only the Ge-doped coatings actually achieve the level of protection expected of a pure silica layer.

Broadly similar behavior to the Ti_5Si_3 coatings has been found by Taniguchi *et al.*[65] for the bulk phase. In this case, rutile (TiO_2) had formed above the silica layer and clearly contributed to the weight

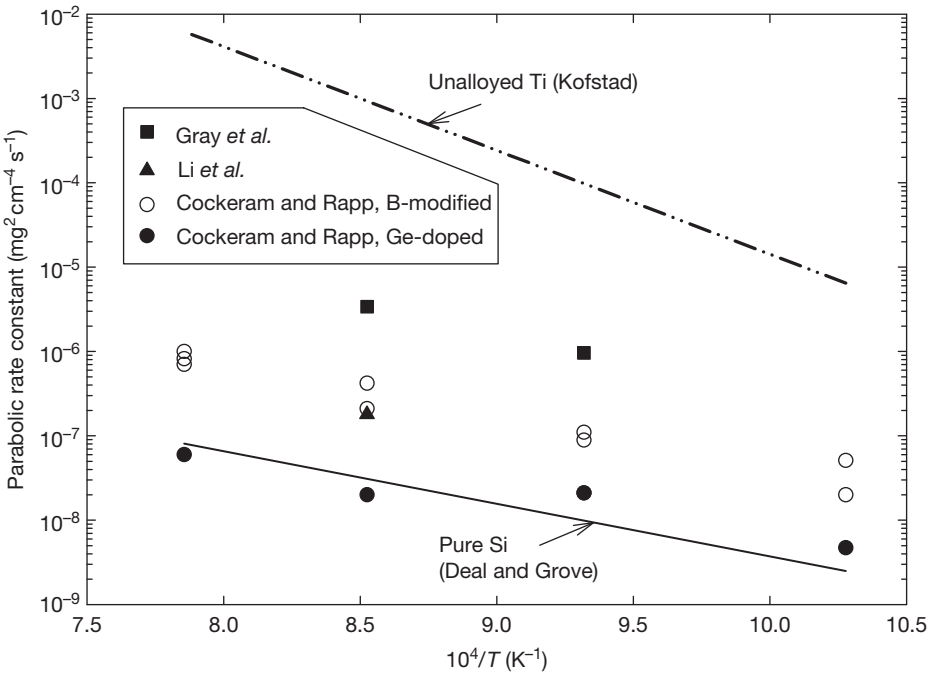

Figure 9 Parabolic rate constants for some silicide-coated titanium-rich alloys compared with the behavior of unalloyed titanium and silicon.

gain of the specimen. An implication is that the beneficial influence of Ge-doping (Figure 9) arises by limiting the transport of titanium through the silica layer.

1.27.3.4 Thermal Barrier Coatings

When discussing the need for high temperature coatings in Section 1.27.1, emphasis on placed solely on achieving adequate oxidation and corrosion resistance. However, under modern turbine conditions and in other applications, such as diesel engines, it can also be necessary to protect the substrate alloys from combustion temperatures by means of TBCs. This developmental trend for aeroengines and associated Ni-based superalloys is shown in simplified form in Figure 10.

It can be seen how in the first 20 years or so, blade alloys had adequate properties in the wrought and unprotected form to satisfy turbine requirements. In the early 1960s, a significant change in blade design permitted the use of some intake air to provide cooling and this increased the turbine entry temperature (TET) significantly above the inherent capabilities of the substrate alloys. During this period from 1940 to approximately 1990, successive generations of superalloys were developed with improved mechanical properties and, hence, higher temperature capabilities. This has been shown simply as a linear trend in Figure 10 but more details can be found elsewhere.[1] The main change during this period was to move from wrought to cast, directionally-solidified structures. The most recent development is the use of cast, single-crystal alloys, such as CMSX-4 (see Table 1), for blades which remain cooled and also are now coated with TBC systems. The use of these can improve engine efficiency and can also extend service lifetimes.[66,67] This same general developmental trend is mirrored in land-based turbines although TETs in these cases tend to be lower and the moves toward TBC usage lag behind those of aeroengines. A cross-section of a typical TBC system is shown schematically in Figure 11.

A TBC system consists of the outer thermal barrier topcoat which is attached to the alloy substrate by means of a mechanically-compliant, oxidation-resistant BC. The topcoat is generally zirconia, containing ~7–8 wt% yttria. This addition provides partial stabilization of the tetragonal (and cubic) zirconia phases and avoids the volume changes associated with the formation of the monoclinic phase. This yttria-stabilized zirconia (YSZ) layer (sometimes termed yttria partially stabilized zirconia (YPSZ)) has a low thermal conductivity, ~1 Wm^{-1} K^{-1}, which is approximately an order of magnitude lower than that for alumina. It means that for cooled turbine blades, a temperature drop of perhaps 150 °C can be obtained across a 250–300-μm-thick topcoat during service which provides considerable benefit to the load-bearing capability of the Ni-based superalloy. It needs to be emphasized, however, that the YSZ topcoat is permeable to oxygen and will not provide oxidation protection. This is achieved by means of the BC which is intended to be alumina-forming and can be based on

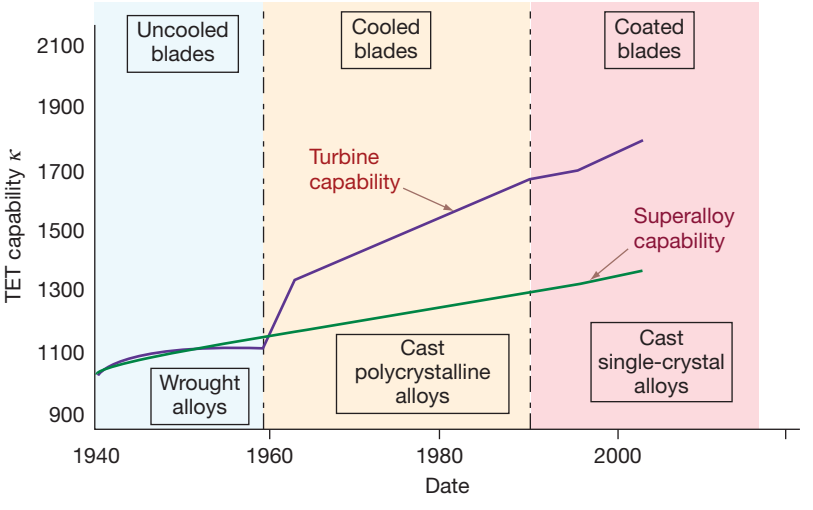

Figure 10 A comparison of the historical increase in turbine entry temperature (TET) for aeroengines and the associated temperature capability of the alloys used for turbine blades.

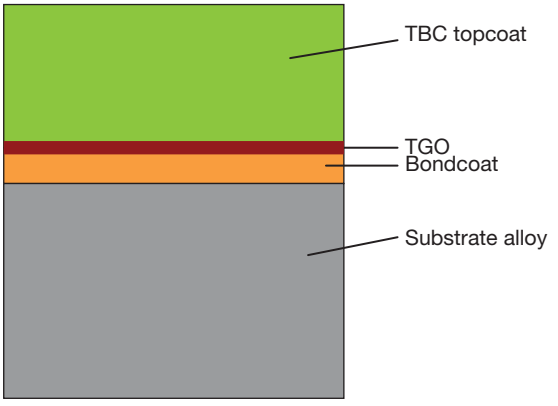

Figure 11 Schematic cross-section of a thermal barrier coating system.

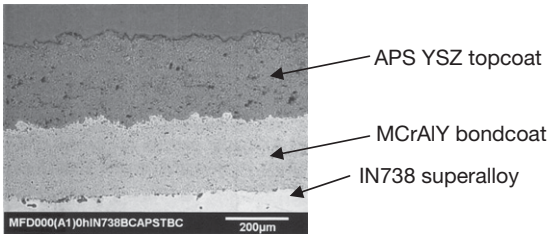

Figure 12 Cross-section of a typical land-based TBC coating system consisting of an air plasma sprayed (APS) YSZ topcoat with a MCrAlY BC[68] on an IN738 Ni-based superalloy substrate. Note the relatively rough BC surface and the limited interdiffusion zone compared with the TBC system shown in **Figure 8(a)**.

one of the MCrAlY overlays discussed previously or on diffusion coatings of the Pt-aluminide or platinized variants. The oxidation of these BCs forms a layer of thermally grown oxide (TGO) over time between the BC and TBC topcoat as shown schematically in **Figure 11**. As will be discussed in some depth in **Section 1.27.5**, the formation of the TGO plays a significant role in the failure by spallation of the TBC.

TBC systems used in practice on Ni-based superalloys for turbine applications tend to be of two distinct types. For large, land-based units, a system consisting of a MCrAlY BC, deposited by any of the processes discussed previously, with a YSZ topcoat produced by APS is usually used. An example of this system is shown in **Figure 12**. In smaller machines, such as aeroengines or, increasingly, small land-based turbines, YSZ layers deposited by electron-beam physical vapor deposition (EB-PVD) are favored. These TBC systems can use MCrAlY BCs also but more typically have Pt-aluminide or, in Rolls-Royce aeroengines, platinized diffusion coatings. A typical cross-section of a system consisting of an EB-PVD topcoat and a Pt-aluminide diffusion BC is shown in **Figure 8(a)**. The columnar nature of the EB-PVD topcoat is evident and can be contrasted with the splat structure of that produced by APS. A much more extensive interdiffusion zone than in the MCrAlY system is also formed during coating manufacture.

To date, the commercial exploitation of TBC systems has been dominated by applications using Ni-based alloys but there is also foreseeable potential for their use on other high temperature structural materials such as the Ti–Al series. Significant progress has already been made in the production of aluminide diffusion coatings on Ti-based alloys[69–71] and recently these have been used as a BC under an APS YSZ topcoat in a TBC system.[72]

1.27.4 Case Study I: Oxidation and Lifing of MCrAlY Overlays

1.27.4.1 Protective Oxidation

In the initial stages of exposure of a complex alloy such as the (Ni, Co)CrAlYs, all constituents which can oxidize will do so and nonprotective oxides such as NiO together with spinels such as $NiCr_2O_4$ are likely to form. Eventually, however, a continuous α-alumina layer will develop underneath these oxides and oxidation rates will rapidly decrease. The formation of metastable aluminas, even at the relatively low temperature of 950 °C, was not found in a study[73] using *in situ* high temperature XRD on a CoNiCrAlY coating. This transitional behavior may not be an issue with these systems at relevant operating temperatures although with FeCrAlY alloys at the slightly lower temperatures of 900 and 925 °C, the transition from θ- to α-alumina took tens of hours.[74]

The growth kinetics of the α-alumina layer on MCrAlY-type alloys have been variously reported to be parabolic (eqn. [1])[75,76] or subparabolic[77] as in the general eqn. [11] for increase in oxide thickness, h, with exposure time, t, at a constant temperature.

$$h = h_o + k_n t^{1/n} \qquad [11]$$

Here, h_o is the preexisting oxide thickness at $t = 0$, n is a time-invariant numerical constant, and k_n is the corresponding rate constant. Ideal parabolic conditions exist when $h_o = 0$ and $n = 2$ (eqn. [1]) but subparabolic kinetics obtain when $n > 2$. The reasons for the differences in kinetics are poorly understood

although there are considerable implications for the longevity of the coatings. Subparabolic kinetics can arise, in principle, as a result of an increase with time of compressive growth stress within the oxide layer.[38,78] They will also arise[79] if oxide grain size increases during exposure and diffusion of reactive species occurs principally by grain boundary diffusion. It is also feasible, particularly with a stoichiometric compound such as alumina, that the gradual incorporation of coating or alloy (minor) constituents affects any doping of the oxide layer so as to decrease diffusion rates progressively with time. Apparent subparabolic kinetics will also occur in those systems and exposure conditions in which metastable alumina forms and transforms over time to the α phase.[80] The situation is unclear and, for present purposes, it will be assumed that the α-alumina layer grows parabolically with time with $h_o = 0$ and $n = 2$ in eqn. [11]. This assumption leads to conservative estimates of coating lifetimes.

The temperature dependence of the parabolic rate constant for the growth of a protective α-alumina layer on various coating-type alloys is shown in **Figure 13**,[75,76] but expressed in terms of mass gain, Δm, per unit surface area. A reasonable mid-range expression for the rate constant, k_p', from **Figure 13** is

$$k_p' = 2.68 \times 10^4 \exp\left(-\frac{275\,000}{8.314T}\right), \text{mg}^2\text{cm}^{-4}\text{s}^{-1} \quad [12]$$

where T is absolute temperature and the mass gain has been expressed in the more common units of mg cm^{-2}. This equation can be expressed in terms of the parabolic rate constant k_p, which uses oxide thickness rather than mass gain, by means of eqn. [13].

$$k_p = \left[\frac{M_{ox}}{3M_o\rho_{ox}}\right]^2 k_p' \quad [13]$$

Here, ρ_{ox} is the density of α-alumina (taken as 4000 mg cm^{-3}), M_{ox} is the molecular mass of alumina and M_o is that of oxygen; the factor three arises because there are three oxygen atoms in Al_2O_3. This conversion equates 1 mg cm^{-2} mass gain to an ~5.3 μm thick layer of α-alumina. Using eqn. [13] to substitute into eqn. [12] then gives:

$$k_p = 7.56 \times 10^{-7} \exp\left(-\frac{275\,000}{8.314T}\right) \text{m}^2\text{s}^{-1} \quad [14]$$

The protection offered by the alumina layer can be appreciated by using eqn. [14] in eqn. [1] to show that the oxide thickness after 30 000 h at 1000 °C is still only ~20 μm. This corresponds to a section loss, x_h, of the coating of[38]

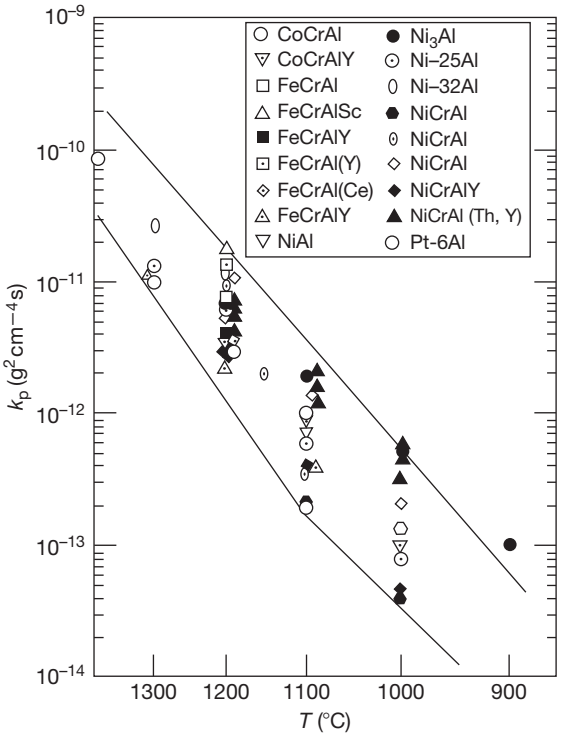

Figure 13 Parabolic rate constants for the formation of alumina on coating-type alloys.[76]

$$x_h \approx \frac{h}{\phi} \approx \frac{20}{1.28} \approx 15.6\,\mu\text{m} \quad [15]$$

where ϕ is the Pilling–Bedworth ratio for alumina (1.28). This level of loss in an MCrAlY coating some 200 μm thick after this exposure period would be excellent behavior but, unfortunately, other degradation processes also occur which limit lifetimes. Principal among these is the loss of aluminum from the coating and the consequences of this. Depletion will occur as a result of selective oxidation, as described in **Section 1.27.2.2**, and will increase with time at temperature. In addition, it will be exacerbated by spallation or cracking (and rehealing) of the protective oxide layer, geometrical factors, internal oxidation, and interdiffusion with the substrate alloy. All of these factors will be considered in this section.

1.27.4.2 Spallation and Cracking of the Protective Alumina Layer

Spallation and cracking of the protective oxide layer results from the generation of strains and associated stresses arising from the oxide growth process,

from temperature changes or imposed upon the component. The issues are particularly complex since they depend on the nature of the oxidation process (the balance between growth by cation or anion fluxes), on the curvature of the substrate and on the elastic, plastic and, particularly, creep properties of the respective layers of the coating system. A background review is available[38] and phenomenological approaches to failure which combine strains from multiple sources have also been developed.[81–83] These predictive approaches have been formulated specifically for TBC systems but contain general principles.

This chapter emphasizes solely the influence of thermal strains in producing oxide spallation from a MCrAlY substrate in order to establish mechanisms. Strains deriving from oxide growth will be significant only if creep relaxation rates are low or, on curved surfaces, if the oxide thickness is of similar magnitude to the local radius of curvature.[38] For now they are neglected but, if significant, can simply be introduced as an additive term.[82] The implication is that the alumina–MCrAlY interface is sensibly flat, that is, there are no locations where the local radius of curvature is of similar magnitude to the oxide thickness. During cooling there are then negligible out-of-plane strains, provided the oxide remains adherent, but a substantial biaxial compressive in-plane strain can develop within the oxide layer. If elastic conditions are assumed, this strain corresponds to an in-plane oxide stress, σ_{ox}, given by[84]:

$$\sigma_{ox} = \frac{E_{ox}\ \Delta T(\alpha_m - \alpha_{ox})}{(1-\upsilon)\left(1+\frac{E_{ox}h}{E_m w}\right)} \qquad [16]$$

Here, ΔT $(=T - T_{ox})$ is the temperature drop, taken as a negative quantity, E_{ox} and E_m are the Young's moduli of, respectively, oxide and metal; α is the corresponding linear thermal expansion coefficient; υ is the Poisson's ratio, assumed to be the same for oxide and metal; h is the oxide thickness, and w is half the specimen thickness. For thin oxides relative to the metal substrate, the equation can be simplified to (compare eqn. [7]):

$$\sigma_{ox} = \frac{E_{ox}\ \Delta T(\alpha_m - \alpha_{ox})}{(1-\upsilon)} \qquad [17]$$

It is also reasonable to assume that the underlying superalloy is much thicker than the coating and, of course, the oxide so that the alloy's dimensional changes are imposed upon the oxide. This means that in eqn. [17], the expansion coefficient, α_m, should be that for the superalloy rather than for the coating. Using representative values of, $\upsilon = 0.3$, $E_{ox} = 387$ GPa, $\alpha_{ox} = 7.9 \times 10^{-6}$ K^{-1}, and $\alpha_m = 15.0 \times 10^{-6}$ K^{-1} in eqn. [17] predicts a residual in-plane oxide stress of ~ -3.9 GPa after a temperature drop of 1000°C. Values of stress of this magnitude have been measured in related alloys and coatings.[68,85,86] Since the values of expansion coefficients and Young's modulus are assumed to be independent of temperature, the elastic oxide stress varies proportionately with temperature change and will be tensile for temperature increases above the oxidation temperature.

Spallation under in-plane compression can occur by two nominally distinct routes depending on the relative strengths of oxide and oxide–coating interface,[38,39] as shown schematically in **Figure 14**. The critical stress for buckling of the oxide layer (**Figure 14(a)**) can be obtained from standard text[87] and converted[38] to a critical temperature drop, ΔT_b, of

$$-\Delta T_b = \frac{1.22}{(1-\upsilon^2)(\alpha_m - \alpha_{ox})}\left(\frac{h}{R}\right)^2 \qquad [18]$$

where the symbols have the same meaning as previously and R is the radius of the circular zone of prior decohesion at the oxide–coating interface. It can be appreciated that for a given value of R, the temperature drop required to effect buckling increases with oxide thickness. For typical values of the various parameters, the zone diameter needs to be approximately at least 20× the thickness of the oxide layer

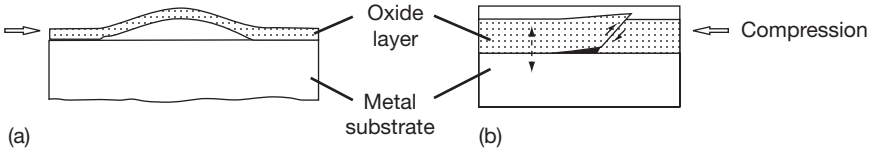

Figure 14 Spallation of the oxide layer under in-plane compression from the metallic MCrAlY substrate can occur by either (a) a buckling or (b) a wedging process.

before the buckle configuration can develop. Thus, for a typical oxide thickness of 5 μm, a circular interfacial zone of some 100 μm would be required. This is a problematic issue since such large areas of decohesion are not seen at the alumina–MCrAlY interface in these simple overlay coatings. The intrinsically good adherence of the alumina layer is related to the addition of yttrium into these coatings which appears to mitigate the potentially harmful effects of sulfur segregation in lowering interface adhesion.[88,89]

In the presence of good adhesion between oxide and coating, a thick protective layer can develop but this, as found on related systems, still contains porosity and crack-like defects.[90,91] At some critical value of the compressive thermal stress generated during the cooling transient, a shear crack can be initiated from one or more of these defects, as shown schematically in **Figure 14(b)**. Continued cooling and contraction of the oxide layer will produce further shear on the crack-like surface and the development of out-of-plane tensile stresses at the oxide–coating interface. A consequence is that a wedge crack will grow along this interface as cooling continues and may cause spallation of the overlying oxide layer. Extensive finite-element (FE) modeling of this wedging process has now been undertaken for chromia and alumina layers on various metallic substrates.[92–94] A consistent result from this work is that the growth rate of the interfacial wedge crack is significantly retarded during cooling as a result of the relaxation of crack-tip stresses by creep of the adjoining metal. Some results[93] for a 5-μm-thick alumina layer on Haynes 214 are given in **Figure 15**. They show that the wedge crack nucleates quickly but its growth rate is then stopped until some lower temperature at which rapid propagation occurs over a narrow temperature range. This period of quiescence corresponds to the period of significant stress relaxation by alloy creep and its extent decreases with increased cooling rate, as shown.

The general behavior shown in **Figure 15** can be approximated by the dashed horizontal and vertical lines superimposed, for clarity, only on the FE results for a cooling rate of 10^4 °C h^{-1}. They can be interpreted as showing that the oxide remains adherent to the alloy or coating until a critical temperature drop, ΔT_c, at which stage the stored strain energy, W^*, per unit volume in the oxide layer is sufficient to produce decohesion of the oxide–metal interface. For a thin planar biaxially strained oxide layer of thickness h, the strain energy in the oxide layer per unit area of

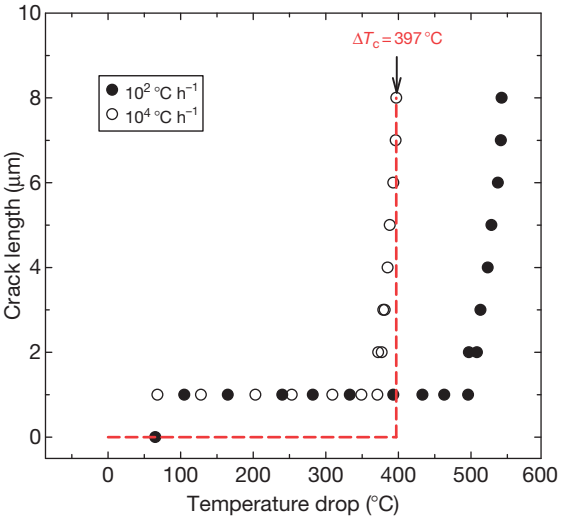

Figure 15 Finite-element predictions of the kinetics of interfacial wedge crack growth for an alumina layer on Haynes 214 cooled from 1100 °C at the rates shown. The dashed line reflects ideal behavior for spallation to occur at a critical value of oxide strain energy.

oxide–metal interface at a temperature drop ΔT is given as[95]:

$$hW^* = hE_{ox}(1-\upsilon)(\Delta T)^2(\alpha_m - \alpha_{ox})^2 \qquad [19]$$

Equating this to the fracture energy, γ_F, of unit area of interface gives the critical temperature drop for spallation as:

$$-\Delta T_c = \left[\frac{\gamma_F}{hE_{ox}(\alpha_m - \alpha_{ox})^2(1-\upsilon)}\right]^{1/2} \qquad [20]$$

This shows that the critical temperature drop decreases with oxide thickness, that is, spallation becomes easier for thicker oxides which is a common observation. It contrasts with the buckling mode (eqn. [18]) which becomes more difficult with increasing oxide thickness.

In applying eqn. [20] for prediction it should be noted that the fracture energy is an effective value since most of the strain energy is lost by creep relaxation during the cooling transient.[92–94] Its value can be obtained from eqn. [20] using the FE predictions of ΔT_c and is always larger than the intrinsic fracture energy of the interface when relaxation processes are present. Thus, for the example shown in **Figure 15**, γ_F is calculated to be ~33 J m^{-2} for the higher cooling rate and ~62 J m^{-2} for the lower. Using a similar approach for a free-standing NiCrAlY coating,[93] the values of the effective fracture energy shown in

Table 3 Estimated effective fracture energies, γ_F, for the spallation of a 5-μm-thick alumina layer from a free-standing NiCrAlY coating[92]

Cooling rate ($^\circ C\ h^{-1}$; $^\circ C\ s^{-1}$)	*Computed* ΔT_c ($^\circ C$)	γ_F ($J\ m^{-2}$)
10^2	745	40
10^3	620	28
10^4	550	22
10^5	382	10
10^6	314	7

Table 3 are obtained as a function of cooling rate. This decrease of γ_F with increasing rate reflects the decreased contribution from creep relaxation and shows that no unique value of the fracture energy can be assumed. It is possible, however, to interpolate between these results for any given conditions within the range shown. The values of γ_F given in the table are typically 10–100 greater than the likely intrinsic interfacial fracture energy but are of similar magnitude to those measured by blister testing[96] and spallation[93,94,97,98] on other systems.

This discussion has highlighted the benefits of stress relaxation within the coating to the spallation resistance of the oxide during a simple cooling transient. It should not necessarily be generalized from this, however, that weak coatings should be preferred over strong. An important consideration is that creep relaxation during thermal cycling can generate a mechanical hysteresis loop[94,99] which can place the oxide layer into in-plane tension on the return to temperature. Consequent tensile cracking will, of course, impair the protective function of the oxide layer. Strong coatings are also desirable to maintain mechanical stability in rapidly rotating components. The balance of creep properties between high and low strength will depend on the application, for example, the magnitude of external stresses, the frequency of thermal cycling, the rate of change of temperature, and the presence of hold periods within the creep regime.

1.27.4.3 Aluminum Depletion

1.27.4.3.1 Uniform depletion

The second main form of coating degradation is through the loss of aluminum and the consequent inability to maintain and reform the protective alumina layer. A general discussion of the depletion occurring as a result of the selective oxidation of aluminum has been given in Section 1.27.2.2. It is shown in that section, how the aluminum concentration can be decreased beneath the oxide but that the aluminum reservoir within the bulk of the coating could maintain concentrations sufficiently to ensure reformation of the alumina layer in the event of its spallation or cracking. Nevertheless, the depletion of aluminum by selective oxidation will destabilize Al-rich phases in the vicinity of the surface oxide. In particular, dissolution of the β-NiAl phase will occur in a zone near the alumina layer[100,101] and, as expected for parabolic oxidation kinetics, the depth of this β-free zone will thicken parabolically with time. In addition, loss of aluminum by interdiffusion with the substrate can also result in the formation of a β-free zone at this inner interface. With continued exposure, the entire coating can become free of the β-phase and this has been used as a failure condition for the coating.[100] This is a useful pragmatic approach but is conservative since sufficient aluminum will usually still be present to provide a rehealing capability.

Even so, substantial exposure periods can be obtained while still retaining some β-phase. Anton *et al.*,[101] for example, find a total β-depletion zone, from inner and outer coating surfaces, of 160 μm in a 250-μm-thick LPPS CoNiCrAlY coating after 10 000 h at 1000 °C. This particular coating contained only 8 wt% Al but exhibited substantial interdiffusion with the IN738LC alloy substrate and formation of Kirkendall voids within the interdiffusion zone (IDZ). The extent of β depletion was decreased, as expected, by increasing the aluminum content to 12 wt% in a NiCoCrAlY coating but rhenium additions also decreased the extent of interdiffusion. In this case the total β-depletion zone was only ~75 μm after 10 000 h at 1000 °C.[101]

Although the extent of aluminum depletion resulting from selective oxidation can be predicted based on the concepts outlined in Section 1.27.2.2, it is much more difficult to model the interdiffusion process. Analytical and numerical attempts have been made for MCrAlY systems[83,102] but it is difficult to deal with diffusion and concurrent precipitation without knowing the appropriate interaction terms for the diffusion coefficients or, equivalently, the chemical activities of the diffusing species. Taylor, *et al.*,[102] for example, report how the diffusion of aluminum from a LPPS CoNiCrAlY coating into a CM186 substrate alloy, in the early stages of exposure at 1200 °C, is limited by the formation of Al-rich phases, associated with tantalum, within the IDZ. With continued exposure and further aluminum

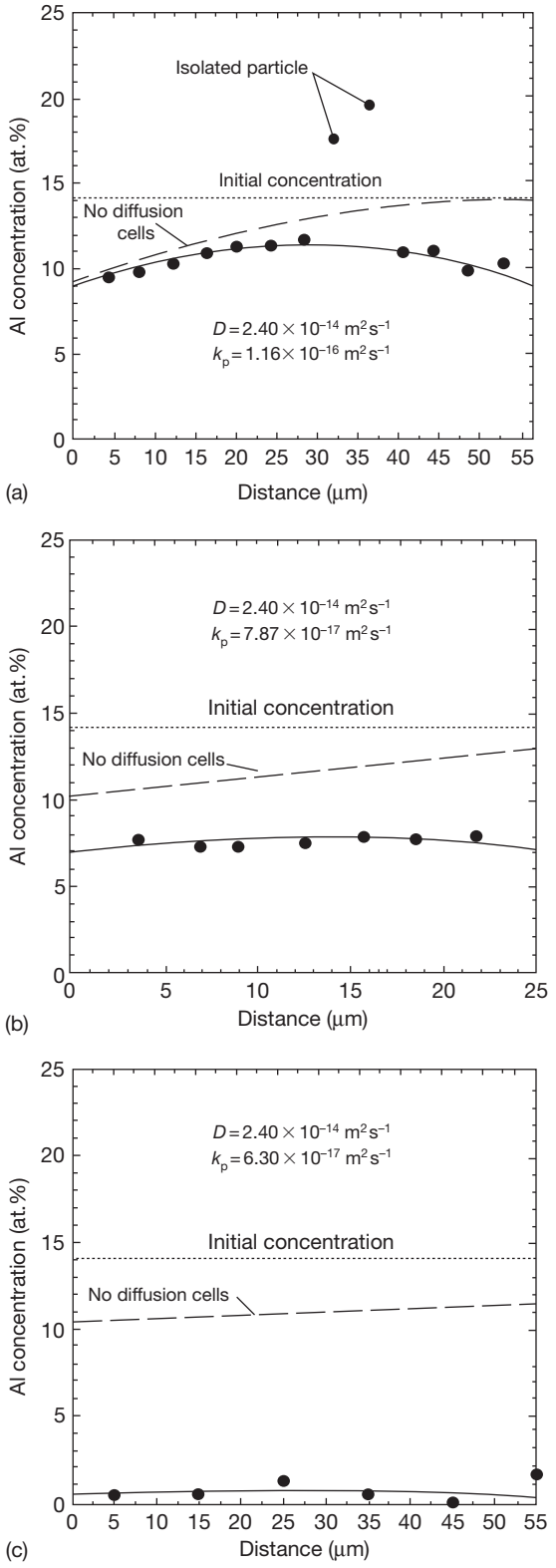

Figure 16 Enhanced aluminum depletion measured in individual diffusion cells in an APS CoNiCrAlY coating. The points are measured using SEM/EDS and the solid line is the best-fit solution to eqn. [21] using the values shown for D and k_p. See text for more details. The dashed line is the expected depletion profile, using the same values of D and k_p, if diffusion cells were absent. Oxidation was performed in air for (a) 4 h, (b) 4 h, and (c) 100 h.[105]

depletion within the coating, these phases dissociate and act as a reservoir to resupply aluminum back into the coating. These counter-flows of diffusive flux reflect the changing aluminum activities within the coating and IDZ. They emphasize that, in such complex situations, modeling using single-valued diffusion coefficients and chemical potential gradients approximated by gradients in concentration can lead to erroneous results.

Interesting future developments to limit interdiffusion are likely to involve the control of aluminum chemical activity within the coating[103] or the use of diffusion barriers such as α-Cr or Re-based alloys.[104]

1.27.4.3.2 *Diffusion cells and chemical failure*

In practice, exceptions to the ideal condition of uniform depletion will exist. These include the diffusional isolation of volumes of the coating as a result of internal oxidation or geometric factors. As highlighted in **Figure 3**, MCrAlY coatings deposited by plasma spraying in air (APS) are of relatively low density as a result of oxidation of the sprayed particles during coating formation. Bonding between the splats within the coating is impaired and internal oxidation at the splat surfaces can continue during subsequent exposure. ASPS and even HVOF coatings probably also suffer from this but to a lesser extent. The alumina layers formed internally in APS MCrAlY coatings have been shown[105] to act as diffusion barriers which isolate the splat volume from the reservoir of aluminum in the remainder of the coating. As a consequence, aluminum depletion within the relatively small splat volume occurs at a much greater rate than would be expected for the coating as a whole. This is shown in **Figure 16** for an APS CoNiCrAlY coating oxidized in air at 1100 °C.[105] Here the measurements of aluminum concentration were obtained across separate diffusion cells which were located at the surface of the coating and bounded around their surface by an alumina layer. The lines in the figures are predictions from eqn. [21] which considers the cell to be approximated as a long 2-dimensional slab, on both flat surfaces on which alumina grows parabolically.

$$C = C_b - \frac{50}{\phi}\left(\frac{\pi k_p}{D}\right)^{1/2} \cdot \sum_{n=0}^{\infty}\left[\mathrm{erfc}\left(\frac{2nw+x}{2(Dt)^{\frac{1}{2}}}\right) + \mathrm{erfc}\left(\frac{2(n+1)w-x}{2(Dt)^{\frac{1}{2}}}\right)\right] \quad [21]$$

Here, C is the aluminum concentration in at.%, C_b is the initial value within the cell, D is the aluminum interdiffusion coefficient, $2w$ is the cell width, x is the distance from the oxide–metal interface, and t is the exposure time. The predictions were made using a single-valued interdiffusion coefficient 2.4×10^{-14} m^2 s^{-1} (N.B. the sites were remote from any interdiffusion effects from the substrate) consistent with measurements on NiCrAl[106] and CoCrAl[107] systems. The corresponding k_p values to give the observed fit vary within a factor 2 but lie within the data spread of **Figure 13** (shown there in terms of mass gain). The expected depletion profile without diffusion cells is shown by the dashed line. The agreement with the data is good and confirms that oxidation is continuing at similar rates at both the external and internal surfaces in these coatings. It can be seen that depletion is much more pronounced in the small cell of **Figure 16(b)** than in the larger one of **Figure 16(a)** even after 4 h at 1100 °C. After 100 h exposure, aluminum has been essentially consumed in the 55 μm cell, **Figure 16(c)**.

The decrease in aluminum concentration can make these cell volumes susceptible to chemical failure (CF) at which stage fast-growing nonalumina oxides will form. A framework theory of CF can be found elsewhere.[108] The cell will be susceptible to mechanically induced chemical failure (MICF) when the aluminum concentration anywhere within it (usually, at the center plane) falls below that needed to reform the alumina layer should the original crack or spall. Intrinsic chemical failure (InCF), unlike MICF, is a thermodynamic boundary at which the aluminum concentration at the oxide–metal interface falls to that below which alumina can be reduced by another of the coating constituents, chromia for example. This critical concentration is very close to zero for the reduction of alumina by chromium but there is experimental evidence for the formation of Cr-rich oxides beneath an alumina layer in NiCrAlY coatings.[109]

A CF map for MCrAlY coatings can be constructed using eqn. [21] as shown in **Figure 17**. The calculations were performed using $D = 2.4 \times 10^{-14}$ m^2 s^{-1}, as above, and a mid-range value of $k_p = 9.0 \times 10^{-17}$ m^2 s^{-1}. The threshold line for

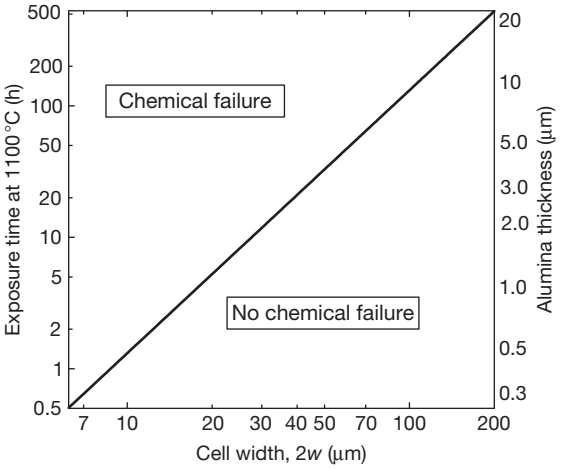

Figure 17 A chemical failure (CF) map for a MCrAlY coating (M = Co,Ni). The left-hand ordinate refers to exposure times at 1100 °C but the oxide thickness of the right-hand ordinate is independent of temperature.

initiating CF is relevant to the MICF condition assuming a critical aluminum concentration of 5 at.%. The exposure times shown as the left-hand vertical axis refer to 1100 °C but the oxide thicknesses (right-hand axis) apply at other temperatures also. Clearly, small cells are susceptible to early MICF leading to the consumption of the entire cell volume with the formation of porous and friable nonprotective oxides. For dense coatings, however, for example those produced by LPPS, internal oxidation is negligible and small diffusion cells do not form.[110]

MCrAlY coatings produced by spraying tend to have convoluted surfaces consisting of protuberances with dimensions relating to those of the original sprayed particles. They may also be postprocessed to change this topography but usually have a significant residual surface roughness. The significance is that a surface protuberance will have a surface-to-volume ratio larger than that of a flat coating. Aluminum depletion will then occur at an enhanced rate and early CF of the protuberance can be expected. Calculation of the rate of depletion is difficult to undertake analytically because the protuberance is not isolated from the bulk of the coating, as with the diffusion cells discussed earlier. Some resupply of aluminum will occur *via* the neck of the protuberance. Useful progress in prediction can be made, however, using numerical finite-difference methods and an example of some results, obtained using the 2-dimensional ODIN (Oxidation and INterdiffusion) code, is shown in **Figure 18**. These results apply to a

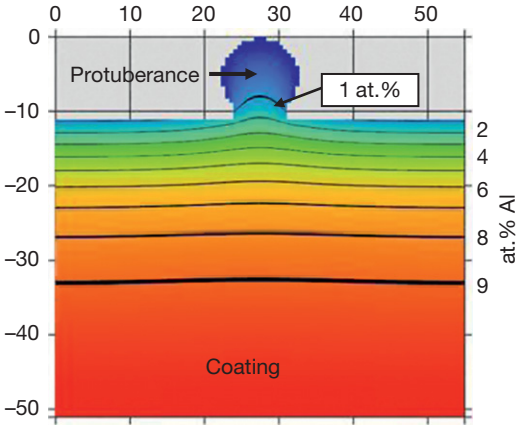

Figure 18 Finite-difference predictions of the Al depletion produced in a surface protuberance of a MCrAlY coating after oxidation at 1100 °C for 1 h. The left-hand and top axes give distances in microns. The right-hand axis gives the aluminum concentration corresponding to the iso-concentration lines drawn on the figure. Courtesy of Dr. W.M. Pragnell.

100 μm thick MCrAlY coating oxidized at 1000 °C for 1 h but with, for purposes of illustration, a relatively low initial concentration of 10 at.% Al. It can be appreciated that selective oxidation to form the alumina layer causes a significant decrease in aluminum content at the surface of the bulk coating with concentration increasing with distance from this interface. More details can be found elsewhere.[111] This level of depletion is similar to the schematic line for an uncoated alloy, of similar aluminum content, shown in Figure 2. In this particular example, there remains sufficient aluminum at depths of ~10 μm to reform the protective alumina layer. This contrasts with the situation within the protuberance, however, where concentrations have dropped everywhere to <1 at.% after 1 h exposure. Early MICF of this is then likely and, indeed, was observed.[111] This failure time is somewhat less but of similar magnitude to that shown for diffusion cells in Figure 17.

1.27.5 Case Study II: Oxidation-Induced Failure of TBC Systems

1.27.5.1 Failure Times under Oxidizing Conditions

An overview of TBC systems and principal types has been given in Section 1.27.3.4. They are an essential part of present-day strategies to operate high temperature machinery, particularly aeroengines and gas turbines, with increased fuel efficiency and longevity. In order to achieve this and to develop the full potential of TBC systems safely and reliably, it is necessary to understand and predict the degradation and failure processes within the system leading to spallation of the insulating topcoat. As a consequence, a tremendous amount of research activity has been undertaken worldwide, particularly in the last decade, to try and achieve these goals. At the time of writing, success has been elusive although large amounts of experimental data have been produced and a plethora of theoretical models have been suggested. It is beyond the scope of this present work to provide a detailed and comprehensive review of this large body of work which is often contradictory. Rather, a personal view will be presented which will attempt to identify key experimental observations and materials' properties and favor theoretical models which are consistent with these.

In some applications, for example, on rotating blades in gas turbines, TBC systems will experience mechanically-imposed strains in addition to those developed by the oxidation process. As discussed in relation to MCrAlY overlay coatings (Section 1.27.4.2), it may be feasible to sum these various strains and define a critical total value at which TBC failure will occur.[81–83] The approach is phenomenological in that no detailed mechanisms of failure are considered. It is, therefore, difficult to generalize complex situations where strains may be tensile or compressive and may act in different directions at different locations within the TBC system. Nevertheless, the approach does attempt to address the difficult subject of the interaction between applied external stresses and those produced by oxidation. For present purposes, however, as earlier with MCrAlY overlays, the intention is to examine only the role of oxidation and thermal loading in TBC failure.

It was pointed out in Section 1.27.3.4 that oxygen can penetrate the YSZ TBC layer and oxidize the underlying BC. The TGO, designed to be alumina, forms as an interlayer between the topcoat and BC as shown schematically in Figure 11. The development of this layer has been implicated in TBC spallation for many years and a simple failure criterion, used in practice, is to assume that spallation will occur at a critical TGO thickness. As shown in Figure 19, this can be a useful approach.

The time-to-failure data shown in Figure 19 derive from previous compilations,[112,113] but have been simplified to distinguish only between the common types of TBC system in commercial use: Pt-aluminide/EB-PVD YSZ, MCrAlY/EB-PVD YSZ, and MCrAlY/APS YSZ. Results on experimental

systems, which can show improved behavior to the above, have been omitted from this graph intentionally although they are prominent in current research literature. These include the use of platinum over- and under-layers to MCrAlY BCs,[114] preoxidation of MCrAlY BCs,[115,116] polishing of the BC surface,[117] and platinized BCs[51,52] see also **Section 1.27.3.3.3**). This body of work is of interest and may point the way to future improvements in TBC systems. The results have been omitted from **Figure 19** simply because they add other variables which will confuse the trends present in the failure-life compilation for conventional systems.

The data shown in **Figure 19** include results from tests ranging from nominally isothermal exposure to those using hourly thermal cycles, for which the accumulated time at peak temperature is used in the figure. A striking feature of the results is the very large scatter in lifetime – a factor 10 – at any given temperature. Within this scatter, there appears to be no systematic difference in behavior between the coating types or with the frequency of cycling.[112] This is a valuable working premise with which to find a path through the diverse competing models of failure. The solid line in the figure is the expected behavior if topcoat spallation occurred at a critical TGO thickness of 4 μm. It is calculated from eqn. [14], assuming an initially bare BC surface. It should be noted, though, that those systems with an EB-PVD topcoat will usually have a preformed alumina layer, ~0.5 μm thick on the BC surface. The agreement with the solid-line prediction is, nevertheless, quite reasonable and supports the use of this simple criterion as a pragmatic lifing method. It also supports the view,[118,119] that time and temperature are the principal parameters affecting lifetimes. The scatter can then be thought of as reflecting the underlying variability in the oxidation process together with the influence of uncontrolled variables, many of which are likely to arise from the manufacturing process. These will include BC surface roughness,[112,113,117] defects within the topcoat which may initiate interfacial cracks,[120] segregation of elements such as titanium from the substrate alloy,[52] and variable sulfur contents, particularly in Y-free BCs and alloys.[91,121]

1.27.5.2 Failure Characteristics

The failure times plotted in **Figure 19** refer to the loss of typically 20% or more of the area covered by the YSZ topcoat. Often this occurs by the spallation of the topcoat in sheets measuring some mm across as shown in **Figure 20**.[117] The morphology of these failed regions in terms of the ratio of the diameter

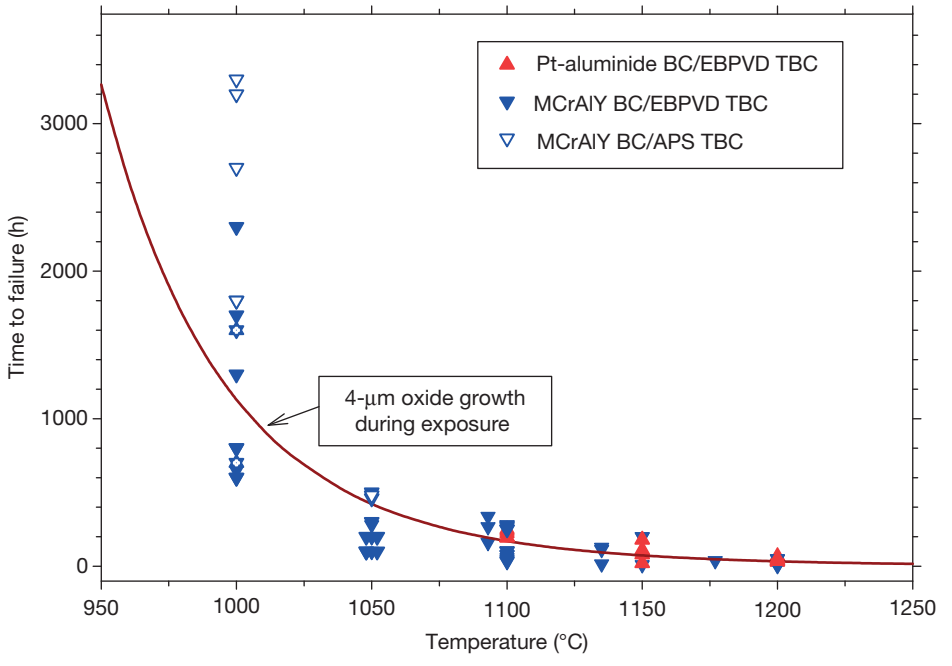

Figure 19 The temperature dependence of the time to spallation of the ceramic topcoat in various TBC systems in general commercial use.

Figure 20 Decohesion of large sheets of the YSZ TBC on a coated 25 mm diameter specimen.[117]

of the area of decohesion to the thickness of the coating (~20) is consistent with buckling occurring during cooling (**Section 1.27.4.2**). This is supported by examination of cross-sections of partially failed coatings[122] and by extensive modeling.[123] Edge cracking can also, in principle, produce spallation of large areas of the coating[123] but this appears to be a much more variable event than buckling. It has not occurred, for example, in the specimen shown in **Figure 20** but there are other cases of laboratory samples where coating failure at edges has occurred[117] but also accompanied by failure remote from these sites.[124]

As discussed in **Section 1.27.4.2**, catastrophic buckling will occur during cooling only when a delamination zone of critical radius has formed under the coating. Preexisting zones of this size are not present in the as-manufactured coating and must form during the high temperature exposure. The relatively slow growth of these subcritical defects determines the life of the TBC system and, understandably, there has been much interest in techniques which can assess the extent of this damage nondestructively. Studies of the use of impedance spectroscopy have been made[125] but a more developed technique to date is that of laser-activated luminescence of trace Cr^{3+} ions within alumina. Application of this to TBC systems has been pioneered by Clarke and coworkers.[126–128] A particularly powerful aspect of the technique is its ability to determine regions in which the alumina TGO within TBC systems has relatively low stress after cooling to room temperature. By laser scanning the specimen, it is possible to construct a map showing the extent of these low-stress regions as a function of exposure time. A particularly satisfying example is shown in **Figure 21**[129] for a platinized BC system exposed to repeated thermal cycles from 1150 °C.

The darker regions in this figure are those of relatively low in-plane compressive stress compared with the lighter regions. The low-stress regions can be interpreted as damaged, involving cracks at either the TGO–BC interface or within the TGO itself. For this particular example, it is clear that the extent of the damaged regions increases markedly only after 190 h leading to spallation of some of the TBC topcoat after 225 h.

The attractions of using this nondestructive technique to evaluate the residual life of TBC systems *in situ* within turbines are considerable but there are cautionary factors. The first to note is that although an EB-PVD YSZ topcoat is transparent to the laser light there is lateral spread of the beam so that return signals are obtained from an area of ~20–60 μm diameter.[128,129] It follows that early-stage cracks, perhaps 5 μm long, will not readily be detected. This may be why there appears to be an extensive damage-free period in the example shown in **Figure 21** whereas, in reality, small cracks may already have nucleated. For APS topcoats, the applicability of the technique is less clear since the lateral splat boundaries now form internal interfaces across the path of the impinging laser beam and significant attenuation of the return signal is likely.

The other important consideration is the location of the spallation interface. In practice, cracks can form within the topcoat near the TGO, at the TGO–topcoat interface, within the TGO, and at the TGO–BC interface. The luminescence technique relates damage to a decrease in stress within the TGO and this will occur only if cracking occurs within the TGO itself or along its interface with the BC. Fracture damage occurring at the other locations will not be detected by the luminescence technique. For the example of the platinized BC shown in **Figure 21**, fracture damage did indeed develop both at the TGO–BC interface and within the TGO. The luminescence technique would detect this, subject to the limits on spatial resolution. There are many examples in the literature of crack formation in TBC systems and a perceived tendency for the spallation path to be at the TGO–BC interface in Pt-aluminide/EB-PVD YSZ systems. This is indeed frequently the case but it does not seem to be an intrinsic feature of this system, however, since fracture along the TGO–topcoat or within the topcoat

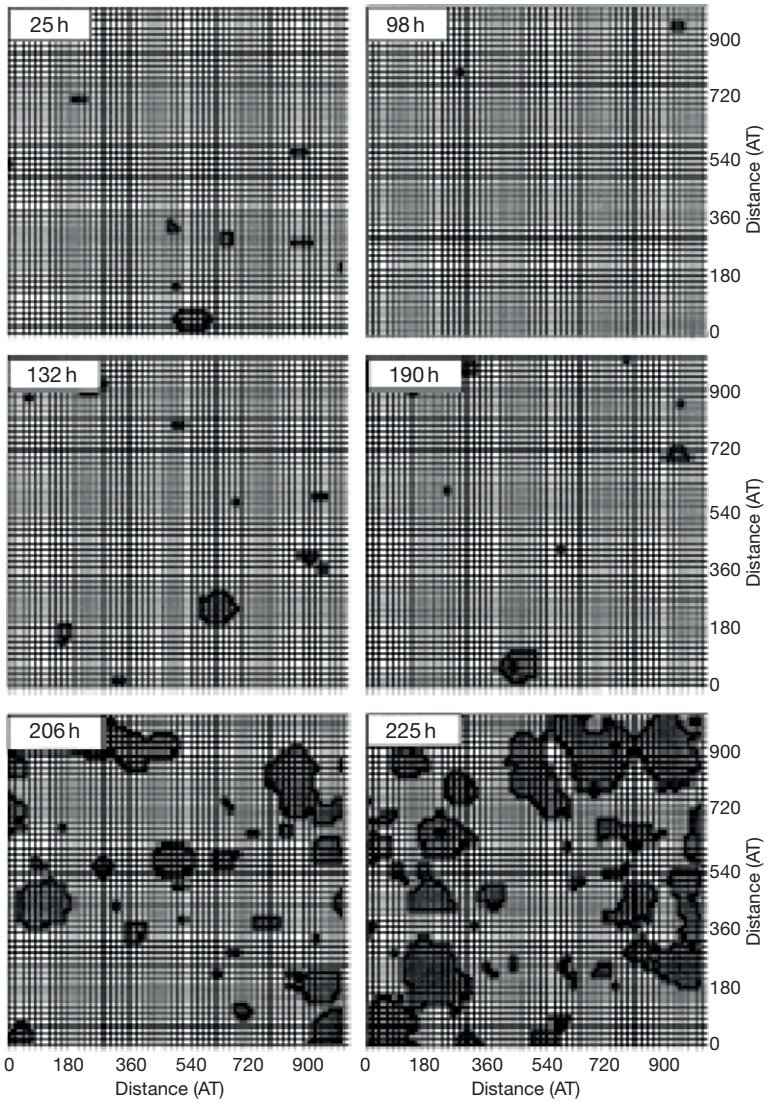

Figure 21 Map showing the development of low-stress regions (dark areas) with increasing number of cycles, containing 1 h hold periods at 1150 °C, for a TBC system consisting of an EB-PVD YSZ topcoat and platinized BC. Note that a single specimen was examined sequentially but not the same area.[129]

has also been observed.[117] This cracking is often associated with BC protuberances, that is, with increased roughness of the BC. An example of the early stages of cracking within the topcoat of a (rough) Pt-aluminide/EB-PVD YSZ system is shown in Figure 22.

By contrast, the perceived tendency with MCrAlY/APS YSZ systems is for the fracture path to lie mainly within the topcoat. Again, this is not an intrinsic property of the system but is associated with the generally rough BC surface. An example of multiple fracture sites, that is, within the topcoat, within the TGO and at the TGO–BC interface in such a system is shown in Figure 23. Here, the principal crack, marked A, is hundreds of microns long and lies at the base of the topcoat. It intersects sites, marked B, of porous nonprotective oxides resulting from CF. There is also a crack, marked C, along the TGO–BC interface which appears to be linked to an inclined shear crack traversing the thickness of the TGO. This is a similar morphology to that expected for wedge cracking (Section 1.27.4.2).

1.27.5.3 Strain Energy Considerations

The driving force for spallation within the TBC system is the release of the stored strain energy

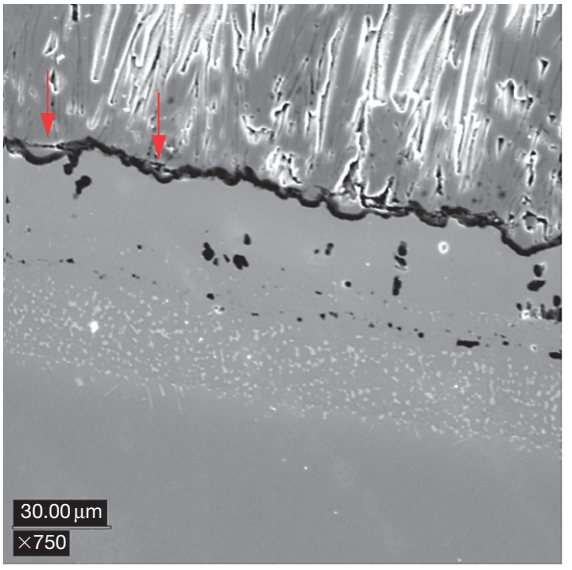

Figure 22 SEM image of a section through a TBC system consisting of a Pt-aluminide bond coat with an EBPVD YSZ top coat that has been held at 1200 °C for 3 h. Small cracks have developed, arrowed, at the flanks of BC protuberances. Courtesy of Dr. M.P. Taylor.

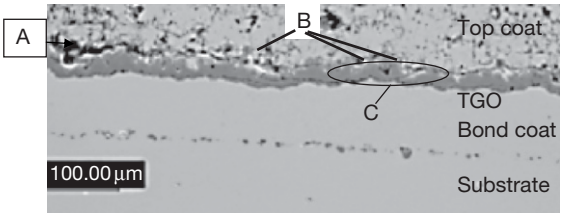

Figure 23 Section through a TBC system consisting of an electroplated CoNiCrAlY BC and an APS topcoat after oxidation in air at 1100 °C for 600 h. Different cracking sites are indicated and described in the text. See text for discussion. Courtesy of Dr. M.P. Taylor.

within the respective layers. It is an analogous situation to the spallation of the alumina layer from a MCrAlY coating discussed in **Section 1.27.4.2**. As in that case, eqn. [19] can be used as a first approach but it needs to be noted that this is a 'thin-layer' approximation which makes no allowance for any strain energy stored within the coating and alloy substrates. As pointed out earlier, it also assumes that negligible stress exists at the exposure temperature and that the strain energy derives only from thermal loading.

The stored energy within the topcoat will depend linearly on the in-plane Young's modulus (eqn. [19]) but this parameter is not well defined, particularly for EB-PVD topcoats. Here the in-plane modulus will vary through the coating thickness and is likely to reach its highest value at its base. Nevertheless, for purposes of illustration, consider a topcoat of thickness 200 µm with an average Young's modulus of 50 GPa, which is representative of literature values. Using linear thermal expansion coefficients of 12×10^{-6} K^{-1} for the topcoat and 15×10^{-6} K^{-1} for the superalloy and 0.1 for the Poisson's ratio of the topcoat within eqn. [19] yields a value for the stored strain energy within the topcoat of 81 J m^{-2} on cooling to 100 °C from 1100 °C. It is the release of this energy that will develop cracks at the TGO–topcoat interface or within the topcoat near the TGO. It should be noted that this strain energy may change with time as a result of sintering of the topcoat and an increase in its Young's modulus[130] or it may decrease as a result of thinning due to chemical or physical erosion.[131]

The specific strain energy within the TGO will increase as the oxide thickens and, in principle, should be added to that within the topcoat to produce cracking either within the oxide layer or at the interface between the TGO and the coating. The strain energy within the TGO can be calculated from eqn. [19]. For an oxide thickness of 4 µm, that is, corresponding to the failure line drawn in **Figure 19**, and using similar parametric values as previously, gives a specific stored energy within the TGO of 53 J m^{-2}. The total energy available to produce fracture within the TGO or along the oxide–coating interface is then 134 J m^{-2} for the example used.

These values of specific strain energy should certainly be sufficient to produce cracking even with the dissipation of energy by creep anticipated for typical (MCrAlY) BCs – see, for example, **Section 1.27.4.2** and **Table 3**. Interestingly, the stored energy within the topcoat is available to produce cracks within the TBC layer or at its interface with the TGO from the onset of exposure. The reason that cracking is deferred and that TBC systems survive beyond the first thermal cycle is that there must also develop a mechanism for producing cracking and releasing this energy. This is a product of the high temperature exposure and various suggested possibilities will be described briefly in the next section.

1.27.5.4 Formation of Subcritical Cracks

1.27.5.4.1 Transformation strains

The removal of aluminum from the BC both by selective oxidation and interdiffusion will result in phase transformation and associated volume changes.

The most obvious of these, evident in Figure 8(b) for example, is the transformation from β to γ′ phases. Tolpygo and Clarke[132] have estimated an associated volume contraction during this process of ~38% and have suggested that this transformation strain could induce BC rumpling and decohesion. A difficulty with the calculation is that, in the vicinity of the TGO, the transformation occurs as a direct result of the removal and oxidation of aluminum. The volume change at this location should then also include the expansion arising from formation of alumina. When this is done,[133] the transformation (and concurrent oxidation), is found to produce a volume expansion, rather than contraction, which is of similar magnitude to that produced by direct oxidation of aluminum. Little effect of the β to γ′ transformation on TGO adherence and mechanical stability of the BC surface should then be expected and this seems to be borne out by observations.[134,135] It can also be seen from Figure 8(b) that there is no marked indentation of the coating–oxide interface above the large γ′ phase. It is worth noting, though, that at the inner surface of the BC where interdiffusion is occurring with the alloy substrate, the volume change associated with alumina formation should not be included in the calculation of total volume. The transformation may result in contraction strains in this case which could contribute to the cavity development sometimes found at these locations. It is not easy to calculate these transformation strains, however, since other, often poorly characterized, phases will form within the interdiffusion zone and the volume changes associated with these should also be taken into account.

Another transformation of interest is that of martensite formation of the β phase during cooling. This has been recognized for many years for β-NiAl[136,137] and has also recently been confirmed in β-(Ni, Pt)Al coatings.[134,138,139] Typical of martensitic transformations, a critical cooling rate is required but this seems remarkably low in this case where martensite has been found after air cooling [138] and even after furnace cooling.[139] The former, at least, is consistent with earlier observations on β-NiAl.[140] These recent results suggest that martensitic transformation of the β-(Ni, Pt)Al phase should be a common occurrence during cooling.

The formation of martensite will result in a volume change estimated at ~−2%, that is, a linear contraction of ~0.7%.[138,139] Unlike the β → γ′ transformation discussed earlier, the expansion due to alumina formation will not mitigate this transformation strain and out-of-plane tensile stresses may be produced across the TGO–BC interface at the transformation temperature of ~450–500 °C.[139] The magnitude of these is unclear since the strains may also be accommodated by void formation within the original β grain and some thermal or athermal relaxation may still be possible at this temperature. There is a strong circumstantial argument, however, that the transformation is not a significantly damaging event. If it were so, both Pt-aluminide and MCrAlY coatings would tend to fail before β-depletion had occurred. In practice, much of the life of MCrAlY coatings, for example, is spent with a β-depleted zone adjacent to the TGO layer. Platinized γ/γ′ coatings, of course, never form the β phase.

1.27.5.4.2 Mechanical instabilities

The alumina TGO layer is under compression during cooling and will also be so at temperature if growth stresses are compressive. The strain energy within the layer can be released and contribute to decohesion if the oxide layer can relax and extend to its stress-free dimensions. The linear relaxation strain per cooling transient will be no more than ~0.5%, equivalent to an extension of 0.1 μm over a 20 μm distance. Large dimensional changes of the TGO layer over these small lengths would then require multiple thermal cycles.

One suggested mechanism is that of ratcheting.[135,141] The initiating event, in this case, is the formation of small cracks within the TBC above preexisting undulations of the BC, essentially as shown arrowed in Figure 22. These cracks remove mechanical constraint from the underlying TGO which, as discussed earlier, may be under a compressive growth stress at the oxidation temperature but will certainly experience large in-plane compressive stresses during cooling. Within the model, it is envisaged that, with increasing number of cycles, these stresses can drive the oxide layer as an indent into the BC and, in doing so, enlarge the crack at the base of the topcoat. The model seems feasible, in principle, and experimental support has been provided[135] although the incidence of failure by this route does not seem widespread. It is often observed, for example, that the main fracture site in TBC systems with such diffusion BCs is at the TGO–BC interface[51,52,128] rather than within the TBC topcoat. A key aspect is that there needs to be either a certain roughness to the BC surface so that cracks such as those in Figure 22 can form or there needs to be a defect at the base of the topcoat which offers no

constraint to the downward migration of the TGO. The issue of surface roughness will be addressed in later sections.

There will probably exist a window of BC strengths within which the ratcheting process could occur. It is not possible to quantify this because modeling the progressive indentation is difficult and has tended to assume[135,141] that the BC deforms by athermal plasticity characterized by yield behavior. In fact, creep processes will dominate,[142,143] even during cooling.[133] Low creep strength is necessary to move the BC away from the indenting oxide but this deformation occurs at constant volume. There must, thus, also be an upwelling of the displaced matter against the TBC topcoat adjacent to the indent. In this case, the creep strength of the BC must be high enough to displace the topcoat upward and allow continued penetration of the indenting oxide layer into the BC. These two contradictory requirements of the BC creep strength may be satisfied only within a limited temperature and composition range.

Another interesting mechanical instability is rumpling. This has been recognized for some years and has been shown to occur in aluminized and Pt-aluminized coatings under thermal cycling conditions[132,144,145] but in the absence of a topcoat. It is manifested by a roughening of the specimen surface and is clearly associated with thermal cycling because isothermally-tested specimens do not show the phenomenon.[144] The basic underlying reasons for the surface instability are well understood[146,147] and are broadly the same as discussed above for the ratcheting process. In both cases, deformation of the coating permits the compressively stressed TGO to increase its length and, thereby, relax its strain energy. As pointed out earlier, this increase in length per temperature transient is small, ~0.5%, and repeated thermal cycles are needed to produce readily observable deformation.

The rumpling process has been implicated[147] in failure of the TBC system because the instability would develop significant out-of-plane stresses in the vicinity of the TGO with associated crack initiation. Modeling of the process again assumes plastic yielding rather than creep behavior and, although the presence of the topcoat is considered, no mechanical constraint is attributed to it. This constraint will be present in real cases and, for the reasons given above when discussing ratcheting, is likely to limit the applicability of the process in TBC systems. Again, exceptions will arise when defects exist in the topcoat such that, locally, mechanical constraint is absent and upward displacement of the TGO and BC becomes feasible.

1.27.5.4.3 Roughness of the BC surface

It has been known for some time that the roughness of the BC surface will have a significant influence on the development of stresses in the TBC system during cooling.[148,149] Various attemspts have been made to evaluate these using FE methods[113,130,133,150–153] which incorporate materials' behavior of varying degrees of relevance. Most recently, it has also become clear that out-of-plane tensile stresses can also develop at the oxidation temperature as a consequence of the volume increase on oxide formation.[112,113]

The development of these numerical models has to some extent mirrored the expansion in computing power. Thus, initial approaches tended to assume entirely elastic behavior of the respective layers but, importantly, creep behavior has been subsequently incorporated and recognition made that the TGO thickens during exposure. The most recent models[113,130,133] incorporate creep of both BC and TGO, allow for growth of the latter together with the associated volume change at temperature during the computation. In addition, they permit densification of the YSZ topcoat, again during the simulated exposure time, and consider a variation in BC surface roughness. Some predicted results for two different BC-roughness geometries are shown in **Figure 24**.[133]

As described in the caption, the stress contours of **Figure 24** apply to the situation at the test temperature of 1100 °C. For the case examined, the total thickness of the alumina TGO had increased to 3.3 μm during the simulated 100 h isothermal exposure at this temperature. The parameters b and a are the amplitude and half-wavelength, respectively, of the surface undulations shown in **Figure 24**. For the rougher surface, **Figure 24(a)**, out-of-plane tensile stresses of ~150 MPa, have developed within the topcoat along the flank of the BC protuberance. For the less-rough surface, however (**Figure 24(b)**), these stresses are absent, showing the strong sensitivity of isothermal stress development to BC surface roughness. In both cases, tensile stresses also develop in the valleys of the undulations.

The out-of-plane tensile stresses on the flanks of the BC protuberance arise from continuity strains[112] which are required if the topcoat is to remain uncracked. Their origins can be understood by recognizing that the outward displacement due to the formation of the TGO is normal to the BC interface and, so, changes direction around the protuberance shown in **Figure 24**. The out-of-plane component, the x_{22} direction, of this displacement also varies around the protuberance and reaches a

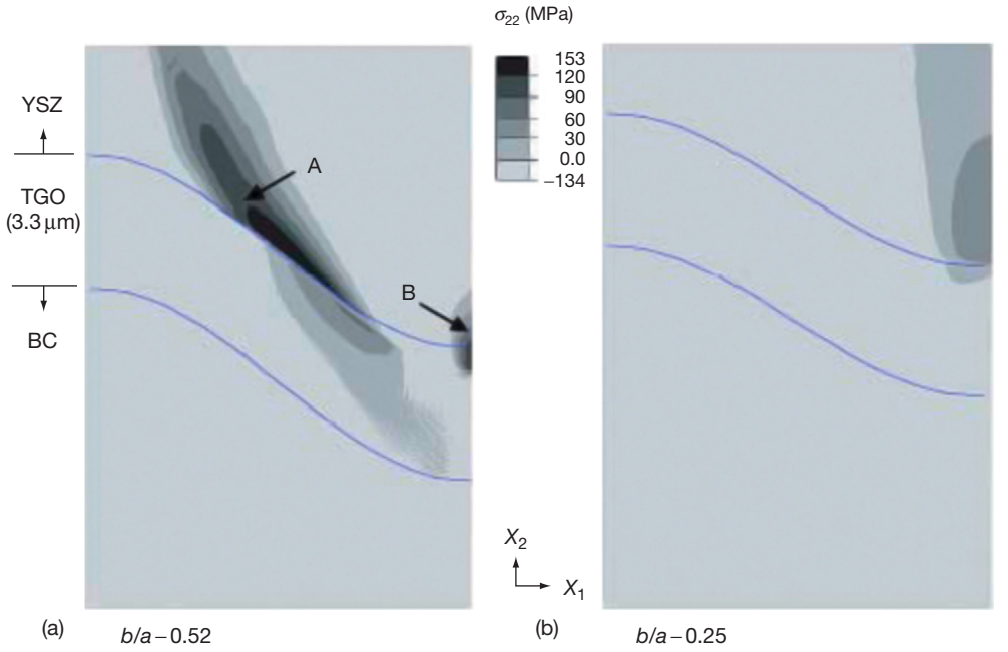

Figure 24 FE predictions[133] of the σ_{22} stress contours at 1100 °C after 100 h oxidation at the same temperature for an EB-PVD YSZ TBC system containing a Pt-aluminide BC. Creep of the BC and TGO, sintering of the topcoat and outward strains due to TGO growth are considered in the stress analysis. The BC creep properties used were those of Taylor *et al*.,[143] The arrowed locations mark the general sites of high stress at the flank (a) and valley (b) regions.

minimum on its flank. To maintain continuity of the topcoat, tensile stresses must then develop to strain the topcoat in these locations to account for the out-of-plane deficit in the displacements resulting from oxide growth.

The effect, on the σ_{22} stress distribution, of cooling the specimen to 25 °C after the isothermal exposure for 100 h at 1100 °C is shown in **Figure 25**, again for the two BC surface roughnesses.[133] The out-of-plane flank stresses in the rougher specimen, **Figure 25(a)**, are largely unaffected by this transient and no new stress is developed in these locations in the less-rough specimen, **Figure 25(b)**. There is a large increase, however, in the tensile stress developed in the topcoat in the valley regions and across the TBC–TGO interface. For the rougher surface, this is ~700 MPa but is appreciably smaller (~200 MPa) for the smoother surface. Significant tensile stresses are also developed at the TGO–BC interface during cooling as a result of differential contraction strains between oxide and coating (see Ref. [37] for a general review of such issues). Broadly, the same behavior has also been found with MCrAlY BCs where, again, appropriate creep and oxide growth kinetics were incorporated into the FE modeling.[113]

These regions of high stress correspond to locations where cracks form in TBC systems. Examples of those found at flank and valley locations are arrowed in **Figure 22** and may well have formed at temperature. Crack initiation, presumably during cooling, has also been reported[113] at the TGO–BC interface at the peak of the BC protuberances. These nucleation processes will occur, however, only with relatively rough BCs. Cracking events should be less easy and TBC lifetimes would be expected to be longer with flatter BC surfaces. This has been clearly demonstrated recently by Yanar *et al.*[117] who found an approximate factor 10 increase in the lifetime of a NiCoCrAlY/EB-PVD YSZ system by hand polishing the BC prior to deposition of the topcoat.

1.27.5.4.4 Chemical failure

A discussion of CF processes in relation to aluminum depletion and the endurance of overlay coatings has been given earlier in **Section 1.27.4.3.2**. Identical concepts apply to BCs in TBC systems but, in this case, spallation of the YSZ topcoat may be induced prior to complete CF of the BC.[105] This can arise because CF will result in the fast growth of nonalumina, breakaway-type oxides which will produce upward displacements of the topcoat. This is an oxide-jacking

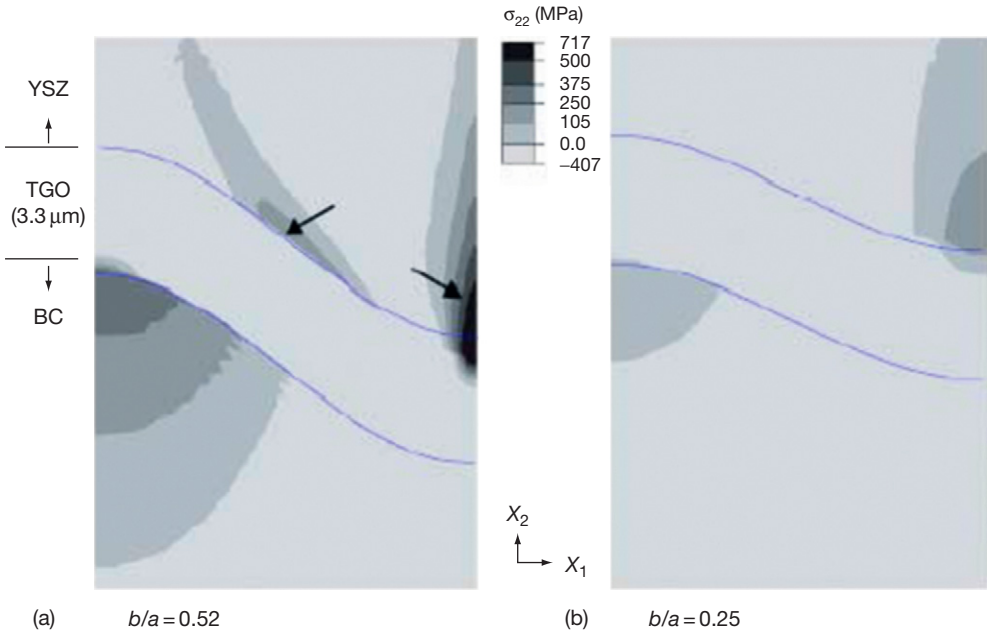

Figure 25 FE contour plots of the σ_{22} stress for the same specimen as shown in **Figure 24** but after cooling to 25 °C after exposure at 1100 °C for 100 h.[133] The arrows indicate the general areas in which out-of-plane stresses had developed prior to cooling.

process which will result in the development of out-of-plane tensile stresses within the topcoat when the CF sites are discrete (**Figure 26**). Possible localized sites for enhanced aluminum depletion and the early initiation of CF are diffusion cells (splats) within sprayed MCrAlY BCs,[105] protuberances (roughness) at the BC surface,[109,111,153] and locally thin cross-sections.

The jacking associated with the formation of the mound of fast-growing (Ni, Cr)-rich breakaway oxides, shown schematically in **Figure 26**, will tend to nucleate and propagate delamination cracks within the topcoat near the TGO. This process will occur at the oxidation temperature and will not need thermal cycles to produce this damage. It is likely that this type of process was responsible for the long crack (marked A) in the cross-section shown in **Figure 23**. This particular specimen had been exposed isothermally until the final cooling transient and several discrete regions of breakaway oxides (marked B), associated, in this case, with BC protuberances, had formed.

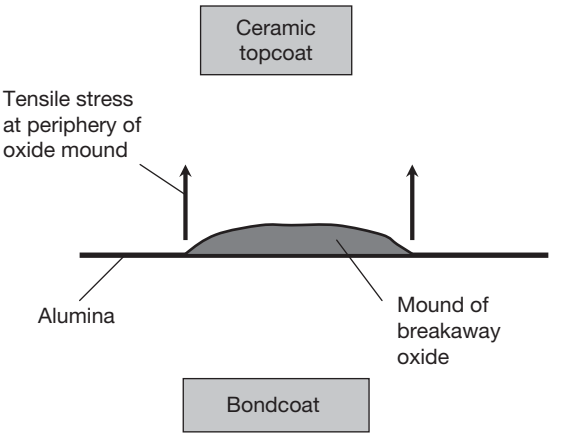

Figure 26 A schematic diagram showing how the growth of fast-growing 'breakaway' oxides resulting from CF will generate out-of-plane tensile stresses within the topcoat.

1.27.5.5 Surface Roughness: A Common Factor?

A number of the degradation mechanisms described in **Section 1.27.5.4** have been observed experimentally and, consequently, have validity. The importance of others (phase transformation strains, rumpling) to TBC failure is less clear and awaits more robust experimental support. Of those mechanisms which have been shown to nucleate and propagate subcritical cracks, some are either aided by or, indeed, require BC surface roughness (e.g., CF, out-of-plane tensile stress development at temperature or during cooling, ratcheting) and others (wedging) are likely to operate only on relatively flat interfaces. The

experiments of Yanar *et al.*,[117] in particular, show very well that decreasing the surface roughness of a MCrAlY BC can increase the lifetime of a TBC system by an order of magnitude. The improved behavior was similar in their experiments to the behavior of a Pt-aluminide BC which had similarly flat BC surfaces. As can be appreciated from **Figure 22**, however, flat Pt-aluminide BCs with EB-PVD topcoats need not always be the case and will depend on the extent of grit blasting performed by the manufacturer. The factor 10 improvement in lifetimes found by Yanar *et al.* is of the same order of magnitude found in the compilation of published lifetime results from commercial systems shown in **Figure 19**. It is certainly tempting to suggest that much of this scatter in lifetimes can be attributed to an uncontrolled variation in the surface roughness of the BCs. There will be other sources of scatter, inevitably included within these various tests, but the first-order importance of BC surface roughness to the scatter at any given temperature can be taken as a working hypothesis.[113]

The dependence of the various delamination mechanisms on surface roughness are only now being assessed quantitatively using realistic numerical models which, as described in earlier sections, allow for creep processes and the volume expansion due to oxide formation. Work in this area is incomplete but some rather qualitative trend lines are shown schematically in **Figure 27** which relates TBC lifetimes to the BC surface roughness.

Relatively flat surfaces (low values of b/a) provide the longest lifetimes since opportunities for crack nucleation caused by continuity strains and CF will be limited. Studies of failure processes in such ideal structures are limited although in localized areas of otherwise rough BCs, wedge-type cracks have been found (**Figure 23** but see also **Section 1.27.4.2**). The red line, representing continuity cracking in **Figure 27**, shows a decrease in lifetimes as BC roughness increases. It refers to the development of subcritical cracks at the flanks of BC protuberances at temperature, possible ratcheting nucleation, and the nucleation of cracks at the TGO/BC interface during cooling. The stresses produced increase with oxide thickness and, so, time at temperature is an important factor. They will also increase with the roughness factor b/a (**Section 1.27.5.4.3**)[113] and it is expected that TBC lifetimes will decrease as this increases. For large values of b/a, aluminum depletion within BC protuberances will be enhanced (e.g., **Figure 18**) and CF with the formation of breakaway-type oxides will take place. These will increase the stresses produced within the TBC layer at temperature and failure will occur earlier than in the absence of breakaway. This trend is shown as the downward-sloping blue line in **Figure 27**. Again, time at temperature will also be an

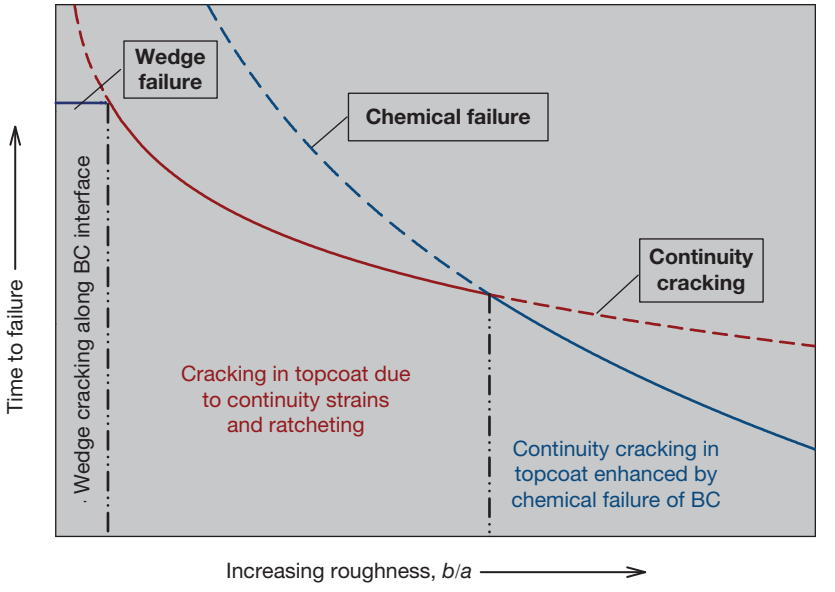

Figure 27 A schematic map showing how variously proposed mechanisms for the nucleation and growth of subcritical cracks may depend on the surface roughness of the BC. The colored lines show possible dependences of continuity cracking and CF on roughness.

important parameter since the depletion of aluminum will be directly related to this.

As a final note of caution, it should be emphasized that the discussion in this section relates to typical laboratory experience in which the test specimens have relatively simple shapes. The map of **Figure 27** then provides a mechanistic framework for these conditions but the concepts are also expected to be valid for service conditions although some modification might well be required. There may be thin regions, for example, within the complex geometry of actual components in which the local total aluminum reservoir is insufficient to maintain a protective TGO. Bulk depletion and breakaway oxidation could then occur prematurely and failure by this route might then be only weakly dependent on the surface roughness of the BC. In another example, local regions of components may be designed with a high radius of convex curvature and could develop significant out-of-plane tensile strains during cooling. These would contribute to the continuity strains developed solely from the surface roughness of the BC. As discussed earlier, similar issues would apply for the case of imposed service strains.

References

1. Reed, R. C. *The Superalloys: Fundamentals and Applications*; Cambridge University Press: Cambridge, 2006.
2. Evans, H. E.; Taylor, M. P. *Proc. IMechE, Part G: J. Aerospace Eng.* **2006**, *220*, 1–10.
3. Giggins, G. S.; Pettit, F. S. *J. Electrochem. Soc.* **1971**, *118*, 1782–1790.
4. Bennett, M. J.; Tuson, A. T.; Knights, C. F.; Ayres, C. F. *Mater. Sci. Technol.* **1989**, *5*, 841–852.
5. Chan, W. Y.; Evans, H. E.; Ponton, C. B.; Nicholls, J. R.; Simms, N. J. *Mater. High Temp.* **2000**, *17*, 173–178.
6. Akhtar, A.; Hook, M. S.; Reed, R. C. *Metall. Mater. Trans. A* **2005**, *36A*, 3001–3017.
7. Luthra, K. L.; Shores, D. A. *J. Electrochem. Soc.* **1980**, *127*, 2202–2210.
8. Strife, J. R.; Sheehan, J. E. *Ceram. Bull.* **1988**, *67*, 369.
9. Wagner, C. *J. Electrochem. Soc.* **1952**, *99*, 369–380.
10. Crank, J. *The Mathematics of Diffusion*; Oxford University Press: Oxford, 1975.
11. Evans, H. E.; Hilton, D. A.; Holm, R. A.; Webster, S. J. *Oxid. Met.* **1980**, *14*, 235–247.
12. Talboom, F. T.; Elam, R. C.; Wilson, L. W. NASA Report CR7813, NASA: Houston, 1970.
13. Saunders, S. R. J.; Nicholls, J. R. *Mater. Sci. Technol.* **1989**, *5*, 780–798.
14. Mévrel, R. *Mater. Sci. Eng. A* **1989**, *120*, 13–24.
15. Hocking, G.; Vasantasree, V.; Sidkey, P. S. *Metallic and Ceramic Coatings*; Longman: Harrow, 1989.
16. Stern, K. H. Ed., *Metallurgical and Ceramic Protective Coatings*; Chapman and Hall: London, 1996.
17. Goward, G. W. *Surf. Coat. Technol.* **1998**, *108–109*, 73–79.
18. Coddet, C. *Mater. Sci. Forum* **2004**, *461–464*, 193–212.
19. Taylor, A.; Floyd, R. W. *J. Inst. Met.* **1952–53**, *81*, 451–464.
20. Muñoz-Arroyo, R.; Clemens, D.; Tietz, F.; Anton, R.; Quadakkers, W. J.; Singheiser, L. *Mater. Sci. Forum* **2001**, *369–372*, 165–172.
21. Brindley, W. J.; Whittenberger, J. D. *Mater. Sci. Eng. A* **1993**, *163*, 33–41.
22. Taylor, M. P.; Evans, H. E.; Ponton, C. B.; Nicholls, J. R. *Surf. Coat. Technol.* **2000**, *124*, 13–18.
23. Fritscher, K.; Leyens, C.; Peters, M. *Mater. Sci. Eng. A* **1995**, *190*, 253–258.
24. Gupta, D. K.; Duval, D. S. *US Patent* **1986**, *4*, 585, 481.
25. Goebel, J. A.; Giggins, C. S.; Krasij, M.; Stringer, J. EPRI Report 2639SR; Palo Alto, CA, 1981.
26. Chan, W. Y.; Evans, H. E.; Ponton, C. B.; Nicholls, J. R.; Simms, N. J. *Mater. High Temp.* **2000**, *17*, 173–178.
27. Leyens, C.; van Liere, J.-W.; Peters, M.; Kaysser, W. A. *Surf. Coat. Technol.* **1998**, *108–109*, 30–35.
28. Leyens, C.; Peters, M.; Kaysser, W. A. *Mater. Sci. Forum* **1997**, *251–254*, 769–776.
29. Gray, S.; Ponton, C. B.; Jacobs, M. H.; Evans, H. E. *United States Patent* **2002**, *6*, 387, 541 B1, May 14.
30. Martinz, H.-P.; Rieger, M. *Mater. Sci. Forum* **1997**, *251–254*, 761–768.
31. Fukomoto, M.; Matsumara, Y.; Hayashi, S.; Sakamoto, K.; Kasama, A.; Tanaka, R.; Narita, T. *Oxid. Met.* **2003**, *60*, 335–346.
32. Bennett, M. J. In *Coatings for High Temperature Applications*; Lang, E., Ed.; Applied Science, 1983; pp 169, 192.
33. Crouch, A. G.; Dooley, R. B. *Corros. Sci.* **1976**, *16*, 341–347.
34. Coley, K. S.; Tuson, A. T.; Saunders, S. R. J.; Bennett, M. J.; Knights, C. F. *Mater. Sci. Eng. A* **1989**, *121*, 461–466.
35. Bennett, M. J.; Tuson, A. T.; Knights, C. F.; Ayres, C. F. *Mater. Sci. Technol.* **1989**, *5*, 841–852.
36. Pennisi, F. J.; Gupta, D. K. *Thin Solid Films* **1981**, *84*, 49–58.
37. Lobb, R. C.; Bennett, M. J. *Oxid. Met.* **1991**, *35*, 35–52.
38. Evans, H. E. *Int. Mater. Rev.* **1995**, *40*, 1–40.
39. Nicholls, J. R.; Lawson, K. J.; Al Yasiri, L. H.; Hancock, P. *Corros. Sci.* **1993**, *35*, 1209–1223.
40. Nicholls, J. R.; Simms, N. J.; Neseyif, S.; Ponton, C.; Evans, H. E.; Taylor, M. In *High Temperature Corrosion and Materials Chemistry*; The Electrochemical Society Proceedings; McNallan, M., Opila, E., Maruyama, T., Narita, T., Eds.; 2000; Vol, 99–38, pp 270–281.
41. Nicholls, J. R.; Simms, N. J.; Chan, W. Y.; Evans, H. E. *Surf. Coat. Technol.* **2002**, *149*, 236–244.
42. Choquet, P. A.; Naylor, E. R.; Rapp, R. A. *Mater. Sci. Eng. A* **1989**, *121*, 413–418.
43. Pérez, F. J.; Trilleros, J. A.; Hierro, M. P.; Milewska, A.; Carpintero, M. C.; Bolivar, F. J. *Mater. Sci. Forum* **2004**, *461–464*, 313–320.
44. Harper, M. A.; Rapp, R. A. In *Surface Modification Technologies*; Sudarshan, T. S., Bhat, D. G., Jeandin, M., Eds.; AIME, 1991; Vol. IV, 415–428.
45. Lehnert, G.; Meinhardt, H. *Surface Treatment* **1972** *1*, 72.
46. Meelu, M. C.; McMordie, B. G.; Loretto, M. H.; Jones, A. In *The Processing, Properties and Applications of Metallic and Ceramic Materials*; Loretto, M. H., Beevers, C. J., Eds.; The University of Birmingham, Birmingham, UK, 1992; pp 1247–1252.
47. Gleeson, B.; Wang, W.; Hayashi, S.; Sordelet, D. *Mater. Sci. Forum* **2004**, *461–464*, 213–222.
48. Cadoret, Y.; Bacos, M.-P.; Josso, P.; Maurice, V.; Marcus, P.; Zanna, S. *Mater. Sci. Forum* **2004**, *461–464*, 247–254.

49. Zhang, Y.; Haynes, J. A.; Lee, W. Y.; Wright, I. G.; Pint, B. A.; Cooley, K. M.; Liaw, P. K. *Metall. Mater. Trans.* **2001**, *32A*, 1727.
50. Rickerby, D. S.; Bell, S. R.; Wing, R. G. *United States Patent* **1999**, *5*, 981 091, November 9.
51. Bouhanek, K.; Adesanya, O. A.; Stott, F. H.; Skeldon, P.; Lees, D. G.; Wood, G. C. *Mater. Sci. Forum* **2001**, *369–372*, 615–622.
52. Adesanya, O. A.; Bouhanek, K.; Stott, F. H.; Skeldon, P.; Lees, D. G.; Wood, G. C. *Mater. Sci. Forum* **2001**, *369–372*, 639–646.
53. Fitzer, E. *Archiv. Eisenhüttenwesen* **1954**, *25*, 45–5.
54. Grünling, H. W.; Bauer, R. *Thin Solid Films* **1982**, *95*, 3–20.
55. Itzhak, D.; Tuller, F. R.; Schieber, M. *Thin Solid Films* **1980**, *73*, 379–384.
56. Young, S. G.; Deadmore, D. L. *Thin Solid Films* **1980**, *73*, 373–378.
57. Cockeram, B. V.; Rapp, R. A. *Oxid. Met.* **1995**, *45*, 375–425.
58. Gaillard-Allemand, B.; Vilasi, M.; Belmonte, T.; Steinmentz, J. *Mater. Sci. Forum* **2001**, *369–372*, 727–734.
59. Li, X. Y.; Taniguchi, S.; Matsunaga, Y.; Nayagawa, K.; Fujita, K. *Intermetallics* **2003**, *11*, 143–150.
60. Voytěch, D.; Kubatik, T.; Jurek, K.; Maixner, J. *Oxid. Met.* **2005**, *63*, 305–323.
61. Cockeram, B. V.; Rapp, R. A. *Mater. Sci. Forum* **1997**, *251–254*, 723–736.
62. Gray, S.; Jacobs, M. H.; Ponton, C. B.; Voice, W.; Evans, H. E. *Mater. Sci. Eng. A* **2004**, *384*, 77–82.
63. Kofstad, P. *High Temperature Corrosion*; Elsevier, 1988.
64. Deal, B. E.; Grove, A. S. *J. Appl. Phys.* **1965**, *36*, 3770–3778.
65. Taniguchi, S.; Minamida, T.; Shibata, T. *Mater. Sci. Forum* **1997**, *251–254*, 227–234.
66. Wortman, D. J.; Nagaraj, B. A.; Dunderstadt, E. C. *Mater. Sci. Eng. A* **1989**, *121*, 433–440.
67. Rhys-Jones, T. N.; Toriz, F. C. *High Temp. Technol.* **1989**, *7*, 73–81.
68. Saunders, S. R. J.; Banks, J. P.; Chunnilall, C. NPL Report MATC(A)113, An evaluation of thermal barrier coated specimens exposed to long-term ageing tests, Teddington, July 2002.
69. Munro, T. C.; Gleeson, B. *Mater. Sci. Forum* **1997**, *251–254*, 753–760.
70. Mabuchi, H.; Asai, T.; Nakayama, Y. *Scripta Metall.* **1989**, *23*, 685–689.
71. Gauthier, V.; Dettenwanger, F.; Schütze, M.; Shemet, V.; Quadakkers, W. J. *Oxid. Met.* **2003**, *59*, 233–254.
72. Gauthier, V.; Dettenwanger, F.; Schütze, M. *Intermetallics* **2002**, *10*, 667–674.
73. Czech, N.; Kolarik, V.; Quadakkers, W. J.; Stamm, W. *Surf. Eng.* **1997**, *13*, 384–388.
74. Naumenko, D.; Quadakkers, W. J.; Galerie, A.; Wouters, Y.; Jourdain, S. *Mater. High Temp.* **2003**, *20*, 287–293.
75. Hindam, H.; Whittle, D. P. *Oxid. Met.* **1982**, *18*, 245–284.
76. Natesan, K.; Liu, Y. Y. *Mater. Sci. Eng. A* **1989**, *121*, 571–580.
77. Clemens, D.; Vosberg, V. R.; Penkalla, H. J.; Breuer, U.; Quadakkers, W. J.; Nickel, H. *Fresenius J. Anal. Chem.* **1997**, *358*, 122–126.
78. Evans, H. E.; Norfolk, D. J.; Swan, T. *J. Electrochem. Soc.* **1978**, *115*, 1180–1185.
79. Sabol, G. P.; Dalgaard, S. B. *J. Electrochem. Soc.* **1975**, *122*, 316–317.
80. Pragnell, W. M.; Evans, H. E.; Naumenko, D.; Quadakkers, W. J. *Mater. High Temp.* **2005**, *22*, 561–566.
81. Miller, R. A. *Trans. ASME* **1987**, *109*, 448–451.
82. Renusch, D.; Echsler, H.; Schütze, M. In *Lifetime Modelling of High Temperature Corrosion Processes*; Schütze, M., Quadakkers, W. J., Nicholls, J. R., Eds.; Maney, Publishing: London, 2001; pp 324–336.
83. Renusch, D.; Echsler, H.; Schütze, M. *Mater. Sci. Forum* **2004**, *461–464*, 729–736.
84. Tien, J. K.; Davidson, J. M. In *Stress Effects and the Oxidation of Metals*; Cathcart, J. V., Ed.; AIME, New York, 197; pp. 200–219.
85. Lipkin, D. M.; Clarke, D. R.; Hollatz, M.; Bobeth, M.; Pompe, W. *Corros. Sci.* **1997**, *39*, 231–242.
86. Echsler, H.; Martinez, E. A.; Singheiser, L.; Quadakkers, W. J. *Mater. Sci. Eng. A* **2004**, *384*, 1–11.
87. Timoshenko, S. *Theory of Elastic Stability*; McGraw-Hill: New York, 1936; 367.
88. Hou, P. Y. *Mater. Sci. Forum* **2001**, *369–372*, 23–28.
89. Smialek, J. L.; Pint, B. A. *Mater. Sci. Forum* **2001**, *369–372*, 459–466.
90. Banks, J. P.; Gohil, D. D.; Evans, H. E.; Hall, D. J.; Saunders, S. R. J. In *Materials for Advanced Power Engineering*; Coutsouradis, D., *et al*., Eds.; Kluwer Academic: The Netherlands, 1994; Part II, pp 1543–1552.
91. Pint, B. A.; Wright, I. G.; Lee, W. Y.; Zhang, Y.; Prüßner; Alexander, K. B. *Mater. Sci. Eng.* **1998**, *245*, 201–211.
92. Evans, H. E.; Mitchell, G. P.; Lobb, R. C.; Owen, D. R. J. *Proc. R. Soc. A* **1993**, *440*, 1–22.
93. Evans, H. E.; Strawbridge, A.; Carolan, R. A.; Ponton, C. B. *Mater. Sci. Eng. A* **1997**, *225*, 1–8.
94. Evans, H. E.; Osgerby, S.; Saunders, S. R. J. In *Proceedings of John Stringer Symposium on High Temperature Corrosion*; Tortorelli, P. F., Wright, I. G., Hou, P. Y., Eds.; ASM International: Ohio, 2003; pp 122–130.
95. Evans, H. E.; Lobb, R. C. *Corros. Sci.* **1984**, *24*, 209–222.
96. Galerie, A.; Dupeux, M.; Wouters, Y.; Toscan, F. *Mater. Sci. Forum* **2006**, *522–523*, 441–450.
97. Bouhanek, K.; Oquab, D.; Pieraggi, B. *Mater. Sci. Forum* **1997**, *251–254*, 33–40.
98. Baleix, S.; Bernhart, G.; Lours, P. *Mater. Sci. Forum* **2001**, *369–372*, 539–546.
99. Osgerby, S.; Berriche-Bouhanek, K.; Evans, H. E. *Mater. Sci. Eng. A* **2005**, *412*, 182–190.
100. Chan, K. S.; Cheruvu, N. S.; Leverant, G. R. *Mater. Sci. Forum* **2001**, *369–372*, 623–630.
101. Anton, R.; Birkner, J.; Czech, N.; Stamm, W. *Mater. Sci. Forum* **2001**, *369–372*, 719–726.
102. Taylor, M. P.; Pragnell, W. M.; Evans, H. E. *Mater. Sci. Forum* **2004**, *461–464*, 239–246.
103. Sato, A.; Harada, H.; Kawagishi, K. *Mater. Sci. Forum* **2006**, *522–523*, 361–368.
104. Matsumaru, H.; Hayashi, S.; Narita, T. *Mater. Sci. Forum* **2006**, *522–523*, 285–292.
105. Evans, H. E.; Taylor, M. P. *Oxid. Met.* **2001**, *55*, 17–34.
106. Nesbitt, J. A.; Heckel, R. W. *Metall. Trans.* **1987**, *18A*, 2075.
107. Roper, G. W.; Whittle, D. P. *Met. Sci.* **1981** *15,* 148.
108. Evans, H. E.; Donaldson, A. T.; Gilmour, T. C. *Oxid. Met.* **1999**, *52*, 379–402.
109. Niranatlumpong, P.; Ponton, C. B.; Evans, H. E. *Oxid. Met.* **2000**, *53*, 241–258.
110. Taylor, M. P.; Evans, H. E. *Mater. High Temp.* **2003**, *20*, 461–466.
111. Taylor, M.P.; Pragnell, W.M.; Evans, H.E. *Mater. Corros.* **2008**, *59*, 508–513.
112. Evans, H. E.; Taylor, M. P. *J. Corros. Sci. Eng.* **2003**, 6, Paper H011.

113. Busso, E. P.; Wright, L.; Evans, H. E.; McCartney, L. N.; Saunders, S. R. J.; Osgerby, S.; Nunn, J. *Acta Mater.* **2007**, *55*, 1491–1503.
114. Yanar, N. M.; Meier, G. H.; Pettit, F. S. *Scripta Mater.* **2002**, *46*, 325–330.
115. Lih, W.; Chang, E.; Wu, B. C.; Chao, C. H. *Oxid. Met.* **1991**, *36*, 221–238.
116. Nijdam, T. J.; Jeurgens, L. P. H.; Chen, J. H.; Sloof, W. G. *Oxid. Met.* **2005**, *64*, 355–377.
117. Yanar, N. M.; Pettit, F. S.; Meier, G. H. *Metall. Mater. Trans.* **2006**, *37A*, 1563–1580.
118. Tolpygo, V. K.; Clarke, D. R.; Murphy, K. S. *Surf. Coat. Tech.* **2001**, *146–147*, 124–131.
119. Kim, G. M.; Yanar, N. M.; Hewitt, E. N.; Pettit, F. S.; Meier, G. H. *Scripta Mater.* **2002**, *46*, 489–495.
120. Evans, A. G.; Mumm, D. R.; Hutchinson, J. W.; Meier, G. H.; Pettit, F. S. *Prog. Mater. Sci.* **2001**, *46*, 505–553.
121. Rouzou, I.; Molins, R.; Rémy, L.; Jomard, F. *Mater. Sci. Forum* **2004**, *461–464*, 101–108.
122. Padture, N. P.; Gell, M.; Jordan, E. H. *Science* **2002**, *296*, 280–284.
123. Choi, S. R.; Hutchinson, J. W.; Evans, A. G. *Mech. Mater.* **1999**, *31*, 431–447.
124. Nunn, J.; Saunders, S. R. J.; Banks, J. P. In *Microscopy of Oxidation* Tatlock, G. J., Evans, H. E., Eds.; Science Reviews, 2006; Vol 6, pp 219–226.
125. Md Shawkat Ali; Shenhua Song; Ping Xiao *J. Eur. Ceram. Soc.* **2002**, *22*, 101–107.
126. Christensen, R.; Lipkin, D. M.; Clarke, D. R.; Murphy, K. *Appl. Phys. Lett.* **1996**, *69*, 3754–3756.
127. Peng, X.; Clarke, D. R. *J. Am. Ceram. Soc.* **2000**, *83*, 1165–1170.
128. Tolpygo, V. K.; Clarke, D. R.; Murphy, K. S. *Surf. Coat. Technol.* **2001**, *146*, 124–131.
129. Selçuk, A.; Atkinson, A. A. *Acta Mater.* **2003**, *51*, 535–549.
130. Busso, E. P.; Qian, Z. Q. *Acta Mater.* **2006**, *54*, 325–338.
131. Wellman, R. G.; Nicholls, J. R. *Surf. Coat. Technol.*, **2004**, *177*, 80–88.
132. Tolpygo, V. K.; Clarke, D. R. *Acta Mater.* **2000**, *48*, 3283–3293.
133. Busso, E.P.; Qian, Z.Q.; Taylor, M.P.; Evans, H.E. *Acta Mater.*, in press.
134. Reid, M.; Pomeroy, M. J.; Robinson, J. S. *Mater. Sci. Forum* **2004**, *461–464*, 343–350.
135. Mumm, D. R.; Evans, A. G.; Spitsberg, I. T. *Acta Mater.* in press.
136. Rosen, S.; Goebel, J. A. *Trans. AIME* **1968**, *242*, 722.
137. Smialek, J. L. *Metall. Trans.* **1971**, *2*, 913.
138. Zhang, Y.; Haynes, J. A.; Pint, B. A.; Wright, I. G.; Lee, W. Y. *Surf. Coat. Technol.* **2003**, *163–164*, 19–24.
139. Chen, M. W.; Ott, R. T.; Hufnagel, T. C.; Wright, P. K.; Hemker, K. J. *Surf. Coat. Technol.* **2003**, *163–164*, 25–30.
140. Smialek, J. L.; Hehemann, R. F. *Metall. Trans.* **1973**, *4*, 1571.
141. Karlsson, A. M.; Hutchinson, J. W.; Evans, A. G. *Mater. Sci. Eng. A* **2003**, *351*, 244–257.
142. Pan, D.; Chen, M. W.; Wright, P. K.; Hemker, K. J. *Acta Mater.* **2003**, *51*, 2205–2217.
143. Taylor, M. P.; Evans, H. E.; Busso, E. P.; Qian, Z. Q. *Acta Mater.* **2006**, *54*, 3241–3252.
144. Deb, P.; Boone, D. H.; Manley, T. F. *J. Vac. Sci. Technol. A* **1987**, *5*, 3366–3372.
145. Tolpygo, V. K.; Clarke, D. R. *Acta Mater.* **2004**, *52*, 5129–5141.
146. Suo, Z. *J. Mech. Phys. Solids* **1995**, *43*, 829–846.
147. He, M. Y.; Evans, A. G.; Hutchinson, J. W. *Acta Mater.* **2000**, *48*, 2593–2601.
148. Miller, R. A.; Lowell, C. E. *Thin Solid Films* **1982**, *95*, 265–273.
149. Bartlett, A. H.; Maschio, R. D. *J. Am. Ceram. Soc.* **1995**, *78*, 1018–1024.
150. Chang, G. C.; Phucharoen, W.; Miller, R. A. *Surf. Coat. Technol.* **1987**, *32*, 307–325.
151. Freborg, A. M.; Ferguson, B. L.; Brindley, W. J.; Petrus, G. J. *Mater. Sci. Eng.A* **1998**, *245*, 182–190.
152. Kerkhoff, G.; Vaßen; Stover, D. In *Cyclic Oxidation of High Temperature Materials*; Schütze, M., Quadakkers, W. J., Eds.; IOM Communications: London, 1999; pp 373–382.
153. Hsueh, C.-H.; Haynes, J. A.; Lance, M. J.; Becher, P. F.; Ferber, M. K.; Fuller, E. R., Jr.; Langer, S. A.; Carter, W. C.; Cannon, W. R. *J. Am. Ceram. Soc.* **1999**, *82*, 1073–1075.